

AD-A169 794

①

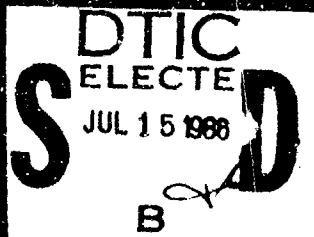
Second  
International  
Conference on

# Numerical Ship Hydrodynamics

September 1977

University of California, Berkeley

DTIC FILE COPY



DISTRIBUTION STATEMENT R

Approved for public release  
Distribution Unlimited

86 7 3 065

AD-A169 794

The  
Proceedings

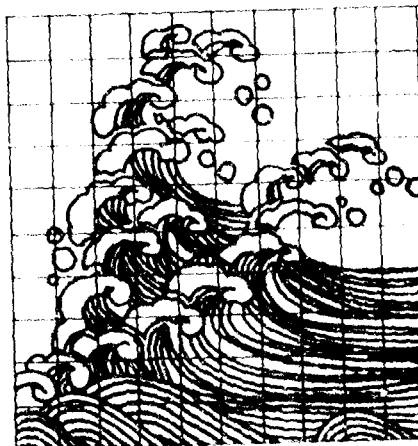
Second  
International  
Conference on

Numerical  
Ship Hydrodynamics

Edited by  
John V. Wehausen  
and  
Nils Saivesen

Sponsored by  
The David W. Taylor  
Naval Ship Research and Development Center  
The Department of Naval Architecture  
College of Engineering, and University Extension  
University of California, Berkeley  
The Office of Naval Research

September 19-21, 1977



University of California, Berkeley  
University Extension Publications  
223 Fulton Street  
Berkeley, CA 94720

DTIC  
ELECTE  
JUL 15 1986  
S B D

Approved for Public Release: Distribution Unlimited



ROGER BRARD  
1907 - 1977

## DEDICATION

These Proceedings are dedicated to the memory of Roger Brard. He expected to attend this Conference together with his wife Thérèse and was to take part in it both as a speaker and as a chairman. A short illness ended with his death on July 15th, a culmination of many years of uncertain health.

Roger Brard's involvement with ships was both broad and deep, touching upon almost every aspect of naval architecture. However, ship-hydrodynamic problems were an ever recurring theme, and in recent years he devoted his efforts principally to these. Earlier he was also known for his contributions to probability theory and he regularly lectured on this subject during his years at the Ecole Polytechnique. Few of those who know only his recent work on resistance and maneuverability or his earlier pioneering work on pitching and rolling of ships under way are likely to be aware of the breadth of his activities in ship theory, fluid dynamics and mathematics. In the following paragraph we try to give some idea of this breadth.

Brard's doctoral thesis (in mathematics) was "On some properties of the geometry of ship hulls" (1929). The following year there was a paper on the reheating of boiler feed water and the year after that, one on the exhaust of internal combustion engines. To give a further idea of the almost incredible extent of his activities, a sampling of topics on which there are published papers follows: theory and design of propellers, added mass in rolling, effect of added mass and wave generation on stopping of ships, nonlinear oscillations, statistical theory of turbulence, the law of large numbers, stationary random processes, model testing of towed barges, representation of hulls by source-sink distributions, self-propelled model tests, sea trials of various ships and comparison with model tests, flow about deformable profiles, cavitation. And of course the topics mentioned earlier. The list is not exhaustive. Furthermore, during 1932-36 while at the Arsenal at Brest he was in charge of repairs to several cruisers, of the construction of another, and of the armament of three battleships.

His talents and contributions were not unrecognized in France and abroad. We mention first a few of his prizes, chosen to show their diversity: a medal from the Office National des

Recherches Scientifiques et des Inventions for his work on the exhaust of internal combustion motors (1932), a prize from the Académie des Sciences for his design of the propellers of the liner Normandie (1937), a further prize from the Académie for contributions to ship hydrodynamics (1955), and the David W. Taylor medal of SNAME (1974). He was a Commandeur of the Légion d'Honneur, a member of the Académie de Marine and a member of the Académie des Sciences. He served as president of the latter during 1972-73. He was also a member of the National Academy of Engineering of the U.S.A. In 1950, he was president of the French Mathematical Society. Much more could be added to this list.

It is not surprising that Roger Brard should have been given positions and responsibilities corresponding to his abilities. Again the list is not complete. In 1941, he was chief of the French towing tank, the Bassin d'Essais des Carènes, and was its director from 1962-1970. He was Professor of Applied Mathematics at the Ecole Polytechnique from 1942-1969 and also Professor of Hydrodynamics from 1944-1969 at the Ecole Nationale Supérieure du Génie Maritime, the French school of naval architecture. He was director of this school from 1958-1962. After retiring from the Ecole Polytechnique and the Ecole du Génie Maritime, he began a new academic career in 1970 at the Ecole Nationale Supérieure de Mécanique of the University of Nantes. Here he developed a special course for advanced training in naval hydrodynamics. In 1973 he was invited to give the David Taylor Lectures at the David Taylor Ship Research and Development Center and on two occasions gave courses of lectures at the University of Michigan. He had been chairman of the Resistance Committee of the ITTC since 1963.

In addition to having outstanding scientific and administrative talents, Roger Brard was also a warm human being, reserved rather than ebullient, but also a good companion and a witty raconteur and conversationalist. To many of us he was a cherished friend. He was an indefatigable worker in spite of his poor health and strove constantly for excellence. He was just past 70 when he died and would certainly have accomplished much more if he had been spared. We shall miss him.

*John Wehausen*



# ORDERING INFORMATION

*Second International Conference on Numerical Ship Hydrodynamics*  
may be ordered by mailing a request to the following address:

Mrs. Betty Dowell  
University Extension Publications  
2223 Fulton Street  
University of California  
Berkeley, California 94720  
U.S.A.

\$20 per copy; \$10 student price  
Please include name, address, zip code and country in all requests.

*First International Conference on Numerical Ship Hydrodynamics*  
may be ordered by mailing a request to the following address:

Ms. Anne Centineo  
Code 184S  
David W. Taylor Naval Ship Research and  
Development Center  
Bethesda, Maryland 20084  
U.S.A.

\$25 per copy; \$12.50 student price  
Please include name, address, zip code and country in all requests.

The Defense Technical Information Center and  
the National Technical Information Service  
have permission to reproduce and sell this  
book.

Per Ms. Norma Dobay, DTNSRDC/Code 5223

International Standard Book Number: 0-917936-11-6  
University Extension Publications  
University of California  
Berkeley, California 94720

Accession For	
NTIS GRA&I	<input checked="" type="checkbox"/>
DTIC TAB	<input type="checkbox"/>
Unannounced	<input type="checkbox"/>
Justification	
By _____	
Distribution/	
Availability Code	
Dist	Avail and Special
A-1	



## PREFACE

Although theoretical ship hydrodynamics has made steady if not dramatic progress during the last thirty years, it seems evident that this progress has been achieved for the most part by application of various methods for replacing the difficult nonlinear equations by approximate ones, in particular by the use of perturbation methods. The simultaneous spectacular growth of computing machines and their impact on the development of numerical analysis were not ignored, but their influence on ship hydrodynamics was primarily in widening the possibilities of computing derived formulas and almost not at all in altering the methods of approach to the problems themselves. It had been evident for several years that the time was appropriate for taking formal notice of this fact and of encouraging wider participation in ship hydrodynamics of persons with strong backgrounds in numerical analysis and computing. The First International Conference on Numerical Ship Hydrodynamics was in response to this need. It brought together researchers of rather diverse backgrounds, with the aim of giving to each a forum for his own approach to ship-hydrodynamic calculations and of providing opportunities for interaction.

This first Conference, held in October 1975 in the National Bureau of Standards in Gaithersburg, Md., was by all criteria a notable success. The papers were interesting and the opportunities for discussion, both formal and informal, were adequate. Furthermore, the Proceedings appeared in a remarkably short time as such things go. It was evident that a second Conference was both desirable and desired. The present Proceedings are the result of this second Conference, held in Berkeley on September 19-21, 1977 and sponsored jointly by the David Taylor Naval Ship Research and Development Center, the Office of Naval Research and the University of California Berkeley. The mere mention of the Office of Naval Research as a sponsor does not do justice to the continuous, effective and informed support that it has given to the development of numerical methods in ship hydrodynamics in recent years. Without this, neither Conference would have taken place, and much of the reported research would not have been done. The actual organization of the meeting, aside from selection of papers, was carried out by the Extension Division of the University through the capable hands of Linda Reid. Since authors provided manuscripts in final form for reproduction, only minor editorial changes were possible and no attempt was made to achieve consistency in format or reference style.

Finally, it seems appropriate to call attention to the remarkable diversity of the papers. Even when the same problem is being treated, the methods are different. It was one of the purposes of the Conference to encourage this diversity and to bring the results into juxtaposition. Diversity extended beyond subject matter. Over a dozen countries were represented among the participants. Such juxtaposition is also important.

## ORGANIZATION AND PAPERS COMMITTEE

### Co-chairmen

John V. Wehausen

Nils Salvesen

### Members

Ralph D. Cooper

Hane J. Lugt

Justin H. McCarthy

Joanna W. Schot

William C. Webster

## CONTENTS

Dedication .....	li
Preface .....	v
<b>KEYNOTE ADDRESS</b>	
<b>Numerical Ship Hydrodynamics, Then and Now</b> , L. Landweber, University of Iowa .....	1
<b>SESSION I: THREE-DIMENSIONAL SHIP-WAVE PROBLEMS</b>	
Chairman: J.C. Dern, Bassin d'Essais des Carènes, Paris France	
Invited Paper: <b>Survey of Numerical Solutions for Ship Free-Surface Problems</b> , R.B. Chapman .....	5
<b>Numerical Evaluation of a Wave-Resistance Theory for Slow Ships</b> , E. Baba and M. Hara .....	17
<b>A Practical Computer Method for Solving Ship-Wave Problems</b> , C.W. Dawson .....	30
<b>Finite Difference Simulation of the Planar Motion of a Ship</b> , R.K.-C. Chan .....	39
Discussion: Session I Papers: J.N. Newman, Massachusetts Institute of Technology, USA, Invited Discussor .....	53
<b>SESSION II: THREE-DIMENSIONAL SHIP-WAVE PROBLEMS</b>	
Chairman: R.J. Lundegard, Office of Naval Research, Washington, D.C., USA	
<b>PART I</b>	
<b>Existence, Uniqueness and Regularity of the Solution of the Neumann-Kelvin Problem for Two- or Three-Dimensional Submerged Bodies</b> , J.C. Dern .....	57
<b>A Localized Finite-Element Method for Steady, Three-Dimensional Ship-Wave Problems</b> , K.J. Bai .....	78
<b>Numerical Solutions of Transient Three-Dimensional Ship-Wave Problems</b> , S. Ohring and J. Talste .....	88
Discussion: Part I, Session II Papers: E.O. Tuck, University of Adelaide, Australia, Invited Discussor .....	104
<b>PART II</b>	
<b>Numerical Solution of the Neumann-Kelvin Problem by the Method of Singularities</b> , M. Guével, G. Delhommeau, and J.P. Cordonnier .....	107
<b>Computations of Three-Dimensional Ship-Motions with Forward Speed</b> , M.-S. Chang .....	124
<b>Computation of the First- and Second-Order Wave Forces on Oscillating Bodies in Regular Waves</b> , J.A. Pinkster and G. Van Oortmarssen .....	136
Discussion: Part II, Session II Papers: F. Ursell, University of Manchester, England, Invited Discussor .....	157
<b>SESSION III: TWO-DIMENSIONAL BODY-WAVE PROBLEMS</b>	
Chairman: W.C. Webster, University of California, Berkeley, USA	
<b>PART I</b>	
<b>Hybrid Integral-Equation Method for the Steady Ship-Wave Problem</b> , R.W. Yeung and Y.C. Bouger .....	160
<b>Integral Equation Methods for Calculating the Virtual Mass in Water of Finite Depth</b> , P. Sayer and F. Ursell .....	176
<b>Theory of Compliant Planing Surfaces</b> , L.J. Doctors .....	185
Discussion: Part I, Session III Papers: H. Maruo, University of Yokohama, Japan, Invited Discussor .....	196

## PART II

<b>Numerical Solution of the Navier-Stokes Equation for 2-D Hydrofoils in or Below a Free Surface</b> , S.P. Shanks and J.F. Thompson .....	202
<b>Finite-Difference Computations Using Boundary-Fitted Coordinate Systems for Free-Surface Potential Flows Generated by Submerged Bodies</b> , H.J. Haussling and R.M. Coleman .....	221
<i>Discussion: Part II, Session III Papers: J.W. Schot, David W. Taylor Naval Ship Research and Development Center, Bethesda, Maryland, USA</i> .....	234

## SESSION IV: CAVITY FLOW

Chairman: G.H. Gleissner, David W. Taylor Naval Ship Research and Development Center, Bethesda, Maryland, USA	
<i>Invited Paper: Review of Numerical Methods for Solution of Three-Dimensional Cavity-Flow Problems</i> , R.L. Street .....	237
<b>A Numerical Method for Determining Forces and Moments on Supercavitating Hydrofoils of Finite Span</b> , C.W. Jiang and P. Leehey .....	250
<b>Supercavitating Foil of an Arbitrary Shape Beneath or Above a Free Surface or in a Cascade</b> , B. Yim .....	258
<b>An Application of the Boundary Integral Equation Method to Cavity and Jet Flows</b> , B.E. Larock .....	269
<i>Discussion: Session IV Papers: M.P. Tulin, Hydronautics, Incorporated, Laurel, Maryland, USA, Invited Discussor</i> .....	275

## SESSION V: NONLINEAR SOLUTIONS TO BODY-WAVE PROBLEMS

Chairman: H. Maruo, University of Yokohama, Japan

### PART I:

<b>Progress in the Calculation of Nonlinear Free-Surface Problems by Surface-Singularity Techniques</b> , J.L. Hess .....	278
<b>The Wave Resistance for Flow Problems with a Free Surface</b> , C. Korving and A.J. Hermans .....	285
<b>Nonlinear Free-Surface Effects—The Dependence on Froude Number</b> , C. von Kerczek and N. Salvesen .....	292
<i>Discussion: Part I, Session V Papers: T.F. Ogilvie, University of Michigan, USA, Invited Discussor</i> .....	301

### PART II:

<b>Finite Element and Finite Difference Solutions of Nonlinear Free-Surface Wave Problems</b> , S.M. Yen, K.D. Lee, and T.-w. Akai .....	305
<b>Transient Free-Surface Hydrodynamics</b> , M.J. Fritts and J.P. Boris .....	319
<i>Discussion: Part I, Session V Papers: A.J. Hermans, Technische Hogeschool Delft, The Netherlands, Invited Discussor</i> .....	329

## SESSION VI: NONLINEAR SOLUTION TO BODY-WAVE PROBLEMS

Chairman: W.E. Cummins, David W. Taylor Naval Research and Development Center, Bethesda, Maryland, USA

<i>Invited Paper: Advances in the Calculation of Steep Surface Waves and Plunging Breakers</i> , M.S. Longuet-Higgins, University of Cambridge, England .....	332
<b>Numerical Solutions of Transient Nonlinear Free-Surface Motion Outside or Inside Moving Bodies</b> , O.M. Faltinsen .....	347
<b>Numerical Simulation of Ship Motion by Eulerian Hydrodynamic Techniques</b> , G.I. Bourlaniou and B.R. Penumallu .....	358
<b>Computation of Near-Bow or Stern Flows, Using Series Expansion in the Froude Number</b> , J.-M. Vanden Broeck and E.O. Tuck .....	371
<b>Nonlinear Hydrodynamic Forces on Floating Bodies</b> , B.D. Nichols and C.W. Hirt .....	382
<i>Discussion: Session VI Papers: J.V. Wehausen, University of California, Berkeley, USA, Invited Discussor</i> .....	395
<b>List of Participants</b> .....	397

## SHIP HYDRODYNAMICS—THEN AND NOW

L. Landweber  
The University of Iowa  
Institute of Hydraulic Research  
Iowa City, Iowa 52242

"Then" in the title refers to the year 1932 when, without previous knowledge of the field of ship hydrodynamics, or preparation for it, I joined the staff of the U.S. Experimental Model Basin, located in the Washington, D.C. Navy Yard. My immediate supervisor was Karl Schoenherr, and Captain Eggert was the Director. Two of the young Naval Officers on the staff at the time, Al Mumma and Harold Saunders, eventually became Directors of the David Taylor Model Basin.

The activity at the Laboratory was then primarily of an experimental nature. The towing tank was mainly occupied with conducting resistance, propulsion, and maneuvering tests of ship models for the Preliminary Design Section of the Bureau of Ships. Propellers were tested in a variable-pressure water tunnel. Initially, my first assignment was to fair the characteristic curves of thrust and torque coefficients, and efficiency of a large family of propellers, with systematically varied parameters. Since the three characteristic curves are mathematically related, a shift in one in the course of the curve fairing, affected the other two. Consequently, after weeks of annoying drawing and redrawing, I designed and had the shop construct a simple mechanism which drew the efficiency curve corresponding to selected curves of the thrust and torque coefficients. This nearly terminated my association with the ship problems, since Schoenherr felt that, in the time spent designing the machine, I could have finished the project.

Schoenherr was one of two staff members knowledgeable in Ship Hydrodynamics. A well-worn copy of Hydro- and Aeromechanics, by Prandtl and Tietjens, in German, lying on his table, was the main reference source for his Ph.D. thesis on the frictional resistance of flat plates, which culminated in the well-known Kármán-Schoenherr formula. Schoenherr was unique among the Naval Architects of that period in that, having studied in Germany, he was aware of developments in fluid mechanics and was successfully applying this knowledge to propeller and rudder design, as well as to the flat-plate resistance problem. One could compare his impact on Naval Architecture with that of Hunter Rouse on the sister field of Hydraulics. Rouse completed his Ph.D. studies at Karlsruhe, Germany, and returned to the U.S. imbued with the idea that Hydraulics could be taught as a science, rather than an art. Schoenherr made important personal contributions, but did not attempt to

develop a group of ship hydrodynamicists. Rouse was essentially an educator who, through his books and classes, and Directorship of the Iowa Institute of Hydraulic Research, effectively spread the new gospel.

After about a year, I was assigned to work under J.G. Thews, the other staff member knowledgeable in Ship Hydrodynamics. Like myself, Thews was classified as a Physicist. We operated a small towing tank of dimensions 80 ft by 7 ft by 4 ft, equipped with a gravity-type dynamometer, in which we studied planing phenomena, ship rolling, ship resistance in restricted waters, and the vibration of cylinders due to their Kármán streets. The results of this work appeared as EMB Reports. Journal outlets for work of this nature were nonexistent at the time.

Thews and I were more fortunate than most of the staff members in that Capt. Eggert had selected us to conduct research in the aforementioned areas, while other staff members were mainly occupied with routine tasks. In those days, the undergraduate engineering curriculum included a year of calculus, and a year of Freshman Physics, and the Calculus was quickly forgotten if the job didn't require its application, as was usually the case. Of a professional staff of about 30, only two, an aeronautical Engineer and myself, were enrolled for graduate study. This required great motivation, since the Laboratory made no concessions or allowances for this purpose.

In some respects, Captain Eggert was ahead his time. He instigated not only the researches by Thews and myself, which he followed with keen interest, but also experimental studies of the pressure distribution and the boundary layer on both a ship model and the full scale ship, an experimental model study of form resistance, model and full scale studies of maneuverability, and the routine measurement, in the course of resistance tests, of the wave profile alongside the hull, and the lines of flow along the bilges for determining the optimum alignment of bilge keels. Numerical analysis of these problems was performed with slide rules, issued by the laboratory in a 20-inch variety.

In the decade from 1930 to 1940, to which the foregoing remarks apply, several books appeared which contributed importantly to the

dissemination of knowledge and the encouragement of research in Ship Hydrodynamics. These were the English translation of Prandtl and Tietjens, the publication of Hydrodynamics, by Dryden, Murnaghan, and Bateman, by the National Research Council, and the six volumes of Aerodynamic Theory, edited by Durand. Methods of computing the potential flow about two dimensional and axisymmetric forms had been published by von Kármán, and in NACA Reports by Theodoresen and Kaplan. A method of computing the turbulent boundary layer for axisymmetric flow about a body of revolution was the subject of Clark Millikan's Ph.D. thesis. The computational labor of applying these methods was, however, discouraging. Wave theory of ships was also being developed in England, Germany and Sweden, but only the most dedicated workers were willing to undertake the tedious numerical evaluations of theoretically-derived results. Analysis had outstripped computational capability, and there was little incentive to extend the theory beyond its linearized form for a thin ship.

In retrospect, the war years, 1940-1945, were not a period in which research in ship hydrodynamics flourished. The emphasis was on constructing many ships rapidly, and overcoming engineering problems with heuristic solutions. Countermeasures, many of a hydrodynamic nature, had to be developed in response to sophisticated mines which detected the presence of a ship by its acoustic, magnetic, or pressure fields. An important consequence, however, was that talented engineers, physicists and mathematicians who would normally have pursued careers in Universities or industry, joined Naval laboratories. Others acted as consultants or undertook Naval projects in their University laboratories. Thus a much wider group became aware of the interesting and challenging problems of ship hydrodynamics, and several Universities subsequently acquired ship research facilities, such as towing tanks and water tunnels.

This influx strongly affected the nature of Naval laboratories. Where previously a project engineer spent most of his time at a drawing board designing equipment for a test, the new breed sought solutions by physical reasoning, formulation of equations, and mathematical analysis. While most of the original professional staff had only the bachelor's degree, most of the newcomers, and of course the professional consultants, had graduate degrees. Among these were the renowned aerodynamicist, Max Munk, the applied mathematician, Alex Weinstein, and the physicist E.H. Kennard, who also affiliated with Universities in the Washington, D.C. area. This strengthening of the local universities in areas related to fluid mechanics was an important factor in encouraging the staff of Naval laboratories to undertake graduate study.

Four factors contributed greatly to the advancement of ship hydrodynamics in the post-war years. First was the reaction to the years of seeking immediate practical solutions to military problems. It was felt that basic research on ship problems was sorely needed. At the Taylor Model Basin, the organization was

restructured in accordance with the new goal. More importantly, the staff selected for assignment to the blocks in the organization chart grew in stature as they mastered their assigned fields, made fundamental contributions and became recognized as authorities in their various subjects. I hesitate to mention names, for fear of omitting some, but I will mention a few. Wehausen and Pond on ship-wave theory; Cummins on the unsteady Lagally theorem; Eisenberg on cavitation; Tulin for many brilliant contributions, including the theory of supercavitating hydrofoils and the determination of the viscous drag of ships by means of wake surveys; Granville on viscous resistance of bodies of revolution; Abkowitz on dynamic stability and maneuverability of ships; St. Denis, Szebehegyi and the Ochis on ship motions and slamming in waves, and Breslin on propeller-induced ship vibration.

Nor was the momentum of University contributions to ship hydrodynamics lost after the war, through the activity of a new organization, The Office of Naval Research. By sponsoring research at other institutions, participating in the organizing of symposia, such as the present one, contributing to the publication of major works and journals such as the Collected Papers of Havelock and the Applied Mechanics Reviews, and establishing international relationships between researchers, the Office of Naval Research has been an important factor in promoting interest and productivity in ship hydrodynamics. Subsequently, the Taylor Model Basin, under its GHR program, also undertook the sponsorship of ship-hydrodynamic research.

Before the War, there were practically no outlets for publication of research in applied mathematics or ship hydrodynamics. The Transactions of the Society of Naval Architects could hardly serve this purpose since it accepts few papers each year, and these were rarely of a ship-hydrodynamic nature. This has been called the "integral gap" in the Transactions. The appearance of several new journals, such as the Quarterly of Applied Mathematics, the Journal of Rational Mechanics, the Journal of Ship Research, and the Journal of Hydronautics, has eased the publication problem. Indeed, with the recent announcement of several new publications, there is danger that we may be overwhelmed by too much literature, and overburdened referees may lower their reviewing standards.

The second factor contributing to the advancement of ship hydrodynamics was a new policy of the Naval laboratories to encourage and promote graduate study by its professional staff. Shortly after the War, arrangements were made with the University of Maryland to offer some classes in Mathematics and Physics (including Hydrodynamics) at the Taylor Model Basin. In addition, the laboratory granted time for students to attend late afternoon classes at the University of Maryland campus. Under this program, many staff members elected to initiate or continue their graduate studies. A few selected students were fully supported while they pursued their graduate studies at Berkeley. In my opinion, this was a wise and far-sighted policy which soon paid valuable

dividends in the ability of the staff to keep abreast of theoretical developments and to employ more sophisticated analytical techniques in the solution of its problems. One need only compare the nature of the TMB (or USEMB, U.S. Experimental Model Basin) reports before 1940 and after 1950 to verify the foregoing statement. A quantum jump in the scientific level of these reports had occurred over that decade.

The third factor was the influence of two outstanding German scientists, Herman Lerbs and Georg Weinblum, who joined the staff of the Taylor Model Basin after the War. Lerbs was an authority on propeller theory. Weinblum stimulated his colleagues to learn and extend the Lagally theorem, to learn and apply ship-wave theory, to study ship motions, and to plan for the acquisition of facilities for testing ship models in waves. After Weinblum and Lerbs returned to Germany, the former as the first Director of the Institut für Schiffbau, the latter as the Director of the Hamburg Model Basin, their former U.S. colleagues, with whom they had formed close friendships, were frequently welcomed in Hamburg where they met the staff of these Institutions and discussed their researches. Weinblum himself was not a strong analyst; but his sense of the direction of ship-hydrodynamic research, his physical perceptions of the approach to a solution, and his ability to encourage others to undertake important problems, make his contributions to the field of immeasurable value.

The last of the four factors contributing to the advancement of ship-hydrodynamics in the post-war years was the advent of the high-speed computer. Eliminated was the drudgery of long calculations with a slide rule or desk calculator, and algorithms for obtaining a numerical result, which were previously impractical, could be routinely performed with the computer. Where, previously, as in ship-wave theory, mathematics had outstripped computational capacity, after the computer became available, the situation was reversed. Now the researcher was challenged to solve his problems more accurately, with fewer assumptions, or even without any simplifying assumptions. On the experimental side, the analog digital computer, designed to interface with an experiment, control the sequence of measurements and store and operate upon the data in digital form, was equally important in freeing the experimenter from the drudgery of reading data against scales, tapes, or film, and enabling previously unthinkable types of experiments to be undertaken.

For free-surface problems, we may take the "now" of the title to be the papers to be presented at this Conference. These illustrate very well how broadly based and world-wide is the research effort in ship hydrodynamics, with 8 papers from the David Taylor Center, 11 from others in the USA, and 9 from abroad. The speed and capacity of computers have increased to a level where, at least for two-dimensional problems, the Navier-Stokes equations and the exact boundary conditions are treated in two of the papers, by the method of finite differences. Six other papers also employ finite-difference methods, but for the irrotational

flow of an inviscid fluid, most employing the exact free-surface boundary condition. Three of these papers require a preliminary mapping of the boundaries of the body and the free surface into coordinate planes of a rectangular grid, a major task even in two dimensions where methods of conformal mapping could be used.

The most popular method, used in twelve of the papers, is that of singularity distributions, determined by integral equations. I must correct the statement in one of the papers that this method is twenty years old. Actually, the basis of the method lies in the theory of symmetrizable kernels and the fact that the kernels of potential theory are symmetrizable, established by Poincaré and Marty at about the turn of the century. The first numerical application of integral equations to a flow problem is that of von Kármán, in the 1920's, for a body of revolution, followed by other methods by Kaplan, Vandrey and myself, also for bodies of revolution. It is true, however, that A.M.O. Smith was the first to succeed, about 20 years ago, in applying the integral equation for the Neumann problem of potential theory to arbitrary three-dimensional forms.

My own feeling is that, because of the intimate connection between potential theory and integral equations, it is most natural to employ them to obtain numerical solutions. There is a tendency for computer virtuosos to ignore possible mathematical reduction of a problem to a simpler form, and to operate directly on the equations and boundary conditions in finite-difference form. This is undoubtedly an inefficient use of computer time, since the nodal points of the calculation lie in the problem space, rather than on its boundaries. Furthermore, integrals can be represented by quadrature formulas more accurately than differential equations by differences. Lastly, when the domain is of infinite extent, the method of finite differences must accept an error due to the upstream and downstream truncations of the region.

All but two of the papers have assumed irrotational flow, and none considered the effects of the turbulent boundary layer and wake. The remarkable agreement with "measurements" of the calculations of Baba and Hara, using a higher-order irrotational flow theory, suggests that the boundary layer and wake of a ship have no influence on the wave resistance. Here "measurements" are in quotes because wave resistance cannot be measured directly, and its experimentally derived values are subject to assumptions and corresponding uncertainties. Our own studies at Iowa of the effect of wake on wave resistance, in which the wave resistance was determined by the longitudinal-cut technique, showed large effects of the boundary layer and wake, in disagreement with the results of Baba and Hara. Thus, although we have made great progress in obtaining more exact solutions of ship hydrodynamic problems, as is evidenced by the unusual collection of papers at this Conference, we still have a long way to go. Until we have learned how to compute the three-dimensional boundary layer on a ship form,

including free-surface effects and vortex formation, and the wavemaking of the ship in the presence of the boundary layer and wake, the problem will continue to confront us.



## SURVEY OF NUMERICAL SOLUTIONS FOR SHIP FREE-SURFACE PROBLEMS

R. Bruce Chapman  
Science Applications, Inc.  
La Jolla, California

### Abstract

Recent methods for numerical solution of free-surface problems in ship hydrodynamics are reviewed. Quasi-analytic methods which model a linearized free surface outside a body of arbitrary shape are discussed in detail for body motion problems. Also reviewed are methods for the wave-making of translating three-dimensional bodies and two-dimensional methods for nonlinear flow.

### Introduction

Interest in numerical methods for solving free-surface problems in ship hydrodynamics has grown rapidly. These methods can eliminate many of the approximations necessary for analytic solution. Capabilities such as arbitrary hull form obviously extend the practical value of any method. The most useful methods may not be the most general ones or those with the fewest assumptions, however. More limited techniques such as the quasi-analytic methods discussed in this paper can be better design tools for large numbers of problems, while more general methods can check the validity of approximations. The purpose of this paper is to describe briefly some recent advances in numerical ship hydrodynamics and to suggest likely areas for the near future. Three general areas which will be reviewed are: (1) quasi-analytic methods for body motion; (2) numerical simulation of the wave-making of translating three-dimensional ship hulls; and (3) two-dimensional methods for highly nonlinear flows.

### Quasi-Analytic Methods

The gap between numerical and analytic free-surface methods in ship hydrodynamics is bridged by a class of methods which combine analytic linearized free-surface solutions with numerically general representations of the body. Quasi-analytic methods will be defined by these two characteristics:

- (1) Analytic linearized free-surface representations eliminate the need to solve the flow over a large volume surrounding the body.
- (2) The body boundary is satisfied exactly on an arbitrary hull.

Thus, quasi-analytic methods are not confined to simple geometric shapes and are easily applied to practical hull forms. The usual formulation is that of a surface integral with singularities distributed over the body and, in some cases, the free surface. Other formulations have also been developed, such as the localized finite element method of Bai [1], which combines a finite element representation near the body with an analytic solution outside this restricted region.

The efficiency of using available analytic solutions for problems with a linearized free surface cannot be disputed. Unless nonlinear free-surface effects are to be included, there is no reason not to take advantage of analytic representations. The validity of this approach depends on the validity of the linearized free-surface approximation. Two classes of commonly solved problems are those in which the free surface disturbance is caused by motion of the body about a mean position, the body motion problem, and those in which the disturbance is caused by steady translation of the body, the wave-making problem. In the former case the linearized free surface is valid for small amplitude motion. For a translating body, the linearized free surface is valid for a deeply submerged body or a thin or slender body, but not for a surface-piercing hull of finite thickness. The physical validity of the problem of a finite surface-piercing hull moving through a linearized free surface hull, i.e. the Neumann-Kelvin problem investigated by Brard [2], can only be established by comparing computed results with experiment. Quasi-analytic methods for body motion will be discussed first.

### Body Motion Problems

The generalized geometry for body motion problems is shown in Figure [1]. For simplicity, methods will be described in three dimensions with all fundamental concepts easily generalized to three dimensions. Flow is defined in a Cartesian coordinate system  $(x, y) = x$ , with  $y$  upward. The static free-surface  $S_f$  corresponds to  $y = 0$ . It is divided into a portion outside the body  $S_{fe}$  and a portion inside the body  $S_{fi}$  which vanishes when the body is submerged. The submerged portion of the body surface is  $S_b$ . The fluid boundary is  $S_w$ , which is assumed infinite and represented by

$S_{\infty}$  unless otherwise specified. The lower half-plane is divided into two regions--Q inside the body bounded by  $S_B$  and  $S_{Fi}$ , and R outside the body bounded by  $S_B$ ,  $S_{Fi}$ , and  $S_{Fe}$ .

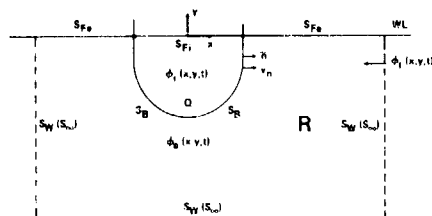


FIGURE 1. GEOMETRY FOR BGJ MOTION PROBLEM

A free-surface disturbance is created by body motion, and, for some problems, by the scattering of an incident wave field defined by  $\phi_1(x,y,t)$ . Body motion is defined by velocity  $\vec{v}_B(x,y,t)$  on  $S_B$  with a normal component

$$v_n = \vec{v}_B \cdot \vec{n} \quad (1)$$

where  $\vec{n}$  is the unit vector normal to  $S_B$ , positive outward.

The flow in region R is defined by a velocity potential  $\phi_0(x,y,t)$ . A velocity potential  $\phi_1(x,y,t)$  is also defined in region Q. This inner potential is non-unique and depends on the formulation. Over region R, the potential satisfies Laplace's equation

$$\nabla^2 \phi_0(x,y,t) = 0 \quad \vec{x} \in R \quad (2)$$

the body boundary condition,

$$\frac{\partial \phi_0}{\partial n}(x,y,t) = v_n(x,y,t) \quad \vec{x} \in S_B \quad (3)$$

the linearized free-surface condition,

$$\frac{\partial^2}{\partial t^2} \phi_0(x,y,t) + g \frac{\partial \phi_0}{\partial y}(x,y,t) = 0 \quad \vec{x} \in S_{Fe} \quad (4)$$

and appropriate boundary and initial conditions.

It is useful to divide the potential into a free-surface component and a body component which vanishes on the free surface,

$$\phi_0(x,y,t) = \phi_f(x,y,t) + \phi_{Be}(x,y,t) + \phi_1(x,y,t) \quad \vec{x} \in R \quad (5)$$

$$\phi_1(x,y,t) = \phi_f(x,y,t) + \phi_{Bi}(x,y,t) + \phi_1(x,y,t) \quad \vec{x} \in Q \quad (6)$$

where  $\phi_1(x,y,t)$  is the scattering wave, present only in certain problems. The free-surface and incident potentials,  $\phi_f(x,y,t)$  and  $\phi_1(x,y,t)$ , are analytic over the entire lower half-plane while the body potentials,  $\phi_{Be}(x,y,t)$  and  $\phi_{Bi}(x,y,t)$ , both vanish on the free surface,

$$\phi_{Be}(x,y,t) = 0 \quad (x,y) \in S_{Fe} \quad (7)$$

$$\phi_{Bi}(x,y,t) = 0 \quad (x,y) \in S_{Fi} \quad (8)$$

The incident wave, if present, satisfies the linearized free surface condition identically. Thus, the free-surface component satisfies the linearized free-surface condition,

$$\frac{\partial^2}{\partial t^2} \phi_f(x,y,t) + g \frac{\partial \phi_f}{\partial y}(x,y,t) = -h(x,t) \quad (x,y) \in S_{Fe} = S_{Fi} \cup S_{Fe} \quad (9)$$

where  $h(x,t)$  represents the free-surface influence of the body potential,

$$h(x,t) = g \frac{\partial \phi_1}{\partial y}(x,0,t) \quad (x,0) \in S_{Fi} \quad (10)$$

$$+ g \frac{\partial \phi_{Be}}{\partial y}(x,0,t) \quad (x,0) \in S_{Fe} \quad (11)$$

Note that  $\phi_f(x,y,t)$  is equivalent to the classical problem of a time-dependent disturbance acting on a linearized free surface and can be solved analytically in terms of  $h(x,t)$ . If  $\phi_f(x,y,t)$  and its time derivative are initially zero for example,

$$\phi_f(x,y,t) = -\frac{1}{g} \int_0^t \int_{-\infty}^{\infty} h(x_1,t_1) \int_0^{\infty} \frac{e^{-ky} \cosh(k(x-x_1))}{\sqrt{gk}} \sin((t-t_1)\sqrt{gk}) dk dx_1 dt_1 \quad (12)$$

For the body source and the body dipole method,  $\phi_f(x,y,t)$  is represented by the integral of the free-surface portion of a Green's function over the body surface.

The body component of the velocity potential vanishes on the free surface and satisfies the body boundary condition

$$\frac{\partial \phi_{Be}}{\partial n}(x,y,t) = v_n(x,y,t) - \frac{\partial \phi_1}{\partial n}(x,y,t) - \frac{\partial \phi_{Bi}}{\partial n}(x,y,t) \quad \vec{x} \in S_B \quad (13)$$

over region R. The body boundary condition for  $\phi_{Bi}(x,y,t)$  is arbitrary.

Quasi-analytic methods are usually applied in the form of a surface integral derived from Green's theorem. Let

$$G(\bar{x}, \bar{x}_1) = G(x, y, \xi, \eta) \quad (14)$$

be the Green's function vanishing on the free surface. In two dimensions,

$$G(x, y, \xi, \eta) = \frac{1}{2\pi} \left\{ \log[(x-\xi)^2 + (y-\eta)^2] - \frac{1}{2} \log[(x-\xi)^2 + (y+\eta)^2] \right\} \quad (15)$$

Assume for now that the fluid is unbounded. Then from Green's theorem the body potential

$$\begin{aligned} \phi_B(\bar{x}, t) &= \phi_{Be}(\bar{x}, t) \quad \bar{x} \in R \\ &= \phi_{Bi}(\bar{x}, t) \quad \bar{x} \in Q \end{aligned} \quad (16)$$

can be represented over the lower half-plane by

$$\begin{aligned} \phi_B(\bar{x}, t) &= \int_{S_B} \left[ \frac{\partial \phi_{Bi}}{\partial n_1}(\bar{x}_1, t) - \frac{\partial \phi_{Be}}{\partial n_1}(\bar{x}_1, t) \right] G(\bar{x}, \bar{x}_1) dS \\ &+ \int_{S_B} [\phi_{Be}(\bar{x}_1, t) - \phi_{Bi}(\bar{x}_1, t)] \frac{\partial}{\partial n_1} G(\bar{x}, \bar{x}_1) dS \end{aligned} \quad (17)$$

This is equivalent to a source distribution over  $S_B$  and a dipole distribution over  $S_B$ . The body boundary condition for  $\phi_{Bi}$  is arbitrary. The most common assumption is that the potential is continuous across the body

$$\phi_{Be}(\bar{x}, t) - \phi_{Bi}(\bar{x}, t) = 0 \quad \bar{x} \in S_B \quad (18)$$

In this case, the normal velocity is discontinuous across the body surface and the body component of the potential is of the form,

$$\phi_B(\bar{x}, t) = \int_{S_B} D(\bar{x}_1, t) G(\bar{x}, \bar{x}_1) dS \quad (19)$$

which is equivalent to a source distribution of strength  $D(\bar{x}, t)$  over the body surface.

#### Body Source Method

The body source method was applied by Frank [3] to the problem of harmonic oscillation of a two-dimensional ship section. In this case, the body boundary condition (13) may be represented as

$$\frac{\partial \phi_B}{\partial n}(\bar{x}, t) = A i \omega v_n^*(\bar{x}) e^{i \omega t} - \frac{\partial \phi_f}{\partial n}(\bar{x}, t) \quad \bar{x} \in S_B \quad (20)$$

where  $A$  is the amplitude and  $\omega$  is the frequency of the oscillation. The nondimensional normal velocity  $v_n^*(\bar{x})$  depends on the mode of motion. The free surface condition reduces to

$$\omega^2 \phi_f(\bar{x}) + g \frac{\partial \phi_f}{\partial y}(\bar{x}) = -g \frac{\partial \phi_B}{\partial y}(\bar{x}), \quad (21)$$

where  $\phi_B(\bar{x})$  is represented by a source distribution over  $S_B$ .

$$\phi_B(\bar{x}, t) = e^{i \omega t} \int_{S_B} D(\bar{x}_1) G(\bar{x}, \bar{x}_1) dS \quad (22)$$

It can be shown analytically that  $\phi_f(\bar{x}, t)$  satisfying the free surface condition (21) may be written as

$$\phi_f(\bar{x}, t) = e^{i \omega t} \int_{S_B} D(\bar{x}_1) G_2(\bar{x}, \bar{x}_1) dS \quad (23)$$

where the free-surface portion of the Green's function,

$$\begin{aligned} G_2(x, x_1) &= \text{Re} \left[ 2 \text{P.V.} \int_0^\infty \frac{e^{-ik(x-x_1) + k(y+y_1)}}{\omega^2/g - k} dk \right] \\ &- i \text{Re} \left[ e^{-\omega^2/g(l(x-x_1) + (y+y_1))} \right] \end{aligned} \quad (24)$$

satisfies

$$\omega^2 + g \frac{\partial}{\partial y} G_2(\bar{x}, \bar{x}_1) = -g \frac{\partial}{\partial y} G_1(\bar{x}, \bar{x}_1) \quad \bar{x} \in S_f \quad (25)$$

and the radiation condition at infinity.

Thus, the body boundary condition (20) becomes an integral equation of the form,

$$\int_{S_B} D(\bar{x}_1) \left[ \frac{\partial}{\partial n} G(\bar{x}, \bar{x}_1) + \frac{\partial}{\partial n} G_2(\bar{x}, \bar{x}_1) \right] dS = i \omega A v_n^*(\bar{x}) \quad (26)$$

This integral equation can be approximated numerically by dividing  $S_B$  into  $N_B$  finite segments of constant source density. Equation (26) applied at the center of each segment produces a set of linear equations for the  $N_B$  source densities. From this density distribution, forces and velocities can be computed from equations (22) and (23).

This well-known method has been successfully applied to a variety of problems. One undesirable feature is a set of anomalous eigenfrequencies corresponding to nontrivial solutions of the inner potential  $\phi_i^*(\bar{x})$  satisfying Laplace's equation over region  $Q$  and boundary conditions

$$\omega_n^2 \phi_i^*(\bar{x}) + g \frac{\partial \phi_i^*}{\partial y}(\bar{x}) = 0 \quad \bar{x} \in S_{f1} \quad (27)$$

$$\phi_i^*(\bar{x}) = 0 \quad \bar{x} \in S_B \quad (28)$$

The inner potential and therefore the source density is non-unique at these frequencies. The problem is not fundamental, however, since the external potential and therefore the pressure remains unchanged. The linear equations for the density distribution are singular at these frequencies. This singularity can be removed by several methods, including placing a lid on the body and submerging it a small distance. These internal modes can also be excited for initial value problems solved by the body source method but they only influence the source distribution and have no effect on the pressure [4].

The utility of the body source method for practical three-dimensional ship hulls is well illustrated by van Oortmerssen's [5] study of the motions of a tanker hull in shallow water. Hydrodynamic coefficients and wave exciting forces were calculated as functions of frequency and compared with experimental data. The method is a three-dimensional generalization of the Frank [3] method with a Green's function for the body component of potential defined by

$$G(\bar{x}, \bar{x}_1) = \frac{1}{4\pi} \left( \frac{1}{r} - \frac{1}{r^*} \right) \quad (29)$$

where  $r$  is the distance between points  $\bar{x}$  and  $\bar{x}_1$  and  $r^*$  is the distance between  $\bar{x}$  and the image of  $\bar{x}_1$  across the undeflected free surface. The free-surface portion of the Green's function  $G_2(\bar{x}, \bar{x}_1)$  corresponds to the disturbance created by an oscillating source below a linearized free surface in a fluid of constant depth. In some calculations the effect of a nearby wall is represented by image terms in the Green's function.

The tanker was represented by 160 triangular and quadrilateral panels no larger than one-fifth of the smallest wave length. Wave induced forces were in good agreement with experiment except for surge and pitch in beam seas which only result from the small longitudinal asymmetry. Added mass and damping coefficients also showed good general agreement with experiment except for viscous effects in roll damping and some differences in roll and pitch added mass. In general, van Oortmerssen's work is strong evidence of the practical utility of the simple source distribution for ship motion problems. No forward speed effects were included, but the results should remain valid for slowly moving ships.

#### Body Dipole Method

Another quasi-analytic method closely related to the body source method is the body dipole method developed by Chang and Pien [6]. This method was developed for a three-dimensional submerged body translating at a steady speed. Chang and Pien [6] demonstrated that a more accurate solution could be obtained with fewer body panels with a dipole distribution than with

a source distribution. Later, the method was extended to wave excited forces and moments [7]. Recent work of Chang shows good results for the hydrodynamic coefficients of a three-dimensional ship hull.

The same formulation developed for the source method can be applied to the dipole method for a submerged body. A surface-piercing body can also be represented as the limiting case of a submerged body with a flat top an infinitesimal distance below the free surface, although this involves a line integral (point sources and dipoles in two dimensions) except for special cases including steady harmonic oscillations.

For a submerged body with the velocity normal to the body continuous across the body surface, equation (17) reduces to

$$\phi_B(\bar{x}, t) = \int_{S_B} D(\bar{x}_1, t) \frac{\partial}{\partial n_1} G(\bar{x}, \bar{x}_1) dS \quad (30)$$

where  $D(\bar{x})$  is the strength of the surface dipole distribution. This body potential  $\phi_B(\bar{x}, t)$  is discontinuous across the body surface but has a continuous normal velocity. As in the source distribution method, the free-surface potential is continuous over the lower half-plane and satisfies equation (21) on the undeflected free surface.

The greatest difference between the source and dipole methods is the technique for determining the strength distribution  $D(\bar{x}, t)$ . For the source method, the body boundary condition is applied directly. For the dipole method, it is applied indirectly by a known internal potential  $\phi_i(\bar{x}, t)$  satisfying

$$\frac{\partial \phi_i}{\partial n}(\bar{x}, t) = v_n(\bar{x}, t) \quad \bar{x} \in S_B \quad (31)$$

If the body translates in the  $x$  direction with speed  $U(t)$ , for example, the inner potential is simply

$$\phi_i(x, t) = x U(t) \quad (32)$$

The dipole density is determined from an integral equation representation of equations (6) and (3)

$$\phi_i(\bar{x}, t) = \phi_f(\bar{x}, t) + \phi_r(\bar{x}, t) + \int_{S_B} D(\bar{x}_1, t) \frac{\partial}{\partial n_1} G(\bar{x}, \bar{x}_1, t) dS \quad (33)$$

where  $\phi_i(\bar{x}, t)$  is the known internal potential and  $\phi_f(\bar{x}, t)$  is the solution of equations (10) and (11).

The wave-induced forces acting on a three-dimensional deeply submerged body moving through a wave field at constant speed were calculated by Chang and Pien [7] under the simplifying assumption that the free-surface potential

generated by the body  $\phi_f(\bar{x}, t)$  can be neglected. Equation (33) then becomes

$$u_x = \phi_1(\bar{x}, t) + \int_{S_B} D(\bar{x}, t) \frac{\partial G(\bar{x}, \bar{x}_1)}{\partial n_1} dS \quad (34)$$

$\bar{x} \in S_B$

which can be converted into a set of  $N_B$  linear equations for the dipole density distribution  $D(\bar{x}_1, t)$  over  $N_B$  finite panels. The resulting induced forces agree with an analytic result of Havelock for a test case of a sphere.

With the same theory, Chang and Pien [7] simulated the free motion of a submerged body in waves. One interesting phenomenon is wave coupling in bidirectional seas. The motion induced by one set of waves alters the forces induced by the other depending on initial conditions, relative direction, and phasing. The result can be a steady drift in yaw, for example, until in some cases a stable relative angle is reached.

As mentioned above, the dipole method can be applied to a surface-piercing body by applying the present formulation to a closed body with a flat top an infinitesimal distance below the free surface. No line integral is involved for steady harmonic oscillation of a three-dimensional ship hull. Chang has in fact, successfully applied the dipole method to a practical ship hull [8]. These results and those of Frank [3] and van Oortmerssen [5] demonstrate the practical utility of quasi-analytic methods for seakeeping prediction. A realistic simulation could be achieved by including the effects of forward speed, nonlinear hydrostatic terms, and viscous effects.

#### Hybrid Method

For the body source and body dipole methods, singularities are distributed over the body surface, with the free-surface potential represented by the free-surface portion of the Green's function which is also integrated over the body surface. Another method for linear harmonic oscillations of a body immersed in a fluid is the hybrid method described by Bai and Yeung [9], which matches a numerical solution in a small region surrounding the body with analytic solutions outside this region. Bai and Yeung [9] give two alternate techniques for implementing the method; a finite element variational method and a surface integral method. The surface integral method will be briefly described in the form developed and applied by Yeung [10].

This method is characterized by a Green's function in the form of a simple source

$$G(x, y, z, n) = \frac{1}{2\pi} \log[(x-\xi)^2 + (y-\eta)^2]^{1/2} \quad (35)$$

distributed over the surface  $S$  bounding region I, the region surrounding the body as shown in

Figure [2]. This bounding surface includes the submerged portion of the body  $S_B$ , the free surface  $S_F$ , the bottom  $S_W$ , and the left and right radiation boundaries  $S_L$  and  $S_R$ . The bottom surface  $S_W$  can be irregular if the depth is constant in regions II and III. The body boundary condition is

$$\frac{\partial \phi}{\partial n}(\bar{x}) = v_n(\bar{x}) \quad \bar{x} \in S_B \quad (36)$$

where  $v_n(\bar{x})$  is a specified function and  $\phi(\bar{x})$  is a complex potential defined by

$$\phi(\bar{x}, t) = \text{Re}\{\phi(\bar{x}) e^{-i\omega t}\} \quad (37)$$

The free-surface and body boundary conditions are

$$\omega^2 g^{-1} \phi(\bar{x}) - \frac{\partial \phi}{\partial y}(\bar{x}) = 0 \quad \bar{x} \in S_F \quad (38)$$

and

$$\frac{\partial \phi}{\partial n}(\bar{x}) = 0 \quad \bar{x} \in S_W \quad (39)$$

The potentials in regions II and III are finite summations of the form,

$$\phi(x) = \sum_{k=0}^{N_R} C_k^R f_k^R(\bar{x}) \quad (\bar{x}) \in \text{II} \quad (40)$$

and

$$\phi(\bar{x}) = \sum_{k=0}^{N_L} C_k^L f_k^L(\bar{x}) \quad (\bar{x}) \in \text{III} \quad (41)$$

with the potential and its normal derivative continuous across the radiation boundaries. When the boundary conditions (36)-(41) are applied to Green's theorem,

$$\phi(\bar{x}) = \int_{S_B} \phi(\bar{x}_1) \frac{\partial G(\bar{x}, \bar{x}_1)}{\partial n_1} - G(\bar{x}, \bar{x}_1) \frac{\partial \phi(\bar{x}_1)}{\partial n_1} dS \quad \bar{x} \in \text{I} \quad (42)$$

all terms involving  $\frac{\partial \phi(\bar{x}_1)}{\partial n_1}$  can be eliminated, giving

$$\begin{aligned} \phi(\bar{x}) = & \int_{S_B \cup S_F \cup S_W} \phi(\bar{x}_1) \frac{\partial G}{\partial n_1}(\bar{x}, \bar{x}_1) - \omega^2 g^{-1} \int_{S_F} \phi(\bar{x}_1) G(\bar{x}, \bar{x}_1) \\ & + \int_{S_R} dS \sum_{k=0}^{N_R} C_k^R (f_k^R(\bar{x}_1) \frac{\partial G}{\partial n_1}(\bar{x}, \bar{x}_1) - \frac{\partial f_k^R}{\partial n_1}(\bar{x}_1) G(\bar{x}, \bar{x}_1)) \\ & + \int_{S_L} dS \sum_{k=0}^{N_L} C_k^L (f_k^L(\bar{x}_1) \frac{\partial G}{\partial n_1}(\bar{x}, \bar{x}_1) - \frac{\partial f_k^L}{\partial n_1}(\bar{x}_1) G(\bar{x}, \bar{x}_1)) \\ & - \int_{S_B} dS v_n(\bar{x}_1) G(\bar{x}, \bar{x}_1) \end{aligned} \quad (43)$$

This integral equation can be reduced to a set of simultaneous linear equations for the potential  $\phi(\bar{x})$  on surfaces  $S_B$ ,  $S_F$ , and  $S_W$  and the coefficients of the two expansions by dividing the boundary surface of region I into small segments of constant potential including  $N_B$  segments on  $S_B$  and  $N_L$  segments on  $S_L$ . Equation (43) then gives the potential at any point in I. An incident wave can be easily included by adding it to the representation at the radiation boundaries (40)-(41). The method can also be applied to body oscillations in deep water.

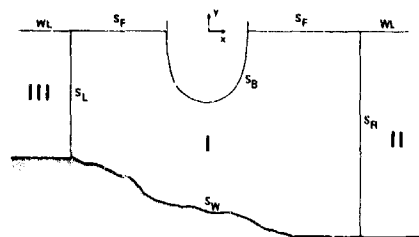


FIGURE 2. GEOMETRY FOR HYBRID METHOD

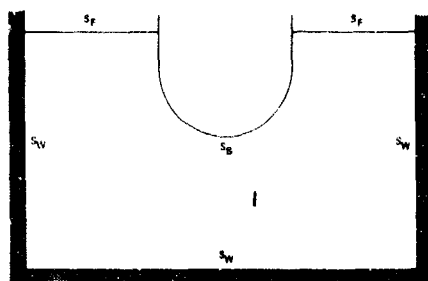


FIGURE 3. GEOMETRY FOR BODY MOTION PROBLEM

#### Initial Value Methods

Although steady harmonic oscillations are the most common form for free-surface body motion problems, initial value problems with arbitrary body motion are of interest as well. Two alternatives to the time-dependent Green's function for initial value problems will be

described - the TDIET (Time-dependent Differential-Integral Equation Technique) method described by Harten [11], and spectral representation of the free-surface potential for the body source method.

Like the hybrid method, the TDIET method distributes simple source and dipole singularities over the surface which bounds the region of computation and uses the boundary conditions to remove the normal velocity from the Green's integral representation for the velocity potential. As an initial value problem, it can be formulated in a closed basin. Radiation boundaries may be included but they complicate the formulation. Consider a two-dimensional closed region I shown in Figure [3] bounded by a body surface  $S_B$ , the basin surface  $S_W$ , and a free surface  $S_F$ . The body boundary condition may be written as

$$\frac{\partial \phi}{\partial n}(\bar{x}, t) = v_n(\bar{x}, t) = \sum_{j=1}^3 b_j(\bar{x}) V_j(t) \quad (44)$$

$$\bar{x} \in S_B, t > 0$$

where  $V_j(t)$  is the velocity of the  $j^{\text{th}}$  mode of body motion. The boundary conditions on the basin surface and the free surface are

$$\frac{\partial \phi}{\partial n}(\bar{x}, t) = 0 \quad \bar{x} \in S_W, t > 0 \quad (45)$$

and

$$\frac{\partial^2 \phi}{\partial t^2}(\bar{x}, t) + g \frac{\partial \phi}{\partial y}(\bar{x}, t) = 0 \quad (46)$$

$$\bar{x} \in S_F, t > 0$$

where  $\phi(\bar{x}, t)$  and  $\eta(\bar{x}, t) = g^{-1} \frac{\partial \phi}{\partial t}(\bar{x}, t)$  are both specified as initial conditions for  $t = 0$ . When these boundary conditions are applied to Green's theorem (42), the result is an integral equation of the form

$$\begin{aligned} \phi(\bar{x}, t) &= \int_{S_B \cup S_W} dS \phi(\bar{x}_1, t) \frac{\partial G(\bar{x}, \bar{x}_1)}{\partial n_1} - \frac{1}{g} \int_{S_F} dS \phi_{tt}(\bar{x}_1, t) G(\bar{x}, \bar{x}_1) \\ &= \int_{S_B} dS v_n(\bar{x}_1, t) G(\bar{x}, \bar{x}_1) \\ &= \sum_{j=1}^3 V_j(t) b_j^*(\bar{x}) \end{aligned} \quad (47)$$

where  $G(\bar{x}, \bar{x}_1)$  is the simple source defined for two dimensions by (35).

Equation (47) is reduced to numerical form by dividing the boundary surface into finite segments with the potential specified at  $N = N_B + N_F$  points. The first  $N_B$  points are on the free surface. Let  $\phi_B(\bar{x}_1, t)$   $1 \leq 1 \leq N$  denote the potential on the body and basin, and let  $\phi_F(\bar{x}_1, t)$   $N_B + 1 \leq 1 \leq N$  denote the potential at  $N_F$  points on the free surface. Harten [11]

shows that a spline fit reduces the integral equation (47) to a set of linear equations of the form

$$\sum_{i=1}^{N+N_F} E_{ki} \mu_i(t) = \sum_{j=1}^3 V_j(t) \delta_k \quad (48)$$

where  $\mu_i(t)$  is a vector with  $N+N_F$  elements defined as

$$\begin{aligned} \mu_i &= \phi_R(\bar{x}_i, t) \quad 1 \leq i \leq N_R \\ &= \frac{\partial^2}{\partial t^2} \phi_F(\bar{x}_i, t) \quad N_R+1 \leq i \leq N \\ &= \phi_F(\bar{x}_{i-N_F}, t) \quad N+1 \leq i \leq N+N_F \end{aligned} \quad (49)$$

The matrix  $E_{ki}$  has  $N$  by  $N+N_F$  elements which are independent of time and depend only on the geometry. Harten [11] shows that by Gaussian elimination, the body and basin potentials can be removed from the last  $N_F$  equations which then assume the form

$$\sum_{i=1}^N [U_{ki} \frac{\partial^2}{\partial t^2} \phi_F(\bar{x}_i, t) + U_{ki} \phi_F(\bar{x}_i, t)] = \sum_{j=1}^3 f_j(t) \delta_k \quad k=1, \dots, N_F \quad (50)$$

which is a system of  $N_F$  linear differential equations for the surface potential  $\phi_F(\bar{x}_i, t)$ . The potentials on the free surface can then be integrated from their initial values without considering the potentials on the body or the basin. These potentials can be calculated from the first  $N_R$  equations of (49) once the free-surface potentials have been determined.

Another method well suited for initial value problems is the body source method described in a previous section with the free surface potential  $\phi_F(\bar{x}, t)$  and the incident wave, if present, described by their spectral components.

Spectral representations of the free surface have been applied to both linear and nonlinear problems by Haussling and Van Eseltine [12], [13]. The combined body source and free surface spectral method described here was applied by Chapman [4] to the problem of large amplitude motion of floating bodies with a linearized free surface. The free surface potential  $\phi_F(x, y, t)$  defined by equations (5), (6) and (9) is analytic over the lower half-plane and can be approximated in deep water by a finite summation of harmonics,

$$\phi_F(x, y, t) = g \sum_{n=1}^{N_W} B_n(t) \sigma_n^{-1} e^{k_n(ix-y)} \quad (51)$$

where  $B_n(t)$  is the complex amplitude of the  $n$ -th harmonic,  $k_n$  is the wave number, and

$\sigma_n = (g k_n)^{1/2}$  is the frequency. This finite summation is, in fact, an approximation to an infinite integral with an error which vanishes as the wave spacing  $\Delta k_n = k_{n+1} - k_n$  approaches zero and the maximum wave number  $k_{N_W}$ , which corresponds to the shortest wave length, approaches infinity.

The free surface elevation,

$$\eta(x, t) = -\frac{1}{g} \frac{\partial \phi_F}{\partial t}(x, 0, t) \quad (52)$$

is also represented by a summation,

$$\eta(x, t) = \sum_{n=1}^{N_W} A_n(t) e^{ik_n x} \quad (53)$$

where  $A_n(t)$  is a complex vector. The free surface is thus represented by a pair of complex vectors,  $A_n(t)$  and  $B_n(t)$ . The linearized free surface equation (9) and the dynamic condition (52) can then be expressed by  $N_W$  pairs of simple differential equations of the form

$$\frac{d}{dt} A_n(t) + \sigma_n B_n(t) = C_n(t) \quad (54)$$

$$\frac{d}{dt} B_n(t) - \sigma_n A_n(t) = 0 \quad (55)$$

where  $C_n(t)$  represents the body source potential in the form of the harmonics of  $h(x, t)$  defined in (9),

$$h(\bar{x}, t) = g \sum_{n=1}^{N_W} C_n(t) e^{ik_n x} \quad (56)$$

These equations can be integrated analytically for a series of small time steps over which the body source distribution, and therefore  $C_n(t)$ , are assumed to be constant. Since the body potential is expressed numerically as a collection of finite sources,  $C_n(t)$  is easily computed by adding the analytic result for the free-surface harmonics generated by an impulsive submerged source [4]. The free surface velocity  $\frac{\partial \phi_F}{\partial n}(x, y, t)$  which appears in the body boundary condition (13) determining the body source distribution can be evaluated by analytic differentiation of the harmonic components in (51). In this way an initial value problem can be advanced in small time steps. If the body is free, forces acting on the body are computed each time step and the accelerations determined from the equations of motion.

One advantage of the spectral rather than a physical representation of the free surface is that wave spacing can be non-uniform with smaller spacing at the low wave numbers which correspond to the long wave lengths.

This increases the time interval over which the long wave lengths and therefore the solution remains valid. In a physical representation these long wave lengths are the first reflected from the boundary of the calculation since they propagate the fastest.

Small body motion is a sufficient but not a necessary condition for a valid linearized free surface. The linear approximation can remain valid, if the body moves slowly, over large changes in the geometry of the submerged portion of the body which induce hydrostatic and hydrodynamic nonlinearities. The body source method with a spectral free-surface representation has been applied to this type of large amplitude motion and tested for a few cases [4], including water entry and large amplitude free oscillation of floating rectangular cylinders.

#### Wave-Making Problems

The problem of a body translating with steady speed through an inviscid fluid with a free-surface is usually solved for the purpose of estimating the resistance due to wave-making. Also of interest are sinkage and trim forces and the streamlines over the hull, including the wave profile. If the body is well submerged, the linear free surface is valid and quasi-analytic methods are applicable. With modification, basic quasi-analytic techniques discussed for body motion problems can be applied to a translating submerged body.

The body source method, for example, was applied to steady flow past submerged two-dimensional hydrofoils by Geising and Smith [14] with a Green's function in the form of a Kelvin source, i.e. a source translating with steady speed under a linearized free surface. Later, Chang and Pien [6] demonstrated the advantages of the surface dipole method for translating, submerged three-dimensional bodies. Both Bai [11] and Chen and Mei [15] have solved two-dimensional flows past submerged bodies with localized finite element, or hybrid, methods based on variational principles for a linearized free surface.

When the body is near or intersects the free surface, linearization is valid only in limiting cases such as thin or flat ships or at zero Froude number where the free-surface acts as a rigid boundary and the flow is identical to flow over a double model--the hull and its reflection in an unbounded fluid. It is not unreasonable though, to attempt an improvement of the thin ship approximation for the wave-making of finite thickness hulls piercing a free surface by placing sources on the hull surface rather than the centerplane while retaining the simplicity inherent in a free-surface potential linearized about the free stream flow. The validity of this method can only be established empirically by comparing predicted and experimental wave-making resistance.

An early investigation of this type was that of Breslin and Eng [16] who computed the wave

resistance induced by the surface source distribution calculated for the flow past a Series-60 hull in the zero Froude number (double hull) limit by Hess and Smith [17]. Although this method neglects the effect of the free-surface disturbance on the body boundary condition and therefore on the source distribution, it should give a strong indication of the effect of satisfying the exact body boundary condition for low Froude numbers. The experimental residuary resistance was compared with predictions from thin ship theory and the surface source distribution over a range of Froude numbers. No improvement was obtained by placing the sources on the actual surface. Breslin and Eng point out that part of the disagreement between theory and experiment may be due to interaction between viscous and wave-making components of resistance.

Adee [18], [19] applied the body source method to a Series-60 hull. The free-surface potential, calculated for a Kelvin source, was included in the body boundary condition so that an exact numerical solution of the Neumann-Kelvin problem was obtained. Adee did not calculate wave-making resistance since he did not expect any fundamental improvement over thin ship theory. Instead, he sought an estimate of the effects of a linearized free surface on the double hull streamlines over the hull surface.

The dipole method was applied to a surface-piercing ellipse by Chang and Pien [6] with a formulation equivalent to a submerged body with a flat top an infinitesimal distance below a linearized free surface. This formulation contained the two-dimensional equivalent of the line integral for three-dimensional surface-piercing bodies.

Two analytic papers concerning a three-dimensional surface-piercing body of finite thickness translating through a linearized free surface, the Neumann-Kelvin problem, should be mentioned. Brard [2] and Bessho [20] both discuss a line integral about the intersection of the body and the linearized free surface. This line integral may be obtained analytically from Green's theorem for a Kelvin source by integrating by parts over the linearized free surface exterior to the body. Some numerical formulations, such as the body source method, do not explicitly contain line integrals while others such as the dipole method do. All methods provide solutions of the Neumann-Kelvin problem within the limitations of numerical approximations such as element size.

The uniqueness and even the existence of a solution to the Neumann-Kelvin problem has not been established for surface-piercing bodies, although Bessho [20] has demonstrated that the flow can be unique if the surface-piercing body is regarded as a submerged body with a flat top an infinitesimal distance below a linearized surface with zero water depth above the hull. Perhaps more importantly, the physical significance of the Neumann-Kelvin problem for surface-piercing bodies is questionable. There is a net flux into the body, for example,



which Bessho [20] shows can only be cancelled by removing one term in the line integral.

Thus, while quasi-analytic methods have been proven valuable for body motion problems and wave-making of well submerged bodies, the important problem of the wave-making resistance of a surface-piercing body seems to require a more realistic representation of the free surface than is provided by the classical linearized theory.

#### Nonlinear Free Surface Solutions for Ship Hull Wave-Making

Before more numerical methods are discussed, some mention should be made of what is essentially an analytic approach to nonlinear flow past a finite ship hull--second order perturbation about a thin ship representation. Formulations of this type have been invented or developed by Wehausen [21], Yim [22], Eggers and Choi [23], Guilloton, Noblesse [24], and Dagan [25]. Comparisons between wave resistance computed by these methods and experimental data have been published by Gadd [26] and by Hong [27]. These methods are shown to improve the theoretical prediction for some Froude numbers but not consistently.

Another approach, easily applied to numerical methods, is to perturb the flow about the double hull or zero Froude number flow rather than about the free stream. Thus, the velocity potential  $\phi(\bar{x})$  is written as

$$\phi(\bar{x}) = \phi_p(\bar{x}) + \psi(\bar{x})$$

where  $\phi_p(\bar{x})$  satisfies the exact body boundary condition and the condition of zero vertical velocity on the static free surface plane. In this way, the free surface disturbance is perturbed about a flow which goes around a finite hull rather than through it. An analytic perturbation of this type is valid in the limiting case of a slowly moving ship [28]. This perturbation has been applied numerically by Baba [29] to low speed flow past blunt ship bows with good agreement with experimental coefficients of wave resistance over a range of low Froude numbers.

Other authors have also had success with perturbation about the double hull streamlines. Dawson [30] has solved the flow about a Wigley hull in this manner and has obtained good agreement with experimental wave profiles for Froude numbers as high as 0.50. Chan [31] uses the double hull flow as a starting estimate for an exact nonlinear solution. Chan and Stuhmiller [32] have also applied perturbation about the double hull flow to unsteady motion of a semisubmerged sphere. Double hull perturbation has limited application however, for body motion problems which are usually linearized on the basis of small amplitude motion rather than body thickness. Terms associated with flow about the body, whether linearized about the double hull or the free stream, are

significant only for cases of large amplitude motion. In these cases, perturbing the double hull flow should provide a correction, valid at low frequencies (Froude numbers), to the nonlinear portion of the damping coefficient--an effect closely related to wave-making.

The limited results now available indicate improved wave-making resistance predictions by perturbing about the double hull flow, even at moderate Froude numbers. This suggests that horizontal transport terms in the free-surface conditions are important factors in the wave-making resistance of realistic ship hulls. It should be expected however, that in the moderate to high range of Froude numbers the horizontal velocities on the free surface will cease to be modeled by the double hull flow.

A more general method was developed by Gadd [33], who formulated a free surface representation, nonlinear in the horizontal plane and second order in the vertical direction. Surface panels are distributed over the body and the undeflected free surface near the body. The source densities on the panels are computed by alternately applying the kinematic condition and correcting for the error in the dynamic condition. Although the method for terminating the free-surface panels and the use of smoothing are perhaps undesirable, Gadd obtained excellent results as evidenced by comparisons with experimental wave profiles and resistance for a hull over a limited range of Froude numbers tested, and particularly by comparisons with free-surface contours and induced pressures for flow over a blunt bow.

Perhaps because investigators have been deterred by the possibility of large computation times, there have been few attempts to solve the exact nonlinear problem of flow past a ship hull numerically. Nichols and Hirt [34] calculated the nonlinear free-surface disturbance generated by a blunt three-dimensional body impulsively started in a basin with a variation of the Marker-and-Cell method, but this calculation has no direct connection to the wave-making of a ship hull. Recently, Chan [31] has developed a numerical method for ship hulls based on double hull flow without linearization so that the solution is exact within the limitations of inviscid flow.

#### Two-Dimensional Nonlinear Free-Surface Problems

Fundamental aspects of nonlinear free surface flow are most easily studied in two dimensions. A few nonlinear solutions of interest for ship hydrodynamics will be mentioned in this section. One class of problems is steady nonlinear flow past a two-dimensional disturbance. Problems of this type, including flows past submerged vortices, flows past foils, and shallow water effects have been studied extensively by Salvesen and von Kerczek [35], [36], [37]. Of particular interest are comparisons with perturbation theory and with experiments with a foil. Nonlinear effects contained in second and third order perturbation

expansions are evident in the numerical nonlinear free-surface elevations for flow past a submerged vortex. For positive circulation, third order theory provides an excellent approximation to the nonlinear wave-making resistance. The basic method is to repeatedly solve Laplace's equation and correct the free surface elevations for the error in the dynamic condition until the solution converges. In this manner, Salvesen and von Kerczek could generate waves near the maximum experimental steepness. Other investigators have generated steady nonlinear flows with unsteady methods using small time steps. Haussling and Van Eeseltine [12], [38], for example, have applied both spectral and finite difference methods to steady flow past a pressure patch.

Unsteady nonlinear methods in two dimensions are of direct interest for ship motion problems, including seakeeping and free-surface effects on maneuvering. One reason for this is that unlike wave-making resistance, which is essentially three-dimensional for practical ship hulls, body motion problems can be reduced to a set of two-dimensional problems by the strip theory approximation, or at high Froude numbers by the slender body approximation. Quasi-analytic and two-dimensional nonlinear methods complement each other in this regard, with the former providing three-dimensional effects and the latter inviscid nonlinear effects. Another reason for the relative importance of two-dimensional methods is that the simplification is useful. Relative to wave-making problems, a large number of calculations are required at various wave lengths and headings to characterize the response of a three-dimensional body in waves; and the problem is compounded if it is nonlinear.

An example of a two-dimensional nonlinear solution related to maneuvering characteristics is the steady force acting on a yawed vertical plate piercing a nonlinear free surface as calculated by Chapman [39]. In this case, slender body theory reduced the nonlinear three-dimensional problem to an unsteady nonlinear two-dimensional problem.

The nonlinear force acting on a heaving rectangular cylinder was computed by Nichols and Hirt [34] with the SOLA-SURF code, a variation of the Marker-and-Cell method. Added mass and damping coefficients were compared with linear theory and with experiment. Chan and Hirt [40] solved the nonlinear problem of the free-surface disturbance and forces generated by the motion of a semisubmerged cylinder. Both a second-order finite difference and a Lagrangian (GALE) method were applied. Lagrangian methods such as GALE or the triangular mesh method developed by Boris, et al. [41] could potentially simulate extreme nonlinear flows, which with strip or slender body theory could be applied to capsizing or ship slamming.

Another class of problems with application to ship hydrodynamics concerns free-surface effects for liquid cargoes or anti-roll tanks. These effects can influence the roll charac-

teristics of ships. A review of numerical methods, including Marker-and-Cell, applicable to the general problem of sloshing in containers is contained in a review paper of von Kerczek [42]. None of these methods have been specifically applied to liquid cargo sloshing, however. Faltinsen [43] has modeled nonlinear sloshing in rectangular containers with a perturbation method and has more recently developed a numerical method applicable to the problem.

#### Summary

A review of recent progress in numerical solutions of free-surface problems in ship hydrodynamics suggests some problems which are likely to be solved in the near future. These are briefly discussed in this section.

Quasi-analytic methods, which combine a linearized free surface with an exact body boundary condition, have already shown their practical value for problems involving three-dimensional ship motion. Future work should soon expand these methods to include the effects of forward speed. It would be useful to combine a three-dimensional quasi-analytic representation for ship motion with an empirical representation for viscous damping and nonlinear hydrostatic terms in a six degree-of-freedom simulation.

Realistic modeling of the wave-making of a translating three-dimensional hull appears to require at least a partial representation of nonlinear free-surface effects. Perturbing about the double hull flow rather than about the free stream appears promising for the wave-making problem for low and moderate Froude numbers. Also, an exact inviscid solution of a nonlinear three-dimensional wave-making problem has been obtained numerically. Further comparisons should be made with experimental wave profiles and wave-making resistance coefficients. Complete agreement between theoretical and experimental resistance depends, in part, on resolving the interaction between wave-making and viscous components of resistance. One simple example is the wetted surface area covered by a bow wave, or at high speeds by a spray sheet.

Two-dimensional nonlinear methods are valuable for simulating nonlinear hydrodynamic effects for large amplitude body motion. Strip theory and slender body theory can extend these methods to practical ship hulls. Thus, while quasi-analytic methods yield three-dimensional effects, nonlinear two-dimensional methods yield nonlinear hydrodynamic effects for extreme motions including possibly capsizing and slamming.

Finally, it should be emphasized that all numerical methods should, if possible, be compared with experimental data over as wide a range as possible. In this way the limitations of the various explicit or implicit assumptions can be evaluated and the simplest valid methods developed.

# References

1. Bai, K.J., "A Localized Finite-Element Method for Steady, Two-Dimensional Free-Surface Flow Problems," First International Conference on Numerical Ship Hydrodynamics, October 1975.
2. Brard, R., "The Representation of a Given Ship Form by Singularity Distribution When the Condition on the Free Surface is Linearized," Journal of Ship Research, Vol. 16, No. 1, pp. 79-92, 1972.
3. Frank, W., "Oscillation of Cylinders in or Below the Free Surface of Deep Fluids," Naval Ship Research and Development Center Report Number 2375, October 1967.
4. Chapman, R.B., "Large Amplitude Transient Motion of Two-Dimensional Floating Bodies," submitted to the Journal of Ship Research.
5. van Dortmerssen, G., "The Motions of a Ship in Shallow Water," Ocean Engineering, Vol. 3, pp. 221-255, 1976.
6. Chang, M.S. and Pien, P.C., "Hydrodynamic Forces on a Body Moving Beneath a Free Surface," First International Conference on Numerical Ship Hydrodynamics, October 1975.
7. Chang, M.S. and Pien, P.C., "Velocity Potentials of Submerged Bodies Near a Free Surface - Application to Wave-Excited Forces and Motions," Eleventh Symposium on Naval Hydrodynamics, March 1976.
8. Chang, M.S., unpublished.
9. Bai, K.J. and Yeung, R.W., "Numerical Solutions to Free Surface Flows," Tenth Symposium on Naval Hydrodynamics, June 1974.
10. Yeung, R.W., "A Hybrid Integral-Equation Method for Time-Harmonic Free-Surface Flow," First International Conference on Numerical Ship Hydrodynamics, October 1975.
11. Harten, A., "An Efficient Differential-Integral Equation Technique for Time-Dependent Flows with a Free Surface," First International Conference on Numerical Ship Hydrodynamics, October 1975.
12. Haussling, H.J. and Van Eseltine, R.T., "A Combined Spectral Finite-Difference Method for Linear and Nonlinear Water Wave Problems," Naval Ship and Research Development Center Report Number 4580, 1974.
13. Haussling, H.J. and Van Eseltine, R.T., "Unsteady Air Cushion Vehicle Hydrodynamics Using Fourier Series," Journal of Ship Research, Vol. 20, No. 2, pp. 79-84, 1976.
14. Giesing, J.P. and Smith, A.M.O., "Potential Flow About Two-Dimensional Hydrofoils," Journal of Fluid Mechanics, Vol. 28, Part 1, pp. 113-129, 1967.
15. Chen, H.S. and Mei, C.C., "Calculation of Two-Dimensional Ship Waves By a Hybrid Element Method Based on Variational Principles," First International Conference on Numerical Ship Hydrodynamics, October 1975.
16. Breslin, J.P. and Eng, K., "Calculation of the Wave Resistance of a Ship Represented by Sources Distributed Over the Hull Surface," International Seminar on Theoretical Wave-Resistance, University of Michigan, 1963.
17. Hess, J.L. and Smith, A.M.O., "Calculation of Nonlifting Potential Flow About Arbitrary Three-Dimensional Bodies," Journal of Ship Research, Vol. 8, No. 2, pp. 22-44, September 1973.
18. Adey, B., "Calculation of the Streamlines About a Ship Assuming a Linearized Free-Surface Boundary Condition," Journal of Ship Research, Vol. 17, No. 3, pp. 140-146, September 1973.
19. Adey, B., "Fluid Flow Around a Ship's Hull," First International Conference on Numerical Ship Hydrodynamics, October 1975.
20. Bessho, M., "Line Integral, Uniqueness and Diffraction of Wave in the Linearized Theory," International Seminar on Wave-Resistance, Tokyo, 1976.
21. Wehausen, J.V., "Use of Lagrangian Coordinates for Ship Wave Resistance (First- and Second-Order Thin Ship Theory)," Journal of Ship Research, Vol. 13, No. 1, pp. 12-22, March 1969.
22. Yim, B., "Higher Order Wave Theory of Ships," Journal of Ship Research, Vol. 12, No. 4, pp. 237-245, December 1968.
23. Eggers, K.W.H. and Choi, H.S., "On the Calculation of Stationary Ship Flow Components," First International Conference on Numerical Ship Hydrodynamics, October 1975.
24. Noblesse, F., "A Perturbation Analysis of the Wavemaking of a Ship with an Interpretation of Guilloton's Method," Journal of Ship Research, Vol. 19, No. 3, pp. 140-148, September 1975.
25. Dagan, G., "A Method of Computing Nonlinear Wave Resistance of Thin Ships by Coordinate Straining," Vol. 19, No. 3, pp. 149-154, September 1975.
26. Gadd, G.E., "Wave Resistance Calculations by Guilloton's Method," Transactions Royal Institution of Naval Architects, Vol. 115, pp. 377-392, 1973.
27. Hong, Y.S., "Numerical Calculation of Second-Order Wave Resistance," Journal of Ship Research, Vol. 21, No. 2, June 1977.

28. Newman, J.N., "Linearized Wave Resistance Theory," International Seminar on Wave Resistance, Tokyo, 1976.
29. Baba, E., "Blunt Bow Forms and Wave Breaking," First Ship Technology and Research Symposium, August 1975.
30. Dawson, C.W., unpublished.
31. Chan, R.K.C., unpublished.
32. Chan, R.K.C. and Stuhmiller, J.H., "Numerical Solution of Unsteady Ship Wave Problems," Eleventh Symposium on Naval Hydrodynamics, March 1976.
33. Gadd, G.E., "A Method of Computing the Flow and Surface Wave Pattern Around Full Forms," Transactions Royal Institution of Naval Architects, 1976.
34. Nichols, B.D. and Hirt, C.W., "Methods for Calculating Multi-Dimensional Transient, Free Surface Flows Past Bodies," First International Conference on Numerical Ship Hydrodynamics, October 1975.
35. von Kerczek, C.H. and Salvesen, N., "Numerical Solutions of Two-Dimensional Nonlinear Wave Problems," Tenth Symposium on Naval Hydrodynamics, June 1974.
36. Salvesen, N. and von Kerczek, C.H., "Numerical Solutions of Two-Dimensional Nonlinear Body-Wave Problems," First International Conference on Numerical Ship Hydrodynamics, October 1975.
37. Salvesen, N. and von Kerczek, C.H., "Comparison of Numerical and Perturbation Solutions of Two-Dimensional Nonlinear Water-Wave Problems," Journal of Ship Research, Vol. 20, No. 3, pp. 160-170, September 1976.
38. Haussling, H.J. and Van Eseltine, R.T., "Finite-Difference Methods for Transient Potential Flows with Free Surfaces," First International Conference on Numerical Ship Hydrodynamics, October 1975.
39. Chapman, R.B., "Free-Surface Effects for Yawed Surface-Piercing Plates," Journal of Ship Research, Vol. 20, No. 3, pp. 125-136, September 1976.
40. Chan, R.K.C. and Hirt, C.W., "Two-Dimensional Calculations of the Motion of Floating Bodies," Tenth Symposium on Naval Hydrodynamics, June 1974.
41. Boris, J., Hain, K.L., and Fritts, M.J., "Free Surface Hydrodynamics Using a Lagrangian Triangular Mesh," First International Conference on Numerical Ship Hydrodynamics, October 1975.
42. von Kerczek, C.H., "Numerical Solution of Naval Free-Surface Hydrodynamics Problems," First International Conference on Numerical Ship Hydrodynamics, October 1975.
43. Faltinsen, O.M., "A Nonlinear Theory of Sloshing in Rectangular Containers," Journal of Ship Research, Vol. 18, No. 4, pp. 224-241, December 1974.

## NUMERICAL EVALUATION OF A WAVE-RESISTANCE THEORY FOR SLOW SHIPS

E. Baba and M. Hara  
Nagasaki Technical Institute,  
Mitsubishi Heavy Industries, Ltd.  
1-1 Akunoura-machi  
Nagasaki, Japan

### Abstract

A procedure is presented for the numerical calculation of wave resistance of conventional ship forms. Wave-resistance theory used in the present calculation takes account of the non-linear effect on the free-surface condition. Because of this a remarkable attenuation of the humps and hollows of wave resistance curve is attained in the practical speed range of conventional commercial ships. Taking a semisubmerged sphere as an example, each stage of numerical calculations is examined by comparing with the analytical values. Finally wave resistance of conventional ship forms is calculated and compared with experimental values. Within a practically acceptable order of magnitude wave resistance can be estimated by the present theory.

### 1. Introduction

A wave resistance theory which takes account of the nonlinear effect on the free-surface condition in low speeds has been developed by Baba and Takekuma [1,2]. In this paper a procedure is presented for the numerical calculation of conventional ship forms based on this theory.

The theory is an extension of Ogilvie's two-dimensional low-speed wave resistance theory [3] to the three-dimensional bodies piercing the free surface. It is a characteristic of the theory that the double-body velocity potential is used as the zero-order solution. As the next-order solution a surface-layer velocity potential which represents a wave motion is determined in such a way that the sum of both velocity potentials satisfies a free-surface condition. The free-surface condition used in the present paper is a linear equation for the surface-layer potential. However, products of derivatives of zero-order potential are included. Therefore the coefficients for the equation are dependent on space variables.

In section 2 an outline of the present theory is given. It is then shown that wave resistance derived from the present theory consists of three parts. One is due to the singularity distributions over the body surface, the second is due to the singularity distributions around the intersection between the body and the still-water surface (the so called line-integral term), and the third is due to the free-surface disturbance expressed in terms of products of derivatives of double-body potential. The last one is considered as the nonlinear effect on the free-surface condition.

In section 3 a quantitative discussion on the characteristics of the present theory is given by applying the theory to a vertical circular cylinder piercing the free surface. It is then shown that the contribution from the singularity distributions on the body surface is cancelled out by the lower-order terms of the contribution from the line-integral term. The remaining higher-order terms are the same order of magnitude as that of the third part of the free-surface disturbance. It is further shown that this third part contributes especially to the reduction of transverse-wave components. As a result, humps and hollows of the wave resistance coefficient curve are attenuated remarkably.

In section 4 a procedure to calculate wave resistance of conventional ship forms is explained. In the computation an asymptotic expression of the amplitude function in low-speed limit is used. Necessary quantities for the computation are double-body velocity components around the load waterline. They can be obtained by finite-element method such as the one developed by Hess and Smith for nonlifting bodies [4]. Details of numerical calculation of wave resistance are described. In the procedure validity of the numerical calculation is examined by applying the computer program to a semisubmerged sphere whose wave resistance is obtained analytically by the present theory.

In section 5 several examples of wave resistance calculations for conventional ship forms are shown and compared with wave resistance determined by towing tests.

## 2. Outline of the theory for slow ships

Taking a rectangular coordinate system fixed in the body with the origin on the still water surface, we set x-axis directed to the uniform flow  $U$  and z-axis directed upwards as shown in Fig. 1. The total velocity potential is defined:

$$\phi_T(x, y, z) = \phi(x, y, z),$$

where  $\phi_T$  is the double-body potential obtained from the rigid-wall problem.  $\phi$  is the surface-layer velocity potential which represents a wave motion.

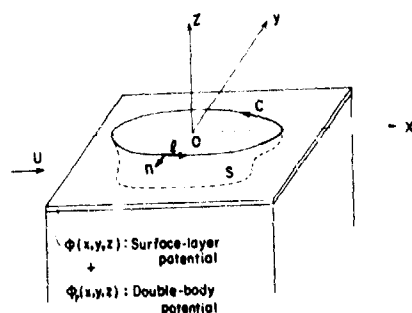


Fig. 1. Coordinate system.

The boundary-value problem presented by Baba and Takekuma[1] for the surface-layer velocity potential  $\phi(x, y, z)$  is written as

$$0 = \phi_{xx}(x, y, z) + \phi_{yy}(x, y, z) + \phi_{zz}(x, y, z), \quad z < 0, \quad (1)$$

$$\frac{1}{g} \left[ \phi_{rx}(x, y, 0) \frac{\partial}{\partial x} + \phi_{ry}(x, y, 0) \frac{\partial}{\partial y} \right] \phi(x, y, z) + \phi_z(x, y, z) = D(x, y), \quad \text{on } z = 0, \quad (2)$$

where  $g$  is the acceleration of gravity,  $\phi_{rx}(x, y, 0)$ ,  $\phi_{ry}(x, y, 0)$  are the velocity components at the still-water surface.

$$D(x, y) = \frac{\partial}{\partial x} \left[ \phi_{rx}(x, y, 0) \zeta_r(x, y) \right] + \frac{\partial}{\partial y} \left[ \phi_{ry}(x, y, 0) \zeta_r(x, y) \right], \quad (3)$$

$$\zeta_r(x, y) = \frac{1}{2g} \left[ U^2 - \phi_{rx}^2(x, y, 0) - \phi_{ry}^2(x, y, 0) \right]. \quad (4)$$

In equations (1) and (2),  $z = 0$  corresponds to the free-surface elevation expressed by the term  $\zeta_r(x, y)$ . Besides the equations (1) and (2), the radiation condition should be satisfied by  $\phi(x, y, z)$ . It should be noted further that in the present theory the surface-layer potential  $\phi(x, y, z)$  does not satisfy the body boundary condition. The zero-order potential  $\phi_T(x, y, z)$  alone satisfies the condition. Recently Newman[5] derived independently the same boundary-value problem for slow ships as the equations (1) and (2). The details of the derivation of the above boundary-value problem and the following results are found in the reference[6].

An asymptotic solution  $\phi(x, y, z)$  in the low-speed limit is obtained as

$$\begin{aligned} \phi(x, y, z) = & \frac{1}{2\pi^2} \iint_{-\infty}^{\infty} dx' dy' D(x', y') \\ & \times \int_{-\pi/2}^{\pi/2} d\theta k_0(x, y, \theta) \left\{ \int_{-\infty}^{\infty} dk \frac{e^{kz} \cos(k\omega)}{k_0(x, y, \theta) - k} \right. \\ & + \frac{1}{2\pi} \iint_{-\infty}^{\infty} dx'' dy'' D(x'', y'') \\ & \times \int_{-\pi/2}^{\pi/2} d\theta k_0(x, y, \theta) e^{zk_0(x, y, \theta)} \sin[k_0(x, y, \theta)\omega] \end{aligned} \quad (5)$$

where

$$k_0(x, y, \theta) = g / \left[ \phi_{rx}(x, y, 0) \cos \theta + \phi_{ry}(x, y, 0) \sin \theta \right]^2, \quad (6)$$

$$\omega = (x - x') \cos \theta + (y - y') \sin \theta. \quad (7)$$

Wave resistance derived from the velocity potential  $\phi(x, y, z)$  is expressed as

$$R_w = \rho U^2 \int_{-\pi/2}^{\pi/2} |A(\theta)|^2 \cos^3 \theta d\theta, \quad (8)$$

where  $\rho$  is the density of water,  $A(\theta)$  is the amplitude function:

$$A(\theta) = -\frac{v}{\pi U} \sec^3 \theta \int_{-\infty}^{\infty} dx dy D(x, y) \times \exp[i v \sec^2 \theta (x \cos \theta + y \sin \theta)], \quad (9)$$

where  $v = g/U^2$ .

It is a characteristic of the present wave-resistance formula that the amplitude function is expressed as an integral of disturbance  $D(x, y)$  over the free surface. Recently Maruo has derived independently the same wave-resistance formula as (9) and (8) [7].

The disturbance  $D(x, y)$  is rewritten as the sum of two parts:

$$D(x, y) = -\frac{1}{v} \phi_{xx}(x, y, 0) + N(x, y, 0), \quad (10)$$

where  $\phi$  is the perturbation velocity potential of the double body, i.e.

$$\phi(x, y, z) = \phi_F(x, y, z) + \phi_A,$$

$$N(x, y, 0) = -\frac{U}{2g} \frac{\partial}{\partial x} (\phi_x^2 + \phi_y^2) - \phi_x \left[ \frac{U}{g} \phi_{xx} + \frac{1}{2g} \frac{\partial}{\partial x} (\phi_x^2 + \phi_y^2) \right] - \phi_y \left[ \frac{U}{g} \phi_{xy} + \frac{1}{2g} \frac{\partial}{\partial y} (\phi_x^2 + \phi_y^2) \right] + \frac{1}{2g} \phi_{zz} [2U \phi_x + \phi_x^2 + \phi_y^2], \quad z = 0. \quad (11)$$

It should be noted that  $N(x, y, 0)$  is expressed in terms of products of derivatives of the perturbation potential. Within the framework of the linearized theory, this term is usually neglected as higher order quantities, as done by Guevel et al. [8]. In the present theory, however, it is shown that the contribution from  $N(x, y, 0)$  plays an important role in the wave resistance at low speeds. The present authors consider that this term represents a nonlinear effect on the free-surface condition.

Substituting (10) into (9), we have

$$A(\theta) = -\frac{1}{\pi U} \sec^3 \theta \int_{-\infty}^{\infty} dx dy \phi_{xx}(x, y, 0) \times \exp[i v \sec^2 \theta (x \cos \theta + y \sin \theta)] - \frac{v}{\pi U} \sec^3 \theta \int_{-\infty}^{\infty} dx dy N(x, y, 0) \times \exp[i v \sec^2 \theta (x \cos \theta + y \sin \theta)]. \quad (12)$$

Excluding the cross section between the body and the still water surface from

the integral range, and integrating by parts, the first term of (12) is written:

$$-\frac{1}{\pi U} \sec^3 \theta \oint_c dy \phi_x(x, y, 0) \times \exp[i v \sec^2 \theta (x \cos \theta + y \sin \theta)] + \frac{1}{\pi U} \sec^3 \theta (i v \sec \theta) \oint_c dy \phi(x, y, 0) \times \exp[i v \sec^2 \theta (x \cos \theta + y \sin \theta)] + \frac{1}{\pi U} \sec^3 \theta (i v \sec \theta)^2 \int_{-\infty}^{\infty} dy dx \phi(x, y, 0) \times \exp[i v \sec^2 \theta (x \cos \theta + y \sin \theta)], \quad (13)$$

where  $c$  is the curve of intersection between the body and the still water surface.

When a body is expressed by surface source distribution  $\sigma(x, y, z)$  and normal doublet distribution  $\mu(x, y, z)$  so as to give zero-value of perturbation potential inside the body, we have the following relations:

$$\phi_x(x, y, 0) = 4\pi \left[ \sigma(x, y, 0) \cos(\phi_x, \vec{n}) + \frac{\partial \mu}{\partial l} \sin(\phi_x, \vec{n}) \right] \text{ on } c,$$

$$\phi(x, y, 0) = -4\pi \mu(x, y, 0) \text{ on } c,$$

$$\phi(x, y, z) = - \iint_S \sigma(x', y', z') \left[ \frac{1}{r} + \frac{1}{r'} \right] dS - \iint_S \mu(x', y', z') \frac{\partial}{\partial n} \left[ \frac{1}{r} + \frac{1}{r'} \right] dS, \quad (14)$$

where  $n$  is the outward normal to the surface at the intersection  $c$ , and  $l$  is the tangent.  $S$  is the surface of the submerged part of the body. Here, a body is considered which has a vertical hull surface at the intersection  $c$ . Also,

$$r = [(x-x')^2 + (y-y')^2 + (z-z')^2]^{1/2}, \\ r' = [(x-x')^2 + (y-y')^2 + (z+z')^2]^{1/2}.$$

Further, we have a relation

$$\int_{-\infty}^{\infty} dx dy \left[ \frac{1}{r} + \frac{1}{r'} \right]_{z=0} \times \exp[i v \sec^2 \theta (x \cos \theta + y \sin \theta)] = \frac{4\pi}{v \sec^2 \theta} \exp[i v \sec^2 \theta (x' \cos \theta + y' \sin \theta)].$$

Thus we have

$$A(\theta) = A_S(\theta) + A_L(\theta) + A_F(\theta), \quad (15)$$

where

$$A_S(\theta) = \frac{4v}{U} \sec^3 \theta \iint_S dS \sigma(x, y, z) \times \exp[v \sec^2 \theta \{z + i(x \cos \theta + y \sin \theta)\}] + \frac{4v}{U} \sec^3 \theta \iint_S dS \mu(x, y, z) \frac{\partial}{\partial n} \times \exp[v \sec^2 \theta \{z + i(x \cos \theta + y \sin \theta)\}],$$

$$A_L(\theta) = -\frac{4}{U} \sec^3 \theta \oint_C dy [\sigma(x, y, 0) \cos(\vec{\alpha}, \vec{n}) + i v \sec \theta \mu(x, y, 0) + \frac{\partial \mu}{\partial l} \sin(\vec{\alpha}, \vec{n})] \times \exp[i v \sec^2 \theta (x \cos \theta + y \sin \theta)],$$

$$A_F(\theta) = -\frac{v}{\pi U} \sec^3 \theta \iint_{-\infty}^{\infty} dx dy N(x, y, 0) \times \exp[i v \sec^2 \theta (x \cos \theta + y \sin \theta)]. \quad (16)$$

It is understood that the amplitude function consists of three parts. One is due to the surface singularity distributions over the body surface. This term gives the conventional wave-resistance formula which was derived by Havelock for submerged bodies [9]. The second is due to the singularity distributions around the intersection between the body and the still-water surface. This term is the so called line-integral term. The third is due to the free-surface disturbance expressed in terms of products of derivatives of double-body potential.

### 3. Wave resistance of simple forms

In order to evaluate numerically the characteristics of the present theory, the above mentioned three parts of the amplitude function are calculated for a vertical circular cylinder piercing the free surface.

The density of source and doublet distributions for a vertical circular cylinder of radius  $a$  are given as follows:

$$\sigma(x, y, z) = -\frac{Ux}{4\pi a}, \quad \mu(x, y, z) = -\frac{Uy}{4\pi a}. \quad (17)$$

The double-body potential  $\phi(x, y, z)$  for a circular cylinder is written as

$$\phi(x, y, z) = \frac{Ua^2 x}{x^2 + y^2}, \quad x^2 + y^2 \geq a^2. \quad (18)$$

Substituting (17) into  $A_S(\theta)$  and  $A_L(\theta)$  of (16), we have

$$A_S(\theta) = -2ia J_1\left(-\frac{1}{2F_n^2} \sec^2 \theta\right) - \frac{ia}{2F_n^2} \sec^2 \theta \left[ J_0\left(-\frac{1}{2F_n^2} \sec^2 \theta\right) - J_2\left(-\frac{1}{2F_n^2} \sec^2 \theta\right) \right], \quad (19)$$

$$A_L(\theta) = 2ia J_1\left(-\frac{1}{2F_n^2} \sec^2 \theta\right) + \frac{ia}{2F_n^2} \sec^2 \theta \left[ J_0\left(-\frac{1}{2F_n^2} \sec^2 \theta\right) - J_2\left(-\frac{1}{2F_n^2} \sec^2 \theta\right) \right] + 8ia F_n^2 \sec \theta \cos 3\theta J_2\left(-\frac{1}{2F_n^2} \sec^2 \theta\right) - 32ia F_n^4 \cos \theta \cos 3\theta J_1\left(-\frac{1}{2F_n^2} \sec^2 \theta\right), \quad (20)$$

where  $F_n = U/\sqrt{2ga}$ , and  $J_0, J_1, J_2$  are the Bessel functions of the first kind. The first term of (19) is the contribution from the surface source distribution, and the second is from doublet distribution.

It is observed that the amplitude function due to the surface singularities  $A_S(\theta)$  is cancelled out by the first two terms of the amplitude function due to the line integral term  $A_L(\theta)$ . This fact was first pointed out by Brard within the framework of the linearized theory [10].

The asymptotic expression of the sum of  $A_S(\theta)$  and  $A_L(\theta)$  is written in the low speed limit:

$$A_S(\theta) + A_L(\theta) = i \frac{16a}{\sqrt{\pi}} F_n^3 \cos 3\theta \times \cos\left(-\frac{1}{2F_n^2} \sec^2 \theta - \frac{\pi}{4}\right) + O(F_n^4). \quad (21)$$

Next, substituting (18) into (11), we have  $N(x, y, 0)$  as follows:



$$N(x, y, 0) = 4U F_n^2 \left( \frac{2a^5 x}{r^4} - \frac{a^7 x}{r^6} \right)$$

$$\text{for } r = \sqrt{x^2 + y^2} \geq a.$$

From  $A_F(\theta)$  of (16) we then have

$$\begin{aligned} A_F(\theta) &= -4i \sec^2 \theta \int_a^\infty \left( \frac{2a^4}{r^4} - \frac{a^6}{r^6} \right) \\ &\quad \times J_1(vr \sec^2 \theta) dr \\ &= -i \frac{16a}{\sqrt{\pi}} F_n^3 \cos \theta \cos \left( \frac{\sec^2 \theta}{2F_n^2} - \frac{\pi}{4} \right) \\ &\quad + O(F_n^5). \end{aligned} \quad (22)$$

It is thus shown that in the low-speed limit  $A_S(\theta) + A_L(\theta)$  is of same order of magnitude as that of  $A_F(\theta)$ . Fig. 2 shows a comparison of the asymptotic values of  $\bar{A}_S(\theta) + \bar{A}_L(\theta)$  and  $\bar{A}_F(\theta)$  at  $F_n = 0.20$ , where

$$\bar{A}_S(\theta) = A_S(\theta)/2a, \quad \bar{A}_L(\theta) = A_L(\theta)/2a,$$

$$\bar{A}_F(\theta) = A_F(\theta)/2a.$$

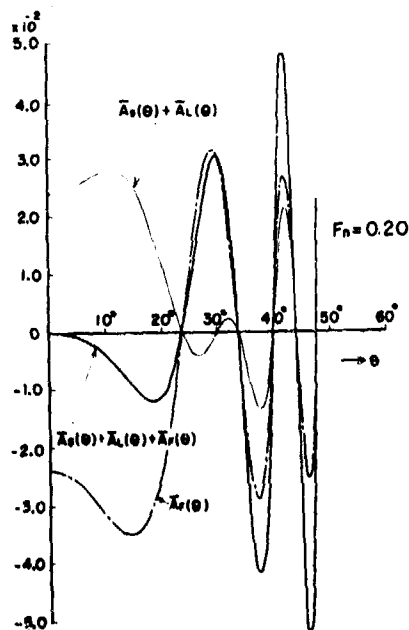


Fig. 2. Comparison of amplitude functions of vertical circular cylinder in low speeds.

From the figure it is found that  $A_F(\theta)$  contributes especially to the reduction of transverse wave component (small  $\theta$ -values). As the result, humps and hollows of the wave-resistance curve are attenuated remarkably.

In the low-speed limit wave resistance due to the sum of  $A_S(\theta)$  and  $A_L(\theta)$  is obtained by means of stationary phase in (8):

$$\begin{aligned} C_w &= \frac{R_w}{\frac{1}{2}\rho U^2 (2a)^2} \\ &= \frac{6656}{315} F_n^4 + 32\sqrt{\pi} F_n^7 \sin\left(\frac{1}{F_n^2} + \frac{\pi}{4}\right) \\ &\quad + O(F_n^6). \end{aligned} \quad (23)$$

On the other hand, the wave resistance due to the sum of three parts  $A_S(\theta)$ ,  $A_L(\theta)$  and  $A_F(\theta)$  is obtained as

$$C_w = \frac{8192}{315} F_n^4 + O(F_n^6). \quad (24)$$

Fig. 3 shows a comparison of the wave resistance curves for both cases. From this figure it is found that  $A_F(\theta)$ , which represents the nonlinear effect on the free-surface condition, plays an important role on the attenuation of humps and hollows of wave-resistance curve in low-speed range.

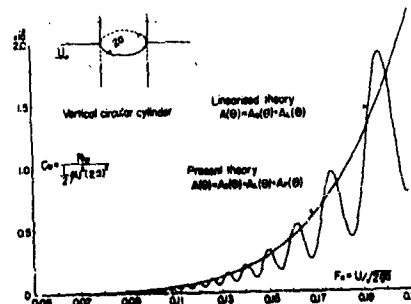


Fig. 3. Comparison of  $C_w$ -values of vertical circular cylinder.

An additional example of calculation is shown in Fig. 4, where the wave resistance curves of a semisubmerged sphere are compared. The wave resistance coefficient obtained from the sum of two parts  $A_S(\theta)$  and  $A_L(\theta)$  is given as follows:

$$C_w = \frac{224}{5} F_n^6 + 72\sqrt{\pi} F_n^7 \sin\left(\frac{1}{F_n^2} + \frac{\pi}{4}\right) + O(F_n^8). \quad (25)$$

On the other hand, the wave-resistance coefficient obtained from the sum of three parts  $A_S(\theta)$ ,  $A_L(\theta)$  and  $A_F(\theta)$  for the semisubmerged sphere is given by

$$C_w = \frac{633}{70} F_n^6 + \frac{9}{2}\sqrt{\pi} F_n^7 \sin\left(\frac{1}{F_n^2} + \frac{\pi}{4}\right) + O(F_n^8). \quad (26)$$

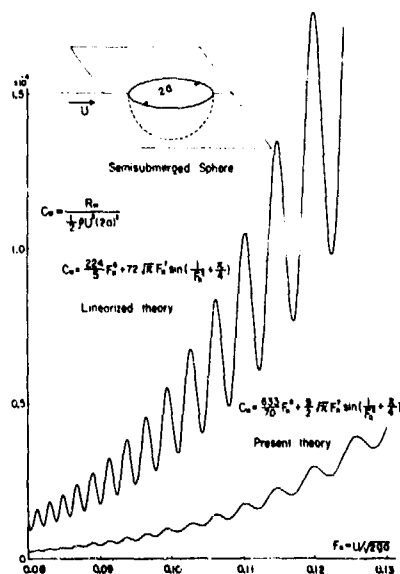


Fig.4. Comparison of  $C_w$ -values of semisubmerged sphere.

In this case, not only an attenuation of humps and hollows but also a large reduction of the basic term which is of order  $F_n^6$  is attained by the addition of the amplitude function  $A_F(\theta)$ . The details of the derivation of (25) and (26) are explained in Appendix A.

#### 4. Numerical method to calculate wave resistance

In the previous sections analytical studies are given on the contribution of each term of amplitude functions to the wave resistance. In the present section a procedure is explained to calculate numerically the wave resistance of arbitrary forms. For convenience of computation, the expression of amplitude function(9) is used directly instead of the expression (15).

By the partial integration with respect to  $x$  in (9), an asymptotic expression of the amplitude function in low-speed limit is obtained as a line integral around the intersection of the body and the still-water surface:

$$A(\theta) = -i \frac{\sec^2 \theta}{\pi l} \oint_C dy D(x, y) \times \exp[i v \sec^2 \theta (x \cos \theta + y \sin \theta)]. \quad (27)$$

In this calculation the cross section between the body and the still-water surface is excluded from the integral range in (9).

When the equation of the intersection is expressed by the following relations:

$$\frac{x}{L} = \frac{1}{2} \cos \beta, \quad \frac{y}{L} = \sum_{n=1}^{\infty} B_n \sin(n\beta),$$

where  $L$  is the length of a body and  $B_n$  are the Fourier coefficients, the amplitude function is rewritten:

$$\frac{A(\theta)}{L} = -i \frac{\sec^2 \theta}{2\pi} F_n^2 \int_0^{2\pi} d\beta F(\beta) \times \exp\left[i \frac{\sec^2 \theta}{2F_n^2} \psi(\beta, \theta)\right], \quad (28)$$

where  $F_n = U/\sqrt{gL}$ ,

$$\psi(\beta, \theta) = \cos \beta \cos \theta + \left(2 \sum_{n=1}^{\infty} B_n \sin n\beta\right) \sin \theta,$$

$$F(\beta) = v \frac{dp}{d\beta} - p w_z \frac{dy}{dz},$$

$$p(\beta) = 1 - u^2 - v^2,$$

$$u = \phi_x(x, y, 0)/U, \quad v = \phi_y(x, y, 0)/U,$$

$$w_z = \phi_{zz}(x, y, 0) L/U.$$

The amplitude function can be calculated by use of the velocity components around the load waterline. The wave resistance is then calculated by (8).

Taking a semisubmerged sphere as an example, the validity of each stage of numerical calculations is examined as follows. First, the integration with respect to  $\beta$  is carried out in (28) by use of the exact expression of  $F(\beta)$  for a semisubmerged sphere [2,6]:

$$F(\beta) = \frac{3}{2} \cos^2 \beta \left( \frac{9}{4} \sin^2 \beta + 1 \right). \quad (29)$$

For this numerical calculation Simpson's rule is applied with the interval  $\Delta\theta = \pi F n^2 / 47$ . At  $\theta = 75^\circ$ , this interval provides more than 15 ordinates in a range from one peak to the next peak of the highly oscillating integrand. Next, the integration with respect to  $\theta$  is carried out in the wave resistance integral (8). In this computation zero-points of  $A(\theta)$  with respect to  $\theta$  are searched first and then each interval from one zero-point to the next zero-point is numerically integrated by Simpson's rule in such a way that the number of ordinates in one interval is not less than 10. It is confirmed that the value of wave resistance usually converges to a certain value when the upper limit of the integral range is close to  $\theta = 75^\circ$  as shown in Fig. 5; an example of calculation on the semisubmerged sphere.

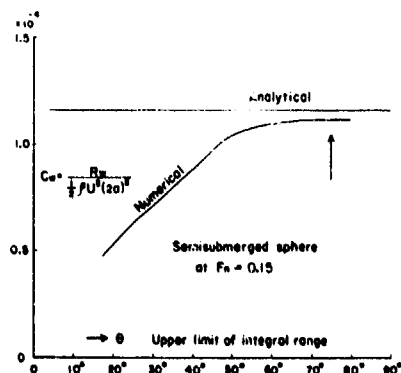


Fig. 5. Variation of  $C_w$ -values with respect to the upper limit of the integral range.

In Table 1 the computed wave-resistance values are shown compared with the analytical values which are obtained by the method of stationary phase with respect to  $\beta$  in (28) and  $\theta$  in (8) for a semisubmerged sphere as expressed by (26) in the previous section.

Table 1. Evaluation of numerical integration with respect to  $\beta$  and  $\theta$ .

Froude number	$C_{w1}$ Numerical	$C_{w2}$ Analytical	$C_{w1}/C_{w2}$
0.15	0.116463-3	0.115927-3	1.005
0.20	0.635963-3	0.640767-3	0.993
0.25	0.189489-2	0.177887-2	1.065

This result shows the validity of the numerical integration for practical use.

In the above mentioned examination of the numerical integration, the exact expression of  $F(\beta)$  is used. In practice, however,  $F(\beta)$  for an arbitrary body has to be obtained numerically.

Representing the body by finite number of surface elements on the body, velocity components at the null point of each surface element can be obtained. Taking again the semisubmerged sphere as an example, computed values of  $v(\beta)$ ,  $p(\beta)$ ,  $dp/d\beta$ ,  $w_z(\beta)$ ,  $dy/d\beta$  and  $F(\beta)$  are compared with the exact values at the load waterline:

$$\begin{aligned} v(\beta) &= -\frac{3}{2} \cos \beta \sin \beta, & w_z(\beta) &= -3 \cos \beta, \\ p(\beta) &= 1 - \frac{9}{4} \sin^2 \beta, & \frac{dy}{d\beta} &= \frac{1}{2} \cos \beta, \\ \frac{dp(\beta)}{d\beta} &= -\frac{9}{2} \sin \beta \cos \beta. \end{aligned}$$

In this computation, half of the surface of submerged part of the sphere is approximated by  $18 \times 18$  surface elements. The source density is assumed constant over each of the elements. Table 2 shows the comparison of analytical and numerical values.

For the calculation of  $dp/d\beta$ ,  $p(\beta)$  is approximated first by a set of parabolic curves determined by  $p(\beta)$  at the null points of surface elements at the load waterline. Then  $dp/d\beta$  is obtained by a curve fitting through the derivatives of  $p(\beta)$  which is approximated by the parabolic curves. For the calculation of  $w_z(\beta)$  in the present paper,  $w(\beta)$  is obtained first at the point which is a little apart from the surface element closest to the load waterline. The distance from the load waterline which is suitable for calculation was investigated in the trial and error process. As the result, the most reliable values for  $w_z$  were found in this case for the point which is 3% of the half breadth of the body in  $y$ -direction from the upper edge  $E$  and 3% of the draft of the body in negative  $z$ -direction ( $=\delta$ ) from the  $z=0$  level as shown in Fig. 6.  $w_z(\beta)$  is then determined by dividing the value of  $w(\beta)$  by  $\delta$ .

In practice, a rather small number, say

Table 2. Comparison of numerical and analytical values of  $v(\beta)$ ,  $p(\beta)$ ,  $dp/d\beta$ ,  $w_2(\beta)$ ,  $dy/d\beta$ , and  $F(\beta)$ .

$\beta$	$v(\beta)$		$p(\beta)$		$dp/d\beta$	
	Numerical	Analytical	Numerical	Analytical	Numerical	Analytical
0.14245	-0.19796	-0.21080	0.96319	0.95465	-0.58765	-0.63239
0.27564	-0.40290	-0.39283	0.82567	0.83333	-1.2215	-1.1785
0.44442	-0.58736	-0.58226	0.57906	0.58410	-1.6852	-1.7468
0.61628	-0.70839	-0.70751	0.25025	0.24830	-2.0385	-2.1225
0.78920	-0.74859	-0.74998	-0.12401	-0.13355	-2.1624	-2.2499
0.96259	-0.70103	-0.70340	-0.49861	-0.51539	-2.0299	-2.1102
1.1362	-0.57045	-0.57286	-0.82839	-0.85112	-1.6548	-1.7186
1.3100	-0.37198	-0.37370	-1.0735	-1.1004	-1.0807	-1.1211
1.4839	-0.12913	-0.12969	-1.2040	-1.2331	-0.37549	-0.38907

$\beta$	$w_2(\beta)$		$dy/d\beta$		$F(\beta)$	
	Numerical	Analytical	Numerical	Analytical	Numerical	Analytical
0.14245	-2.8776	-2.9696	0.49269	0.49494	1.4778	1.5364
0.27564	-2.8769	-2.8868	0.47999	0.48113	1.6323	1.6204
0.44442	-2.7145	-2.7086	0.45056	0.45143	1.6980	1.7313
0.61628	-2.4527	-2.4481	0.40732	0.40802	1.6941	1.7497
0.78920	-2.1115	-2.1132	0.35165	0.35221	1.5267	1.5879
0.96259	-1.7031	-1.7142	0.28527	0.28570	1.1808	1.2319
1.1362	-1.2500	-1.2631	0.21021	0.21052	0.72631	0.75816
1.3100	-0.76229	-0.77355	0.12874	0.12893	0.29665	0.30920
1.4839	-0.25609	-0.26036	0.43357-1	0.43394-1	0.35119-1	0.36527-1

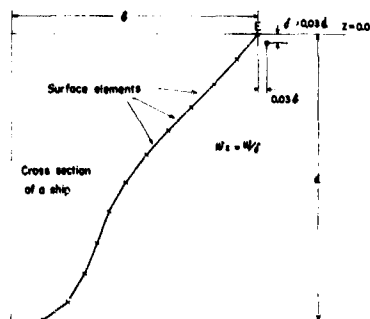


Fig. 6. Calculation of  $w_2$ -values.

350, are used from the economical view point. Therefore, the present authors consider that such a method mentioned above is necessary in determining the values of  $w_2(\beta)$  efficiently. It is needless to say that the suitable distance of the point where  $w(\beta)$  is calculated should be searched in accordance with the numbers, the size and the shape of the surface elements.

Finally, Table 3 shows a comparison of wave resistance obtained by analytical method with the wave resistance obtained numerically in all the steps of calculations.

Table 3. Comparison of wave resistance numerical and analytical.

Froude number	$Cw_3$	$Cw_2$	$Cw_3/Cw_2$
	Numerical	Analytical	
0.15	0.111583-3	0.115927-3	0.963
0.16	0.164280-3	0.169636-3	0.968
0.17	0.188316-3	0.194107-3	0.970
0.18	0.300873-3	0.318895-3	0.940
0.19	0.406422-3	0.410392-3	0.990
0.20	0.605154-3	0.640767-3	0.944
0.21	0.613495-3	0.632632-3	0.970
0.22	0.114399-2	0.112825-2	1.014
0.23	0.146388-2	0.154081-2	0.950
0.24	0.135996-2	0.149167-2	0.912
0.25	0.178262-2	0.177887-2	1.002

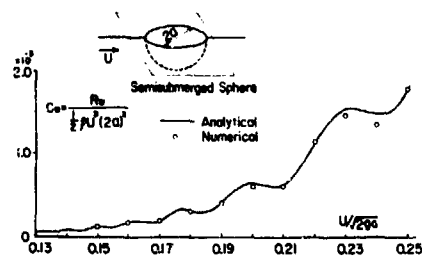


Fig. 7. Comparison of numerical and analytical  $C_w$ -values of semisubmerged sphere.

Fig. 7 shows a wave-resistance curve obtained analytically compared with the values obtained numerically. From this study it is claimed that the present procedure for numerical calculation of wave resistance in low speeds has sufficient accuracy for practical use.

#### 5. Calculation of wave resistance of conventional ship forms

In this section results of numerical calculation of wave resistance of five different ship forms are shown. Table 4 shows the particulars of the ship forms.

Table 4. Particulars of ship forms and numbers of surface elements.

M.No.	$C_b$	L/B	B/d	Surface elements
1719, 20	0.4444	10.000	1.600	$30 \times 10$
1955	0.5576	6.720	2.581	$27 \times 18$
2330C	0.7391	6.770	2.381	$27 \times 19$
1360	0.7764	6.966	2.510	$23 \times 12$
1914B	0.8624	6.358	2.561	$23 \times 14$

The first example of the calculations is for Wigley's parabolic forms M.1719, and M.1720 which are geometrically similar and defined by

$$y = 2B \left[ \left( \frac{1}{L} \right)^2 - \left( \frac{x}{L} \right)^2 \right] \left[ 1 - \left( \frac{z}{d} \right)^2 \right],$$

$$L/B = 10, \quad d/L = 0.0625.$$

In this computation  $30 \times 10$  surface elements are used. Near the fore and aft ends smaller elements are used, because velocity components vary rapidly with position in those regions. The breadth of the elements at fore and aft ends is  $0.5 \lambda$  as shown in Fig. 8. In addition to this case, two other cases, i.e. the breadth of the elements being  $0.25 \lambda$  and  $0.05 \lambda$  are also studied so as to know a change of wave resistance with respect to the breadth of the surface elements.

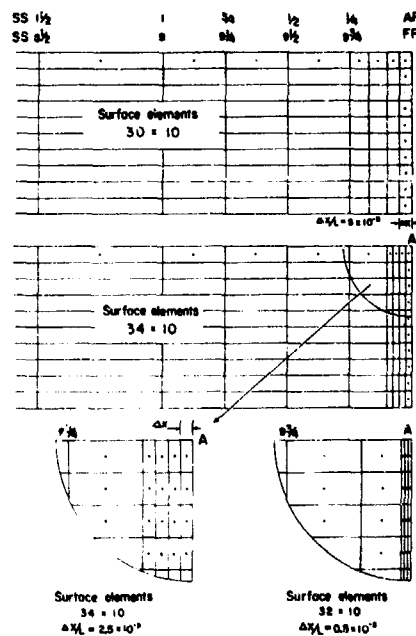


Fig. 8. Arrangements of surface elements near the fore and aft ends of Wigley's form.

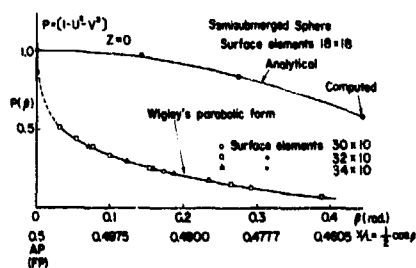


Fig. 9.  $p(\beta)$ -values near the fore and aft ends.

In Fig. 9 the calculated values of  $p(\beta)$  are shown compared with the values for a semisubmerged sphere. It is understood that near the fore and aft ends  $p(\beta)$  of Wigley's form varies rapidly. It is also seen that  $p(\beta)$  of Wigley's form is almost unchanged for a large difference of the breadth of the surface elements.

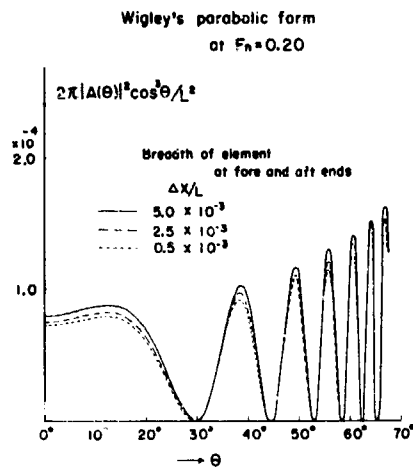


Fig.10. Comparison of wave spectra with different breadth of surface element at fore and aft ends.

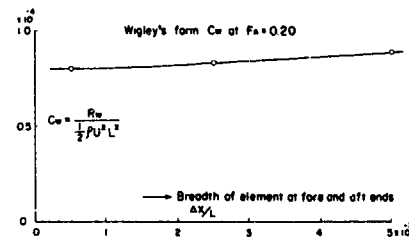


Fig.11. Change of  $C_w$  with respect to the breadth of surface element.

Fig.10 shows a comparison of wave spectra at  $F_n = 0.20$ . With a decrease of the breadth of the surface element, wave spectrum decreases. However, its change is small. Fig.11 shows the result of integration of wave spectra with respect to  $\theta$ . From this figure it is found that wave resistance is not so sensitive to the difference of the breadth of the surface element used in the present study.

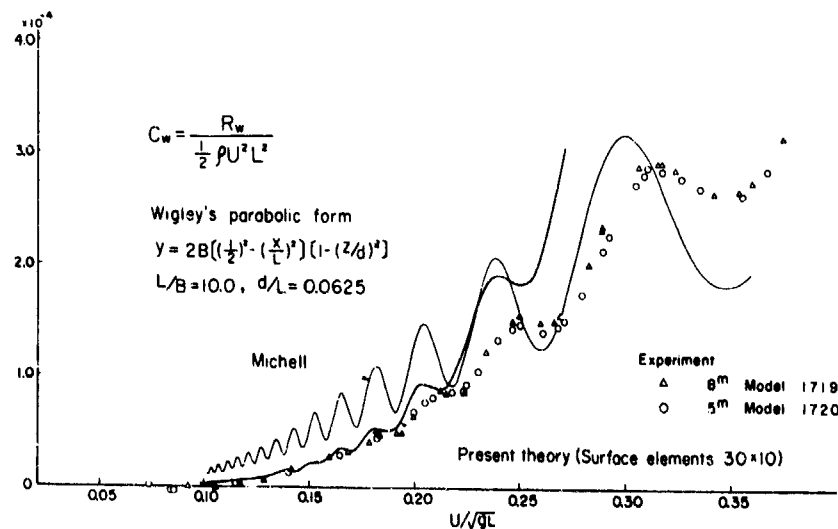


Fig.12. Comparison of calculated and measured wave resistance of Wigley's form.

Fig.12 shows the computed wave resistance for a wide range of Froude number compared with the wave resistance obtained by Michell's linearized theory. In this figure wave resistance determined from the towing tests of geometrically similar models of 8 meters and 5 meters are also shown. A remarkable attenuation of the humps and hollows in the range  $F_n < 0.20$  is attained by the present theory. A quantitative agreement is also observed between the present theory and the experiment. It should be noted, however, that in higher speed range the present theory gives poorer estimate than Michell's theory.

Fig.13 shows a comparison of wave spectra at  $F_n = 0.20$ . When compared with Michell's theory, it is a characteristic of the present theory that the wave spectrum corresponding to the transverse waves (small  $\theta$ -values) is considerably reduced as observed for vertical circular cylinder. This is the reason for the attenuation of humps and hollows in wave-resistance curve.

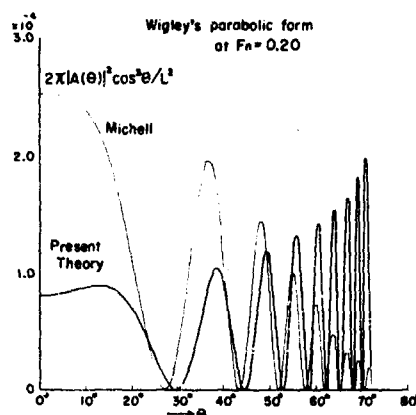


Fig.13. Comparison of calculated wave spectra of Wigley's form.

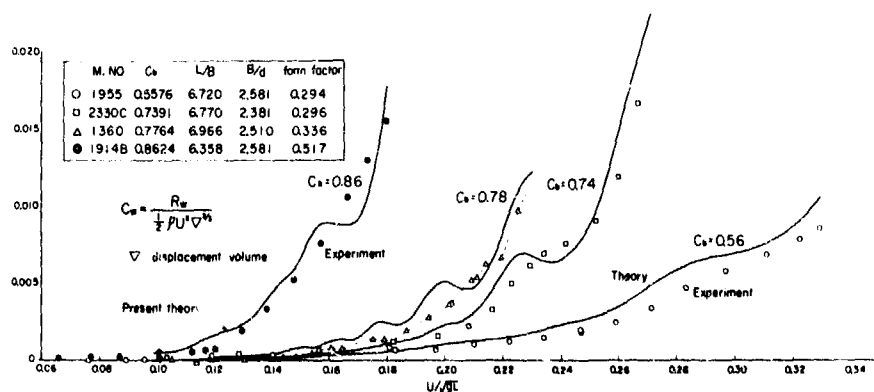


Fig.14. Comparison of calculated and measured wave resistance of conventional ship forms.

Fig.14 shows computed wave resistance of four conventional ship forms ( $L/B=6.4-7.0$ ,  $C_b = 0.56 - 0.86$ ). For those ship forms, the number of surface elements in the longitudinal direction corresponds to the number of square stations which are used for the drawing of hull in routine.

It is observed that in a wide range of block coefficient the calculated values of wave resistance are in the same order of magnitude as those of experimental values which are determined by Hughes method, where the form factor is determined by assuming that the total

resistance is the viscous resistance in very low speed range ( $F_n \sim 0.06$ ).

When comparing carefully the computed wave resistance with experiment, it is noted that theoretical curves are shifted a little toward lower speed range. This tendency is also observed in the case of Wigley's form in the range  $F_n > 0.20$ .

#### 6. Concluding remarks

In the present paper a procedure is explained for the calculation of wave resistance of ships in low speeds. The surface-layer velocity potential used in the present study is an asymptotic solution in low-speed limit. In accordance with this fact, an asymptotic wave-resistance formula in low-speed limit is used for the calculation of wave resistance.

From a number of computations based on the present theory it is found that in the practical speed range the wave resistance of conventional ship forms can be estimated within a practically acceptable order of magnitude. The wave resistance of those ship forms has not been tractable by the thin-ship theory. It is the breakthrough which has been achieved by taking into account the nonlinear effect of the free-surface condition in the present theory.

From the practical view point, it is expected that the present theory can be used to find a ship form of small wave resistance in an early stage of development of ship forms. It is also expected that the present theory can be used for the determination of the level of viscous resistance in low-speed range. Then a reliable value of form factor is determined. This contributes to the increase of accuracy of power prediction of ships from the model tests.

There is, however, room for an improvement of the present asymptotic theory. In the future a correction should be added to the surface-layer potential so as to satisfy the body boundary condition. By doing this it is expected that a better estimate of wave resistance may be possible. Further, trim and sinkage of a ship should be considered.

#### 7. Acknowledgments

The authors wish to express their deep appreciation to Mr. Kinya Tamura, manager of Resistance and Propulsion Laboratory, Nagasaki Technical Institute and Dr. Yoshio Kayo for their stimulating and encouraging discussions.

#### 8. References

- [1] Baba, E., and Takekuma, K. (1975), A Study on Free-Surface Flow around the Bow of Slowly Moving Full Forms, *Journal of The Society of Naval Architects of Japan*, Vol.137, 1-10.
- [2] Baba, E. (1975). Blunt Bow Forms and Wave Breaking, *The First STAR Symposium*, Washington, D.C.
- [3] Ogilvie, T.F. (1968). Wave Resistance: The Low Speed Limit, University of Michigan, Naval Architecture and Marine Engineering, No.002.
- [4] Hess, J.L., and Smith, A.M.O. (1964). Calculation of Nonlifting Potential Flow About Arbitrary Three-Dimensional Bodies, *Journal of Ship Research*, Vol.8, No.2, 22-44.
- [5] Newman, J.N. (1976). Linearized Wave Resistance Theory, *Proceedings of International Seminar on Wave Resistance*, Tokyo, 31-43.
- [6] Baba, E. (1976). Wave Resistance of Ships in Low Speed, *Mitsubishi Technical Bulletin*, No.109, Mitsubishi Heavy Industries, Ltd.
- [7] Maruo, H. (1977). Wave Resistance of a Ship with Finite Beam at Low Froude Numbers, *Bulletin of The Faculty of Engineering, Yokohama National University*, Vol.26.
- [8] Guével, P., Vaussy, P., and Kobus, J.M. (1974). The Distribution of Singularities Kinematically Equivalent to a Moving Hull in the Presence of a Free Surface, *International Shipbuilding Progress*, Vol.21, 311-324.
- [9] Havelock, T.H. (1932). The Theory of Wave Resistance, *Proceedings of the Royal Society, A*, Vol.138, 339-348.
- [10] Brard, R. (1972). The Representation of a Given Ship Form by Singularity Distributions When the Boundary Condition on the Free Surface is Linearized, *Journal of Ship Research*, Vol.16, No.1, 79-92.



# Appendix A. Wave resistance of semisubmerged sphere

The perturbation velocity potential of a semisubmerged sphere in the rigid-wall problem is given as

$$\phi(x, y, z) = \frac{Ua^3 x}{2(x^2 + y^2 + z^2)^{3/2}}, \quad (A-1)$$

where  $a$  is the radius of the sphere. The first term of  $D(x, y)$  defined by (10) in the text is obtained as

$$\begin{aligned} -\frac{1}{v} \phi_{xx}(x, y, 0) &= -\frac{a^3 U^3}{2g} \left[ -\frac{9x}{r^3} + \frac{15x^3}{r^5} \right] \\ &= 4U F_n^2 \left[ \left( \frac{9}{4s^3} - \frac{45}{16s^5} \right) \cos \theta - \frac{15}{16s^5} \cos 3\theta \right], \end{aligned} \quad (A-2)$$

for  $s \geq 1$ ,

where  $F_n = U/\sqrt{2ga}$ ,  $r = \sqrt{x^2 + y^2}$ ,  $s = r/a$ ,  
 $\cos \theta = x/a$ ,  $\sin \theta = y/a$ .

On the other hand,  $N(x, y, 0)$ , the second term of  $D(x, y)$  is obtained as

$$\begin{aligned} N(x, y, 0) &= 4U F_n^2 \left[ \left( -\frac{9}{16s^3} - \frac{9}{4s^5} + \frac{177}{32s^7} - \frac{201}{128s^9} \right) \right. \\ &\quad \times \cos \theta + \left( -\frac{15}{16s^5} + \frac{63}{32s^7} - \frac{39}{128s^9} \right) \cos 3\theta \left. \right] \end{aligned} \quad (A-3)$$

for  $s \geq 1$ .

The amplitude function due to the surface singularity distributions and the line singularity distributions around the load waterline is expressed by the first term of (12):

$$\begin{aligned} A_S(\theta) + A_L(\theta) &= -\frac{v}{\pi U} \sec^3 \theta \iint_{-\infty}^{\infty} dx dy \left( -\frac{1}{v} \phi_{xx}(x, y, 0) \right) \\ &\quad \times \exp[ i v \sec^2 \theta (x \cos \theta + y \sin \theta) ]. \end{aligned} \quad (A-4)$$

The amplitude function due to the free-surface disturbance  $N(x, y, 0)$  is expressed by the second term of (12):

$$\begin{aligned} A_F(\theta) &= -\frac{v}{\pi U} \sec^3 \theta \iint_{-\infty}^{\infty} dx dy N(x, y, 0) \\ &\quad \times \exp[ i v \sec^2 \theta (x \cos \theta + y \sin \theta) ]. \end{aligned} \quad (A-5)$$

Substituting (A-2) into (A-4), we have in

the low-speed limit:

$$\begin{aligned} A_S(\theta) + A_L(\theta) &= i \frac{16a}{\sqrt{\pi}} F_n^3 \left[ \frac{72}{128} \cos \theta \right. \\ &\quad \left. + \frac{120}{128} \cos 3\theta \right] \cos \left( \frac{1}{2F_n^2} \sec^2 \theta - \frac{\pi}{4} \right) + O(F_n^5). \end{aligned} \quad (A-6)$$

Substituting (A-3) into (A-5), we have in the low-speed limit:

$$\begin{aligned} A_F(\theta) &= -i \frac{16a}{\sqrt{\pi}} F_n^3 \left[ \frac{147}{128} \cos \theta + \frac{93}{128} \cos 3\theta \right] \\ &\quad \times \cos \left( \frac{1}{2F_n^2} \sec^2 \theta - \frac{\pi}{4} \right) + O(F_n^5). \end{aligned} \quad (A-7)$$

The sum of three parts  $A_S(\theta)$ ,  $A_L(\theta)$  and  $A_F(\theta)$  is thus written:

$$\begin{aligned} A_S(\theta) + A_L(\theta) + A_F(\theta) &= -i \frac{16a}{\sqrt{\pi}} F_n^3 \left[ \frac{75}{128} \cos \theta - \frac{27}{128} \cos 3\theta \right] \\ &\quad \times \cos \left( \frac{1}{2F_n^2} \sec^2 \theta - \frac{\pi}{4} \right) + O(F_n^5). \end{aligned} \quad (A-8)$$

Substituting (A-6) into (8) in the text and using the stationary phase method, we have a wave-resistance formula of a semisubmerged sphere when the free surface condition is linearized:

$$\begin{aligned} C_w &= \frac{R_w}{\frac{1}{2} \rho U^2 (2a)^2} \\ &= \frac{224}{5} F_n^6 + 72\sqrt{\pi} F_n^7 \sin \left( \frac{1}{F_n^2} + \frac{\pi}{4} \right) \\ &\quad + O(F_n^8). \end{aligned} \quad (A-10)$$

When the contribution from the free-surface disturbance  $N(x, y, 0)$  is included, the wave resistance is obtained by the use of the expression (A-8):

$$\begin{aligned} C_w &= \frac{633}{70} F_n^6 + \frac{9}{2} \sqrt{\pi} F_n^7 \sin \left( \frac{1}{F_n^2} + \frac{\pi}{4} \right) \\ &\quad + O(F_n^8). \end{aligned} \quad (A-11)$$

## A PRACTICAL COMPUTER METHOD FOR SOLVING SHIP-WAVE PROBLEMS

C. W. Dawson  
David W. Taylor Naval Ship Research and Development Center  
Bethesda, Maryland 20084

### Abstract

A computer method is described for computing the three-dimensional, steady state, potential flow about a ship-like body in or near the free surface. The two-dimensional work which formed the foundation for the three-dimensional program is also described. The method uses a simple source density distribution over both the body surface and a local portion of the undisturbed free surface. The free surface condition is linearized in terms of the double-model velocity. Upstream waves are prevented by the use of a one-sided, upstream, finite difference operator for the free surface condition. Results are given for Wigley Model 1805A and for a Series 60, Block 60 ship. The results were obtained at reasonable cost and show that the method is practical for the evaluation of ship designs.

### I. Introduction

This paper describes a computer method for computing the three-dimensional, steady state, potential flow past an arbitrarily shaped body in or near the free surface. A FORTRAN program (XYZFS) has been developed using the method. The output of XYZFS includes the velocity field, pressure distribution, and streamlines over the body surface plus the wave resistance and elevation of the free surface. A Texas Instruments "Advanced Scientific Computer" was used to solve test problems.

The method of solution is a modification of the surface source method developed by Hess and Smith [1,2]. A method similar to the method described here has been developed by Gadd [3]. The body and a local portion of the undisturbed free surface are geometrically represented by quadrilateral panels. The source density is determined so that the boundary conditions on the panels are approximately satisfied.

The Series 60, Block 60 ship, used as a test problem, was run with 208 (8x26) panels on the body surface and 360 (10x36) panels on the undisturbed free surface. Because of center-plane symmetry, only half of the body and free surface were directly represented. This problem took 5 minutes of central processor time and cost \$87.00 for the first Froude number. Each additional Froude number took

2 minutes and cost \$39.00. For many problems, the time and labor cost for preparation of the input will be greater than the cost of computer time for running the problems.

The method was first developed for two-dimensional problems and then extended to three dimensions. The two-dimensional work will be described first as it is the foundation for the three-dimensional method.

### II. Mathematical Statement of the Problem

The velocity potential  $\phi$  must satisfy the following conditions:

$$\nabla^2 \phi = 0 \quad \text{in the fluid} \quad (1)$$

$$\phi_n = 0 \quad \text{on the body} \quad (2)$$

$$g_n + \frac{1}{2}(\phi_x^2 + \phi_y^2 + \phi_z^2 - U_\infty^2) = 0 \quad \text{on the free surface} \quad (3)$$

$$\phi_x n_x + \phi_y n_y - \phi_z = 0$$

$$\nabla \phi = (U_\infty, 0, 0) \quad \text{at } \infty \quad (\text{except where there are waves and waves must be present only downstream from the body}) \quad (4)$$

where  $n$  refers to the direction normal to the body surface,

subscripts  $n, x, y, z$  denote partial differentiation,

$z$  is the vertical coordinate, and

$n$  is the value of  $z$  at the free surface.

The free surface condition is replaced by a linearized condition and approximations are made to discretize the problem. However, it is the way in which waves are made to radiate only in the downstream direction that is special to the method of solution described here.

### III. Method for Two-Dimensional Problems

Consider a body beneath the free surface of a moving fluid as shown in Figure 1. The simplest approximation to the free surface is a line of symmetry. Then the problem is easily solved by placing an image of the body above the line of symmetry. This formulation is called the double-model problem.

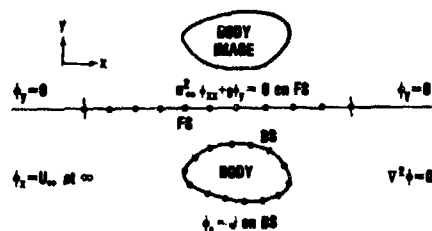


Figure 1. Geometry of a Two-Dimensional Problem

To improve on the double-model solution, a portion of the free surface (FS) near the body is treated separately from the outer part of the free surface. The free surface condition is linearized in terms of the free stream velocity and is satisfied by the addition of a source density on the line of the undisturbed surface. The undisturbed surface is used to preserve the symmetry condition for the outer part of the surface as well as to simplify the calculations.

This symmetry condition is a very good approximation upstream from the body where the surface has not been disturbed. Downstream it is not correct but it still represents the average condition. That is, some parts of the surface are moving up, others are moving down so that the average vertical motion is zero.

The problem just defined does not have a unique solution. Upstream waves satisfy the free surface condition just as well as downstream waves. Normally the solution is made unique by imposing a radiation boundary condition upstream from the body. Since it is difficult to set up a radiation condition in three dimensions, another approach is used here.

When a numerical procedure is applied to a problem that does not have a unique solution, the result can still be a reasonable solution of the problem; and if the procedure is set up just right, the solution will be the desired one. In this case the desired solution is achieved by using a one-sided, upstream, finite difference operator to approximate the free surface condition. In this way a disturbance in the free surface is propagated downstream by the free surface condition but will influence the flow upstream only through the application of Laplace's equation to the bulk of the fluid. This process is analogous to the natural process in which a disturbance is carried downstream by momentum but is felt upstream only as changes in the pressure.

The solution is generated in terms of a source density distributed on the body surface (BS), on the image of the body, and on the local part of the undisturbed free surface (FS), and is represented as follows:

$$\phi(x,y) = U_\infty x + \int_{BS} S(x',y') (\ln r + \ln \bar{r}) dz' + \int_{FS} S(x',y') \ln r dz' \quad (5)$$

where  $S(x',y')$  is the source density,

$U_\infty$  is the free stream velocity,

$r$  is  $[(x-x')^2 + (y-y')^2]^{1/2}$ ,

$\bar{r}$  is  $[(x-x')^2 + (y+y')^2]^{1/2}$ , ( $\bar{r}$  applies to the image of the body),

and  $x',y'$  is a point on BS or FS. Laplace's equation, the infinity condition, and the symmetry condition for the outer part of the free surface are satisfied by  $\phi$  regardless of the values of  $S$ . Thus  $S$  may be found so as to satisfy the boundary conditions on BS and FS.

Both BS and FS are divided into straight line segments, and the source density is approximated by a constant value in each segment. Integration is thus replaced by summation. The velocity components are given by Equations (6) and (7).

$$u(x,y) = \phi_x = U_\infty + \sum_{j=1}^M S_j CX_j(x,y) \quad (6)$$

$$v(x,y) = \phi_y = \sum_{j=1}^M S_j CY_j(x,y) \quad (7)$$

where  $M$  is the number of segments

$$CX_j(x,y) = \int_{BS_j} \left( \frac{x-x'}{r^2} + \frac{x-x'}{\bar{r}^2} \right) dz'$$

$$\text{or } \int_{FS_j} \frac{x-x'}{r^2} dz'$$

and

$$CY_j(x,y) = \int_{BS_j} \left( \frac{y-y'}{r^2} + \frac{y+y'}{\bar{r}^2} \right) dz'$$

$$\text{or } \int_{FS_j} \frac{y}{r^2} dz'$$

The appropriate boundary condition will be satisfied at the center of each line segment. On BS the boundary condition (2) at segment  $i$  is

$$0 = \phi_n = u_i N_{xi} + v_i N_{yi} \quad (8)$$

$$= u_i N_{xi} + \sum_{j=1}^M (C_{xi,j} N_{xi} + C_{yi,j} N_{yi}) S_j$$

where  $(N_{xi}, N_{yi})$  is the unit normal vector to segment  $i$ . (Note that  $C_{xi,j} N_{xi} + C_{yi,j} N_{yi}$  equals  $\pi$  plus the contribution from the image of segment  $i$  for  $i$  in BS.)

On FS a four-point, upstream, finite difference operator is used to obtain  $\phi_{xx}$  so that

$$\phi_{xx} = u_x \approx C_{A_i} u_i + C_{B_i} u_{i-1} + C_{C_i} u_{i-2} + C_{D_i} u_{i-3} \quad (9)$$

$$\approx \sum_{j=1}^M [C_{A_i} C_{xi,j} + C_{B_i} C_{xi-1,j} + C_{C_i} C_{xi-2,j} + C_{D_i} C_{xi-3,j}] S_j$$

where  $C_{A_i}$ ,  $C_{B_i}$ ,  $C_{C_i}$ ,  $C_{D_i}$  are functions of the segment lengths and  $i$  increases in the downstream direction. When the free surface equations are linearized in terms of the free stream velocity and  $\eta$  is eliminated, the result is:

$$0 = U_x^2 \phi_{xx} + g \phi_y$$

$$= U_x^2 \sum_{j=1}^M [C_{A_i} C_{xi,j} + C_{B_i} C_{xi-1,j} + C_{C_i} C_{xi-2,j} + C_{D_i} C_{xi-3,j}] S_j - g \phi_y = S_i \quad (10)$$

Near the upstream end of FS, a smaller number of points is used in the finite difference operator. For the first point,  $S$  is either set equal to zero or determined in some other manner.

Thus a system of  $M$  equations in  $M$  unknown values of  $S$  must be solved. The matrix is full and is not symmetric or diagonally dominate but does seem to be well-conditioned. The system of equations is solved by the Gaussian Elimination procedure with double precision arithmetic.

#### IV. Two-Dimensional Results

Experiments with simple two-dimensional problems have shown that the method does work. Waves develop downstream from a disturbance and not upstream. The experiments have also shown that:

(1) A two-point finite difference operator used in the free surface boundary condition results in waves that are strongly damped downstream from a disturbance. A three-point finite difference operator which eliminates errors from  $u_{xx}$  is better than the two-

point operator but still damps the waves too much. A four-point operator which eliminates errors from  $u_{xx}$  and  $u_{xxx}$  results in waves that grow in amplitude downstream from a disturbance. A four-point operator which eliminates errors from  $u_{xx}$  and  $u_{xxxx}$  but not  $u_{xxx}$  results in reasonable conservation of wave height and was therefore used in the computations. A five-point operator which eliminates errors from  $u_{xx}$ ,  $u_{xxx}$ , and  $u_{xxxx}$  conserves wave height reasonably well but does not work as well as the four-point operator with large segments or near large changes in the slope of the surface.

The coefficients of the four-point operator are:

$$C_{D_i} = (x_{i-1} - x_i)^2 (x_{i-2} - x_i)^2 (x_{i-2} - x_{i-1}) (x_{i-2} + x_{i-1} - 2x_i) / D_i$$

$$C_{C_i} = -(x_{i-1} - x_i)^2 (x_{i-3} - x_i)^2 (x_{i-3} - x_{i-1}) (x_{i-3} + x_{i-1} - 2x_i) / D_i$$

$$C_{B_i} = (x_{i-2} - x_i)^2 (x_{i-3} - x_i)^2 (x_{i-3} - x_{i-2}) (x_{i-3} + x_{i-2} - 2x_i) / D_i$$

$$C_{A_i} = -(C_{B_i} + C_{C_i} + C_{D_i})$$

$$D_i = ((x_{i-1} - x_i)(x_{i-2} - x_i)(x_{i-3} - x_i)(x_{i-3} - x_{i-1})(x_{i-2} - x_{i-1})(x_{i-3} - x_{i-2})(x_{i-2} + x_{i-1} - 3x_i))$$
(11)

where the four points are  $x_i$ ,  $x_{i-1}$ ,  $x_{i-2}$ ,  $x_{i-3}$ .

(2) The wave length will be too short by about 5%.

(3) A large abrupt change in the lengths of the segments will cause a large point-to-point oscillation in the free surface upstream from the change. Changes in segment size smaller than a factor of 1.5 do not cause noticeable oscillations.

(4) The downstream boundary will also cause oscillations unless a damping region is placed next to it. An adequate damping region is provided by the use of the two-point difference operator for the last two segments.

(5) The effect of the downstream boundary is significant for only a short distance upstream. Most of the downstream boundary effect disappears after 1/4 of a wave length. Figure 2 shows three solutions to the problem of flow past a point dipole. The solution with the shorter downstream region is almost the same as the solution with the longer region except for the last three points. Although errors at the upstream boundary are usually small, they are serious as they can affect the entire solution. The solution in Figure 2 with the short upstream region has a phase shift

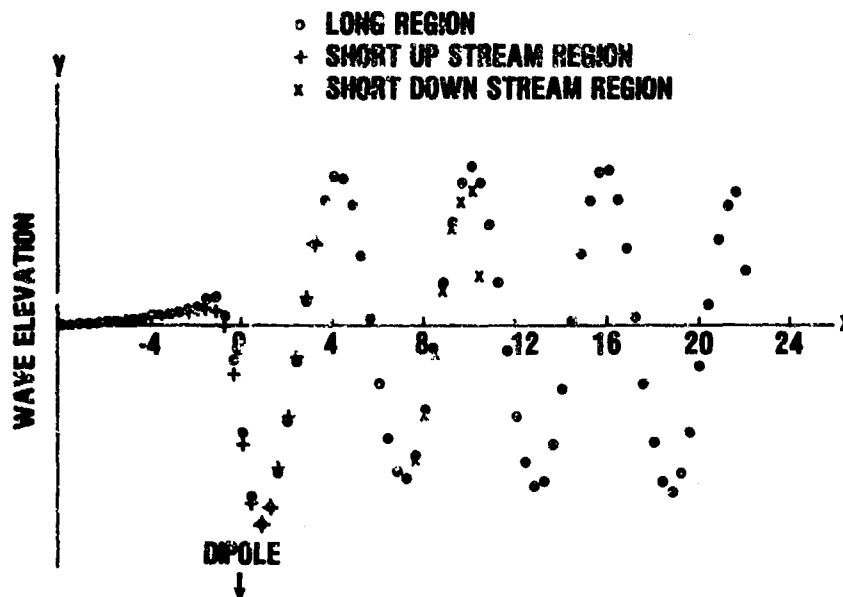


Figure 2. Boundary Effects on Flow Past a Dipole

relative to the long region solution.

(6) Good results can be obtained with only 14 segments per wave length and useful results with only 8 segments per wave length.

In Figure 1 and Equation (10), the free surface condition was linearized in terms of the free stream velocity. The free surface condition can also be linearized in terms of the double-model velocity. A good discussion of double-model linearization is provided by Neuman in reference [4].

Two test problems were run to compare double-model linearization with free-stream linearization. The first problem, that of flow past a point vortex, was used by Salvesen and von Kerczek [5] to compare perturbation methods with a nonlinear calculation. Figure 3 is a comparison of wave profiles. Double-model linearization produced a wave more nearly in phase with the nonlinear wave than did free stream linearization. Figure 4 is a comparison of the drag on the vortex. For positive vortices the double model linearization produced very good results. For negative vortices the results were not as good but were still much better than those for free-stream linearization and were comparable to the perturbation solutions.

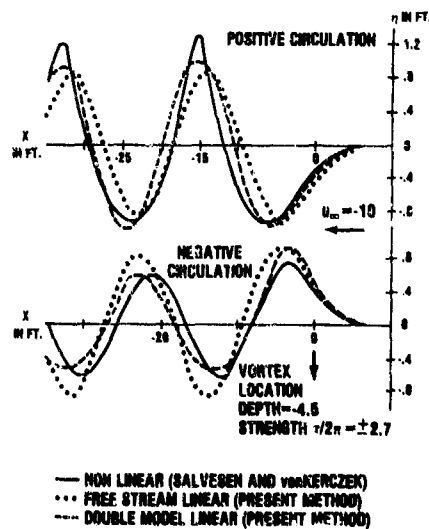


Figure 3. Wave Elevations for a Submerged Vortex

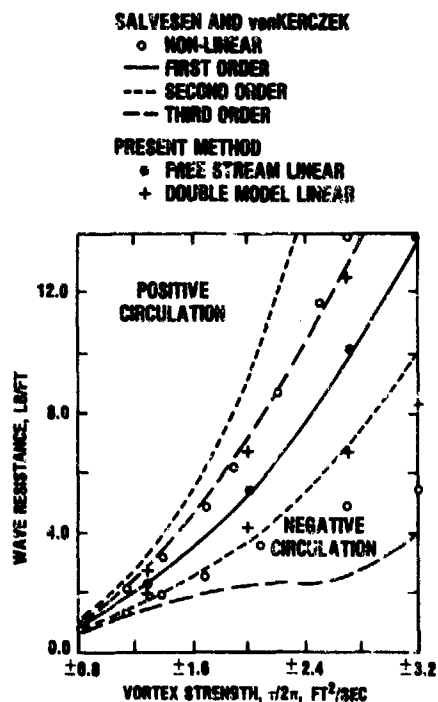


Figure 4. Wave Resistance as a Function of Vortex Strength

The second problem was that of flow past a submerged body represented by 3 point sources and 8 point sinks as shown in Figure 5. This

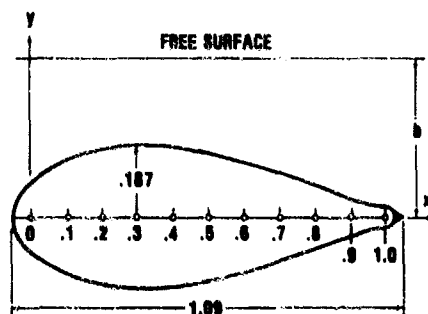


Figure 5. Singularity Representation and the Cross Section of the Body

problem was used by Salvesen [6] for a comparison of perturbation calculations with experimental results. Figure 6 shows the wave profiles for three different depths of submergence. The improvement produced by double-model linearization was small for the deeper submergence but quite large when the body approached the surface.

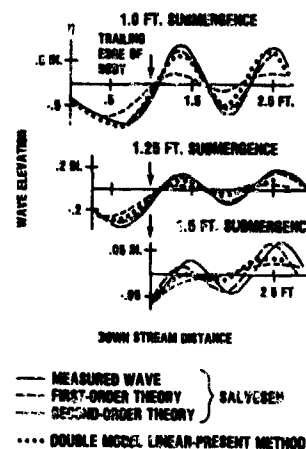


Figure 6. Wave Elevations for Different Depths of Submergence of the Body

#### V. Method for Three-Dimensional Problems

For three-dimensional problems the free surface condition (3) is always linearized in terms of the double-model velocity potential  $\phi$ , that is,  $\phi = \phi + \phi'$  and nonlinear terms of  $\phi'$  are dropped. Also Equations (3) are applied at  $z=0$ , not at the free surface. When  $n$  is eliminated, Equations (3) reduce to:

$$\frac{1}{2}(\phi_x^2 + \phi_y^2 + \phi_z^2)_x + \phi_y(\phi_x^2 + \phi_y^2 + \phi_z^2)_y + g\phi_z = 0$$

Now for any function  $F$

$$\phi_x F_x + \phi_y F_y = \phi_z F_z \quad (12)$$

where the subscript  $z$  denotes differentiation along a streamline of  $\phi$ . Thus the free surface condition becomes

$$\begin{aligned} \frac{1}{2}[\phi_x(\phi_x^2 + 2\phi_x\phi_x') + \phi_x'(\phi_x^2 + \phi_y^2)_x \\ + \phi_y'(\phi_x^2 + \phi_y^2)_y] + g\phi_z' = 0 \end{aligned} \quad (13)$$

$$\begin{aligned}
& \text{but } \frac{1}{2}[\phi'_x(\phi_x^2 + \phi_y^2)_x + \phi'_y(\phi_x^2 + \phi_y^2)_y] \\
& = \phi'_x(\phi'_x\phi_x + \phi'_y\phi_y)_x - \phi'_x(\phi_x\phi'_{xx} + \phi_y\phi'_{xy}) \\
& + \phi'_y(\phi'_x\phi_x + \phi'_y\phi_y)_y - \phi'_y(\phi_x\phi'_{xy} + \phi_y\phi'_{yy}) \\
& = \phi'_x(\phi'_x\phi'_x)_x - \phi_x^2\phi'_{xx} = \phi'_x\phi'_{xx}
\end{aligned}$$

so that

$$\phi'^2_{xx} + (\phi'_x\phi'_x)_x + g\phi'_z = 0$$

Now replace  $\phi'$  with  $\phi - \phi$  to get

$$(\phi'_x\phi'_x)_x + g\phi'_z = -\phi'^2_{xx} \quad (14)$$

Equation (14) is the same as the double-model linearized free surface condition for two dimensions except that  $x$  has been replaced by  $z$ .

For three-dimensional problems, quadrilateral panels are used in place of the line segments of the two-dimensional problems. The body is assumed to have symmetry about the center plane so that only half of the body and free surface need be directly represented. The  $\ln r$  of the two-dimensional kernel is replaced by  $1/r$ . The integrals over each panel are evaluated by the method used by Hess and Smith [1,2]. Exact integration is used for the shorter distances, a quadrupole source is used for intermediate distances, and a monopole source is used for large distances.

The panels for the free surface are arranged in sets so that each set is bounded by streamlines of the double-model problem. Thus Equation (14) may be applied to each set and approximated by the four-point, upstream, finite difference operator that was used for two dimensions. The result as in two-dimensional problems is a system of  $M$  equations in  $M$  unknowns that is solved by Gaussian Elimination.

All the double-model streamlines go around the body whereas some free stream streamlines go through the body. Thus the problem of starting the free surface condition at the body surface has been avoided. This was the original reason for using double-model linearization. The increased accuracy shown by the two-dimensional experiments is a bonus.

The free surface panels adjacent to the body are extended a short distance into the body. Otherwise there would be a singularity in the source density where the body panels meet the free surface panels. This idea was borrowed from Gadd [3].

In the present method and Gadd's method use a double-model of the body and represent the body and a local portion of the free surface by source panels. The methods differ in that Gadd uses artificial smoothing to eliminate unwanted oscillations and a nonlinear form of the free surface condition. It is not clear

from reference [3] how Gadd prevents upstream waves.

#### VI. Three-Dimensional Results

Two three-dimensional problems have been studied. The first problem was that of flow about "Wigley Model 1805A". This body is referred to as Model 2891 by Shearer [7] and Wehausen [8]. Model 1805A is ship-like with the body surface defined by

$$y = .75(1-z^2)(1 - \frac{x^2}{64})(1 - .6\frac{x^2}{64}) \quad (15)$$

Numerical experiments were run with Model 1805A using 64 panels (4x16) for the body surface and various numbers of panels for the free surface. These experiments showed that:

- (1) The paneled region of the free surface must be about 3/8 of the body length wide. Otherwise waves reflected from the boundary will alter the flow at the stern of the body.
- (2) The paneled region of the free surface need be extended downstream only about 1/4 wave length. (About 1/4 body length for the problems considered here.)
- (3) The paneled region of the free surface must be extended about 1/4 of the body length upstream from the body.
- (4) Much smaller panels are required near the bow than over the remainder of the body.
- (5) The free surface panels should be swept back at about a 45° angle so that the small panels near the bow follow the bow wave.

The final panel arrangement in these experiments had 288 panels with 64 on the body and 224 (8x28) on the free surface. Wigley Model 1805A was then run with 484 panels, 144 (6x24) on the body and 340 (10x34) on the free surface.

The wave profiles and drag curves for Model 1805A are shown in Figures 7 and 8. These figures include experimental data and thin ship calculations from Shearer [7] (also available in ref. [8]). The wave profile was taken from the surface elevation at the panels next to the body, which resulted in some error near the bow.

The solutions from the 288-panel model and the 484-panel model agree quite well at smaller Froude numbers. At higher Froude numbers the two solutions differ by an increasing amount, indicating a need for smaller panels. This result was unexpected since the waves are longer for higher Froude numbers.

The error in the wave length predicted by the two-dimensional results shows up as a Froude number shift in the drag curves. Otherwise the results are an improvement over the thin ship calculations.

The second problem involved the flow past a Series 60 Block 60 ship. For this problem 208 panels (8x26) were used for the ship and 360

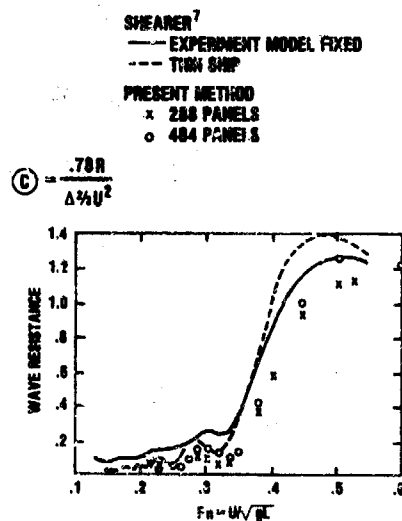


Figure 7. Wave Resistance for Wigley Model 1805A

panels (10x36) for the free surface. The arrangement of the panels, viewed from the side and below, is shown in Figure 9.

The drag curves for the Series 60 ship are shown in Figure 10. The band for the residual drag represents the envelope of the experimental data from Huang and von Kerczek [9], Tsai and Landreber [10] and Todd [11]. The drag curve does not show the expected Froude number shift.

The wave profiles for the Series 60 ship are shown in Figure 11. Experimental data and calculations by Guilloton's method [9] are also shown. The wave profiles computed by the present method show a dip in the top of the bow wave that is not shown by the other curves. The bow is slightly concave near the dip so the dip may be real. Because the dip is small and would be hidden by the bow wave itself, it could have been missed in the experiments.

For Froude number .35 the surface elevation at the next set of panels is also shown. The center of these panels is .035 L/2 from the ship. The dip in the bow wave is very small at this distance and cannot be detected further out.

The experimental wave profiles show larger oscillations near the middle of the ship than do those obtained by the present method. The error may be caused by the non-linear terms that are omitted or by inadequate resolution. This question needs additional study.

Streamlines on the surface of the Series 60 ship have also been computed. Figure 12

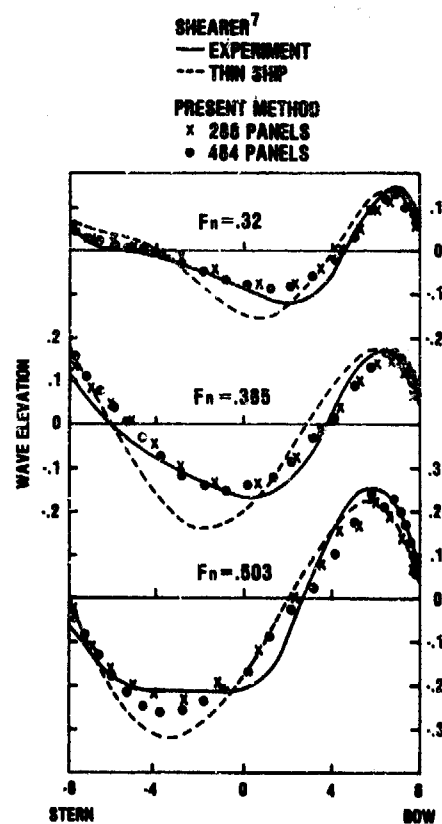


Figure 8. Wave Profiles for Wigley Model 1805A

shows the streamlines viewed from the side for the double-model solution and for Froude number .359. The change in the streamlines indicates the importance, at higher Froude numbers, of the free surface to the flow over all parts of a ship.

#### VII. Conclusion

With the method presented here, it is practical to examine the steady state performance of ship designs. The cost is reasonable and the accuracy of the results is better than that provided by thin ship theory or by Guilloton's method [9].

#### VIII. Acknowledgment

The author wishes to thank Mr. Paul Morawski for running the three-dimensional calculations. This work was supported by the 6.1 and 6.2 Mathematical Sciences Research Programs





Figure 9. Panel Arrangement for Series 60 Ship

• PRESENT METHOD (WAVE RESISTANCE)  
 — EXPERIMENT<sup>2</sup> (RESIDUAL RESISTANCE)

$$C_R = \frac{D}{\rho U^2 L}$$

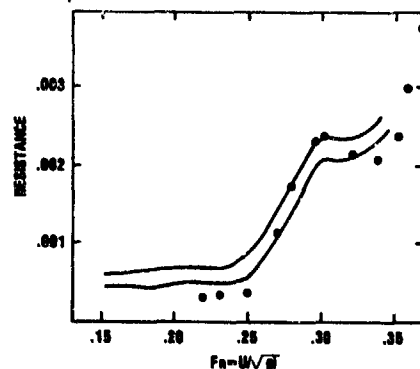


Figure 10. Wave Resistance for Series 60 Block 60 Ship

sponsored by the Naval Sea Systems Command (Task Area SR 0140301: Mathematical Sciences) and the Naval Material Command (Task Area ZF53532001: Logistics Technology).

#### References

1. Hess, John L. and A.M.O. Smith, "Calculation of Potential Flow About Arbitrary Bodies," Pergamon Press Series "Progress in Aeronautical Science," Volume 8, 1966.
2. Hess, John L. and A.M.O. Smith, "Calculation of Non-Lifting Potential Flow About Arbitrary Three-Dimensional Bodies," Douglas Aircraft Company Report No. 40622, March 1962.
3. Gadd, G.E., "A Method of Computing the Flow and Surface Wave Pattern Around Full Forms," The Royal Institution of Naval

HUANG & vanKERCZEK  
 — EXPERIMENT  
 - - - COMPUTED BY  
 GULLOTON METHOD

PRESENT METHOD  
 ... PANELS NEXT TO BODY  
 \* \* \* SECOND ROW OF PANELS

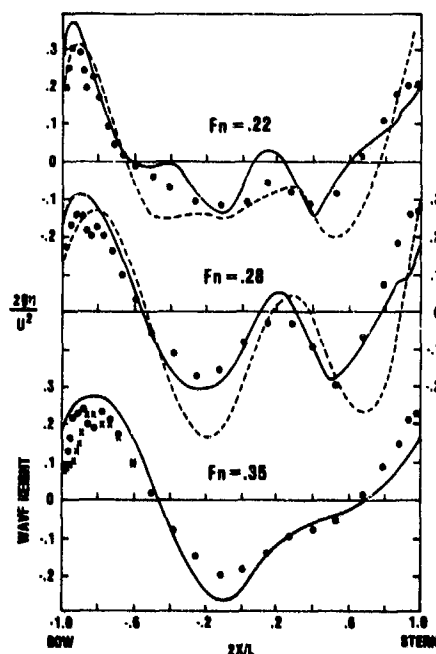


Figure 11. Wave Profiles for the Series 60 Ship

Architects, volume 118 (1976).

4. Neuman, J.N., "Linearized Wave Resistance Theory," Proceedings of International Seminar on Wave Resistance, Society of Naval Architects of Japan, 1976.

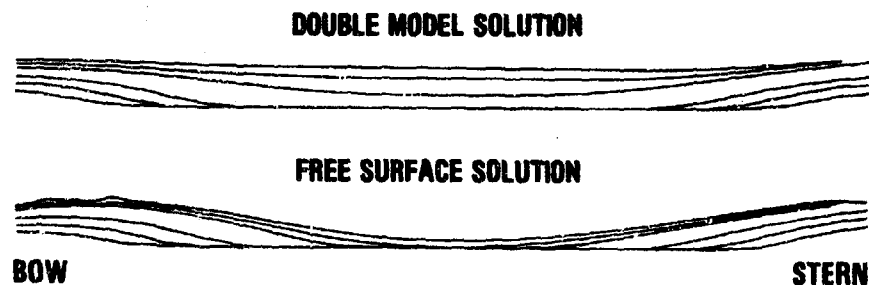


Figure 12. Streamlines on the Series 60 Ship,  $F_n = .359$

5. Salvesen, N. and C.H. von Kerczek, "Comparison of Numerical and Perturbation Solutions of Two-Dimensional Nonlinear Water-Wave Problems," *Journal of Ship Research*, vol. 20, No. 3, September 1976.
6. Salvesen, N., "Second-Order Wave Theory for Submerged Two-Dimensional Bodies," 6th Naval Hydrodynamics Symposium, Office of Naval Research, ARC 136, 1966, pp. 595-636.
7. Shearer, J.R., "A Preliminary Investigation of the Discrepancies between the Calculated and Measured Wave-making of Hull Forms," *North-East Coast Inst. Eng. Shipbld. Trans.* 67, 1951.
8. Mehausen, J.V., "The Wave Resistance of Ships," *Advances in Applied Mechanics*, vol. 13, 1973.
9. Huang, T.T. and C.H. von Kerczek, "Shear Stress and Pressure Distribution on a Surface Ship Model: Theory and Experiment," Ninth Symposium on Naval Hydrodynamics, Office of Naval Research, ARC 203, vol. 2, 1972, pp. 163-2010.
10. Tsai, C.E. and L. Landweber, "Total and Viscous Resistance of Four Series-60 Models," 13th International Towing Tank Conference, Berlin, Hamburg, Sept. 1972.
11. Todd, R.H., "Series 60-Methodical Experiments with Models of Single-Screw Merchant Ships," *David Taylor Model Basin Research and Development Report 1712*, 1963.

## FINITE DIFFERENCE SIMULATION OF THE PLANAR MOTION OF A SHIP\*

Robert K.-C. Chen  
JAYCOR  
Del Mar, California

### Abstract

A finite difference solution procedure has been developed to study three-dimensional potential flows, both transient and steady, about a shiplike floating body. The primary features of this paper include the use of special coordinate transformations so that proper boundary conditions can be applied at the exact locations of the body surface and free surface, the application of Orlanski's numerical radiation condition to prevent unwanted wave reflections, and a new upwind-centered finite-difference scheme for numerical integration of the time-dependent free surface conditions. The forward motion of a shiplike floating body and that of a submerged body are studied. Both nonlinear and linearized free surface conditions were used for comparison purposes. The nonlinear results were found to be significantly different from the linear solution for finite-amplitude waves. Also, Orlanski's numerical radiation condition was found to be extremely effective in reducing spurious wave reflections.

### 1. Introduction

This paper describes a finite-difference, numerical technique for simulating transient, three-dimensional potential flow about a floating body. The primary objective is the development of a computational procedure which allows arbitrary planar motions for a fairly large class of shiplike floating bodies. This work is the continuation of the author's previous numerical study of the flow about an accelerating floating sphere.<sup>1</sup> In earlier studies, the basic approach was the separation of the flow field into a base flow and the perturbation from it. As an example, in studying the forward motion of a ship, we choose as the base flow the one that would exist if the free surface were replaced by a rigid plate, instead of using a uniform stream with the magnitude of the velocity equal to the speed of the ship, as is usually done in analyses to render the mathematics tractable. The advantage of this approach is that it is more efficient in achieving a given level of accuracy for the perturbation field because accumulated errors due to computation of the bulk of the flow pattern, i.e., the base flow, can not arise. The penalty, however, is that additional storage on

the computer is required, and that the resulting equations are much longer and harder to program, especially when simulating finite-amplitude waves. Consequently, this approach is not taken in the present study. Rather, the full nonlinear equations are used directly.

Several difficulties arise when calculating three-dimensional, time-dependent flows about a ship. Because of limitation in computer storage, one is allowed to use a relatively small computation domain, e.g.,  $40 \times 20 \times 20$  mesh points. Besides, one almost must employ a body-fixed frame of reference, so that the precious mesh points can be used to give the best resolution in the vicinity of the ship. In this frame of reference, the ship appears stationary in a running stream. Numerically, this situation creates two problems. The first problem concerns boundary conditions at "open boundaries," where the flow and/or waves leave the computation region. Improper treatment of open boundaries will result in spurious reflections that make the computations meaningless. Fortunately, with the appearance of Orlanski's<sup>2</sup> excellent technique for numerically implementing the Sommerfeld radiation condition for unbounded hyperbolic flows, this obstacle can now be removed. The second problem associated with streaming flows is that the advection terms in the governing equations (Eqs. (18) and (19) in Section II) demand careful construction of finite difference schemes. Various conventional explicit schemes, such that the first-order, forward-time, central-space difference, have been tried and found unstable. Other schemes, like the first-order upwind differencing, are so dissipative that the waves are severely damped. Implicit or other higher-order methods, on the other hand, greatly increase the programming task and cost of computation. In this paper an upwind-centered finite-difference scheme, which has some attractive properties, is proposed. The details are found in Section III. Another category of difficulties is related to the geometry of some boundaries. Proper boundary conditions must be applied at the exact, instantaneous positions of the hull surface and the free surface, so that large-amplitude motions can be accommodated. To this end, a series of coordinate transformations is made (Section II). Essentially, a body-fitted, but otherwise stationary coordinate system is used

\*This work was sponsored by the Office of Naval Research under Contract N00014-76-C-0455.

to describe the interior of the flow field, while a second system, which conforms to both the hull surface and the instantaneous free surface, is employed to implement the free surface conditions.

The class of body shapes considered here is limited to those representable by a single-valued function on the ship's center plane. Thus, the technique here is particularly useful in calculating flow about a sharp-edged ship. For blunt bodies other coordinate systems must be used, but the formulation and computational procedure remains the same. The present method can also be applied to flows about a submerged body, or surface piercing structures, such as a bridge pier.

## II. Governing Equations

In this section a series of coordinate transformations are performed to obtain the governing equations in forms convenient for applying correct boundary conditions at the solid surface of a ship and at the instantaneous position of the free surface.

### Equations in a Moving Frame of Reference

As shown in Fig. 1, let  $(X, Y, Z, T)$  be the cartesian coordinates referred to an absolute, inertial frame, and  $(x, y, z, t)$  be their counterparts with reference to a moving frame which is fixed in the ship. Within the scope of the present study, let us assume further that the ship undergoes an arbitrary planar motion such that its mast (i.e., the vertical axis of the ship) always points vertically upward. The choice of the moving axes  $(x, y, z)$  will be such that the positive  $x$ -direction is the same as the longitudinal axis of the ship, pointing to the front.

Employing a procedure similar to that given by Stoker,<sup>3</sup> we obtain the following relations between the two coordinate systems:

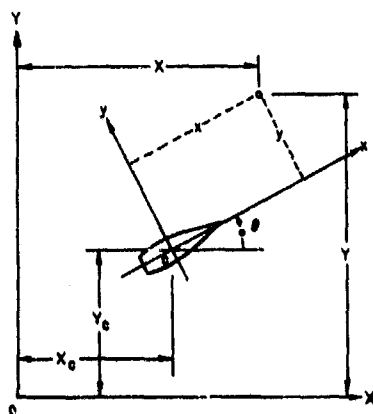


Figure 1. Frames of Reference

$$X = X_c + x \cos \theta - y \sin \theta$$

$$Y = Y_c + x \sin \theta + y \cos \theta$$

$$Z = z$$

$$T = t$$

where  $\theta$  is the angle which the ship makes with the  $X$ -axis, and  $(X_c, Y_c)$  are the coordinates in the  $(X, Y, Z)$  system of the instantaneous position of the ship's center of rotation;  $\theta$ ,  $X_c$ , and  $Y_c$  are generally functions of the time ( $T$  or  $t$ ).

Potential flow is assumed in this study. Using  $\phi$  for the velocity potential, we have

$$\phi_X = \phi_x \cos \theta - \phi_y \sin \theta$$

$$\phi_Y = \phi_x \sin \theta + \phi_y \cos \theta$$

$$\phi_Z = \phi_z$$

$$\phi_T = \phi_t + \bar{u}\phi_x + \bar{v}\phi_y$$

(1)

where

$$\bar{u} = -u_0 + \omega y$$

$$\bar{v} = -v_0 - \omega x$$

$$u_0 = (X_c)_t \cos \theta + (Y_c)_t \sin \theta$$

$$v_0 = -(X_c)_t \sin \theta + (Y_c)_t \cos \theta$$

$$\omega = \theta_t$$

In the equations above, subscripts imply partial differentiation, e.g.,

$$\phi_X \equiv \frac{\partial \phi}{\partial X} \Big|_{Y, Z, T}$$

while

$$\phi_x \equiv \frac{\partial \phi}{\partial x} \Big|_{y, z, t}$$

In the  $(X, Y, Z, T)$  system, two of the governing equations are the Laplace equation

$$\phi_{XX} + \phi_{YY} + \phi_{ZZ} = 0$$

(3)

and the Bernoulli equation

$$\phi_T + \frac{1}{2} [(\phi_X)^2 + (\phi_Y)^2 + (\phi_Z)^2] + gZ + \frac{p}{\rho} = 0$$

(4)

In Eq. (4),  $p$  is the fluid pressure and  $\rho$  the density. Using Eqs. (1), Eqs. (3) and (4) can be written as

$$\phi_{xx} + \phi_{yy} + \phi_{zz} = 0$$

(5)

and

$$\phi_t + \bar{u}\phi_x + \bar{v}\phi_y + \frac{1}{2}[(\phi_x)^2 + (\phi_y)^2 + (\phi_z)^2] + gz + \frac{p}{\rho} = 0. \quad (6)$$

The boundary condition at the hull surface is simply given by

$$(\vec{v}_B - \vec{v}_F) \cdot \vec{n} = 0 \quad (7)$$

where  $\vec{v}_B$  is the velocity of a point at the body surface,  $\vec{v}_F$  the velocity of the fluid particle which happens to be at the surface point under consideration, and  $\vec{n}$  is the unit normal vector at that point. In the  $(x, y, z, t)$  system, Eq. (7) is expressed explicitly as

$$\phi_x n_1 + \phi_y n_2 + \phi_z n_3 = -\bar{u}n_1 - \bar{v}n_2 \quad (8)$$

where  $(n_1, n_2, n_3)$  are the cartesian components of the vector  $\vec{n}$ . As shown in Fig. 2, let the single-valued function  $y = f(x, z)$  describe the distance of the hull from the ship's center plane. Then the components of  $\vec{n}$  can be written as

$$n_1 = -f_x/A$$

$$n_2 = 1/A$$

$$n_3 = -f_z/A$$

where

$$A = \sqrt{1 + (f_x)^2 + (f_z)^2}.$$

Thus, the hull-surface boundary condition, Eq. (8), becomes

$$f_x(\bar{u} + \phi_x) + f_z\phi_z - \phi_y - \bar{v} = 0. \quad (9)$$

Note that generally  $f(x, z) \neq 0$  in the projected area of the ship hull on the center plane, and  $f(x, z) \equiv 0$  outside that area.

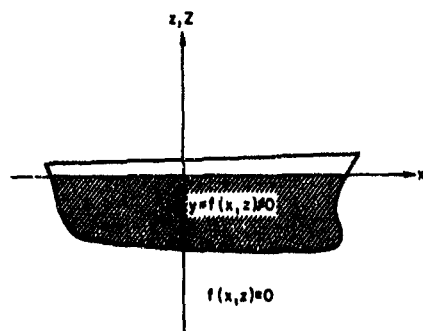


Figure 2. Distribution of  $f(x, z)$  on the Ship's Center Plane

#### Body-Fitted Coordinate System

It is convenient to use a curvilinear coordinate system with the property that one of its coordinate planes coincides with the hull surface. Consider a new coordinate system  $(x', y', z', t')$  which is related to the  $(x, y, z, t)$  system by

$$\begin{aligned} x' &= x \\ y' &= y - f(x, z) \\ z' &= z \\ t' &= t. \end{aligned} \quad (10)$$

Let  $Q$  be any scalar quantity, then by the chain rule we have

$$\begin{aligned} Q_x &= Q_{x'} - f_{x'} Q_{y'} \\ Q_y &= Q_{y'} \\ Q_z &= Q_{z'} - f_{z'} Q_{y'} \\ Q_t &= Q_{t'}. \end{aligned} \quad (11)$$

Using these relations in Eq. (5), the Laplace equation becomes

$$\begin{aligned} \phi_{x'x'} + [1 + (f_{x'})^2 + (f_{z'})^2] \phi_{y'y'} + \phi_{z'z'} \\ - 2(f_{x'}\phi_{x'y'} + f_{z'}\phi_{y'z'}) \\ - (f_{xx'} + f_{zz'})\phi_{y'} = 0, \end{aligned} \quad (12)$$

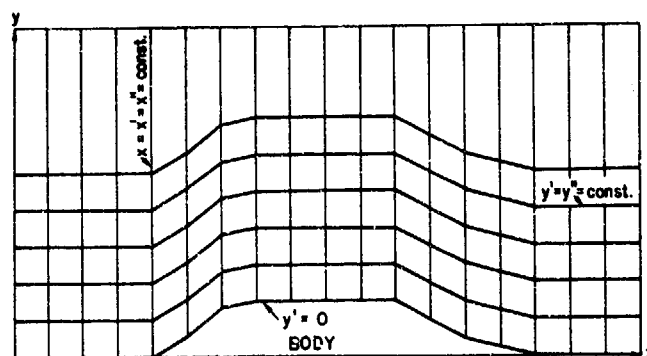
and the Bernoulli equation

$$\begin{aligned} \phi_{t'} + \bar{u}\phi_{x'} + (\bar{v} - \bar{u}f_{x'})\phi_{y'} \\ + \frac{1}{2}\{(\phi_{x'} - f_{x'}\phi_{y'})^2 + (\phi_{y'})^2 + (\phi_{z'} - f_{z'}\phi_{y'})^2\} \\ + gz' + \frac{p}{\rho} = 0. \end{aligned} \quad (13)$$

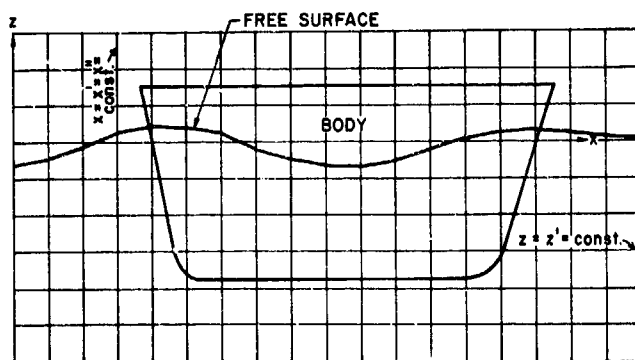
The hull surface boundary condition, Eq. (9), now takes the form

$$\phi_{y'} = [f_{x'}(\bar{u} + \phi_{x'}) - \bar{v} + f_{z'}\phi_{z'}] / [1 + (f_{x'})^2 + (f_{z'})^2]. \quad (14)$$

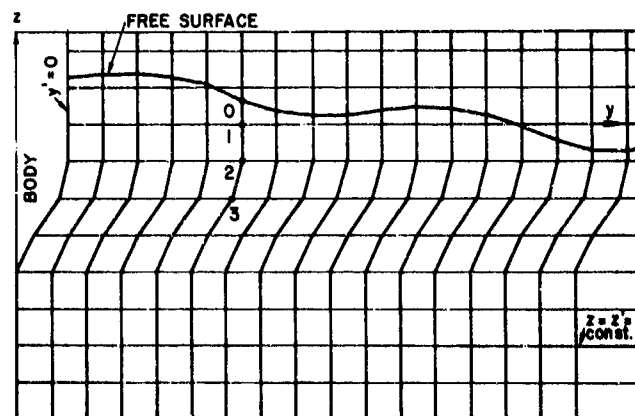
The location of the free surface can be described by defining a scalar function  $\zeta(x', y', z', t') \equiv z' - \eta(x', y', t')$ ;  $\eta$  is the height of the point at which the  $z'$  coordinate line pierces through the free surface (Figs. 3(b) and (c)). Using this description, the class of free surface shapes is limited to those representable by a single-valued function of  $(x', y')$ . Since  $\zeta \equiv 0$  at the free surface for all times, the particle derivative  $D\zeta/Dt$  vanishes there, viz.



(a) Top View



(b) Side View



(c) Front View

Figure 3. Coordinate Systems and Computation Mesh

$$\frac{D\zeta}{Dt} = \zeta_T + \phi_X \zeta_X + \phi_Y \zeta_Y + \phi_Z \zeta_Z = 0. \quad (15)$$

Applying the transformations Eqs. (1) and (11), this leads to

$$\begin{aligned} \eta_{t''} + (\bar{u} + \phi_X) \eta_{x''} + [\bar{v} + \phi_Y \\ - (\bar{u} + \phi_X) f_X - \phi_Z f_Z] \eta_{y''} = \phi_Z \end{aligned} \quad (16)$$

which governs the displacement of the free surface. In the equations above, quantities like  $\phi_X$ ,  $\phi_Y$ ,  $\phi_Z$ , etc. are to be evaluated by Eqs. (11).

#### Coordinate System for Free Surface Conditions

To impose correctly the free surface conditions for finite-amplitude waves, it is important that Eqs. (13) and (16) be applied at the instantaneous position of the free surface. This is cumbersome to do in the  $(x', y', z', t')$  system because in general none of the coordinate planes coincides with the free surface.

Consider the following change of variables.

$$\begin{aligned} x'' &= x' \\ y'' &= y' \\ z'' &= z' - \eta(x', y', t') \\ t'' &= t'. \end{aligned} \quad (17)$$

Equations (13) and (16) can be written, respectively, as

$$\begin{aligned} \phi_{t''} + \bar{u} \phi_{x''} + (\bar{v} - \bar{u} f_X - f_X \phi_{x''}) \phi_{y''} + \Delta \\ + g\eta + \frac{p}{\rho} = 0 \end{aligned} \quad (18)$$

$$\begin{aligned} \eta_{t''} + (\bar{u} + \phi_X) \eta_{x''} + [\bar{v} + \phi_Y - (\bar{u} + \phi_X) f_X \\ - \phi_Z f_Z] \eta_{y''} = \phi_Z \end{aligned} \quad (19)$$

where

$$\begin{aligned} \Delta = \frac{1}{2} \left\{ \phi_{x''}^2 + (1 + f_X^2 + f_Z^2) \phi_{y''}^2 \right. \\ \left. - \left[ 1 + \eta_{x''}^2 + (1 + f_X^2 + f_Z^2) \eta_{y''}^2 \right. \right. \\ \left. \left. + 2\eta_{y''} (f_Z - f_X \eta_{x''}) \right] \phi_{z''}^2 \right\}. \end{aligned}$$

These equations are to be used at the free surface where  $z'' = \eta$  (or  $z'' = 0$ ). Thus, the term  $g\eta$  has been replaced by  $g\eta$  in Eq. (18). The following relations are used to evaluate  $\phi_X$ ,  $\phi_Y$ , and  $\phi_Z$ , which appear in the equations above.

$$\begin{aligned} \phi_X &= \phi_{x''} - f_X \phi_{y''} + (f_X \eta_{y''} - \eta_{x''}) \phi_{z''} \\ \phi_Y &= \phi_{y''} - \eta_{y''} \phi_{z''} \\ \phi_Z &= (1 + f_Z \eta_{y''}) \phi_{z''} - f_Z \phi_{y''}. \end{aligned} \quad (20)$$

Note that in Eqs. (18)-(20) all space derivatives can be evaluated on the plane  $z'' = 0$ , the only exception being  $\phi_{z''}$  which involves variation of  $\phi$  below the free surface. Since  $\phi_{z''} = \phi_{z'}$ ,  $\phi_{z''}$  can be easily computed by using the  $(x', y', z', t')$  system which describes the interior flow field.

The hull surface condition, Eq. (14), becomes

$$\begin{aligned} \phi_{y''} \\ = \frac{f_X (\bar{u} + \phi_X) - \bar{v} + [1 + f_X^2 + f_Z^2] \eta_{y''} + f_Z - f_X \eta_{x''}}{1 + f_X^2 + f_Z^2} \phi_{z''} \end{aligned} \quad (21)$$

and, using Eq. (9), Eq. (19) reduces to

$$\eta_{t''} + (\bar{u} + \phi_X) \eta_{x''} = \phi_Z \quad (22)$$

for use at the intersection of free surface and the solid body.

#### Other Boundary Conditions

Temporal integration of Eqs. (18) and (19) provides values of  $\phi$  and  $\eta$  at the free surface at any instant of time. At the bottom of the computational "tank,"  $\phi_Z = 0$ . At large  $y'$ , the disturbance should vanish, so that  $\phi = 0$ . This condition also applies at a sufficiently large distance upstream of the ship for forward motion. At the downstream end of the computation domain proper radiation condition must be imposed so that waves can leave the region of interest with minimum amount of nonphysical reflections. This condition is so crucial to successful computation of wave propagation in a limited domain, we shall describe it in a separate section (Section IV).

#### Outline of the Computational Procedure

The basic computational mesh is rectangular in the  $(x', y', z')$  space, as shown in Figs. 3(a)-(c). The only quantities to be computed in the  $(x'', y'', z'')$  system are  $\eta$  and  $\phi$  at the free surface. The following is a sketch of the steps required to advance the flow field in time.

1. Apply radiation boundary condition to obtain advanced values of  $\eta$  and  $\phi$  at the downstream end of the computation domain.
2. Use Eqs. (18) and (19) to advance  $\phi$  and  $\eta$  at the instantaneous position of the free surface.

3. Obtain the  $\phi$ -field by solving Eq. (12), subject to appropriate boundary conditions, e.g., Eq. (14).

### III. Finite Difference Schemes

For illustrative purposes, let us assume constant mesh spacings  $\delta x''$ ,  $\delta y''$ , and  $\delta z''$ . It was found early in this study that the computation is unstable when the familiar scheme of explicit central difference is employed. Since in forward motion, the flow clearly has a preferred direction, one immediately thinks of the one-sided, upwind difference. Unfortunately, the usual upwind difference schemes introduce so much artificial damping that the accuracy is seriously impaired. In this study we use a new upwind-centered scheme which introduces no artificial viscosity for pure advections at a constant velocity.

Let  $Q$  be any quantity, such as  $\phi$  or  $\eta$ , defined at the free surface. We use the indices  $(i, j, n)$  to discretize  $Q$  over the free surface, such that

$$Q_{i,j}^n \equiv Q(i \delta x'', j \delta y'', n \delta t'')$$

where  $\delta x''$  and  $\delta y''$  are the spatial mesh spacings and  $\delta t''$  is the time increment. Equations (18) and (19) can be cast in the general form

$$Q_t'' + u^* Q_x'' + v^* Q_y'' + \xi = 0 \quad (23)$$

where  $u^* = \bar{u}$ ,  $v^* = \bar{v} - \bar{u} f_x - f_x \phi_x''$  for Eq. (18) and  $u^* = \bar{u} + \phi_x$ ,  $v^* = \bar{v} + \phi_y - (\bar{u} + \phi_x) f_x - \phi_z f_z$  for Eq. (19). Since in forward motion (i.e., the ship moving toward the negative  $x''$ -direction)  $u^* \geq 0$ , we may develop our finite difference schemes about an upstream point  $O$  as shown in Figs. 4(a) and (b), using the following rules:

$$[Q_t]_O^n = (Q_A - Q_B) / \delta t''$$

$$[Q_x]_O^n = (Q_{i,j}^n - Q_{i-1,j}^n) / \delta x''$$

$$[Q]_O^n = \frac{1}{2} (Q_{i,j}^n + Q_{i-1,j}^n)$$

$$[Q_y]_O^n = \frac{1}{2} (Q_{i,j+1}^n - Q_{i,j-1}^n + Q_{i-1,j+1}^n - Q_{i-1,j-1}^n) / (2\delta y'')$$

where

$$Q_A \equiv \frac{1}{2} (Q_{i,j}^{n+1} + Q_{i-1,j}^n) \quad (24)$$

$$Q_B \equiv \frac{1}{2} (Q_{i,j}^n + Q_{i-1,j}^{n-1})$$

Using these rules, Eqs. (18) and (19) lead to explicit, one-step, but three-level difference schemes for advancing  $\eta$  and  $\phi$  at the free surface. It can be shown that Eqs. (24), when applied to the simple advection equation  $Q_t'' + uQ_x'' + vQ_y'' = 0$  ( $u$  and  $v$  are constants),

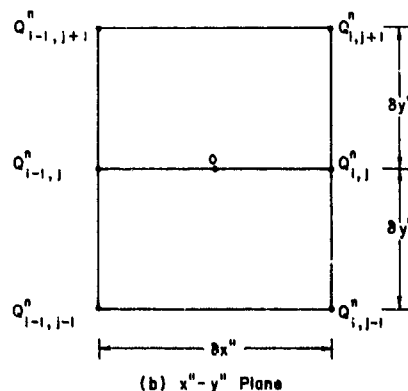
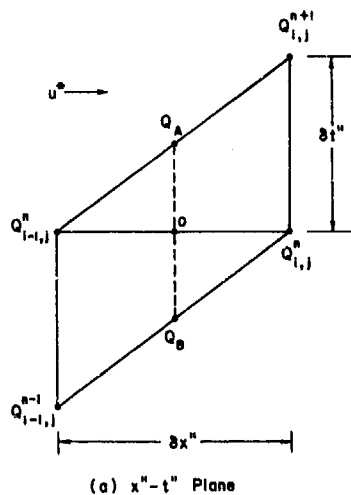


Figure 4. Upwind Centered Difference Scheme

lead to a finite difference algorithm that does not contain any artificial viscosity.

In solving Eqs. (18) and (19), one has to evaluate  $\phi_{z''}$  at the free surface (see also Eqs. (20)). Since  $\phi_{z''} = \phi_z'$ , we only have to calculate  $\phi_z'$  at the free surface. In Fig. 3(c) let  $\phi_0$  be the value of  $\phi$  at a free-surface point  $O$ , then a one-sided difference gives

$$[\phi_z]_O^n = (\phi_0^n - \phi_1^n) / (z_0^n - z_1^n) \quad (25)$$

The boundary condition, Eq. (21), for  $\phi$  at the free surface is represented by a one-sided difference in the  $y''$ -direction, but by central difference in the other two directions.



Because interior values of  $\phi$ , such as  $\phi_1^n$  in Eq. (25), are needed in solving Eqs. (18) and (19), one must solve Eq. (12) to obtain the internal distribution of  $\phi$ . This is done by using the following difference expressions

$$\begin{aligned} [\phi_{xx}]_{i,j,k}^n &= \left\{ \phi_{i+1,j,k}^n - 2\phi_{i,j,k}^n + \phi_{i-1,j,k}^n \right\} \\ &\quad \cdot (\delta x)^{-2} \\ [\phi_{yy}]_{i,j,k}^n &= \left\{ \phi_{i,j+1,k}^n - 2\phi_{i,j,k}^n + \phi_{i,j-1,k}^n \right\} \\ &\quad \cdot (\delta y)^{-2} \\ [\phi_{zz}]_{i,j,k}^n &= \left\{ \phi_{i,j,k+1}^n - 2\phi_{i,j,k}^n + \phi_{i,j,k-1}^n \right\} \\ &\quad \cdot (\delta z)^{-2} \\ [\phi_{xy}]_{i,j,k}^n &= \left\{ \phi_{i+1,j+1,k}^n - \phi_{i-1,j+1,k}^n \right. \\ &\quad \left. - \phi_{i+1,j-1,k}^n + \phi_{i-1,j-1,k}^n \right\} \\ &\quad \cdot (4 \delta x \delta y)^{-1} \\ [\phi_{yz}]_{i,j,k}^n &= \left\{ \phi_{i,j+1,k+1}^n - \phi_{i,j-1,k+1}^n \right. \\ &\quad \left. - \phi_{i,j+1,k-1}^n + \phi_{i,j-1,k-1}^n \right\} \\ &\quad \cdot (4 \delta y \delta z)^{-1} \\ [\phi_{xz}]_{i,j,k}^n &= \left\{ \phi_{i,j+1,k}^n - \phi_{i,j-1,k}^n \right\} / (2\delta y) = 0 \end{aligned} \quad (26)$$

in Eq. (12) and solving the resulting system of difference equations by the standard procedure of successive over-relaxation (SOR), subject to appropriate boundary conditions. Note that  $\delta x'' = \delta x$  and  $\delta y'' = \delta y$  in Eqs. (26). At the hull surface, Eq. (14) is represented by a one-sided difference in the  $y'$ -direction, while central difference is used in the other two directions. In forward motion the boundary condition at the upstream (or inflow) plane and at large  $y'$  is simply  $\phi \equiv 0$ . At the free surface,  $\phi$  is provided by Eqs. (18) and (19), as just described. For an internal mesh point near the free surface, such as point 1 in Fig. 3(c),  $\phi_1$  is obtained by interpolation from  $\phi_0$ ,  $\phi_2$ , and  $\phi_3$ . At the downstream (or outflow) plane, values of  $\phi$  are provided by the radiation condition described below.

#### IV. Radiation Condition

Wave reflections from "outflow" or open boundaries have traditionally presented a special difficulty in finite-difference simulation of hyperbolic systems. Various devices, such as simple extrapolation or artificial damping near the outflow region, have been proposed by

a number of authors in the past. Experience indicates, however, that none of these methods is effective in reducing wave reflections to a negligible degree. Recently, Orlanski<sup>2</sup> published a simple, but very effective treatment of such boundaries. His method consists of imposing a Sommerfeld radiation condition at the outflow boundary and numerically evaluating the phase velocity in the vicinity of the boundary. Since Orlanski's original finite difference representation of the radiation condition is dissipative, we have replaced it with a nondissipative, neutrally stable scheme in this paper. The reader is referred to the original paper for details on Orlanski's scheme. We shall describe here the improved version.

The Sommerfeld radiation condition is

$$Q_t + CQ_x = 0, \quad (27)$$

where  $Q$  is any variable, and  $C$  is the phase velocity of the waves. Because the dispersion characteristics of a complicated hyperbolic system are not generally known, it is desirable to have a simple procedure for finding the value of  $C$  needed to effect the condition (27).

Using the finite differences in Eqs. (24), Eq. (27) becomes

$$Q_{iB}^{n+1} = Q_{iB-1}^{n-1} + (1 - 2\alpha) \left\{ Q_{iB}^n - Q_{iB-1}^n \right\} \quad (28)$$

where the mesh index  $i = iB$  at the outflow boundary point and

$$\alpha \equiv \frac{C\delta t}{\delta x}.$$

The time step  $\delta t$  is chosen such that  $0 \leq \alpha \leq 1$ . By inserting a Fourier component solution in Eq. (28), it can be shown that the amplitude of wave components of all lengths is preserved under the algebraic operations in Eq. (28).

Equation (28) allows one to advance  $Q$  at the outflow boundary if  $\alpha$  is known. This is accomplished by reducing the values of both the superscripts and subscripts in Eq. (28) by one unit and rearranging to give

$$\alpha = \frac{1}{2} \left( Q_{iB-1}^n + Q_{iB-2}^{n-1} - Q_{iB-1}^{n-1} - Q_{iB-2}^{n-2} \right) / \left( Q_{iB-1}^{n-1} - Q_{iB-1}^{n-2} \right). \quad (29)$$

By Eq. (29) we now have all the information to compute  $\alpha$  and, in turn by Eq. (28),  $Q_{iB}^{n+1}$ .

Note that Eq. (29) is equivalent to finding  $C$  by rearranging Eq. (27) into the form

$$C = -Q_t/Q_x. \quad (30)$$

When a wave crest or trough approaches the outflow boundary, Eq. (30) can result in division of zero by zero, a singular situation that must be treated separately. Thus, when the absolute value of the denominator in Eq. (29) becomes very small, e.g.,

$$|Q_{IB-2}^{n-1} - Q_{IB-1}^{n-1}| < 10^{-10} |Q_{\max} - Q_{\min}|$$

where  $Q_{\max}$  and  $Q_{\min}$  are the extreme values of  $Q$  in the flow field, we simply set

$$Q_{IB}^{n+1} = Q_{IB}^n \quad (31)$$

to replace Eq. (28). This is a valid procedure because when a wave crest or trough reaches the boundary,  $Q_{IB}$  changes very little in one time step. However, in applying Eq. (29) there is still the possibility of dividing a small number by another small number, leading to a large error in  $\alpha$ . As Orlanski pointed out, the following constraints on  $\alpha$  are sufficient to handle such singular cases. Let the right side of Eq. (29) be  $\alpha^*$ , then

$$\alpha = \begin{cases} 0, & \text{if } \alpha^* < 0 \\ \alpha^*, & \text{if } 0 \leq \alpha^* \leq 1 \\ 1, & \text{if } \alpha^* > 1 \end{cases} \quad (32)$$

In the present study, Eqs. (28)-(32) are applied to  $\phi$  in the interior near the outflow plane of the computation domain. The effectiveness of this treatment will be discussed in the next section.

#### V. Discussion of Sample Results

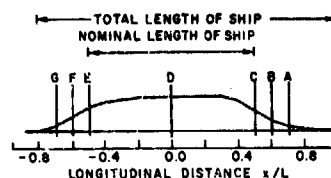
To demonstrate the present approach, consider a shiplike floating body depicted in Figs. 5(a) and (b). Throughout this section, we shall consider only the forward motion. For comparison purposes, calculations were performed using linearized equations as well as the full, nonlinear equations. The linearized free surface conditions are obtained by neglecting higher order terms in Eqs. (13) and (16):

$$\phi_t + u^* \phi_x + g\eta = \frac{p}{\rho} = 0 \quad (33)$$

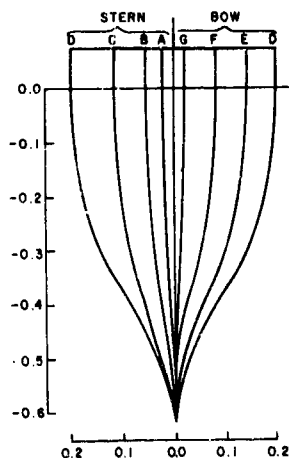
$$\eta_t + u^* \eta_x = \phi_z \quad (34)$$

where  $u^* = -u_0 = -(X_c)_t$  and  $gz$  has been replaced by  $g\eta$ . Equations (33) and (34) are to be applied at the initial, undisturbed position of the free surface.

Dimensionless variables will be used throughout this discussion. Let  $L$  be a characteristic length of the flow, such as the nominal length of ship (Fig. 5(a)). All lengths will be normalized by  $L$ , all velocities by  $\sqrt{gL}$ , accelerations by  $g$ , and time by  $\sqrt{L/g}$ . In a typical calculation the computation domain consists of 40 mesh points in the  $x$ -direction, 20 in the  $y$ -direction, and 20 in the  $z$ -direction. Variable mesh spacings are employed to meet resolution requirements in different parts of the flow field. The values  $\delta x = \delta y = \delta z = 0.1$  are used near the ship. The motion of the ship is prescribed by



(a) Top View



(b) Cross Sections

Figure 5. Shiplike Body Used in Sample Calculations

$$u_0 = (X_c)_t = \begin{cases} 0, & t \leq 0 \\ (u_0)_{\max} \cdot (t/t_{\max}), & 0 < t < t_{\max} \\ (u_0)_{\max}, & t \geq t_{\max} \end{cases} \quad (35)$$

Figures 6(a) and (b) compare the free surface profiles along  $y' = 0$  (Fig. 3(a)) between linear and nonlinear calculations for  $(u_0)_{\max} = 1.0$  and  $t_{\max} = 4.0$ . Figure 6(a) corresponds to  $t = 2.5$  when the ship is still accelerating, and the flow is unsteady. At  $t = 10.0$  (Fig. 6(b)) the flow in the computation domain has reached steady state. At steady state, the Froude number  $|u_0|/\sqrt{gL} = 1.0$ . The nonlinear result is quite different from the linear one, something to be expected because in this case  $ka = 0.65$  for the linear solution ( $k$  is the wave number and  $a$  the amplitude). The wave pattern at three different times for the nonlinear calculation is shown in Figs. 7(a)-(c) in terms of contour plots of  $\eta$ .

The method of this paper is also applicable to a submerged body. As a numerical

experiment, both linear and nonlinear calculations were made for the forward motion of a body with nondimensional length equal to 1.0, and a diameter of 0.2. The depth of submergence is 0.58. The motion is again prescribed by Eq. (35), with  $(u_0)_{\max} = -1.0$  and  $t_{\max} = 4.0$ . The nonlinear and linear free surface profiles at  $y' = 0$  are compared in Figs. 8(a) and (b). Note that the profiles in Fig. 8(b) are in steady state. In this submerged case, as opposed to the surface ship above, the source of disturbance is farther from the free surface, and the linearized free surface conditions are expected to be good approximations, as is evident in these comparisons. In this case,  $ka = 0.1$ . The contour plots of the free surface are shown in Figs. 9(a)-(c) for three different times. The flow field in the computational domain has reached steady state in Fig. 9(c).

In the examples above, the body was initially at rest and then accelerated to a final, constant velocity. In due time the flow field in the computation domain should reach a steady state. It is interesting to see how the steady state is approached in different parts of the field. Furthermore, it is a nontrivial question whether the same steady-state solution is obtained if the ship accelerates in different manners before reaching the prescribed final velocity, because the flow is nonlinear and it is not clear how the numerical radiation condition and truncation errors in general affect the well-posedness of the overall problem. To answer this question, an additional calculation was made for the nonlinear problem in Figs. 6, this time the ship being impulsively set into forward motion with  $u_0 = -1.0$  in one time step. Figure 10(a) compares the steady-state free surface profile at  $y' = 0$  between the gradually started case (i.e., the problem associated with Figs. 6) and the impulsively started one. The agreement is excellent except for minor discrepancy at the last few points. Note that the last point (point C) is subject to numerical radiation condition. This kind of agreement is observed throughout the entire computation domain. The time history of  $\eta$  at three selected points A, B, and C (see Fig. 10(a) for definitions) is compared in Fig. 10(b). It is seen that, independent of starting conditions, a unique steady state is approached, except for minor variations at points very close to the outflow boundary.

To investigate the effectiveness of the radiation condition, two linear calculations were made for the problem associated with Figs. 6, one with a short computation domain ( $-2.36 \leq x' \leq 2.45$ ) and the other with a long domain ( $-2.36 \leq x' \leq 8.45$ ). These two runs are compared in Figs. 11(a) and (b) for the transient and steady states, respectively, in terms of the wave profile at  $y' = 0$ . Similarly good agreement is found throughout the flow field. Thus, we have some concrete evidence that Orlanski's radiation condition leads to practically no spurious reflection at all.

Although validations and extensive application of the present methodology is not within the scope of this paper, one potential

application is worth mentioning. Suppose that the calculation of a particular flow situation has been validated by comparing with experimental data in terms of quantities that can be easily measured, such as the drag (with the viscous contribution subtracted) and the wave height distribution. The wealth of information contained in the numerical solution can then be processed to gain some insight into various simplifications made in analytical models. This may help identify those areas needing improvements in the simplified theories. For the nonlinear problem considered in Figs. 6, as an example, one can examine the validity of the linearized equations (33) and (34) along  $y' = 0.1$  at the free surface when steady state is reached. In Fig. 12(a), the terms  $u^*\phi_x$  and  $-gn$  are compared. These two terms are supposed to be in balance by Eq. (33). The agreement is good in general, except near the bow and the stern. The curve for  $u^*\phi_x$ , which is used in conventional linear analysis, shows a greater deviation from the  $-gn$  curve. Next, we compare  $u^*\eta_x$  with  $\phi_z$  in Fig. 12(b) and find fairly good agreement. Again, the term  $u^*\eta_x$ , used in conventional analysis, differs considerably from  $\phi_z$  near the stern. Thus it appears that Eq. (34) is a good approximation for the full equation, while Eq. (33) is not. This observation is also true when the analysis above is repeated for flow variations along  $y' = 0$ . Since more extensive analysis of this type is anticipated in the future, we shall not draw any conclusions that may be premature.

#### References

1. Chan, R. K.-C. and J. S. Stuhmiller, "Numerical Solution of Unsteady Ship Wave Problems," Eleventh Symposium on Naval Hydrodynamics, London, 1976.
2. Orlanski, I., "A Simple Boundary Condition for Unbounded Hyperbolic Flows," Journal of Computational Physics, 21, 1976.
3. Stoker, J. J., Water Waves, Interscience Publishers, Inc., New York, 1966.

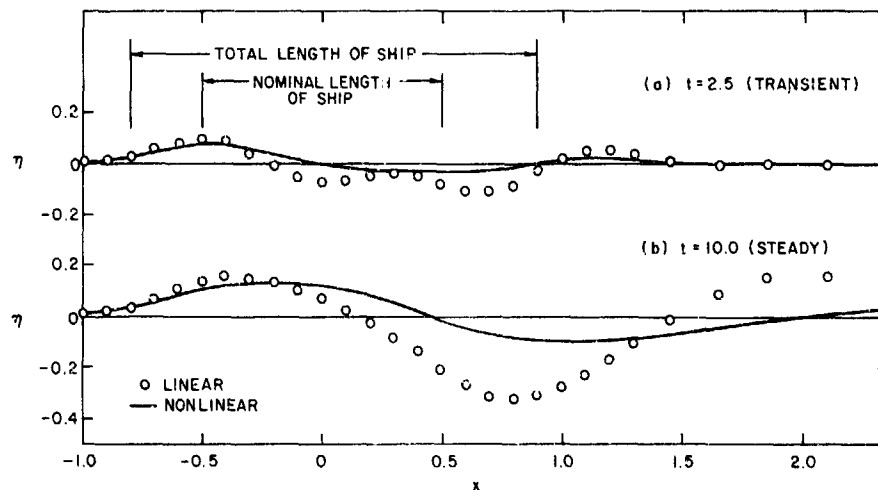
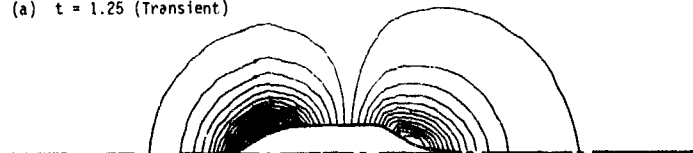


Figure 6. Comparison of Wave Profiles at  $y' = 0$  for the Forward Motion of the Shiplike Body Shown in Figure 5

(a)  $t = 1.25$  (Transient)



(b)  $t = 3.75$  (Transient)



(c)  $t = 15.0$  (Steady State)

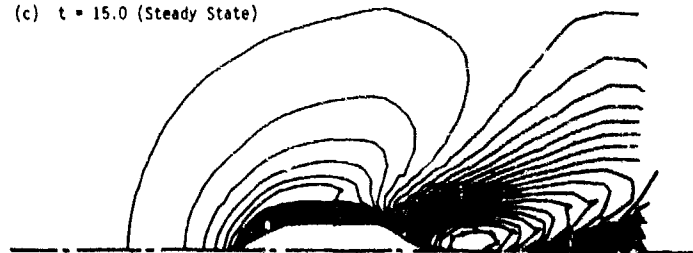


Figure 7. Free Surface Contour Maps for the Problem in Figure 6

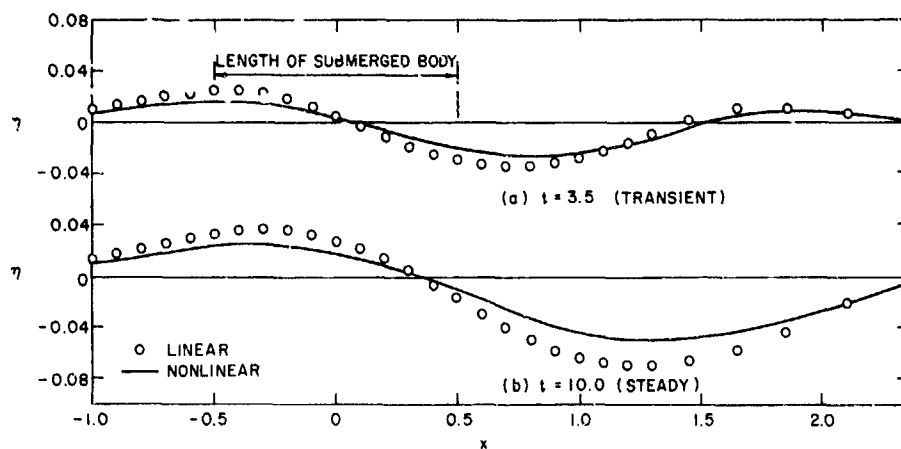


Figure 8. Comparison of Wave Profiles at  $y' = 0$  for the Forward Motion of a Submerged Body

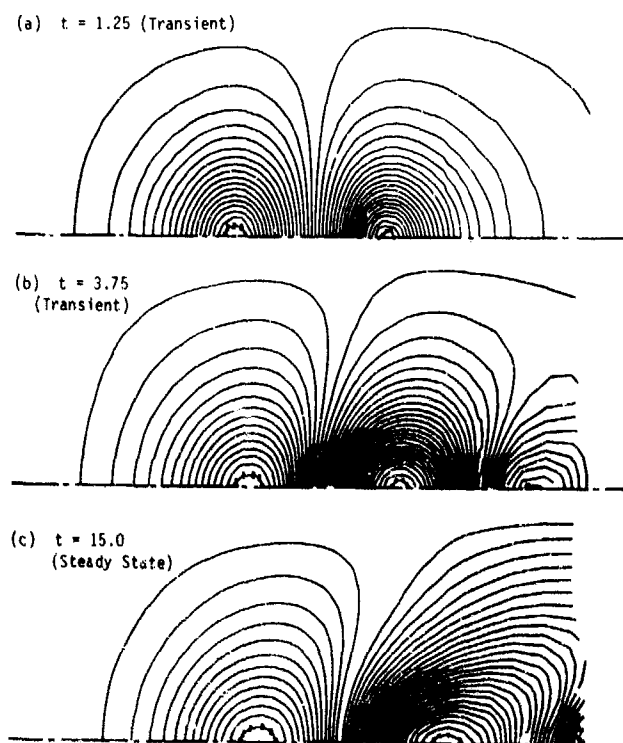


Figure 9. Free Surface Contour Maps for the Problem in Figure 8

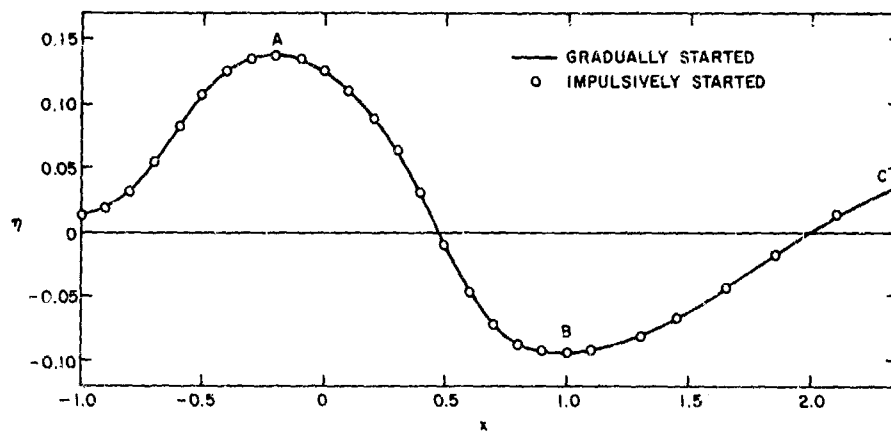


Figure 10(a). Comparison of Steady-State Wave Profiles at  $y' = 0$

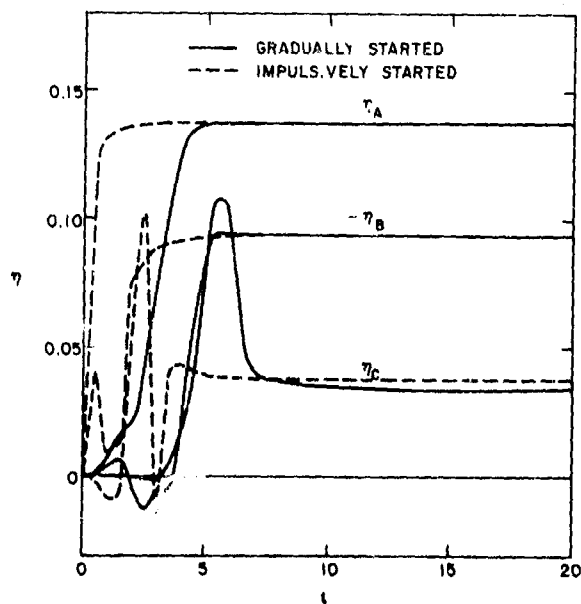
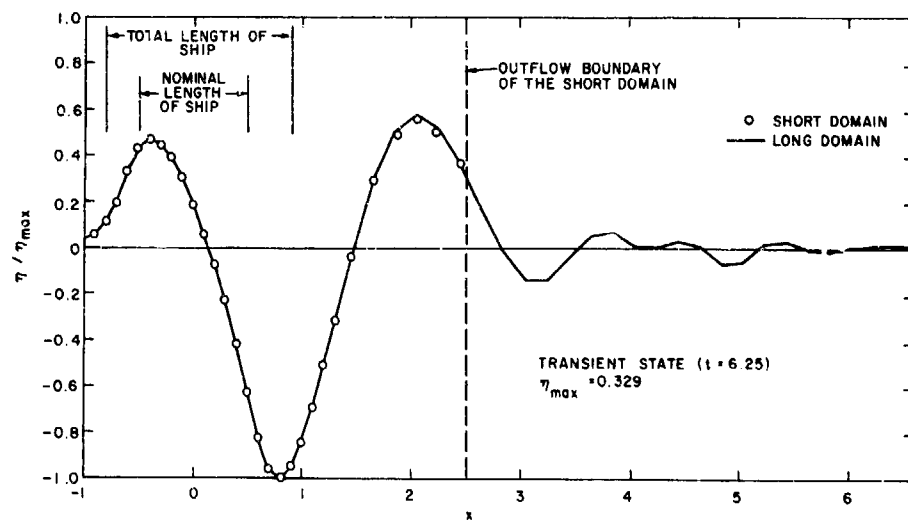
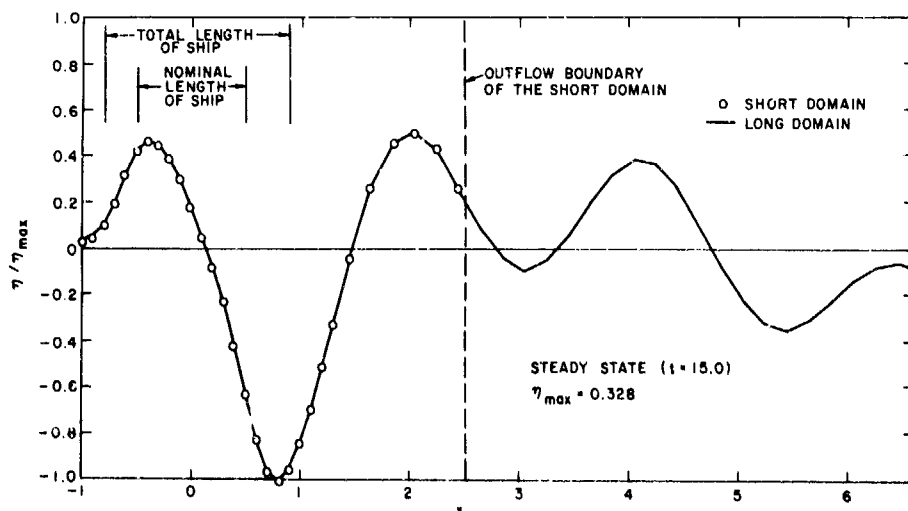


Figure 10(b). Comparison of Time History of Surface Heights at Three Selected Points



(a)



(b)

Figure 11. Calculations for Assessing the Effectiveness of Radiation Condition.

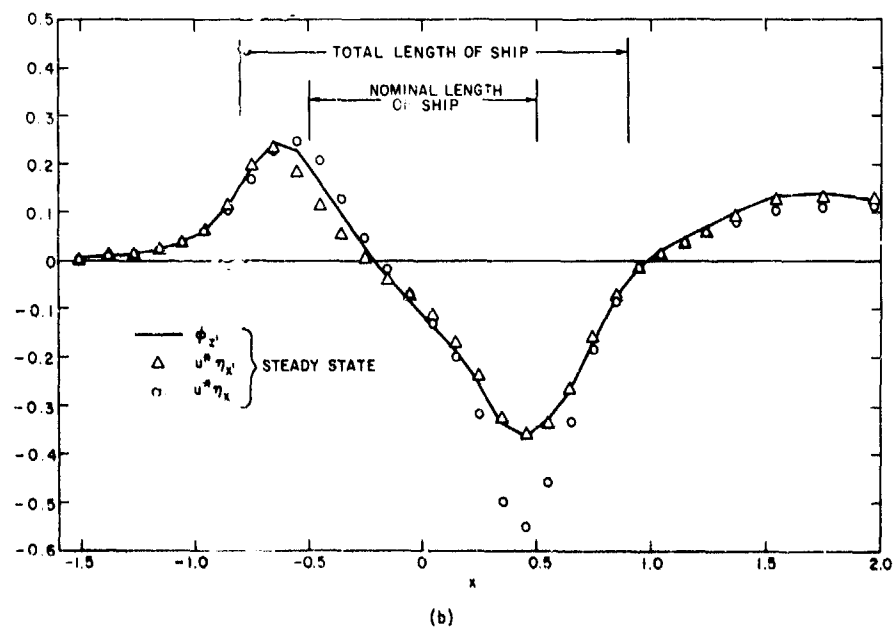
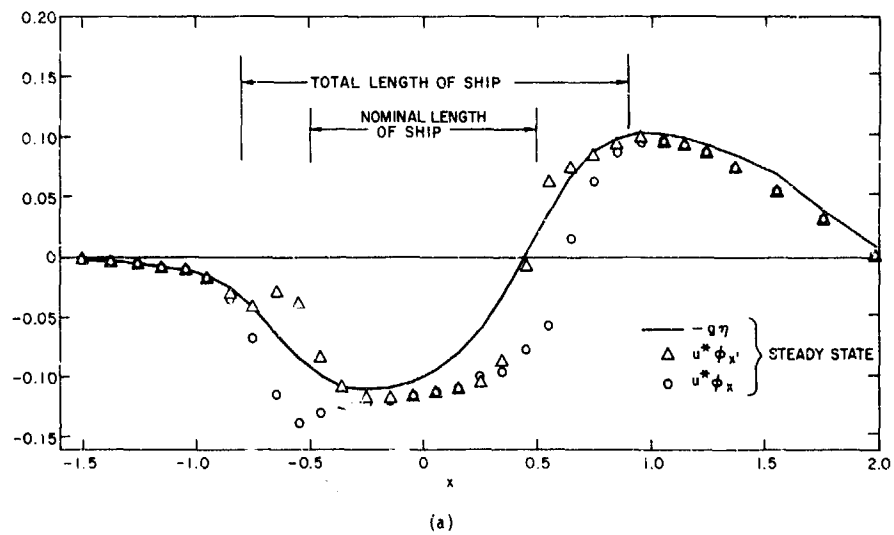


Figure 12. Evaluation of the Adequacy of Linear Approximations



DISCUSSIONS  
of three papers

NUMERICAL EVALUATION OF WAVE-RESISTANCE THEORY FOR SLOW SHIPS

E. Baba and M. Hara

A PRACTICAL COMPUTER METHOD FOR SOLVING SHIP-WAVE PROBLEMS

C. W. Dawson

FINITE DIFFERENCE SIMULATION OF THE PLANAR MOTION OF A SHIP

Robert K. C. Chan

Invited Discussion

J.N. Newman  
Massachusetts Institute of Technology

These three papers represent remarkable progress in analysing the three-dimensional ship-wave problem, in comparison with the state of the art at Gaithersburg two years ago. The paper presented by Dr. Baba is quasi-analytical in its approach, and uses extensions of integral representations that are familiar in the classical ship-wave theory. By comparison, Drs. Dawson and Chan have obtained direct numerical solutions that include unsteady and nonlinear effects.

The work of Baba and Hara is based on the low Froude-number assumption; and thus it might be judged less ambitious than the following papers, but the results are very complete and impressive. The slow-ship approximation is appealing from the practical standpoint, especially for large merchant ships. This is essentially a short-wavelength approximation, with all the subtleties thereof. In particular, the waves are driven by a slowly-varying double-body field. Since the short waves are not efficiently driven by this slowly-varying generator, I wonder if the result is correct to leading order in a perturbation sense, in comparison with other higher-order terms that have been neglected. Also, how serious are the singularities at the bow and stern, where the double-body flow is not slowly varying as assumed?

The paper by Dr. Dawson includes calculations of the free-surface elevation and of the wave resistance; the crucial step of one-sided finite-differencing appears to embrace the radiation condition as a part of the free-surface condition. From the analytic viewpoint this seems a marriage of convenience, but the results are impressive. One detailed comment is that the double-hull linearized free-surface condition differs from that derived by Dr. Baba and myself; Dr. Dawson applies the free-surface boundary condition on  $z=0$ , as opposed to the "double-body free surface", with differences that appear to be of leading order. It would seem no more difficult to use the more complete free-surface condition equation (2) of Drs. Baba and Hara. However the comparison in wave-resistance calculations between these two papers is striking and

suggests that the difference in the free-surface condition is not too significant.

The paper of Dr. Chan is doubly impressive in treating the full nonlinear problem, for unsteady motion. Much weight is placed on the utilization of a numerical scheme of Orlansky for imposing the radiation condition. The need for such a condition in this initial-value problem is a bit surprising. Moreover, as utilized here the scheme ensures that a single wave moving parallel to the x-axis will propagate downstream. The unsteady ship-wave radiation condition is more complicated than this, and even in the steady-state the usual linear solution includes two separate transverse and diverging waves, to which the radiation conditions must be applied separately. It is difficult to assess the results without extending the domain further upstream and downstream. That of course is expensive and possibly inaccurate. Within the domain shown the characteristic wavelength seems to be much shorter than is appropriate for steady motion where, with the units adopted,  $\lambda=2\epsilon$ . Perhaps this is the result of unsteadiness as well as the bounded domain on which the waves are being studied.

We should appreciate especially the comparisons for the common Wigley model that have been added by Drs. Dawson and Chan following Dr. Baba's introduction of this hull form in his preliminary summary. There is clearly great value in the use of common hull forms in comparing different numerical techniques, as in the analogous towing-tank tests fostered by the ITTC.

In summary, while there are a few details that remain to be refined, all three of these papers represent impressive progress toward our implicit goal, of predicting ship-wave interactions for practical hull forms. All of the authors are to be commended for their efforts in that quest.

Discussion  
by H. Maruo  
of paper by E. Baba and  
M. Hara

The authors claim that the computation of the wave resistance by means of the slow ship formulation gives good agreement with the measured results. I have carried out a similar calculation and obtained some new results, from which I derive a slightly different conclusion. The basic theory is based on the expression for the velocity potential derived by the direct application of Green's theorem:

$$\begin{aligned} \phi(P) = & -\frac{1}{4\pi} \iint_S \left[ G(P,Q) \frac{\partial \phi(Q)}{\partial n_Q} - \phi(Q) \frac{\partial G(P,Q)}{\partial n_Q} \right] dS_Q \\ & + \frac{1}{4\pi\gamma_0} \int_0 \left[ G(P,Q) \frac{\partial \phi(Q)}{\partial x_1} - \phi(Q) \frac{\partial G(P,Q)}{\partial x_1} \right]_{z'=0} dy' \\ & - \frac{1}{4\pi\gamma_0} \iint_{L_0} \phi(x',y') G(P,Q) \Big|_{z'=0} dx' dy' \end{aligned} \quad (1)$$

$$\begin{aligned} \phi(x,y) = & \frac{1}{2} \left[ \left( 2 \frac{\partial}{\partial x} + u \frac{\partial}{\partial x} + v \frac{\partial}{\partial y} + w \frac{\partial}{\partial z} \right) (u^2 + v^2 \right. \\ & \left. + w^2) - \frac{\partial w}{\partial z} (2u + u^2 + v^2 + w^2) \right]_{z=0} \end{aligned} \quad (2)$$

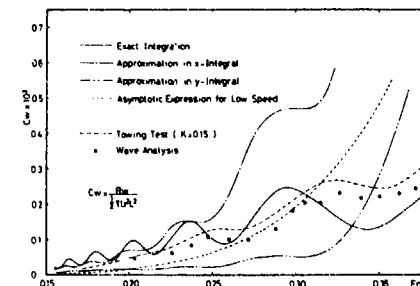
The first term on the right-hand side of (1) gives the singularity distribution over the immersed hull surface  $S$  and the second term is the line integral. The third term represents a plane  $z=0$  or the undisturbed free surface outside the hull, with the source density given by (2). The fluid motion far behind the ship is characterized by the generalized Kochin function defined by

$$\begin{aligned} H(k,\theta) = & -\frac{1}{4\pi} \iint_S \left( \frac{\partial \phi}{\partial n} - \phi \frac{\partial}{\partial n} \right) \exp[kz + k(x \cos \theta \\ & + y \sin \theta)] dS + \frac{1}{4\pi\gamma_0} \int_0 \left( \frac{\partial \phi}{\partial x} \right. \\ & \left. - k \cos \theta \phi \right)_{z=0} \exp[k(x \cos \theta + y \sin \theta)] dy \\ & - \frac{1}{4\pi\gamma_0} \iint_{L_0} \phi(x,y) \exp[k(x \cos \theta + y \sin \theta)] dx dy \end{aligned} \quad (3)$$

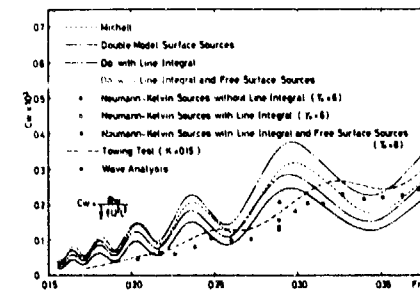
and the wave resistance is given by Havelock's formulae.

$$R_w = 8\pi U^2 \gamma_0^2 \int_{-\pi/2}^{\pi/2} |H(\gamma_0 \sec^2 \theta, \theta)|^2 \sec^3 \theta d\theta. \quad (4)$$

If the Froude number is assumed small, the first approximation is the double model flow. Therefore the wave resistance at low Froude numbers is given by substituting for  $\phi$  the double-model solution  $\phi_0$  in the calculation of the function  $H(k,\theta)$  expressed by (3). For a numerical example, I calculated the case of Wigley's parabolic model. Because of the assumption of the low Froude number, the double integral of the second term of (3) can be further simplified. The result of calculation is given in Fig. 1



which shows several stages of approximate integration. The calculation of Baba and Hara corresponds to the result when the integration with respect to  $x$  is approximated. There are considerable differences between various approximations and the exact integration of the double integral term. Numerical results deviate from the measured values at moderate and higher Froude numbers. For a trial, the solution that satisfies the exact hull-surface condition and the linearized free-surface condition is calculated by assuming a source distribution. This so-called Neumann-Kelvin solution is employed for the calculation of (3). Since the numerical work is very tedious, only results for one Froude number were obtained.



They are shown in Fig. 2. The result including the line-integral and the free surface sources gives plausible agreement with the measured wave-pattern resistance. In conclusion, I wish to point out as a warning that a calculation based on the double model solution is

likely to show a considerable deviation from the measured results at moderate and higher Froude numbers, and the effect of the distortion of the free surface must be taken into account to determine the singularity distribution over the hull surface.

Discussion  
by C. M. Lee  
of paper by E. Baba and  
M. Hara

This paper presents information of great interest to me. I would like to sincerely congratulate the authors for their excellent work.

In a practical sense, the question of the usefulness and the validity of the perturbation expansion about the zero-speed limit in the wave resistance theory seems to be no longer a bothersome issue. However, I will not completely dismiss this question until I can fully digest the paper to be presented by Professor Tuck and Mr. Vanden Broek.

In 1969 at the 12th ITTC meeting, Dr. Baba's work on the so-called wave-breaking resistance was introduced. This has led to an impetus for many investigators to review the decomposition of ship resistance. Essentially, Dr. Baba decomposed the total ship resistance into the viscous resistance and the wave resistance. The viscous resistance was defined by the pressure head loss through the transverse control plane behind a ship. This head loss was divided into one contributed by the frictional wake, and the other by the wave breaking by the bow. The wave resistance was defined as that obtainable from the wave analysis behind the ship.

The present paper appears to give an impression that there is a shift in the position for defining the wave resistance. That is, the experimental results presented in Figures 12 and 14, according to the paper, were obtained by Hughes' form-factor method. As we know, any correlation of theoretical wave resistance with model experimental results can be significantly influenced by the definition of wave resistance obtained by experiments. It would be interesting to know why the authors did not compare the theoretical results with the wave-cut results, which can be truly defined as wave resistance, consistent with the theoretical definition. Could it be possible that the results presented in Figures 12 and 14 contained the wave-breaking resistance, especially for the fuller models?

I understand that a numerical integration of rapidly oscillating function such as the amplitude function  $|A(\theta)|^2$  can be more effectively performed by Filon's method. I would like to know if the authors tried this method instead of Simpson's rule which could be time-consuming and erroneous when applied to rapidly oscillating functions.

Author's Reply  
by E. Baba and M. Hara  
to discussion by C.M. Lee

There are three reasons why we do not use the wave-cut results for the comparison with theoretical results.

(1) The wave-cut results do not always give the wave resistance. The term "wave resistance" used here is defined as the resistance component due to the generation of gravity waves. For conventional ship forms, this component is written as the sum of two components:

Wave Resistance = resistance component due  
to the generation of  
propagating gravity waves  
+ resistance component due  
to wave breaking

(2) The measured wave heights are the results of wave-wave interaction. The wave-cut results contain interaction effects between the propagating waves and the viscous wake. Therefore, the wave-cut results do not always represent the resistance component due to the propagating gravity waves as was pointed out by Prof. Landweber in the keynote address.

(3) The process of analysing the measured wave heights is not always accurate enough. The theory used in the analysis is the linearized theory for an ideal flow.

However, the comparison with the wave-cut results is useful for the investigation into the detailed mechanism of wave propagation. The order of magnitude of wave-cut results is about 80% of the wave resistance defined by the Hughes method for fine ship forms such as a high speed container ship. For full forms, the wave-cut results are much less than the values given by the Hughes method. There are two reasons for this. One is due to wave breaking and the other is due to wave-wave interaction.

The theoretical value of wave resistance is originally defined as the resistance component due to wave generation. Therefore, in the present paper, we considered that, within the limitation of our present knowledge of the resistance components, the calculated wave resistance should be compared with the results obtained from a method such as the one by Hughes where the form effect is considered.

Author's Reply  
by Robert K. C. Chan

Professor Newman's comments on my paper may be summarized as (1) that the need for the radiation condition in an initial-value problem was unexpected, (2) a single radiation condition was imposed, instead of two separate ones, and (3) that the calculated wavelength seems much shorter than expected. To answer Professor Newman's first question, I must admit that there is confusion of terminology. In the usual analytic approach to initial-value wave-resistance problems, an infinite domain is assumed where the only far-field condition is

that all disturbances die out at infinity. If the ship is the only source of disturbance in the whole field, there will be outgoing waves only. The situation of a discrete numerical simulation in a truncated domain is quite different. If one had the resources to use a computational mesh that is so large that, throughout the physical time of interest, the disturbances generated by the ship never reach the far-field boundaries, then the radiation condition would not be needed in initial-value problems. In practice, however, the flow field is arbitrarily truncated to fit the capacity of the computational equipment, as well as the budget. Unlike the case of real infinite domain, where one can simply specify  $\phi = \eta = 0$  at infinity, one does not know a priori what boundary conditions to apply at those arbitrarily defined boundaries. The basic assumption which allows one to truncate the domain is that at some distance from the ship the flow field becomes hyperbolic so that information propagates away from the ship. Under this assumption one can describe the flow field in the vicinity of the artificial boundaries in a characteristic form. Orlandi's method essentially makes use of this characteristic form to "extrapolate" the interior information to the artificial boundaries, such that unwanted wave reflection is sharply reduced. In contrast, the function of radiation condition in steady-state analysis is to help determine the one solution that satisfies the physical requirement of outgoing wave systems. Thus, there is difference, both in purpose and technique, between Orlandi's radiation condition and the radiation condition in classical hydrodynamics. I am in favor of relabeling the former as "open-boundary condition" to avoid confusion. This would also have answered Professor Newman's comment No. 2. As for his last comment, concerning the wavelength, I am afraid I do not have any satisfactory explanation at this time. However, I am positive that the short wavelengths are not the results of unsteadiness or the bounded domain, since these calculations were carried to steady state and various boundary sizes were tested. I plan to clarify it by using a point source pressure disturbance at the free surface in the near future. I am glad that Professor Newman pointed this out, because the computational results were very preliminary and a great deal of additional work is required to understand the various properties of the numerical solution technique.

# EXISTENCE, UNIQUENESS AND REGULARITY OF THE SOLUTION OF NEUMANN-KELVIN PROBLEM FOR TWO OR THREE DIMENSIONAL SUBMERGED BODIES

J. G. Dorn  
Bassin d'Essais des Carènes  
Paris, France

## Summary

The Neumann-Kelvin problem associated with a steady flow above a horizontal bottom presenting a bump of limited area is considered. In the case of the height of the bump being small, but not infinitely small, the existence and uniqueness of the solution is demonstrated. This result is valid for two or three-dimensional flows. The Method of Singularities is discussed and it is shown that the bump is kinematically equivalent to a distribution of sources, and/or dipoles on its surface. Furthermore, it is shown that the integral equation employed to calculate the density of these singularities has a unique solution.

## Contents

1. Introduction.
2. Notations.
3. Main results.
4. The flat bump approach, I generalized solution.
5. The flat bump approach, II strict solution.
6. Two auxiliary boundary value problems.
7. Existence, uniqueness and regularity of the solution : proofs of theorem I and II.
8. The Method of Singularities : proof of theorem III.

## References

### 1. Introduction

Frequently, numerical methods in ship hydrodynamics are developed before it has been proved that an exact solution to the problem really exists. From a practical point of view, one may maintain this procedure when good numerical evaluations can be made which compare reasonably well with experimental results. For example, the Method of Singularities has been applied successfully to calculate the diffraction and radiation forces acting upon a body in heaving motion in waves. Nevertheless, even in this case, difficulties are occasionally met : for example, in the two-dimensional problems, the Method of Frank is not applicable (13) when the body section is not vertical at flotation : this is due to the fact that such a body is not kinematically equivalent to a distribution of sources on its surface. It is known,

however, that even in the case of a body kinematically equivalent to a distribution of singularities, the integral equation used to calculate the density of these singularities may have a number of solutions for some, so-called, irregular frequencies (28).

These are, however, minor drawbacks and the Method of Singularities is largely used in diffraction and radiation problems.

Therefore, to calculate the wave resistance of a body of any shape piercing or not piercing a free surface, one is tempted to use the Method of Singularities. Unfortunately, the numerical experience seems to prove that it is rather a delicate matter to use the Method of Singularities in the Neumann-Kelvin problem. This fact induces one to think it is advisable, even essential, to carry out mathematical studies concurrently with a numerical analysis.

The present paper is intended to determine certain conditions under which the Method of Singularities can be used to solve the wave resistance problem for submerged bodies.

As far as this problem is concerned, the Method of Singularities may be divided into three parts :

- (i) the linearisation of the free surface condition ; this leads to the so-called Neumann-Kelvin problem (N-K problem) (4), (5)
- (ii) the representation of the solution as a distribution of sources, and/or dipoles, disposed on the surface of the body
- (iii) the expression of the flow condition on the body by means of an integral equation.

One is then led to ask the following questions on the above points (i) to (iii).

- (i) has the Neumann-Kelvin problem a unique solution and what is the regularity of this solution ? Above all, is the regularity sufficient to provide a physically acceptable solution ?

- (ii) is the body kinematically equivalent to a distribution of sources, and/or dipoles, on its surface ?  
 (iii) has the integral equation a unique solution ?

Few studies on the existence and uniqueness of the N-K problem have been published.

For 2-D or 3-D submerged bodies, N.E. Kochin (17) has proved the existence and uniqueness of the problem as follows : the velocity potential  $\Phi(X)$  of the fluid at point  $X$  is represented by a distribution of Kelvin sources on the body surface  $\Gamma$  : if  $K(X,Y)$  is the velocity potential at point  $X$  of a Kelvin unit source at point  $Y$ , the potential  $\Phi(X)$  is assumed to be :

$$(1.1) \quad \Phi(X) = \int_{\Gamma} K(X,Y) \sigma(Y) d_Y \Gamma$$

The flow condition on  $\Gamma$  is :

$$(1.2) \quad \frac{\partial \Phi}{\partial N} = v(X), \quad X \in \Gamma$$

where  $N$  is the normal towards the outside relative to the body and  $v(X)$  is a given function.

(1.1) and (1.2) give :

$$(1.3) \quad -\frac{1}{2} \sigma(X) + \int_{\Gamma} \sigma(Y) \frac{\partial K}{\partial N_X}(X,Y) d_Y \Gamma = v(X)$$

which is an integral equation of the second kind for the unknown  $\sigma(\cdot)$ . Let  $V$  be the integral operator

$$(1.4) \quad \sigma(\cdot) \mapsto \int_{\Gamma} \sigma(Y) \frac{\partial K}{\partial N_X}(\cdot, Y) d_Y \Gamma$$

the equation (1.3) can also be written as :

$$(1.5) \quad (V - \frac{1}{2}) \sigma = v$$

N.E. Kochin uses the Fredholm Alternative Theorems to show that, if the Froude number is sufficiently small,  $\frac{1}{2}$  is not an eigenvalue of the operator  $V$ . Therefore, the operator  $(V - \frac{1}{2})$  is invertible. This proof of existence and uniqueness assumes, however, that (i) the operator  $V$  fulfills the conditions of Fredholm's Theorems (e.g. :  $V$  must be completely continuous), (ii)  $\|V\| ; L^2(\Gamma)$  is a continuous function of  $k_0 = \frac{g}{c^2}$  in the vicinity of the critical value  $k_0 = 0$ . Here  $g$  is the acceleration of gravity ;  $c$ , the velocity of the body ;  $L^2(\Gamma)$  the space of square summable functions on  $\Gamma$ ,  $\|V\| ; L^2(\Gamma)$ , the norm of the operator  $V$  considered as a continuous mapping from  $L^2(\Gamma)$  into  $L^2(\Gamma)$  i.e.  $V \in \mathcal{L}(L^2(\Gamma), L^2(\Gamma))$ . These properties are not explicitly proven by N.E. Kochin.

The study of the existence and uniqueness, for bodies piercing the free surface is very complicated. Curiously, it was J.N. Michell (23) who first proved it in the limit case of infinitely thin ships. However, his argument would not be considered a rigorous proof by modern standards. The uniqueness of the solution of the N-K problem in the case of a body of any given shape was questioned by J. Kotik and R. Morgan (18) in the hypothesis of the zero Froude number. Their proof which neglected the existence of the water-line was improved by R. Brard (4), (5) with the aid of the line integral, and later by P. Guevel *et al.* (12) who used the modified Kochin function. However,

it is clear that the non-uniqueness of the solution in the hypothesis of the zero Froude number does not necessarily entail an analogous property for the corresponding solution with an exact Froude number.

M. Bessho (2) has given an interesting proof of the non-uniqueness in the case of a 2-D vertical plate partly immersed in water. For 3-D surface piercing bodies, M. Bessho (3) has proposed a method for proving the uniqueness but further studies are needed to clarify the method.

The above discussion demonstrates the difficulty presented by the study of the existence and uniqueness of the solution to the N-K problem. When the body pierces the free surface the mathematical problems are enormous. To begin with, it seems to be preferable to study the simplest case of immersed bodies and especially of bodies lying on the bottom of the sea (2-D or 3-D bump) and subjected to the effect of a flow of constant and uniform velocity  $c$ . The potential  $\Phi(X)$  corresponding to the flow over this bump is solution of a N-K problem, which shall be noted as NKd ( $Fh, \Sigma$ ) ;  $d$  is the dimension of the physical space ( $d = 2$  or  $3$ ) ;  $Fh = c/\sqrt{gh}$  is the Froude number allied to the depth  $h$ ,  $\Sigma = \Sigma(X')$  is the height of the bump at point  $X'$ , positively counted from the bottom.

To prove the existence and uniqueness, the NKd ( $Fh, \Sigma$ ) problem shall be considered as an elliptic boundary value problem (but with a non-conventional boundary condition at the free surface) and the perturbation theory of linear operators (16) will be used to prove the following chain : existence and uniqueness of the flat bump  $\Rightarrow$  N-K uniqueness  $\Rightarrow$  N-K existence.

Another possible method would be to consider the NKd ( $Fh, \Sigma$ ) problem as the steady state limit of an initial value problem of hyperbolic type. But, this method, used in water wave theory (32) does not directly give the uniqueness, which is the crux of the problem.

## 2. Notations

The system of reference axis,  $OX_1X_2X_3$ , is right handed orthonormal and is bound to the bottom of the sea. The  $OX_1X_2$  plane is that of the free surface at rest. The  $OX_3$  axis is vertical, directed towards the bottom. The  $OX_1$  axis is parallel to the incident velocity  $c$ , of the fluid and runs in the opposite direction to it. The bottom of the sea has a bump of limited area. The part  $B$  of the bottom which is situated without this bump is horizontal. The bump  $\Gamma$  has either a two-dimensional shape with a generatrix parallel to  $OX_2$ , or has a three-dimensional shape. The equation of the bump is :

$$(2.1) \quad \Gamma : X_3 = h - \Sigma(X'), \quad X' \in K$$

$X'$  is a real ( $X' \in X_1$ ) if  $d=2$  and a pair of reals  $X' = (X_1, X_2)$  if  $d=3$ .  $K = \text{supp } \Sigma$  is the support of  $\Sigma$ , compactum of  $\mathbb{R}^{d-1}$ . If  $\Sigma$  is defined outside  $K$  by  $\Sigma(X') = 0$  for  $X' \notin K$ , (2.1) is the equation of the bottom  $\Gamma \cup B$ . For what follows it is convenient to introduce the following notations :

$$\begin{aligned}
(2.2) \quad \epsilon &\triangleq \max_{X' \in K} |\Sigma(X')| \\
(2.3) \quad \Sigma^{(1)}(X') &\triangleq \epsilon^{-1} \Sigma(X') \\
(2.4) \quad \phi^{(1)}(X') &\triangleq \epsilon^{-1} \phi(X') \\
(2.5) \quad N_1^{(1)}(X') &\triangleq \epsilon^{-1} N_1(X')
\end{aligned}$$

It should be remembered that:  $\phi(X)$  is the velocity potential at point  $X$ ,  $N$  is the normal from the bump towards the outside relative to the fluid domain.

$$(2.6) \quad N = (N_1, N_2, N_3) \text{ or } (N_1, N_3)$$

according to  $d=3$  or  $2$ .

With these notations the fluid domain  $\Omega_\epsilon$  is given by:

$$(2.7) \quad \Omega_\epsilon \triangleq \{X = (X', X_3) : X' \in \mathbb{R}^{d-1}, 0 < X_3 < h - \epsilon \Sigma^{(1)}(X')\}.$$

The fluid domain is therefore in terms of parameter  $\epsilon$ .

In particular:

$$(2.8) \quad \Omega_0 \triangleq \bigcup_{\epsilon=0} \Omega_\epsilon = \{X = (X', X_3) : X' \in \mathbb{R}^{d-1}, 0 < X_3 < h\}$$

### Functional spaces

The terminology and the notations are for the most part those of L. Schwartz [31]. Let  $\omega$  be an open subset of  $\mathbb{R}^n$ ,  $n \geq 1$ ,  $\text{bdry } \omega$ , the boundary of  $\omega$  and  $\bar{\omega} = \omega \cup \text{bdry } \omega$ . A function  $u(X)$ ,  $X \in \omega$ , belongs to the class  $C^m$  in  $\omega$  (in  $\bar{\omega}$ ) iff  $u$  has continuous partial derivatives up to the  $m$ -th order in  $\omega$  (in  $\bar{\omega}$ ). It is said that  $u$  belongs to the class  $C^{m,\alpha}$  in  $\bar{\omega}$  iff  $u$  belongs to the class  $C^m$  in  $\bar{\omega}$  and if the partial derivatives  $\partial^\alpha u$  of the  $m$ -th order, are  $\alpha$ -holderian ( $0 < \alpha$ ).

$$(2.9) \quad |\partial^\alpha u(X) - \partial^\alpha u(Y)| \leq M |X-Y|^\alpha, X, Y \in \bar{\omega}$$

where  $M$  is  $X, Y$  independent and where  $|\cdot|$  is the Euclidian norm on  $\mathbb{R}^n$ .

The following normed linear spaces are used:  $u \in \mathcal{B}^m(\omega)$  iff  $u$  is a function of the class  $C^m$  in  $\omega$  and all the derivatives of which up to the  $m$ -th order are bounded in  $\omega$ . The norm:  $\|u\|_{\mathcal{B}^m(\omega)}$  is the norm of the uniform convergence on  $\omega$  of  $u$  and of all its derivatives of order  $\leq m$ .

$u \in \mathcal{B}^{m,\alpha}(\bar{\omega})$  the same as above with  $\bar{\omega}$  replaced by  $\bar{\omega}$   $u \in \mathcal{B}^{m,\alpha}(\bar{\omega})$  iff  $u$  is a function of the class  $C^{m,\alpha}$  in  $\bar{\omega}$ .

The norm is  $\|u\|_{\mathcal{B}^{m,\alpha}(\bar{\omega})} = \|u\|_{\mathcal{B}^m(\bar{\omega})} +$

$$\sum_{|\alpha|=m} \sup_{X,Y \in \bar{\omega}} |\partial^\alpha u(X) - \partial^\alpha u(Y)| \cdot |X-Y|^{-\alpha}, X, Y \in \bar{\omega},$$

where the summation is taken for all derivatives up to the  $m$ -th order.

All the spaces above are Banach spaces.

$u \in C^m(\omega)$  iff  $u$  is a function of the class  $C^m$  in  $\omega$   
 $u \in C^m(\bar{\omega})$  iff  $u$  is a function of the class  $C^m$  in  $\bar{\omega}$   
 $u \in \mathcal{C}(\omega)$  iff  $u \in C^m(\omega)$  for all  $m \geq 0$   
 $u \in \mathcal{C}(\bar{\omega})$  iff  $u \in C^m(\bar{\omega})$  for all  $m \geq 0$ .

These four spaces are equipped with the topology of uniform convergence of  $u$  and its derivatives up to the  $m$ -th order.

vatives up to the  $m$ -th order ( $m < \infty$ ) on the compact subsets of  $\omega$  (of  $\bar{\omega}$ ). If  $\bar{\omega}$  is compact  $\mathcal{C}^m(\bar{\omega}) \equiv \mathcal{B}^m(\bar{\omega})$ .

$u \in \mathcal{D}^m(\omega)$  iff  $u \in \mathcal{B}^m(\omega)$  has compact support,  $\text{supp } u$ , in  $\omega$ .

$u \in \mathcal{D}(\omega)$  iff  $u \in \mathcal{D}^m(\omega)$  for all  $m \geq 0$ .

For the topologies of these spaces see [31]

$u \in \mathcal{B}_0^m(\mathbb{R}^{d-1})$  iff  $u \in \mathcal{B}^m(\mathbb{R}^{d-1})$  and  $u$  vanishes at infinity

$u \in \mathcal{B}_K^{\alpha}(\mathbb{R}^{d-1})$ , where  $K$  is a compactum of  $\mathbb{R}^{d-1}$

iff  $u \in \mathcal{B}^{m,\alpha}(\mathbb{R}^{d-1})$  and  $\text{supp } u \subset K$ . The Banach space  $\mathcal{B}_K^{m,\alpha}(\mathbb{R}^{d-1})$  is a Banach Algebra, that is:

$$u, v \in \mathcal{B}_K^{m,\alpha}(\mathbb{R}^{d-1}) \Rightarrow uv \in \mathcal{B}_K^{m,\alpha}(\mathbb{R}^{d-1}) \text{ and}$$

$$(2.11) \quad \|uv\|_{\mathcal{B}_K^{m,\alpha}(\mathbb{R}^{d-1})} \leq \|u\|_{\mathcal{B}_K^{m,\alpha}(\mathbb{R}^{d-1})} \|v\|_{\mathcal{B}_K^{m,\alpha}(\mathbb{R}^{d-1})}$$

$$\|v\|_{\mathcal{B}_K^{m,\alpha}(\mathbb{R}^{d-1})}$$

$$u \in \mathcal{B}_R^{m,\alpha}(\Omega_\epsilon) \text{ iff } u \in \mathcal{B}^{m,\alpha}(\Omega_\epsilon) \text{ and } u \in \mathcal{B}^0(\Omega_\epsilon)$$

where one has set:

$$(2.12) \quad R(X) = \begin{cases} (1+|X'|^2)^{\frac{d-1}{2}}, & \text{if } X_3 > 0, \\ (1+|X'|^2)^{\frac{d-2}{4}}, & \text{if } X_3 < 0. \end{cases}$$

$\mathcal{B}_R^{m,\alpha}(\Omega_\epsilon)$  is a Banach space with the norm:

$$\|u\|_{\mathcal{B}_R^{m,\alpha}(\Omega_\epsilon)} = \|u\|_{\mathcal{B}^{m,\alpha}(\Omega_\epsilon)} + \|uR\|_{\mathcal{B}^0(\Omega_\epsilon)}.$$

If  $u \in \mathcal{B}_K^{m,\alpha}(\mathbb{R}^{d-1})$ ,  $m \geq 2$ , it shall be said that the function  $u(X)$  defined on  $\bar{\Gamma}$  belongs to  $\mathcal{B}_1^{1,\alpha}(\bar{\Gamma})$  iff  $u(X', h - \epsilon \Sigma(X')) \in \mathcal{B}_K^{1,\alpha}(\mathbb{R}^{d-1})$ .

### 3. Main results

It should be remembered that  $\Omega_\epsilon$  is the fluid domain defined by (2.7),  $N$  is the normal to the bottom, with  $(N_1, N_2, N_3)$  or  $(N_1, N_3)$  components with respect to  $\partial X_1 \partial X_2 \partial X_3$  or  $\partial X_1 \partial X_3$ ,  $\phi(X)$  is the potential at point  $X$  allied to the fluid movement of which the velocity is:

$$(3.1) \quad U(X) = \nabla_X \phi(X)$$

with

$$(3.2) \quad \nabla_X = \left( \frac{\partial}{\partial X_1}, \frac{\partial}{\partial X_2}, \frac{\partial}{\partial X_3} \right) \text{ or } \left( \frac{\partial}{\partial X_1}, \frac{\partial}{\partial X_3} \right)$$

according to  $d=3$  or  $2$ .

Let  $\Sigma(X')$  be the height of the bump at point  $X'$ . We define

$$(3.3) \quad \begin{cases} \Sigma^{(1)} = \Sigma^{(1)}(X') \\ \phi^{(1)} = \phi^{(1)}(X; \epsilon, \Sigma^{(1)}) \\ N_1^{(1)} = N_1^{(1)}(X'; \epsilon, \Sigma^{(1)}) \end{cases}$$

by formulae (2.2) to (2.5).

In the Neumann-Kelvin formulation (4),  $\phi$  is solution of a boundary value problem  $\text{NKd}(\text{Ph}, \Sigma)$  which takes the following form when  $\phi^{(1)}$  is chosen as the unknown function.

NKd(Ph,  $\epsilon$ ,  $\Sigma^{(1)}$ ) problem

Find  $\phi^{(1)} = \phi^{(1)}(X; \epsilon, \Sigma^{(1)})$  such that

$$(NK_1) \quad \nabla_x^2 \phi^{(1)}(x; \varepsilon, \Sigma^{(1)}) = 0, \quad x \in \Omega_\varepsilon$$

$$(NK_2) \quad \frac{\partial^2 \phi^{(1)}}{\partial x_1^2} - k_0 \frac{\partial \phi^{(1)}}{\partial x_3} = 0, \quad x_3 = 0$$

$$(NK_3) \quad \frac{\partial \phi^{(1)}}{\partial n} = cN_1^{(1)}(x'; \varepsilon, \Sigma^{(1)}), \quad x_3 = h - \varepsilon \Sigma^{(1)}(x')$$

$$(NK_4) \text{ radiation condition: } R\phi^{(1)} \in \mathcal{B}^0(\Omega_\varepsilon)$$

$$\text{where } k_0 = \frac{\varepsilon_0}{c^2}$$

Given :

$K$  compactum of  $\mathbb{R}^{d-1}$ , support of the bump  $(s)$   
 $m$  integer  $\geq 2$   
a real  $0 < \alpha < 1$

We set :

$$(3.4) \quad \mathcal{K} = \mathcal{B}_R^{m, \alpha}(\Omega_\varepsilon) \text{ (space of solutions } \phi^{(1)})$$

$$(3.5) \quad \mathcal{U} = \mathcal{B}_K^{m, \alpha}(\mathbb{R}^{d-1}) \text{ (space of data } \Sigma^{(1)})$$

The two following results are proven :

**Theorem 1 :** Let us assume  $d=2$  and  $Fh=1$ . For each  $\Sigma^{(1)} \in \mathcal{U}$ , the  $NKd(Fh, \Sigma)$  problem has no solution in  $\mathcal{K}$ .

In fact, it is shown that no solution exists in the space of bounded functions.

**Theorem 2 :** Let us assume whatever be  $Fh$  when  $d=3$  and  $Fh \neq 1$  if  $d=2$ . For each  $\Sigma^{(1)} \in \mathcal{U}$ ,  $\varepsilon_0 > 0$  exists such that for all  $\varepsilon \in [0, \varepsilon_0[$  :

(i) the  $NKd(Fh, \Sigma)$  problem has a unique solution  $\phi^{(1)} \in \mathcal{K}$

(ii)  $\phi^{(1)} = \phi^{(1)}(x; \varepsilon, \Sigma^{(1)})$  analytically depends on  $\varepsilon$  :

$$\phi^{(1)}(x; \varepsilon, \Sigma^{(1)}) = \phi^{(1)}(x; 0, \Sigma^{(1)}) + \sum_{n=1}^{\infty} \varepsilon^n \phi_n(x; \Sigma^{(1)})$$

This series converges uniformly with respect to  $x$  and can be differentiated with respect to  $x$ , term by term until the  $m$ -th order.

(iii)  $\phi^{(1)}(x; \varepsilon, \Sigma^{(1)}) - \phi^{(1)}(x; 0, \Sigma^{(1)})$  and the  $\phi_n(x; \Sigma^{(1)})$  belong to  $\mathcal{L}(\mathcal{U}, \mathcal{K})$  i.e. they are linear and continuous mapping from  $\mathcal{U}$  into  $\mathcal{K}$ .

#### The Method of Singularities

Let  $K(X, Y)$  be the potential created at  $X$  by a Kelvin unit source placed at  $Y \in \Omega_\varepsilon \cup \Gamma$ .

The operators "source" and "dipole" are defined as follows :

$$(3.6) \quad S\sigma = \int_{\Gamma} K(X, Y) \sigma(Y) d_Y \Gamma$$

$$(3.7) \quad D\mu = \int_{\Gamma} \frac{\partial K}{\partial N_Y}(X, Y) \mu(Y) d_Y \Gamma,$$

and the restrictions of  $S\sigma$  and  $D\mu$  to the surface  $\Gamma$  of the bump are noted as  $S\sigma$  and  $D\mu$ . The following is also defined :

$$(3.8) \quad V\sigma = \int_{\Gamma} \frac{\partial K}{\partial N_X}(X, Y) \sigma(Y) d_Y \Gamma.$$

**Theorem 3 :** Under the conditions of theorem 2, the unique solution of the  $NKd(Fh, \Sigma)$  problem can be expressed equally well in any of the three following different forms :

(i) single layer potential :  $\phi(X) = S\sigma$  where  $\sigma$  is the unique solution in  $L^2(\Gamma)$  of the integral equation,

$$(V - \frac{1}{2})\sigma = v, \quad v \in cN_1$$

(ii) double layer potential :  $\phi(X) = D\mu$  where  $\mu$  is the unique solution in  $\mathcal{B}^{1, \alpha}(\Gamma)$  of the integral equation,

$$(D - \frac{1}{2})\mu = u, \quad u = \text{restriction of } (cX_1) \text{ to } \Gamma$$

(iii) mixed potential :  $\phi(X) = D\mu - S\sigma$  where  $\mu$  is the unique solution in  $\mathcal{B}^{1, \alpha}(\Gamma)$  of the integral equation

$$(D - \frac{1}{2})\mu = S\sigma.$$

#### 4. The Flat-Bump Approach I, Generalized Solution

Before resolving the  $NKd(Fh, \varepsilon, \Sigma^{(1)})$  problem for any given value of  $\varepsilon$ , the problem is to be resolved for  $\varepsilon = 0$ . In this case, the solution is well known :

For  $d=2$ , it is possible to refer to Lamb (20 p.409) who explains the method followed by Rayleigh (1883 ; artificial frictional forces) and the method used by Kelvin (1886, Fourier Integral Decomposition) ;

For  $d=3$ , it is possible to refer to Ekman (1907) (11). Also, the articles of Palm (29) and Harband (14) who used the Initial Value Method can be quoted. All these methods clearly demonstrate the existence of a solution of the  $NKd(Fh, 0, \Sigma^{(1)})$  problem, by actually constructing it. In return the uniqueness of the solution is not rigorously proven by methods of Rayleigh, Kelvin and Ekman, whereas the Initial Value Method cannot, in essence, prove it.

In fact, it is possible to prove the existence and the uniqueness of the solution by using a modernised version of the method of Kelvin : The Method of the Fourier Transform in the space of L. Schwartz's Distributions.

Using distributions the proof is routine but lengthy. Therefore, only the essential stages of the proof (which is expounded in detail in (9)) will be shown.

#### Notations

For the sake of brevity the following notations will be used :

$$I = \{x_3 : 0 < x_3 < h\} \text{ so that } \Omega_0 = \mathbb{R}^{d-1} \times I$$

$$I_0 = \{x_3 : 0 \leq x_3 < h\}$$

$$\bar{I} = \{x_3 : 0 \leq x_3 \leq h\} \text{ so that } \bar{\Omega}_0 = \mathbb{R}^{d-1} \times \bar{I}$$

$$f(x_1, x_2, x_3) \text{ is the mapping } x_1 \mapsto f(x_1, x_2, x_3)$$

$$\phi_0(x) \neq \phi^{(1)}(x; 0, \Sigma^{(1)}) \text{ solution of the}$$



NKd (Fh, 0,  $\Sigma^{(1)}$ ) problem.

$u \in \mathcal{D}'(\mathbb{R}^{d-1})$  iff  $u$  is a function of the class  $C^p$  with compact support

$u \in \mathcal{D}(\mathbb{R}^{d-1})$  iff  $u \in \mathcal{D}'(\mathbb{R}^{d-1})$  for any  $p \geq 0$

$u \in \mathcal{D}_L(\mathbb{R}^{d-1})$  iff (i)  $u$  is a function of the class  $C^\infty$   
(ii)  $u$  and all its derivatives belong to  $L^p(\mathbb{R}^{d-1})$

$u \in \mathcal{S}(\mathbb{R}^{d-1})$  iff (i)  $u$  is a function of the class  $C^\infty$   
(ii)  $u$  and all its derivatives are rapidly decreasing at infinity

$u \in \mathcal{O}_M(\mathbb{R}^{d-1})$  iff (i)  $u$  is a function of the class  $C^\infty$   
(ii)  $u$  is a function slowly increasing at infinity.

The respective duals of the above spaces are introduced:

$\mathcal{D}'(\mathbb{R}^{d-1})$  space of distributions of order  $\leq p$ . For  $p=0$  we have the space of Radon measure; which is denoted also by  $\mathcal{M}(\mathbb{R}^{d-1})$

$\mathcal{D}'(\mathbb{R}^{d-1})$  space of L. Schwartz's Distributions

$\mathcal{D}'_L(\mathbb{R}^{d-1})$  with  $p^{-1}+q^{-1}=1$  We denote by

$\mathcal{D}_L'(\mathbb{R}^{d-1})$  the dual of  $\mathcal{D}_L(\mathbb{R}^{d-1})$

$\mathcal{S}'(\mathbb{R}^{d-1})$  space of tempered distributions

$\mathcal{O}'_M(\mathbb{R}^{d-1})$  space of distributions rapidly decreasing at infinity.

For the properties of these spaces and their topology, see [31].  $\mathcal{C}^k(I, \mathcal{S}(\mathbb{R}^{d-1}))$  is the space of the functions  $\phi(X) = \phi(X', X_3)$  which are differentiable with respect to  $X_3 \in I$  up to the  $k$ -th order and are valued in the vector space  $\mathcal{S}'(\mathbb{R}^{d-1})$  i.e.  $\phi(X', X_3) \in \mathcal{S}'(\mathbb{R}^{d-1})$  see [30 p.49].

#### Fourier Transform (FT) and Inverse Fourier Transform (IFT).

The direct Fourier Transform (FT) of  $f(X', X_3) \in \mathcal{S}'(\mathbb{R}^{d-1})$  is:

$$(4.1) \quad \hat{f}(k', X_3) = \int_{\mathbb{R}^{d-1}} f(X', X_3) e^{-ik'X'} dX'$$

where  $k' = (k_1, k_2)$  if  $d=3$ ,  $k' = k_1 k_2$  if  $d=2$  and where  $k'X'$  is the scalar product  $k'X' = k_1 X_1 + k_2 X_2$  or  $kX_1$  depending on  $d=3$  or 2.

It shall be noted by  $\mathcal{F}_{k'}$   $\{f(X', X_3)\}$  the extension to  $\mathcal{S}'(\mathbb{R}^{d-1})$  of  $\mathcal{F}_{k'}$  the operator defined by (4.1).

The inverse Fourier Transform (IFT) of  $\hat{f}(k', X_3) \in \mathcal{S}'(\mathbb{R}^{d-1})$  is

$$(4.2) \quad f(X', X_3) = \frac{1}{(2\pi)^{d-1}} \int_{\mathbb{R}^{d-1}} \hat{f}(k', X_3) e^{ik'X'} dk'$$

and it shall be noted by  $\mathcal{F}_{k'}^{-1}$   $\{\hat{f}(k', X_3)\}$  the extension to  $\mathcal{S}'(\mathbb{R}^{d-1})$  of the operator defined by (4.2).

It should be remembered that the operator  $\mathcal{F}$  is a topological isomorphism from  $\mathcal{S}'(\mathbb{R}^{d-1})$  to  $\mathcal{S}'(\mathbb{R}^{d-1})$ .

onto  $\mathcal{S}'(\mathbb{R}^{d-1})$ .

If  $\partial$  is taken as the symbol of classical differentiation (i.e.  $\frac{\partial \phi_0}{\partial X_1}$ ), the symbol of differentiation in the sense of  $\mathcal{D}'$  is noted by  $D$  (i.e.  $\frac{D\phi_0}{DX_1}$ ). To the classical Laplacien operator  $\nabla_X^2$  corresponds the operator  $\Delta_X^2$  in the sense of  $\mathcal{D}'$ .

#### Definition 4.1 -

A function of  $\mathcal{C}^2(I, \mathcal{S}'(\mathbb{R}^{d-1}))$  is said to be a generalized solution of NKd(Fh, 0,  $\Sigma^{(1)}$ ) if it is a solution of NK1, NK2 and NK3 in the sense of distributions.

It is not necessarily assumed that the NK4 condition is satisfied.

Let us show that NK1, NK2 and NK3 has meaning if  $\phi_0 \in \mathcal{C}^2(I, \mathcal{S}'(\mathbb{R}^{d-1}))$ : NK1 can be written as:

$$(4.4) \quad \Delta_X^2 \phi_0 = \Delta_X^2 \phi_0 + \frac{D^2 \phi_0}{DX_3^2} = 0$$

which is really an equality in  $\mathcal{S}'(\mathbb{R}^{d-1})$

The operators depending on the parameter  $X_3 \in I$  are then defined by:

$$(4.5) \quad B_1(X_3) \phi_0 = \frac{D^2 \phi_0}{DX_3^2} - k_0 \frac{D\phi_0}{DX_3} \in \mathcal{S}'(\mathbb{R}^{d-1})$$

$$(4.6) \quad B_2(X_3) \phi_0 = \frac{D\phi_0}{DX_3} \in \mathcal{S}'(\mathbb{R}^{d-1})$$

$\phi_0$  satisfies NK2 and NK3 in the sense of distributions if:

$$(4.7) \quad B_1(X_3) \phi_0 = 0 \text{ in } \mathcal{S}'(\mathbb{R}^{d-1}) \text{ when } X_3 = 0$$

$$(4.8) \quad B_2(X_3) \phi_0 = c \frac{D\Sigma^{(1)}}{DX_1} \text{ in } \mathcal{S}'(\mathbb{R}^{d-1}) \text{ when } X_3 = h$$

where it is assumed that  $\frac{D\Sigma^{(1)}}{DX_1} \in \mathcal{S}'(\mathbb{R}^{d-1})$ .

#### Definition 4.2 -

A distribution belonging to  $\mathcal{C}^2(I, \mathcal{S}'(\mathbb{R}^{d-1}))$  is said to be a generalized Green Potential of the NKd(Fh, 0,  $\Sigma^{(1)}$ ) problem if it satisfies in the sense of distributions, the following equations:

$$(G1) \quad \Delta_X^2 Gd(X) = 0 \text{ in } \Omega_0$$

$$(G2) \quad \frac{\partial^2 Gd}{\partial X_1^2} - k_0 \frac{\partial Gd}{\partial X_3} = 0 \quad X_3 = 0$$

$$(G3) \quad \frac{\partial Gd}{\partial X_3} = \delta(X) \quad X_3 = h$$

$\delta(X)$  is the Dirac measure at point  $X' = 0$ .

The two following lemmata are well known

**Lemma 4.1** - The following equation for the unknown  $\gamma$ :

$$\text{th } \gamma h = \frac{\gamma}{k_0}$$

has no solution if  $Fh > 1$  i.e.  $k_0 h < 1$ , has a unique positive solution  $\gamma_0$  if

$$Fh < 1 \text{ i.e. } k_0 h > 1$$

has the double solution  $\gamma_0 = 0$  if

$$Fh = 1 \text{ i.e. } k_0 h = 1$$

When  $k_0 h$  increases from 1 to  $+\infty$ ,  $\gamma_0$  increases from 0 to  $+\infty$  and verifies:

$$k_0^2 h^2 > \gamma_0^2 h^2 > k_0^2 h^2 - k_0 h$$

**Lemma 4.2** - The positive solution  $\gamma = \gamma(t)$  of the equation:

$$\text{th } \gamma h = \frac{\gamma \cos^2 t}{k_0}, \quad t \in [0, 2\pi]$$

has the following properties:

- (i)  $\gamma(\pi - t) = \gamma(t)$
- (ii)  $\gamma(-t) = \gamma(t)$

One can therefore restrict the study of

$$\gamma(t) \text{ to } t \in [0, \frac{\pi}{2}]$$

- (iii) if  $Fh < 1$ ,  $\gamma(t)$  increases from  $\gamma_0$  to  $+\infty$  when  $t$  increases from 0 to  $\frac{\pi}{2}$  ( $\gamma_0$ : see lemma 4.1)

- (iv) if  $Fh = 1$ ,  $\gamma(t)$  increases from 0 to  $+\infty$  when  $t$  increases from  $t_0 = 0$  to  $\frac{\pi}{2}$

- (v) if  $Fh > 1$ ,  $\gamma(t)$  only exists if  $t \geq t_0$  where  $t_0$  is the solution in  $[0, \frac{\pi}{2}]$  of  $\cos t_0 = \sqrt{k_0 h}$ . When  $t$  increases from  $t_0$  to  $\frac{\pi}{2}$ ,  $\gamma(t)$  increases from 0 to  $+\infty$

- (vi) for each  $Fh$ ,  $\gamma'(t) = \frac{\gamma(t) \sin 2t}{k_0 h \left[ \frac{\text{th } \gamma h}{\gamma h} - \frac{1}{\text{ch}^2 \gamma h} \right]} \geq 0$ ,  $\gamma(t) = 0$  only for  $Fh < 1$  in which case  $t = 0$ .

- (vii) for each  $Fh$  when  $t = \frac{\pi}{2}$ ,  $h\gamma(t) = k_0 h \sec^2 t$

- (viii) if  $Fh \geq 1$  and if  $t = t_0$ ,  $h\gamma(t) = \sqrt{3} \left( 1 - \frac{\cos^2 t_0}{k_0 h} \right)^{\frac{1}{2}}$  and  $h\gamma'(t) = \frac{3 \sin 2t_0}{2 k_0 h \text{th } \gamma(t)}$

- (ix) in the plane  $k' = (k_1, k_2) = (k \cos t, k \sin t)$  the manifold (C) with polar equation  $k = \gamma(t)$  consists of two different curves without any point of intersection if  $Fh < 1$ . If  $Fh \geq 1$ , (C) consists of a connected curve with a double point at the origin.

#### Theorem 4.1

There exists an infinite number of generalized Green potentials that are given by the following formulas:

$$G_d(X) = H_d(X) + \Psi_d(X) + g_d(X)$$

where  $H_d$ ,  $\Psi_d$  and  $g_d$  are given by the following formulas:

- (i) in the case of  $d=2$

$$\text{if } Fh \neq 1 \quad g_2(X) = a_0 + a_1 X_1$$

$$\text{if } Fh = 1 \quad g_2(X) = a_0 + a_1 X_1 + a_2 (X_1^2 - X_2^2 + 2hX_1) + a_3 (X_1^3 - 3X_1 X_2^2 + 6hX_1 X_2)$$

$$\text{if } Fh \geq 1 \quad \Psi_2(X) = 0$$

$$\text{if } Fh < 1 \quad \Psi_2(X) = \left( \text{ch } \frac{X_1}{k_0} - \frac{\gamma_0}{k_0} \right) \text{th } \gamma_0 X_2$$

$$(b_1 \cos \gamma_0 X_1 + b_2 \sin \gamma_0 X_1)$$

$a_j (j=0, 3)$  and  $b_j (j=1, 2)$  are arbitrary constants.  $\gamma_0$  is defined by lemma 4.1

$$\hat{H}_2(k, X_3) = \text{Pf } h_2(k, X_3)$$

$$H_2(X_1, X_3) = \mathcal{F}_{X_1}^{-1} \{ \hat{H}_2(k, X_3) \}$$

with

$$h_2(k, X_3) = \frac{-k_0 (\text{ch } k X_3 - \frac{k}{k_0} \text{sh } k X_3)}{k^2 (\text{ch } k h - k_0 \frac{\text{sh } k h}{k})}$$

$\text{Pf}$  = Hadamard-Schwartz pseudo-function with respect to variable  $k$ .

- (ii) in the case of  $d=3$

$$\text{if } Fh \neq 1 \quad g_3(X) = a_0 + a_1 X_1 + a_2 X_2 + a_3 X_1 X_2$$

$$\text{if } Fh = 1 \quad g_3(X) = a_0 + a_1 X_1 + a_2 X_2 + a_3 X_1 X_2 + \sum_{m=0,1} a_{3m} (X_1^2 - X_2^2 - 2hX_1) X_2^m + a_{3m} (X_1^3 - 3X_1^2 X_2 + 6hX_1 X_2^2) X_2^m$$

$$\hat{H}_3(k_1, k_2, X_3) = \text{Pf } h_3(k_1, k_2, X_3)$$

$$h_3(k_1, k_2, X_3) = \frac{-k_0 (\text{ch } k X_3 - \frac{k_1^2}{k k_0} \text{sh } k X_3)}{k^2 \left[ \left( \frac{k_1}{k} \right)^2 \text{ch } k h - k_0 \frac{\text{sh } k h}{k} \right]}$$

with  $k = \sqrt{k_1^2 + k_2^2}$ ,  $a_j$  and  $a_{3m}$  arbitrary constants

$$\hat{\Psi}_3(k_1, k_2, X_3) = \left( \text{ch } k X_3 - \frac{k_1^2}{k k_0} \text{sh } k X_3 \right) \bar{T}_C$$

$\bar{T}_C$  extension to  $\mathbb{R}^2$  of an arbitrary distribution  $T_C$  whose support is in (C) (see lemma 4.2ix)

$$H_3(X) = \mathcal{F}_X^{-1} \{ \hat{H}_3(k_1, k_2, X_3) \}$$

$$\Psi_3(X) = \mathcal{F}_X^{-1} \{ \hat{\Psi}_3(k_1, k_2, X_3) \}$$

$\text{Pf}$  = pseudo function with respect to variable  $k' = (k_1, k_2)$

The precise meaning of the symbol  $\text{Pf}$  will be given at the end of this chapter, as well as the expression which is corresponding to the distribution  $\bar{T}_C$ .

#### Theorem 4.2 -

Let us assume that  $Fh$  has any given value and  $\frac{D\Gamma(1)}{DX_1} \in \mathcal{O}'(\mathbb{R}^{d-1})$ . Then the  $\text{NKd}(Fh, 0, \Gamma(1))$  problem has an infinity of generalized solutions given by:

$$\Phi_0(X) = c \frac{D\Gamma(1)}{DX_1}(X') \cdot G_d(X', X_3) + \pi_d(X)$$

where  $G_d$  is any one of the generalized Green potentials of theorem 4.1 and where  $\pi_d$  is an arbitrary polynomial, that can be chosen independently of  $G_d$  but having the same form as the  $u_d$  polynomials defined in theorem 4.1.

The symbol  $(X')$  denotes the convolution with respect to variable  $X'$ .

Before demonstrating the proof of theorems 4.1 and 4.2 the following results should be noted:

Let us set

$$0(k', X_3) = \text{ch } k X_3 - \frac{k_1^2}{k k_0} \text{sh } k X_3$$

where  $k = |k'|$  ( $=k_1$  if  $d=2$ )

Lemma 4.3 - The distribution  $U(X) \in C^2(I, S^{d-1})$  is a solution of (a) and (b) :

$$(a) \quad D_X^2 U = 0 \quad X \in \Omega_0$$

$$(b) \quad D_{X_1}^2 U - k_0 D_{X_3} U = 0 \quad X_3 = 0$$

if its IFT  $\hat{U}(k', X_3)$  is of the following form :

$$\hat{U}(k', X_3) = \hat{O}(k', X_3) V(k')$$

where  $V(k')$  is any tempered distribution such that  $0 \leq V \in S'(\mathbb{R}^{d-1})$ .

Lemma 4.3 is proven easily using the FT of (a) and (b).

Proof of theorems 4.1 and 4.2 -

(i) Case  $d=3$  - Let  $\hat{\phi}_0(k', X_3)$  be the FT of  $\phi_0(X', X_3)$ .

$$\begin{aligned} \text{The FT of (4.6) is :} \\ \left[ B_2(X_3) \hat{\phi}_0 \right]^\sim(k', X_3) &= \left[ \frac{D\hat{\phi}_0}{DX_3} \right]^\sim(k', X_3) \\ &= -\frac{k^2}{k_0} \left[ \left( \frac{k_1}{k} \right)^2 \text{chkh} - k_0 \frac{\text{shkh}}{k} \right] V(k') \end{aligned}$$

where lemma 4.3 is used.

$$\text{Let us set : } \hat{U}(X') = c \frac{D\hat{\phi}_0}{DX_3} (X')$$

The relation (4.8) gives :

$$-\frac{k^2}{k_0} \left[ \left( \frac{k_1}{k} \right)^2 \text{chkh} - k_0 \frac{\text{shkh}}{k} \right] V(k') = \hat{U}(k')$$

From which after multiplication by  $-k_0 \hat{O}(k', X_3)$

$$(4.9) \quad k^2 \left[ \left( \frac{k_1}{k} \right)^2 \text{chkh} - k_0 \frac{\text{shkh}}{k} \right] \hat{\phi}_0(k', X_3) = -k_0 \hat{O}(k', X_3) \hat{U}(k').$$

The general solution of this problem of division in  $\mathbb{R}^2$  is :

$$(4.10) \quad \hat{\phi}_0(k', X_3) = \text{Pf} \left[ \frac{-k_0 \hat{O}(k', X_3)}{k^2 \left[ \left( \frac{k_1}{k} \right)^2 \text{chkh} - k_0 \frac{\text{shkh}}{k} \right]} \right] \hat{U}(k') + \left[ a_0 \delta(k') + a_1 \frac{D\delta(k')}{Dk_1} + a_2 \frac{D\delta(k')}{Dk_2} + a_3 \frac{D^2\delta(k')}{Dk_1 Dk_2} \right] \hat{U}(k') + \sum_{l,m=0,1}^{\infty} \frac{D^{l+m}\delta(k')}{Dk_1^{l+1} Dk_2^{m+1}} \hat{O}(k', X_3) \hat{U}(k') + \hat{O}(k', X_3) \hat{U}(k')$$

where  $T_C$  is a single layer on (C) (i.e. a distribution with support in (C)) and  $\hat{T}_C$  is the extension of this distribution to the  $(k_1, k_2)$  - plane - see [31, theor. XXXVI p.102, formula (IV.5;7) p.114 and theor. VIII p.127]. The terms  $a_j$  and  $a_{lm}$  are arbitrary constants and  $a_{lm}=0$  if  $l+m \neq 1$ .

The solution (4.10) is somewhat formal and it still has to be precisely expounded by giving a definition of the pseudo-function Pf and of the distribution  $\hat{T}_C$  so that the right-hand side of (4.10) is a tempered distribution. See the end of the present chapter.

By using the IFT of (4.10) the formulae of theorems 4.1 and 4.2 are obtained. These theorems are therefore completely proven once the regularity of  $G_2$  and  $\phi_0$  has been proven i.e. :

$$G_2, \phi_0 \in C^2(I, S'(\mathbb{R}^{d-1}))$$

The details of the proof are not given here (see case  $d=2$ ).

(ii) case  $d=2$  - The same operation is carried out and instead of (4.9) one obtains :

$$(4.9A) \quad k^2 \left( \text{chkh} - k_0 \frac{\text{shkh}}{k} \right) \hat{\phi}_0(k, X_3) = -k_0 \hat{O}(k, X_3) \hat{U}(k')$$

The general solution of this problem of division in  $\mathbb{R}$  is :

$$(4.10A) \quad \hat{\phi}_0(k, X_3) = \text{Pf} \left[ \frac{-k_0 \hat{O}(k, X_3)}{k^2 \left( \text{chkh} - k_0 \frac{\text{shkh}}{k} \right)} \right] \hat{U}(k) + \left[ a_0 \delta(k) + a_1 \delta^{(1)}(k) + a_2 \delta^{(2)}(k) + a_3 \delta^{(3)}(k) \right] \hat{U}(k) + b_1 \hat{O}(k, X_3) \hat{U}(k) + b_2 \hat{O}(k, X_3) \hat{U}(k) \delta(k - \gamma_0)$$

where the terms  $a_i$  and  $b_j$  are arbitrary constants and  $a_2=a_3=0$  if  $\text{Fh} \neq 1$  and  $b_1=b_2=0$  if  $\gamma_0$  does not exist, i.e. if  $\text{Fh} > 1$ .

Compared with (4.10) the solution is simpler because :

(i) Pf is perfectly defined as a Hadamard-Schwartz pseudo-function in  $\mathbb{R}$

(ii) The manifold (C) is here reduced to two points and the meaning of  $\hat{T}_C$  is therefore elementary.

By taking the IFT of (4.10A) the formulae of theorems 4.1 and 4.2 are obtained. The study of regularity is simple. For example :

$G_2 \in C^2(I, S'(\mathbb{R}^{d-1}))$ , because that is true for  $\psi_2$  and  $g_2$  ; for  $H_2$  according to [31 theor. XV p.268] it is known that :

$$X_3 \in I \Rightarrow H_2(k, X_3) \in O_C^1(\mathbb{R}^{d-1}) \Rightarrow H_2(X_1, X_3) \in O_H(\mathbb{R}^{d-1}).$$

According to [21 p.20] it is also known that  $\hat{h}_2(k, X_3) \in C^\infty(I, S'(\mathbb{R})) \Rightarrow \hat{h}_2(k, X_3) \in C^\infty(I, S'(\mathbb{R})) \Rightarrow H_2(X_1, X_3) \in C^\infty(I, S'(\mathbb{R}))$

From the regularity of  $G_2$ , the hypothesis  $U \in O^1(\mathbb{R}^{d-1})$  and from the theorem XI of [31 p.247] the regularity of  $\phi_0$  is proved. Q.E.D.

Study of  $\hat{T}_C$  distribution

The precise definition of  $\hat{T}_C$  shall be given only in the case  $\text{Fh} < 1$ . Before hand a meaning must be given to the pseudo-function which defines

$$H_3(k_1, k_2, X_3) = \text{Pf} h_3(k_1, k_2, X_3).$$

On the outside of disc  $\{k \geq \eta\}$  where  $\eta > 0$  is given, the change of variables  $(k_1, k_2) = (k \cos t, k \sin t)$  is a diffeomorphism and the following can be posed without any difficulties:

$$(4.11) \quad \hat{h}_3(k, t, X_3) = h_3(k \cos t, k \sin t, X_3)$$

$$(4.12) \quad \hat{\phi}(k, t) = \hat{\phi}(k \cos t, k \sin t)$$

$$\text{where } \hat{\phi}(k_1, k_2) : S(\mathbb{R}_{k_1, k_2}^2)$$

$$(4.13) \quad I_{0+}(t, \phi) = \int_0^\infty \hat{h}_3(k, t, X_3) \hat{\phi}(k, t) k dk$$

where  $\int$  is the finite part of the integral.

For what follows it is sufficient to consider the elements of  $S(\mathbb{R}^2)$  such that :

$$(4.14) \quad \bar{\phi}(k, t) = \bar{\phi}(k, -t) = \bar{\phi}(k, \pi - t)$$

It is not difficult then to prove that :

**Proposition 4.1** - When  $Fh < 1$ ,  $I_{0+}(t, \phi)$

$\in L(S(\mathbb{R}^2), \mathcal{B}^0([0, \frac{\pi}{2}]))$  from which follows that  $\int_{-\pi}^{+\pi} I_{0+}(t, \phi) dt$  exists and varies continuously when  $\phi$  varies in  $S(\mathbb{R}^2)$ .

Therefore the following definition can be put forward.

**Definition 4.3** - When  $Fh < 1$  the pseudo-function  $Pfh_3(k_1, k_2, X_3)$  is defined for each  $\phi \in S(\mathbb{R}^2)$  by:

$$\langle Pfh_3(k_1, k_2, X_3), \phi(k_1, k_2) \rangle = \int_{-\pi}^{+\pi} I_{0+}(t, \phi) dt \text{ where } \langle \dots \rangle \text{ is the duality pairing on } S'(\mathbb{R}^2) \times S(\mathbb{R}^2). \text{ If } X_3 \neq h \text{ the above formula retains its meaning if } \phi \in \mathcal{D}_{L^\infty}(\mathbb{R}^2).$$

In fact  $h_3(k, t, X_3)$  is rapidly decreasing at infinity and the integral (4.13) remains convergent if  $\phi$  is only bounded.

It is now possible to give the expression of  $\bar{T}_C$ : since  $\text{supp } T_C \subset (C)$  a distribution  $T_C$  exists such that for all  $\phi \in S(\mathbb{R}^2)$  satisfying (4.14):

$$(4.15) \quad \langle \bar{T}_C, \phi(k_1, k_2) \rangle = \langle T_C, \bar{\phi}(\gamma(t), t) \rangle$$

where it is assumed that  $t$  varies in  $[-\frac{\pi}{2}, \frac{\pi}{2}]$ . Knowing the properties of  $\gamma(t)$  (lemma 4.2) and  $\phi \in S(\mathbb{R}^2)$ , it is easy to prove that  $\bar{\phi}(\gamma(t), t)$  is a continuous function of  $t$  and is bounded in  $[-\frac{\pi}{2}, \frac{\pi}{2}]$ . Thus  $T_C$  is a Radon measure i.e. a complex measure  $\mu(\bar{t})$  exists such that:

$$(4.16) \quad \langle \bar{T}_C, \phi(k_1, k_2) \rangle = \int_{-\frac{\pi}{2}}^{+\frac{\pi}{2}} \bar{\phi}(\gamma(t), t) \frac{d\mu(t)}{\text{ch}(\gamma(t)h)}.$$

In other words  $\bar{T}_C$  has the form:

$$(4.17) \quad \bar{T}_C = \mu(t) \text{sech}(\gamma(t)h) \delta(k - \gamma(t))$$

and the term  $\bar{\Psi}_3(k_1, k_2, X_3)$  given in the statement of theorem 4.1(ii) becomes:

$$(4.18) \quad \bar{\Psi}_3(k_1, k_2, X_3) = \frac{\text{ch}[\gamma(t)(X_3 - h)]}{\text{ch}^2[\gamma(t)h]} \mu(t) \delta(k - \gamma(t))$$

This leads to the FT that takes the following form since  $\mu \in \mathcal{D}'_{L^\infty}(\mathbb{R})$ :

$$\bar{\Psi}_3(X) = \langle \bar{\Psi}_3, \frac{e^{ik'X'}}{(2\pi)^2} \rangle$$

$$\bar{\Psi}_3(X) = (2\pi)^{-2} \int_{-\pi}^{+\pi} \frac{\text{ch}(\gamma(t)(X_3 - h))}{\text{ch}^2 \gamma(t)h} \exp[i\bar{\omega}_t] \gamma(t) d\mu(t)$$

where  $\gamma_t = \gamma(t)$ ,  $X' = (X_1, X_2) = (r \cos \theta, r \sin \theta)$  and  $\bar{\omega}_t = \gamma_t r \cos(t - \theta)$ .

By setting  $\mu(t) = \mu_1(t) + i\mu_2(t)$ , one has:  $\mu_1(\pi - t) = \mu_1(t)$ ,  $\mu_2(\pi - t) = -\mu_2(t)$  since  $\bar{\Psi}_3(X)$  is real, from which:

$$(4.19) \quad \bar{\Psi}_3(X) = (2\pi)^{-2} \int_{-\pi}^{+\pi} \frac{\text{ch}(\gamma_t(X_3 - h))}{\text{ch}^2 \gamma_t h} \cdot$$

$$\cdot \gamma(t) \{ \cos \bar{\omega}_t d\mu_1(t) - \sin \bar{\omega}_t d\mu_2(t) \}$$

This and other easily established results can be summed up by:

**Theorem 4.3** - General properties of  $Gd(X)$  for any given value of  $Fh$ .

(i)  $Gd(X) = Hd(X) + \Psi d(X) + gd(X)$   
See theorem 4.1

(ii)  $Gd(X)$  is of the class  $C^\infty$  in  $\Omega_0$  and on the free surface  $X_3 = 0$

(iii) For  $0 \leq X_3 < h$  one has:

$$H_2(X) = -\frac{k_0}{2\pi} \int_{-\infty}^{+\infty} \frac{\text{chk}X_3 - \frac{k}{k_0} \text{shk}X_3}{k^2 (\text{chkh} - \frac{k}{k_0} \text{shkh})} e^{ikX_1} dk$$

$$H_3(X) = -\frac{k_0}{(2\pi)^2} \int_{-\pi}^{+\pi} dt \int_0^{+\infty} \frac{\left[ \text{chk}X_3 - \frac{k}{k_0} \text{shk}X_3 \right] e^{ik'X'}}{k \left[ \cos^2 t \text{chkh} - \frac{k_0}{k} \right]}$$

where  $\int$  denotes the finite part of the integral.

(iv)  $\Psi_2(X) = 0$  if  $Fh \geq 1$

$$\Psi_2(X) = \frac{\text{ch}Y_0(X_3 - h)}{\text{ch}Y_0 h} (b_1 \cos Y_0 X_1 + b_2 \sin Y_0 X_1)$$

if  $Fh < 1$ ,  $b_1, b_2$  being arbitrary constants.

$$\text{if } Fh < 1 \quad \Psi_3(X) = (2\pi)^{-2} \int_{-\pi}^{+\pi} \frac{\text{ch}(\gamma_t(X_3 - h))}{\text{ch}^2 \gamma_t h} \cdot$$

$$\cdot \gamma(t) \{ \cos \bar{\omega}_t d\mu_1(t) - \sin \bar{\omega}_t d\mu_2(t) \}$$

$$\text{if } Fh \geq 1 \quad \frac{\partial^2 \Psi_3(X)}{\partial X_1^2} = -(2\pi)^{-2} \int_{-\pi}^{+\pi} \frac{\text{ch}(\gamma_t(X_3 - h))}{\text{ch}^2 \gamma_t h} \cos^2 t \cdot$$

$$\cdot \gamma^3(t) \{ \cos \bar{\omega}_t d\mu_1(t) - \sin \bar{\omega}_t d\mu_2(t) \}$$

$\mu_1(t)$  and  $\mu_2(t)$  are arbitrary signed measure and  $\bar{\omega}_t = \gamma_t r \cos(t - \theta)$ .

Now the Method of Stationary Phase and the Riemann-Lebesgue Lemma yield the following result.

**Theorem 4.4** - Far Field of the Generalized Green Potentials for any given value of  $Fh$ .

When  $d=2$  and  $3$ ,  $Hd, \Psi d$  and  $gd$  are defined by theorems 4.1 and 4.3 and the following results are obtained:

In the case of  $d=2$

(A2) If  $Fh < 1$

$$G_2(X_1, X_3) = \frac{1}{2} \frac{k_0}{1 - \frac{k_0}{h}} |X_1| + g_2(X) + X_2(X)$$

$$+ \frac{1}{2} \frac{k_0}{h} \frac{\text{ch}Y_0(X_3 - h)}{\text{ch}Y_0 h} \sin(Y_0 X_1) \sin Y_1 + \Psi_2(X)$$

with

$$B_0 = \frac{2}{Y_0 h} \left[ \frac{\text{sh}Y_0 h}{Y_0 h} - \frac{1}{\text{ch}Y_0 h} \right]^{-1}$$

$$X_2(X_1, X_3) \in \mathcal{C}(\mathbb{R}^*) \cap \mathcal{O}'_C(\mathbb{R})$$

$$(B2) \text{ If } Fh = 1 \quad \frac{1}{4} \left| \frac{X_1}{h} \right|^3 + \frac{3}{4} \frac{X_1}{h} \left( \frac{X_3}{h} \right)^2 - 2 \left( \frac{X_3}{h} \right) \cdot \frac{1}{5}$$

$$+ g_2(X) + \Psi_2(X) + X_2(X)$$

with  $X_2(X_1, X_3) \in \mathcal{C}(\mathbb{R}^*) \cap \mathcal{O}'_C(\mathbb{R})$

(C2) if  $Ph > 1$

$$G_2(X_1, X_3) = \frac{1}{2} \frac{k_0}{1-k_0h} |X_1| + g_2(X) + \psi_2(X) + X_2(X)$$

with

$$X_2(X_1, X_3) \in \mathcal{E}(\mathbb{R}^*) \cap \mathcal{O}'_c(\mathbb{R})$$

In the case of  $d=3$

(A3) If  $Ph < 1$

$$G_3(X_1, X_3) = \frac{k_0}{2\pi} \int_{-\frac{\pi}{2}}^{\frac{\pi}{2}} \frac{\text{ch} \gamma_t (X_3 - h)}{\text{ch}^2 \gamma_t h} \frac{\gamma'(t) \sin |\bar{\omega}_t|}{\sin 2t \gamma(t)} dt$$

$$+ g_3(X) + \psi_3(X) + X_3(X)$$

$$\omega_t = \gamma_t r \cos(t - \theta)$$

$$X_3(X_1, X_3) \in \mathcal{E}(\mathbb{R}^2 \setminus \{0, 0\})$$

$$\text{When } r \rightarrow \infty, X_3 = A \log r + B(\theta) + \mathcal{O}\left(\frac{1}{r}\right) \quad r = |X'|$$

(B3) If  $Ph \geq 1$

$$\frac{\partial^2 G_3}{\partial X_1^2}(X', X_3) = -\frac{k_0}{4\pi} \left[ \int_{t_0}^{\frac{\pi}{2}} + \int_{-\frac{\pi}{2}}^{-t_0} \right] \frac{\text{ch} \gamma_t (X_3 - h)}{\text{ch}^2 \gamma_t h} \cdot$$

$$\sin[\gamma_t r \cos(t - \theta)] \cotgt \gamma(t) \gamma'(t) dt$$

$$+ g_3(X) + \psi_3(X) + X_3(X)$$

$$X_3(X', X_3) \in \mathcal{E}(\mathbb{R}^2 \setminus \{0, 0\})$$

$$X_3 = \mathcal{O}\left(\frac{1}{r}\right) \text{ when } r \rightarrow \infty$$

#### 5. The Flat-Bump Approach II. Strict Solution

Chapter 4 has given the set of all generalized solutions of NKd  $(Ph, 0, \Sigma^{(1)})$  problem.

Now, from among these general solutions, these, which are strict solutions must be found i.e.

(i) those which are sufficiently regular in order that the partial derivatives occurring in NK1, NK2, NK3 would be derivatives in the classical sense (ii) those which satisfy besides others, the radiation conditions NK4.

Let  $K$  be a given compactum of  $\mathbb{R}^{d-1}$ :

**Proposition 5.1** - "Regularity of the generalized solution  $\phi_0$  of the NKd  $(Ph, 0, \Sigma^{(1)})$  problem".

(i)  $\frac{\partial \phi_0}{\partial X_1} \in \mathcal{E}'(\mathbb{R}^{d-1}) \Rightarrow \phi_0 \in \mathcal{E}(\Omega_0 \cup S_0)$  where

$S_0: X_3=0$  is the free surface at rest

(ii)  $\Sigma^{(1)} \in \mathcal{B}_k^1(\mathbb{R}^{d-1}) \Rightarrow \phi_0 \in \mathcal{C}^0(\bar{\Omega}_0) \cap \mathcal{E}(\Omega_0 \cup S_0)$  and

has a correct normal derivative on  $X_3 = h$  that is, its normal derivative exists as a directional derivative on  $X_3=h$  and is the continuous limit-value of  $\frac{\partial \phi_0}{\partial X_3}(X', X_3)$  when  $X_3 \rightarrow h$ .

**Proof:** According to theorem 4.3 (ii) we have  $\phi_0(X) \in \mathcal{E}(\Omega_0 \cup S_0)$ . In theorem 4.2 it is assumed that

$$\frac{\partial \phi_0}{\partial X_1} \in \mathcal{E}'(\mathbb{R}^{d-1}) \subset \mathcal{O}'_c(\mathbb{R}^{d-1}).$$

Therefore (i) is deduced from theorem XII of [31 p.167] and from its corollaries. If besides  $\Sigma^{(1)} \in \mathcal{B}_k^1(\mathbb{R}^{d-1})$  this same theorem XII proves

$$\phi_0 \in \mathcal{C}^0(\bar{\Omega}_0).$$

To prove that  $\phi_0$  has a correct normal derivative it is shown that first of all when  $X_3 \rightarrow h$ ,  $\frac{DGd}{DX_3}(X', X_3) + \delta(X')$  in the space  $\mathcal{M}(\mathbb{R}^{d-1})$  of Radon measures on  $\mathbb{R}^{d-1}$  (compared with the definition 4.2 (G3) where the preceding limit is set in  $\mathcal{D}'(\mathbb{R}^{d-1})$  only). The theorem XII mentioned above is then used to prove the result.

Q.E.D.

**Theorem 5.1** - It is assumed that  $d=2$  and  $Ph=1$ . For all  $\Sigma^{(1)} \in \mathcal{B}_k^1(\mathbb{R}^{d-1})$ , the NKd  $(Ph, 0, \Sigma^{(1)})$  problem admits no strict solution.

**Proof** - When  $|X_1| \rightarrow \infty$  the behaviour described in theorem 4.4 results, thus the generalized solution is as follows:

$$\begin{aligned} (5.1) \quad \phi_0(X_1, X_3) &= c \frac{\partial \Sigma^{(1)}}{\partial X_1}(X_1) + G_2(X_1, X_3) \\ &= -\frac{c}{4h^3} \frac{\partial \Sigma^{(1)}}{\partial X_1}(X_1) \cdot |X_1|^3 \\ &\quad + \frac{3c}{4h} \left[ \frac{X_3^2}{h} - 2 \left( \frac{X_3}{h} - \frac{1}{5} \right) \right] \frac{\partial \Sigma^{(1)}}{\partial X_1}(X_1) \cdot |X_1| \\ &\quad + c \frac{\partial \Sigma}{\partial X_1}(X_1) \cdot \omega_2(X_1) + \pi_2(X) \\ &\quad + c \frac{\partial \Sigma^{(1)}}{\partial X_1}(X_1) \cdot X_2(X_1) \end{aligned}$$

$$\text{with } \pi_2(X) = \alpha_0 + \alpha_1 X_1 + \alpha_2 (X_1^2 - X_3^2 + 2hX_3)$$

$$+ \alpha_3 (X_1^3 - 3X_3^2 X_1 + 6hX_1 X_3)$$

Let us set:

$$(5.2) \quad m_k = \int_K X_1^k \Sigma^{(1)}(X_1) dX_1$$

so that

$$(5.3) \quad \int_K X_1^k \frac{\partial \Sigma^{(1)}}{\partial X_1} dX_1 = -k m_{k-1}$$

$$\begin{aligned} (5.4) \quad \phi_0(X_1, X_3) &= -\frac{c}{4h^3} \left[ 3m_0 X_1^2 - 6m_1 X_1 + 3m_2 \right] \text{sg} X_1 \\ &\quad + \frac{3c}{4h} \left[ \left( \frac{X_3}{h} \right)^2 - 2 \left( \frac{X_3}{h} - \frac{1}{5} \right) \right] m_0 \text{sg} X_1 \\ &\quad - a_1 m_0 c + 2a_2 c m_1 - 2a_3 m_0 X_1 c - 3a_3 c m_2 + 3a_3 c X_1 m_1 \\ &\quad - 3a_3 c X_1^2 m_0 + 3a_3 c X_3^2 m_0 - 6h X_3 m_0 a_3 c + \pi_2(X) + o(1) \end{aligned}$$

because the last term of (5.1) is  $o(1)$ .

Now, it must be seen, if for a suitable choice of coefficients  $a_j$ , the generalized solution (5.4) is a strict one, and in particular bounded at infinity.

The principal terms of (5.4) are:

$$(5.5) \quad \alpha_3 X_1^3 - \frac{3c}{4h} m_0 X_1^2 \text{sg} X_1 - 3a_3 m_0 c X_1^7 + \alpha_2 X_1^2$$

$\alpha_3=0$  but whatever be the choice of  $a_3$  and  $\alpha_2$ , the solution will always be non-bounded when  $X_1^3 \rightarrow \infty$  or  $X_1 \rightarrow -\infty$ .

Q.E.D.

**Theorem 5.2** - It is assumed that  $\text{Ph}$  is of any value if  $d=3$  and  $\text{Ph} \neq 1$  when  $d=2$ . For each  $\Sigma^{(1)} \in \mathcal{B}_K^{(1)}(d-1)$  the NKd  $(\text{Ph}, 0, \Sigma^{(1)})$  problem admits a strict unique solution with a correct normal derivative on  $X_3 = h$ .

**Proof:** As an example the proof will be given when  $\text{Ph} < 1$  and  $d=2$  and 3.

(A)  $d = 2$

According to theorem (4.4) the generalized solution is written as follows:

$$(5.6) \quad \Phi_0(X_1, X_3) = \frac{c}{2} \frac{k_0}{1-k_0 h} \frac{\partial \Sigma^{(1)}}{\partial X_1}(X_1) + |X_1| + \frac{c}{2} B_0 (\text{ch} \gamma_0 X_3 - \frac{\gamma_0}{k_0} \text{sh} \gamma_0 X_3) \frac{\partial \Sigma^{(1)}}{\partial X_1}(X_1) \sin(\gamma_0 |X_1|) + c \frac{\partial \Sigma^{(1)}}{\partial X_1}(X_1) + g_2(X_1) + c \frac{\partial \Sigma^{(1)}}{\partial X_1}(X_1) (X_1^*)^2 g_2(X_1, X_3) + c \frac{\partial \Sigma^{(1)}}{\partial X_1}(X_1) (X_1^*) X_2(X_1, X_3) + \pi_2(X_1)$$

Let us set:

$$(5.7) \quad \hat{\Sigma}^{(1)} = \Sigma_c^{(1)} - i \Sigma_s^{(1)} = \int_K \Sigma^{(1)}(X_1) e^{-ikX_1} dX_1$$

then it follows that when  $|X_1| \rightarrow \infty$

$$(5.8) \quad \Phi_0(X_1, X_3) = \frac{c}{2} \frac{k_0}{1-k_0 h} m_0 \text{sg}(X_1) - \frac{1}{2} \gamma_0 B_0 c (\text{ch} \gamma_0 X_3 - \frac{\gamma_0}{k_0} \text{sh} \gamma_0 X_3) \cdot \left[ \Sigma_s^{(1)} \sin \gamma_0 X_1 + \Sigma_c^{(1)} \cos \gamma_0 X_1 \right] \text{sg} X_1 + a_1 m_0 c + a_0 + a_1 X_1 + \gamma_0 (\text{ch} \gamma_0 X_3 - \frac{\gamma_0}{k_0} \text{sh} \gamma_0 X_3) \left[ (b_1 \Sigma_s^{(1)} - b_2 \Sigma_c^{(1)}) \sin \gamma_0 X_1 + (b_1 \Sigma_c^{(1)} + b_2 \Sigma_s^{(1)}) \cos \gamma_0 X_1 \right] + o(1)$$

The constants  $a_i$  and  $b_i$  must now be determined in order that (5.8) would satisfy (NK4) condition.

If  $X_1 \rightarrow +\infty$

$$\alpha_1 = 0 \\ \alpha_0 + a_1 m_0 c + \frac{c}{2} \frac{k_0}{1-k_0 h} m_0 = 0$$

It follows for example  $\alpha_0 = 0$  and  $a_1 = -\frac{1}{2} \frac{k_0}{1-k_0 h}$

$$(5.9) \quad \begin{cases} b_1 \Sigma_s^{(1)} - b_2 \Sigma_c^{(1)} = \frac{1}{2} \Sigma_s^{(1)} B_0 c \\ b_1 \Sigma_c^{(1)} + b_2 \Sigma_s^{(1)} = \frac{1}{2} \Sigma_c^{(1)} B_0 c \end{cases}$$

which gives the unique solution

$$(5.10) \quad b_1 = \frac{1}{2} B_0 c, \quad b_2 = 0$$

The behaviour at infinity down-stream ( $X_1 \rightarrow -\infty$ ) is then deduced

$$(5.11) \quad \Phi_0(X_1, X_3) = -c \frac{k_0}{1-k_0 h} m_0 - \gamma_0 B_0 c (\text{ch} \gamma_0 X_3 - \frac{\gamma_0}{k_0} \text{sh} \gamma_0 X_3) \cdot \left[ \Sigma_s^{(1)} \sin \gamma_0 X_1 + \Sigma_c^{(1)} \cos \gamma_0 X_1 \right] + o(1)$$

which is consistent with NK4.

(B)  $d = 3$

According to theorem (4.4) the generalized solution is written as:

$$(5.12) \quad \Phi_0(X', X_3) = c \frac{\partial \Sigma^{(1)}}{\partial X_1}(X', X_3) (X')^2 I_3(X', X_3) + c \frac{\partial \Sigma^{(1)}}{\partial X_1}(X', X_3) (X')^2 g_3(X') + c \frac{\partial \Sigma^{(1)}}{\partial X_1}(X', X_3) (X')^2 X_3(X', X_3) + \pi_3(X')$$

with

$$(5.13) \quad I_3(X', X_3) = \frac{k_0}{2\pi} \int_{-\pi/2}^{\pi/2} \frac{\text{ch} \gamma_0 X_3 - n}{c^2 \gamma_0^2} \cdot \left[ \frac{\gamma(t)}{k_0 \pi} \cos \left[ \gamma_0 t \cos(t) \right] \frac{du_1}{dt} + \left[ \frac{\gamma'(t)}{\sin 2t \gamma(t)} \text{sg} [\cos(t-\theta)] - \frac{\gamma(t)}{k_0 \pi} \frac{du_2}{dt} \right] \cdot \sin \left[ \gamma_0 t \cos(t-\theta) \right] \right] dt$$

The second term of (5.12) equals:

$$(5.14) \quad c \frac{\partial \Sigma^{(1)}}{\partial X_1}(X', X_3) \cdot g_3(X') = -c m_{00} a_1$$

with notation:

$$(5.15) \quad m_{kl} = \int_K X_1^k X_2^l \Sigma^{(1)}(X') dX'$$

The third term is  $O(\frac{1}{r})$ , the fourth term equals:

$$\pi_3(X') = \alpha_0 + \alpha_1 X_1 + \alpha_2 X_2$$

The arbitrary signed measures  $\mu_1$  and  $\mu_2$  and the arbitrary constants  $\alpha_i$  must now be defined for (5.12) to satisfy NK4. It immediately follows that:

$$\alpha_1 = \alpha_2 = 0 \\ \alpha_0 - c m_{00} a_1 = 0$$

hence, for example,  $\alpha_0 = a_0 = a_1 = a_2 = 0$

As far as the integral (5.13) is concerned, when using the steady phase method it is noteworthy that the first term when  $r \rightarrow \infty$  gives a contribution which is  $O(r^{-1/2})$  for nearly all the values of  $\theta$ . The same applies to the second term if  $\mu_2$  is of any value, and the contributions of both terms cannot vanish. Thus to satisfy NK4 condition with  $X_1 \rightarrow +\infty$ ,  $X_2 = \text{constant}$ , it is necessary to choose

$$\frac{d\mu_1}{dt}(t) \equiv 0 \\ \frac{\gamma(t)}{k_0 \pi} \frac{d\mu_2(t)}{dt} = \frac{\gamma'(t)}{\sin 2t \gamma(t)}$$

hence the behaviour at infinity  $X_1 \rightarrow -\infty$   $X_2 = \text{constant}$

$$(5.16) \quad \Phi_0(X) = c \frac{\partial \Sigma^{(1)}}{\partial X_1}(X') (X')^2 \cdot \left( -\frac{k_0}{\pi} \int_{-\pi/2}^{\pi/2} \frac{\text{ch} \gamma_0 (X_3-h)}{\text{ch}^2 \gamma_0 h} \frac{\gamma'(t)}{\sin 2t \gamma(t)} \sin \mu_1 dt \right) + o(\frac{1}{r})$$

and the steady phase method shows that (5.16) is  $O(r^{-1/2})$  which satisfies NK4 condition. Q.E.D.

**Corollary 5.1 - "Far Field in the two-dimensional case and blockage with a free surface".**

It is assumed that  $d=2$ ,  $Ph \neq 1$  and  $\Gamma^{(1)} \in \mathcal{B}_k^1(\mathbb{R})$ . Let  $B_0$  be vanished if  $Ph > 1$  and  $B_0$  equals the expression of 4.4 (A2) theorem if  $Ph < 1$ .

Let us set :

$$m_0 = \int_K \Gamma^{(1)}(X_1) dX_1 \text{ and } Y(X_1) = 0 \text{ if } X_1 < 0$$

$= 1$  if  $X_1 > 0$  (Heaviside function)

The behaviour of the potential  $\phi_0(X_1, X_3)$  at infinity  $X_1 \rightarrow \pm\infty$  is given by :

$$\phi_0(X_1, X_3) = \frac{c}{2} \frac{k_0}{1-k_0 h} m_0 (\operatorname{sg}(X_1) - 1) - [1 - Y(X_1)] \gamma_0 B_0 c \frac{\operatorname{ch} \gamma_0 (X_3 - h)}{\operatorname{ch} \gamma_0 h} \left[ \Gamma_S^{(1)} \sin \gamma_0 X_1 + \Gamma_C^{(1)} \cos \gamma_0 X_1 \right]$$

$+ \lambda_2 \dots \lambda_n(X_3)$

the function  $\lambda_2$  vanishes at infinity.

$\lambda_2(X_1, X_3) \in \mathcal{B}(\mathbb{R}^*)$  and  $\Gamma_S^{(1)}$  and  $\Gamma_C^{(1)}$  are defined by

$$\hat{\Gamma}^{(1)} = \Gamma^{(1)}(\gamma_0) = \Gamma_C^{(1)} - i \Gamma_S^{(1)} = \int_K \Gamma^{(1)}(X_1) e^{-i \gamma_0 X_1} dX_1$$

The above formula particularly shows that the magnitude  $A_C$  and  $A_S$  of cosine and sine waves at downstream infinity are given by the very simple following relation :

$$A_C - i A_S = i k_0^{-1} B_0 \gamma_0^2 \hat{\Gamma}^{(1)}$$

This corollary is a direct consequence of formulae (5.8 - 5.11) and should be compared with result given in [27 p.201 formula (13)] .

**Corollary 5.2 - "Far Field in the three-dimensional case".**

It is assumed that  $d=3$  and  $Ph < 1$ . Let us set:

$$\hat{\Gamma}(0, t) = \frac{\gamma_0}{2\pi} \int_K \Gamma^{(1)}(X_1, X_2) e^{-i \gamma_0 (X_1 \cos t + X_2 \sin t)} dX_1 dX_2$$

$Y(u) = 0$  if  $u < 0$ ,  $= 1$  if  $u > 0$

Therefore the behaviour of the potential  $\phi_0$  at infinity  $|X'| \rightarrow \infty$  is represented by :

$$\phi_0(X) = \frac{c}{\gamma_0} \int_{-\pi/2}^{\pi/2} \frac{\operatorname{ch} \gamma_0 (X_3 - h)}{\operatorname{ch} \gamma_0 h} \left[ 1 - Y(\cos(t - \theta)) \right] \cdot$$

$$\hat{\Gamma}^{(1)}(t) \cos \gamma_0 X_1 e^{-i \gamma_0 X_2 \sin t} \left[ \gamma_0 \cos t + i \sin t \right] dt + O\left(\frac{1}{r}\right)$$

This formula shows in particular that the amplitudes  $A_C(t)$  and  $A_S(t)$  of cosine and sine waves at downstream infinity are given by the very simple following relation :

$$A_C(t) - i A_S(t) = i k_0^{-1} B_0 \gamma_0^2 \hat{\Gamma}^{(1)}(t)$$

where

$$B(t) = \frac{2}{\gamma_0 h} \cos^2 t \left[ \frac{\operatorname{sh} \gamma_0 h}{\gamma_0 h} - \frac{1}{\operatorname{ch} \gamma_0 h} \right]^{-1}$$

Compare with  $B_0$  given by Theor. 4.4 (A.2)

**Corollary 5.3 - "Velocity potential and Green potential of NKd  $(Ph, 0, \Gamma^{(1)})$  problem".**

The strict unique solution of the NKd  $(Ph, 0, \Gamma^{(1)})$  problem which was constructed in theorem 5.2 can be expounded in the following form :

$$\phi_0(X) = c \frac{\partial \Gamma^{(1)}}{\partial X_1}(X') \cdot \nabla G_d(X', X_3)$$

where Green potential  $G_d$  is given by :

(A) when  $d=2$

$$G_2(X) = H_2(X) + \psi_2(X) + \frac{1}{2} \frac{k_0}{1-k_0 h} [|X_1| - X_1]$$

$$\text{if } X_3 \neq h, H_2(X) = - \frac{k_0}{2\pi} \int_{-\infty}^{+\infty} \frac{\operatorname{ch} k X_3 - \frac{k}{k_0} \operatorname{sh} k X_3}{k^2 (\operatorname{ch} k h - \frac{k}{k_0} \operatorname{sh} k h)} e^{i k X_1} dk$$

$$\psi_2(X) = \frac{1}{2} B_0 \frac{\operatorname{ch} \gamma_0 (X_3 - h)}{\operatorname{ch} \gamma_0 h} \sin \gamma_0 X_1$$

$B_0 = 0$  if  $Ph > 1$

$$B_0 = \frac{2}{\gamma_0 h} \frac{\operatorname{ch} \gamma_0 h}{\operatorname{sh} 2 \gamma_0 h} \text{ if } Ph < 1$$

(B) When  $d=3$  (in the case of  $Ph < 1$  only)

$$G_3(X) = H_3(X) + \psi_3(X)$$

$$\text{if } X_3 \neq h, H_3(X) = - \frac{k_0}{(2\pi)^2} \int_{-\pi/2}^{\pi/2} dt \cdot$$

$$\int_0^{\infty} \frac{\operatorname{ch} k X_3 - \frac{k \cos^2 t}{k_0} \operatorname{sh} k X_3}{k [\cos^2 t \operatorname{ch} k h - \frac{k}{k_0} \operatorname{sh} k h]} e^{i k r \cos(t - \theta)} dk$$

$$\psi_3(X) = - \frac{k_0}{2\pi} \int_{-\pi/2}^{\pi/2} \frac{\operatorname{ch} \gamma(t) (X_3 - h)}{\operatorname{ch} \gamma(t) h} \frac{\gamma'(t)}{\sin 2t \cdot \gamma(t)} dt$$

**Corollary 5.4 - The solution  $\phi_0$  of the NKd  $(Ph, 0, \Gamma^{(1)})$  problem defined in corollary 5.3 is as follows.**

$$(*) \|\phi_0\|_{\mathcal{B}_k^0(\bar{\Omega}_0)} \leq M_0 \|\Gamma^{(1)}\|_{\mathcal{B}_k^1(\mathbb{R}^{d-1})}$$

$$(**) \|R \phi_0\|_{\mathcal{B}_k^0(\bar{\Omega}_0)} \leq M_1 \|\Gamma^{(1)}\|_{\mathcal{B}_k^1(\mathbb{R}^{d-1})}$$

where  $M_0$  and  $M_1$  are two constants.

This corollary which is deduced from corollary 5.3 and theorem 4.4 is admitted here without demonstration.

**Theorem 5.3 - "Existence, Uniqueness and Regularity of the strict solution of the problem NKd  $(Ph, 0, \Gamma^{(1)})$ . It is assumed that  $Ph$  is of any value if  $d=3$ , and  $Ph \neq 1$  if  $d=2$ .**

Let  $m$  be an integer  $\geq 2$  and  $K$  a given compactum of  $\mathbb{R}^{d-1}$ . For each  $\Gamma^{(1)} \in \mathcal{B}_k^{m, \alpha}(\mathbb{R}^{d-1})$  the NKd  $(Ph, 0, \Gamma^{(1)})$  problem admits a unique solution

$\phi_0 \in \mathcal{B}_k^{m, \alpha}(\bar{\Omega}_0)$  (ii)  $\phi_0$  depends continuously on  $\Gamma^{(1)}$  i.e. the mapping  $\Gamma^{(1)} \mapsto \phi_0$  belongs to  $\mathcal{L}(\mathcal{B}_k^{m, \alpha}(\mathbb{R}^{d-1}), \mathcal{B}_k^{m, \alpha}(\bar{\Omega}_0))$ .

**Proof** - Having proved existence and uniqueness in theorem 5.2 we still have to prove the regularity of this solution and its dependence with respect to data  $\Sigma^{(1)}$ . Let  $T$  be the solution operator  $(\Sigma^{(1)} \rightarrow \Phi)$ . The proof that is given follows closely method used in (15).

**First step -**

$\Sigma^{(1)} \in \mathcal{B}_K(\mathbb{R}^{d-1}) \Rightarrow \Phi_0 \in \mathcal{B}(\bar{\Omega}_0) \cap \mathcal{B}^{2,\alpha}(\bar{\Omega}_0)$ . This follows from theorem 1.3 of [19 p.115] where the result is established for bounded domains i.e. the boundary of which is compact. Although, here, the domain  $\Omega$  is not bounded the result of (19) remains valid if it is taken into account that  $\nabla_{\mathbb{R}^d} \Phi$  is continuous, bounded and that it vanishes at infinity as all its derivatives.

**Second step -**  $T \in \mathcal{L}(\mathcal{B}_K(\mathbb{R}^{d-1}), \mathcal{B}^{2,\alpha}(\bar{\Omega}_0))$ .

First of all the following is established :

**Proposition 5.2 -**

$T \in \mathcal{L}(\mathcal{E}'(\mathbb{R}^{d-1}), \mathcal{C}^2(\mathbb{I}, \mathcal{S}'(\mathbb{R}^{d-1})))$

The proposition 5.2 is an immediate consequence of theorem XI of [31, p.247]. The result to be demonstrated is deduced from this proposition because the graph of  $T$  is closed and therefore continuous according to closed graph theorem.

**Third step -**  $\Sigma^{(1)} \in \mathcal{B}_K^{m,\alpha}(\mathbb{R}^{d-1}) \Rightarrow \Phi_0 \in \mathcal{B}^{2,\alpha}(\bar{\Omega}_0)$   
We have  $\mathcal{B}_K(\mathbb{R}^{d-1}) \subset \mathcal{B}_K^{m,\alpha}(\mathbb{R}^{d-1})$  with dense injection. By forming the mollifiers (regularization) of  $\Sigma^{(1)}$ , it is possible to find a sequence  $(\Sigma_n^{(1)}, n \geq 1, \Sigma_n^{(1)} \in \mathcal{B}_K(\mathbb{R}^{d-1}))$  bounded in  $\mathcal{B}_K^{2,\alpha}$  and convergent to  $\Sigma^{(1)}$  in  $\mathcal{B}_K(\mathbb{R}^{d-1})$ .

At each  $\Sigma_n^{(1)}$  there is a unique corresponding solution  $\Phi_n \in \mathcal{B}^{2,\alpha}(\bar{\Omega}_0)$ , see second step. Schauder's a priori estimates [1, theore 7.3 p.668] can be then applied :

$$(5.20) \quad \|\Phi_n\|_{\mathcal{B}^{2,\alpha}(\bar{\Omega}_0)} \leq C_0 \left[ \|\Phi_n\|_{\mathcal{B}^0(\bar{\Omega}_0)} + \|\Sigma_n^{(1)}\|_{\mathcal{B}_K^{2,\alpha}(\mathbb{R}^{d-1})} \right]$$

where  $C_0$  is a constant. However, according to corollary 5.4 :

$$(5.21) \quad \|\Phi_n\|_{\mathcal{B}^0(\bar{\Omega}_0)} \leq M_0 \|\Sigma_n^{(1)}\|_{\mathcal{B}_K^1(\mathbb{R}^{d-1})} \leq M_0 \|\Sigma_n^{(1)}\|_{\mathcal{B}_K^{2,\alpha}(\mathbb{R}^{d-1})}$$

Then it follows :

$$(5.22) \quad \|\Phi_n\|_{\mathcal{B}^{2,\alpha}(\bar{\Omega}_0)} \leq C_1 \|\Sigma_n^{(1)}\|_{\mathcal{B}_K^{2,\alpha}(\mathbb{R}^{d-1})}$$

where  $C_1 = C_0(1+M_0) < \infty$ . Thus the sequence  $\Phi_n$  is bounded in  $\mathcal{B}^{2,\alpha}(\bar{\Omega}_0)$ . Now for all compact  $\omega \subset \mathcal{B}^{2,\alpha}(\omega) \subset \mathcal{B}^2(\omega)$  the injection being completely continuous.

Therefore if  $\omega \subset \bar{\Omega}_0$  it is possible to obtain from sequence  $\Phi_n$  a subsequence also noted as  $\Phi_n$  which is convergent in  $\mathcal{B}^2(\omega)$ . The limit of this sequence can only be  $\Phi_0(X)$  which according

to (5.22) satisfies then :

$$(5.23) \quad \|\Phi_0\|_{\mathcal{B}^{2,\alpha}(\bar{\Omega}_0)} \leq C_1 \|\Sigma^{(1)}\|_{\mathcal{B}_K^{2,\alpha}(\mathbb{R}^{d-1})} < \infty$$

which proves the third step.

**Fourth step -**

$\Sigma^{(1)} \in \mathcal{B}_K^{m,\alpha}(\mathbb{R}^{d-1}) \Rightarrow \Phi_0 \in \mathcal{B}^{m,\alpha}(\bar{\Omega}_0)$

By, once again, applying Schauder's a priori estimates one has successively :

$$(5.24) \quad \|\Phi_0\|_{\mathcal{B}^{m,\alpha}(\bar{\Omega}_0)} \leq C_2 \left[ \|\Phi_0\|_{\mathcal{B}^0(\bar{\Omega}_0)} + \|\Sigma^{(1)}\|_{\mathcal{B}_K^{m,\alpha}(\mathbb{R}^{d-1})} \right]$$

$$(5.25) \quad \|\Phi_0\|_{\mathcal{B}^0(\bar{\Omega}_0)} \leq C_3 \|\Sigma^{(1)}\|_{\mathcal{B}_K^{m,\alpha}(\mathbb{R}^{d-1})}$$

Which is proven in the same way as for (5.22). Then it follows :

$$(5.26) \quad \|\Phi_0\|_{\mathcal{B}^{m,\alpha}(\bar{\Omega}_0)} \leq C_4 \|\Sigma^{(1)}\|_{\mathcal{B}_K^{m,\alpha}(\mathbb{R}^{d-1})}$$

**Fifth step -**  $T \in \mathcal{L}(\mathcal{B}_K^{m,\alpha}(\mathbb{R}^{d-1}), \mathcal{B}^{m,\alpha}(\bar{\Omega}_0))$

Which is a consequence of (5.26)

**Sixth step -**  $T \in \mathcal{L}(\mathcal{B}_K^{m,\alpha}(\mathbb{R}^{d-1}), \mathcal{B}_R^{m,\alpha}(\bar{\Omega}_0))$

Which is a consequence of the fifth step and the corollary 5.4. Q.E.D. theorem 5.3

**6. Two Auxiliary Boundary Value Problems**

The two problems studied here will be useful later on. The V.P. problem (Variation Problem in the sense of calculus of variations) allied to NKd (Ph,  $\Sigma$ ) problem and a D.P. problem (Dirichlet Problem).

**V.P.  $(f, \phi_1, \phi_2)$  problem -**

The following three functions are given :  $f(x), x \in \bar{\Omega}_0$  ;  $\phi_1(x'), x' \in \mathbb{R}^{d-1}$  ;  $\phi_2(x'), x' \in \mathbb{R}^{d-1}$  and one is searching for  $w(x), x \in \bar{\Omega}_0$  such that :

$$(VP1) \quad \nabla_x^2 w(x) = f(x), \quad x \in \bar{\Omega}_0$$

$$(VP2) \quad \frac{\partial^2 w}{\partial x_1^2} - k_0 \frac{\partial w}{\partial x_3} = \phi_1(x'), \quad x_3 = 0$$

$$(VP3) \quad \frac{\partial w}{\partial x_3} = \phi_2(x'), \quad x_3 = h$$

$$(VP4) \quad R w \in \mathcal{B}^0(\bar{\Omega}_0)$$

Here,  $R(x)$  is defined by (2.10) where, to make the following easier, the notation change  $X = (X', X_3) \cap x = (x', x_3)$  is used.

It is noted that  $VP(0, 0, cN_1^{(0)}) = NKd(Ph, 0, \Sigma^{(1)})$

The following theorem is a generalization of theorem 5.3.

**Theorem 6.1 -**  $Ph$  is assumed of any value if  $d=3$ , and  $Ph \neq 1$  if  $d=2$ . Given  $f(x)$  such that  $f(x)=0$  for  $x_3=0$  the  $VP(f, 0, \phi_2)$  problem admits a unique solution  $w \in \mathcal{B}_R^{m,\alpha}(\bar{\Omega}_0)$  as soon as  $f \in \mathcal{B}^{m-2,\alpha}(\bar{\Omega}_0) \cap \mathcal{C}^1(\mathbb{R}^{d-1})$  and



**Theorem 6.2** - It is assumed that  $Fh$  is of any value  $\alpha \in \mathbb{R}$ ,  $\alpha \neq 1$  if  $d=2$ . Let  $m$  be an integer  $\geq 2$ . For each  $(f, \phi_1, \phi_2) \in \mathcal{U}_h$  (i) the  $VP(f, \phi_1, \phi_2)$  problem admits a unique solution  $\psi \in \mathcal{B}_R^{m, \alpha}(\bar{\Omega}_0)$  (ii)  $\psi$  depends continuously on  $(f, \phi_1, \phi_2)$  i.e. the mapping  $(f, \phi_1, \phi_2) \mapsto \psi$  belongs to  $\mathcal{L}(\mathcal{U}_h, \mathcal{B})$ .

The notations are as follows:

$$\mathcal{U}_0 = \{f(x) \in \mathcal{B}^{m-2, \alpha}(\bar{\Omega}_0) : (1+|x'|^2)^{\frac{d-1}{2}} f(x', x_3) \in L^1(\mathbb{R}^{d-1})\}$$

$$\mathcal{U}_1 = \{\phi_1(x') \in \mathcal{B}^{m-2, \alpha}(\mathbb{R}^{d-1}) : (1+|x'|^2)^{\frac{d-1}{2}} \phi_1(x') \in L^1(\mathbb{R}^{d-1})\}$$

$$\mathcal{U}_2 = \{\phi_2(x') \in \mathcal{B}^{m-1, \alpha}(\mathbb{R}^{d-1}) : (1+|x'|^2)^{\frac{d-1}{2}} \phi_2(x') \in L^1(\mathbb{R}^{d-1})\}$$

$L^1(\mathbb{R}^{d-1})$  is the space of measurable  $u(x')$  functions defined on  $\mathbb{R}^{d-1}$ , for which the Lebesgue integral

$$\|u\|_{L^1(\mathbb{R}^{d-1})} = \int_{\mathbb{R}^{d-1}} |u(x')| dx'$$

is finite.

$\mathcal{U}_0, \mathcal{U}_1, \mathcal{U}_2$  are Banach spaces with the norms

$$\|f\|_{\mathcal{U}_0} = \|f\|_{\mathcal{B}^{m-2, \alpha}(\bar{\Omega}_0)} + \sup_{x_3 \in \mathbb{R}} \|(1+|x'|^2)^{\frac{d-1}{2}} f(x', x_3)\|_{L^1(\mathbb{R}^{d-1})}$$

$$\|\phi_1\|_{\mathcal{U}_1} = \|\phi_1\|_{\mathcal{B}^{m-2, \alpha}(\mathbb{R}^{d-1})} + \|(1+|x'|^2)^{\frac{d-1}{2}} \phi_1(x')\|_{L^1(\mathbb{R}^{d-1})}$$

$$\|\phi_2\|_{\mathcal{U}_2} = \|\phi_2\|_{\mathcal{B}^{m-1, \alpha}(\mathbb{R}^{d-1})} + \|(1+|x'|^2)^{\frac{d-1}{2}} \phi_2(x')\|_{L^1(\mathbb{R}^{d-1})}$$

and the product space  $\mathcal{U}_0 \times \mathcal{U}_1 \times \mathcal{U}_2$  is also a Banach space.  $\mathcal{U}_h$  is the subspace of  $\mathcal{U}_0 \times \mathcal{U}_1 \times \mathcal{U}_2$  for which  $(f, \phi_1, \phi_2)$  verifies the compatibility condition

$$\int_{\mathbb{R}^{d-1}} \left[ \phi_2(x') + \frac{1}{k_0} \phi_1(x') \right] dx' = \int_{\Omega_0} f(x) dx = 0$$

$\mathcal{U}_h$  is a closed subspace of  $\mathcal{U}_0 \times \mathcal{U}_1 \times \mathcal{U}_2$ , hence a Banach space.

**Proofs of theorem 6.1 and 6.2** : The proofs are identical to the proofs of theorem 5.1 and 5.3 and are based on the use of the Fourier transform in the space of ultradistributions. We recall the main four steps of the argument :

- (i) we look for the generalized solutions of  $VP(f, \phi_1, \phi_2)$  i.e. the solutions which are not necessarily regular and for which the  $VP_4$  condition is not necessarily satisfied.
- (ii) then the strict solutions of  $VP(f, \phi_1, \phi_2)$  are found, i.e. the solutions with sufficient regularity which satisfy the radiation condition  $VP_4$ . This condition can be satisfied only if the compatibility condition is verified by the data  $f, \phi_1, \phi_2$ . If it is so the strict solution is unique.
- (iii) the following result is proven which is analogous to corollary 5.4 :

$$\|w\|_{\mathcal{B}_0^{m, \alpha}(\bar{\Omega}_0)} \leq C \|u\|_{\mathcal{B}_0^{m, \alpha}(\bar{\Omega}_0)}$$

$$\|Rw\|_{\mathcal{B}_0^{m, \alpha}(\bar{\Omega}_0)} \leq M_1 \|u\|_{\mathcal{B}_0^{m, \alpha}(\bar{\Omega}_0)}$$

where  $u = (f, \phi_1, \phi_2)$  and  $M_1, M_2$  are two constants.

(iv) finally the regularity of the strict solution is proven by the method used in the proof of theorem 5.

**DP( $\mathcal{E}^{(1)}$ ) problem**

$\mathcal{E}^{(1)}(x')$  is given and  $\phi^D(x')$  is looked for

such that :

$$(DP1) \quad \Delta \phi^D(x') = 0, \quad x' \in \mathbb{R}^{d-1}$$

$$(DP2) \quad \phi^D(x') \in \mathcal{B}_0^{m, \alpha}(\mathbb{R}^{d-1}), \quad x' \in \mathbb{R}^{d-1}$$

$$(DP3) \quad \phi^D(x') \in \mathcal{B}_0^{m, \alpha}(\mathbb{R}^{d-1}), \quad x' \in \mathbb{R}^{d-1}$$

**Definition 6.1** - We say that  $\phi^D(x')$  is a generalized Green potential of the DP( $\mathcal{E}^{(1)}$ ) problem if it satisfies the generalized distributions :

$$(GD1) \quad \Delta \phi^D(x') = 0, \quad x' \in \mathbb{R}^{d-1}$$

$$(GD2) \quad \phi^D(x') \in \mathcal{B}_0^{m, \alpha}(\mathbb{R}^{d-1}), \quad x' \in \mathbb{R}^{d-1}$$

$$(GD3) \quad \phi^D(x') \in \mathcal{B}_0^{m, \alpha}(\mathbb{R}^{d-1}), \quad x' \in \mathbb{R}^{d-1}$$

**Lemma 6.1**

(i) There exists a unique generalized Green potential  $G^D$  and it is a unique Green potential, i.e. infinitely differentiable. Furthermore for each compact

$$K \subset \mathbb{R}^{d-1} \quad (K \cap \mathbb{R}^{d-1} \neq \emptyset)$$

we have :  $G^D(x') \in \mathcal{B}_0^{m, \alpha}(\mathbb{R}^{d-1})$

(ii)  $G^D$  is given by

$$G^D(x') = \frac{1}{(2\pi)^{d-1}} \frac{\sin(\frac{\pi}{2} x_3)}{\operatorname{ch}(\frac{\pi}{2} x_3) + \cos(\frac{\pi}{2} x_3)} \quad (x', x_3) \in \mathbb{R}^d$$

$$G^D(x') = \frac{1}{(2\pi)^{d-1}} \sum_{n=1}^{\infty} (-i)^{n-1} n \sin(n \frac{\pi}{2} x_3) K_n(\frac{\pi}{2} |x'|)$$

where  $|x'| \neq 0$  and  $K_n$  is the modified Bessel function.

(iii)  $G^D(x') > 0, \quad x' \in \mathbb{R}^{d-1}$

$$(iv) \quad \int_{\mathbb{R}^{d-1}} G^D(x', x_3) dx' = \frac{x_3}{h}$$

(v) When  $x_3 \rightarrow 0, G^D(x', x_3) \rightarrow 0$  in  $\mathcal{B}_0^{m, \alpha}(\mathbb{R}^{d-1})$

(vi) When  $x_3 \rightarrow h, G^D(x', x_3) \rightarrow \delta(x' - \frac{1}{2} \mathbb{R}^{d-1})$ , space of Radon measures on  $\mathbb{R}^{d-1}$ .

(vii)  $G^D(x', x_3)$  is a function rapidly decreasing at infinity as well as all its derivatives.

**Theorem 6.3** -

Let  $K$  be a given compactum of  $\mathbb{R}^{d-1}$ . For each  $\mathcal{E}^{(1)} \in \mathcal{B}_K^{m, \alpha}(\mathbb{R}^{d-1})$  the DP( $\mathcal{E}^{(1)}$ ) problem admits in  $\mathcal{B}_0^{m, \alpha}(\bar{\Omega}_0)$  the following unique solution:

$$\phi^D(x) = \mathcal{E}^{(1)}(x') \int_{\mathbb{R}^{d-1}} G^D(x', x_3) dx'$$

The solution  $\phi^D$  has the following properties

$$(i) \quad \phi^D(x', x_3) \in \mathcal{B}_0^{m, \alpha}(\mathbb{R}^{d-1}), \quad 0 \leq x_3 < h$$

$$(ii) \quad \|\phi^D(x)\| \leq \|\mathcal{E}^{(1)}\|_{\mathcal{B}_K^{m, \alpha}(\mathbb{R}^{d-1})} = 1$$

The proof of lemma 6.1 and theorem 6.2 are analogous yet much simpler than the proof of theorems 4.1, 4.2 and 4.3, see [6] for details.

## 7. Proof of Theorems 1 and 2

Chapter 8 gave the conditions of existence and uniqueness of the solution of the problem NKd  $(\Phi, 0, \Sigma^{(1)})$ . One is tempted to use the conventional perturbation theory of linear operators, to deduce the conditions of existence and uniqueness of the solution of problem NKd  $(\Phi, \epsilon, \Sigma^{(1)})$ , e.g. theorem 5.17 [16 p.235]. In this theory it is assumed an operator  $A(\epsilon)$  is given:  $X \rightarrow Y$  depending on a real or complex parameter  $\epsilon$ .  $X$  and  $Y$  are Banach spaces independent of  $\epsilon$ . For the NKd  $(\Phi, \epsilon, \Sigma^{(1)})$  it would be possible to take, for example  $Y = \mathcal{B}^k(\bar{\Omega}_\epsilon)$  with  $k \geq 2$ , but this choice is not suitable as on one hand  $Y$  depends on  $\epsilon$  and on the other the choice of  $\mathcal{B}^k$  instead of  $\mathcal{B}^{k,\alpha}$ ,  $\alpha \in ]0, 1[$  would lead to non-optimal results.

The conventional method to obtain functional spaces independent of  $\epsilon$  is to carry out a mapping which induces a one-to-one correspondence between the "unperturbed domain"  $\Omega$  and the "perturbed domain"  $\Omega_\epsilon$ , see [8, section 6.26 pp.420-423], [16, section 7.65 pp.423-426], etc... This mapping is not unique and it has been chosen to simplify as much as possible the demonstration of the final result.

Let  $p: \Omega_0 \rightarrow \mathbb{R}^d$  be the mapping

$$(7.1) \quad X = p(x) = x - \epsilon \frac{x_3}{h} \phi^D(x) e_3, \quad x \in \Omega_0$$

where  $e_3$  is the unit vector of  $Ox_3$  axis.

### Proposition 7.1 -

It is assumed that  $\Sigma^{(1)} \in \mathcal{B}^{m,\alpha}(\mathbb{R}^{d-1})$ ,  $m \geq 2$ . There exists  $\epsilon_0 > 0$  such that for  $0 \leq \epsilon < \epsilon_0$  the mapping  $p$  has the following properties:

- (i)  $p$  is a diffeomorphism from  $\Omega_0$  onto  $\Omega$ , of the class  $[C^{m,\alpha}(\bar{\Omega}_0)]^d$ .
- (ii)  $x_3 = 0 \cap X_3 = 0$
- (iii)  $x_3 = h \cap X_3 = h - \epsilon \Sigma^{(1)}(X')$

### Proof of proposition 7.1 -

From (7.1) (ii) and (iii) are obvious.

To prove (i) it must be shown that:

- (a)  $p(\Omega_0) \subset \Omega_\epsilon$
- (b)  $p$  is of the class  $[C^{m,\alpha}(\bar{\Omega}_0)]^d$
- (c)  $p$  is a bijection from  $\Omega_0$  onto  $\Omega_\epsilon$  and the inverse mapping  $q$  is of the class  $[C^{m,\alpha}(\bar{\Omega}_\epsilon)]^d$ .

The (a) is obvious. The (b) results from the expression (7.1) of  $p$  which takes the form of a sum of 2 mappings of the class  $[C^{m,\alpha}(\bar{\Omega}_0)]^d$ . The (c) is a consequence of the two following lemmas:

### Lemma 7.1 -

There exists  $\epsilon' > 0$  such that for  $0 \leq \epsilon < \epsilon'$  the differential mapping  $p'$  is an invertible endomorphism of  $\mathbb{R}^d$ .

### Lemma 7.2 -

There exists  $\epsilon_0'' > 0$  such that for  $0 \leq \epsilon < \epsilon_0''$  the mapping  $p$  is a homeomorphism from  $\Omega_0$  onto  $\Omega_\epsilon$  of the class  $C^m$ .

It remains to be seen therefore whether  $q$  is of the class  $[C^{m,\alpha}(\bar{\Omega}_\epsilon)]^d$  and to use  $\epsilon_1 = \min(\epsilon_0', \epsilon_0'')$  to thoroughly prove (i). Now  $q$  having derivatives of the  $m$ -th order  $\partial^m q$  which are continuous and bounded according to lemma 7.2, these derivatives are  $\alpha$ -Holderian.

### Proof of lemma 7.1 -

We have:

$$(7.2) \quad p'(x) = \begin{bmatrix} 1 & 0 & 0 \\ 0 & 1 & 0 \\ -\epsilon \frac{x_3}{h} \frac{\partial \phi^D}{\partial x_1} & -\epsilon \frac{x_3}{h} \frac{\partial \phi^D}{\partial x_2} & 1 - \epsilon \left( \phi^D + x_3 \frac{\partial \phi^D}{\partial x_3} \right) \end{bmatrix}$$

Then it follows

$$(7.3) \quad \det p'(x) = 1 - \epsilon \frac{x_3}{h} \left[ \phi^D + x_3 \frac{\partial \phi^D}{\partial x_3} \right]$$

$$|\det p'(x)| \geq 1 - \epsilon \frac{h}{h} \left[ \|\phi^D; \mathcal{B}^{m,\alpha}(\bar{\Omega}_0)\| + h \|\phi^D; \mathcal{B}^{m,\alpha}(\bar{\Omega}_0)\| \right]$$

$$(7.4) \quad |\det p'(x)| \geq 1 - \epsilon \frac{1+h}{h} \|\phi^D; \mathcal{B}^{m,\alpha}(\bar{\Omega}_0)\|$$

Then the lemma is proved with:

$$\frac{1}{\epsilon_0} = \frac{1+h}{h} \|\phi^D; \mathcal{B}^{m,\alpha}(\bar{\Omega}_0)\|$$

Q.E.D. lemma 7.1

### Proof of lemma 7.2 -

The following is shown

$$(7.5) \quad \Omega_\epsilon \subset p(\Omega_0)$$

which will prove with (a) that  $p$  is a bijection from  $\Omega_0$  onto  $\Omega_\epsilon$ .

The system of equations with unknowns  $x_1, x_2, x_3$  defined by 7.1 is reduced in fact to:

$$(7.6) \quad x_3 = X_3 + \epsilon \frac{x_3}{h} \phi^D(x', x_3)$$

which is an equation of the form:

$$(7.7) \quad x_3 = f(X_3, x_3)$$

where  $f$  has the following properties:

- (a) for each  $x_3$  fixed in  $[0, h]$ , the mapping  $X_3 \mapsto f(X_3, x_3)$  is affine thus continuous, from  $\bar{\Omega}_\epsilon$  into  $\bar{\Omega}_\epsilon$ .
- (b) for each  $X_3$  fixed the mapping  $x_3 \mapsto f(X_3, x_3)$  is a contraction of  $\bar{\Omega}_0$  with a ratio independent of  $X_3$ .

This results from (7.6) and theorem 6.2(ii) because:

$$\mathcal{B}^{m,\alpha}(\bar{\Omega}_\epsilon) \subset \mathcal{B}^{0,1}(\bar{\Omega}_0) \text{ implies:}$$

$$|f(X_3, x_3) - f(X_3, y_3)| = \epsilon \left| x_3 \phi^D(x', x_3) - y_3 \phi^D(x', y_3) \right|$$

$$\leq \epsilon \left| (x_3 - y_3) \phi^D(x', x_3) + y_3 (\phi^D(x', x_3) - \phi^D(x', y_3)) \right|$$

$$\leq \epsilon \frac{1+h}{h} \|\phi^D; \mathcal{B}^{0,1}(\bar{\Omega}_0)\| |x_3 - y_3|$$

If therefore  $\varepsilon \in [0, \varepsilon_0']$  is chosen, with  $\frac{1}{\varepsilon_0'} = \frac{1+h}{h} \|\phi\|; \mathcal{B}^{\alpha,1}(\bar{U}_0)$ , (B) is the result.

The properties (a) and (B) and fixed point theorem (10, theor. 10.1.2 p. 271) show that equation 7.6 admits a unique solution of the class  $C^m$  with respect to  $X_3$ , therefore the system  $X=p(x)$  admits a unique solution  $x=q(X)$  of the class  $C^m(\bar{U}_0)$  i.e.  $p$  is a bicontinuous bijection and thus a homeomorphism of the class  $C^m$ .

#### Some useful formulae

The following properties of coordinate change should be remembered.

If the following is posed

$$(7.8) \quad f(x) = \frac{x_3}{h} \phi^D(x) e_3$$

Then

$$(7.9) \quad X = p(x) = x - \varepsilon f(x)$$

and the inverse mapping shall be written in an analogous form:

$$(7.10) \quad x = q(X) = X + \varepsilon g(X)$$

The differential mappings satisfy:

$$(7.11) \quad \frac{dp}{dx} = I - \varepsilon \frac{df}{dx}$$

$$(7.12) \quad \frac{dq}{dX} = I + \varepsilon \frac{dg}{dX}$$

where  $I$  is the identity function in  $\mathbb{R}^d$ .

To calculate the differential mapping  $g \cdot \frac{dg}{dX}$  one begins with:

$$(7.13) \quad p \circ q = X$$

which by differentiation gives:

$$(7.14) \quad \frac{dp}{dx} \frac{dq}{dX} = I$$

$$\text{that is } \left[ I - \varepsilon \frac{df}{dx} \right] \left[ I + \varepsilon \frac{dg}{dX} \right] = I$$

Then it follows

$$(7.15) \quad \left[ I - \varepsilon \frac{df}{dx} \right] \frac{dg}{dX} = \frac{df}{dx}$$

Thus by using the matrix notation and by setting:

$$(7.16) \quad \frac{df}{dx} = \left[ \frac{\partial f_i}{\partial x_k} \right] = [f'_{jk}], \text{ dxd matrix}$$

we obtain the matrix equation

$$(7.17) \quad [p'_{jk}] [g'_{kl}] = [f'_{jl}]$$

of which the resolution by Cramer's rule gives:

$$(7.18) \quad g'_{kl} = 0 \text{ for } k \neq 3$$

$$(7.19) \quad g'_{3l} = \frac{f'_{3l}}{\det p'} = \frac{f'_{3l}}{1 - \varepsilon f'_{33}}$$

Then it follows:

$$(7.20) \quad \frac{dq}{dX} = [q'_{kl}] \text{ dxd matrix}$$

with

$$(7.21) \quad q'_{11} = q'_{22} = 1$$

$$(7.22) \quad q'_{33} = \frac{1}{1 - \varepsilon f'_{33}}$$

$$(7.23) \quad q'_{3l} = \frac{\varepsilon f'_{3l}}{1 - \varepsilon f'_{33}} \quad l = 1, 2$$

all the others  $q'_{kl}$  vanish.

In the same way, the following is introduced

$$(7.24) \quad q''_{klm} = \frac{\partial^2 q_k}{\partial X_l \partial X_m}$$

$$(7.25) \quad \frac{d^2 q}{dX^2} = [q''_{klm}] \text{, dxd}^2 \text{ matrix}$$

$$(7.26) \quad q''_{3lm} = \frac{\varepsilon f''_{3lm}(1 - \varepsilon f'_{33}) + \varepsilon^2 f'_{3l} f'_{33m}}{(1 - \varepsilon f'_{33})^3}, m=3$$

$l = 1, 2$ , alike formula for  $m=1, 2$ ;

$$(7.27) \quad q''_{33m} = \frac{\varepsilon f''_{33m}}{(1 - \varepsilon f'_{33})^3} \quad m = 3;$$

alike formula for  $m=1, 2$ ; all the others  $q''_{klm}$  vanish.

Finally the following tensor product is introduced:

$$(7.28) \quad \frac{dq}{dX} \otimes \frac{dq}{dX} = [q'_{kl} q'_{mn}] \text{ d}^2 \text{xd}^2 \text{ matrix.}$$

#### The $P_c(Ph, \varepsilon^{(1)})$ problem

The problem  $NKd(Ph, \varepsilon, \varepsilon^{(1)})$  will now be transformed by the diffeomorphism  $X = p(x)$ .

The following is posed:

$$(7.29) \quad \phi(x) = \phi(x, \varepsilon, \varepsilon^{(1)}) \triangleq \phi^{(1)}(X, \varepsilon, \varepsilon^{(1)}) \Big|_{X=p(x)}$$

$$(7.30) \quad \phi^{(1)}(X, \varepsilon, \varepsilon^{(1)}) = \phi(x, \varepsilon, \varepsilon^{(1)}) \Big|_{x=q(X)}$$

The following formulae result:

$$(7.31) \quad \frac{d\phi^{(1)}}{dX} = \frac{d\phi}{dx} \frac{dq}{dX}$$

$$(7.32) \quad \frac{d^2 \phi^{(1)}}{dX^2} = \frac{d^2 \phi}{dx^2} \left( \frac{dq}{dX} \otimes \frac{dq}{dX} \right) + \frac{d\phi}{dx} \frac{d^2 q}{dX^2}$$

with

$$(7.33) \quad \frac{d\phi}{dx} = \left[ \frac{\partial \phi}{\partial x_k} \right] \text{ 1xd matrix}$$

$$(7.34) \quad \frac{d^2 \phi^{(1)}}{dX^2} = \left[ \frac{\partial^2 \phi^{(1)}}{\partial X_k \partial X_l} \right] \text{ 1xd}^2 \text{ matrix}$$

the same for  $\frac{d\phi}{dx}$  and  $\frac{d^2 \phi}{dX^2}$

From these formulae it is possible to deduce easily the formulae that  $\phi(x)$  satisfies namely:

#### $P_c(Ph, \varepsilon^{(1)})$ problem

Find  $\phi(x)$  so that

$$(P1) \quad L^{(\varepsilon)} \phi = 0 \text{ in } \Omega_0$$

$$(P2) \quad B_1^{(\varepsilon)} \phi = 0$$

$$(P3) \quad B_2^{(\varepsilon)} \phi = c \frac{\partial \varepsilon^{(1)}}{\partial X_1} (x')$$

$$(P4) \text{ radiation condition when } |x_1| \rightarrow \infty$$

The following has been posed:

$$(7.35) \quad L^{(\varepsilon)} \phi = \left[ \frac{\partial \phi}{\partial x_j} \right] \frac{\partial \varepsilon}{\partial x_i} + \left[ \frac{\partial \phi}{\partial x_i} \right] \frac{\partial \varepsilon}{\partial x_j}$$

where indices  $i$  and  $j$  have values  $\{1,2,3\}$  or  $\{1,3\}$  according to whether  $d=3$  or  $2$ .

$$(7.35B) \begin{cases} a_{ij}^{(e)} = 1 \text{ for } i=j=1 \text{ and } 2 \\ a_{ij}^{(e)} = 0 \text{ for } (i,j) = (1,2) \text{ and } (2,1) \\ a_{i3}^{(e)} = e g_{3i}^{(e)} = e f_{3i}^{(e)} (1 - e f_{33}^{(e)})^{-1} \quad i=1,2 \\ a_{3i}^{(e)} = e g_{3i}^{(e)} = e f_{3i}^{(e)} (1 - e f_{33}^{(e)})^{-1} \quad j=1,2 \\ a_{33}^{(e)} = 1 + 2e g_{33}^{(e)} + e^2 (g_{31}^{(e)2} + g_{32}^{(e)2} + g_{33}^{(e)2}) \\ = \left[ 1 + e^2 (f_{31}^{(e)2} + f_{32}^{(e)2} + f_{33}^{(e)2}) \right] \left[ 1 - e f_{33}^{(e)} \right]^{-2} \end{cases}$$

$$(7.36) b_i(x) = 0 \quad i=1,2$$

$$(7.37) b_3(x) = e(g_{31}^{(e)} + g_{32}^{(e)} + g_{33}^{(e)})$$

$$(7.38) B_1^{(e)} \phi = B_1 \phi - \left[ \frac{e}{8} \frac{\partial^2 \phi}{\partial x_1^2} - \frac{\partial \phi}{\partial x_3} \right]_{x_3=0} \text{ independent of } e$$

$$(7.39) B_2^{(e)} \phi = \text{restriction to } x_3 = h \text{ of}$$

$$\left\{ \frac{\partial \phi}{\partial x_3} + e \left[ \sigma_1^{(e)}(x') \frac{\partial \phi}{\partial x_1} + \sigma_2^{(e)}(x') \frac{\partial \phi}{\partial x_2} + \frac{f_{33}^{(e)}}{1 - e f_{33}^{(e)}} \frac{\partial \phi}{\partial x_3} \right] + e^2 (\sigma_1^{(e)2} + \sigma_2^{(e)2}) (1 - e f_{33}^{(e)})^{-1} \frac{\partial \phi}{\partial x_3} \right\}$$

$$\text{with} \\ (7.40) \sigma(x') = \Sigma^{(1)}(x'), \sigma_1^{(e)}(x') = \frac{\partial \phi}{\partial x_1}, \text{ etc. ...}$$

The main properties of  $P_e = P_e(\Phi, \Sigma^{(1)})$  problem are as follows: (1)

Proposition 7.2 - Let us assume  $\Gamma \in \mathcal{B}_K^m, \alpha \in \mathbb{R}^{d-1}, m \geq 2$ . There exists  $\epsilon_0 > 0$  such that for  $0 \leq \epsilon < \epsilon_0^2$  the  $P_e(\Phi, \Sigma^{(1)})$  and  $NKd(\Phi, \epsilon, \Sigma^{(1)})$  problems are equivalent: in other words the  $NKd(\Phi, \epsilon, \Sigma^{(1)})$  problem admits a unique solution  $\phi^{(1)} \in \mathcal{B}_R^m, \alpha \in \mathbb{R}^{d-1}$  iff the  $P_e(\Phi, \Sigma^{(1)})$  problem admits a unique solution  $\phi \in \mathcal{B}_R^m, \alpha \in \mathbb{R}^{d-1}$  and we have

$$(7.41) \phi(x) = \phi^{(1)} \left[ \begin{matrix} p(x) \\ q(x) \end{matrix} \right]$$

$$(7.42) \phi^{(1)}(X) = \phi \left[ \begin{matrix} p(X) \\ q(X) \end{matrix} \right]$$

In particular  $P_e(\Phi, \Sigma^{(1)})|_{\epsilon=0} = VP(0,0,c \frac{\partial \Sigma}{\partial x_1}) \in NKd(\Phi,0,\Sigma^{(1)})$  which shows that the problem  $P_e$  has a unique solution when  $\epsilon=0$ .

#### Proof of theorems 1 and 2

The  $P_e(\Phi, \Sigma^{(1)})$  problem can be written as follows:

$$(7.43) \mathcal{K} = \mathcal{B}_R^m, \alpha \in \mathbb{R}^{d-1}$$

$$(7.44) \mathcal{U} = \mathcal{B}^{m-2, \alpha}(\mathbb{R}_0^d) \times \mathcal{B}^{m-2, \alpha}(\mathbb{R}_K^{d-1}) \times \mathcal{B}^{m-1, \alpha}(\mathbb{R}_K^{d-1})$$

$\mathcal{U}_1$  = subspace of  $\mathcal{U}$  defined in theorem 6.2

$$(7.45) \mathcal{U}_0 = \{u = (f, \phi_1, \phi_2), \mathcal{U}_1 : \phi_1 = 0\}$$

so that  $u = (f, \phi_1, \phi_2) \in \mathcal{U}_1$  implies that

$$(7.46) \int_{\mathbb{R}^{d-1}} \phi_2(x') dx = \int_{\mathbb{R}_K^{d-1}} f(x) dx = 0$$

The space  $\mathcal{U}_0$  is a Banach space.

Let us consider the following operator:

$$(7.47) T(e) : \begin{cases} \mathcal{K} \cap \mathcal{U} \\ \phi \in \mathcal{U} \text{ with } \mathcal{B}_1^{(e)} \phi = 0 \text{ and } 0 \leq \epsilon < \epsilon_0^2 \end{cases}$$

Hence the domain of definition  $DT(e)$  of the operator  $T(e)$  is strictly lying in  $\mathcal{K}$ . Then

$$(7.48) \mathcal{K}_0 = \{\phi \in \mathcal{K} : T(o)\phi \in \mathcal{U}_0\}$$

is defined and we choose  $DT(o) = \mathcal{K}_0$ .

$$\text{Lemma 7.3} - \phi \in \mathcal{K}_0 \Rightarrow T(e)\phi \in \mathcal{U}_0$$

This lemma can be obtained from Green's second formula and from properties of each term of (7.35A) and (7.39) which follow from theorem 6.3

Lemma 7.3 allows us to choose  $DT(e) = \mathcal{K}_0$ .

Now we introduce the following notions

see (16) for more details:

$$\text{range of } T(e) = RT(e) = \{u \in \mathcal{U}_0 : \exists \phi \in DT(e), u = T(e)\phi\}$$

$$\text{nullity of } T(e) = \text{nul } T(e) = \dim \{\phi \in DT(e) : T(e)\phi = 0\}$$

where  $\dim \{ \cdot \}$  is the dimension of the space  $\{ \cdot \}$

$$\text{deficiency of } T(e) = \text{def } T(e) = \dim \{ \mathcal{U}_0 / RT(e) \}$$

$\mathcal{U}_0 / RT(e)$  is the set of the equivalence

classes with respect to  $RT(e)$  that is to say:

$$\tilde{u}_1, \tilde{u}_2 \in \mathcal{U}_0 / RT(e) \text{ and } \tilde{u}_1 = \tilde{u}_2 \Rightarrow u_1 - u_2 \in RT(e)$$

$$\text{index of } T(e) = \text{ind } T(e) = \text{nul } T(e) - \text{def } T(e)$$

The minimum modulus of  $T(e) = \gamma T(e)$  is defined as:

$$\gamma T(e) = \inf \{ \|T(e)\phi\| : \|\phi\| = 1, \phi \in DT(e) \}$$

This definition has meaning only if  $\text{nul } T(e) > 0$

Following Kato (16p230) a closed operator  $S$  is said to be Fredholm if  $RS$  is closed and both  $\text{nul } S$  and  $\text{def } S$  are finite.  $S$  is said to be semi-Fredholm if  $RS$  is closed and at least one of  $\text{nul } S$  and  $\text{def } S$  is finite.

Lemma 7.4 - For all  $\epsilon \in [0, \epsilon_0^2]$ , the operator  $T(e)$  is linear, bounded, closed and such that

$$\|T(e) - T(o) : \mathcal{L}(\mathcal{K}_0, \mathcal{U}_0)\| \rightarrow 0 \text{ as } \epsilon \rightarrow 0$$

Lemma 7.5 - Moreover, the operator  $T(o)$  has the following properties:

A-In the case of  $(d, \Phi) \neq (2, 1)$

(i)  $T(o)$  has an inverse  $T^{-1}(o)$  belonging to  $\mathcal{L}(\mathcal{U}_0, \mathcal{K}_0)$

(ii)  $T(o)$  is a Fredholm operator with index zero

$\text{nul } T(o) = \text{def } T(o) = \text{ind } T(o) = 0$

(iii) the minimum modulus  $\gamma = \gamma T(o)$  of  $T(o)$  is such that  $0 < \gamma < +\infty$

B-In the case of  $(d, \Phi) = (2, 1)$

(i)  $T(o)$  is not invertible except for zero element of  $\mathcal{U}_0$

(ii)  $T(o)$  is a semi-Fredholm operator.

$$\begin{aligned} \text{nul } T(o) &= 0 \\ \text{def } T(o) &= \dim \mathcal{U}_0 \end{aligned}$$

(iii) the minimum modulus of  $T(o)$  is  $\gamma = \gamma T(o) = +\infty$

Lemmas 7.4 and 7.5 are easily proven. For instance, in lemma 7.5 (Ai) and (Aii) are direct consequence of theorem 6.2, (Bi) and (Bii) are direct consequence of theorem 6.1.

Lemmas 7.4 and 7.5 enable us to use the general stability theorem for linear operator (16 p 235, theor. 5.17)

#### Case (d,Fh) = (2,1) : proof of theorem 2

By virtue of the general stability theorem for linear operator we have :

$$\begin{aligned} \text{nul } T(\epsilon) &\leq \text{nul } T(0) \\ \text{def } T(\epsilon) &\leq \text{def } T(0) \end{aligned}$$

provided that  $\epsilon$  is sufficiently small (let us say  $\epsilon < \epsilon_0^3$ ) for  $T(\epsilon)$  to be closed to  $T(0)$ , see lemma 7.6 and lemma 7.5 (Aiii)

By using lemma 7.5(Aii), it is concluded that :

$$\text{nul } T(\epsilon) = \text{def } T(\epsilon) = 0$$

Thus  $T(\epsilon)$  is a topological isomorphism from  $\mathcal{U}_0$  into  $\mathcal{V}_0$ , see theorem 1.16 in (16 p 196).

On the other hand  $T(\epsilon)$  is an analytic (or real holomorphic) operator-valued function and the family  $\{T(\epsilon)\}$  is of type A, see definition chapter VII § 2 p 375 in [30] : it is then concluded that  $T^{-1}(\epsilon)u$  for  $u \in \mathcal{U}_0$  and  $\epsilon < \epsilon_0^4$  has a Taylor expansion :

$$T^{-1}(\epsilon)u = T^{-1}(0)u + \epsilon T_1 u + \epsilon^2 T_2 u + \dots$$

which converges for  $\epsilon < \epsilon_0^4$  independent of  $u$ .

What is true for  $u \in \mathcal{U}_0$  is therefore true for

$$u = (0, 0, c \frac{\partial \Sigma(1)}{\partial X_1}) \text{ with } \Sigma(1) \in \mathcal{U}$$

If  $\epsilon_0 = \min(\epsilon_0^2, \epsilon_0^3, \epsilon_0^4)$  theorem 2 is proven.

#### Case (d,Fh) = (2,1) : proof of theorem 1

By virtue of theorem (5.22) in (16 p 236) we have :

$$\begin{aligned} \text{nul } T(\epsilon) &\geq \text{nul } T(0) \\ \text{def } T(\epsilon) &\leq \text{def } T(0) \\ \text{ind } T(\epsilon) &= \text{ind } T(0) \end{aligned}$$

provided that  $\epsilon$  is sufficiently small, let us say  $\epsilon < \epsilon_0^5$ .

By using lemma 7.5 (Bii), it is concluded that :

$$\begin{aligned} \text{nul } T(\epsilon) &= 0 \\ \text{def } T(\epsilon) &= \dim \mathcal{U}_0 \end{aligned}$$

If  $\epsilon_0 = \min(\epsilon_0^2, \epsilon_0^3)$ , then for each  $\epsilon \in [0, \epsilon_0]$  the operator  $T(\epsilon)$  is not invertible except for zero element of  $\mathcal{U}$ . Theorem 1 is thus proven.

Q.E.D. theor. 1 and 2

#### 8. The Method of Singularities

It is thanks to R.Brard (4) to (7) that the rigorous bases of this method in the general case of a body, immersed or piercing the free surface have been established. In the particular case of a body totally immersed such as that of the bump, Brard's results are conventional and have been known for a long time. However, it is useful to rapidly go over R. Brard's reasoning steps.

Before doing so some new notations will be introduced and a new boundary value problem will be studied.

##### Notations -

The fluid domain which until now has been noted as  $\Omega = \Omega_c$  shall henceforth be noted as  $\Omega_e$  and  $\Omega_i$  shall represent the domain situated beneath the bump i.e.

$$\Omega_i = \{X = (X', X_3) : X' \in K, h - \epsilon(X') < X_3 < h\}$$

where it should be remembered that  $K$  is the support of the bump,  $K$  is the interior of compactum  $K$  and  $\text{bdry } K$  is the boundary of  $K$  on the bottom  $X_3 = h : K = \bar{K} \cup \text{bdry } K$ .

The velocity potential, solution of the NKd(Fh,  $\Sigma$ ) problem, which till now has been noted as  $\Phi(X)$ , shall be noted henceforth as  $\Phi_e(X)$  where index  $e$  indicates that the potential is defined in  $\Omega_e$  and where the sign  $+$  indicates that the velocity  $c$  of the flow is positive (running flow in the negative  $X$  - direction).

In the same manner  $K_e^+(X, Y)$  shall be the potential of the Kelvin unit source and  $\Sigma_e^+, D_e^+, V_e^+$  the operators defined from (3.6) to (3.8)

NKd(-Fh,  $\Sigma$ ) can correspond to the NKd(Fh,  $\Sigma$ ) problem. NKd(-Fh,  $\Sigma$ ) is obtained by changing the sign  $c$  (reverse flow problem).  $\Phi_e^-(X)$ ,  $K_e^-(X, Y)$ ,  $\Sigma_e^-$ , etc... shall signify the magnitudes corresponding to this new problem.

##### IP(Fh, $\Sigma$ , $\alpha, \beta, \gamma$ ) problem -

The IP(Fh,  $\Sigma$ ,  $\alpha, \beta, \gamma$ ) problem (Interior Problem) is associated with the NKd(Fh,  $\Sigma$ ) problem in accordance with the following :

Let  $\alpha, \beta, \gamma$  be given functions defined on  $\Gamma$ . The solution  $\Phi_e^+$  of the NKd(Fh,  $\Sigma$ ) problem is assumed known and a function  $\Phi_i^+$  is searched for, such that :

$$(PI1) \quad \nabla^2 \Phi_i^+ = 0 \text{ in } \Omega_i$$

$$(PI2) \quad \frac{\partial \Phi_i^+}{\partial N} = 0, \quad X_3 = h, \quad X' \in K$$

$$(PI3) \quad \alpha \Phi_i^+ + \beta \frac{\partial \Phi_i^+}{\partial N} = \gamma + \alpha \Phi_e^+ + \beta \frac{\partial \Phi_e^+}{\partial N}, \quad X \in \Gamma$$

A particularity of the IP problem is that it is defined in a not very regular domain  $\Omega_i$  in the sense that the boundary of this domain is of the class  $C^{1,1}$  piecewise but along the  $\text{bdry } K$  it presents a simple cusp which will complicate the regularity problems of the solution of the IP problem.

Hence the two particular cases of the problem IP are studied :

(i)  $\beta = \gamma = 0$ ,  $\alpha = 1$  thus  $\phi_i^+ = \phi_e^+$  on  $\Gamma$ .

$\phi_i^+$  is therefore a solution to a mixed problem with a Neumann condition on  $X_3=h$  and a Dirichlet condition on  $\Gamma$ . In fact, by the principle of images this problem is equivalent to a Dirichlet problem in the domain interior to  $\Gamma \cup \Gamma'$  ( $\Gamma'$  is the image of  $\Gamma$  with respect to  $X_3=h$ ). In these conditions it is known that the problem has a unique solution  $\phi_i^+$  in  $H^1(\Omega_i)$  and that this solution is also in  $B^0(\Omega_i)$ , see for example [26p. 329, theorems 3.2 and 3.3]. Furthermore for any compactum  $\omega \subset \Omega_i$  not having any common point with bdy  $K$ , the solution is of the class  $C^{2,\alpha}(\omega)$  according to the Schauder's a priori estimates. The behaviour of the solution when  $X$  tends towards a point in bdy  $K$  is difficult to study because of the presence of the simple cusp. Is it possible to say particularly, that  $\frac{\partial \phi_i^+}{\partial N}$

is of the class  $C^{1,\alpha}$  on  $\Gamma = \Gamma \cup \text{bdy } K$ ? This question shall not be answered but it is noted that  $\frac{\partial \phi_i^+}{\partial N} \in L^2(\Gamma)$  [26 p.247, lemma 1.4].

(ii)  $\alpha = \gamma = 0$ ,  $\beta = 1$  thus  $\frac{\partial \phi_i^+}{\partial N} = \frac{\partial \phi_e^+}{\partial N}$  on  $\Gamma$

$\phi_i^+$  is therefore a solution of a Neumann problem. This solution exists and is unique in the space  $H^1(\Omega_i)$  one arbitrary constant more or less. More again the regularity of  $\phi_i^+$  on  $\Gamma$  is difficult to study but it shall be noted that  $\phi_i^+ \in H^1(\Gamma)$  [26 p.256, theorem 2.2]. In fact all is for the best as the particular solution  $\phi_i^+ = c X_1 + \text{constant}$  is known and which is the general solution of the problem.

Properties of operators  $S^+$ ,  $D^+$ ,  $V^+$

In the following the results and terminology of [34] will be used. We shall use, the fact that  $\Gamma$  is a manifold of the class  $C^{2,\alpha}$  without boundary but which connect up in a very regular way with the bottom  $X_3=h$  so that Privalov's theorem is true, see as an example [25,p.46] for  $d=2$  and [24 p.50] for  $d=3$ .

The operator  $S^+$  is a Fredholm's operator from  $L^2(\Gamma)$  into  $L^2(\Gamma)$  and from  $B^{1,\alpha}(\Gamma)$  into  $B^{1,\alpha}(\Gamma)$  according to Privalov's theorem.

The operators  $D^+$  and  $V^+$  are weakly singular operators from  $L^2(\Gamma)$  into  $L^2(\Gamma)$ , from  $B^{1,\alpha}(\Gamma)$  into  $B^{1,\alpha}(\Gamma)$ .

The adjoint (operator) of  $D^+$  in  $L^2(\Gamma)$  is  $V^+$  and the adjoint of  $S^+$  in  $L^2(\Gamma)$  is  $S^+$ . This is a consequence of the argument exposed in [5p.83 formula (7)].

(\*)  $H^1(\Omega_i)$  denotes the usual Sobolev Space :  
 $u \in H^1(\Omega_i)$  iff  $u, Du \in L^2(\Omega_i)$  where  $L^2(\Omega_i)$  is the set of measurable  $f(x)$  functions defined on the domain  $\Omega_i$ , for which the Lebesgue integral  $\int_{\Omega_i} |f(x)|^p dx < \infty$

#### Proof of theorem 3 (iii)

In admitting the hypothesis of theorem 2,  $\phi_e^+$  therefore exists and is unique. If the third Green's formula is applied to the pair  $\phi_e^+(X), K^+(X,Y)$ . The following is obtained (see (8) and (9) for details) :

$$(8.1) \quad \phi_e^+(X) = D_e^+ \left[ \phi_e^+ \right] - S_e^+ \left[ \frac{\partial \phi_e^+}{\partial N} \right]$$

where  $[f]$  denotes the restriction to  $\Gamma$  of a function  $f$  defined in  $\Omega_e$  or  $\Omega_i$ .

Likewise, the application of the third Green's formula to the pair  $\phi_e^+(X), K_i^+(X,Y)$  gives :

$$(8.2) \quad 0 = D_i^+ \left[ \phi_e^+ \right] - S_i^+ \left[ \frac{\partial \phi_e^+}{\partial N} \right]$$

In making  $X \in \Omega_e$  tend towards a point on  $\Gamma$  (8.1) gives :

$$\left[ \phi_e^+ \right] = \frac{1}{2} \left[ \phi_e^+ \right] + D^+ \left[ \phi_e^+ \right] - S^+ \left[ \frac{\partial \phi_e^+}{\partial N} \right]$$

hence by setting :  $\mu^+ = \left[ \phi_e^+ \right]$  and  $v = \left[ \frac{\partial \phi_e^+}{\partial N} \right] = c N_1$

$$(8.3) \quad \left( D^+ - \frac{1}{2} \right) \mu^+ = S^+ v$$

In its construction this equation admits at least one solution  $\mu^+$ . This solution is unique in  $L^2(\Gamma)$  according to the following lemma :

Lemma 8.1 -

$$\text{nul} \left( D^+ - \frac{1}{2} \right) = 0 \text{ in } L^2(\Gamma)$$

Proof of lemma 8.1 -

In fact any solution  $\mu_0$  of  $(D - \frac{1}{2})\mu_0 = 0$  is such that

$$(8.4) \quad \phi_e \in D_e \mu_0 \text{ satisfies}$$

$$(8.5) \quad \phi_e = D_e \left[ \phi_e \right] - S_e \left[ \frac{\partial \phi_e}{\partial N} \right] \text{ (3rd Green's formula)}$$

$$(8.6) \quad \left[ \phi_e \right] = \frac{1}{2} \mu_0 + D \mu_0 = \mu_0 \text{ (by passing to the limit } X \rightarrow \Gamma)$$

Therefore

$$(8.7) \quad S_e \left[ \frac{\partial \phi_e}{\partial N} \right] = 0$$

On the other hand,

$\phi_i \in D_i \left[ \phi_e \right]$  satisfies in the same way

$$\phi_i = -\frac{1}{2} \left[ \phi_e \right] + D \left[ \phi_e \right] = 0 \text{ by definition of } \left[ \phi_e \right] = \mu_0$$

therefore  $\phi_i$  is harmonic, vanishes on  $\Gamma$  and its derivative vanishes on  $X_3=h$ ,  $X' \in K$  thus

$$\phi_i = D_i \left[ \phi_e \right] \equiv 0$$

$\phi_i$  also satisfies an analogous relation to (8.2)

$$0 = D_i \left[ \phi_e \right] - S_i \left[ \frac{\partial \phi_e}{\partial N} \right]$$

Then it follows

$$(8.8) \quad S_i \left[ \frac{\partial \phi_e}{\partial N} \right] = 0$$

(8.7) and (8.6) imply that  $\frac{\partial \phi}{\partial n} = 0$ . Also  $\phi_e$  is a solution of the NED (Ph.1) problem corresponding to  $\frac{\partial \phi}{\partial n} = 0$ .

Following the property of uniqueness of NED (Ph.1) one obtains:

$$\phi_e = 0 \text{ therefore } \left[ \phi_e \right]_n = 0$$

Q.E.D. lemma 8.1

Thus the integral equation (8.3) admits a unique solution in  $L^2(\Gamma)$ . In fact this solution is in  $B^{1,0}(\Gamma)$  since  $\phi_e = \left[ \phi_e \right]_n$  and  $\phi_e^* \in B^{2,0}(\bar{\Omega}_e)$  and  $\phi_e^* \in B^{1,0}(\Gamma)$ .

Q.E.D. theorem 3 (iii)

Proof of theorem 3 (i)

The third Green's formula is applied to the pair  $\phi_1^*(X), K_1^*(X,Y)$  and to the pair  $\phi_1^*(X), \phi_1^*(X,Y)$  where  $\phi_1^*$  is the unique solution of the IP (Ph.1,0,0) problem.

$$(8.9) \quad \phi_1^*(X) = \int_{\Gamma} \left[ \frac{\partial \phi_1^*}{\partial n} \right] - D_1^* \left[ \phi_1^* \right]$$

$$(8.10) \quad 0 = \int_{\Gamma} \left[ \frac{\partial \phi_1^*}{\partial n} \right] - D_1^* \left[ \phi_1^* \right]$$

In adding member to member (8.9) and (8.10) then (8.2) and (8.9) it follows:

$$(8.11) \quad \phi_1^*(X) = \int_{\Gamma} \phi^*$$

$$(8.12) \quad \phi_1^*(X) = \int_{\Gamma} \phi^*$$

where one has set

$$(8.13) \quad \phi^* = \left[ \frac{\partial \phi}{\partial n} \right] - \left[ \frac{\partial \phi}{\partial n} \right]$$

and according to what has been seen in the discussion of IP problem,  $\frac{\partial \phi}{\partial n}$  exists in  $L^2(\Gamma)$ , therefore  $\phi^*$  exists in  $L^2(\Gamma)$ .

In making  $X \rightarrow \Gamma_e$  and towards a point on the boundary: the normal derivative  $\frac{\partial \phi}{\partial n}$  tends towards  $\left[ \frac{\partial \phi}{\partial n} \right] = -\frac{1}{2} \phi^* + V^* \phi^*$

$$(8.14) \quad \left( V^* - \frac{1}{2} \right) \phi^* = \left[ \frac{\partial \phi}{\partial n} \right] = v$$

This integral equation admits a unique solution in  $L^2(\Gamma)$  according to the following lemma:

Lemma 8.2 - sol  $(V^* - \frac{1}{2}) \phi^* = 0$  in  $L^2(\Gamma)$

Proof of lemma 8.2 -

In fact the solution  $\phi_0$  to  $(V - \frac{1}{2}) \phi = 0$  is such that  $\phi_0 \in \mathcal{H}_0$  satisfies  $\left[ \frac{\partial \phi_0}{\partial n} \right] = 0$  hence, according to the property of uniqueness stated in theorem 2,  $\phi_0 = 0$  in particular  $\left[ \phi_0 \right]_n = 0$  therefore  $\phi_0 = 0$  (uniqueness for IP), from (8.14) it follows then:  $\phi_0 = 0$

Q.E.D. lemma 8.2

It should be noticed that it would have been possible to prove lemma (8.2) by using lemma 8.1 the Riesz-Schauder theory and the fact that  $V^*$  is the adjoint of  $V^*$ . Nevertheless we would have also to prove that  $V^*$  or one among its iterates is a compact operator.

Theorem 3 (iii) is thus proven. It gives a weaker result than theorem 3 (i) as far as the regularity of the unknown density is concerned. This is due to the fact that a sufficient property of regularity has not been proven for the normal derivative  $\frac{\partial \phi}{\partial n}$ . solution of  $PI(Ph,1,0,0)$ .

Q.E.D. theorem 3 (ii)

Proof of theorem 3 (ii) -

This proof is similar to the preceding proofs. Therefore only the major points of the proof shall be given.

The third Green formula is applied to the pair  $\phi_1^*(X), K_1^*(X,Y)$  and the pair

$\phi_1^*(X), \phi_1^*(X,Y)$  where  $\phi_1^*$  is the unique solution of the IP (Ph.1,0,1,0) problem. Also equation identical to (8.9) and (8.10) are obtained. By combining as before these equations with the equation (8.1) and (8.2) the following is now obtained:

$$(8.15) \quad \phi_1^*(X) = D_1^* \phi^*$$

$$(8.16) \quad \phi_1^*(X) = D_1^* \phi^*$$

where one has set:

$$(8.17) \quad \phi^* = \left[ \frac{\partial \phi}{\partial n} \right] - \left[ \frac{\partial \phi}{\partial n} \right]$$

and according to what has been seen in the discussion of the IP problem,  $\frac{\partial \phi}{\partial n}$  exists in  $L^2(\Gamma)$ , hence  $\phi^*$  exists in  $B^{1,0}(\Gamma)$ .

In making  $X \rightarrow \Gamma_e$  and towards a point on  $\Gamma$ , it follows:

$$\left[ \phi_1^* \right] = -\frac{1}{2} \phi^* + D^* \phi^*$$

or even:

$$(8.18) \quad (D^* - \frac{1}{2}) \phi^* = u$$

where  $u$  is the restriction of  $\phi_1^*$  to  $\Gamma$  i.e.  $\{ \phi_1^* \}$

According to lemma 8.1, the integral equation (8.18) admits a unique solution in  $B^{1,0}(\Gamma)$ .

It is to be noted that in the equation (8.18)  $u$  is defined to within a constant because the solution of

$$(8.19) \quad (D^* - \frac{1}{2}) \phi^* = \text{constant} = \mu_0$$

is none other than  $\phi^* = 2\mu_0$  and it is remembered that the corresponding potential is in  $\mathcal{H}_0$ .

$$(8.20) \quad D_1^* \mu^* = 2 \mu_0^* \mu_0 = 0$$

so that this term contributes nothing to the

potential  $\phi_e^*$ , solution of NKd (Ph, E).

This remark ends the proof of theorem 3 and it should be noted that this theorem could have been proved by using the Riesz-Schauder theory. Nevertheless in order to use this theorem, we should have to prove that  $V^2$  or one among its iterates is a compact operator and that  $\frac{1}{\lambda}$  is not an eigenvalue of  $D^2$ . We have dispensed with the proof of these properties by using theorem 2.

# REFERENCES

- (1) AGMON S., DOUGLIS A., NIRENBERG L. - *Estimates near the Boundary for Solutions of Elliptic Partial Differential Equations Satisfying General Boundary Conditions*. - Part I Communications on Pure and Applied Mathematics vol. XII (1959).
- (2) BESSHO M. - *On the Wave-Making Resistance of a Vertical Plate Partly Immersed in Water (Two-dimensional Problem)* - Transactions of the West-Japan Society of Naval Architects n°51, March 1976
- (3) BESSHO M. - *Line Integral, Uniqueness and diffraction of Waves in the Linearized Theory* - International Seminar on Wave Resistance, Japan, 1976
- (4) BRARD R. - *The Neumann-Kelvin Problem for Surface Ships* - Report n° 11 CST, January 1971, Bassin d'Essais des Carènes, Paris
- (5) BRARD R. - *The Representation of a Given Ship Form by Singularity Distributions when the Boundary Condition on the Free Surface is Linearized* - Journal of Ship Research, 16, n°1, March 1972
- (6) BRARD R. - *Le Problème de Neumann-Kelvin* Comptes-rendus de l'Académie des Sciences Paris, t.278 (14 jan. 1974)
- (7) BRARD R. - *Compléments sur le Problème de Neumann-Kelvin* - Comptes-rendus de l'Académie des Sciences, Paris, t.278, (28 janv. 1974)
- (8) COURANT R., HILBERT D. - *Methods of Mathematical Physics* - Vol.1, Interscience Publishers, 1953.
- (9) DERN J.C. - *Existence, Unicité et Régularité de la Solution du Problème de Neumann-Kelvin Associé à l'Écoulement d'un Fluide au-dessus d'un Fond Présentant une Bosse Bi-dimensionnelle ou Tri-dimensionnelle* - Rapport Bassin d'Essais des Carènes (à paraître).
- (10) DIEUDONNE J. - *Foundations of Modern Analysis* - Pure and Applied Mathematics, vol.10 Academic Press, New York, 1960
- (11) EKMAN V.W. - *On Stationary Waves in Running Water* - Arkiv för Matematik, Astronomi Och Fysik, band 3, n°2, 1907
- (12) GUEVEL P., VAUSSY P., KOBUS J.M. - *The Distribution of Singularities Kinematically Equivalent to a Moving Hull in the Presence of a Free Surface* - International Shipbuilding Progress, Vol.21, n°243 Nov. 1974
- (13) GUEVEL P., KOBUS J.M. - *Horizontal Cylindrical Floating Bodies Forced into Simple Harmonic Motion of Very Small Amplitude (in French)* - Association Technique Maritime et Aéronautique (ATMA), Session 1975.
- (14) HARBAND J. - *Three Dimensional Flow Over a Submerged Object* - Journal of Engineering Mathematics, vol.10, n°1, Jan. 1976
- (15) HOITSMA D.H. Jr - *Existence and Uniqueness of Axisymmetric Free Boundary Flows* - Communications on Pure and Applied Mathematics, vol.28, 1975, pp. 375-402.
- (16) KATO T. - *Perturbation Theory for Linear Operators* - 2<sup>nd</sup> edition, Springer Verlag 1976
- (17) KOCHIN N.E. - *On the Wave-Making Resistance and Lift of Bodies Submerged in Water*. Transactions of the Conference on Wave Resistance Theory, Collected Articles, Vol.11 USSR Academy of Sciences, 1949. Translation available as Publication n° 1-8, Society of Naval Architects and Marine Engineers.
- (18) KOTIK J., MORGAN R. - *The Uniqueness Problem for Wave Resistance Calculated from Singularity Distributions Which are Exact at Zero Froude Number* - Journal of Ship Research, vol.13, n°1, March 1969
- (19) LADYZHENSKAYA O.A., URAL'TSEVA, N.K. - *Linear and Quasi-linear Elliptic Equations* - Academic Press, 1963.
- (20) LAMB H. - *Hydrodynamics* - Dover (1932)
- (21) LAVOINE J. - *Calcul Symbolique, Distributions et pseudo-Fonctions* - Editions du Centre National de la Recherche Scientifique (CNRS), 1961.
- (22) LIONS J.L., MAGENES F. - *Problèmes aux Limites Non Homogènes et Applications*, Vol.1 - Dunod, Paris, 1968
- (23) MICHELL J.H. - *The wave-Resistance of a Ship* - Philosophical Magazine, 5, Vol.45, 1898
- (24) MIKHLIN S.G. - *Multidimensional Singular Integrals and Integral Equations* - Pergamon Press 1965.



- (25) MUSKHELISHVILI - *Singular Integral Equations* - Noordhoff Holland, 1946
- (26) NECAS J. - *Les Méthodes Directes en Théorie des Equations Elliptiques* - Masson et Cie, Paris 1967
- (27) NEWMAN J.N - *Blockage with a Free Surface* Journal of Ship Research, Vol.20, n°4 Dec.1976.
- (28) OHMATSU S. - *On the Irregular Frequencies in the Theory of Oscillating Bodies in a Free Surface* - Papers of Ship Research Institute, Jan. 1975
- (29) PALM E.- *On the Formation of Surface Waves in a Fluid Flowing Over a Corrugated Bed and on the Development of Mountain Waves* - Astrophysica Norvegica Vol.5, n°3, 1953
- (30) SCHWARTZ L.- *Theorie des Distributions à Valeurs Vectorielles* - Annales de l'Institut Fourier, Tomes 7 et 8, 1959
- (31) SCHWARTZ L. - *Theorie des Distributions*, Hermann, Paris, 1973
- (32) STOKER J.J. - *Water Waves* - Interscience Publishers, 1957
- (33) YOSIDA K. - *Functional Analysis* - Springer Verlag 4<sup>th</sup> edition, 1974
- (34) ZABREYKO P.P. et al. - *Integral Equations, a Reference Text* - Noordhoff International Publishing, Leyden, 1975

# **A LOCALIZED FINITE-ELEMENT METHOD FOR STEADY, THREE-DIMENSIONAL FREE-SURFACE FLOW PROBLEMS**

Kwang June Bai  
David W. Taylor Naval Ship Research and Development Center  
Bethesda, Maryland 20084

## **ABSTRACT**

A finite-element method is presented for solving steady free-surface flow past three-dimensional disturbances. The free-surface boundary condition is linearized. The boundary-value problem governed by Laplace's equation is replaced by Galerkin's formulation with certain essential conditions. The method used is a localized finite-element method. The fluid domain where the numerical computations are performed is reduced to a small local domain which surrounds the disturbance. This reduction of the domain is achieved by making use of the known solution space (eigenfunction or Green's function) in the choice of the trial and test function bases. In the localized finite-element domain, a simple polynomial trial and test function basis is used. Proper junction conditions are also used to match (couple) the eigenfunction and polynomial function bases. The present method was used previously to solve two-dimensional free-surface problems by Bai (1975, 1978).

Some numerical results for a pressure distribution on a free surface are presented and compared with the analytic results of Newman & Poole (1962). Wave resistance results are also given for a ship moving along the centerline in a canal and compared with the results obtained by Kirsch (1966). Agreement between numerical and analytical predictions of resistance for both the pressure distribution and for the ship is very good. The results of preliminary calculations for a surface effect ship (SES), with rigid side-walls are also discussed.

## **1. INTRODUCTION**

Steady flow of an inviscid, incompressible fluid past a body in the presence of a free surface is described by a boundary-value problem governed by Laplace's equation. In the past, problems of this type were generally solved by distributing sources (and/or dipoles) on the body boundary and using Green's theorem to obtain an integral equation for the strength of these boundary singularities or, alternatively, by using sources and higher order multipole expansions at an interior point within the body, the strengths of these singularities being determined so as to satisfy the body boundary condition. In all cases, it is conventional to utilize the singularities which are solutions of the boundary-value problem stated above, except that the body boundary condition is invoked separately to determine the strength of the singularity distribution.

As an alternative approach, a localized finite element method was used by Bai (1975, 1978) to solve the steady two-dimensional uniform-flow problem. Chen & Mei (1975) and Mei & Chen (1976) have applied a similar numerical method to solve two dimensional problems. In the present paper Bai's method is extended to three-dimensional problems. When this method is applied to an arbitrary

three-dimensional ship, a line integral along the intersection between the free surface and the ship hull appear in Galerkin's formulation. However, if the waterplane is assumed to be sufficiently thin, the contribution from the line integral may be ignored.

Some numerical results for the pressure distribution on the free surface are presented and compared with analytic solutions obtained by Newman & Poole (1962). Computations have also been made for a ship moving along the centerline of a canal. Specifically we present here the wave resistance, the wave profile, the blockage parameter, the velocity profile on the ship hull, and the pressure on the bottom. The wave resistance of a thin ship is compared with the result obtained by Kirsch (1966). Agreement between the numerical and analytical predictions for both the pressure distribution and for the thin ship is very good. The ship hull boundary condition is treated in two ways. First, the ship hull boundary condition is applied on the centerplane according to the thin ship approximation, and next, the exact hull condition is used with the line integral being ignored. We also tested for a few Froude numbers the problem of a pressure distribution with infinitely thin side walls which is a simplified model for a surface effect ship (SES).

The main advantage of the present method is that the complex geometry of a hull boundary can be easily accommodated. The method also provides values for the velocity potential in the entire fluid domain as part of the results.

## **2. FORMULATION OF THE STEADY UNIFORM FLOW IN A CANAL**

We consider here steady uniform flow past a fixed three-dimensional disturbance in a canal with a rectangular uniform cross section. The coordinate system is right-handed and rectangular. The y-axis is directed oppositely to the force of gravity, and the xz-plane coincides with the undisturbed free surface. The bottom of the canal is in the y = -H plane and the side walls in the z = ±b planes. The uniform flow is coming from the negative x-axis. We neglect surface tension and assume that the fluid is inviscid and incompressible and that the motions are irrotational.

The steady three-dimensional flow is described by a total velocity potential

$$\Phi(x, y, z) = Ux + \phi(x, y, z) \quad (2.1)$$

where  $\phi$  is the perturbation potential, which must satisfy

$$\nabla^2 \phi(x, y, z) = 0 \quad (2.2)$$

in the fluid domain D. It will be assumed that the free-surface disturbances are all small so that the linearized free-surface

boundary condition

$$U^2 \phi_{xx} + g \phi_y = \begin{cases} 0 & \text{on } S_1 \\ -\frac{U}{\rho} \frac{\partial}{\partial x} P_0(x, z) & \text{on } S_p \end{cases} \quad (2.3)$$

can be applied, where  $P_0(x, z)$  is a specified non-zero pressure applied over a portion of the free surface,  $S_p$ .  $S_1$  is the remaining free-surface, and  $\rho$  is the density of water. The boundary condition on the ship hull,  $S_0$ , is

$$\phi_n = V_n \quad \text{on } S_0 \quad (2.4)$$

Here the normal velocity  $V_n$  is given as

$$V_n = -U n_1 \quad (2.5)$$

where  $\mathbf{n} = (n_1, n_2, n_3)$  is the outward unit normal vector. The boundary conditions on the bottom,  $S_B$ , and side walls,  $S_W$ , of a canal are

$$\phi_n = 0 \quad \text{on } S_B \cup S_W \quad (2.6)$$

As the radiation condition we require that no disturbances exist far upstream, i.e.,

$$\lim_{x \rightarrow -\infty} |\nabla \phi| = 0 \quad (2.7)$$

and that the potential  $\phi$  be bounded far downstream

$$\lim_{x \rightarrow +\infty} \phi < \infty \quad (2.8)$$

The solution of equations (2.2) through (2.8) is unique to within an arbitrary additive constant. To eliminate the arbitrary constant in the solution, we require a Dirichlet-type boundary condition at any one point in the fluid domain or on its boundary. For this purpose, we simply require

$$\phi(x_0, y_0, z_0) = 0 \quad (2.9)$$

where  $(x_0, y_0, z_0)$  is a point in the fluid or on its boundary. Now the solution of equations (2.2) through (2.9) can be determined uniquely.

### 3. LOCALIZED FINITE-ELEMENT METHOD

In this section we shall describe a numerical method based on a weak formulation or Galerkin's form. A description of the weak formulation or Galerkin's form will not be given here since many references on this subject exist. The reader who is not familiar with this subject may find an extensive treatment in Strang and Fix (1973).

The fluid domain of our problem is infinite along the  $x$ -axis. For numerical computations, it is desirable that the fluid domain be reduced to as small a region as possible. The goal of reducing the original infinite domain to a finite domain is achieved by making use of the known solution space in truncated infinite subdomains which will be defined later. Finally the domain of the fluid to be treated in the computations is reduced to a local region which may barely include any source of the disturbance in the steady flow. The present numerical method is termed a localized finite-element method since finite-element numerical computations are made only for a local domain which will be defined later. This procedure has been applied to steady two-dimensional uniform-flow problems by Bai (1975, 1978).

Let us draw two imaginary vertical planes  $J_1$  and  $J_2$  which separate the original fluid into the three sub-domains:  $D_0$ ,  $D_1$ , and  $D_2$ , shown in Figure 1. We assume that  $D_0$  includes the ship and/or the pressure distributions. The boundary surfaces of  $D_0$ ,  $D_1$ , and  $D_2$  are denoted, respectively, by

$$\begin{aligned} \partial D_0 &= S_{10} + S_{B0} + S_{W0} + J_1 + J_2 + S_0 + S_p \\ \partial D_i &= S_{1i} + S_{Wi} + S_{Bi} + J_i + S_{Ri}, \quad i = 1, 2 \end{aligned} \quad (3.1)$$

where  $S_{1i}$ ,  $S_{Bi}$ , and  $S_{Wi}$  denote, respectively, the free surface, the bottom, and the canal side walls, in the sub-domains  $D_i$  ( $i = 0, 1, 2$ ), and where  $S_{Ri}$  ( $i = 1, 2$ ) are the boundaries at infinity. Here  $\Gamma_0$  is the intersection line between the free surface  $S_{10}$  and the ship hull surface  $S_0$ . The lines  $\Gamma_1(x_1, 0, z)$ ,  $\Gamma_2(x_2, 0, z)$ ,  $\Gamma_3(x_3, 0, z)$ , and  $\Gamma_4(x_4, 0, z)$  are, respectively, the intersection lines of the surfaces  $J_1$ ,  $S_{R1}$ ,  $J_2$ , and  $S_{R2}$  with the free surface.  $S_p$  denotes the region of pressure distribution on the free surface, if any, in  $D_0$ .

Let  $\phi_0$ ,  $\phi_1$ , and  $\phi_2$  denote the perturbation potentials defined in the subdomains  $D_0$ ,  $D_1$ , and  $D_2$ , and on the boundaries,  $\partial D_0$ ,  $\partial D_1$ ,  $\partial D_2$ , respectively. Then we have, from equations (2.2) through (2.9), that  $\phi_0$  must satisfy

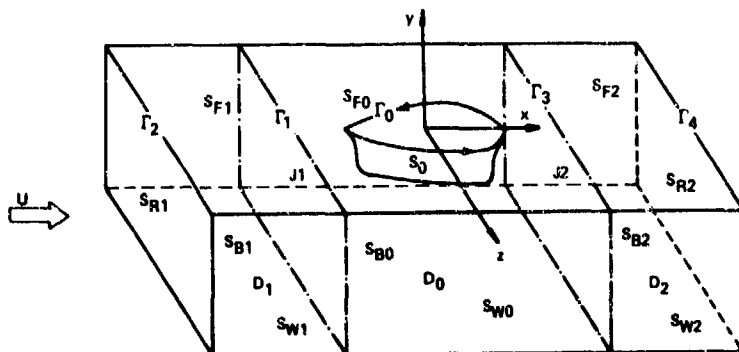


Figure 1 -- Boundary Configurations of the Three Subdivided Fluid Domain.

$$\begin{aligned} \nabla^2 \phi_0 &= 0 & \text{in } D_0 \\ \phi_{0n} &= \begin{cases} -\frac{U^2}{g} \phi_{0xx} & \text{on } S_{10} \\ -\frac{U^2}{g} \phi_{0xx} - \frac{U}{\rho g} \frac{\partial}{\partial x} P_0(x, z) & \text{on } S_p \end{cases} & (3.2) \\ \phi_{0n} &= 0 & \text{on } S_{w0} \cup S_{B0} \\ \phi_n &= -Un_1 & \text{on } S_0 \\ \phi_0(x_0, y_0, z_0) &= 0 \end{aligned}$$

and that  $\phi_i, i = 1, 2$ , must satisfy

$$\begin{aligned} \nabla^2 \phi_i &= 0 \\ \phi_{iy} &= -\frac{U^2}{g} \phi_{ixx} & \text{on } S_{1i} \\ \phi_{in} &= 0 & \text{on } S_{wi} \cup S_{wi} \end{aligned} \quad (3.3)$$

with the upstream condition

$$\lim_{x \rightarrow -\infty} |\nabla \phi_i| = 0$$

and with the downstream condition

$$\lim_{x \rightarrow +\infty} \phi_i < \infty$$

In addition, we have the matching conditions

$$\left. \begin{aligned} \phi_0 &= \phi_i \\ \phi_{0n} + \phi_{in} &= 0 \end{aligned} \right\} \text{ on } J_i, i = 1, 2 \quad (3.4)$$

where the normal vector  $n$  is taken outwards from the fluid region, i.e.,

$$\begin{aligned} \phi_{1n} &= \phi_{1x}, \phi_{0n} = -\phi_{0x} & \text{on } J_1 \\ \phi_{2n} &= -\phi_{2x}, \phi_{0n} = \phi_{0x} & \text{on } J_2 \end{aligned} \quad (3.5)$$

It is easy to show, by use of Green's theorem, that the solutions,  $\phi_0, \phi_1, \phi_2$  of the above problems, (3.2) through (3.4), are identical in each corresponding subdomain to the solution  $\phi$  of (2.2) through (2.9)

As the basis of the present numerical procedure, a weak formulation will be used, as mentioned earlier. One important step in the localized finite-element method is the construction of three coupled functionals by applying the weak formulation (Strang and Fix, 1975, pp. 116-125) in each of the three subdomains:

$$\iiint_{D_i} (\nabla^2 \phi_i) \psi_i dv = 0, \quad (i = 0, 1, 2) \quad (3.6)$$

for all  $\psi_i$  in some test space. Integrating by parts, (3.6) reduces to

$$\iiint_{D_0} \nabla \phi_0 \cdot \nabla \psi_0 dv - \iint_{\partial D_0} \phi_{0n} \psi_0 ds = 0, \quad \text{for all } \psi_0, \quad (3.7)$$

and,

$$\iint_{\partial D_i} (\phi_{in} \psi_i - \phi_i \psi_{in}) ds = 0 \quad (3.8)$$

for all  $\psi_i, i = 1, 2$ . Here  $\phi_i$  and  $\psi_i, i = 1, 2$ , are solutions of Laplace's equation.

Let  $\bar{\phi}_0, \bar{\phi}_1$ , and  $\bar{\phi}_2$  denote the trial functions in the subspace of the solution space in the subdomains  $D_0, D_1$ , and  $D_2$ , respectively and let  $\bar{\psi}_0, \bar{\psi}_1$  and  $\bar{\psi}_2$  denote the test functions in the subspace of the test space in  $D_0, D_1$ , and  $D_2$ , respectively. We define the functionals  $F_0, F_1$ , and  $F_2$  in  $D_0, D_1$ , and  $D_2$ , respectively, as follows

$$\begin{aligned} F_0\{\bar{\phi}_0, \bar{\phi}_1, \bar{\phi}_2; \bar{\psi}_0\} &= \iiint_{D_0} \nabla \bar{\phi}_0 \cdot \nabla \bar{\psi}_0 dv - \frac{U^2}{g} \iint_{S_{10} \cup S_p} \bar{\phi}_{0x} \bar{\psi}_{0x} ds \\ &+ \frac{U}{\rho g} \iint_{S_p} P_{0x} \bar{\psi}_0 ds + \frac{U^2}{g} \int_{\Gamma_0} \bar{\phi}_{0x} \bar{\psi}_0 dz + U \iint_{S_0} n_1 \bar{\psi}_0 ds \\ &+ \iint_{J_1} \bar{\phi}_{1x} \bar{\psi}_0 ds - \frac{U^2}{g} \int_{\Gamma_1} \bar{\phi}_{1x} \bar{\psi}_0 d\ell \\ &- \iint_{J_2} \bar{\phi}_{2x} \bar{\psi}_0 ds + \frac{U^2}{g} \int_{\Gamma_3} \bar{\phi}_{2x} \bar{\psi}_0 d\ell, \end{aligned} \quad (3.9)$$

where the line integration along the closed contour  $\Gamma_0$  is understood to proceed in the counterclockwise direction as shown in Fig. 1. (Note that  $dz < 0$  around the stem and  $dz > 0$  around the stem).

$$\begin{aligned} F_1\{\bar{\phi}_1, \bar{\phi}_0; \bar{\psi}_1\} &= \iint_{J_1} (\bar{\psi}_{1x} \bar{\phi}_0 - \bar{\phi}_{1x} \bar{\psi}_1) ds \\ &- \frac{U^2}{g} \int_{\Gamma_1} (\bar{\psi}_{1x} \bar{\phi}_0 - \bar{\phi}_{1x} \bar{\psi}_1) d\ell \\ &- \iint_{S_{R1}} (\bar{\psi}_{1x} \bar{\phi}_1 - \bar{\phi}_{1x} \bar{\psi}_1) ds \\ &+ \frac{U^2}{g} \int_{\Gamma_2} (\bar{\psi}_{1x} \bar{\phi}_1 - \bar{\phi}_{1x} \bar{\psi}_1) d\ell \end{aligned} \quad (3.10)$$

$$\begin{aligned} F_2\{\bar{\phi}_2, \bar{\phi}_0; \bar{\psi}_2\} &= - \iint_{J_2} (\bar{\psi}_{2x} \bar{\phi}_0 - \bar{\phi}_{2x} \bar{\psi}_2) ds \\ &+ \frac{U^2}{g} \int_{\Gamma_3} (\bar{\psi}_{2x} \bar{\phi}_0 - \bar{\phi}_{2x} \bar{\psi}_2) d\ell \\ &+ \iint_{S_{R2}} (\bar{\psi}_{2x} \bar{\phi}_2 - \bar{\phi}_{2x} \bar{\psi}_2) ds \\ &- \frac{U^2}{g} \int_{\Gamma_4} (\bar{\psi}_{2x} \bar{\phi}_2 - \bar{\phi}_{2x} \bar{\psi}_2) d\ell \end{aligned} \quad (3.11)$$

In constructing the above functionals given in (3.9) through (3.11), the following "additional" conditions were used to keep the desirable property of eigenfunction orthogonality (see Bai (1978)) in the solution space (eigenfunction space) to be used later:

$$\left. \begin{aligned} \bar{\phi}_{1,x} &= \bar{\phi}_{0,x} \\ \bar{\phi}_1 &= \bar{\phi}_0 \end{aligned} \right\} \text{ at } \Gamma_1(x_1, 0, z) \quad (3.12)$$

and

$$\left. \begin{aligned} \bar{\phi}_{2,x} &= \bar{\phi}_{0,x} \\ \bar{\phi}_2 &= \bar{\phi}_0 \end{aligned} \right\} \text{ at } \Gamma_2(x_2, 0, z) \quad (3.13)$$

These conditions are imposed to insure continuity of  $\phi$  and  $\phi_x$  across the lines  $\Gamma_1$  and  $\Gamma_2$  because the second derivative  $\phi_{xx}$  is involved in the free-surface boundary condition. (Obviously (3.12) and (3.13) are conditions stronger than the boundary conditions on the surfaces  $J_1$  and  $J_2$ , (3.4)). It is of particular interest to note that functional  $F_0$  given by (3.9) contains a line integral along the intersection of the ship hull and the free surface. This line integral is similar to the well-known line integral (also known as the sheltering effect) which is present in the Green's function formulation of the wave-resistance problems.

Finally we obtain the following functional equations with certain essential boundary conditions:

$$F_0 \{ \bar{\phi}_0, \bar{\phi}_1, \bar{\phi}_2, \bar{\psi}_0 \} = 0, \quad \text{for all } \bar{\psi}_0 \quad (3.14)$$

with the essential condition

$$\left. \begin{aligned} \bar{\phi}_0(x_0, y_0, z_0) &= 0 \\ F_1 \{ \bar{\phi}_1, \bar{\phi}_0, \bar{\psi}_1 \} &= 0, \quad \text{for all } \bar{\psi}_1 \end{aligned} \right\} \quad (3.15)$$

with the condition

$$\lim_{x \rightarrow -\infty} |\nabla \bar{\phi}_1| = 0;$$

and

$$F_2 \{ \bar{\phi}_2, \bar{\phi}_0, \bar{\psi}_2 \} = 0, \quad \text{for all } \bar{\psi}_2 \quad (3.16)$$

with the condition that  $\bar{\phi}_2$  is bounded as  $x \rightarrow \infty$ .

In the coupled functional equation (3.14) through (3.16), all the boundary conditions are properly taken into account as natural boundary conditions except for the essential conditions specified in the above functional equations. The essential conditions play the role of an additional condition on the functional equations given in (3.14) through (3.16) and have to be properly taken into account when constructing the trial functions.

In the region  $D_0$ , the bases for the trial and test functions are chosen from a polynomial basis. Specifically, 8-node isoparametric linear three-dimensional elements were used in the present numerical procedure. We will omit a description of this representation and of the computation of (3.9). One can read about this element in Wilson (1972).

As mentioned earlier, the trial and test functions in  $D_1$  and  $D_2$  will be chosen from a subspace of the solution space which satisfies the Laplace equation with the free-surface condition, the side wall condition and the bottom condition. The eigenfunctions or the Green functions of the above problem can represent the solution space. We will choose the eigenfunction space in this paper for its simplicity.  $F_1$  and  $F_2$  can be given in simple analytic forms except for the integrals along the juncture boundaries, i.e.,  $J_1$  and  $J_2$ . Therefore, the integral expressions for the functionals are involved only with subdomain  $D_0$ , which we shall call the localized finite-element domain. If one takes the localized finite-element domain to

be small, then the domain over which the integrals have to be computed will also be small. On the other hand, one has to take many terms (eigenfunctions) to represent the trial and test functions for  $\bar{\phi}_1$  and  $\bar{\psi}_1$  or  $\bar{\phi}_2$  and  $\bar{\psi}_2$  in the computation of the approximate solutions, and vice versa.

The coupled Galerkin equations (3.14) through (3.16) go into operational form in the following way. Let  $q_{i1}, \dots, q_{iN_i}, (i = 0, 1, 2)$  be the basis for the  $M_i$ -dimensional subspace of the solution space and let

$$\psi_{i1}, \psi_{i2}, \dots, \psi_{iN_i}, (i = 0, 1, 2)$$

be the basis for the  $N_i$ -dimensional subspace of the test space defined in the subdomains  $D_i, i = 0, 1, 2$ . Then the solution is assumed to be

$$\phi_i = \sum_{j=1}^{M_i} \varphi_{ij} q_{ij} \text{ in } D_i, \quad i = 0, 1, 2, \quad (3.17)$$

where  $\varphi_{ij}$  are coefficients to be determined. By substituting (3.17) into the coupled functional equations (3.14) through (3.16), finally reduce to sets of linear algebraic equations. Since the detailed procedures can be found in Bai (1978), we omit these here.

A complete set of the eigenfunctions which satisfy Laplace's equation and the homogeneous boundary conditions on the free surface, the bottom,  $y = -H$ , and the canal side walls ( $x = \pm b$ ) are given (see Wehausen (1973, p. 110)) as

$$\left\{ x, 1, \left( \frac{\cos k_n x}{\sin k_n x} \right) \cosh \mu_n (y + H) \cos \frac{n\pi}{2b} (z - b), \right. \\ \left. \exp k_{np} x \cos \mu_{np} (y + H) \cos \frac{n\pi}{2b} (z - b) \right\}, \quad (3.18)$$

where  $\mu_n > 0, k_n > 0, \mu_{np} > 0, k_{np} > 0$ , and where

$$\left. \begin{aligned} k_n^2 &= \mu_n^2 - (n\pi/2b)^2, \\ k_{np}^2 &= \mu_{np}^2 + (n\pi/2b)^2. \end{aligned} \right\} \quad (3.19)$$

The  $\mu_n$  must satisfy

$$\frac{U^2}{gH} \left[ \mu H - \left( \frac{n\pi H}{2b} \right) \frac{1}{\mu H} \right] = \tanh \mu H, \quad (3.20)$$

and the  $\mu_{np}$  must satisfy

$$\frac{U^2}{gH} \left[ \mu H + \left( \frac{n\pi H}{2b} \right) \frac{1}{\mu H} \right] = \tanh \mu H \quad (3.21)$$

If  $n \geq 1$ , there is a single solution for  $\mu_n$  for each value of  $U^2/gH$ . If  $n = 0$ , there is one positive solution for  $\mu_0$  if  $U^2/gH < 1$ , but none if  $U^2/gH > 1$ . There are infinitely many solutions for  $\mu_{np}$ , which we shall number with  $p = 0, 1, 2, \dots$  in order of increasing value. If  $n = 0$ , there is no solution  $\mu_{00}$  if  $U^2/gH < 1$ , but  $\mu_{00}$  exists if  $U^2/gH > 1$ . There is no steady-state solution if  $U^2/gH = 1$ .

In the numerical procedure it is understood that for convenience the  $yz$ -plane is shifted to coincide with  $J_1$  and  $J_2$  for the computations of  $F_1$  and  $F_2$ .

From the complete set of eigenfunctions, the basis for the trial functions is chosen so that all the trial functions satisfy the essential boundary conditions. In the choice of

the basis for the test functions, we eliminate the terms which result in a trivial zero row vector, a row vector linearly dependent on another row vector, or an unbounded integral.

The bases for the upstream region are chosen as

$$\{\psi_{11}, \dots, \psi_{1M1}\} = \left\{ 1, e^{k_{np}x} \cos \mu_{np}(y+H) \cos \frac{n\pi}{2b}(z-b) \right\} \quad (3.22)$$

and

$$\{\psi_{11}, \dots, \psi_{1M1}\} = \left\{ x, \sin k_n x \cosh \mu_n(y+H) \cos \frac{n\pi}{2b}(z-b), e^{k_{np}x} \cos \mu_{np}(y+H) \cos \frac{n\pi}{2b}(z-b) \right\} \quad (3.23)$$

where  $n$  and  $p$  are properly chosen from the lowest so as to make the total number of terms on both sides the same. Similarly, the bases for the downstream region are

$$\{\psi_{21}, \dots, \psi_{2M2}\} = \left\{ 1, \cos k_n x \cosh \mu_n(y+H) \cos \frac{n\pi}{2b}(z-b), \sin k_n x \cosh \mu_n(y+H) \cos \frac{n\pi}{2b}(z-b), e^{k_{np}x} \cos \mu_{np}(y+H) \cos \frac{n\pi}{2b}(z-b) \right\} \quad (3.24)$$

and

$$\{\psi_{21}, \dots, \psi_{2M2}\} = \left\{ x, \sin k_n x \cosh \mu_n(y+H) \cos \frac{n\pi}{2b}(z-b), e^{k_{np}x} \cos \mu_{np}(y+H) \cos \frac{n\pi}{2b}(z-b) \right\} \quad (3.25)$$

It is of interest to note that the final total matrix is banded. Furthermore, it should be noted that the submatrix obtained from the polynomial trial and test functions in  $D_0$  and the local-terms eigenfunctions in  $D_1$  and  $D_2$  is symmetric as well as banded. In the present numerical computations, this symmetric submatrix is solved first in terms of unknown coefficients of the free-wave eigenfunctions and constants. Then, the asymmetric submatrix of the rest of the matrix is solved.

#### 4. HYDRODYNAMIC PRESSURES, FORCES, MOMENTS, AND BLOCKAGE PARAMETER

The solution of the final matrix equation gives the velocity potential  $\phi(x, y, z)$  in the localized finite element domain  $D_0$  as well as the coefficients of the eigenfunctions in both the upstream and downstream half-infinite domains,  $D_1$  and  $D_2$ . For example, the potential  $\phi$  in the downstream region can be written as (see Wehausen (1973), p. 111)

$$\phi(x, y, z) = C_2 + \sum_n (a_n \cos k_n x + b_n \sin k_n x) \cdot \frac{\cosh \mu_n(y+H)}{\cosh \mu_n H} \cos \frac{n\pi}{2b}(z-b) + \sum_n \sum_p c_{np} e^{-k_{np}x} \cos \mu_{np}(y+H) \cos \frac{n\pi}{2b}(z-b) \quad (4.1)$$

Since the free-surface elevation in the linear theory is

$$\eta(x, z) = -\frac{U}{g} \phi_x(x, 0, z) \quad (4.2)$$

the free-surface elevation associated with the potential in (4.1) is then given by

$$\eta(x, z) = \frac{U}{g} \sum_n k_n t_{an} \sin k_n x - b_n \cos k_n x \cos \frac{n\pi}{2b}(z-b) + \frac{U}{g} \sum_n \sum_p k_{np} c_{np} e^{-k_{np}x} \cos \mu_{np} H \cos \frac{n\pi}{2b}(z-b) \quad (4.3)$$

The first summation starts with  $n=0$  or  $n=1$  according as  $U/\sqrt{gH} < 1$  or  $U/\sqrt{gH} > 1$ , respectively. In the second summation the term corresponding to  $n=p=0$  is absent in the first case, but present in the second. Here the coefficients  $C_2$ ,  $a_n$ ,  $b_n$ , and  $c_{np}$  are the coefficients,  $\phi_{2j}$ , defined in (3.17).

After the velocity potential has been obtained, the pressure can be computed by Bernoulli's equation

$$p = -\rho U \phi_x - \frac{\rho}{2} (\phi_x^2 + \phi_y^2 + \phi_z^2) \quad (4.4)$$

where the hydrostatic pressure has been omitted. Then the non-dimensional pressure coefficient  $C_p$  is defined as

$$C_p = p / \frac{1}{2} \rho U^2 = 1 - \frac{|\nabla(\phi_x + \phi)|^2}{U^2} \quad (4.5)$$

where  $C_p$  is unity at the stagnation point. The force and moment acting on a ship hull  $S_0$  are, respectively,

$$F = \iint_{S_0} p n \, dS$$

$$M = \iint_{S_0} p(r \times n) \, dS \quad (4.6)$$

where  $r = (x, y, z)$ ,  $r = (x, y, z)$  is the position vector, and  $n = (n_x, n_y, n_z)$  is the unit normal vector into the body. The drag force  $X$  can also be expressed in terms of the far-downstream free waves as

$$X = \frac{\rho b U^2}{2g} \sum_{n=0 \text{ or } 1}^{\infty} \epsilon_n^{-1} k_n^2 (a_n^2 + b_n^2) \left[ 1 - \frac{1}{2} \frac{gH}{U^2} \frac{\tanh \mu_n H}{\mu_n H} \left( 1 + \frac{2\mu_n H}{\sinh 2\mu_n H} \right) \right] \quad (4.7)$$

where

$$\epsilon_0 = \frac{1}{2}, \quad \epsilon_n = 1 \quad \text{for } n \geq 1,$$

It is of interest to note that, for steady flow in a canal, the mean potentials far upstream and far downstream are different. This mean-potential jump between the two infinities, i.e.,  $x = \pm \infty$ , defines the so-called blockage parameter which is discussed by Newman (1976) for the

two-dimensional case. The potential jump is defined by the difference in the two constants at both infinities. In his two-dimensional analysis, Newman (1976) pointed out that the potential jump  $C$  is related to the doublet strength,  $(UH/2\pi)\mu$ , by

$$\mu = \frac{C}{UH} \left( 1 - \frac{U^2}{gH} \right) \quad (4.8)$$

In presenting our numerical results, we will make use of the water-depth Froude number  $F_H$  and the ship length Froude number  $F_L$ , respectively defined by:

$$F_H = \frac{U}{\sqrt{gH}}$$

and

$$F_L = \frac{UL}{\sqrt{gL}}$$

where  $H$  and  $L$  are the water depth and the ship length, respectively.

In most of our computations, two sets of finite-element mesh subdivisions were used: a rather coarse mesh subdivision, with 500 elements and 26 nodes (10, 5, and 10 elements along the  $x$ ,  $y$ , and  $z$  axis, respectively) and a fine mesh, with 1120 total elements and 1496 total nodes (16 x 7 x 10 elements along the  $x$ ,  $y$ , and  $z$  axes). In both sets of mesh subdivisions, the approximately 30 eigenfunctions were taken (10 free-wave terms were taken). The average CPU execution time for each Froude number on the Texas Instrument Advanced Scientific Computer at the Naval Research Laboratory was 36 and 96 seconds, for the coarse and fine meshes, respectively. (The costs were approximately, \$10.00 and \$39.00, respectively.)

## 5. RESULTS AND DISCUSSIONS

We present some test results in this section. Specifically, a pressure distribution on the free surface is treated first, and a parabolic ship moving along the center of a canal is treated next. Throughout the computations, only half of the canal domain, i.e.,  $0 < z < b$  is considered due to the symmetry with respect to the  $xy$ -plane. Here the width of the canal  $W$  is given as  $W = 2b$ .

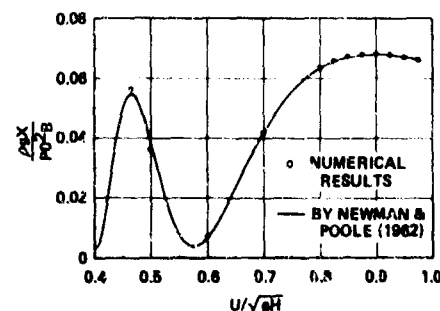


Figure 2 - Wave Resistance of a Pressure Distribution  
( $B/L = 1$ ,  $H/L = 0.5$ ,  $W/L = 2$ )

## Pressure Distribution on the Free Surface

A rectangular pressure distribution on the free surface was used to test the present numerical method since there exist analytic expressions for this simple geometry. The pressure distribution is given as

$$\begin{aligned} p_0(x, z) &= p_0 \quad \text{for } |x| < \frac{L}{2} \text{ and } |z| < \frac{B}{2} \\ p_0(x, z) &= 0 \quad \text{for } |x| > \frac{L}{2} \text{ or } |z| > \frac{B}{2} \end{aligned} \quad (5.1)$$

where  $L$  and  $B$  are the length and beam respectively and  $p_0$  is a constant. The wave resistance for this case is given in Newman & Poole (1962) as

$$\begin{aligned} X &= \frac{\pi}{2} \frac{p_0^2 W}{\rho g} \sum_{n=0}^{\infty} \frac{\epsilon_n}{n^2} \\ &\quad \frac{\mu_n H \sin^2 \left( \frac{n\pi B}{W} \right) \sin^2 \frac{1}{2H} \sqrt{\nu H \mu_n H} \tanh \mu_n H}{2\mu_n H - \nu H + \tanh \mu_n H - \nu H + \mu_n H + \text{sech}^2 \mu_n H} \end{aligned} \quad (5.2)$$

where  $\epsilon_n$  is defined earlier in (4.7),  $\nu = g/U^2$ , and where  $\mu_n$  are the positive real roots of equation (3.20) with  $'2b'$  replaced by  $'b'$ , i.e.,  $W/2$ , since the symmetry with respect to the  $xy$ -plane is used in the above formula.

In Figure 2 and Table 1, our numerical results are compared with the analytic results given by (5.2). As shown in Table 1, finer finite-element meshes were used for the low Froude numbers. Table 1 shows that the accuracy of the numerical results improves if finer finite-element meshes are used and that finer meshes should be used as the Froude number decreases. The comparison in Figure 2 shows good agreement between the numerical and analytic results for the higher Froude numbers. The slight disagreement shown for the low Froude-number cases results from insufficiently fine finite-element meshes. It is of interest to note that the blockage parameter  $\mu$  defined in (4.8) was a constant throughout the entire Froude-number range tested:  $\mu = p_0/\rho gH$ , for  $H/L = 0.5$ ,  $B/L = 1$ , and  $W/L = 2$ .

Table 1 - Comparison of the Wave Resistance,  $\rho g X/p_0^2 B$ , Computed by the Numerical and Analytic Methods for the Pressure Distribution on the Free Surface  
( $B/L = 1$ ,  $H/L = 0.5$ ,  $W/L = 2$ )

$F_H$	Numerical Results		Analytic Results (100 Terms)
	726 Nodes	1496 Nodes	
0.975	0.0660		0.0661
0.950	0.0671		0.0670
0.925	0.0678		0.0677
0.900	0.0682	0.0680	0.0680
0.875	0.0682		0.0679
0.850	0.0675		0.0671
0.825	0.0661		0.0656
0.800	0.0636	0.0633	0.0632
0.700	0.0443	0.0418	0.0415
0.600	0.0077	0.0072	0.0069
0.500	0.0290	0.0384	0.0382
0.465		0.0670	0.0649

In order to investigate surface effect ships (SES), we also tested the pressure distribution with infinitely thin side plates. The computed wave resistance with side plates was approximately double the wave resistance without the side hull plates when the draft of the side plates was  $T = 0.02 L$  for  $F_L = 0.95$ . We have some reservations with regard to these numerical values, because we did not take very fine meshes and because we did not take into account the Kutta condition along the edge of the side plates. Neglect of the Kutta condition resulted in an infinite cross velocity along the plate edge.

#### Parabolic Ship

Computations have been made for a parabolic ship moving along the centerline of a canal. A mathematical hull surface  $f(x, z)$  with symmetry about the  $x$ - and  $z$ -axes and with rectangular cross section is defined by

$$f(x, z) = z \pm \frac{B}{2} \left[ 1 - \left( \frac{x}{L/2} \right)^2 \right] = 0, \text{ for } 0 \leq y \leq T. \quad (5.3)$$

Here  $B$  and  $L$  are the beam and length of the ship, respectively. The draft of the ship is  $T$  and the depth and width of a canal are  $H$  and  $W$ , respectively. This hull form was chosen since there exist extensive results for this model in a canal by Kirsch (1966). We made two sets of computations, one using the linearized hull boundary condition on the centerplane, and the other using the exact hull boundary condition. In both cases the line integral along  $\Gamma_0$ , the intersection between the ship hull and the free surface, in (3.9) is ignored. We will give here a brief discussion for why this line integral may be ignored under certain assumptions.

It is convenient to nondimensionalize the functional  $F_0$  defined in (3.9) by  $U^2 L^3$ , i.e.,

$$F_0^* = \frac{F_0}{U^2 L^3} \quad (5.4)$$

Then the line integral along the intersection boundary  $\Gamma_0$ , from (3.9), can be written as

$$\frac{1}{g L^2} \oint_{\Gamma_0} \bar{\phi}_{0x} \bar{\psi}_0 d\left(\frac{z}{L}\right) = K \cdot \left(\frac{B}{L}\right) \quad (5.5)$$

where  $K$  is a constant of  $O(1)$ . By assuming that the ship is thin, i.e.,

$$\left(\frac{B}{L}\right) = o(1) \quad (5.6)$$

one can see from (5.5) that the line integral in (3.9) can be ignored since it is of  $O(B/L)$ . Similarly one can also show that the rest of the integral terms in (3.9) should be retained since they are of  $O(1)$  in the nondimensional forms.

The computed wave resistance using both the linear and exact boundary conditions on the hull surface are shown in Figure 3 and also given in Table 2.

Table 2 - Computed Wave Resistance\* Obtained by Using the Linear and Exact Hull Conditions for a Parabolic Ship  
( $B/L = 0.2$ ,  $T/L = 0.1$ ,  $H/L = 0.3$ ,  $W/L = 1$ )

$F_L$	Linear Boundary Condition		Exact Hull Boundary Condition 1496 Nodes
	728 Nodes	1496 Nodes	
0.800	0.9665		
0.570	1.0250		
0.530	3.3913	3.4155	5.8229
0.500	2.7764	2.8390	3.2590
0.475	2.2508	2.3287	2.7352
0.450	1.7638	1.7844	2.4412
0.425	1.3647	1.2240	1.4025
0.400		0.7371	
0.350		0.1791	
0.300		0.0056	

\*The nondimensional wave resistance is defined as

$$X / \left( \frac{B}{\pi} \rho g \frac{B^2 T^2}{L} \right)$$

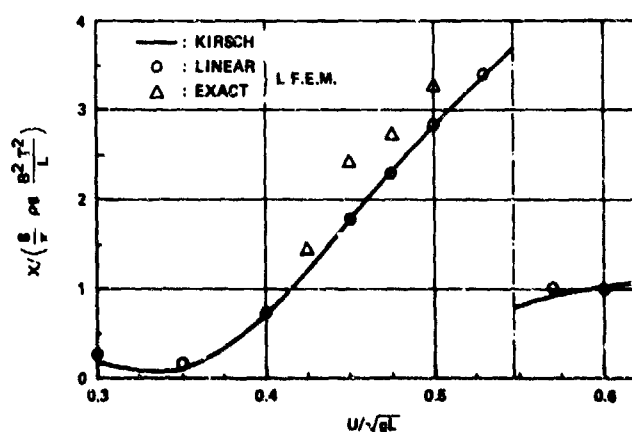


Figure 3 - Wave Resistance of a Parabolic Ship in a Canal  
( $B/L = 0.2$ ,  $T/L = 0.1$ ,  $H/L = 0.3$ ,  $W/L = 1$ )



The linear results are compared with those obtained by Kirsch (1966) in Figure 3. The agreement is good, for both sub-critical and super-critical flows. However, the results obtained by using the exact hull boundary condition are higher than those obtained by using the linear hull condition on the centerplane. This qualitative tendency can also be observed in the results shown by Inui (1957, p. 348; see also Wehausen, 1973, p. 195).

The velocity potentials and the free-surface elevations along the ship hull surface, the canal centerplane forward and aft of the hull, and along the canal side walls for  $F_L = 0.5$  are shown in Figure 4. The mean potential jump is also shown in Figure 4. It is of interest to note that the zeroth-mode free wave (i.e.,  $\mu_0 H = K_0 H = 0.790284$  in Table 3) is dominant along the canal side walls whereas along the hull surface, the higher-mode free waves are significant as well as the zeroth mode (the lowest mode). It appears that the higher-mode free waves have not quite propagated to the side walls even though all modes of free waves (as well as the local-disturbance terms) have been generated by the hull surface.

As a part of the numerical solution, we also obtained the coefficients of the eigenfunctions (the free-wave terms

as well as the local-disturbance terms). The coefficients of the ten-mode free waves (from the lowest mode) are given in Table 3 for  $F_L = 0.5$ , and for the linear and exact hull conditions, respectively. It is of great interest to note that the results in Table 3 provide not only the wave resistance from (4.7), but also provide the wave amplitude spectrum for discrete wave numbers. This wave amplitude spectrum is an intermediate result commonly obtained in the towing tank wave measurement by the transverse or longitudinal wave-cut methods. Therefore, since this method can simulate closely the towing tank experiments, it can be regarded as 'a numerical towing-tank experiment'.

The velocity vectors,  $\nabla(Ux + \phi)$ , on the hull surface (i.e., the tangential velocity) are computed from the potential obtained using the exact hull boundary condition. They are shown in Figure 5a for a Froude number,  $F_L = 0.5$ . The side of the hull surface is divided into three panels along the depth and ten panels along the length. The corresponding finite element nodes in the body plan are shown in Figure 5b. The accuracy of the velocity vectors can easily be improved by taking finer meshes (panels). Such results can then be used as input values for computation of the viscous boundary layer on a ship hull.

Table 3 - The Coefficients of the Downstream Free Waves in (4.1) for  $F_L = 0.5$   
( $B/L = 0.2$ ,  $T/L = 0.1$ ,  $H/L = 0.3$ ,  $W/L = 1$ )

n	$\mu_n H$	$K_n H$	Linearized Condition (On the Centerplane)		Exact Hull Condition	
			$a_n/UH$	$b_n/UH$	$a_n/UH$	$b_n/UH$
0	0.790284	0.790284	0.435529	0.736219	0.372829	0.728139
1	2.589032	1.745526	-0.014155	0.116152	0.017700	0.026130
2	4.417158	2.301966	-0.028785	-0.007874	0.030042	0.067346
3	6.286605	2.746611	-0.000609	0.000673	-0.054492	-0.000575
4	8.163857	3.129918	-0.003859	-0.008078	0.007485	-0.010914
5	10.043856	3.471690	0.010569	0.000794	-0.006729	-0.008545
6	11.925636	3.782958	-0.005156	0.005677	0.019083	-0.015158
7	13.808326	4.070825	-0.001105	-0.003588	0.008250	0.030843
8	15.691578	4.339341	0.000962	0.000311	-0.018894	-0.008766
9	17.575206	4.592412	0.000723	-0.000285	-0.008122	-0.002158

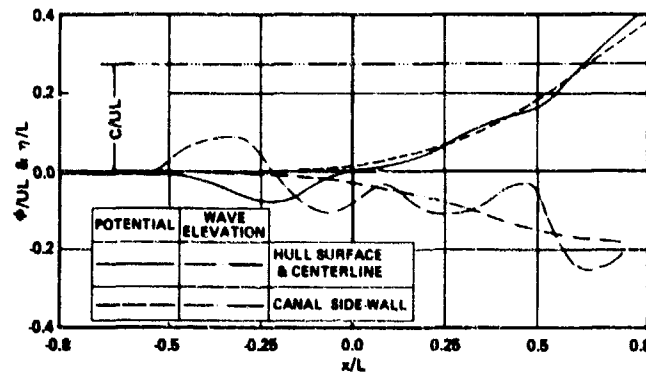


Figure 4 - The Velocity Potentials and Free Surface Elevations  
( $B/L = 0.2$ ,  $T/L = 0.1$ ,  $H/L = 0.3$ ,  $W/L = 1$ )

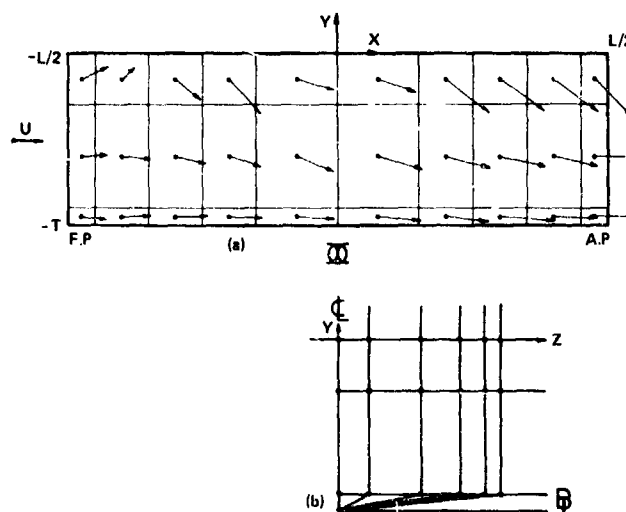


Figure 5 - (a) Velocity Profiles and  
(b) Finite Element Nodes on the Body Plan

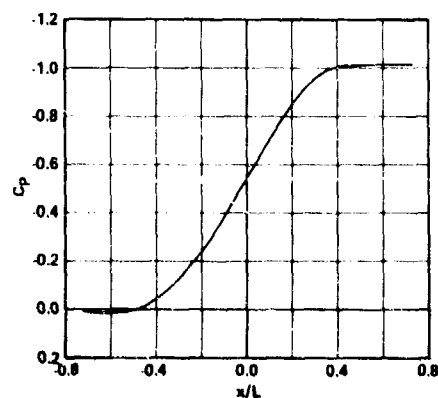


Figure 6 - Pressure Coefficient on the Bottom  
( $y = -H$ ,  $z = 0$ )  
( $B/L = 0.2$ ,  $T/L = 0.1$ ,  $H/L = 0.3$ ,  $W/L = 1$ )

The pressure coefficient  $C_p$  (defined in (4.5)) on the canal bottom below the centerline ( $y = -H$  and  $z = 0$ ) for  $F_L = 0.5$  is shown in Figure 6. The negative peak pressure occurs underneath the stern. The oscillatory behavior of the pressure coefficient appears downstream of the hull and is not shown in this figure. This is because the zeroth mode (the most significant term) free wave is very long in this case.

The blockage parameter  $\mu$  for the ship hull is given in Table 4. It is of interest to note that the value of  $\mu$  is constant, throughout the Froude numbers tested, when using the linear hull boundary condition. This is similar to the case of the pressure distribution on the free surface

Table 4 - Blockage Parameter  $\mu$  of a  
Parabolic Ship in a Canal  
( $B/L = 0.2$ ,  $T/L = 0.1$ ,  $H/L = 0.3$ ,  $W/L = 1$ )

$F_L$	Exact Hull Boundary Condition (1496 Nodes)
0.53	0.15749
0.50	0.15809
0.475	0.15926
0.450	0.16223
0.425	0.16604
With the linearized Boundary Condition on the Centerplane, $\mu = 0.14815$ throughout all the Froude numbers tested.	

discussed earlier. However, when the exact hull boundary condition is used, the values of  $\mu$  no longer remain constant, as shown in Table 4. It would be interesting to investigate the relation, if any, between the blockage parameter discussed here and that employed when analyzing towing tank experiments. In the latter case one can find extensive discussions and empirical formulas in the recent proceedings of the International Towing Tank Conference.

#### CONCLUDING REMARKS

As the preliminary test results show in the previous section, the present numerical method provides all the information in the potential flow accurately if a sufficiently large number of finite-element meshes are used. If one thinks of the fact that the capacity of computers (i.e., the main central core memory) is getting larger and the CPU execution time is becoming less and less as time goes on, it seems worthwhile to tackle quite complicated problems by the present numerical method. The present computations required approximately 16 and 96 seconds of CPU time (costing \$10.00 and \$29.00) respectively for 726 nodes and

1496 nodes. Since we can not claim that the present computer program is the most efficient to use as a production computer-program, one can easily reduce the cost more significantly by optimizing the present code.

It should be emphasized that the following additional investigations can and should be readily undertaken:

- (1) Inclusion in the method of the line-integral term given in (5.5).
- (2) Extension of the method to solve the exact nonlinear steady-flow problem by satisfying the exact free-surface condition locally around the ship and by using the eigenfunctions or singularity distributions (a fundamental source or a complete Green's function) around the juncture boundary on the localized finite element sub-domain.

#### ACKNOWLEDGEMENTS

This work was supported by the Numerical Naval Hydrodynamics Program at the David W. Taylor Naval Ship Research and Development Center. This Program is jointly supported by the DTNSRDC and the Office of Naval Research. The author also thanks Mr. Richard T. Van Eseltine at DTNSRDC for his assistance in converting the original CDC Computer Program to the TI-ASC Computer Program.

#### REFERENCES

- Bai, K.J., 1975, "A Localized Finite-Element Method for the Uniform Flow Problem with a Free Surface," Proc. First Int. Conf. Num. Ship Hydro., Sponsored by the David Taylor Naval Ship R&D Center, Bethesda, Md.
- Bai, K.J., 1978, "A Localized Finite-Element Method for Two-Dimensional Steady Potential Flows with a Free Surface," (submitted to J. of Ship Research).
- Chen, H.S. and Mei, C.C., 1975, "Calculations of Two-Dimensional Ship Waves by a Hybrid Element Method Based on Variational Principles," Proc. First Int. Conf. Num. Ship Hydrodynamics, Sponsored by David Taylor Naval Ship Research and Development Center, Bethesda, 95-111.
- Inui, Takao, 1957, "Study on Wave-Making Resistance of Ships," Soc. Nav. Architects Japan, 60th Anniv., Ser. 2, 173-355.
- Kirsch, Maria, 1966, "Shallow Water and Channel Effects on Wave Resistance," J. Ship Res., Vol. 10, No. 3, 164-181.
- Mei, C.C. and Chen, H.S., 1976, "A Hybrid Element Method for Steady Linearized Free-Surface Flows," Int. J. Numer. Method in Engrg., 10, 1153-1175.
- Newman, J.N., 1976, "Blockage with a Free Surface," J. Ship Res., Vol. 20, No. 4, 199-203.
- Newman, J.N. and Poole, F.A.P., 1962, "The Wave Resistance of a Moving Pressure Distribution in a Canal," Schiffstechnik, Vol. 9, 21-26.
- Wehausen, J.V., 1973, "The Wave Resistance of Ships," Advances in Appl. Mechanics, 13, 93-245.
- Wilson, E.L., 1972, "Solid Sap," UC/SESM 71-19, Structural Engineering Lab., Univ. of Calif., Berkeley, Cal.

## NUMERICAL SOLUTIONS OF TRANSIENT THREE-DIMENSIONAL SHIP-WAVE PROBLEMS

Samuel Ohring and John Telate  
David W. Taylor Naval Ship Research and Development Center  
Bethesda, Maryland 20084

### Abstract

An efficient 3-D finite difference implicit scheme based on a fast direct matrix solver has been developed to obtain transient solutions of the flow about a ship translating with uniform speed in a channel from its abrupt start in calm water. Both "thin ship" and exact body boundary conditions are considered. The problem is linearized in terms of the free stream velocity. Abrupt changes in the ship's uniform translational speed are considered in addition to abrupt starts in calm water. The present method can also handle ship accelerations and decelerations. Wigley hulls, characterized by small beam and draft-to-length ratios, have been used to represent the ship. For Froude numbers based on ship length above .5 it is found that the transient approach to a locally steady state about the ship from an abrupt start is rapid. This approach becomes significantly slower with decreasing Froude number with the wave resistance oscillating in time about a mean value which is approximately the steady state value of the appropriate comparison method.

In addition to a hull integration of pressure, wave resistance has also been computed for locally steady state cases by integrating an expression over a transverse plane aft of the ship based on energy conservation for the steady state flow region upstream of this plane. Wave resistance computed from these two methods as well as wave resistance versus time curves and ship wave profiles for all Froude number cases considered generally agree well with available comparison methods (analytic, observed, etc.). Energy conservation is monitored and wave patterns are computed in the entire channel at each time step.

### 1. Introduction

The problem of wave making and wave resistance of ships has been one of the central areas of marine research for many years. The wave resistance of an accelerating ship has been of particular interest in connection with towing-tank experiments. This paper presents a very efficient numerical technique for obtaining the transient solution about a ship translating with uniform speed in a channel

from an abrupt start in calm water. The abrupt start is viewed as a very rapid acceleration from rest. This numerical technique can easily handle accelerations and decelerations of the ship although this has not been done in this paper. However, abrupt changes in the ship's uniform translational speed are considered.

The numerical technique described in this paper, in addition to being very efficient, has the advantage of delivering the potential flow solution and the ship wave pattern in the entire channel at each time step. Such a solution permits the calculation of wave resistance from the wave energy. Although analytic approaches to the accelerating ship problem based on linear theory exist (see refs. [1] through [3]), these approaches must ultimately resort to numerical evaluation of certain series or integrals which require a large amount of computation. This is especially true when the exact body condition is satisfied. Thus the development of an efficient technique [such as that in the present paper] for handling these ship problems is well justified.

Both the "thin ship" and exact body boundary conditions are considered in this paper. Linearization of the free surface equations with respect to the free stream velocity was used. The numerical technique used is based on fast, direct matrix solvers for Laplace's equation. For the "thin ship" body condition the fast solver is diagonal decomposition as described in [4] but applied to second order differencing. For the exact body condition an imbedding technique is used as described in [5] and [6]. The numerical technique used at each time step couples the fast solution of Laplace's equation to the solution of the free surface equations accomplished by fourth-order line inversions. The coupling ordinarily involves a few iterations in a "predictor-corrector" manner with convergence on the vertical fluid velocity at the free surface. Therefore the overall numerical technique is implicit in time and is second order accurate. Results are obtained with this technique for Wigley ship hulls characterized by small beam and draft-to-length ratios and are compared with those of other available methods.

## II. Mathematical Formulation

We consider a right-handed Cartesian coordinate reference frame fixed to a ship translating with uniform speed  $U$  in a channel from its abrupt start in calm water (Figure 1). (Note that the origin of the reference frame is placed upstream of the ship.)

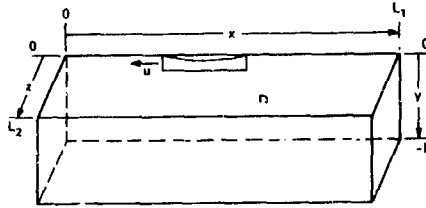


Figure 1. The Reference Frame

Assuming potential flow of an incompressible fluid the problem (which is symmetric about the centerplane  $z=0$  of the channel) can be represented mathematically by the following set of equations:

$$\eta_t = -\eta_x + \phi_y \quad \text{at } y=0 \text{ exterior to the ship} \quad (1)$$

$$\phi_t = -\phi_x - \eta/\text{Fr}^2 \quad \text{at } y=0 \text{ exterior to the ship} \quad (2)$$

$$\phi_{xx} + \phi_{yy} + \phi_{zz} = 0 \quad \text{in the region D exterior to the ship} \quad (3)$$

subject to the boundary conditions

$$\phi_x = 0 \quad \text{at } x=0, L_1 \quad (4)$$

$$\phi_y = 0 \quad \text{at } y=-h \quad (5)$$

$$\phi_z = 0 \quad \text{at } z=L_2 \quad (6)$$

$$\phi_z = 0 \quad \text{at } z=0 \text{ exterior to the ship} \quad (7)$$

$$\phi_n = h_x/\sqrt{1+h_x^2+h_y^2} \quad \text{at the hull } z=h(x,y) \quad (8)$$

The initial conditions representing the abrupt start are

$$\eta=0; \phi=0 \quad \text{at } y=0 \text{ exterior to the ship; } t=0 \quad (9)$$

All variables in Equations (1) through (9) have been nondimensionalized according to the scheme

$$(x,y,z) = L(x,y,z) \quad t' = \frac{L}{U} t \quad (10)$$

$$\phi' = LU\phi \quad \eta' = L\eta \quad h' = Lh$$

and the limits  $L_1, L_2$ , and  $h$  of the computational region D (representing half the channel) in Figure 1 are already nondimensional. In Equation (10) the primes denote dimensional

variables,  $\phi(x,y,z,t)$  is the velocity potential relative to a non moving reference frame,  $\eta(x,z,t)$  is the free surface elevation,  $t$  is the time,  $h$  is the hull function, and  $L$  is the length of the ship. The free surface equations have been linearized in terms of the free stream velocity  $U$  with the dimensionless Froude number  $\text{Fr} = U/\sqrt{gL}$ , where  $g$  is the gravitational acceleration. In Equation (8)  $n$  refers to the direction of the unit outward normal vector  $\hat{n}$  from the ship pointing into the fluid. When the "thin ship" boundary condition is used, the exact body boundary condition of Equation (8) is replaced by

$$\phi_z = h_x \quad \text{at the hull's projection onto the centerplane } z=0 \quad (11)$$

The wave resistance coefficient is given by

$$C_R = \frac{R'}{\rho U^2 L d} = \frac{2}{\rho U^2 L d} \int_{\text{ship}} -p' n_x dS / (\rho U^2 L d) \quad (12)$$

$$= \frac{2L}{d} \iint_A (\phi_t + \phi_x) (n_x/n_z) dx dy$$

where  $R'$  is dimensional resistance,  $p'$  is dimensional dynamic pressure,  $\rho$  is the constant density,  $d$  is the draft of the ship,  $n_x, n_y$ , and  $n_z$  are elements of the unit outward normal vector  $\hat{n}$ , i.e.,  $\hat{n} = (n_x, n_y, n_z)$ , and  $A$  is the projection of the ship's surface onto the centerplane  $z=0$ . The nondimensional dynamic pressure  $p$  within the linearization is given by

$$p = \frac{p'}{\rho U^2} = -(\phi_t + \phi_x) \quad (13)$$

It should be noted that the integrand in Equation (12) is evaluated at the ship hull, although the integration is performed on the projection  $A$ .

For steady state free surface flow about a ship translating with constant speed  $U$  in a channel, the dimensional wave resistance  $R'$  is also given by

$$R' = \frac{\rho U^2}{2g} \int_{-W}^W [(\phi_x')^2 - \phi' \phi_{xx}']_{y'=0} dz' \quad (14)$$

$$- \frac{\rho}{2} \int_{-W}^W dz' \int_{-h}^0 [(\phi_x')^2 - \phi' \phi_{xx}'] dy'$$

as derived in Lund (1971). Here the integrations are performed on a transverse plane aft of the ship and perpendicular to its motion ( $W'$  is the width of the channel). The derivation of (14) is based on considering energy conservation in the region upstream of the transverse plane. Flow in this region is assumed to be steady. Nondimensionalizing  $R'$  in Equation (14) and considering only one-half of the channel because of symmetry in the centerplane  $z=0$  we obtain the wave resistance coefficient  $C_R$ :

$$C_R = \frac{R'}{\rho U^2 L d} = \text{Fr}^2 \left( \frac{L}{d} \right) \int_0^W [(\phi_x')^2 - \phi' \phi_{xx}']_{y=0} dz \quad (15)$$

$$- \frac{L}{d} \int_0^W dz \int_{-h}^0 [(\phi_x')^2 - \phi' \phi_{xx}'] dy$$

Wave resistance computed this way is usually considered to be more reliable than computing it from integration at the body surface.

Energy conservation can be used to check and monitor numerical solutions. The nondimensional time rate of work performed by the ship on the fluid is given by

$$\dot{W} = \frac{dW'/dt'}{\rho U^3 L^2} = 2 \iint_A (\phi_t + \phi_x) \frac{n_x}{n_z} dx dy \quad (16)$$

with the integrand evaluated at the ship's surface. The nondimensional time rates of kinetic and potential energy of the fluid are, respectively,

$$\begin{aligned} \dot{KE} = \frac{d(KE)'/dt'}{\rho U^3 L^2} &= \frac{d}{dt'} \left[ \iint_{FS} \phi \phi_y dz \right. \\ &\quad \left. + \iint_A \phi \frac{n_x}{n_z} dx dy \right] \end{aligned} \quad (17)$$

$$\dot{PE} = \frac{d(PE)'/dt'}{\rho U^3 L^2} = \frac{d}{dt'} \left[ \frac{1}{Fr^2} \iint_{FS} n^2 dx dz \right] \quad (18)$$

In Equations (17) and (18) FS refers to the free surface and the integrand of the second integral in Equation (17) is evaluated at the ship's hull. Energy conservation is expressed as

$$\dot{W} = \dot{KE} + \dot{PE} \quad (19)$$

### III. The Numerical Method

The ship problem was discretized with a numerical grid defined as follows:  $(x_j, y_i, z_k)$  denotes a grid point:  $[x_j = j\Delta x, y_i = i(-\Delta y), z_k = k\Delta z]$  with  $j=0, 1, 2, \dots, L-1$ ;  $i=0, 1, 2, \dots, m-1$ ;  $k=0, 1, 2, \dots, n-1$  where  $(L-1)\Delta x = L_1$ ,  $(m-1)(-\Delta y) = -h$ ,  $(n-1)\Delta z = L_2$ . (See Figure 1.) For most cases treated in this paper the grid parameters for what we shall call the standard grid are  $\Delta x = \Delta z = .05$ ,  $\Delta y = 1/1.36$ ,  $L-1 = 128$ ,  $m-1 = 128$ ,  $n-1 = 16$ . Thus the standard grid represents a channel 6.4 ship lengths long, one ship length deep and 1.6 ship lengths wide. When different grid parameters are used, they will be specified.

The numerical method consists basically of coupling at each time step the solution of the free surface equations to the solution of Laplace's equation through convergence on the vertical velocity at the free surface with a few iterations. The numerical method, when using the exact body condition (Equation (8)) is a substantial alteration of the numerical method for the "thin ship" condition. Therefore the two body conditions are discussed separately in more detail.

#### "Thin Ship" Condition

Laplace's equation, subject to the boundary conditions of Equations (4) through (7) and (11), was solved on the box region of Figure 1 by the diagonal decomposition technique described in [4] but applied to second-order finite differencing. For most cases the

"thin ship" condition (Eq. (11)) was applied on the standard grid at points  $(x_j, y_i, z_k)$  with  $j=31, \dots, 50$ ;  $i=1, \dots, 8$ ;  $k=0$  for a total of 160 points. However, the ship was assumed to extend from  $x = (30.5)(\Delta x)$  to  $(50.5)(\Delta x)$  and from  $y = 0$  to  $8.5(\Delta y)$  since the unit normal vector to the ship's surface is undefined along lines of intersection of the ship with the centerplane  $z=0$ . (See Figure 1.) We shall call this a standard ship placement. Those cases with different ship placements will have the placements described.

The free surface equations (Eq. (1) and (2)) were discretized in accordance with Euler's modified method, i.e., they were replaced by difference equations of the form

$$\eta_j^{m+1} = \eta_j^m + \frac{\Delta t}{2} (F_j^{m+1} + F_j^m) \quad (20)$$

$$\phi_j^{m+1} = \phi_j^m + \frac{\Delta t}{2} (G_j^{m+1} + G_j^m) \quad (21)$$

where the superscripts refer to time levels,  $\Delta t$  is the time increment,  $F$  and  $G$  are finite difference approximations to the right-hand sides of Equations (1) and (2) respectively, and the subscript  $j$  refers to the  $j$ th grid point in the  $x$ -direction. (The subscripts  $i, k$  have been suppressed since  $i=0$  and  $k$  can be considered fixed because Equations (20) and (21) involve finite differencing only in the  $x$ -direction.) The derivatives  $n_x$  and  $\phi_x$  in  $F$  and  $G$ , respectively, are replaced with fourth-order central differences. Given  $\phi_y$  at the  $m$  and  $m+1$  levels, Equations (20) and (21) can be viewed as one-dimensional finite difference equations for the unknowns  $\eta_j^{m+1}$  and  $\phi_j^{m+1}$ , respectively (for  $k$  fixed), i.e., for each  $k$ ,  $k=0, \dots, n-1$  and for  $j=0, \dots, L-1$ , Equations (20) and (21) each yield a set of simultaneous linear equations for the unknowns  $\eta_j^{m+1}$  and  $\phi_j^{m+1}$ , respectively, which are solved by direct inversion along a grid line in the  $x$ -direction.

The complete numerical scheme for each time step is described as follows. Second-order extrapolation for  $(\phi_y)_{y=0}^{m+1}$  is followed by line inversions of Equation (20) (for all lines  $k=0, \dots, n-1$ ) to obtain  $\eta_j^{m+1}$  which is then used in the line inversions of Equation (21) to obtain  $\phi_j^{m+1}$ . Subject to this Dirichlet condition for  $\phi$  at  $y=0$ , Laplace's equation is solved to give  $\phi_y^{m+1}$  at  $y=0$ . This constitutes one iteration and the cycles through Equations (20), (21) and Laplace's equation are repeated, using the latest values for  $\phi_y^{m+1}$ ,  $\eta_j^{m+1}$ , and  $\phi_j^{m+1}$  as soon as they are available. The iteration process is halted after the  $J$ th iteration when

$$|\phi_y^{m+1, J+1} - \phi_y^{m+1, J}| \leq \epsilon, |\eta_j^{m+1, J+1} - \eta_j^{m+1, J}| \leq \epsilon \quad \text{at } y=0 \quad (22)$$

where  $|\phi_{y^{m+1,j+1}}| \leq \epsilon_2$ . For all cases,  $\epsilon_1$  and  $\epsilon_2$  were .05 and .001, respectively. The complete numerical scheme is second-order accurate in time and space.

#### Exact Body Condition

Laplace's equation, subject to the boundary conditions of Equations (4) through (8) was solved in the region D by an imbedding technique known as the "capacitance matrix" technique [5],[6] in which the ship was imbedded in the box of Figure 1. Finite difference approximations to this boundary value problem for Laplace's equation result in a matrix system for  $\phi$  which is perturbed by perturbed finite difference operators or "irregular stars" in the neighborhood of the ship hull. The formulation of these irregular stars is quite arbitrary but must include the body condition of Equation (8). The curvature of the ship hull as well as the body condition (Eq. (8)) is represented in our formulation of the irregular stars which are second-order accurate and given in [6]. In all cases having the exact body condition the irregular stars were centered at grid points  $(x_i, y_i, z_k)$  with  $j=31, \dots, 50$ ;  $i=1, \dots, 8$ ;  $k=1$ . (The ship had standard placement.) Briefly our formulation of the irregular stars (see Fig. 2) consists of (i) Selecting two out of three arc-length directions on the hull surface passing through the hull contact point a (which is not a grid point) of the irregular star centered at the grid point 0. (Our selection was  $s_1$  and  $s_2$  which lie in planes parallel to the  $y=0$  and  $x=0$  planes, respectively.) (ii) Taking a linear combination of the expressions for  $\phi_n$ ,  $\phi_{ns_1}$ ,  $\phi_{ns_2}$ ,  $\phi_{nx}$  evaluated at the point a to eliminate the cross derivatives (the choice of  $\phi_{nx}$  from among  $\phi_{nx}$ ,  $\phi_{ny}$ ,  $\phi_{nz}$  is arbitrary). (iii) Replacing the derivatives in the resultant linear combination by finite differences centered at the grid point 0 to certain orders of accuracy and also incorporating Laplace's equation. This formulation cannot be used if at least one from among  $\phi_n$ ,  $\phi_{ns_1}$ ,  $\phi_{ns_2}$ ,  $\phi_{nx}$  at the point a is zero.

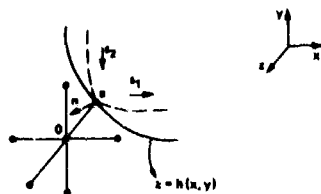


Figure 2. An Irregular Star

The perturbed matrix system for  $\phi$  was solved efficiently using an algorithm [5],[6] based on the Woodbury formula for a perturbed matrix. This algorithm consists essentially of

two fast direct partial solutions of the unperturbed matrix system and the solution of a small full "capacitance" matrix system whose order is equal to the number of irregular stars. The direct solver for the two solutions of the unperturbed matrix system was chosen to be that of [4] but applied to second-order differencing. In addition to the 160 irregular stars just discussed there were an additional 36 perturbed Laplacians centered on the plane  $z=0$  surrounding the hull's intersection with  $z=0$ . Thus the order of the "capacitance" matrix was 196. Since the ship problem we are considering is time dependent, it was necessary only to compute and store the inverse of the "capacitance" matrix initially and then replace the solution of the "capacitance" matrix each time it was required by multiplication of a vector with this inverse.

The free surface equations were solved by line inversions as described for the "thin ship" condition. However, the grid line along  $z=0$  was interrupted by the ship and required special treatment. Figure 3 shows this interruption behind the stern of the ship. For the derivatives  $\eta_x$ ,  $\phi_x$  at the point 0 in

Figure 3, upstream differencing given by

$$\eta_x = \frac{-4\eta_1 + \eta_2 + 3\eta_0}{2h} + O(h^2) \quad (23)$$

was used; the subscripts refer to evaluation at the numbered grid points, and  $h=\Delta x=\Delta z$ . The line inversion of the shortened line behind the stern could then proceed without being a closed system. Similar considerations would apply to other grid lines that might be interrupted by the ship.



Figure 3. Grid Neighborhood of Stern (Aerial View)

The complete numerical scheme for each time step proceeds iteratively as for the "thin ship" condition and is second-order accurate in time and space.

#### IV. Results

The results discussed in this section were obtained for the Wigley 1805A hull [2] given by

$$z = h(x,y) = \frac{3}{64} (1-256y^2)(1-6.4(x-x_c)^2 + 9.6(x-x_c)^4) \quad (24)$$

where  $x_c$  is the x-coordinate of the center of the ship. For all Froude number cases using the standard grid, ship placement was also standard with  $x_c = 2.025$ . When other grids are used,  $x_c$  is specified. The Wigley 1805A hull

is characterized by a half-beam-to-length ratio of 3/64 and draft-to-length ratio of 1/16 so that, on the standard grid representing the half channel in which the computation takes place (because of symmetry) this hull is not as wide as the mesh space, i.e.,  $3/64 < \Delta z = .05$ .

It was found that advancing solutions in time caused numerical "noise" to emanate from the leading edge of the bow which is singular. This "noise" caused low-level upstream waves. To prevent this emanation, a filtering scheme based on [7] was applied at the free surface from the bow to the upstream boundary at each time step within the iterative process. A second-order filtering function [7], which removes the shortest wave component but preserves the longer wave components, was used for  $\eta = \eta_f$  and averaged with the calculated  $\eta = \eta_c$  within the iterative process for each time step. This weighted averaging at grid points  $(x_j, 0, z_k)$  upstream of the bow's leading edge was for  $k=0, \dots, n-1$ .

$$\eta = .9\eta_c + .1\eta_f \quad \text{for } j=28, 29, 30$$

$$\eta = .8\eta_c + .2\eta_f \quad \text{for } j=25, 26, 27$$

$$\eta = .7\eta_c + .3\eta_f \quad \text{for } j=22, 23, 24$$

$$\eta = .6\eta_c + .4\eta_f \quad \text{for } j=19, 20, 21$$

$$\eta = .5\eta_c + .5\eta_f \quad \text{for } j=0, \dots, 18$$

The same weighted averaging was applied to  $\phi$  at  $y=0$ . This filtering scheme worked very nicely.

The solution could be advanced several units in time, i.e., the ship could be advanced several of its lengths, before waves reached the downstream boundary. In some cases, when necessary, the numerical solution was advanced somewhat beyond this point in time without affecting the local solution about the ship. Results for the "thin ship" condition are presented first; for the exact body condition, second.

#### "Thin Ship" Condition

Figures 4 through 16 represent "thin ship" condition results.

Figure 4 shows wave resistance versus time curves for five different Froude numbers. Analytic, steady state values are taken from [8],[9]. All Froude number cases involved abrupt starts from rest except for  $Fr = .385$  which involved an abrupt start from a locally steady state solution for  $Fr = .503$ . After the initial transient effects, the oscillations in the wave resistance curves about the steady state values are of constant wave length for each Froude number, the wave length increasing with increasing Froude number. In addition the amplitude of the oscillations decreases with increasing Froude number and with increasing time. All of these results are in agreement with an asymptotic expansion for large time obtained by Mehausen [3] for the wave resistance of a thin ship started abruptly from rest.

This asymptotic expansion up to terms of  $O(1/t^2)$  gives the following dimensional wave length in dimensional time of the oscillations.

$$\lambda' = \frac{8U\pi}{g} \quad (26)$$

Nondimensionally the wave length is

$$\lambda = 8Fr^2\pi \quad (27)$$

The wave lengths of the resistance curves in Figure 4 satisfy Equation (27) fairly closely. The behavior of  $Fr = .385$  is a little surprising since it was not an abrupt start from rest.

The analytic values of resistance in Figure 4 are from [8],[9] and are for infinite fluid. However in all cases the channel is so wide and deep that these analytic values are valid for comparison. Wave resistance  $C_p$  in Figure 4 was calculated from Equation (12) with nondimensional time representing ship lengths traveled. All cases were calculated on the standard grid with standard ship placement except Froude numbers .32 and .385. For .32,  $\Delta y = 1/72$ ,  $m=1 = 64$  with the other grid parameters those of the standard grid while the "thin ship" condition was applied at grid points  $(x_j, y_i, z_k)$  with  $j=31, \dots, 50$ ;  $i=1, \dots, 4$ ; and  $k=0$  with  $x_c = 2.025$ . For .385, the parameter  $z=1=256$ ; the others were standard with the "thin ship" condition applied at  $(x_j, y_i, z_k)$  with  $j=101, \dots, 120$ ;  $i=1, \dots, 8$ ; and  $k=0$  with  $x_c=5.525$ .

All cases were run on the IBM 360-91 in double precision with time step  $\Delta t = .03$  (except for  $Fr = .32$  run on the CDC 6600). A time step with two iterations on the standard grid took 1.21 seconds on the IBM 360-91 so that the case  $Fr = .503$ , for example, used 145 seconds to compute 120 time steps in attaining locally steady state. Increasingly less computer time is required to attain steady state for the higher Froude number cases.

Finally, we mention that for  $Fr = .32$  only the upstream filtering scheme already discussed was applied to the entire free surface with the weighted average  $\eta = .5\eta_c + .5\eta_f$ . It was felt that such filtering for  $Fr = .32$  only was necessary since the standard grid might not resolve the shorter waves resulting in numerical noise. The calculation of resistance and wave profiles for this case is not believed to be significantly affected by the filtering. Numerical evidence supporting this statement is presented later in this section.

Approximately steady state wave resistance was also computed for  $Fr = .503$  and  $Fr = .557$  using Equation (15) at three consecutive transverse planes given by  $x_j = j\Delta x$  ( $\Delta x = .05$ ) with  $j=125, 126$ , and  $127$ . (These two Froude number cases were also run on a grid, standard except for  $z=1 = 256$  with the "thin ship" condition applied at  $(x_j, y_i, z_k)$ ;  $j=101, \dots, 120$ ;  $i=1, \dots, 8$ ;  $k=0$  with  $x_c = 5.525$ .) For  $Fr = .503$ , the calculated resistance values at planes  $j=125, 126$ , and  $127$  were  $C_p = .005102, .005108$ , and  $.005006$ , respectively. This compares with the computed value from Equation (12) at  $t=3.6$



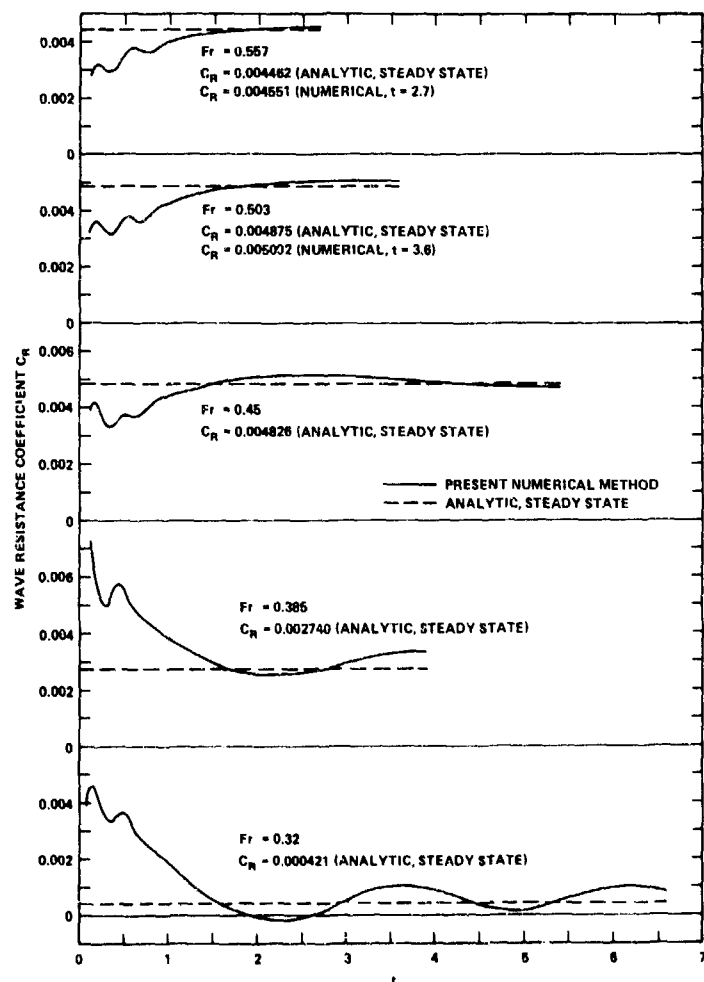


Figure 4. Wave Resistance Versus Time for Selected Froude Numbers

of  $C_R = .005092$  and the analytic value of  $C_R = .004875$ . For  $Fr = .557$ , the calculated resistance values at planes  $j=125$ ,  $126$ , and  $127$  were  $C_R = .004568$ ,  $.004710$ , and  $.004734$ , respectively. This compares with the computed value from Equation (12) at  $t = 2.7$  of  $C_R = .004551$  and the analytic value  $C_R = .004462$ . In these computations derivatives were replaced by second-order finite differences in Equations (12) and (15) and integrations performed by the rectangular and Simpson's rule in both coordinate directions in Equations (12) and (15), respectively.

Corresponding to Figure 4, Figure 5 shows the wave profiles at the ship computed for the

various Froude numbers at the times indicated. For the smaller Froude numbers .32, .385, and .45 the numerically obtained wave profiles at times  $t$  of the last minimum and maximum of the corresponding resistance curves are compared. The profiles change little with time, and what change there is occurs mostly in the stern area. Analytic steady state wave profile data for  $Fr = .45$  and  $.557$  were not available.

Figure 6 shows how well energy is conserved in the channel. Near  $t=0$ , changes occur so rapidly that they cannot be resolved accurately by the numerical scheme. For Froude number .32 the energy loss is due to the filtering scheme already discussed as applied to this case. For

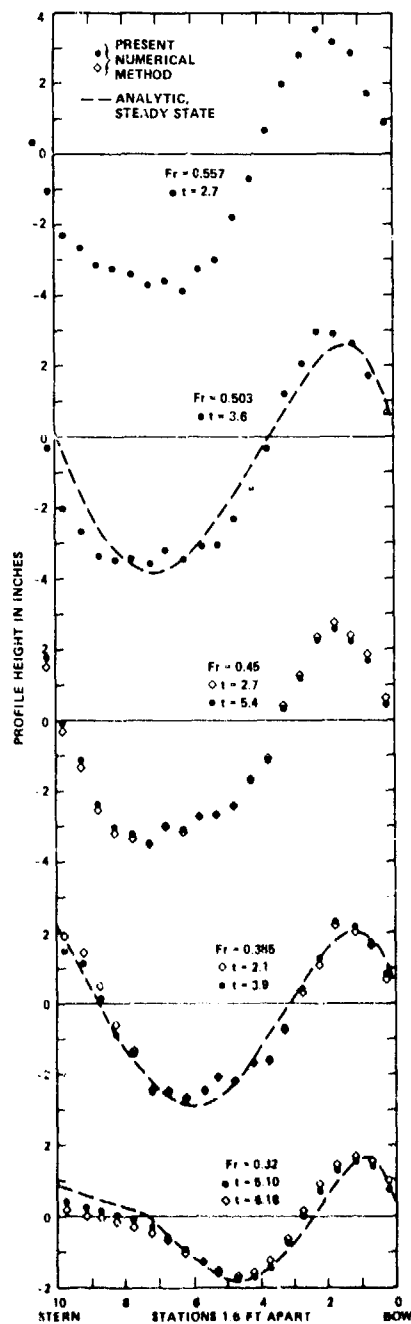


Figure 5. Comparison of Numerical and Analytic Wave Profiles for Selected Froude Numbers

For  $Fr = .45$ , energy is not conserved as well after  $t \geq 4.2$  as it was earlier because waves have reached the downstream boundary. However, this boundary is so far away as not to affect the local solution about the ship. The quantities  $W$ ,  $KE$ , and  $PE$  in Equations (16), (17), and (18), respectively, were computed numerically with second-order finite differences replacing derivatives and the rectangular and Simpson's rule used to compute the integrals at the body and free surface, respectively.

Free surface elevation contour values obtained numerically have been plotted by computer on the Stromberg Carlson 4060 as shown in Figures 7, 8, 9, and 10 for Froude numbers .32, .385, .503, and .557, respectively. The free surface of the channel is plotted in all pictures for a region extending from one-half a ship length upstream of the ship to two and one-half ship lengths downstream of the ship and from sidewall to sidewall of the channel (channel walls are not drawn). The ship is traveling to the left. The ranges of the free surface elevation contour values plotted are tabulated:

Froude No.	Range
.32	-.008 to .007
.385	-.017 to .016
.503	-.020 to .017
.557	-.021 to .018

Contour values were incremented by .001. Solid and dotted contour lines correspond to positive and negative contour values, respectively, i.e., they indicate wave crests and troughs, respectively. Divergent and transverse waves are present in all pictures. Any waves upstream of the bow in any of the pictures are of very low value and insignificant.

In addition to the abrupt start from rest for  $Fr = .557$ ,  $Fr = .503$  (in the same manner as the  $Fr = .385$  case) was also abruptly started from a locally steady state solution obtained numerically for  $Fr = .503$ . The two solutions are compared in Figures 11 and 12. The steady state solutions are virtually identical.

Because the filtering scheme used for  $Fr = .32$  resulted in a loss of energy, it was decided to determine its effect on a higher Froude number such as  $Fr = .503$ . The result was a significant loss of energy with some wave distortion. However, the wave resistance is affected to only a small degree as shown in Figure 13. The conclusion is that filtering over the entire free surface for the higher Froude numbers is not necessary and should not be used because it dampens the larger transverse waves. At the lower Froude numbers, for  $Fr = .32$ , this effect is diminished although less filtering could be used.

One solution for an abrupt start from rest of another Wigley hull [10] given by

$$z = h(x,y) = \frac{1}{20} (1-256y^2)(1-4(x-x_c)^2) \quad (28)$$

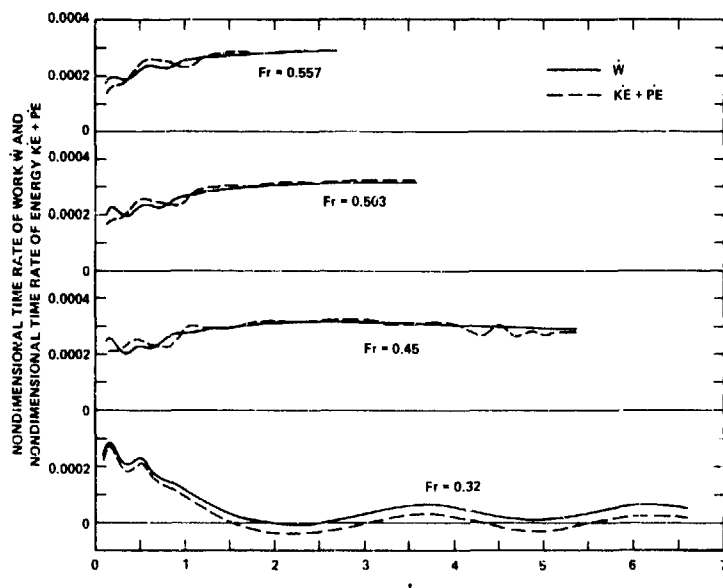


Figure 6. Conservation of Energy Versus Time for Selected Froude Numbers

for  $Fr = .3162$  was obtained on the same grid used for  $Fr = .385$ . This hull has a block coefficient equal to .44 compared to .39 for the hull given by Equation (24). The filtering scheme for  $Fr = .32$  was used here also. Results are presented in Figures 14, 15, and 16. Note that wave profiles in Figure 15 are compared with the measured (not the analytic) wave profile. Contour values in Figure 16 ranged from -.010 to .011 with values incremented by .001.

#### Exact Body Condition

The major difficulty in editing accurate flow results at the hull surface from the field solution when the hull is imbedded in a Cartesian grid is that hull surface points are generally not grid points. Thus although the numerical scheme (which is subject to a Neumann condition for  $\phi$  at the hull surface) is second-order accurate at field grid points and is efficient, the velocity potential  $\phi$  and surface elevation  $\eta$  at the hull must still be accurately determined. These quantities are used in computing  $C_D$ ,  $W$ ,  $KE$ , and  $PE$  of Equations (12), (16), (17), and (18), respectively. They therefore can significantly affect the computation of wave resistance and energy conservation. Determining  $\phi$  and  $\eta$  at the hull can be accomplished through finite differencing of Equations (2), (3), and (8) and/or through interpolation to desired orders of accuracy depending on how many field grid points one is willing to use. We have chosen

to obtain the velocity potential  $\phi$  at the hull by applying the exact body condition (Equation (8)) at grid point 0 (Figure 2) using finite differencing. This method is easy to implement but only first-order accurate. In Equations (12), (16), (17), and (18) the rectangular rule was used to compute hull integrals; a double application of the trapezoidal rule was used to compute the remaining integrals. Results were obtained for Froude number .32 (without filtering) and for Froude number .503 on the standard grid with standard ship placement.

Figure 17 shows numerically computed wave resistance  $C_D$  (Equation (12)) plotted against time and compared with steady state, observed (free to trim) results [8]. The time behavior of  $C_D$ , as expected, is quite similar to results already discussed for the "thin ship" condition. However, for both Froude numbers  $Fr = .32$  and .503 the numerical editing predicts a smaller wave resistance than expected. This situation most likely would be improved by finer Cartesian grid resolution about the body.

On the IBM 360-91, using double precision arithmetic, it took 295.81 seconds to compute 90 time steps (with  $\Delta t = .03$ ) in obtaining steady state for  $Fr = .503$ . Almost all time steps for this case used two iterations. Thus each such time step on the standard grid required 3.18 seconds of computer time. Higher Froude numbers would require less total computer time in achieving steady state. For  $Fr = .32$ ,

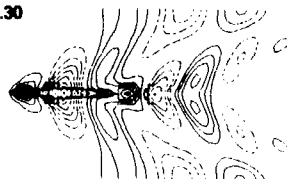
t = 0.16



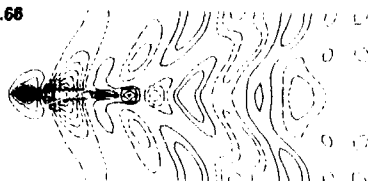
t = 0.62



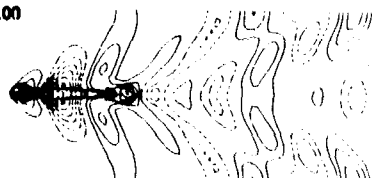
t = 2.30



t = 3.68



t = 5.00



t = 6.18

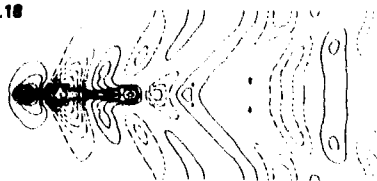


Figure 7. Time Sequence of Free Surface Contours for Fr = .32

819.06 seconds were used to compute 170 time steps (most requiring three iterations) with  $\Delta t = .03$ . Preprocessing the capacitance matrix (of order 196) and its inverse took 90.11 seconds. This preprocessing was done only once since it is independent of the Froude number.

Approximately steady state wave resistance for Fr = .503 at t = 2.7 was also computed using Equation (15) at three consecutive transverse planes given by  $x_j = j\Delta x$  ( $\Delta x = .05$ ) with j = 55, 56, and 57 (ship placement was standard). Since wave resistance  $C_R$  (using Equation (15)), is computed to second-order accuracy from a second-order accurate field solution, this calculation is more accurate and reliable than that for obtaining  $C_R$  using Equation (12). The calculated resistance values at planes j = 55, 56, and 57 were  $C_R = .004265$ ,  $.004441$ , and  $.004811$ , respectively, with a mean value of  $.004506$ . This value compares favorably with the observed (fixed to trim) value of  $C_R = .00444$  and with the computed value from Equation (12) at t = 2.7 of  $C_R = .003756$ .

Wave profiles along the ship hull are compared in Figure 18. The numerical wave profiles were computed from the following expression obtained by taking the outward normal derivative of Equation (2) at the body.

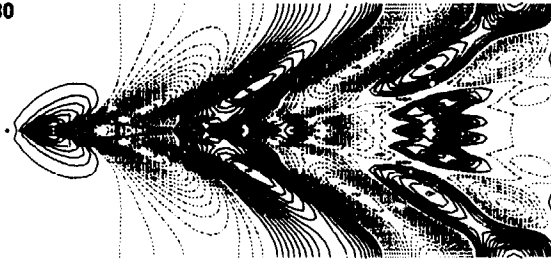
$$\{n_n = -(Fr)^2 \phi_{nx}\}_{\text{body}} \quad (29)$$

Second-order differencing for  $n_n$  using second-order Lagrange interpolated free surface values of  $n$  (with  $\phi_{nx}$  body known analytically) was introduced into Equation (29) so that the unknown  $\{n\}_{\text{body}}$  could be solved for in terms of known quantities. It is seen in Figure 18 that most numerical errors occur in the stern area of the ship. Also most of the change with time for Fr = .32 is in this area as it was for the "thin ship" condition.

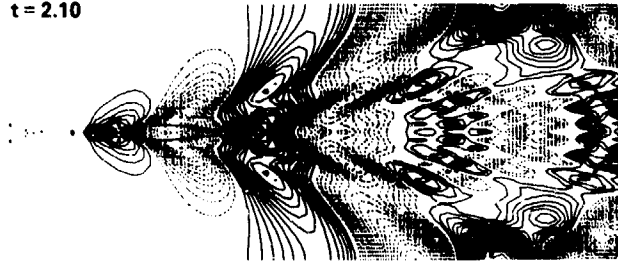
Figure 19 shows the attempt to prove energy conservation in the channel. It is evident that the numerical editing has failed to resolve, for the initial transient effects, the rate of work and energy growth. It is likely that the discretization, including the time step ( $\Delta t = .03$ ) and mesh spacing, was too coarse to make this resolution possible.

Free surface elevation contours have been plotted by computer on the Calcomp 936 Plotter (Figures 20 and 21). With contour values incremented by .001 and solid and dotted lines indicating positive and negative contour values, respectively, the ranges of contour values for Fr = .32 and .503 were -.007 to .010 and -.017 to .022, respectively. As expected, the wave patterns produced by the exact body condition are similar to patterns shown earlier in this paper for the "thin ship" condition.

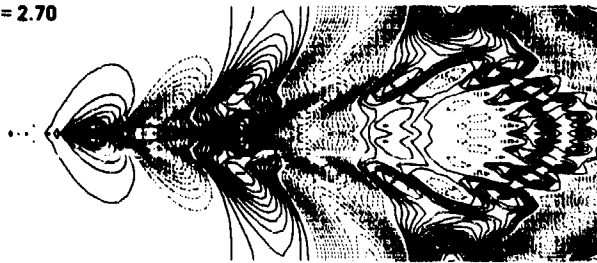
**t = 0.30**



**t = 2.10**



**t = 2.70**



**t = 3.90**

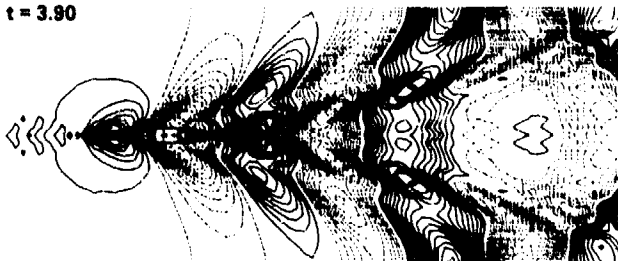
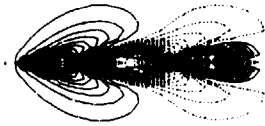
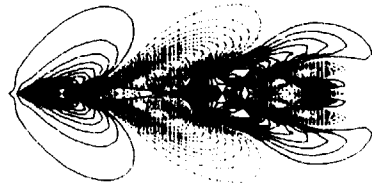


Figure 8. Time Sequence of Free Surface Contours for  $Fr = .385$

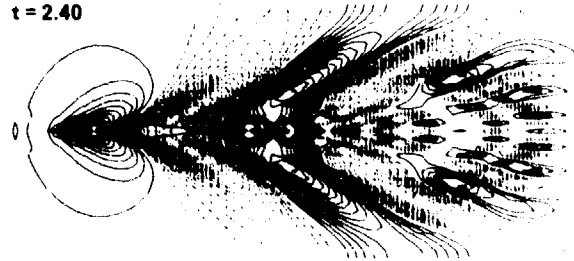
$t = 0.60$



$t = 1.20$



$t = 2.40$



$t = 3.60$

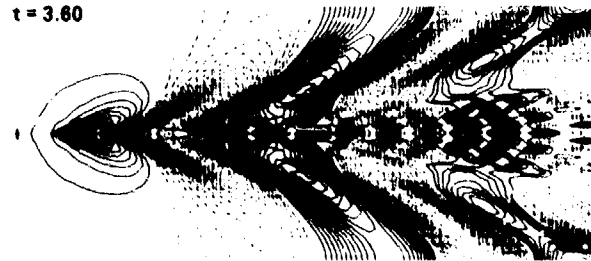


Figure 9. Time Sequence of Free Surface Contours for  $Gr = .503$

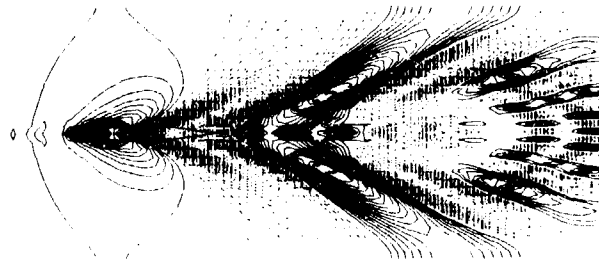


Figure 10. Free Surface Contours for  $Fr = .557$  at  $t = 2.7$

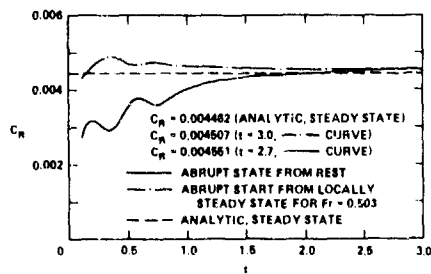


Figure 11. Wave Resistance Coefficient  $C_R$  Versus Time for  $Fr = .557$

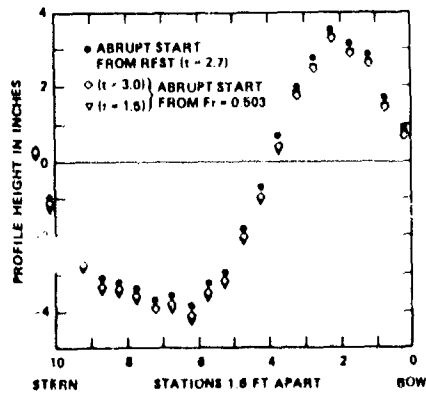


Figure 12. Numerical Wave Profiles for  $Fr = .557$

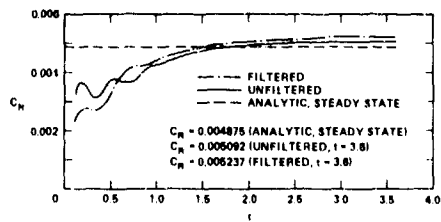


Figure 13. Wave Resistance Coefficient  $C_R$  Versus time for  $Fr = .503$

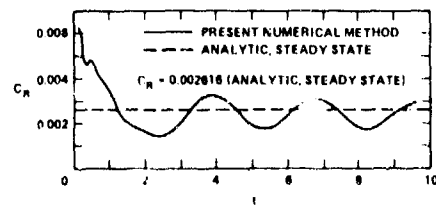


Figure 14. Wave Resistance Versus Time for  $Fr = .3162$  and Hull of Eq. (28)

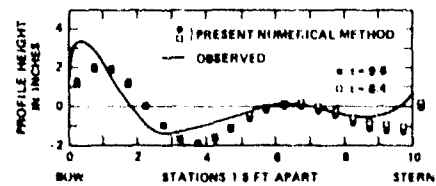


Figure 15. Comparison of Wave Profiles for  $Fr = .3162$  and Hull of Eq. (28)

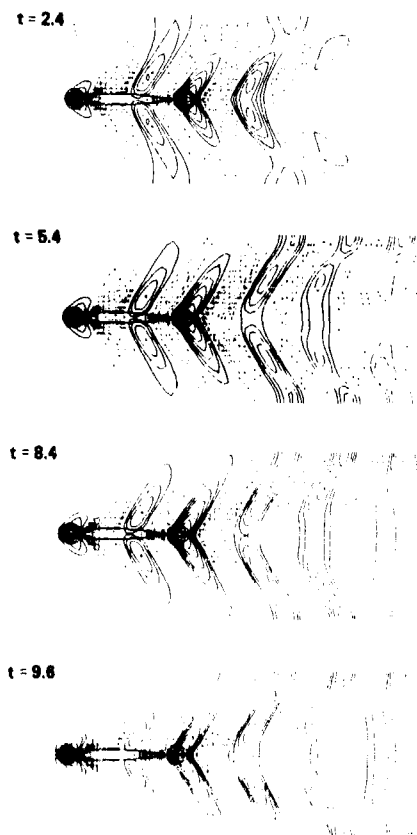


Figure 16. Time Sequence of Free Surface Contours for  $Fr = 0.3162$  and Hull of Eq. (28)

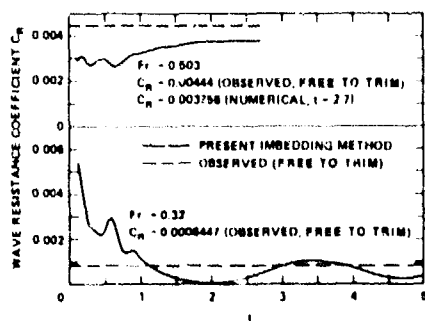


Figure 17. Wave Resistance Versus Time for Selected Froude Numbers (Exact Body Condition)

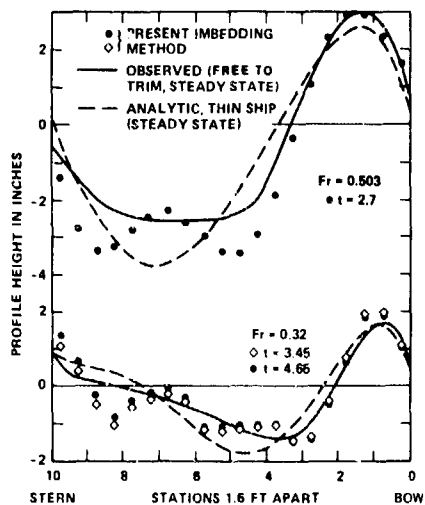


Figure 18. Comparison of Wave Profiles for Selected Froude Numbers (Exact Body Condition)

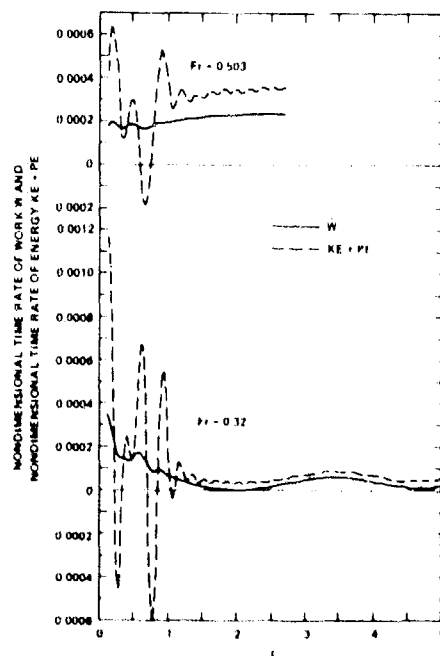


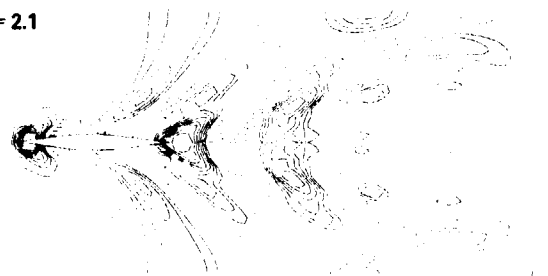
Figure 19. Conservation of Energy Versus Time for Selected Froude Numbers (Exact Body Condition)



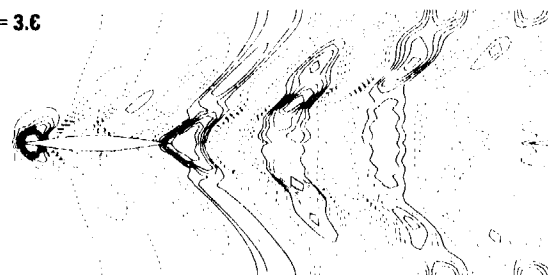
$t = 0.3$



$t = 2.1$



$t = 3.6$



$t = 4.8$

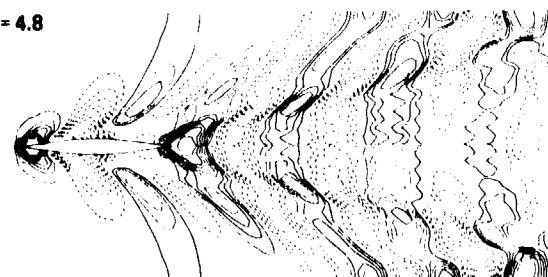
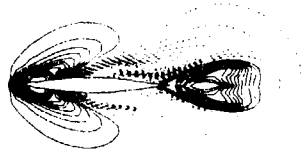
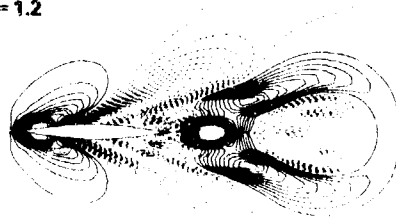


Figure 20. Time Sequence of Free Surface Contours for  $Fr = .32$   
(Exact Body Condition)

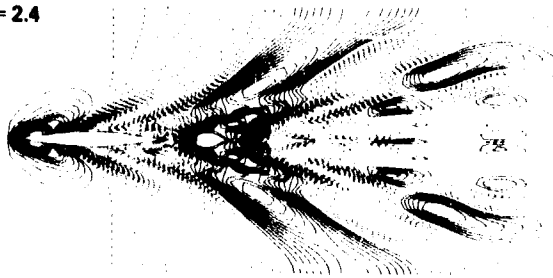
$t = 0.6$



$t = 1.2$



$t = 2.4$



$t = 2.7$

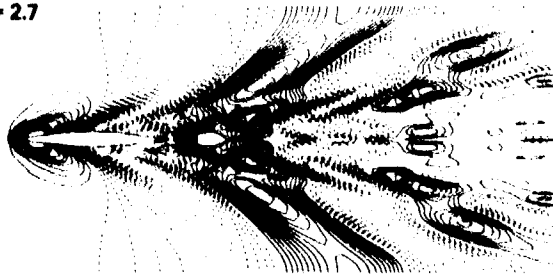


Figure 21. Time Sequence of Free Surface Contours for  $Fr = .503$   
(Exact Body Condition)

#### V. Conclusions

The numerical methods used in this paper have proved useful in efficiently obtaining solutions for transient ship problems. For problems with the exact body condition, finer Cartesian grids than were used in this paper should be used for better local flow resolution in the neighborhood of the body. Variants of the numerical methods used in this paper can be applied efficiently on locally stretched grids.

#### References

1. Lunde, J.K., "On the Linearized Theory of Wave Resistance for Displacement Ships in Steady and Accelerated Motion," Trans. SNAME, Vol. 59, 1951, pp. 24-76; discussion pp. 76-85.
2. Lunde, J.K., "The Linearized Theory of Wave Resistance and its Application to Ship-Shaped Bodies in Motion on the Surface of a Deep, Previously Undisturbed Fluid," Technical and Research Bulletin No. 1-18, SNAME, 1957.
3. Wehausen, J.V., "Effect of the Initial Acceleration Upon the Wave Resistance of Ship Models," Journ. of Ship Research, pp. 38-50, January 1964.
4. Ohring, S., "A Fast Fourth-Order Laplace Solver for Application to Numerical Three-Dimensional Water Wave Problems," Proceedings of the First International Conference on Numerical Ship Hydrodynamics, NBS, Gaithersburg, Maryland (Oct. 1975).
5. Buzbee, B.L., et al, "The Direct Solution of the Discrete Poisson Equation on Irregular Regions," Journ. SIAM, vol. 8, pp. 722-736, (Dec. 1971).
6. Ohring, S. and J.G. Telste, "The Direct Matrix Imbedding Technique for Three-Dimensional Potential Flow and Water Wave Problems With Arbitrarily Shaped Bodies," to be published.
7. Shapiro, R., "Linear Filtering," Math. of Comp., vol. 29, pp. 1094-1097 (Oct. 1975).
8. Shearer, J.R., "A Preliminary Investigation of the Discrepancies between the Calculated and Measured Wavemaking of Hull Forms," North-East Coast Inst. Eng. Shipbldg., Trans. 67, 43-68; discussion, D21-D34 (1951).
9. Wehausen, J.V., "The Wave Resistance of Ships," Advances in Applied Mechanics, vol. 13, Academic Press (1973).
10. Hishida, ., "Investigation on Equivalent Singularity Distributions for Ship Forms-- Particularly on the Effect of the Line Integral," University of Tokyo Report, December 1974.

DISCUSSIONS  
of three papers

EXISTENCE, UNIQUENESS AND REGULARITY OF THE SOLUTION OF NEUMANN-KELVIN  
PROBLEM FOR TWO OR THREE DIMENSIONAL SUBMERGED BODIES

J.C. Derr

A LOCALIZED FINITE-ELEMENT METHOD FOR STEADY, THREE-DIMENSIONAL  
FREE-SURFACE FLOW PROBLEMS

Kwang June Bai

NUMERICAL SOLUTIONS OF TRANSIENT THREE-DIMENSIONAL SHIP WAVE PROBLEMS

Samuel Ohring and John Telste

Invited Discussion

E.O. Tuck  
University of Adelaide

I would like to commence with a few words of general congratulations to the authors presenting papers at this conference using direct numerical computations, whether by field methods (finite element or finite difference) or by boundary-integral-equation methods. I have found, on discussing ship hydrodynamic problems with my mathematical colleagues in the area of numerical analysis, a lack of appreciation of the extreme difficulty faced by those attempting direct numerical solution for free-surface problems. Professional numerical analysts tend to be rather timid characters, who are ever-ready to tell us what we cannot do for fear of leaving too large an error term, and who tend to confine themselves to well-behaved and understood functions, difference schemes or kernels. Our problems are beset with difficulties involved with the non-linearity and unknown shape of the free surface, with rapid variability and singularity of the kernel functions, and with the radiation condition at infinity. Many herculean successful or almost successful efforts have been made, a number of which are reported in this meeting, including the papers by Bai and by Ohring and Telste in this session.

The organizers have perhaps been a little perverse in asking me, a known enemy of the Neumann-Kelvin problem, to be the official discussor of three papers in which this approximation is used, at least in part. Before returning to more complimentary discussion, let me state once again my extreme view on this topic.

There is no rational justification for linearizing the free-surface condition for non-thin surface-piercing bodies. If the body is bluff, it makes big waves. If this is not the case, then not only the free-surface condition, but also the body boundary condition, should be linearized for consistency.

Now an inconsistent problem is not necessarily an incorrect one. The Neumann-Kelvin problem must give results at least as good as Michell's theory; it may give better results. In the spirit of pure scientific research there

is no reason why it should not be tried, just in case this happens. As a mathematician, I can only applaud such efforts. However, it is an expensive undertaking, both in professional time and computer time, so that one would expect any proposals for research on such an irrational but mathematically interesting approach to be subject to a searching evaluation, compared to other perhaps more rational approaches.

In addition, there is serious doubt that a bounded solution of the Neumann-Kelvin problem even exists for the surface-piercing case. If true, this would be an instance of nature making us pay for being irrational. For example, the free-surface elevation at a forward stagnation point is necessarily  $U^2/2g$ , and is not small unless the Froude number is small. Hence linearization cannot be justified near such a point. It seems likely that the price to be paid for such a forbidden action is a singularity in the Neumann-Kelvin problem, at the very least, or at worst a lack of existence of any solution at all.

Doubts of this sort have been expressed in the past by workers such as Brard, and Dr. Derr's fine paper here is a continuation of research along the lines of Brard. However, the present paper confines itself to submerged bodies. In that case there is no such localized singularity, and few of us would have doubted existence of the solution to the Neumann-Kelvin problem. I am sure that Dr. Derr is as keen as I am to see this issue settled for the surface-piercing case.

I also draw Dr. Derr's attention to an existence question with the full non-linear condition. For example, in the paper by Vanden Broeck and myself at this conference, we speculate on non-existence for a particular class of near-bow problems. However, our evidence is purely numerical, and of course one can never prove non-existence numerically; rather one can only demonstrate one's failure to find solution. Careful function-space analysis such as that in the present paper by Derr could perhaps settle this issue also.

The paper by Dr. Bai continues his successful series of studies of free-surface problems using the finite-element method. The most notable feature of the present paper is a full-fledged attack on a three-dimensional problem for a translating ship, a heroic achievement.

The "localized" sense of the title refers to the fact that the finite elements can be terminated on control surfaces quite close to the ship, the region exterior to these surfaces being represented by series of eigenfunctions whose coefficients are appended to the list of nodal unknowns. This approach seems to me clearly superior to one where mesh elements must in principle continue to infinity.

No details are given of the "matrix inversion" or linear-equation-solution procedure used. As mentioned in my discussion of the 1974 paper of Bai and Yeung at the 10th Symposium on Naval Hydrodynamics, relative-efficiency comparison between field and boundary discretization methods depends crucially on the efficiency of iterative inversion of the large (order of thousands) but sparse matrices in the former, compared to direct inversion of the much smaller (order of hundreds) dense matrices in the latter method. This question applies also to the paper by Ohring and Telste who simply describe their inversion as a "fast" Laplace solver. As a proponent of boundary-integral-equation methods, I tend to be skeptical of claims for speed for field methods, which necessarily involve an order of magnitude more unknowns due to the extra dimension. However, I am prepared to be convinced, providing the "time to invert" varies as not more than the  $3/2$  power of the number of unknowns in two dimensions, or the second power in three dimensions. These estimates assume a conservative  $n^3$  time to invert a small dense matrix of order  $n$ ; any improvement on that time would make it even harder for the large-sparse-matrix methods to compete.

Both Bai and Ohring and Telste, use the Neumann-Kelvin approximation implicitly, when they solve with the exact body condition, but linearized free-surface condition. I am sure all would accept that they would really prefer to use the exact free-surface condition, but want first to try their method on a simpler problem, and I certainly have no quarrel with such an approach. In both papers, linearized body-boundary conditions are also used as test cases. Of course there is no need to use direct numerical methods for such problems, since analytic solutions either are already available, or are easy to compute by just evaluating integrals.

In contrast to the paper by Bai, in that by Ohring and Telste the finite-difference mesh must be truncated at an effective infinity. I am surprised at the accuracy obtained by Ohring and Telste with truncation points as close to the ship as they chose. Further evidence as to the effect of changing the truncation points would be welcome. Of course, the fact that they are solving a transient problem helps; the choice of truncation point then mainly affects the transition to steady state. In both numerical papers, I would have liked to have seen also evidence regarding the effect of reducing the mesh spacing.

In conclusion, in spite of doubts expressed above about the significance of the Neumann-Kelvin problem, I feel that the papers under discussion represent a worthwhile advance in our

knowledge in this area. I have the greatest respect for authors such as Derr who are able to pursue deep mathematical analysis to a rigorous existence conclusion, and for the other authors in this session, whose tenacity in the numerical area is no less remarkable.

#### Discussion

by T. Francis Ogilvie

I agree with Tuck that the authors at this meeting have not presented good reasons for undertaking the monstrous chore of solving the Kelvin-Neumann problem numerically. But I feel that Tuck's negative comments are too strong. There are some good reasons to expect that the solution of the Kelvin-Neumann problem may be decidedly more accurate than the solution of any of the usual "consistent" first approximations.

One such reason is that information has become available in recent years showing that diffraction of the ship-generated waves by the ship itself has a significant effect on, say, wave resistance. This effect is close to what is often called "sheltering effect." It should be possible to make a fairly good prediction of such diffraction on the basis of a model involving the linearized free-surface conditions, and the Kelvin-Neumann model should suffice for this purpose. We cannot say that other higher-order effects in thin-ship theory are not also important. But we do know that this one diffraction phenomenon is important and should be included in our theories. This is enough reason by itself to consider the possibility of solving the Kelvin-Neumann problem.

If the advocates of the Kelvin-Neumann problem are successful and if the results are an improvement over existing procedures, then we might better spend our time in trying to justify the problem formulation than in trying to dispute its validity.

#### Discussion

by L. Landweber

According to Dr. Tuck, the Neumann-Kelvin problem is only of mathematical interest and of little value in solving the exact irrotational gravity-wave problem. In a recent paper by Francis Noblesse, it is shown, however, that the N.-K. problem can serve as a good first approximation in an iteration procedure for solving the nonlinear free-surface problem. (This paper has been submitted to the Journal of Ship Research.) He shows this by demonstrating that the nonlinear terms of the free-surface boundary conditions are small relative to the linear terms even for the observed bow wave, at low Froude numbers.

Prof. Ursell has indicated that Fredholm integral equations of the first kind are of little value because a theory concerning the existence and nature of their solutions is lacking. Actually, there is a theorem due to Piccard which gives necessary and sufficient conditions for the existence of a solution for Fredholm integral equations of the first kind. When a

solution exists, this theorem displays the solution, but this is of little value since it is expressible in terms of the eigenfunctions and eigenvalues of the kernel, as an infinite series. It has been shown, however, that numerical solutions can be obtained by means of an iteration formula which can give useful approximations, even when an exact solution does not exist. An example of this is the van Karman method of solving the irrotational, axisymmetric flow about a body of revolution, which, it is known, gives reasonably good solutions when a moderate number of intervals is used, but yields poor solutions when too many intervals, say greater than 20, are employed.

ber of operation steps in the present method is comparable to or less than  $N^{2/3}$  in two dimensions and  $N^2$  in three dimensions. However, one should not emphasize too much the time to invert the matrix by considering only the total number of unknowns. There are more important factors that govern the computation time: they are, for example, the size of the central-core memory space, the time in I/O operations when an out-of-core memory is used, and any capability or features such as the vectorized execution used in the present computer program written for the ASC of Texas Instruments Company.

Author's Reply  
by Sam Ohring and John G. Telste  
to discussion by E.O. Tuck

We would like to mention an important point that was not emphasized in our paper and therefore was overlooked in Professor Tuck's discussion pertaining to the computational time of field methods. The high speed of computation of our finite difference technique is due in large part to the fact that only a very small portion of the grid, mostly in the neighborhood of the ship and free surface, is "involved". Being direct (noniterative), the fast Laplace solver used for the field equation permits us to do this as shown in reference 4.

Author's Reply  
by Kwang June Bai  
to discussion by E.O. Tuck

I would like to thank Prof. Tuck for his comments. I would like to reply to his question about matrix inversion. In my paper, Gaussian elimination is used in solving the matrix equation.

The number of operation-steps required for solving a banded symmetric matrix is proportional to  $NM^2$ , where  $N$  is the total number of unknowns and  $M$  is the half bandwidth. As an illustration, the fluid domain is subdivided into 4-point quadrilateral elements. The total number of nodes are  $I$  and  $J$  along the  $x$ - and  $y$ -axes, respectively, so that the total number of unknowns is  $N = IJ$ . The half bandwidth  $M$  is approximately  $I$  (or  $J$  if  $J < I$ ). The time to invert the matrix is then proportional to  $NI^2 \leq N^2$ . In three dimensions, where  $K$  is the number of nodes along the  $z$ -axis, the half bandwidth becomes  $M = JK \leq N^{2/3}$ , where  $N = IJK$ , and the time to invert is proportional to  $N(JK)^2 \leq N^{7/3}$ . In practical ship problems,  $JK$  is considerably less than  $N^{2/3}$ , since a ship is much longer along the  $x$ -axis than along the  $y$ - or  $z$ -axes. Furthermore, all the matrix elements are zero except the nine non-zero elements in two dimensions. In other words, this banded matrix is still very sparse. This fact can be taken into consideration in the computer program by using an 'if test' to reduce the computation time substantially. Another feature in the finite-element method is that the time to compute the matrix elements is much less than the time to invert the matrix. Therefore, the num-

# NUMERICAL SOLUTION OF THE NEUMANN-KELVIN PROBLEM BY THE METHOD OF SINGULARITIES

P. Guével, G. Delhommeau and J. P. Cordonnier  
Ecole Nationale Supérieure de Mécanique  
44072 Nantes Cedex, France

## Abstract

We present the main lines of the method used for setting up the computer programs giving an estimate of the wave resistance of a surface ship moving at constant speed in calm water. We use the Neumann-Kelvin model based on the following hypothesis: the fluid flow derives from an harmonic potential; the free surface condition is linearised and written on the horizontal plane which is the water level at forward infinity. The gliding condition on the hull is exactly satisfied. The problem is solved by the method of Kelvin singularities distributed over the hull surface. Their density is obtained by solving a Fredholm integral equation. The surface ship case is treated using the notion of line integral. The numerical solution of this equation is approximately obtained by considering the hull as a juxtaposition of plane polygonal elements, bearing a constant singularity distribution. The wave resistance is computed by the Havelock formula. We perfected three computer programs using respectively sources, normal dipoles and mixed distributions. The computing times being extremely long, we have only made tests on the easier case of a completely submerged ellipsoid. The stability of the results is obtained if the hull is discretised with a very large number of elements.

## 1. Introduction

If the influences of boundary layer and wake are neglected, the problem of evaluating the wave resistance of a ship moving at constant speed  $C$  on calm water, is reduced to determining an harmonic potential function  $\phi$ , defined in the whole liquid domain and satisfying the following boundary conditions

$$\frac{\partial \phi}{\partial n} = \dot{C} \cdot \vec{n} \quad \text{on the hull surface } (\Sigma) \quad (1.1)$$

$$\frac{\partial \phi}{\partial n} = \dot{C} \cdot \vec{n} \quad \text{on the free surface } (S) \text{ whose equation is } z=h(x,y) \quad (1.2)$$

$$h = \frac{1}{g} \left\{ C \frac{\partial \phi}{\partial x} - \frac{1}{2} \left[ \left( \frac{\partial \phi}{\partial x} \right)^2 + \left( \frac{\partial \phi}{\partial y} \right)^2 + \left( \frac{\partial \phi}{\partial z} \right)^2 \right] \right\}_{z=h} \quad (1.3)$$

$$\phi \rightarrow 0 \text{ as } x \rightarrow -\infty \quad (1.4)$$

$$\phi \rightarrow 0 \text{ as } z \rightarrow -\infty \quad (1.5)$$

... symbols are explained on figure (1).

The equation (1.1) expresses the gliding condition over the hull  $(\Sigma)$ .  
The equation (1.2) expresses that the free surface is a material surface.  
The equation (1.3) is the Bernoulli equation in which the pressure is a constant over the free surface.  
The equation (1.4) is the non-radiation condition which expresses that the fluid stays still at forward infinity.  
The equation (1.5) expresses that the fluid does not move at very large depth.

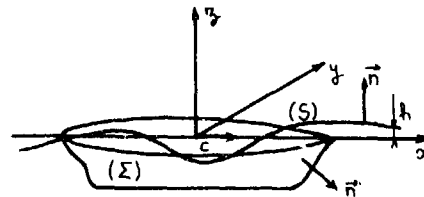


Figure 1

The  $xOy$  plane is the horizontal plane which is the water level at forward infinity.  
The  $Ox$  axis, situated in the longitudinal plane of symmetry, is directed towards the ship's bow.  
The  $Oz$  axis is the upward vertical.  
The free-surface equation is:  $z - h(x,y) = 0$ .  
 $\phi = \phi(x,y,z)$  is the absolute potential expressed in the  $(O,x,y,z)$  coordinate system attached to the ship.

The free-surface conditions (1.2) and (1.3) can be replaced by the following conditions, in which  $V$  is the absolute speed modulus:

$$\frac{\partial^2 \phi}{\partial x^2} + k_0 \frac{\partial \phi}{\partial x} - \frac{1}{C} \frac{\partial V^2}{\partial x} + \frac{1}{2C^2} \nabla^2 \phi \bigg|_{z=h} = 0 \quad (2)$$

$$h = \frac{1}{g} \left( C \frac{\partial \phi}{\partial x} - \frac{V^2}{2} \right) \bigg|_{z=h} \quad (3)$$

$$\text{in which } k_0 = \frac{g}{C^2}$$

In spite of the great simplification which consists in classing the real flow as a perfect fluid flow, the free boundary problem, defined by the system of equations (1) is still too complex to be numerically solved. It is therefore necessary to introduce new approximations simplifying the mathematical model. The one we adopted is the Neumann-Kelvin model [4] which is based on the following hypothesis:

- The fluid, considered as a perfect one, is the seat of a flow deriving from an harmonic potential; this flow is steady with respect to the coordinate system attached to the ship.
- The camber of the free surface elevation is small enough to be able to write the boundary condition, not on the real free surface, but on the plane  $z = 0$  which is the water level at forward infinity.
- The absolute speeds are small enough so that squares are negligible over the whole free surface. In fact, we also neglect the derivatives of the absolute speed squared; this approximation is very doubtful in the vicinity of the ship bow. On the other hand, the gliding condition is exactly satisfied over the hull.

The equations of the simplified problem are:

$$\left. \begin{aligned} \Delta \phi &= 0 & (4.1) \\ \frac{\partial \phi}{\partial n} \Big|_{\Sigma} &= C \cdot n & (4.2) \\ \frac{\partial^2 \phi}{\partial x^2} + k_0 \frac{\partial \phi}{\partial z} \Big|_{z=0} &= 0 & (4.3) \\ \phi &\rightarrow 0 \text{ as } x \rightarrow \infty & (4.4) \\ \phi &\rightarrow 0 \text{ as } z \rightarrow -\infty & (4.5) \end{aligned} \right\} (4)$$

The non-radiation condition at forward infinity is implicitly expressed by allowing the fluid to be slightly energy-dissipative [2].

The equation (4.4) can be suppressed and the equation (4.3) is then replaced by the free surface condition corresponding to nearly perfect fluids:

$$\frac{\partial^2 \phi}{\partial x^2} - \frac{2\varepsilon}{C} \frac{\partial \phi}{\partial x} + k_0 \frac{\partial \phi}{\partial z} \Big|_{z=0} = 0 \quad (4.3')$$

where  $\varepsilon$  is a fictitious viscous coefficient, very small and essentially greater than zero.

The second free surface condition,

$$h = \frac{C}{g} \frac{\partial \phi}{\partial x} \quad (5)$$

is no longer expressed in the boundary problem; this will be used at the end of the computations when the potential is already determined, in order to evaluate the free surface elevation.

To solve the Neumann-Kelvin problem, we used the method of singularities.

## VI. Computing method

The idea on which the method of singularities is based is suggested by the fact that all the equations, formulating the Neumann-Kelvin problem, are linear ones. The potential function  $\phi$  can be considered as a superposition of elementary solutions  $\Psi$  satisfying the Laplace equation, the free surface condition as well as the conditions at infinity.

These elementary potentials can be generated by Kelvin singularities such as sources, dipoles, vortices or multipoles, placed either on the ship hull ( $\Sigma$ ) or inside it. The singularity distribution must be determined, in each particular case, in such a manner that the gliding condition is satisfied in each point of the surface ( $\Sigma$ ). When this is so, the singularity distribution is said to be "kinematically equivalent to the moving hull". Here, we only considered superficial distributions of sources and normal dipoles.

To sum up, to use the method of singularities we will have first to solve a Kelvin problem consisting in building elementary operators generating harmonic potentials satisfying automatically the linearised free surface condition and the conditions at infinity.

Then, in mixing these operators, we will satisfy the gliding condition over the given hull; this last problem is an exterior Neumann problem.

In the exposition, we use the following symbols:

- $\phi = \phi(M)$ , the absolute potential in  $M(x, y, z)$  expressed in the coordinate system attached to the hull.
- $C = C \cdot i_x$ , the speed of the ship.
- $L$ , an arbitrary reference length.
- $\vec{n}$ , the outward normal to the hull surface ( $\Sigma$ ).
- $k_0 = \frac{g}{C^2}$ , the wave number associated with the speed  $C$ .
- $K_0 = \frac{g L}{C^3}$ , the nondimensional wave number.
- $F = \frac{C}{\sqrt{g L}} = \frac{1}{\sqrt{K_0}}$ , the Froude number.
- $\sigma = \sigma(M')$ , the superficial density of sources at  $M'(x', y', z')$  on the hull surface.
- $\mu = \mu(M')$ , the superficial density of normal dipoles in  $M'$ .
- $H(\theta, k)$ , the Kochin function.
- $\hat{H}_k(\theta, k)$ , the modified Kochin function.
- $\hat{f}(\theta, k)$ , the direct Fourier transform of a function  $f(x, y)$ .
- $\rho$ , the mass density of the fluid.

## III. Kelvin operators

### Kelvin source

So is called a point singularity, placed at  $M'(x', y', z' < 0)$ , generating in each point  $M$  of the space  $z < 0$  an harmonic potential whose particularities are:

- It automatically satisfies the linearised free surface condition.
- It goes to zero as  $x \rightarrow \infty$  and  $z \rightarrow -\infty$ .



Its principal value as  $M \rightarrow M'$  is such that

$$\phi_0(M) = -\frac{Q}{4\pi} \frac{1}{|MM'|}$$

which is the potential generated by a source of intensity  $Q$  in an unbounded liquid.

The potential  $\phi$  having these properties can be expressed by:

$$\phi(M) = \phi_1(M) + \psi(M) \quad (6)$$

with

$$\phi_1(M) = -\frac{Q}{4\pi} \left( \frac{1}{|MM'|} + \frac{1}{|MM'_1|} \right) \quad (7)$$

$M'_1$  is the point symmetric to  $M$  with respect to the plane  $z = 0$ .

$$\psi(M) = \frac{Q}{2\pi} R_0 \int_{-\pi/2}^{\pi/2} d\theta \int_0^\infty \frac{e^{k(z+z' + i\omega)} k dk}{k - k_0 \sec^2 \theta + i(0)} \quad (8)$$

assuming

$$\omega = (x-x') \cos \theta + (y-y') \sin \theta. \quad (9)$$

Calculating the integral corresponding to the variable  $k$ , we finally obtain:

$$\phi(M) = -\frac{Q}{2\pi} \left( \frac{1}{|MM'|} + \frac{1}{|MM'_1|} \right) + \frac{Qk_0}{2\pi} R_0 \int_{-\pi/2}^{\pi/2} \sec^2 \theta \frac{d}{d\zeta} \left[ e^\zeta \mathcal{E}_1(\zeta) \right] d\theta \quad (10)$$

with

$$\zeta = \zeta + i\eta \quad (11)$$

$$= k_0 \sec^2 \theta \left\{ z+z' + i[(x-x') \cos \theta + (y-y') \sin \theta] \right\}$$

$\mathcal{E}_1(\zeta)$  being a function we call "modified exponential integral" which is related to the classical exponential integral by:

$$\left. \begin{aligned} \mathcal{E}_1(\zeta) &= E_1(\zeta) & , \text{ if } \operatorname{Im}(\zeta) > 0 \\ \mathcal{E}_1(\zeta) &= E_1(\zeta) - 2i\pi & , \text{ if } \operatorname{Im}(\zeta) < 0 \end{aligned} \right\} \quad (12)$$

where

$$E_1(\zeta) = \int_{\zeta}^{\infty} \frac{e^{-t}}{t} dt, \quad -\pi < \operatorname{Arg} \zeta < \pi$$

The major advantage in introducing this modified exponential integral  $\mathcal{E}_1(\zeta)$  is that the potential  $\phi$  can be expressed by an integral defined inside an interval independent of the relative position of  $M$  and  $M'$ ; moreover, the integral kernel is continued inside this interval. There is no particular care to be taken in differentiating or integrating under the integral sign.

From (5) and (10), the wave elevation is:

$$h = h^P + h^\ell \quad (14)$$

$$h^P = \frac{Qk_0}{2\pi} R_0 \int_{-\pi/2}^{\pi/2} i \sec^3 \theta \left[ e^\zeta \mathcal{E}_1(\zeta) - \frac{1}{\zeta} \right] d\theta \quad (15)$$

$$h^\ell = \begin{cases} \frac{Qk_0}{\pi C} R_0 \int_{-\pi/2}^{\pi/2} \sec^3 \theta e^\zeta d\theta, & \text{if } y-y' > 0 \\ \frac{Qk_0}{\pi C} R_0 \int_{\pi/2}^{\pi/2} \sec^3 \theta e^\zeta d\theta, & \text{if } y-y' < 0 \end{cases} \quad (16)$$

and

$$R = -\operatorname{tg}^{-1} \left( \frac{x-x'}{y-y'} \right).$$

We show, after some elementary calculations, that  $h^P$  goes rapidly to zero when we go far from the source in any direction; its asymptotic value is equal to

$$\frac{Q}{2\pi} \frac{C}{q} \frac{x-x'}{r^3}, \quad r = \sqrt{(x-x')^2 + (y-y')^2}.$$

$h^P$ , decreasing at least as  $\frac{1}{r^2}$  when  $r \rightarrow \infty$ , is the elevation of the nearfield waves.

The asymptotic expression of  $h^\ell$  is obtained by using the stationary phase method;  $h^\ell$  goes to zero as  $1/r$  outside the Kelvin dihedral, as  $1/\sqrt{r}$  inside it and as only  $\frac{1}{\sqrt{r}}$  on the boundary of this dihedral.  $h^\ell$ , which goes to zero much slower than  $h^P$ , is the elevation of the farfield waves.

The figure (2a) shows the free surface elevation corresponding to a point source, immersed at a depth  $H$ , moving at constant speed such as  $k_0 H > 1$ , and having a constant intensity

$$Q = \frac{\pi}{2} C H^2.$$

On the figure (2b), we have drawn the contribution of the nearfield waves; we can see that the corresponding elevation is localised in the vicinity of the source projection onto the plane  $z = 0$ . This remark will be used later on.

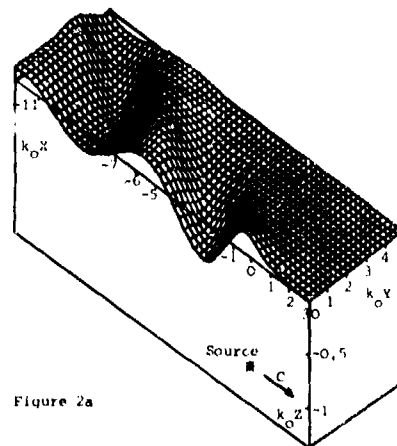


Figure 2a

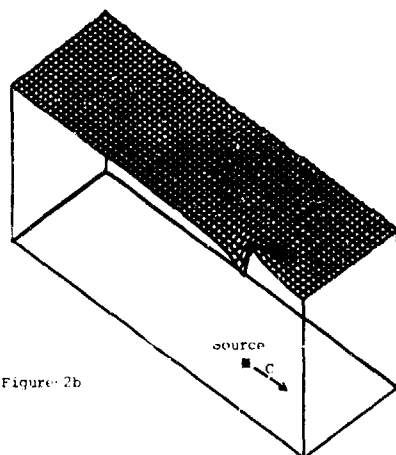


Figure 2b

#### Kelvin dipole

Let  $m_x, m_y, m_z$  be the components of a dipole  $\vec{m}$  having a constant intensity and a fixed direction, moving with an horizontal constant speed  $\vec{C} = C \vec{i}_x$ .

We can immediately express every quantity  $f_d$  depending linearly on  $\vec{m}$  knowing the expression of the same quantity due to a source of intensity  $Q$ ; we only have to use the relation:

$$f_d = \vec{m} \cdot \text{grad}_{M'} \left( \frac{f_s}{Q} \right). \quad (18)$$

In particular, the potential, obtained from the formula (10), is:

$$\begin{aligned} \Phi(M) = & -\frac{\vec{m}}{4\pi} \cdot \text{grad}_{M'} \left( \frac{1}{|\vec{MM}'|} + \frac{1}{|\vec{MM}'_1|} \right) \\ & + \frac{k_0^2}{2\pi^2} R_e \int_{-\frac{\pi}{2}}^{\frac{\pi}{2}} \sec^2 \theta \left[ m_z - 1(m_x \cos \theta + m_y \sin \theta) \right] \\ & \times \frac{d^2}{dz^2} \left[ e^{i\zeta} \mathcal{L}_1(\zeta) \right] d\theta \end{aligned}$$

#### Wave field generated by a singularity distribution

##### 1. Kochin function

Let us recall the following formulas corresponding to the potential due to a Kelvin source:

$$\begin{aligned} v &= \Phi_1 + \Psi \\ \Phi_1 &= -\frac{Q}{4\pi} \left( \frac{1}{|\vec{MM}'|} + \frac{1}{|\vec{MM}'_1|} \right) \\ \Psi &= \frac{Q}{2\pi^2} R_e \int_{-\frac{\pi}{2}}^{\frac{\pi}{2}} d\theta \int_0^\infty \frac{k(z+z'+i0)}{k-k_0 \sec^2 \theta + i(0)} k dk \end{aligned}$$

For a source distribution of intensity  $\sigma(M')$ , localised in a domain  $(\mathcal{D})$ , completely submerged, we have:

$$\begin{aligned} \Phi_1 &= -\frac{1}{4\pi} \int_{\mathcal{D}} \sigma(M') \left[ \frac{1}{|\vec{MM}'|} + \frac{1}{|\vec{MM}'_1|} \right] d\mathcal{D}(M') \\ \text{and} \\ \Psi &= -\frac{2}{\pi} R_e \int_{-\frac{\pi}{2}}^{\frac{\pi}{2}} d\theta \int_0^\infty H(\theta, k) \times \frac{e^{k(z+i(x \cos \theta + y \sin \theta))}}{k-k_0 \sec^2 \theta + i(0)} k dk \end{aligned} \quad (20)$$

where  $H(\theta, k)$  is the Kochin function:

$$\begin{aligned} H(\theta, k) = & -\frac{1}{4\pi} \int_{\mathcal{D}} \sigma(M') \\ & \times e^{k[z'-i(x' \cos \theta + y' \sin \theta)]} d\mathcal{D}(M') \end{aligned} \quad (21)$$

In the case of a dipole distribution of density  $\vec{u}(M')$ , the potential  $\Psi$  is still given by the formula (20) if  $H(\theta, k)$  is replaced by:

$$\begin{aligned} H(\theta, k) = & -\frac{k}{4\pi} \int_{\mathcal{D}} \left[ u_z - i(u_x \cos \theta + u_y \sin \theta) \right] \\ & \times e^{k[z'-i(x' \cos \theta + y' \sin \theta)]} d\mathcal{D}(M'). \end{aligned} \quad (22)$$

Particularly, if we consider, on a surface  $(\Sigma)$  with a normal vector  $\vec{n}$ , a superficial distribution of sources and normal dipoles of intensities  $\sigma(M')$  and  $\vec{u}(M') = u(M') \vec{n}(M')$  respectively we have:

$$\begin{aligned} H(\theta, k) = & -\frac{1}{4\pi} \int_{\Sigma} \sigma(M') \\ & \times e^{k[z'-i(x' \cos \theta + y' \sin \theta)]} d\Sigma(M') \\ & - \frac{1}{4\pi} \int_{\Sigma} u(M') \\ & \times \frac{\partial}{\partial n_{M'}} e^{k[z'-i(x' \cos \theta + y' \sin \theta)]} d\Sigma(M') \end{aligned} \quad (23)$$

$$\begin{aligned} \text{or:} \\ H(\theta, k) = & -\frac{1}{4\pi} \int_{\Sigma} \sigma(M') \\ & \times e^{k[z'-i(x' \cos \theta + y' \sin \theta)]} d\Sigma(M') \\ & - \frac{k}{4\pi} \int_{\Sigma} u(M') \left[ r'-i(p' \cos \theta + q' \sin \theta) \right] \\ & \times e^{k[z'-i(x' \cos \theta + y' \sin \theta)]} d\Sigma(M'), \end{aligned} \quad (23')$$

$p', q', r'$  being the components of the normal vector  $\vec{n}(M')$ .

This superficial distribution of sources and normal dipoles, considered as an ordinary singularity distribution, generates in the whole space a potential  $\psi$ .

If these singularities are distributed over a closed surface  $(\Sigma)$  entirely situated in the domain  $z < 0$ , this potential has two determinations,  $\psi^e$  and  $\psi^i$  corresponding to the exterior and the interior of  $(\Sigma)$ . (Fig. 3).

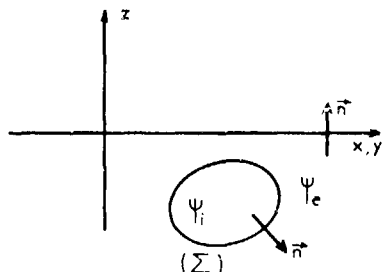


Figure 3

The discontinuities of  $\psi$  and  $\frac{\partial \psi}{\partial n}$  are related to the densities  $\sigma$  and  $\mu$  by :

$$\sigma = \frac{\partial \psi^e}{\partial n} - \frac{\partial \psi^i}{\partial n}, \quad \mu = -(\psi^e - \psi^i) \quad (24)$$

Substituting in (23), one finds

$$H(\theta, k) = \frac{1}{4\pi} \left\{ \int_{\Sigma} \left[ \psi^e \frac{\partial}{\partial n} e^{k[z-i(x \cos \theta + y \sin \theta)]} - \frac{\partial \psi^e}{\partial n} e^{k[z-i(x \cos \theta + y \sin \theta)]} \right] d\sigma - \frac{1}{4\pi} \left\{ \int_{\Sigma} \left[ \psi^i \frac{\partial}{\partial n} e^{k[z-i(x \cos \theta + y \sin \theta)]} - \frac{\partial \psi^i}{\partial n} e^{k[z-i(x \cos \theta + y \sin \theta)]} \right] d\sigma \right\} \right.$$

These integrals can still be modified using Green's second equation. For the first one, we choose the domain  $(D_0)$  exterior to  $(\Sigma)$  situated beneath the plane  $z = 0$ ; for the second one, we choose the interior domain  $(D_1)$ .

Noticing that  $\psi$  and  $e^{k[z-i(x \cos \theta + y \sin \theta)]}$  are harmonic functions, we have :

$$H(\theta, k) = \frac{1}{4\pi} \left\{ \int_{-\infty}^{\infty} \int_{-\infty}^{\infty} \left( k \psi^e - \frac{\partial \psi^e}{\partial z} \right) \Big|_{z=0} \times e^{-ik(x \cos \theta + y \sin \theta)} dx dy \right.$$

that is :

$$H(\theta, k) = \frac{k}{2} \hat{\psi}(\theta, k) - \frac{1}{2} \frac{\partial \hat{\psi}}{\partial z}(\theta, k) \quad (25)$$

$\hat{\psi}(\theta, k)$  and  $\frac{\partial \hat{\psi}}{\partial z}(\theta, k)$  denoting respectively the direct Fourier transforms of  $\psi^e$  and  $\frac{\partial \psi^e}{\partial z}$  for  $z = 0$ .

We can still simplify the expression (25) of  $H(\theta, k)$  noticing that  $\psi$ , a regular function in the whole domain  $z > 0$ , can be written as :

$$\psi = \frac{1}{2\pi} \int_{-\pi}^{\pi} d\theta \int_0^{\infty} \hat{\psi}(\theta, k) \times e^{-k[z-i(x \cos \theta + y \sin \theta)]} k dk \quad z > 0$$

from which we deduce :

$$\frac{\partial \psi}{\partial z} \Big|_{z=0} = -\frac{1}{2\pi} \int_{-\pi}^{\pi} d\theta \int_0^{\infty} k \hat{\psi}(\theta, k) \times e^{ik(x \cos \theta + y \sin \theta)} k dk$$

and therefore :

$$\frac{\partial \hat{\psi}}{\partial z}(\theta, k) = -k \hat{\psi}(\theta, k), \quad (26)$$

Substituting in (25) :

$$H(\theta, k) = k \hat{\psi}(\theta, k) \quad (27)$$

or

$$H(\theta, k) = -\frac{\partial \hat{\psi}}{\partial z}(\theta, k). \quad (28)$$

Let us note that if  $\psi_1$  is the potential due to a given distribution  $(\Sigma_1)$ , associated with a symmetric distribution  $(\Sigma_2)$  placed on a surface  $(\Gamma_1)$ , symmetric to  $(\Gamma_2)$  with respect to the plane  $z = 0$ , we have  $\psi_1 = 2\psi$  for  $z > 0$ ; from (27) we then have :

$$H(\theta, k) = \frac{k}{2} \hat{\psi}_1(\theta, k). \quad (29)$$

The wave resistance generated by a singularity distribution is given by Havelock's formula:

$$R_w = H \pi_1 k_0^2 \int_{-\pi/2}^{\pi/2} \sec^3 \theta \left| H(\theta, k_0 \sec^2 \theta) \right|^2 d\theta \quad (30)$$

in which  $H(\theta, k_0 \sec^2 \theta) = H(\theta)$  is the value of the Kochin function for  $k = k_0 \sec^2 \theta$ .

The computation of the function  $H(\theta)$  can be made using the defining formula (23) or one of the formulas (27), (28) or (29).

## 2. Modified Kochin formula [7]

The preceding results cannot be generalized without care if the singularities are distributed over an open surface  $(\Gamma)$  cutting the plane  $z = 0$  along a contour  $(c)$ . In fact, the theory used to obtain the previous results is essentially based on the identity :

$$\frac{1}{(MM')} \Big|_{z=0} = \frac{1}{\pi} R_0 \int_{-\pi/2}^{\pi/2} d\theta \int_0^{\infty} e^{k(z' + i\omega)} dk \quad (31)$$

A particular study is therefore necessary for evaluating the contribution of the singularities placed close to the plane  $z = 0$ .

Figure 4

$$\Phi(M) = \Phi_1(M) + \Psi(M) \quad (32)$$
$$\varphi(M) = \frac{1}{\pi} R e \int_{-\frac{\pi}{2}}^{\frac{\pi}{2}} d\theta \int_0^{\infty} \hat{\varphi}(0, k) \times e^{k[z+i(x \cos \theta + y \sin \theta)]} k dk \quad (33)$$

The harmonic function  $\varphi$  satisfies the following condition :

$$\left( \frac{\partial^2 \psi}{\partial x^2} - \frac{2v}{C} \frac{\partial \psi}{\partial x} + k_0 \frac{\partial \psi}{\partial z} \right) \Big|_{z=0} = - \left( \frac{\partial^2 \psi}{\partial x^2} \right) \Big|_{z=0},$$

It follows immediately that

$$\hat{\psi}(\theta, k) = \frac{\sec^2 \theta}{k[k - k_0 \sec^2 \theta + 1(0)]} \hat{\phi}_1(\theta, k),$$

$$\left. \frac{\partial^2 \Phi_1}{\partial x^2} \right|_{x=0}$$
$$\varphi = \frac{1}{\pi} R_0 \int_{-\frac{\pi}{2}}^{\frac{\pi}{2}} \sec^2 \theta \, d\theta \int_0^{\widehat{\varphi}_1(\theta, k)} \frac{e^{k[x+1(x \cos \theta + y \sin \theta)]}}{k - k_0 \sec^2 \theta + 1(0)} dk \quad (34)$$
$$\eta(\theta, k) = -\frac{\sec^2 \theta}{2k} \hat{\phi}_1(\theta, k) \quad (35)$$

We can now show that the difference,  $\eta(\theta, k) - H(\theta, k)$ , can be expressed in term of a line integral in which we find the values taken by the superficial densities  $\sigma$  and  $\mu$  along the waterline (c).

3. Line integral [3], [4], [7]

$$\left( \frac{\partial^2}{\partial x^2} \right)_{z=0}$$
 is defined by :

$$\hat{\chi}_1(0, k) = \frac{1}{2\pi} \iint_{SL} \frac{\partial^2 \phi}{\partial x^2} e^{-ik(x \cos \theta + y \sin \theta)} dS + \frac{1}{2\pi} \iint_{SE} \frac{\partial^2 \phi}{\partial x^2} e^{-ik(x \cos \theta + y \sin \theta)} dS,$$

$\phi_1^i$  is the value of  $\phi_1$  on the free surface (SF) inside the hull. (Fig. 5).

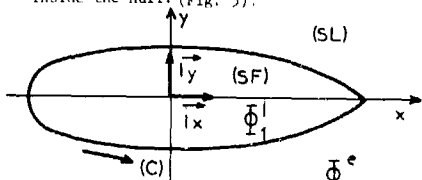


Figure 5

We can modify this expression of  $\Phi_1(\theta, k)$  :

$$\hat{\phi}_1(\theta, k) = -\frac{k^2 \cos^2 \theta}{2\pi} \left\{ \phi_1 \right\}_{SL+SF} \\ + \frac{1}{2\pi} \left\{ \frac{\partial}{\partial x} \left\{ \left[ ik \cos \theta \phi_1 + \frac{\partial \phi_1}{\partial x} \right] \right. \right. \\ \left. \left. \times e^{-ik(x \cos \theta + y \sin \theta)} \right\} \right\}_{SL} \\ + \frac{1}{2\pi} \left\{ \frac{\partial}{\partial x} \left\{ \left[ ik \cos \theta \phi_1 + \frac{\partial \phi_1}{\partial x} \right] \right. \right. \\ \left. \left. \times e^{-ik(x \cos \theta + y \sin \theta)} \right\} \right\}_{SF} \\ \left. \times e^{-ik(x \cos \theta + y \sin \theta)} \right\}_{SL}$$

The two last integrals can be modified using the Green-Riemann equation in the domains (SL) and (SF) where they are respectively defined.

Thus, we have:

$$\begin{aligned} \hat{\phi}_1(\theta, k) &= -k^2 \cos^2 \theta \cdot \hat{\phi}_1(\theta, k) \\ &- \frac{1}{2\pi} \int_C \left[ ik \cos \theta (\phi_1^e - \phi_1^i) + \left( \frac{\partial \phi_1^e}{\partial x} - \frac{\partial \phi_1^i}{\partial x} \right) \right] \\ &\quad \times e^{-ik(x \cos \theta + y \sin \theta)} dy \end{aligned} \quad (36)$$

the contour (c) being described in the positive direction.

From the defining formula (35), the modified Kochin function is then expressed by:

$$\begin{aligned} \mathcal{K}(\theta, k) &= \frac{k}{2} \hat{\phi}_1(\theta, k) + \frac{\sec^2 \theta}{4k} \\ &\times \left[ ik \cos \theta (\phi_1^e - \phi_1^i) + \left( \frac{\partial \phi_1^e}{\partial x} - \frac{\partial \phi_1^i}{\partial x} \right) \right] \\ &\times e^{-ik(x \cos \theta + y \sin \theta)} dy \end{aligned} \quad (37)$$

The equation (29) can be generalized using the same proof: one always has:

$$H(\theta, k) = \frac{k}{2} \hat{\phi}_1(\theta, k) \quad (29)$$

even if the singularity distribution ends on the plane  $z = 0$ .

Substituting in (37), we obtain:

$$\mathcal{K}(\theta, k) = H(\theta, k) + \delta H(\theta, k) \quad (38)$$

with

$$\begin{aligned} \delta H(\theta, k) &= \frac{\sec^2 \theta}{4k} \int_C \left[ ik \cos \theta (\phi_1^e - \phi_1^i) + \left( \frac{\partial \phi_1^e}{\partial x} - \frac{\partial \phi_1^i}{\partial x} \right) \right] \\ &\quad \times e^{-ik(x \cos \theta + y \sin \theta)} dy \end{aligned} \quad (39)$$

The line integral  $\delta H(\theta, k)$  appears to be a correction which has to be made to the classical Kochin function to obtain the "modified Kochin function".

The terms  $(\phi_1^e - \phi_1^i)$  and  $(\frac{\partial \phi_1^e}{\partial x} - \frac{\partial \phi_1^i}{\partial x})$  in  $\delta H(\theta, k)$  are directly related to the nature of superficial singularity chosen for generating the potential  $\phi_1$ .

For a superficial source distribution of intensity  $\sigma$ , we simply have:

$$\left. \begin{aligned} \phi_1^e - \phi_1^i &= 0 \\ \frac{\partial \phi_1^e}{\partial x} - \frac{\partial \phi_1^i}{\partial x} &= \sigma(\vec{n}, \vec{i}_x) \end{aligned} \right\} \quad (40)$$

$\vec{n}$  is the outward normal to the surface (F) in a point belonging to the contour (c).

For a superficial normal dipole distribution of intensity  $\mu$ , we have:

$$\left. \begin{aligned} \phi_1^e - \phi_1^i &= -\mu \\ \frac{\partial \phi_1^e}{\partial x} - \frac{\partial \phi_1^i}{\partial x} &= - \left[ \frac{\partial \mu}{\partial \xi} (\vec{\ell}, \vec{i}_x) + \frac{\partial \mu}{\partial s} (\vec{s}, \vec{i}_x) \right] \end{aligned} \right\} \quad (41)$$

$\vec{\ell}$  is the unit vector tangent to the contour (c) oriented in the positive direction.

$\vec{s} = \vec{n} \wedge \vec{\ell}$  is the unit vector normal to  $\vec{n}$  and to  $\vec{\ell}$  such that the trihedral  $(\vec{n}, \vec{\ell}, \vec{s})$  is right-handed (Fig. 6).

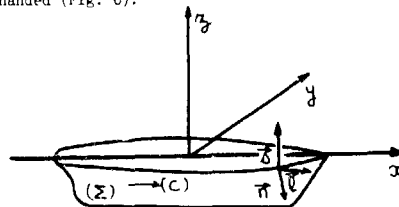


Figure 6

The potential  $\delta \phi$ , associated with the line integral, is expressed from (20) and (39):

$$\begin{aligned} \delta \phi &= \frac{1}{2\pi} \int_C \left( \phi_1^e - \phi_1^i \right)_{M'} dy' R_c \int_{-\pi/2}^{\pi/2} i \sec^2 \theta d\theta \\ &\times \int_0^\infty \frac{k(z + i0)}{k - k_0 \sec^2 \theta + i(0)} k dk \\ &- \frac{1}{2\pi} \int_C \left( \frac{\partial \phi_1^e}{\partial x} - \frac{\partial \phi_1^i}{\partial x} \right)_{M'} dy' R_c \int_{-\pi/2}^{\pi/2} \sec^2 \theta d\theta \\ &\times \int_0^\infty \frac{k(z + i0)}{k - k_0 \sec^2 \theta + i(0)} dk, \end{aligned}$$

Both integrals corresponding to the variable  $k$  can be performed using the modified exponential integral: in fact, we have:

$$\begin{aligned} \int_0^\infty \frac{k(z + i0)}{k - k_0 \sec^2 \theta + i(0)} k dk &= k_0 \sec^2 \theta \frac{d}{d\ell} \left[ e^{\ell} \mathcal{E}_1(\ell) \right] \\ \int_0^\infty \frac{k(z + i0)}{k - k_0 \sec^2 \theta + i(0)} dk &= e^{\ell} \mathcal{E}_1(\ell), \end{aligned}$$

$$\text{where } \ell \text{ is now: } \ell = k_0 \sec^2 \theta (z + i0) \quad (42)$$

Finally, we deduce the expression of the potential associated with the line integral :

$$\Delta \varphi(M) = -\frac{k_0}{2\pi^2} \int_C \left( \frac{\partial \varphi}{\partial x} - \frac{\partial \varphi}{\partial y} \right)_{M'} dy' R_e \int_{-\frac{\pi}{2}}^{\frac{\pi}{2}} \frac{1}{i} \sec^2 \theta \times \frac{d}{d\zeta} \left[ e^{i\zeta} \mathcal{L}_1(\zeta) \right] d\theta \quad (43)$$

$$- \frac{1}{2\pi^2} \int_C \left( \frac{\partial \varphi}{\partial x} - \frac{\partial \varphi}{\partial y} \right)_{M'} dy' R_e \int_{-\frac{\pi}{2}}^{\frac{\pi}{2}} \sec^2 \theta \times e^{i\zeta} \mathcal{L}_1(\zeta) d\theta.$$

The values of the discontinuities  $\mathcal{L}_1^+ - \mathcal{L}_1^-$ ,  $\frac{\partial \mathcal{L}_1^+}{\partial x} - \frac{\partial \mathcal{L}_1^-}{\partial x}$  are given by the equation (40) or (41) if the superficial singularities distributed over the hull surface are either sources or normal dipoles.

#### Singularity distribution kinematically equivalent to a hull

In all the preceding computations, we considered Kelvin singularities to have the following properties :

- they induce in the whole space  $z > 0$ , a speed field  $\vec{V}$  deriving from an harmonic potential  $\varphi$ ;
- they satisfy the linearised free surface condition ;
- they satisfy the conditions at infinity for  $x \rightarrow \infty$  and  $z \rightarrow \infty$ .

We now have to find, in each particular case, a Kelvin singularity distribution, kinematically equivalent to the given hull : such a distribution must satisfy the gliding condition :

$$\frac{\partial \varphi}{\partial n} = \dot{C} \cdot \vec{n}$$

in every point of the hull surface  $\Sigma$ .

Writing this gliding condition, we finally obtain an integral equation whose solution is the superficial density of the considered singularities.

We established this integral equation for superficial distributions of sources, normal dipoles and for a mixture of sources and normal dipoles called mixed distribution.

#### 1. Integral equation for a source distribution

From (40), (43), (44), superficial sources of density  $\sigma = \sigma(M')$ , distributed over a surface  $(E)$  with a contour  $(c)$  in the plane  $z = 0$ , generate in the whole space  $z > 0$  a potential :

$$\varphi(M) = \iint_E \sigma(M') A(M, M') dE(M') + \int_C \sigma(M') \mathcal{H}(M, M') d\ell(M'), \quad (44)$$

with

$$A(M, M') = -\frac{1}{4\pi} \left[ \frac{1}{|MM'|} + \frac{1}{|MM'_1|} - \frac{2k_0}{\pi} \times R_e \int_{-\frac{\pi}{2}}^{\frac{\pi}{2}} \sec^2 \theta \left[ e^{i\zeta} \mathcal{L}_1(\zeta) - \frac{1}{\zeta} \right] d\theta \right] \quad (45)$$

and

$$\mathcal{H}(M, M') = -\frac{1}{2\pi^2} \left[ (\vec{n}, \vec{i}_x) (\vec{\ell}, \vec{i}_y) \right]_{M'} \times R_e \int_{-\frac{\pi}{2}}^{\frac{\pi}{2}} \sec^2 \theta e^{i\zeta} \mathcal{L}_1(\zeta) d\theta, \quad (46)$$

The normal component of the speed in a point  $M$  belonging to the surface  $(E)$  is then :

$$(\vec{V}, \vec{n})_M = \iint_E \sigma(M') K(M, M') dE(M') + \int_C \sigma(M') \chi(M, M') d\ell(M')$$

with

$$K(M, M') = \vec{n}(M) \cdot \text{grad}_{M'} A(M, M'), \quad (47)$$

$$\chi(M, M') = \vec{n}(M) \cdot \text{grad}_M \mathcal{H}(M, M'). \quad (48)$$

In a point  $M_p$ , infinitely close to a point  $M$  but situated in the domain outside the hull, we have, taking care of the discontinuity of the normal speed induced by a source distribution :

$$(\vec{V}, \vec{n})_{M_p} = \frac{1}{2} \sigma(M) + \iint_E \sigma(M') K(M, M') dE(M') + \int_C \sigma(M') \chi(M, M') d\ell(M').$$

Whence, finally, the integral equation which has to be satisfied in each point  $M$  of

$$\frac{1}{2} \sigma(M) + \iint_E \sigma(M') K(M, M') dE(M') + \int_C \sigma(M') \chi(M, M') d\ell(M') = (\dot{C}, \vec{n})_M. \quad (49)$$

## 2. Integral equation for a normal dipole distribution

From (18), (41), (43), a superficial normal dipole distribution of density  $\mu = \mu(M')$ , generates a potential:

$$\begin{aligned} \Phi(M) = & \iint_{\Sigma} \mu(M') B(M, M') d\Omega(M') \\ & + \int_C \mu(M') \mathcal{B}(M, M') d\ell(M') \\ & + \int_C \left( \frac{\partial \mu}{\partial n} \right)_{M'} \mathcal{B}(M, M') d\ell(M') \\ & + \int_C \left( \frac{\partial \mu}{\partial n} \right)_{M'} \omega(M, M') d\ell(M') \end{aligned} \quad (50)$$

with:

$$B(M, M') = \vec{n}(M') \cdot \vec{\text{grad}}_{M'} A(M, M') \quad (51)$$

where  $A(M, M')$  is the already defined function given by (45), and:

$$\begin{aligned} \mathcal{B}(M, M') = & \frac{\lambda_0}{2\pi} \left( \vec{\ell} \cdot \vec{i}_y \right)_{M'} R_c \int_{-\frac{\pi}{2}}^{\frac{\pi}{2}} \sec^2 \theta \\ & \times \left[ e^{\frac{1}{2} \mathcal{C}_1} \mathcal{C}_1(z) - \frac{1}{\ell} \right] d\theta, \end{aligned} \quad (52)$$

$$\begin{aligned} \omega(M, M') = & \frac{1}{2\pi^2} \left[ \left( \vec{\ell} \cdot \vec{i}_y \right) \left( \vec{\ell} \cdot \vec{i}_x \right) \right]_{M'} R_c \int_{-\frac{\pi}{2}}^{\frac{\pi}{2}} \sec^2 \theta \\ & \times e^{\frac{1}{2} \mathcal{C}_1} \mathcal{C}_1(z) d\theta, \end{aligned} \quad (53)$$

$$\begin{aligned} \omega(M, M') = & \frac{1}{2\pi^2} \left[ \left( \vec{\ell} \cdot \vec{i}_y \right) \left( \vec{s} \cdot \vec{i}_x \right) \right]_{M'} R_c \int_{-\frac{\pi}{2}}^{\frac{\pi}{2}} \sec^2 \theta \\ & \times e^{\frac{1}{2} \mathcal{C}_1} \mathcal{C}_1(z) d\theta. \end{aligned} \quad (54)$$

Here, the gliding condition is directly expressed in writing that the potential  $\Phi^1$ , generated inside the hull, is equal to the leading potential  $\Phi_E = C.x$ .

Whence, taking care of the potential discontinuity due to a normal dipole distribution, the integral equation which has to be satisfied in each point  $M$  of the hull ( $\Sigma$ ) is

$$\begin{aligned} \frac{1}{2} \mu(M) + & \iint_{\Sigma} \mu(M') B(M, M') d\Omega(M') \\ & + \int_C \mu(M') \mathcal{B}(M, M') d\ell(M') \\ & + \int_C \left( \frac{\partial \mu}{\partial n} \right)_{M'} \mathcal{B}(M, M') d\ell(M') \\ & + \int_C \left( \frac{\partial \mu}{\partial n} \right)_{M'} \omega(M, M') d\ell(M') = (Cx)_M. \end{aligned} \quad (55)$$

## 3. Integral equation for a mixed distribution

Here, we consider the Green mixed distribution made of superficial distributions of sources and normal dipoles whose densities are:

$$\left. \begin{aligned} \sigma(M) &= \left( \frac{\partial \Phi}{\partial n} \right)_{M'} \\ \mu(M) &= -\dot{\Phi}(M) \end{aligned} \right\} \quad (56)$$

The source intensity is known, since, from the gliding condition, we have  $\frac{\partial \Phi}{\partial n} = \vec{C} \cdot \vec{i}$  and therefore:

$$\sigma(M) = (\vec{C} \cdot \vec{n})_M \quad (57)$$

In order to determine the dipole distribution which is still unknown, we write that the Green mixed distribution generates inside the hull a potential  $\Phi^1$  which is identically zero; we thus obtain the following integral equation:

$$\begin{aligned} \frac{1}{2} \mu(M) + & \iint_{\Sigma} \mu(M') B(M, M') d\Omega(M') \\ & + \int_C \mu(M') \mathcal{B}(M, M') d\ell(M') \\ & + \int_C \left( \frac{\partial \mu}{\partial n} \right)_{M'} \mathcal{B}(M, M') d\ell(M') \\ & + \int_C \left( \frac{\partial \mu}{\partial n} \right)_{M'} \omega(M, M') d\ell(M') \\ & - \iint_{\Sigma} (\vec{C} \cdot \vec{n})_{M'} A(M, M') d\Omega(M') \\ & + \int_C (\vec{C} \cdot \vec{n})_{M'} \mathcal{A}(M, M') d\ell(M') \end{aligned} \quad (58)$$

## 4. Equivalent linear system

When the solution is sought in the form of a superficial singularity distribution, one obtains integral equations which can be approximately solved by considering singularity densities remaining constant over very small elements belonging to the hull. The hull surface is then discretised in  $N$  plane quadrilateral elements  $a_j$

bearing a uniform singularity distribution; the elements  $s_j$  numbered from 1 to  $M$ , ending at the free surface, cut out of the waterline  $M$  elements of arc  $\ell_j$ .

Thus, in the case of superficial distribution of sources, the integral equation (49) is replaced by the following linear system of  $N$  equations with  $N$  unknowns, the gliding condition being satisfied at the center  $M_i$  of each element  $s_i$ :

$$\frac{\sigma_i}{2} + \sum_{j=1}^N \sigma_j K_{ij} + \sum_{j=1}^M \sigma_j \chi_{ij} = (\vec{C} \cdot \vec{n})_{M_i}, \quad i = 1, 2, \dots, N \quad (59)$$

$$K_{ij} = \iint_{s_j} K(M_i, M'), dE(M') \quad (60)$$

$$\chi_{ij} = \int_{\ell_j} \chi(M_i, M'), d\ell(M') \quad (61)$$

The coefficients  $K_{ij}$  are called "influence coefficient" of the element  $s_j$  upon the point  $M_i$ ; likewise,  $\chi_{ij}$  is the influence coefficient of the arc  $\ell_j$  upon the point  $M_i$ .

In the case of a superficial distribution of normal dipoles, an additional difficulty appears due to the fact that, in the line integral, there are terms depending not only on the density  $\mu(M')$ , but also on the derivatives  $(\frac{\partial \mu}{\partial \ell})_{M'}$  and  $(\frac{\partial \mu}{\partial s})_{M'}$ .

$$\text{Concerning the term: } \int_C (\frac{\partial \mu}{\partial \ell})_{M'} \Omega(M, M'), d\ell(M')$$

which is in equations (55) and (56), the difficulty is immediately removed in integrating by parts; as  $\mu$  is a uniform function, at least for a symmetrical hull moving without incidence, we simply have:

$$\int_C (\frac{\partial \mu}{\partial \ell})_{M'} \Omega(M, M'), d\ell(M') = \int_C \mu(M') d[\Omega(M, M')].$$

On the other hand, the contribution of the term

$$(\frac{\partial \mu}{\partial s})_{M'}$$

is not so easy to compute.

A way which could be used to solve the discretized problem is to consider the terms  $(\frac{\partial \mu}{\partial s})_{M'}$  for

$1 \leq j \leq M$  as additional unknowns; at that moment, the condition  $\phi^I = 0$  or  $\phi^I = 0$  should be satisfied not only at the center of the element  $s_1$  but also at the middle of the segment  $\ell_1$ . This should give a linear system of  $N+M$  equations with  $N+M$  unknowns.

But in the particular case of a hull surface ending perpendicularly at the free surface, this stratagem doesn't work; in fact, the integral which depends on  $(\frac{\partial \mu}{\partial s})_{M'}$ , disappears due to the fact that the product  $(\vec{s} \cdot \vec{i}_x)$  is zero.

Up to now, we limit ourselves in considering hulls having this characteristic: thus, we are not able to assert that the proposed stratagem can be easily used to solve the general case.

##### 5. Explicit form of the influence coefficients

Before writing a computer program solving the Neumann Kelvin problem, we have to perform analytical computations as completely as possible in order to perform numerically only the quadratures which are absolutely necessary.

The surface and the line integrals occurring inside the influence coefficients corresponding to source or dipole distributions cannot be exactly computed unless the elements  $s_j$  are plane polygonal elements.

The hull surface ( $E$ ) will thus be discretised taking care of this necessity; besides, it seems that this approximation, which is discretising the hull into plane elements, is consistent with the one which is assuming that the singularity density remains constant on each of these elements.

Whatever the type of singularity adopted, all influence coefficients are practically computed in the same way. Thus, we only explain the method used to express the coefficient  $K_{ij}$  occurring in the linear system (59); from equations (45), (47) and (60), this is:

$$K_{ij} = k_{ij} + \tilde{k}_{ij} \quad (62)$$

with

$$k_{ij} = -\frac{1}{4\pi} n(M_i) \cdot \iint_{s_j} \text{grad}_{M_i} \left( \frac{1}{|M_i M'|} + \frac{1}{|M_i M'_1|} \right) \chi dE(M') \quad (63)$$

$$\tilde{k}_{ij} = -\frac{k_0^2}{2\pi} R_e \int_{-\frac{\pi}{2}}^{\frac{\pi}{2}} \left[ r_1 + 1/p_1 \cos \theta + q_1 \sin \theta \right]$$

$$\chi \sec^2 \theta \sin \theta \iint_{s_j} G(\zeta) dE(M'), \quad (64)$$

$k_1, q_1, r_1$  are the components of the normal vector  $\vec{n}(M_i)$ ;  $G(\zeta)$  is the function  $e^{\zeta} \mathcal{E}_1(\zeta)$  and  $G(\zeta)$  its second derivative.

The coefficient  $k_{ij}$  is simply the normal speed generated, in the point  $M_i$  on the element  $s_i$ , by the element  $s_j$  and its symmetrical one  $s_j^*$  with respect to the plane  $\sigma = 0$ , if they are bearing a constant distribution of ordinary sources with a unit intensity.



This coefficient, which occurs also in solving the problem of a moving solid inside an unbounded fluid, is easily computed from the Hess and Smith formulas.

Then, we only have to put the coefficient  $\tilde{k}_{ij}$  into a form as sophisticated as possible; as it cannot be expressed in an analytical form, we compute only the surface integral:

$$I = I(\theta) = \iint_{s_j} \ddot{G}(\zeta) d\Omega(M') \quad (65)$$

Let  $O$  be any point of the element  $s_j$  and  $P_j$  a moving point of it. The equation of the element plane is then:

$$\vec{n}_j \cdot \vec{OP}_j = 0$$

or

$$p_j(x_j - x_0) + q_j(y_j - y_0) + r_j(z_j - z_0) = 0 \quad (66)$$

$\vec{n}_j$ , whose components are  $p_j, q_j, r_j$ , is the unit vector normal to the element.

On  $s_j$ , the variable  $\zeta$ :

$$\zeta = k_0 \sec^2 \theta \left\{ z_i + z_j + i[(x_i - x_j) \cos \theta + (y_i - y_j) \sin \theta] \right\} \quad (67)$$

is only a function of two independent variables.

To begin with, let assume  $p_j \neq 0$ ; from (66) we can write:

$$x_j = x_0 - \frac{q_j}{p_j}(y_j - y_0) + \frac{r_j}{p_j}(z_j - z_0)$$

so that  $\zeta$  could be considered as a function of two independent variables  $y_j, z_j$ .

Therefore, the surface integral  $I$  can be written in the form:

$$I = \frac{\cos^2 \theta}{k_0} \frac{1}{p_j + i r_j \cos \theta} \iint_{s_j} p_j \frac{\partial}{\partial z_j} \ddot{G}(\zeta) dS$$

We can use the Stokes formula; we obtain:

$$I = - \frac{\cos^2 \theta}{k_0} \frac{1}{p_j + i r_j \cos \theta} \int_{C_j} \ddot{G}(\zeta) dy_j \quad (68)$$

or

$$I = - \frac{\cos^2 \theta}{k_0} \frac{p_j - i r_j \cos \theta}{p_j^2 + r_j^2 \cos^2 \theta} \int_{C_j} \ddot{G}(\zeta) dy_j \quad (69)$$

$C_j$  being the contour of the element  $s_j$ , described in the positive direction determined by the normal vector  $\vec{n}_j$ :

If  $q_j \neq 0$ , we can write in the same way:

$$I = \frac{\cos^2 \theta}{k_0} \frac{q_j - i r_j \cos \theta}{q_j^2 + r_j^2 \cos^2 \theta} \int_{C_j} \ddot{G}(\zeta) dx_j \quad (70)$$

The comparison of (69) and (70) gives a way to express  $I$  in a form which is always valid:

$$I = \frac{\cos^2 \theta}{k_0} \int_{C_j} \left\{ \ddot{G}(\zeta) [(q_j - i r_j \sin \theta) dx_j - (p_j - i r_j \cos \theta) dy_j] \right\} \quad (71)$$

This equation is valid for any plane element of any shape: we go on with the computations in the case of polygonal elements.

The contour  $C_j$  is then made of  $m$  segments  $s_{j,k}$  whose ends  $P_{j,k}, P_{j,k+1}$  are numbered from 1 to  $m$ , turning in the positive direction;  $I$  is then:

$$I = \frac{\cos^2 \theta}{k_0} \sum_{k=1}^m I_{j,k} \quad (72)$$

with

$$I_{j,k} = (q_j - i r_j \sin \theta) \int_{x_{j,k}}^{x_{j,k+1}} \ddot{G}(\zeta) dx_j - (p_j - i r_j \cos \theta) \int_{y_{j,k}}^{y_{j,k+1}} \ddot{G}(\zeta) dy_j$$

On a straight element,  $\zeta$  is a linear function of one of the variables  $x_j, y_j$  or  $z_j$ ; we have, in particular, on the segment  $s_{j,k}$ , if  $\zeta_{j,k+1} - \zeta_{j,k} \neq 0$ ,

$$dx_j = \frac{x_{j,k+1} - x_{j,k}}{\zeta_{j,k+1} - \zeta_{j,k}} d\zeta$$

$$dy_j = \frac{y_{j,k+1} - y_{j,k}}{\zeta_{j,k+1} - \zeta_{j,k}} d\zeta$$

and therefore:

$$I_{j,k} = \left[ (q_j - i r_j \sin \theta) (x_{j,k+1} - x_{j,k}) - (p_j - i r_j \cos \theta) (y_{j,k+1} - y_{j,k}) \right] \times \frac{G(\zeta_{j,k+1}) - G(\zeta_{j,k})}{\zeta_{j,k+1} - \zeta_{j,k}} \quad (74)$$

For  $\zeta_{j,k+1} - \zeta_{j,k} = 0$ , we have :

$$I_{j,k} = \left[ (q_j - ir_j \sin \theta) (x_{j,k+1} - x_{j,k}) - (p_j - ir_j \cos \theta) (y_{j,k+1} - y_{j,k}) \right] \bar{G}(\zeta_k) \quad (75)$$

Finally, we can write the influence coefficient  $\hat{K}_{ij}$  :

$$\hat{K}_{ij} = \frac{k_0}{2a^2} R_e \left\{ \begin{aligned} & \int_{-\frac{\pi}{2}}^{\frac{\pi}{2}} \left[ x_i + i(p_i \cos \theta + q_i \sin \theta) \right] \\ & \times K_{ij}(\theta) \sec^2 \theta d\theta \\ & K_{ij}(\theta) = \sum_{k=1}^m \left[ (q_j - ir_j \sin \theta) (x_{j,k+1} - x_{j,k}) - (p_j - ir_j \cos \theta) (y_{j,k+1} - y_{j,k}) \right] K_{ij,k} \\ & K_{ij,k} = \frac{1}{\zeta_{j,k+1} - \zeta_{j,k}} \left[ G(\zeta_{j,k+1}) - G(\zeta_{j,k}) \right] \\ & \quad \text{if } |\zeta_{j,k+1} - \zeta_{j,k}| > \epsilon \\ & K_{ij,k} = \frac{1}{2} \left[ G(\zeta_{j,k+1}) - G(\zeta_{j,k}) - \left( \frac{1}{\zeta_{j,k+1}} - \frac{1}{\zeta_{j,k}} \right) \right] \\ & \quad \text{if } |\zeta_{j,k+1} - \zeta_{j,k}| < \epsilon \end{aligned} \right. \quad (76)$$

$\epsilon$  is a numerical constant generally equal to  $10^{-4}$ .

#### 6. Computation of the wave resistance

After determining the singularity distribution kinematically equivalent to the hull, the wave resistance is calculated using Havelock's formula:

$$R_w = 8\pi \rho k_0^2 \int_{-\frac{\pi}{2}}^{\frac{\pi}{2}} \sec^3 \theta \left| \eta_k(\theta, k_0 \sec^2 \theta) \right|^2 d\theta \quad (77)$$

In which  $\eta_k(\theta, k_0 \sec^2 \theta) = \eta_k(\theta)$  is the value taken by the "modified Kochin function" for  $k = k_0 \sec^2 \theta$ . To start with, we write the value  $\eta_j(\theta)$  due to a plane element  $s_j$ , completely submerged, bearing a constant distribution of

sources of unit strength ; from the defining equation (21), we have :

$$H_j(\theta) = -\frac{1}{4\pi} \iint_{s_j} k_0 \sec^2 \theta [z - i(x \cos \theta + y \sin \theta)] d\Gamma$$

This integral can be compared to the one in :

$$I(\theta) = \iint_{s_j} \bar{G}(\zeta) d\Gamma$$

which is computed to evaluate the influence coefficients.

The results can be transposed without new computation using the following substitutions :

$$\begin{cases} G(\zeta) + e^\zeta \\ \zeta + k_0 \sec^2 \theta [z - i(x \cos \theta + y \sin \theta)] \end{cases}$$

From (71) we deduce :

$$H_j(\theta) = -\frac{1}{4\pi} \frac{\cos^2 \theta}{k_0} \int_{C_j} \left[ (q_j - ir_j \sin \theta) dx_j - (p_j - ir_j \cos \theta) dy_j \right] e^\zeta$$

and, in the case of a polygonal element with  $m$  sides :

$$H_j(\theta) = -\frac{\cos^2 \theta}{4\pi k_0} \sum_{k=1}^m \left[ (q_j - ir_j \sin \theta) (x_{j,k+1} - x_{j,k}) - (p_j - ir_j \cos \theta) (y_{j,k+1} - y_{j,k}) \right] H_{j,k}$$

$$\left. \begin{aligned} H_{j,k} &= \frac{1}{\zeta_{j,k+1} - \zeta_{j,k}} (e^{\zeta_{j,k+1}} - e^{\zeta_{j,k}}) \\ &\quad \text{if } |\zeta_{j,k+1} - \zeta_{j,k}| > \epsilon \\ H_{j,k} &= \frac{1}{2} \left[ e^{\zeta_{j,k+1}} + e^{\zeta_{j,k}} \right] \\ &\quad \text{if } |\zeta_{j,k+1} - \zeta_{j,k}| \leq \epsilon \end{aligned} \right\} \quad (78)$$

$$\zeta_{j,k} = k_0 \sec^2 \theta [x_{j,k} - i(x_{j,k} \cos \theta + y_{j,k} \sin \theta)]$$

We obtain, in the same way, the contribution of a completely submerged element bearing a constant distribution of normal dipoles :

$$H_j^*(\theta) = \frac{1}{4\pi k_0} \sum_{k=1}^m \left[ \sin \theta (x_{j,k+1} - x_{j,k}) - \cos \theta (y_{j,k+1} - y_{j,k}) \right] H_{j,k}^*$$

where  $H_{j,k}$  is the function defined in equation (78).

Finally, for a segment  $L_j$  belonging to the contour  $c$ , intersection of the hull with the plane  $z = 0$ , we have from (39), (40) and (41):

+ For a superficial distribution of sources of unit strength:

$$\eta_j^s(\theta) = -\frac{1}{4\pi k_0} p_j (y_{j+1} - y_j) H_j, \quad (80)$$

$$p_j = \vec{n}_j \cdot \vec{i}_x$$

with:

$$\left. \begin{aligned} H_j &= \frac{1}{\zeta_{j+1} - \zeta_j} (e^{\zeta_{j+1}} - e^{\zeta_j}), \\ &\quad \text{for } |\zeta_{j+1} - \zeta_j| > \epsilon \\ H_j &= \frac{1}{2} (e^{\zeta_{j+1}} + e^{\zeta_j}), \text{ for } |\zeta_{j+1} - \zeta_j| \leq \epsilon \end{aligned} \right\} \quad (81)$$

$$\zeta_j = -ik_0 \sec^2 \theta (x_j \cos \theta + y_j \sin \theta)$$

+ For a superficial distribution of normal dipoles of unit density, when the hull is perpendicular to the plane  $z = 0$ :

$$\eta_j^d(\theta) = -\frac{1}{4\pi} \frac{\sec^2 \theta}{k_0} (y_{j+1} - y_j) H_j + \frac{1}{4\pi k_0} p_j \frac{(x_{j+1} - x_j)}{|\vec{M}_j \vec{M}_{j+1}|} \left[ e^{\zeta_{j+1}} - e^{\zeta_j} \right] \quad (82)$$

$H_j$  being again the function defined in formula (81).

#### IV. Solution of the discretised problem

There is no peculiar difficulty in establishing the computer program solving the Neumann Kelvin problem for a singularity distribution made of sources, normal dipoles or mixed. However, the computing times are extremely long, due to the fact that each influence coefficient is given by an integral whose kernel  $F(\theta)$  is a very oscillatory function of the variable  $\theta$ ; when the influencing element  $s_j$  and the influenced point  $M_i$  are situated near the free surface the high frequency oscillations occur when the kernel values are still of importance. On figure (7), we show the kernel variations we had to consider in a concrete example.

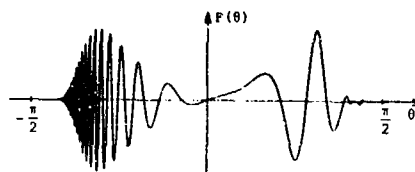


Figure 7

This case corresponds to an influence coefficient due to a rectangular element, bearing a constant distribution of normal dipoles, whose vertices  $P_k$  are:

$$\begin{array}{lll} X_1 = -0.01 & Y_1 = -0.2 & Z_1 = -0.02 \\ X_2 = +0.01 & Y_2 = -0.2 & Z_2 = -0.02 \\ X_3 = +0.01 & Y_3 = -0.2 & Z_3 = -0.01 \\ X_4 = -0.01 & Y_4 = -0.2 & Z_4 = -0.01 \end{array}$$

The influenced point  $M_i$  is:

$$X_i = -1 \quad Y_i = 0 \quad Z_i = -0.015$$

the wave number being  $K_0 = 25$ .

It appears that the influence coefficient computation needs a lot of care; when we study the whole hull, there exists a great diversity in the ten thousands of functions we have to integrate.

To achieve the computations, we used various stratagems\* and we tested a great number of classical quadrature methods; but, up to now, the computing time necessary to solve the problem is still very important for any chosen solution.

We then realise that it is very disappointing to spend a lot of computing time for a result showing great discrepancies depending on the singularity type and the way of discretising the hull surface.

\* To compute separately the farfield and the nearfield contributions.

To use asymptotic formulas valid when the influenced point is very far from the influencing element.

To integrate by parts in order to put  $F(\theta)d\theta$  under the form  $P(\theta) d[Q(\theta)]$ , where  $P(\theta)$  is a function having no rapid variations.

To our knowledge, only the Japan researchers, using superficial distributions of singularities made of sources, gave coherent results able to be compared with experiments; however, their papers are generally illustrated by curves showing a very few number of points obtained by numerical computations. We may, therefore, imagine that, if their programs are operational, they must spend important computing times, even on big computers.

A priori, the resultant dispersion, observed using our own programs, can be due to one of the following facts:

- The Neumann Kelvin problem is not, mathematically, well formulated since we are not sure that it does admit one solution; the solutions obtained numerically are then without sense.

- The computation of the influence coefficients has not been performed with enough accuracy in every cases; it is not totally excluded that peculiar difficulties could escape for certain relative dispositions of the influencing element  $s_i$  and the influenced point  $M_j$ . Now, it is sufficient to render the solution completely aberrant if only one influence coefficient is not very well computed.

- The Neumann Kelvin problem needs a very finely discretised hull surface.

In order to localise the difficulties, we gave up, for the moment, the idea of solving the case of a surface ship. In fact, when we consider a completely submerged hull, we get rid of the two first difficulties, pointed out above.

On the one hand, we are nearly sure that the Neumann Kelvin problem has a unique solution\*. On the other hand, the influence coefficient computation is much easier than in the case of a surface ship; the computing times becoming reasonable, it is then possible to perform systematic tests.

To achieve those tests, we adopted elongated ellipsoids of revolution; they are placed near the free surface in order to obtain a significant wave resistance when they move in a direction parallel to their revolution axis. The ellipsoids are discretised with plane elements such as shown on figure (8).

The computer programs are those established for solving the case of surface ships; we simply suppressed the special instructions for elements ending on the free surface. We denoted by (S), (D), (S+D) the programs solving the problem with sources, normal dipoles and mixed Green distribution respectively.

\* Kochin showed the uniqueness of the solution except for some values of the Froude number.

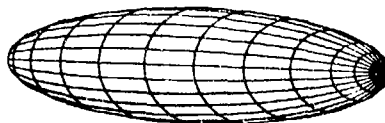


Figure 8

#### Stability of Numerical Results

Here, we are looking for the numerical results sensitivity to the way of discretising the hull.

The tests are made on an ellipsoid of length  $L = 14$  meters, of main radius  $r = 1$  meter, whose revolution axis is submerged to the depth  $H = 2$  meters.

The table (I) sums up the results obtained for  $\mathcal{F}^2 = \frac{c^2}{gL} = 0.5$ ;  $R_w$  is the wave resistance expressed in kgf,  $N$  is the number of elements in the ellipsoid discretisation.

Table I

$N \backslash R_w$	Program S	Program D	Program S+D
60	888	715	708
144	920	781	783
192	894	782	786

It appears that the results are nearly identical when the problem is solved with a dipole distribution or with a mixed distribution; however, the wave resistance value obtained with a source distribution is very different from the preceding one.

Besides, the values of  $R_w$ , given by the program (S) and the program (D), are very rapidly varying with  $N$ .

It would be obviously of a great interest to see if  $R_w$  tends to the same limit, whatever the type of singularities chosen, when the hull is discretised with more and more elements.

We had to give up temporarily this idea, the estimated computing time to perform this work being too important with the present formulation.

We preferred systematic tests, much less expensive, using the zero Froude number hypothesis.

The wave resistance values, obtained always for the same ellipsoid, are in the table (II); the theoretical value given in the last column is the result of an analytical computation performed by C. Farell. [5]

Table II  
(zero Froude number hypothesis)

N	R <sub>w</sub>	Program S	Program D	Program (S+D)	R <sub>w</sub> Analytical
60		1028	820	/	982
144		1066	901	/	
192		1037	901	/	
288		1026	938	939	
540		1016	956	/	

For  $N = 288$ , we again remark the identity of the results given by a dipole distribution and a mixed distribution. This fact cannot be a result of chance since both curves showing the variations of the Kochin function  $H(\theta, k_0 \sec^2 \theta) = H(\theta)$  are nearly identical along the interval  $-\frac{\pi}{2} < \theta < +\frac{\pi}{2}$ .

This is the reason why we did not use any more the program (S+D).

Here again, the  $R_w$  values, not the same according as they are obtained by the program (S) or (D), are rapidly varying with  $N$ ; for  $N = 540$  there is still a divergence of 6 % between the values obtained with a source distribution and with a dipole distribution.

The results of tables I and II are also given on the figure (9). The examination of these curves suggests the following remarks, which can very well be coincidence since we are not yet able to justify them:

a) With the zero Froude number hypothesis, the mean wave resistance,  $R_{w \text{ mean}}$ , computed by making the half sum of the values obtained with a source distribution and a dipole distribution is not very sensitive to the hull discretisation, at least for  $N \geq 144$  (Table III).

Table III

N	60	144	192	288	540
R <sub>w</sub> mean	924	984	969	982	986
R <sub>w</sub> analytical	982				

b) For a singularity distribution of a given type, the gap,  $\Delta R_w$ , between the values computed at exact Froude number and in the hypothesis of zero Froude number, seems to be little sensitive to the hull discretisation (Table IV).

Table IV

N	60	144	192
$\Delta R_w$ (sources)	- 140	- 146	- 143
$\Delta R_w$ (dipoles)	- 105	- 120	- 119

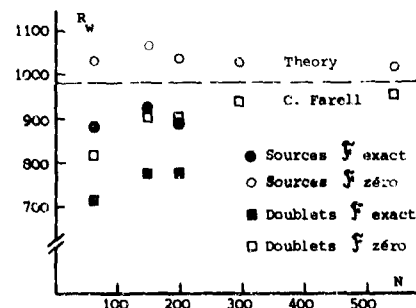


Figure 9

#### Comparisons with experiments

In order to perform these comparisons, we chose an ellipsoid tested by C. Farell for which he gave an estimate of the wave resistance coefficient  $C_W$ .

The geometrical characteristics of this ellipsoid are the following:

$L = 10$  meters ,  $r = 1$  meter ,  $H = 1.6$  meter.

The points computed for only  $N = 60$  are drawn on the figure (10).

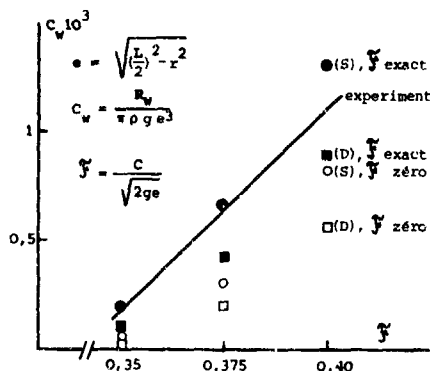


Figure 10

These results, given by an inexpensive computation, show that theoretical values, though they are scattered according to the program (S) or (D) used, are not extremely far from experimental values, as they should be in computing them with the zero Froude number hypothesis.

#### V. Conclusions

This study on completely submerged hulls, even if it seems to be far from our initial goal gives us some lessons ; it shows that :

- a) the difficulties, met in the case of a surface ship, are not totally due to the junction between the hull and the free surface.
- b) to compute correctly the wave resistance of a ship, even completely submerged, we cannot be satisfied with a rough discretisation .

\* When we determine, with enough precision for practical use, the hydrodynamic coefficients of a floating body subjected to forced oscillations, only one hundred elements are necessary ; to solve correctly the Neumann Kelvin problem, the hull should be discretised with at least 500 elements.

Due to these facts, we modified our plan of work. To start with, as we had a rather poor, but safe, computing tool, we tried to take advantage of it immediately in order to compare the results with experimental data ; to reach this aim as fast as possible, it was not unreasonable for us to spend a lot of money on computers, leaving for a following stage the uninspiring job of improving the cost of our computer program. Now, it appears that experimental comparisons are not significant unless the hull is very well discretised ; hence, we have to concentrate on the following points :

- Find a new formulation of the influence coefficients, in order to integrate more rapidly the very oscillatory functions. For that, many solutions are available ; actually, we are developing two computing methods based on various ideas.

After determining the discrete singularity densities kinematically equivalent to the hull, make a numerical interpolation in order to be sure that instabilities are not only due to an inadequate way of computing the Kochin function ; we are now improving a program performing that numerical interpolation.

Finally, the computer programs, already built, will solve the Neumann Kelvin problem if there is no limitation on computing time or on computing cost.

But comparisons with experiments, to determine if the mathematical model represents well physical reality, will not be done unless numerical difficulties are overcome. Even if this experience were unfavourable, we are sure that the effort made to solve the linear problem is useful ; in fact, to improve a perturbation method, whatever its principle may be, to take partially care of non-linear terms, seems to be without any success if there is numerical doubt, about 20 %, on the results given by the linear theory.

#### Acknowledgements

We were applying ourself to the writing of this paper when we have heard that Admiral Brard "Professeur Associé" at the "Ecole Nationale Supérieure de Mécanique" in Nantes, was dead. Our emotion and our sadness, due to our intimate relationship with Professor Brard for many years, became more acute precisely because we started our study under his advice and because he recommended our paper to be presented.

Professor Brard wanted to apply a perturbation method he recently put into shape, in order to improve the results given in solving the Neumann Kelvin problem.

We want to dedicate to Professor Brard's memory our present work on the Neumann Kelvin problem as well as the continuation we are going to give to it.

# References

- [1] BABA E. - TAKEKUMA K.  
"A study on free-surface flow around bow of slowly moving full forms"  
Journal of the Society of Nav. Arch. of Japan - Vol. 137 June 1975 p. 1-10
- [2] BRARD R.  
"The Neumann Kelvin problem for surface ships"  
Bassin d'Essais des Carènes, Report 11 CST, 1971 (unpublished)
- [3] BRARD R.  
"The representation of a given ship form by singularity distributions when the boundary condition on the free surface is linearized"  
J. Ship. Res. 16 (1972) 79-92
- [4] BRARD R.  
"The fundamentals and applications of the Neumann Kelvin problem theory"  
Bassin d'Essais des Carènes, Report 18 CST, 1973 p. 7-56
- [5] FARELL C.  
"On the wave resistance of a submerged spheroid"  
J. Ship Res. 17 (1973) 1-11
- [6] FARELL C. - GÜVEN O.  
"On the experimental determination of the resistance components of a submerged spheroid"  
J. Ship. Res. 17 (1973) 72-79
- [7] GUEVEL P. - VAUSSY P. - KOBUS J.M.  
"The distribution of singularities kinematically equivalent to a moving hull in the presence of a free surface"  
Int. Shipbuilding Progress 21 (1974) 311-324
- [8] GUEVEL P. - DELHOMMEAU G.  
"Méthode de calcul de la résistance de vagues"  
E.N.S.M. report I.R.C.N. 1976 (unpublished)
- [9] HESS J.L. - SMITH A.M.O.  
"Calculation of non-lifting potential flow about arbitrary three dimensional bodies"  
Douglas Aircraft Company Report E.S. 40622 March 1962
- [10] INUI T. - KAJITANI H. - KUSAKA Y.  
"Analysis of hydrodynamical source singularities for surface ships"  
Written contribution to the resistance Committee 14th ITTC, Ottawa, Sept. 1975
- [11] KOTIK J. - MORGAN R.  
"The uniqueness problem for wave resistance calculated from singularity distributions which are exact at zero Froude number"  
J. Ship. Res. 13 (1969) 61-68
- [12] KUSAKA Y.  
"On the hydrodynamical singularities for surface ships with special reference to line Integral."  
Doctoral Thesis, Department of Naval Architecture, The U. of Tokyo 1974
- [13] MORI K.  
"On the singularity distribution representing surface ships"  
Memoirs of the Faculty of Eng. Hiroshima University Vol. 5 n° 2, November 1974, p. 15-26.
- [14] MEHAUSEN J.V.  
"The wave resistance of ships"  
Advances in applied mechanics. Vol. 13 p. 23-245 - Academic Press N.Y. 1973.

## COMPUTATIONS OF THREE-DIMENSIONAL SHIP-MOTIONS WITH FORWARD SPEED

Ming-Shun Chang

David W. Taylor Naval Ship Research and Development Center  
Bethesda, Maryland 20884

### ABSTRACT

A singularity distribution method has been developed to calculate the motion coefficients and wave exciting forces and moments for ships with forward speed. This method accounts for the speed effect on the hull boundary condition as well as its effect on the free-surface boundary condition. Hence, the zero-speed motion computation and the wave resistance computation are two limiting cases of the present calculations; the former corresponds to the case of forward speed approaching zero while the frequency of the oscillation remains finite and the latter corresponds to the frequency of oscillation approaching zero while the forward speed remains finite.

Numerical results for the wave resistance, motion coefficients and wave forces are presented. The wave resistance calculation for a Wigley hull has been compared to the experimental data as well as to thin-ship theory results. Agreement between the experiment and the theories is satisfactory.

Motion coefficients and wave forces for a Series 60 hull have been computed and compared to experimental data and to strip theory results. The present calculations are very good for the case of zero speed and are much improved over the strip-theory results at lower frequencies. For the case of a Froude number of 0.2, the present computations are not as good as those for zero speed. Yet the results are satisfactory and are also an improvement over strip theory predictions.

### INTRODUCTION

Since the development of a two-dimensional roll-damping theory by Ursell<sup>1</sup> and the introduction of strip theory to ship motions by Korvin Kroukovsky,<sup>2</sup> the strip-theory method has become the most universally used technique for analyzing ship motions. The most extensively documented six-degree-of-freedom ship-motion prediction procedure based on strip theory was developed by Salvesen, Tuck and Faltinsen.<sup>3</sup> Good agreement between strip-theory predictions and experimental data has been found for many classes of ships. In essence strip theory converts a three-dimensional body into hydrodynamically independent two-dimensional sections, and the numerical computations of flow about these independent sections are quite simple. The computation time and the memory space required for strip-theory computations are very small in comparison with those required for three-dimensional flow calculations. Strip theory represented a very practical approach to the calculation of ship motions on digital computers available ten years ago when computations for a three-dimensional body in a free-surface were impractical if not impossible.

Computer technology has been drastically improved during the past few years. Not only has the memory space

been expanded, but the speed of computation has been increased and the relative cost has been drastically reduced. With further improvements of the computers, the computational advantages of strip theory will become less and less significant. Techniques<sup>4,5,6</sup> for calculating three-dimensional ship motions have been under development for a number of years; while general application of some of these techniques are still restricted by the limitations of current-generation computers, the method should have potential for practical applications in the very near future.

The method of three-dimensional singularity distributions developed by Chang and Pien<sup>4,7</sup> has been successfully applied to wave resistance and time-dependent motion computations for submerged bodies. Since this method does not require a large memory space, it is workable on most presently available computers. Extension of the singularity method to the calculation of ship motions at zero forward speed is trivial while its application to non-zero speed cases requires modifications. This paper presents calculations of motion coefficients and wave-excitation forces for bodies at both zero and non-zero forward speed. Sample calculations for a Series 60 hull<sup>8</sup> with a block coefficient,  $C_B$ , of 0.70, are compared with strip theory predictions and experimental data. For the zero speed case the results of the motion-coefficient comparison indicate that the present method gives good results with a small number of control panels. In the intermediate-frequency region computed motion coefficients agree well with both strip theory and experimental data. In the low frequency region, the computed motion coefficients agree well with experimental data whereas the strip theory approximation gives less satisfactory agreement. A comparison of wave-excitation forces shows good agreement between the present and strip-theory calculations and experimental data over a wide range of wave frequencies. Comparisons of wave-excitation moments show deviations between the two theories and between the theories and experiments. This discrepancy may be due to experimental difficulties in determining the rotation centers. Non-zero speed calculations are presented for Froude number 0.2. Agreement with experimental data is not as good as for the zero forward-speed-case.

If the steady part of the free-surface effect is neglected, the influence of ship speed on the calculation of unsteady hydrodynamics forces on a ship appears through its modifications of the pressure calculation, body-boundary condition and the free-surface condition. Inclusion of the speed effect on the pressure calculation and the body boundary condition is simple for both the strip theory approximation and the three-dimensional calculation. However, the speed effect on the free-surface condition can not be easily included in strip theory. Most strip theory calculations for non-zero speed cases neglect the speed terms in the free-surface condition by assuming the frequency is sufficiently high, such that  $u/\partial/\partial x \ll \omega$ . For a fully three-dimensional theory, the effect of forward speed on the



free-surface condition can be taken into account by modifying the fundamental singularity. In comparison to the zero-speed case, this modification only leads to an additional line-singularity distribution at the intersection of the ship and the free surface. Numerical evaluation of the modified fundamental singularity is similar to the computations of wave resistance. Hence, the effect of the forward speed in the free-surface condition only increases the computation time for a three-dimensional theory without introducing any complications. This contrasts sharply with strip theory. Forward-speed computations are presented here both with and without speed modifications to the free-surface condition. In comparison with the experimental data, the calculations that neglect the speed effect on the free surface are not good. The calculations that account for the modified free-surface conditions are satisfactory except in the cases of predicted coefficients of pitch and roll damping. The discrepancies between the calculated and the experimental pitch damping coefficients are possibly due to neglect of the steady part of the perturbing potential in the present calculation. But this is not certain at the present time, and requires further investigation.

### FORMULATION

In calculating the ship motions the major difficulty is to determine the hydrodynamic forces due to the presence of a free surface. If viscous stresses are neglected, the hydrodynamic forces,  $\vec{F}_T$  and  $\vec{M}_T$ , can be described by a pressure field,  $P$ , determined from a potential field,  $\phi_T$ ; that is

$$\vec{F}_T = - \int_{S_B} P \vec{N} dS \quad \text{and} \quad \vec{M}_T = - \int_{S_B} P \vec{r} \times \vec{N} dS, \quad (1)$$

with

$$P/\rho = \frac{\partial}{\partial t} \phi_T - \frac{1}{2} (\nabla \phi_T)^2, \quad (2)$$

where  $S_B$  denotes the hull surface and  $\vec{N}$  is its normal vector directed into the fluid,  $\vec{r}$  is the displacement vector,  $t$  is the time parameter,  $\nabla$  is the gradient operator, and  $\rho$  is the density of the fluid. Thus, the analysis of ship motions can be derived from solution of a potential field with boundary conditions specified on the hull surface,  $S_B$ , and the free surface,  $S_F$ . The boundary conditions corresponding to a ship moving forward with small oscillatory motions in otherwise calm water have been given by Timman and Newman.<sup>9</sup> The system that governs the potential field,  $\phi_T$ , can be summarized as follows.

Let  $(x, y, z)$  be the right-hand coordinate system with  $z$  directed vertically upwards and origin at the water line of the center plane of the ship. For a ship moving forward in the  $x$ -direction with speed  $U$  and oscillating at a frequency  $\omega$ , the corresponding potential field,  $\phi_T$ , is the sum of two potential fields: a time-independent potential field,  $U\phi_0$ , due to the ship's steady forward motion, and a periodic potential field,  $\phi$ , due to the ship's oscillatory motions. If the gradients of the steady potential,  $U\phi_0$ , and the oscillatory potential,  $\phi$ , are both small, the system of equations may be linearized; the potential fields  $U\phi_0$  and  $\phi$  then become uncoupled and can be solved independently. The governing equations can be solved as

$$\phi_T = U(x + \phi_0) + \phi e^{-i\omega t}, \quad (3)$$

with Laplace equations

$$\nabla^2 \phi_0 = 0 \quad \text{and} \quad \nabla^2 \phi = 0 \quad \text{in the fluid}, \quad (4)$$

the hull boundary conditions

$$\frac{\partial}{\partial n} (x + \phi_0) = 0 \quad \text{and} \quad -\frac{\partial}{\partial n} \phi = \sum_{i=1}^6 (-i\omega n_i \xi_i + U m_i \xi_i) \quad \text{on } S_B, \quad (5)$$

and the free-surface conditions

$$U^2 \frac{\partial^2}{\partial x^2} \phi_0 + g \frac{\partial}{\partial z} \phi_0 = 0$$

$$\text{and} \quad \left( i\omega + U \frac{\partial}{\partial x} \right)^2 \phi + g \frac{\partial}{\partial z} \phi = 0 \quad \text{at } z = 0. \quad (6)$$

where

$g$  is the gravitational acceleration

$(n_1, n_2, n_3) = \vec{N}$  are the components of the normal vector  $\vec{N}$

$(n_4, n_5, n_6) = \vec{r} \times \vec{N}$  are the components of the normal vector with respect to the rotational motion,  $\vec{r} \times \vec{N}$

$(m_1, m_2, m_3) = + \frac{\partial}{\partial n} \nabla(x + \phi_0)$  are the normal velocity gradients of the steady motion

$(m_4, m_5, m_6) = \vec{r} \times \vec{m} - \nabla(x + \phi_0) \times \vec{N}$  are the rotational parts of the  $(m_1, m_2, m_3)$

and  $(\xi_1, \xi_2, \xi_3)$  and  $(\xi_4, \xi_5, \xi_6)$  are the displacement amplitudes of the linear and rotational oscillatory motions, respectively.

The system of equations (3) to (6) is, in general, applicable to three-dimensional ships. If a ship is slender and  $(U/\omega)(\partial/\partial x)$  is very small, one may neglect the  $x$ -derivative terms in (4) and (6) and reduce the problem to a sequence of computations for two-dimensional sections. This is the strip theory approximation. It should be noted that the neglect of  $(U/\omega)(\partial/\partial x)$  on the free surface is the same as the neglect of the speed effect on the free surface, since the speed term appears only in the form of  $(U/\omega)(\partial/\partial x)$ . The present paper will not assume that the  $x$ -derivative of  $\phi$  is small and  $\phi$  will be found by a three-dimensional source distribution method. Note that since the cross products between the steady potential  $U\phi_0$  and the oscillatory potential  $\phi$  are of higher order,  $\phi_0$  may be neglected in the computations of  $m_i$  in the hull boundary condition (5). For the results presented in this paper this simplification has been made.

### SOLUTION FOR POTENTIAL

A fundamental singularity<sup>10,11</sup> which behaves as  $1/R$  and satisfies the free-surface condition (6) is

$$G(x, y, z; x_0, y_0, z_0) = \left( \frac{1}{R} - \frac{1}{R_1} \right) + \frac{2g}{\pi} \int_0^\pi d\theta \int_0^\infty dk F(\theta, k)$$

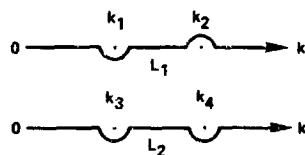
$$+ \frac{2g}{\pi} \int_{-\pi/2}^{\pi/2} d\theta \int_{L_1} dk F(\theta, k) + \frac{2g}{\pi} \int_{\pi/2}^\pi d\theta \int_{L_2} dk F(\theta, k), \quad (7)$$

where

$$F(\theta, k) = \frac{k e^{k[(z+z_0) + i(x-x_0)\cos\theta]} \cos[k(y-y_0)\sin\theta]}{gk - (\omega + kU\cos\theta)^2},$$

$$\beta = U\omega/g, \quad (8)$$

$$\nu = \begin{cases} 0 & \text{if } \beta < \frac{1}{4} \\ \arccos \frac{1}{4\beta} & \text{if } \beta \geq \frac{1}{4} \end{cases}$$



$$\sqrt{gk_1} \cdot \sqrt{gk_3} = \frac{1 - \sqrt{1 - 4\beta \cos \vartheta}}{2\beta \cos \vartheta} \omega,$$

$$\sqrt{gk_2} \cdot \sqrt{gk_4} = \frac{1 + \sqrt{1 - 4\beta \cos \vartheta}}{2\beta \cos \vartheta} \omega,$$

$$R^2 = (x - x_0)^2 + (y - y_0)^2 + (z - z_0)^2,$$

$$R_1^2 = (x - x_0)^2 + (y - y_0)^2 + (z + z_0)^2,$$

and

$(x_0, y_0, z_0)$  is the position of a singularity.

With this fundamental singularity, from Green's theorem, and the fact that the potential  $\phi$  satisfies a radiation condition at infinity and the free-surface condition (6) at  $z = 0$ , it follows that the potential  $\phi$  at any point  $p$  inside the fluid can be expressed<sup>12</sup> as

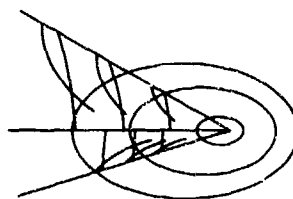
$$\begin{aligned} \phi(p) = & -\frac{1}{4\pi} \left\{ \iint_{S_B} [G(p, q) \frac{\partial}{\partial n} \phi(q) - \phi(q) \frac{\partial}{\partial n} G(p, q)] dS \right. \\ & - \frac{1}{g} \oint [2i\omega U G(p, q) \phi(q) - U^2 G(p, q) \frac{\partial}{\partial x} \phi(q) \\ & \left. + U^2 \phi(q) \frac{\partial}{\partial x} G(p, q)] dy \right\}. \end{aligned} \quad (9)$$

where the contour integral is over the intersection of the hull surface  $S_B$  and the free surface. For a submerged body or the zero forward speed case, the contour integral vanishes identically. Examination of equation (9) shows that the potential  $\phi$  is the sum of contributions from two types of surface singularities in addition to the contribution from the line singularity: one source distribution and one doublet distribution. These two surface distributions can be reduced to either a source or a doublet distribution when one extends the potential field into the ship hull and applies Green's theorem.<sup>12</sup> For the case when the line integral vanishes, it has been pointed out by Chang and Pien that the doublet distribution representation is a more direct and convenient approach. However, for a ship at nonzero speed, the presence of the contour integral makes it uncertain whether the doublet method is more efficient than the source method. The present paper converts the surface distributions into a source distribution so that the line singularity and the surface singularity are of the same type. Equation (9) then becomes

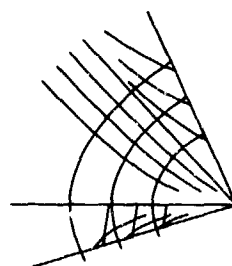
$$\begin{aligned} \phi(p) = & -\frac{1}{4\pi} \left[ \iint_{S_B} G(p, q) Q(q) dS \right. \\ & \left. + \frac{U^2}{g} \oint G(p, q) Q(q) n_1(q) dy \right], \end{aligned} \quad (10)$$

where  $Q$  is the source distribution determined from boundary condition (5).

The fundamental singularity  $G$  defined in Eq. (7) is a function of parameters  $\beta = U\omega/g$  and  $\omega^2/g$ . The behavior of this function is similar to the Kelvin singularity but produces four free waves.<sup>10</sup> A schematic representation of its wave system is shown in Figure 1. It is seen that with  $\beta < 1/4$  there are three waves downstream and one wave



$\beta < 1/4$



$\beta > 1/4$

Figure 1 - A Schematic Representation of the Wave System Associated with a Moving and Oscillating Source (from reference 10)

upstream. When  $\beta > 1/4$  the wave upstream disappears and waves are only downstream. In the limiting case when  $\beta \rightarrow 0$  while  $\omega^2/g$  remains finite,  $G$  approaches the fundamental singularity for body oscillations at zero forward speed. When  $\beta \rightarrow 0$  while  $U^2/g$  remains finite, the singularity  $G$  approaches the Kelvin singularity for steady motion. Thus, the solutions for  $\phi_0$  and  $\phi$  with zero forward speed are two limiting solutions of equations (10) and (5).

#### CALCULATION OF UNSTEADY HYDRODYNAMIC FORCES

One can evaluate the hydrodynamic force and moment from equations (1) and (2) after the potential  $\phi$  is obtained from (5) and (10). These hydrodynamic forces are composed of steady and unsteady contributions as well as linear and non-linear contributions, since the pressure has a velocity-squared term. In the following only the calculations for the linear unsteady force will be discussed. The calculations for steady force have been discussed in Chang and Pien, reference 4.

Substitution of equation (3) into (2) and neglect of the non-linear terms in  $\phi$ , results in

$$\begin{aligned} P/\rho = & -i\omega \phi e^{-i\omega t} - \{U \nabla(x + \phi_0) \cdot \nabla \phi\} e^{-i\omega t} \\ & - \frac{1}{2} U^2 [\nabla(x + \phi_0)]^2, \end{aligned} \quad (11)$$

where the last term on the right-hand side of equation (11) is time-independent and associated with the wave resistance and the lift. The other terms in equation (11) are time dependent due to multiplying by  $e^{-i\omega t}$  and give rise to unsteady forces. Now, let us denote the amplitudes of these unsteady forces and moments by

$$\vec{F} = \rho \int_{S_B} \{ i\omega\phi + U[\nabla(x + \phi_0) \cdot \nabla\phi] \} \vec{N} dS \quad (12)$$

and

$$\vec{M} = \rho \int_{S_B} \{ i\omega\phi + U[\nabla(x + \phi_0) \cdot \nabla\phi] \} \vec{r} \times \vec{N} dS. \quad (13)$$

Then, from the fact that

$$\frac{\partial}{\partial n} (x + \phi_0) = 0 \quad \text{on } S_B,$$

one has

$$\vec{F} = \rho \int_{S_B} \{ i\omega\phi + U[\nabla_T(x + \phi_0) \cdot \nabla_T\phi] \} \vec{N} dS \quad (14)$$

and

$$\vec{M} = \rho \int_{S_B} \{ i\omega\phi + U[\nabla_T(x + \phi_0) \cdot \nabla_T\phi] \} \vec{r} \times \vec{N} dS, \quad (15)$$

where  $\nabla_T$  denotes the gradient along the hull surface. Calculation of  $\vec{F}$  and  $\vec{M}$  from equations (14) and (15) will involve the calculation of gradients of  $\nabla_T\phi_0$  and  $\nabla_T\phi$  along the ship hull. With proper choice of the panels used to represent the three-dimensional body, the calculations for  $\nabla_T\phi_0$  and  $\nabla_T\phi$  present no difficulties. However, with a small number of panels, numerical evaluation of  $\nabla_T$  may not obtain sufficient accuracy. Alternative expressions for  $\vec{F}$  and  $\vec{M}$ , which do not contain the form  $\nabla_T\phi$ , have been given by Tuck.<sup>13</sup> They are

$$\vec{F} = \rho \int_{S_B} \{ i\omega\phi \vec{N} + U\phi \nabla[\nabla(x + \phi_0)] \cdot \vec{N} \} dS - \rho \oint U\phi d\vec{e} \times \nabla(x + \phi_0) \quad (16)$$

and

$$\vec{M} = \rho \int_{S_B} \{ i\omega\phi \vec{r} \times \vec{N} + U\phi(\vec{r} \times \nabla)[\nabla(x + \phi_0)] \cdot \vec{N} + U\phi \nabla(x + \phi_0) \times \vec{N} \} dS + \rho \oint U\phi \vec{r} \times [\nabla(x + \phi_0) \times d\vec{e}]. \quad (17)$$

where the contour integral is over the intersection of the ship hull and the free surface. These expressions for  $\vec{F}$  and  $\vec{M}$  are especially useful for thin ships where the steady potential  $\phi_0$  and the contour integral may both be neglected. The common strip-theory calculation for non-zero speed possesses this advantage. Also, the strip-theory approximation replaces the potential  $\phi$  in equations (16) and (17) by a corresponding zero-speed two-dimensional potential. This is because, as mentioned previously, the neglect of  $x$ -derivatives is equivalent to the approximation of zero forward speed on the free surface.

#### WAVE EXCITATION FORCE

When a ship moves forward in a given wave field  $\phi_w e^{-i\omega_e t}$ , having encounter frequency  $\omega_e$ , the ship creates not only the potential field  $\phi$  but also a diffraction field,  $\phi_D$ . Since the wave field is periodic, the system determines the diffraction potential  $\phi_D$ ; and the associated wave forces are the same as those for  $\phi$ , but with boundary condition (5) replaced by

$$\frac{\partial}{\partial n} (\phi_w + \phi_D) = 0 \quad \text{on } S_B \quad (18)$$

and  $\phi$  replaced by  $\phi_w + \phi_D$  in the calculations of the unsteady forces given in equations (16) and (17). This is because  $\phi_D$  is determined in the same manner as  $\phi$  but with different hull boundary conditions. The diffraction potential and wave-excitation forces are calculated directly in the present method, while the strip-theory approximation calculates it from the Haskind relations.

#### NUMERICAL RESULTS

Theoretically, equations (5), (10), (11), (16), and (17) complete the formulation of linear ship motions with forward speed. Numerically, further approximations are necessary in order to represent a three-dimensional body and to determine the singularity distribution. For the present computer program, the representation of a ship is taken to be the same as that for strip-theory computations, except that the input offsets at each station are further connected to the neighboring stations to form three-dimensional panels.<sup>14</sup> In the determination of the singularity distribution, the fundamental singularity is evaluated using the method developed by Chang and Pien,<sup>4</sup> and only minor modifications are made in the fundamental singularity. As discussed previously, the wave resistance and the zero-speed motion problems are the two limiting cases of the present computations. The computer program was first applied to these two cases, for which reliable and extensive information is available for comparison.

##### A. Wave Resistance

The wave resistance of a submerged body has been evaluated by Chang and Pien from a doublet-distribution method. The present program with  $\omega U/g = 10^{-3}$  and  $\omega^2/g = 10^{-6} \times g/U^2$  was applied to the calculation of the wave resistance of a submerged sphere and the results were compared to those of Chang and Pien. The two results were shown to agree well. The present program was then applied to ship forms. The resulting wave resistance for Wigley Hull 2892<sup>15</sup> is shown in Figure 2. In comparison with the experimental data, the present calculation agrees well with the data for a fixed model at high Froude numbers. At low Froude numbers the calculation tends to agree better with the data for the model which is free to trim. As pointed out in reference 15, this is because at low Froude numbers the experiments for model 2892 did not achieve steady-state flow conditions. In comparison with the results of thin-ship theoretical calculations, the present calculations show the wave resistance to have less-pronounced hollows. This is as expected because in thin-ship theory the source distribution is pre-determined and neglects the interactions among the singularities. The present calculation method evaluates the singularity distribution as well as the wave resistance. It includes the wave interferences between the singularities which in turn smooth out the hollows in the wave resistance curve. More comparisons on the wave resistance computation will be reported in the future.

##### B. Zero-Speed Motion Coefficients

Careful ship-motion experiments have been conducted by Gerritsma<sup>16</sup> and Vugts<sup>17</sup> for Series 60,  $C_B = 0.70$ , ship models. Experimental data as well as strip-theory predictions for this ship model are given by both Gerritsma and Vugts. It is known that, in the practical frequency region, strip theory yields good motion predictions for this class of ships.<sup>11</sup> Hence, the present program is applied to the same ship for verification. Figure 3 presents the added-mass and damping coefficients. The strip-theory results shown in Figure 5 were taken from reference 17 and the present calculations were obtained by representing the half-ship by 49 panels.

The solid lines in Figure 3 denote the strip theory predictions while the filled and the opened symbols denote the results of the present calculation and the measurements

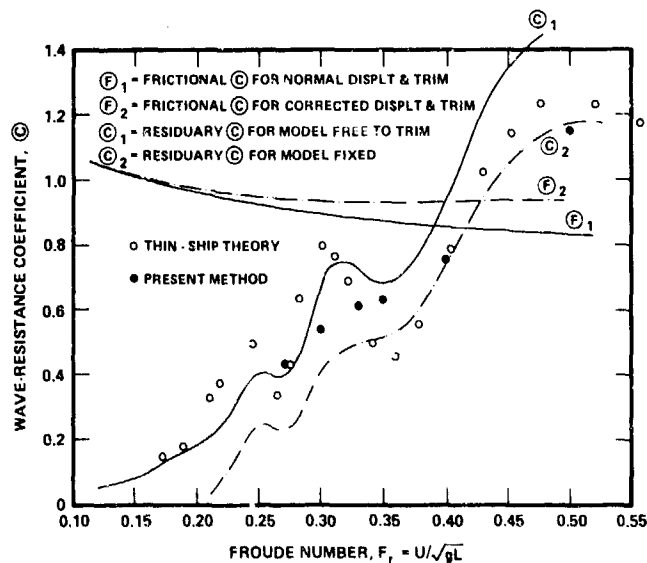


Figure 2 - Comparison of Measured and Calculated Wave Resistance for Wigley Hull 2892

respectively; two measurements are shown: one obtained for the whole model,  $\square$ , and one obtained from the sum of sectional measurements,  $\circ$ . Motion coefficients are presented for added masses of pitch, heave, pitch-heave and yaw, and for damping coefficients of pitch, roll, sway-roll and sway. It is seen from Figure 3 that the present calculations of added mass agree very well with the experimental data over most of the frequency region presented, i.e., for values of  $\omega$  from 2 to 6  $\text{sec}^{-1}$ . This is in contrast to the strip-theory predictions which deviate considerably from the measurements except for the pitch-heave mode. For other modes of motion at frequencies above 5  $\text{sec}^{-1}$ , strip theory predicts fairly good motion coefficients. In the case of damping, the present calculations of pitch agree well with the experimental data. However, for other modes: roll, sway and sway-roll, the predictions are not very good; they are especially bad for the roll mode. Calculated damping coefficients for the sway and sway-roll modes agree fairly well with the measurements for the whole model at frequencies lower than 4.5  $\text{sec}^{-1}$ ; at higher frequencies the magnitudes of the calculated damping coefficients start to deviate from the measured values; the calculated values are approximately twenty percent lower than the corresponding measurements at a frequency near 6  $\text{sec}^{-1}$ . The agreement between the measured and calculated roll dampings is worse than that for sway and sway-roll. The calculated roll dampings are much too small; nevertheless, the form of the roll damping as a function of frequency resembles the form of the measurements. However, in examining the measurements, it is seen that the measured results obtained from the whole model,  $\square$ , and the measured results obtained from the sum of the sections,  $\circ$ , are also very different. It seems that the measured roll damping coefficients may not be sufficiently reliable for verifying the predictions; more measurements are required for verification. The pitch damping coefficients predicted by strip theory are not very good; the strip-theory prediction shifts the frequency of maximum damping from 5  $\text{sec}^{-1}$  to approximately 3.6  $\text{sec}^{-1}$  and overpredicts the magnitude of the damping coefficient.

At the predicted maximum frequency, the predicted value of the damping coefficient from strip theory is approximately twice as large as the measured value. The strip theory predicts the sway and sway-roll damping coefficients very well at all frequencies including the low frequencies. The roll damping coefficient predicted by strip theory does not agree with the measurements as well as the predictions of the present three-dimensional calculation method. As mentioned previously, some of the discrepancies could be due to experimental difficulties.

The insufficiency of strip theory for the prediction of motion coefficients at low frequencies is well known. It remains to be shown how well the three-dimensional calculation method can improve the prediction and how important the improvements are. The present calculations indicate that the three-dimensional method can predict motion coefficients quite well even with a small number of panels - 49 panels for the present predictions. The importance of the improvement is certainly dependent upon the phenomenon one is observing and the characteristics of the ship hull. For hull forms where strip theory fails to apply even in theory, the need for the three-dimensional calculation should be obvious.

#### C. Wave-Excitation Force with Zero Forward Speed

Wave excitation forces and moments for a Series 60,  $C_B = 0.70$ , ship model were also measured by Geurtsma<sup>16</sup> and Vugts.<sup>17</sup> The excitation forces and moments for incoming waves at 30 degrees and 120 degrees are shown in Figure 4. Figure 4 also shows the results of calculations using strip theory and the present computational method. The symbolic representations in Figure 4 are the same as used in Figure 3 and will also be applied later to Figures 5 and 7. It is seen from the figure that the predictions of strip theory and the present computational method both agree well with the measurements at all frequencies and all modes of motions except roll and yaw. For yaw moment, the measurements appear to agree with the present

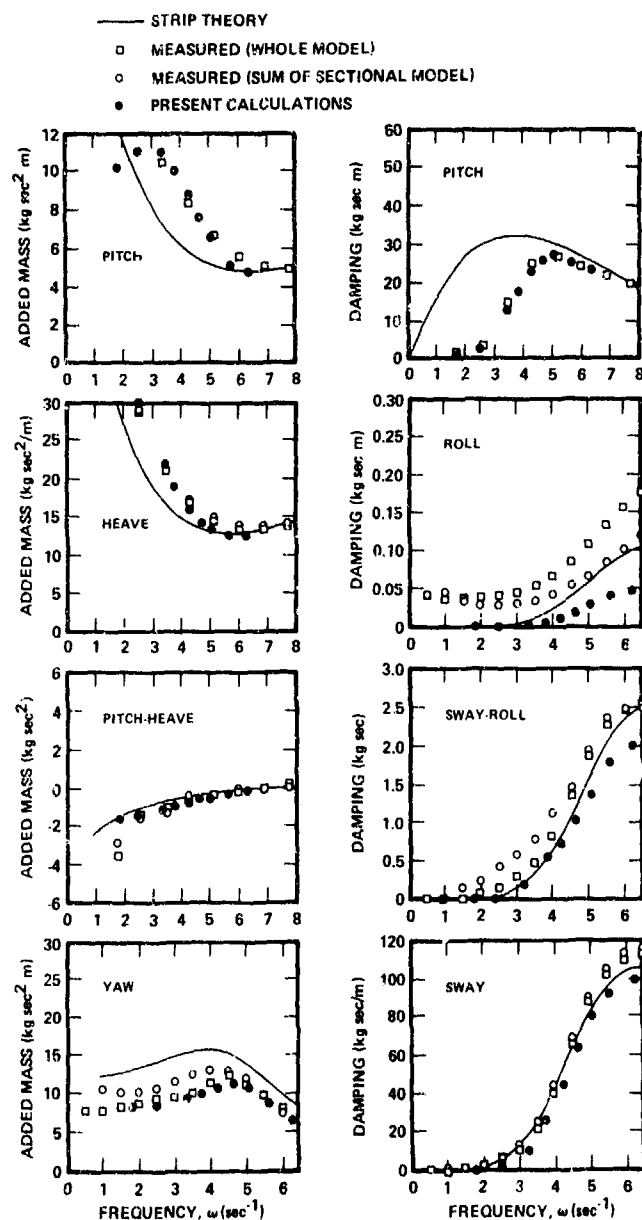


Figure 3 - Zero-Speed Motion Coefficients for Series 60,  $C_B = 0.70$  Hull Model

calculations a bit better than with the strip-theory calculations; however the measurements are rather too scattered to permit decisive conclusions. In the comparison of roll moments, the three-dimensional calculations agree well with the two-dimensional strip-theory calculation for a wave

heading of 30 degrees, although both predictions deviate from the measurements considerably. For a wave heading of 120 degrees, the agreement between the measurements and the present three-dimensional calculations seem to be improved, but decisive conclusions may not be drawn.

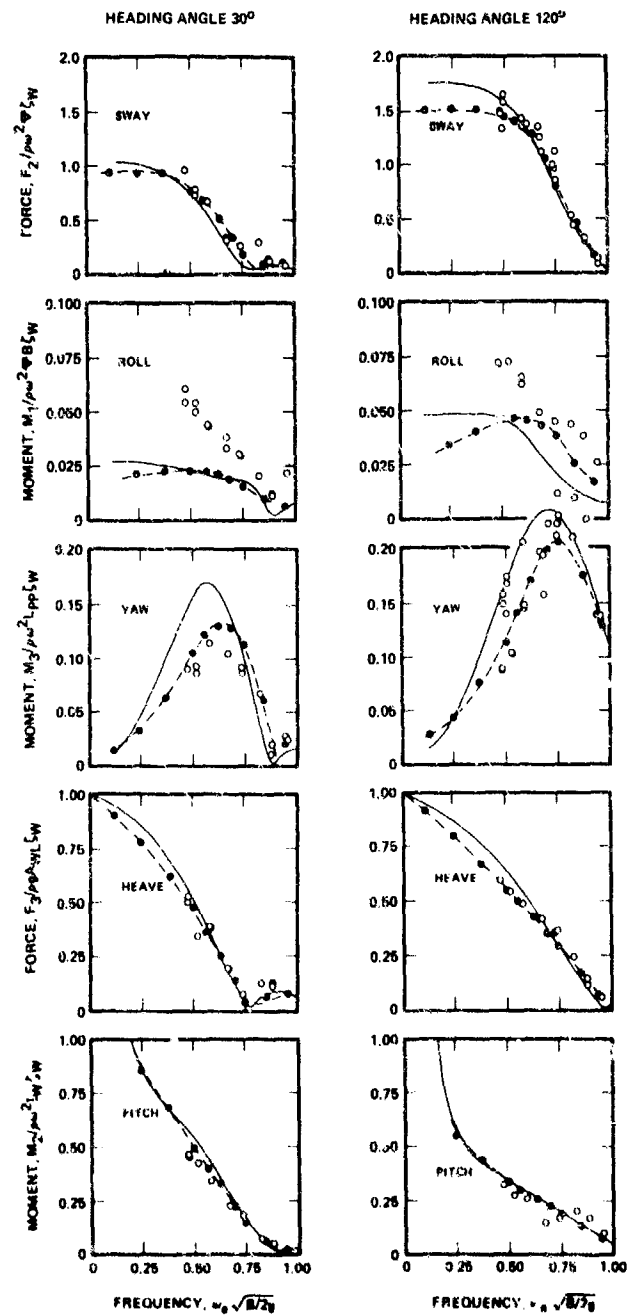


Figure 4 - Zero-Speed Wave Forces and Moments for Series 60,  $C_B = 0.70$  Hull Model, Non-Dimensionalized by Wave Amplitude,  $\zeta_W$ , Displacement,  $\nabla$ , Beam,  $B$ , Length,  $L_{PP}$ , Water Plane Area,  $A_{WL}$ , and Inertia of Water Plane,  $I_{WL}$ .

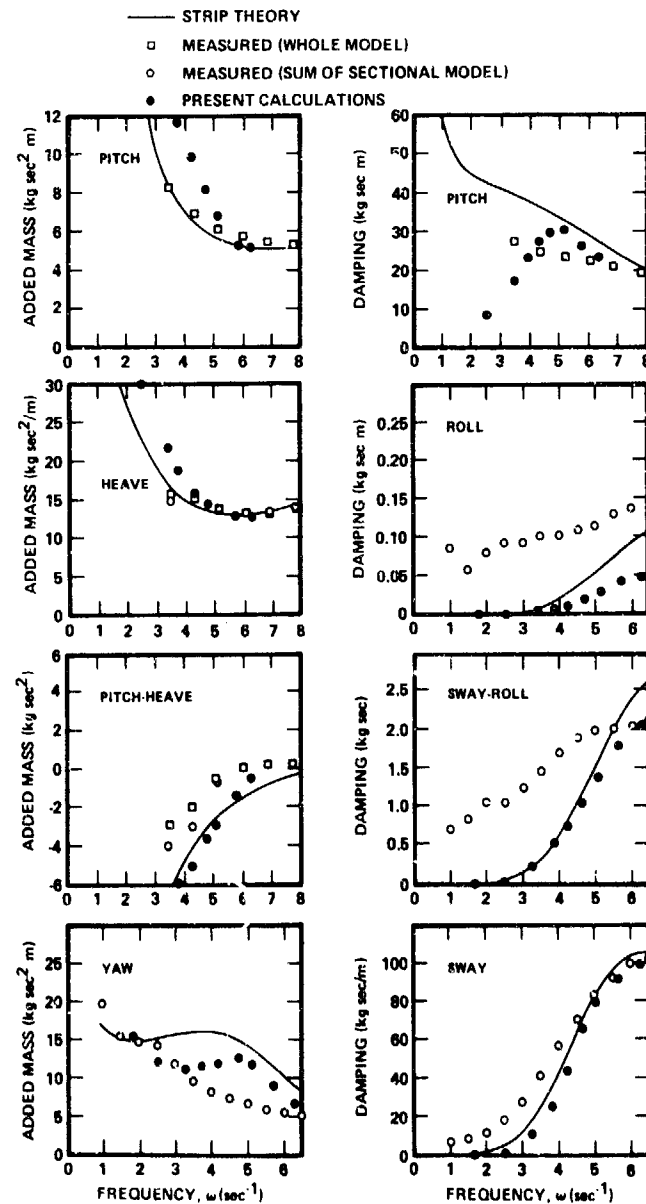


Figure 5 - Motion Coefficients with Simple Speed Correction  
 for Series 60,  $C_B = 0.70$  Hull Model at  $F_r = 0.20$

#### D. Motion Coefficients with Forward Speed

Reference 17 also provides motion coefficients for a Series 60,  $C_B = 0.70$ , ship model at a Froude number of 0.2. The present computation program has thus been

applied to calculate motion coefficients at this Froude number. The measurements, the strip-theory predictions and the results of the present calculations, neglecting the steady part of the perturbing motion, are presented in Figures 5 and 7 for comparison.

As has been mentioned, the forward speed effects on the computations of motion coefficients come from the free-surface condition, the modifications of the body boundary condition, and the modification of the computation of pressure on the body surface. By neglecting the effect from the free-surface condition the motion coefficients with forward speed can be expressed in terms of corresponding zero-speed coefficients. The formulae for calculating the unsteady hydrodynamic forces, equations (16) and (17), then lead to simple speed corrections,<sup>13</sup> i.e., for the heave added mass and sway, sway-roll and roll damping, the coefficients are speed independent. The simple speed-correction formulae are applicable to strip-theory calculations as well as the three-dimensional computations. Thus, neglect of the speed effect on the free-surface condition makes the method for computing three-dimensional motion coefficients with non-zero forward speed the same as that for strip theory, except that the two-dimensional zero-speed coefficients are replaced by their corresponding three-dimensional values. Figure 5 shows the results of three-dimensional calculations using the simple speed corrections. It is seen from the figure that, in comparison to the measurements, the present results denoted by  $\bullet$ , do not agree very well with the experimental results, denoted by  $\square$  and  $\circ$ ; this contrasts with the zero-speed results, where the comparisons were quite good except for the roll damping coefficients. The predicted magnitudes of the added masses at a Froude number of 0.2 are too high in comparison to the measurements whereas the predictions for zero speed were very good, as was shown in Figure 4.

In examining the strip-theory predictions, it is seen from Figure 5 that the predictions of the added masses for pitch and heave at Froude number 0.2 are good, and much better than the corresponding zero-speed predictions. In spite of the fact that strip-theory predictions for the other modes are not good, it is clear that at a Froude number of 0.2, the strip-theory predictions of pitch and heave added masses are better than the corresponding three-dimensional predictions which employ simple speed corrections. This result is rather astonishing because, to the order of the linear approximation, the formulae for the speed corrections are exact and the three-dimensional predictions for zero speed have been shown to be very good. Thus, one would expect better predictions from three-dimensional calculations than from strip theory, whose zero-speed predictions for heave and pitch added masses have been shown to be considerably lower than the experimental values. In order to better understand the reasons for this contradiction, the measured added masses of pitch and heave at Froude numbers of 0.0 and 0.2 are plotted together in Figure 6. It is seen that from a Froude number of 0.0 to a Froude number of 0.2, the added masses of both pitch and heave are significantly reduced, except at high frequencies where no significant change occurs. One may conclude from these measurements that the speed effect on the pitch and heave added masses over the frequency region presented is to reduce their magnitudes. Now, if one examines the formulae for the simple speed corrections to pitch and heave added masses, it will be found that the heave added masses are speed independent whereas the pitch added masses should increase with increasing speed since the measured heave added masses at zero Froude number take on positive values. This implies that the behavior of the measurements does not follow the simple speed corrections for pitch and heave added masses, which may explain the poor three-dimensional predictions using correct zero-speed predictions. It is then clear why the strip theory predictions were improved at a Froude number of 0.2: the zero-speed predictions from strip theory were underestimated so that when the measured added masses decreased with increasing speed the agreement between strip theory and experiment became better.

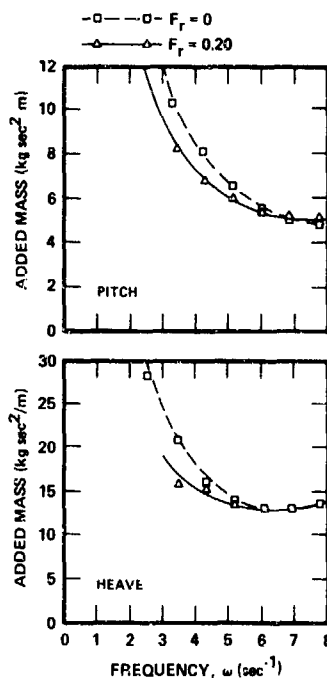


Figure 6 — Measured Pitch and Heaving Added Masses for Froude = 0.0 and 0.20

Consideration of the measurements at Froude numbers of 0.0 and 0.2, suggests that the speed effect on the free-surface condition may not be neglected in the present motion-coefficient computations. Motion coefficients were, thus, recomputed with the inclusion of the speed effect through the free-surface condition. That is, one computes the perturbation potential,  $\phi$ , from the fundamental singularity distribution using the exact values of  $\omega U/g$  instead of setting it equal to a very small number as in the previous calculations. The resulting predictions are plotted as Figure 7. In comparison with the measurements, the predictions of added masses at a Froude number of 0.2 are almost as good as the corresponding zero-speed predictions. It is interesting to note that the curve for the measured added mass for yaw has changed from convex at zero Froude number to concave at a Froude number of 0.2 and this change of characteristic is correctly predicted by including the speed effect of the free-surface condition. This was not predicted from either strip theory nor three-dimensional theory when using simple speed corrections. Note that the measured values, denoted by  $\circ$ , are the sum of sectional measurements which may not be identical to the measurements for the whole ship model, denoted by  $\square$ ; for example, for the yaw added mass, the values of the measurements  $\square$  at zero speed are lower than the values of the corresponding sectional sum  $\circ$ . In view of this, the present prediction of yaw added mass might have been considerably improved if the measurements  $\square$  had been available. The predictions of sway-roll and sway damping coefficients at a Froude number of 0.2 have about the same accuracies as their corresponding zero Froude-number predictions. The predictions are not



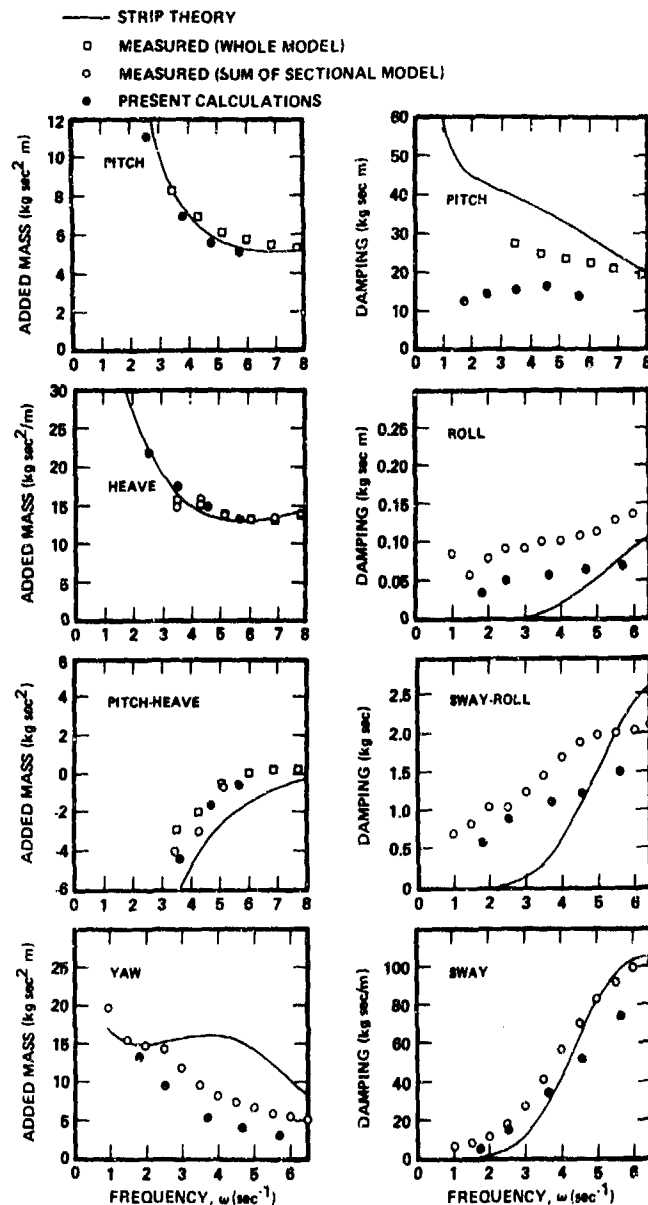


Figure 7 - Motion Coefficients for Series 60,  $C_B = 0.70$  at  $Fr = 0.20$

only better than those from strip theory, which are speed independent, but also resemble fairly well the measured speed effects as functions of frequencies; that is, above a frequency of about  $5 \text{ sec}^{-1}$  the speed effect decreases the values of the damping coefficients and below that frequency the speed effect increases the damping coefficients. The

predictions of roll damping coefficients do not appear to be good. However, the speed effect in increasing the roll damping coefficient at low values of frequency is clearly shown in both the experimental results and the predictions. The comparison between the predicted and measured pitch damping coefficient is not good. It is hard to understand

why the predicted pitch damping coefficients at a Froude number of 0.2 are so much lower than the measured values in view of the fact that the corresponding zero-speed predictions are very accurate. To check the present numerical results the computer program was applied to calculation of the pitch damping coefficients for a modified Wigley hull<sup>18</sup> specified by:

$$y = \frac{B}{2} \left\{ \left[ 1 - \left( \frac{2x}{L} \right)^2 \right] - \left[ \left( \frac{2x}{L} \right)^2 - \left( \frac{2x}{L} \right)^4 \right] \left( \frac{z}{D} \right)^{10} \right\} \left[ 1 - 0.3 \left( \frac{z}{D} \right)^8 - 0.7 \left( \frac{z}{D} \right)^{150} \right] \quad (19)$$

where L, B and D are the length, breadth and draft of the hull, respectively. Figure 8 shows comparison of pitch damping coefficients determined by the present calculation method, measurements,<sup>19</sup> and the thin-ship calculations by Newman.<sup>19</sup> It is seen from the figure that the present calculations agree quite well with the measurements and also agree qualitatively with the results of Newman, which were calculated from a polynomial representation of the hull. It seems, then, that the measured pitch damping coefficients for a Series 60,  $C_B = 0.70$ , model hull at a Froude number of 0.2 may include physical effects which are not included

in the present mathematical model, e.g., the steady part of the perturbations, non-linear effects, etc. To further improve the computation of pitch damping coefficients, one may have to include these additional speed-dependent terms.

## CONCLUDING REMARKS

A computer program developed for calculating the steady and unsteady forces on a ship moving in waves has been described. The program calculates the wave resistance, lift, motion coefficients and wave forces from a source distribution method. Unlike thin-ship theory and strip theory computations, the present computations employ three-dimensional source singularities which satisfy the body boundary condition at its mean position. The computer program has been used to evaluate the wave resistance of a Wigley hull tested by Shearer and the motion coefficients and wave forces of a Series 60,  $C_B = 0.7$  ship hull. Computations were also made for a modified Wigley hull tested by Golovato, in order to verify pitch damping coefficient predictions.

For Wigley Hull 2892, in the Froude number range of 0.25 to 0.60, it has been shown that the wave resistance predicted by the present method agrees well with experimental data. It has also been shown for this case that the wave resistance curve predicted by the present method has much smaller "humps" and "hollows" than those predicted by thin-ship theory.

A major effort was made in the present work to investigate the possible improvements of a three-dimensional theory for the calculation of ship motion coefficients and the wave exciting forces and moments. It was found from the zero forward speed calculations, that, for most of the frequency range, the agreement between the added mass coefficients computed by the present method and the experimental data is better than for strip theory. In general, the damping coefficients and the exciting forces and moments predicted by the present method and by strip theory are shown to agree well with experimental data, but for the pitch damping coefficient it was found that strip theory agrees poorly with both the present method and the experimental data. For the roll case there are some unresolved discrepancies between the present method, strip theory and experiments.

Finally, it is shown that the simple-speed correction normally used in strip theory does not adequately characterize the actual speed effects observed in the measurements. The speed term in the free-surface condition has to be included in order to obtain reasonable quantitative and qualitative predictions. When the speed terms are included in the free-surface condition, it is shown that the present results agree quite well with experimental data except in the cases of the roll-damping and pitch-damping coefficients. It seems that the discrepancy in the predicted pitch-damping coefficient of a Series 60,  $C_B = 0.7$ , hull form at a Froude number of 0.20 may result from some physical effects which have not been included in the present mathematical model. To improve the predictions for the pitch-damping coefficients consideration should be given to inclusion of the cross product terms between the oscillating potential and the steady perturbation potential which have been neglected in the present calculations.

The numerical results presented in this paper were obtained from the Texas Instrument Advanced Scientific Computer at the Naval Research Laboratory. The computation time for a zero forward speed case (or zero frequency case) was approximately 50 seconds for each frequency (or each Froude number). The cost is about \$15. For non-zero speed and non-zero frequency case the required computing

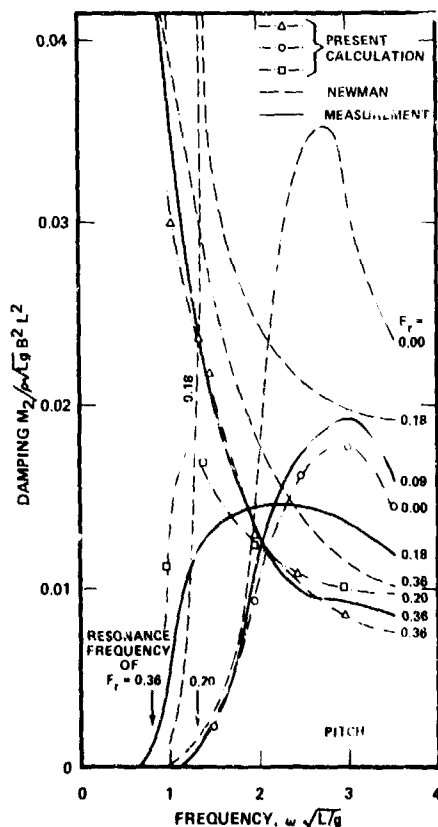


Figure 8 - Pitch Damping Coefficients for a Modified Wigley Hull

time and cost were approximately triple the zero-speed computing time and cost.

Although these calculations were performed on a fast new-generation computer, the computer program was developed for more conventional computers with smaller memory spaces such as the CDC 6600 or IBM 360. Therefore, the present computer program has not taken full advantage of the new larger computers. If one modifies the present program and vectorizes the statements, the speed of the computations will be increased. It is expected that the computing time can then be reduced by a factor of about three and the cost will be reduced to approximately \$5.00 and \$15.00 for each zero-speed run and each non-zero speed run, respectively. A further reduction in computation time can be expected to result from modifying the computations to take advantage of the large memory space of new computers.

#### ACKNOWLEDGMENT

The author wishes to express her thanks to Mr. Justin McCarthy for his continuous support of the work and to Dr. Nils Salvesen for valuable discussions during the course of this work. The author also wishes to thank Mr. Richard T. Van Eseltine for his assistance in converting the CDC program to a TI-ASC program. The work reported here was funded partially by the Naval Sea Systems Command General Hydrodynamics Research Program, Task Area SR 023 0101, program Element 61135N, Work Unit 1552-015 and partially by the Numerical Naval Hydrodynamics Program at the David W. Taylor Naval Ship Research and Development Center.

#### REFERENCES

1. Ursell, F., "On the Rolling Motion of Cylinders in the Surface of a Fluid," *Quarterly Journal of Mechanics and Applied Mathematics*, Vol. 2, 1949.
2. Korvin-Kroukovsky, B.V., "Investigation of Ship Motions in Regular Waves," *Transactions SNAME*, Vol. 63, 1955.
3. Salvesen, N., E.O. Tuck and O. Faltinsen, "Ship Motions and Sea Loads," *Transactions SNAME*, Vol. 78, 1970.
4. Chang, M-S. and P.C. Pien, "Hydrodynamic Forces on a Body Moving Beneath a Free Surface," 1st Int. Conference on Computational Ship Hydrodynamics, 1975.
5. Bai, K.J. and R.W. Yeung, "Numerical Solutions to Free-Surface Flow Problems," Proc. of 10th Symp. on Naval Hydrodynamics, Cambridge, Mass., 1974.
6. Kim, W.D., "On the Harmonic Oscillation of a Rigid Body on a Free Surface," *Journal of Fluid Mechanics*, Vol. 21, 1965.
7. Chang, M-S and P.C. Pien, "Velocity Potentials of Submerged Bodies Near a Free Surface—Application to Wave-Excited Forces and Motions," Proc. of 11th Symp. on Naval Hydrodynamics, London, England, 1976.
8. Todd, F.H., "Series 60, Methodical Experiments with Models of Single-Screw Merchant Ships," David Taylor Model Basin Report 1712, 1963.
9. Timman, R. and J.N. Newman, "The Coupled Damping Coefficients of a Symmetric Ship," *Journal of Ship Research*, Vol. 5, March 1962.
10. Wehausen, J.V., and E.V. Laitone, "Surface Waves," *Handbuch der Physik*, Vol. 9, Springer Verlag, Berlin, 1960.
11. Havelock, T.H., "The Effect of Speed of Advance upon the Damping of the Heave and Pitch," *Transactions Inst. Naval Arch.* Vol. 100, 1952.
12. Brard, R., "The Representation of a Given Ship Form by Singularity Distribution when the Boundary Condition on the Free Surface is Linearized," *Journal of Ship Research*, Vol. 16, No. 1, 1972.
13. Tuck, E.O., "A New Approach to the Strip Theory of Forced Ship Motions," Hydromechanics Lab., David Taylor Model Basin, Department Report, 1966.
14. Pien, P.C., "Calculation of Non-Lifting Potential Flow About Arbitrary Three-Dimensional Bodies Based on Doublet Distributions," David Taylor Naval Ship Research and Development Center, Department Report SPD 601-01, 1975.
15. Shearer, J.R., "A Preliminary Investigation of the Discrepancies Between the Calculated and Measured Wave-making of Hull Forms," *Trans. North East Coast Inst. Eng and Ship Builders*, Vol. 67, 1950.
16. Gerritsma, J. and W. Burkelman, "The Distribution of the Hydrodynamic Forces on a Heaving and Pitching Ship Model in Still Water," *Proc. of the 5th Symp. on Naval Hydrodynamics*, Bergen, Norway, 1964.
17. Vugts, J.H., "The Hydrodynamic Forces and Ship Motions in Waves," Ph. D. Thesis, Delft University of Technology, 1970.
18. Gotovato, P., "The Forces and Moments on a Heaving Ship," *Journal of Ship Research*, Vol. 1, 1957.
19. Newman, J.N., "The Damping and Wave Resistance of a Pitching and Heaving Ship," *Journal of Ship Research*, Vol. 3, 1959.

## COMPUTATION OF THE FIRST AND SECOND ORDER WAVE FORCES ON OSCILLATING BODIES IN REGULAR WAVES

J. F. Pinkster and G. van Oortmerssen  
Netherlands Ship Model Basin  
Wageningen, The Netherlands

### Abstract

A method is described to obtain first order wave forces, hydrodynamic reaction forces, mean second order wave forces on, as well as the wave induced motions of, floating bodies in regular waves by means of linear potential theory. The first order potential function which describes the flow is obtained numerically using a singularity distribution on the wetted surface of the body in its equilibrium position. The mean second order wave drift force is calculated by means of direct integration of the pressures on the hull as derived from the first order potential.

Results of computations are presented for a pipe lay-barge and compared with the results of model tests. The agreement between theoretical and experimental results appears to be satisfactory.

### Introduction

In offshore activities, stationary vessels play an important role as work platforms, storage and production units. In order to design such units from the point of view of vessel motions and mooring loads induced by environmental forces, prediction of the behaviour of the vessels is essential.

A major part of the environmental forces is due to the action of waves. The forces due to waves may be split into two parts, viz.

- oscillating wave forces with zero mean and frequency equal to the wave frequency. (First order wave forces.)
- mean and slowly varying forces with frequencies below wave frequencies.

(Low frequency second order wave forces)  
The first order wave forces are responsible for the well known ship motions with wave frequencies. The second order wave forces are, in many instances, the cause of low frequency, large amplitude horizontal motions of moored vessels. This low frequency behaviour is of importance from the point of view of mooring loads. From observations, both in reality and on model scale, of low frequency components in the vertical motions of for instance gravity platforms during towing

and submergence and submersibles, it has become obvious that second order wave exciting loads are of importance here also.

The first order wave exciting loads and motion response in irregular waves may be predicted from the normal frequency transfer functions which can be obtained from computations or tests in monochromatic waves. The low frequency wave exciting forces in irregular waves should be determined from knowledge of the wave excitation in bichromatic waves (regular wave groups). See for instance Newman [1] and Dalzell [2].

At the N.S.M.B. a program is being developed to predict the second order wave forces in bichromatic waves. The first phase of this development comprises the calculation of the mean second order forces and moments in regular waves. In this paper, results are presented of calculations of first order wave loads and motions and mean second order forces on a free floating vessel at zero forward speed and compared with the results of model tests. First and second order fluid forces can be obtained from a first order approximation of the potential function, which is obtained numerically by means of a three-dimensional singularity distribution (Green's functions) on the body surface in its equilibrium position.

This technique has been applied frequently during the last few years for large volume structures and many comparisons with experimental results have been reported. See for instance [3], [4]. The method used to predict the mean second order loads is based on a direct integration of pressures on the complete wetted surface of the body, while most existing methods (Salvesen [5], Michelsen and Faltinsen [6]) make use of the far field behaviour of the fluid. The advantage of the present method is that it provides more insight into the physical processes involved and will allow evaluation of the second order wave drift forces in bichromatic waves [7].

# Description of the theory

## First order wave loads and motions

The ship is considered as a rigid body, oscillating sinusoidally about a state of rest, in response to excitation by a long crested regular wave. The amplitudes of the motions of the ship as well as of the wave are supposed to be small while the fluid is assumed to be ideal and irrotational. A right handed, fixed system of coordinates  $OX_1X_2X_3$ , is defined with the origin in the mean position of the centre of gravity of the body and the  $OX_3$  axis vertically upwards. The oscillating motion of the ship in the  $j$ th mode is given by:

$$x_j = \zeta_j e^{-i\omega t} \quad j = 1, \dots, 6 \quad (1)$$

in which  $\zeta_j$  is the amplitude of motion in the  $j$ th mode and  $\omega$  the circular frequency.

The motion variables  $x_1$ ,  $x_2$  and  $x_3$  stand for the translations, surge, sway and heave, while  $x_4$ ,  $x_5$  and  $x_6$  denote rotations around the  $OX_1$ ,  $OX_2$  and  $OX_3$  axis respectively.

The free surface at great distance from the ship is defined by:

$$z = \zeta_0 e^{ik(x_1 \cos \alpha + x_2 \sin \alpha) - i\omega t} \quad (2)$$

where:

$\zeta_0$  = amplitude of the wave  
 $k$  = wave number  $= 2\pi/\lambda$ , where  $\lambda$  is the wave length  
 $\alpha$  = angle of incidence

The flow field can be characterized by a first order velocity potential

$$\phi(x_1, x_2, x_3, t) = \phi(x_1, x_2, x_3) e^{-i\omega t} \quad (3)$$

The potential function  $\phi$  can be separated into contributions from all modes of motion and from the incident and diffracted wave fields:

$$\phi = i\omega \sum_{j=1}^6 (\phi_{0j} + \phi_{7j}) - i\omega \sum_{j=1}^6 \phi_j \zeta_j \quad (4)$$

The incident wave potential is given by:

$$\phi_0 = \frac{1}{v} \frac{\cosh k(x_3 + c)}{\cosh kd} e^{ik(x_1 \cos \alpha + x_2 \sin \alpha)} \quad (5)$$

in which:

$v = \omega^2/g$   
 $c$  = the distance from the origin to the sea bed  
 $d$  = water depth

The cases  $j = 1, 2, \dots, 6$  correspond to the potentials due to the motion of the ship in the  $j$ th mode, while  $\phi_7$  is the potential of the diffracted waves. The individual potentials are all solutions of the Laplace equation which satisfy the linearized free surface condition and the boundary conditions on the sea floor, on the body's surface and at

infinity.

The potential function  $\phi_j$  can be represented by a continuous distribution of single sources on the boundary surface  $S$ :

$$\begin{aligned} \phi_j(x_1, x_2, x_3) &= \frac{1}{4\pi} \int_S \sigma_j(a_1, a_2, a_3) \cdot \\ &\gamma_j(x_1, x_2, x_3, a_1, a_2, a_3) dS \\ (j=1, 2, \dots, 7) \quad (6) \end{aligned}$$

where  $\gamma_j(x_1, x_2, x_3, a_1, a_2, a_3) =$   
= The Green's function of a source, singular in  $a_1, a_2, a_3$   
 $a_1, a_2, a_3$  = the vector, describing  $S^2$   
 $\sigma_j(a_1, a_2, a_3)$  = the complex source strength

For the Green's function a function is chosen which satisfies the Laplace equation and the boundary conditions on the sea bottom, in the free surface and at infinity. This function is given by (see Wehausen and Laitone [8]):

$$\begin{aligned} \gamma &= \frac{1}{r} + \frac{1}{r_1} \\ &+ PV \int_0^\infty \frac{\omega^2 (\xi + v) e^{-\xi d} \cosh \xi(a_3 + c)}{\xi \sinh \xi d - v \cosh \xi d} \\ &\frac{\cosh \xi(x_3 + c)}{\cosh \xi(x_3 + c)} \cdot J_0(\xi R) d\xi \\ &+ i \frac{2\pi (k^2 - v^2) \cosh k(a_3 + c) \cosh k(x_3 + c)}{k^2 d - v^2 d + v} \\ &\cdot J_0(kR) \quad (7) \end{aligned}$$

in which

$$\begin{aligned} r &= \sqrt{(x_1 - a_1)^2 + (x_2 - a_2)^2 + (x_3 - a_3)^2} \\ r_1 &= \sqrt{(x_1 - a_1)^2 + (x_2 - a_2)^2 + (x_3 + 2c + a_3)^2} \\ R &= \sqrt{(x_1 - a_1)^2 + (x_2 - a_2)^2} \end{aligned}$$

John [9] has derived the following series for  $\gamma$ , which is the analogue of (7):

$$\begin{aligned} \gamma &= 2\pi \frac{v^2 - k^2}{k^2 d - v^2 d + v} \cosh k(a_3 + c) \cosh k(x_3 + c) \\ &\cdot \{Y_0(kR) - i J_0(kR)\} \\ &+ \sum_{i=1}^\infty \frac{4(\mu_i^2 + v^2)}{d\mu_i^2 + dv^2 - v} \cdot \cos \mu_i(x_3 + c) \cos \mu_i(a_3 + c) \\ &\cdot K_0(\mu_i R) \quad (8) \end{aligned}$$

where  $\mu_i$  are the positive solutions of:

$$\mu_i \tan(\mu_i d) + v = 0 \quad (9)$$

Although these two representations are equivalent, one of the two may have preference for numerical computations, depending on the values of the variables. In general, equation (8) is the most convenient representation for calculations, but when  $R=0$  the value of  $K_0$  becomes infinite, and therefore equation (7) must be used when  $R$  is small or zero.

The unknown source strength function  $\sigma$  must be determined such, that the boundary condition on the body's surface  $S$  is fulfilled. Due to the linearization, this boundary condition is applied to

the surface in its equilibrium position  $S_0$ .

$$-\frac{1}{2} \sigma_j (x_1, x_2, x_3) + \frac{1}{4\pi} \iint_{S_0} \sigma_j (a_1, a_2, a_3) \frac{\partial \gamma_j}{\partial n} (x_1, x_2, x_3, a_1, a_2, a_3) dS =$$

$$= n_j \frac{\partial \Phi_0}{\partial n} \quad \text{for } j = 1, \dots, 6$$

$$= -\frac{\partial \Phi_0}{\partial n} \quad \text{for } j = 7 \quad (10)$$

$n_1$  through  $n_6$  are the generalized direction cosines on  $S_0$ , defined by:

$$\begin{aligned} n_1 &= \cos(n, x_1) \\ n_2 &= \cos(n, x_2) \\ n_3 &= \cos(n, x_3) \\ n_4 &= x_2 n_3 - x_3 n_2 \\ n_5 &= x_3 n_1 - x_1 n_3 \\ n_6 &= x_1 n_2 - x_2 n_1 \end{aligned} \quad (11)$$

To solve equation (6) numerically, the surface  $S$  is subdivided into a number of finite, plane elements on which the source strength is constant. The boundary condition is applied in one control point on each element being the centre of the element. The integral equation (6) then reduces to a set of algebraic equations in the unknown source strengths. In general, the Green function  $\gamma$  may be computed with sufficient accuracy as if the source strength is concentrated in the centre (control point) of each element. When, however, the influence of an element on its own control point is evaluated,  $\gamma$  has a singularity of the type  $1/r$ , which can be removed by spreading the source uniformly over the panel. When the influence of a panel on a control point which is at a close distance of this panel and not lying in the same plane, is considered, the source is spread uniformly and integrated numerically to obtain its contribution to  $\Phi$  or  $\frac{\partial \Phi}{\partial n}$ .

After solving the equations for the source strengths, the first order potential function is known. The pressure on the surface  $S$  can then be found from Bernoulli's theorem. The linearized hydrodynamic pressure is given by:

$$p(x_1, x_2, x_3, t) = -\rho \frac{\partial \Phi}{\partial t}$$

$$= \left[ \rho \omega^2 \zeta_0 (\Phi_0 + \Phi_7) + \rho \omega \sum_{j=1}^6 \zeta_j \Phi_j \right] e^{-i\omega t} \quad (12)$$

Subsequently, the first order wave exciting forces and moments can be found from:

$$X_k = -\rho \omega^2 \zeta_0 e^{-i\omega t} \iint_{S_0} (\Phi_0 + \Phi_7) n_k dS \quad (13)$$

The oscillating hydrodynamic forces ( $k=1, 2, 3$ ) and moments ( $k=4, 5, 6$ ) in the  $k$ th direction are:

$$F_k = -\rho \omega^2 \sum_{j=1}^6 \zeta_j e^{-i\omega t} \iint_{S_0} \Phi_j n_k dS \quad (14)$$

According to common practice the hydrodynamic forces are represented by means of added mass and damping coefficients:

$$a_{kj} = -\rho \operatorname{Re} \left\{ \iint_{S_0} \Phi_j n_k dS \right\} \quad (15)$$

$$b_{kj} = -\rho \omega \operatorname{Im} \left\{ \iint_{S_0} \Phi_j n_k dS \right\} \quad (16)$$

where:

$a_{kj}$  = the added mass coefficient in the  $k$ -mode due to motion in the  $j$ -mode  
 $b_{kj}$  = the damping coefficient in the  $k$ -mode due to motion in the  $j$ -mode

Finally, the motion response to first order excitation is computed by means of the well known equations of motion in the frequency domain:

$$\sum_{j=1}^6 \{ -\omega^2 (M_{kj} + a_{kj}) \sin(\omega t + \epsilon_j) + b_{kj} \omega \cos(\omega t + \epsilon_j) + c_{kj} \sin(\omega t + \epsilon_j) \} \zeta_j = X_k \sin(\omega t + \delta_k)$$

$$k=1, \dots, 6 \quad (17)$$

in which:

$X_k$  = wave excited force in the  $k$ th mode  
 $\epsilon_j, \delta_k$  = phase angles

$M_{kj}$  is an inertia matrix. Since the origin of the system of axes coincides with the centre of gravity of the ship in its rest position, it is found that

$$M_{kj} = \begin{bmatrix} m & 0 & 0 & 0 & 0 & 0 \\ 0 & m & 0 & 0 & 0 & 0 \\ 0 & 0 & m & 0 & 0 & 0 \\ 0 & 0 & 0 & I_4 & 0 & -I_{46} \\ 0 & 0 & 0 & 0 & I_5 & 0 \\ 0 & 0 & 0 & -I_{64} & 0 & I_6 \end{bmatrix} \quad (18)$$

where:

$m$  = mass of the ship  
 $I_k$  = moment of inertia in the  $k$ th mode  
 $I_{kj}$  = product of inertia

#### Mean second order wave loads

In vector notation the mean second order wave exciting forces and moments about the fixed  $OX_1X_2X_3$  system of co-ordinate axes are as follows:

$$\bar{F}^{(2)} = -\rho \sum_{j=1}^6 \zeta_j \overline{\zeta_j^{(1)} \zeta_j^{(1)}} \bar{n} dS -$$

$$\iint_{S_0} \left[ -\frac{1}{2} \rho \overline{|\nabla \Phi^{(1)}|^2} \bar{n} dS - \right.$$

$$\left. - \iint_{S_0} \rho \overline{(\bar{x}^{(1)} \cdot \nabla \Phi^{(1)})} \bar{n} dS + M_R \overline{\frac{1}{R} \cdot \bar{x}^{(1)}} \right] \bar{n} dS \quad (19)$$

$$\begin{aligned}
\text{and} \\
\bar{M}^{(2)} = & -\oint_{WL} \frac{1}{2} \rho g \bar{\zeta}_t^{(1)2} (\bar{x} \times \bar{n}) d\bar{l} \\
& - \iint_{S_0} \frac{1}{2} \rho |\bar{\nabla} \bar{\phi}_t^{(1)}|^2 (\bar{x} \times \bar{n}) d\bar{S} \\
& - \iint_{S_0} \bar{p} (\bar{x}^{(1)} \cdot \bar{\nabla} \bar{\phi}_t^{(1)}) (\bar{x} \times \bar{n}) d\bar{S} \\
& + \bar{I} \bar{R}^{(1)} \cdot \bar{x}_a^{(1)} - \bar{x}_g^{(1)} \cdot \bar{F}^{(1)} \quad (20)
\end{aligned}$$

where the heavy bar indicates that the time average has to be taken. The above expressions are derived in the appendix. In the above expression quantities marked (1) are first order quantities derived from the solution of the linear problem described in the previous section. The potential  $\bar{\phi}^{(1)}$  is composed of the first order potentials of the undisturbed incoming wave, the diffraction potential and the potential due to body motions. The relative wave height  $\bar{\zeta}_t^{(1)}$  at a point along the mean waterline is composed of contributions from the vertical motion of the point, and the potentials due to incoming waves, diffraction and body motions.

#### Calculations and model tests

##### The vessel

Calculations and model tests were carried out for a lay barge type vessel with the following main particulars.

Length	150 m.
Breadth	50 m.
Draft	10 m.
Displacement	73750 m <sup>3</sup>
KG	10 m.
Radius of gyration in air	
Roll	20 m.
Pitch	39 m.
Yaw	39 m.

A body plan of the vessel is shown in Fig 1. The water depth amounted to 50 m.

Model tests and calculations were carried out for regular waves with frequencies ranging from 0.3 rad/sec to 1.1 rad/sec and wave directions of 90°, 135° and 180°.

##### Calculations

For the calculations of the first order wave exciting forces, added mass and damping coefficients, first order motion responses and mean second order wave drifting forces and moments, the mean wetted surface of the vessel was subdivided in 138 facets as is shown in Fig 1. For the calculation of the relative wave height contribution to the mean second order forces, the water line was subdivided in 48 length elements, the length of each element corresponding to the length of the facet below. The relative wave height was calculated at the

half length of each line element.

The calculations were carried out for 15 frequencies. The average computing time of the FORTRAN program for one frequency amounted to 210 seconds on a CDC 6600 computer.

##### Model tests

The model tests were carried out in the shallow water laboratory of the Netherlands Ship Model Basin. This basin has the following principal dimensions:

Length	210 m.
Breadth	15.75 m.
Water depth	1.0 m.

A paddle type wave generator is fitted at one end of the basin. A perforated sloping beach at the other end of the basin serves to damp out the waves.

The model tests were carried out with a scale 1 : 50 model.

All tests were carried out in regular waves. The wave amplitudes varied slightly with the wave frequency. The amplitudes amounted to approximately 1.0 m. in reality.

The following tests were carried out

- Tests with the free-floating model moored between soft springs to determine the frequency response of the six ship motions and the mean longitudinal and transverse wave drifting forces and yawing moment. The test set-up is shown in Fig 2.
- Tests with a captive model to determine the frequency response of the first order wave excited forces and moments. The test set-up is shown in Fig 3.

**Measurements.** During the tests with the free-floating model, the linear motions of the centre of gravity of the vessel were measured by means of an optical tracking device following a point light source mounted in G. The pitch and roll motions were measured by means of gyroscopes in the model. The yaw motion was measured by means of an optical device mounted on the model which tracked a fixed light source.

The mean second order drifting forces and yawing moment were determined from the forces measured in the soft mooring system. Since the mean yawing moment is derived from the measured lateral forces fore and aft, and the horizontal rods containing the force transducers remain at a fixed distance fore and aft of the centre of gravity of the vessel, the measured yawing moment applies to a vertical axis through G and not to the vertical axis OX<sub>3</sub> of the fixed OX<sub>1</sub>X<sub>2</sub>X<sub>3</sub> system of axes. In order to make a proper comparison between calculations and measurements, the calculations of the yawing moment are carried out for the same axes. This means that in eqn. (20) the last term is omitted. During the tests with the captive model,

the model was connected to a rigid six component force transducer as shown in Fig 3. The forces and moments measured in the transducers were transformed to apply to the body axes through G. Force measurements were carried out using strain gauge transducers.

Test conditions. Both series of tests were carried out for a range of frequencies from 0.3 rad/sec to 1.1 rad/sec full scale and for wave directions of  $90^\circ$  (beam waves),  $135^\circ$  (bow quartering waves) and  $180^\circ$  (head waves)

Recording and analysis of measurements. The measured signals were recorded on FM magnetic tape and subjected to harmonic analysis.

#### Results of Measurements and Calculations

The results of measurements and calculations are shown in Fig 4 through Fig 32. In Fig 33 and Fig 34 a breakdown is given of the calculated mean longitudinal and transverse drifting forces in head waves and beam waves respectively while Fig 35 and Fig 36 show the calculated mean vertical wave drifting forces.

#### Discussion of the results

##### First order wave exciting forces and moments

In general, the agreement between calculations and measurements is good. In all cases the trends suggested by the measurements are predicted by the calculations. For a wave direction of  $180^\circ$  (head waves) the agreement is better than for the other wave directions.

##### First order motions

Here again the agreement between theory and experiment is good. As is usual, the roll motions, at the resonance frequency for beam waves ( $90^\circ$ ) and quartering waves ( $135^\circ$ ), are overestimated by the calculations due to the omission of the effect of viscous damping which occurs in reality.

##### Mean second order wave drifting forces and yaw moment

The agreement between measurements and calculations is, considering the magnitude of the forces involved, good. The agreement is best for the longitudinal force shown in Fig 32 for a wave direction of  $180^\circ$  (head waves).

For a wave direction of  $90^\circ$  (beam waves) the calculations predict a high value of the mean lateral force at roll resonance (see Fig 28). This is due to the fact that the first order roll motion is overestimated by the calculations.

For waves from  $135^\circ$  (quartering

waves), the mean longitudinal and lateral forces and yawing moment are shown in Fig 29 through Fig 31. The calculated mean longitudinal force predicts peak values at roll and pitch resonance which appear to be confirmed by the measurements. Some scattering of the measured data occurs at higher frequencies.

The calculated mean lateral force predicts a peak at roll resonance only. Unfortunately, no measurements were available at this frequency to confirm this peak. Considering, however, the overall agreement, the occurrence of this peak is felt to be realistic.

The experimental values of the mean yawing moment in quartering waves ( $135^\circ$ ) are calculated from the difference between the lateral forces measured fore and aft (see Fig 2). This yawing moment is small and consequently the accuracy of the measurements is less for this quantity.

In order to show the effect of the four components in the mean wave drifting force given in eqn. (19), a breakdown of the mean longitudinal force in head waves and the mean lateral force in beam waves is given in Fig 33 and Fig 34 respectively. The numerals I to IV shown in these Figures refer to the first, second, third and fourth terms in equation (19). In both cases, it is seen that the contribution due to the relative wave height is dominant. The contributions due to the product of motion and angular displacements have, as may be expected, largest values when there is a considerable amount of motion response. At higher frequencies these contributions vanish and only the relative wave height and the second order pressure due to the fluid velocity remain. For frequencies tending to infinity the vessel acts as a vertical wall. In this case the relative wave height contribution is double the velocity contribution, the sign being opposite. This is confirmed by the trend of the calculations.

The calculated mean vertical drift forces shown in Fig 35 and Fig 36 are small and will not result in a significant change in draft of this vessel. In the case of floating structures with relatively small waterplane areas the change of draft due to this force need not be insignificant as has been found from model tests.

#### Conclusions

The results of the investigation have confirmed again that accurate predictions can be made of the first order motions in regular waves of a floating body by means of a three dimensional singularity distribution on the body surface in its equilibrium position.

The method of direct integration over the wetted part of the hull of all contributions to the second order wave exciting forces and moments leads to



results which are confirmed to a large extent by the results of the model tests.

Results of calculations show that, in the case of horizontal forces on the body, the mean second order wave drift forces are predominantly due to the contribution originating from the relative wave height. Contributions due to second order pressures on the hull counteract the relative wave height contribution and are directed into the incoming waves. The predominance of the effect of the relative wave height has also been noted in previous investigations concerning the low frequency surge motions of a moored barge in irregular waves (see ref [7]).

A direct, practical, application of the theoretical formulation for the second order wave drifting forces is being investigated at present at the NSMB. This involves the instantaneous evaluation of the relative wave height contribution to the second order, low frequency, longitudinal and lateral forces and yawing moment through the measurement of the relative wave height at a number of points along the waterline of a stationary vessel in arbitrary wave conditions. In this way, a partial wave feed forward control signal is generated which may be of practical use in, for instance, dynamic positioning of vessels in irregular waves.

#### References

- 1 Newman, J.N.;  
Second-order, slowly-varying forces on vessels in irregular waves. Paper 19, Int. Symp. on the dynamics of Marine vehicles and structures in waves, London 1974.
- 2 Dalzell, J.;  
Application of the functional polynomial model to the added resistance problem. Eleventh symposium on naval hydrodynamics, London, 1976.
- 3 Boreel, L.J.;  
"Wave action on large offshore structures". Conference on offshore structures, Inst. of Civil Engineers, London, 1974.
- 4 Van Oortmerssen, G.;  
"The motions of a ship in shallow water". Ocean Engineering, Vol. 3, pp 221-255, 1976.
- 5 Salvesen, N.;  
Second-order steady-state forces and moments on surface ships in oblique regular waves. Paper 22, International symposium on the dynamics of marine vehicles and structures in waves, London, 1974.
- 6 Faltinsen, O., Michelsen, F.C.;  
Motions of large structures in waves at zero Froude number, Paper 11, International symposium on the dynam-

ics of marine vehicles and structures in waves, London, 1974.

- 7 Pinkster, J.A.;  
"Low frequency second order wave forces on vessels moored at sea". Eleventh symposium on naval hydrodynamic, London, 1976.
- 8 Wehausen, J.V., Laitone, E.V.;  
"Handbuch der Physik". Vol. 9, Springer Verlag, Berlin 1960.
- 9 John, F.;  
"On the motion of floating bodies". Comm. on pure and applied mathematics, Part I : 2, 1949, pp. 13-57; Part II : 3, 1950, pp. 45-100.
- 10 Stoker, J.J.;  
"Water waves". Interscience publishers INC., New York, 1957.
- 11 Joseph, D.D.;  
"Domain perturbations: the higher order theory of infinitesimal water waves". Arch. Rational Mech. Anal. Vol. 51 (295-303) 1973.

# Appendix: Second order wave forces on a body floating in waves

For the determination of the second order wave drifting forces and moments it is first assumed that the body is floating in arbitrary irregular waves. Although this is not necessary for the determination of the mean drifting force in regular waves, it has been followed here since the expressions derived will be more general. The restriction to regular waves will be introduced at the end.

## Co-ordinate systems

Use is made of three systems of co-ordinate axes (see Fig 37). The first is a right handed system of  $Gx_1x_2x_3$  body axes with as origin the centre of gravity  $G$  and with positive  $Gx_3$  axis vertically upwards in the mean position of the oscillating vessel. The surface of the hull is uniquely defined relative to this system of axes. A point on the surface has as position the vector  $x$ . The orientation of a surface element in this system of axes is defined by the outward pointing normal vector  $n$ . In the development of the expressions for the wave drifting forces we assume that the motions of the body consist of a part which is due to the first order wave exciting forces (motions indicated by (1)) and a part which is due to the second order wave exciting forces (motions indicated by (2)).

The second system of co-ordinate axes is a  $Gx_1\bar{x}_2\bar{x}_3$  system with the centre of gravity as origin. The  $Gx_1$  axis coincides with the  $Gx_1$  axis of the body axes. The  $G\bar{x}_3$  axis is at all times vertically upwards. The  $G\bar{x}_2$  axis is at all times horizontal and at right angles to both  $Gx_1$  and  $G\bar{x}_3$  axes. The angular displacements of the body  $x_4, x_5, x_6$  (roll, pitch, yaw) are about the  $Gx_1, Gx_2$  and  $Gx_3$  axes respectively.

The third system of co-ordinate axes is a fixed righthanded  $OX_1X_2X_3$  system which coincides with the  $Gx_1x_2x_3$  and  $Gx_1\bar{x}_2\bar{x}_3$  systems when the vessel is in the mean position. The linear motions  $\bar{x}_g$  of the centre of gravity of the vessel are defined relative to this system of axes.

The position vector relative to the fixed system of axes of any point on the hull which has the position vector  $\bar{x}$  relative to the body axes follows from

$$\bar{x} = \bar{x}_g + R \cdot x \quad (21)$$

where  $R$  is the matrix:

$$R = \begin{bmatrix} a_{11} & a_{12} & a_{13} \\ a_{21} & a_{22} & a_{23} \\ a_{31} & a_{32} & a_{33} \end{bmatrix} \quad (22)$$

and

$$\begin{aligned} a_{11} &= \cos x_5 \cos x_6 \\ a_{12} &= \sin x_4 \sin x_5 \cos x_6 - \cos x_4 \sin x_6 \\ a_{13} &= \cos x_4 \sin x_5 \cos x_6 + \sin x_4 \sin x_6 \\ a_{21} &= \cos x_5 \sin x_6 \\ a_{22} &= \sin x_4 \sin x_5 \sin x_6 + \cos x_4 \cos x_6 \\ a_{23} &= \cos x_4 \sin x_5 \sin x_6 - \sin x_4 \cos x_6 \\ a_{31} &= -\sin x_5 \\ a_{32} &= \sin x_4 \cos x_5 \\ a_{33} &= \cos x_4 \cos x_5 \end{aligned} \quad (23)$$

If all angular displacement are zero  $R$  becomes

$$R = R^{(0)} = \begin{bmatrix} 1 & 0 & 0 \\ 0 & 1 & 0 \\ 0 & 0 & 1 \end{bmatrix} \quad (24)$$

If the body is carrying out small amplitude motions the linearized (first order) displacements follow from

$$\bar{x}^{(1)} = \bar{x}_g^{(1)} + R^{(1)} \cdot x \quad (25)$$

$$\text{where } R^{(1)} = \begin{bmatrix} 0 & -x_6^{(1)} & x_5^{(1)} \\ x_6^{(1)} & 0 & -x_4^{(1)} \\ -x_5^{(1)} & x_4^{(1)} & 0 \end{bmatrix} \quad (26)$$

If the body is carrying out motions which are a combination of first order motions and small, low frequency motions induced by the second order wave drifting forces, the second order displacements follow from:

$$\bar{x}^{(2)} = \bar{x}_g^{(2)} + R^{(2)} \cdot x \quad (27)$$

$$\text{where } R^{(2)} = \begin{bmatrix} b_{11} & b_{12} & b_{13} \\ b_{21} & b_{22} & b_{23} \\ b_{31} & b_{32} & b_{33} \end{bmatrix} \quad (28)$$

in which:

$$\begin{aligned} b_{11} &= -\frac{1}{2}(x_5^{(1)2} + x_6^{(1)2}) \\ b_{12} &= -x_6^{(2)} + x_4^{(1)}x_5^{(1)} \\ b_{13} &= x_5^{(2)} + x_4^{(1)}x_6^{(1)} \\ b_{21} &= x_6^{(2)} \\ b_{22} &= -\frac{1}{2}(x_6^{(1)2} + x_4^{(1)2}) \\ b_{23} &= -x_4^{(2)} + x_5^{(1)}x_6^{(1)} \\ b_{31} &= -x_5^{(2)} \\ b_{32} &= x_4^{(2)} \\ b_{33} &= -\frac{1}{2}(x_4^{(1)2} + x_5^{(1)2}) \end{aligned} \quad (29)$$

### Fluid motions

The fluid domain is bounded by the free surface, the surface of the body and the sea floor. Assuming that the fluid is inviscid, irrotational, homogeneous and incompressible, the fluid motion may be described by means of the velocity potential  $\phi$  [10]:

$$\phi = \epsilon \phi^{(1)} + \epsilon^2 \phi^{(2)} + \dots \quad (30)$$

The potentials are defined relative to the fixed system of  $Ox_1, x_2, x_3$  axes.

The first order potential  $\phi^{(1)}$  consists of the sum of three potentials associated with the undisturbed incoming waves, the diffracted waves and waves due to the first order body motion respectively:

$$\phi^{(1)} = \phi_w^{(1)} + \phi_d^{(1)} + \phi_b^{(1)} \quad (31)$$

Both the first and second order potential must satisfy the equation of continuity within the fluid domain and to first and second order respectively the boundary condition on the moving surface of the body and the fixed horizontal surface of the sea-floor.

The boundary condition at the mean free surface becomes:

$$g \phi_{x_3}^{(1)} + \phi_{tt}^{(1)} = 0 \quad (32)$$

$$g \phi_{x_3}^{(2)} + \phi_{tt}^{(2)} = -2 \bar{\nabla} \phi^{(1)} \cdot \bar{\nabla} \phi_t^{(1)} + \frac{1}{g} \phi_t^{(1)} \phi_{x_3 x_3}^{(1)} + \frac{1}{g} \phi_{tt x_3}^{(1)} \quad (33)$$

For derivation of eqn. 32 and eqn. 33 see for instance ref. [10].

Since this paper is concerned with the first order and mean second order forces in regular waves, the second order potential  $\phi^{(2)}$  contribution disappears, (see ref. [5]). For further details of boundary condition for  $\phi^{(1)}$  and its components see for instance ref. [4].

### Pressure in a point mooring within the fluid domain

We consider a point within the fluid domain with mean position  $\bar{x}^{(0)}$  relative to the fixed system of axes  $Ox_1, x_2, x_3$ . We furthermore assume that the point is carrying out small oscillations relative to the mean position:

$$\bar{x} = \bar{x}^{(0)} + \epsilon \bar{x}^{(1)} + \epsilon^2 \bar{x}^{(2)} \quad (34)$$

The pressure in the moving point follows from the Bernoulli equation:

$$p = -\rho g (x_3 - d) - \rho \phi_t - \frac{1}{2} \rho |\bar{\nabla} \phi|^2 \quad (35)$$

where  $(x_3 - d)$  denotes its instantaneous vertical distance below the mean free surface and  $\phi$  and its derivatives are taken at the instantaneous position.

Using the small amplitude motion assumption the pressure in the instantaneous position may be given in terms of the derivatives of  $\phi$  in the mean position. Up to second order the pressure  $p$  becomes:

$$p = p^{(0)} + \epsilon p^{(1)} + \epsilon^2 p^{(2)} \quad (36)$$

where:

$$p^{(0)} = -\rho g (x_3 - d) \quad (37)$$

$$p^{(1)} = -\rho g \bar{x}_3^{(1)} - \rho \phi_t^{(1)} \quad (38)$$

$$p^{(2)} = -\rho g \bar{x}_3^{(2)} - \rho (\bar{x}^{(1)} \cdot \bar{\nabla} \phi_t^{(1)}) - \frac{1}{2} \rho |\bar{\nabla} \phi^{(1)}|^2 - \rho \phi_t^{(2)} \quad (39)$$

Up to now we have assumed that the point is moving within the fluid domain. The same expression will be used to determine the pressure on a point on the hull of the body. This means that derivatives of the potentials are taken at the mean position of the hull which is alternately within and outside the actual fluid domain. This appears to be permissible if the potential functions are sufficiently "smooth" at the boundaries (see ref. [11]). This is assumed to be satisfied in this case.

### Fluid forces on the body

The forces exerted on the body, relative to the fixed  $Ox_1, x_2, x_3$  system of axes follow from:

$$\bar{F} = - \int_S p \bar{N} dS \quad (40)$$

where  $S$  is the instantaneous wetted surface and  $\bar{N}$  is the instantaneous normal vector of the surface element  $dS$  relative to the fixed system of axes and  $p$  is the pressure given in eqn. 36.

Since the body is moving in all six degrees of freedom,  $\bar{N}$  is also an oscillating quantity of the following form:

$$\bar{N} = \bar{N}^{(0)} + \epsilon \bar{N}^{(1)} + \epsilon^2 \bar{N}^{(2)} \quad (41)$$

where  $\bar{N}^{(0)}$  is the normal vector relative to the fixed system of axes in the mean position and hence equal to the normal vector  $\bar{n}$  relative to the body axes  $Gx_1, x_2, x_3$ .  $\bar{N}^{(1)}$  is an oscillatory component of  $\bar{N}$  due to first order oscillatory angular displacements.

$$\bar{N}^{(1)} = R^{(1)} \cdot \bar{n} \quad (42)$$

in which  $R^{(1)}$  is according to eqn. 26

A similar equation to 42 may be set up for  $\bar{N}^{(2)}$ :

$$\bar{N}^{(2)} = R^{(2)} \cdot \bar{n} \quad (43)$$

in which  $R^{(2)}$  is according to eqn. 28

The instantaneous wetted surface  $S$  may be split up into a mean surface  $S^0$  extending up to the mean waterline of the vessel and an oscillatory part  $s$

which is continually submerging and emerging.

The expression for the fluid force then becomes:

$$\vec{F} = - \iint_{S_0} p \vec{N} dS - \iint_S p \vec{N} dS \quad (44)$$

Substitution of the pressure  $p$  as given in eqn 36 and the normal vector  $\vec{N}$  given in eqn. 41 gives:

$$\begin{aligned} \vec{F} = & - \iint_{S_0} (p^{(0)} + \epsilon p^{(1)} + \epsilon^2 p^{(2)}) (\vec{n} + \epsilon \vec{N}^{(1)} + \epsilon^2 \vec{N}^{(2)}) dS - \iint_S (p^{(0)} + \epsilon p^{(1)} + \epsilon^2 p^{(2)}) (\vec{n} + \epsilon \vec{N}^{(1)} + \epsilon^2 \vec{N}^{(2)}) dS \end{aligned} \quad (45)$$

Integration of the various components in 45 using eqn. 37, 38, 39 and 42 and taking into account that the surface  $s$  is an oscillating quantity gives the following result for the total fluid force up to the second order:

$$\vec{F} = \vec{F}^{(0)} + \epsilon \vec{F}^{(1)} + \epsilon^2 \vec{F}^{(2)} \quad (46)$$

where,

$$\vec{F}^{(0)} = - \iint_{S_0} \rho g (X_3 - d) \vec{n} dS \quad (47)$$

$$\vec{F}^{(1)} = - \iint_{S_0} \rho g X_3^{(1)} \vec{n} dS - \iint_{S_0} \rho \phi_t^{(1)} \vec{n} dS \quad (48)$$

$$\begin{aligned} \vec{F}^{(2)} = & - \phi_t \rho g \zeta_r^{(1)} \vec{n} dS - \iint_{S_0} \phi_t^{(1)} \vec{n} dS - \iint_{S_0} \rho \phi_t^{(2)} \vec{n} dS - \iint_{S_0} \rho (\vec{x}^{(1)} \cdot \vec{\nabla} \phi_t^{(1)}) \vec{n} dS - \iint_{S_0} \rho \phi_t^{(2)} \vec{n} dS + R^{(1)} \cdot \vec{F}^{(1)} - \iint_{S_0} \rho g X_3^{(2)} \vec{n} dS \end{aligned} \quad (49)$$

in which:

$$X_3^{(2)} = X_g^{(2)} - x_g^{(2)} \cdot x_1 + x_4^{(2)} x_2 \quad (50)$$

and  $R^{(1)}$  is according to eqn. 26

Equation 47, 48 and 49 give the total hydrostatic, first order and second order fluid forces acting on the body oscillating under the influence of waves. The first and second order forces  $\vec{F}^{(1)}$  and  $\vec{F}^{(2)}$  contain not only the wave exciting forces but also the hydrostatic and hydrodynamic reaction forces due to body motions in first and second order respectively. As such the term containing  $\vec{F}^{(1)}$  in eqn. 49 may be simplified by using the following relationship:

$$\vec{F}^{(1)} = M \cdot \vec{X}_g^{(1)} \quad (51)$$

where:

$$M = \begin{bmatrix} m & 0 & 0 \\ 0 & m & 0 \\ 0 & 0 & m \end{bmatrix} \quad (52)$$

and  $\vec{X}_g^{(1)}$  are the first order motions of the body under the influence of the first

order wave forces calculated at the centre of gravity of the body. From the afore going it is clear that in order to be able to determine the second order force, the complete solution to the first order excitation must be known. The method used for this is discussed in the paper.

#### Mean second order force in regular waves

Up to now, the approach has been as general as possible in that no restrictions were placed on the nature of incoming waves. We will now place the restriction that the incoming waves are regular. In that case the contribution of  $\phi^{(2)}$  to the second order force given in eqn. 49 disappears (see ref. [5]). We will also disregard the second order hydrostatic reaction term since this is in fact a reaction force due to second order displacements under the influence of the mean second order wave exciting force which then follows from:

$$\begin{aligned} \vec{F}^{(2)} = & - \phi_t \rho g \zeta_r^{(1)} \vec{n} dS - \iint_{S_0} \phi_t^{(1)} \vec{n} dS - \iint_{S_0} \rho \phi_t^{(2)} \vec{n} dS - \iint_{S_0} \rho (\vec{x}^{(1)} \cdot \vec{\nabla} \phi_t^{(1)}) \vec{n} dS + M \cdot \vec{R}^{(1)} \cdot \vec{X}_g^{(1)} \end{aligned} \quad (53)$$

where the heavy bar indicates the time average of the quantity under the bar.

#### Mean second order moments in regular waves

The mean second order moments about the axes of the fixed  $OX_1X_2X_3$  system of axes are found by the same development as was used for the forces. We give here the final results:

$$\begin{aligned} \vec{M}^{(2)} = & - \phi_t \rho g \zeta_r^{(1)} \vec{x} \cdot \vec{n} dS - \iint_{S_0} \phi_t^{(1)} \vec{x} \cdot \vec{n} dS - \iint_{S_0} \rho \phi_t^{(2)} \vec{x} \cdot \vec{n} dS - \iint_{S_0} \rho (\vec{x}^{(1)} \cdot \vec{\nabla} \phi_t^{(1)}) \vec{x} \cdot \vec{n} dS + I \cdot \vec{R}^{(1)} \cdot \vec{X}_g^{(1)} - \vec{X}_g^{(1)} \cdot \vec{F}^{(1)} \end{aligned} \quad (54)$$

where:

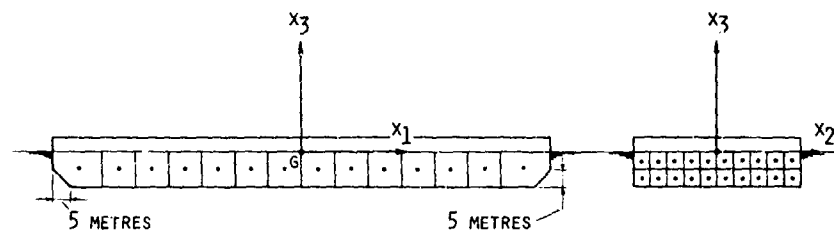
$$I = \begin{bmatrix} I_4 & 0 & -I_{46} \\ 0 & I_5 & 0 \\ -I_{64} & 0 & I_6 \end{bmatrix} \quad (55)$$

In the term involving  $I$ ,  $\vec{X}_g^{(1)}$  refers to the first order angular acceleration vector and  $\vec{R}^{(1)}$  is according to eqn. 26 and  $\vec{F}^{(1)}$  according to eqn. 51.

#### Nomenclature

$\omega$	frequency in rad/sec.
$x_k$	first order linear motions for $k=1,2,3$
	first order angular motions for $k=4,5,6$
$\vec{X}^{(1)}$	first order linear motion vector in fixed system of axes
$\vec{X}_a^{(1)}$	first order angular motion vector

$\bar{X}_g^{(1)}$	tor about $Gx, X_1, X_2$ axes first order linear motion vector of centre of gravity in fixed system of axes	mean free surface in reposition.
$\bar{x}$	position vector of a point relative to body axes	
$\bar{n}$	normal vector defined relative to body axes	
$\bar{N}$	normal vector defined relative to fixed system of axes	
$x_k^{(1)}$	first order angular motion about $Gx, X_1, X_2$ axes for $k=4, 5, 6$ . Components of $\bar{X}_a$	
$R$	Transformation matrix containing angular motions about $Gx, X_1, X_2$ axes	
$\bar{X}$	position vector in fixed system of axes	
$\bar{X}^{(0)}$	constant part of position vector in fixed system of axes	
$\bar{X}^{(2)}$	second order linear motion vector in fixed system of axes	
$x_k^{(2)}$	second order linear displacements in fixed system of axes for $k=1, 2, 3$ . Components of $\bar{X}^{(2)}$	
$x_k^{(2)}$	second order angular motion about $Gx, X_1, X_2$ axes for $k=4, 5, 6$ due to second order wave forces	
$m$	mass of body	
$I_4, I_5, I_6$	mass moments of inertia	
$I_{46}, I_{64}$	products of inertia	
$\zeta_r^{(1)}$	first order relative wave height in a point along the mean waterline	
$S$	instantaneous wetted surface	
$S_0$	mean wetted surface	
$s$	periodically emerging and submerging part of wetted surface	
$WL$	waterline	
$dS$	element of surface $S, S_0$ or $s$	
$dl$	length element of waterline	
$\rho$	specific mass of fluid	
$g$	acceleration of gravity	
$x_1, x_2, x_3$	first order wave exciting moments about $OX_1, OX_2, OX_3$ axes respectively of the fixed system of axes	
$\phi$	total potential describing fluid motion	
$\phi^{(1)}, \phi^{(2)}$	first and second order approximations for the total potential $\phi$	
$\epsilon$	a small parameter $\epsilon \ll 1$	
$\bar{F}_1, \bar{F}_2, \bar{F}_3$	mean second order wave exciting forces along the $OX_1, OX_2$ and $OX_3$ axes respectively of the fixed system of axes	
$\bar{M}_3$	mean second order wave exciting yaw moment about a vertical axis through the centre of gravity $G$ of the body	
$\epsilon_0$	wave amplitude	
$k$	wave number	
$V$	displaced volume of the barge	
$L$	length of the barge	
$B$	breadth of the barge	
$d$	Vertical distance of $G$ below	



LENGTH 150 METRES  
 BREADTH 50 METRES  
 DRAFT 10 METRES

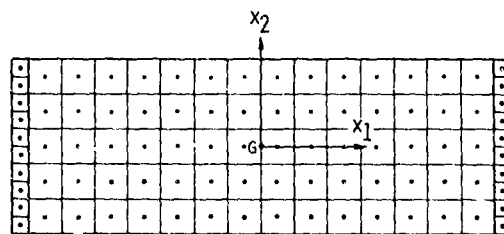


FIG. 1: BODY PLAN OF LAY BARGE INCLUDING FACET AND CONTROL POINT DISTRIBUTION

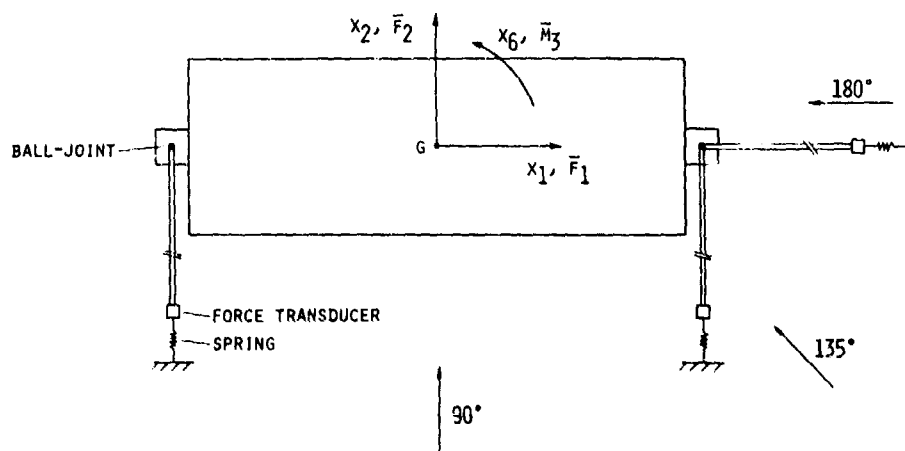


FIG. 2: SET-UP FOR TESTS TO DETERMINE MOTIONS AND MEAN DRIFT FORCES

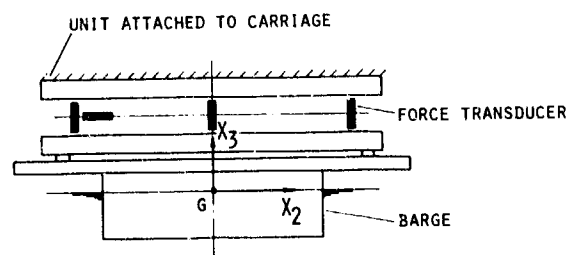
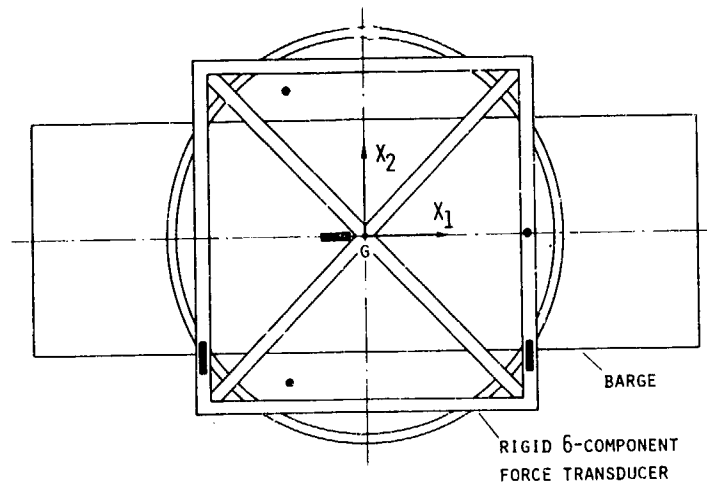


FIG. 3: SET-UP FOR WAVE FORCE TESTS

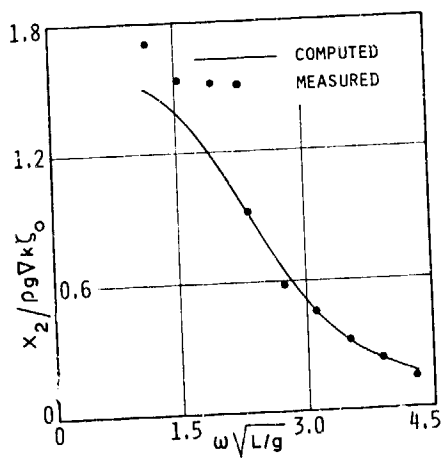


FIG. 4: AMPLITUDE OF TRANSVERSE WAVE  
FORCE  
WAVE DIRECTION 90°

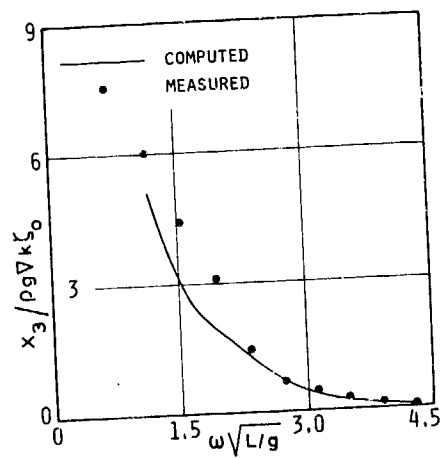


FIG. 5: AMPLITUDE OF VERTICAL WAVE  
FORCE  
WAVE DIRECTION 90°

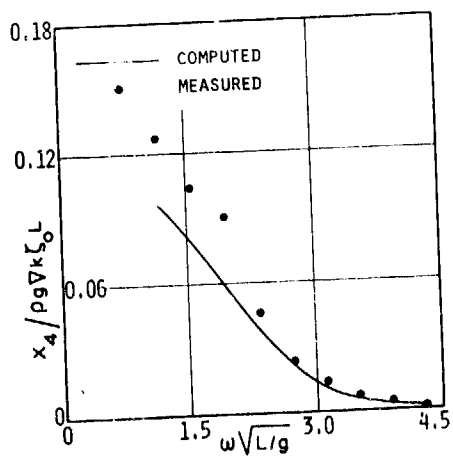


FIG. 6: AMPLITUDE OF ROLL MOMENT  
WAVE DIRECTION 90°

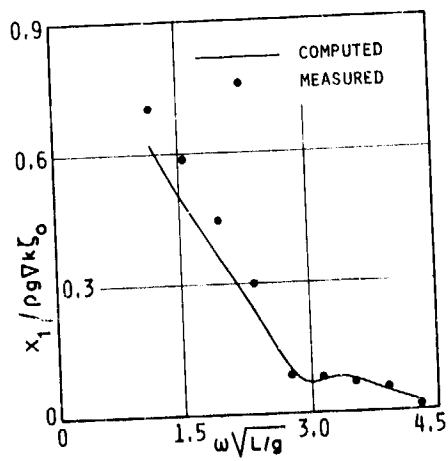


FIG. 7: AMPLITUDE OF LONGITUDINAL WAVE  
FORCE  
WAVE DIRECTION 135°



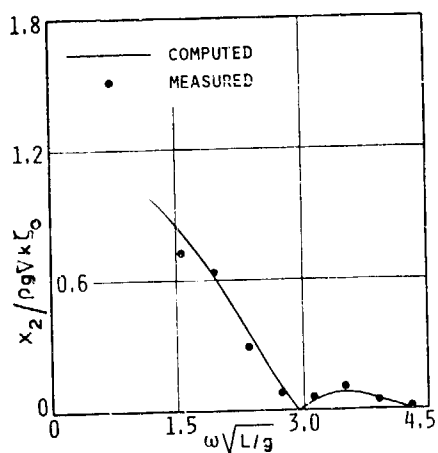


FIG. 8: AMPLITUDE OF TRANSVERSE WAVE  
FORCE  
WAVE DIRECTION 135°

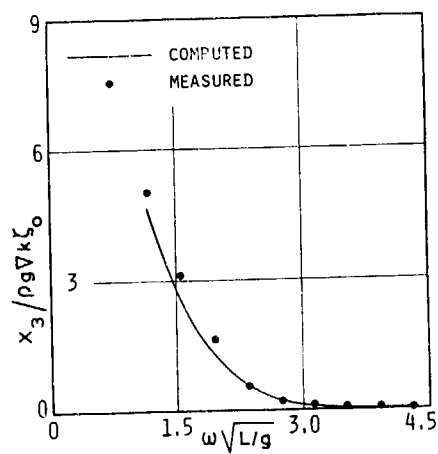


FIG. 9: AMPLITUDE OF VERTICAL WAVE  
FORCE  
WAVE DIRECTION 135°

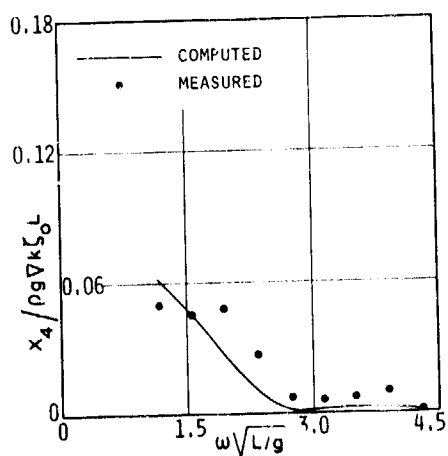


FIG. 10: AMPLITUDE OF ROLL MOMENT  
WAVE DIRECTION 135°

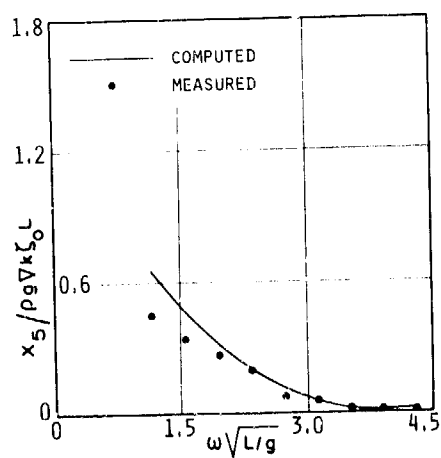


FIG. 11: AMPLITUDE OF PITCH MOMENT  
WAVE DIRECTION 135°

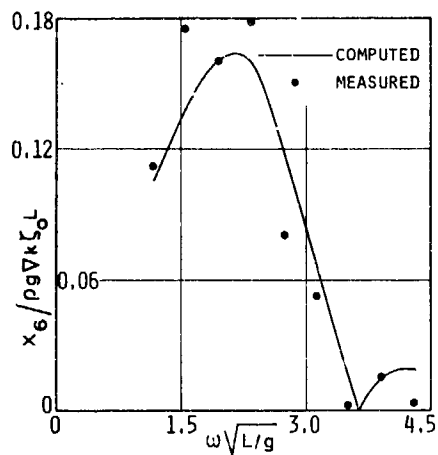


FIG. 12: AMPLITUDE OF YAW MOMENT  
WAVE DIRECTION 135°

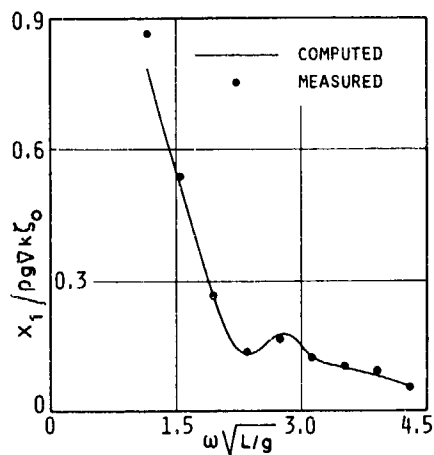


FIG. 13: AMPLITUDE OF LONGITUDINAL WAVE  
FORCE  
WAVE DIRECTION 180°

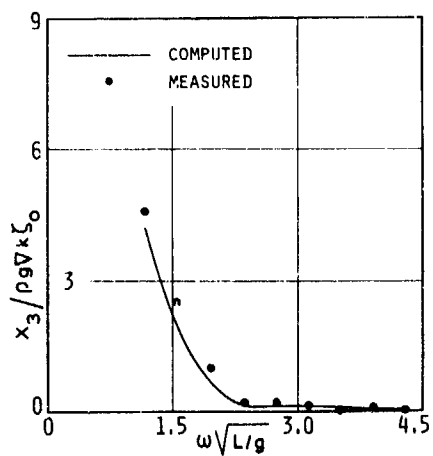


FIG. 14: AMPLITUDE OF VERTICAL WAVE  
FORCE  
WAVE DIRECTION 180°

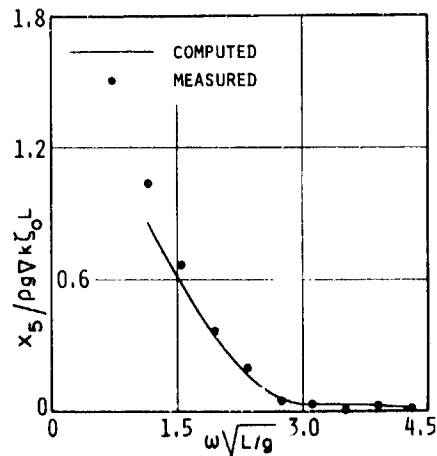


FIG. 15: AMPLITUDE OF PITCH MOMENT  
WAVE DIRECTION 180°

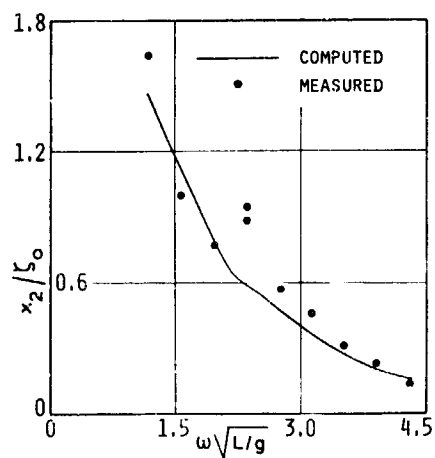


FIG. 16: AMPLITUDE OF SWAY MOTION  
WAVE DIRECTION 90°

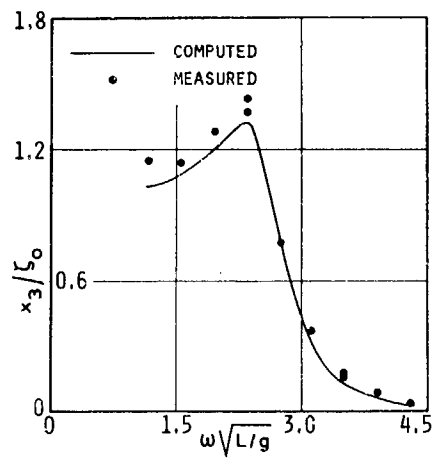


FIG. 17: AMPLITUDE OF HEAVE MOTION  
WAVE DIRECTION 90°

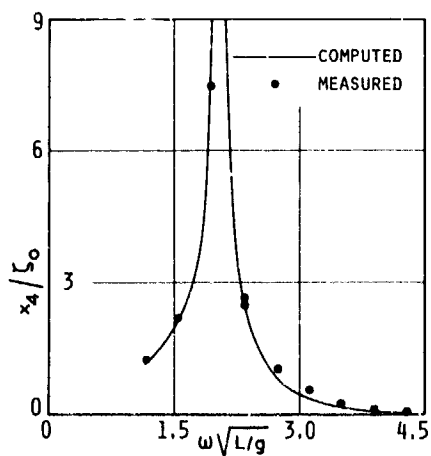


FIG. 18: AMPLITUDE OF ROLL MOTION  
WAVE DIRECTION 90°

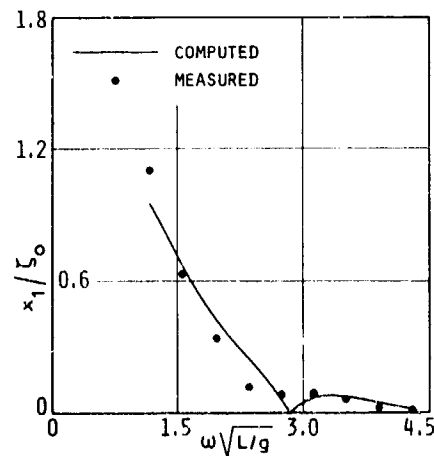


FIG. 19: AMPLITUDE OF SURGE MOTION  
WAVE DIRECTION 135°

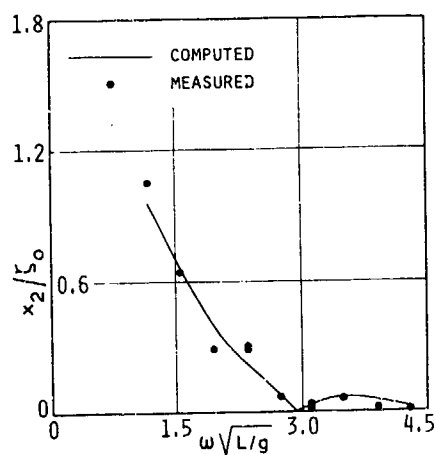


FIG. 20: AMPLITUDE OF SWAY MOTION  
WAVE DIRECTION 135°

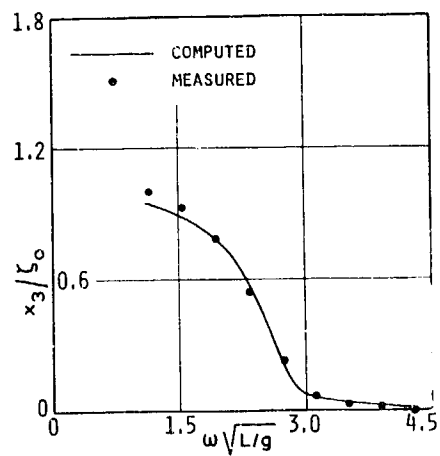


FIG. 21: AMPLITUDE OF HEAVE MOTION  
WAVE DIRECTION 135°

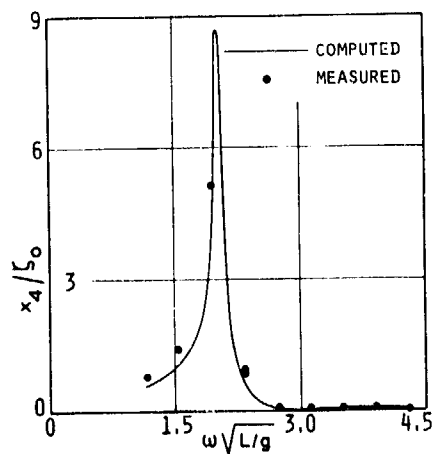


FIG. 22: AMPLITUDE OF ROLL MOTION  
WAVE DIRECTION 135°

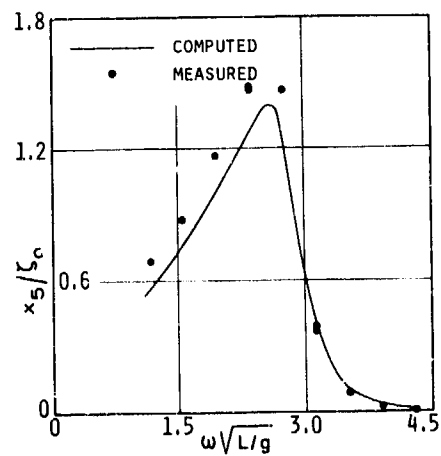


FIG. 23: AMPLITUDE OF PITCH MOTION  
WAVE DIRECTION 135°

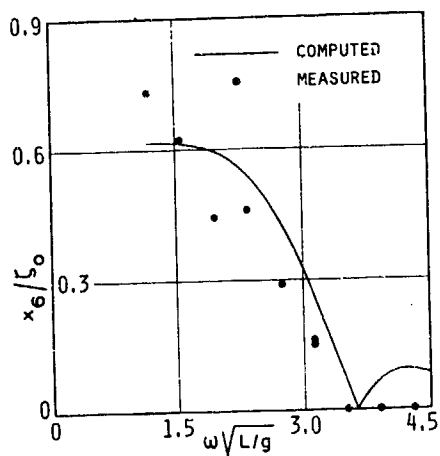


FIG. 24: AMPLITUDE OF YAW MOTION  
WAVE DIRECTION 135°

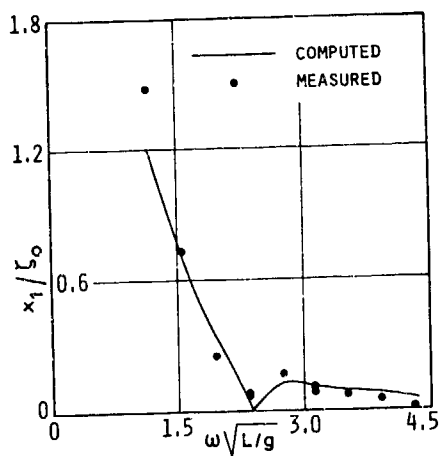


FIG. 25: AMPLITUDE OF SURGE MOTION  
WAVE DIRECTION 180°

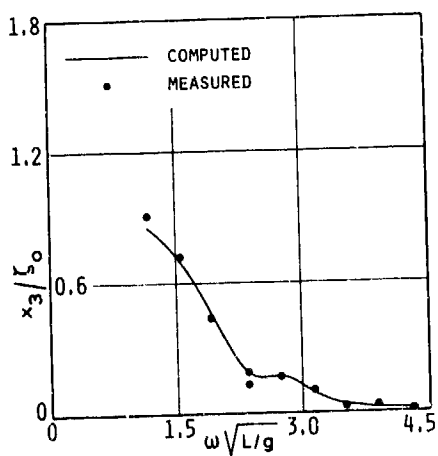


FIG. 26: AMPLITUDE OF HEAVE MOTION  
WAVE DIRECTION 180°

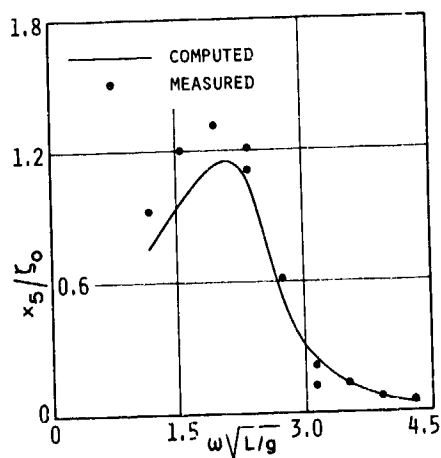


FIG. 27: AMPLITUDE OF PITCH MOTION  
WAVE DIRECTION 180°

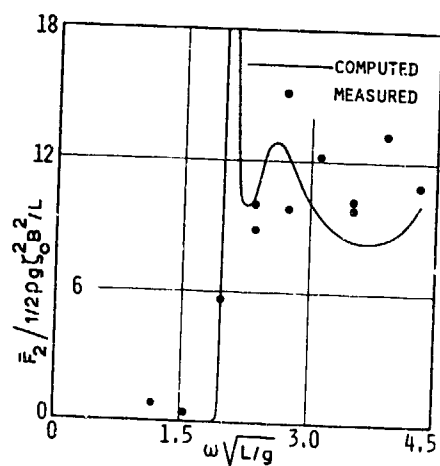


FIG. 28: MEAN TRANSVERSE DRIFT FORCE  
WAVE DIRECTION 90°

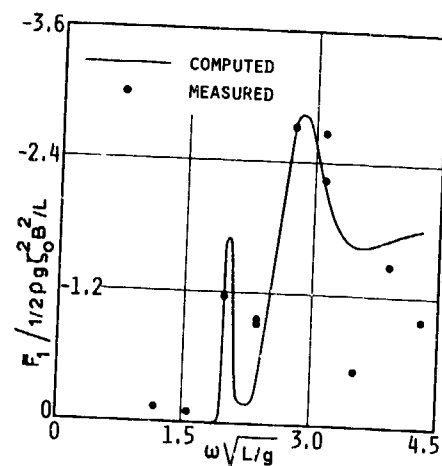


FIG. 29: MEAN LONGITUDINAL DRIFT FORCE  
WAVE DIRECTION 135°

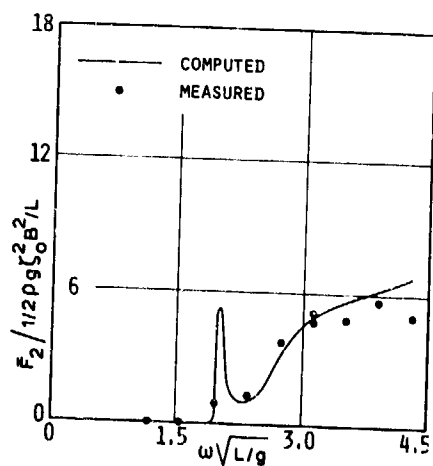


FIG. 30: MEAN TRANSVERSE DRIFT FORCE  
WAVE DIRECTION 135°

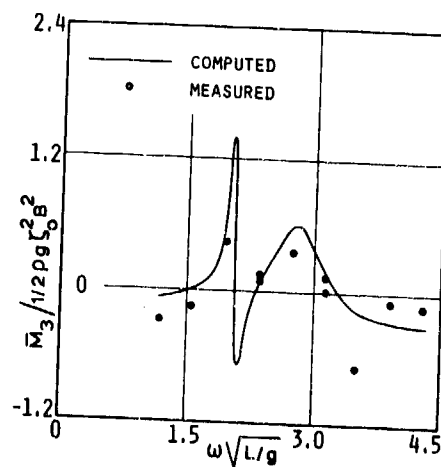


FIG. 31: MEAN YAW DRIFT MOMENT  
WAVE DIRECTION 135°

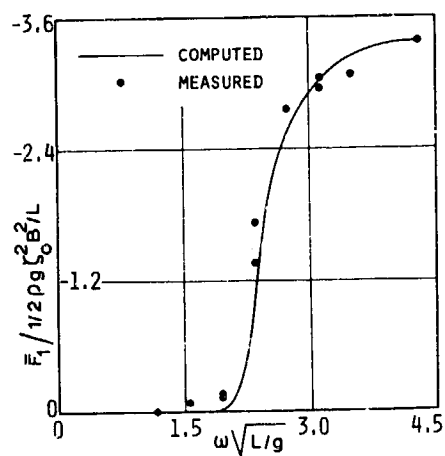


FIG. 32: MEAN LONGITUDINAL DRIFT FORCE  
WAVE DIRECTION 180°

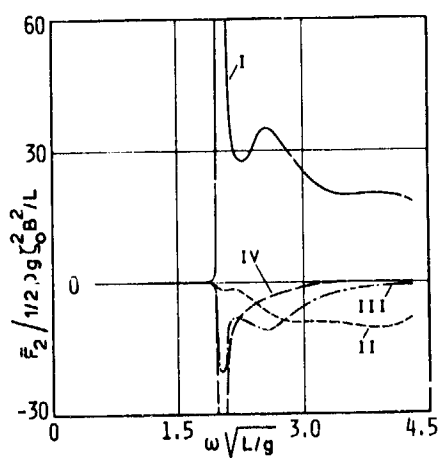


FIG. 33: COMPONENTS OF COMPUTED MEAN  
TRANSVERSE DRIFT FORCE  
WAVE DIRECTION 90°

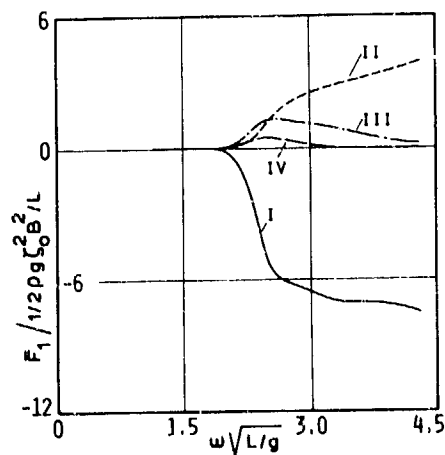


FIG. 34: COMPONENTS OF COMPUTED MEAN  
LONGITUDINAL DRIFT FORCE  
WAVE DIRECTION 180°

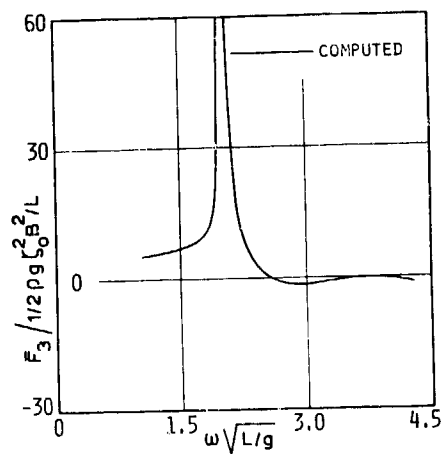


FIG. 35: MEAN VERTICAL DRIFT FORCE  
WAVE DIPECTION  $90^\circ$

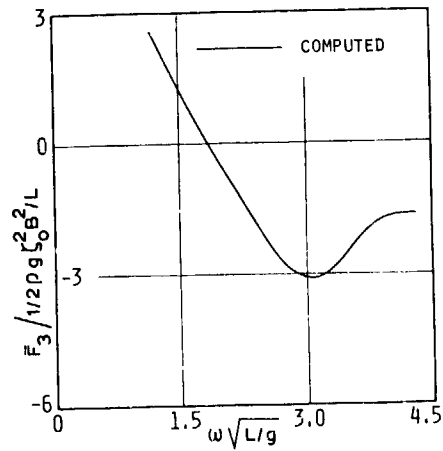


FIG. 36: MEAN VERTICAL DRIFT FORCE  
WAVE DIRECTION  $180^\circ$

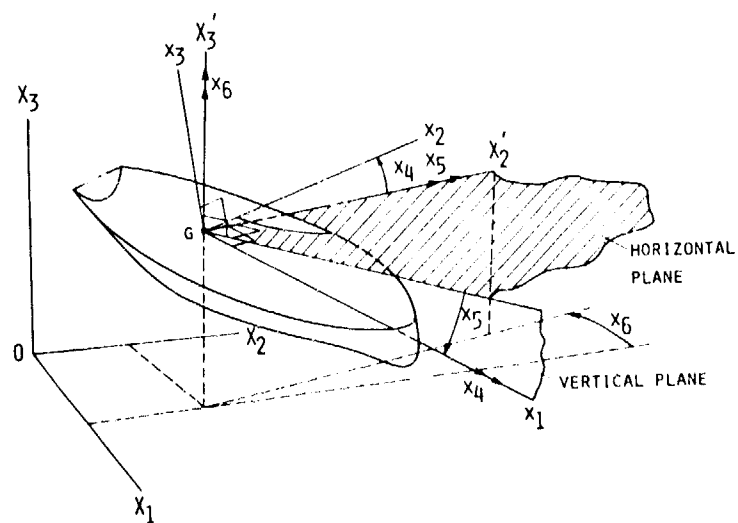


FIG. 37: CO-ORDINATE SYSTEMS  $O, x_1, x_2, x_3$ ;  $G, x_1, x_2, x_3$   
AND  $G, x_1, x'_2, x'_3$



DISCUSSIONS  
of three papers.

NUMERICAL SOLUTION OF THE NEUMANN KELVIN PROBLEM  
BY THE METHOD OF SINGULARITIES  
P. Guével, G. Delhommeau and J.P. Cordonnier

COMPUTATIONS OF THREE-DIMENSIONAL SHIP-MOTIONS WITH FORWARD SPEED  
Ming-Shun Chang

COMPUTATION OF THE FIRST AND SECOND ORDER WAVE FORCES ON  
OSCILLATING BODIES IN REGULAR WAVES  
J.A. Pinkster and G. van Oortmerssen

Invited Discussion

F. Ursell  
University of Manchester

I shall discuss mainly the paper by Miss Chang but my comments are in fact applicable to several other papers concerned with linear equations, and perhaps also to non-linear equations. To fix ideas I shall confine myself to zero speed.

To derive her integral equations, Miss Chang uses interior potentials. In particular, let us consider the integral representation quoted in her abstract, which can be derived in the following way. Let  $\phi_0$  be the potential function defined outside the body; we want the values of  $\phi_0$  on the body. Two integral relations are obtained by applying Green's theorem twice, first to the wave source  $G$  and a simple potential function  $\phi_1$  defined everywhere inside the body, secondly to  $G$  and the potential function  $\phi_0$  defined outside the body. (On the body we have  $\partial\phi_0/\partial n = \partial\phi_1/\partial n$ .) By combining the two integral relations the dipole representation given in the abstract is obtained: The interior potential  $\phi_1(P)$  can be represented by a distribution of wave dipoles over the body closed by a lid, and the dipole strength on the body is seen to involve the values of  $\phi_0$  on the body. (A similar expression can be given for the exterior potential.)

Now let the point  $P$  approach the boundary of the body from the inside. Then the representation becomes an integral equation which is actually a Fredholm equation of the second kind although this is not immediately evident. If  $P$  were not made to approach the boundary, then the integral equation would be an equation of the first kind.

I wish to make the following points.

- (i) There is a complete mathematical theory for the solution of equations of the second kind whereas for equations of the first kind little is known about existence and uniqueness of solutions.
- (ii) When  $\phi_0$  is required on the body there are infinitely many ways of formulating equations of the second kind for this unknown function. (Miss Chang, for instance, uses a simple interior potential defined throughout the interior of the body, while Sayer and myself use a wave source

potential which is singular at an interior point. Since interior potentials have no actual physical meaning they need not be bounded or even defined everywhere inside the body.) These equations may have very different numerical properties.

(iii) The solution procedure breaks down at the irregular frequency, at which the Fredholm determinant is zero, but different integral equations in general have different Fredholm determinants and different irregular frequencies. With some care the equation can be arranged so that the Fredholm determinant is not zero in the frequency range of interest. (I suspect that at zero speed Miss Chang's equation does lead to irregular frequencies.) Much less is known about forward speed.

(iv) At the present time many workers, including Miss Chang, have gained much valuable experience with various formulations of wave problems, all mathematically valid. What is desirable now is a comparative study of the relative merits of these methods, and I believe that a knowledge of mathematical theory will be very helpful here. In our paper at this conference, Philip Sayer and I have made a first attempt at such a comparison; see our Table 1. We realize that this is only a modest beginning. If more studies of this kind could be undertaken, by Miss Chang and other experienced workers present here, and if we could receive reports at later conferences, I believe that these would prove to be of great value.

Discussion  
by J.N. Newman  
of paper by M.S. Chang

The results shown in this paper are very impressive, but not too surprising. It is well known that the strip theory gives good predictions of ship motion characteristics only for high frequencies, and for zero speed the comparisons shown here with exact three-dimensional calculations are qualitatively similar to various previous studies. The use of the strip-theory forward-speed corrections in conjunction with the three-dimensional zero-speed damping and added-mass coefficients is inconsistent, and the resulting poor comparison with experiments is to be expected. But, Dr. Chang is to be congratulated for going on to solve the forward-speed problem with the correct free-surface condition and source potential. The resulting agreement with experiments is generally satis-

factory, although some discrepancies remain to be explained. On the whole, this is a milestone in the study of ship motions, and the author deserves credit for this accomplishment.

#### Discussion

by H. Maruo  
of paper by M.S. Chang

The author has carried out an elaborate computation using the method of singularity distributions over the hull surface of an oscillating ship. I know of a similar calculation that was made by Takagi of Hitachi Shipbuilding Co. He told me that it was not easy to attain a satisfactory accuracy by a numerical method of this kind in spite of the tedious and time-consuming calculation. On the other hand, it is known that the strip method shows deviations from the measured result at lower wave numbers due to the three-dimensional effect. Therefore some improvement of the calculation method is needed, and the present work may suffice for this purpose. However, from the practical point of view, the computer time should be as short as possible. The three-dimensional effect in the hydrodynamic forces on an oscillating ship can be taken into account quite easily by application of the slender-ship theory. I believe this allows much simpler computation than the purely numerical method of the present work. The basic formula for the slender ship oscillating with zero forward speed is the following expression for the velocity potential:

$$\phi = \phi^{(2D)} + \frac{1}{2}(\gamma + Kz) \int a_0'(x') N(K|x-x'|) \operatorname{sgn}(x - x') dx,$$

where

$$N(u) = -\gamma - i\pi 2u + \frac{\pi}{2} \int_0^u H_0(u') du' + \frac{\pi}{2} \int_0^u \gamma_0(u') du' - \pi i + \pi \int_0^u \gamma_0(u') du'.$$

$\phi^{(2D)}$  is the two-dimensional solution for an oscillating cylinder and  $a_0(x)$  is the source term in the expansion of the two-dimensional potential. The boundary-value problem on the hull surface is formulated in the form

$$\frac{\partial \phi}{\partial n}^{(2D)} = [U(x) - W(x)] n_z,$$

where  $U(x)$  is the relative vertical velocity of a section and  $n_z$  the z-component of the direction cosines of the normal. It can be easily understood that the three-dimensional effect appears in the function  $W(x)$  which is similar to the induced velocity of wing theory. I calculated a numerical example for a Series 60, C = 0.7 model. The result for the added mass  $B$  and damping in heave is shown in the figure and denoted as the "improved slender-ship theory." The "original slender-ship theory" means the result obtained by the formula introduced in Newman's review. Thus the analytical method of the slender-ship formula can serve as an accurate prediction method for practical purposes. So far we have considered the case of zero forward speed. For the case of finite forward speed, similar calculations have been

carried out by Kobayashi of Mitsui Shipbuilding Co. However, his results suffer from strong criticism: first, that the formulation is not consistent, and second, that it neglects the line integral that must appear at the intersection of the hull surface and the undisturbed free surface.

#### Discussion

by Y. Kayo  
of paper by P. Guevel, G. Delhommeau and J.P. Cordonnier

In a previous paper (Int. Shipb. Progress, vol. 21, 1974, pp. 311-324), one of the authors proposed a wave-making resistance formula when the double-body potential is used as the zero-order approximation:

$$R_w = 8\pi\rho k_0^2 \int_{-\pi/2}^{\pi/2} |H(\theta, k_0 \sec^2 \theta)|^2 \sec^3 \theta d\theta$$

where

$$H(\theta, k_0 \sec^2 \theta) = -\frac{1}{4\pi} \iint_{SL} \frac{\partial^2 \phi}{\partial x^2} \Big|_{z=0} \exp[-ik_0 \sec^2 \theta (x \cos \theta + y \sin \theta)] dx dy. (1)$$

The modified Kochin function  $H$ , defined above, is determined by the source distribution

$$\frac{\partial^2 \phi_1}{\partial x^2}$$

which is spread over the entire free surface  $z = 0$ . Since the double-body potential  $\phi_1$  is arbitrary inside the body, we have various values of

$$\frac{\partial^2 \phi_1}{\partial x^2}$$

on  $z = 0$  inside the body. Therefore the wave-making resistance derived from (1) is indeterminate.

Since the fluid domain inside the body is independent of the exterior one, the indeterminacy of the wave-making resistance can be eliminated by the proper use of Green's formula for the double-body potential field inside the body.

The result, in the form of the corresponding Kochin function, is

$$H(\theta, k_0 \sec^2 \theta) = -\frac{1}{4\pi} \iint_{SL} \frac{\partial^2 \phi}{\partial x^2} \Big|_{z=0} \exp[-ik_0 \sec^2 \theta (x \cos \theta + y \sin \theta)] dx dy. (2)$$

where  $SL$  is the free surface outside the body. This Kochin function is independent of the kind of singularities used to represent the double-body. It may be seen that the wave-making resistance from (2) is determined uniquely. A detailed discussion of this method can be found in my paper entitled "A note on the uniqueness of wave-making resistance when the double-body potential is used as the zero-order approximation" which is to be read at the joint meeting of the three Japanese Societies of Naval Architects in November 1977.

#### Discussion

by Y. Kusaka  
of paper by P. Guevel, G. Delhommeau and  
J.P. Cordonnier

The discussor wishes to express his respects to the authors for their efforts to obtain a numerical solution of the Neumann-Kelvin problem. It took more than 10 hours of computer time for the discussor to obtain only one solution of this problem using the very large and high-speed computer HITAC 8800/8700. As the authors also point out in their paper, it's necessary to find out the new formulation of the influence coefficients. However, from the discussor's experience, the interpolation method seems very dangerous because of the oscillatory characteristic of that coefficient.

The discussor has been very interested in the uniqueness of the solution of Neumann-Kelvin problem. It seems very difficult to prove uniqueness by mathematical methods. Consequently the discussor believes it's necessary to create numerical techniques that can convince one of the uniqueness of this problem.

#### Author's Reply

by M.S. Chang  
to discussions by F. Ursell and H. Maruo

I would like to thank both discussors of my paper for their interesting comments. It is interesting that Professor Ursell, as a formal discussor, chooses the particular subject of "irregular frequency" for discussion. I believe that Professor Ursell must have some interesting thoughts on the subject and I look forward to reading his paper.

The problem of "irregular frequency" associated with the two-dimensional source method has been known for many years. Not only has the cause of this problem been known, but also simple remedies have been established. I will not discuss this in detail at this time. However, it is worthwhile to note that Professor Ursell's choice of using the inner-potential method to demonstrate his point appears to be misleading; the inner-potential method that Dr. Pien and I applied has a unique inner potential and is not subject to the problem of "irregular frequency." Our inner-potential method determines the doublet distribution  $D(Q)$  from an inner potential  $\phi_i(P)$  that is specified on the closed contour  $S_B + S_{F1}$  by the equation

$$\phi_i(P) = \int_{S_B + S_{F1}} D(Q)K(P,Q)dS(Q); P, Q \in S_B + S_{F1} \quad (1)$$

From potential theory,  $D$  has to be unique, unless the outside potential is non-unique. One should not confuse this inner-potential method with the mathematical model

$$\phi_i(P) = \int_{S_B} D(Q)K(P,Q)dS(Q); P, Q \in S_B \quad (2)$$

for in the latter model,  $\phi_i(P)$  is specified only on  $S_B$ . It is wellknown that the "irregular frequency" does exist in this model--because in this mathematical model the inner potential is

specified on the closed boundary  $S_B + S_{F1}$ .

It is nice to see that the heave-damping and added-mass coefficients obtained by Dr. Maruo are also in very good agreement with the experimental data. However, one has to bear in mind that slender-ship theory is not as general as three-dimensional theory. Mostly it will not work well for coefficients for horizontal modes of the motion, even at zero-forward speed. Moreover, in my opinion, the method of slender-ship theory is not as analytical as Dr. Maruo states it to be; numerical computations using slender-ship theory require the evaluation of the functions  $J_0$ ,  $Y_0$ , and  $H_0$ , which is similar to evaluations required in the three-dimensional method.

# HYBRID INTEGRAL-EQUATION METHOD FOR THE STEADY SHIP-WAVE PROBLEM

Ronald W. Yeung and Yann C. Bouger  
Massachusetts Institute of Technology  
Cambridge, Massachusetts

## ABSTRACT

This paper presents a novel integral-equation technique for solving the steady-state wave-resistance problem. The free-surface condition is linearized, but the body condition is satisfied exactly. An integral relation describing the flow inside an arbitrarily truncated internal region is first obtained by applying Green's Theorem, using only the simple source function for an infinite fluid. The internal flow is next matched with eigen expansions in the upstream and downstream outer regions. The radiation condition can be satisfied exactly simply by a proper choice of the solution form in these outer regions. The method is applied to investigate flows about both lifting and non-lifting two dimensional bodies. Agreement with existing results is excellent. The present formulation provides a simple yet rational basis for tackling the practical three-dimensional ship-wave problem.

## 1. INTRODUCTION

The practical importance of the problem of predicting the lift and drag of a body moving in or near a free surface is well known. Much attention has been devoted to the subject matter in recent literature. This paper describes a novel integral-equation formulation for tackling the steady-state problem with a linearized free-surface but exact body boundary condition. Emphasis is placed on validating the numerical formulation by applying it to obtain flow solutions for various two-dimensional bodies. The formulation permits the body to have circulation, if present. The extension of the present method to three-dimensional problems will also be discussed.

A brief review of the literature pertinent to techniques used in solving such steady-flow problems is included here. By expanding the solution in an infinite series of wave singularities which satisfy the free-surface and radiation conditions, Havelock (1936) obtained the wave resistance and lift force on a circular cylinder in a uniform stream. His formulation permits the body boundary condition to be satisfied exactly. The problem of the flow about an arbitrary

cylinder remained unsolved until much later when the modern digital computer became available. Giesing and Smith (1967) tackled this by distributing on the body contour the traditional wave sources, which satisfies the free-surface condition. By applying the body boundary condition, an integral equation for the source density was obtained. This was solved numerically and they presented some sample results for flow about hydrofoils, including ones with slotted flaps. The relative importance of the exact body boundary condition versus the exact free-surface condition was examined by Tuck (1965) and Salvesen (1969). Both noted the importance of nonlinearities associated with the free-surface condition when the conventional Froude number is large. But, for Froude numbers associated with the operation speeds of most surface vessels, the exact satisfaction of the body condition appears important (Gadd, 1976).

Recently, a number of numerical methods, successfully applied in other branches of applied science, are being employed to solve free-surface flow problems, with the aim of tackling the fully nonlinear free-surface condition. The numerical analysts were faced with two obstacles, one being that the fluid domain is infinite, the other being the difficulty of implementing the steady-state radiation condition numerically. Most workers circumvent the necessity of applying a radiation condition by using an initial-value formulation; see, for example, Chan & Stuhmiller (1976) and Haussling and Van Eseltine (1976). However, if only the steady-state results are desired, such a formulation is computationally lengthy. In addition, the final steady-state results may suffer from the problem of error accumulation and numerical instability. Moreover, unless a proper flow-through condition is applied at the truncation boundaries, the fluid region used in the calculations will have to be enlarged as time progresses. Bai and Yeung (1974), in developing a finite-element variational formulation as well as a new integral-equation technique for the time-harmonic zero forward-speed problems, introduced the concept of solution matching at an arbitrary "radiation" boundary (see also Chen and Mei, 1974). But the extension of such a technique using a finite-element formulation from time-harmonic type flows to the case of steady forward

motion was found to be nontrivial. Mei and Chen (1976) considered the forward-motion problem as the sum of two fictitious problems that were complex in time: a radiation and a scattering problem, each of which can be solved by their earlier hybrid-element variational method. The two solutions were then combined in such a way that the upstream waves cancelled. On the contrary, Bai (1975), who also used finite-element techniques, found it necessary to use a Galerkin's type formulation with a rather unusual choice of trial-function and test-function spaces before he could obtain a unique solution satisfying the radiation condition.

In this work, the hybrid integral-equation technique investigated previously by the first author (Yeung, 1975) for time-harmonic problems is extended to tackle the steady-state forward-speed problem. Most interestingly, the extension turned out to be rather straightforward: the radiation condition can be satisfied explicitly simply by omitting wave functions on the upstream outer region. Further, the problem can be solved in the real domain without resorting to any complex-time formulation. The method is thoroughly tested in this paper. Its potential is obvious. The remarkably simple formulation can provide a rational mathematical basis for solving the more practical three-dimensional Neumann-Kelvin ship-wave problem.

## 2. THE BOUNDARY-VALUE PROBLEM

Consider a two-dimensional body undergoing uniform translation in a fluid of depth  $h$ . As shown in Figure 1, the body coordinate system  $Oxy$  is chosen with the  $x$ -axis pointing opposite to the direction of

motion and coincident with the  $x$ -axis of the undisturbed free surface. Let  $\phi(x,y,t)$  be the disturbance potential at  $(x,y,t)$  due to the motion of the body.

$$\nabla^2 \phi(x,y,t) = 0 \quad (2.1)$$

for  $(x,y)$  in the fluid. The kinematic boundary condition to be satisfied on the body surface  $S_0$  is given by

$$\frac{\partial \phi}{\partial t} + U \frac{\partial \phi}{\partial x} = 0 \quad (2.2)$$

where  $U$  is the speed of the body and  $\hat{n}$  a unit external normal to the fluid. The bottom condition to be satisfied is

$$\frac{\partial \phi}{\partial y} \bigg|_{y=-h} = 0 \quad (2.3)$$

In this moving coordinate system, the linearized free surface condition takes the following form:

$$\left( \frac{\partial}{\partial t} + U \frac{\partial}{\partial x} \right)^2 \phi(x,0,t) + g \phi_y = 0 \quad (2.4)$$

where  $g$  is the constant of gravitational acceleration. Equation (2.4) is valid for the general case when the motion is unsteady. If the body undergoes only steady translational motion parallel to the bottom, then (2.4) reduces to

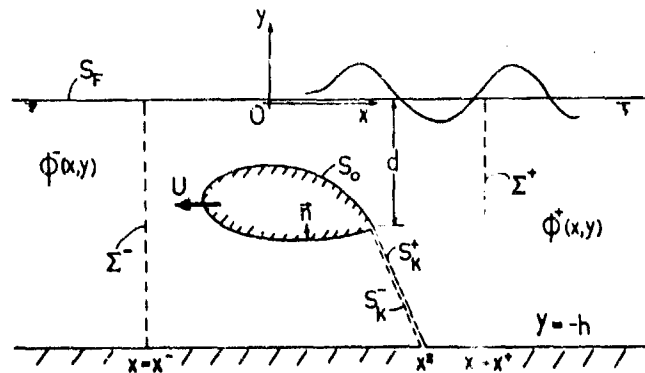


Figure 1. Coordinate Systems and Notations

$$\kappa \phi_{xx}(x,0) + \phi_y = 0, \quad \kappa = \frac{U^2}{g}. \quad (2.5)$$

For such a case of steady flow, the radiation condition may be stated mathematically as

$$\phi(x,y) = \begin{cases} C^- + o(1) & \text{as } x \rightarrow -\infty \\ C^+ + W(x,y) & \text{as } x \rightarrow +\infty \end{cases} \quad (2.6)$$

where  $W(x,y)$  corresponds to a standing wave pattern.  $C^\pm$  are constants associated with the upstream and downstream ends. It is worthwhile to point out that either  $C^-$ , or  $C^+$ , or  $\phi$  at any one point in the fluid can be specified arbitrarily, for the boundary value problem (2.1) to (2.3), (2.5), and (2.6) can only be determined uniquely to an arbitrary constant.

The mathematical formulation is now complete. However, to facilitate the process of seeking a numerical solution, it is convenient to introduce two artificial vertical boundaries,  $\Sigma^+$  and  $\Sigma^-$ . These will be called the radiation boundaries. They separate the inner region enclosing the body from two outer regions on the upstream and downstream sides. Furthermore, keeping in mind that if there is a net circulation around the body, the potential will be discontinuous in the fluid, we introduce a Riemann type cut  $S_K$  joining the trailing edge of the body to, say, the bottom. Across this cut we note that

$$\frac{\partial \phi}{\partial n} \Big|_{S_K^+} = - \frac{\partial \phi}{\partial n} \Big|_{S_K^-} \quad (2.7)$$

$$\phi \Big|_{S_K^+} - \phi \Big|_{S_K^-} = \Gamma \quad (2.8)$$

where  $\Gamma$  is the circulation of the body and  $S_K^\pm$  denotes the two boundary contours surrounding the cut. The introduction of circulation into the problem requires an additional condition to render the problem unique. A Kutta condition to be applied at the trailing edge is plausible. This may be stated as

$$\frac{\partial}{\partial s} (Ux + \phi) \Big|_{T.E.}^{\text{upper}} = - \frac{\partial}{\partial s} (Ux + \phi) \Big|_{T.E.}^{\text{lower}} \quad (2.9)$$

where  $s$  is an arc-length parameter along the body. This ensures the vanishing of loading in the neighborhood of the trailing edge (Hess, 1975). If the body does not have a sharp trailing edge, the potential is continuous everywhere in the fluid, in which case the cut  $S_K$  is obviously unnecessary.

The physical quantities that are of interest in the steady-state problem are the free-surface elevation  $\eta(x)$ , wave-resistance  $R$ , and lift force  $L$ . By the use of Bernoulli's equation, these can be written in terms of the potential as

$$\eta(x) = - \frac{U}{g} \phi_x(x,0) \quad (2.10)$$

$$C_p = \frac{p-p_\infty}{\frac{1}{2}\rho U^2} = \frac{-\phi_x}{U} + \frac{1}{2} \frac{|\nabla \phi|^2}{U^2} \quad (2.11)$$

$$\left( \frac{R}{L} \right) = \rho \oint_{S_0} \left[ -U \phi_x + \frac{1}{2} |\nabla \phi|^2 \right] \begin{pmatrix} dy \\ dx \end{pmatrix} \quad (2.12)$$

where  $C_p$  is the dynamic pressure coefficient. Note that  $L$  as defined does not include the hydrostatic force.

### 3. THE HYBRID INTEGRAL-EQUATION TECHNIQUE

The term hybrid integral-equation is used to designate the numerical formulation described below, applications of which were initially made to time-harmonic free-surface flow problems (Yeung, 1975, see also Yeung, 1973). The present approach represents, perhaps, a straightforward conceptual extension of the previous technique. In comparison with the traditional integral-equation technique of using the Green function of the problem (Wehausen and Laitone, 1960, § 13) our hybrid method is unique in two senses. First, in formulating the integral equation only the simple source function for an infinite fluid,  $\log 1/r$ , is used; second, the originally external boundary-value problem is solved as an interior problem, but with an appropriate matching of the solution between the inner region and the outer regions.

#### 3.1 Representations of the Solution

In the inner region where all geometrical complications occur, the velocity potential  $\phi$  will be described by Green's Theorem. First, let us recall that the following identity holds for any two harmonic functions  $\psi_1$  and  $\psi_2$  which are continuous in a region bounded by the contour  $R$ :

$$\oint_R \left( \psi_1 \frac{\partial \psi_2}{\partial n} - \psi_2 \frac{\partial \psi_1}{\partial n} \right) ds = 0 \quad (3.1)$$

where  $ds$  denotes an infinitesimal arc-length element along the boundary. We now choose  $\psi_1$  to be the unknown potential  $\phi$ , and  $\psi_2$  to be  $\log r$ , where  $r$  is the distance between a boundary point  $Q$  and a field point  $P$ , viz.  $r = |PQ|$ . If  $S$  denotes the contour enclosing the inner region, i.e.,  $S_0 \cup S_F \cup S_B \cup S_K \cup \Sigma^+ \cup \Sigma^-$ , (3.1) becomes

$$2\pi\phi(P) = \oint_S \phi \frac{\partial}{\partial n} \log r \, ds - \oint_S \phi_n \log r \, ds \quad (3.2)$$

where

$$\frac{\partial}{\partial n} = \vec{n} \cdot \left( \frac{\partial}{\partial \xi} + \frac{\partial}{\partial \eta} \right)$$

with  $(\xi, \eta)$  being the variables of integration along  $S$ . Now, by substituting the conditions (2.2), (2.3), (2.5), (2.7), and (2.8) into (3.2), we obtain

$$\begin{aligned} 2\pi\phi(P) = & \int_{S_F} \left[ \phi \frac{\partial}{\partial n} \log r + \kappa \phi_{xx} \log r \right] ds \\ & + \int_{\Sigma^+ \cup \Sigma^-} \left[ \phi \frac{\partial}{\partial n} \log r - \phi_n \log r \right] ds \\ & + \int_{S_B} \phi \frac{\partial}{\partial n} \log r \, ds + \int_{S_K^+ \cup S_K^-} \phi \frac{\partial}{\partial n} \log r \, ds \\ & + \int_{S_0} \phi \frac{\partial}{\partial n} \log r + U \int_{S_0} n_x \log r \, ds \quad (3.3) \end{aligned}$$

With the exception of the radiation boundaries, we observe that  $\phi$  is the only unknown quantity along each boundary. If we are not studying a flow about an undulating bottom, the integral along  $S_B$  can be eliminated by reflection about the line  $y = -h$ . Otherwise  $\phi$  on  $S_B$  should be treated as unknown like any other boundaries. Proceeding along with the assumption that the bottom is flat, we construct an image system below the bottom by defining

$$\log r' = \log |z - \bar{z}^*| = \log \sqrt{(x-\xi)^2 + (y+2h+\eta)^2}.$$

where  $Q^*$  is an image point about the line  $y = -h$ . Accordingly, if  $P$  is a point on  $S$ , (3.3) reduces to

$$\begin{aligned} -\pi\phi(P) + & \int_{S_F} \left[ \phi \frac{\partial}{\partial n} \log(rr') + \kappa \phi_{xx} \log(rr') \right] ds \\ & + \int_{\Sigma^+ \cup \Sigma^-} \left[ \phi \frac{\partial}{\partial n} \log(rr') + \phi_n \log(rr') \right] ds \\ & + \int_{S_0} \phi \frac{\partial}{\partial n} \log(rr') \, ds + \Gamma \int_{S_K^+} \phi \frac{\partial}{\partial n} \log(rr') \, ds \\ & - U \int_{S_0} n_x \log(rr') \, ds, \quad P \in S \quad (3.4) \end{aligned}$$

which can be regarded as an integro-differential equation for  $\phi$  on  $S_F$  and  $S_0$ .  $\phi$  and its normal derivative on  $\Sigma^\pm$ , however, should be matched with the outer representations, to which we now turn our attention.

In the outer regions, which consist of only vertical and horizontal boundaries, the solution  $\phi^+$ , on the downstream side, and  $\phi^-$ , on the upstream side, can be written simply in terms of eigen expansions. By introducing the set of eigen functions which satisfy (2.1), (2.3), and (2.5), as well as (2.6) asymptotically, we can write:

$$\phi^\pm(x, y) = C_0^\pm + H(x^\pm) H(1-F_h) \times$$

$$(A \cos m_0 x + B \sin m_0 x) \frac{\cosh m_0 (y+h)}{\cosh m_0 h}$$

$$+ \sum_{k=1}^{\infty} C_k e^{\frac{1}{2} m_k x} \cos m_k (y+h),$$

$$\text{for } x \gtrless x^\pm \quad (3.5)$$

where  $H$  is the heavyside function and  $F_h$  is the depth-Froude number  $U/\sqrt{gh}$ . The eigenvalues  $m_0, im_k, k=1, 2, \dots$  are roots of the transcendental equation:

$$\kappa m = \tanh mh \quad (3.6)$$

where  $m$  represents either  $m_0$  or  $im_k$  with  $i^2 = -1$ . The values of the coefficients  $A, B$ , and  $C_k, k=0, 1, 2, \dots$ , are unknown and have to be determined from the inner region via

matching. The matching of  $\phi$  and  $\phi_n$  at  $\Sigma^+$  and  $\Sigma^-$  is now accomplished by substituting (3.5) into the second integral of (3.4). This ensures the continuity of the normal and tangential velocities at the juncture boundaries. The final result is given by the following integral identity:

$$\begin{aligned} -\pi\phi(P) + \int_{S_F} \left[ \phi \frac{\partial}{\partial n} \log(rr') + \kappa \phi_{xx} \log(rr') \right] ds \\ + \int_{S_0} \phi \frac{\partial}{\partial n} \log(rr') ds + \Gamma \int_{S_K^+} \phi \frac{\partial}{\partial n} \log(rr') ds \\ + C_0^+ \int_{\Sigma^+} \phi \frac{\partial}{\partial n} \log(rr') ds - C_0^- \int_{\Sigma^-} \phi \frac{\partial}{\partial n} \log(rr') ds \\ + A \left[ F_0 \cos m_0 x + G_0 \sin m_0 x \right] \\ + B \left[ F_0 \sin m_0 x - G_0 \cos m_0 x \right] \\ + \sum_{k=1}^{\infty} \tilde{C}_k^+ (F_k^+ + G_k^+) + \tilde{C}_k^- (-F_k^- + G_k^-) \\ = -U \int_{S_0} n_x \log(rr') ds, \quad P \in S \quad (3.7) \end{aligned}$$

where the integrals  $F_0, G_0, F_k, G_k$  are defined by

$$\begin{aligned} F_0^+(x-\xi^+, y) &= \int_{-h}^0 \frac{\cosh m_0(\eta+h)}{\cosh m_0 h} \left[ \frac{\partial}{\partial \eta} \log rr' \right] \\ G_0^+(x-\xi^+, y) &= \int_{-h}^0 \left[ m_0 \log rr' \right] \\ &\quad (3.8) \end{aligned}$$

$$\begin{aligned} F_k^+(x-\xi^+, y) &= \int_{-h}^0 \frac{\cosh m_k(\eta+h)}{\cosh m_k h} \left[ \frac{\partial}{\partial \eta} \log rr' \right] \\ G_k^+(x-\xi^+, y) &= \int_{-h}^0 \left[ m_k \log rr' \right] \\ &\quad (3.9) \end{aligned}$$

For convenience, the coefficients  $C_k^{\pm}$  and  $\tilde{C}_k^{\pm}$  have been replaced by  $\tilde{C}_k^{\pm}$  above. Equation (3.7) is the foundation of the present numerical procedure for the solution of the problem. That there are more unknowns on the

downstream region than the upstream side is immaterial in our formulation. This is because (3.7) is an identity valid everywhere on  $S$ . We note that if  $P$  is located on  $\Sigma^{\pm}$ , the first term of (3.7) should be replaced by the series defined by (3.5) with  $x$  evaluated at  $x^{\pm}$ . It is of some interest to note that the integrals (3.8) and (3.9) are completely identical to those studied in the time-harmonic problem (Yeung, 1975) with the trivial exception that the  $m_k$ 's are given by a different equation. To avoid performing numerical integration of an oscillatory function, a closed form solution of (3.9) has been derived. The details and results are given in Appendix A.

### 3.2 Discretization of Integral Equation

Discretization techniques of various degrees of sophistication may be used to solve (3.7). In the previous work associated with time-harmonic problems, a step discretization along the free surface and the body boundaries (as well as the fluid bottom, if it was not flat) was used. Since the free-surface boundary condition now contains tangential derivatives of a second order, the discretization function for  $\phi$  should be at least a parabola. For the representation of  $\phi$  on  $S_F$ , we chose to use spline functions, which have the desirable property that the approximating functions possess continuous second derivatives everywhere along the entire range of discretization. Let  $(\xi_1, \xi_2, \dots, \xi_N)$  be a set of grid points in  $[x^-, x^+]$ . The potential on the free surface  $\phi(x, 0)$  can therefore be written as

$$\phi(x, 0) = \sum_{j=1}^N p_j(x) \phi_j^F + q_1(x) (\phi_1^F)' + q_N(x) (\phi_N^F)' \quad (3.10)$$

where

$$\begin{aligned} \phi_1^F &= \phi(x_1, 0) \\ (\phi_1^F)' &= \phi'(x^-, 0) \\ (\phi_N^F)' &= \phi'(x^+, 0) \end{aligned} \quad (3.11)$$

with the prime denotes differentiation with respect to  $x$ . The quantities  $\phi_j^F$ ,  $j=1, 2, \dots, N$ ,  $(\phi_1^F)'$ , and  $(\phi_N^F)'$  are of course unknown. However, the spline functions  $p_j(x)$ ,  $q_1$  and  $q_N$  depend only on the values of the grid points. They satisfy the conditions



$$p_j(x_1) = \frac{1}{2} \left( p_j(x_1) + p_j(x_1) \right) =$$

$$\text{for } i, j = 1, 2, \dots, N$$

$$q_1(x_1) = 0, \quad q_1'(x_1) = \frac{1}{2} \left( q_1'(x_1) + q_1'(x_1) \right)$$

$$\text{for } i = 1, 2, \dots, N$$

$$q_N(x_1) = 0, \quad q_N'(x_1) = \frac{1}{2} \left( q_N'(x_1) + q_N'(x_1) \right)$$

$$\text{for } i = 1, 2, \dots, N$$

where  $\delta_{ij}$  is the Kronecker delta between two consecutive grid points,  $h_j$  and  $g_j$ 's are merely constants. The functions  $p_j$  and  $q_j$  are integrals of (3.7) now reduced to

$$\left[ \int_{S_F} \right] ds \sum_{j=1}^N p_j(x, y)$$

$$= Q^F(x, y) (\phi_1^F)$$

$$= Q_N^F(x, y) (\phi_N^F) \quad (3.13)$$

where

$$\begin{aligned} p_j^F(x, y) &= \int_{x_1}^{x_2} \left[ \frac{p_j(\xi)}{q_j(\xi)} \right] \frac{\partial}{\partial \eta} \log rr' \\ q_j^F(x, y) &= \int_{x_1}^{x_2} \left[ \frac{p_j''(\xi)}{q_j''(\xi)} \right] \log rr' d\xi \end{aligned} \quad (3.14)$$

The integrals of (3.14) are elementary. The resulting expressions can be evaluated numerically very expediently.

On the boundary  $S_0$ , which will be represented by straight-line segments as in Yeung (1975), a scheme involving mid-point discretization of  $\phi$  is used. This enables us to write the third integral of (3.7) and the right-hand side (3.7) respectively as

$$\sum_{j=1}^{N^0} Q_j(x, y) \phi_j^0, \quad -U \sum_{j=1}^{N^0} (n_x)_j p_j(x, y) \quad (3.15)$$

where

$$\begin{aligned} Q_j(x, y, \xi_j^0, \eta_j^0, \xi_{j+1}^0, \eta_{j+1}^0) &= \left[ \log(rr') \right] \\ Q_j(x, y, \xi_j^0, \eta_j^0, \xi_{j+1}^0, \eta_{j+1}^0) &= \left[ \frac{\partial}{\partial \eta} \log(rr') \right] \end{aligned} \quad (3.16)$$

here,  $(\xi_j^0, \eta_j^0)$ ,  $j=1, 2, \dots, N^0$  denotes the set of points defining  $S_0$ . With the help of (3.13) and (3.15), (3.7) can now be expressed in terms of a finite number of unknowns as follows:

$$\phi(v) = \sum_{j=1}^N p_j^F \phi_j^F + Q_1^F(\phi_1^F) + Q_N^F(\phi_N^F)$$

$$\sum_{j=1}^{N^0} Q_j \phi_j^0 + \Gamma Q(x, y; \xi_{T,E}, \eta_{T,E}, \xi^*, -h)$$

$$+ C_0^+ Q(x, y, x^+, -h) + C_0^- Q(x, y, x^-, o, x^-, -h)$$

$$+ A(F_0 \cos m_0 x + G_0 \sin m_0 x)$$

$$+ B(F_0 \sin m_0 x - G_0 \cos m_0 x)$$

$$+ \sum_{k=1}^{N^+} \tilde{C}_k^+ (r_k^+ + G_k^+) + \sum_{k=1}^{N^-} \tilde{C}_k^- (-r_k^- + G_k^-)$$

$$= -U \sum_{j=1}^{N^0} (n_x)_j p_j, \quad \text{for any } P \in S_0$$

$$(3.17)$$

Here, the number of terms used in the eigen expansions are denoted by  $N^+$  and  $N^-$ , for the upstream and downstream outer regions respectively. The integral  $Q$  above is that defined by (3.16).

At this point, we inspect how the unknowns are distributed along the boundary. They are listed as follows:

On	Number of Unknowns
$S_F$ :	$N+2$
$S_O$ :	$N^0$
$\Sigma^+$ :	$N^++3$
$\Sigma^-$ :	$N^-+1$
$S_K$ :	1

We now examine the number of equations available. On  $S_O$ , the midpoint of each segment provides one equation. On  $S_F$ , we should apply (3.17) only to the interior grid points, i.e.,  $N-2$  of them. This is because tangential derivatives of  $\phi$ , which occur on  $S_F$ , are not defined in Green's Theorem at the intersection of  $S_F \cap \Sigma^+$  and  $S_F \cap \Sigma^-$ . Hence, (3.17) is not a valid relation at these corner points. In view of the fact that we are treating the potential on the free surface and that on the radiation boundaries at these corners as separate unknowns, the proper conditions should instead be:

$$\frac{d^n}{dx^n} \phi(x^+, 0) = \frac{d^n}{dx^n} \phi^+(x^+, 0), \quad \text{for } n=0,1,2$$

(3.18)

where  $\phi$  on the left-hand side is given by (3.10) and  $\phi^+$  are the outer representations (3.5). These equalities ensure the continuity of the solution up to the second derivatives on the free surface. The unknowns on  $\Sigma^+$  and  $\Sigma^-$  can be determined by applying (3.17) at  $(N^++1)$  and  $(N^-+1)$  points on  $\Sigma^+$  and  $\Sigma^-$  respectively. The exact locations of these points are insignificant since Equation (3.7) is an identity. Finally, the Kutta condition (2.9) provides the additional equation for determining  $\Gamma$ . Thus, all in all, the number of unknowns and conditions are equal. The applications of the conditions (3.17), (3.18) and (3.19) are illustrated symbolically in Figure 2.

We note in passing that one of the equations obtained by applying (3.17) in the manner described above will be redundant. This does not seem so surprising if we recall that the boundary-value problem stated in § 2 can only be determined up to an arbitrary constant. Interestingly enough, the redundancy is of an implicit type for no one particular field point is more preferable than the others. However, this redundancy can be easily removed by assigning an arbitrary non-zero value to  $C_0^-$  (or  $C_0^+$ ) during the reduction stage of the

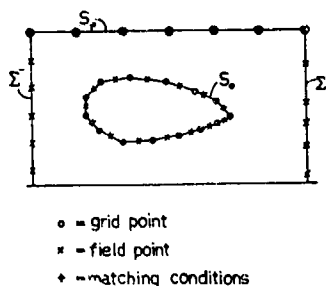


Figure 2. Schematic Showing Grid Systems and Conditions

equations. The resulting system then has a unique solution.

Two relations useful for checking the consistency of the numerical results are given below. The first is well known and can be derived from energy conservation

$$R = \frac{\rho g n^2}{4} \left( 1 - \frac{2m_0 h}{\sinh 2m_0 h} \right) \quad (3.19)$$

where  $n_0$  is the wave amplitude. The second relates the jump in the potential at both infinities,  $C_0^+ - C_0^-$ , to the body potential. This relation was previously considered by Newman (1976). A new derivation, which makes use of the asymptotic behavior of the outer solutions only, is given in Appendix B. The identity given below also accounts for the presence of circulation in the problem:

$$C_0^+ - C_0^- = \left[ - \oint_{S_O \cup S_B} (Ux + \phi) n_x ds + \Gamma(y_{T.E.} + h) \right] / h(1 - F_h^2) \quad (3.20)$$

In (3.20), the first integral on the right represents merely the sum of area enclosed in the body and that protruded on the bottom.

#### 4. RESULTS AND DISCUSSION

A number of tests have been conducted to verify the results of our numerical method. We will first show that the real formulation described in this paper yields the same results as those obtained by superposing two fictitious time-harmonic problems, a procedure used previously by Mei and Chen (1976).

In the complex(-time) formulation, one introduces two fictitious problems  $\psi(\tau)$  and  $\psi(s)$  as follows:

$$\psi(r), (s) (x, y, t) = \phi(r), (s) (x, y) e^{-it}, \quad i = \sqrt{-1}$$

where  $t$  is time and the spatial functions  $\phi(r)$  and  $\phi(s)$  now correspond to fictitious radiation and scattering potentials respectively. Each of them satisfies (2.1), (2.3) and (2.5), but

$$\frac{\partial \phi(r)}{\partial n} = -Un_x, \quad \text{whereas} \quad \frac{\partial \phi(s)}{\partial n} = 0.$$

Moreover, they are required to behave asymptotically like

$$\begin{aligned} \phi(r) &\rightarrow C_0(r) + A^{\pm} e^{\pm i m_0 x} \frac{\cosh m_0(y+h)}{\cosh m_0 h} \quad \text{as } x \rightarrow \infty \\ \phi(s) &\rightarrow \begin{cases} C_0(s) + (e^{-i m_0 x} + R e^{i m_0 x}) \frac{\cosh m_0(y+h)}{\cosh m_0 h} & \text{as } x \rightarrow \infty \\ C_0(s) + T e^{-i m_0 x} \frac{\cosh m_0(y+h)}{\cosh m_0 h} & \text{as } x \rightarrow -\infty \end{cases} \end{aligned}$$

Here,  $A^{\pm}$  can be thought of as the complex amplitudes of the radiated waves due to a

$$F_h = 0.8 \quad d/a = 2 \quad h/a = 5$$

(dimensional solution for  $a=1.0$  m)

real formulation						$\phi(r) = \phi(r) - \frac{A}{T} \phi(s)$	
		PHI	ELEVATION	PHI	ELEVATION		
ON FREE SURFACE							
1	-1.00000	0.0	-5.28469	0.00103	-5.20898	0.00113	-5.26410
2	-0.60870	0.0	-5.30357	0.08492	-5.26410	0.08532	-5.26410
3	-0.20010	0.0	-5.35110	0.05935	-5.32101	0.05967	-5.32101
4	0.20000	0.0	-5.39406	0.02523	-5.35098	0.02599	-5.35098
5	0.60000	0.0	-5.38771	-0.04775	-5.35287	-0.04725	-5.35287
6	1.00000	0.0	-5.42258	-0.14058	-5.28798	-0.14075	-5.28798
SLOPES AT BOTH CORNERS							
		CORFF		CORFF			
		$X^+1$	-0.18188			-0.18205	
		$X^+1$	0.24619			0.24649	
ON POOT							
51	0.40776	-1.92275	-1.81568	-1.41608	-1.41608		
56	0.44002	-1.77580	-1.81826	-1.41868	-1.41868		
57	0.31920	-1.65040	-2.50491	-2.50936	-2.50936		
58	0.22420	-1.55998	-3.35195	-3.35238	-3.35238		
59	0.07725	-1.51224	-4.27935	-4.27973	-4.27973		
60	-0.07725	-1.51224	-5.20276	-5.20107	-5.20107		
61	-0.22420	-1.55998	-6.06067	-6.06097	-6.06097		
62	-0.31920	-1.65040	-6.72128	-6.72151	-6.72151		
63	-0.44002	-1.77580	-7.18453	-7.18472	-7.18472		
64	-0.48776	-1.92275	-7.58419	-7.58436	-7.58436		
65	-0.48776	-2.07725	-7.93119	-7.93132	-7.93132		
66	-0.44002	-2.22420	-8.13770	-8.13782	-8.13782		
67	-0.31920	-2.34920	-8.21497	-8.21508	-8.21508		
68	-0.22420	-2.44002	-8.25220	-8.25233	-8.25233		
69	-0.07725	-2.48776	-8.25453	-8.25467	-8.25467		
70	0.07725	-2.48776	-8.25948	-8.25965	-8.25965		
71	0.22420	-2.44002	-8.20276	-8.20299	-8.20299		
72	0.31920	-2.34920	-8.07162	-8.07168	-8.07168		
73	0.44002	-2.22420	-7.88170	-7.88180	-7.88180		
74	0.48776	-2.07725	-7.61966	-7.61970	-7.61970		
BLOCKAGE CONSTANT $C_0 = -C_0$							
				-5.03526	-5.03531		
WAVE TERMS $\cos(k_0 x)$ , $\sin(k_0 x)$							
				-5.65992	-5.66014		
				-0.22502	-0.22517		
BLOCH EXPANSION AT LEFT							
$C_k$	1	0.72937	0.72937	1	0.72937	1	0.72937
	2	0.02740	0.02740	2	0.02740	2	0.02740
	3	-0.20019	-0.20019	3	-0.20019	3	-0.20019
	4	0.06321	0.06321	4	0.06321	4	0.06321
	5	0.03467	0.03467	5	0.03467	5	0.03467
	6	-0.02926	-0.02926	6	-0.02926	6	-0.02926
	7	0.00020	0.00020	7	0.00020	7	0.00020
	8	0.00031	0.00031	8	0.00031	8	0.00031
	9	-0.00267	-0.00267	9	-0.00267	9	-0.00267
	10	-0.00140	-0.00140	10	-0.00140	10	-0.00140
	11	0.00131	0.00131	11	0.00131	11	0.00131
BLOCH EXPANSION AT RIGHT							
$C_k$	1	-0.48607	-0.48607	1	-0.48607	1	-0.48607
	2	0.07378	0.07378	2	0.07378	2	0.07378
	3	-0.20019	-0.20019	3	-0.20019	3	-0.20019
	4	-0.05325	-0.05325	4	-0.05325	4	-0.05325
	5	-0.04053	-0.04053	5	-0.04053	5	-0.04053
	6	0.02072	0.02072	6	0.02072	6	0.02072
	7	0.00177	0.00177	7	0.00177	7	0.00177
	8	-0.00277	-0.00277	8	-0.00277	8	-0.00277
	9	0.00238	0.00238	9	0.00238	9	0.00238
	10	0.00175	0.00175	10	0.00175	10	0.00175
	11	-0.00124	-0.00124	11	-0.00124	11	-0.00124
BLOCH EXPANSION AT LEFT							
	1	0.72937	0.72937	1	0.72937	1	0.72937
	2	0.02740	0.02740	2	0.02740	2	0.02740
	3	-0.20019	-0.20019	3	-0.20019	3	-0.20019
	4	0.06321	0.06321	4	0.06321	4	0.06321
	5	0.03467	0.03467	5	0.03467	5	0.03467
	6	-0.02926	-0.02926	6	-0.02926	6	-0.02926
	7	0.00020	0.00020	7	0.00020	7	0.00020
	8	0.00031	0.00031	8	0.00031	8	0.00031
	9	-0.00267	-0.00267	9	-0.00267	9	-0.00267
	10	-0.00140	-0.00140	10	-0.00140	10	-0.00140
	11	0.00131	0.00131	11	0.00131	11	0.00131
BLOCH EXPANSION AT RIGHT							
	1	-0.48607	-0.48607	1	-0.48607	1	-0.48607
	2	0.07378	0.07378	2	0.07378	2	0.07378
	3	-0.20019	-0.20019	3	-0.20019	3	-0.20019
	4	-0.05325	-0.05325	4	-0.05325	4	-0.05325
	5	-0.04053	-0.04053	5	-0.04053	5	-0.04053
	6	0.02072	0.02072	6	0.02072	6	0.02072
	7	0.00177	0.00177	7	0.00177	7	0.00177
	8	-0.00277	-0.00277	8	-0.00277	8	-0.00277
	9	0.00238	0.00238	9	0.00238	9	0.00238
	10	0.00175	0.00175	10	0.00175	10	0.00175
	11	-0.00124	-0.00124	11	-0.00124	11	-0.00124

Table 1  
Comparison of Solutions Based on Real Formulation  
and Complex (-time) Formulation

surging motion of the body,  $R$  as the reflection coefficient and  $T$  the transmission coefficient due to an incident wave from the downstream side. Thus, in contrast to the asymptotic behavior described by (2.6) for the real formulation, these time-harmonic problems possess a certain amount of mathematical symmetry on the upstream and downstream ends. They are amenable to the solution technique described by Yeung (1975) which was well validated. The solution for the original steady-state problem can next be obtained by the relation

$$\phi = \phi(r) - \frac{A^-}{T} \phi(s)$$

which satisfies the radiation condition (2.6) by construction. The calculations involved in this approach are considerably lengthier than the real formulation described earlier in § 3, but the procedure was nevertheless programmed to provide a consistency check of our results. Table 1 compiles the solutions of a uniform subcritical flow about a circular cylinder with its center submerged at two times its radius. Results for both the real and complex formulations are shown side by side for the purpose of comparison. Within the accuracy of a 6 significant-figure machine (IBM-360), it is clear that the two sets of numbers are practically identical. This provides the evidence that the integral-equation technique discussed in this paper can be used to solve the steady-state problem in the real domain without resorting to the more complicated and expensive complex-time formulation.

Next, a uniqueness check on the coefficients of the eigen expansion was conducted in the following fashion. The problem of the flow about a circular cylinder is solved thrice with three different locations of the radiation boundaries,  $\Sigma^+$  and  $\Sigma^-$ . A correct formulation should yield the same solution regardless of the location of these boundaries. Table 2 is a collection of the numerical results obtained by using the formulation in § 3 for  $x^+ / a = \pm 2, \pm 4, \pm 8$ , where  $a$  is the radius of the cylinder. Note the excellent agreement of the predicted free-surface elevation  $\eta(x)/d$  among all 3 cases. The coefficients of the eigen expansion are also quite consistent, although the accuracy of the higher-order coefficients in the expansion tend to deteriorate as  $x^+$  or  $x^-$  becomes large. In view of the fact that the solution in the outer region is always dominated by the first few terms, due to the exponential decaying factor in front of  $C_n$  in (3.5), such inaccuracies have little overall effect on the solution.

In Figure 3a, the velocity potential and the free-surface elevation correspond to a subcritical flow about a circle submerged at two times its radius are plotted. At this particular speed, even though the depth/wavelength ratio is 0.995, the effect of the bottom is not entirely negligible. The computed

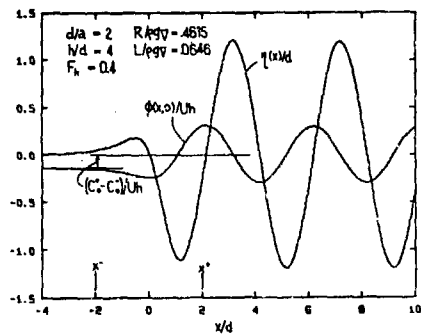
$\gamma_0 = 0.8$   
 $d/a = 2.0$   
 $H/d = 5.$

	$x^+ = 2a$	$x^+ = 4a$	$x^+ = 8a$
<u>free-surface elevation: <math>\eta(x)/d</math></u>			
at $x/d = -2.0$	.0633	.0632	.0633
-1.0	.1945	.1947	.1945
-0.5	.3248	.3248	.3248
0.	.3907	.3911	.3912
0.5	.2418	.2416	.2411
1.0	-.0014	-.0015	-.0017
2.0	-.3812	-.3812	-.3812
3.0	-.6419	-.6419	-.6419
4.0	-.8255	-.8255	-.8255
<u>wave amplitude:</u>			
A: (cos $m_0 x$ mode)	-6.2007	-6.2039	-6.2034
B: (sin $m_0 x$ mode)	-0.4637	-0.4633	-0.4625
<u>blockage:</u>			
$C_0^+ C_0^-$	4.5103	4.5116	4.5111
<u>expansion:</u>			
$C_1^+ e^{-m_1 x^+}$	.27759	.27752	.27750
$C_2^+ e^{-m_2 x^+}$	-.07772	-.07765	-.07759
$C_3^+ e^{-m_3 x^+}$	.01664	.01663	.01666
$C_4^+ e^{-m_4 x^+}$	-.00163	-.00157	-.00140
$C_5^+ e^{-m_5 x^+}$	-.00056	-.00057	-.00050
$C_6^+ e^{-m_6 x^+}$	-.29854	-.29862	-.29877
$C_7^+ e^{-m_7 x^+}$	.07611	.07595	.07366
$C_8^+ e^{-m_8 x^+}$	-.01419	-.01428	-.01900
$C_9^+ e^{-m_9 x^+}$	.00057	.00046	.00020
$C_{10}^+ e^{-m_{10} x^+}$	.00086	.00081	.00005

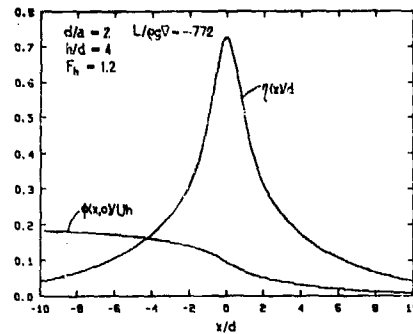
Table 2.  
Solution of Flow about Circular Cylinder  
for Different Values of  $\Sigma^+$  and  $\Sigma^-$

resistance and lift coefficients are in very good agreement with the results of Mei and Chen (1976). Comparing with Havelock's (1936) infinite-depth results, one may notice that the fluid bottom has a stronger influence on the wave resistance than the lift for this particular configuration. The wave pattern for a supercritical case of the same configuration is shown in Figure 3b in which one notices that only a local disturbance exists. Once again, the lift force is in good agreement with Mei and Chen (1976). In checking our computed results, it was noticed that Bai's (1975) published results for the vertical force coefficient was in error while his resistance coefficient was in apparent agreement with the present authors and Mei and Chen.

In Figure 4a and 4b, we display the results of  $C_R$  and  $C_L$  versus  $F_h$  for ellipses of various length ratios of minor to major axes. The center of the ellipse is located at one body length below the free



3a. - Subcritical



3b. - Supercritical

Figure 3. Potential and Wave Elevation for Flow About a Circular Cylinder

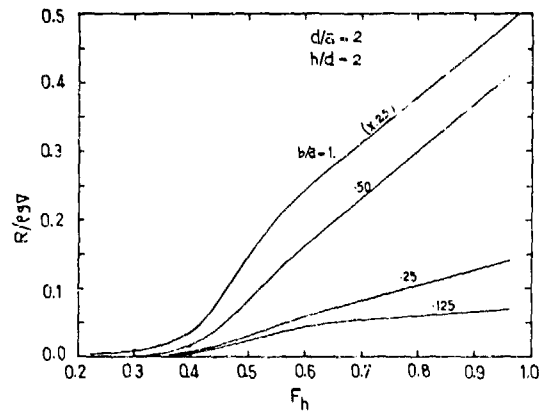


Figure 4a. - Wave Resistance of Elliptical Cylinders of Various Thickness at 10° Angle of Attack

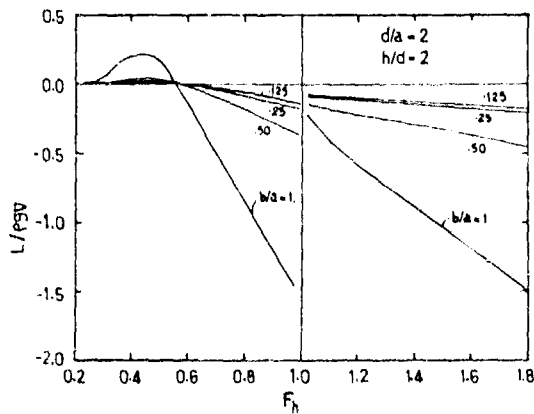


Figure 4b. - Lift Force on Elliptical Cylinders of Various Thickness at 10° Angle of Attack

surface with the major axis tilted  $10^\circ$  upwards from the horizontal. These results assume the absence of circulation in the flow. From the figures one notes the rapid decrease in wave resistance as the body thickness is reduced. Another interesting feature is that while the horizontal force increases monotonically as the speed increases, the vertical force reverses its sign at  $F_n$  approximately 0.6. The discontinuity of the linearized solution at the critical Froude number is well known. This can be remedied only by considering a non-linear solution of the problem.

For a body with circulation, our formulation was tested by calculating the flow about a NACA 4412 hydrofoil submerged at one chord length from the undisturbed free surface. Figure 5 shows the pressure coefficient on both surfaces of the airfoil. Only 34 segments were used to represent the foil geometry. The Kutta condition (2.9) was handled by a three-point finite-difference scheme and was evaluated at the field points adjacent to the trailing edge. The results are in good agreement with those of Giesing and Smith (1967), particularly in view of the sensitivity of the solution to a precise treatment of the Kutta condition (see Hess, 1975). Figure 6 shows the wave profiles generated by such a hydrofoil translating in water of depth equal to four times the chord length. It is interesting to note that the initial depression of the free surface moves further upstream as the speed decreases. In subcritical flow, in the supercritical case, the disturbance generated by the body is felt at a much larger distance upstream. Figure 7 shows the hydrodynamic lift and drag coefficient of the same hydrofoil versus the depth Froude

number. When nondimensionalized in the conventional manner, both lift and drag coefficients are observed to have turning points in the subcritical range. For most of the range of the Froude number, the lift coefficient is considerably lower than the infinite-fluid value of 1.08.

## 5. CONCLUSION

In this paper, a novel integral-equation method of solving the steady-state ship-wave problem with the linearized free-surface and exact-body condition is presented. The method is tested for lifting- and non-lifting flows about a number of two dimensional bodies. Numerical results obtained using our method agree very well with existing calculations. The formulation incorporates a rational, yet remarkably simple, treatment of the radiation condition. The current investigation shall provide a sound mathematical basis for tackling the more practical three-dimensional problem. Such an extension is conceptually straightforward. The source function will be the simple three-dimensional Rankine source,  $1/R$ . The contour integrals will now be replaced by surface integrals. Extensions using similar techniques have already been carried out successfully for the time-harmonic problems (Yeung, 1973). The present mathematical formulation should provide additional insight into the understanding of the Neumann-Kelvin ship-wave problem. Since our approach does not utilize the traditional Havelock source function, it will allow us to bypass the controversial issue of what the rational treatment of the "line integral" (see Brard, 1972) around the ship hull is.

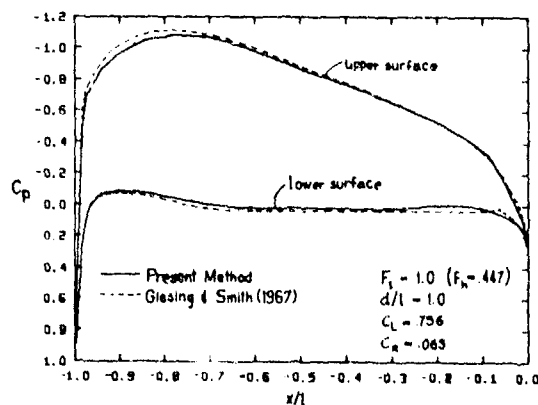


Figure 5. Pressure Distribution on a NACA-4412 Hydrofoil at  $5^\circ$  Angle of Attack

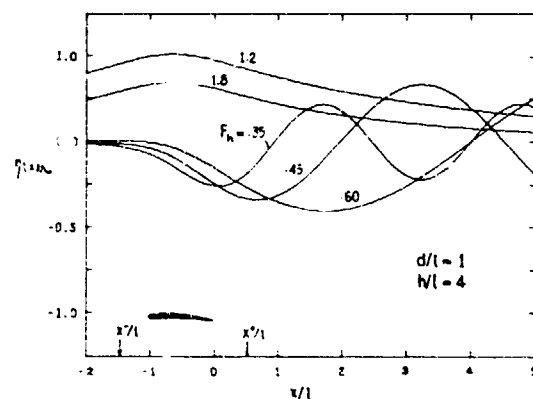


Figure 6. Wave Profiles of a NACA-4412 Hydrofoil at 5° Angle of Attack at Various Froude Numbers

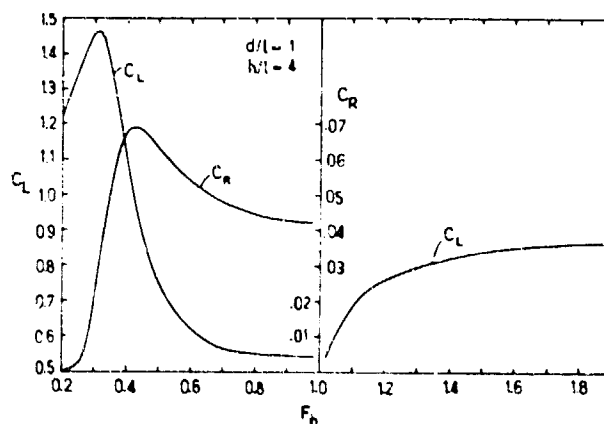


Figure 7. Lift and Wave Drag of a NACA-4412 Hydrofoil at 5° Angle of Attack Versus Depth-Froude Number

#### ACKNOWLEDGMENT

We would like to thank Dr. K.J. Bai of DUTNSRDC and Professor C.C. Mei of MIT for providing some computer printouts for the purpose of checking our program.

Acknowledgement for support of this research is made to the Naval Sea Systems Command General Hydromechanics Research Program, Subproject SRO73 0101, administered by the David W. Taylor Naval Ship Research and Development Center, Contract N0014-77-C-0083.

#### REFERENCES

- Abramowitz, M; Stegun, I.A. Handbook of Mathematical Functions. National Bureau of Standards, 1968.
- Bai, K. J. A Localized Finite-Element Method for Steady Two-Dimensional Free-Surface Flow Problems. 1st Int. Conf. Numer. Ship Hydrodyn., 1975, 309-310.
- Bai, K. J. A Localized Finite-Element Method for Potential-Flow About Two-Dimensional Hydrofoils. Manuscript for J. Ship Res., 1976.

- Bai, K. J.; Yeung, R. W. Numerical Solutions to Free-Surface Flow Problems. *10th Symp. Naval Hydrodyn.*, Cambridge, Mass., 1974, 609-633.
- Brard, R. The Representation of a Given Ship Form by Singularity Distribution When the Boundary Condition on the Free Surface is Linearized. *J. Ship Res.*, Vol. 16 (1972), 79-92.
- Chan, R. K.; Stuhmiller, J.H. Numerical Solution of Unsteady Ship-Wave Problems. *11th Symp. Naval Hydrodyn.*, London, 1976, 303-313.
- Chen, H.S.; Mei, C. C. Oscillations and Wave-Forces in a Man-Made Harbor in the Open Sea. *10th Symp. Naval Hydrodyn.*, Cambridge, Mass., 1974, 573-594.
- Gadd, G. E. A Method of Computing the Flow and Surface Wave Pattern Around Full Forms. *Trans. RINA* (1976), 207-216.
- Giesing, J. P.; Smith, A.M.O. Potential Flow about Two-Dimensional Hydrofoils. *J. Fluid Mech.*, Vol. 28 (1967), 113-129.
- Havelock, T.H. The Forces on a Circular Cylinder Submerged in a Uniform Stream. *Proc. Roy. Soc., Ser. A.*, Vol. 157 (1936), 526-534.
- Hausling, H. J.; Van Eseltine, R. T. Numerical Solution of Planing-Body Problems. D.W. Taylor NSRDC Report 76-0118, 1976.
- Hess, J. L. The Use of Higher-Order Surface Singularity Distributions to Obtain Improved Potential-Flow Solutions for Two-Dimensional Lifting Airfoils. *Comp. Meth. Appl. Mech. and Engrg.*, Vol. 5 (1975), 11-35.
- Mei, C. C.; Chen, H. S. A Hybrid Element Method for Steady Linearized Free-Surface Flows. *Int. J. Numer. Methods in Engrg.*, Vol. 10 (1976), 1153-1175.
- Newman, J. N. Blockage with a Free Surface. *J. Ship Res.*, vol. 20 (1976), 199-203.
- Salvesen, N. On Higher-Order Wave-Theory for Submerged Two-Dimensional Bodies. *J. Fluid Mech.*, Vol. 29 (1969), 415-432.
- Tuck, E. O. The Effect of Non-Linearity at the Free Surface on Flow Past a Submerged Cylinder. *J. Fluid Mech.*, Vol. 22 (1965), 401-414.
- Wehausen, J. V.; Laitone, E.V. Surface Waves. "Handbuch der Physik," Vol. IX, pp. 446-778. Springer-Verlag, Berlin, 1960.
- Yeung, R. W. A Singularity-Distribution Method for Free-Surface Flow Problems with an Oscillating Body. College of Engrg., University of California, Berkeley, Report NA73-6, 1973.
- Yeung, R. W. A Hybrid Integral-Equation Method for Time-Harmonic Free-Surface Flows. *1st Int. Conf. Numer. Ship Hydrodyn.*, Gaithersburg, Maryland, 1975, 581-608.



# APPENDIX A

## The Integrals $F_k$ and $G_k$

Consider the integrals  $F$  and  $G$  defined by

$$F(x-\xi, y) = \int_{-h}^0 d\eta \cos m(\eta+ih) \left\{ \frac{-\partial}{\partial x} \log r \right\} \quad (A.1)$$

$$G(x-\xi, y) = \int_{-h}^0 d\eta \cos m(\eta+ih) \left\{ \frac{-\partial}{\partial x} \log r \right\} \quad (A.1)$$

We will show that they can be written in terms of exponential integrals. The derivation to follow is considerably simpler if we introduce the following complex variables:

$$z = \alpha + iy, \quad \alpha = x - \xi,$$

$$\zeta = \rho + i\eta,$$

where for practical purposes one only has to consider the case  $(x-\xi) < 0$  since  $G$  remains the same while  $F$  differs only by a sign for the opposite case. In the complex plane  $\rho(z)$  is given by:

$$G(\alpha, y) = E_1(z) - E_1(z) \left\{ -1 \int_{C_0} d\zeta \cosh m(\zeta+ih) \log(z-\zeta) \right\}$$

$$= E_1(z) - W(z) \quad (A.2)$$

where the contour of integration  $C_0$  is a vertical line from  $\zeta = -ih$  to  $\zeta = 0$  as shown in Fig. A.1.

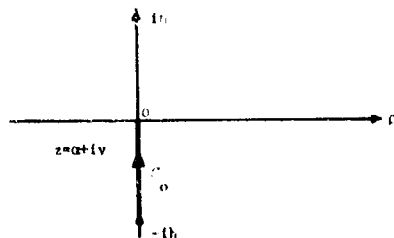


Fig. A.1

If  $W(z)$  were known, the evaluation of  $F$  would be straightforward since

$$F(\alpha, y) = -\frac{1}{m} \operatorname{Re} \left[ \frac{d}{dz} W(z) \right] \quad (A.3)$$

which follows from the fact that the derivative of any analytic function is independent of the direction of approach. Now to evaluate  $W(z)$ , an integration by parts yields

$$W(z) = -i \left\{ \sinh(imh) \log z + \int_{C_0} \frac{\sinh m(\zeta+ih)}{z-\zeta} d\zeta \right\}$$

$$= \sin(mh) \log z + \frac{i}{2} e^{m(\zeta+ih)} \int_{-m(z+ih)}^{mz} \frac{e^{-u}}{u} du$$

$$- \frac{i}{2} e^{-m(z+ih)} \int_{-m(z+ih)}^{-mz} \frac{e^{-u}}{u} du \quad (A.4)$$

The paths of the integrals of (A.4) in the  $u$ -plane are shown in Fig. A.2.

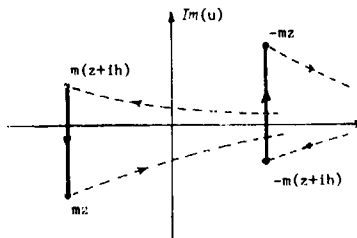


Fig. A.2

Both integrals can be replaced by a pair of integrals extending from the end points to  $z \rightarrow \infty$ . Exploiting the definition of the exponential integral  $E_1(z)$

$$E_1(z) = \int_z^\infty \frac{e^{-t}}{t} dt, \quad |\arg z| < \pi \quad (A.5)$$

where the Riemann cut is along the negative real axis, we obtain for (A.4), after accounting for the pole at  $u=0$  for the first integral, the following expression:

$$W(z) = \sin(mh) \log z$$

$$+ \frac{i}{2} e^{m(z+ih)} [-E_1(mz) + E_1(m(z+ih)) - 2\pi]$$

$$- \frac{i}{2} e^{-m(z+ih)} [-E_1(-mz) + E_1(-m(z+ih))] \quad (A.6)$$

Whence,

$$G(\alpha, y) = \sin(mh) \log [\alpha^2 + y^2]^{1/2} - \pi \cos m(y+h) e^{m\alpha} \\ + \frac{1}{2} \operatorname{Im} \left\{ e^{m(z+ih)} [E_1(mz) - E_1(m(z+ih))] \right. \\ \left. - e^{-m(z+ih)} [E_1(-mz) - E_1(-m(z+ih))] \right\} \quad (A.7)$$

Next for  $F(\alpha, y)$ , we recall that by Leibnitz' rule

$$\frac{d}{dz} e^z E_1(z) = e^z E_1(z) - 1/z \quad (A.8)$$

By (A.3) and (A.6), the normal-derivative integral is given as follows:

$$F(\alpha, y) = -\pi \operatorname{sign}(\alpha) e^{-m|\alpha|} \cos m(y+h) \\ + \frac{1}{2} \operatorname{Im} \left\{ e^{m(z+ih)} [E_1(m(z+ih)) - E_1(mz)] \right. \\ \left. + e^{-m(z+ih)} [E_1(-m(z+ih)) - E_1(-mz)] \right\} \quad (A.9)$$

Note that as  $\alpha \rightarrow 0$  the exponential-integral terms vanish in pairs because

$$E_1(z^*) = [E_1(z)]^* \quad (A.10)$$

and (A.9) reduces to merely

$$F(0^{\pm}, y) = -\pi \operatorname{sign}(\alpha) \cos m(y+h) \quad (A.11)$$

which follows naturally from the physical interpretation of the integral as the normal velocity of a source-distribution. In this same limit,  $G(\alpha, y)$  can be written as the sine- and cosine-integrals:

$$G(0, y) = \sin \psi \log |y| \\ + \sin m(y+h) [Ci(m(y+h)) - Ci(-my)] \\ - \cos m(y+h) [Si(m(y+h)) - Si(-my)] \quad (A.12)$$

where  $Ci$  and  $Si$  are those defined in Abramowitz and Stegun (1964).

For the integrals defined by (3.9), which involves  $\log rr'$ , one simply observes that the

image terms corresponds to a choice of

$$z = \alpha - i(2h+y) \quad (A.13)$$

in (A.2) and (A.3). Thus, the point  $mz$  in Figure A.2 is always above the real axis, which implies that the contribution from the pole at  $u=0$  (the term " $2\pi$ " in A.6) should be discarded. Equation (A.7) without the second term and Equation (A.9) without the first term are now the results, with  $z$  defined by (A.13) and  $y$  replaced by  $-(2h+y)$ .

## APPENDIX B

### Relation Between Blockage Constant and Body Potential

A simple relation exists between the difference in upstream and downstream potential,  $C_0^+ - C_0^-$ , and the potential on the body. This can be obtained rather expediently by applying Green's second identity. The derivation below does not appear to be available in the literature.

Let us consider applying (3.1) to the harmonic functions  $\psi_1 \equiv Ux + \phi$ , and  $\psi_2 \equiv \phi$  where  $\phi$  is the disturbance potential. This time, we take  $x^+$  to be sufficiently large so that

$$\phi(x^+, y) = C_0^+ + \alpha h(x^+) \sin(m_0 x + \delta) \frac{\cosh m_0(y+h)}{\cosh m_0 h} \quad (B.1)$$

where  $\alpha$  is a constant and  $\delta$  is a phase angle. By the free-surface condition, the integral along  $S_F$  can be written as

$$\int_{S_F} \left( \psi_1 \frac{\partial \psi_2}{\partial n} - \psi_2 \frac{\partial \psi_1}{\partial n} \right) ds = -\kappa \left[ x \phi_x(x, 0) - \phi \right]_{x^-}^{x^+} \quad (B.2)$$

Now by making use of (B.1), the integrals over  $\Gamma^+$  and  $\Gamma^-$  can be carried out in a straightforward manner, and when combined with (B.2), the result is

$$\int_{S_F \cup \Gamma^+ \cup \Gamma^-} \left( \psi_1 \frac{\partial \psi_2}{\partial n} - \psi_2 \frac{\partial \psi_1}{\partial n} \right) ds = U h (C_0^+ - C_0^-) (P_h^2 - 1) \quad (B.3)$$

Next, we note that because of the body condition (2.2),

$$\int_{S_0 \cup S_B} \left( \psi_1 \frac{\partial \psi_2}{\partial n} - \psi_2 \frac{\partial \psi_1}{\partial n} \right) ds = U^2 (V_0 + V_B) - U \oint_{S_0} \phi n_x ds \quad (B.4)$$

where  $(V_0 + V_B)$  is the sum of the submerged area of the body and the net protruded area of the bottom. Finally, by the conditions (2.7) and (2.8) across the Riemann cut

$$\int_{S_K} \left( \psi \frac{\partial \psi_2}{\partial n} - \psi_2 \frac{\partial \psi_1}{\partial n} \right) ds = -U \Gamma \int_{S_K^+} n_x ds = U \Gamma (h + y_{T.E.}) \quad (B.5)$$

where  $y_{T.E.}$  denotes the vertical coordinate of the trailing edge.

If we now equate the sum of (B.3), (B.4) and (B.5) to zero, the following simple formula results

$$C_o^+ - C_o^- = \left[ U(V_o + V_B) - \oint_{S_o \cup S_B} \phi n_x ds + \Gamma(h + y_{T.E.}) \right] / h(1 - F_h^2) \quad (B.6)$$

which is actually valid even for supercritical ( $F_h > 1$ ) flow. Recalling that the first two terms represent the dipole strength associated with the body and the bottom, one notes that Newman's (1976) result is recovered when  $\Gamma = 0$ .

# INTEGRAL-EQUATION METHODS FOR CALCULATING THE VIRTUAL MASS IN WATER OF FINITE DEPTH

P. Sayer and F. Ursell  
Department of Mathematics,  
University of Manchester  
Manchester M13 9PL, England

## Abstract

In the present work Green's theorem is applied to the potential and to a fundamental solution (wave source) satisfying the conditions at the free surface, at the bottom and at infinity, but not necessarily on the body. An integral equation for the potential on the body is thus obtained. For the simplest choice of fundamental solution the method breaks down at a discrete infinite set of frequencies, as is well known. When the fundamental solution is modified, however, a different integral equation is obtained which is found not to break down at any frequency. A theoretical discussion is given, and numerical results are presented for the half-immersed circle and the half-immersed ellipse. If only the virtual mass is required (rather than the distribution of pressure) much time can be saved by using an integral equation with the transposed kernel and a simplified right-hand side. The numerical results are in good agreement with earlier results using the method of multipoles which for the circle is better than the method of integral equations but is not readily applicable to other sections.

## 1. Introduction

In earlier numerical work on the circle we expressed the potential as the sum of a wave source and multipoles, which are simple but specially appropriate only for the circle. For more general shapes the method of integral equations may be used. In our work, Green's theorem is applied to the potential and to a fundamental solution (wave source). If the fundamental solution satisfies the boundary conditions at the free surface, at the bottom and at infinity, but not necessarily on the body, then the resulting integral equation has a complicated kernel but involves only the values of the potential on the body. This formulation has the advantage that the mathematical theory is well understood but that the solution is usually associated with resonance difficulties. There is however much theoretical work (beginning with Ursell 1953) which shows that resonance difficulties can often be avoided by modifying the fundamental solution. In this way a different integral equation can be obtained for the same unknown function. In the present work this idea will

be applied to the numerical solution of problems involving the half-immersed circle and the half-immersed ellipse. We hope to publish some of the theoretical considerations in greater detail elsewhere.

## 2. Formulation of the problem

A smooth cylinder is partially immersed in a fluid with its axis in the free surface (see Figure 1 below), and undergoes a periodic heaving motion with prescribed velocity  $U_0 \exp(-i\sigma t)$ , where  $\sigma$  is the radian frequency of the oscillation. Viscosity and surface tension are neglected; thus a velocity potential exists. The origin of rectangular Cartesian coordinates, in the mean free surface, is taken at the mean position of the axis of the cylinder. The x-axis is horizontal and perpendicular to the axis of the cylinder; the y-axis is vertical, y increasing with depth. Also polar coordinates  $(r, \theta)$  are defined by the equations  $x = r \sin \theta$ ,  $y = r \cos \theta$ . Then the velocity potential  $\phi(x, y, t) = \phi(x, y) \exp(-i\sigma t)$  satisfies Laplace's equation

$$\left( \frac{\partial^2}{\partial x^2} + \frac{\partial^2}{\partial y^2} \right) \phi(x, y, t) = 0 \quad (2.1)$$

in the fluid. The linearized boundary conditions are

$$\left( K + \frac{\partial}{\partial y} \right) \phi(x, y, t) = 0 \text{ on the free surface} \\ y=0, \quad x < x_1, \quad x > x_2, \quad (2.2)$$

where  $K = \sigma^2/g$ ;

$$\frac{\partial \phi}{\partial y}(x, y, t) = 0 \text{ on the bottom } y=h; \quad (2.3)$$

$$\frac{\partial \phi}{\partial n}(x, y, t) = U_0 \frac{\partial y}{\partial n} \exp(-i\sigma t) \text{ on the} \quad (2.4)$$

submerged part  $\partial D_1$  of the cylinder.

Also, waves at a distance from the cylinder travel outwards: thus there is a radiation condition

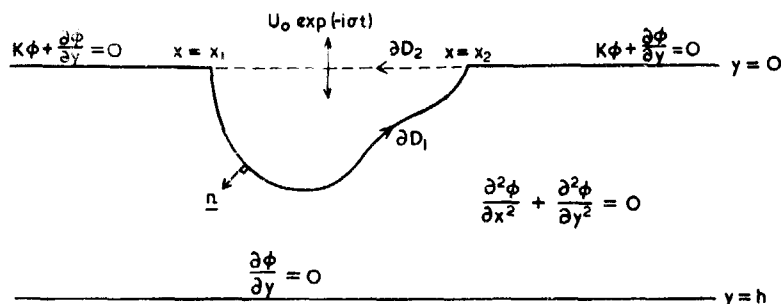


Figure 1.

$$\left\{ \frac{\partial}{\partial x} + ik_0 \right\} \phi(x, y, t) \rightarrow 0 \text{ as } x \rightarrow \pm \infty, \quad (2.5)$$

where  $k_0$  is the unique real positive root of the equation

$$K = k_0 \tanh k_0 h. \quad (2.6)$$

If the cross-sectional profile lies entirely between the two vertical planes  $x=x_1$  and  $x=x_2$  then it is known (cf. John 1950) that the above boundary-value problem has a unique solution. For simplicity we shall consider only the heaving motion of a smooth cylinder which is symmetric about  $x=0$  and which intersects the free surface  $y=0$  at  $x=a$ , but the method is applicable to unsymmetrical sections and to other motions.

The problem is solved when the value of the potential  $\phi(x, y)$  is known on the submerged portion  $\partial D_1$  of the cylinder, for then  $\phi(x, y)$  can be found everywhere in the fluid by Green's theorem (cf. Ursell 1953). In an earlier paper (Sayer and Ursell 1976) numerical results for a circular cylinder were found by using a wave source and multipoles, which are simple but specially appropriate only for the circle. For this reason, an integral equation for the boundary values of  $\phi$  on  $\partial D_1$  is used in the present work. This equation can be obtained by applying Green's theorem to the two harmonic functions  $\phi(x, y)$  and  $G(x, y; \xi, \eta)$ , (defined in (2.8) below), where  $(\xi, \eta)$  is on  $\partial D_1$ . Thus

$$\left\{ \phi(x, y) \frac{\partial}{\partial n} - G(x, y; \xi, \eta) \frac{\partial}{\partial n} \right\} ds(x, y) = 0. \quad (2.7)$$

Here  $\partial/\partial n$  denotes differentiation normal to the line element  $ds(x, y)$  into the fluid. The line integral (2.7) is taken along  $\partial D_1$ , indented by a small semi-circular arc round  $(\xi, \eta)$  where  $G(x, y; \xi, \eta)$  has a source singularity. The contributions to Green's theorem from the free surface, the bottom and infinity all vanish by virtue of the conditions satisfied by  $\phi$  and  $G$ . It will be assumed that  $\partial D_1$  meets the free surface normally; then an integral equation with a square-integrable kernel is obtained.

The Green's function  $G(x, y; \xi, \eta)$  is a potential which is harmonic everywhere in the fluid except at the point  $(x, y) = (\xi, \eta)$  where it has a source singularity. It also satisfies (2.2), (2.3) and (2.5). Such a potential is given by Thorne (1952):

$$\begin{aligned} G(x, y; \xi, \eta) &= \frac{1}{2} \log \frac{(x-\xi)^2 + (y-\eta)^2}{(x-\xi)^2 + (y+\eta)^2} \\ &+ 2 \int_0^\infty \frac{\cosh k(h-y) \cosh k(h-\eta)}{K \cosh kh - k \sinh kh} \\ &- \frac{e^{-kh}}{k} \sinh ky \sinh k\eta \left\{ \frac{\cos k(x-\xi)}{\cosh kh} \right. dk \\ &- \frac{4\pi i \cosh k_0(h-y) \cosh k_0(h-\eta) \cos k_0(x-\xi)}{2k_0 h + \sinh 2k_0 h} \\ &= \frac{1}{2} \log \frac{(x-\xi)^2 + (y-\eta)^2}{(x-\xi)^2 + (y+\eta)^2} + G_*(x, y; \xi, \eta), \text{ say.} \end{aligned} \quad (2.8)$$

The bar through the integral indicates that the Cauchy principal value is to be taken.

(i) Circular cylinder  $r = a, |0| \leq \theta \leq \pi$

This was the problem studied by Sayer and Ursell (1976) using the method of multipoles. Here  $\partial D_1$  consists of the semi-circle  $r = a, |0| \leq \theta \leq \pi$ . We write  $\phi(a) = \phi(a \sin \theta, a \cos \theta)$  and  $G(\theta, \eta) = G(a \sin \theta, a \cos \theta; a \sin \eta, a \cos \eta)$ . Then  $\phi(a)$  satisfies the following Fredholm integral equation of the second kind (Ursell 1953)

$$\begin{aligned} \pi \phi(a) &+ \int_{-\pi}^{\pi} \phi(\theta) \left\{ \frac{\partial}{\partial r} G_*(\theta, \eta) \right\} a d\theta \\ &= -\pi a U_0 \cos a + U_0 \int_{-\pi}^{\pi} \cos \theta \left\{ G_*(\theta, \eta) \right\} a d\theta \end{aligned} \quad (2.9)$$

The first term on the left-hand side of (2.9) is the contribution from the small semi-circle round  $(a \sin \alpha, a \cos \alpha)$ . Observe also that

$$\left\langle \frac{\partial}{\partial r} \log \frac{(x-\xi)^2 + (y-\eta)^2}{(x-\xi)^2 + (y+\eta)^2} \right\rangle = 0. \quad (2.10)$$

where, here and elsewhere, angular brackets denote that  $r$  is to be put equal to  $a$ .

The expansion of  $G_*(x, y; \xi, \eta)$  near the origin is (cf. Yu and Ursell 1961) given by

$$\begin{aligned} G_*(x, y; \xi, \eta) = & \langle \log Kr^* \rangle \sum_{s=0}^{\infty} \frac{(-Kr^*)^s}{s!} \cos s\theta^* \\ & - \theta^* \sum_{s=1}^{\infty} \frac{(-Kr^*)^s}{s!} \sin s\theta^* \\ & - \sum_{s=1}^{\infty} \frac{(-Kr^*)^s}{s!} \left( \frac{1}{2} + \dots + \frac{1}{s} \right) \cos s\theta^* \\ & + Kh \sum_{s=0}^{\infty} \frac{G_{2s+1}(Kh)}{(2s+1)!} \left( \frac{r^*}{h} \right)^{2s+1} \cos(2s+1)\theta^* \\ & - \sum_{s=0}^{\infty} \frac{G_{2s+1}(Kh)}{(2s)!} \left( \frac{r^*}{h} \right)^{2s} \cos 2s\theta^* \\ & - i \sum_{s=1}^{\infty} \frac{G_{2s-1}(Kh)}{(2s)!} \left( \frac{r^*}{h} \right)^{2s} \cos 2s\theta^* \\ & - \left( \frac{r^*}{h} \right)^{2s} \cos 2s\theta^* \Big\} \\ & - \frac{2\pi i \cosh k_0(h-y) \cosh k_0(h-\eta) \cos k_0(x-\xi)}{2k_0 h + \sinh^2 2k_0 h}, \end{aligned} \quad (2.11)$$

where

$$G_{2s+1}(Kh) = \int_0^{\infty} \frac{u^{2s+1} e^{-u}}{(Kh+u)(Kh \cosh u - u)} du, \quad (2.12)$$

$$G_{2s-1}(Kh) = \int_0^{\infty} \frac{(Kh+u)^2}{Kh} \frac{e^{-u}}{\sinh u - u} \frac{du}{\sinh u}, \quad (2.13)$$

$$= (Kh)^2 G_{2s-1}(Kh) - G_{2s+1}(Kh),$$

and  $(r^*, \theta^*)$  and  $(r^+, \theta^+)$  are polar coordinates with origins at  $(\xi, -\eta)$  and  $(\xi, \eta)$  respectively ( $\eta > 0$ ).

(ii) Elliptical cylinder  $x = c \sinh \theta_0 \sin \alpha$ ,  $y = c \cosh \theta_0 \cos \alpha$ ,  $|\alpha| \leq \frac{1}{2}\pi$ .

Again an application of Green's theorem to  $\phi(x, y)$  and  $G(x, y; \xi, \eta)$  yields a Fredholm integral of the second kind:

$$\pi \phi(a_0) + \int_{-\frac{1}{2}\pi}^{\frac{1}{2}\pi} \phi(\alpha) \frac{\partial}{\partial \beta} G(\alpha, a_0) \Big|_{\beta=\beta_0} d\alpha = U_0 c \sinh \beta_0 \int_{-\frac{1}{2}\pi}^{\frac{1}{2}\pi} \cos \alpha G(\alpha, a_0) \Big|_{\beta=\beta_0} d\alpha \quad (2.14)$$

where an obvious abbreviated notation has been used. The term  $U_0 c \sinh \beta_0 \cos \alpha$  is the normal velocity on the ellipse, where

$$\frac{\partial \phi}{\partial n} ds = \frac{\partial \phi}{\partial \beta} d\alpha.$$

### 3. Uniqueness of solution of integral equation

The solution of the physical problem is certainly unique (cf. John 1950), but our mathematical formulation may not possess a unique solution for every  $K$ . In this section we are concerned with properties of the integral equations (2.9) and (2.14). These equations are non-singular (i.e. the Fredholm determinant  $\neq 0$ ) if and only if the transposed equations are non-singular. It can be shown that the latter equation occurs in the solution of the exterior Neumann problem by sources and it is well known (cf. John) that this is singular only when  $K$  is an eigenvalue of the associated interior Dirichlet problem. These eigenvalues occur at an infinite discrete set of values of  $K$ ; the theory is treated by John. The difficulty at these frequencies, due to the use of frequency-dependent Green's functions, also arises in many other wave problems, e.g. the problems of acoustics (cf. Jones 1974). (We may note that  $K = 0$  is obviously not an eigenvalue of the interior Dirichlet problem.) For wavenumbers  $Ka \gg 1$  it is known that this difficulty can be overcome by putting a wave source of a certain definite strength at the origin (cf. Ursell 1953, 1961; Rhodes-Robinson 1970), and we shall do this in the present work. Much of the remainder of the present work has been influenced by the observation of Ogilvie (1976) that in the modified integral equation the choice of source strength at the origin was not at all critical in his computations. We shall now explain Ogilvie's observation by showing that the integral equation formed with a modified source function

$$\tilde{G}(P, Q) = G(P, Q) + A G(P, 0) G(Q, 0) \quad (3.1)$$

is in general non-singular, where  $P, Q$  denote points of the fluid. (We shall use  $p, q$  to denote points of  $\partial D_1$ ), and where  $A \equiv A(k_0 h)$  is a frequency-dependent strength parameter. The multiplicative factor  $G(Q, 0)$  is included so that  $\tilde{G}(P, Q)$  is symmetric (and hence the kernel of (3.3) below is the transpose of the kernel of (2.9), with  $G$  replaced by  $\tilde{G}$ ).

Consider the potential

$$\phi(P) = \int_{\partial D_1} u(q) \tilde{G}(P, q) ds_q \quad (3.2)$$

where  $\tilde{G}(P, Q)$  is defined in (3.1) above. Then the homogeneous exterior Neumann problem yields the integral equation

$$\pi u(p) + \int_{\partial D_1} u(q) \frac{\partial}{\partial n_p} \tilde{G}(p, q) ds_q = 0 \quad (3.3)$$

If we write

$$B = \int_{\partial D_1} u(q) G(q, 0) ds_q \quad (3.4)$$

it can be shown that (3.3) has a non-trivial solution only if

$$|B|^2 \{A - \bar{A} - 2i|A|^2 C(k_0 h)\} = 0, \quad (3.5)$$

where, by definition,

$$C(k_0 h) = \frac{-4\pi \cosh^2 k_0 h}{2k_0 h + \sinh 2k_0 h} \quad (3.6)$$

Put  $A = A_1 + iA_2$ , where  $A_1$  and  $A_2$  are real. Then if  $A_1$  and  $A_2$  do not lie on the circle

$$A^2 - \left\{A_2 - \frac{1}{2C(k_0 h)}\right\}^2 = \left\{\frac{1}{2C(k_0 h)}\right\}^2 \quad (3.7)$$

the solution of (3.3) (and hence (2.9) and (2.14)) is unique except at those Dirichlet eigenfrequencies for which the corresponding eigenfunction also vanishes at the origin. It is believed that there are no such eigenfrequencies. We have carried out calculations for  $A = 1, 1, i$  and we find they agree to three significant figures. The calculations at the end of the paper are those for which  $A = 1$ .

In his analysis, Ogilvie considers the simpler case of the oscillations between two vertical plates in infinite depth. He shows that the interior Dirichlet eigenvalues are removed if the central source strength  $A$  is chosen suitably, but within wide limits; his criterion is a limiting case of ours.

#### 4. Singular behaviour of the solution of the integral equation

This section deals with the singular behaviour of the solution of the unmodified integral equations (2.9) and (2.14). We shall show that the singular values of the numerical schemes (see §7 below) do in fact occur at the

eigenvalues of the interior Dirichlet problem, as is predicted by the theory.

The numerical study of (2.9) indicated instability at certain values of the wavenumber  $Ka$ ; in particular, when  $Ka$  was increased from zero it was found that instability first occurred in the range  $1.80 < Ka < 1.85$  approximately. It was therefore suspected that the first eigenvalue of the associated interior Dirichlet problem occurred within these limits, and the following observations confirm this.

It is possible to obtain an estimate of the fundamental eigenvalue  $K_1$  by using a form of Rayleigh's Principle (cf. Lamb 1932, §72, for his treatment of the analogous Neumann problem). Let  $V(x)$  be a prescribed normal velocity on  $\partial D_2$ , vanishing at the ends, ( $\partial D_2$  is that part of  $y=0$  lying between  $x=x_1$  and  $x=x_2$ ), and let  $\phi(x, y)$  be the corresponding harmonic potential satisfying  $\phi=0$  on  $\partial D_1$ . We then define a Rayleigh quotient  $Q[V]$  by the ratio

$$Q[V] = \frac{- \int_{\partial D_2} \phi(x, 0) V(x) dx}{\int_{\partial D_2} \{V(x)\}^2 dx} \quad (4.1)$$

where the numerator and denominator are related to the kinetic and potential energies respectively. Then it can be shown that

$$Q[V] \geq \frac{1}{K_1} \quad (4.2)$$

and a method analogous to that adopted by Lamb gives the estimate  $K_1 a \approx 1.822$  for the fundamental eigenvalue of the circle. This is close to the value at which the solution was found to break down. Higher eigenvalues can be obtained in a similar manner, but the process is more complicated since the  $m$ th eigenfunction must be orthogonal to the previous  $(m-1)$  eigenfunctions. Estimates of 3.289 and 4.891 for the second (anti-symmetrical) and third (symmetrical) eigenvalues of the circle have been obtained. We note that the eigenvalues are independent of depth.

#### 5. Additional modifications

##### (i) Enforcement of symmetry

$\phi(a)$  is an even function of  $a$  and thus (2.9) may be written in the form

$$\begin{aligned} \pi \phi(a) + \int_0^{\frac{1}{2}\pi} \phi(\theta) \left\{ \frac{\partial}{\partial r} \{G_a(\theta, a) + G_a(-\theta, a)\} \right\} a d\theta \\ = -\pi u_0 \cos a \\ + u_0 \int_0^{\frac{1}{2}\pi} \cos \theta \{G_a(\theta, a) + G_a(-\theta, a)\} a d\theta. \end{aligned} \quad (5.1)$$

Although the kernel and the integrand on the right-hand side of (5.1) are more complicated than the corresponding terms in (2.9), the range of integration is halved. Numerical computations indicate that both (2.9) and (5.1) take comparable times to solve. (5.1), however, was found to have the advantage that only those eigenvalues occur which correspond to symmetric oscillations, and that the calculation did not break down at the anti-symmetric eigenvalues.

(ii) Use of the transposed integral equation

The virtual mass is defined by the quotient  
virtual mass =

$$\frac{\left( \begin{array}{l} \text{upward hydrodynamic force per unit length} \\ \text{of cylinder in phase with acceleration} \end{array} \right)}{\left( \begin{array}{l} \text{acceleration} \\ \text{mass per unit length of} \\ \text{of cylinder} \end{array} \right) \left( \begin{array}{l} \text{cylinder immersed in fluid} \end{array} \right)}$$

(5.2)

From Bernoulli's equation, the hydrodynamic force is  $-\rho \frac{\partial \phi}{\partial t}(x, y, t) = \text{Re} \{ i \omega \phi(x, y) \exp(-i \omega t) \}$ . Thus, for the circle, the upward hydrodynamic force per unit length of the cylinder in phase with the acceleration is

$$2 \int_0^{\pi/2} i \omega \{ \text{Re} \langle \phi \rangle \} \exp(-i \omega t) \cos \theta \, a \, d\theta, \text{ whence}$$

$$\text{virtual mass} = \frac{2 \int_0^{\pi/2} i \omega \{ \text{Re} \langle \phi \rangle \} \exp(-i \omega t) \cos \theta \, a \, d\theta}{(-i \omega U_0 \exp(-i \omega t)) \left( \frac{1}{2} \pi a^2 \rho \right)}$$

(5.3)

Hence only the quantity  $\int_0^{\pi/2} \text{Re} \{ \phi(\theta) \} \cos \theta \, d\theta$ ,

rather than the potential explicitly, is required for the virtual mass of the circle. Since the major part of the computational time is consumed in evaluating certain matrix elements (see (7.14) below) it is worth considering the integral equation which has the transposed kernel of (2.9) but a much simpler right-hand side, viz.  $\cos \theta$ , where  $\theta$  is the angle between the downward vertical and the normal to the circle. In this case it can readily be shown that

$$\int_0^{\pi/2} \phi(\theta) \cos \theta \, d\theta = \int_0^{\pi/2} F(\theta) \psi(\theta) \, d\theta, \quad (5.4)$$

where

$$\phi(\alpha) + \int_{-\pi}^{\pi} K(\theta, \alpha) \phi(\theta) \, d\theta = F(\alpha) \quad (5.5)$$

and

$$\psi(\theta) + \int_{-\pi}^{\pi} K(\theta, \theta) \psi(\theta) \, d\theta = \cos \theta \quad (5.6)$$

The numerical solution of (5.6), together with the evaluation of (5.4), took approximately one-third of the computational time required for the solution of (5.5).

## 6. Long-wave behaviour of virtual mass

In an earlier paper (Sayer and Ursell 1976), on a heaving circular cylinder, an analytical and numerical study of the behaviour of the virtual mass as a function of wavenumber showed that, for sufficiently deep water, a turning point (maximum) occurs at a certain small wavenumber. The result

$$\left. \frac{d}{d(Ka)} (\text{virtual mass}) \right|_{\text{zero frequency}} \sim \frac{16}{\pi^4} \frac{h}{a} \sum_{n=1}^{\infty} \frac{1}{n^3},$$

$$\text{as } \frac{a}{h} \rightarrow 0, \quad (6.1)$$

was derived from the multipole method (cf. Sayer and Ursell, equation (3.3)). The virtual mass was found to be greater than unity as  $a/h \rightarrow 0$  in the limit of zero frequency, but equal to  $1 + O(a/h)^2$  for  $Ka \gg 1$ ; (6.1) then shows that a turning point (maximum) exists for  $Ka$  and  $a/h$  sufficiently small. This was found to occur in the neighbourhood of  $Kh = 1$ , where the wavelength is of the same order as the depth. The same result has recently been derived by us in a different way by matching the velocity potentials in both the inner and outer regions, and in this form the argument is applicable to other sections.

Thus, by considering the behaviour of  $\phi$  at zero frequency on the ellipse, it can be deduced that

$$\left. \frac{d}{d(Kt)} (\text{virtual mass}) \right|_{\text{zero frequency}} \sim \frac{16}{\pi^4} \frac{h}{t} \sum_{n=1}^{\infty} \frac{1}{n^3}$$

in sufficiently deep water, where  $a, b$  are the draft, half-beam respectively, and  $t$  is a typical body dimension. Hence the virtual mass has a maximum which is also found to occur near  $Kh = 1$ .

## 7. Numerical methods and results

Two numerical methods were employed to solve the integral equation



$$\phi(\alpha) + \int_a^b K(\theta, \alpha) \phi(\theta) d\theta = F(\alpha) \quad (7.1)$$

numerically.

(i) The classical Galerkin procedure

Let us consider the functional

$$L[\phi] = \phi(\alpha) + \int_a^b K(\theta, \alpha) \phi(\theta) d\theta - F(\alpha) \quad (7.2)$$

and seek a solution

$$Y_n(\alpha) = F(\alpha) + \sum_{i=0}^n a_i \phi_i(\alpha) \quad (7.3)$$

such that

$$L[Y_n] = 0. \quad (7.4)$$

$\phi_0, \phi_1, \dots, \phi_n$  are any linearly independent functions of  $\alpha$ .

Substitution of (7.3) into (7.2) gives

$$\begin{aligned} L[Y_n] &= \sum_{i=0}^n a_i \left\{ \phi_i(\alpha) + \int_a^b K(\theta, \alpha) \phi_i(\theta) d\theta \right\} \\ &\quad - F(\alpha) \\ &= \phi(\alpha; a_0, a_1, \dots, a_n), \text{ say} \end{aligned} \quad (7.5)$$

Now, by virtue of (7.4),

$$\int_a^b L[Y_n(\alpha)] \phi_i(\alpha) d\alpha = 0, \quad i=0, 1, 2, \dots, n \quad (7.6)$$

whence

$$\sum_{j=0}^n a_j (A_{ij}^* + B_{ij}^*) = -C_i^*, \quad i=0, 1, 2, \dots, n, \quad (7.7)$$

where

$$\begin{aligned} A_{ij}^* &= \int_a^b \phi_i(\alpha) \phi_j(\alpha) d\alpha \\ B_{ij}^* &= \int_a^b \int_a^b K(\theta, \alpha) \phi_j(\theta) \phi_i(\alpha) d\theta d\alpha \\ C_i^* &= \int_a^b K(\theta, \alpha) F(\theta) \phi_i(\alpha) d\theta d\alpha. \end{aligned} \quad (7.8)$$

For the circle,  $a = -\frac{1}{2}n$  and  $b = \frac{1}{2}n$ ; choose  $\phi_j(\alpha) = \cos 2ju$ .

$$\text{Then } A_{00}^* = n; \quad A_{ij}^* = \frac{1}{2}n\delta_{ij}, \quad i, j=1, 2, \dots, n.$$

$$\text{Also write } B_{0j} = \frac{1}{n} B_{0j}^*; \quad B_{ij} = \frac{2}{n} B_{ij}^*, \quad i, j=1, 2, \dots, n. \quad (7.9)$$

$$C_0 = \frac{1}{n} C_0^*; \quad C_i = \frac{2}{n} C_i^*, \quad i=1, 2, \dots, n.$$

Hence (7.8) reduces to

$$\sum_{j=0}^n a_j (\delta_{ij} + B_{ij}) = -C_i, \quad i=0, 1, 2, \dots, n. \quad (7.10)$$

By choosing for  $K(\theta, \alpha)$  the modified kernel  $\langle \frac{\partial}{\partial r} G_1(\theta, \alpha) \rangle$  we can immediately conclude from the results of §3 that (7.10) is a non-singular system of linear equations, subject to the restriction (3.7), except at those Dirichlet eigenfrequencies (if any) for which the corresponding eigenfunction vanishes at the origin. No instabilities were recorded in the range  $0 < Ka < 10$ .

(ii) Quadrature method; Fox-Goodwin algorithm

This second method reduces the integral equation (7.1) to a system of linear equations by employing an elementary trapezium rule to evaluate the integral term:

$$\begin{aligned} \phi(a+ih) + h \sum_{j=0}^n K(a+ih, a+jh) \phi(a+jh) \\ = F(a+ih) + E_i, \quad i=0, 1, 2, \dots, n, \end{aligned}$$

where

$$\sum_{j=0}^n = \frac{1}{2} \{ j=0 \text{ term} + j=n \text{ term} \} + \sum_{j=1}^{n-1}. \quad (7.12)$$

and  $E_i$  is the  $i^{\text{th}}$  correction arising from the error in the trapezium rule. We then solve the system of linear equations

$$A \underline{\phi} = \underline{F} + \underline{E}(\underline{\phi}) \quad (7.13)$$

where  $\underline{\phi}$ ,  $\underline{F}$  and  $\underline{E}$  are column vectors whose  $i^{\text{th}}$  elements are  $\phi(a+ih)$ ,  $F(a+ih)$  and  $E_i$  respectively.  $A$  is the matrix

$$A = \begin{pmatrix} 1 - \frac{1}{2}hK(a, a) & -hK(a, a+h) & \dots & -\frac{1}{2}hK(a, b) \\ -\frac{1}{2}hK(a+h, a) & 1 - hK(a+h, a+h) & \dots & -\frac{1}{2}hK(a+h, b) \\ \vdots & \vdots & \ddots & \vdots \\ -\frac{1}{2}hK(b, a) & -hK(b, a+h) & \dots & 1 - \frac{1}{2}hK(b, b) \end{pmatrix} \quad (7.14)$$

Fox and Goodwin (1953) suggest solving successively the equations

$$\begin{aligned} A \phi^{(0)} &= F \\ A \phi^{(1)} &= h E(\phi^{(0)}) \\ &\vdots \\ A \phi^{(m)} &= h E(\phi^{(m-1)}) \end{aligned} \quad (7.15)$$

giving the solution

$$\phi = \phi^{(0)} + \phi^{(1)} + \dots + \phi^{(m)} \quad (7.16)$$

The  $i^{\text{th}}$  element  $E_i(j)$  of the column vector  $E \phi(j)$  is given by Gregory's finite-difference formula (cf. Jeffreys and Jeffreys, §9.083)

$$\begin{aligned} E_i(j) &= \left( -\frac{1}{12} \nabla^1 - \frac{1}{24} \nabla^2 - \dots \right) K(a+ih, b) \phi^{(j)}(b) \\ &+ \left( +\frac{1}{12} \Delta^1 - \frac{1}{24} \Delta^2 + \dots \right) K(a+ih, a) \phi^{(j)}(a) \end{aligned} \quad (7.17)$$

The solution of (7.13) used Crout factorisation and iteratively refined the solution vectors to some specified tolerance (see (7.15)). Typical numerical results for the circle and ellipse are given in Table 2 and Table 3 at the end of the paper.

It is instructive to compare the times required by the various numerical methods. Let  $T$  be a typical time required to compute the virtual mass of the circle at one particular frequency by the multipole method. Then the corresponding times needed by us for the integral-equation methods (to achieve the same accuracy) were approximately as given in Table 1 below.

Method	Time
Multipoles	$T$
Unmodified integral equation	$10T$
Modified integral equation	$20T$
Unmodified transposed integral equation	$3T$
Modified transposed integral equation	$6T$

Table 1.

Both the Galerkin method and the quadrature method due to Fox and Goodwin required comparable computer times. For  $Ka = 1.0$  a typical value of  $T$  was four seconds on the CDC7600 computer, to achieve an accuracy of four significant figures.

## 8. Conclusions

In the present work we have formulated the boundary-value problem as an integral equation by means of Green's theorem applied to the velocity potential, and to a fundamental solution satisfying the free-surface condition and the conditions on the bottom and at infinity. The unknown function is then the potential on the body, and the kernel is complicated. There are many such integral equations, one for each choice of fundamental solution. We began by choosing the simplest fundamental solution, a wave source in a strip of constant depth. The numerical solution was satisfactory for small  $Ka$  but instabilities developed near  $Ka = 1.8$ . Such instabilities are familiar in these problems; we showed theoretically that they would be expected at eigenvalues of the corresponding interior Dirichlet problem, for which the smallest such eigenvalue was found to be indeed near  $Ka = 1.8$ . It was also known that the fundamental solution could be modified so that the corresponding integral equation would have no resonances for large  $Ka$ ; this equation was studied numerically and was found to be free from resonances for all  $Ka$ . Following a suggestion by Ogilvie, we have shown both theoretically and numerically that the choice of useful fundamental solutions is wider than was expected. We conclude that resonances are probably not a serious difficulty in two-dimensional problems with constant finite depth if the fundamental solution is appropriately chosen. Integral equations with modified kernels were solved numerically for half-immersed circles and ellipses, by the Galerkin method and by a quadrature method due to Fox and Goodwin. These results agreed with each other, and (for the circle) with the results of the multipole method, to at least three significant figures. Typical results are given in Tables 2 and 3.

We found that the virtual mass for the circle could be obtained more efficiently by solving an integral equation with the transposed kernel and a simpler right-hand side; this reduced the work by about 70 per cent.

We should point out that our values of the virtual mass of the circle for low wavenumbers and shallow water ( $a/h > 0.4$ ) exceed the upper bound given by Bai (1977) for zero frequency. Our results appear to be in good agreement with the results of Bai and of Yeung (1975) except perhaps at small wavenumbers. Neither Bai nor Yeung report any difficulty with resonances, and it may be that in their methods they do not occur.

Circle,  $a/h = 0.5$

Ka	VIRTUAL MASS		
	Multipole Method	Modified	Modified
		Integral Equation, A=1: (i) Galerkin Method	Integral Equation, A=1: (ii) Fox-Goodwin
0.00001	0.49843	0.49850	0.49850
0.00005	0.49845	0.49851	0.49850
0.0001	0.49848	0.49851	0.49850
0.0005	0.49851	0.49854	0.49853
0.001	0.49855	0.49858	0.49856
0.005	0.49880	0.49885	0.49882
0.01	0.49912	0.49917	0.49914
0.05	0.50180	0.50189	0.50184
0.1	0.50541	0.50549	0.50545
0.2	0.51344	0.51354	0.51349
0.3	0.52274	0.52283	0.52279
0.4	0.53342	0.53355	0.53350
0.5	0.54567	0.54583	0.54576
0.6	0.55957	0.55972	0.55966
0.7	0.57514	0.57530	0.57523
0.8	0.59233	0.59251	0.59243
0.9	0.61099	0.61119	0.61110
1.0	0.63090	0.63111	0.63101
1.822	0.80133	0.80156	0.80144
2.5	0.90606	0.90630	0.90618
3.289	0.98583	0.98611	0.98599
4.891	1.07320	1.07350	1.07336
5.0	1.07705	1.07736	1.07725
10.0	1.18048	1.18082	1.18070

Table 1.

Ellipse,  $\tanh \beta_0 = 0.5$ ,  $\frac{\text{draft}}{\text{water depth}} = 0.5$

Kh	VIRTUAL MASS	
	Modified	Modified
	Integral Equation, A=1: (i) Galerkin Method	Integral Equation, A=1: (ii) Fox-Goodwin
0.00001	0.22432	0.22431
0.00005	0.22432	0.22430
0.0001	0.22431	0.22430
0.0005	0.22430	0.22430
0.001	0.22423	0.22421
0.005	0.22401	0.22396
0.01	0.22368	0.22362
0.05	0.22237	0.22230
0.1	0.22094	0.22086
0.2	0.21964	0.21953
0.3	0.21914	0.21901
0.4	0.21909	0.21900
0.5	0.21950	0.21939
0.6	0.22026	0.22014
0.7	0.22135	0.22123
0.8	0.22279	0.22268
0.9	0.22460	0.22449
1.0	0.22681	0.22671
2.5	0.32557	0.32548
5.0	0.45093	0.45084
10.0	0.56160	0.56149

Table 2.

# References

- BAI, K.J., 1977. The added mass of two-dimensional cylinders heaving in water of finite depth. *J. Fluid Mech.*, 81, 85-105.
- FOX, L. and GOODWIN, E.T., 1953. Numerical solution of non-singular linear integral equations. *Phil. Trans. Roy. Soc.*, A245, 501-534.
- JEFFREYS, H. and JEFFREYS, B.S., 1946. *Methods of mathematical physics*, §9.083.
- JOHN, F., 1950. On the motion of floating bodies, II. *Comm. Pure and Appl. Maths.*, 3, 45-101.
- JONES, D.S., 1974. Integral equations for the exterior acoustic problem. *Q. Jl. Mech. appl. Math.*, 27, 129-142.
- OGILVIE, T.F., 1976. Private communication.
- RHODES-ROBINSON, P.F., 1970. On the short-wave asymptotic motion due to a cylinder heaving on water of finite depth. *Proc. Cambridge Phil. Soc.*, 67, 423-468.
- SAYER, P. and URSELL, F., 1976. On the virtual mass, at long wavelengths, of a half-immersed circular cylinder heaving on water of finite depth. 11th. Symposium on Naval Hydrodynamics, University College London.
- THORNE, R.C., 1953. Multipole expansions in the theory of surface waves. *Proc. Cambridge Phil. Soc.*, 49, 707-716.
- URSELL, F., 1953. Short surface waves due to an oscillating immersed body. *Proc. Roy. Soc.*, A220, 90-103.
- URSELL, F., 1961. The transmission of surface waves under surface obstacles. *Proc. Cambridge Phil. Soc.*, 57, 638-668.
- YU, Y.S. and URSELL, F., 1961. Surface waves generated by an oscillating immersed body. *J. Fluid Mech.*, 11, 529-551.
- YEUNG, R.W., 1975. A hybrid integral-equation method for time-harmonic free-surface flow. 1st. International Conference on Numerical Ship Hydrodynamics, Gaithersburg, Maryland.

## THEORY OF COMPLIANT PLANING SURFACES

Lawrence J. Doctors\*

Aviation and Surface Effects Department  
David W. Taylor Ship Research and Development Center  
Bethesda, Maryland 20084

### Abstract

This report describes a theoretical model for the hydrodynamics of flexible planing surfaces. Linearized potential-flow theory is used to obtain the hydrodynamic effects, and the surface itself is replaced by a finite-element representation of the pressure distribution. The flexural behavior of the planing surface is computed with small-deflection beam theory, and the plate is discretized into structural finite elements. A series of numerical experiments shows that a sufficient degree of convergence is achieved with forty elements. The resultant pressure distributions reproduce the leading-edge square-root singularity - which is well known in airfoil theory. The rigidity of the plate is found to have a major effect on all the results: the lift and drag are reduced, with this influence being stronger at higher speeds. Tapering towards the trailing edge has a similar effect. The pressure distributions show that there is a possibility of negative pressure regions under the deflected shape of the surface - indicating that cavitation might occur in some conditions. Curves of the free-surface elevation are presented, and in addition, the results of applying a pressure on the plate are described.

### 1. Introduction

#### Background

The work described in this paper was prompted by an interest in the application of flexible planing surfaces to advanced marine craft. One such possible use is to support the weight of the vehicle on three or more suitably spaced surfaces. A careful choice of the degree of flexibility - and appropriate damping - would produce a much smoother ride in rough water than is given by a rigid shape.

Another application of the concept is to the seals of a surface-effect ship (SES). A typical layout of an SES fitted with sidewalls and bow and stern seals is shown in Figure 1. The main design feature of the seals is that they can deflect in order to permit travel in a sea state without excessive loss of pressure from the air cushion which supports the craft. The details of the seal design will not be given here, but the reader is referred instead to other works on this subject.

One of the phenomena of great interest - as well as the generated forces - is the wave system developed under the vehicle. If the sidewalls are not sufficiently deep then venting of cushion air can occur in those regions where a wave trough exists. This results in a lower attitude of the SES with an attendant rise in hydrodynamic drag due to the buildup of water against the seals.

\*Permanent address:

School of Mechanical and Industrial Engineering  
University of New South Wales, Sydney, Australia

Regarding the theory of planing, this problem has always been attacked using the assumptions of inviscid incompressible potential flow. The assumption has also been made that the main effect of viscosity is to generate a frictional drag which can be accounted for separately. Sretenskii [1 and 2] and Sedov [3] were two of the earliest workers in the field of two-dimensional planing. The use of potential-flow theory allows one to represent the action of the planing surface by a pressure distribution, which they expressed as an infinite series. The first term of the series contains the square-root singularity at the leading edge - a phenomenon which also occurs in airfoil theory. In linearized planing theory this singularity models the splash jet that is thrown forward of the boat.

Maruo [4, 5, 6 and 7] also developed the linearized theory, and in the last paper, obtained experimental pressure distributions, which tended to verify the theory. The agreement, not unexpectedly, was better at small trim angles, and in regions away from the singularity at the leading edge.

The work of Squire [8] will be remembered, particularly, because he carefully explained the importance of satisfying the Kutta condition at the trailing edge. A consequence of this is that if one decides on the wetted length, then the height of the craft relative to the undisturbed free surface has to be treated as unknown. (This means that the load, and the center of lift, are parts of the solution.) Another approach is the high-Froude-number approximation of Cumberbatch [9]. He also developed a parabolic-shaped plate which was more efficient than a flat plate since it eliminated the splash jet. A review of the above work was given by Wehausen and Laitone [10].

Nonlinear aspects of planing in two dimensions have also been examined. Thus Green [11, 12 and 13] solved the problem of a flat plate gliding at infinite Froude number in both finite and infinite depth water. Other gravity-free planing research was performed by Wu and Whitney [14] and Ting and Keller [15]. They derived shapes that resulted in a splash-free condition. The situation of *high* (but not infinite) Froude number was examined by Wu [16] and Ting and Keller [17], who used a singular perturbation scheme. The latter paper took into account the impingement of the spray jet on the water ahead of the plate.

Doctors [18] developed a finite-element approach for handling plates of arbitrary shape, including the effects of gravity waves. The method also allowed the prediction of optimum forms which coincided with those of Cumberbatch.

With regard to three-dimensional planing, the main problem here is that the wetted area of the surface is unknown and must be found as part of the solution. (As mentioned previously, this difficulty is skirted in two dimen-

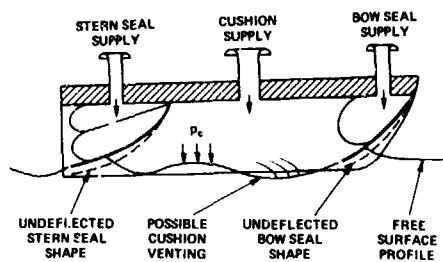


Figure 1 - Typical Layout of Sidewall Craft

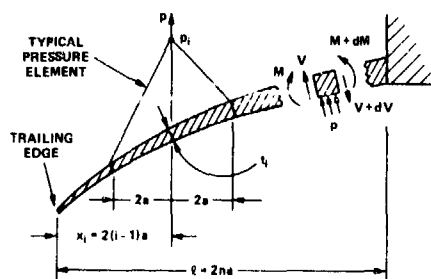


Figure 2 - Finite-Element Breakdown of a Seal

sions - in an inverse manner - by fixing the wetted length, and considering the weight supported by it to be unknown.)

The three-dimensional problem can be simplified in various ways. For example, Wagner [19], Tulin [20], Shuford [21] and Casling [22] used a low-aspect-ratio assumption, while Shen [23] and Shen and Ogilvie [24] assumed that the aspect ratio was high. Wagner [25] and Wadlin and Christopher [26] assumed that the speed was infinite. Maruo [27] examined the limits of high and low aspect ratios separately.

Weinstein and Kapryan [28] carried out high-speed experiments and their results compared well with data from other tests.

Wang and Rispin [29] applied a high-Froude-number theory but simply assumed a rectangular wetted area, while Tuck [30] and Oertel [31] discussed the problem of not knowing the correct wetted area.

Further papers have presented experimental results. These include work by Clement and Blount [32], Hadler [33] and Savitsky [34, 35 and 36].

#### Present Work

The aim of this study is to develop an analytic theory for the hydrodynamics of flexible planing surfaces, which could then be applied to an SES. One simplifying assumption to be utilized is that of two-dimensionality.

It is, of course, well known that the flow under the craft is actually three-dimensional, and it would therefore seem appropriate to use the three-dimensional finite-element planing technique of Doctors [37]. This could be combined with the theory for the waves generated by a pressure patch (in order to model the cushion) reported by Huang and Wong [38], Hausaling and Van Eseltine [39] and Doctors [40]

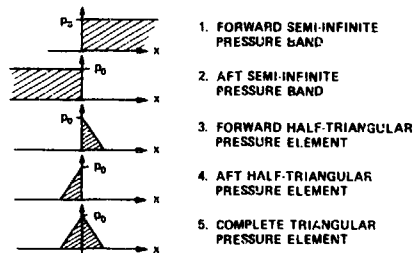
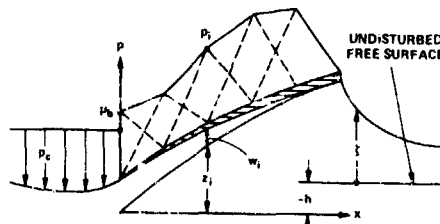


Figure 3 - The Different Pressure Elements



NOTES: 1. PRESSURE SHOWN ACTS DOWN ON WATER, AND UPWARDS ON SEAL. SEAL PRESSURE,  $p_s$ , NOT SHOWN.  
2. CUSHION AND BOW END PRESSURES USUALLY EQUAL:  
 $p_c = p_b$

Figure 4 - Theoretical Model of Seal and Cushion

Although the rise-height and wetted-area predictions of Doctors [37] were within a few percent of experimental results for arbitrary Froude number, aspect ratio and dead-rise, the pressure distributions were not well behaved. This problem has been traced to the curved singularity line at the leading edge.

It was therefore decided to employ a two-dimensional approach since the beam-to-wetted-length ratio of the seals is quite large. Also, the effect of the sidewalls is to confine the generated wave pattern and to encourage its two-dimensional character.

Figure 2 illustrates the finite-element representation of the seal itself, while Figure 3 shows the different pressure elements to be used in the hydrodynamic model, which is illustrated in Figure 4.

## II. Flexural Model of Seal

### Theory

**Background.** A cross-section of a seal in the deflected position is shown in Figure 2. This diagram also defines the sign convention for the moment  $M$ , the shear force  $V$ , and the loading  $p$ . The relations between these quantities and the deflection  $w$  are given by standard beam theory (see Timoshenko and Young [41, p. 197]):

$$p = \frac{dV}{dx} \quad (1)$$

$$V = \frac{dM}{dx} \quad (2)$$

$$\text{and} \quad M = D \frac{d^2 w}{dx^2} \quad (3)$$

where  $D = EI$  is the local flexural rigidity, in which  $E$  is the Young's modulus of the material, and  $I$  is the local second moment of area. The distance  $x$  is measured forward from the trailing edge.

We now consider loading of the beam by four types of elements illustrated in Figure 3: a *uniform loading* over the entire seal (Type 1), a *forward half-triangular element* (Type 3), an *aft half-triangular element* (Type 4), and a *complete triangular element* (Type 5).

The uniform loading can be used to represent the cushion pressure acting down on the seal, while a series of overlapping complete triangular elements (whose strengths have to be found) will be used to represent the hydrodynamic pressure distribution resulting from the water. The half-triangular elements are used for blending purposes at the seal ends, as seen in Figure 4.

**Uniform Loading.** Using Eqs. (1) and (2), the shear force and moment acting on the beam due to a loading  $p_s$  are

$$V = p_s x \quad (4)$$

$$\text{and} \quad M = \frac{1}{2} p_s x^2. \quad (5)$$

We consider the deflection of the beam between stations  $i$  and  $i+1$ . The rigidity is assumed to vary linearly between stations, so that

$$D = D_i (1 + \alpha_i \xi), \quad (6)$$

in which  $\alpha_i = D_{i+1}/D_i$  and  $\xi = (x_{i+1} - x_i)/2a$  and  $2a$  is the station spacing. For convenience, the  $i$  index on  $\alpha$  will be dropped.

The slope of the deflection may be obtained by a single integration of Eq. (3), after substituting Eqs. (5) and (6). After substitution of the limits  $\xi = 0$  and  $1$ , the result is

$$w'_i = w'_{i+1} - \frac{4 p_s a^2}{D_i \alpha^3} \left[ -\alpha + \left( 2i_1 + \frac{1}{2} \right) \alpha^2 + (1 - i_1 \alpha)^2 \ln(1 + \alpha) \right], \quad (7)$$

in which  $i_1 = i - 1$ . The deflection is obtained by a second integration of Eq. (3), but with a free lower limit of  $\xi$  rather than 0 used after the first integration. After some algebra, one obtains

$$w_i = w_{i+1} - 2a w'_{i+1} + \frac{8 p_s a^4}{D_i \alpha^4} \left[ \alpha - \left( \frac{1}{2} + 2i_1 \right) \alpha^2 + \left( \frac{1}{3} + i_1 + i_1^2 \right) \alpha^3 - (1 - i_1 \alpha)^2 \ln(1 + \alpha) \right]. \quad (8)$$

The expressions for the deflection, given by Eqs. (7) and (8) are used repetitively, working backwards from the leading edge. The case of local uniform rigidity, namely  $\alpha = 0$ , is easily obtained by taking the limit of these two equations. The other limit, when  $\alpha = \infty$ , is needed for representing the first element of the beam ( $i = 1$ ) when the thickness tapers down to zero there. For the sake of brevity, these two pairs of limits are not given here.

**Forward Half-Triangular Element.** For this element it is necessary to consider three cases separately: the field point ahead of the source element ( $i > j$ ), the field point located at the source element ( $i = j$ ), and that of the field point behind the element ( $i < j$ ). (The last case is not actually needed for the calculations here, but is trivial to obtain.)

If the field point is ahead of the source element, then the moment acting on the beam between stations  $i$  and  $i+1$  is

$$M = 4 p_j a^2 (r + \xi)/\gamma, \quad (9)$$

$$\text{where} \quad r = i - j + \frac{1}{3}. \quad (10)$$

Eq. (10) gives the dimensionless lever arm between the centroid of the source element and the field point. The purpose of the  $\gamma$  factor is to be able to handle the complete element when its value would be 1. Here,  $\gamma = 2$ .

We use these expressions in order to integrate Eq. (3) once for the deflection slope, and a second time for the deflection itself, in a manner similar to that explained in the previous section:

$$w'_i = w'_{i+1} - \frac{8 p_j a^3}{\gamma D_i \alpha^2} [\alpha - (1 - \alpha r) \ln(1 + \alpha)] \quad (11)$$

$$\text{and} \quad w_i = w_{i+1} - 2a w'_{i+1} + \frac{8 p_j a^4}{\gamma D_i \alpha^3} \left[ \alpha^2 + 2(1 - \alpha r) \{ \ln(1 + \alpha) - \alpha \} \right]. \quad (12)$$

As before, the limit of  $\alpha = 0$  (a uniform segment) may be easily obtained, but the case of  $\alpha = \infty$  has no physical application.

We now consider the second situation, namely  $i = j$ . The loading, shear force and moment between stations  $i$  and  $i+1$  are

$$p = p_j (1 - \xi), \quad (13)$$

$$V = p_j a (2\xi - \xi^2) \quad (14)$$

$$\text{and} \quad M = 2 p_j a^2 \left( \xi^2 - \frac{1}{3} \xi^3 \right). \quad (15)$$

The last equation may be used in Eq. (3) to yield the gradient of the deflection, and the deflection itself, after appropriate integrations.

$$w'_i = w'_{i+1} - \frac{4 p_j a^3}{3 D_i \alpha^4} \left[ -\alpha + \frac{2}{3} \alpha^2 + \frac{7}{6} \alpha^3 + (1 + 3\alpha) \ln(1 + \alpha) \right] \quad (16)$$

$$\text{and} \quad w_i = w_{i+1} - 2a w'_{i+1} + \frac{8 p_j a^4}{3 D_i \alpha^5} \left[ \alpha + \frac{5}{2} \alpha^2 - \frac{7}{6} \alpha^3 + \frac{3}{4} \alpha^4 - (1 + 3\alpha) \ln(1 + \alpha) \right] \quad (17)$$

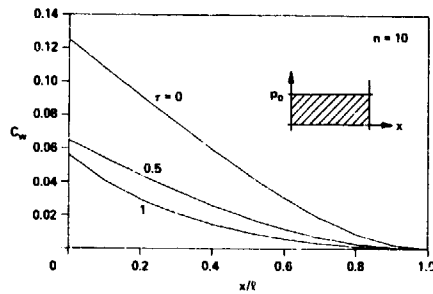


Figure 5 - Flexural Influence Coefficients  
(a) Uniform Loading

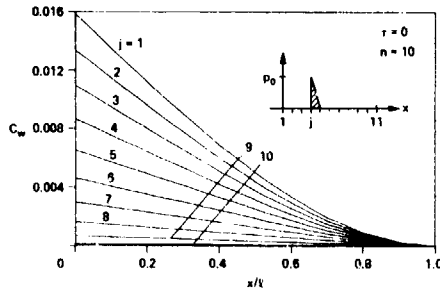


Figure 5 - Flexural Influence Coefficients  
(b) Forward Half-Triangular Element

The third case, namely  $i < j$  is the simplest of all. The two equations are just

$$w'_i = w'_{i+1} \quad (18)$$

$$\text{and} \quad w_i = w_{i+1} - 2aw'_{i+1} \quad (19)$$

**Aft Half-Triangular Element.** We consider the three different relations between the source element and the field point - as for the forward half-triangular element. The results for the first case, namely  $i \geq j$ , can be obtained directly from those of the forward element. The only difference occurs in computing the moment arm in Eq. (10) which should now read

$$r = i - j + \frac{1}{3} \quad (20)$$

so that Eqs. (11) and (12) are still valid

The case of  $i = j - 1$  has to be handled separately, however. The equations for loading, shear force and moment are respectively

$$p = p_j \xi \quad (21)$$

$$V = p_j a \xi^2 \quad (22)$$

$$\text{and} \quad M = \frac{2}{3} p_j a^2 \xi^3 \quad (23)$$

The deflection slope, and deflection may then be derived

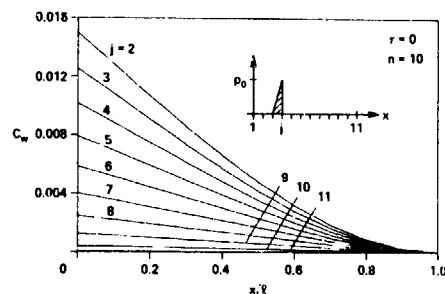


Figure 5 - Flexural Influence Coefficients  
(c) Aft Half-Triangular Element

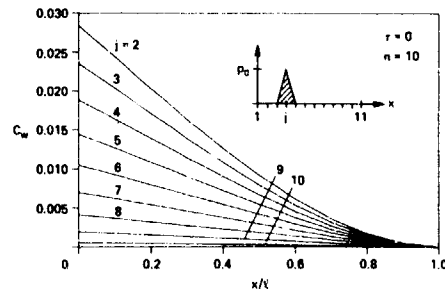


Figure 5 - Flexural Influence Coefficients  
(d) Complete Triangular Element

$$w'_i = w'_{i+1} - \frac{4p_j a^3}{3D_j \alpha^3} \left[ \alpha - \frac{\alpha^2}{2} + \frac{\alpha^3}{3} - \ln(1 + \alpha) \right] \quad (24)$$

$$\text{and} \quad w_i = w_{i+1} - 2aw'_{i+1} + \frac{8p_j a^4}{3D_j \alpha^4} \left[ -\alpha + \frac{\alpha^2}{2} - \frac{\alpha^3}{3} + \frac{\alpha^4}{4} + \ln(1 + \alpha) \right] \quad (25)$$

The third case - that of the field point being located behind the source element ( $i < j - 1$ ) - has already been treated, by Eqs. (18) and (19).

**Complete Triangular Element.** This element is actually the basic one and is used over the entire length of the plating surface, whereas the half elements are only used at the ends. We have four distinct cases to consider - as far as the relative positions of the source element and field point are concerned. For the first case, that of the field point ahead of the source element ( $i \geq j + 1$ ), we can use Eqs. (11) and (12), but with  $\gamma = 1$  and the moment arm altered to

$$r = i - j \quad (26)$$

The next case is that of the field point coinciding with the source element ( $i = j$ ). We combine Eq. (11) (with  $\gamma = 2$  and  $r = 1/3$ ) with Eq. (16) to obtain

$$w'_i = w'_{i+1} - \frac{4p_j a^3}{3D_j \alpha^3} \left[ -\alpha - \frac{5}{2}\alpha^2 + \frac{25}{6}\alpha^3 + (1 + 3\alpha - 3\alpha^2 + \alpha^3) \ln(1 + \alpha) \right] \quad (27)$$



and similarly

$$w_i = w_{i+1} - 2\alpha w'_{i+1} + \frac{8p_i a^4}{3D_i \alpha^5} \left[ \alpha + \frac{5}{2} \alpha^2 - \frac{25}{6} \alpha^3 + \frac{13}{4} \alpha^4 - (1 + 3\alpha - 3\alpha^2 + \alpha^3) \ln(1 + \alpha) \right] \quad (28)$$

The third case, that of the field point coinciding with the aft end of the triangle ( $i = j - 1$ ), is equivalent to that for the aft half-triangular element, so that Eqs. (24) and (25) apply.

The fourth case occurs when the field point is behind the source element ( $i < j - 1$ ), and Eqs. (18) and (19) may be used here.

#### Results

Some sample beam deflections, due to the application of these pressure elements, are now presented in Figure 5.

The case of a uniform loading, in particular, is seen in Figure 5(a). The deflection coefficient,

$$C_w = \frac{w D_m}{p_0 \ell^4} \quad (29)$$

is plotted against position along the beam of length  $\ell$ . Here  $p_0$  is the loading and  $D_m$  is the rigidity of the beam at its midpoint. Three constant tapers,  $\tau$ , are considered. The taper is defined as the thickness at the anchored end ( $x/\ell = 1$ ) minus that at the free end ( $x/\ell = 0$ ), divided by twice the average thickness. This means that the rigidity can be represented as a third-order polynomial:

$$D = D_m \left[ (1 - \tau) + 2\tau \frac{x}{\ell} \right]^3 \quad (30)$$

Figure 5(a) shows that increasing the taper decreases the overall deflection. This is due to the fact that keeping  $D_m$  constant, but increasing  $\tau$  results in a general strengthening of the beam because of the relation  $D \propto t^3$ . A taper of unity implies a tip thickness of zero, and consequently greater curvature in the deflection near the tip occurs.

The flexural response due to the three triangular elements is shown in Figures 5(b), (c), and (d), respectively. Due to a need for brevity, an example of zero taper only is presented. For these elements there are respectively 10, 10 and 9 curves - appropriate to the number of possible locations of the source element. The deflections from the forward half element (Figure 5(b)) are slightly less than those due to the aft half element (Figure 5(c)) because of the smaller bending moments. The portion of the curve behind the source element is a straight line, as seen by Eqs. (18) and (19).

The case of a complete triangular element is plotted in Figure 5(d). As noted before, these results may be obtained by summing the deflections from the two half triangles (using a common  $j$  index).

### III. Hydrodynamic Model of Seal

#### Theory

**Background.** We make the usual assumptions of inviscid incompressible flow. A further simplification is to linearize the free-surface conditions. The theory for the wave disturbance resulting from the application of a pressure distribution on the water surface is well known, and will not be repeated here. Instead, the reader is referred to Wehausen and Laitone [10, p. 601] and other standard textbooks on this subject.

Rather than solve the wave elevation generated by each type of pressure element, we will construct the results by the superposition method. This technique is valid since the equations of motion for the fluid have been linearized. The building blocks for our pressure distribution will be the results for semi-infinite uniform pressure bands given by Lamb [42, p. 404].

**Forward Semi-Infinite Band.** In the present notation, Lamb's result for a uniform pressure  $p_0$  extending between 0 and  $\infty$  is

$$\rho g \xi / p_0 = -\frac{1}{\pi} \operatorname{sgn}(\lambda_0) f(\lambda_0) - 2H(-\lambda_0) \cos(\lambda_0) - H(\lambda_0), \quad (31)$$

$$\text{where} \quad \lambda_0 = x k_0 \quad (32)$$

$$\text{and} \quad k_0 = g/c^2, \quad (33)$$

in which  $\rho$  is the water density,  $g$  is the acceleration of gravity,  $\xi$  is the wave elevation,  $c$  is the velocity of the travelling pressure, and  $x$  is measured forwards from the point of discontinuity in the pressure. Also,  $H$  is the Heaviside step function and  $f$  is one of the two auxiliary functions for the sine- and cosine-integrals, which are defined by

$$f(\lambda) = \int_0^\infty \frac{\sin(t)}{\lambda + t} dt \quad (34)$$

in Abramowitz and Stegun [43, p. 232].

The asymptotic form of the downstream wave profile is

$$\rho g \xi / p_0 = -2 \cos(\lambda_0) \quad \text{as } \lambda_0 \rightarrow -\infty. \quad (35)$$

**Aft Semi-Infinite Band.** The results from Lamb are

$$\rho g \xi / p_0 = \frac{1}{\pi} \operatorname{sgn}(\lambda_0) f(\lambda_0) + H(-\lambda_0) \{ 2 \cos(\lambda_0) - 1 \}, \quad (36)$$

$$= 2 \cos(\lambda_0) \quad \text{as } \lambda_0 \rightarrow -\infty. \quad (37)$$

**Forward Half-Triangular Element.** We may construct the required pressure distribution by integrating a large number of aft semi-infinite bands, each of magnitude  $dp' = (p_0/2a) dx'$ . For each of these bands  $\lambda = k_0(x - x')$ , where  $x'$  is the starting point of that band. Thus

$$\rho g \xi / p_0 = \frac{1}{2a} \int_0^{2a} \left[ \frac{1}{\pi} \operatorname{sgn}(\lambda) f(\lambda) + H(-\lambda) \{ 2 \cos(\lambda) - 1 \} \right] dx' - \left[ \frac{1}{\pi} \operatorname{sgn}(\lambda_0) f(\lambda_0) + H(-\lambda_0) \{ 2 \cos(\lambda_0) - 1 \} \right]$$

Care has been taken here to subtract an aft step of magnitude  $p_0$  - necessary to bring the pressure of the element back to zero at  $x = -a$ .

For the purpose of the integration, one needs the following relationship:

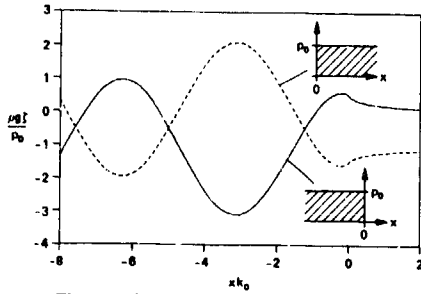


Figure 6 - Hydrodynamic Influence Coefficients  
(a) Semi-Infinite Pressure Bands

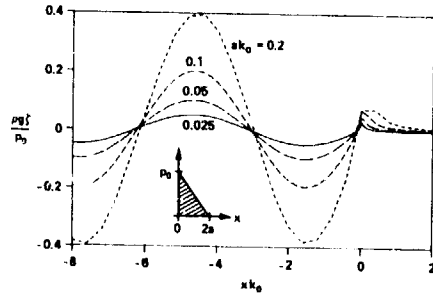


Figure 6 - Hydrodynamic Influence Coefficients  
(b) Forward Half-Triangular Element

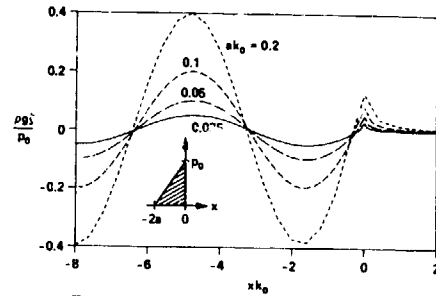


Figure 6 - Hydrodynamic Influence Coefficients  
(c) Aft Half-Triangular Element

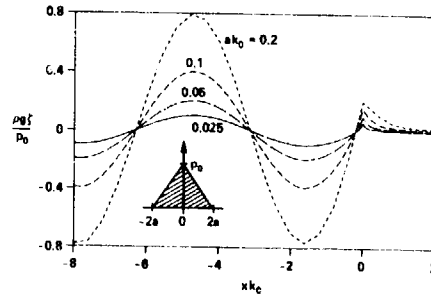


Figure 6 - Hydrodynamic Influence Coefficients  
(d) Complete Triangular Element

$$\int \operatorname{sgn}(\lambda) f(\lambda) d\lambda = g(\lambda) + \ln(\lambda) \\ = g(\lambda). \quad (38)$$

The results for the wave elevation, and its asymptotic form, are

$$\rho g \zeta / p_0 = \frac{1}{2 a k_0} \left\{ \left[ \frac{1}{\pi} g(\lambda_0) + H(-\lambda_0) \{ 2 \sin(\lambda_0) - \lambda_0 \} \right] \right. \\ \left. - \left[ \frac{1}{\pi} g(\lambda_1) + H(-\lambda_1) \{ 2 \sin(\lambda_1) - \lambda_1 \} \right] \right\} \\ - \left[ \frac{1}{\pi} \operatorname{sgn}(\lambda_0) f(\lambda_0) + H(-\lambda_0) \{ 2 \cos(\lambda_0) - 1 \} \right] \\ \sim \frac{1}{a k_0} \{ \sin(\lambda_0) - \sin(\lambda_1) \} - 2 \cos(\lambda_0) \text{ as } \lambda_0 \rightarrow -\infty, \quad (39)$$

$$\text{where } \lambda_1 = (x - 2a) k_0. \quad (40)$$

**Aft Half-Triangular Element.** In a similar manner to the previous case one can construct this element using a (positive) aft semi-infinite band starting at \$x = 0\$, and then subtracting an integrated series of bands. The final result is

$$\rho g \zeta / p_0 = \frac{1}{2 a k_0} \left\{ \left[ \frac{1}{\pi} g(\lambda_0) + H(-\lambda_0) \{ 2 \sin(\lambda_0) - \lambda_0 \} \right] \right.$$

$$\left. - \left[ \frac{1}{\pi} g(\lambda_2) + H(-\lambda_2) \{ 2 \sin(\lambda_2) - \lambda_2 \} \right] \right\} \\ + \left[ \frac{1}{\pi} \operatorname{sgn}(\lambda_0) f(\lambda_0) + H(-\lambda_0) \{ 2 \cos(\lambda_0) - 1 \} \right] \quad (42)$$

$$= \frac{1}{a k_0} \{ \sin(\lambda_0) - \sin(\lambda_2) \} + 2 \cos(\lambda_0) \text{ as } \lambda_0 \rightarrow -\infty, \quad (43)$$

$$\text{where } \lambda_2 = (x + 2a) k_0. \quad (44)$$

**Complete Triangular Element.** We could build this element with a series of small-magnitude pressure bands. However, it is easier to add Eq. (39) to Eq. (42), and Eq. (40) to Eq. (43):

$$\rho g \zeta / p_0 = \frac{1}{2 a k_0} \left\{ - \left[ \frac{1}{\pi} g(\lambda_1) + H(-\lambda_1) \{ 2 \sin(\lambda_1) - \lambda_1 \} \right] \right. \\ \left. + 2 \left[ \frac{1}{\pi} g(\lambda_0) + H(-\lambda_0) \{ 2 \sin(\lambda_0) - \lambda_0 \} \right] \right. \\ \left. - \left[ \frac{1}{\pi} g(\lambda_2) + H(-\lambda_2) \{ 2 \sin(\lambda_2) - \lambda_2 \} \right] \right\} \quad (45)$$

$$= \frac{4 \sin^2(a k_0)}{a k_0} \sin(\lambda_0) \text{ as } \lambda_0 \rightarrow -\infty, \quad (46)$$

after some simplification.

## Results

Figures 6(a) through (d) display wave profiles generated by the five different pressure forms. For example, the two semi-infinite pressure bands are shown in Figure 6(a). It is seen that the profiles very quickly develop their asymptotic forms downstream - perhaps within half a wavelength. Of interest too, is that the slope of the free surface at  $x = 0$ , as given by Eqs. (31) and (36) for these two cases is theoretically infinite (according to linearized theory). However, this behavior is so localized that it is not really apparent on this plotting scale.

The three triangular elements are shown respectively in Figures 6(b), (c) and (d). Again the asymptotic downstream wave profiles are very quickly obtained. It is seen that the amplitudes of the wave is, to the first order,  $2ak_0$  for the half elements, and  $4ak_0$  for the complete element.

The kinks visible in the curves for  $ak_0 = 0.2$  are due to the fact that points were computed only for values of  $x$  which were an integral multiple of the element length  $2a$ . They could have been avoided by using a closer spacing of points.

## IV. Combining the Elements

### Kinematic Condition

We now apply the results of the previous two sections to that of a flexible planing seal travelling ahead of a cushion pressure on the free surface. The configuration is shown in Figure 4. The cushion pressure,  $p_c$ , and the seal pressure,  $p_s$ , are normally identical, but will be kept separate in the problem formulation.

The solution to the problem is obtained by summing the wave profiles resulting from all the pressure elements, and equating this to the profile of the deformed plate:

$$\sum_{j=2}^n p_j (\hat{\xi}_{ij}^{(5)} - \hat{w}_{ij}^{(5)}) = \rho g (h + z_i) - p_c \hat{\xi}_i^{(2)} - p_s \hat{w}_i^{(1)} - p_b (\hat{\xi}_i^{(3)} - \hat{w}_i^{(3)}) \quad \text{for } i = 1 \text{ to } n. \quad (47)$$

Here the superscript  $\wedge$  means that the variable has been made dimensionless using  $\rho$ ,  $g$  and the pressure for that element. The double subscript  $ij$  refers to the influence at the  $i$ 'th field point due to a source element at station  $j$ . A single subscript  $i$  implies that  $j = 1$ , that is, the source element is located at the seal trailing edge. The superscripts (1) through (5) refer to the five pressure forms considered in the previous section, and in the section on beam deflection (although type 2 does not occur there).

Eq. (47) contains, as input, the undeflected seal profile,  $z_i$ . (Arbitrary seal shapes can be handled by the procedure - as well as the obvious flat form.) The wetted length is fixed, and as a consequence, the equilibrium height,  $h$ , must be considered to be unknown. The set of  $n$  equations in  $n$  unknowns represented by Eq. (47) may be solved by a standard matrix inversion technique.

### Free-Surface Elevation

This calculation may be carried out once the pressure distribution has been determined:

$$\rho g \hat{\xi}_i = p_c \hat{\xi}_i^{(2)} + p_b \hat{\xi}_i^{(3)} + \sum_{j=2}^n p_j \hat{\xi}_{ij}^{(5)}. \quad (48)$$

## The Seal Deflection

Geometry considerations are used to find the distortion in the seal:

$$w_i = \xi_i - z_i - h \quad \text{for } 1 \leq i \leq n. \quad (49)$$

## The Seal Forces

Simple summation may be used to compute the lift, drag and moment about the seal trailing edge:

$$L = a p_b + 2a \sum_{i=2}^n p_i, \quad (50)$$

$$D = \frac{1}{2} p_b (z_2 + w_2 - z_1 - w_1) + \frac{1}{2} \sum_{i=2}^n p_i (z_{i+1} + w_{i+1} - z_i - w_i) \quad (51)$$

$$\text{and } M = \frac{2a^2}{3} p_b + \sum_{j=2}^n x_j p_j, \quad (52)$$

while the center of lift developed by the seal is just

$$\bar{x} = M/L. \quad (53)$$

## The Wave Resistance

The downstream amplitude of the waves may be expressed in terms of its two components:

$$\xi = A_c \cos(xk_0) + A_s \sin(xk_0). \quad (54)$$

The wave resistance is then given by Lamb [p. 415]:

$$D_w = \frac{1}{4} \rho g (A_c^2 + A_s^2). \quad (55)$$

One therefore needs to find these two wave components. Eqs. (37), (40) and (46) are used, after taking into account the longitudinal displacements of the source points of the contributions to the downstream wave:

$$\rho g A_c = 2 p_c + p_b \left\{ \frac{\sin(2ak_0)}{ak_0} - 2 \right\} - \frac{4 \sin^2(ak_0)}{ak_0} \sum_{i=2}^n p_i \sin(x_i k_0) \quad (56)$$

and

$$\rho g A_s = 2 p_b \frac{\sin^2(ak_0)}{ak_0} + \frac{4 \sin^2(ak_0)}{ak_0} \sum_{i=2}^n p_i \cos(x_i k_0). \quad (57)$$

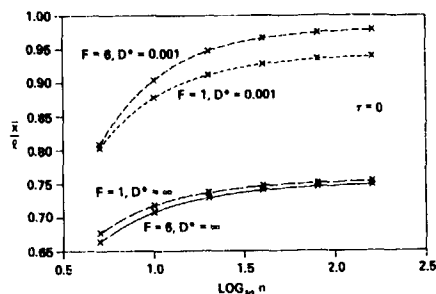


Figure 7 - Convergence of the Numerical Scheme  
(a) Center of Pressure

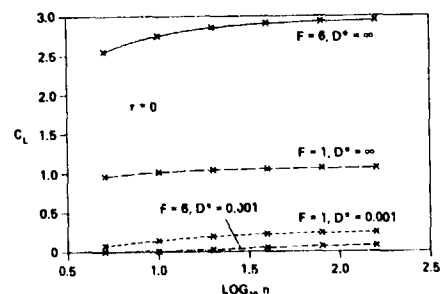


Figure 7 - Convergence of the Numerical Scheme  
(b) Lift Coefficient

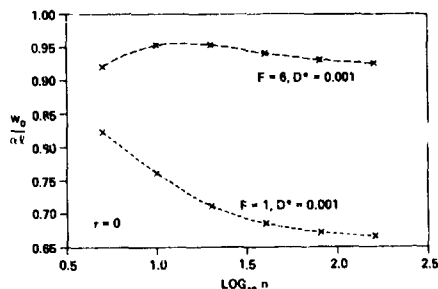


Figure 7 - Convergence of the Numerical Scheme  
(c) Tip Deflection

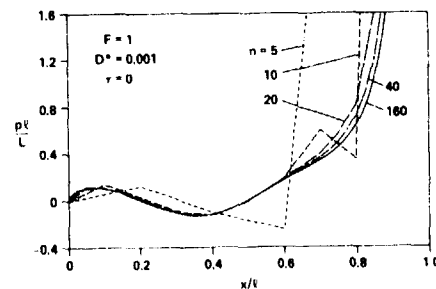


Figure 7 - Convergence of the Numerical Scheme  
(d) Pressure Distribution

## V. Results

### Convergence

Figure 7(a), (b) and (c) demonstrate the convergence rate for some of the integrated quantities with respect to the number of elements used. Cases of  $n = 5, 10, 20, 40, 80$  and  $160$  are shown. The definitions of the dimensionless parameters are:

$$\text{Froude number: } F = c/\sqrt{g\ell} \quad (58)$$

$$\text{Dimensionless rigidity: } D^* = D/\rho g \ell^4 \quad (59)$$

$$\text{Lift coefficient: } C_L = L/\frac{1}{2} \rho c^2 \ell \alpha \quad (60)$$

$$\text{Drag coefficient: } C_D = D/\frac{1}{2} \rho c^2 \ell \alpha^2 \quad (61)$$

The seal under consideration is flat before deflection; that is, its profile is given by  $z = \alpha x$ , where  $\alpha$  is the angle of attack.

The error in the results appears to be inversely proportional to the number of elements used. It is seen that for the two Froude numbers and two stiffnesses considered that there is little difference between the cases of 80 and 160 elements. For most purposes, in fact, 40 elements should yield sufficiently accurate results, perhaps even for the case of tip deflection,  $w_0$ , in Figure 7(c).

Figure 7(d) illustrates the rate of convergence of the pressure distribution under a relatively soft seal. Not surprisingly, the rate of convergence is fastest away from the leading edge - where the spray jet is formed.

### Basic Quantities

We now examine the effect of the basic parameter in the present work - the seal stiffness. This is illustrated in Figures 8(a) through (d). In these examples, the seal possesses a constant thickness. The effect of cushion and seal pressures will be shown later.

Figure 8 shows the dramatic effect of stiffness. For example, in Figure 8(a), the center of pressure moves forward as the rigidity is decreased. This is a result of the seal bending, and the load being carried only near the leading edge.

One sees in Figures 8(b) and (c) that the lift and drag are also greatly reduced when the seal is made softer. There is a general drop in these two quantities at the critical speed of the seal, that is, near  $F = 0.9$ . A couple of interesting checks may be used. At high Froude numbers (when gravity effects approach zero) the lift and drag coefficient for a rigid seal ( $D^* = \infty$ ) both approach  $\pi$  - a result well known in airfoil theory. Furthermore, for this case, the dimensionless center of pressure approaches the required value of  $3/4$ .

Figure 8(d) shows the tip deflection. Obviously, increasing the rigidity decreases the deflection, and there are interesting dips in the curves at Froude numbers less than 1.0.

The influence of a uniform taper in the thickness of the planing surface is shown in Figure 9. (The stiffness at the midpoint has been kept constant here, at a value of  $D^* = 0.05$ .) The center of pressure in Figure 9(a) is seen to move aft with increasing taper - although the change is

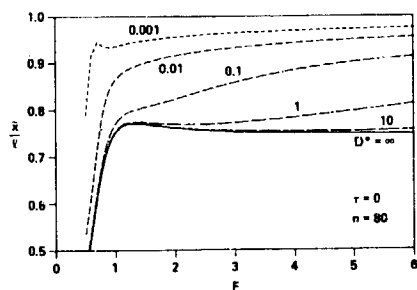


Figure 8 - Variation of Seal Stiffness  
(a) Center of Pressure

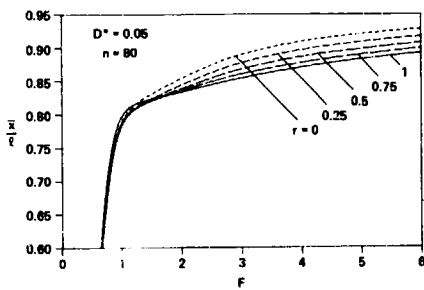


Figure 9 - Variation of Seal Taper  
(a) Center of Pressure

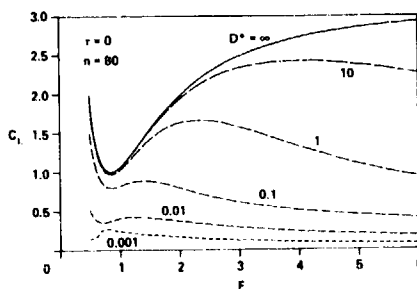


Figure 8 - Variation of Seal Stiffness  
(b) Lift Coefficient

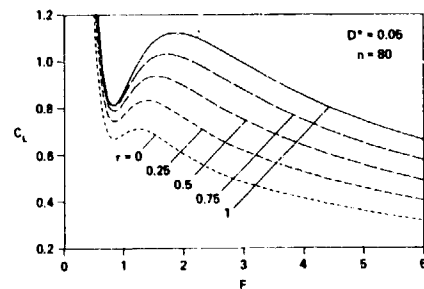


Figure 9 - Variation of Seal Taper  
(b) Lift Coefficient

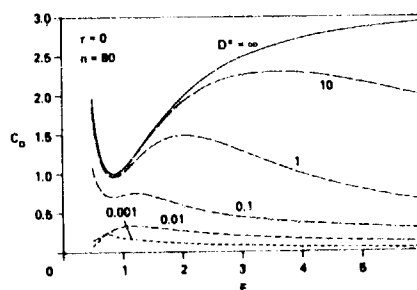


Figure 8 - Variation of Seal Stiffness  
(c) Drag Coefficient

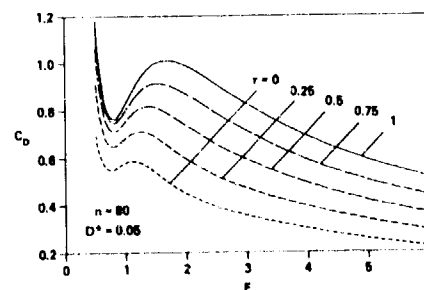


Figure 9 - Variation of Seal Taper  
(c) Drag Coefficient

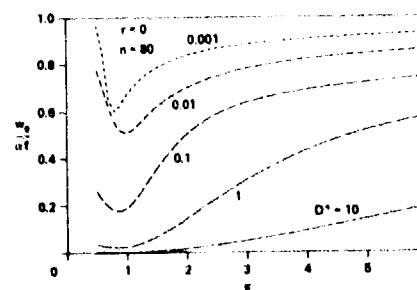


Figure 8 - Variation of Seal Stiffness  
(d) Tip Deflection

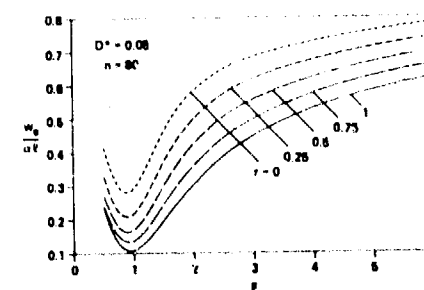


Figure 9 - Variation of Seal Taper  
(d) Tip Deflection

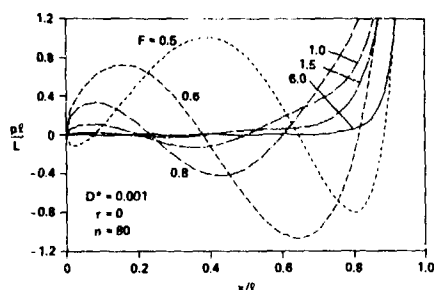


Figure 10 - Pressure Distribution  
(a)  $D^* = 0.001$  and  $\tau = 0$

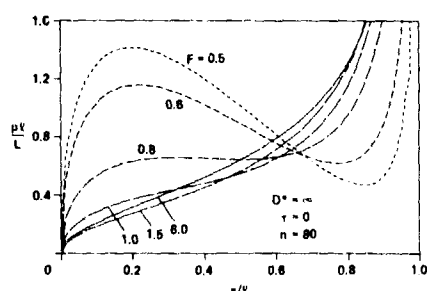


Figure 10 - Pressure Distribution  
(b)  $D^* = \infty$  and  $\tau = 0$

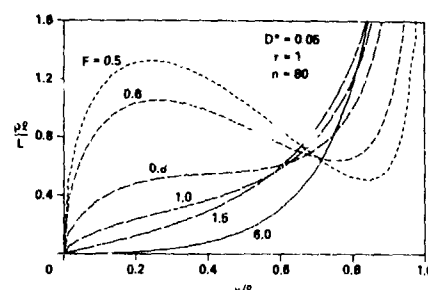


Figure 10 - Pressure Distribution  
(c)  $D^* = 0.05$  and  $\tau = 1$

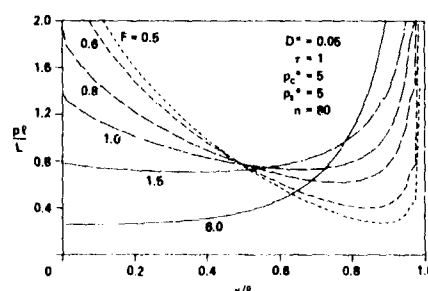


Figure 10 - Pressure Distribution  
(d)  $D^* = 0.05$ ,  $\tau = 1$  and  $p_c^* = p_s^* = 5$

fairly small. The lift and drag in Figures 9(b) and (c) are greatly influenced by the taper. Increasing the taper raises the values of the lift and drag coefficients - not that dissimilar to the effect of increasing the rigidity in Figure 8. Pronounced dips in the curves are still evident.

The tip deflection (Figure 9(d)) is also a strong function of the taper. The deflection is always reduced when the taper is increased. The effect of Froude number is also very evident.

#### Pressure Distributions

We now turn to Figure 10 whose four parts illustrate the vivid effects of the various parameters introduced above. For the purpose of illustration, the pressure has been made dimensionless using the lift of the seal,  $L$ , and its length,  $\ell$ .

A relatively flexible seal is considered in Figure 10(a). As a result, negative pressures are evident over some regions of the surface. At low Froude numbers, the wavelength of the pressure oscillations is practically the same as the standard result from linear theory. Thus the seal is essentially conforming to the natural water wave generated by the forward portion of the seal, whose deflection is obviously less.

At higher speeds, very little lift is carried by the aft portion of the surface. Also, regions of negative or very low relative pressures still occur. Of note, is the fact that the wavelength of the oscillation is much smaller for the higher speeds. This contradicts simple unconstrained water wave theory and points up the influence of the stiffness (albeit small) of the seal.

In Figure 10(b), a rigid surface has been considered. The curves of pressure are somewhat simpler in form than for the flexible case, in Figure 10(a). The fact that the center of pressure moves forward with increasing Froude number is demonstrated.

The case of a taper of unity is presented in Figure 10(c). At high speeds, the amount of load carried near the stern is even less than in previous cases. Comparison with Figures 10(a) and (b) shows that the taper has radically altered the form of the pressure distribution.

Finally, in Figure 10(d), we consider a situation in which a dimensionless cushion pressure and seal pressure of 5 are applied. These are defined by the formulas

$$p_c^* = p_c / \rho g \ell \alpha \quad (6.2)$$

$$\text{and} \quad p_s^* = p_s / \rho g \ell \alpha, \quad (6.3)$$

respectively. The taper and rigidity are the same as in Figure 10(c), so a comparison can be made there.

The pressures in all cases approach the cushion pressure at the stern ( $x/\ell = 0$ ) in a smooth manner. (The apparently different values of the pressure at the stern is a result of the particular pressure parameter being plotted.) At low speeds, up to a Froude number of 1.5, the pressure curves all appear to pass through the same point ( $x/\ell = 0.5$ ,  $p/L = 0.8$ ). However, no particular significance for this has been discovered.

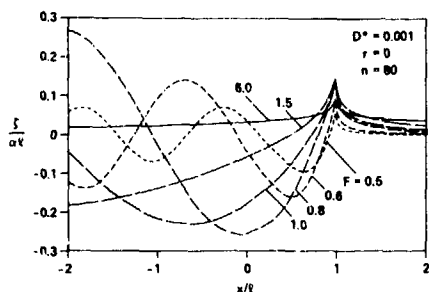


Figure 11 - Wave Profile  
(a)  $D^* = 0.001$  and  $r = 0$

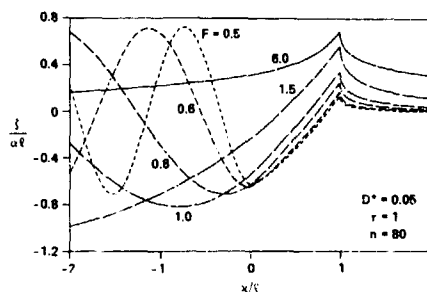


Figure 11 - Wave Profile  
(c)  $D^* = 0.05$  and  $r = 1$

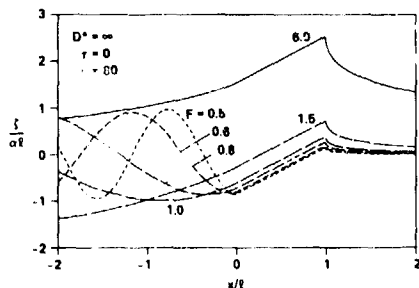


Figure 11 - Wave Profile  
(b)  $D^* = \infty$  and  $r = 0$

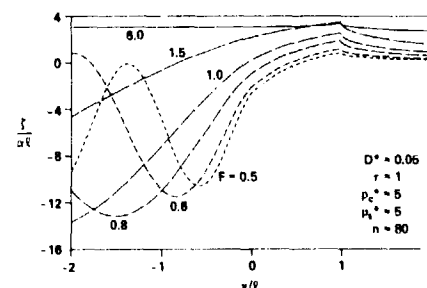


Figure 11 - Wave Profile  
(d)  $D^* = 0.05$ ,  $r = 1$  and  $p_c^* = p_s^* = 5$

#### Wave Profiles

The last set of results, in Figure 11, show the form of the water surface for the same four cases presented in Figure 10.

In the examples shown, the plate lies in the region  $0 < x/l < 1$ . Thus, Figure 11(a) also illustrates how much deformation the plate suffers at different speeds. At the lower Froude numbers, in fact, the plate possesses a negative slope over the stern region. The buildup of the water ahead of the plate is also seen. In addition, the downstream wave system becomes established in a short distance.

The plate remains flat in Figure 11(b) since it is rigid. The water is seen to separate smoothly off the trailing edge - as it also does in Figure 11(a).

A taper of unity was used in the calculations leading to Figure 11(c). Once again, the water buildup ahead of the surface, and the wave train in the downstream region are prominent. So too, is the plate deflection.

The last figure to be presented, Figure 11(d), demonstrates the powerful effect of applying a pressure in the cushion on the seal. In this case, the seal deflects downward (that is, a negative deflection occurs). This effect is due to the pressure acting down on the seal. Very large downstream waves are also generated. A comparison of wave heights with the previous parts of Figure 11 highlights this feature.

Incidentally, it should be pointed out here that the value of the blending pressure element,  $p_b$ , was chosen to provide a continuous pressure distribution in Figures 10(d)

and 11(d). That is,  $p_b = p_c = p_s$ . As expected, if a different value of the blending pressure were chosen, then a badly behaved pressure distribution resulted. Surprisingly, however, the choice of blending pressure had little effect on lift, drag, center of pressure, and tip deflection.

#### VI. Conclusions

##### Present Work

The principal object of the research described in this paper was to introduce the effect of compliance of the body into planing theory. Flexibility is seen to have a profound effect on all the quantities of interest. In brief, increasing the flexibility results in a loss of lift and a reduction in drag. Also, the center of pressure moves forward. Increasing the Froude number makes the importance of compliance greater.

The effect of taper is found to influence the lift, drag, center of pressure and tip deflection in a manner similar to that of increasing the rigidity.

It was also found that application of a pressure on the seal, and on the water behind, has a major effect on its performance. The lift is increased, and at low speeds the drag is much larger.

##### Future Work

An obvious improvement in the rate of convergence of the numerical scheme could be achieved through use of a special pressure element at the leading edge of the planing surface. This element would need to possess the square-root singularity referred to before. Examination of some of the

pressure distributions presented in this paper would indicate that somewhat fewer than 80 elements should be needed to faithfully represent them, if the singularity at the leading edge were handled in this manner.

The work should definitely be extended in various directions. For example, a three-dimensional model of the surface would be an improvement on the present two-dimensional one. However, the greater performance of the theory would be at the expense of somewhat more analytic and computational effort.

The final goal, naturally, is a complete model of an SES. Such a theory would have to include the influence of both the stern and the bow seal - as well as the effects of the two sidehulls.

#### Acknowledgements

The research described in this paper was performed while the writer was located in the Aviation and Surface Effects Department (ASED) of the David W. Taylor Naval Ship Research and Development Center (DTNSRDC), during leave from the University of New South Wales in Sydney, Australia.

The writer would particularly like to thank those who helped to make his stay in the U.S. possible. These include Mr. S. Davis of the Surface Effect Ships Program Office (SESPO), Mr. A.G. Ford (ASED, DTNSRDC), Mr. R.D. Cooper of the Office of Naval Research (ONR), and Professor J.P. Breslin of the Stevens Institute of Technology.

The work was supported by the Naval Sea Systems Command (SESPO) and administered by ONR through Contract No. N00014-77-C-0121, Task No. NR062-567.

The writer would also like to thank Dr. P.R. Zarda of the Numerical Structural Mechanics Branch of DTNSRDC for help that he gave.

#### References

1. Sretenski, I.N., "On the Motion of a Glider on Deep Water," *Izv. Akad. Nauk SSSR, Otdel. Mat. Estest. Nauk*, Vol. 1933, pp. 817-818 (in English) (1933).
2. Sretenski, I.N., "On the Theory of the Glider," *Izv. Akad. Nauk SSSR, Otdel. Tekhn. Nauk*, Vol. 1940, No. 7, pp. 3-26 (in Russian) (1940).
3. Sedov, L.I., "The Plane Problem of Gliding on the Surface of a Heavy Fluid," *Trudy Konferentsii po Teorii Volnovogo Sooprotivleniya*, Moscow, pp. 7-30 (in Russian) (1946). Also *Tsentral Aero-Gidrodinam. Inst. Moscow* (1937).
4. Maruo, H., "Two-dimensional Theory of the Hydroplane," *Proc. First Japan Nat. Cong. Appl. Mech.*, Science Council of Japan, Tokyo, pp. 409-415 (1952).
5. Maruo, H., "Hydrodynamic Researches of the Hydroplane, Part 1," *J. Zosen Kiokai (J. Soc. Nav. Arch. Japan)*, Vol. 91, pp. 9-16 (in Japanese) (1956).
6. Maruo, H., *Ibid.*, Part 2, Vol. 92, pp. 57-63 (1957).
7. Maruo, H., *Ibid.*, Part 3, Vol. 95, pp. 23-26 (1959).
8. Squire, H.B., "The Motion of a Simple Wedge along the Water Surface," *Proc. Roy. Soc. London, Series A*, Vol. 243, pp. 40-64 (1957).
9. Cumberbatch, E., "Two-dimensional Planing at High Froude Number," *J. Fluid Mechanics*, Vol. 4, Part 5, pp. 466-478 (1958).
10. Wehausen, J.V. and Laitone, E.V., "Surface Waves," *Encyclopedia of Physics*, Vol. 9, Fluid Dynamics 3, ed. by S. Flügge, Springer-Verlag, Berlin, pp. 446-815 (1960).
11. Green, A.E., "The Gliding of a Plate on a Stream of Finite Depth, Part 1," *Proc. Cambridge Phil. Soc.*, Vol. 31, pp. 589-603 (1935).
12. Green, A.E., *Ibid.*, Part 2, Vol. 32, pp. 67-85 (1936).
13. Green, A.E., "Note on the Gliding of a Plate on the Surface of a Stream," *Proc. Cambridge Phil. Soc.*, Vol. 32, pp. 248-252 (1936).
14. Wu, T.Y. and Whitney, A.K., "Theory of Optimum Shapes in Free-Surface Flows, Part 1, Optimum Profile of Sprayless Planing Surface," *J. Fluid Mechanics*, Vol. 55, Part 3, pp. 439-455 (1972).
15. Ting, L. and Keller, J.B., "Optimal Shape of a Planing Surface at High Froude Number," *J. Ship Research*, Vol. 21, No. 1, pp. 40-43 (1977).
16. Wu, T.Y., "A Singular Perturbation Theory for Nonlinear Free-Surface Flow Problems," *Int. Shipbuilding Progress*, Vol. 14, No. 151, pp. 88-97 (1967).
17. Ting, L. and Keller, J.B., "Planing of a Flat Plate at High Froude Number," *The Physics of Fluids*, Vol. 17, No. 6, pp. 1080-1086 (1974).
18. Doctors, I.J., "Representation of Planing Surfaces by Finite Pressure Elements," *Proc. Fifth Australasian Conference on Hydraulics and Fluid Mechanics*, Vol. 2, pp. 480-488 (1974).
19. Wagner, H., "Über Stoss- und Gleitvorgänge an der Oberfläche von Flüssigkeiten," *Zeitschrift für Angewandte Mathematik und Mechanik*, Vol. 12, No. 4, pp. 193-215 (1932).
20. Tulin, M.P., "The Theory of Slender Surfaces Planing at High Speeds," *Schiffstechnik*, Vol. 4, No. 21, pp. 125-133 (in English) (1957).
21. Shuford, C.L., "A Theoretical and Experimental Study of Planing Surfaces Including Effects of Cross Section and Plan Form," National Advisory Committee for Aeronautics (NACA), Report 1333, 35 pp. (1958).
22. Casling, E.M., "The Planing of a Low Aspect-Ratio Flat Ship at Infinite Froude Number," to be published in *J. Engineering Mathematics*, 31 pp. (1977).
23. Shen, Y.T., "Theory of High-Aspect-Ratio Planing Surfaces," Dept. Nav. Arch. and Marine Eng., Univ. Michigan, Ann Arbor, Michigan, Rep. 102, 123 + vii pp. (1970).
24. Shen, Y.T. and Ogilvie, I.F., "Nonlinear Hydrodynamic Theory for Finite-Span Planing Surfaces," *J. Ship Research*, Vol. 16, No. 1, pp. 3-20 (1972).
25. Wagner, H., "Planing of Watercraft," National Advisory Committee for Aeronautics (NACA), TM 1139, 41 pp. (1948). (Translation of "Über das Gleiten von



Wassersfahrzeuge," Leitbuch der Schiffbautechnik, Vol. 34, pp. 205-227 (1933).

26. Wadlin, K.L. and Christopher, Y.W., "A Method for Calculation of Hydrodynamic Lift for Submerged and Planing Rectangular Lifting Surfaces," National Aeronautics and Space Administration (NASA), LR R-14, 13 pp. (1959).

27. Maruo, H., "High- and Low-Aspect Ratio Approximations of Planing Surfaces," Schiffstechnik, Vol. 14, No. 72, pp. 57-64 (in English) (1967).

28. Weinstein, I. and Kapryan, W.J., "The High Speed Planing Characteristics of a Rectangular Flat Plate over a Wide Range of Trim," National Advisory Committee for Aeronautics (NACA), TN 2981, 29 pp. (1953).

29. Wang, D.P. and Rispin, P., "Three-dimensional Planing at High Froude Number," J. Ship Research, Vol. 15, No. 3, pp. 221-230 (1971).

30. Tuck, E.O., "Low-Aspect-Ratio Flat-Ship Theory," J. Hydronautics, Vol. 9, No. 1, pp. 3-12 (1975).

31. Oertel, R.P., "The Steady Motion of a Flat Ship Including an Investigation of Local Flow near the Bow," Ph. D. thesis, Dept. Applied Mathematics, Univ. Adelaide, Adelaide, Australia, 113 + vii pp. (1975).

32. Clement, E.P. and Blount, D.L., "Resistance Tests of a Systematic Series of Planing Hull Forms," Trans. Soc. Naval Architects and Marine Engineers, Vol. 71, pp. 491-579 (1963).

33. Hadler, J., "The Prediction of Power Performance on Planing Craft," Trans. Soc. Naval Architects and Marine Engineers, Vol. 74, pp. 563-610 (1966).

34. Savitsky, D., "Hydrodynamic Design of Planing Hulls," Marine Technology, Vol. 1, No. 1, pp. 71-95 (1964).

35. Savitsky, D., "Planing Craft," Panel Discussion, Proc. Seventh Symposium on Naval Hydrodynamics, Office of Naval Research, August 25-30, Rome, pp. 1163-1168 (1968).

36. Savitsky, D., "Hydrodynamic Development of a High Speed Planing Hull for Rough Water," Proc. Ninth Symposium on Naval Hydrodynamics, Office of Naval Research, August 20-25, Paris, pp. 419-461 (1972).

37. Doctors, L.J., "Representation of Three-Dimensional Planing Surfaces by Finite Elements," Proc. First International Conference on Numerical Ship Hydrodynamics, David W. Taylor Naval Ship Research and Development Center and the Office of Naval Research, Washington, pp. 517-537 (1975).

38. Huang, T.T. and Wong, K.K., "Disturbance Induced by a Pressure Distribution Moving Over a Free Surface," J. Ship Research, Vol. 14, No. 3, pp. 195-203 (1970).

39. Haussling, H.J. and Van Eseltine, R.T., "Unsteady Air-Cushion Vehicle Hydrodynamics Using Fourier Series," J. Ship Research, Vol. 20, No. 2, pp. 79-84 (1976).

40. Doctors, L.J., "The Effect of Air Compressibility on the Nonlinear Motion of an Air-Cushion Vehicle over Waves," Proc. Eleventh Symposium on Naval Hydrodynamics, Office of Naval Research, Washington, 16 pp. (1976).

41. Timoshenko, S. and Young, D.H., "Elements of Strength of Materials," 4th Ed., D. Van Nostrand Company, Inc., Princeton, 377 + x pp. (1962).

42. Lamb, H., "Hydrodynamics," 6th Ed., Dover Publications, New York, 738 + xv pp. (1945).

43. Abramowitz, M. and Stegun, I.A., "Handbook of Mathematical Functions," Applied Mathematics Series-55, Nat. Bureau of Standards, U.S. Govt. Printing Office, Washington, 1046 + xiv pp. (1965).

DISCUSSIONS  
of three papers

HYBRID INTEGRAL-EQUATION METHOD FOR THE STEADY SHIP-WAVE PROBLEM

Ronald W. Yeung and Yann C. Bouger

INTEGRAL-EQUATION METHODS FOR CALCULATING THE VIRTUAL MASS  
IN WATER OF FINITE DEPTH

P. Sayer and F. Ursell

THEORY OF COMPLIANT PLANING SURFACES

L.J. Doctors

Invited Discussion

H. Maruo  
Yokohama National University

Dr. Yeung and Mr. Bouger have developed a method that looks quite novel as a treatment of steady free-surface flow problems. The special feature of this method is first, the employment of the ordinary source potential in place of the conventional Havelock source, and second, the division of the fluid domain into an inner region and outer regions. The first point is advantageous in making the computation of the kernel much simpler but the evaluation of the second derivative of the velocity potential on the undisturbed free surface necessitates some special technique such as the employment of the spline function. The division of the fluid domain in inner and outer regions at proper radiation boundary is convenient especially for the case of an irregular bottom. This idea reminds us of the method adopted by Yamamoto in 1975. In the outer regions the potential is expressed by an asymptotic expansion. If the radiation boundaries are taken far enough from the body and from the irregularity of the bottom, only a few terms are necessary; otherwise the local irregularity will cause some complication. This situation is particularly important in the case that the bottom is not flat. Unfortunately, only the case of a flat bottom is given as a numerical example. Further calculation for irregular bottoms is expected. The authors have also referred to the Neumann-Kelvin problem and have expressed optimism about the resolution of the line-integral controversy. However, the discussor is rather skeptical about this. A numerical method of this kind can be safely applied to a problem for which the existence of a unique solution has been proved. In the case of fully submerged bodies, this might be all right, but there is no evidence of existence of a stable unique solution in the case of surface-piercing bodies, because the linearized free-surface condition is quite artificial. An interesting result obtained by Bessho concerning a vertical plate inserted in a uniform flow with free surface showed a non-uniqueness of the solution of the boundary-value problem with exact boundary condition on the plate and linearized free-surface condition. Bessho has proved that the integral equation has eigensolutions that satisfy the homogeneous

equation. Some singular behavior is anticipated at the intersection between the body boundary and the free surface, which apparently is related to the line-integral ... three-dimensional problem.

The paper of Dr. Sayer and Professor Ursell deals with several problems of practical as well as theoretical interest relating to the classical problem of heaving two-dimensional cylinders in a free surface. The authors employ the method of integral equations in the computation for arbitrary shape of cross section. The discussor wonders if conformal mapping, which is conveniently used in the case of infinite depth, is applicable to the case of finite depth too. When the integral equation is employed to solve the boundary-value problem, there appear frequencies at which the solution cannot be determined. These so-called irregular frequencies correspond to a physical phenomenon of resonant oscillation of water inside the cylinder which is assumed to exist when the boundary of the cylinder is replaced by some singularity distribution. The existence of the irregular frequencies does not present as serious a problem in the computation of hydrodynamic forces in steady oscillation of a cylinder, but makes a trouble in the analysis of the transient oscillations. This problem has been studied by Ohmatsu of the Ship Research Institute. He pointed out that the irregular frequency could be removed by suppressing the resonant oscillation inside the cylinder by means of a source distribution over the interior free surface. If the irregular frequency can be removed by a single wave source at the center, the computation becomes much simpler than the application of the source distribution. The discussor wonders if the elimination of the irregular frequency by means of the modification of the kernel has a connexion with some kind of physical phenomenon in the interior region. In this work, the authors employ an expression derived by Green's theorem, but there is another formulation expressed by the distribution of wave sources only. The authors propose a transposed integral equation which is simpler than the original equation. The discussor feels that the transposed equation looks, in appearance, like the integral equation which appears in the source method, and the solution determines the source density. There is a simple relation, first indicated by Bessho, that determines the integrated pressure by a simple integral of the source density. Therefore the authors' conclusion seems to imply the superior-

ity of the source method. The discussor wishes to know whether the irregular frequencies are the same in the source method and the present method. Another question is the following. The irregular frequencies result from the resonant oscillation in the inner Dirichlet problem, while the resonant oscillation of the liquid in the container is related to the Neumann problem. Are the eigen frequencies in both cases the same or not?

Dr. Doctors has presented a method for solving the flexible planing-surface problem. The determination of the pressure distribution on two-dimensional planing surfaces is now a classical problem. Nevertheless there still remains an unsolved difficulty, the indeterminateness of the wetted surface. The length of the wetted surface depends on the elevation of the free surface to a great extent. Although the elevation is a small quantity of  $O(\alpha)$ ,  $\alpha$  being the angle of attack, the change of the wetted surface due to the surface elevation is  $O(1)$ . Therefore the position of the leading edge cannot be determined beforehand. This fact may not matter much in the case of steady planing of a plane surface, but it seems to yield a considerable difficulty in the determination for a flexible planing surface. The boundary-value problem of the two-dimensional planing surface is formulated as a Fredholm equation of the first kind. The author's calculation is, in effect, the solution of this integral equation by means of the discretization of the integral equation. According to my experience, the method of discretization of an integral equation of the first kind with logarithmic kernel is likely to show an unsatisfactory accuracy sometimes, especially at low Froude numbers. In this case, the expansion by mode functions may give a more stable result.

#### Discussion

by T. Francis Ogilvie  
of paper by P. Sayer and F. Ursell

It is worthwhile to say something about the practical utility of what authors have demonstrated. Many organizations have computer programs similar to Frank's for computing ship motions and wave loads on ships. Of course, these all give difficulty at the irregular frequencies discussed here. But these programs can all be modified by the insertion of a single step, equivalent to Equation (3.1) in the paper presented here (with any non-zero value assigned to the constant  $A$ ). Then, regardless of the frequency under consideration, one can be certain that the eigen-frequencies of the internal Dirichlet problem will have been displaced to other frequencies.

This seems to me to be a much happier solution of the practical difficulty than using such devices as putting a "lid" on the inner-flow region.

#### Discussion

by Kwang June Bai  
of paper by Ronald W. Yeung and Yann C. Bouger

The method presented here was applied previously by Yeung to two-dimensional time-harmonic free-surface flow problems and the results were presented at the First International Conference on Numerical Ship Hydrodynamics in 1975. The same method was also applied to the same time-harmonic problem by Kim (1976).

For solving the uniform steady-flow problem considered here and the time-harmonic problems considered in Yeung (1975) and Kim (1976), I personally do not see any advantage in using the present hybrid integral-equation technique over the conventional Green-function method (distributing singularities on only the body boundary). It seems to me that the computation of the coupling terms, which result from matching the eigenfunction representations (i.e.,  $\cosh m_j(y+h)$ ,  $\cos m_j(y+h)$  and the fundamental singularity distributions (i.e.,  $\log r$ ) along the artificial juncture boundaries, is as complicated as the computations involved in the conventional Green-function method for the finite constant depth case. This fact is obvious when the Green function (in the conventional Green-function method is expressed in series form.

In the earlier work of Yeung (1973) and Bai & Yeung (1974) the fundamental singularity method is used without matching of the eigenfunctions. In this case there is a computational advantage over the conventional Green-function method since the kernel is much simpler. However, in this approach, the computational boundary domain is increased as a trade-off since the fundamental singularities ( $\log r$ ) are distributed along the entire (closed) boundary.

I would appreciate it if the authors could express their view on the advantages (or disadvantages) of the present method over the conventional Green-function method for the case of constant water depth. It would also be useful for the authors to discuss the improvement of the Yeung (1975) and Kim (1976) methods over the earlier work by Yeung (1973) and Bai & Yeung (1974) for the general cases including the case of variable depth.

My second comment concerns the authors' use of spline-function approximations along the free surface in the present work. It seems to be necessary in the present formulation to use the spline functions due to the presence of the second derivative  $\phi_{xx}$  in the free surface integral. However, the second derivative  $\phi_{xx}$  in the integral along the free surface in Equation (3.3) can be eliminated by integrating by parts, resulting in a slightly different form which involves only the first derivative as the highest-order derivative. Then, in the new formulation, it is not necessary to use complicated (and more sophisticated) spline functions. From my own experience, it is much easier to use simple piecewise polynomial functions which permit discontinuities in the first derivative,  $\phi_x$ , at intersecting points of two adjacent segments. I would like to ask the authors if there is any other significance or advantage in using the spline functions.

Finally I would like to point out that the

error in the vertical force in Figure 7 of Bai (1975) which Yeung and Bowyer referred to in the present paper is not due to any error in my numerical computations, but to an unfortunate misprint. The vertical force scale should have been  $1/(5\text{segwa}^2)$  in Figure 7. Also I would like to take this opportunity to point out one more typographical error in Bai (1975), namely, the scale factors ( $10^2$ ) and ( $10^{-1}$ ) in the abscissa of Figures 10 and 11 should have been interchanged. I would also like to correct two misprints in Bai and Yeung (1974) which were also pointed out by Yeung (1975). In Figure 5.7 of Bai & Yeung (1974), the abscissa scale should have been divided by the factor of four and  $m_0 h$  should have been  $m_0 b$ . The correct scale was given in my original paper (Bai, 1972) and the results were confirmed by Kim (1976).

Bai, K.J., 1972, "A variational method in potential flows with a free surface," Ph.D. Thesis, Dept. of Naval Arch., University of Calif., Berkeley

Kim, Y.H., 1976, "Hydrodynamics of cylinders in water of arbitrary varying depth," Master's Thesis, Dept. of Ocean Engineering, MIT, Cambridge Mass. 67 pages.

#### Author's Reply

by R.W.Yeung

to discussions by H. Maruo and Kwang June Bai

First, concerning Professor Maruo's comment on the possibility of complications in applying the method to the case of non-flat bottom, I would like to point out that similar techniques were used very successfully for such a case in my previous work (Yeung, 1975) for the time-harmonic problems. Although we give no results in the present paper, we anticipate no difficulties in that direction. A distinct advantage of our hybrid method is that the choice of the truncation boundary can be quite arbitrary and in fact can be as close to the body or the irregularities of the bottom as one desires. Any local disturbances can be absorbed automatically in the series expansion.

The idea of matching a solution expressed in analytical form with a local numerical solution using an integral-equation formulation was carried out to fruition in my initial work in 1973. At that time, only a single (wave) term was taken. This was later generalized in Bai and Yeung (1974). I am glad to learn of Yamamoto's (1974) work, related to stress calculation problems, which was also in that direction. His later work, related to free-surface flows and presented at the First Conference, indicates that we have a common philosophy of approach.

Professor Maruo's point on the uniqueness of solution of the Neumann-Kelvin problem is a point of common concern in our field. Bessho's work on the two-dimensional semi-submerged vertical-plate problem is an interesting contribution. It is clear that he experienced difficulty in constructing a physically plausible solution. However, it is not entirely clear whether or not this difficulty was implicitly associated with the method of solution. His solutions always produce a continuous free-surface elevation across the plate which seems to be against intuition. Also, I don't believe he has proved that the integral equation has eigen solutions satisfying homogeneous condi-

tions of the problem. We all hope to get to the bottom of the matter soon.

In response to Dr. Bai's first query, related to the computational difference between our hybrid method and a traditional Green-function approach, I want to point out that the coupling terms that Dr. Bai refers to, when computed from the expressions in closed form that we obtained, are about the same order of complication as the Green function itself. However, in applying the Green-function technique, one is required not merely to be able to compute the Green function, but also to be able to integrate such a function over a segment of finite-size. This requirement of the distribution of singularities is well known to those applying the singularity method. Generally, integration of a Green function over a segment cannot be carried out in closed form; thus it must be integrated numerically. Therefore, our ability to obtain closed-form solutions of the integrals associated with the radiation boundaries means that we are one step ahead of the Green-function method. Such closed-form solutions are central to the success of our scheme, a fact that was pointed out previously in Yeung (1975) and in my student Y. H. Kim's thesis (1976). As far as computation time is concerned, the hybrid method of Yeung (1975) was about two to three times more efficient than the original formulation of Yeung (1973). A recent work due to Harten and Efrony (1977, J. of Comp. Physics) indicates that by block structuring the matrix a further improvement by a factor of 10 is possible. Thus it appears that our hybrid formulation has a tremendous amount of potential in computation economy.

While computation costs may be important in the production stages of every method, it is not of primary concern in this paper. This paper serves to demonstrate that the hybrid-integral-equation formulation is applicable to either time-harmonic or steady-flow problems. This is in great contrast to the finite-element formulation of Bai and Yeung (1974), which had to undergo fundamental modifications to tackle the steady-flow problem (Bai, 1975).

With respect to the point concerning comparison of computation time of the traditional Green-function method with our method, it appears that there exists no published computational data using the finite-depth Green function for two-dimensional steady flow; hence such a comparison is not possible. Perhaps this is an indication of the fact that the Green-function approach has not been too attractive computationally.

The second point concerns the treatment of the second derivative term of  $\phi$  on the free surface. We want to emphasize that a spline approximation is not absolutely necessary, although it was found to be most helpful. We could have used piecewise polynomial approximation between successive grid points on the free surface and this will result in the same type of integrals as in (3.14). Inasmuch as the usage of the spline functions hardly complicated the calculations, that one obtains smooth first and second-derivatives at every grid point, and that very few points are necessary to represent  $\phi$  in  $[x^-, x^+]$ . The high quality of the differentiated curve as shown confirms the usefulness of the technique. The application of spline functions to finite-element methods such as Dr. Bai's, however,

would likely destroy the banded structure of the resulting matrix and is therefore, not very desirable in that respect.

Finally, concerning whether one should perform an integration by parts to reduce the order of differentiation of the  $\phi_{xx}$  term: we examined this during the course of the work and found that no particular advantage resulted. In fact, this will bring about concentrated singularities at the end of the interval of integration, which is highly undesirable.

I am glad that Dr. Bai agrees upon the errors we found in both our joint work as well as his paper in the First conference. Both discussor's comments on this paper are appreciated by us.

#### Author's Reply

by P. Sayer and F. Ursell  
to discussions by H. Maruo and  
T. Francis Ogilvie

We are grateful to Professor Maruo and to Professor Ogilvie for their illuminating comments. In addition, Professor Maruo has put some searching questions to which we offer the following replies:

- (i) We have not succeeded in applying conformal mapping to the finite-depth problem.
- (ii) We should be glad to know more about Ohmatsu's work on transient problems. The work done on transient problems at Manchester has proceeded along different lines and does not involve the complete determination of the water motion. (See S.J. Maskell and F. Ursell, J. Fluid Mech. 44, 1970, 303-313).
- (iii) We agree that our device of using the transposed kernel must be equivalent to the source method used earlier by Bessho, and that the advantages of that method (provided that only the total force is required) deserve further study. The irregular frequencies remain the same when the kernel of an integral equation is replaced by the transposed kernel. Thus they are the same for the Green-function method as for the source method.
- (iv) The eigenfrequencies of the interior Dirichlet problem are in general distinct from the eigenfrequencies of the interior Neumann problem. We find it difficult to attribute a physical meaning to the interior Dirichlet problem in the present calculations. Indeed, if the source potential is modified, then the corresponding irregular frequencies are also modified and are no longer related to the interior Dirichlet problem.

#### Author's Reply

by L.J. Doctors  
to discussion by H. Mauro

The author would like to thank Professor Maruo for his interesting comments.

The first point concerns the unknown length of the wetted surface. As pointed out, the position of the leading edge cannot be determined beforehand--assuming, of course, that the height of the leading edge is specified. The only practical method of skirting this difficulty

is to specify the wetted length instead, and consequently the planing height is found as part of the solution. Although not carried out here, one could then iterate the wetted length until the desired planing height is achieved.

In the case of a flexible planing surface, the identical stumbling block occurs, except, of course, the planing height is now reduced by the influence of plate compliance. Once again, an iteration procedure would be needed to determine the actual wetted length in a practical situation.

With regard to the second comment, the writer found no problems in accuracy for low Froude numbers--suggested by Professor Maruo. Typically, it was found that the number of elements needed to achieve, say, one percent accuracy in the lift force, was independent of the speed. Perhaps the reason for this is that the logarithmic kernel is smoothed out by the use of triangular pressure elements. These yield a continuous pressure distribution, which could not be obtained by cruder elements--such as rectangular ones.

A second advantage of the use of triangular pressure elements--as opposed to mode functions--is that one can more easily obtain the flexural influence coefficients for a plate of arbitrary stiffness distribution.

## NUMERICAL SOLUTION OF THE NAVIER-STOKES EQUATIONS FOR 2D HYDROFOILS IN OR BELOW A FREE SURFACE\*

Samuel P. Shanks\*\* and Joe F. Thompson†  
Mississippi State University  
Department of Aerophysics and Aerospace Engineering  
Mississippi State, MS 39762

### Abstract

The results of an investigation of the application of numerically-generated boundary-fitted curvilinear coordinate systems in the finite-difference solution of the time-dependent, two-dimensional Navier-Stokes equations for the laminar viscous flow about hydrofoils moving either in a free surface or submerged at a finite depth in a fluid of infinite or finite depth are presented. The hydrofoil may be of arbitrary shape, and its motion may include pitching oscillation or oscillation normal or parallel to the plane of the undisturbed free surface as well as translation parallel to this plane. A computer code has been developed that is capable of predicting the flow field, pressure distributions, and force coefficients for this configuration at low Reynolds numbers. The finite-difference solution is implicit in time so that all the difference equations are solved simultaneously by iteration at each time step.

### 1. Introduction

This report presents the results of an investigation of the application of numerically-generated boundary-fitted curvilinear coordinate systems in the finite-difference solution of the time-dependent, two-dimensional Navier-Stokes equations for the laminar viscous flow about hydrofoils moving either in a free surface or in a fluid of finite or infinite depth. The hydrofoil may be of arbitrary shape, and its motion may include pitching oscillation or oscillation normal or parallel to the plane of the undisturbed free surface as well as translation parallel to this plane. A computer code has been developed that is capable of predicting the flow field, pressure distributions, and force coefficients at low Reynolds numbers. The finite-difference solution is implicit in time, so that all the difference equations are solved simultaneously by iteration at each time step.

The numerical solution of the Navier-Stokes equations for flow with a free surface is complicated in particular by the fact that part of the boundary of the calculation region, i.e., the free surface, is deforming. This makes the accurate representation of boundary conditions on the free surface difficult; yet this solution, as other partial differential equation solutions, is most strongly influenced by the boundary conditions. The most critical need for accuracy thus lies in precisely the region of the most difficulty of attainment.

The basis of the present numerical solution is the technique of numerically-generated boundary-fitted curvilinear coordinate systems reported earlier in Reference 1. This is a procedure for automatic numerical generation of curvilinear coordinate systems with coordinate lines coincident with all boundaries of a general multi-connected, two-dimensional region containing any number of arbitrarily shaped bodies. The curvilinear coordinates are generated as the solution of an elliptic partial differential system. No restrictions are placed on the shape of the boundaries, which may even be time-dependent, and the approach is not restricted in principle to two dimensions. With this procedure the numerical solution of a partial differential system may be done on a fixed rectangular field with a square mesh with no interpolation required regardless of the shape of the physical boundaries, regardless of the spacing of the curvilinear coordinate lines in the physical field, and regardless of the movement of the coordinate system in the physical plane. A number of examples of coordinate systems and application thereof to the solution of partial differential equations are given in [2] along with a discussion of the technique. This procedure essentially eliminates the boundary geometry as a complicating factor in the numerical solution of partial differential equations. The use of boundary-fitted coordinate systems for the solution of the incompressible Navier-Stokes equations for the flow

\* This research was sponsored principally by ONR, Contract N00014-74-C-0373. The work reported in Section VI was sponsored by NSRDC, Contract N00167-76M-8359.

\*\* Ph.D., Present affiliation: General Dynamics, Ft. Worth, TX

† Professor, Ph.D.

about two-dimensional airfoils has been reported by Thames, et. al. [3] and by Hodge [4]. The latter reference uses the pressure-velocity formulation used in the present work.

The use of boundary-fitted coordinate systems is particularly attractive for free surface problems, since a coordinate line will remain coincident with the free surface as it deforms under wave action. The physical flow field is transformed to the curvilinear coordinate system as discussed in more detail in Section II. The field in the transformed plane is rectangular with a fixed square grid regardless of the movement of the physical boundaries. With the partial differential equations of motion and their associated boundary conditions transformed to the curvilinear system, all computation can be done on the fixed square grid in the transformed plane regardless of the motion of the free surface or the hydrofoil. It is even possible to allow the hydrofoil to oscillate without really complicating the problem, since a coordinate line can also remain coincident with the hydrofoil surface as it oscillates.

The present solution is capable of treating the low Reynolds number viscous flow about a translating hydrofoil in or below the free surface of a fluid of any depth. The hydrofoil may also be in pitching, plunging, or longitudinal oscillation as well as translation. The hydrofoil starts from rest with a flat surface and accelerates to full speed at any acceleration desired. The general solution procedure is discussed in Sections II-IV, and facets peculiar to each of the parts of the study together with typical results are given in Sections V-VII.

## II. Boundary-Fitted Coordinate System

The basic idea of the boundary-fitted coordinate systems is to numerically generate a curvilinear coordinate system having some coordinate line coincident with each boundary of the physical region of interest, regardless of the shape of these boundaries. This is done by taking the curvilinear coordinates to be solutions of an elliptic partial differential system, with constant values of one of the curvilinear coordinates specified as Dirichlet boundary conditions on each boundary. Values of the other coordinate are either specified in a monotonic variation over a boundary as Dirichlet boundary conditions, or are determined by Neumann boundary conditions thereon. In the latter case, the curvilinear coordinate lines can be made to intersect the boundary according to some specified condition, such as normalcy or parallel to some given direction. It is also possible to exercise control over the spacing of the curvilinear coordinate lines in the field in order to concentrate lines in regions of expected high gradients.

In any case, the numerical generation of the coordinate system is done automatically for any shape boundaries, requiring only the input of points on the boundary. The technique has been described in detail in earlier reports [1-2], and the computer code, together with instructions for and examples of its use in the numerical solution of partial differential equations, is given in Ref. [5].

The technique is described in general in this section. Each of the three parts of the present study used a different variation of the basic procedure as is discussed for each configuration in Sections V-VII.

As mentioned previously, the curvilinear coordinates are generated by solving an elliptic system of suitable form. One such system is

$$\xi_{xx} + \xi_{yy} = P(\xi, \eta) \quad (1a)$$

$$\eta_{xx} + \eta_{yy} = Q(\xi, \eta) \quad (1b)$$

with Dirichlet boundary conditions, one coordinate being specified to be equal to a constant on the body and equal to another constant on the outer boundary, with the other coordinate varying monotonically over the same range around both the body and the outer boundary.

Since it is desired to perform all numerical computations in the uniform rectangular transformed plane, the dependent and independent variables must be interchanged in Eq. (1). This results in the coupled system

$$\begin{aligned} \alpha \xi_{\xi\xi} - 2\beta \xi_{\xi\eta} + \gamma \eta_{\xi\xi} \\ = -J^2 [x_{\xi} P(\xi, \eta) + x_{\eta} Q(\xi, \eta)] \end{aligned} \quad (2a)$$

$$\begin{aligned} \alpha \eta_{\xi\xi} - 2\beta \eta_{\xi\eta} + \gamma \eta_{\eta\eta} \\ = -J^2 [y_{\xi} P(\xi, \eta) + y_{\eta} Q(\xi, \eta)] \end{aligned} \quad (2b)$$

where

$$\begin{aligned} \alpha &= x_{\eta}^2 + y_{\eta}^2 & \gamma &= x_{\xi}^2 + y_{\xi}^2 \\ \beta &= x_{\xi} x_{\eta} + y_{\xi} y_{\eta} & J &= x_{\xi} y_{\eta} - x_{\eta} y_{\xi} \end{aligned}$$

The system described by Eq. (2) is a quasi-linear elliptic system for the coordinate functions  $x(\xi, \eta)$  and  $y(\xi, \eta)$  in the transformed plane. This set is considerably more complex than the linear system specified by Eq. (1), but the boundary conditions are specified on straight boundaries, and the coordinate spacing in the transformed plane is uniform.

The coordinate lines may be spaced as desired around the boundaries, since the assignment of the coordinate values to the  $[x, y]$  boundary points is arbitrary. Control of the radial

spacing of the coordinate lines is accomplished by varying the functions  $P(\xi, \eta)$  and  $Q(\xi, \eta)$  in (2).

The effect of changing the functions  $P(\xi, \eta)$  and  $Q(\xi, \eta)$  on the coordinate system is discussed in Ref. 2. One particularly effective procedure, used here for the submerged hydrofoil solutions, is to choose  $P$  and  $Q$  as exponential terms, so that the coordinates are generated as the solutions of

$$\begin{aligned}\xi_{xx} + \xi_{yy} &= -\sum_{i=1}^n a_i \operatorname{sgn}(\xi - \xi_i) \cdot \\ \exp(-c_i |\xi - \xi_i|) - \sum_{j=1}^m b_j \operatorname{sgn}(\xi - \xi_j) \cdot \\ \exp(-d_j \sqrt{(\xi - \xi_j)^2 + (\eta - \eta_j)^2}) &\equiv P(\xi, \eta) \quad (3a)\end{aligned}$$

$$\begin{aligned}\eta_{xx} + \eta_{yy} &= -\sum_{i=1}^n a_i \operatorname{sgn}(\eta - \eta_i) \exp(-c_i |\eta - \eta_i|) - \\ - \sum_{j=1}^m b_j \operatorname{sgn}(\eta - \eta_j) \cdot \\ \exp(-d_j \sqrt{(\xi - \xi_j)^2 + (\eta - \eta_j)^2}) &\equiv Q(\xi, \eta) \quad (3b)\end{aligned}$$

where the positive amplitudes and decay factors are not necessarily the same in the two equations. Here the first terms have the effect of attracting the  $\xi = \text{constant}$  lines to the  $\xi = \xi_i$  lines in Equation (3a), and attracting  $\eta = \text{constant}$  lines to the  $\eta = \eta_i$  lines in Equation (3b). The second terms cause  $\xi = \text{constant}$  lines to be attracted to the points  $(\xi_j, \eta_j)$  in (3a), with similar effect on  $\eta = \text{constant}$  lines in (3b). Several examples of the use of coordinate system control are given in Ref. 2.

As discussed previously, the physical plane grid system is generated by solving the set of elliptic partial differential equations, (2), with one of the  $(\xi, \eta)$  coordinates specified to be constant on the boundaries of the physical plane, and the other  $(\xi, \eta)$  coordinate distributed along the boundaries as desired. If the boundary values of  $x$  and  $y$  are changed in the physical plane by the movement of the free surface contours a new solution of the elliptic system with the changed boundary values is obtained over the same range of values of  $\xi$  and  $\eta$  in the field. Thus, the transformed plane remains unchanged as the coordinate grid system moves in the physical plane. Only the values of the physical coordinates  $(x, y)$  change with time at the fixed grid points in the transformed plane.

The transformed time derivative is

$$\begin{aligned}\left(\frac{\partial f}{\partial t}\right)_{x,y} &= \frac{\partial(x,y,t)}{\partial(\xi,\eta,t)} \bigg/ \frac{\partial(x,y,t)}{\partial(\xi,\eta,t)} = \left(\frac{\partial f}{\partial t}\right)_{\xi,\eta} \\ &- \frac{1}{J} \left( \frac{\partial f}{\partial \xi} \frac{\partial y}{\partial \eta} - \frac{\partial f}{\partial \eta} \frac{\partial y}{\partial \xi} \right) \left( \frac{\partial x}{\partial \xi} \right)_{\xi,\eta} \\ &+ \frac{1}{J} \left( \frac{\partial f}{\partial \xi} \frac{\partial x}{\partial \eta} - \frac{\partial f}{\partial \eta} \frac{\partial x}{\partial \xi} \right) \left( \frac{\partial y}{\partial \xi} \right)_{\xi,\eta} \quad (4)\end{aligned}$$

All derivatives are expressed in the transformed variables  $(\xi, \eta)$ ; thus eliminating the need for interpolation between points in the physical plane. The movement of the physical plane grid points is accounted for by the time rate of change of  $x$  and  $y$ ,  $\left(\frac{\partial x}{\partial t}\right)_{\xi,\eta}$  and  $\left(\frac{\partial y}{\partial t}\right)_{\xi,\eta}$  in the above expression.

### III. Equations of Motion

The equations of motion are the complete time-dependent Navier-Stokes equations with the gravity term included. The no-slip boundary condition is applied on the hydrofoil, and the viscous stress conditions are applied on the free surface. The free surface deforms in time as waves are formed thereon.

All quantities are non-dimensionalized with respect to the translation velocity of the hydrofoil and the hydrofoil chord. The Reynolds and Froude numbers are defined in terms of these reference values. The physical coordinate system is taken to be fixed relative to the translational motion of the hydrofoil. In the physical plane the equations of motion are

$$\begin{aligned}u_t + (u^2)_x + (uv)_y \\ = -p_x + (u_{xx} + u_{yy})/R - \psi \quad (5a)\end{aligned}$$

$$\begin{aligned}v_t + (uv)_x + (v^2)_y \\ = -p_y + (v_{xx} + v_{yy})/R - 1/F^2 \quad (5b)\end{aligned}$$

$$p_{xx} + p_{yy} = -u_x^2 - 2u_x v_x - v_y^2 - D_t \quad (5c)$$

where  $R = \frac{V_0 c}{\nu}$  and  $F = \frac{V_0}{\sqrt{g c}}$  are the Reynolds and Froude numbers, respectively,  $V_0$  being the magnitude of a reference hydrofoil translational velocity,  $V$  the instantaneous velocity,  $c$  the chord,  $\nu$  the kinematic viscosity, and  $g$  the acceleration of gravity. The third of these equations is the Poisson equation for the



pressure, derived by taking the divergence of the Navier-Stokes equations and requiring that the continuity equation ( $D \equiv u_x + v_y = 0$ ) be satisfied. The time derivative of  $D$ , ideally zero, has been retained in this equation as a corrective term in the manner of Hirt and Harlow [6].

The boundary conditions are as follows:

(a) On the hydrofoil (no-slip condition):  
 $u = u_B(x, y, t)$ ,  $v = v_B(x, y, t)$  where  $(u_B, v_B)$  are the velocity components of the hydrofoil surface at  $(x, y, t)$  relative to the coordinate system translating with the hydrofoil. (These values are zero if the hydrofoil is not oscillating.)

(b) On the surface (viscous stress condition):

$$\frac{2}{R} u_x n_1 + \frac{1}{R} (u_y + v_x) n_2 = (p - p_o) n_1 \quad (6a)$$

$$\frac{2}{R} v_y n_2 + \frac{1}{R} (u_y + v_x) n_1 = (p - p_o) n_2 \quad (6b)$$

where  $p_o$  is the applied pressure from the atmosphere, and  $n_1$  and  $n_2$  are the components of the unit normal to the surface in the  $x$  and  $y$  directions, respectively. These relations assume no wind stress on the surface.

(c) On the remote boundary (undisturbed flow):  
 $u = -V_o$ ,  $v = 0$ ,  $p = p_o + (y_o - y)/F^2$ . (These conditions apply on the remote boundary strictly only until surface waves reach it. At low  $R$ , sufficient viscous dissipation is present to damp the waves before the remote boundary 10 chords distant is reached.)

Using the derivative transformation relations given in the appendices of Ref. 5, these equations may be transformed to the curvilinear coordinate system, so that the equations of motion in the transformed plane are

$$\begin{aligned} u_\xi - x_\xi (y_\eta u_\xi - y_\xi u_\eta) / J - y_\xi (x_\xi u_\eta - x_\eta u_\xi) / J \\ + [y_\eta (u^2)_\xi - y_\xi (u^2)_\eta] / J \\ + [x_\xi (uv)_\eta - x_\eta (uv)_\xi] / J \\ + (y_\eta p_\xi - y_\xi p_\eta) / J = (\alpha u_{\xi\xi} - 2\beta u_{\xi\eta} + \gamma u_{\eta\eta} \\ + \sigma u_\eta + \tau u_\xi) / RJ^2 + \dot{v} \end{aligned} \quad (7a)$$

$$v_\xi - x_\xi (y_\eta v_\xi - y_\xi v_\eta) / J - y_\xi (x_\xi v_\eta - x_\eta v_\xi) / J$$

$$\begin{aligned} + [y_\eta (uv)_\xi - y_\xi (uv)_\eta] / J + [x_\xi (v^2)_\eta - x_\eta (v^2)_\xi] / J \\ + (x_\xi p_\eta - x_\eta p_\xi) / J = (\alpha v_{\xi\xi} - 2\beta v_{\xi\eta} + \gamma v_{\eta\eta} \\ + \sigma v_\eta + \tau v_\xi) / RJ^2 - 1/F^2 \end{aligned} \quad (7b)$$

$$\begin{aligned} \alpha p_{\xi\xi} - 2\beta p_{\xi\eta} + \gamma p_{\eta\eta} + \sigma p_\eta + \tau p_\xi \\ = - (y_\eta u_\xi - y_\xi u_\eta)^2 \\ - 2(x_\xi u_\eta - x_\eta u_\xi)(y_\eta v_\xi - y_\xi v_\eta) \\ - (x_\xi v_\eta - x_\eta v_\xi)^2 - J^2 D_t \\ + x_\xi (D_\xi y_\eta - D_\eta y_\xi) J - y_\xi (D_\xi x_\eta - D_\eta x_\xi) J \end{aligned} \quad (7c)$$

where

$$D = (y_\eta u_\xi - y_\xi u_\eta + x_\xi v_\eta - x_\eta v_\xi) / J \quad (7d)$$

and

$$\sigma \equiv J^2 \partial(\xi, \eta), \quad \tau \equiv J^2 \partial(t, \eta).$$

The coefficients  $\alpha$ ,  $\beta$ ,  $\gamma$ , and  $J$  have been defined in the previous section.

The time derivatives have also been transformed in these equations. Thus, time derivatives in Eq. (7) are taken with  $\xi$  and  $\eta$  fixed, while those in Eq. (5) were taken with  $x$  and  $y$  fixed. This transformation of time derivatives allows the computation to be done on a fixed grid in the transformed plane even though the physical grid is in motion due to the free surface and hydrofoil movement.

The transformed boundary conditions are

(a) On the hydrofoil (no-slip conditions):  
 $u = u_B(\xi, t)$ ,  $v = v_B(\xi, t)$

(b) On the free surface (viscous stress conditions):

$$\begin{aligned} u_\xi = \frac{1}{\alpha^2} [(\alpha\beta - Jx_\eta y_\eta) u_\eta + (Jx_\eta^2) v_\eta \\ + \frac{RJ\sigma}{2} y_\eta (p - p_o)] \end{aligned} \quad (8a)$$

$$\begin{aligned} v_\xi = \frac{1}{\alpha^2} [(-Jy_\eta^2) u_\eta + (\alpha\beta + Jx_\eta y_\eta) v_\eta \\ - \frac{RJ\sigma}{2} x_\eta (p - p_o)] \end{aligned} \quad (8b)$$

(c) On the remote boundary (undisturbed flow):  
 $u = -V_o$ ,  $v = 0$ ,  $p = p_o + (y_o - y)/F^2$ .

The two free surface boundary conditions given above result from transforming the two viscous

stress equations (6) to the curvilinear coordinate system and solving these two simultaneous equations for  $u_\xi$  and  $v_\xi$  in terms of  $u_\eta$ , the free surface being a line of constant  $\xi$  in the configuration used. (See the appendix of [7] for this development.)

On the hydrofoil contour and the free surface the pressure is determined by iteratively adjusting the pressure at each point on the hydrofoil in proportion to the divergence of the velocity at the same point, so that upon convergence the continuity equation is satisfied at the hydrofoil surface. Thus on the hydrofoil surface, since  $u_\xi = v_\xi = 0$  by the no-slip condition, we have, using (7d),

$$p^{(k+1)} = p^{(k)} - K(x_\xi v_\eta - y_\xi u_\eta)/J \quad (9a)$$

while on the free surface,

$$p^{(k+1)} = p^{(k)} - KD \quad (9b)$$

with  $D$  given by (7d). Here  $(k)$  is the iteration counter, and  $K$  is a proportionality factor given by  $K = \frac{2\omega J^2}{(a + \gamma)\Delta t}$  on the hydrofoil and

by  $K = \frac{1}{R}$  on the free surface,  $\omega$  being an acceleration parameter. The different form on the free surface results from the need to prevent positive feedback from the surface stress condition to the surface pressure iteration. (See Appendix D of [8] for the development of these relations.)

The  $y$  coordinate on the free surface is determined at each time from the movement of the free surface. Since the free surface can be described by  $y = f(x, t)$  or  $f(x, t) - y = 0$ , the convective derivative of the latter function must vanish:

$$0 = \frac{d}{dt} [f(x, t) - y] = \left(\frac{\partial f}{\partial t}\right)_x + \left(\frac{\partial f}{\partial x}\right)_t \frac{dx}{dt} - \frac{dy}{dt}$$

Then since  $y = f$ , and the surface is a line of constant  $\xi$ ,

$$\left(\frac{\partial y}{\partial x}\right)_t = \left(\frac{\partial y}{\partial x}\right)_\xi = \frac{y_\eta}{x_\eta}$$

and then

$$\left(\frac{\partial y}{\partial t}\right)_x = v - u \frac{y_\eta}{x_\eta}$$

#### IV. Numerical Solution

All space derivatives in the field are approximated by second-order, central difference expressions. ( $\Delta\xi$  and  $\Delta\eta$  are both unity by construction, the actual values of  $\xi$  and  $\eta$  being immaterial since cancellation occurs

after substitution in the transformed equations.) Derivatives along coordinate lines emanating from the hydrofoil surface or from the free surface are evaluated using second-order, one-sided difference expressions.

Finally all the time derivatives are approximated by first-order, backward difference expressions, so that the solution is implicit in time. The set of five simultaneous difference equations from (2) and (7), three equations of motion and two coordinate system equations, with the boundary conditions are solved at each time step by SOR iteration. The result from the previous time step serves as the initial guess for the iteration at the next. The solution starts from rest with a flat free surface and proceeds with a specified acceleration to full speed.

The body force components are obtained from the integration of the pressure and shear forces around the wetted portion of the hydrofoil surface:

$$F_x = -2 \oint p y_\xi d\xi + \frac{2}{R} \oint \omega x_\xi d\xi \quad (11a)$$

$$F_y = +2 \oint p x_\xi d\xi + \frac{2}{R} \oint \omega y_\xi d\xi \quad (11b)$$

with vorticity,  $\omega$ , given by

$$\omega = (y_\eta v_\xi - y_\xi v_\eta - x_\xi u_\eta + x_\eta u_\xi)/J \quad (12)$$

Here the  $\eta$ -derivatives are evaluated by the second-order, one-sided difference expressions given above, while the second-order central expressions are used for the  $\xi$ -derivatives. Finally, the lift and drag coefficients are given by

$$C_L = F_y \cos\theta - F_x \sin\theta \quad (13a)$$

$$C_D = F_y \sin\theta + F_x \cos\theta \quad (13b)$$

where  $\theta$  is the angle of attack.

#### V. Submerged Hydrofoil - Infinite Depth [7]

##### Solution Configuration

Figure 1 shows the basic doubly-connected transformation with a free surface. This type of configuration has been used successfully for airfoils in previous studies [3]. For a free surface problem  $C_1$  would be the arbitrary hydrofoil,  $C_2$  would be the "infinity" boundary, and  $C_3$  would be the free surface. Since the "infinity" boundary is chosen to be ten chords from the hydrofoil in the present research, the contour  $C_2$  would be approximately twenty chords long. Thus, fewer points would be on  $C_2$  to cover 20 chord lengths than would be on  $C_1$  to cover approximately 2 chord lengths. Unless many  $\xi$ -points were used the wide grid spacing

on the free surface would cause large truncation error.

Several modified coordinate systems were investigated in order to provide more points on the free surface [7]. The transformation shown in Fig. 2 was chosen because the number of free surface ( $C_7$  and  $C_8$ ) grid points is independent of the number of points on the body ( $C_1$ ). The transformed plane of Figure 2 forms a T-shaped region. The lower part of the coordinate system is the same as the basic transformation of Figure 1. The cut  $C_1^*$  is taken at  $11 - \frac{1}{2}(12 + \frac{1}{2})$ , thus creating the two common reentrant boundaries  $C_3^*$  and  $C_4^*$ . The upper part of the transformed plane bounded by the constant  $\eta$ -line ( $JM - \frac{1}{2}$ ),  $C_8$ ,  $C_7$ ,  $C_2$  are added to the basic transformed plane to provide free surface and "infinity" boundaries. The two common reentrant boundaries,  $C_6$  and  $C_5$ , are created to provide more points on the infinity boundary than are on the body ( $C_1$ ). The cuts are taken at half indices because the point  $(11 - \frac{1}{2}, JM - \frac{1}{2})$  has a zero Jacobian. By taking the cut at half indices, the zero Jacobian point is eliminated from the field calculations.

The system of finite difference equations is solved simultaneously by the successive-over-relaxation (SOR) iterative method. The number of simultaneous equations to be solved is  $(JMAX - JM + 1)(IMAX - 1) + (JM - 1)(12 - 11 + 1)$ . Boundary values are specified on  $J = JMAX$  for all  $i \in [1, IMAX]$ . Also, boundary values are specified on  $j = JMAX$  for all  $i \in [1, 12]$ . Boundary values or the Neumann boundary condition  $x_c = 0$  (normal  $\eta$ -lines to free surface) may be expressed on the free surface contours,  $i = 1$  and  $i = IMAX$ . At the branch cut for the constant  $\eta$ -line  $J = JM$  and  $i \in [1, 11 - 1]$ , we have  $(i, j - 1) = (IMAX - 1 + 1, JM)$ . Also, at the branch cut for the constant  $\eta$ -line  $J = JM$  and  $i \in [12 + 1, IMAX]$ , we have  $(i, j - 1) = (IMAX - 1 + 1, JM)$ . At the branch cut for the constant  $\xi$ -line  $i = 11$  and  $j \in [1, JM - 1]$ , we have  $i - 1 = 12$ . At the branch cut for the constant  $\xi$ -line  $i = 12$  and  $j \in [1, JM - 1]$ , we have  $i + 1 = 11$ .

The basic hydrofoil geometry and coordinates are shown in Figure 3. The equations of motion are those given in Section III except that the non-conservative form of the convective terms in the Navier-Stokes equations was used for this solution.

#### Translating Karman-Trefftz Airfoil

Typical results of the numerical solution are given in Figs. 4-9 for a Karman-Trefftz hydrofoil (Fig. 4) and in Figs. 10-11 for a circular cylinder hydrofoil. The airfoil was defined by 37 coordinate points and was located one chord below the free surface. The field size of the coordinate grid was  $54 \times 30$ . The "outer" boundary was located 10 chords from the airfoil.

Using Fig. 2,  $JM = 6$ ,  $11 = 10$  and  $12 = 45$ . Six  $\eta$ -lines were attracted to the airfoil with an amplitude of 1000 and a decay factor of 1.0.

Fig. 5 shows the effect of Froude number on the free surface movement. Three Froude numbers of 0.5, 1.0 and 2.0 are shown for a constant Reynolds number of 20 and at a time of 8.0. All three cases were accelerated gradually over a time of 4.0. Also, the same time step size ( $\Delta t = .01$ ) was used in all three cases. At a time of 8.0 the airfoil had moved 4 chords. Comparison of Figs. 5a, b, and c shows that the effect of the airfoil on the free surface increases as the Froude number increases, as would be expected since the Froude number is the ratio of inertial forces to gravitational forces.

Figs. 6-8 demonstrate the effect of Froude number on the drag, lift, and pressure. The time histories for three Froude numbers, 0.5, 1.0 and 2.0, are presented for  $Re = 20$  and  $t = 8.0$ . Referring to the peak drag in each figure, the drag is reduced as the Froude number is increased, because as the Froude number increases the free surface rises over the airfoil thus changing the local angle of attack. From Fig. 7, the lift changes drastically because as the Froude number decreases, the buoyancy forces become more dominant. From Fig. 8 the effect of Froude number on the pressure distribution can be seen. Buoyancy forces are dominant at a Froude number of 0.5 (Fig. 8a), and inertial forces are dominant at a Froude number of 2.0 (Fig. 8d).

Figure 9 shows the pressure distributions about the Karman-Trefftz airfoil for two Reynolds numbers,  $Re = 20$  and  $Re = 100$ . The constant parameters are  $F = 0.5$  and  $t = 6$ . The pressure coefficients for  $Re = 20$  are larger than the pressure coefficients for  $Re = 100$ . The lift coefficient for both cases is due mainly to the buoyancy forces.

#### Translating Circular Cylinder

Fig. 10 shows the coordinate system for a circular cylinder located one chord below the free surface at three times. The flow parameters are  $Re = 20$  and  $F = 0.5$ . Two wave peaks are shown on the free surface. The circular cylinder affects the free surface more than the airfoil, which should be expected. Fig. 11 shows the velocity vectors for the circular cylinder. At a time of 6, the stagnation point started to move up the front of the cylinder.

#### Oscillating Karman-Trefftz Airfoil

Results are presented in Figs. 12-14 for a hydrofoil in pitching, plunging, and longitudinal oscillation. All solutions are presented in the free stream-fixed coordinate reference frame. Also all solutions were run using the flow parameters,  $Re = 20$  and  $F = 1.0$ . The same coordinate system was used for all solutions. The Karman-Trefftz airfoil was placed at one chord below the free surface. The infinity boundary was located 10 chords from the airfoil.

In Fig. 12, the airfoil is moving in the negative x-direction. This solution is equivalent to the other solutions of previous sections. However, the hydrofoil is moving relative to the "outer" boundary. The coordinate lines close to the body are moving with the airfoil. The free stream-fixed reference frame clearly shows the fluid being pushed by the airfoil. Also, fluid is moving in at the trailing edge to fill the space evacuated by the airfoil.

In Fig. 13, the airfoil is moving toward the free surface. As the airfoil moves toward the free surface, fluid is pushed up and to the sides. Vortices are created at the leading edge and at the trailing edge of the airfoil because the fluid is moving from the upper side to the lower side. The fluid that is moved up by the airfoil disturbs the free surfaces by pushing up the free surface above the airfoil.

In Fig. 14, the airfoil is pitching  $5^\circ$  about its center chord. Three times ( $t = 1, 5, 8$ ) are shown. The airfoil takes a time of 10 to pitch from  $0^\circ$  to  $5^\circ$  and back to  $0^\circ$ . The vortices can be seen forming as the airfoil pitches.

#### Computer Time

Some of the solutions were generated on the UNIVAC 1106 single processor and the latest solutions were generated on the upgraded UNIVAC 1106 dual processor. There are many factors which determine the computer time required for a solution, for example, the way the object program is loaded in the computer code. The uncontracted coordinate system requires from 3 to 6 minutes to converge depending on the field size and convergence criteria. Depending on the type of attraction required, the contracted coordinate system took up to 30 minutes. The acceleration parameter for pressure was 1.8 and the acceleration parameter for velocity was 0.8. The constant of 0.1 was used in the pressure iteration on the body. At  $Re = 20$  and  $F = 1$ , the solution took 239 minutes to generate 600 time steps. The maximum number of iterations for a time step to converge was 11 at time step 313.

#### VI. Submerged Hydrofoil - Finite Channel Depth [11]

The only modification necessary to the submerged hydrofoil solution discussed in the previous section here was the change of the configuration in the physical plane to include inflow and outflow boundaries with a solid bottom between. In regard to the coordinate system, this change is merely a matter of changes in the input to the program, replacing the semi-circular outer boundary located at a great distance from the hydrofoil with a boundary consisting of three segments--inlet, outlet, and bottom. The undisturbed flow boundary conditions used on the semi-circular outer boundary were then replaced with undisturbed flow on the inlet and outlet segments, and free-slip boundary conditions on the solid bottom. Inviscid boundary conditions were

applied on the free surface, rather than viscous conditions as in Section V. The transformation configuration is the same as that used for the infinite depth channel as shown in Fig. 2.

The two configurations, shown in Fig. 15, were considered from the data supplied by Salvesen [9]. Fig. 16 shows the cross section of the hydrofoil. To define the hydrofoil, twelve locations along the chord were specified with the local thickness. To have the freedom to arbitrarily place points on the hydrofoil surface, the data for the hydrofoil was fitted to the general equation for a NACA modified four-digit airfoil. The resulting hydrofoil is shown in Fig. 16. Using a chord of 1.0, the maximum thickness of 0.345 chords is located at 0.32 chords from the leading edge. After investigating several airfoil shapes, the leading edge radius was chosen to be 0.04 chords and the trailing edge angle was chosen to be  $16.5^\circ$ . The resulting hydrofoil thickness distribution agrees closely with the twelve coordinate points that were given.

The field size was chosen to be  $62 \times 60$  with  $JH = 21$ ,  $I1 = 20$  and  $I2 = 53$ . The coordinate system was converged to  $10^{-6}$  using the SOR iterative method. Next, the uncontracted coordinate system was used as the initial guess for the contracted coordinate system. Eleven  $n$ -lines were attracted to the body. The first 10  $n$ -lines were attracted using an amplitude of 20,000 and a decay factor of 0.4, and the eleventh  $n$ -line was attracted using an amplitude of 250 and a decay factor of 0.2. Detail of the first 17  $n$ -lines is shown in Fig. 17. The results of viscous flow about the submerged hydrofoil for low Reynolds numbers are shown in Figs. 18-28. Three cases were run: The first case (Fig. 18) involved the deep-water configuration with  $Re = 100$  and  $F = 0.33$ . The second case (Figs. 19-23) presents results for the deep-water configuration with  $Re = 100$  and  $F = 2.0$ . Finally, the third case (Figs. 24-28) presents results for the shallow-water configuration with  $Re = 100$  and  $F = 2.0$ .

All three cases had several things in common. In each case the hydrofoil was accelerated from a velocity of zero over a time period of 4. For the first case the field size was  $62 \times 55$  and for the second and third cases the field size was  $62 \times 60$ . In each case,  $JH = 21$ ,  $I1 = 10$ , and  $I2 = 53$ . The time step size for each case was chosen to be 0.01.

The trailing edge pressure was calculated by extrapolation of the adjacent surface pressure. An inviscid condition was used on the free surface in each case. The free surface pressure was set equal to the atmospheric pressure, and the free surface velocity boundary conditions become

Convergence of the viscous solution was chosen to be dependent on the change of the velocity and the coordinate system at each iteration. When the change of velocity and the coordinate system became less than the convergence criteria of  $10^{-5}$  the solution for that time step was stopped at that iteration. The pressure change was not required to meet a convergence criteria, but the pressure was monitored.

The deep-water configuration with  $Re = 100$  and  $F = 0.33$  of Fig. 18 shows a vortex developing on the lower surface of the hydrofoil, and the leading edge stagnation point moving up the leading edge of the hydrofoil as a result of the small movement of the free surface for this low Froude number. This separation did not occur in the results for  $F = 2$  given below. Additional results at  $F = 0.33$  are given in Ref. 11.

The deep-water configuration with  $Re = 100$  and  $F = 2.0$  of Fig. 19 shows the large movement of the free surface. In Fig. 21, the pressure distribution is almost symmetrical, except for the slight movement of the leading edge stagnation point. The time history of the free surface shows the large movement of the free surface. Also one can see the movement of the first peak from the front of the hydrofoil to the rear of the hydrofoil.

The shallow-water configuration results with  $Re = 100$  and  $F = 2.0$  show the effect of the hydrofoil being close to the bottom. In Fig. 25 the leading edge stagnation point is moving down to the lower side of the hydrofoil. Also a slight separation is developing on the upper side of the hydrofoil. In Fig. 26, the effect of the hydrofoil being close to the bottom on the pressure can be seen.

The configuration of Figs. 24-28 corresponds to one of the test configurations of Ref. 9 (depth 0.99 ft., foil 0.15 ft. above bottom). However, the depth-Froude number in the present simulation is 1.09, while the experimental results of Ref. 9 had a depth-Froude number of 0.706 for this configuration. More significantly, the chord Reynolds number of this simulation is only 100, while that for the experimental results was about 200,000. Each of these discrepancies tends to shift the local disturbance aft in the simulation.

Both experimental results [10] and the present numerical solution indicate that the aft local disturbance moves aft as the Froude number increases (cf. Fig. 5). The Reynolds number effect in the present results is even greater, however. The local disturbance is broader and extends farther aft in the numerical results at the lower Reynolds number. At the same time, the initial rise forward of the hydrofoil is broader at the higher Reynolds number and extends farther forward.

Following this trend, it is conjectured that at low Reynolds numbers the forward propagation of the rise in surface level above the hydrofoil that occurs at high Reynolds numbers [9]

is rapidly damped by the strong viscous effects so that the rise is confined to the immediate vicinity of the hydrofoil. Furthermore, the front stagnation pressure on the hydrofoil increases as the Reynolds number decreases, since the strong viscous pull of the free stream on the flow being deflected around the hydrofoil is greater. These effects tend to produce a pronounced local upward deflection of the free surface in the immediate vicinity of the hydrofoil at low Reynolds numbers. The strong viscous pull of the free stream flow tends to shift this disturbance downstream and hence aft of the hydrofoil.

## VII. Hydrofoil in Free Surface [8]

The physical and transformed planes used in this solution are shown in Fig. 29. Since the hydrofoil is in the free surface, rather than submerged, the physical region is simply-connected, its boundaries being the wetted portion of the hydrofoil contour, 2 - 3, the free surface fore, 1 - 2, and aft, 3 - 4, and a remote semi-circular boundary, 1 - 4, located at a sufficient distance from the hydrofoil to be undisturbed by the flow. The transformed plane is a rectangle, with the wetted portion of the hydrofoil contour transforming to the upper horizontal side, the free surface fore and aft transforming to the left and right vertical sides, respectively, and the semi-circular remote boundary transforming to the lower horizontal side as indicated in Fig. 29. This configuration differs from that used for the submerged hydrofoil in that the physical region was doubly-connected with the submerged body.

As noted above, the curvilinear coordinates  $(\xi, \eta)$  are taken as the solution of two elliptic partial differential equations. The particular equations used in the present solution are those of [12], which differ from the original system of [5], used for the submerged hydrofoil, only in the form of the coordinate system control terms (the terms involving the functions  $P$  and  $Q$  below and in Eq. (2) above.) Thus  $\xi$  and  $\eta$  are determined by the solution of

$$\xi_{xx} + \xi_{yy} = (\xi_x^2 + \xi_y^2) P(\xi, \eta) \quad (14a)$$

$$\eta_{xx} + \eta_{yy} = (\eta_x^2 + \eta_y^2) Q(\xi, \eta) \quad (14b)$$

With reference again to Fig. 29, the boundary conditions for these equations are as follows:

- (a) on the wetted portion of the hydrofoil contour, 2 - 3 :  $\eta = \eta_2 = \text{constant}$ ,  $\xi$  varying monotonically from  $\xi_1$  to  $\xi_2$  ( $\xi_2 > \xi_1$ ) from 2 to 3.
- (b) on the free surface, 1 - 2, and 3 - 4 :  $\xi = \xi_1 = \text{constant}$  on 1 - 2,  $\xi = \xi_2 = \text{constant} > \xi_1$  on 3 - 4,  $\eta$  varying monotonically from  $\eta_1$  to  $\eta_2$  ( $\eta_2 > \eta_1$ ) from 1 to 2 and from 4 to 3.

(c) on the remote boundary,  $1 - 4$ .

$\eta = \eta_1 = \text{constant} < \eta_2$ .  $\xi$  varying monotonically from  $\xi_1$  to  $\xi_2$  from 1 to 4.

In the present application, the control functions,  $P$  and  $Q$ , are determined from the specified spacing of points on the hydrofoil contour and free surface, those on the body being concentrated near the free surface and those on the surface being concentrated near the hydrofoil as in Fig. 30. The details of this determination of  $P$  and  $Q$  are given in [8]. The resultant concentration of coordinate lines near the body and free surface is evident in Fig. 30.

In the initial stages of this study, the control functions,  $P$  and  $Q$ , were taken as sums of decaying exponentials that cause attraction of coordinate lines to specified lines and/or points as used for the submerged hydrofoil. Some of the results given below were obtained on coordinate systems using this type of control as will be noted. The new control procedure has the advantage of automating the control and eliminating the need for judgmental estimation of the attraction amplitudes and decay factors necessary to achieve a desired degree of line concentration.

With the current modification in the control functions, Eq. 2 in the transformed plane are replaced by

$$u_{\xi\xi} - 2Bx_{\xi\eta} + \gamma x_{\eta\eta} + \alpha Px_{\xi} + \gamma Qx_{\eta} = 0 \quad (15a)$$

$$u_{\eta\eta} - 2By_{\xi\eta} + \gamma y_{\eta\eta} + \alpha Py_{\xi} + \gamma Qy_{\eta} = 0 \quad (15b)$$

The boundary conditions for  $x$  and  $y$  are as follows:

(a) On the hydrofoil:

$x$  and  $y$  specified by the chosen spacing of points around the hydrofoil contour. These points move on the contour with time as a result of motion of the hydrofoil and also because of movement of the free surface-body contact points on the contour.

(b) On the free surface:

$x_{\xi} = 0$  initially, fixed thereafter,  $y$  from the surface movement, Eq. (10). (The first of these allows the points to slide along the free surface so that the coordinate lines are initially vertical at the free surface.)

(c) On the remote boundary:

$x$  and  $y$  fixed and specified by the chosen spacing of points along the remote boundary.

This point distribution on the body and remote boundary was taken according to equiangular spacing over the body and remote

boundary arcs in the earlier stages of the present investigation. Later an unequal spacing was used, with the angular separation of points varying on a sine curve, so that the closest spacing occurs adjacent to the free surface.

Since the free surface deforms in time, with consequent motion of its intersections with the hydrofoil contour, only the relative distribution of points on the hydrofoil contour is kept fixed. The points thus slide along the wetted portion of the hydrofoil while maintaining the same relative spacing from adjacent points as time progresses. This is accomplished by locating the points on the contour at fixed percentages of the angle subtended by the arc between the two intersections with the free surface. This subtended angle, of course, changes in time. When the hydrofoil oscillates, the movement follows the oscillating motion of the body as well.

The points on the free surface are initially determined by a Neumann boundary condition that requires the coordinate lines to be vertical at the moving surface. The local elevation of the surface is determined by the equations of motion for the free surface as discussed in Section III. The points thus slide along the free surface as the surface deforms in time.

Results of the numerical solution are presented for a circular cylinder hydrofoil in two flow configurations:

- (a) Accelerating translational motion parallel to the plane of the initially undisturbed flat free surface.
- (b) Oscillatory plunging motion normal to the plane of the initially undisturbed flat free surface.

In each case the axis of the cylinder is in the plane of the initially undisturbed flat free surface. The fluid is physically unbounded except by the free surface, with no disturbance remote from the hydrofoil.

In the translational case (a) the acceleration is linear, with the Reynolds and Froude numbers given by

$$R = 20t \quad F = 2t$$

these numbers being based on the cylinder diameter and current velocity.

For the plunging case the motion of the hydrofoil is sinusoidal with the elevation of the cylinder axis relative to the plane of the initially undisturbed free surface given by

$$y = A \sin\left(\frac{2\pi t}{P}\right) \text{ where } A \text{ and } P \text{ are the amplitude and period, respectively, of the motion. The velocity of the cylinder is thus}$$

$$\dot{y} = \frac{2\pi A}{P} \cos\left(\frac{2\pi t}{P}\right) \text{ and the Reynolds and Froude numbers are then given by } R = 20\dot{y} \text{ and } F = 2\dot{y}, \text{ respectively.}$$

In each case the coordinate system is of the form shown in Fig. 30 and discussed above in this section, with 37 points on the body and 30 points on the free surface on each side of the body. The remote boundary where the fluid is undisturbed is located at a radius of 10 cylinder diameters. The convergence acceleration parameters used were 1.0 for the momentum equations (7a-b), 1.8 for the Poisson equation (7c), 0.45 for the surface pressure equation (9), and 1.85 for the coordinate system equations (15). The iterative convergence criteria used were  $10^{-5}$  for the coordinate system and  $10^{-4}$  for the velocity and pressure.

The initial point distribution on the cylinder was determined by a sine curve, with points distributed asymmetrically and concentrated near each free surface contact point. The initial distribution on the free surface was determined by an exponential curve, with points concentrated near the body. It was found necessary to have the points adjacent to the free surface-body contact point approximately equidistant from the contact point else stability problems arose with the surface. The points move on both the hydrofoil and free surface as time passes, but the same relative distributions are maintained as discussed in the previous section.

As noted in the discussions above, the curvilinear coordinate system continually deforms as time progresses, always keeping a coordinate line coincident with the deforming free surface. This behavior is evident in Fig. 30 which shows the coordinate system at four times for the translating hydrofoil. The free surface rises in front of the hydrofoil, and the fore contact point slides up along the hydrofoil contour. At the rear of the hydrofoil, the surface falls, and the aft contact point moves downward.

Velocity vectors and the hydrofoil pressure distribution for this solution are shown at one time in Fig. 31. The vectors clearly show the fore and aft stagnation points to be well below the corresponding surface contact points on the hydrofoil. The pressure distribution shows a positive pressure spike adjacent to both contact points, but a smooth distribution elsewhere on the hydrofoil. This spike is due to numerical error resulting probably from the modeling of the contact point movement.

The initially undeformed coordinate system used in the oscillatory solution is shown in Fig. 32. A stronger concentration of lines near the free surface and hydrofoil contour was used in view of the results discussed above. Fig. 33 shows the temporal oscillation of the lift coefficient. The curve is seen to be deformed from a pure sinusoidal oscillation. After an initial rise, the force remains upward throughout the cycle.

Fig. 34 shows a series of plots of velocity vectors at several times during the cycle, while Fig. 35 shows the same thing, but in detail of the region around the right surface-body contact point. As the body rises initially, the fluid moves downward from the surface

and inward toward the void being left by the rising body. However, due to the viscous no-slip boundary condition, a vortex is created near the contact point ( $T = 0.01$  in Fig. 35). (A similar vortex, but of the opposite rotation is, of course, created off the left contact point.) These vortices move away from the body and decrease in intensity as the quarter-cycle is approached (cf.  $T = 0.11$  in Fig. 35).

At the quarter-cycle (0.157), the body reaches its highest point and then reverses its motion to move downward. This forces the fluid beneath the body to the sides. The beginning of this sideward motion can be seen at  $T = 0.17$  in Fig. 34 just beneath the body. At this time, inertia causes most of the fluid to still reflect the previous upward movement of the body. This inertial effect is evident also in the corresponding detail plot in Fig. 35, where the fluid adjacent to the body has reversed its motion and is moving downward with the body while the rest of the fluid motion is qualitatively similar to that at  $T = 0.15$  before the quarter-cycle.

As time passes, the influence of the downward motion of the body spreads progressively throughout the fluid so that more and more of the fluid acquires downward and sideward motion beneath the body, with consequent upward motion toward the surface (cf.  $T = 0.21$  and  $0.31$  in Fig. 34). This annihilates the vortices, and new vortices of opposite rotation to the original form just off each surface-body contact point (cf.  $T = 0.21$  in Fig. 35). These vortices also move away from the body and decrease in intensity as the body moves toward its lowest point at the three-quarter cycle time ( $T = 0.471$ ).

At this time the motion of the body again reverses, and the body starts back upward. This causes inward motion to begin just beneath the body ( $T = 0.49$  in Fig. 34) with upward motion adjacent to the body ( $T = 0.49$  in Fig. 35). This new pattern of motion then spreads out into the remainder of the fluid, competing initially with the inertially persisting motion from before the last body reversal. As at the quarter-cycle, the existing vortices are annihilated, and new ones of opposite rotation again form off the contact points (cf.  $T = 0.53$  in Fig. 35). The general fluid motion is again downward from the surface, with inward and upward motion beneath the rising body (cf.  $T = 0.61$  in Fig. 34) as at the beginning of the cycle.

The movement of the hydrofoil free surface contact points along the hydrofoil contour is modeled by a condition of continuity as discussed in detail in Ref. 8. Essentially this model causes the contact points to slide along the hydrofoil contour in response to a net imbalance of flow into the cell at the contact point. Net inflow will thus cause that contact point to slide upward along the contour. Another model based on a condition of zero stress at the contact point was also investigated but was found to be unsatisfactory as also discussed in Ref. 8.

Figs. 36 and 37 show the surface elevation and pressure at approximately the quarter, half, three-quarter, and full cycle times. The elevation curves show that the mean surface position is not flat, but is depressed in the vicinity of the body. This result is in qualitative agreement with a periodic boundary layer solution and experimental flow visualization results given in Schlichting [13] for a circular cylinder oscillating in an unbounded fluid. There it is shown that a mean secondary motion exists in which fluid moves from the sides toward the body (normal to the direction of oscillation) and then away from the body parallel to the oscillation direction (cf. Fig. 11.7 of [13]). In the present case this type of mean flow would be toward the body, parallel to the free surface, and then away from the surface beneath the body. This then would result in a mean surface depression.

#### VIII. Conclusion

The technique of numerically generated boundary-fitted coordinate systems is clearly an effective aid in treating flow problems involving both free surfaces and solid boundaries. With this technique the complication of the boundary shape is essentially removed from the problem. It is possible to obtain numerical solutions for viscous flow, with viscous boundary conditions on the free surface as well as on the solid body.

The research results presented in this report leave several problems unresolved. Regarding the submerged hydrofoil solution, the coordinate configuration used had a zero Jacobian between grid points in the field of calculation. This zero Jacobian made it difficult to contract coordinate lines near the branch. Also, an ambiguity in the finite difference expressions for the cross derivatives at the point of zero Jacobian led to ambiguous results in the coordinate solutions. Thirdly, the coordinate control functions were found to be inadequate in controlling coordinate lines in the field. An arbitrary change in the coordinate control often led to unpredictable results for the physical coordinates. Some progress was made in this area during the latter stages concerning the hydrofoil in the free surface with the incorporation of an automated control. Finally, at project termination, the solution could not be run successfully for Reynolds numbers greater than 100 for the submerged hydrofoil. The combination of the coordinate contraction functions and the field point with a zero Jacobian is believed to be the cause of a pressure source that occurred at the trailing edge of hydrofoils for  $Re > 100$ . Finally, since higher Reynolds numbers were not obtained, the method could not be verified with the experimental data available for submerged hydrofoils.

The presence of a zero Jacobian in the field is not a universal feature in the boundary-fitted coordinate systems, but is peculiar to the type of configuration adopted for the transformed plane in the submerged hydrofoil solution. This configuration did have certain

advantages as noted in spite of the presence of the zero Jacobian. The configurations used for the hydrofoil in the free surface (and for the external flow about airfoils in other studies) do not have any zeros of the Jacobian in the field. Further study would be necessary to develop better configurations for the submerged hydrofoil case.

Concerning the hydrofoil in the surface, the coordinate configuration was less of a problem, and no zeros of the Jacobian occurred in the field. The results given in the present work are all at very low Reynolds number, but the solution can in principle be run at any Reynolds number by increasing the attraction of the coordinate lines to the body and free surface at higher Reynolds numbers in order to maintain a sufficient number of lines in the viscous layers. Such a procedure is currently under investigation in connection with the flow about airfoils. The problem is made more difficult, however, with increasing Reynolds number. More investigation of the control of the coordinate system so that sufficiently close spacing is maintained near the free surface as it deforms is necessary, as is further study of the modeling of the hydrofoil-free surface contact point movement.

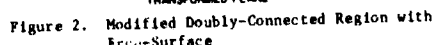
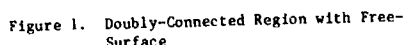
Finally, the hydrofoil and/or bottom could be allowed to deform in time without complicating the problem unduly. This is because all of the computation is done on the fixed rectangular transformed grid regardless of the shape or movement of the physical boundaries. Wind shear on the free surface could also be added by a change in surface boundary conditions to include applied external shear as well as pressure.

#### References

1. Thompson, J. F., Thames, F. C., and Mastin, C. W., "Automatic Numerical Generation of Body-fitted Curvilinear Coordinate System for Field Containing any Number of Arbitrary Two-Dimensional Bodies," *Journal of Computational Physics*, 15, 299 (1974).
2. Thompson, J. F., Thames, F. C., Mastin, C. W., "TOMCAT - A Code for Numerical Generation of Boundary-Fitted Curvilinear Coordinate Systems on Fields Containing any Number of Arbitrary Two-Dimensional Bodies," *Journal of Computational Physics*, 24, 274 (1977).
3. Thames, F. C., Thompson, J. F., et. al., "Numerical Solutions for Viscous and Potential Flow about Arbitrary Two-Dimensional Bodies using Body-Fitted Coordinate Systems," *Journal of Computational Physics*, 24, 245 (1977).
4. Hodge, J. K., "Numerical Solution of Incompressible Laminar Flow about Arbitrary Bodies in Body-Fitted Curvilinear Coordinates," Ph.D. Dissertation, Mississippi State University, Mississippi State, Mississippi (1975).



- Note: In the interest of space, all figures have been made small, and consequently, some scales are difficult to read. Therefore, extreme ordinate values have been added in larger type. Larger versions of all figures can be found in References 8 and 11, available from Mississippi State University through the second author.



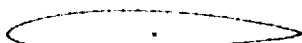
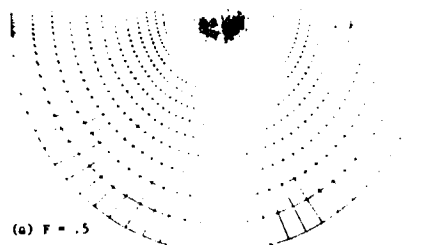
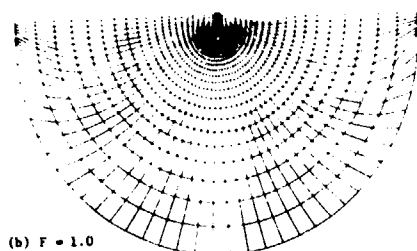


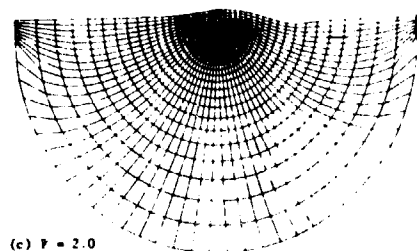
Figure 4. Karman-Trefftz Airfoil



(a)  $F = 0.5$

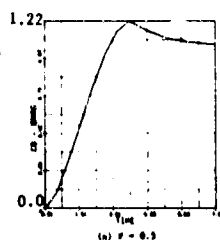


(b)  $F = 1.0$



(c)  $F = 2.0$

Figure 5. Coordinate system for three Froude numbers,  $Re = 20$ ,  $t = 8.0$  - Karman-Trefftz Airfoil located 1 chord below free surface.



(a)  $F = 0.5$

Figure 6. Time history of drag for three Froude numbers,  $Re = 20$  - Karman-Trefftz Airfoil located 1 chord below free surface.

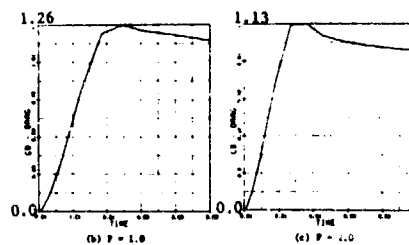
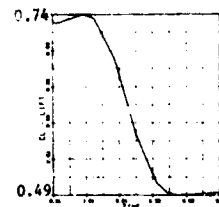


Figure 6. Continued



(a)  $F = 0.5$

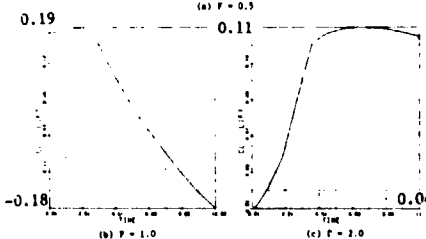
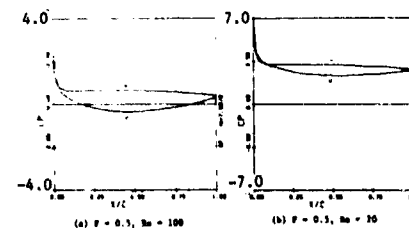
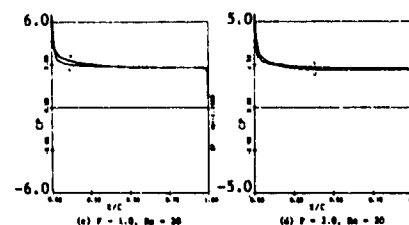


Figure 7. Time history of lift for three Froude numbers,  $Re = 2.0$  - Karman-Trefftz Airfoil located 1 chord below free surface.



(a)  $F = 0.5$ ,  $Re = 100$

(b)  $F = 0.5$ ,  $Re = 10$



(c)  $F = 1.0$ ,  $Re = 100$

(d)  $F = 1.0$ ,  $Re = 10$

Figure 8. Pressure distribution for various Reynolds and Froude numbers at  $t = 8.0$  - Karman-Trefftz Airfoil located 1 chord below free surface.

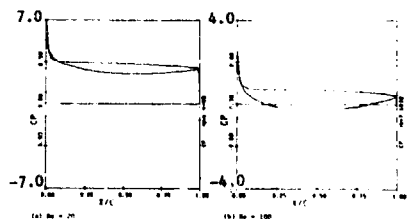
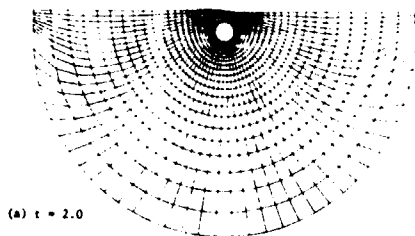
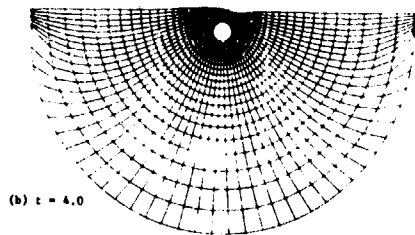


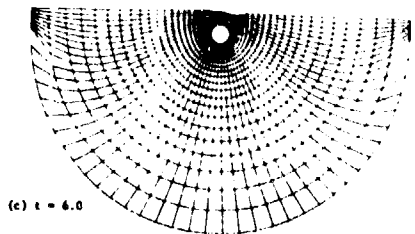
Figure 9. Pressure distribution for two Reynolds numbers,  $F = 0.5$ ,  $t = 6.0$  - Karman-Trefftz Airfoil located 1 chord below a free surface.



(a)  $t = 2.0$



(b)  $t = 4.0$



(c)  $t = 6.0$

Figure 10. Coordinate system at three times,  $Re = 20$ ,  $F = 0.5$  - Circular cylinder located 1 chord below free-surface.

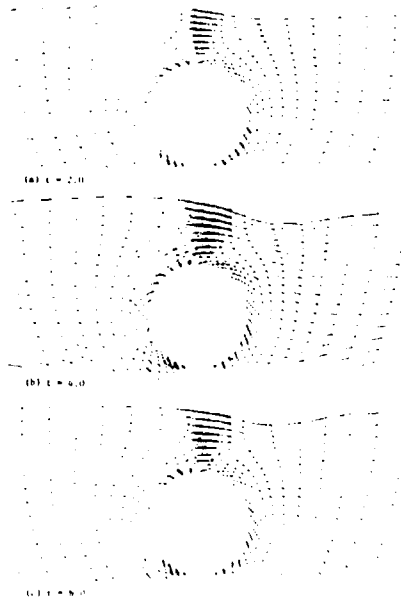


Figure 11. Velocity vector field at three times,  $Re = 20$ ,  $F = 0.5$  - Circular cylinder located 1 chord below free-surface.



Figure 12. Velocity vector field of Karman-Trefftz Airfoil translating in the negative  $x$  - direction.

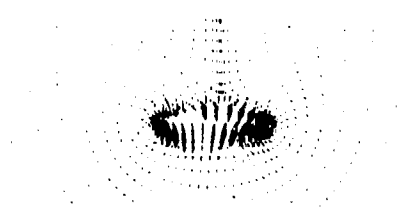


Figure 13. Velocity vector field of Karman-Trefftz Airfoil translating toward free surface,  $Re = 20$ ,  $F = 1.0$  and  $t = 1.75$  (free stream-fixed coordinates).

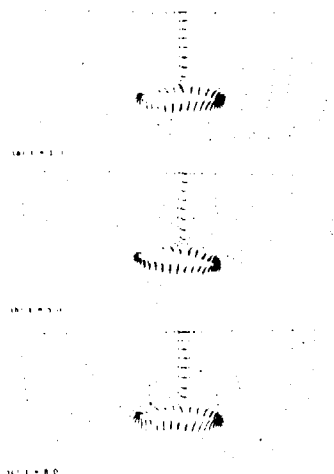


Figure 14. Velocity vector field of Karman-Trefftz slowly pitching  $5^\circ$  about its center chord at three times,  $Re = 20$ ,  $F = 1.0$  (free stream-fixed coordinates).

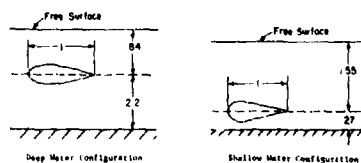
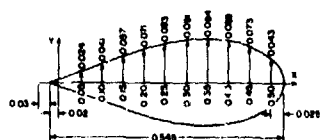


Figure 15. Deep and Shallow Water Configurations (Non-Dimensional)



Test Hydrofoil (Dimensions in Feet)



Figure 16. NACA Airfoil approximating the test hydrofoil. Chord = 1, maximum thickness = 0.345 located at 32% chord, leading edge radius = 0.04, and trailing angle =  $16.5^\circ$ .



Figure 17. Coordinate System - First 17  $\eta$ -lines

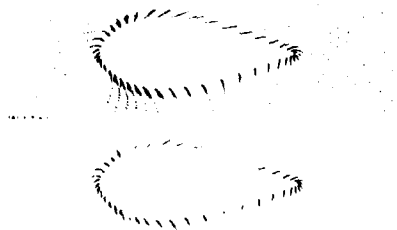


Figure 18. Velocity vector field at two times showing close-up of body,  $Re = 100$ ,  $F = 0.33$  - Airfoil located 0.841 chords below free surface and 2.2 chords from bottom.

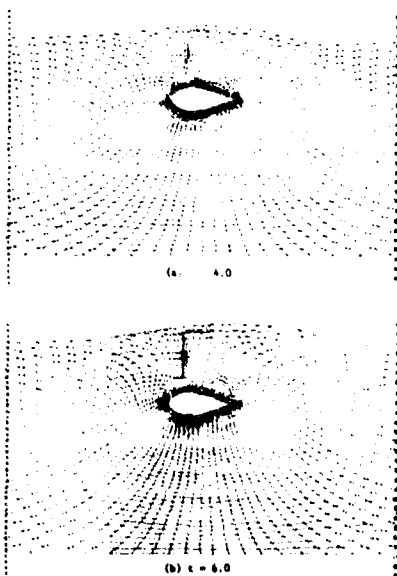


Figure 19. Coordinate system at two times,  $Re = 100$ ,  $F = 2.0$  - Airfoil located 0.841 chords below free surface and 2.2 chords from bottom.

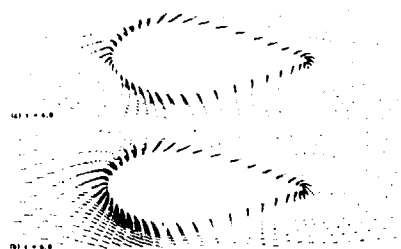


Figure 20. Velocity vector field at two times showing close-up of body,  $Re = 100$ ,  $F = 2.0$  - Airfoil located 0.841 chords below free-surface and 2.22 chords from bottom.

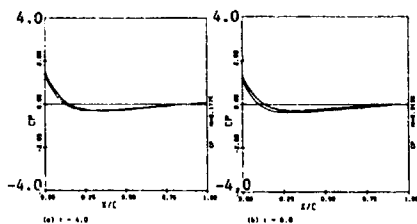


Figure 21. Pressure distribution at two times,  $Re = 100$ ,  $F = 2.0$  - Airfoil located 0.841 chords below free surface and 2.22 chords from bottom.

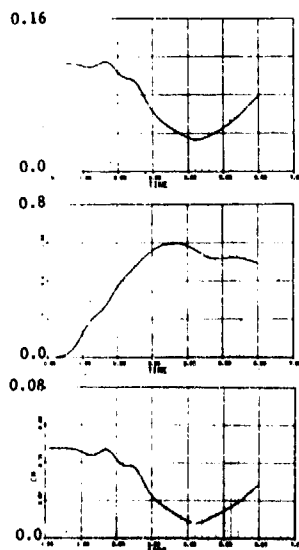


Figure 22. Time history of lift, drag and leading edge moment,  $Re = 100$ ,  $F = 2.0$  - Airfoil located 0.841 chords below free surface and 2.2 chords from bottom.

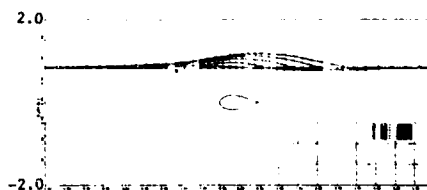


Figure 23. Time history of free-surface movement,  $Re = 100$ ,  $F = 2.0$  - Airfoil located 0.841 chords below free-surface and 2.22 chords from bottom.

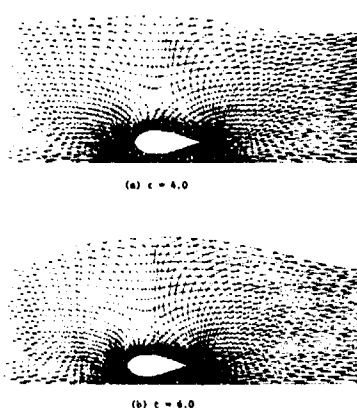


Figure 24. Coordinate system at two times,  $Re = 100$ ,  $F = 2.0$  - Airfoil located 1.56 chords below free surface and 0.27 chords from bottom.

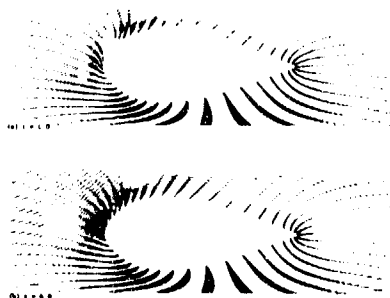


Figure 25. Velocity vector field at two times showing close-up of body,  $Re = 100$ ,  $F = 2.0$  - Airfoil located 1.56 chords below free-surface and 0.27 chords from bottom.

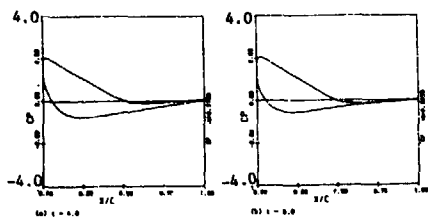


Figure 26. Pressure distribution at two times,  $Re = 100$ ,  $F = 2.0$  - Airfoil located 1.56 chords below free surface and 0.27 chords from bottom.

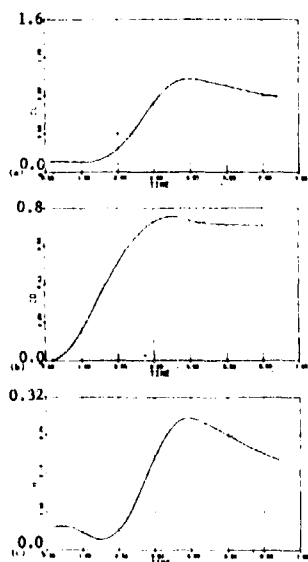


Figure 27. Time history of lift, drag and leading edge moments,  $Re = 100$ ,  $F = 2.0$  - Airfoil located 1.56 chords below free surface and 0.27 chords from bottom.

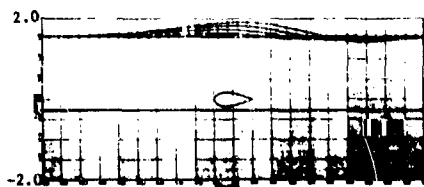


Figure 28. Time history of free-surface movement,  $Re = 100$ ,  $F = 2.0$  - Airfoil located 1.56 chords below free-surface and 0.27 chords from bottom.

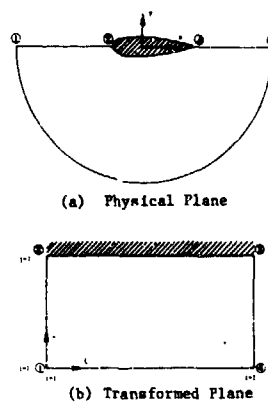


Figure 29. Relation Between Physical and Transformed Planes

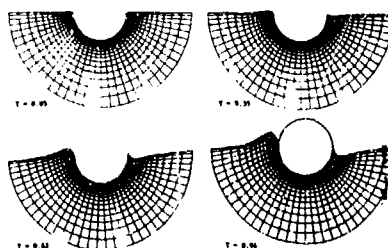


Figure 30. Deforming Coordinate System - Translating Hydrofoil

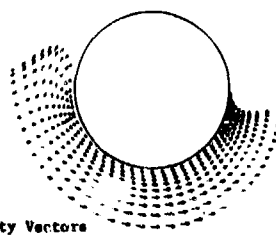
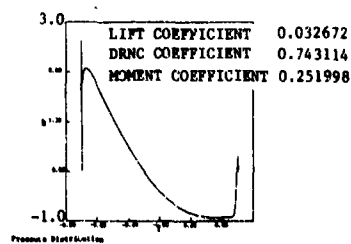


Figure 31. Flow Solution - Translating Hydrofoil.  $T = 0.84$

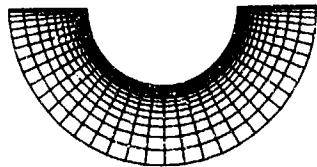


Figure 32. Initial Coordinate System - Plunging Hydrofoil

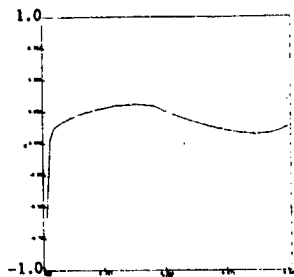


Figure 33. Lift Coefficient - Plunging Hydrofoil

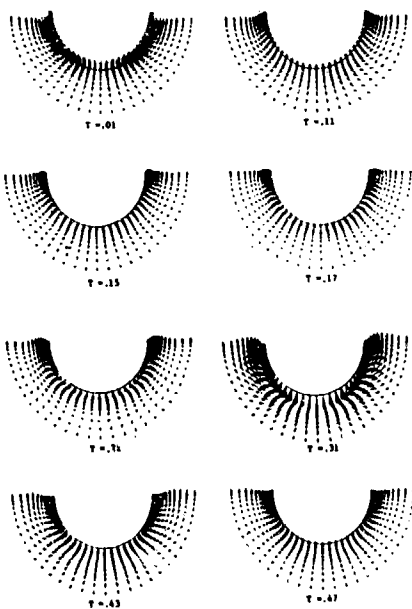


Figure 34. Velocity Vectors - Plunging Hydrofoil (0.001 Amplitude, 0.628 Period)

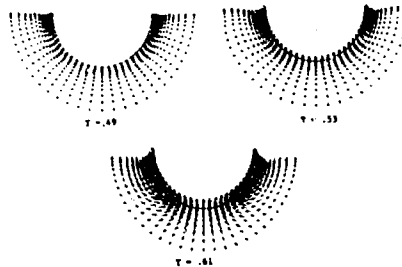


Figure 34. Continued

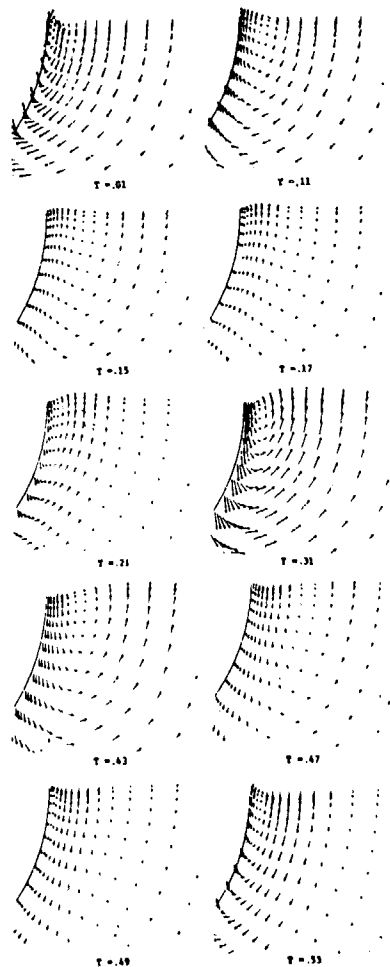


Figure 35. Detail of Surface - Body Contact Region - Plunging Hydrofoil (0.001 Amplitude, 0.628 Period)

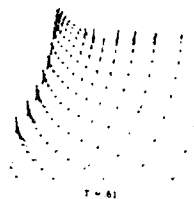


Figure 35. Continued

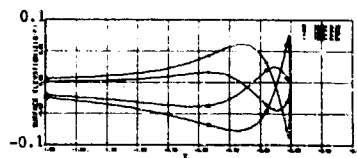


Figure 36. Surface Elevation - Plunging Hydrofoil (0.001 Amplitude, 0.628 Period)

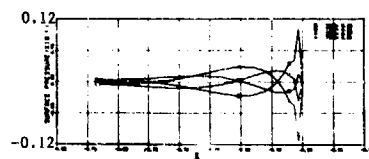


Figure 37. Surface Pressure - Plunging Hydrofoil (0.001 Amplitude, 0.628 Period)



# FINITE-DIFFERENCE COMPUTATIONS USING BOUNDARY-FITTED COORDINATES FOR FREE-SURFACE POTENTIAL FLOWS GENERATED BY SUBMERGED BODIES

H. J. Hausling and R. M. Coleman  
David W. Taylor Naval Ship Research and Development Center  
Bethesda, Maryland 20864

## Abstract

Finite-difference techniques are used with boundary-fitted coordinates to compute the two-dimensional unsteady potential flow generated by a circular cylinder in motion below a free water surface. Both linearized and nonlinear boundary conditions are employed for swaying and translating cylinders. The time-dependent physical region is transformed into an H-shaped computational region. Since the geometry of the flow region is not known in advance, but is part of the solution, the transformation must be computed simultaneously with the flow field for each time step. When nonlinear free-surface boundary conditions are used, a numerical filtering procedure is needed to eliminate numerical instability. A comparison of linear results for surface elevation and forces with existing steady-state solutions shows that accurate results can be obtained with such a numerical scheme. Nonlinear results indicate that the scheme is useful for analyzing nonlinear free-surface flows involving nonbreaking waves.

## I. Introduction

In a previous paper Hausling and Van Eseltine [1] discussed the application of finite-difference methods to two-dimensional potential flows generated by pressure distributions moving over a free water surface. Such unsteady problems were solved with a scheme which combined a numerical solution of the Laplace equation with numerical approximations to the time-dependent free-surface boundary conditions. Both linear and nonlinear boundary conditions were considered. In the linear case the Laplace equation was solved in a rectangular region. In the nonlinear case, the physical region, bounded above by the wavy free surface, was transformed into a rectangle to facilitate the numerical solution of the Laplace equation.

When the flow is generated by a body rather than by a surface pressure distribution, the numerical problem is more difficult. The geometry, even in the linear case, is much more complex, and the simple transformation used in [1] for the nonlinear problem cannot be applied. Such complex geometries are often treated with a rectangular finite-difference

grid using finite-difference formulae for unequal mesh spacing (irregular stars) at the boundaries as in the marker-and-cell method [2]. Irregular stars can sometimes be handled efficiently with imbedding techniques [3]. In another approach, which is used in the present work, numerical transformations map arbitrary geometries into rectangular regions [4]. The resulting boundary-fitted coordinate systems simplify the application of boundary conditions at curved boundaries, are applicable to three-dimensional problems, and are particularly useful with time-dependent geometries such as those found with unsteady nonlinear water-wave problems.

This paper describes the application of boundary-fitted coordinates to the computation of unsteady potential flows generated by a circular cylinder in swaying or translating motion below a free surface. Both linear and nonlinear problems have been considered.

In the nonlinear case, the initial numerical scheme was found to be unstable. Therefore, a numerical filtering scheme proposed by Shapiro [5] and used by Longuet-Higgins and Cokelet [6] was used to stabilize the calculations. Comparison of the linear results for surface elevation and forces with solutions obtained by other methods indicates that these finite-difference techniques can yield accurate results. Results for nonlinear problems indicate that the method is useful for analyzing nonlinear free-surface flows as long as wave breaking does not occur.

## II. Mathematical Formulation

### The Initial/Boundary-Value Flow Problem

Consider a circular cylinder in motion in water of depth  $d$  with submergence  $h$  below a free surface as shown in Figure 1. An  $(x,y)$ -coordinate system is chosen with the origin in the undisturbed free surface. The coordinate system may be fixed or it may move with the body. It is assumed that the flow is irrotational and that the fluid is incompressible and lacks surface tension. It is also assumed that the surface elevation can be described at any time  $t$  by specifying  $y$  as a single-valued function of  $x$ :  $y = Y(x,t)$ . This assumption is made for convenience and is not valid if the

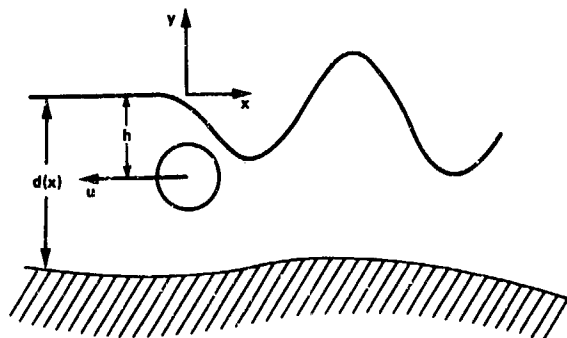


Figure 1. Body in Motion in Water of Depth  $d(x)$ .

waves approach breaking conditions.

The variables are nondimensionalized according to the scheme

$$\begin{aligned} (x', y') &= L(x, y), \quad t' = Lt/U, \\ \phi' &= LU\phi, \quad p' = \rho U^2 p, \quad Y' = LY \end{aligned} \quad (1)$$

where the primes denote dimensional variables,  $\phi(x, y, t)$  is the velocity potential,  $p$  is the pressure,  $\rho$  is the density, and  $U$  and  $L$  are characteristic speed and length scales associated with the body.

The initial/boundary-value problem is defined by

$$\phi_{xx} + \phi_{yy} = 0, \quad -\infty < x < \infty, \quad -d < y < Y \quad (2)$$

$$Y_t = \delta u(t) Y_x - \phi_x Y_x + \phi_y \quad \text{at } y=Y \quad (3)$$

$$\phi_t = \delta u(t) \phi_x - Y/Fr^2 - (\phi_x^2 + \phi_y^2)/2 \quad \text{at } y=Y \quad (4)$$

$$\nabla \phi \cdot \hat{n} = \begin{cases} 0 & \text{at } y = -d \\ \hat{v} \cdot \hat{n} & \text{at the body surface} \end{cases} \quad (5)$$

$$\phi_x = 0 \quad \text{at } x = \pm\infty \quad (6)$$

$$\phi = \phi_0, \quad Y = Y_0 \quad \text{at } t=0 \quad (7)$$

The subscripts  $x$ ,  $y$ , and  $t$  denote differentiation. The velocity of the body is  $\vec{V}(t)$  with horizontal component  $u$ . For a reference frame moving with horizontal speed  $u$ ,  $\delta=1$  and appropriate convective terms are present in (3) and (4). For a fixed frame,  $\delta=0$  and those terms are absent. The dimensionless parameter is the Froude number

$$Fr = U/(gL)^{1/2} \quad (8)$$

where  $g$  is the gravitational acceleration. The unit normal vector to a boundary is

represented by  $\hat{n}$ . Arbitrary initial conditions are represented by  $\phi_0$  and  $Y_0$ .

The dynamic pressure on the body surface can be computed from the Bernoulli equation without the hydrostatic term as

$$p = -\phi_t + \delta u \phi_x - (\phi_x^2 + \phi_y^2)/2 \quad (9)$$

The resistance and lift coefficients are

$$R = \text{resistance}/\rho LU^2 = -\int \hat{p} \cdot \hat{i} \, ds \quad (10)$$

$$L = \text{lift}/\rho LU^2 = \int \hat{p} \cdot \hat{j} \, ds \quad (11)$$

where  $\hat{i}$  and  $\hat{j}$  are unit vectors in the  $x$ - and  $y$ -directions, respectively, and where the integrations are over the body surface.

When wave slopes are small, the linearized free-surface boundary conditions

$$\left. \begin{aligned} Y_t &= \delta u Y_x + \phi_y \\ \phi_t &= \delta u \phi_x - Y/Fr^2 \end{aligned} \right\} \quad \text{at } y=0 \quad (12)$$

often provide sufficient accuracy. Similarly, if the body displacements are small, the body boundary condition in (6) can be applied at the mean body position.

#### The Transformation

To simplify the numerical solution of the problem, the time-dependent physical region (Figure 1), cut off suitably far upstream and downstream, is transformed to a time-dependent computational region which, as shown in Figure 2, is composed solely of rectangles. The body is mapped onto the slit  $LE$ , the free surface onto  $AB$ , the bottom of the water onto  $IH$ , the upstream boundary onto  $AH$  and  $JI$ , and the downstream boundary onto  $BC$  and  $GH$ . The boundaries  $JKLMN$  and  $CDEFG$  represent cuts within the fluid.

Similar transformations represented by

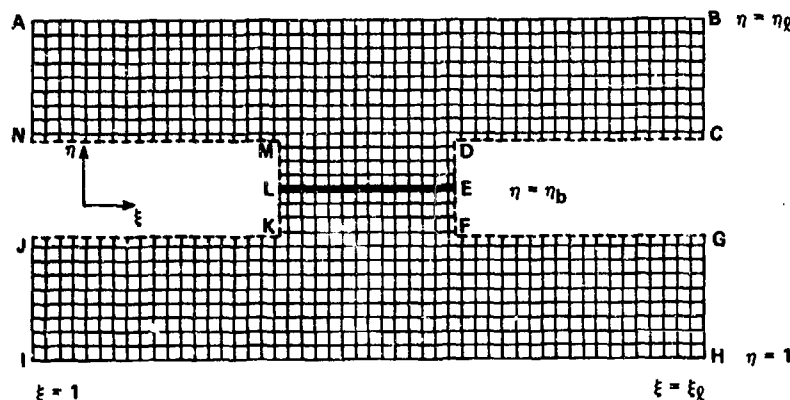


Figure 2. The Transformed Computational Region.

$$\xi = \xi(x, y, t) \quad \eta = \eta(x, y, t) \quad (13)$$

have been computed by Thompson et al [4] as solutions to the Poisson equations

$$\xi_{xx} + \xi_{yy} = P(\xi, \eta, t) \quad (14)$$

$$\eta_{xx} + \eta_{yy} = Q(\xi, \eta, t) \quad (15)$$

with appropriate boundary conditions. The source functions  $P$  and  $Q$  are specified such that an efficient numerical scheme results. The use of the H-shaped region in Figure 2 is an extension of the work of Thompson and his co-workers which, as will be seen, leads to a numerical scheme with nice properties for the problems under consideration.

For computational purposes, the generating system (14) and (15) is transformed to the computational space by interchanging dependent and independent variables to yield

$$\alpha \xi_{\xi\xi} - 2\beta \xi_{\xi\eta} + \gamma \eta_{\eta\eta} + J^2(P\xi + Q\eta) = 0 \quad (16)$$

$$\alpha \eta_{\xi\xi} - 2\beta \eta_{\xi\eta} + \gamma \eta_{\eta\eta} + J^2(P\eta + Q\xi) = 0 \quad (17)$$

where

$$\begin{aligned} \alpha &= x_\eta^2 + y_\eta^2 & \beta &= x_\xi x_\eta + y_\xi y_\eta \\ \gamma &= x_\xi^2 + y_\xi^2 & J &= x_\xi y_\eta - x_\eta y_\xi \end{aligned} \quad (18)$$

The transformation can then be determined by solving (16) and (17) subject to the following boundary conditions: The  $(x, y)$ -coordinates of the free surface are specified on AB (Figure 2), the coordinates of the body are given on LE (top and bottom), the coordinates of the lower boundary are given on HI, and the coordinates of the upstream and downstream boundaries are specified on AN, JI, BC, and GH. Reentrant-type boundary conditions are applied on the cuts as follows: The  $(x, y)$ -coordinates on CD match those on GF; the boundary pairs MN and

KJ, ML and KL, and DE and FE are similarly matched.

For a circular cylinder in water of constant depth this transformation yields the coordinate system displayed in Figure 3. Lines of constant  $\eta$  extend between the upstream and downstream boundaries except near the body which they encircle. Lines of constant  $\xi$  run between the free surface and the bottom of the water except where they intersect the body surface. The coordinate system is cylindrical near the body but also conforms to the shape of the region occupied by the water.

Again for computational reasons, the governing equations and boundary conditions are transformed to the  $(\xi, \eta)$ -coordinate system. Equation (2) is rewritten

$$\alpha \phi_{\xi\xi} - 2\beta \phi_{\xi\eta} + \gamma \phi_{\eta\eta} + \sigma \phi_\eta + \tau \phi_\xi = 0 \quad (19)$$

where

$$\sigma = J^2 Q \quad \tau = J^2 P \quad (20)$$

Equations (3) and (4) transform to

$$(Y_t)_{x=\text{constant}} = [\delta u - (y_\eta \phi_\xi - y_\xi \phi_\eta) / J] y_\xi / \quad (21)$$

$$x_\xi + (x_\xi \phi_\eta - x_\eta \phi_\xi) / J \quad \text{at } \eta = \eta_b$$

$$(\phi_t)_{\xi, \eta=\text{constant}} = x_\xi (\phi_\xi y_\eta - \phi_\eta y_\xi) / J - y_\xi (\phi_\xi x_\eta$$

$$- \phi_\eta x_\xi) / J + \delta u (y_\eta \phi_\xi - y_\xi \phi_\eta) / J - Y / Fr^2 \quad (22)$$

$$- [(y_\eta \phi_\xi - y_\xi \phi_\eta)^2 + (x_\xi \phi_\eta - x_\eta \phi_\xi)^2] / (2J^2)$$

$$\text{at } \eta = \eta_b$$

Since the coordinate system is time dependent, time derivatives of the  $x$ - and  $y$ -coordinates appear in (22). At the upstream and downstream boundaries (6) is replaced by

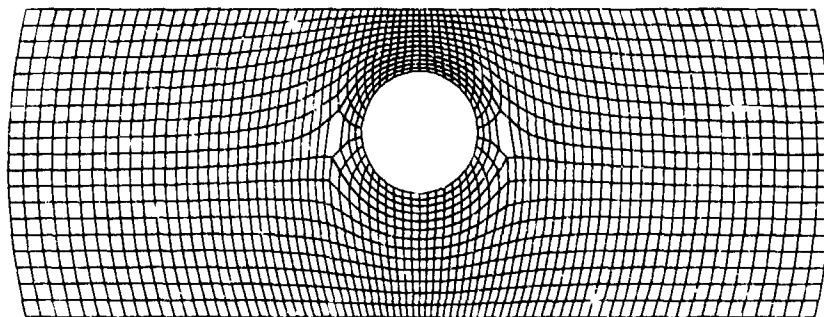


Figure 3. The Boundary-Fitted Coordinate System as it Appears in Physical Space for Both the Linear Problem and the Nonlinear Problem at  $t=0$ .

$$y_n \phi_{\xi} - y_{\xi} \phi_n = 0 \text{ at } \xi = \xi_1 \text{ and } \xi = \xi_2 \quad (23)$$

The normal derivative of  $\phi$  at a boundary can be written in the form (ref. [7])

$$\nabla \phi \cdot \hat{n} = [\phi_{\xi}(g'y_n + x_n) - \phi_n(g'y_{\xi} + x_{\xi})] / [J(1+g'^2)^{1/2}] \quad (24)$$

where  $g' = dy/dx$  is the slope of the boundary. By multiplying numerator and denominator by  $x_{\xi}$ , equation (24) can be rewritten in the form

$$\nabla \phi \cdot \hat{n} = (\phi_{\xi} B - \phi_n) / (J y^{1/2}) \quad (25)$$

Thus (5) becomes

$$(\phi_{\xi} B - \phi_n) / (J y^{1/2}) = \begin{cases} 0 & \text{at } n = n_1 \\ \vec{v} \cdot \hat{n} & \text{at } n = n_b \end{cases} \quad (26)$$

Since the shape of the fluid region is not known in advance but is part of the solution, the transformation cannot be carried out in advance. Equations (16) and (17), which generate the transformation, must be solved at each time in conjunction with the solution of the fluid flow problem (19), (21)-(23), and (26).

### III. The Numerical Scheme

This section presents the numerical aspects of both the transformation and flow problem solution. Further details concerning the numerical transformation can be found in ref. [8].

The domain of integration in the  $(\xi, n)$ -plane is replaced by a uniform network of points specified by  $(i, j = 1, n_j = j)$ , with  $i=1, \dots, 149$  and  $j=1, \dots, 28$  (Figure 2). The differential equations are replaced by difference equations involving the values of the variables at these grid points.

To compute the transformation, equations

(16) and (17) are replaced by central difference formulae yielding

$$\begin{aligned} \begin{Bmatrix} x_{i,j} \\ y_{i,j} \end{Bmatrix} &= \left[ (a_{i,j} + j^2_{i,j} p_{i,j}/2) \begin{Bmatrix} x_{i+1,j} \\ y_{i+1,j} \end{Bmatrix} \right. \\ &\quad + (a_{i,j} - j^2_{i,j} p_{i,j}/2) \begin{Bmatrix} x_{i-1,j} \\ y_{i-1,j} \end{Bmatrix} \\ &\quad + (y_{i,j} + j^2_{i,j} q_{i,j}/2) \begin{Bmatrix} x_{i,j+1} \\ y_{i,j+1} \end{Bmatrix} \\ &\quad \left. + (y_{i,j} - j^2_{i,j} q_{i,j}/2) \begin{Bmatrix} x_{i,j-1} \\ y_{i,j-1} \end{Bmatrix} \right] \\ &\quad - (B_{i,j}/2) \begin{Bmatrix} x_{i+1,j+1} + x_{i-1,j-1} - x_{i-1,j+1} \\ y_{i+1,j+1} + y_{i-1,j-1} - y_{i-1,j+1} \\ -x_{i+1,j-1} \\ -y_{i+1,j-1} \end{Bmatrix} / 2(a_{i,j} + y_{i,j}) \end{aligned} \quad (27)$$

where  $a_{i,j}$ ,  $B_{i,j}$ ,  $y_{i,j}$  and  $j_{i,j}$  are central difference approximations to (18).

The transformation has singularities at the points M, K, O, and F in the transformed plane (Figure 2) which correspond to only two points in physical space. With zero source terms,  $(P=Q=0)$ , very large grid cells would be present near these points. The source terms are specified so as to attract grid points toward these singularities to improve the resolution in their neighborhood. Source terms of exponential form as suggested by Thompson et al [9] are used for this purpose.

For convenience, equation (27) is solved by successive overrelaxation (SOR). Similar difference equations have been solved with alternating-direction implicit schemes by Ghia, Ghia, and Stauder [10]. Although the present calculations were carried out on a CDC 6400 computer, other research [11] has shown that

with a vector processing computer such as the Texas Instruments Advanced Scientific Computer mesh generation equations such as (27) can be solved very efficiently using SOR by sweeping the mesh in the so-called "red-black" manner.

Equation (19) is replaced by the difference equation

$$\begin{aligned} \phi_{i,j} = & [(a_{i,j} + \tau_{i,j}/2)\phi_{i+1,j} \\ & + (a_{i,j} - \tau_{i,j}/2)\phi_{i-1,j} + (\gamma_{i,j} + \sigma_{i,j}/2)\phi_{i,j+1} \\ & + (\gamma_{i,j} - \sigma_{i,j}/2)\phi_{i,j-1} - (b_{i,j}/2)(\phi_{i+1,j+1} \\ & - \phi_{i-1,j-1} - \phi_{i+1,j-1} - \phi_{i-1,j+1})]/2(a_{i,j} + \tau_{i,j}) \end{aligned} \quad (28)$$

which is also solved with SOR.

Euler's modified method of time differencing is used to replace the free-surface boundary conditions (21) and (22) by

$$Y_i^{n+1} = Y_i^n + \Delta t(F_i^{n+1} + F_i^n)/2 \quad (29)$$

and

$$\phi_{i,n_z}^{n+1} = \phi_{i,n_z}^n + \Delta t(G_i^{n+1} + G_i^n)/2 \quad (30)$$

where the superscripts refer to time levels,  $\Delta t$  is the time increment, and  $F_i$  and  $G_i$  are finite-difference approximations to the right-hand sides of (21) and (22).

The implicit equations (29) and (30) are solved iteratively for  $\phi$  and  $Y$  at the advanced time level. The iterative solution of these equations is combined with the iterative solution for the velocity potential and the mesh point coordinates. A time advancement of the surface elevation and the potential on the surface according to (29) and (30) is followed by an updating of the grid point coordinates according to (27) and then an adjustment of  $\phi$  below the surface according to (28) and finite-difference approximations to the boundary conditions (23) and (26). Thus the new grid point distribution and flow field are computed simultaneously. The iteration procedure is started with initial estimates of  $Y_i^{n+1}$ ,  $\phi_{i,j}^{n+1}$ ,  $\phi_{i,j}^{n+1}$ , and  $Y_i^{n+1}$  obtained by extrapolation from two previous time levels. The iterations are halted when the percentage change of  $x$ ,  $y$ ,  $\phi$ , and  $Y$  from iteration to iteration is less than some specified small number, usually on the order of 0.1%.

When linearized boundary conditions are applied, the Laplace equation is solved in a time-independent region in  $(x,y)$ -space. Thus, for the linear case, the grid system need be generated only once.

To eliminate the numerical instability encountered earlier by Haussling and Van Eseltine [1] using a similar nonlinear numerical scheme, a filtering procedure is applied. After each advancement of

$Y_i^{n+1}$  and  $\phi_{i,n_z}^{n+1}$ , new values of the quantities are computed according to the smoothing formula

$$f_i^1 = [-f_{i+2} - f_{i-2} + 4(f_{i+1} + f_{i-1}) + 10f_i]/16 \quad (31)$$

Such filtering schemes were discussed by Shapiro [5]. They were used successfully by Longuet-Higgins and Cokelet [6] to eliminate a similar instability encountered in the numerical calculation of the development of breaking waves.

#### IV. Results

The translating cylinder is considered with nonlinear boundary conditions for three submergence depths. For the smallest submergence the linear boundary conditions are also used for comparison with other linear solutions. The swaying cylinder is considered with linear and nonlinear boundary conditions for one submergence depth.

##### Translating Cylinder

The first problem considered is the linearized one for a circular cylinder accelerating from rest to a constant speed. The moving coordinate system is used. Thus  $\delta=1$  in (21) and (22). The characteristic length scale  $L$  is the diameter of the body and the speed scale  $U$  is the final speed. The center of the cylinder is one diameter below the undisturbed free surface and the depth of the water is 2.5 diameters. The body is accelerated with constant acceleration from rest at  $t=0$  to dimensionless speed  $-1$  at dimensionless time  $1$ . Thus

$$u = \begin{cases} -t & 0 \leq t \leq 1 \\ -1 & 1 \leq t \end{cases} \quad (32)$$

The grid used is shown in Figure 3. The Froude number is  $Fr = 0.566$ . This particular case was considered first for accuracy comparison since Giesing and Smith [12] have presented solutions to the steady version of this problem.

The evolution of the free surface is shown in Figure 4. Initially the surface is pushed upward ahead of and pulled downward behind the cylinder in an antisymmetric manner. Then a wave train gradually develops downstream. By  $t = 9.6$  the surface elevation near the body is close to the steady profile predicted by Giesing and Smith [11]. This linear result predicts that the free surface is tangent to the body surface. Such a solution must be far from reality since the exact boundary conditions applied to such a surface configuration would predict that no water flows over the top of the body.

In Figure 5 the corresponding lift and resistance coefficients for the linear problem are plotted against time. The resistance is nonzero at  $t=0$  because of the acceleration

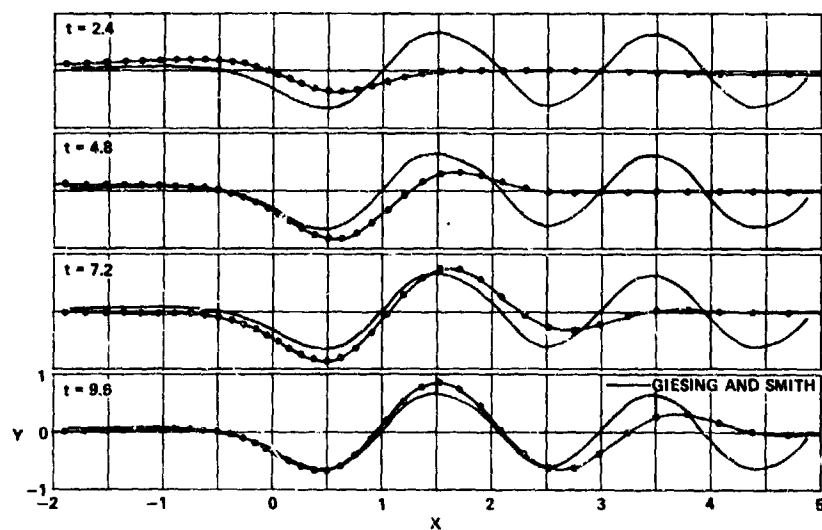


Figure 4. Linear Free Surface Evolution for the Translating Cylinder Compared with the Steady-State Results of Giesing and Smith [12]:  $h = 1$ ,  $d = 2.5$ ,  $Fr = 0.566$ .

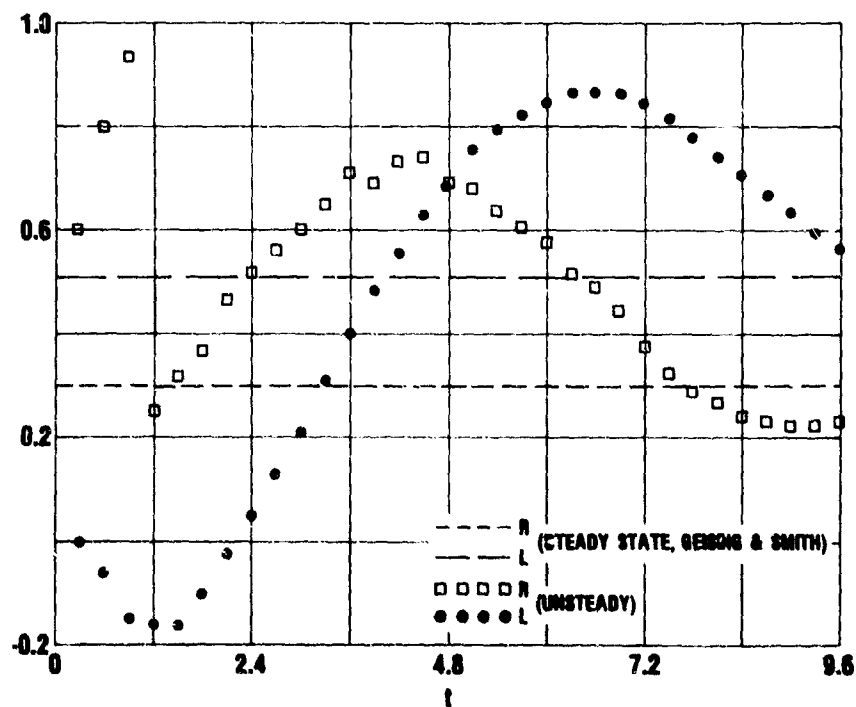


Figure 5. Time History of Linear Resistance and Lift Corresponding to Figure 4 Compared with the Steady-State Results of Giesing and Smith.

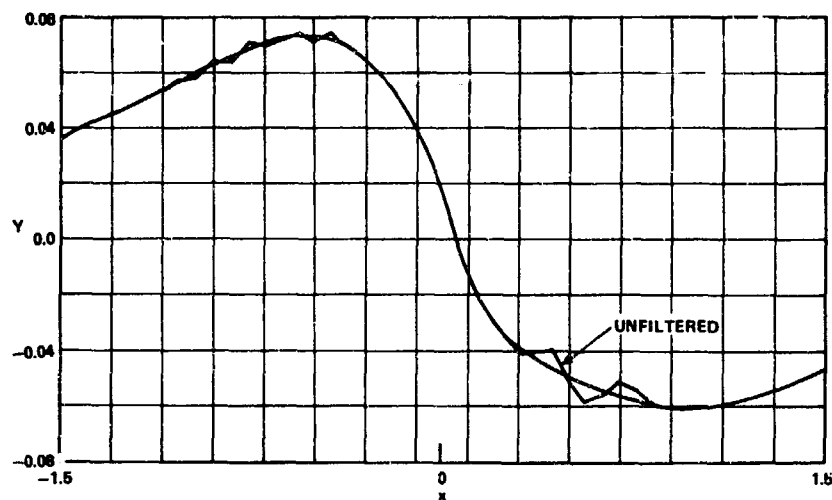


Figure 6. Nonlinear Free-Surface Profiles for the Translating Cylinder at  $t = 0.75$  Computed With and Without Numerical Filtering:  $h = 1$ ,  $d = 2.5$ .

reaction. There is a discontinuity in the resistance at  $t = 1$  when the acceleration ceases. The forces appear to be approaching the steady values predicted by Giesing and Smith, although at  $t = 9.6$  the force values are still changing significantly.

The next case considered is the fully nonlinear version of the same problem. Calculations were carried out without the filtering or equation (31) from  $t = 0$  to  $t = 0.75$  when growing free-surface oscillations of small wavelength were noted. The calculations were rerun from  $t = 0.6$  to  $t = 0.75$  with the filtering. The filtered and unfiltered results are compared in Figure 6. Note that the smoothing eliminates the unwanted high frequency waves without otherwise significantly altering the surface elevation.

The calculations, however, could not be continued much beyond  $t = 0.78$  since by this time features had appeared in the velocity potential near the surface which could not be resolved by the finite-difference grid. These features are displayed in Figure 7 where the free-surface potential is plotted for several times. Continuation of the computations would be meaningless. Such a breakdown of the calculations might indicate a deficiency of the numerical scheme—for instance, inadequate resolution. On the other hand, a deficiency of the mathematical model might also be indicated—for example, wave breaking cannot be handled within the present potential-flow theory. Comparisons with other nonlinear solutions and experiments can help determine which of these two possibilities is being encountered.

It is appropriate to note at this point that steady, large-amplitude, nonbreaking waves

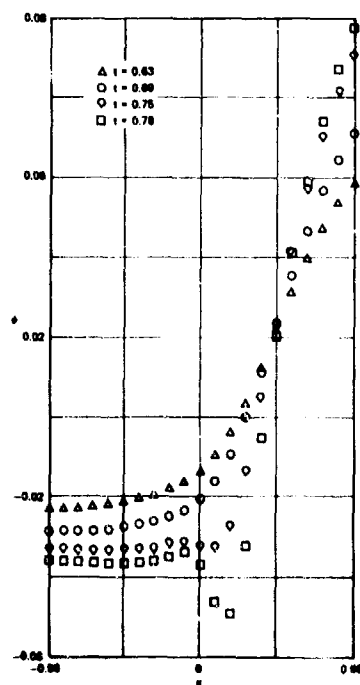


Figure 7. Evolution of the Nonlinear Free-Surface Potential for the Translating Cylinder:  $h = 1$ ,  $d = 2.5$ .

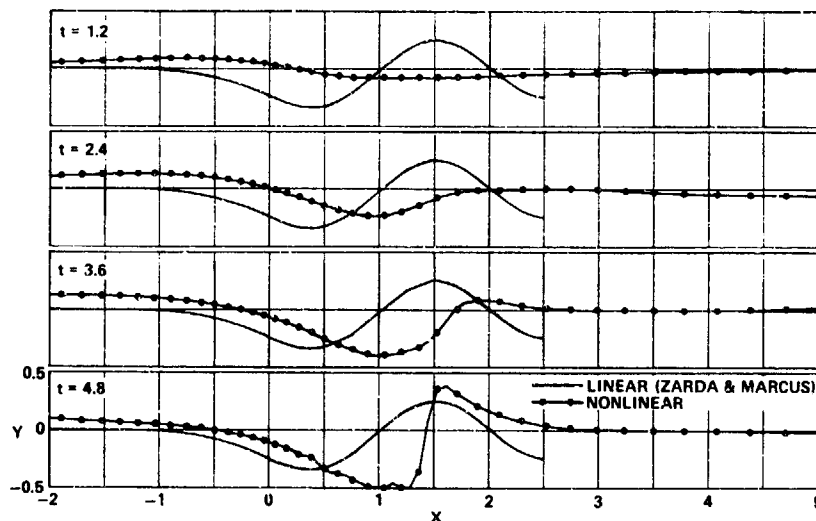


Figure 8. Nonlinear Free-Surface Evolution for the Translating Cylinder Compared with Steady-State Linear Results of Zarda and Marcus [13]:  $h = 1.25$ ,  $d = 2.75$ .

can exist in certain situations where an attempt to reach such a steady state with an unsteady numerical calculation for an accelerated body would fail because of wave breaking during the transient period. Such steady, nonlinear solutions might have to be approached in a different manner. It seems quite likely that at least some of the nonlinear problems considered here fall into this category.

The translating cylinder was next considered with a submergence of 1.25 instead of 1 and a depth of 2.75 instead of 2.5. Once again filtering is needed to eliminate an instability which appears early in the calculations, but in this case the flow development can be followed to  $t = 4.8$  before features develop which cannot be adequately handled by the numerical scheme. Figure 8 shows the free-surface evolution along with the steady linear surface profile computed by Zarda and Marcus [13]. A trough develops downstream from the body. As the gap between the body and the surface narrows, the flow speed in the gap increases. This increased flow speed leads to increased downstream convection which prevents the trough from moving to a position over the body as it does in the linear case. The computed pressure distribution on the body at  $t = 4.8$  is compared with the linear steady-state distribution computed by Zarda and Marcus in Figure 9. Although the linear and nonlinear pressures are essentially the same on the bottom of the cylinder, the high flow speed over the top of the cylinder in the nonlinear case results in a shift of the pressure minimum on the upper surface toward the trailing end.

By  $t = 4.8$  a very steep slope  $dy/dx \approx 3.3$

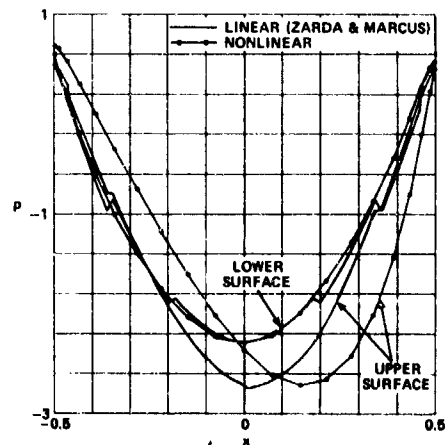


Figure 9. The Nonlinear Pressure Distribution on the Translating Cylinder at  $t = 4.8$  Compared with Steady-State Linear Results of Zarda and Marcus:  $h = 1.25$ ,  $d = 2.75$ .

exists on the upstream face of the growing wave. In reality a wave developing in this manner would break, and continuing the calculations without a more sophisticated mathematical model would be meaningless. In any case, the grid cannot adequately resolve such a surface configuration and the calculations break down.



Figure 10, which shows the computed grid at  $t = 4.8$ , reveals that the resolution is bad in the area of high surface curvature in the trough and near the wave crest. If meaningful, the calculations could be continued with better resolution by allowing grid points to move along the surface to critical areas and by attracting constant  $n$  grid lines toward the surface through use of the transformation source terms  $P$  and  $Q$ .

By increasing the submergence to 1.5, the relative magnitude of the nonlinear terms is further reduced. In Figure 11 the nonlinear results computed with filtering are again com-

pared with linear steady-state results of Zarda and Marcus. Once more a very steep wave slope of about 3.5 develops and the calculations break down. However this condition is not reached until  $t \approx 6.0$ . The trough near the body is not as deep as with the smaller submergence but its horizontal location is roughly the same in both cases. Since the steady-state linear solution exhibits a maximum slope of about 0.3, it is very likely that this is a case where a steady-state nonbreaking nonlinear solution exists but cannot be reached with the present approach because of breaking during the transient period.

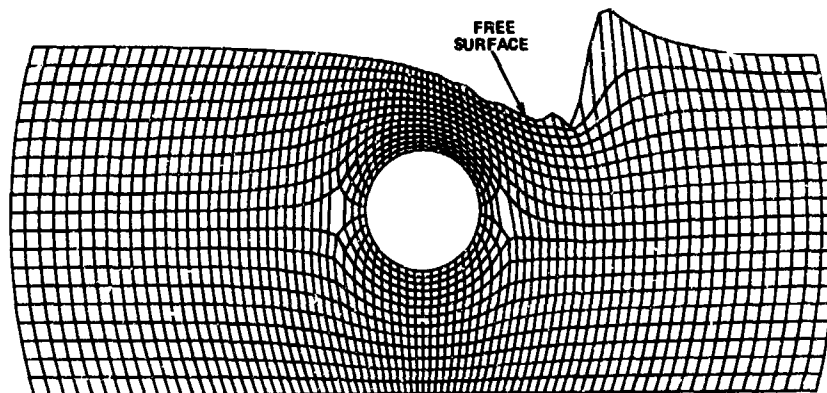


Figure 10. The Boundary-Fitted Coordinate System for the Translating Cylinder at  $t = 4.8$ :  $h = 1.25$ ,  $d = 2.75$ .

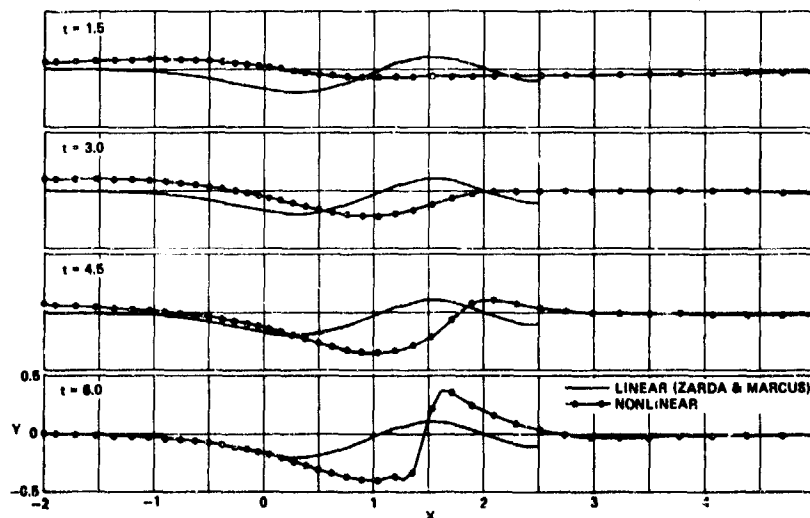


Figure 11. Nonlinear Free Surface Evolution for the Translating Cylinder Compared With Steady-State Linear Results of Zarda and Marcus:  $h = 1.5$ ,  $d = 3.0$ .

### Swaying Cylinder

In addition to the translating cylinder, a swaying cylinder is considered. A fixed reference frame is used so that  $\delta = 0$  in (21) and (22). In the nonlinear case the finite-difference grid must deform in response to both the surface waves and the movement of the body. The center of the cylinder is one cylinder diameter below the undisturbed surface, and the water depth is 2.5 diameters. The characteristic speed  $U$  is the maximum speed of the cylinder. The dimensionless frequency (frequency  $\cdot L/U$ ) is 4 and the Froude number is  $Fr = 0.354$ . The horizontal position of the center of the body is

$$x = 0.25 \cos(4t) \quad (33)$$

The evolution of the free surface, computed with both linearized (free-surface and body) and exact boundary conditions, is shown in Figure 12. For this problem there is no significant difference between the linear and nonlinear results. Comparison of the surface at  $t = 2.1$  with the profile at  $t = 3$ , the two times being roughly 1/2 period apart, shows that the surface elevations above the cylinder (near  $x = 0$ ) are essentially temporally periodic by  $t = 3$ .

Figure 13 shows the time-dependent grid system. By the time the body reaches its maximum displacement (near  $t = 1.5$ ) a large grid cell is present on one side. Time-dependent source terms  $P$  and  $Q$  in the grid generating equations should be helpful in maintaining a suitable mesh system.

The nonlinear swaying body calculations remained stable without filtering. Perhaps the instability would have appeared if the calculations had been continued or if the nonlinearities had been more important. On the other hand the increased stability might be due to the form of the equations in the fixed frame of reference. Additional research should be carried out to determine the conditions which necessitate the use of the filtering.

### V. Conclusions

Finite-difference techniques have been applied with boundary fitted coordinates to solve water wave problems for flow generated by a submerged circular cylinder. The coordinate system used (Figures 2 and 3) leads to efficient distribution of grid points for free surface problems. The method is general and can be extended to three-dimensional, time-dependent, arbitrary geometries. Kutta conditions can be applied when necessary.

A comparison of the numerical solutions of unsteady linearized problems with other solutions to steady-state problems (Figures 4 and 5) indicates that the finite-difference schemes can provide accurate estimates of such phenomena as surface elevations and wave forces. Numerical filtering is useful for stabilizing nonlinear calculations (Figure 6). When high

velocity gradients or very steep waves develop, the calculations break down (Figures 7, 8 and 11). Higher resolution and/or improved mathematical models are needed. Adjustments to the coordinate system are needed to resolve flow fields associated with steep waves and moving bodies (Figures 10 and 13).

For the cylinder translating near the free surface nonlinear effects are important. The wave trough associated with the body is further downstream than in the linear case (Figures 8 and 11). Low pressure values occur on the body between the top and trailing end (Figure 9). Nonlinear free-surface effects are not significant for the particular swaying cylinder problem considered (Figure 12).

### VI. Acknowledgment

This work was supported by the Numerical Naval Hydrodynamics Program at the David W. Taylor Naval Ship Research and Development Center. This program is jointly sponsored by the DTNSRDC and Office of Naval Research.

### References

1. Haussling, H.J. and R.T. Van Eeseltine, "Finite-Difference Methods for Transient Potential Flows with Free Surfaces," Proc. of the First International Conference on Numerical Ship Hydrodynamics, David W. Taylor Naval Ship Research and Development Center, Bethesda, Md., 1976, p. 295.
2. Nichols, B.D. and C.W. Hirt, "Calculating Three-Dimensional Free Surface Flows in the Vicinity of Submerged and Exposed Structures," J. Comp. Phys., Vol. 12, 1973, p. 234.
3. Ohring, S. and J. Telste, "Numerical Solutions of Transient Three-Dimensional Ship Wave Problems," Second International Conference on Numerical Ship Hydrodynamics, Berkeley, Calif., Sept. 1977.
4. Thompson, J.F., et al, "Solutions of the Navier-Stokes Equations in Various Flow Regimes on Fields Containing Any Number of Arbitrary Bodies Using Boundary-Fitted Coordinate Systems," Lecture Notes in Physics, Vol. 59, Springer-Verlag, Berlin/Heidelberg/New York, 1976, p. 421.
5. Shapiro, R., "Linear Filtering," Mathematics of Computation, Vol. 29, 1975, p. 1094.
6. Longuet-Higgins, M.S. and E.D. Cokelet, "The Deformation of Steep Surface Waves. I. A Numerical Method of Computation," Proc. Roy. Soc. Lond. A, Vol. 350, 1976, p. 1.
7. Thompson, J.F., F.C. Thames, and C.W. Mastin, "Automatic Numerical Generation of Body-Fitted Curvilinear Coordinate System for Field Containing Any Number of Arbitrary Two-Dimensional Bodies," J. Comp. Phys., Vol. 15, 1974, p. 99.

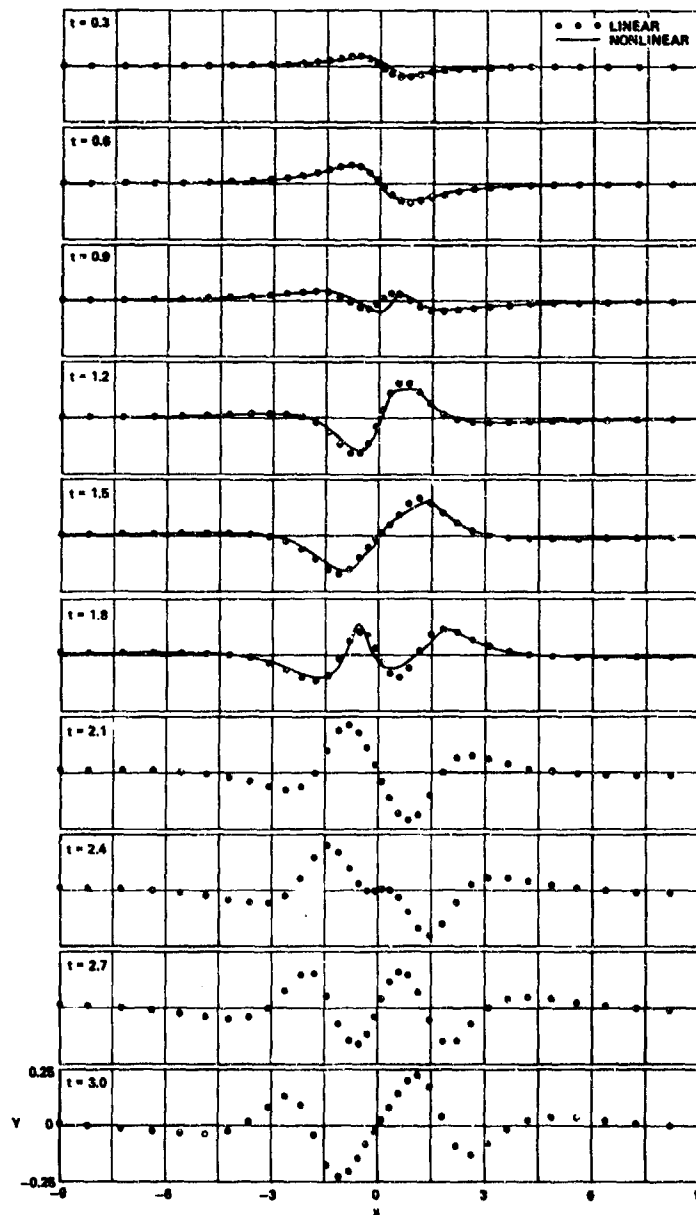
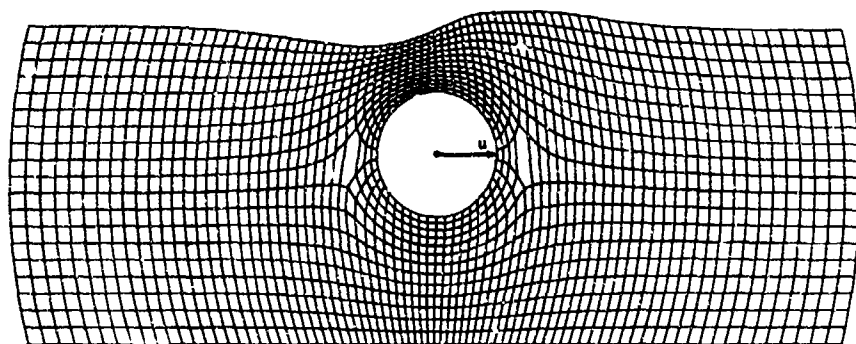
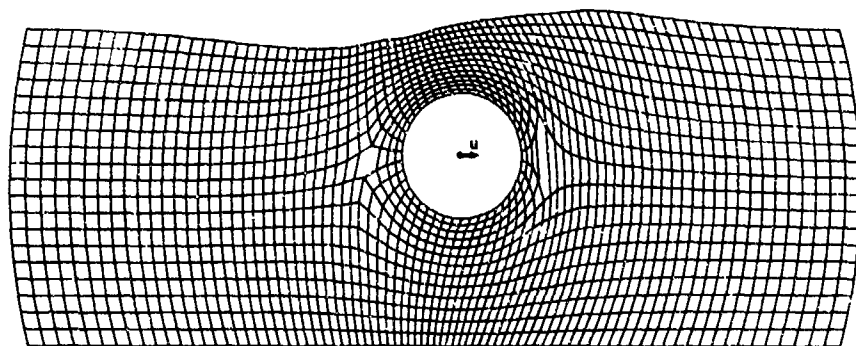


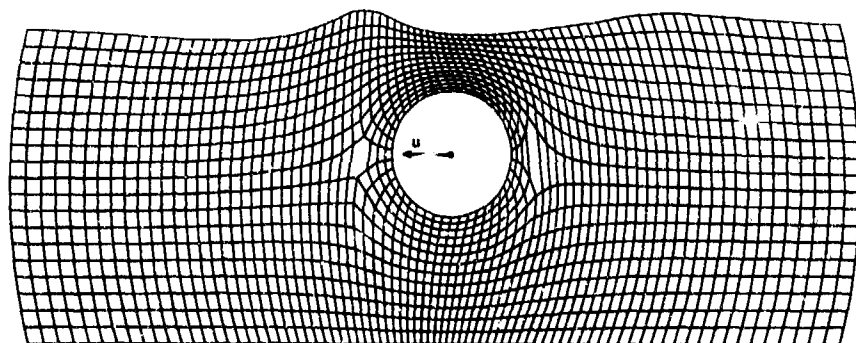
Figure 12. Free Surface Evolution for the Swaying Cylinder.



$t = 1.2$



$t = 1.5$



$t = 1.8$

Figure 13. Time-Dependent Coordinate System for the Swaying Cylinder.

8. Coleman, R.M., "NUMESH: A Computer Program to Generate Finite-Difference Meshes for Arbitrary Doubly-Connected Two-Dimensional Regions." Computation, Mathematics, and Logistics Department Report CHLD-77-05, David W. Taylor Naval Ship Research and Development Center, March 1977.
9. Thompson, J.F., F.C. Thames, C.W. Mastin, and S.P. Shanks, "Use of Numerically Generated Body Fitted Coordinate Systems for Solution of the Navier-Stokes Equations," AIAA Second Computational Fluid Dynamics Conference, Hartford, Conn., June 19-20, 1975.
10. Ghia, U., K.N. Ghia, and C.J. Studerus, "Use of Surface-Oriented Coordinates in the Numerical Simulation of Flow in a Turbine Cascade," Lecture Notes in Physics, Vol. 59, Springer-Verlag, Berlin/Heidelberg/New York, 1976, p. 197.
11. Haussling, H.J., "Boundary-Fitted Coordinates for Accurate Numerical Solution of Multi-Body Flow Problems," to appear, 1977.
12. Giesing, J.P. and A.M.O. Smith, "Potential Flow about Two-Dimensional Hydrofoils," J. Fluid Mech., Vol. 28, 1967, p. 113.
13. Zarda, P.R. and M.S. Marcus, "Finite Element Solutions of Free-Surface Flows," NASTRAN: Users' Experiences, NASA Technical Memorandum, to appear, Oct. 1977.

DISCUSSIONS  
of two papers

NUMERICAL SOLUTION OF THE NAVIER-STOKES EQUATIONS FOR 2D HYDROFOILS  
IN OR BELOW A FREE SURFACE  
Samuel P. Shanks and Joe F. Thompson

FINITE-DIFFERENCE COMPUTATIONS USING BOUNDARY-FITTED COORDINATES  
FOR FREE-SURFACE POTENTIAL FLOWS GENERATED BY SUBMERGED BODIES  
H.J. Haussling and R.M. Coleman

Invited Discussion

Joanna W. Schot  
David W. Taylor Naval Ship Research and  
Development Center

The two papers just presented demonstrate quite impressively how far finite-difference methods have evolved in dealing with initial-boundary-value problems for two-dimensional irregularly shaped flow domains that deform with time. The authors circumvent the well-known difficulties associated with the use of rectangular coordinates for computing free-surface flows around arbitrarily shaped bodies by employing numerically generated curvilinear-coordinate systems in which a coordinate line coincides with each of the boundaries of the physical region. This means that the curvilinear finite-difference grid must be numerically determined at each time step along with the solution of the fluid-flow equations.

It is especially interesting to note that the technique for generating such curvilinear coordinate systems is very general (conformal mapping is a special case), and is independent of the flow equations to be solved. Thus, it is appropriate that at this Conference we are exposed to the results obtained with the use of this approach for two different types of flow formulations. Shanks and Thompson have solved the difficult Navier-Stokes equations of viscous flow past hydrofoils moving in or near a free surface at relatively low Reynolds numbers. In a complementary effort, Haussling and Coleman have treated the infinite-Reynolds-number case of unsteady potential flow past submerged circular cylinders with both linear and non-linear free-surface conditions.

While there are various ways of setting up the numerical procedure for defining the curvilinear grid system and performing the flow calculations, both papers here use an elliptic system of equations with Dirichlet or Neumann boundary conditions to transform the physical flow domain in  $(x,y)$ -spatial coordinates into a region composed of rectangles in  $(\xi,\eta)$ -coordinates with constant mesh size. The use of elliptic equations for the coordinate-generating scheme appears to be a natural choice suggested by the extremum principle for certain elliptic boundary-value problems. The dependent and

independent variables of the coordinate transformation are then interchanged so that the flow-field computations can be conveniently performed on the fixed  $(\xi,\eta)$  grid which does not change with time. The flow equations to be solved must also be transformed to this computational grid. Although this step introduces cross derivatives and complicates the solution of these equations somewhat, the advantages gained by performing the calculations in the transformed region include the convenience of a uniform rectangular grid and greater accuracy in applying the boundary conditions along straight lines. There is considerable flexibility in the choice of the configuration for the transformed region which depends both upon the geometry of the physical flow domain and the extent to which grid-point density is desired in critical locations. For submerged-body problems, Haussling and Coleman chose an H-shaped transformed region which exhibits certain advantages over the T-shaped region employed by Shanks and Thompson.

The grid-generating elliptic systems used in both papers are Poisson equations with special functions  $P(\xi,\eta)$  and  $Q(\xi,\eta)$  for the inhomogeneous terms. It is these functions, called source terms or driving functions, which provide a means of controlling the density or spacing of the curvilinear-coordinate lines so that greater accuracy may be obtained where details of the flow behavior are important. Although neither Shanks and Thompson nor Haussling and Coleman discuss how the functions  $P$  and  $Q$  are determined, they define them in terms of exponential functions in their papers. I would like to suggest that further research be undertaken by the authors on a rationale for choosing, or specifying, these functions because of their influence on the spacing of the curvilinear-coordinate lines. In this connection, the use of computer graphics consoles as an aid to visualizing and influencing the final choice of the grid system becomes very important, especially for computing free surface flows around large, complex ship structures.

Another important aspect of the numerical procedure is the behavior of the Jacobian of the coordinate transformation. If the Jacobian vanishes, or becomes sufficiently close to zero at certain grid points, inaccuracies in the solution of the flow problem may result, depending on various circumstances. Shanks and Thompson point out, as a result of their experience with a variety of problems, that the pres-

ence of a zero Jacobian depends on the type of configuration chosen for the transformed plane. In order to avoid unacceptable configurations and the ensuing inaccuracies, it is probably advisable to automatically monitor the Jacobian as part of the grid definition procedure, as recommended by Oberkampf [1].

In both papers, the systems of finite-difference equations approximating the coordinate transformation equations and the flow equations and the flow equations are solved simultaneously using the easy-to-program SOR (Successive Over-Relaxation) method. Much faster methods could be applied, and are indeed under investigation by several researchers, for example K. Ghia and U. Ghia of the University of Cincinnati. Haussling and Coleman refer to their work on alternating-direction implicit methods in their paper, and they have recently reported further advances which will lead to even faster methods [2].

The four authors of these two significant papers are to be congratulated for carrying forward the numerical solution of very challenging flow problems to a point where they can begin to be applied to three-dimensional ship hydrodynamic problems. However, as these authors indicate, there is still much work to be done, not the least part of which is to improve the handling of steep surface waves in the case of potential flow, and to increase the range of the Reynolds number for viscous-flow problems.

[1] Oberkampf, W.L., "Domain Mappings for the Numerical Solution of Partial Differential Equations," *Int'l. J. Numerical Methods in Engineering*, Vol. 10, 211-223 (1976).

[2] Ghia, U., Hodge, J.K., and Hankey, W.L., "An Optimization Study for Numerically Generating Surface-Oriented Coordinates for Higher Reynolds Number Flow," Wright-Patterson AFB AFDD-TR Report (to appear, Fall 1977).

#### Discussion

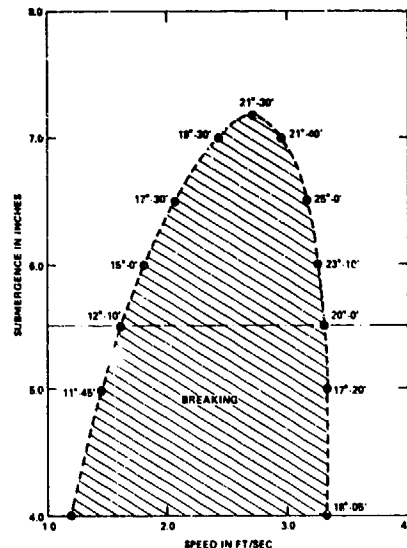
by Nils Salvesen

of paper by H.J. Haussling and R.M. Coleman

The steady-state nonlinear problem of uniform flow past a body may be solved by two approaches: (1) It may be solved in the time domain as an initial-value problem advancing in time until a steady-state condition has been reached, and (2) it may be solved as a steady-state problem where the free-surface shape is initially assumed and then through an iteration scheme systematically changed until the free-surface conditions are satisfied. Since it would be extremely difficult to construct an iteration scheme that would work for the three-dimensional ship-wave problem, it might seem that the initial-value approach would be the most suitable for three-dimensional problems, even though we have had more success with iteration techniques than with the initial-value approach for two-dimensional problems.

However, as shown by Haussling and Coleman, the numerical time-domain solution may often break down before a steady-state condition has been reached. Model-tank experiments have

shown that there are steady-state conditions with stable non-breaking waves that can only be obtained by accelerating the body through intermediate conditions where wave breaking is present. Figure 1 shows the results from an experiment conducted at the David W. Taylor Naval Ship Research and Development Center in a 40-foot tank having two-by-two-foot cross section. A submerged foil which spanned the width of the tank was used as the wave generator. The foil which was towed by a submerged wire, generated waves which were sufficiently uniform across the tank to be considered as two-dimensional waves.



The shaded region in Figure 1 indicates the combined conditions of foil submergence and speed for which breaking occurred. The numbers next to each point in the figure give the maximum slopes measured at the first crest of unbroken waves. The inception of wave breaking is affected by the acceleration of the foil before breaking occurs. The left- and right-hand parts of the dotted lines in Figure 1, which we shall refer to as the lower and upper speed limits for nonbreaking waves, have been obtained by two different acceleration patterns. For the lower speed limits, the foil was accelerated very slowly until breaking occurred, whereas for the upper speed limits, the foil was accelerated rapidly to a speed somewhat higher than the limiting speed; then after uniform nonbreaking waves had formed behind the foil, it was slowly decelerated until breaking occurred. Thus, the breaking conditions were always obtained by approaching from an established stable condition.

These experimental results seem to indicate that there are steady-state conditions that cannot be obtained by accelerating the body from

rest without wave breaking occurring at intermediate stages and therefore it seems likely that any numerical scheme modeling such cases would also have to break down at some intermediate time step. I would like to use this opportunity to suggest some initial-value time-domain approaches where this wave-breaking problem can be avoided. For the two-dimensional case of a submerged body as investigated by Haussling and Coleman, one could, for example, let the starting condition be the uniform flow past a deeply-submerged body and then slowly decrease the submergence until the desired condition is reached. One could also let the starting condition be the uniform flow past an infinitesimal thin body, and then slowly increase the thickness of the body. Such an approach would be applicable to both two- and three-dimensional bodies. However, these approaches have the disadvantage that the geometry of the problem would change with each time step. Therefore, the best approach seems to be one suggested to me by K.J. Bai, namely, to consider the body as a porous medium. One would start with uniform flow, going completely through the body and then in the time domain change the body-boundary condition so that less and less fluid goes through the body until it finally becomes a solid body.

#### Author's Reply

by H.J. Haussling and R.M. Coleman  
to discussion by Nils Salvesen

We would like to thank Dr. Salvesen for presenting some interesting experimental results which support the plausibility of our numerical solutions. To continue his discussion of methods for avoiding transient breaking waves we point out once more that the boundary-fitted coordinate systems can handle time-dependent geometries. Thus changes in body thickness or depth of submergence could be treated. However, the most satisfying solution to the wave-breaking problem might evolve from the current studies of the physics of this phenomenon. With the development of mathematical-numerical models of breaking waves calculations could be carried out beyond the time at which breaking first occurs.



## A REVIEW OF NUMERICAL METHODS FOR SOLUTION OF THREE DIMENSIONAL CAVITY FLOW PROBLEMS\*

Robert L. Street  
Stanford University  
Stanford, California 94305

### Abstract

Available and developing techniques for the numerical solution of three-dimensional, fully-cavitating flows about hydrofoils and other bodies are reviewed. Three areas are examined, viz., linearized methods, methods based on matched asymptotic expansions, and fully nonlinear methods. For the first two areas there are presently available two specific techniques usable for quantitatively accurate design; interestingly both techniques rely on the use of two-dimensional characteristics of the flow applied stripwise in the three-dimensional flow field. The area of fully nonlinear methods is still developing. The finite element method and the inverse, stream function and potential method have both been applied successfully to three-dimensional free surface flows.

### Introduction

It was just over eleven years ago that Widnall (1966) published her numerical simulation of three-dimensional, fully-cavitating flow about hydrofoils. That work and work preceding it incorporated a number of limiting assumptions. Only within the last year or so new techniques have become available so that there are now available quantitatively accurate methods for the design and analysis of three-dimensional, fully-cavitating flows.

The purpose of this paper is to review a set of available and potentially valuable techniques for the numerical solution of steady-state, three-dimensional, fully-cavitating flows about hydrofoils. This review is not intended to be comprehensive; indeed, it is focused on a few techniques and a representative set of references.

We assume that the reader is well acquainted with the inviscid theory for steady-state, fully-cavitating flow and with the state-of-the-art in two-dimensional, in axisymmetric, and in the

three-dimensional, linearized asymptotic theories where numerical computation is not a major feature. Reference to Gilbarg (1960), Gurevich (1965), Wu (1968, 1972) and Acosta (1973) provides the basic background. Wu (1975) gives a more recent overview. Lechey (1973) and Lechey and Stellingner (1975) cover the linearized asymptotic theories. We also shall not review the classic numerical calculations performed prior to, say, 1965 as these are well reviewed in the literature just cited.

We focus on three aspects of the numerical simulation of steady-state three dimensional flows. We begin with an examination of the linearized techniques. Next we review the use of matched asymptotic expansions. Finally we close with an examination of fully nonlinear techniques. While the linearized and asymptotic expansion methods yield viable design techniques for finite span hydrofoils, none of the nonlinear techniques is yet ready for design application. Several of the fully nonlinear methods do look ripe for exploitation, however, and in the end we focus on the finite element method.

### Linearized Methods

Widnall (1966) derived a linearized three-dimensional, lifting-surface theory for fully-cavitating hydrofoils of finite span in steady or oscillatory motion through an infinite fluid. The planform of the cavity was assumed to be a rectangle of finite length and of span equal to that of the foil. Widnall (1966) argued that the prediction of lift and moment on the foil is not sensitive to the assumed cavity length when it exceeds about twice the chord of the foil. It is well known that this approximation does not hold for shorter cavities, and indeed is not an accurate representation of the cavity shape for longer ones (see the discussion of Furuya and Acosta, 1976, below).

\*This work was supported in part by the Naval Sea Systems Command General Hydromechanics Research Program, Subproject SR 023 01 01, administered by the David W. Taylor Naval Ship Research and Development Center, Contract N00014-75-C-0277.

In Widnall's (1966) analysis a pair of coupled integral equations are derived by use of the pressure potential and Green's theorem. The known boundary conditions on the foil and the assumed cavity pressure (i.e., cavitation number) provide enough information to determine the unknown distributions of pressure doublets on the foil and pressure sources on the foil-cavity surfaces if the cavity planform shape and length are assumed and the cavity is terminated by requiring the pressure source distribution to go to zero beyond the cavity trailing edge.

The numerical problem is solved by representing the pressure-doublets distribution in a series with unknown coefficients while the source terms are represented as simple delta functions. The coefficients are found by satisfying the boundary conditions at a suitable series of collocation points. The results showed reasonable agreement with available experimental data, indicating the efficacy of the lifting-surface theory.

Nishiyama (1970) made an important contribution to the linearized theory by illustrating how two-dimensional theory is relevant to the three-dimensional problem (this had been done many years ago, of course, for the fully wetted flow; see Van Dyke, 1964). This concept of using essentially two-dimensional (or streamwise) components of the flow was to reappear in the paper of Jiang and Leehey (1977), which in many ways is a synthesis of the Nishiyama (1970) and Widnall (1966) concepts, and in the work of Shen and Ogilvie (1972) and Furuya (1975b).

Nishiyama (1970) expressed the flowfield over a fully-cavitating hydrofoil as the superposition of pressure doublets on the foil and sources over the foil-cavity surface. For linearized flow and large aspect ratio (span  $b \gg$  chord  $c$ ), he demonstrated that, with sufficient accuracy, two-dimensional flow is maintained at each spanwise location over the foil with respect to an effective angle of attack. This angle is the actual physical angle of attack less the induced angle, produced at each spanwise location by the induced velocity of the trailing vortex sheet springing downwards from the cavity termination. The induced angle depends on the circulation about the foil plus cavity in each streamwise plane.

Nishiyama (1970) formulated and solved an integral equation for the circulation with a specified cavitation number. He expanded the circulation in a trigonometric series and satisfied the integral equation at an appropriate number of points over the foil to find the unknown coefficients in the series. A key is that no a priori specification is needed for the cavity length which is found to vary with spanwise position.

Interestingly, Nishiyama's results seem to follow the trend of the lift data, as it varies with cavitation number, better than Widnall's results do. However, her results are generally closer in magnitude to the actual data, except in the case of lowest angle of attack and largest aspect ratio presented by Nishiyama (1970). Although Nishiyama begins with a lifting-surface theory, he effectively reduces it to a lifting-line theory through the use of large aspect ratio approximations. It is not surprising then that his theory works best for large aspect ratio, but that there is little to choose between the Widnall (1966) and Nishiyama (1970) results.

Tsen and Guilbaud (1974) solved the lifting surface, linearized flow problem, using a refined version of Widnall's (1966) approach. While they apparently achieved improved results, the results of a comparison with theory were not satisfactory according to them because the angles of attack for much of the experimental data were beyond the range of linearized theory and because the nonlinear lift from tip vortices is important for smaller aspect ratios. Their paper suggests strongly the need for nonlinear methods.

Jiang and Leehey (1977) have refined the linearized lifting surface theory and achieved an impressive correlation between linearized calculations and their experimental data for an elliptical-planform, flat-plate foil of aspect ratio 5. Interestingly, the angles of attack for the experiments range from  $11^\circ$  to  $18^\circ$ , well beyond the normal range of linearized theory.

Jiang and Leehey (1977) employ distributions of discrete vortices (on the foil) and sources on the foil and cavity. The unknown distributions of the strengths of the singularities are found by satisfying coupled integral equations at collocation points on the projection of the foil plus cavity planform. A key element in their solution is an iteration procedure in which the spanwise variation of cavity length is adjusted until a uniform cavitation number is achieved across the entire spanwise range of the cavity. Thus, Jiang and Leehey (1977) combine two of the most important features of Widnall's (1966) lifting-surface theory and Nishiyama's lifting-line theory in their new method.

Jiang and Leehey's (1977) method appears to represent the best that can be obtained with linearized theory and clearly provides a usable design tool of quantitative accuracy. While the linearized method has well known limits and has been developed so far only for infinite fluid flows, it does offer simplicity and reasonable cost as attractive features.

### Asymptotic Expansion Methods

Van Dyke (1964) describes the concepts of singular perturbation analyses. He gives a rule, viz., a perturbation solution is uniformly valid unless the perturbation parameter is the ratio of two lengths. In cases where the perturbation parameter is a ratio of two lengths singular behavior is to be expected and the method of matched asymptotic expansions is applicable. The flow past large aspect ratio wetted and fully-cavitating hydrofoils both offer cases in which the perturbation parameter, the aspect ratio, is the ratio of two lengths, namely the span and the effective chord (strictly speaking, the chord of the foil plus the cavity is the proper length for scaling). Far from the body the primary reference length is the span. Near the body we recognize a secondary length scale, the local chord length. Thus, these large aspect ratio problems are natural for solution by the method of matched asymptotic expansions in which the asymptotic expansion of the far field solution is expressed in terms of the inner variables (i.e., variables scaled on the chord) and then matched term-by-term to the asymptotic expansion of the near field solution expressed in terms of the outer variables (i.e., variables scaled on the span).

Leehey (1973) and Leehey and Stellingner (1975) have successfully applied the method of matched asymptotic expansions to linearized flow past large aspect ratio fully-cavitating hydrofoils. However, their method is essentially analytic, involving no substantial numerical analysis. Accordingly, we do not review their work here.

Shen and Ogilvie (1972) developed a nonlinear hydrodynamic theory for the planing of large aspect ratio surfaces by the use of the theory of matched asymptotic expansions. Although their work is also essentially analytic, we describe it briefly because of its relevance to the numerical method developed by Furuya (1975b) which is the focus of this section.

Shen and Ogilvie (1972) treated the three-dimensional flow generated by a high-aspect-ratio planing surface gliding with constant speed and at arbitrary angle on the free surface of an infinitely deep weightless fluid. After defining the small parameter  $\epsilon = AR^{-1}$  where the aspect ratio  $AR = (\text{Span})^2 / \text{Wetted-Planing-Area}$ , they sought a solution asymptotically valid as  $\epsilon \rightarrow 0$ . This leads to the definition of a near field where distance from the planing surface is comparable to the chord length of the planing surface and of a far field where distance from the planing surface is comparable to its span. If the span is normalized to 2, then the chord vanishes in the far field view as  $\epsilon \rightarrow 0$ . In the far field view the

planing surface becomes representable by a line of doublets in a uniform flow. In the near field view we hold the local chord constant as  $\epsilon \rightarrow 0$  so that the span approaches infinity and the flow in this region becomes approximately two-dimensional.

Solution of the far field problem is straightforward. The key idea of Shen and Ogilvie (1972) was to solve the two-dimensional near field problem exactly, i.e., without introducing linearizing approximations. The method of matched asymptotic expansions was then used to match the near field and far field solutions. The result is a uniformly valid nonlinear solution matched (in this case) to the second order in the small parameter  $\epsilon = AR^{-1}$ . In addition, this method yields an unambiguous definition of the height of the planing surface above the undisturbed free surface at infinity.

The hydrofoil problem corresponding to Shen and Ogilvie's planing problem was solved by Furuya (1975b). His objective was "to provide a simple yet accurate method for design of super-cavitating hydrofoils of large aspect ratio near a free surface, having practically no limitations on the admissible foil profile and angle of attack." In the context of matched asymptotic expansions as described above, Furuya (1975b) employs a two dimensional nonlinear free-streamline theory for the near field flow region and Prandtl's lifting-line theory for the far field. The small parameter  $\epsilon = 1/(\text{Aspect Ratio})$  is used as in Shen and Ogilvie (1972), with  $(\text{Aspect Ratio}) = (\text{span})^2 / (\text{projected area of the foil on the horizontal plane})$ . The matched asymptotic expansions are taken in the limit as  $\epsilon \rightarrow 0$ . The effect of this approach, it should be remembered, is to eliminate consideration of the behavior of the flow near the foil tips. Thus, the cavity width (spanwise) is equal to the foil span exactly at and near the foil. Furthermore, for the far field problem to be a lifting line flow, it is necessary that the foil plus cavity chord be small compared to the span. Accordingly, the theory is valid in principle only for "short" cavities.

Furuya's (1975b) configuration is shown in Fig. 1; the notation is self-explanatory. The spanwise foil submergence  $h(\epsilon)$  is taken to be of the order of the chord length so  $h/(\text{span}) = O(\epsilon)$ .

In the limit as  $\epsilon \rightarrow 0$  with foil span ( $=2$ ) held constant the far field flow appears as a lifting line (the foil) with trailing vortices, all lying in the free surface (Fig. 2). The solution to this problem to order  $\epsilon^2$  has exactly the same form as that for a fully wetted foil except for a factor of 2 in the first-order term, caused by the imaging at the free surface. This lifting line solution has in it an unknown vortex strength

$\gamma(z)$ , to be determined in the matching process.

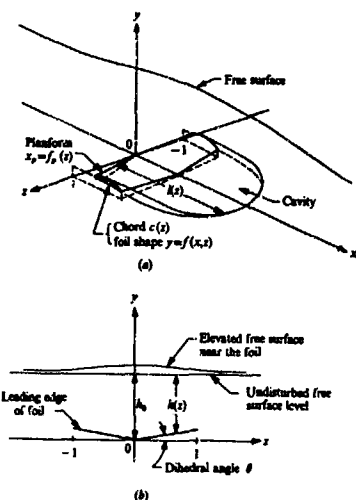


Figure 1. Schematic of Three-Dimensional Flow About Hydrofoil Near a Free Surface. (a) Flow configuration. (b) View from upstream [After Furuya (1975b)].

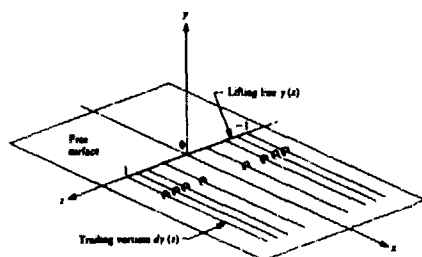


Figure 2. Schematic of Far Field Flow About Large Aspect Ratio Hydrofoil [After Furuya (1975b)].

The near field configuration is found by letting  $\epsilon \rightarrow 0$  with the chord held fixed. This is accomplished by describing the near field in terms of the stretched coordinates  $(X, Y, Z) = (x/\epsilon, y/\epsilon, z/\epsilon)$ . As in the case of Shen and Ogilvie (1972), the near field flow is nonlinear and two-dimensional. The solution used is that of Furuya (1975a) which employs the Tulin double-spiral vortex model (Fig. 3).

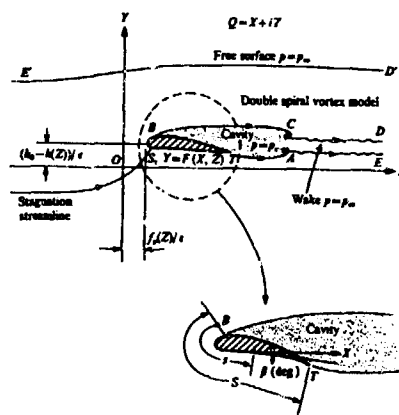


Figure 3. Schematic of Near Field, Two-Dimensional Flow in Stretched Coordinates [After Furuya (1975b)].

The corresponding boundary-value problems for the near and far fields are given in Table 1.

	Far field	Near field
Foil shape	$y = f(x, z)$	$Y = F(X, Z), \quad \epsilon F(X, Z) = f(x, z)$
Chord length	$a(x)$	$\epsilon A(X), \quad \epsilon A(X) = a(x)$
Submergence	$h(x)$	$H(X), \quad \epsilon H(X) = h(x)$
Laplace equation	$\phi_{xx} + \phi_{zz} = 0$	$\phi_{XX} + \phi_{ZZ} + \epsilon^2 \phi_{ZZ} = 0, \quad \epsilon^2 \phi = \phi$
Boundary conditions		
(i) Free surface and wake	$\phi_x^2 + \phi_z^2 = 1$	$\phi_X^2 + \phi_Z^2 + \epsilon^2 \phi_Z^2 = 1$
(ii) Cavity	$\phi_x^2 + \phi_z^2 = 1 + \epsilon$	$\phi_X^2 + \phi_Z^2 + \epsilon^2 \phi_Z^2 = 1 + \epsilon$
(iii) Foil	$\phi_{x,z} - \phi_z = \phi_{x,z} = 0$	$\phi_X \phi_Z - \phi_Z = \phi_X \phi_Z = 0$

Table 1. Near and Far Field Boundary Value Problems for Hydrofoil [After Furuya (1975b)].

There the cavitation number is

$$\sigma = \frac{p_\infty - p_c}{\frac{1}{2} \rho q_\infty^2} \quad (1)$$

as usual. While the lifting-line solution for the far field is easily expanded in powers of  $\epsilon$ , the two-dimensional, nonlinear near-field solution is more complex, requiring first expansion of the solution in terms of a transform plane parameter.

The submergence depth  $h(x)$  is related to the rest of the problem by calculation of the location of the stagnation streamline. Furuya (1975b) uses the method of additive composition as described by Van Dyke (1964). The result is achieved by summing the near and far field solutions for  $h(x)$  and then subtracting their common part. This yields a stable and well defined submergence depth (as contrasted to the problem found in two dimensions).

The full set of nonlinear equations relating to parameters of the problem contains five unknowns. The last of the equations is obtained by specifying the flow angle of the upper cavity sheet at downstream infinity in the two-dimensional solution to be equal to the "downwash" angle obtained in the three-dimensional solution. Of the previous four equations, two were generated by the near field solution and two by the far field solution through the matching procedure.

Furuya (1975b) describes a numerical iterative procedure to solve the system of five nonlinear equations described above. His procedure converges rapidly and stably in 4 to 8 iterations to relative errors of less than  $3 \times 10^{-3}$  for rectangular flat-plate foils. For these foils the numerical results are in excellent agreement (for lift and drag) with experimental data for aspect ratios of 2, 5, 4 and 6 at various angles of attack and cavitation numbers. Although the theory assumes large aspect ratio, short cavity and shallow submergence the numerical results are good even for  $\epsilon = 0.4$ ,  $\sigma = 0.1$  and  $h = 2$  chords.

Furuya and Acosta (1976) present a set of experimental data taken to test the Furuya (1975b) theory. The test hydrofoil had a flat lower surface, sharp and straight leading edge, and a partially tapered planform. The taper served to simulate somewhat an elliptic loading and to avoid strong tip vortices observed on rectangular planforms. The theoretical predictions are excellent for lift and drag (Fig. 4 and 5) and give impressive agreement for cavity shape (Fig. 6). It is clear, from Fig. 6, that the variable cavity length with span approach is an appropriate improvement employed in the recent models of Furuya (1975b) and Jiang and Leehey (1977).

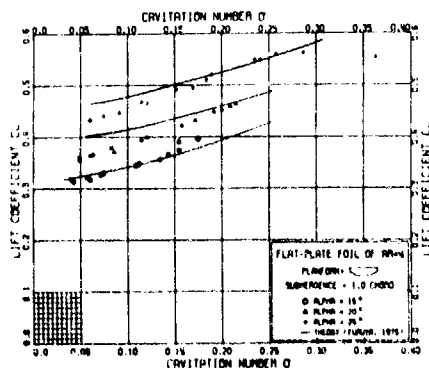


Figure 4. Typical Lift Coefficient Versus Cavitation Number  $\sigma$  and Angle of Attack  $\alpha$  [After Furuya and Acosta (1976)].

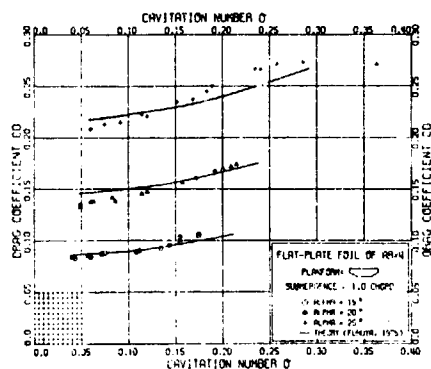


Figure 5. Typical Results for Drag Coefficient Versus Cavitation Number  $\sigma$  and Angle of Attack  $\alpha$  [After Furuya and Acosta (1976)].

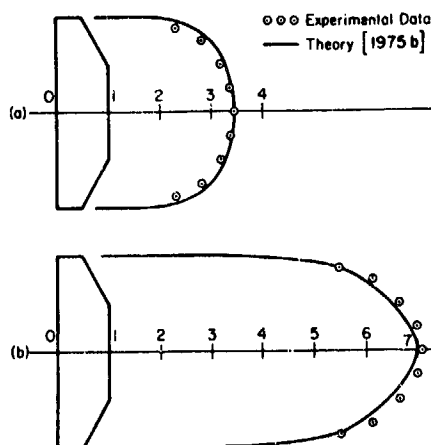


Figure 6. Spanwise Variation of Cavity Length at One Chord Submergence and  $\alpha = 15^\circ$ . (a)  $\sigma = 0.13$ , (b)  $\sigma = 0.072$ .

Furuya (1975b) notes that, while the method has only been applied to flat plate foils, the technique is applicable to arbitrary planform and foil profile, including a rounded leading edge and a small dihedral angle. Thus, although the actual flow behavior near the foil tips has yet to be treated, this nonlinear method is a powerful and accurate design tool for large aspect ratio fully-cavitating hydrofoils near a free surface.

## Fully Nonlinear Methods

### An Overview

There are several major categories of numerical techniques applied to free surface flows, including finite-difference and finite-element methods. Amongst the finite-difference methods we also find formulations in which the problem is solved in a stream function and velocity potential space or in which the formulation is based on the distribution of singularities on the free surface of the flow (normally called a boundary integral equation technique).

Our work in numerical simulation began with a study by Mogel and Street (1974) involving two-dimensional cavitating flows. We used a finite-difference technique and solved a problem of flow past a plate in a water tunnel by employing a Ritzboushinsky model and imaging to achieve an exact formulation. Irregular finite-difference stars were employed along the curved free surface boundary. We also employed a refinement of the finite difference grid in the neighborhood of the separation point on the flat plate. The solution of the finite-difference equations for the velocity components was achieved by successive over-relaxation (SOR). Because the velocity components were employed as the unknowns, the solution required simultaneous satisfaction of the Laplace equation for each velocity component and of the nonlinear free surface boundary conditions. The solution converged and gave reasonable results. However, the cost for the two-dimensional case was equal to the cost for a solution of similar accuracy for a three-dimensional disk-in-water-tunnel flow by the finite-element method.

Brennen (1969) combined a finite-difference technique with a mapping to the stream function and velocity potential space to solve the axisymmetric flow past a circular disk in a circular water tunnel using a Ritzboushinsky model. A difficulty with the extension of this technique to more general bodies is that the solution is inverse because the stream function and velocity potential space solution must be mapped back to physical space to obtain the final geometry.

White and Kline (1975) developed a general method for the solution of turbulent separated axisymmetric flows. In their general development they employed a boundary integral technique for the potential flowfield outside the boundary layers developing in their diffuser flows. Unlike grid techniques, the boundary integral method requires computation of unknowns only over the flow boundary. The solution technique obtains the potential flow from the numerical solution of Green's third identity and iteratively solves for the correct

location of an initially unknown free surface (see Larock, 1977, in these proceedings). In principle this technique can be extended to general three-dimensional flows. Interestingly, a very similar technique was developed by Armstrong and Dunham (1953). They applied a vortex sheet singularity to free streamline flows, thereby generating an integral equation whose solution formed part of an iterative procedure to locate the initially unknown free surface. They solved several axisymmetric cavity flows in an infinite fluid field and obtained reasonable agreement with experiment.

The application of the finite-element method to free streamline flows was first made by Chan, et al. (1973a, 1973b). They showed that the finite-element method could be used to solve for the velocity potential in two-dimensional and axisymmetric ideal fluid flows involving a free surface. The trial-free-boundary technique used involved assumption of the location of the free surface, solution of the resulting well posed problem, and relocation of the free surface according to the free streamline boundary condition.

In the next two sections we follow up on two methods. First, we review a three-dimensional formulation of the inverse stream function and velocity potential by Jeppson (1972). Second, we describe our own progress in the application of the finite element method to three-dimensional flows.

### The Inverse Method

Working independently Jeppson and Brennen both developed inverse solution methods for free streamline flows and presented these results in their Ph. D. dissertations in 1966 (see Brennen, 1969, and Jeppson, 1969 and 1970, for example). Jeppson (1972) and Davis and Jeppson (1973) subsequently developed an inverse formulation for three-dimensional flows in which a velocity potential and two stream functions were used. By changing the conventional roles played by the variables of the problem, the inverse method converts a free surface with an unknown position in physical space into a plane of known position in the inverse stream function and velocity potential space. The major disadvantage of the method is that the shape of curved solid bodies cannot be exactly prescribed in advance in physical space. However, Jeppson's method has been successfully applied to a three-dimensional groundwater flow with a free surface and to fully-wetted flow past a body moving beneath a free surface. Accordingly, it seemed appropriate to review here the fundamentals of his formulation.

Consider an inviscid, steady-state flow in three-dimensions past a body in the presence of free surfaces or cavities. Let the magnitude

of the cartesian coordinates  $(x, y, z)$  be the dependent variables and define a velocity potential  $\Phi$  and two additional functions  $(\psi, \psi^*)$  as the independent variables. The two stream functions defined by Yih (1957) as surfaces normal to equipotential surfaces and tangential to the velocity vector (such that their intersections define the stream lines of the flow) meet the necessary requirements. As a result

$$u = \frac{\partial \psi}{\partial y} \frac{\partial \psi^*}{\partial z} - \frac{\partial \psi}{\partial z} \frac{\partial \psi^*}{\partial y} = \frac{\partial \Phi}{\partial x} \quad (2)$$

$$v = \frac{\partial \psi}{\partial x} \frac{\partial \psi^*}{\partial z} - \frac{\partial \psi}{\partial z} \frac{\partial \psi^*}{\partial x} = \frac{\partial \Phi}{\partial y} \quad (3)$$

$$w = \frac{\partial \psi}{\partial x} \frac{\partial \psi^*}{\partial y} - \frac{\partial \psi}{\partial y} \frac{\partial \psi^*}{\partial x} = \frac{\partial \Phi}{\partial z} \quad (4)$$

in which,  $u$ ,  $v$ , and  $w$  are the components of velocity vector  $\vec{V}$  in the  $x$ ,  $y$ , and  $z$  coordinate directions, respectively, i.e.,  $\vec{V} = u\vec{i} + v\vec{j} + w\vec{k}$ . Using vector notations Eqns. 2, 3, and 4 can be written as

$$\vec{V} = \text{grad } \Phi = \begin{vmatrix} \vec{i} & \vec{j} & \vec{k} \\ \frac{\partial \psi}{\partial x} & \frac{\partial \psi}{\partial y} & \frac{\partial \psi}{\partial z} \\ \frac{\partial \psi^*}{\partial x} & \frac{\partial \psi^*}{\partial y} & \frac{\partial \psi^*}{\partial z} \end{vmatrix} = \text{grad } \psi \times \text{grad } \psi^* \quad (5)$$

It follows that  $\nabla \cdot \vec{V} = 0$ , i.e., the incompressible, steady-state continuity equation is satisfied.

The surfaces formed by holding  $\psi$  and  $\psi^*$  constant are orthogonal to equipotential surfaces. However, the two surfaces formed by holding  $\psi$  and  $\psi^*$  constant are not necessarily orthogonal. Jeppson (1972) imposes the requirement that  $\psi$  and  $\psi^*$  are orthogonal axes and demonstrates that the selected functions are orthogonal. This yields a well defined orthogonal 3-space for  $(\Phi, \psi, \psi^*)$ .

Employing implicit function theory one finds the mathematical formulation governing the inverse functions  $x(\Phi, \psi, \psi^*)$ ,  $y(\Phi, \psi, \psi^*)$  and  $z(\Phi, \psi, \psi^*)$ , viz.,

$$\frac{\partial x}{\partial \Phi} = \frac{\partial y}{\partial \psi} \frac{\partial \psi^*}{\partial \psi^*} - \frac{\partial y}{\partial \psi^*} \frac{\partial \psi^*}{\partial \psi} \quad (6)$$

$$\frac{\partial y}{\partial \Phi} = \frac{\partial x}{\partial \psi^*} \frac{\partial \psi^*}{\partial \psi} - \frac{\partial x}{\partial \psi} \frac{\partial \psi^*}{\partial \psi^*} \quad (7)$$

$$\frac{\partial z}{\partial \Phi} = \frac{\partial x}{\partial \psi} \frac{\partial y}{\partial \psi^*} - \frac{\partial x}{\partial \psi^*} \frac{\partial y}{\partial \psi} \quad (8)$$

These are a set of coupled, nonlinear, first-order partial differential equations. When combined with appropriate boundary conditions this set comprises a well-posed boundary value problem. This coupled set of first-order equations must be solved simultaneously and has been a major stumbling block to more aggressive use of the method. Jeppson (1972) says, "They cannot be combined, at least in an obvious manner, by differentiation, for example, to obtain a reasonably simple higher order equation for only one dependent variable." [cf., Brennen, 1969.] Davis and Jeppson (1973) add, "The writers believe a more satisfactory method (or methods) must exist for solving the space boundary value problems associated with three simultaneous, nonlinear partial differential equations."

Suppose we consider the flow past a body in a rectangular channel. Then Figs. 7 and 8 from Davis and Jeppson (1973) illustrate the coordinate systems and boundary conditions in

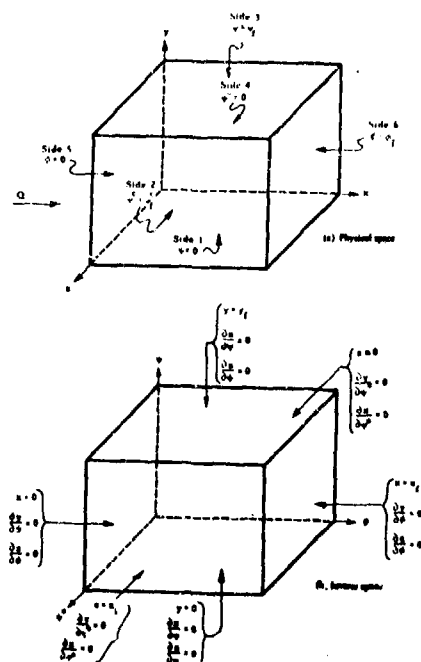


Figure 7 Coordinate Systems and Boundary Conditions for a Rectangular Channel in the Physical and Inverse Spaces. [After Davis and Jeppson (1973).]

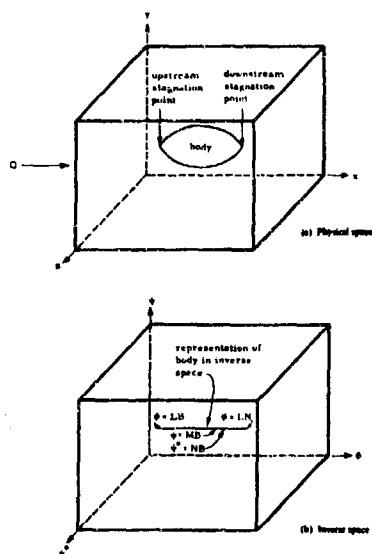


Figure 8. Illustration of the Formulation of the Problem of Flow Around a Three-Dimensional Body in a Rectangular Channel in (a) the Physical Space and (b) the Inverse Space. [After Davis and Jeppson (1973).]

the physical and inverse spaces. Sides 5 and 6 represent the inflow and outflow sections. Sides 1, 2 and 4 are solid boundaries, while side 3 is the free surface. The location of the free surface can be found from application of the Bernoulli equation during the solution process if the total head in the flow is specified.

Equations (6-8) are solved by the method of finite differences. The  $\Phi\psi\psi^*$  space is replaced by a three-dimensional finite-difference grid, with the values  $x_{ijk}$ ,  $y_{ijk}$ ,  $s_{ijk}$  to be found at the node points of the grid. Jeppson (1972) did not difference these equations directly. He first combined them by differentiation to obtain separate second-order equations for  $x$ ,  $y$ ,  $s$  in different planes within  $\Phi\psi\psi^*$  space under the assumption that certain relatively small cross-terms could be taken as known at each level of an iteration scheme. He then solved the resulting porous media flow problem by SOR and LSOR methods. The details are given in Jeppson (1972).

On the other hand Davis and Jeppson (1973) attacked the first-order equation system directly. After testing several methods they

settled on a modified Gauss-Seidel method. Because only first-order differences appear in the three, coupled nonlinear equations, which must be solved simultaneously, only first-order differences can be used in the finite-difference scheme; otherwise, point-iterative methods will not converge. Eight possible combinations of first-order differences (forward and backward) exist and can be used to represent Eqs. (6-8). Davis and Jeppson (1973) use a weighted sum of these eight, the weights depending on the location of a given node point in the  $\Phi\psi\psi^*$  finite-difference grid.

Jeppson (1972) presented a successful simulation of a three-dimensional porous media flow with a free surface. Davis and Jeppson (1973) solved three-dimensional flow past prolate spheroids in a rectangular duct and in a rectangular channel with a free surface. They also formulated, but did not solve, the cavity flow problem. No comparisons to experimental results were made.

A major advantage of the inverse method is that the solution is carried out in a simple domain of known geometric properties, in spite of the unknown locations of free surfaces. Major disadvantages lie in the inability to prescribe curved body surfaces directly in the physical space (the shape is given parametrically in the  $\Phi\psi\psi^*$  space and known in physical space only after the solution is obtained) and in the difficulties associated with solving the set of coupled, nonlinear, first order partial differential equations. It appears, however, that this method deserves further study.

#### The Finite Element Method

Larock and Taylor (1976) applied finite-element techniques to solve the jetflow from a circular pipe and orifice under the influence of gravity. The resulting flow is three-dimensional, namely, the jet remains essentially circular but droops under the action of gravity creating a three-dimensional flowfield. They employed the velocity potential as the dependent variable and allowed it to vary quadratically within each isoparametric hexahedron element. An iterative approach was used to determine the free surface position whose precise location is initially unknown. The formulation of their problem is relatively straightforward and they are able to prescribe the flowrate in the pipe and then proceed with their iteration to find the location of the stream surface.

Street and Ko (1977) solved the problem of a fully cavitating flow past a disk in a water tunnel. To illustrate the use of a finite-element technique, we repeat their formulation here



and apply it to the case of flow past an elliptic plate in a rectangular water tunnel.

The flow is assumed to be incompressible, steady, and irrotational. Hence, it is governed by a velocity potential  $\phi(x, y, z)$  which satisfies the Laplace Equation  $\nabla^2 \phi = 0$  within the fluid and generally

$$\vec{V} = -\nabla \phi \quad (9)$$

so, in the usual notation and Cartesian coordinate system,

$$u = -\partial \phi / \partial x; \quad v = -\partial \phi / \partial y; \quad w = -\partial \phi / \partial z \quad (10)$$

The streamline conditions

$$\frac{dy}{dx} = \frac{v}{u}; \quad \frac{dz}{dx} = \frac{w}{u} \quad (11)$$

describe the free surface, where in the absence of gravity influence

$$u^2 + v^2 + w^2 = q_c^2 = \text{constant} \quad (12)$$

As a consequence, in terms of a coordinate system oriented along the streamline, the change of potential on the free surface is given by

$$-\frac{\partial \phi}{\partial s} = q_c \quad (13)$$

In the finite-element method we represent a problem solution as a continuous function in terms of values at the edges of finite volumes in the problem domain and with a specified variation locally within such volumes as functions of the edge value. Partial differential equations are replaced by integrals which are subsequently replaced by a set of algebraic equations which can be solved directly and exactly.

There are three parts to a finite-element method formulation:

(a) The variational principle.

Functional:

$$\chi = \int_V \frac{1}{2} \left[ \left( \frac{\partial \phi}{\partial x} \right)^2 + \left( \frac{\partial \phi}{\partial y} \right)^2 + \left( \frac{\partial \phi}{\partial z} \right)^2 \right] dV \quad (14)$$

in which the functional  $\chi$  is minimized with respect to the velocity potential values specified at finite element nodes  $\phi_i$ .

(b) The functional representation within an element.

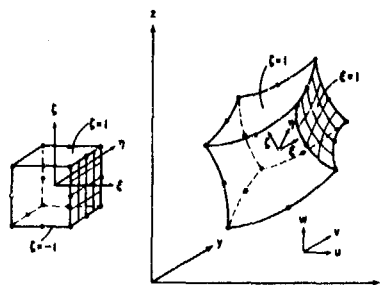
Within element:

$$\phi = [N_1, N_2, \dots, N_{20}] \begin{Bmatrix} \phi_1 \\ \phi_2 \\ \vdots \\ \phi_{20} \end{Bmatrix} = [N] \{\phi\}^e \quad (15)$$

We employ a quadratic variation within the hexahedral 20-node element. In Eqn. (15) the  $\phi_i$  are the values of the velocity potential at the corner and mid-side nodes of the element, while the  $N_i$  are the well-known shape functions.

(c) The isoparametric element.

We have chosen, as noted above, a 20-node hexahedron element. Figure 9 shows a schematic of our isoparametric element in the physical Cartesian space and in its transformed space.



Local (Natural) Co-ordinates

Cartesian Co-ordinates

Figure 9. The Isoparametric Element.

Now the functional in Eqn. (14) is minimized with respect to the nodal values  $\phi_i$  within each element (Huebner, 1975). Thus,

$$\frac{\partial \chi^e}{\partial \phi_i^e} = \int_V \left\{ \frac{\partial N_i}{\partial x} \frac{\partial \phi}{\partial x} + \frac{\partial N_i}{\partial y} \frac{\partial \phi}{\partial y} + \frac{\partial N_i}{\partial z} \frac{\partial \phi}{\partial z} \right\} |\phi|^e dV = 0 \quad (16)$$

or for each element

$$\frac{\partial \chi^e}{\partial \phi_i^e} = [h] \{\phi\}^e = 0 \quad (17)$$

The global sum over all elements produces a linear algebraic equation set

$$[H] \{\phi\} = 0 \quad (18)$$

A unique solution is guaranteed by specification

of the  $\phi_i$  or  $\psi$  derivatives along the flow boundaries.

For the isoparametric element of Fig. 9 we write a transform from the physical space to a set of natural local coordinates  $(\xi, \eta, \zeta)$  such that each element occupies the cube bounded by  $|\xi, \eta, \zeta| \leq 1$ . Generally then (Huebner, 1975)

$$\left. \begin{aligned} x(\xi, \eta, \zeta) &= \sum_{i=1}^{20} N_i(\xi, \eta, \zeta) x_i \\ y(\xi, \eta, \zeta) &= \sum_{i=1}^{20} N_i(\xi, \eta, \zeta) y_i \\ z(\xi, \eta, \zeta) &= \sum_{i=1}^{20} N_i(\xi, \eta, \zeta) z_i \\ \phi(\xi, \eta, \zeta) &= \sum_{i=1}^{20} N_i(\xi, \eta, \zeta) \phi_i \end{aligned} \right\} \quad (19)$$

where  $x_i$ ,  $y_i$ ,  $z_i$ , and  $\phi_i$  are the nodal values in each element. The key idea is that the mathematical formulation is easily made on a set of cubes while physically we can handle complex curved boundary surfaces.

The essence of the transformation [Eqn. (19)] is in the Jacobian

$$[J] = \begin{bmatrix} \partial x / \partial \xi & \partial y / \partial \xi & \partial z / \partial \xi \\ \partial x / \partial \eta & \partial y / \partial \eta & \partial z / \partial \eta \\ \partial x / \partial \zeta & \partial y / \partial \zeta & \partial z / \partial \zeta \end{bmatrix} \quad (20)$$

which relates, for example,

$$dx dy dz = |J|^{-1} d\xi d\eta d\zeta \quad (21)$$

and

$$\begin{bmatrix} \frac{\partial N_i}{\partial \xi} \\ \frac{\partial N_i}{\partial \eta} \\ \frac{\partial N_i}{\partial \zeta} \end{bmatrix} = [J] \cdot \begin{bmatrix} \frac{\partial N_i}{\partial x} \\ \frac{\partial N_i}{\partial y} \\ \frac{\partial N_i}{\partial z} \end{bmatrix} \quad (22)$$

Figure 10 is a schematic of the physical problem. We model the flow past an elliptic plate of semi-axes  $P$  and  $Q$  in a rectangular water tunnel of half-width  $W$  and depth  $D$ . The elliptic plate is assumed to be supported on one side of the tunnel. In Fig. 10 is shown a

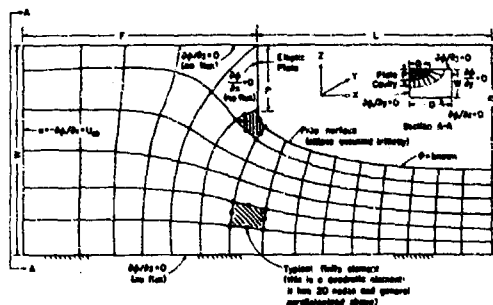


Figure 10. Schematic of Cavity Flow Problem.

centerline section for one quarter of the flow. The flow velocity is prescribed upstream while a Riabouchinsky cavity model is used; thus, only the forward half of the cavity is shown. The upper half of the flow (not shown) is symmetric to the part shown.

The boundary conditions for a fully-cavitating flow in a water tunnel are straight forward. With a Riabouchinsky model, the downstream boundary is an equipotential line. If the potential downstream is taken to be zero, then when a free surface shape is known (assumed or calculated) the potential can be computed on the free surface by Eqn. (13). The remainder of the flow boundaries are solid or no flow boundaries, except upstream from the plate. Typical boundary conditions are illustrated in Fig. 10.

If  $F$ ,  $W$ ,  $D$ ,  $P$ ,  $Q$ , and  $L$  are given, there exists a unique value of the cavitation number

$$\sigma = \left( \frac{q_c}{U_\infty} \right)^2 - 1 = \frac{p_\infty - p_c}{\frac{1}{2} \rho U_\infty^2} \quad (23)$$

in which  $q_c$  is the magnitude of the velocity on the free surface,  $U_\infty$  is the prescribed upstream  $u$ -component of velocity,  $p_\infty$  is the upstream pressure,  $p_c$  is the cavity pressure, and  $\rho$  is the fluid density. In our case we elect to prescribe  $U_\infty$  and to determine  $q_c$  and  $\sigma$  as part of the solution process.

With the given boundary conditions (cf., Fig. 10), an assumed free surface location, and specified geometry of plate and tunnel, the finite element method can be used to find the nodal values  $\phi_i$  of the velocity potential and to determine the fluid velocities  $u$ ,  $v$  and  $w$ . We next move the free stream surface to a better location.

The total process can be summarized as follows:

a. Establish the geometry. Input all data including locations of all corner nodes, assumed form of free surface, assumed  $U_{\infty}$ , etc. The computer program then locates all the mid-nodes.

b. Generate "stiffness" matrix  $H$  (Eqn. 18). Account for various boundary conditions where  $\phi_i$  or  $\phi$  derivatives are specified and for isoparametric mappings.

c. Solve for  $\phi_i$  by Gaussian elimination and back substitution.

d. Calculate fluid velocities.

e. Move the free surface. Movement is accomplished by integration (cf., Larock and Taylor, 1976) along free streamlines beginning at element corner nodes on the edge of the plate. This establishes a set of lines which are tangent to the velocity in accordance with the streamline equations

$$\frac{dy}{dx} = \frac{v}{u} \quad \text{and} \quad \frac{dz}{dx} = \frac{w}{u} \quad (24)$$

A periodic cubic spline interpolation is employed in planes  $x = \text{constant}$  to locate the element transverse mid-nodes which are missed by the integration process.

f. Establish new values of  $\phi$  on the free surface.

g. Modify the "stiffness" matrix  $H$ . Only elements near the free surface are changed by the move so only a small part of  $H$  is changed.

h. Return to Step c unless free surface movement is less than an arbitrary, preset, small amount. If this happens the solution is complete.

The solution program has been implemented on the IBM 360/91 and 370/168 Triplex System at the Stanford Linear Accelerator Center. With 1325 nodes and 224 elements in a typical case, one iteration (Steps a through h) takes about 45 seconds and solution is achieved in about 15 iterations.

Street and Ko (1977) applied the above technique to two geometries. First, they reproduced the geometry used by Brennen (1969), viz., a Riabouchinsky model of flow past a circular disk in a circular tunnel. The finite element results for  $\sigma$  and cavity radius  $B$  agreed to within 2 percent with Brennen's results when the physical geometry was specified. Second, they examined flow past a disk in a square water tunnel, demonstrating for the first time (a) a fully nonlinear, three-dimensional cavity flow and (b) the effect of three-dimensionality on the wall effect in this flow (as compared to that in the axisymmetric case).

Figure 11 shows the wall effects for flows past disks in both circular and square water tunnels (in Fig. 10, the square tunnel flow corresponds to  $Q = 0$  and  $D = W$ ). The square-tunnel flow (which is three dimensional) deviates

noticeably from its axisymmetric counterpart for small  $W/P$ , i.e., where wall effects are large.

We have begun the simulation of cavitating flow past the elliptic plate in a rectangular water tunnel. No definitive results have been obtained, but the cavity shape appears to remain elliptical during the first few iteration steps.

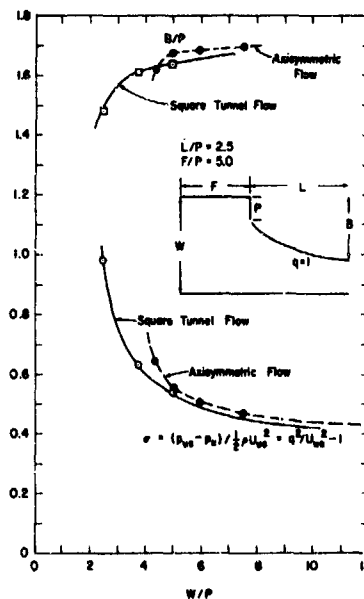


Figure 11. Wall Effects in Cavitating Flow Past Disks.

### Prognosis

The prognosis for numerical simulation of three-dimensional, fully-cavitating, steady-state flows is good. Jiang and Leehey (1977) have developed a linearized method which is in good agreement with experimental data and is not limited to large aspect ratio or short cavities. The method of Furuya (1975b), while having such limitations in principle, works well outside those limits and is nonlinear with respect to angle of attack. Neither of these methods accurately models the tip regions of the flow, but this does not seem to be a major limitation at the moment.

Street and Ko (1977) have successfully applied a finite-element method which is fully

nonlinear to simple pure drag flows. As illustrated herein their simulation can be extended and is applicable in principle to hydrofoils in lifting flow. This method directly handles the tip regions, but may experience difficulties at low angles of attack due to the rapid changes in flow near separation and the extreme curvature of the free surface there.

The inverse method of Jeppson (1972) and Davis and Jeppson (1973) deserves further study. In spite of the difficulties associated with solving the governing equations, the method has been successfully applied to free-surface, non-cavitating flows. An extension to cavitating flow based on a Riabouchinsky model appears feasible.

A method likely to make a major contribution to fully nonlinear flow simulation is the boundary integral equation technique. White and Kline (1975) used it successfully for axisymmetric free-surface flows. Larock (1977) presents an application of the method in these proceedings. Finally, Hess (1972) has demonstrated the power of the technique in fully-wetted, three-dimensional, lifting potential flows.

#### Acknowledgments

The finite element work for three-dimensional cavitating flows reported herein is a joint effort of the author with Peter Y. Ko under the sponsorship of the Naval Sea Systems Command General Hydromechanics Research Program, Subproject SR 023 01 01, administered by the David W. Taylor Naval Ship Research and Development Center, Contract N00014-75-C-0277.

#### References

1. A. J. Acosta (1973). "Hydrofoils and Hydrofoil Craft" *Ann. Rev. Fluid Mech.*, **5**, pp. 161-184.
2. A. H. Armstrong and J. H. Dunham (1953). "Axisymmetric Cavity Flow" *Ann. Research Estab.*, Kent, England, Rep. 12/53.
3. C. Brennen (1969). "A numerical solution of axisymmetric cavity flows" *J. Fluid Mech.*, **37**, pp. 671-688.
4. S. T. K. Chan and B. E. Larock (1973a). "Fluid Flows from Axisymmetric Orifices and Valves" *J. Hydr. Div., Proc. ASCE*, **99**, pp. 81-97.
5. S. T. K. Chan, B. E. Larock and L. R. Herrmann (1973b). "Free-Surface Ideal Fluid Flows by Finite Elements" *J. Hydr. Div., Proc. ASCE*, **99**, pp. 959-974.
6. A. L. Davis and R. W. Jeppson (1973). "Solving Three-Dimensional Potential Flow Problems by Means of an Inverse Formulation and Finite Differences" *Utah Wat. Research Lab. Rep. PRWG-96-2*, Utah State Univ., Logan.
7. O. Furuya (1975a). "Nonlinear calculation of arbitrarily shaped supercavitating hydrofoils near a free surface" *J. Fluid Mech.*, **68**, pp. 21-40.
8. O. Furuya (1975b). "Three-dimensional theory on supercavitating hydrofoils near a free surface" *J. Fluid Mech.*, **71**, pp. 339-359.
9. O. Furuya and A. J. Acosta (1976). "An Experimental Study of a Supercavitating Finite Aspect Ratio Hydrofoil Near a Free Surface" *Proc. Eleventh Naval Hydrodyn. Symp.*, London.
10. D. Gilbarg (1960). "Jets and Cavities" *Handbuch Der Physik, Strömungsmechanik III*, **9**, Springer-Verlag, pp. 311-445.
11. M. I. Gurevich (1965). *Theory of Jets in Ideal Fluids* (Transl. from Russian) Academic Press.
12. J. L. Hess (1972). "Calculation of Potential Flow About Arbitrary Three-Dimensional Lifting Bodies" *Douglas Aircraft Co., McDonnell Douglas Corp.*, Rep. No. MDG J5679-01.
13. K. H. Huebner (1975). *The Finite Element Method for Engineers* Wiley-Interscience.
14. R. W. Jeppson (1969). "Numerical Solutions to Free-Surface Axisymmetric Flows" *J. Engrg. Mech. Div., Proc. ASCE*, **95**, pp. 1-20.
15. R. W. Jeppson (1970). "Inverse formulation and finite difference solution for flow from a circular orifice" *J. Fluid Mech.*, **40**, pp. 215-223.
16. R. W. Jeppson (1972). "Inverse Solution to Three-Dimensional Potential Flows" *J. Engrg. Mech. Div., Proc. ASCE*, **98**, pp. 789-812.
17. C. W. Jiang and P. Leehey (1977). "A Numerical Method for Determining Forces and Moments on Supercavitating Hydrofoils of Finite Span" *Second Int'l. Conf. Numer. Ship Hydrodyn.*, Berkeley, Sept. 19-21.
18. B. E. Larock (1977). "An Application of the Boundary Integral Equation Method to Cavity and Jet Flows" *Second Int'l. Conf. Numer. Ship Hydrodyn.*, Berkeley, Sept. 19-21.
19. B. E. Larock and C. Taylor (1976). "Computing Three-Dimensional Free Surface Flows" *Int'l. J. Numer. Meth. Engrg.*, **10**, pp. 1143-1152.
20. P. Leehey (1973). "Supercavitating Hydrofoil of Finite Span" *Proc. IUTAM Symp. on Non-Steady Flow of Water at High Speed*, Leningrad (June 1971), Moscow, pp. 277-298.
21. P. Leehey and T. S. Stallinger (1975). "Force and Moment Measurements of

- Supercavitating Hydrofoils of Finite Span with Comparison to Theory" J. Fluids Engrg., Transact. ASME, 97, pp. 453-464.
22. T. R. Mogel and R. L. Street (1974). "A Numerical Method for Steady-State Cavity Flows" J. Ship Res., 18, pp. 22-31.
  23. T. Nishiyama (1970). "Lifting-line Theory of Supercavitating Hydrofoil of Finite Span" ZAMM, 50, pp. 645-653.
  24. Y. T. Shen and T. F. Ogilvie (1972). "Nonlinear Hydrodynamic Theory for Finite-Span Planing Surfaces" J. Ship Res., 16, pp. 3-20.
  25. R. L. Street and P. Y. Ko (1977). "Numerical Methods Applied to Fully Cavitating Flows, with Emphasis on the Finite Element Method" Symp. Hydrodyn. Ship and Offshore Propul. Sys., Det Norske Veritas, Høvik, March 20-25.
  26. L. F. Tsien and M. Gullbaud (1974). "A Theoretical and Experimental Study on the Planform of Superventilated Wings" J. Ship Res., 18, pp. 169-184.
  27. M. Van Dyke (1964). Perturbation Methods in Fluid Mechanics Academic Press.
  28. J. W. White and S. J. Kline (1975). "A Calculation Method for Incompressible Axisymmetric Flows, Including Unseparated, Fully Separated, and Free Surface Flows" Dept. Mech. Engrg., Thermosci. Div., Rept. MD-35, Stanford Univ., Stanford, CA.
  29. S. E. Widnall (1966). "Unsteady Loads on Supercavitating Hydrofoils" J. Ship Res., 9, pp. 107-118.
  30. T. Y. Wu (1968). "Inviscid Cavity and Wake Flows" Basic Develop. Fluid Dyn., 2, Academic Press, pp. 1-116.
  31. T. Y. Wu (1972). "Cavity and Wake Flows" Ann. Rev. Fluid Mech., 4, pp. 243-284.
  32. T. Y. Wu (1975). "Cavity Flow and Numerical Methods" First Int'l. Symp. Numer. Ship Hydrodyn., pp. 113-153.
  33. C. S. Yih (1957). "Stream Functions in Three-dimensional Flows" LaHouille Blanche, 12, pp. 445-450.

# A NUMERICAL METHOD FOR DETERMINING FORCES AND MOMENTS ON SUPERCAVITATING HYDROFOILS OF FINITE SPAN

C. W. Jiang and P. Leehey  
Massachusetts Institute of Technology  
Cambridge, Massachusetts 02139

## Abstract

A numerical lifting surface theory was derived for a supercavitating hydrofoil of finite span in steady flow. Discrete vortices and sources were used to represent the physical model, and the coupled integral equations were reduced to a set of simultaneous algebraic equations. The cavity length was iterated to get the desired cavitation number over the cavitated planform. The calculation of supercavitating hydrofoils of elliptic planform was performed and compared with analytical solutions and with experiments. Results of these calculations indicate that this numerical solution gave a more accurate prediction of lift and moment coefficients on a supercavitating hydrofoil than existing asymptotic theories.

## I Introduction

Considerable theoretical and experimental work has been done on three-dimensional supercavitating hydrofoils, but the agreement between the theory and experiment is not fully satisfactory.

A few attempts have been made to apply a numerical lifting surface technique to cavitating hydrofoils. Widnall (1966) and Unruh and Bass (1974) used a double lattice - source representation for the prediction of forces on supercavitating hydrofoils of finite span. Both make priori assumptions of cavity length which are not appropriate for short cavities. Efremov and Soroka (1975) used the Lawrence approximations and an elliptic source, vortex distribution along the span to transform the three-dimensional problem to two-dimensional equations for rectangular supercavitated wings. Nishiyama (1970) made no a priori assumptions regarding the cavity length, which was determined from the two-dimensional results and corrected by using induced angle of attack. The integral equations were simplified by the condition of large aspect ratio. A matched asymptotic

solution for large aspect ratio has been derived by Leehey (1973). The paper by Leehey and Stellingner (1975) showed good agreement between asymptotic theory and experiments for lift and drag coefficients in a certain range of  $\sigma/\alpha$  (cavitation number divided by angle of attack). Theoretical moments were too large, indicating the need for lifting surface corrections.

This numerical method is a lifting surface theory for a supercavitating hydrofoil of finite span. The discrete vortex and source method is used to formulate the equations. The governing equations for this problem are a pair of coupled-integral equations relating the unknown boundary values of the upwash and the cavity pressure to the unknown distribution of vortices and sources on the foil-cavity surfaces. An iteration scheme is used to alter the cavity length until the desired cavitation number is reached over the cavitated planform.

The numerical accuracy of the present method is tested in two-dimensional flow. The results compare well with the linearized analytical solution of Geurst (1960). The predicted results of elliptic foil were compared with analytical solutions by Leehey (1973), and with experiments by Leehey and Stellingner (1975). The results show that the improvement has been made after considering the lifting surface effect.

## II Linearized Theory

The linearized problem for a cavitating hydrofoil of finite span in steady flow can be represented by a set of coupled integral equations. The derivation proceeds either from Green's theorem or from the solution for the velocity field induced by a distribution of vortices and sources. This distribution must be chosen to satisfy the relevant boundary conditions. The numerical model we are about to describe

is shown in Figure 1.

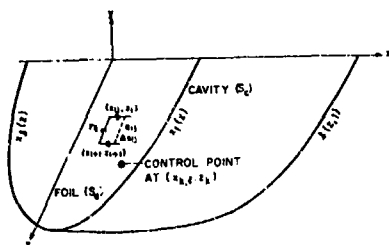


Figure 1. Foil Planform and Typical Vortex Source Element

The source distribution  $q(x, z)$  represents the slope difference between the upper cavity surface and the mean camber line of the foil or the lower cavity surface at the point  $(x, 0, z)$ . The vortex distributions  $\gamma(x, z), \delta(x, z)$  create the perturbation velocity differences in the  $x$  and  $z$  components between the upper and lower surfaces at the point  $(x, 0, z)$ . This leads to the result

$$\begin{aligned} g(x, z) &= \frac{1}{U_\infty} (V(x, 0, z) - V(x, -0, z)), \\ \gamma(x, z) &= \frac{1}{U_\infty} (u(x, -0, z) - u(x, 0, z)), \\ \delta(x, z) &= \frac{1}{U_\infty} (w(x, 0, z) - w(x, -0, z)). \end{aligned} \quad (1)$$

The boundary conditions specified are the normal velocity on the wetted surface of the foil, a constant pressure in the cavity, and closure of the cavity.

$$\begin{aligned} V(x, -0, z) &= U_\infty \frac{\partial h(x, z)}{\partial x}, \\ P_c &= P(x, 0, z), \\ 0 &= \iint_{S_c} g(\xi, \zeta) d\xi d\zeta, \end{aligned} \quad (2)$$

where  $h(x, z)$  is the  $y$ -ordinate of the wetted surface.  $S_c$  is the surface of the cavity as projected onto the  $x$ - $z$  plane.  $P_c$  is cavity pressure. Gaustad

(1961) proved that for two-dimensional steady flow, the re-entrant jet and Riabouchinsky models for cavity termination reduced upon linearization to a statement that the cavity is closed at its end. The requirement that the source strength be zero beyond the cavity trailing edge and the sum of sources is zero are necessary to meet this condition.

Based on the boundary conditions, the integral equations for three-dimensional steady flow can be written as

$$\begin{aligned} V(x, -0, z) &= -\frac{1}{2} g(x, z) \\ &+ \frac{1}{4\pi} \iint_{S_c} \frac{g(\xi, \zeta) [(x-\xi)^2 + (z-\zeta)^2]^{3/2}}{[(x-\xi)^2 + (z-\zeta)^2]^{3/2}} d\xi d\zeta \\ &+ \frac{1}{4\pi} \iint_{S_w} \frac{\delta_w(\xi, \zeta) [(x-\xi)^2 + (z-\zeta)^2]^{3/2}}{[(x-\xi)^2 + (z-\zeta)^2]^{3/2}} d\xi d\zeta, \end{aligned} \quad (3)$$

$$\begin{aligned} 0 &= \frac{P_c - P_\infty}{\frac{1}{2} \rho U_\infty^2} \\ &= -\gamma(x, z, t) \\ &+ \frac{1}{2\pi} \iint_{S_c} \frac{g(\xi, \zeta) [(x-\xi)^2 + (z-\zeta)^2]^{3/2}}{[(x-\xi)^2 + (z-\zeta)^2]^{3/2}} d\xi d\zeta, \end{aligned} \quad (4)$$

$$0 = \iint_{S_c} g(\xi, \zeta) d\xi d\zeta, \quad (5)$$

where  $S_a$  is the projection of the foil surface on to the  $x$ - $z$  plane and  $S_w$  is the projection of the wake region on to the same plane.  $P_\infty$  is free stream pressure. The unknowns are the source strength, vortex strength and cavity surface location.

The solution of these integral equations will represent the linearized, supercavitating hydrofoil of finite span in steady flow. The forces and moments can be calculated using the Bernoulli equation.

### III Numerical Method

The solution of the problem is

obtained by reducing the coupled integral equations to a set of simultaneous algebraic equations.

The surface is divided into small elements. The element used in this model is one obtained by dividing the foil and cavity semispan into strips with cosine spacing, while the chord is divided into strips of constant spacing on the foil and on the cavity behind the foil. In order to increase the rate of convergence for the number of elements used, the first two elements of each chordwise strip, near the leading edge, have only one-half the chord spacing of the rest of the elements on the foil.

The model uses discrete vortices and sources to represent the foil and cavity. Each element contains a bound line vortex, a trailing vortex and a line source. The quarter-chord line of each element contains the bound vortex, and the induced velocities are calculated for all elements at their midspan, three-quarter chord positions. James (1972) showed that for the best efficiency the vortex and control points should be arranged according to the Pistolesi approximation, i.e., at the quarter and three-quarter chord points on each element. The concentrated line source is taken to be a constant distribution across each element at its three-quarter chord position. Since the source distribution is singular at the cavity leading edge and termination point, these control points should be placed away from the singularities. Therefore, the first control point is located at the three-quarter chord and the source is located at the quarter chord. The local vortex or source strength is given by the discrete vortex or source strength divided by the element width.

Since the cavity length is unknown, a closure condition is applied to individual spanwise strips in the calculation. Otherwise, the iteration technique does not converge. This condition satisfies the overall global condition. It also allows the variation of cavity length along the span to vary. This approach is exact for a symmetric foil. The source integration along a strip between  $s = -x_1$  and  $s = x_1$  is

$$\int_{-x_1}^{x_1} \int_{\eta_1}^{\eta_2} g(\xi, s) d\xi ds, \quad (6)$$

where  $x_1(\zeta)$  and  $\eta_1(\zeta)$  are the spanwise profiles of the leading edge and cavity termination points, respectively. Let  $g(\xi, s)$  represent the profile of the cavity-foil combination. Then the strip-

wise integration becomes

$$\begin{aligned} & \int_{-x_1}^{x_1} \int_{\eta_1}^{\eta_2} \left( \frac{\partial g}{\partial \xi} + \frac{\partial g}{\partial s} - \frac{\partial g}{\partial \xi} - \frac{\partial g}{\partial s} \right) d\xi ds \\ &= \int_{-x_1}^{x_1} \left( g_+(\xi, s) - g_-(\xi, s) \right) \Big|_{\eta_1}^{\eta_2} ds \\ &+ \int_{\eta_1}^{\eta_2} \left( g_+(\xi, s) - g_-(\xi, s) \right) \Big|_{-x_1}^{x_1} d\xi \\ &= 0. \end{aligned} \quad (7)$$

The first integral is zero if the cavity is closed both at its leading edge and trailing edge. The second integral is zero due to the symmetry of the cavity. This integral therefore represents the stripwise closure condition.

The effect of all singularities must be calculated at each control point. The Biot-Savart's law is used to calculate the induced velocity at a control point due to a constant strength discrete vortex segment. The Kirchhoff's law and Kelvin's theorem must be satisfied for the vortex distribution. Consider the vortex segment  $(x_1, 0, z_1)$  to  $(x_2, 0, z_2)$  with strength  $\gamma$  per unit length. Defining  $(\xi, \zeta)$  as the coordinates of a general point on the vortex, and  $(x, z)$  as the coordinates of a control point, the induced velocity at  $(x, z)$  due to the bound vorticity,  $\gamma_A$ , is

$$\frac{4\pi U(x, 0, z)}{\gamma_A} = \frac{2a\gamma + b}{2d(2s^2 + b^2 + c^2)} \Big|_{\eta_1}^{\eta_2}, \quad (8)$$

$$a = 1 + t^2,$$

$$b = -2(\epsilon t + \delta),$$

$$t = (x_2 - x_1) / (x_2 - \delta),$$

$$e = x - x_1 + t\delta,$$

$$d = x - x_1 + t\delta - \epsilon\delta,$$

$$c = e^2 + \delta^2. \quad (9)$$



The induced velocity due to the trailing vortex  $(x, 0, z_1)$  to  $(x_3, 0, z_3)$  with strength  $\Gamma_a$  is

$$\frac{4\pi U(x, z, \delta)}{\delta_a} = \frac{\Gamma_a}{\delta - \delta_1} \frac{1}{((x-\xi)^2 + (\delta - \delta_1)^2)^{3/2}} \Big|_{\xi=z_1}^{\xi=z_3} \quad (10)$$

The total velocity induced by a vortex distribution is the sum of the influence of all the spanwise and chordwise vortices.

According to the linearized Bernoulli equation, the pressure induced by the source component is

$$P_s = -2 \frac{\partial \varphi_s}{\partial x} = -2 u_s, \quad (11)$$

where  $\varphi_s$  is the source potential. The  $P_s$  due to the line source  $((x_1, 0, z_1)$  to  $(x_2, 0, z_2))$  can be calculated by the line integration

$$P_s = -\frac{1}{2\pi} \int_{(x, \delta_1)}^{(x_2, \delta_2)} \frac{(x-\xi) d\xi}{((x-\xi)^2 + (\delta - \xi)^2)^{3/2}} \\ = -\frac{1}{2\pi} \frac{a^{3/2} (\delta - \delta_1)}{d ((x-\xi)^2 + (\delta - \xi)^2)^{3/2}} \Big|_{\delta_1}^{\delta_2}, \quad (12)$$

where  $a, b, d$  are defined the same as before.

Equations (8) and (12) are not suitable for numerical computation if  $d/\sqrt{a}$  becomes small (Kirwin and Oppenheim (1974)). The following approximate formulas are used for this special case.

(1) for  $z_1 \leq z \leq z_2$

$$\frac{4\pi U}{\delta_a} \approx 2a^{3/2} \left[ \frac{1}{d} - \frac{d}{(2a\delta_1 + b)^2} - \frac{d}{(2a\delta_2 + b)^2} \right], \quad (13)$$

$$\frac{4\pi u_s}{\delta} \approx \frac{a^{3/2}}{d} \frac{\delta - \delta_1}{(a\delta^2 + b\delta + c)^{3/2}} \Big|_{\delta_1}^{\delta_2}. \quad (14)$$

(2) for  $z < z_1$

$$\frac{4\pi U}{\delta_a} \approx 2a^{3/2} \left[ \frac{d}{(2a\delta_1 + b)^2} - \frac{d}{(2a\delta_2 + b)^2} \right], \quad (15)$$

$$\frac{4\pi u_s}{\delta} \approx 2d \left[ \frac{1}{(2a\delta_1 + b)^2} - \frac{1}{(2a\delta_2 + b)^2} \right] + 2d \left( \left| \frac{1}{2a\delta_2 + b} \right| - \left| \frac{1}{2a\delta_1 + b} \right| \right). \quad (16)$$

(3) for  $z > z_2$

$$\frac{4\pi U}{\delta_a} \approx 2a^{3/2} \left[ \frac{d}{(2a\delta_2 + b)^2} - \frac{d}{(2a\delta_1 + b)^2} \right], \quad (17)$$

$$\frac{4\pi u_s}{\delta} \approx 2d \left[ \frac{1}{(2a\delta_1 + b)^2} - \frac{1}{(2a\delta_2 + b)^2} \right] + 2d \left( \left| \frac{1}{2a\delta_1 + b} \right| - \left| \frac{1}{2a\delta_2 + b} \right| \right). \quad (18)$$

An iteration is used to alter the cavity length until the desired cavitation number is reached over the cavitated planform. A cavity length is assumed and the matrix coefficients are calculated. Solving the matrix with appropriate boundary conditions, we can get the distribution of vortices and sources, and the cavitation number on each strip. Then a new cavity length is chosen using the calculated cavitation number. The length is adjusted by using Newton's method with Geurst's steady state analytic solution.

The linear algebraic equations which satisfy the boundary conditions are solved by using Gauss elimination with equilibration and partial pivoting (e.g. Isaacson and Keller (1966)). The convergence tests had been made both on two-dimensional cavity flow (Uhlman and Jiang (1977)) and three-dimensional supercavitating hydrofoils. Table 1 gives the number of elements chosen in the numerical calculation.

Table 1 Values of Vortex and Source Element

No. of element along the chord on the foil	12
No. of element in the cavity behind the foil	8 to 14
No. of element along the semispan	6

#### IV. Comparison Between Theory & Experiment

Present numerical results for two-dimensional supercavitating flow are compared with Geurst's analytic solution (1960) and Golden's numerical scheme (1975). Golden used a uniform distribution of the singularity in each element and the best choice of control points. Figure 2 simply confirms that these methods of solution lead to identical results.

The lift and moment calculation for supercavitating hydrofoils of elliptic planform was performed and compared with analytic solutions by Leehey (1973), experiments by Leehey and Stellingner (1975) and experiments by Maixner (1977). Leehey utilized the method of matched asymptotic-expansions. The theory is valid to first order in angle of attack and second order in the reciprocal of aspect ratio. In the experiments of Leehey and Stellingner forces, moments and cavity lengths were measured for aspect ratio 3 and 5 supercavitating hydrofoils of elliptic planform. Maixner investigated the water tunnel wall effects on supercavitating

hydrofoils of finite span by using a geometrically similar family of three hydrofoils ( $R = 5$ ). He showed that the previous tests by Leehey and Stellingner were reliable. The standard wind tunnel wall correction is adequate when the foil span is equal to or less than half of the tunnel depth. It should be noted that the data of Leehey and Stellingner was based on the cavitation number calculated by using the vapor pressure rather than the measured cavity pressure. In the comparison with present results, for the aspect ratio 5 foil, experimental data for the medium foil is taken from Maixner's results where measured cavity pressure were used.

Figures 3 and 4 show the ratio of the lift coefficient to the angle of attack,  $C_L/\alpha$ , versus  $\sigma/\alpha$  for the aspect ratio 5 and 3 hydrofoils, respectively. The agreement between theory and experiment is good. For small values of  $\sigma/\alpha$ , there is much better agreement with the present numerical theory than with Leehey's asymptotic theory. The foil and cavity combination is no longer of large aspect ratio at small  $\sigma/\alpha$ , so the asymptotic theory is not valid.

The moment coefficient is taken about the mid-chord, consistent with the right hand rule. Figures 5 and 6 show the moment coefficient for the aspect ratio 5 and 3 hydrofoils. Since Leehey's matched asymptotic expansion theory neglects the lifting surface effect, it is expected that the present numerical lifting surface theory would show better agreement with experiments.

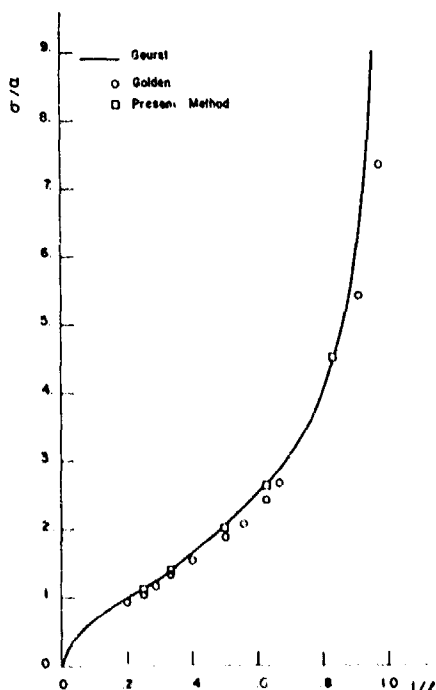


Figure 2. Cavity Length vs.  $\sigma/\alpha$  Flat Plate

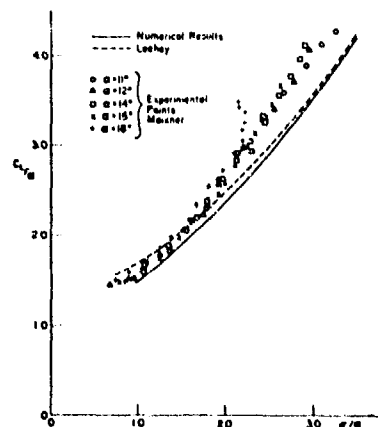


Figure 3.  $C_L/\alpha$  vs.  $\sigma/\alpha$ ,  $R=5$

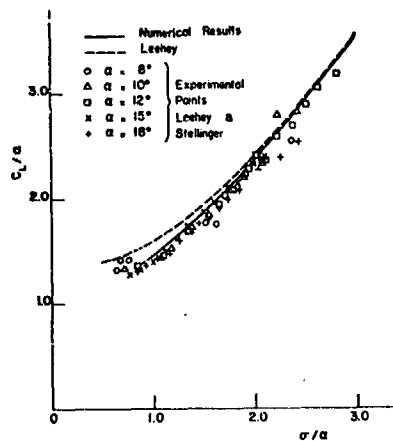


Figure 4.  $C_L/a$  vs.  $\sigma/a$ ,  $R=3$

The nondimensional cavity length versus the ratio of cavitation number to angle of attack is shown in Figures 7 and 8. The cavity length is measured from the leading edge at the spanwise location of the centroid of the foil area. Generally speaking, the agreement between the theory and experiments is very good.

In Maixner's experiment, the cavity pressure was measured with a foil surface pressure tap. A noticeable "hook" was found in the lift and moment data at higher angles of attack (Figures 3 & 5). Ram effects on the cavity pressure measurement, due to the dynamic pressure, were further investigated on the large foil used in Maixner's test. The cavity pressure readings are taken both inside the cavity, using a total head tube, and on the foil surface. The L-shaped total head tube protruded

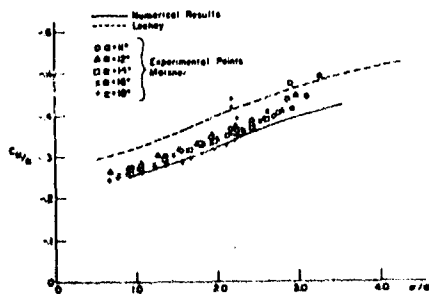


Figure 5.  $C_M/a$  vs.  $\sigma/a$ ,  $R=5$

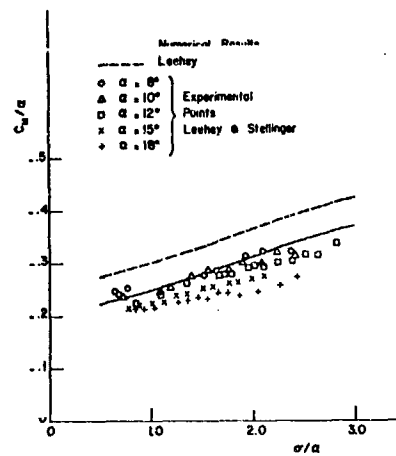


Figure 6.  $C_H/a$  vs.  $\sigma/a$ ,  $R=3$

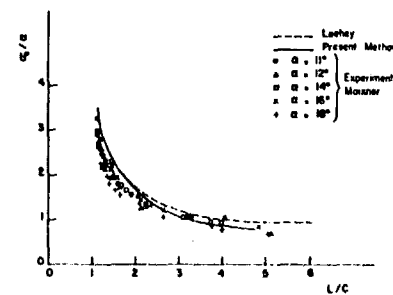


Figure 7.  $\sigma_c/a$  vs.  $L/C$ ,  $R=3$

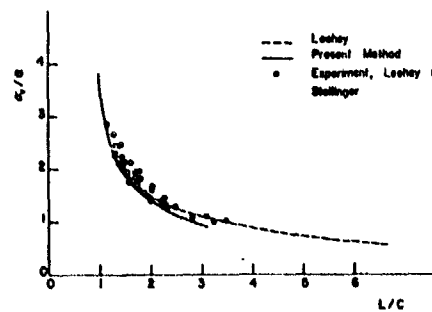


Figure 8.  $\sigma_v/a$ ,  $L/C$ ,  $R=3$

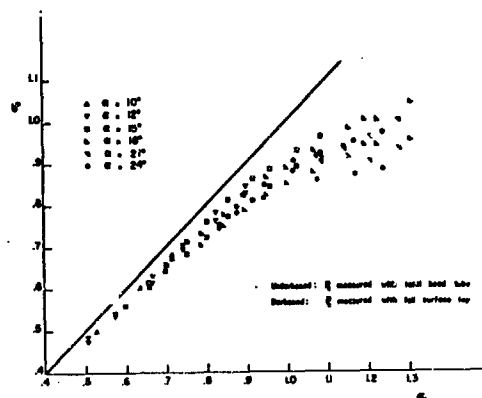


Figure 9.  $\sigma_c$  vs.  $\sigma_v$

downwards into the cavity from the upper tunnel wall so that it was parallel to the foil surface and pointed towards the leading edge, away from the impinging re-entrant jet. Figure 9 shows that the readings from the foil surface pressure tap are consistently higher than the measured cavity pressure, especially at higher angles of attack and shorter cavity lengths. If the improved cavity pressure measurements had been taken in the experiments of Maixner, the discrepancy from theory at higher angles of attack and shorter cavities would probably have been smaller.

#### V Conclusions

The discrete vortex and source method was developed for supercavitating hydrofoils. The cavity length was iterated to get a uniform cavitation number over the cavity planform. The lift and moment coefficients for supercavitating hydrofoils of elliptic planform in steady flow was performed and compared well with previous experiments. A more accurate prediction of lift and moment coefficients was obtained by the present numerical method than with existing asymptotic theories.

#### Acknowledgement

This research was carried out under the Naval Ship Systems Command, General Hydromechanics Research Program, Subproject SR 009 01 01, administered by the Naval Ship Research and Development Center.

#### References

- 1 Efremov, I. I. & Soroka, R. A. 1975 Approximate Computation of the Cavitation Flow Around Small Span Wing. *Fluid Dynamics*.
- 2 Geurst, J. A. 1960 Linearized Theory for Fully Cavitated Hydrofoils. *Int. Shipbuilding Progress*, Vol 7, No. 65.
- 3 Geurst, J. A. 1961 Linearized Theory of Two-dimensional Cavity Flows, Doctoral Dissertation, Technical Univ., Delft, The Netherlands.
- 4 Golden, D. W. 1975 A Numerical Method for Two-dimensional Cavitating, Lifting Flows, M. S. Thesis, MIT.
- 5 Isaacson, E. & Keller, H. B. 1966 Analysis of Numerical Methods. John Wiley & Sons.
- 6 James, R. M. 1972 On the Remarkable Accuracy on the Vortex Lattice Method, *Computer Methods in Applied Mechanics and Engineering*, 1.
- 7 Kerwin, J. E. & Oppenheim, B. W. 1974 A Lifting-Surface Program For Tricoidal Control Surfaces With Flaps, Rep. No. 74-15, MIT.
- 8 Leehey, P. 1973 Supercavitating Hydrofoils of Finite Span, Proceedings of the IUTAM Symposium in Leningrad, Nauka Publishing House, Moscow.
- 9 Leehey, P. & Stallinger, T. C. 1975 Force and Moment Measurement of Supercavitating Hydrofoils of Finite Span With Comparison to Theory, *J. of Fluids Engineering*, ASME.
- 10 Maixner, R. M. 1977 An Experimental Investigation of Wall Effects on Supercavitating Hydrofoils of Finite Span, MIT Dept. Ocean Eng. Report No. 83481-3
- 11 Nishiyama, T. 1970 Lifting Line Theory of Supercavitating Hydrofoil of Finite Span, *IAMM*, Vol. 50.

12 Uhlman, J. S., Jr. & Jiang, C. W.,  
Experiments on a Partially Cavitating  
Plano-Convex Hydrofoil With Comparison  
to Theory, MIT Dept. Ocean Eng. Report  
No. 83481-2

13 Unruh, J. R. & Bass, R. L. 1974  
A General Theory of Unsteady Load on  
Cavitating Hydrofoils, J. Hydraulics,  
Vol. 8, No. 4.

14 Widnall, S. E. 1966 Unsteady Loads  
on Supercavitating Hydrofoils of Finite  
Span, J. Ship Research, Vol. 10, No. 2.

# SUPERCAVITATING FOIL OF AN ARBITRARY SHAPE BENEATH OR ABOVE A FREE SURFACE OR IN A CASCADE

B. Yip

David W. Taylor Naval Ship Research and Development Center  
Bethesda, Maryland 20884

## 1. INTRODUCTION

Linear and nonlinear models of supercavitating foils have been investigated extensively.<sup>1-14</sup> All investigations involve a considerable amount of numerical work. Thus the advent of high speed computers naturally requires efficient numerical methods to be applied to the solution of the flow field and the design of supercavitating foils. Recently a large effort has been exerted toward numerical computation of cavity flows<sup>15</sup> either by the singularity method,<sup>16</sup> the finite difference scheme<sup>17</sup> or by the finite element technique.<sup>18</sup> This effort seems to be particularly fruitful for three-dimensional flow, highly complicated boundary, and consideration of nonlinear effects. In the present study, an application of numerical technique to a linear two-dimensional supercavitating foil is considered, especially from a design point of view.

Fourier series have long been used in linear airfoil theory.<sup>19</sup> And a theory of hydrofoil-airfoil correspondence<sup>1,10</sup> has made the Fourier series useful for the linear theory of supercavitating foils. However, when the boundary conditions become complicated as for foils in a cascade Fourier series become cumbersome<sup>7</sup> when carrying out computations. Fortunately, as in other applications of Fourier series, such as to information theory, the use of the Fast Fourier Transform (FFT) technique<sup>20</sup> greatly assist numerical computations.

In the present theory, in order to use the FFT effectively, many physical quantities are conveniently represented by Fourier series and its coefficients. It is demonstrated that FFT computations can be performed accurately in a relatively short time. By a simple change of the transformation function, the method can be easily applied to different boundary conditions such as those for a infinite medium, beneath a free surface, or in a cascade.

The linear theory of supercavitating foils is particularly useful for designing the foil, since, in addition to the great advantages of superposition, the usual foil at its design condition has a small angle of attack and a thin cavity. Besides, many parameters such as cavity thickness, angle of attack, lift coefficient, and camber can be controlled easily in the linear theory.

There are three important interrelated general requirements for supercavitating foils: large lift-drag ratio, no face cavitation, and adequate cavity thickness. Although the linear theory indicates<sup>1,10</sup> that the center of pressure should be near the trailing edge, for the requirement of large lift-drag ratio, this kind of foil may have negative cavity thickness.<sup>3</sup> A negative cavity thickness could be avoided by superposing angle of attack, but still the camber shape may be vulnerable to face cavitation. Although the conventional design method has been considered to give a favorable

pressure distribution,<sup>1,5,10</sup> this does not guarantee satisfactory foil performance. One other possible design method would be to specify the favorable camber shape first and then determine the angle of attack and the leading edge cavity thickness. For this purpose, it is necessary to have a method for computing the flow field about a supercavitating foil of arbitrary shape. The significant physical quantities of the flow field include not only the pressure distribution, the lift and the drag coefficients, but also the shock-free angle of attack,<sup>4</sup> and the foil cavity shape.

The present study deals with these problems, exploiting many advantages of FFT. A particular advantage is that the shock-free angle of attack is readily supplied by FFT. Numerous results of computations are shown for the case of a cascade. The design of a supercavitating foil is accomplished by combining three different elementary foils: a shock-free foil with a given camber shape, a flat plate with an angle of attack, and a point drag<sup>5</sup> to increase the leading edge thickness. The relative effectiveness of the angle of attack and the point drag in increasing cavity thickness is examined numerically.

The present method and the computer program may be utilized effectively for the design of any supercavitating foil for a high speed hydrofoil or a supercavitating propeller.

## 2. FORMULATION OF PROBLEM

A supercavitating foil with an infinitely long cavity is first considered near a free surface or in a cascade. The angle of attack of the foil is small and the flow perturbation due to the foil is assumed to be small. Thus a linear theory is considered to be applicable here. The linearized mathematical boundary for the foil and cavity is considered to be along the  $x$  axis which is parallel to the velocity at  $x = \infty$  where the velocity is unity. Four possible flow geometries of a foil-cavity boundary near a free surface or in a cascade is shown in Figures 1-4.

For convenience, the complex perturbation velocity,  $u - iv$ , is changed to a modified complex velocity  $F(z) = u - v/2 - i(v - v_\infty)$  where  $u$  is the real function,  $v$  is defined by the pressure at  $x = \infty$ ,  $P_\infty$ , and the pressure on the cavity,  $P_c$ .

$$F(z) = \frac{P_\infty - P_c}{2\rho\sqrt{z}}$$

where  $\rho$  is the density of water. The boundaries are transformed to the half planes shown in Figures 1b, c, 4b, c, and the corresponding transformation functions are shown in Figures 1c, 4c. Then according to the hydrofoil-airfoil correspondence<sup>1,10</sup> the transformed plane becomes the airfoil plane where airfoil theory can be applied.

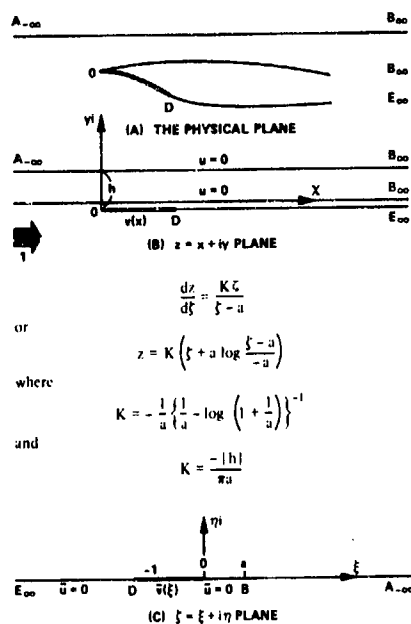


Figure 1 - A Supercavitating Foil Beneath a Free Surface

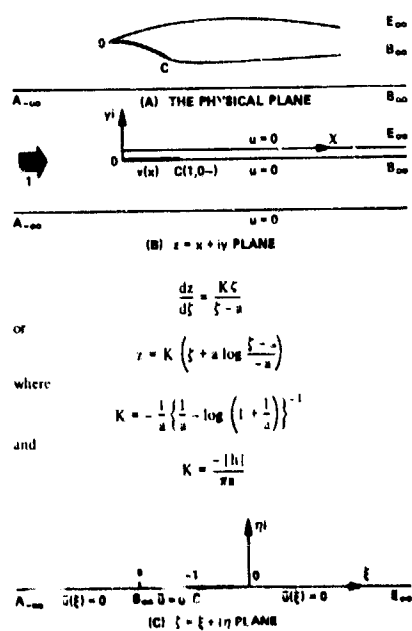


Figure 2 - A Supercavitating Foil Above a Free Surface

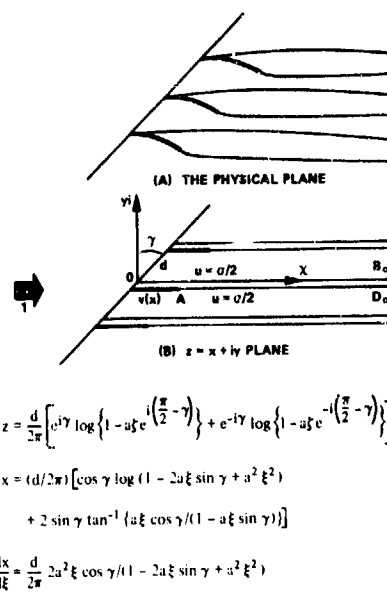


Figure 3 - An Infinite Cavity Cascade

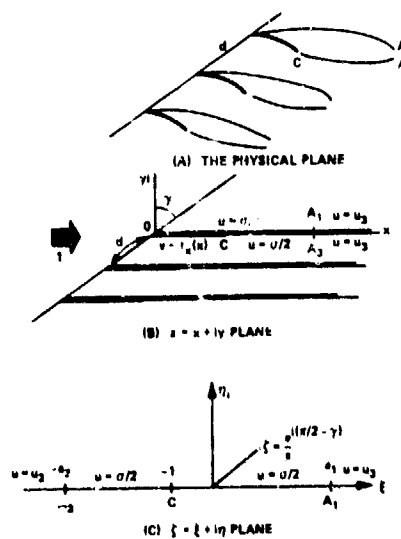


Figure 4 - Finite Cavity Cascade

### 3. FOURIER SERIES EXPANSION

It is well known in airfoil theory<sup>19</sup> that when the circulation distribution is represented by an expression

$$\frac{G}{2} = A \cot \frac{\theta}{2} + \sum_{n=1}^{\infty} A_n \sin n\theta \quad (1)$$

on the two-dimensional wing in the domain

$$0 > \xi > -1$$

$$\xi = -\frac{1}{2}(1 - \cos \theta) \quad 0 < \theta < \pi$$

$$d\xi = -\frac{1}{2} \sin \theta d\theta \quad (2)$$

then the velocity  $F$  normal to the  $\xi$  axis on the wing can be written

$$v_n = -A + \sum_{n=1}^{\infty} A_n \cos n\theta \quad (3)$$

and

$$G/2 = a/2 - u$$

$$v_n = v - v_{\infty}$$

$$A \equiv v_{\infty} - A_0 \quad (3a)$$

That is, in the transformed plane, equations (1)-(3) hold where  $\xi = 0$  is the leading edge, and  $\xi = -1$  is the trailing edge of the foil. The normal velocity represented by

$$v = \sum_{n=0}^{\infty} A_n \cos n\theta = f_x \quad (3b)$$

is the Fourier expansion of the foil shape  $dy/dx = f_x(x)$  in the transformed plane. Thus the coefficients  $A_n$  change when the transformed plane changes. Then, even if the same foil is given in the physical plane, the angle of attack,  $A_0$ , is different depending on the boundary shape. That is,  $A_0$  is not only related to the geometry of the foil itself in relation to the velocity at  $x = -\infty$  but also depends upon the boundary surfaces of the fluid. On the other hand, the effective angle,  $A$ , is uniquely related to the pressure singularity at the leading edge as is seen in equation (1). According to equations (3a, b)  $A_0$  is the angle of attack with respect to the velocity at  $x = -\infty$  and  $A$  is the angle of attack with respect to the direction of the flow at  $x = \infty$ .

According to Table I, when the lift distribution is assumed to be given by

$$-4\tilde{u}(\xi) = 2(\sigma - 2u) T(\xi) \quad (4)$$

where  $T(\xi) = 1$  in an infinite medium,

$$T(\xi) = \frac{K}{\xi - a} \text{ for above or below the free surface, and}$$

$$T(\xi) = \frac{K}{1 - 2a\xi \sin \gamma + a^2 \xi^2} \text{ in a cascade,}$$

then there exist simple relations between the coefficients of lift, moment and drag in the physical and transformed spaces. To obtain coefficients of lift and moment,  $C_L$  and  $C_M$  in the transformed plane,  $T(\xi)$  in equation (4) is represented by a Fourier series,

$$T(\xi) = \sum_{n=0}^{\infty} B_n \cos n\theta \quad (5)$$

in

$$0 > \xi = -\frac{1}{2}(1 - \cos \theta) > -1$$

$$0 < \theta < \pi$$

### 4. LIFT, DRAG, AND NORMAL VELOCITY

In equations (1), (3) and (5), Fourier coefficients can be easily and quickly computed on a high speed computer by the Fast Fourier Transform (FFT) technique. Then the lift coefficient of the transformed airfoil is:

$$\begin{aligned} \bar{C}_L &= \int_{-1}^0 \frac{(\sigma - 2u) 2K d\xi}{1 - 2a\xi \sin \gamma + a^2 \xi^2} \\ &= 2 \int_0^\pi \frac{K(A \cot \frac{\theta}{2} + \sum_{n=1}^{\infty} A_n \sin n\theta) \sin \theta}{1 + a(1 - \cos \theta) \sin \gamma + \frac{a^2}{4}(1 - \cos \theta)^2} d\theta \\ &= 2 \int_0^\pi \left\{ A(1 + \cos \theta) \sum_{n=1}^{\infty} B_n \cos n\theta \right. \\ &\quad \left. + \sum_{n=1}^{\infty} A_n \sin n\theta \sum_{n=0}^{\infty} B_n \cos n\theta \sin \theta \right\} d\theta \\ &= 2\pi A \left( B_0 + \frac{1}{2} B_1 \right) + \int_0^\pi \sum_{n=1}^{\infty} A_n \left\{ \cos(n-1)\theta \right. \\ &\quad \left. - \cos(n+1)\theta \right\} \sum_{n=0}^{\infty} B_n \cos n\theta d\theta \\ &= 2\pi A \left( B_0 + \frac{1}{2} B_1 \right) + \pi B_0 A_1 + \frac{\pi}{2} \{ B_1 A_2 \\ &\quad + \sum_{n=2}^{\infty} B_n (A_{n+1} - A_{n-1}) \} \quad (6) \end{aligned}$$

The moment coefficient of the transformed airfoil is

$$\begin{aligned} \bar{C}_M &= - \int_{-1}^0 \frac{2(\sigma - 2u) K \xi d\xi}{1 - 2a\xi \sin \gamma + a^2 \xi^2} \\ &= - \int_0^\pi \left\{ A(1 - \cos^2 \theta) \sum_{n=0}^{\infty} B_n \cos n\theta \right. \\ &\quad \left. + \sum_{n=1}^{\infty} A_n \sin n\theta \sum_{n=0}^{\infty} B_n \cos n\theta (1 - \cos \theta) \sin \theta \right\} d\theta \\ &= - \int_0^\pi \left[ A \left( 1 - \frac{1}{2} - \frac{1}{2} \cos 2\theta \right) \sum_{n=0}^{\infty} B_n \cos n\theta \right. \end{aligned}$$



Table 1 - Flow Characteristics of Finite Cavity Foils and Corresponding Airfoils

	Isolate single foils in an infinite medium	Foils above (or below) a free surface	Cascades	Airfoils in the transformed plane
Load distribution $-2u(x) + \sigma$	$-2\bar{u}(\xi)$	$-4\bar{u}(\xi) \frac{\xi - a}{K}$	$-\frac{2}{K} \bar{u}(\xi) (1 - 2a\xi \sin \gamma + a^2 \xi^2)$	$-4\bar{u}(\xi)$
Lift Coefficient $C_L$	$\frac{1}{4\pi}$	$\frac{1}{2\pi} \frac{1}{K}$	$\bar{C}_M$	$\bar{C}_L$
Drag Coefficient $C_D$	$\frac{1}{8\pi}$	$\frac{1}{4\pi} \frac{1}{K}$	$\frac{1}{8\pi K} (\bar{C}_L^2 + 2a \sin \gamma \bar{C}_M \bar{C}_L + a^2 \bar{C}_M^2)$	
$C_L^2/C_D$	$8\pi \bar{C}_M^2/\bar{C}_L^2$	$\frac{4\pi}{K} \frac{\bar{C}_M^2}{\bar{C}_L^2}$	$8\pi K \left( a^2 + 2a \sin \gamma \frac{\bar{C}_L}{\bar{C}_M} + \frac{\bar{C}_L^2}{\bar{C}_M^2} \right)^{-1}$	
Least upper bound of $C_L^2/C_D$	$8\pi$	$\frac{4\pi}{K}$	$8\pi K (a^2 + 2a \sin \gamma + 1)^{-1}$	$h$ = the distance from the leading edge to the free surface
Foil-cavity shape $y$	$y(\xi)$	$y(\xi) = \frac{1}{\pi K} \left( \frac{a\xi}{1 - \xi^2} \right)$	$\bar{y}(\xi) = \frac{1}{4\pi K} \sin \gamma \bar{C}_L x(\xi)$ $C_L = \frac{1}{a \cos \gamma} \left( \tan^{-1} \left( \frac{a\xi - \sin \gamma}{\cos \gamma} \right) + \gamma \right)$	$d^{-1}$ = solidity $\gamma$ = stagger angle $C_M$ = Coefficient of moment about the leading edge of aerofoil
Cavitation No. $\sigma$	0	0	$\frac{1}{K} \bar{C}_L^2 \cos \gamma$	$a$ = Transformation constant
$v_{\infty}$	0	0	$\frac{1}{K} (a \bar{C}_L \sin \gamma + a^2 \bar{C}_M)$	Chord length = 1
$K$		$-\frac{\ln  1 - \xi^2 }{\pi a}$	$\frac{1}{K} \cos \gamma$	
Coordinate Transformation	$x = z$	$x = K \left\{ \xi + a \log \left( \frac{a - \xi}{1 - \xi^2} \right) \right\}$	$x = \frac{1}{2} \int_{-1}^{\xi} [\cos \gamma \log \left( \frac{1 - 2a\xi \sin \gamma + a^2 \xi^2}{1 - \xi^2} \right) + 2 \sin \gamma \tan^{-1} \left( \frac{\xi \cos \gamma}{1 - a\xi \sin \gamma} \right)] d\xi$	

$$\begin{aligned}
 & + \frac{1}{2} \sum_{n=1}^{\infty} A_n \left\{ \cos(n-1)\theta \right. \\
 & \left. - \cos(n+1)\theta \right\} \sum_{n=0}^{\infty} B_n \left\{ \cos n\theta - \frac{1}{2} \cos(n-1)\theta \right. \\
 & \left. - \frac{1}{2} \cos(n+1)\theta \right\} d\theta \\
 & = \frac{\pi}{2} \left[ A \left( B_0 - \frac{1}{2} B_1 \right) - A_1 \left( \frac{1}{2} B_1 - B_0 \right) \right. \\
 & \left. + \frac{1}{2} A_2 \left( B_1 - B_0 - \frac{1}{2} B_2 \right) \right. \\
 & \left. + \sum_{n=2}^{\infty} \frac{1}{2} (A_{n+1} - A_{n-1}) \left( B_n - \frac{1}{2} B_{n+1} - \frac{1}{2} B_{n-1} \right) \right] \quad (7)
 \end{aligned}$$

The coefficients of lift and drag,  $C_L$  and  $C_D$ , are calculated from Table 1.<sup>10</sup>

$$C_L = \bar{C}_M$$

$$C_D = \frac{1}{8\pi K} (\bar{C}_L^2 + 2a \sin \gamma \bar{C}_M \bar{C}_L + a^2 \bar{C}_M^2) \quad (8)$$

The velocity normal to the  $\xi$  axis in  $\xi < -1$ , and in  $\xi > 0$  can be obtained by

$$\begin{aligned}
 v - v_{\infty} &= -\frac{1}{2\pi} \int_{-1}^{\xi} \frac{v - 2u}{1 - \xi} d\xi \\
 &= -\frac{1}{\pi} \int_0^{\pi} \frac{A \cos \frac{\theta}{2} + \sum_{n=1}^{\infty} A_n \sin n\theta \sin \theta}{-2\xi - 1 + \cos \theta} d\theta
 \end{aligned}$$

$\ln \xi < -1$

$$v - v_{\infty} = -\frac{1}{\pi} \int_0^{\pi} \frac{A(1 + \cos \theta) + \frac{1}{2} \sum_{n=1}^{\infty} A_n \{ \cos(n-1)\theta - \cos(n+1)\theta \}}{a + \cos \theta} d\theta$$

$$= -A \frac{1}{\sqrt{a^2-1}} + \frac{\sqrt{a^2-1}-a}{\sqrt{a^2-1}}$$

$$- \sum_{n=1}^{\infty} \frac{1}{2} A_n \frac{(\sqrt{a^2-1}-a)^{n-1} - (\sqrt{a^2-1}-a)^{n+1}}{\sqrt{a^2-1}}$$

$$= A \frac{a-1-\sqrt{a^2-1}}{\sqrt{a^2-1}} + \sum_{n=1}^{\infty} A_n (\sqrt{a^2-1}-a)^n \quad (9)$$

with  $a = -1 - 2\xi > 1$

$\ln \xi > 0$

$$v - v_{\infty} = A \frac{a+1-\sqrt{a^2-1}}{\sqrt{a^2-1}} + \sum_{n=1}^{\infty} A_n (a-\sqrt{a^2-1})^n \quad (10)$$

with  $a = 1 + 2\xi > 1$

The velocity at  $x = \infty$  may be expressed<sup>10</sup> in terms of  $\bar{C}_L$  and  $\bar{C}_M$ :

$$v_{\infty} = \frac{1}{4\pi K} (-a \sin \gamma \bar{C}_L - a^2 \bar{C}_M)$$

$$u_{\infty} = \frac{a}{2} = \frac{a}{4\pi K} \cos \gamma \bar{C}_L \quad (11)$$

## 5. SHOCK FREE ANGLE

From Equations (3), (6), (9) and (11):

$$v_{\infty} = A + A_0 \quad (12)$$

$$= -\frac{A}{4K} \left\{ 2a \left( B_0 + \frac{1}{2} B_1 \right) \sin \gamma + \frac{a^2}{2} \left( B_0 - \frac{1}{2} B_2 \right) \right\} + \frac{F_1}{4K}$$

where

$$F_1 = -a \sin \gamma \left[ B_0 A + \frac{1}{2} \left\{ B_1 A_2 + \sum_{n=2}^{\infty} B_n (A_{n+1} - A_{n-1}) \right\} \right]$$

$$- \frac{a^2}{2} \left\{ -A_1 \left( \frac{1}{2} B_1 - B_2 \right) + \frac{1}{2} A_2 \left( B_1 - B_0 - \frac{1}{2} B_2 \right) \right.$$

$$\left. + \sum_{n=2}^{\infty} \frac{1}{2} (A_{n+1} - A_{n-1}) \cdot \left( B_n - \frac{1}{2} B_{n+1} - \frac{1}{2} B_{n-1} \right) \right\}$$

Hence, the effective angle of attack,  $A$ , is given by

$$A = \frac{F_1 - 4K A_0}{\left\{ 2a \sin \gamma \left( B_0 + \frac{1}{2} B_1 \right) + \frac{a^2}{2} \left( B_0 - \frac{1}{2} B_2 \right) \right\} + 4K} \quad (13)$$

Usually  $A_0$  and  $v_{\infty}$  are negative so that  $A$  has to be positive to prevent face cavitation. Thus, in general,  $|A|$  will be much smaller than  $|A_0|$ . Shock-free entry can be obtained by setting  $A = 0$ , or

$$A_0 = \frac{F_1}{4K} \quad (14)$$

In this analysis, it is interesting to note the relations between the angles of attack and the velocity at  $\infty$ .  $F_1/(4K)$  in Equation (14) is the angle of velocity at  $\infty$  due to pure camber on a shock-free foil. If  $F_1 = 0$ , then in the case of flat plate

$$A = \beta A_0$$

where

$$\beta = \frac{-4K}{\left\{ 2a \sin \gamma \left( B_0 + \frac{1}{2} B_1 \right) + \frac{a^2}{2} \left( B_0 - \frac{1}{2} B_2 \right) \right\} + 4K} \quad (15)$$

In the general case,  $F_1 \neq 0$ , we can write

$$A = \beta (A_0 - F_1/(4K)) \quad (16)$$

Thus, when we consider that any foil is represented by a superposition of attack angle and camber, the effective angle of attack due to camber is the same as that due to a flat plate with the attack angle,  $-F_1/(4K)$ .

## 6. CAVITY THICKNESS

The cavity thickness is obtained by integrating  $y$  shown in equations (9) and (10) along  $x$ . To build an actual supercavitating foil, the cavity thickness has to be thick enough to provide adequate foil strength. The cavity thickness is not known a priori, whether the given value is the pressure distribution on the foil or the shape of the foil.

As in the case of designing a supercavitating foil with a given load distribution, the cavity thickness may still be negative even when a camber shape is given. Then either angle of attack and/or a point drag can be superposed to provide cavity thickness. In the present solution, an unreasonable cavity shape of the given foil near the leading edge can be detected easily by simply observing the sign of the constant  $A$ . Low-drag cambers such as two- or three-term cambers in an infinite medium have been chosen for a shock-free foil in an infinite medium. However when this camber shape is used near a free surface or in a cascade it will no longer be shock free. In the present analysis, from equation (14), it is easy to find the angle of attack that makes the given camber shock-free. If the camber shape has positive curvature everywhere on the foil, the shock-free camber shape has no negative cavity thickness although the cavity thickness near the leading edge may be too small. In general, shock free entry of a low-drag cambered foil does not necessarily make the cavity thickness non-negative everywhere.

The cavity shape due to a flat plate can be obtained by integrating

$$v - v_{2\infty} = (A_0 - v_{2\infty}) \left( 1 - \sqrt{\frac{x+1}{t}} \right) \quad (17)$$

where  $v_{2\infty}$  is the  $y$  component of velocity at  $x = \infty$  due to just the flat plate. The flat-plate contribution to cavity shape is obtained from

$$\int_0^x v(x) dx = \int_0^{\xi} v(\xi) \frac{dx}{d\xi} d\xi$$

$$= \int_0^{\xi} v(\xi) \frac{2K\xi}{1 - 2a\xi \sin \gamma + a^2 \xi^2} d\xi \quad (18)$$

The integrand with respect to  $\xi$  behaves better in the neighborhood of  $\xi = x = 0$  than in the integration with respect to  $x$  without using the transformed coordinates.

The cavity shape due to a unit-strength point-drag singularity at the leading edge is<sup>12</sup>

$$y(\xi) = -\frac{a}{\pi K} \sin \gamma x(\xi) + \frac{2}{\pi} \frac{1}{a \cos \gamma} \left\{ \tan^{-1} \left( \frac{\xi a - \sin \gamma}{\cos \gamma} \right) + \gamma \right\} \quad (19)$$

which results from integration of the  $y$  component of velocity

$$\frac{k_0}{\pi K} \left( \frac{1}{\xi} - a \sin \gamma \right)$$

with respect to  $x$ .

The present analysis can be used for either a given arbitrary shape of foil face or a given load distribution on the foil. If the shape of the foil is given in the physical plane, say

$$y = f(x)$$

then from linear theory,

$$v = f_x(x(\xi))$$

Thus,  $v$  in equation (3) is known. If the foil has a blunt leading edge,  $|f_x|$  may be infinitely large at the leading edge, and equation (3) can not be used. In this case, the foil is considered to consist of two foils: a thin leading-edge foil  $f_1$  and a non-lifting foil consisting of a point drag.<sup>12</sup> That is

$$v = f_x(x(\xi)) = f_{1x}(x(\xi)) + \frac{k_0}{K\pi} \left( \frac{1}{\xi} - a \sin \gamma \right)$$

where  $f_{1x} = f_x - (k_0/K\pi)(1/\xi - a \sin \gamma)$  is small and can be expanded in a Fourier series. After performing an analysis with  $f_{1x}$ , the point drag will be added separately in a simple way as shown in the following sections.

## 7. FOIL DESIGN

The design method for a supercavitating foil near a free surface has been studied for zero cavitation number.<sup>5</sup> For a cascade, a given pressure mode was considered to create a reasonable foil.<sup>11,13</sup> It would be very useful to design a supercavitating foil with a circular-arc camber or so-called two-term camber or any other given camber shapes in a cascade or beneath a free surface. A typical technique<sup>5,13</sup> involves a superposition of three elementary foils: a shock free foil with a given camber shape, a flat plate with an angle of attack, and the point drag, for which all the useful formulae are given in the previous sections.

The philosophy of superposition of the three elementary foils to design a good supercavitating foil involves first making cavity thickness positive by angle of attack and then making the cavity thickness near the leading edge thicker by a point drag. Although this philosophy has been based on a general knowledge of low-drag nonlifting thick foils,<sup>21</sup> the combination of the angle of attack and the point drag was

not intended to be mathematically optimum. This optimization aspect is investigated in the following section for a supercavitating foil in a cascade by systematic change of parameters. A mathematical formulation of a general variational problem is not very neat because with a shock-free foil, neither negative strength of the point drag,  $k_0$ , nor negative angle of attack,  $\alpha$  is allowed. However, when  $\alpha$  increases,  $k_0$  has to decrease because the cavity thickness is given. Thus, the permissible range of  $\alpha$  and  $k_0$  fall in a narrow domain for a given camber shape, rendering an easy numerical plot.

## 8. OPTIMUM ANGLE OF ATTACK

The cavity thickness of the foil is considered at a given point  $x_1$  as a superposition of a shock-free camber, a flat plate, and the cavity of a point drag. The cavity thicknesses may be written respectively as

$$y_1/C_L = c f_1/C_L$$

$$y_2/C_L = \alpha f_2/C_L$$

$$y_3/C_L = k_0 f_3/C_L \quad (20)$$

where  $f_1$ ,  $f_2$  and  $f_3$  are functions of cascade parameters. For convenience  $y_1$ ,  $y_2$ ,  $y_3$ ,  $c$ ,  $\alpha$ ,  $k_0$  and the cavity thickness of the composite foil,  $t(x_1)$  are all considered to be divided by a given design lift coefficient,  $C_L$ , or all the quantities are considered for a unit  $C_L$ . If the composite foil is considered, the cavity thickness is,

$$t = y_1 + y_2 + y_3$$

$$= c f_1 + \alpha f_2 + k_0 f_3 \quad (21)$$

The drag coefficient is, from Table 1,

$$\frac{C_D}{C_L^2} = \frac{1}{8\pi K} \left( \frac{\bar{C}_L^2}{\bar{C}_M^2} + 2a \sin \gamma \frac{\bar{C}_L}{\bar{C}_M} + a^2 \right) \quad (22)$$

where

$$\frac{\bar{C}_L}{\bar{C}_M} = c \bar{C}_{L1} + \alpha \bar{C}_{L2} + k_0 \bar{C}_{L3} \quad (23)$$

and

$$t = c \bar{C}_{M1} + \alpha \bar{C}_{M2}, \text{ or } c = \frac{1 - \alpha \bar{C}_{M2}}{\bar{C}_{M1}} \quad (24)$$

where  $C_{L1}$  and  $C_{M1}$  are given by equations (6), (7), and (13) for a given foil,  $C_{L2}$  and  $C_{M2}$  are very succinctly represented by equations (6), (7), and (13) because for a flat plate,  $A_n \approx 0$  ( $n = 1, 2, \dots$ ) with only non-zero coefficient  $A_0$ , and for a point drag.<sup>13</sup>

$$\bar{C}_{L3} = 4$$

$$\bar{C}_{M3} = 0 \quad (25)$$

Now for a given  $t$ , the ratio of the cavity thickness to the given  $C_L$ ,

$$y_3 = k_0 f_3 = t - \frac{1 - \alpha \bar{C}_{M2}}{\bar{C}_{M1}} f_1 - \alpha f_2 \quad (26)$$

or

$$k_0 = k_1 + k_2 \alpha \quad (27)$$

where

$$k_1 \equiv \frac{1}{f_3} - \frac{f_1}{f_3 C_{M1}} \quad (28)$$

and

$$k_2 \equiv \frac{\bar{C}_{M2} f_1}{f_3 C_{M1}} - \frac{f_2}{f_3} \quad (29)$$

$C_{M1}$  and  $C_{L1}$  are functions of cascade parameters:  $f_1$  are functions of  $x_1$  as well as the cascade parameters. Therefore, if the camber shape, cascade parameters and  $x_1$  are fixed,  $C_{M1}$ ,  $C_{L1}$  and  $f_1$  are all constants. Thus,  $c$  and  $k_0$  are linear functions of  $\alpha$  and  $C_D/C_L^2$  is a quadratic function of  $\alpha$ . Thus the optimum value of  $\alpha$  should be either the point at  $d/d\alpha (C_D/C_L^2) = 0$ , or at the boundary of the significant  $(\alpha, k_0)$  domain.

If  $\alpha = 0$  and  $\alpha = \alpha_1$  in equation (27), and correspondingly  $k_0 = k_g$  and  $k_0 = 0$ , then physically significant values of  $(\alpha, k_0)$  lie in the domain

$$\begin{aligned} 0 < \alpha < \alpha_1 \\ 0 < k_0 < k_g \end{aligned} \quad (30)$$

with increasing  $\alpha$  corresponding to decreasing  $k_0$ .

When the amount of camber factor  $c$  is given, the angle of attack has to be determined from

$$\alpha = \frac{1 - c \bar{C}_{M1}}{\bar{C}_{M2}}$$

Then the condition of the leading edge thickness will determine the strength of the point drag,  $k_0$ . Since the large camber may induce face cavitation, the camber naturally also has an upper limit.

## 9. FINITE CAVITY EFFECT

For a design problem with an arbitrary lift distribution given on the foil, the solution for the supercavitating cascade with a finite cavity length has been readily obtained<sup>12</sup> by a superposition of a simple function of cavity length parameters onto the solution for the infinite-cavity problem with the same lift distribution. When

$$w_1 = u_1 - i v_1 \quad (31)$$

is a complex velocity of infinite cavity length with a lift distribution,

$$p + \gamma$$

then, a solution  $w$  for the finite-cavity length with the same lift distribution can be written

$$w = w_1 + w_2 \quad (32)$$

where

$$w_2(\xi) = \frac{1}{\pi i} \int_{-a_3}^{a_1} \frac{\frac{\sigma}{2} - u_3}{\xi - \xi'} dt = \frac{1}{\pi i} \left( \frac{\sigma}{2} - u_3 \right) \log \frac{a_1 - \xi}{-a_3 - \xi} - u_3 + i v_2 \quad (33)$$

and

$$w_1(\xi) \rightarrow 0, w_2(\xi) \rightarrow 0 \quad \text{for } \xi \rightarrow -\infty$$

$w_2$  is the complex velocity due to a constant negative pressure distribution on the cavity and foil equal to the difference of

the cavity pressure and the down stream pressure, with  $a_1$  and  $a_3$  corresponding to cavity ends as shown in Figure 4. However neither the pressure distributions on the foil nor the foil shapes of the solutions  $w$  and  $w_1$  are necessarily the same, because the cavitation number changes according to the cavity length. If the lift distribution of the infinite-cavity foil is kept the same when designing foils having finite cavity length, the above theory can be conveniently used.

## 10. COMPUTATIONAL PROCEDURE AND NUMERICAL RESULTS

When the foil shape is given in a cascade, or beneath a free surface, the foil offsets in the transformed plane have to be represented by a Fourier series. Thus, for a given boundary geometry, transformation parameters  $a$  and  $K$  are computed. In general, "a" is computed by Newton-Raphson's method for the given geometrical parameters. The initial approximation of "a" can be selected from the corresponding graphs.<sup>10</sup> Then for a given  $\xi$  in the transformed plane, the corresponding  $x$  of the physical plane can easily be computed from the transformation equations in Figures (1) through (3). The offsets in the transformed plane are expanded in a Fourier series by FFT.

There are several FFT routines available at the David W. Taylor Naval Ship Research and Development Center. These can be used to obtain either the Fourier coefficients or the sum of Fourier series at each small interval. The number of intervals or the number of terms in the Fourier series is  $2^n$ . The routine which was used here to get the Fourier coefficients of  $v$  in a cascade in Equation (3b) took 0.18 seconds of computing time with  $n = 8$  and 0.11 seconds with  $n = 7$  on a CDC 6600 computer. With these two sets of Fourier coefficients, the computed values of  $C_L$  and  $C_D/C_L^2$  differ by less than 0.1 percent with the solidity  $c/d = 1$ , and the stagger angle  $\gamma = 1$  radian. If the solidity is larger than 1.5, the accuracy is decreased slightly. Fourier coefficients  $A_0$  from Equation (3b) and  $A_0$  from the shock-free relation in Equation (14) contribute to the actual shock-free angle of attack. The difference between these two numbers,  $\alpha_0$ , is the extra angle of attack to be added to the given foil in order to make it shock-free. Thus, the shock-free nose-tail line is the sum of  $\alpha_0$  and the nose-tail line angle of the given foil with respect to the  $x$  axis. In Figure 5 a circular arc foil and the two-term camber foil in an infinite medium are shown at the shock-free angles. The lift coefficients and the drag-lift ratios at the shock-free angles of these two foils in a cascade are computed from Equations (6) through (8), and are shown in Figures 6 and 7 as normalized by the lift coefficient in an infinite medium. A noticeable feature is that the curve of drag-lift ratio is almost parallel and very close to the curve of nose-tail line shock-free angle. This means, the drag originates mostly from the shock-free angle of attack, and very little drag results from camber. Also shown in the figures are the considerable cascade effects resulting from increasing solidities. However, the circular arc and the two-term cambers have relatively small cascade effects compared with those of a flat plate shown in Figure 7. The two-term camber foil performs very slightly better than the circular arc foil.

The cavity shape is obtained by computing normal velocities on the cavity from Equation (10) and numerically integrating them with respect to  $x$ . For the flat plate, Equations (17) and (18) are used. For the point drag, the cavity shape is available in Equation (19). With these cavity shapes, the cavity thickness is computed and  $f_1$  in Equation (20) is prepared. Thus, foil shapes of composite foils with a given cavity thickness at a given  $x$ , or  $x_1$ , are analyzed for a shock-free circular arc foil. When the leading-edge cavity thickness divided by the chord length and the lift coefficient

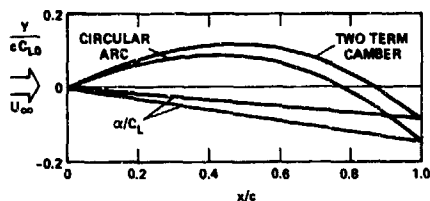


Figure 5 - Supercavitating Shock-Free Foil Shape  $y/C_{L0}$  in an Infinite Medium

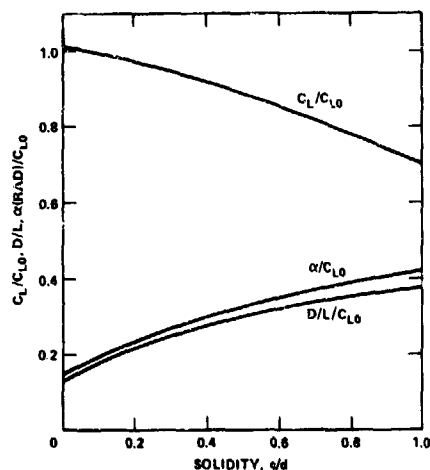


Figure 6 - Lift Coefficient  $C_L$  Drag-Lift Ratio  $D/L$  of Supercavitating Circular-Arc Foil  $y/C_{L0} = 16(x-x^2)/(9\pi)$  in a Cascade of Stagger Angle 1 Radian, at Shock Free Angle  $\alpha/C_{L0}$

is 0.1 at  $x_1 = 0.1$ ,  $C_D/C_L^2$  and the point drag singularity  $k_0/C_L$  versus the angle of the flat plate superposed are shown in Figure 8, where  $(d/da)(C_D/C_L^2)$  is positive. A similar curve at  $x_1 = 0.5$  is shown in Figure 9, where  $(d/da)(C_D/C_L^2)$  is negative. In general, when the cavity thickness is specified near the leading edge  $(d/da)(C_D/C_L^2)$  is positive, i.e., the point drag is more efficient for increasing the leading-edge thickness. When the cavity thickness is specified near the trailing edge,  $(d/da)(C_D/C_L^2)$  is negative, i.e., the flat-plate angle of attack is more efficient to increase the trailing-edge cavity thickness. However, slopes of  $(d/da)(C_D/C_L^2)$  are very small, i.e., the cavity thickness and the amount of camber mostly determine  $C_D/C_L^2$  irrespective of the shape of camber.

To investigate the influence of camber shape on the lift and the drag-lift ratio, a variation of circular-arc camber is considered as in Figure 10. The  $x$ -coordinate of the maximum camber is varied by a factor  $(x/4)(1+bx)$  to the circular arc  $y = 4(x-x^2)$  where  $a = 1/((x_1-x_1^2)(1+bx_1))$  is the factor to make the maximum camber equal to 1, and the  $x$  coordinate of the maximum camber is  $x_1 = (-B + \sqrt{B^2 + 4A})/(2A)$  with  $A = 3b$ , and  $B = 2(1-b)$ . The lift coefficient, the shock-free angle of attack, and the drag-lift ratio of the deformed circular arc are shown in

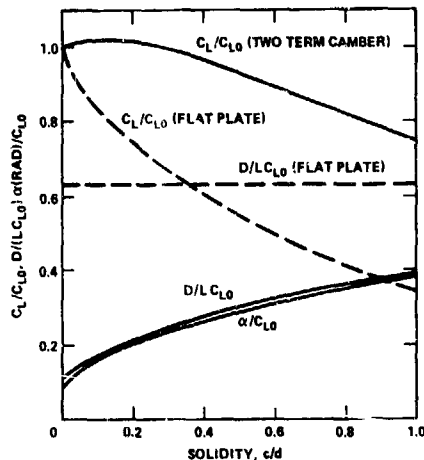


Figure 7 - Lift Coefficient  $C_L$  Drag-Lift Ratio  $D/L$  of Supercavitating Two-Term Camber Foil  $y/C_{L0} = 4/5\pi(x + 8/3x^{3/2} - 4x^2)$  in a Cascade of Stagger Angle 1 Radian, at Shock-Free Nose-Tail Line Angle  $\alpha/C_{L0}$

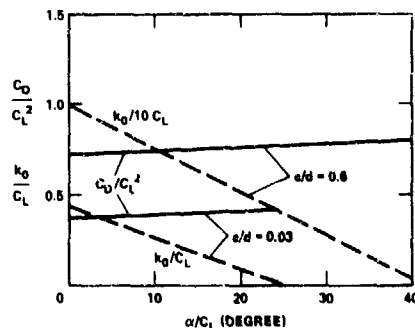


Figure 8 - Drag-Lift Ratio and Strength of Point-Drag Singularity for Composite Foil of Shock-Free Circular Arc, Flat Plate, and Point Drag in a Supercavitating Cascade of Stagger Angle 1 Radian with Cavity Thickness  $t/(cC_L) = 0.1$  at  $x = 0.1$

Figure 11. As expected, the smaller the  $x$ -coordinate of maximum camber, the larger the shock-free angle of attack. The drag due to the camber alone is negative when the  $x$ -coordinate of maximum camber is less than 0.5. That is, the amount of negative pressure near the leading edge overcomes the positive pressure on the foil. The drag-lift ratio of the shock-free deformed circular arc decreases when the  $x$ -coordinate of maximum camber increases, even when the leading edge cavity thickness is specified. As has been discussed often in the past, the influence of camber shape on lift and drag is related to the cavity thickness distribution on the foil. Thus, with a given cavity thickness at only one point, the discussion of the influence of the camber shape on the lift and drag cannot be completely general. In general, when the curvature of the foil face is positive everywhere,

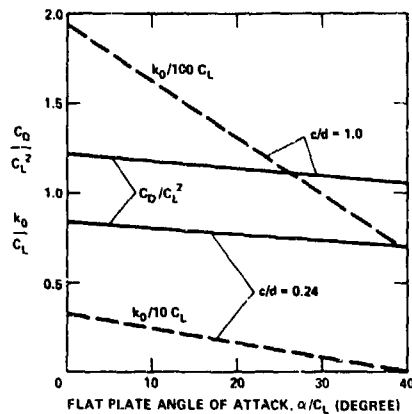


Figure 9 - Drag-Lift Ratio for Composite Foil of Shock-Free Circular Arc, Flat Plate and Point Drag in a Supercavitating Cascade of Stagger Angle 1 Radian with Cavity Thickness  $t/c C_L = 0.5$  at  $x = 0.5$

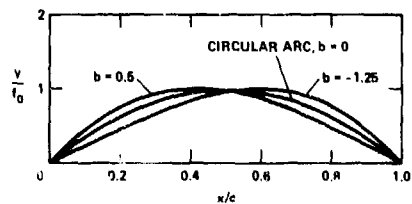


Figure 10 - Variation of Circular Arc  
 $y/f_0 = a(x - x^2)(1 + bx)$

a shift of the maximum camber towards the trailing edge slightly reduces the lift-drag ratio and the section modulus, for a given leading-edge cavity thickness.

An example of a foil cavity shape with two-term camber, and a given leading-edge cavity thickness is shown in Figure 12 together with the corresponding lift distribution. The analysis of a supercavitating cascade is particularly useful for designing supercavitating propellers. As an example, the cascade parameters for a model of a supercavitating propeller tested at the David W. Taylor Naval Ship Research and Development Center (Model 3770) are shown in Figure 13. The ranges of solidities and stagger angles are very large.

The effect of finite cavities is directly related to the cavitation number. Of course, for an isolated supercavitating foil beneath a free surface, the cavitation number is zero when the cavity length is infinite. For a cascade, the choked-flow cavitation number is a function of cascade parameters and the leading-edge thickness. In Figure 14, it is shown that the choked-flow cavitation number is a linear function of the cavity thickness per unit  $C_L$  for a given set of cascade parameters with a fixed  $c$  or  $\alpha$  in Equation (24). (In Figures 14, 15,  $c = 1.5$  to the two term camber). The larger the solidity, the larger the rate of change of the choked-flow cavitation number with respect to the increasing cavity thickness. Assuming that the load distribution on the finite-cavity supercavitating foil is the same as in the case of

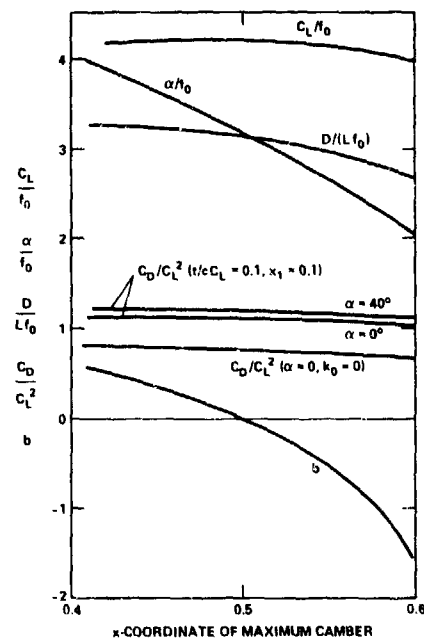


Figure 11 - Lift Coefficient, Drag-Lift Ratio of Supercavitating Deformed Circular Arc  $y/f_0 = a(x - x^2)(1 + bx)$  in a Cascade of Solidity 0.984 and Stagger Angle 1.1868 Radian at Shock-Free Angle of Attack  $\alpha/f_0$ , Normalized by Camber  $f_0$

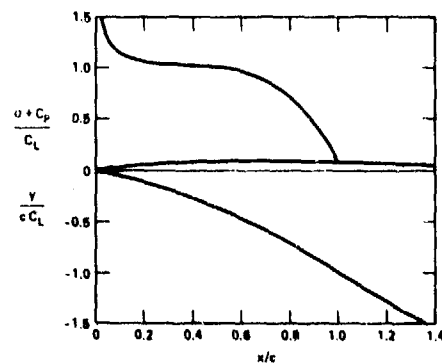


Figure 12 - Foil-Cavity Shape and Lift Distribution in a Supercavitating Cascade with  $c/d = 0.4788$ ,  $\gamma = 1.3015$  and  $C_D/C_L^2 = 0.9231$

choked cavity, the finite cavity effect is analyzed as shown in Equations (71)-(73) using the technique of Reference 12. Then the lift, the drag and the cavity-foil shape will be functions of the cavitation number. Of course, the cavitation number is a function of cavity length.<sup>11</sup> The relations

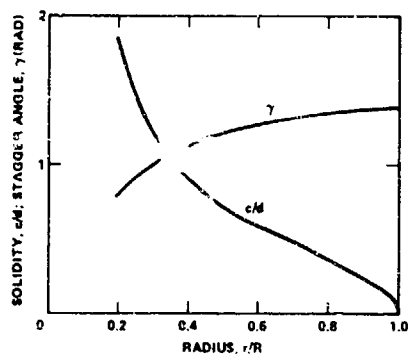


Figure 13 - Cascade Parameters in Supercavitating Propeller Model 3770

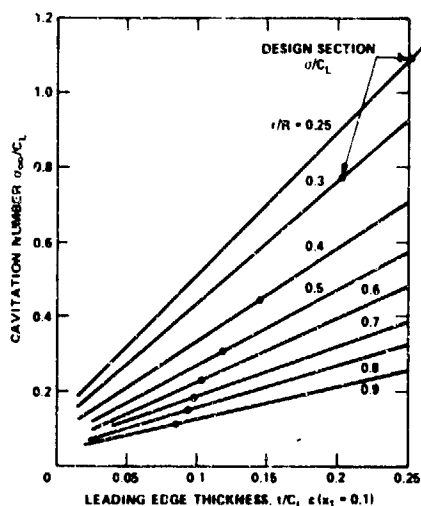


Figure 14 - Relation Between Choked Flow Cavitation Number and Leading-Edge Thickness of Supercavitating Cascade in Blade Sections of Supercavitating Propeller Model 3770

between the cavitation number and the cavity length are shown in Figure 15 for propeller Model 3770. Figure 15 shows that near the hub where the solidity is large, the cavitation number divided by the lift coefficient varies very little with cavity length. Throughout most sections of the propeller-blade a cavity of two and one-half chord lengths gives the same effect as a cavity of infinite length. The design section cavitation number divided by lift coefficient for propeller Model 3770 is shown in Figure 14 for each section. The cavity-thickness of the foil in Figure 15 is adjusted to the design value of cavitation number per unit lift coefficient. According to designer requirements to make the entire section supercavitate, the foil shape could be designed to have enough cavity thickness at a given design section cavitation number.

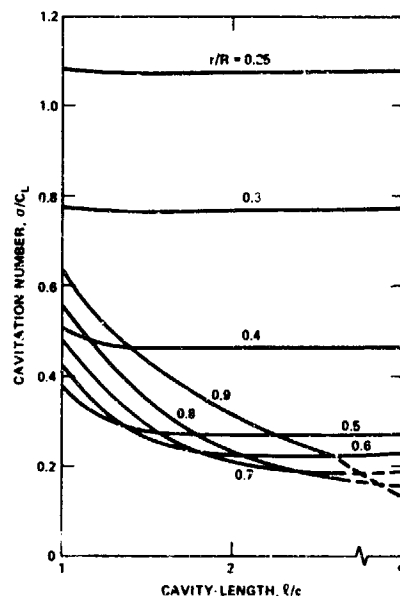


Figure 15 - Relation Between Cavitation Number and Cavity-Length of Supercavitating Cascade in Blade Sections of Supercavitating Propeller Model 3770

Although most examples in the present study are for cascades, the foils beneath or above a free surface can be treated in the same way by just changing the transformation function for the Fourier coefficients  $B_n$  in Equation (5). In the case of an infinite fluid, where  $B_0 = 1$  and  $B_n = 0$  ( $n = 1, 2, \dots$ ), the problem becomes much simpler, and the use of EFT could simplify the analysis of any foil shape.

#### ACKNOWLEDGEMENTS

This work has been supported by the Naval Material Command Direct Laboratory Funding Project on Propellers for High Speed Naval Vehicles. The author also wishes to express his appreciation to Ms. Nadine M. White for assisting him with the computer, and to Dr. William B. Morgan and Mr. Justin H. McCart, Jr. for their many valuable discussions and continuous encouragements.

# REFERENCES

1. Tulin, M.P., "Supercavitating Flows - Small Perturbation Theory," *Journal of Ship Research*, Vol. 7, No. 3 (January 1964).
2. Betz, H., and E. Petersohn, "Application of the Theory of Free Jets," National Advisory Committee for Aeronautics TN 667 (April 1932).
3. Cohen, H., and C.D. Sutherland, "Finite Cavity Cascade Flow," *Proceedings of the 3rd U.S. National Congress of Applied Mechanics* (1958).
4. Johnson, V.E., Jr., "The Influence of Depth of Submergence, Aspect Ratio, and Thickness of Supercavitating Hydrofoils Operating at Zero Cavitation Number," Second Symposium on Naval Hydrodynamics, Office of Naval Research, Washington, D.C., pp. 319-366 (1958).
5. Auslaender, J., "The Linearized Theory for Supercavitating Hydrofoils Operating at High Speeds Near a Free Surface," *Journal of Ship Research*, Vol. 6, No. 2, pp. 8-23 (October 1962).
6. Hsu, C.C., "Some Remarks on the Progress of Cavity Flow Studies," *Transaction of the ASME*, Vol. 97, Series 1, No. 4, pp. 439-452 (Dec 1975).
7. Oba, R., "Theory on Supercavitating Cascade Flow for Arbitrary Form Hydrofoils," *Proceedings ASME Symposium on Cavitation in Fluid Machinery*, pp. 70-90 (1965).
8. Furuya, O., "Exact Supercavitating Cascade Theory," *Journal of Fluid Engineering*, Vol. 97, ASME, pp. 419-429 (Dec 1975).
9. Furuya, O., "Numerical Procedures for the Solution of Two-Dimensional Supercavitating Flows Near a Free Surface," *Proceedings of First International Conference on Numerical Ship Hydrodynamics*, David W. Taylor Naval Ship R&D Center, pp. 155-176 (1975).
10. Yim, B., "On Low-Drag Infinite-Cavity Foils Near a Free Surface or in a Cascade," *Proceedings of the Second International Japanese Society of Mechanical Engineers Symposium*, Tokyo, Japan, pp. 257-266 (1972).
11. Yim, B., and L. Higgins, "A Nonlinear Design Theory of Supercavitating Cascade," *Transaction of the ASME*, Vol. 97, Series 1, No. 4, pp. 430-438 (Dec 1975).
12. Yim, B., "Finite Cavity Cascades with Low-Drag Pressure Distributions," *Transaction of the ASME*, Vol. 95, Series 1, No. 1, pp. 8-16 (Mar 1973).
13. Yim, B., and L. Higgins, "Linear Design of Supercavitating Cascade Sections," David W. Taylor Naval Ship R&D Center, NSRDC Report 4239 (Mar 1974).
14. Larock, B.E., and R.L. Street, "A Nonlinear Solution for a Fully Cavitating Hydrofoil Beneath a Free Surface," *Journal of Ship Research*, Vol. 11, No. 2, pp. 131-139 (1967).
15. Wu, T.Y., "Cavity Flow and Numerical Method," *Proceedings of the First International Conference on Numerical Ship Hydrodynamics*, David W. Taylor Naval Ship R&D Center, pp. 113-136 (1975).
16. Jiang, C.W., and P. Leehey, "A Numerical Method for Determining Forces and Moments on Supercavitating Hydrofoils of Finite Span," *Proceedings of the Second International Conference on Numerical Ship Hydrodynamics*, David W. Taylor Naval Ship R&D Center (1977).
17. Mogel, T.R., and R.L. Street, "A Numerical Method for Steady-State Cavity Flows," *Journal of Ship Research*, Vol. 18, No. 1, pp. 22-31 (1974).
18. Street, R.L., "Review of Numerical Methods for Solution of Cavity Flow Problem," *Proceedings of the Second International Conference on Numerical Ship Hydrodynamics*, David W. Taylor Naval Ship R&D Center (1977).
19. Glauert, H., "The Elements of Aerofoil and Airscrew Theory," Cambridge University Press, London (1926).
20. Cooley, J.W., and J.W. Tukey, "An Algorithm for the Machine Calculation of Complex Fourier Series," *Math. Comp.* 19, 90, pp. 297-301 (Apr 1965).
21. Gilberg, D., "Jets and Cavities," *Encyclopedia of Physics*, Vol. 9, Fluid Dynamics III, Springer-Verlag, Berlin, pp. 311-445 (1960).



# AN APPLICATION OF THE BOUNDARY INTEGRAL EQUATION METHOD TO CAVITY AND JET FLOWS

Bruce E. Larock  
University of California  
Davis, California 95616

## Abstract

A discussion of the use of boundary integral equation techniques to solve cavity and jet flow problems is presented. The need to model such flows as a mixed-boundary-value problem is demonstrated. Application of the basic method requires four steps: a suitable discretization of the problem, formation of the resulting matrix of linear equations, solution of these equations, and use of a systematic shifting algorithm to improve the free surface location. Although progress has been made recently, examples show step four is still in need of further research and improvement. To illustrate procedures, simple two-dimensional jet and cavity flows are presented.

## I. Introduction

In recent years the design of high performance surface vessels and other marine vehicles has continued to focus attention on the need for computationally practical solutions to progressively more complicated jet and cavity flow problems. Hydrodynamicists have now sought these steady-state solutions for over a century; to date no totally satisfactory approach has been presented which allows a convenient and suitably accurate fully non-linear computation of these flows, especially in three dimensions.

During the past decade the use of conformal mapping, finite difference and finite element techniques have all contributed substantially to progress in understanding jet and cavity flows. However, none of these approaches is free of limitations or shortcomings, and the great majority of the work has been restricted to two dimensions. Conformal mapping is of course limited solely to two dimensions. From a conceptual point of view, finite difference and finite element approaches to jet and cavity flows can be formulated in terms of a velocity potential so that there is little if any difference between a two-dimensional and a three-dimensional problem; the shortcomings here are mostly practical ones.

Both finite difference and finite element techniques must fill the entire flow domain. The physical domain is always irregular in shape and often possesses curved boundaries

surfaces. Trial free-boundary techniques depend upon shifting of the free surface portion of these boundaries as the solution proceeds iteratively. Finite difference methods are not ideally suited to the treatment of boundary conditions at non-rectangular boundaries, and so they usually either (i) use irregular computational stags there and suffer some loss of accuracy, or (ii) solve the problem in a velocity potential and stream function domain [1,2] and transform the solution back to the physical domain, thereby sacrificing the ability to prescribe the physical geometry a priori. Finite element techniques do not have these problems but do require an automated mesh adjustment scheme near free surfaces, preferably a quadratic representation of the velocity potential and possibly the use of isoparametric elements along the boundaries.

In jet and cavity flows the most interesting and useful information from a solution are the spatial location of all free surfaces and a knowledge of velocities and/or pressures along the boundaries. This realization causes one to feel that full-domain techniques such as the finite element technique are in a sense computationally inefficient, for in the course of developing the required boundary information it literally generates reams of interior data which is often of minor use.

For these reasons the search for superior computational techniques for high-speed free surface flows continues. This presentation suggests that a variant of the boundary integral equation method holds promise of being such a technique. In this method all computations deal directly with domain boundaries. For free surface flow problems the vital missing ingredient in previous implementations of the method was a systematic algorithm for shifting the trial free-boundary between successive iterations; the present paper presents two possibilities.

## II. Basic Theory

Several basic ideas underlying the method have been understood for a very long time (e.g., see [3]), but most computational progress has occurred in the last 20 years during the computer era. Hess, Smith and co-workers at Douglas Aircraft have been among the most

persistent contributors to developments over this entire period (see review articles [4,5]), while a more diverse interest in applications such as solid mechanics [6] and seepage flow [7] is becoming apparent in the last few years. In retrospect the approach proposed herein is closely related to boundary integral techniques developed at Stanford University by Kline et al. as part of a continuing investigation of stall prediction in diffusers [8-11].

The method is based on Green's theorem for

$$\int_{\Omega} (F \nabla^2 G - G \nabla^2 F) d\Omega = \int_{\Gamma} (F \nabla G - G \nabla F) \cdot \underline{n} d\Gamma \quad (1)$$

a domain  $\Omega$  bounded by a surface  $\Gamma$  having a unit outer normal  $\underline{n}$ . The functions  $F$  and  $G$  are to be continuously differentiable. When both  $F$  and  $G$  satisfy the Laplace equation, the left member vanishes and one obtains a boundary integral equation (BIE). In the present case one function is chosen to be the velocity potential  $\phi$  (let  $F = \phi$ ) and the other to be a fundamental solution of the Laplace equation. The most common choice for  $\Omega$  is

$$G = \ln r \quad \text{in two dimensions} \quad (2)$$

$$G = 1/r \quad \text{in three dimensions} \quad (3)$$

where  $r = r_{pq}$  = the distance from any arbitrarily chosen point  $P$  in  $\Omega$ , to a point  $Q$  on the boundary  $\Gamma$ . By use of a limit process in the neighborhood of  $P$ , one finds

$$\alpha \phi_P = \int_{\Gamma} \left( \phi \frac{\partial G}{\partial n} - G \frac{\partial \phi}{\partial n} \right) d\Gamma \quad (4)$$

noting that  $\nabla G \cdot \underline{n}$  is equivalent to  $\partial G / \partial n$ . If  $P$  does not lie on  $\Gamma$ ,  $\alpha = 2\pi$  in two dimensions,  $\alpha = 4\pi$  in three dimensions. If  $P$  lies on  $\Gamma$ , then  $\alpha$  is the "internal angle" subtended in passing around  $P$ . Subsequent sections of this paper assume  $P$  lies on  $\Gamma$ . When a problem is well posed, either  $\phi$  or  $\partial \phi / \partial n$  will be known at each point along the boundary, and Eq. 4 then becomes an integral equation relating the known function  $G$  and the complementary function  $\phi$  which is to be found. One additional noteworthy point is that the technique is inherently mass-conserving in its exact form; that is,

$$\int_{\Gamma} \frac{\partial \phi}{\partial n} d\Gamma = G \quad (5)$$

Since the form of the fundamental solution chosen for  $G$  has the same mathematical form as the velocity potential for a point source of fluid, the approach is called the surface-source method. Hess et al. have fashioned this technique into a highly efficient method of solving the pure Neumann problem of exterior flow over solid objects of known shape in two and three dimensions. However, Hess correctly remarked [7, p.15] a decade ago that

this particular technique offered at best a "cut and try" approach to adjusting free surface boundaries until all appropriate boundary conditions are satisfied.

The next sections will demonstrate how solutions to jet and cavity flows can be sought systematically by use of Eq. 4 as the basis of a numerical treatment of a mixed boundary value problem.

### III. The Present Technique

Implementation of the current BIE method depends on four steps (Hess [5] has written extensively on the first three steps and can be referred to for a more complete account). These steps are: discretization of the problem, computation of the coefficient matrix for the unknown values of  $\phi$  and  $\partial \phi / \partial n$ , solution of the resulting linear equation system, and adjustment of the free surface.

#### 1. Discretization

Equation 4 normally can not be solved in closed form for  $\phi$  and  $\partial \phi / \partial n$ . The usual approach is therefore to discretize Eq. 4 to obtain a set of  $N$  algebraic equations in the discretized unknowns  $\phi_i$  and  $(\partial \phi / \partial n)_j$ , where  $i = 1, 2, \dots, I$ ,  $j = 1, 2, \dots, J$  and  $I + J = N$  so that the equation system is determinate. This process involves a discretization of both the boundary geometry and the unknowns.

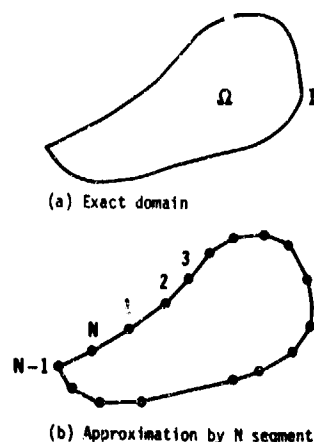


Figure 1. Discretization of boundary

**Geometry.** Figure 1 depicts in two dimensions the process of approximating the true boundary geometry by dividing it into  $N$  segments of known (by choice) shape -- straight-line segments in this case. Straight lines are simplest to use. Higher-order polynomial

segments can better approximate the boundary but require more effort to implement. Circular arcs closely approximate parabolic arcs and are mathematically more tractable [12]. In three dimensions the line segments become plates of quadrilateral or triangular shape; both have been used. Some [13] have rejected the use of quadrilaterals because adjacent segments sometimes can not be aligned to give a  $C^0$  continuous approximation to the original surface and the elements "leak"; Hess [5] discounts this by considering this discretization as a mathematical approximation rather than a physical one.

**Unknowns.** The simplest approach is to assume that  $\phi$  and  $\partial\phi/\partial n$  are constant on a discrete boundary segment, and historically it is the most frequent choice. Assuming a linear variation of the unknowns on a segment is becoming more common, however, and higher order interpolation functions have been used on occasion [12].

The choice of order-of-approximation for the boundary geometry and the discretized unknowns is still regarded by many as an independent pair of decisions, but Hess [12] has shown by series expansion techniques and numerical experiments for the Neumann problem that mathematical consistency requires the approximation of the geometry to be one order higher than the approximation of the unknowns. Although the selection of straight-line segments and linear interpolation of the unknowns is thus deemed an inconsistent approximation, this choice is becoming common and often yields good results. (It will also be used in the examples in this paper.) Finally, for two-dimensional BIE formulations based on complex function theory, order-of-approximation arguments appear not to be applicable because the resulting expressions become path independent so that boundary curvature does not play a role [14].

As an example of approximation of the unknowns, refer to Figure 2. For the linear

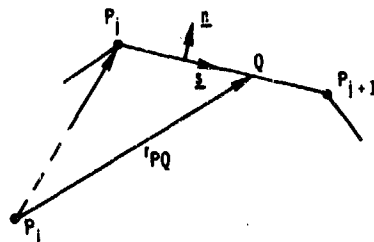


Figure 2. Portion of discretized boundary approximation one may write

$$\phi(s) = \phi_j + (\phi_{j+1} - \phi_j)(s - s_j)/(s_{j+1} - s_j) \quad (6)$$

and

$$\frac{\partial\phi}{\partial n}(s) = \frac{\partial\phi}{\partial n}\bigg|_j + \left(\frac{\partial\phi}{\partial n}\bigg|_{j+1} - \frac{\partial\phi}{\partial n}\bigg|_j\right)(s - s_j)/(s_{j+1} - s_j) \quad (7)$$

where  $s$  is the coordinate along the segment connecting points  $P_j$  and  $P_{j+1}$ .

## 2. Equation Matrix

When Eqs. 6-7 are employed in Eq. 4, the required integrations can be completed in closed form to yield expressions linear in the  $\phi_j$ 's and  $(\partial\phi/\partial n)_j$ 's and involving logarithmic and inverse tangent functions. In a higher-order approximation the superiority of circular arcs over parabolic segments becomes apparent here due to greater ease of integration. In axisymmetric problems where integrals can not conveniently be evaluated in closed form, one must use numerical integration with care to achieve accuracy. On the other hand, when  $rpq$  is several times the segment size it is often possible to use simplified results in place of lengthier, exact expressions; this factor becomes most important when three-dimensional problems are considered.

When Eq. 4 is evaluated for each of the  $N$  points  $P_i$  ( $i = 1, 2, \dots, N$ ), the result is a set of linear algebraic equations of the form

$$a_{ij}\phi_j + a'_{ij}\left(\frac{\partial\phi}{\partial n}\right)_j = 0 \quad (8)$$

where summation over  $j = 1, 2, \dots, N$  is implied. At each of the  $N$  discrete points on the boundary either  $\phi_j$  or  $(\partial\phi/\partial n)_j$  is specified as a known boundary value, and the final  $N$  equations to be solved are

$$A_{ij}q_j = B_j \quad (9)$$

Equation 9 is obtained from Eq. 8 by transposing to the right side the  $N$  terms known from the boundary conditions, and  $q_j$  is the remaining vector of unknowns.

At some points on the boundary of the flow it is desirable to represent exactly a discontinuity in  $\partial\phi/\partial n$ ; in particular, this occurs at a corner where one segment representing a wall connects with another which has fluid flowing across the domain boundary. To model this case exactly, one simply places two nodes  $i$  and  $j$  atop one another at the corner (they are connected by a boundary segment of zero length). One can then assign a boundary value for  $\partial\phi/\partial n$  to node  $i$  and/or node  $j$ ; if only one value of  $\partial\phi/\partial n$  is specified, then  $\phi$  can be specified

at the other node. Equation 9 must also be augmented with the equation  $\phi_1 = \psi_j$ . Normal computations for the segment of zero length are then omitted from Eqs. 8-9.

### 3. Solution of Equations

The coefficient matrix  $A_{ij}$  is full and unsymmetric in distinct contrast to the finite element formulation of these problems, which would yield a symmetric, banded matrix. But the number of equations  $N$  via the BIE method is much smaller than for a full domain method. Moreover, the diagonal coefficients tend to be relatively large although the matrix is not strictly diagonally dominant.

In two dimensions and in smaller three-dimensional problems this kind of linear equation set is solved directly (e.g., Gaussian elimination). For large three-dimensional problems, iterative solution techniques may be preferred.

### 4. The Free Surface

It is the treatment of the free surface itself that spells success or failure for the BIE method in jet and cavity flows. Earlier BIE techniques concentrated on formulation of the pure Neumann problem. Once a tentative free surface location was assumed, a jet flow could be formulated and "solved" as a Neumann problem, but after a check had ascertained that the trial location did not satisfy both the streamline tangency and constant pressure conditions, no algorithm was available to adjust the free surface systematically to an improved location. Cavity flows were even less susceptible to such a treatment.

It now appears that the BIE method should properly treat jet and cavity flows as mixed boundary value problems which are solved in conjunction with the kind of general surface shifting algorithm used by the writer and several other investigators over the past five years [8,9,15-19].

The essence of the scheme is to assure a constant pressure on a trial free surface, Fig. 3, which may initially be incorrectly

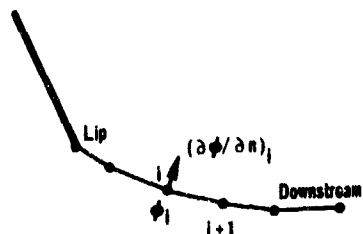


Figure 3. Schematic of free surface located, by assigning nodal boundary values of  $\phi_1$  by integration of  $\partial \phi / \partial s = V$ , usually

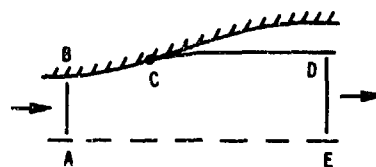
progressing from a downstream reference value of  $\phi$  to the upstream lip from which the free surface springs. Here  $V$  = fluid speed on the free surface. After Eq. 9 is solved for values of  $(\partial \phi / \partial n)_i$  along the free surface, the streamline tangency condition is used to adjust the surface, beginning now at the known coordinates of the lip. First the new local free surface slope  $m^{(n+1)}$  is computed at each node  $i$  in terms of the old slope  $m^{(n)}$ , local tangential speed  $V$  and current value of  $(\partial \phi / \partial n)^{(n)}$ ; the relation is

$$m^{(n+1)} = \frac{V m^{(n)} + (\partial \phi / \partial n)^{(n)}}{V - m^{(n)} (\partial \phi / \partial n)^{(n)}} \quad (10)$$

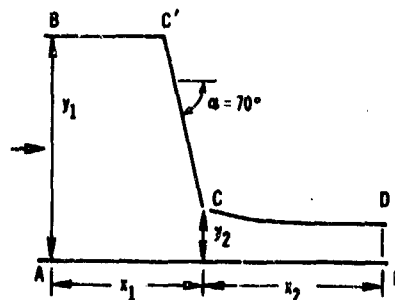
with use of an outer normal. It is convenient to insert these slopes directly into a cubic spline interpolation scheme to find the new free surface. Whether  $V$  varies along the free surface because of gravitational effects is of little consequence. The single remaining problem is proper selection of the downstream value of  $V$ ; as the next section indicates, no one approach currently appears superior for both jet and cavity problems.

### IV. Examples and Discussion

BIE techniques [8-11] at Stanford University have in the last couple years been applied to the (assumed) potential flow core of stalling flows in two-dimensional and axisymmetric diffusers and are typified by the flow shown in Figure 4a. Line AE is the centerline of the diffuser where  $\partial \phi / \partial n = 0$ . Flow across the



(a) Diffuser jet



(b) Jet or cavity

Figure 4. Jet and cavity flow examples

inlet section AB and outlet section DE is two-dimensional; the velocity  $\partial\phi/\partial n$  is prescribed at AE and computed at DE at the beginning of each computational cycle from continuity. Along the solid wall BC  $\partial\phi/\partial n = 0$ . The free surface CD separates from the wall at C; the fluid outside surface CD is assumed to be at constant pressure. With the velocity  $V$  computed at D, boundary values of  $\phi$  are assigned along the trial free surface, and Eq. 9 is formed and solved. The computational cycle is repeated until a convergent solution is attained. In axisymmetric problems [9] the investigators had to undercorrect the amount of the local slope adjustment  $(m(n+1) - m(n))$  strongly to assure convergence of the technique; only 10 to 20% of the computed change in slope was actually used in adjusting the surface at one time. Undercorrection was apparently not needed in two-dimensional problems. All work employed straight-line segments and a linear approximation for unknowns; apparently each free surface experienced a total angle change of  $45^\circ$  or less (local free surface slope  $|m| \leq 1.0$ ) with no more than a  $5^\circ$  change in direction per segment.

The author applied the foregoing procedure to the configuration shown in Figure 4b; it is a two-dimensional jet flow from a slot with  $\alpha = 70^\circ$  and  $y_1/y_2 = 4.0$ . Twelve segments were used to model the free surface; for convenience the velocity across AB was unity. Unaccountably the scheme did not converge to a solution even though the initial trial free boundary was a smooth exponential curve located reasonably close to the expected solution.

With a different physical interpretation and a different assignment of boundary values, figure 4b depicts a Riabouchinsky cavity flow past half a symmetric wedge in a water tunnel. Let AE be the tunnel wall, BC' is a line of symmetry, and C'C is half the wedge; along all these boundaries assign  $\partial\phi/\partial n = 0$ . Thus DE is at midcavity and is a line of constant velocity potential  $\phi$ , but the normal velocity across DE is nonuniform; assign  $\phi = \text{constant}$  across DE. Across AB the oncoming velocity is uniform and  $\phi$  is also constant but unknown; for convenience assign a unit velocity to section AB. On CD  $\phi$  can be prescribed once  $V$  is selected. Again  $y_1/y_2 = 4.0$ , and for this example  $x_1/y_2 = 7.73$  and  $x_2/y_2 = 1.57$ . At this point C a double node was placed so that  $\partial\phi/\partial n = 0$  on the wedge, but  $\phi$  was also prescribed at the lip from free surface considerations.

The free surface was sought by the following procedure. By comparison with the related jet-flow whose solution is known [40],  $V = 6$  was chosen. Several computational cycles were computed without adjustment of  $V$ ; the trial free surface location converged toward a stable location during this process. It was observed that  $\partial\phi/\partial n$  at the lip end of the free surface, which was not prescribed and which can play no role in free surface adjustment because the lip location is fixed, also converged toward a negative value rather than the desired value of zero which would indicate proper flow behavior at the lip. Next  $V$  was changed to a

lower value; several iterations with  $V = 5.9$  caused the value of  $\partial\phi/\partial n$  at the lip to converge toward a positive value. Hence, the correct value of  $V$  must lie in between, and several automated interpolative sequences gave a final free-surface value for  $\partial\phi/\partial n$  at the lip which was approximately  $-0.036$  when  $V = 5.94$ . The initial and final free surface are plotted in Figure 5.

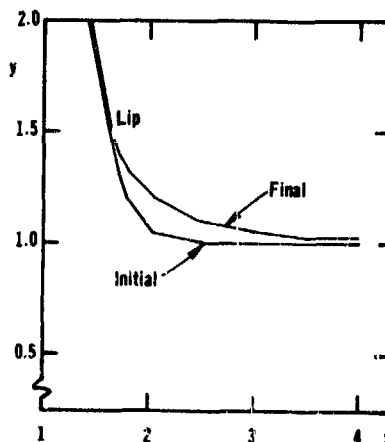


Figure 5. Initial and final cavity free surface

The general free surface adjustment scheme seems to perform differently when implemented in the BIE technique rather than, for example, the finite element method. The probable cause is that the BIE approach is inherently mass-conserving, as Eq. 5 states clearly. Consequently, when a portion of a trial free surface is too low and causes computed local values of  $\partial\phi/\partial n$  to be positive, Eq. 5 apparently ensures that  $\partial\phi/\partial n$  will be negative over another portion of the same free surface to conserve mass. Possibly this effect is more pronounced for axisymmetric flows and led to the need for undercorrection of the free surface.

#### V. Prognosis

Formulation of the boundary integral equation method as a mixed boundary value problem holds promise for the efficient solution of jet and cavity flows. In several respects the technique is still not well developed, however. Although some free surface location techniques have been shown to work for certain kinds of problems, much room for both innovation and for improvement remains. Extension of these techniques to the much more challenging, practical and exciting three-dimensional jet and cavity flows remains to be accomplished, but prospects of eventual success appear reasonably good at this time.

#### References

1. Brennan, C., "A numerical solution of

- axisymmetric cavity flows," J. Fluid Mech., 37, 4, 1969, pp. 671-688.
2. Jeppson, R. W., "Inverse solution to three-dimensional potential flows," J. Engr. Mech. Div., ASCE, 98, EM4, 1972, pp. 789-812.
  3. Kellogg, O. D., Foundations of Potential Theory, Ungar, New York, 1929.
  4. Hess, J. L., and Smith, A.M.O., "Calculation of potential flow about arbitrary bodies," in Progress in Aeronautical Sciences, 8, Pergamon, New York, 1967, pp. 1-138.
  5. Hess, J. L., "Review of integral-equation techniques for solving potential-flow problems with emphasis on the surface source method," Comp. Meth. in Appl. Mech. and Engrg., 5, 1975, pp. 145-196.
  6. Cruse, T. A., and Rizzo, F. J., eds., Boundary-Integral Equation Method: Computational Applications in Applied Mechanics, ASME, AMD 11, 1975.
  7. Liggett, J. A., "Location of free surface in porous media," J. Hyd. Div., ASCE, 103, HY4, April 1977, pp. 353-365.
  8. Wooley, R. L., and Kline, S. J., "A method for calculation of a fully stalled flow," Report MD-33, Thermosciences Div., Mechanical Engineering Dept., Stanford University, November 1973.
  9. White, J. W., and Kline S. J., "A calculation method for incompressible axisymmetric flows, including unseparated, fully separated, and free surface flows," Report MD-35, Thermosciences Div., Mechanical Engineering Dept., Stanford University, May 1975.
  10. Ghose, S., and Kline, S. J., "Prediction of transitory stall in two-dimensional diffusers," Report MD-36, Thermosciences Div., Mechanical Engineering Dept., Stanford University, December 1976.
  11. Rinehart, F., "A boundary integral method for the solution of two-dimensional Laplace's equation using the Plemelj formula," unpublished report, Thermosciences Div., Mechanical Engineering Dept., Stanford University, 1976.
  12. Hess, J. L., "Higher order numerical solution of the integral equation for the two-dimensional Neumann problem," Comp. Meth. in Appl. Mech. and Engrg., 2, 1973, pp. 1-15.
  13. Webster, W. C., "The flow about arbitrary three-dimensional smooth bodies," J. Ship Res., 19, 4, December 1975, pp. 206-218.
  14. Ferziger, J. n., personal communication, 1977.
  15. Chan, S. T. K., and Larock, B. E., "Fluid flows from axisymmetric orifices and valves," J. Hydr. Div., ASCE, 99, HY1, 1973, pp. 81-97.
  16. Chan, S. T. K., Larock, B. E., and Herrmann, L. R., "Free-surface ideal fluid flows by finite elements," J. Hydr. Div., ASCE, 99, HY6, 1973, pp. 959-974.
  17. Mogel, T. R., and Street, R. L., "A numerical method for steady-state cavity flows," J. Ship Res., 18, 1, 1974, pp. 22-31.
  18. Larock, B. E., and Taylor, C., "Computing three-dimensional free surface flows," Int. J. Num. Meth. Engrg., 10, 1976, pp. 1143-1152.
  19. Street, R. L., and Ko, P. Y., "Numerical methods applied to fully cavitating flows, with emphasis on the finite element method," Symposium on Hydrodynamics of Ship and Offshore Propulsion Systems, Det Norske Veritas, Oslo, Norway, March 1977.
  20. Larock, B. E., "Jets from two-dimensional symmetric nozzles of arbitrary shape," J. Fluid Mech., 37, 3, 1969, pp. 479-489.

DISCUSSIONS  
of three papers

A NUMERICAL METHOD FOR DETERMINING FORCES AND MOMENTS ON  
SUPERCAVITATING HYDROFOILS OF FINITE SPAN  
C.W. Jiang and P. Leehey

SUPERCAVITATING FOIL OF AN ARBITRARY SHAPE  
BENEATH OR ABOVE A FREE SURFACE OR IN A CASCADE  
B. Yim

AN APPLICATION OF THE BOUNDARY INTEGRAL EQUATION METHOD  
TO CAVITY AND JET FLOWS  
Bruce E. Larock

Invited Discussion

M.P. Tulin  
Hydronautics Inc.

The vastness of the literature for steady planar free-streamline flow attests to the power of available analytical tools for the solution of certain physical problems (especially supercavitating flows) through their reduction to mixed boundary-value problems. These tools include: suitable modeling (cavity termination and wakes), analytic functions and mapping, boundary integral equations, asymptotic (i.e. linear) approximations, and combinations thereof. A sizeable number of important engineering problems have by now been given adequate solution through the application of theory. I would mention especially the design of supercavitating propellers. The second paper (#18) today, by Yim, is a further and very elegant contribution to this literature. He utilizes known techniques of supercavitating-foil theory: linearizations and mappings to the "airfoil" plane, combinations of incidence, camber, and "parabolic" thickness (really a leading-edge singularity). He has succeeded in a very useful synthesis of these methods and finally applied some fast computing techniques. I was especially pleased to see the hydrofoil-airfoil equivalence generalized, as these rules immediately give much insight as to the relation between the chordwise pressure distribution (at design) and the lift/drag ratio. Yim's results, which include free-surface (infinite Froude number) and cascade effects, attest again to the power of analytical methods, more so in this case than to the power of numerical hydrodynamic techniques.

Useful and general as Yim's results are, I would like to suggest a little warning in connection with their utilization in hydrofoil or propeller design. In both cases, it is often necessary to utilize non-linear corrections based on theory. For foils it is also of some importance to take into account the down-wash due to gravity effects on the cavity. Further, I have some doubts about the utility of the planar cascade model in application to propeller design, except to estimate cavity-section interference during off-design operation--and this is the design region where we most need better methods. In the off-design regime non-linear effects are

due to the large cavity thickness clearly become important. Non-linear cascade calculations have been made earlier by Furuya, (ref. 1), based on the approach of Wu and Wang to the non-linear supercavitating flow past a given isolated hydrofoil, and Yim himself has earlier considered the non-linear problem (ref. 2). The superproblem for the supercavitating propeller and a great challenge for numerical analysis involves the calculation of the flow past the collective blade cavities treated as a fully-three-dimensional problem, but which more resembles a short axisymmetric cavity (in the limit of many blades) shed by a porous disc (the propeller blade) than it does a cascade. I refer to the model I suggested in ref. 3. It is the inflow distribution to this disc just as much as the flow over the blades considered as a blade element that requires numerical calculation, since at the present time we have available for the inflow estimation only the results of supercavitating propeller momentum theory. Yim is, I know, working on the full supercavitating-propeller problem, toward which the present work is a step, and we should all look forward to his future results.

The gap between three-dimensional supercavitating flow theory and the present status is being closed with efforts such as those of Jiang and Leehey (paper #17). It is the latest result in the long effort to develop a practical numerical lifting-surface method for supercavitating wings, a history beginning with the rheo-electric analogy work of T.S. Luu in Paris in the early 1960's (ref. 4). It is a difficult problem, even in its linearized form (as is the case with all numerical attempts), as it involves two coupled integral equations and an unknown area of integration; the authors have made a prodigious effort. They have tested their numerical techniques in the two-dimensional case by comparing with analytic results; they obtained a good comparison, but first I would like to suggest the possibility of an additional perspective that arises through comparison of numerical calculations such as these with approximate theories that are more or less well-proven. I refer to the semi-empirical methods starting with linear two-dimensional theory, factoring in lifting-surface corrections such as the Jones edge connection, plus corrections for non-linear effects based on theory, both for the section effectiveness and cross-flow drag. In 1975, C.C. Hsu presented practical formulae for wing force coefficients together with comparison with the

data for rectangular wings of Reichardt and Sattler, Schiebe and Wetzel, and Dobay, including free-surface effects and for angles of attack as high as  $16^\circ$ . The comparison with the data lend confidence that Hsu's formulae may be used for preliminary design with confidence. The Jones' edge correction for supercavitating wings, originally proposed by V.E. Johnson, has been well-confirmed, incidentally, by the numerical lifting-surface calculations of Tsen and Guilbaud (ref. 5) carried out in France and which are the  $\sigma = 0$  counterpart of the results of Jiang and Leehey, and which would make a very important additional reference in their paper.

In Figure 1, I show a comparison of predictions using Hsu's formulae for the aspect ratio 5 elliptic wing tested by Leehey and Stellingner for  $\alpha = 21^\circ$ . The data are those reported by Maixner at the recent ATTC conference in Annapolis (ref. 6). Note first of all the relative agreement of Hsu with the small foil data, which are, according to Maixner, free of wall effects. Note also that Jiang and Leehey actually lie under Hsu for the values of  $\sigma/\alpha$  reported. This, it seems to me, poses a grave difficulty for the theory of Jiang and Leehey as non-linear effects are very large at this angle of attack. Most probably at this aspect ratio, the non-linear effects must reduce the linear predictions, thus worsening the comparison between the present calculations and experiment. To drive the point home, I show in Fig. 1 the predictions of Hsu's wing theory, omitting the non-linear corrections. I believe that for this aspect ratio any "correct" linear theory must lie closer to the dotted line than to the data, and I wonder whether or not the authors would agree and whether they can illuminate the situation this poses for their numerical results. Incidentally, Tsen and Guilbaud show that for an aspect ratio 4 wing, the data of Schiebe and Wetzel and Kermee lie in general well below both their own linearized numerical calculations and those of Widnall, even at an angle of attack of  $10^\circ$ . Finally, I hope that the authors persevere and eventually go on to consider the practical problems of the free surface for high speeds, and pod-strut interference with wings, for which numerical computation methods should be welcome.

How to do truly non-linear free-surface problems? This is the subject of Larock (paper #19) who has earlier been involved in the numerical calculation of such free-streamline flows as from orifices and valves. In particular, he addresses the question how to carry out a stable iteration for the free-surface configuration in space, in conjunction with boundary integral techniques. The method seems natural, and I believe that essentially the same technique has been used previously in conjunction with finite-element calculations (I refer to the work of Chan, Larock, and Herrmann, and to Sarphaya). I would ask the author two questions, though: 1) is the algorithm optimum in any sense (speed of convergence, for example); that is, why this method rather than any other? and 2) is it possible to optimize an algorithm through mathematical analysis?

Finally, in designing numerical methods and in testing their accuracy, I think it is impor-

tant to keep foremost in mind the results needed from the computation and to test the computations in terms of the accuracy of those results. These may often involve (jet flows, for instance) the pressures in regions where cavitation is to be feared, as at bends—I think of the crest of dams or spillways, which were many decades ago being studied numerically using relaxation techniques, or at the entrance of valves as studied by Chan and Larock. Sometimes very sharp corners or discontinuities in shape or boundary conditions are involved, and it would then seem appropriate and even in some cases necessary to supplant numerical calculations such as proposed by the author with imbedded analytic expansion.

#### REFERENCES

1. Furuya, O., "Exact Supercavitating Cascade Theory," *Trans. ASME, J. Fluids Engineering*, Vol. 97, 1975, pp. 419-429.
2. Yim, B., and Higgins, L., "A Nonlinear Design Theory of Supercavitating Cascade," *Trans. ASME, J. Fluids Engineering*, Vol. 97, 1975, pp. 420-438.
3. Tulin, M.P., "Supercavitating Flows and Practical Applications," *Cavitation in Real Liquids*, Robert Davies (editor), Elsevier Press, Amsterdam, 1977.
4. Luu, T.S., "Hydrofoils supercavitants d'envergure finie. Simulation rhéologique," *Colloque international des techniques de calcul analogique et numérique en aéronautique*, Liège, September 1963.
5. Tsen, L.F. and Guilbaud, M., "Méthode du potentiel d'accélération pour le calcul des ailes supercavitantes finies," *Bull. Assoc. Tech. Mar. Aéron.*, Vol. 70, 1970.
6. Maixner, M.R., "An Experimental Investigation of Wall Effects on Supercavitating Hydrofoils of Finite Span," *Cavitation Committee Report*, 18th ATTC, Annapolis, August 1977.

#### Author's Reply

by C.W. Jiang and P. Leehey  
to discussion by M.P. Tulin

The authors appreciate the comments of invited discussor and will endeavor to reply the questions raised by him.

The discussor made the comparison between our linear numerical results with Hsu's (1975) non-linear empirical expression. Our present numerical lifting surface theory is as good as Hsu's non-linear results (see the figure prepared by the discussor). The empirical expression of two-dimensional results of Hsu was based on the results of Professor Wu (1956). Based upon a comparison of linear and non-linear results of Hsu, discussor expected that our linearized results would overpredict the results. Wu's (or Hsu's) linearized theory, however, is not the same as ours. Our numerical method is based on the linearized two-dimensional theory of Goursat as expressed by our Fig. 1. The following comparison of two-dimensional lift coefficient is instructive:

	$\sigma=0.1$ $\alpha=15^\circ$	$\sigma=0.1$ $\alpha=10^\circ$	$\sigma=0.436$ $\alpha=10^\circ$
non-linear(Wu)	0.37	0.28	0.56
linear(Goursat)	0.47	0.29	0.54



These relative errors are far less than those quoted by the discussor. One may refer this to the discussions following the paper by Leehey and Stellingner (1975) for details.

We also wish to mention that the steady-state experimental data have been taken for different reasons by several investigators during past four years. A dynamometer and the hydrofoils have been modified for special purpose at each test. We do believe those data are reliable.

15. Hsu, C. C., 1975. Some remarks on the progress of cavity flow studies. Trans. ASME. J. Fluids Engineering, vol. 97, pp. 439-448.  
16. Wu, T. Y., 1965. A note on linear and non-linear theories for fully-cavitated hydrofoils. CIT Div. of Eng. & App. Sci. Rept. No. 21-22.

Author's Reply  
by B.E. Larock  
to discussion by M.P. Tulin

Tulin directs two questions to this writer. My responses follow.

1. The major alternative to the present free-surface adjustment scheme is somehow to satisfy initially the streamline tangency condition with chosen boundary values, then solve the corresponding boundary-value problem, and finally employ the constant-pressure condition to adjust the free surface; this scheme apparently is always non-convergent for high speed flows. The algorithm presented in the paper is "optimum" only in the sense that it is successful and the major alternative cited above is not optimum because it fails. In the more conventional sense, the writer would not claim any optimality properties for the present algorithm. It is indeed quite possible that the global adjustment scheme proposed by Hess (paper 20) possesses advantages over the present approach.
2. I do not know if it is possible, but I would welcome the interest of mathematicians and specialists in numerical analysis in free-surface adjustment schemes. Perhaps they could answer the question positively.

# PROGRESS IN THE CALCULATION OF NONLINEAR FREE-SURFACE PROBLEMS BY SURFACE-SINGULARITY TECHNIQUES

John L. Hess  
John L. Hess, Associates  
Long Beach, California

## Abstract

This paper describes the status of a computer program for solving the full nonlinear problem of a two-dimensional body performing steady translation near a free surface. The method of solution is based on distributions of simple Rankine-type singularities on the body and on the true location of the free surface, which must be obtained by iteration. The key is the iterative algorithm for determining free surface shape. It must account for the mutual influence of various portions of the surface. Various stages of development of the procedure are described, including the final successful technique based on a higher-order singularity procedure. Comparisons are presented of free-surface shapes calculated by the present method with those calculated by a previous finite-difference solution for a submerged point vortex. For the higher-order solution, agreement is quite good. Future directions of the work are indicated.

## Introduction

The problem of interest is that of the steady translation of a body in the presence of a free surface. The fluid below the free surface is inviscid and incompressible, and the flow is irrotational so that it is a potential flow governed by Laplace's equation. The fluid pressure is constant all over the free surface. In three-dimensions this problem finds its chief application in the calculation of wave resistance both for surface ships (the surface-piercing case) and for undersea vehicles (the submerged case). In two dimensions the flow about hydrofoils is chief application. Although the problem of main practical interest is the three-dimensional one, because of its very formidable nature, the present effort has been devoted to the two-dimensional problem, where the only solution techniques considered are those with direct three-dimensional analogies.

The intention is to attempt to solve this problem in its full generality, i.e. without any assumptions of small perturbations in regard to either the body or the free surface. This is a nonlinear problem because the location of the free surface is unknown and must be solved for as part of the problem. The method of solution to be used is the surface-singularity approach (reference 1), which utilizes

singularity distributions — source, dipole, vorticity — on the surface of all bodies and on the true location of the free surface. This is in contrast to small-perturbation approaches that use singularity distributions interior to the bodies and/or on the undisturbed location of the free surface. In the surface singularity approach, the strengths of these singularities are determined from the boundary conditions in terms of integral equations, which are approximated by matrix equations for numerical implementation. The singularities used are of the simple "Rankine type," which are appropriate for problems without a free surface. For example, the point source potential is  $\log(1/r)$ , where  $r$  is distance between the source and the point where the potential is evaluated.

## General Description of the Flow Problem

It is supposed that a body is translating parallel to a free surface with uniform velocity  $U$ . By superposing the negative of the body's translational velocity on the entire velocity field, the problem can be stated as shown in Figure 1. The body surface  $S$ , which may be multiply-connected, is stationary in the presence of a uniform onset flow of magnitude  $U$  parallel to the positive  $x$ -axis. Above the body at a location  $y = n(x)$  that must be determined is the free surface, which is a streamline of the flow along which the pressure is constant. The flow field for  $y < n(x)$  is a potential flow, which has zero normal component on  $S$  and approaches the uniform freestream for  $x \rightarrow \pm\infty$  or  $y \rightarrow \pm\infty$ . (For definiteness the infinite-depth case is considered, but the finite-depth case may be handled by use of a single image of the body and free surface.) The undisturbed position of the free surface is  $y = n = 0$ .

If the tangential velocity at any point on the free surface is denoted  $V$ , the constant-pressure condition can be written

$$V^2 + 2gn = U^2 \quad (1)$$

or

$$V = \sqrt{U^2 - 2gn} \quad (2)$$

where  $g$  is the acceleration of gravity.

To solve this problem by a surface singularity approach, the body surface  $S$  is covered

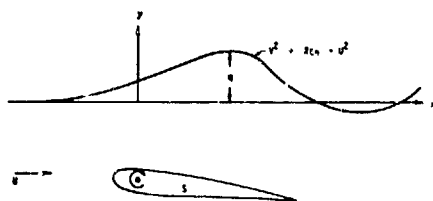


Fig. 1 A two-dimensional lifting body performing steady translation near a free surface.

with a source density distribution. (There is also vorticity to produce circulation about  $S$  in lifting cases.) The free surface is covered with either a source or a vorticity distribution. The two distributions, i.e. on the body and the free surface, are determined from the boundary conditions on the body and free surface. However, there are three boundary conditions, i.e. zero normal velocity on  $S$  and on  $y = \eta(x)$  and constant pressure on  $y = \eta(x)$ . Thus, two singularity distributions are insufficient, and an additional "degree of freedom" is necessary. This is the location  $y = \eta(x)$ , which is determined from the boundary conditions along with the source and vorticity distributions.

The surface singularity method requires that the locations of all boundaries be known. The free-surface problem must be attacked by iteration. At any stage the location of the free surface is assumed and a flow calculation is performed. Presumably one (or both) of the boundary conditions on the free surface are not satisfied. Based on some algorithm the location of the free surface is then changed, and the calculation is repeated. The above process is iterated until convergence (in some sense) is obtained. The algorithm for altering the free-surface location is highly nonunique. Many possibilities can be postulated and probably most of them lead to a divergent process. The main task in applying the surface singularity method to the free-surface problem is selection of a convergent algorithm. This is somewhat similar to the classic inverse problem, where the velocity distribution on a surface is specified and the surface shape must be computed.

Basically the calculation can proceed in one of two general ways. At each stage it can satisfy the condition of zero normal velocity on  $S$  and on  $y = \eta(x)$  and then iterate to obtain constant pressure on  $y = \eta(x)$ . Alternatively, at each stage it can satisfy the condition of zero normal velocity on  $S$  and the condition of constant pressure on  $y = \eta(x)$  and then iterate to obtain zero normal velocity on  $y = \eta(x)$ . While both possibilities must be kept in mind, it is the second one that has been used successfully in inverse problems, and it has been given first attention. Similarly either a source or a vorticity distribution may be used on the free surface. So far the use of a vortex distribution on the free surface has proven more effective.

Strictly speaking, it is not sufficient to consider only the free surface and the body as boundaries of the problem. The domain should be closed by the addition of three more boundaries: (1) an  $x = \text{constant}$  boundary at a large negative value of  $x$  on which freestream conditions (normal velocity equal to  $U$ ) are prescribed; (2) a  $y = \text{constant}$  boundary at a large negative value of  $y$  on which zero normal velocity is prescribed; and (3) an  $x = \text{constant}$  boundary at a large positive value of  $x$  on which a "radiation condition" of downstream waves is applied. However, the philosophy that has been followed in the present work has been to try the simpler approaches first and to add complications only when these simpler approaches prove inadequate. Accordingly, the above three additional boundaries have been ignored in the work to date. This is equivalent to the assumption that these boundaries will have weak enough singularity strengths to give a negligible effect in the vicinity of the body. Almost certainly it will always be possible to ignore boundary (2), but some form of boundary (3) may prove necessary in the future.

#### The Prototype Problem

To conserve computing time during the search for a convergent iteration algorithm, the mechanism responsible for disturbing the free surface has been taken as a submerged point vortex, as shown in Figure 2, rather than a lifting body, as shown in Figure 1. Some distance from the

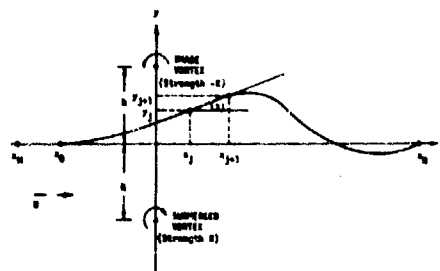


Fig. 2 The prototype problem. Flow about a submerged point vortex.

body its velocity field approaches that of a point vortex, so this appears to be a reasonable approximation. In any case it is known from the literature that the shape of the free surface due to a submerged point vortex is qualitatively similar to that due to a submerged lifting body. Thus, it seems likely that any proposed iteration algorithm for determining the free-surface shape would either converge for both a point vortex and a lifting body or diverge for both. The saving in computing time comes from the fact that only the free surface need be defined by surface elements. Thus, the order of the matrices that must be formed and solved is reduced. Another important reason for considering the point vortex is that this case has been considered by previous investigators, notably von Kerczek and Salvesen (references 2 and 3). Thus, solutions obtained

by the present method of this report can be compared with theirs to yield an essential quantitative test of accuracy.

The essentials of the point vortex problem are illustrated in Figure 2. The vortex which has a strength  $K$ , is located at the point  $x = 0, y = -h$ . Here  $K = \Gamma/2\pi$  where  $\Gamma$  is the circulation. The problem has been addressed both with and without an image vortex of equal and opposite strength at the point  $x = 0, y = +h$ , and it was encouraging to note that the convergent algorithms yielded exactly the same results in both cases. During most of the work to date, an image vortex was included. All cases follow references 2 and 3 in using a freestream velocity  $U$  of 10 feet per second and a submergence depth  $h$  of 4.5 feet. Various vortex strengths  $K$  are considered, which lead to various wave heights. During most of the present effort only reference 2, not reference 3, was available. In this paper all comparisons are for the two vortex strengths of reference 2,  $K = +1.15$  and  $K = -1.4$ . It should also be noted that the results of references 2 and 3 have been obtained for a finite fluid depth of 9.5 feet, so that perfect agreement with the infinite-depth results of the present method cannot be expected.

The free surface is represented by singularity distributions from  $x_0$  or  $x_0$  (see below) to  $x_1$  (Figure 2). From  $x_0$  to  $x_1$  the velocity is required to satisfy the free-surface condition of constant pressure and the shape is allowed to vary to produce a condition of zero normal velocity. The physical variables are  $U, h$ , and  $K$ . The "numerical variables" are  $x_0, x_1, x_2$ , and the element length  $\Delta x = x_{j+1} - x_j$  which is used to define the free surface. In all cases presented, a constant spacing is used, and  $\Delta x$  is a single number.

To implement the surface singularity method of reference 1, the free surface or its approximation is represented by a set of points  $(x_j, y_j)$ . During the course of iterating for the free-surface shape, the  $x_j$  remain fixed and the  $y_j$  are altered. The portion of the surface between two successive points  $(x_j, y_j)$  and  $(x_{j+1}, y_{j+1})$  is a surface element on which singularity (in this case vorticity) is distributed. In the "first-order" version of the method the surface element is a straight line from  $(x_j, y_j)$  to  $(x_{j+1}, y_{j+1})$  on which the singularity is constant. In the more accurate "higher-order" version (references 1 and 4) the element is a parabola and the singularity varies linearly. Boundary conditions are applied at a single control point  $(x_j, y_j)$  of each element, and this point is the midpoint of the element in both versions.

Let  $v_j$  denote the vorticity strength at the control point of the  $j$ th element, and let  $A_{ij}$  and  $B_{ij}$  be, respectively, the normal and tangential components of velocity at the control point  $(x_i, y_i)$  of the  $i$ th element due to a unit value of vorticity at the control point of the  $j$ th element. Further, let  $V_{Ni}$  and  $V_{Ti}$  be, respectively, the normal and tangential components at  $(x_i, y_i)$  due to the point vortex and

its image (if any). Then the total normal and tangential components of velocity at  $(x_i, y_i)$  are

$$V_{Ni} = \sum A_{ij} v_j - U \sin \alpha_i + V_{Ni} \quad (3)$$

$$V_{Ti} = \sum B_{ij} v_j + U \cos \alpha_i + V_{Ti} \quad (4)$$

where  $\alpha_i$  is the slope angle of the  $i$ th element as shown in Figure 2, and where the summations are over all elements. The equations that must be satisfied are

$$V_{Ni} = 0 \quad (5)$$

$$V_{Ti} = \sqrt{U^2 - 2qy_i} = V_i(\bar{y}_i) \quad (6)$$

In the present procedure the free-surface shape is assumed, and the  $v_j$  are obtained as solutions of the simultaneous linear equations (6) with left sides given by (4), i.e. the  $v_j$  are determined to satisfy the constant-pressure boundary condition. These values are then used in (3) to calculate normal velocities, which are not, in general, equal to zero. An iterative algorithm is then applied to alter the free-surface shape.

#### Local Algorithms

The simplest algorithm computes the change of slope angle  $\delta \alpha_i$  of each element as

$$\delta \alpha_i = \tan^{-1}(V_{Ni}/V_{Ti}) \quad (7)$$

These are added to the  $\alpha_i$  to obtain new  $\alpha_i$ , which in turn are used to calculate new  $y_i$  successively, beginning with some fixed upstream value. Then the entire calculation is repeated. This algorithm converges for the classical inverse problem of potential flow, in which the prescribed value of tangential velocity at each  $(x_i, y_i)$  is independent of location, but it diverges in the present application.

This algorithm may be called local because the local slope correction is determined from the local deviation of the calculated results from the satisfaction of the boundary condition. Three such algorithms have been investigated and all diverged.

#### Global Algorithms

To obtain convergence it is necessary to employ a global iterative algorithm which considers the effects at other elements of a change in  $\alpha_i$  and which simultaneously computes (to first order) changes in slope angle and vorticity strength that correct the normal velocities while maintaining the constant pressure condition on all elements. It should be emphasized that the final converged shape is not in any sense a small-perturbation solution. While small-perturbation formulas are used to

compute shape corrections, each iteration performs a full potential-flow solution in the sense of reference 2. Thus, the converged solution has the correct normal velocity (zero) and the correct tangential velocity for constant-pressure. Deviations, if any, of the computed shape from the correct shape can only be due to nonuniqueness of the basic problem and to numerical discretization, namely the finite length of the elements and the finite locations of the  $x_M$ ,  $x_0$  and  $x_N$ .

Basically, a change of shape of the free surface affects the local velocities in four ways:

1. Rotation of the local surface through a fixed velocity field.
2. Change of vorticity strength with fixed induced-velocity matrices.
3. Change of induced-velocity matrices with fixed vorticity strengths.
4. Effect of vertical translation on vortex velocity and on the constant pressure boundary condition.

The local iterative algorithm accounts only for effect 1, while the global algorithm below accounts for effects 1, 2, and 4. Experience indicates that effect 3 may be ignored safely if surface slopes are as low as those occurring in surface wave problems.

When the free-surface shape is altered, first-order changes in the velocity components (3) and (4) are

$$\delta V_{Ni} = \sum A_{ij} \delta u_j - (V_{Ti} - B_{i1} u_1) \delta \alpha_i + \frac{\partial}{\partial y_i} (V_{Ni}) \delta \bar{y}_i \quad (8)$$

$$\delta V_{Ti} = \sum B_{ij} \delta u_j + V_{Ni} \delta \alpha_i + \frac{\partial}{\partial y_i} (V_{Ti}) \delta \bar{y}_i \quad (9)$$

A simple geometric calculation

$$\delta \bar{y}_i = \sum p_j \delta \alpha_j \quad (10)$$

expresses the changes in vertical displacement in terms of slope angle changes. The conditions to be satisfied are

$$\delta V_{Ni} = -V_{Ni} \quad (11)$$

$$\delta V_{Ti} = \delta V_i(\bar{y}_i) - \frac{\partial}{\partial y_i} [V_i(\bar{y}_i)] \delta \bar{y}_i \quad (12)$$

Using (8), (9) and (10) in (11) and (12) gives a set of linear equations for  $\delta u_j$  and  $\delta \alpha_j$ , the latter of which yields a new free-surface shape  $y_j$ . Thus, the flow calculation can be repeated.

In all cases the initial approximation to the free-surface shape is the undisturbed location of the free surface  $y = 0$ .

#### Representation of the Free Surface With No Flat

The initial form of the global algorithm fixed the upstream end of the free surface at  $x = x_0$ ,  $y = 0$  (Figure 2) and applied the above equations to the entire free surface from  $x_0$  to  $x_N$ . Some of the results obtained for the free-surface shape are compared with corresponding results from reference 2 in Figures 3 and 4.

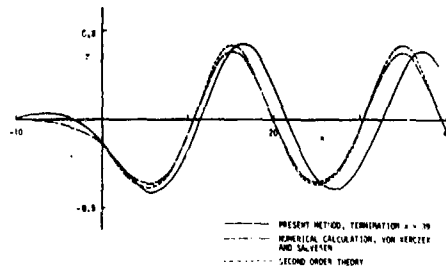


Fig. 3 Free-surface shapes for  $K = +1.15$ . First-order solution, no flat.  $\Delta x = 1$ .

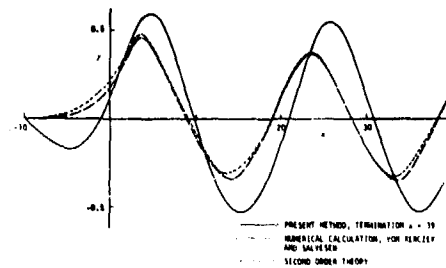


Fig. 4 Free surface shapes for  $K = -1.4$ . First-order solution, no flat.  $\Delta x = 1$ .

One very gratifying result is evident from these figures, namely that the present calculations yield waves. This was not at all obvious a priori. A monotonic shape might have been obtained. However, the one constantly occurring result in applying the present method is that it always gives waves, even in divergent cases. Moreover, the waves have approximately the correct wave lengths.

While the results of Figures 3 and 4 are not absurd, they are clearly unacceptable as results of a method of quantitative prediction. However, attempts to improve the results by decreasing the point spacing  $\Delta x$  lead to divergence. In fact, any change in  $\Delta x$  leads to divergence.

The iterations only converge for  $\Delta x = 1$ , a clearly unacceptable situation that requires a new approach.

#### Representation of the Free Surface with an Initial Flat

To render the calculation more stable, the free surface is preceded by an initial "flat" that is constrained to lie along the x-axis. Specifically, the portion of the free surface from  $x_M$  to  $x_0$  (Figure 2) is required to lie along  $y = 0$ , and the tangential velocity is required to equal the freestream velocity  $U$ . The remainder of the free surface from  $x_0$  to  $x_N$  is treated as described above. On  $x_M < x < x_0$  both source density and vorticity are used to handle the two boundary conditions, and the above iterative equations are modified in that region to account for two singularity changes with no change of shape. It was found by numerical experiment that as long as the flat has a certain minimum length necessary to ensure convergence, further increase in the length of the flat has virtually no effect on the results. Computed results are presented for flats of sufficient length without specifically listing that length. Usually  $x_M = -20$  is sufficient. Moreover, unless otherwise stated the end of the flat  $x_0$  is at  $-10$ .

Calculated results for the two vortex strengths considered are shown in Figures 5 and 6 for a very short representation of the free surface (termination on the figure) and a unit point spacing. The wave heights agree rather well

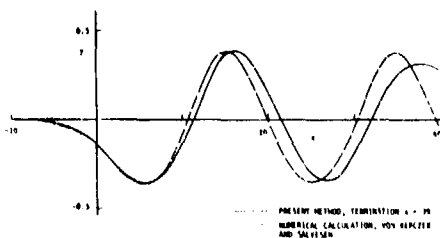


Fig. 5 Free surface shapes for  $K = +1.15$ . First-order solution.  $\Delta x = 1$ .

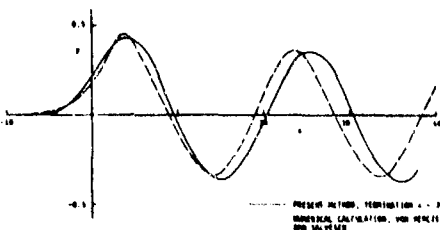


Fig. 6 Free surface shapes for  $K = -1.4$ . First-order solution.  $\Delta x = 1$ .

with those of reference 2, but the wave lengths are somewhat too long. Unfortunately, this

solution is sensitive to the magnitude of the numerical variables. Figure 7 shows free-surface shapes calculated by the present method for three values of the downstream termination point  $x_N$ . All three calculated shapes have the same wave length (which is somewhat in error) and the same locations of peaks and zeros. However, the wave height is evidently dependent on the downstream termination point.

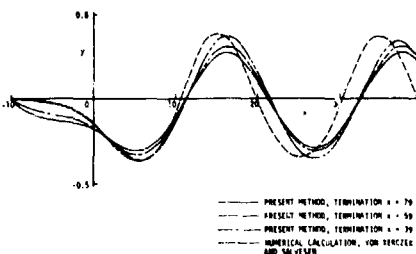


Fig. 7 Free surface shapes for  $K = +1.15$ . First-order solution.  $\Delta x = 1$ . Effect of downstream termination.

An effort to increase the accuracy of the calculated solution by reducing the point spacing to  $\Delta x = 0.5$  is shown in Figure 8. The wave height is significantly overpredicted for the case with the flat extending to  $x_0 = -10$ , and an erroneous "bump" at negative values of  $x$  is evident. Moving the flat termination to  $x_0 = -5$  removes the bump and reduces the wave height, but the wave height is still incorrect and the wave length is still in error.

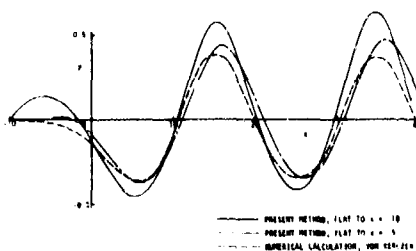


Fig. 8 Free-surface shapes for  $K = +1.15$ . First-order solution.  $\Delta x = 0.5$ . Effect of flat termination.

#### A Nonuniqueness Due to Numerical Inaccuracy

It turns out that the above-described sensitivity of the results to the numerical parameters is due to a nonuniqueness arising from insufficient numerical precision in the first-order formulation of the surface-singularity technique. This can be illustrated by a sample calculation. An original shape was selected that is flat from  $x = -30$  to  $x = -10$  and that has a wave-like shape for  $x > -10$ . It is shown as a solid curve in Figure 9. Flow about this shape in the presence of a uniform onset flow parallel to the

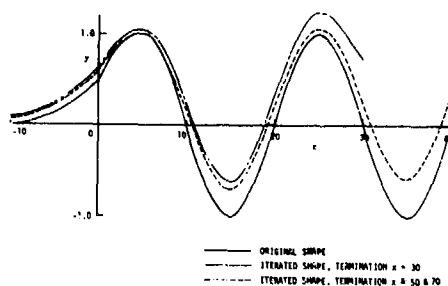


Fig. 9 Nonuniqueness study

x-axis was calculated using a surface source distribution and a point spacing  $\Delta x = 1$ . The resulting surface velocity distribution was input into a program using surface vorticity that was required to reproduce the surface velocity. If the problem had a unique solution, the resulting normal velocity distribution should be vanishingly small. Instead it was a periodic function with maximum value equal to 5% of freestream velocity. When the shape was allowed to alter itself iteratively to produce both the prescribed tangential velocity and zero normal velocity, shapes like those shown in Figure 9 were obtained for different downstream terminations. These differ from the original curve by amounts similar to those of the preceding figure. It is not a question of the finite length of the shape, because termination at  $x > 50$  give essentially the same results as that for  $x = 50$  (Figure 9).

If the above procedure is carried out with the same point spacing using the higher-order version of the surface singularity technique (references 1 and 4), the magnitude of the normal velocity that expresses the degree of nonuniqueness is reduced from 5% of freestream velocity to 0.5%. Thus, with some suitable upstream point fixed, the iterated shape would be only about a tenth as far from the original shape as the iterated shapes of Figure 9. This would be quite acceptable accuracy, and it implies that use of the higher-order version is the key to quantitative accuracy of the present method. This appears to be the case.

#### Higher-Order Procedure

When the higher-order surface singularity procedure of reference 4 is incorporated into the above-described global iteration procedure with initial flat, the result is a method that appears to be quite successful in predicting free-surface shapes. Moreover, it appears to be stable with respect to the numerical parameters. Calculated results for vortex strengths of +1.15 and -1.4 are shown in Figures 10 and 11, respectively. The agreement of the wave shapes obtained by the present method with those from reference 2, is essentially exact when due account is taken of the fact that the shapes from reference 2 have been calculated for a finite depth by a numerical procedure. The curve of the present method in Figure 10 represents three graphically indistinguishable

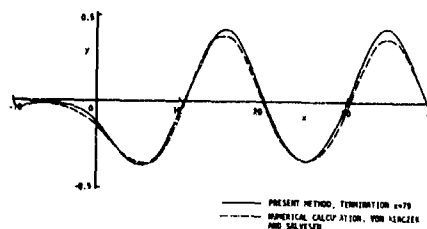


Fig. 10 Free-surface shapes for  $K = +1.15$ . Higher-order solution.  $\Delta x = 1$ .

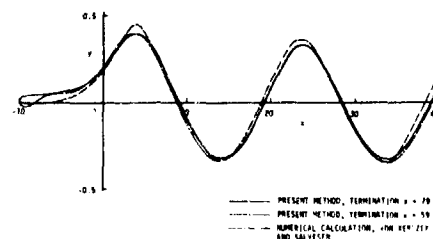


Fig. 11 Free-surface shapes for  $K = -1.4$ . Higher-order solution.  $\Delta x = 1$ .

solutions obtained for the same three locations of downstream termination that are shown in Figure 7. Figure 11 shows two barely distinguishable results obtained for two downstream terminations. Thus the higher-order iterative procedure is apparently an accurate reliable method of obtaining nonlinear free-surface shapes that had previously been obtained only by a much more time-consuming finite-difference technique. No further refinement seems to be required at least for the two vortex strengths shown, although some additional testing with different spacing  $\Delta x$  is planned. Stronger vortices having greater wave heights remain to be investigated (see below).

#### Summary of Iterative Algorithms

For the two vortex strengths considered above the results of tests of the iterative algorithms may be summarized as follows:

1. Local algorithms — always divergent.
2. Global algorithms, no flat — divergent except for  $\Delta x = 1$ .
3. Global algorithm with flat — convergent but results sensitive to numerical parameters.
4. Higher-order global algorithm with flat — always convergent. Results insensitive to numerical parameters.

#### Directions of Future Work

One modification will be made to the higher-order procedure. It can be noticed in Figures

10 and 11 that the calculated curves have erroneous bumps or bulges immediately downstream of  $x = -10$ , the end of the flat. These are due to the fact that the numerical differentiation procedures in the higher-order method are somewhat unstable at the junction of the flat and the curved portion of the free surface. A straightforward modification should remove the instability and smooth the bulges. Evidently, this flaw in the method does not have a large effect on the calculated free surface for these vortex strengths, but it might at larger strengths.

Some improvement of the iteration procedure seems desirable and quite possible. Figure 12 shows the free surface shape computed by the present method in the first iteration and in the final sixth iteration for which the normal velocity is everywhere less than 0.1% of freestream

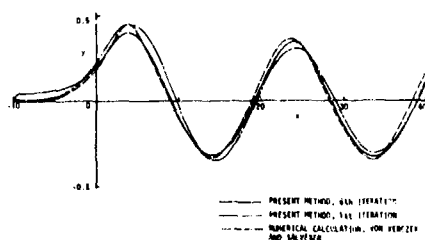


Fig. 12 Free-surface shapes for  $K = -1.4$ . Higher-order solution.  $\Delta x = 1$ . First and final iterations.

velocity. Thus, one iteration carries the solution from the  $x$ -axis (the initial guess) to the substantially correct first-iteration curve, while five more iterations are required to make the relatively small adjustment from this curve to the sixth-iteration curve. It seems likely that this performance could be improved and the number of iterations reduced.

The most important area of future effort is the calculation of free surfaces having larger wave heights. Recently data were obtained from Dr. von Kerczek that define the free-surface shapes obtained for a large number of vortex strengths as reported (but not presented) in reference 3. Cases have been successfully computed using the present method for vortex strengths of +1.7 and -2.3 for which the wave heights are approximately 50% larger than those for +1.15 and -1.4. The calculated free-surface shapes are only slightly less accurate and slightly more sensitive to downstream termination than the cases shown in Figures 10 and 11. Time did not permit inclusion of graphs of these results in the present paper. A case has been attempted for  $K = +2.7$  for which the wave heights are twice as high as the above and of the size that experimental results indicate are on the verge of breaking. This case did not converge, and it is planned to devote considerable effort to obtaining convergence in cases of large wave height.

#### References

1. Hess, J.L.: Review of Integral-Equation Techniques for Solving Potential-Flow Problems with Emphasis on the Surface-Source Method. Computer Methods in Applied Mechanics and Engineering, Vol. 5, No. 2, March 1975.
2. von Kerczek, C.H. and Salvesen, N.: Numerical Solutions of Two-Dimensional Nonlinear Wave Problems. Presented at the 10th ONP Symposium on Naval Hydrodynamics at M.I.T., June 1974.
3. Salvesen, N. and von Kerczek, C.H.: Comparison of Numerical and Perturbation Solutions of Two-Dimensional Nonlinear Water-Wave Problems. Journal of Ship Research, Vol. 20, No. 3, pp. 160-170, September 1976.
4. Hess, J.L.: Higher-Order Numerical Solution of the Integral Equation for the Two-Dimensional Neumann Problem. Computer Methods in Applied Mechanics and Engineering, Vol. 2, No. 1, February 1973.



# THE WAVE RESISTANCE FOR FLOW PROBLEMS WITH A FREE SURFACE

C. Koring and A. J. Hermans  
Delft University of Technology  
Department of Mathematics  
The Netherlands

## Abstract

A numerical procedure is presented for solving free surface flow problems. The boundary value problem in terms of Laplace's equation subject to non-linear free-surface boundary conditions is considered to be composed of two fundamental subproblems. The first problem is defined on a fluid domain with a fixed boundary and is known as the Neumann problem whereas the second problem consists of the determination of an improved position of this boundary. The solution is obtained by a process of successive iteration on both subproblems. In view of the intended extension to the three-dimensional case, the Neumann problem is solved by a procedure using finite elements in a dimension lowered by one as a result of an approximation by splines. Up to now the correction of the free surface has been developed in a two-dimensional version. The procedure was applied to the two-dimensional steady state problem of a running stream with a flat bottom. Then, somewhere upstream a disturbance of the free surface is introduced in order to calculate the effect in downstream direction. Besides this, numerical results were obtained for a running stream, upstream undisturbed, with a bump on the bottom.

## I. Introduction

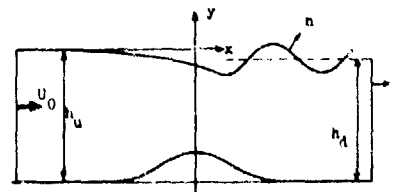
Contrary to methods using singularities\* at the boundary of the flow region, the solution of the problem of determining the wave resistance of a moving obstacle partially immersed in the fluid is based on a direct numerical method. The advantage of this approach arises when the method is extended to cover the case where the non-linear effects resulting from the dynamic free-surface boundary condition is taken into account and attempts are made to solve the three-dimensional problem. The direct approach appears from the simplicity of the procedure to solve basically the Neumann problem on the one hand, and the problem of improving the free-surface elevation on the other hand. The difficulty, however, is whether convergence can be achieved when both subproblems are solved in an iterative way. Starting to solve the Neumann problem which is formulated on a fluid domain of a known shape, it is evident that the results can be used to calculate a new free-surface elevation from the dynamic free-surface boundary condition. The kinematic free-surface

\* ref. 1, 2, 3, 4, 5

condition is again satisfied if the calculation is continued by solving the Neumann problem for the new fluid domain etc., but generally the correct solution is not obtained. This is illustrated in the example of a symmetrical bump on the bottom of a running stream. Assuming undisturbed flow upstream of the bump the above-mentioned procedure leads to a solution which reproduces an unchanged symmetry of the free surface with respect to the vertical axis through the top of the bump. In fact, a singularity is created at the free surface. As a result, no waves are found downstream of the bump. The example demonstrates that the procedure must be extended in order to satisfy the radiation condition downstream of the obstruction. This paper contains an explanation of this extension in the two-dimensional representation.

The Neumann problem is solved by a procedure which is based on an approximation with splines along one coordinate. This coordinate is eliminated by a collocation method which is combined with a transformation of the system of differential equations into a system of dominant diagonal terms. Each equation, described in a lower dimension is individually solved by a Galerkin finite element method, this operation being part of a process of successive iteration on the complete set of equations. The procedure was developed for three-dimensional flows\*\* but in view of the low computation time the method is successfully used in the two-dimensional version for the problems in consideration.

## II. Mathematical Formulation



We consider steady uniform flow past a fixed two-dimensional bump on the bottom. The undisturbed free surface upstream of the bump is at

\*\* ref. 7,8

a constant value  $h_d$  above the bottom. The flow is treated as steady and irrotational. It is assumed that the fluid is inviscid, incompressible and without surface tension. This two-dimensional steady-state potential flow problem is formulated in terms of a velocity potential  $\phi(x, y)$  which satisfies Laplace's equation

$$\nabla^2 \phi = 0 \quad (2.1)$$

everywhere in the fluid domain. The potential must also satisfy the following boundary conditions:

- 1) on the unknown free surface  $y = \eta(x)$ 
  - a) the kinematic condition is:

$$-\phi_y + \phi_x \eta_x = 0 \quad (2.2a)$$

- b) the dynamic condition

$$\frac{1}{2} \left( \phi_x^2 + \phi_y^2 \right) + g \eta = \frac{1}{2} U_0^2 \quad (2.2b)$$

where  $g$  is the acceleration of gravity and  $U_0$  is the undisturbed uniform velocity in upstream direction.

- 2) Far upstream the flow is assumed to be uniform with no waves:

$$\frac{\partial \phi}{\partial n} = -U_0 \quad (2.3)$$

- 3) Far downstream at a station where the mean value  $h_d$  of the free surface above bottom is originally unknown, the flow is also assumed to be uniform, hence

$$\frac{\partial \phi}{\partial n} = \frac{h_d}{h_d} U_0 \quad (2.4)$$

- 4) The bottom condition at depth  $y = -H(x)$

$$\frac{\partial \phi}{\partial n} = 0. \quad (2.5)$$

### III. Computation of the free-surface elevation

An important part in the solution procedure consists of a correction of the position of the free surface with respect to the fixed position of this curve during the preceding calculation. Consequently the Neumann problem being solved with a free-surface elevation  $y = \eta_0$  the dynamic free-surface condition is generally not satisfied. Since the pressure distribution, then involved at the free surface can't lead to convergence of the perturbation method, outlined below, first the value of  $\eta_0$  has to be replaced by the corrected value  $\eta_0^*$ . It is calculated from the dynamic free-surface condition after the substitution of the surface velocities following from the solution of the Neumann problem.

We consider the problem in a curvilinear system of coordinates where  $x^3$  is defined as a coordinate which follows the bottom and the

free surface  $y = \eta_0^*(x)$ . The  $x^3$  coordinate coincides with the vertical coordinate  $y$  and  $x^2$  is the coordinate perpendicular to both  $x^2$  and  $x^3$ . (Fig. 3.1).

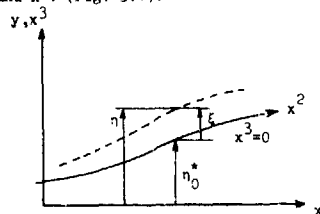


Fig. 3.1

The known free surface elevation  $y = \eta_0^*$  corresponds to  $x^3 = 0$  and the bottom  $y = -H(x)$  corresponds to  $x^3 = -1$ . Using the metric tensor quantities  $g_{ij}$ , Laplace's equation is described by the equation:

$$\frac{\partial}{\partial x^i} \left( G^{ij} \frac{\partial \phi}{\partial x^j} \right) = 0 \quad (3.1)$$

where  $G^{ij} = \sqrt{g} g^{ij}$

and

$$\tilde{g} = \det |g_{ij}|$$

(note:  $g$  is the acceleration of gravity, to be distinguished from  $\tilde{g}$ )

The dynamic free surface condition (2.2b) changes into:

$$\frac{1}{\sqrt{g}} \left[ G^{22} \left( \frac{\partial \phi}{\partial x^2} \right)^2 + 2G^{23} \frac{\partial \phi}{\partial x^2} \frac{\partial \phi}{\partial x^3} + G^{33} \left( \frac{\partial \phi}{\partial x^3} \right)^2 \right] +$$

$$g \eta = \frac{1}{2} U_0^2 \quad (3.2a)$$

Instead of  $y = \eta_0^*(x)$  we look for a new position of the free surface determined by

$$y = \eta(x) = \eta_0^*(x) + \xi(x)$$

or

$$x^3 = \tilde{\xi}(x^2)$$

The transformation to the new variable  $\tilde{\xi}$  using the relations

$$G^{22} + \frac{d\eta_0^*}{dx} + \frac{d\tilde{\xi}}{dx} = G^{22} \frac{d\tilde{\xi}}{dx}$$

$$\text{or } \frac{d\tilde{\xi}}{dx} = G^{22} \frac{d\tilde{\xi}}{dx} = \sqrt{g_{33}} \frac{d\tilde{\xi}}{dx}$$

( $\eta$  can be approximated by  $\eta = \eta_0^* + \sqrt{g_{33}} \tilde{\xi}$ )

leads to the kinematic free-surface condition

$$G_{33} \frac{\partial \phi}{\partial x^3} + G_{23} \frac{\partial \phi}{\partial x^2} = \frac{d\tilde{f}}{dx^2} (G_{22} \frac{\partial \phi}{\partial x^2} + G_{23} \frac{\partial \phi}{\partial x^3}) \quad (3.2b)$$

Now, the potential  $\phi$  is considered to be composed of a contribution of the potential  $\psi$  determined by the solution of the preceding Neumann problem and a perturbation potential  $\phi$  with the assumed property:

$$\frac{\partial \phi}{\partial x^2} \ll \frac{\partial \psi}{\partial x^2}, \quad \frac{\partial \phi}{\partial x^3} \ll 1$$

Besides this, the derivative of  $\tilde{f}$  with respect to  $x^2$  is assumed to be much smaller than 1.

The new variables  $\phi = \phi - \psi$  and  $\xi = \eta - \eta_0^*$  are substituted into the free-surface boundary conditions (3.2), which are linearized under above assumptions.

As a result, we have

$$q \frac{1}{\sqrt{g_{22}}} \frac{\partial \phi}{\partial x^2} + g \sqrt{g_{33}} \tilde{f} = \frac{1}{2} (U_0^2 - q^2) - g \eta_0^* \quad (3.3a)$$

and

$$G_{33} \frac{\partial \phi}{\partial x^3} + G_{23} \frac{\partial \phi}{\partial x^2} = \frac{d\tilde{f}}{dx^2} + \frac{1}{\sqrt{g_{33}}} q \quad (3.3b)$$

$$\text{where } q = \left. \frac{1}{\sqrt{g_{22}}} \frac{\partial \psi}{\partial x^2} \right|_{x^3=0}$$

The potential  $\phi$  in Laplace's equation (3.1) can be replaced by the perturbation potential  $\phi$ . In order to produce an equation which can be treated by the method of separation of the variables the quantity  $x$  is introduced according to the relations:

$$\frac{\partial x}{\partial x^2} = G_{22} \frac{\partial \phi}{\partial x^2} + G_{23} \frac{\partial \phi}{\partial x^3}$$

and

$$\theta(x^2) \frac{\partial x}{\partial x^3} = G_{32} \frac{\partial \phi}{\partial x^2} + G_{33} \frac{\partial \phi}{\partial x^3}$$

This transformation turns out to be an approximation because the necessary condition

$$\frac{\partial}{\partial x^2} \left( \frac{\partial \phi}{\partial x^3} \right) = \frac{\partial}{\partial x^3} \left( \frac{\partial \phi}{\partial x^2} \right) \quad (3.4)$$

can partially be fulfilled f.i. for one position  $x^3 = \text{constant}$  or for an averaged value about  $x^3$ . The best results can be expected if condition (3.4) is prescribed at the free surface  $x^3 = 0$ . From this a relation for  $\theta(x^2)$  can be derived.

Before doing this, the partial differential equation (3.1) expressed in the form

$$\frac{\partial^2 x}{(\partial x^2)^2} + \theta(x^2) \frac{\partial^2 x}{(\partial x^3)^2} = 0$$

is solved by the method of separation of the variables:

Then, we substitute the series

$$x(x^2, x^3) = \sum_i f_i(x^2) h_i(x^3) \quad (3.5)$$

and we arrive at the ordinary differential equations

$$\frac{d^2 f_i}{(dx^2)^2} + \alpha_i^2 \theta(x^2) f_i = 0$$

and

$$\frac{d^2 h_i}{(dx^3)^2} - \alpha_i^2 h_i = 0$$

If the fluid domain is divided into intervals of small  $\Delta x^2$  the solution of above equations in each interval can be represented in the form:

$$f_i = A_i \cos \alpha_i \beta x^2 + B_i \sin \alpha_i \beta x^2 \quad (3.6)$$

$$\text{and } h_i = \frac{\cosh \alpha_i (x^3 + 1)}{\cosh \alpha_i} \quad (3.7)$$

where  $\beta^2$  is equal to the mean value of  $\theta$  in an interval  $\Delta x^2$ .

Furthermore, the boundary condition at the bottom  $x^3 = -1$ :

$$\frac{\partial \phi}{\partial x} = 0 \quad \text{or} \quad \frac{\partial x}{\partial x^3} = 0 \quad \text{is satisfied.}$$

Now, we approximate the function  $\tilde{f}(x^2)$  by the expression

$$\tilde{f} = a_0 + a_1 \cos \alpha_1 \beta x^2 + b_1 \sin \alpha_1 \beta x^2 \quad (3.8)$$

which is also valid in a small interval  $\Delta x^2$ . The constant  $a_0$  is added to the expression in order to eliminate the imaginary parts of the roots  $\alpha_i$ . These roots need not to be considered because their exponential contribution to the free surface elevation corresponds to nearly a constant in a small interval  $\Delta x^2$ . The substitution of the expressions (3.5), (3.6), (3.7) and (3.8) into the free surface conditions (3.3) leads to equations containing terms of three interdependent types. These terms are the constants (the metric tensor quantities, the velocity  $q$  etc. are averaged in an interval), the cosine and sine terms. Comparing the coefficients of similar independent terms we obtain:

$$1) \quad g \sqrt{g_{33}} a_0 = \frac{1}{2} (U_0^2 - q^2) - g \eta_0^* \quad (3.9)$$

where  $q_c$  is a corrected value for  $q$  in relation to the change in the mean level of the free surface.

2) a local dispersion relation for  $\alpha_i$ :

$$\frac{\beta \sqrt{g_{33}}}{q^2} = \frac{\alpha_i}{\tanh \alpha_i} \quad (3.10)$$

If  $\frac{\beta \sqrt{g_{33}}}{q^2} > 1$  we find one real root from this

relation.

The value of  $\beta$  being known, the solution can be found in this step of the iteration process. Starting upstream at  $x^2 = 0$  where  $\xi$  and  $\frac{d\xi}{dx^2}$  are known the value of  $\xi$  can be computed

in the first interval by means of the expression (3.9). This expression gives  $a_0$ , while the initial conditions give  $a_1$  and  $b_1$ . Then, the values of  $\xi$  and  $\frac{d\xi}{dx^2}$  are calculated

at the end of the interval. They are the initial values for the next interval and the calculation of  $\xi$  can be started again. This process is sequentially repeated until the end of the region is reached.

As mentioned earlier, the value of  $\beta$  in an interval is calculated from expression (3.4). Substitution of the approximated solution (3.5) combined with (3.6) and (3.7) produces the relation:

$$(Pb_i + Qa_i) \cos \alpha_i \beta x^2 = (Pa_i - Qb_i) \sin \alpha_i \beta x^2$$

where

$$P = \tanh \alpha_i \left( \beta \frac{\partial G^{23}}{\partial x^2} + \frac{1}{\beta} \frac{\partial}{\partial x^2} (G^{22} \beta^2) \right) + 2 \alpha_i \beta G^{23}$$

and

$$Q = \frac{\partial G^{23}}{\partial x^2} + \frac{\partial G^{33}}{\partial x^2} + \alpha_i \tanh \alpha_i (G^{33} - \beta^2 G^{22})$$

The value of  $\beta$  is calculated from the requirement that the form  $P^2 + Q^2$  has a minimum. In the case when  $G^{23} = 0$  and  $G^{11} = \text{constant}$  which occurs at the first step -  $P$  and  $Q$  can be simplified to:

$$P = 2 \tanh \alpha_i \frac{d\beta}{dx^2} G^{22}$$

$$Q = \alpha_i \tanh \alpha_i (G^{33} - \beta^2 G^{22})$$

and the minimum is arrived at

$$\beta = \sqrt{\frac{G^{33}}{G^{22}}} \quad (3.11)$$

For demonstration, the example is chosen of a uniform flow of velocity  $U_0$  along a flat bottom, being at distance  $H$  below the free surface.

The dispersion relation (3.10) is reduced to:

$$U_0^2 \alpha - g \tanh \alpha H = 0$$

If  $\frac{gH}{U_0^2} > 1$  one real root  $\alpha$  is of significance

in the solution for  $\xi$ . So, starting upstream where f.i. a free-surface elevation occurs of the form:

$$\xi(0) = c, \quad \frac{d\xi}{dx^2} \Big|_0 = 0$$

we find the solution for  $\xi$  ( $= a_0 + a_1 \cos \alpha x + a_2 \sin \alpha x$ ) in the first approximation. From (3.9) follows  $a_0 = 0$  and the initial conditions give:

$$a_0 + a_1 = c \quad \text{and} \quad a_2 = 0.$$

As a result, we get

$$\xi = c \cos \alpha x \quad (3.12)$$

Continuing the process we find that above result represents the solution in the first order approximation for the complete free surface. Subsequently, the Neuman problem is solved for the new fluid domain bounded by a free surface  $\eta_0$  which is equal to above value  $\xi$ . With respect to the velocity field obtained this value is replaced by a value  $\eta^*$  in agreement with the dynamical free surface condition. The procedure for correcting the free surface can be started again and this process is repeated until the free surface elevation does not change in a complete loop of the iteration.

The difference between  $\eta_0$  and  $\eta_0^*$  at the end of the calculation indicates the error as a result of the numerical approximation.

If above procedure is applied to the example of the symmetrical bump the symmetry of the problem disappears and waves come into existence downstream of the bump. The smoothing effect of the method on the course of the free surface suppresses the singularity which arises if the wave making part of the procedure is omitted. Naturally, the character of the solution is completely different if no roots  $\alpha_i \neq 0$  are found from relation (3.10). In the example of the flat bottom this is the case when

$\frac{gH}{U_0^2} < 1$ . The solution of the problem is then

obtained if the expression (3.8) is replaced by a polynomial approximation of the second degree in  $x^2$ :

$$\xi = a_0 + a_1 x^2 + a_2 (x^2)^2 \dots \quad (3.13)$$

One constant is determined from the dynamic free surface condition and similarly to above procedure the other two constants follow from the initial conditions in the considered interval.

#### IV. The solution procedure concerning the Neumann problem

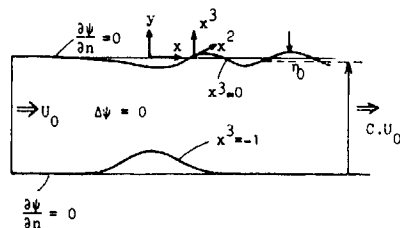


Fig. 4.1

A part of the procedure is represented by the solution of a Neumann problem in terms of Laplace's equation subject to boundary conditions of given normal derivatives (Fig. 4.1). Because of the two-dimensional character of the problem the solution can be obtained by a direct numerical method of integration. Since the solution of this problem is a part of an iteration process in order to solve the complete problem, the computer time required will be reduced as much as possible. This is achieved by adopting the following approach.

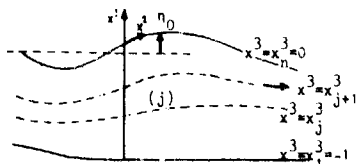


Fig. 4.2

A regular set of curves of constant  $x^3$ , the same system of coordinates is used as in chapter 3, is located in the domain between the bottom and the free surface.

On these curves  $x^3 = x^3_j$  ( $j = 1(1)n$ ) (Fig. 4.2)

the functions  $\psi_p^j(x^2)$  ( $p=0,1$ ) are defined

representing the potential ( $p=0$ ) and its derivative with respect to  $x^3$  ( $p=1$ ).

The potential  $\psi$  at an arbitrary point in a subdomain ( $j$ ) lying between the curves  $x^3 = x^3_j$  and  $x^3 = x^3_{j+1}$  is assumed to be a polynomial

in  $x^3$  with coefficients containing the defined quantities  $\psi_p^j$  at their boundaries. It is expressed by

$$\psi^{(j)}(x^2, x^3) = \sum_{k=0}^1 [l_k^{(j)}(x^3) \psi_0^{j+k}(x^2) + m_k^{(j)}(x^3) \psi_1^{j+k}(x^2)] \quad (4.1)$$

The coefficients of the interpolation polynomials  $l_k$  and  $m_k$  are calculated from the condition that the approximated potential and its derivative with respect to  $x^3$  correspond exactly to the quantities  $\psi_p^j$  at the boundaries

$x^3 = x^3_j$  and  $x^3 = x^3_{j+1}$ , resulting in polynomials of the third degree.

The approximation (4.1) is used to produce a set of ordinary differential equations, following from the requirement that Laplace's equation is only satisfied on the curves  $x^3 = x^3_j$ . Arranging this system, the result of the collocation method is represented in a set of  $n$  ordinary differential equations of the form:

$$\frac{G_{(i)}^{33}}{c} \left( \frac{3}{\delta} A_{ij} \psi_0^j + B_{ij} \psi_1^j \right) + \frac{d}{dx^2} \left( G_{(i)}^{22} \frac{d}{dx^2} \psi_0^i \right) + C_i = 0 \quad (4.2)$$

where  $\delta = x^3_{j+1} - x^3_j$   $i, j = 1(1)n$

$$A_{ij} = \begin{pmatrix} -1 & 1 \\ 1 & -2 \\ 1 & -1 \end{pmatrix}, B_{ij} = \begin{pmatrix} -2 & -1 \\ 1 & 0 \\ 1 & -2 \end{pmatrix}$$

combined with  $n-2$  relations, actually resulting from the requirement of the continuity of the second derivative with respect to  $x^3$  at the intercurves  $x^3 = x^3_j$  ( $j=2(1)n-1$ ).

Next, the complete set of equations in the  $2n$  unknowns  $\psi_p^j$  is obtained if the boundary

condition at the bottom and the free surface are added to the system.

Considering the system of equations (4.2) it can be noted that the interdependency of the various equations is produced by the first two terms. The eigen functions being determined the system of equations can be transformed into a system containing dominant terms with respect to one dependent variable in each of the equations. Each equation can then be solved individually by means of a Galerkin element method, this operation being part of a process of successive iteration. It turns out to be a quicker procedure of solution, in comparison to a two dimensional finite element method.

#### V. Numerical results

In this paper some results of calculations are presented for two different examples. First, the numerical method was checked in the case of a running stream about a flat bottom. A local disturbance at the free surface represented by some deviation with respect to an originally undisturbed level, is introduced to study its effect in downstream direction. The results are shown in Fig. 5.1 indicating the difference between the simple harmonic solution A (3.12) in the first order approximation and the non-linear solution B after three complete loops of the iteration (Fig. 5.1).

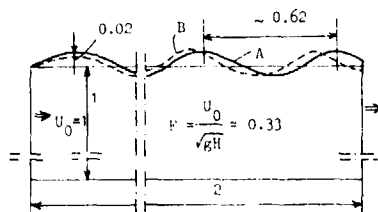


Fig. 5.1

The method turns out to be stable producing results characterised by an unchangeable difference between the free surface elevation  $\eta_0$  and its corrected value  $\eta_0^*$  during the last loop of the iteration. The accuracy of the results expressed by the above mentioned difference is still not sufficient to evaluate the results on its quantitative aspects. Then, the number of subdomains  $n-1$  in the solution of the Neumann problem has to be increased. The computations performed with  $n=3$  involve too large errors, which can be reduced as soon as the computer program is extended to cover the case of a variable  $n$ .

The calculations were carried out on an IBM 360/65. The computation time required amounted to 12 seconds. The number of intervals in  $x^2$  or  $x$  direction was 50 and the Neumann problem was solved for  $n=3$  using 50 elements on one curve  $x^2$  is constant.

A special procedure has been incorporated to take account of the shift the wave undergoes during one loop of the iteration. Effectively the free surface in an interval is iteratively determined from data belonging to a comparable position in the period of the preceding wave. Since uniform flow is imposed at the vertical boundaries of the fluid domain the wave is somewhat deformed in the neighbourhood of the boundaries. Since the example serves for a qualitative analysis of the method no attempts were made to eliminate these effects. The middle of the fluid region provides good results indicated by the conformity with a Stokes wave pattern.

The method is also applied to the problem of a running stream which is assumed to be undisturbed upstream of a smooth bump on the bottom. The results are illustrated for subcritical flow in Fig. 5.2 and for supercritical flow in Fig. 5.3. The latter agree with analytical results as far as the position of the free surface at the end location downstream is concerned. A small shrinkage of the mean level is observed in the case of the subcritical flow. The calculations were done for 35 intervals, and 4 loops were necessary to find the solution. Doubling of the number of intervals did not affect the results, but the same remarks as for above example can be made in relation to the accuracy.

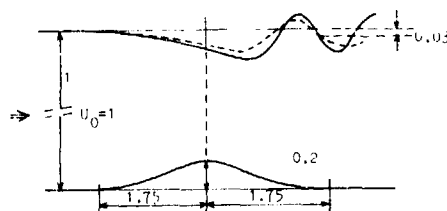


Fig. 5.2

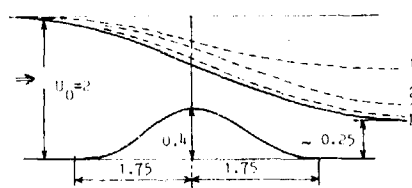


Fig. 5.3

#### VI. Conclusions

A stable method was developed for predicting the wave pattern downstream of an obstruction in a running stream. In this respect the calculations were only performed for an obstruction at the bottom, but the method presented lays the foundation of the solution for the problem to find the wave resistance for obstructions located at the free surface.

The most important contribution to the solution is produced by the addition of the second correction of the free surface elevation to the iteration process. The first correction intended to satisfy the dynamic free surface condition is not accurate enough to prevent the penetration of singularities in the solution. It is demonstrated for the example of a running stream with a symmetrical bump on the bottom where a singularity is created in this way and no waves are found in downstream direction. On the contrary, the second correction generates a curve, the function value and its derivatives being continuous up to and including order two, which is sufficient to preserve the accuracy of this approximation during the iteration. The stability of the method, however, is guaranteed if the first correction precedes the second one. The method was applied to some examples mainly intended to investigate the qualitative aspects. It may be concluded that the calculations produce reliable results being of interest to compare with experimental results. To this purpose the accuracy has to be increased especially as far as the solution of the Neumann problem is concerned. Therefore, the computer program must be adjusted to operate with a variable number of subdomains. In addition the objective in future is to check the method

on the problem of a cylinder partially immersed in the fluid. It should be emphasized that the considerations are presented in order to extend to the three-dimensional case.

#### References

1. A.S. Peters New Treatment of the Ship Wave Problem. Communications on Pure and Applied Mathematics, vol 2, p 123
2. E.O. Tuck On line Distributions of Kelvin Sources. Journal of Ship Research, vol 8,, no. 2, pp. 45-52 (1964).
3. E.O. Tuck Shallow-water flows past slender bodies. J. Fluid Mech. (1966) vol 26, part 1, pp 81-95.
4. Bruce H. Adee Calculation of the Streamlines About a Ship Assuming a Linearized Free-Surface Boundary Condition. Journal of Ship Research, Vol 17, No3, '73, pp 140-146.
5. E.O. Tuck A Systematic Asymptotic Expansion Procedure for Slender Ships. Journal of Ship Research, vol 8, no. 1, 15-23 (1964).
6. Nils Salvesen and C. von Kerczek Comparison of numerical and perturbation solutions of two-dimensional nonlinear Water-Wave problems. Journal of Ship Research, vol. 20 (1976), 160-170.
7. C. Korving, A Three-Dimensional Method for the calculation of Flow in Turbomachines Using Finite Elements on a Blade-to-Blade Surface of Revolution. PhD thesis, Delft, 1974.
8. C. Korving, A Method of Calculation for the Three-Dimensional Fluid Flow in Turbomachines. Proceedings of the Fourth International Conference on Numerical Methods in Fluid Dynamics, (35), 1974, p. 443.
9. K.J. Bai, A Localized Finite-Element Method for Steady, Two-Dimensional Free-Surface Flow Problems, First Int. Conf. on Num. Ship Hydr. 1975.

# NONLINEAR FREE-SURFACE EFFECTS— THE DEPENDENCE ON FROUDE NUMBER

C. von Kerczek and Nils Salvesen  
David W. Taylor Naval Ship Research and Development Center  
Bethesda, Maryland 20884

## ABSTRACT

Numerical solutions of the nonlinear problem of two-dimensional finite-depth potential flow past a fixed pressure distribution on a free surface are given. The numerical method approximates the exact problem by finite differences. The numerical solutions presented here are for a range of values of the Froude number based on the length characterizing the free-surface pressure distribution. The numerical solutions are compared as far as possible with first-, second-, and third-order perturbation-theory solutions and it is found that the second-order perturbation theory can give accurate solutions of this problem for the range of Froude numbers investigated. The details of the free-surface deformation caused by the surface-pressure distribution are presented in graphs. These graphs illustrate the effects of the nonlinearities of the problem on the description of the wave-making action of the surface-pressure distribution.

## NOMENCLATURE

- $C = R\rho g/2p^2$ , wave-resistance coefficient  
 $C_L$ , linear-theory finite-depth wave-resistance coefficient  
 $C_{L\infty}$ , linear-theory infinite-depth wave-resistance coefficient  
 $C_p = 100p/\rho gL$ , pressure coefficient  
 $D$ , water depth  
 $F = U/\sqrt{gL}$ , Froude number  
 $l$ , effective length of pressure distribution defined in Equation (7) and Figure 1  
 $R$ , dimensional wave resistance per unit width  
 $U$ , velocity of pressure disturbance or uniform stream velocity far upstream  
 $g$ , gravitational acceleration  
 $h$ , mesh size  
 $\ell_1, \ell_2$ , lengths defined in Figure 1 and in Equation (7)  
 $p$ , maximum value of pressure distribution  $p_0(x)$   
 $p_0(x)$ , free-surface pressure distribution defined in Equation (7) and in Figure 1  
 $\eta$ , free-surface elevation  
 $\lambda$ , wave length  
 $\lambda_{L\infty}$ , linear-theory infinite-depth wave length  
 $\rho$ , mass density of water  
 $\psi$ , stream function

## Introduction

In this paper we present numerical solutions of the nonlinear problem of two-dimensional finite-depth potential

flow past a fixed pressure distribution on a free surface. The numerical method that we use has been described in Reference [1]. We have used the method previously to investigate the nonlinear free-surface effects of a submerged vortex at a fixed Froude number [2], a submerged cylinder [3], and the subcritical shallow-water flow past an obstruction [4]. We have found in the studies [2-4] that certain nonlinear features of the flow field which can be calculated accurately using perturbation methods are also predicted accurately by our numerical method. For example, in numerous experiments our method (see especially [4]) has accurately predicted the influence of the free-surface nonlinearities on the wave length of free waves. Furthermore, in finite-depth water, there is a lowering of the mean level of the free surface in the downstream wave field behind an obstacle (see [5]). This nonlinear effect depends only on the wave resistance of the obstacle. It has been found in [4] that this characteristic lowering of the mean level of the free surface is predicted well by our numerical method. It is for these and similar reasons that we have come to believe that for a certain range of parameters, our numerical method predicts the wave resistance and free-surface elevations in the vicinity of a body that appear to be accurate to within at least 2 or 3 percent of the exact solutions. Accordingly, the numerical method should be used to obtain as much information as possible about how waves are generated by obstacles in a two-dimensional stream and the effectiveness of perturbation techniques in solving such problems. It is hoped that such information can yield important clues on how to handle the more important and difficult three-dimensional ship-wave problem, although the two-dimensional problem discussed in this paper may also be of some practical importance.

There are two main Froude numbers associated with the two-dimensional wave-resistance problem. One of these Froude numbers is based on the depth  $D$  of the stream and is defined as  $U/\sqrt{gD}$  where  $U$  is the speed of the incoming stream far upstream of the wave-generating obstacle and  $g$  is the acceleration of gravity. The effects on the flow field of the variation of this depth-Froude number which were examined in Reference [4], are not of primary interest in this paper, though they do play an important role here. Our primary interest now is to examine the nonlinear free-surface effects as the length-Froude number  $F = U/\sqrt{gL}$  is varied. The length  $l$  is the characteristic length of the wave-generating obstacle. We are interested in using our results for the two-dimensional wave-resistance problem to speculate about the ship-wave problem. It seemed to us that the two-dimensional obstacle that is closest in some sense to a ship is the free-surface pressure distribution with characteristic length  $l$  and pressure amplitude  $p$ . Furthermore, the wave-making effects of planing hulls and air-cushion vehicles can be modeled by a free-surface pressure distribution. The solution of the two-dimensional free-surface pressure distribution problem may result in a fairly accurate description of the local free surface disturbance between the very thin



and deeply submerged side walls of a low aspect-ratio air-cushion vehicle.

We present in this paper numerical solutions obtained for pressure distributions of the form shown in Figure 1. The numerical solutions were obtained for a range of values of length-Froude number  $F$  and pressure coefficient  $C_p = 100\rho \mu g L$  where  $\rho$  is the density of the water. In particular, we examine the variation of the wave-resistance coefficient,  $C = R\rho g 2p^2$  where  $R$  is the dimensional wave resistance, as a function of  $F$ . We have also computed  $C$  by first-, second-, and third-order perturbation theory for infinite-depth water (denoted by  $C_{1,\infty}$ ,  $C_{2,\infty}$ , and  $C_{3,\infty}$  respectively) and we compare these results as far as possible with the values of  $C$  obtained by the direct numerical solution of the finite-depth nonlinear potential-flow problem. Graphs of the free-surface elevations at various values of Froude number  $F$  and pressure coefficient  $C_p$  are presented to show how the nonlinearities of the problem affect the wave-making action of the pressure distribution.

#### Formulation of the Problem

We describe the motion in a coordinate system fixed with respect to a uniformly translating pressure distribution. In this coordinate system labeled  $(x, y)$  and shown in Figure 2, the pressure distribution is stationary, and the fluid far upstream, as  $x \rightarrow \infty$ , is moving with constant velocity  $\vec{V} = U\vec{i}$ , where  $\vec{i}$  and  $\vec{j}$  are unit vectors tangent to the  $x$  and  $y$  coordinates respectively. The origin of the coordinate system is in the undisturbed free surface and the bottom of the stream is at  $y = -D$ . Gravity acts downward and is given by  $-g\vec{j}$ .

We formulate this problem as an incompressible potential flow in terms of the stream function  $\psi(x, y)$  from which the velocity  $\vec{V} = u\vec{i} + v\vec{j}$  is obtained by

$$\vec{V} = \vec{k} \times \nabla \psi \quad (1)$$

where  $\vec{k} = \vec{i} \times \vec{j}$  and  $\nabla = \vec{i} \frac{\partial}{\partial x} + \vec{j} \frac{\partial}{\partial y}$ . Then  $\psi(x, y)$  satisfies the Laplace equation in the water domain

$$\nabla^2 \psi = 0 \quad (2)$$

and the following boundary conditions: on the free surface,  $y = \eta(x)$ , the dynamic condition is

$$\rho \frac{1}{2} \vec{V} \cdot \vec{V} + \rho g \eta + p_0(x) = 0 \quad (3)$$

and the kinematic condition is

$$\psi = 0 \quad \text{on } y = \eta. \quad (4)$$

On the bottom

$$\psi = -UD. \quad (5)$$

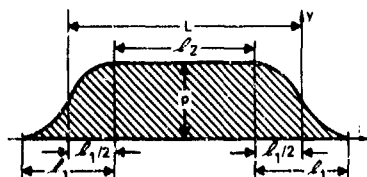


Figure 1 - Free-Surface Pressure Distribution,  $p_0(x)$

Far upstream the flow is uniform,

$$\lim_{x \rightarrow \infty} \psi = Uy. \quad (6)$$

and the free surface is horizontal,  $\eta(x) = 0$ . Far downstream we expect waves having an unknown wave length  $\lambda$ .

The surface pressure distribution  $p_0(x)$  is given by (see Figure 1)

$$p_0(x) = \begin{cases} \frac{1}{2} \rho \left[ 1 - \sin \left( \frac{\pi x}{L} \right) \right] \cdot x e^{-\left[ \frac{x_1}{2}, \frac{x_2}{2} \right]} \\ \rho \cdot x e^{-\left[ \frac{x_1}{2}, \frac{x_2}{2} \right]} \\ \frac{1}{2} \rho \left[ 1 - \sin \left( \frac{\pi}{L} (x + \frac{L}{2}) \right) \right] \cdot x e^{-\left[ \frac{x_1}{2}, \frac{x_2}{2} \right]} \\ 0 \text{ elsewhere} \end{cases} \quad (7)$$

and the characteristic length  $L$  is defined by

$$L = \frac{1}{C_p} + \frac{1}{C_p^2} \quad (8)$$

#### The Numerical Method

The nonlinear problem for  $\psi$  is approximated by a finite-difference representation defined on the grid which overlays the fluid domain as shown in Figure 2. The stream function is computed at the mesh nodes denoted by  $(i, j)$  where each node  $(i, j)$  corresponds to the coordinate  $(x_i, y_j)$  of the mesh nodes. The details of the numerical method are given in Reference [1]. Only the major steps in the procedure are outlined here:

(i) An initial free-surface shape  $\eta(x)$  is assumed (usually a plane free surface).

(ii) The finite-difference equations approximating the field equation (2), subject to the finite-difference approximations of the boundary conditions (4), (5), and (6), are solved by successive overrelaxation (with an overrelaxation constant of 4/3).

(iii) Starting at the free-surface node  $i = 2$ , each term in Equation (3) is computed using finite-difference approximations of  $\vec{V}$ . If (3) is satisfied,  $i$  is increased by one and each term in (3) is again computed. This continues until an  $i = i^*$  is reached where (3) is not satisfied.

(iv) The free-surface height  $\eta_{i^*+1}$  at  $i^* + 1$  is raised an amount  $\Delta \eta$ ,  $\Delta \eta = 0.01 h$ , where  $h$  is the basic grid spacing, on the first try and an amount determined by interpolation or extrapolation on subsequent tries. A new free surface is then interpolated between points  $i^* + 1$  and  $i^* + 1 + \ell$  where  $\ell$  is an integer such that  $\ell h \approx 1/2 \lambda_1$  and where  $\lambda_1$  is the linear-theory wavelength. This interpolation

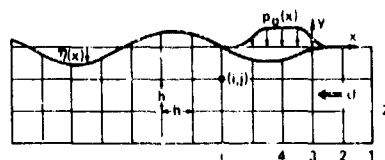


Figure 2 - Flow and Finite Difference Mesh Schematic

i established by an interpolation polynomial of fourth degree. The interpolation polynomial is determined by the height, slope, and curvature of the free surface at  $i^* + 1$  and the height and slope at  $i^* + 1 + \ell$ . The height, slope, and curvature of  $\eta$  at  $i^* + 1$  is determined approximately by finite differences using  $\eta_{i^*+1}$ ,  $\eta_{i^*}$  and  $\eta_{i^*+1}$ . Similarly, the height and slope at  $i^* + 1 + \ell$  is determined from  $\eta_{i^*+1}$  and  $\eta_{i^*+1+\ell}$ .

(iv) Step (iii) is now repeated.

(vi) Each term of Equation (3) is recomputed at  $i^*$ . If (3) is not satisfied,  $i^*$  to some specified accuracy, then the procedure returns to step (iv). If (3) is satisfied at  $i^*$  to the specified accuracy, then the procedure continues to the next step.

(vii)  $i^* + 1$  replaces  $i^*$  but is called  $i^*$  (i.e.,  $i^* + 1 \rightarrow i^*$ ). If  $i^*$  is near the end of the field ( $i^* = N - 5$ ), the problem terminates. If  $i^*$  is not near the end of the field, the procedure returns to step (vi).

The wave resistance of the surface pressure distribution is given by

$$R = - \int p_n(x) \left[ \frac{d\eta}{dx} \right] dx \quad (9)$$

The integral in (9) is over the length of the pressure distribution and is evaluated using trapezoidal quadratures. The free-surface slope ( $d\eta/dx$ ) is computed using first-order central differences.

#### Perturbation Method

It is assumed that the surface pressure distribution is a weak disturber so that the perturbations about the uniform flow are everywhere small, and that the stream function has the following expansion in terms of a perturbation parameter  $\epsilon$ :

$$\psi(x, y) = -Uy + \psi^{(1)} + \psi^{(2)} + \psi^{(3)} + \dots \quad (10)$$

where  $\psi^{(n)}$  is of  $O(\epsilon^n)$ . Furthermore, it is assumed that the free-surface elevation  $\eta(x)$  has the expansion

$$\eta(x) = \eta^{(1)} + \eta^{(2)} + \eta^{(3)} + \dots \quad (11)$$

and that the uniform-stream velocity  $U$  is an unknown of the problem with the expansion

$$U = u + u^{(1)} + u^{(2)} + \dots \quad (12)$$

where  $\eta^{(n)}$  and  $u^{(n)}$  are both of  $O(\epsilon^n)$ .

Substitution of expansions (10), (11), and (12) into the exact free-surface conditions (3) and (4) gives the free-surface conditions

$$\psi_y^{(n)} - \nu \psi^{(n)} = f^{(n)}(x) \quad \text{on } y = 0, \quad n = 1, 2, 3, \dots \quad (13)$$

where  $f^{(1)} = p_0(x)/\rho u$  and  $f^{(n)}(x)$ , with  $n = 2, 3, \dots$ , are functions of the lower-order solutions  $\psi^{(n-1)}$  and  $\eta^{(n-1)}$  (see [6], Equations 2.15 and 2.17) and where  $\nu = g/u^2$  is the wave number. For infinite depth the solutions are given by the convolution integral ([7], p. 601)

$$\psi^{(n)} = \frac{1}{\pi} \int_{-\infty}^{\infty} dk f^{(n)}(x) \text{Re} \{ i \nu \{ -x \} \}, \quad n = 1, 2, 3, \dots \quad (14)$$

where the complex function  $I(\zeta)$  is defined in terms of the exponential integral as

$$I(\zeta) = e^{-\zeta} \int_{-\zeta}^{\infty} \frac{e^{-u}}{u} du \quad (15)$$

The first- and higher-order free-surface elevations are

$$\eta^{(1)} = \frac{1}{u} \psi^{(1)}(x, 0) \quad (17)$$

and

$$\eta^{(n)} = \frac{1}{u} \psi^{(n)}(x, 0) + g^{(n)}(x), \quad n = 2, 3, \dots \quad (18)$$

where  $g^{(n)}(x)$  are functions of the lower-order solutions (see [6], Equations 2.19 and 2.20).

The solutions (14) are bounded only if each function  $f^{(n)}(x)$  is nonoscillatory for large negative values of  $x$ . This requires that the perturbations of the unknown uniform-stream velocity are given by

$$u^{(1)} = 0 \quad (19)$$

and

$$u^{(2)} = \frac{1}{2} \nu^2 \alpha^2 u \quad (20)$$

where  $\alpha$  is the first-order far-downstream wave amplitude. This implies that the wave length, according to the third-order theory, is

$$\lambda_3 = \frac{2\pi}{\nu} = \frac{2\pi}{g} U^2 (1 - \nu^2 \alpha^2) \quad (21)$$

The wave length given by both the linear and second-order theory is  $\lambda_1 = \lambda_2 = (2\pi/g) U^2$ .

The linearized and two higher-order wave resistances for the pressure distribution have been obtained by numerical integration of

$$R_n = - \int p_n(x) \left[ \frac{d\eta_n}{dx} \right] dx, \quad n = 1, 2, \text{ and } 3. \quad (22)$$

A serious deficiency of the comparisons between the numerical and the second- and third-order perturbation-theory results that we will make is that the former is for finite-depth  $D$  and the latter is for infinite depth. Unfortunately, the numerical method is restricted to streams which are insufficiently deep that the bottom effects are completely negligible. Also, we did not have the capability to calculate finite-depth second- and third-order perturbation theory solutions. Such theories remain to be developed and would be of considerable intrinsic interest, but see for instance [4] for a start on this problem. However, it is an elementary matter to compute the finite-depth linear-theory wave-resistance coefficient  $C_1$  using the formula<sup>1)</sup>

$$C_1 = \frac{k_0^2 (a^2 + b^2)}{2p^2 (1 - \nu D \text{sech}^2 k_0 D)} \quad (23)$$

where

<sup>1)</sup>Subscripts are used to indicate that a quantity is correct within the order of the perturbation theory as given by the index.

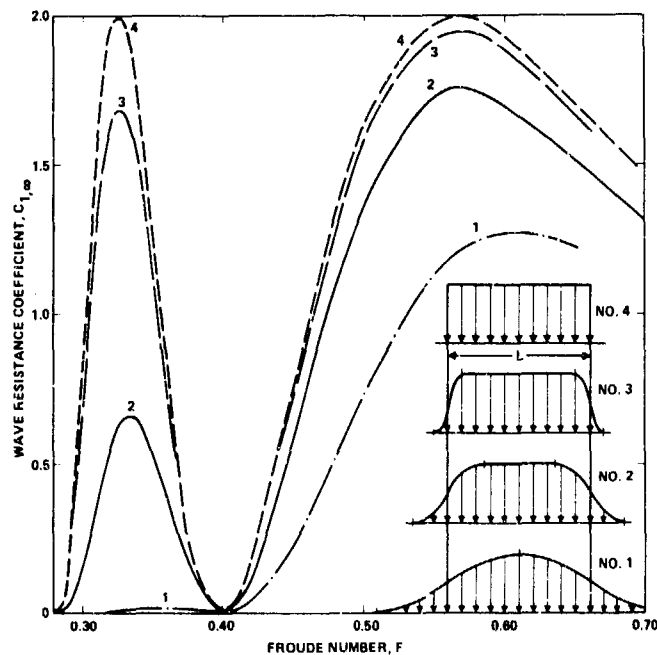


Figure 3 - Infinite-Depth Linear-Theory Wave-Resistance Coefficient versus Froude Number, for Various Pressure Distributions

$$a = \int_{-\infty}^{\infty} p_0(x) \cos k_0 x \, dx$$

$$b = \int_{-\infty}^{\infty} p_0(x) \sin k_0 x \, dx$$

and  $k_0$  is the real positive root of the equation

$$k_0 - \nu \tanh k_0 D = 0.$$

#### Results and Discussion

We first examine the linear-theory wave resistance of free-surface pressure distributions of the form given by (7) and shown in Figure 1. Figure 3 shows the infinite-depth linear-theory wave-resistance coefficient  $C_{1,\infty}$  versus Froude number  $F$  for the four pressure distributions shown (Nos. 1 through 4). The pressure distributions 1-4 all have characteristic length  $L$  and correspond to ratios of  $\ell_1/\ell_2 = \infty$ , 1, 1/4, and 0, respectively; ( $\ell_1$  and  $\ell_2$  are defined in Equation (7) and in Figure 1). We note that the  $C_{1,\infty}$  versus  $F$  graphs exhibit peaks and troughs (there are an infinite number of each converging at  $F = 0$ , but only the two outermost peaks are shown) at values of Froude number  $F$  which correspond to cases in which the resulting linear-theory wavelength  $\lambda_{1,\infty}$  is approximately a certain multiple of  $L$ . We recall that  $\lambda_{1,\infty} = 2\pi U^2/g$  so that  $\lambda_{1,\infty}/L = 2\pi F^2$ . The troughs at which  $F \approx 0.28$  and  $0.40$  correspond to  $L/\lambda_{1,\infty} \approx 2.0$  and  $1.0$ , respectively. The peaks at which  $F \approx 0.3$  and  $0.57$  correspond to  $L/\lambda_{1,\infty} \approx 3/2$  and  $1/2$ , respectively. It will be seen that the linear wave-resistance

theory given by formula (23) describes the main features of the wave-making action of the pressure distribution defined by (7). The main feature of the wave-making is the generation of "bow" and "stern" waves by the front and rear portions of the pressure distribution and the cancellation or reinforcement of these waves depending on the phasing between them. The objective here is to investigate in what ways the nonlinearity of this problem modifies the linear-theory description of the wave-making action of the pressure distribution.

In the modelling of air-cushion vehicles<sup>(8)</sup> it is necessary to use a pressure distribution with a fairly steep variation at its ends, such as distribution number 3 in Figure 3. One can infer this fact from the wave-resistance curves for air-cushion vehicles given in Reference [8] (pp. 3-50). The wave-resistance curves given in Reference [8] exhibit two nearly equally large peaks at roughly the same values of the Froude number  $F$  as the two peaks shown in Figure 3. However, for all of the results given in this paper (other than Figure 3), pressure distribution No. 2 has been used because pressure distributions Nos. 3 and 4 cannot be resolved accurately with the finite-difference mesh sizes used in the numerical method. We are mainly interested in qualitative effects of the nonlinearities so that this choice seems adequate for this purpose.

Figure 4 shows the graph of the linear-theory wave-resistance coefficient  $C_1$  versus the Froude number  $F$  (and the wave length depth ratio,  $\lambda_{1,\infty}/D$ ) for pressure distribution No. 2 and for finite depth  $D$ . In this graph, the depth of the water is constant and equal to one-half the pressure distribution length  $L$ . The points in Figure 4 are the

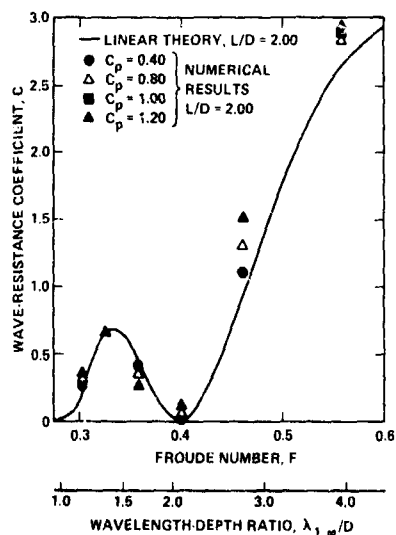


Figure 4 - Wave-Resistance Coefficient versus Froude Number for Various Values of Pressure Coefficient  $C_p$ . Compared to Finite-Depth Linear Theory

numerical predictions of the wave-resistance coefficient  $C$  at various values of the pressure coefficient  $C_p$ . We note from the  $\lambda_{1,\infty}/D$  abscissa that for fixed values of  $L$  and  $D$ , increasing the Froude number  $F$  results in an increase in the wavelength-depth ratio,  $\lambda_{1,\infty}/D$ . Thus at the higher speeds ( $F > 0.40$ ), the wavelength-depth ratio becomes large ( $\lambda_{1,\infty}/D > 2.0$ ) so that the higher-speed cases correspond to shallow water with respect to the wavelength.

We find in Figure 4 that the nonlinear effects are substantial at most of the Froude numbers. The exception is in the areas near the peaks of the linear-theory resistance-coefficient curve. Before discussing these results further, consider the similar graphs of wave-resistance coefficient shown in Figure 5. The numerical results in Figure 5 correspond to a fixed value of the ratio  $\lambda_{1,\infty}/D \approx 2.0$ . Thus, as the Froude number  $F$  increases, the length-depth ratio  $L/D$  decreases, as indicated by the second abscissa in Figure 5. In other words, the water gets shallower relative to the characteristic length  $L$  of the pressure distribution as the Froude number decreases. The physical situation is that of an air-cushion vehicle, say, running into increasingly shallow water and decreasing its speed in such a way that the ratio  $\lambda_{1,\infty}/D$  remains constant.

What is notable in comparing Figures 4 and 5 is their qualitative similarity. An interesting finding is that for the range of  $F$  over which the linear-theory  $C_1$  curve has positive slope, the nonlinear free-surface effects result in increasing values of wave-resistance coefficient  $C$  with increases in the pressure coefficient  $C_p$ . Exactly the opposite effect occurs for the ranges of  $F$  over which the linear-theory  $C_1$  curve has negative slope. This effect of the nonlinearities indicates that the graph of  $C$  versus  $F$  has essentially the same form as the graph of  $C_1$  versus  $F$  but it is shifted to lower values of  $F$  for increasing values of the pressure coefficient  $C_p$ .

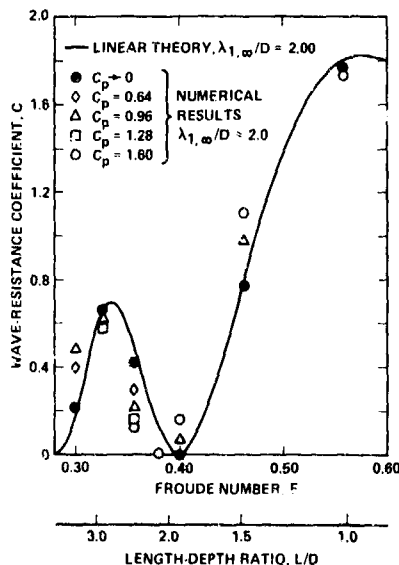


Figure 5 - Wave-Resistance Coefficient versus Froude Number for Various Values of Pressure Coefficient  $C_p$ . Compared to Finite-Depth Linear Theory

It is of essential practical interest to know if higher-order perturbation theory for the two-dimensional wave-resistance problem accurately predicts the nonlinear variations of  $C$  with  $C_p$ , as shown in Figures 4 and 5. The results presented in Figure 6 give some indication that second- and third-order perturbation theory may predict the wave resistance coefficient  $C$  fairly accurately. In this figure, the ratios of the wave-resistance coefficients  $C/C_{1,\infty}$  versus the pressure coefficient  $C_p$  at various values of Froude number,  $F$  are compared. The open symbols denote the numerical finite-depth results and the solid and dashed curves denote the second- and third-order infinite-depth perturbation-theory results. The value of the ratio  $\lambda_{1,\infty}/D$  is less than 2 for all of the numerical results shown in Figure 6; hence this is almost equivalent to infinite depth as far as the description of the waves is concerned. However, examination of the numerical results in Figure 6 shows that the characteristic length  $L$  is too large relative to the depth  $D$  for nonlinear bottom effects on the wave-making action of the pressure distribution to be negligible.

One can estimate (roughly) the wave-resistance coefficient for infinite depth,  $L/D = 0$ , at fixed values of Froude number  $F$  and pressure coefficient  $C_p$  by extrapolating to  $L/D = 0$  the finite-depth numerical data given in Figure 6. A hand-sketch extrapolation of the finite-depth values of  $C/C_{1,\infty}$  is presented in Figure 7 for  $F = 0.461$  and  $0.357$  and it indicates that the exact infinite-depth values of wave-resistance coefficient  $C$  will be either close to the third-order perturbation theory values of  $C$  or at least between the second and third order values of  $C$ . Figures 6 and 7 seem to indicate that for  $F \approx 0.357$ , the third-order theory fails for the larger values of  $C_p$ . We conclude that perturbation theory can be expected to predict fairly well the wave resistance of two-dimensional pressure distributions, at least for Froude numbers  $F > 0.3$ . At high speeds ( $F > 0.55$ )

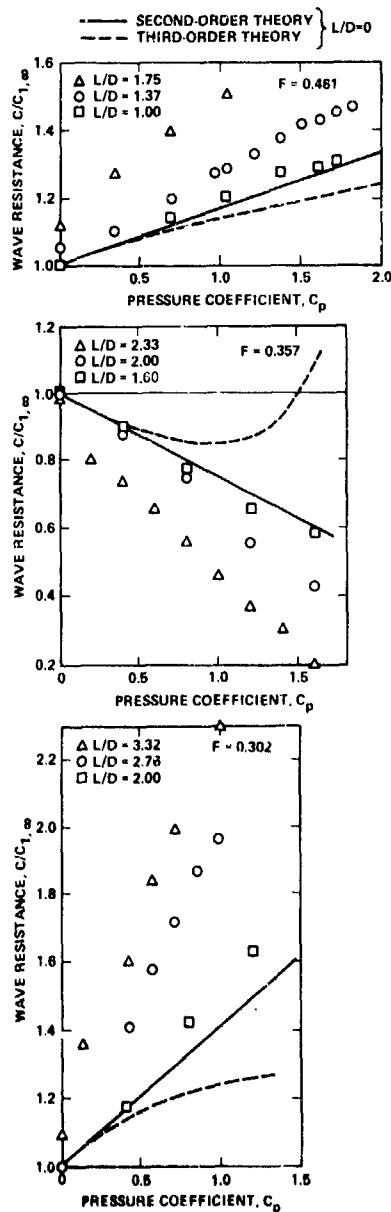


Figure 6 - Wave Resistance versus Pressure Coefficient for Various Froude Numbers

\*For linear theory, the difference in free surface elevations between finite-depth and infinite-depth is less than 1 percent when both  $L/D$  and  $\lambda_{1,\infty}/D$  are less than 2.

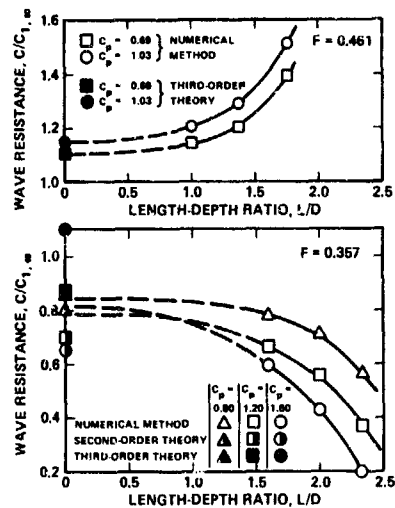


Figure 7 - Wave Resistance versus Ratio of Pressure Distribution Length,  $L$  and Water Depth,  $D$  for  $F = 0.357$  and  $0.461$

near and beyond the second hump of the  $C$  versus  $F$  curves of Figures 4 and 5, linear wave-resistance theory is expected to be fairly accurate in predicting the values of  $C$ .

In Figure 6, the open symbols given for  $C_p = 0$  have been obtained by the linear finite-depth theory, Equation (23). These values show that the differences between finite-depth linear theory and infinite-depth linear theory are no more than  $\pm 10$  percent for the cases presented in Figure 6, whereas the differences between the finite-depth nonlinear numerical results and the infinite-depth perturbation-theory results are much larger. For example, for  $F = 0.302$  and  $C_p = 1.00$ , the finite-depth numerical and the infinite-depth perturbation results differ by about a factor of 2.0. We conclude from this that the finite-depth effects on the wave resistance for two-dimensional flow past free-surface pressure distributions are highly nonlinear and that linear theory cannot be used to estimate accurately the bottom effects even for disturbances with moderate strengths. Similar conclusions were reached in Reference [4] with regard to the finite-depth effects on the wavelength of free running two-dimensional waves.

One can detect a small amount of scatter (or irregularity) of the numerical results shown in Figure 6. The questions of accuracy will be discussed later and some results of numerical experiments to answer some of these questions will be given.

Let us now examine the free-surface elevations in Figure 8 in order to more fully understand the wave-making action of the pressure distribution. We compare in Figure 8 the free-surface profiles obtained by the numerical method with those obtained by linear infinite-depth theory, for three Froude number cases, all with  $C_p = 1.60$ . For the numerical results shown in Figure 8 both  $L/D$  and  $\lambda_{1,\infty}/D$  are sufficiently small (both considerably less than 2) so that they can be compared to infinite-depth linear-theory results.\*

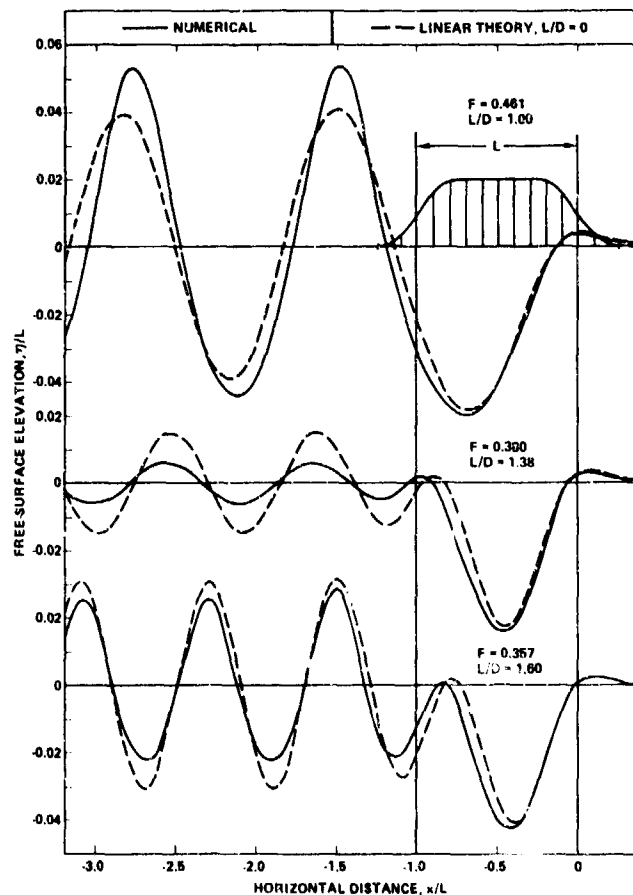


Figure 8 - Free-Surface Elevations Obtained by Numerical Method and Linear Theory for Various Froude Numbers and  $C_p = 1.60$

Figure 8 shows the very interesting fact that the difference between the nonlinear and linear-theory wave resistance must stem almost entirely from the phase shift of the rear portion of the local disturbance relative to the front portions. Note that the amplitude of the forward part of the local disturbance is predicted to be almost the same by the nonlinear and linear calculations. Thus, at the high speeds,  $F > 0.55$ , where the pressure distribution rides entirely on the forward portion of the local disturbance, very small differences are found between linear and nonlinear results.

Free-surface elevations obtained by second- and third-order perturbation theory (which we do not show here) also show the same nonlinear phase shift for the rear portion of the local disturbance. The perturbation results also show that the front portion of the local free-surface elevations predicted by the second- and third-order theory is almost identical to the linear-theory results.

A general conclusion seems to be that the predominate nonlinear effect is the phase shift between the waves generated by different portions of the disturbance. Furthermore, as the speed decreases and the wavelength becomes smaller relative to the disturbance length, this phase shift results in an increasingly larger difference between the exact and the linear theory wave resistance. It seems plausible that this conclusion for the two-dimensional pressure case may carry over to the three-dimensional ship case. Namely, that as the ship speed decreases one may expect larger nonlinearities due to the nonlinear phasing between the waves generated by the bow and the stern. This is in agreement with the well-known fact that linear ship-wave-resistance theory agrees better with experimental results at higher ship speeds.

As previously discussed, the nonlinear effects are very noticeable when  $L/D > 2$ , even when the waves themselves are close to being deep-water waves, i.e.,  $\lambda_{1, \infty}/D < 2$ .

A particularly interesting case with strong nonlinear effects is shown in Figure 9. Here  $L/D = 2.33$  and  $F = 0.357$ . Free-surface elevations are shown for two pressure coefficients,  $C_p = 0.80$  and  $1.60$ . Note that the doubling of the pressure coefficients from  $C_p = 0.8$  to  $C_p = 1.6$  results in only a very slight increase of the wave height (and wave-resistance coefficient  $C$ ) although the amplitude of the local disturbance is almost exactly doubled. Thus, we see that the main effects of the nonlinearities of the problem are to change the phasing (increase the distance between) the front and rear portions of the local disturbance.

An interesting phenomenon connected with the nonlinear variations of the free-surface profile with increases in pressure coefficient  $C_p$  is more thoroughly illustrated in Figure 10. Here we show the variation of the wave-resistance coefficient  $C$  and the actual wave resistance  $R$  (made dimensionless by the hydrostatic head  $\rho g L$ ) with pressure coefficient  $C_p$ . Note that as  $C_p$  increases towards 1.6, the actual wave resistance  $R$  increases to a maximum at  $C_p = 1.4$  and decreases again with a further increase in  $C_p$ .

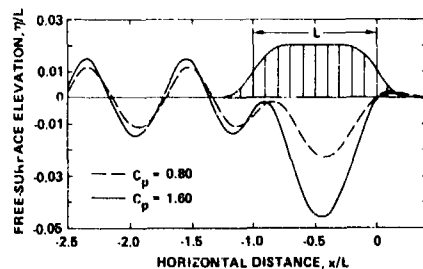


Figure 9 - Free-Surface Elevations Obtained by Numerical Method for  $F = 0.357$ ,  $C_p = 0.80$  and  $1.60$ , and  $L/D = 2.33$

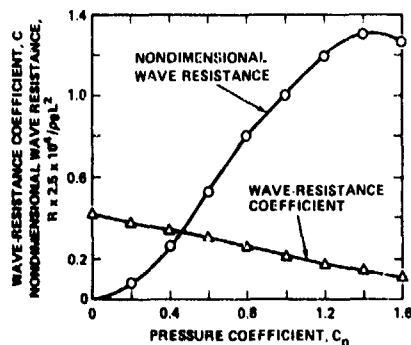


Figure 10 - Nondimensional Wave Resistance and Wave-Resistance Coefficient versus Pressure Coefficient for  $F = 0.357$

This curious phenomenon means that beyond a certain loading, it is economical in an absolute sense to actually increase the loading further (at least when running at Froude number,  $F = 0.357$  in water depth of  $D = L/2.33$ ).

We have alluded to the slight irregularity of some of the numerical results shown in Figure 6. We note in particular that the numerical results for low values of  $C_p$  seem to be displaced from the main trend of the numerical results. This is due to the fact that in the numerical method we use an absolute measure of the local error in the free-surface condition. This results in higher relative accuracy in satisfying the free-surface condition for larger free-surface disturbances. Some numerical results illustrating this effect are shown in Figure 11. This figure shows the effect of the variation of the finite-difference mesh size on the wave-resistance coefficient  $C$  for various values of  $C_p$  at the values  $F = 0.357$  and  $L/D = 2.0$ . Note the somewhat lower accuracy achieved at lower values of  $C_p$  and larger values of the mesh size  $h/L$  if one assumes that the values of  $C$  at  $L/h = 24$  represent accurate values. Most of the numerical results given in this paper were obtained for values of  $L/h = 20$  or  $22$  although some of the results were obtained at  $L/h = 24$ .

#### Concluding Remarks

We have found in the numerical investigations described in this paper that the first- and second-order perturbation theory of [6] is probably adequate for predicting the wave resistance coefficient  $C$  of two-dimensional surface pressure distributions on infinite depth streams and for Froude number  $F \geq 0.3$ . We expect that a second-order perturbation theory for finite-depth streams, similar to the infinite-depth perturbation theory of [6] also will predict accurately the wave-resistance coefficient  $C$  for surface-pressure distributions. We note in Figures 4 and 5 that the relative accuracy of the linear-theory wave-resistance coefficient  $C_1$  is very low at the sloping parts and near the troughs of the  $C$  versus  $F$  graphs. However, the absolute magnitude of the difference between the exact and linear-theory values of  $C$  is not large.

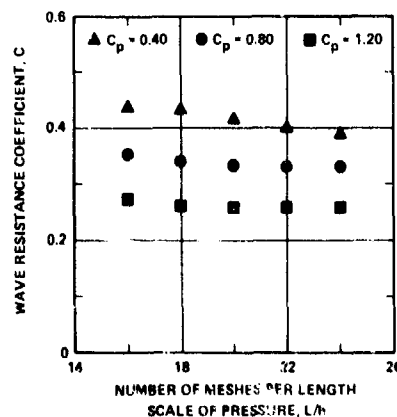


Figure 11 - Wave-Resistance Coefficient versus Number of Meshes per Length Scale for  $F = 0.357$  and  $L/D = 2.00$

\*We recognize that we only have one data point beyond  $C_p = 1.4$  which shows this decrease in the wave resistance, however, considering the wave cancellation mechanisms which are present under the pressure distribution, this decrease is certainly possible.

compared with say the maximum value of  $C$  at  $F = 0.57$ . Thus, it seems that the linear-theory wave-resistance coefficient  $C_L$  is an adequate prediction of the value of  $C$  in most practical circumstances. The improvement of the prediction of the wave-resistance coefficient  $C$  given by second-order theory then gives accurate estimates of  $C$  for Froude numbers  $F \geq 0.3$ . We expect that similar accuracy for first- and second-order wave-resistance theory of three-dimensional surface pressure distributions can be obtained.

#### Acknowledgment

This work was supported by the Numerical Naval Hydrodynamics Program at the David W. Taylor Naval Ship Research and Development Center. This Program is jointly sponsored by the DTNSRDC and the Office of Naval Research.

#### REFERENCES

- [1] von Kerczek, C. and N. Salvesen, "Numerical Solutions of Two-Dimensional Nonlinear Wave Problems," Office of Naval Research Tenth Symposium on Naval Hydrodynamics, Massachusetts Institute of Technology, Cambridge, Mass., pp. 649-666 (1974).
- [2] Salvesen, N. and C. von Kerczek, "Comparison of Numerical and Perturbation Solutions of Two-Dimensional Nonlinear Water-Wave Problems," *Journal of Ship Research*, Vol. 20, No. 3, pp. 160-170 (1976).
- [3] Salvesen, N. and C. von Kerczek, "Numerical Solutions of Two-Dimensional Nonlinear Body-Wave Problems," First International Conference on Numerical Ship Hydrodynamics, Gaithersburg, Md., pp. 279-293 (1975).
- [4] Salvesen, N. and C. von Kerczek, "Nonlinear Aspects of Subcritical Shallow-Water Flow Past Two-Dimensional Obstructions," submitted to *Journal of Ship Research* (1977).
- [5] Benjamin, T. Brooke, "Upstream Influence," *Journal of Fluid Mechanics*, Vol. 40, Part 1, pp. 49-479 (1970).
- [6] Salvesen, N., "On Higher-Order Wave Theory for Submerged Two-Dimensional Bodies," *Journal of Fluid Mechanics*, Vol. 38, Part 2, pp. 415-429 (1969).
- [7] Wehausen, J. V. and E. V. Laitone, "Surface Waves," *Handbuch der Physik*, Vol. 9, Springer, Berlin (1960).
- [8] Mantle, P. J., "A Technical Summary of Air Cushion Craft Development," David W. Taylor Naval Ship R&D Center Report 4727 (1975).



DISCUSSIONS  
of three papers

PROGRESS IN THE CALCULATION OF NONLINEAR FREE-SURFACE PROBLEMS  
BY SURFACE SINGULARITY TECHNIQUES

John L. Heas

THE WAVE RESISTANCE FOR FLOW PROBLEMS WITH A FREE SURFACE  
C. Korving and A.J. Hermans

NONLINEAR FREE-SURFACE EFFECTS — THE DEPENDENCE ON FROUDE NUMBER  
C. von Kerczek and Nils Salvesen

Invited Discussion

T. Francis Ogilvie  
University of Michigan

Before discussing the three papers at hand, I wish to make a general comment about the subject of this meeting: Numerical Ship Hydrodynamics.

I do not believe that the subject exists. Long before the first meeting of this series, I asserted this publicly. Now it is obvious that I have been overruled by consensus, but I still believe what I said several years ago.

There is such a subject as "ship hydrodynamics," but a good ship hydrodynamicist has a tool kit with many tools, including numerical analysis and the computer. It should, however, include many other things, and everything is useful only if the person has a good understanding of the physical phenomena involved. Most important of all is an appreciation of when to use which tool.

I have arrived at my present age without ever having written a computer program. But I am certainly not "against" numerical ship hydrodynamics. I feel that I appreciate the importance of numerical solutions as well as anyone, if they are developed and used sensibly. I established my position many years ago. For example, many of you know the work of Frank (1967), to which reference has been made here several times. When Werner Frank developed his now well-known procedure, I was his supervisor. I had assigned the task to him, after doing a fair part of the numerical analysis myself. We had visions then of eventually doing the full 3-D ship-motion problem in a similar way. But we aborted that effort when we realized that we could combine his 2-D numerical solutions with appropriate analytical techniques to obtain rather good solutions of real-world 3-D problems, even those involving ships in waves with forward speed. We made the best use of numerical and analytical tools.

Those hybrid solutions were very successful for certain important purposes, but they had many defects too. And so we should be studying new and better ways of solving those problems. We should be directing our efforts toward identi-

fying and removing the defects of the previous solutions, not just finding new ways of doing the same old things. And we should be trying to develop numerical methods for those problems that cannot be solved at all by classical analytical methods.

During this meeting, I have heard very few authors give any reasons for undertaking the studies that they are reporting. It would be entirely proper if some of them were justified purely on the grounds that they would improve our basic scientific knowledge of fluid mechanics. I would accept a statement that our practical capabilities in ship hydrodynamics would be improved even ten years from now because of these studies. But, quite frankly, I do not see an indication that most of these papers were prepared with these general goals in mind.

For example, we have heard much discussion about the significance--or lack thereof--of the Kelvin-Neumann problem. But the authors who have addressed this problem have not generally discussed why they are bothering to study the problem at all. It has been the discussers who have brought up the question. I myself tried to defend these authors earlier in this meeting. But why did these authors not investigate thoroughly for themselves whether this problem was relevant to anything at all, especially before beginning the horrendous task of trying to solve it? Or, if they did investigate this matter, why did they not tell us about it?

So now I come to the three papers that I am supposed to discuss. The three deal with practically the same problem, presenting three different approaches. Now, I am quite aware that nonlinear effects may be very significant in many practical problems of ship hydrodynamics. In steady-motion problems, such effects are likely to be most important near the junction of the free surface and the leading edge of the ship (or other body). However, all of the authors have avoided having such a junction in their problems, and none of them suggest how or even whether their methods can be extended to cover such important matters.

Perhaps the difficulties will be less when these methods are applied to 3-D problems. Or will they? Is it worth all of this work on 2-D problems unless we have anticipated how we shall

be able to handle real problems? It is encouraging that these authors do treat the full nonlinear free-surface conditions, and I do not mean to imply that this is easy. But where will it lead?

Leaving aside for the moment the discussion of perturbation theory by von Kerczek and Salvesen, I think that it is fair to say that the major difficulty in all of these papers lies in finding the location of the free surface. A different method is used in each paper, and each seems to be more-or-less successful. This is art, of course, not science. Hess has concluded that a global correction must be made to the free-surface location in each iteration, but the authors seem to have managed to use procedures that adjust the location stepwise in the downstream direction. Perhaps Hess' claim is too strong, but it may still be the best way to proceed.

There is one fundamental difference in approach between Hess and the others. There are two free-surface conditions, of course, and the unknown location of the free surface must be determined as part of the solution. Hess satisfies the dynamic free-surface condition first on an assumed location of the surface, then computes the velocity components and uses the kinematic condition to correct the surface location. The other authors use the two boundary conditions in the opposite order. There are heuristic arguments on both sides, but I cannot see any definitive argument in favor of either approach.

It is remarkable in what a cavalier way these authors can treat the radiation condition. For those of us who are accustomed to performing analytical studies of similar problems, we expect to have to impose explicit radiation conditions, but this seems to be a trivial matter in a purely numerical analysis. Presumably, this situation is characteristic only of a 2-D problem, and radiation conditions may cause much difficulty in the corresponding 3-D problems.

I am troubled by Hess' device for smoothing the incident flow. He requires that both components of the perturbation velocity be zero on an upstream segment of the undisturbed free surface. This kind of overspecification would lead to disaster in an analytical solution: It would require that the perturbation velocity be identically zero everywhere. But there is certainly no disaster here, just some questionable results. Presumably, both components are very small on the upstream "flat," and approximating them numerically as zero is simply a good approximation that causes no fundamental difficulty.

Finally, I wish to make a couple of comments about the perturbation analysis in the paper by von Kerczek and Salvesen.

First of all, it is commendable that two investigators should carry along an impartial parallel development of two quite different approaches. We are all too accustomed to seeing each person going off in his own direction, pursuing a particular approach and, forever

after, each advocating his own approach as best. I congratulate Chris and Nils for their long cooperation on this problem.

Salvesen's early work on this subject was the direct inspiration for me to investigate the asymptotic low-speed problem. My elementary analysis has now been developed by Baba and Hara into an elegant theory that for the first time really appears to explain some important low-speed phenomena of surface ships. This can all be traced back to Salvesen's observation that steady-motion free-surface problems appear to become more and more nonlinear as speed becomes smaller and smaller. Many years ago, I found this to be a very disturbing observation, but I finally rationalized it on the grounds that the generated waves become shorter and shorter as speed decreases, and so gradients and higher derivatives of the field variables could become larger and larger, even though wave amplitude itself becomes negligible. Such behavior could occur only in a surface layer, of course, and so we were led to the low-speed singular perturbation that Baba and Hara have developed.

Now von Kerczek and Salvesen again observe that the linear theory is best if the speed is quite high ( $F > 0.55$ ) and their higher-order perturbation theory is fairly good for moderate speed ( $F > 0.3$ ). But their explanation appears not to be quite equivalent to what I concluded nine years ago. They claim that the phase of the generated waves is sensitive to "nonlinear effects." This strikes me as being quite close to the approach that has been developed recently at the University of Tokyo by Professor Inui and Kajitani, who consider that the ship-generated waves propagate on a nonuniform stream the streaming flow around the body, satisfying the rigid-wall free-surface condition. The phase velocity of waves propagating on such a nonuniform stream may vary remarkably. There is no body in the problem of von Kerczek and Salvesen, but there is a corresponding rigid-wall solution. I wonder whether the observed phase shifts could be obtained from a linear analysis involving perturbations about the rigid-wall solution. I also wonder whether the interpretation of the phase sensitivity is in fact just another way of looking at the surface-layer phenomenon that I analyzed qualitatively many years ago, or is it really something different?

#### Discussion by Nils Salvesen

It is difficult in most cases to determine the accuracy of numerical nonlinear solutions of body-wave problems. First of all, there exist very few published nonlinear solutions and very often the published data are for conditions slightly different from those modeled in our own computer methods. For example, von Kerczek and I were forced to make comparisons between nonlinear numerical results for finite-depth flow and perturbation results for infinite-depth flow. The reasons for this are that a higher-order perturbation theory for finite depth has not been developed and that our numerical method was

not suitable for very large depths. We assumed in our earlier work that the bottom effects could be considered small when the depth was equal to one-half of the wavelength since the differences between finite-depth and infinite-depth linear-theory results are no more than one-half a percent at this depth.

However, our recent results (to be published in the Journal of Ship Research in 1978) show that our assumption is incorrect for the non-linear case. Figure 1 shows, for free waves in finite-depth ( $h/\lambda_1 = 0.486$ ) and infinite-depth, the proportional change in the wavelength  $(\lambda - \lambda_1)/\lambda_1$  as a function of the dimensionless wave height  $H/\lambda_1$ . Here  $\lambda_1$  is the first-order wavelength. It is seen that according to linear theory ( $H/\lambda_1 = 0$ ) the difference between the finite-depth and infinite-depth wavelength is about one-half a percent, whereas for steep waves ( $H/\lambda_1 = 0.10$ ), the fifth-order perturbation theory shows a five-percent difference between finite-depth and infinite-depth wavelength. The nonlinear numerical results agree well with the fifth-order finite-depth results.

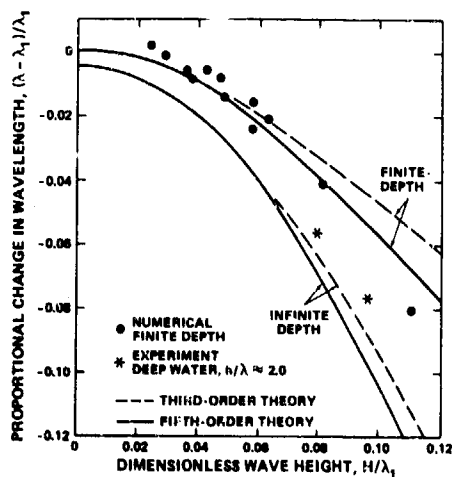


Figure 1

We wanted to bring these results to your attention since the wavelength is often used in evaluating the accuracy of numerical results and since the effect of the bottom on the nonlinear change in wavelength has not generally been recognized.

#### Author's Reply

by A.J. Hermans and C. Korving  
to discussion by T. Francis Ogilvie

The remark of Ogilvie about the radiation condition suggests that in performing analytical studies for similar problems a different radiation condition has to be imposed.

In our numerical analysis we used the following radiation condition:

a) The flow is undisturbed upstream.  
b) A continuity requirement for the surface elevation ( $C^{(2)}$ ).  
The downstream condition is just a condition to close the region in an appropriate way. The region is closed at a position where the mean surface elevation equals zero. In each iteration step this leads to a different position. This disadvantage can be handled easily in the numerical scheme. The advantage is the very simple boundary condition imposed on the normal velocity. This closure condition has nothing to do with the radiation condition. By the way, in nonlinear theory it is an approximation. In linear theory it is fulfilled exactly. Therefore our radiation condition is a) and b). The question arises what "radiation" condition is used in theoretical studies. The analytical studies are on problems with a linearized free-surface condition. In the two-dimensional case use can be made of function theory to construct the solution of a vortex in a moving ideal fluid with a linear free-surface condition. Ogilvie suggests that in that case some sophisticated radiation condition has to be formulated to obtain a unique solution, with a physical meaning. However, the condition that is used is the requirement that the upstream potential is undisturbed. See for instance the book of Kochin, Kibel and Rose on Theoretical Hydrodynamics, page 479. We may say that our continuity requirement implies that the free-surface elevation is an analytic function. It turns out that  $C^{(2)}$  is a condition that is sufficient to lead to a unique numerical procedure. I hope that the discussor agrees that the radiation condition in similar analytical studies is the same trivial matter as in pure numerical analysis. Soon we will solve 3-D problem numerically and I am sure that again we will use the same radiation condition as the one in analytical studies.

#### Author's Reply

by John L. Hess  
to discussion by T. Francis Ogilvie

First, I would like to thank Prof. Ogilvie for his thoughtful comments and to remind him that similar comments of his at a meeting several years ago initiated the work that has led to my present paper. I do not pretend to have answers for all the questions he raises, but I have a few thoughts that seem applicable.

The "tool kit" metaphor is a good one. However, it should be kept in mind that the subject of this conference (only the second such conference) is in its infancy and that the calculational tools we are presently developing are accordingly very primitive ones.

These simple tools probably will not be the ones that are used to solve the problems of real interest, but rather they will be used to construct more powerful tools that will be applied to these problems.

In accordance with the above it seems to be quite appropriate at this stage of development to consider two-dimensional problems, as long as the solution techniques have direct three-dimensional analogies. The failure of a two-dimensional approach would clearly preclude any three-dimensional effort, while its success would furnish a good deal of guidance for the attack on the three-dimensional problem. The history of numerical analysis shows few if any solutions of three-dimensional problems that were not carried out initially in two dimensions. For the same reasons, it seems legitimate to attempt a solution for submerged bodies before addressing the additional complications of the surface-piercing case.

As regards the significance of the Kelvin-Neumann problem, I am not competent to discuss the issue. However, as long as the problem has not been proved to lack significance, work on its solution appears valid, if for no other reason than to determine its significance "empirically". There is after all some doubt as to the significance of the Navier-Stokes equations.

Prof. Ogilvie has put forward several technical points. I can report the results of our numerical experiments but cannot draw any far-reaching conclusions with any degree of certainty. First, we have never obtained convergence with any sort of local iterative algorithm, including ones that use the two boundary conditions in the opposite order. Second, in a case run after the conference, the normal-velocity condition on the upstream "flat" was eliminated with a resultant divergence of the procedure. Elimination of the tangential-velocity boundary condition has not been attempted as yet. Finally, I certainly do not minimize the possibility that a radiation condition will have to be applied on some vertical downstream surface. I consider the inclusion of a radiation condition to be one of the better possibilities for obtaining convergence in cases having large wave heights.

Author's Reply  
by C. von Kerczek  
to discussion by T. Francis Ogilvie

We thank Prof. Ogilvie for his kind comments. We do not fully understand what Prof. Ogilvie means by the "rigid-wall solution" in his first question to us. If he means the uniform free-stream flow under a planar free surface, then the answer to his question seems to be no! The phase shifts do occur at second order when perturbing about the free stream. However, if Prof. Ogilvie means the flow under a rigid free surface whose shape is that of the static free surface under a stationary pressure distribution, then it does seem to us the answer to his question is yes!

The phase shifts do occur at first order. The reason we believe this is that when the perturbation theory is applied to the free-stream solution, the second-order problem, in which the phase shift does occur, accounts mainly for the effects of the local distortion of the free surface in the first-order solution.

## FINITE-ELEMENT AND FINITE-DIFFERENCE SOLUTIONS OF NONLINEAR FREE SURFACE WAVE PROBLEMS\*

S. M. Yen, K. D. Lee and T. J. Akai  
Coordinated Science Laboratory, University of Illinois  
Urbana, Illinois 61801

### Abstract

In this paper two time-dependent numerical schemes for solving steady and unsteady potential flows for nonlinear free surface problems are presented. In one scheme, the finite element method is used to make the field calculation of the velocity potential and the finite difference method is used for the time evolution. The feasibility of this scheme has been demonstrated by numerical solutions obtained for the two-dimensional problems of the pressure distribution and the submerged body. In the other scheme, a finite difference method that couples an explicit, single stage, second order time integration scheme with the solution of the Laplace equation for the velocity potential is used. The feasibility of this scheme has been demonstrated by numerical solutions obtained for a two-dimensional pressure distribution problem and a three-dimensional accelerating strut problem.

### 1. Introduction

Free surface wave problems are characterized by complexities in flow geometry, flow features and boundary conditions. The flow has an unknown free surface and it is propagative and transient. The boundary condition at the free surface is of a mixed, parabolic type and it contains highly nonlinear terms. In the steady state, there also exists a radiation boundary condition, since the waves, once generated, propagate downstream. These complexities have led to several computational difficulties: accurately accommodating the free surface geometry, satisfying the boundary condition uniformly over the free surface, and treating the radiation boundary condition. Computational methods have been developed to deal with some of these difficulties and have been used to solve several free surface problems. These methods have advantages as well as problems in their implementations. Some of these advantages and problems furnish possibly useful guidance for further development of computational schemes.

Von Kercsek and Salvesen [1,2] adopted a marching technique to eliminate the necessity

of the radiation condition by guessing and correcting the free surface for steady, two-dimensional flow. Their downstream closure condition is simply an extrapolation of the streamlines, but it may be useful in evaluating the nonlinear effects. Steady state solutions can also be attained by using a transient approach. The works by Chan and Hirt [3] and Haussling and Van Eseltine [4,5] showed that a local steady state solution is obtained relatively soon after a sudden start. It seems that one of the most general methods for free surface problems is MAC [6-10] or its modified version SURMAC [11-13], which is an Eulerian method with Lagrangian updating of the free surface geometry. However, questions still remain concerning overall efficiency and applications to problems with complex geometry. Lagrangian methods [14-18] look good for simulating free surface flows in confined regions, but are more complex for problems of flow past obstacles. Furthermore, the Lagrangian mesh would be distorted so severely as to produce serious questions of accuracy.

Several investigators [19-26] have succeeded in applying the finite element method to several free surface problems. However, there are many unsolved problems concerning accuracy and convergence of the finite element solutions, especially for nonlinear free surface problems with far-field radiation conditions. Chen and Mei [25] and Bai and Yeung [26] used the known radiation condition at a suitable distance and matched it to their interior numerical solution at the truncation boundary by using an eigenfunction expansion.

Further application of methods developed to find accurate solutions of more complex problems depends on the success of future efforts to alleviate the computational difficulties associated with each of these methods. We shall describe in this paper our research effort in the development of computational methods for nonlinear free surface problems.

The focal point of our study is the nonlinear problem for a disturbance in uniform or accelerated motion on or near a free surface. Our objective is to develop numerical methods for solving steady and unsteady potential flows for free surface problems.

\* Research supported by NSF under Grant ENG-75-15050.

We have developed a time-dependent finite element scheme [27] to deal with the geometrical complexity and the free surface boundary condition of the nonlinear free surface problems. In this scheme, the finite element method is used to make the field calculation and the finite difference method is used for the time evolution. We have used this method to solve two problems: a pressure distribution moving with a constant speed and a moving submerged elliptical cylinder or a hydrofoil.

We have also developed an explicit time-dependent finite difference scheme [28]. Explicit schemes may be more favorable for solving large scale problems on "supercomputers" which have more stringent implementation requirements. We have used this method to solve two problems: a pressure distribution moving with a constant speed and an elliptic cylindrical, surface-piercing strut accelerating from rest. Our solutions serve to demonstrate the feasibility of using the method to solve two-dimensional as well as three-dimensional problems.

## II. Formulation of the Problem

We consider the potential flow produced by a disturbance moving forward on or near a free surface. We assume that there are no secondary motions such as pitch, roll, heave, sway, or surge and that there are no ambient waves. The flow is governed by the potential equation, free surface boundary conditions and conditions at other boundaries. The free surface is characterized by two distinct conditions, kinematic and dynamic conditions.

We shall summarize below the basic equations and the boundary conditions. The coordinate system  $(x, y, z)$  is attached to the disturbance with negative  $y$  oriented toward the acceleration of the gravity. The flow variables are the potential function  $\phi$ , the velocity  $V(V_x, V_y, V_z)$ , and the pressure  $p$ . All the variables in the basic equations and boundary conditions are nondimensionalized with respect to  $U$ ,  $L$ , and  $P_0$  which are the reference values of velocity, length and pressure respectively. We introduce two flow parameters:

$$Fr = \frac{U}{\sqrt{gL}}, \text{ and} \quad (1)$$

$$\sigma = \frac{P_0}{\rho gL}. \quad (2)$$

The free surface height is defined as

$$y = \eta(x, z; t). \quad (3)$$

A two-dimensional problem of a moving disturbance can be defined as follows:

$$\begin{aligned} \phi_{xx} + \phi_{yy} &= 0 & \text{in } \mathcal{D}, \\ \eta_t &= \phi_y - \frac{1}{2} \eta_x^2 & \text{on } y = \eta, \\ \phi_t &= \frac{1}{2} (\phi_x^2 + \phi_y^2) - \frac{1}{Fr^2} \eta - \frac{\sigma}{Fr^2} p & \text{on } y = \eta. \end{aligned} \quad (4)$$

$$\phi = x \quad \text{on cut-off boundaries.}$$

$$\frac{\partial \phi}{\partial n} = 0 \quad \text{on solid boundary.}$$

$$\phi = 0, \quad \eta = -\sigma p \quad \text{at } t = 0 \text{ in } \mathcal{D}.$$

Here  $p$  is the applied pressure on the free surface. When the solid body contains a sharp trailing edge, the Kutta condition is also to be satisfied there. That is

$$\vec{v} = 0 \quad \text{at the trailing edge.} \quad (5)$$

The computational domain is bounded by the free surface and three cut-off boundaries approximating boundaries at infinity.

For the accelerating strut problem, we use the elliptic cylindrical coordinate system  $(\delta, \theta, y)$  to discretize the computational field. The constant  $\delta$  and constant  $\theta$  level curves are respectively confocal ellipses and hyperbolas with foci  $(-c, 0)$  and  $(c, 0)$ . Here,  $c$  is the semifocal distance

$$c = (a^2 - b^2)^{1/2}$$

where  $a$  and  $b$  are the semi-major and semi-minor axes of the base ellipse respectively. The base ellipse is represented by  $\delta_0 = \ln[(a+b)/c]$ .

The metric or scale factor  $h$  associated with the transformation from the Cartesian to the elliptic cylindrical system may be expressed by

$$h^2 = c^2 (\sinh^2 \delta + \sin^2 \theta).$$

The problem considered is defined as follows:

$$\begin{aligned} \phi_{\delta\delta} + \phi_{\theta\theta} + \frac{1}{h^2} \phi_{yy} &= 0 & \text{in } \mathcal{D}, \\ \eta_t &= \phi_y - (\phi_\delta \eta_\delta + \phi_\theta \eta_\theta)/h^2 & \text{on } y = \eta, \\ \phi_t &= cU_t \cosh \delta \cos \theta - \frac{\eta}{Fr^2} & (6) \\ &+ [U^2 - (\nabla \phi)^2]/2 & \text{on } y = \eta, \end{aligned}$$

where  $(\nabla \phi)^2 = \phi_\delta^2 + \phi_\theta^2 + \phi_y^2/h^2$

$$\phi = cU \cosh \delta \cos \theta \quad \text{on } \delta = \delta_0.$$

The cut-off boundary is  $\delta_0$ . At the bottom boundary  $y = y_b$ , it is assumed that  $\phi$  is equivalent to the potential function for a two-dimensional flow past an elliptic cylinder. After a slight modification to obtain compatibility with the boundary condition at  $\delta_0$ , we get

$$\phi = cU (\cosh \delta) (\cos \theta) \left\{ \frac{a \cosh \delta - b \sinh \delta}{a \cosh \delta_0 - b \sinh \delta_0} \right\} \quad \text{on } y = y_b.$$

## III. Finite Element Method

In this method, the finite element method is used for the field calculation of the velocity potential while the time evolution is updated by using the finite difference method. We shall describe here the finite element

formulation and the hybrid approach that we use to solve the free surface problem.

There are two basic steps in formulating a given problem using the finite element method:

1. Discretize the computational field into elements.
2. Select a method to implement the governing equations and the boundary conditions on the discretized field.

For the solution of the free surface problems presented in this paper, we use an iterative scheme to solve the matrix equations resulting from the finite element formulation and a mesh system which is generated numerically in an optimum way. We shall describe here the iterative finite element method, the method we use to generate the mesh system, and their significances.

In the variational finite element method, the form of the unknown solution is assumed in terms of known (trial) functions with unknown adjustable parameters. The assumed trial functions are defined in each element with continuity requirements across the boundaries. The finite element solution is to obtain the combination of trial functions that extremize a given functional for each of the elements in the computational domain. The solution of the Laplace equation over an element is approximated so that the approximate solution minimizes the functional

$$X^E[\phi] = \frac{1}{2} \int (\nabla \phi)^2 dV \quad (7)$$

in that element, thus satisfying the Laplace equation. For the boundary element, both the non-Dirichlet boundary condition and the governing equation should be satisfied.

If the approximate solution in an element is

$$\phi^E = [F(x, y, z)][\phi_1] \quad (8)$$

the necessary condition for Eq. (7) to have a stationary value is

$$\frac{\partial X^E}{\partial [\phi_1]} = \{0\} \quad (9)$$

which yields

$$[K^E][\phi_1] = \{0\} \quad (10)$$

where the matrix  $[K^E]$  is the element stiffness matrix.

The element stiffness matrix is a submatrix of the system stiffness matrix. Hence, the system stiffness matrix can be constructed by

$$[K] = \left[ \sum_{e=1}^{N_e} k_{ij}^e \right] \quad (11)$$

where  $N_e$  is the total number of elements in the domain. The system matrix equation to be solved becomes

$$[K][\phi_1] = [R_1] \quad (12)$$

where the right hand side is obtained from the boundary conditions. That is, Eq. (12) is the discretized form of Eq. (9).

When the finite element method is applied to larger and more complex problems, it becomes increasingly more difficult to construct the system matrix equation and to develop a method to solve it. Also, the implementation may require excessive data handling that usually leads to additional computational errors. We have developed an iterative scheme [27] called the sector method that is more efficient to implement. In our method, a sector is defined by a combination of elements surrounding a node or nodes as shown in Fig. 1. Its boundaries denote the finite cut-off zone of influence of the interior node or nodes since the effect of any node appears only in elements where that point is involved. That is, the field variable at an interior node is affected only by the field variable at other nodes in that sector through the finite element algorithm. The sector stiffness matrix is constructed by the element stiffness matrices of member elements in that sector. Similar to Eq. (11), it is

$$[K^s] = [k_{ij}^s] = \left[ \sum_{e=1}^{N_e} k_{ij}^e \right] \quad (13)$$

where  $N_e$  is the number of elements in that sector. The matrix equation in a sector is therefore

$$[K^s][\phi_1] = \{0\}. \quad (14)$$

Instead of constructing the system stiffness matrix and solving the resulting matrix equation, the solution procedure is to construct the sector stiffness matrix for each sector and to iterate by sweeping all the sectors. Any iterative scheme such as the successive overrelaxation method can be incorporated.

The sector method provides a way to avoid the tedious data handling in constructing the system stiffness matrix and facilitates the treatment of boundary conditions. Since it is used with an iterative scheme, the values at non-Dirichlet boundary points are updated separately from the field computation after each iterative step.

The accuracy of the finite element method can be increased by using smaller elements and/or higher-order polynomials. But the degree of freedom in discretization is limited by considerations of economy and computer capacity. For a given degree of freedom, it is essential to choose a proper mesh system and a finite element algorithm to obtain the maximum possible accuracy. The choice of an optimum mesh system should be based upon a set of guidelines that are applicable to any field of computation. We have made a comprehensive parametric study of the effect of mesh systems on the computational errors. This study has led to the formulation of a set of guidelines that may be followed in designing an optimum finite element mesh system. To meet these

guidelines, the mesh structure should be regular and of simple pattern, the shape of the basic element should also be regular and as equilateral as possible and the distribution of size of elements should be consistent with the flow variables to insure maximum uniformity in the error distribution.

We have developed two methods [27,29] that can be used to numerically generate mesh systems that meet the guidelines listed above. The methods are based on the numerical transformation obtained by solving the Laplace equation to produce an orthogonal grid system in the physical plane. The node distribution of this system satisfies the geometric potential to ensure maximum uniformity, and the structure of mesh is orthogonal and regular. The boundary geometry is accommodated accurately and the implementation of boundary conditions is simple due to the orthogonality. Moreover, all the data for the finite element algorithm are computer-generated, thus reducing the data handling for the input to the finite element program. The mesh generating schemes, therefore, provide a way to construct a mesh system which minimizes errors associated with the finite element method. We believe that it is important to use such an optimum mesh system in the finite element solution of the free surface problems because of their complexities.

The finite element algorithms developed are used to solve the Laplace equation. The computational domain is divided into triangular elements for simplicity, but quadrilateral elements can also be used. The time advancement of the free surface boundary conditions is carried out through the finite difference method. A predictor-corrector method is used for the time updating. Let the free surface boundary conditions be expressed by

$$\eta_t = F(x,y;t)$$

and

$$\phi_t = G(x,y;t).$$

The Euler method predicts the values at a particular  $x$  position at the new time-step by

$$\eta_{n+1} = \eta_n + \Delta t F_n$$

and

$$\phi_{n+1}^* = \phi_n^* + \Delta t G_n,$$

where  $\phi^*$  denotes  $\phi$  on the free surface, the subscript  $n$  refers to the time level, and  $\Delta t$  is the time increment. The values at the new time-step are obtained from the corrector step by

$$\eta_{n+1} = \eta_n + \frac{\Delta t}{2}(F_n + F_{n+1})$$

and

$$\phi_{n+1}^* = \phi_n^* + \frac{\Delta t}{2}(G_n + G_{n+1}).$$

In computing  $F$  and  $G$ , the spatial derivatives can be computed from the finite element

algorithms. However, when the triangular mesh is used, the derivatives have comparably larger errors. In this case, the spatial derivatives are obtained from polynomial approximations after the iterative solutions converge at each time-step.

The successive overrelaxation method is used to solve the Laplace equation iteratively with the specified values of  $\phi^*$  on the given boundary  $\eta$ . The updating of  $\eta$  and  $\phi^*$  is carried out by the predictor-corrector method after the iterative solutions converge within a required limit. The predictor-corrector method has less stringent conditions for stability and converges even in nonlinear problems; however, it does require two solutions for each time-step.

The computational domain always includes the updated free surface boundary in the finite element formulations and computation of the stiffness matrices for the boundary elements is therefore necessary at each time-step. When the elevation of the free surface is large, several rows of elements near the free surface are rearranged periodically to maintain maximum uniformity in element sizes. For example, Fig. 2 shows the case when four rows of elements are rearranged to accommodate the elevation of the free surface. It would be best to find an optimum mesh system at each time-step, but it would be cumbersome to change the whole mesh since new stiffness matrices for all the elements would then have to be recalculated. Since the Eulerian approach is used, no interpolations are necessary for the field variable at new interior points. The mesh rearrangement does not lead to any difficulties since no transformation is included in the formulations. Once the coordinates of new nodal points are assigned, the stiffness matrices for the changed elements are recomputed, but the finite element algorithm is not changed.

The computational domain is expanded downstream periodically as the disturbance on the free surface is propagated close to the downstream boundary. Therefore, the undisturbed condition is always applied on the cut-off downstream boundary. This can save unnecessary computations in the undisturbed regions. The numerical scheme used is tested for the flow generated by a pressure distribution moving across the free surface and is applied to two free surface problems due to an obstacle in a uniform stream.

#### IV. Finite Difference Method

Our finite difference method is to couple an explicit, single stage, second order time integration scheme with the solution of the Laplace equation for the potential function. In this method, the free surface conditions are integrated to provide a Dirichlet condition at the surface for the Laplace equation, the Laplace equation is solved, and the solution is used together with the free surface conditions to determine the derivatives needed for another time integration.

The time integration scheme is expressed by



$$\eta_{n+1} = \eta_n + \Delta t (\eta_t)_n + (\Delta t^2/2) (\eta_{tt})_n \quad (18)$$

and

$$\begin{aligned} \phi_{n+1}^* &= \phi_n^* + \Delta t (\phi_t^*)_n + (\Delta t^2/2) (\phi_{tt}^*)_n \\ &+ \Delta \eta [(\phi_y^*)_n + (\Delta \eta/2) (\phi_{yy}^*)_n + \Delta t (\phi_{yt}^*)_n]. \end{aligned} \quad (19)$$

The subscript  $n$  denotes values at time  $t = t_n$ ,  $\phi^*$  denotes  $\phi$  at  $y = \eta$ ,

$$\Delta t = t_{n+1} - t_n,$$

and

$$\Delta \eta = \eta_{n+1} - \eta_n.$$

Equation (18) is a second-order Taylor series expansion in  $t$ . Equation (19) is an expansion in terms of two variables because  $\phi^*$  is to be computed not only at a new time but also at a new position  $y = \eta_n$ . The attractive features

of the scheme given by Eqs. (18) and (19) are that only one solution of the Laplace equation is required at each time-step (predictor-corrector schemes require more than one and implicit schemes require additional solutions of two simultaneous systems of equations for  $\eta_{n+1}$  and  $\phi_{n+1}^*$ ) and that implementation is straightforward. Also, since separate rather than interdependent computations are made at nodes on the surface, the method is well-suited to creating large problems on parallel process machines which are currently available among modern, large-scale "supercomputers".

The Dirichlet condition at the new surface provided by the application of Eqs. (18) and (19) and the other boundary conditions for the problem are used to solve the Laplace equation. Since there are a variety of conditions that may be encountered, no single method of solving the Laplace equation is suggested here. We simply point out that the method should be chosen on the basis of accuracy, efficiency, and suitability to the problem considered as well as to the computer used to solve the problem.

The final step of the method is to compute the derivatives appearing on the right hand sides of Eqs. (18) and (19). In order to do this, we make use of a set of auxiliary equations which are obtained by differentiating the free surface conditions. For example, the auxiliary equations for a three-dimensional problem in Cartesian coordinates are as follows:

$$\begin{aligned} \eta_{xt} &= \phi_{xy} - \phi_{xx} \eta_x - \phi_{xx} \eta_x - \phi_{xz} \eta_z \\ &- \phi_{zz} \eta_{xz} \quad \text{on } y = \eta \end{aligned} \quad (20)$$

$$\begin{aligned} \eta_{zt} &= \phi_{yz} - \phi_{xz} \eta_x - \phi_{xz} \eta_x - \phi_{zz} \eta_z \\ &- \phi_{zz} \eta_{zz} \quad \text{on } y = \eta \end{aligned} \quad (21)$$

$$\begin{aligned} \eta_{tt} &= \phi_{yt} - \phi_{xt} \eta_x - \phi_{xt} \eta_x - \phi_{zt} \eta_z \\ &- \phi_{zz} \eta_{zz} \quad \text{on } y = \eta \end{aligned} \quad (22)$$

$$\begin{aligned} \phi_{xt} &= (u_\infty)_t - \eta_x / Fr^2 - \sigma p_x / Fr^2 - \phi_{xx} \\ &- \phi_{xy} \eta_y - \phi_{xz} \eta_z \quad \text{on } y = \eta \end{aligned} \quad (23)$$

$$\phi_{yt} = -\phi_{xy} \eta_x - \phi_{yy} \eta_y - \phi_{yz} \eta_z \quad \text{on } y = \eta \quad (24)$$

$$\begin{aligned} \phi_{zt} &= (w_\infty)_t - \eta_z / Fr^2 - \sigma p_z / Fr^2 - \phi_{xz} \\ &- \phi_{yz} \eta_y - \phi_{zz} \eta_z \quad \text{on } y = \eta \end{aligned} \quad (25)$$

$$\begin{aligned} \phi_{tt} &= x(u_\infty)_{tt} + z(w_\infty)_{tt} - \eta_{tt} / Fr^2 + u_\infty (u_\infty)_t \\ &+ w_\infty (w_\infty)_t - \sigma p_t / Fr^2 - \phi_{xt} \\ &- \phi_{yt} \eta_y - \phi_{zt} \eta_z \quad \text{on } y = \eta \end{aligned} \quad (26)$$

The sequence of computations for determining the derivatives in Eqs. (18) and (19) are summarized below.

1. All first and second derivatives of  $\eta_n$  with respect to the space variables by numerical differentiation.
2. All first and second derivatives of  $\phi_n^*$  with respect to the space variables from the solution of the Laplace equation.
3.  $(\eta_{xt})_n$  and  $(\eta_{zt})_n$  from Eqs. (20) and (21).
4.  $(\phi_{xt}^*)_n$ ,  $(\phi_{yt}^*)_n$ , and  $(\phi_{zt}^*)_n$  from Eqs. (23)-(25).
5.  $(\eta_t)_n$  and  $(\phi_t^*)_n$  from the free surface conditions.
6.  $(\eta_{tt})_n$  from Eq. (9) and  $(\phi_{tt}^*)_n$  from Eq. (26).

#### V. Numerical Solutions

##### Finite element Solutions

**Pressure Distributions Problem.** The problem of pressure distribution is shown schematically in Fig. 3. We consider the distribution

$$p = f(x) = \begin{cases} \frac{P_0}{2} (1 - \cos \frac{2\pi x}{L}) & 0 \leq x \leq L \\ 0 & \text{elsewhere} \end{cases} \quad (27)$$

where  $P_0$  is the maximum pressure in the surface distribution. It is initially at rest and starts to move with the uniform speed  $U$  in the negative direction on the  $x$ -axis. The span of the applied pressure is chosen as the length unit. The computational domain is bordered by the free surface and three cut-off boundaries. The grid system extends initially a distance of 6 units on the  $x$ -axis with 2 of

these units on the upstream side of the pressure distribution, i.e.,  $x_u = -2$  and  $x_d = 6$ . The depth of the domain  $y_d$  is chosen as unity.

The downstream boundary is expanded periodically to contain the entire region of disturbance within the computational domain. The domain is initially divided into regular triangular elements with  $\Delta x = \Delta y = 0.05$ .

Equations (4) are solved by the finite element method with the finite-difference time-updating scheme for the pressure distribution of Eq. (27). The linearized boundary condition is also used to show the differences between the linear and nonlinear cases. The time-step used is  $\Delta t = 0.002$  for the nonlinear case and  $\Delta t = 0.005$  for the linear case. In order to make comparisons with the results of Haussling and Van Eseltine [5], the Froude number is chosen as  $(4\pi)^{-1/2}$  and the parameter  $\sigma$  is 0.01. Comparison is also made with the analytic steady state solution derived from Lamb [30] in order to determine the transient development of the flow.

The evolution of the wave height is displayed in Fig. 4 for the linear case and in Fig. 5 for the nonlinear case. In Fig. 6, the nonlinear result at  $t = 1.0$  is compared with the corresponding linear calculation as well as other solutions. These results show that the local steady state solution can be achieved by the proposed  $\epsilon$ -dependent approach and indicate that the numerical scheme developed yields reasonable numerical solutions for the free surface problem. The numerical test given here is only for small heights, but the numerical scheme proposed can be applied easily to cases of larger heights by restructuring the finite element mesh system.

When analytical or experimental results are not available for comparison with numerical solutions, energy conservation serves as a useful check for evaluating the numerical results. For this problem,

$$\frac{\partial E}{\partial t} = \frac{\partial W}{\partial t} \quad (28)$$

in which  $E$  is the total energy and  $W$  is the work. The energy and work are computed by numerical integration, and the rate of energy change is computed by the second-order finite difference scheme

$$\left(\frac{\partial E}{\partial t}\right)^n = (3E^n - 4E^{n-1} + E^{n-2})/2\Delta t \quad (29)$$

and is compared with the rate of work. The result is shown in Fig. 7. It can be seen that the numerical values of the rate of work and the resistance approach asymptotically the analytically predicted steady-state value. The condition of the conservation of energy is preserved throughout the computation.

**Obstacle in a Moving Stream.** The finite element method is now applied to the free surface problem of a submerged body. Such a problem has the additional difficulty in

implementing the boundary condition at the solid surface.

The coordinate system is fixed with respect to the solid body with its origin at the center of the body. Two different shapes are chosen for the solid body: an elliptic cylinder and a symmetric hydrofoil. The length scale in the nondimensionalization is the body length. The body is located at one unit beneath the undisturbed free surface and has a thickness of 0.2 units. The problems are illustrated in Figs. 8 and 9.

For the hydrofoil problem, the implementation of the Kutta condition is not simple in the finite element method, the first-order approximation

$$\phi = \text{Constant for all } e_t$$

is used with  $e_t$  representing the elements which include the trailing edge. This approximation works well when the element sizes near the trailing edge are relatively small.

The mesh generating scheme we have developed is used to obtain the initial finite element mesh system. As time increases, the boundary elements near the free surface follow the free surface geometry and the mesh system is rearranged when the surface elevation becomes large. The initial mesh systems are shown in Fig. 10 for the elliptic cylinder and in Fig. 11 for the hydrofoil.

The development of the wave height with respect to time is displayed in Fig. 12 for the elliptic cylinder problem and in Fig. 13 for the hydrofoil problem. The results tend to approach local steady state solutions.

#### Finite Difference Solutions

**Pressure Distribution.** The problem was solved on a domain bounded by the free surface,  $x_u = -6$ ,  $y_d = -2$ , and  $x_d = 10$ . A uniformly spaced grid with  $\Delta x = \Delta y = \Delta = 0.0625$  was used except for the spacing between nodes at the surface and those at  $y = -\Delta$ . The spacing between such nodes was  $\Delta y = (\Delta + \eta)$ . Successive over-relaxation (SOR) was used to solve the Laplace equation in its finite difference form.

Haussling and Van Eseltine [4,5] used an implicit scheme to solve this problem. Their solutions oscillate about and slowly approach the steady state, and their early linear and nonlinear solutions are similar. Our (nonlinear) solutions at  $t = 0, 1$ , and 2 are shown with the linear, analytic, steady-state solution in Fig. 14. We can see similar oscillations of the wave amplitude about the steady-state solution and the wave trough position about  $x = 0$ . The profiles shown are also in good agreement with those in [4,5]. An overall comparison between the linear results in [4] and our results is shown by the variation of the drag coefficient

$$C_d = -\frac{\sigma}{Fr^2} \int_0^1 p \eta_x dx$$

with time in Fig. 15. The major difference between these results is in the damping rate. Artificial damping was introduced in [4] to maintain stability in the upstream wave height because the upstream boundary was placed relatively close to the pressure distribution. In our case, the upstream boundary was farther away and such measures were unnecessary. Our results indicate that the explicit method yields accurate solutions.

We have compared our finite difference and finite element solutions and have found these two solutions differ after  $t = 1.4$ . The difference is illustrated in Fig. 16 which shows the comparison of results on the drag coefficient. The agreement of the wave height at  $t = 1.0$  is shown in Fig. 17.

**An Accelerating Strut.** The problem was solved on an elliptic cylindrical coordinate system. The parameters of this problem are:  $a = 0.5$ ,  $b = 0.05$ , and  $Fr^2 = 0.025$ . The outer boundary of the domain used is an ellipse with axes

$$a_\infty = c \cosh \delta_\infty$$

$$\text{and } b_\infty = c \sinh \delta_\infty$$

$$\text{where } c^2 = a^2 - b^2$$

$$\text{and } \delta_\infty = \pi + \ln[(a+b)/c].$$

The other boundaries were the free surface, the symmetry axis, the surface of the strut, and  $y = -4\pi/25$ . At the boundary  $y = -4\pi/25$ , the flow is assumed to be completely horizontal as it would be at infinite depth. The two-dimensional flow past an elliptic cylinder is therefore used as a condition at this boundary. The initial conditions for the problem are the conditions at rest. The initial acceleration used is  $g/10$ . The grid used to solve this problem was uniform with spacing  $\Delta = \pi/50$  in all three directions of the elliptic cylindrical coordinate system. As in the previous problem, the spacing between nodes at the surface and those at  $y = -\Delta$  was  $\Delta y = (\Delta + \eta)$ .

Our solutions for the strut problem show the wave formation at the ends of the strut at  $t = 0.05$  in Figs. 18 and 19. Shortly after, at  $t = 0.058$ , wavebreaking occurred near the downstream end of the strut. Profiles along the strut before and just after wavebreaking are shown in Fig. 20. The profile at  $t = 0.05878$  is similar to that of the breaking Stokes wave [31]. The wavebreaking is caused by a combination of the short wavelengths associated with low speeds and the relatively large amplitudes associated with the high initial acceleration.

The solutions for the strut problem exhibit expected behavior and, more importantly, show that a careful choice of initial conditions

must be made if an initial value problem is used to seek steady state solutions. Otherwise, phenomena such as the wavebreaking as in this case may occur. Another important indication is that numerical solutions for three-dimensional problems other than very simple ones are feasible with current computer technology.

## VI. Conclusions

We have developed two time-dependent numerical schemes to solve free surface problems. In one scheme, we use the finite element method to make the field calculation in order to deal with the complex flow geometry and boundary conditions of the free surface problem. The feasibility of this scheme has been demonstrated by numerical solutions obtained for the two-dimensional problems of the pressure distribution and the submerged body. In the other scheme, we use an explicit finite difference method which is simpler to implement and, therefore, can be applied to more complex and large scale problems. Its feasibility has been demonstrated by numerical solutions obtained for a two-dimensional pressure distribution problem and a three-dimensional accelerating strut problem.

It would be of interest to study further application and extension of our methods to more complex problems. For example, a hybrid method that combines the finite element and finite difference grid systems can be devised for complex flow geometry to increase the computational accuracy as well as efficiency. We illustrate in Fig. 21 a hybrid system that has two regions. We propose to use the finite difference method in the outer region and the finite element method in the inner region that has triangles as basic elements. The inner region has a square outer boundary that matches the inner boundary of the outer region. Such a scheme can be applied to problems such as that of an air cushion vehicle.

The application of any time-dependent approach to find the steady state solution of free surface problems is possible only if we are able to find ways to increase the computational efficiency and to control the accumulation of the diffusive error. These two difficult tasks will challenge us in our attempt to solve numerically complex free surface problems.

## References

1. Von Kerczek, C. and Salvesen, N., "Numerical Solutions of Two-Dimensional Nonlinear Wave Problems," Proceedings of the Tenth ONR Symposium on Naval Hydrodynamics, Cambridge, Mass., June 1974, p. 649.
2. Salvesen, N. and von Kerczek, C., "Comparison of Numerical and Perturbation Solutions of Two-Dimensional Nonlinear Water-Wave Problems," J. Ship Res., vol. 20 (1976), pp. 160-170.

3. Chan, R. K.-C and Hirt, C. W., "Two-Dimensional Calculations of the Motion of Floating Bodies," Proceedings of the Tenth ONR Symposium on Naval Hydrodynamics, Cambridge, Mass., June 1974, p. 667.
4. Haussling, H. J. and Van Eseltine, R. T., "A Combined Spectral Finite-Difference Method for Linear and Nonlinear Water Wave Problems," Naval Ship R & D Center Report 4580, Nov. 1974.
5. Haussling, H. J. and Van Eseltine, R. T., "Finite Difference Methods for Transient Potential Flows with Free Surfaces," First International Conference on Numerical Ship Hydrodynamics, Gaithersburg, Maryland, Oct. 1975.
6. Harlow, F. H. and Welch, J. E., "Numerical Calculation of Time-Dependent Viscous Incompressible flow of Fluid with Free Surface," Physics of Fluids, Vol. 8, No. 12, Dec. 1965, p. 2182.
7. Harlow, F. H. and Welch, J. E., "Numerical Study of Large-Amplitude Free-Surface Motions," Physics of Fluids, Vol. 9, No. 5, May 1966, p. 842.
8. Nichols, D. D. and Hirt, C. W., "Improved Free Surface Boundary Conditions for Numerical Incompressible Flow Calculations," Journal of Computational Physics, Vol. 8, No. 3, Dec. 1971, p. 434.
9. Nichols, D. D. and Hirt, C. W., "Calculating Three-Dimensional Free Surface Flows in the Vicinity of Submerged and Exposed Structures," Journal of Computational Physics, Vol. 12, No. 2, June 1973, p. 234.
10. Nichols, D. D. and Hirt, C. W., "Methods for Calculating Multi-Dimensional, Transient Free Surface Flow Past Bodies," First International Conference on Numerical Ship Hydrodynamics, Gaithersburg, Maryland, Oct. 1975.
11. Chan, R. K.-C. and Street, R. L., "A Computer Study of Finite-Amplitude Water Waves," Journal of Computational Physics, Vol. 6, No. 1, Aug. 1970, p. 68.
12. Chan, R. K.-C., Street, R. L., and Fromm, J. E., "The Digital Simulation of Water Waves: An Evaluation of SUMMAC," Lecture Notes in Physics, Vol. 8 (edited by Ehlers, J. et al.), Springer-Verlag, Berlin, 1970, p. 429.
13. Street, R. L., Chan, R. K.-C., and Fromm, J. E., "Two Methods for the Computation of the Motion of Long Water Waves: A Review and Applications," Proceedings of the Eighth ONR Symposium on Naval Hydrodynamics, Rome, Italy, Aug. 1970, p. 147.
14. Hirt, C. W., Cook, J. L., and Butler, T. D., "A Lagrangian Method for Calculating the Dynamics of an Incompressible Fluid with Free Surface," Journal of Computational Physics, Vol. 5, No. 1, Feb. 1970, p. 103.
15. Brennan, C. and Whitney, A. K., "Unsteady Free Surface Flows; Solutions Employing the Lagrangian Description of the Motion," Proceedings of the Eighth ONR Symposium on Naval Hydrodynamics, Rome, Italy, August 1970, p. 117.
16. Brennan, C., "Some Numerical Solutions of Unsteady Free Surface Wave Problems Using the Lagrangian Description of the Flow," Lecture Notes in Physics, Vol. 8 (edited by Ehlers, J. et al.), Springer-Verlag, Berlin, 1970, p. 403.
17. Chan, R. K.-C., "A Generalized Arbitrary Lagrangian-Eulerian Method for Incompressible Flow with Sharp Interfaces," Journal of Computational Physics, Vol. 17, No. 3, Mar. 1975, p. 311.
18. Boris, J. P. and Hain, K. L., "Free Surface Hydrodynamics Using a Lagrangian Triangular Mesh," First International Conference on Numerical Ship Hydrodynamics, Gaithersburg, Maryland, Oct. 1975.
19. Taylor, C. J., France, P. W., and Zienkiewicz, O. C., "Some Free Surface Transient Flow Problems of Seepage and Irrotational Flow," The Mathematics of Finite Elements and Applications (edited by Whiteman, J. R.), Academic Press, New York, 1973, p. 313.
20. Chan, S. T.-K., "Finite Element Analysis of Irrotational Flows of an Ideal Fluid," Thesis, University of California at Davis, California, 1970.
21. Visser, W. and van der Wilt, M., "A Numerical Approach to the Study of Irregular Ship Motions," Finite Element Methods in Flow Problems, (edited by Oden, J. T. et al.) UAH Press, Alabama, 1974, p. 277.
22. van der Wilt, M., "Ship Motions: A Test Case for a Numerical Approach," Thesis Delft University of Technology, the Netherlands, June 1973.
23. Nickell, R. E., Tanner, R. I., and Caswell, B., "The Solution of Viscous Incompressible Jet and Free-Surface Flows Using Finite-Element Methods," Journal of Fluid Mechanics, Vol. 65, pt. 1, 1974, p. 189.
24. Bai, K. J., "A Localized Finite Element Method for the Uniform Flow Problem with a Free Surface," First International Conference on Numerical Ship Hydrodynamics, Gaithersburg, Maryland, Oct. 1975.

25. Chen, H. S. and Mei, C. C., "Calculations of Two-Dimensional Ship Waves by a Hybrid Element Method Based on Variational Principles," First International Conference on Numerical Ship Hydrodynamics, Gaithersburg, Maryland, Oct. 1975.
26. Bai, K. J. and Yeung, R. W., "Numerical Solutions to Free-Surface Flow Problems," Proceedings of the Tenth ONR Symposium on Naval Hydrodynamics, Cambridge, Mass., June 1974, p. 609.
27. Lee, K. D., "Application of the Finite Element Method to Potential Flow Problems," Report T-32, Coordinated Science Laboratory, University of Illinois, Oct. 1976.
28. Akai, T. J., "Numerical Solutions of Nonlinear Potential Flows with Free Surfaces," Report T-30, Coordinated Science Laboratory, University of Illinois, Sept. 1976.
29. Yen, S. M. and Lee, K. D., "Application of Finite Element Method to Potential Flow Problems," Proceedings of the Second International Symposium on Finite Element Methods in Flow Problems, Rapallo, Italy, June 1976, p. 539.
30. Lamb, H., "Surface Waves," Hydrodynamics, Chapter 9, Sixth edition, Dover Publications, New York, 1932, p. 363.
31. Stokes, J. J., Water Waves, Interscience Publishers, Inc., New York, 1957.

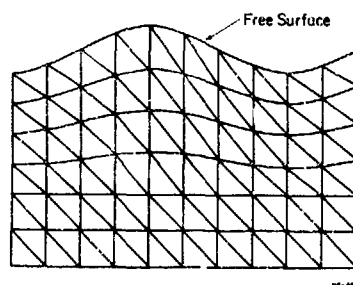


Fig. 2. An Example of Restructuring Elements near the Free Surface.

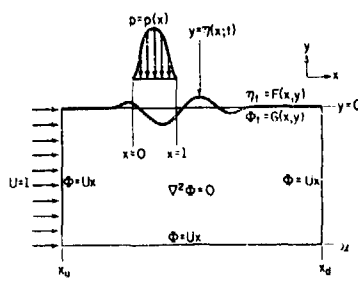


Fig. 3. Schematic of the Two-dimensional Pressure Distribution Problem.

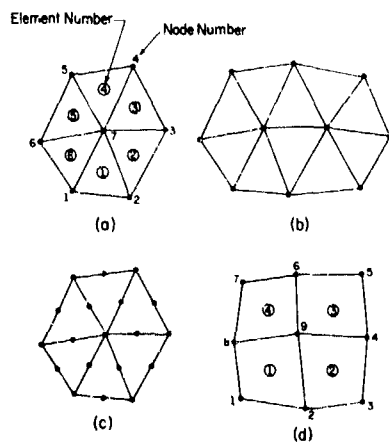


Fig. 1. Finite Element Sectors: (a) Six triangular elements, one interior node, (b) Ten triangular elements, two interior nodes, (c) Six triangular elements, seven interior nodes, (d) Four quadrilateral elements, one interior node

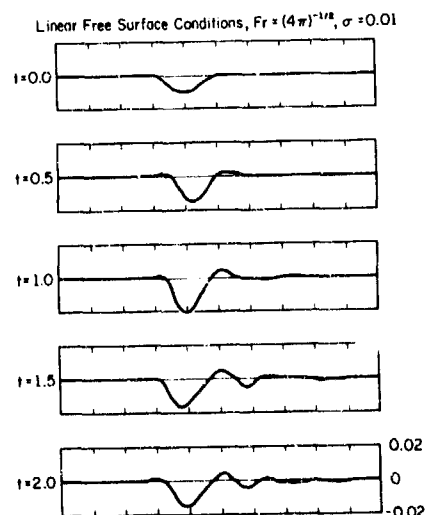


Fig. 4. Time Evolution of Wave Height Computed with Linear Free Surface Conditions.  $Fr = (4\pi)^{-1/2}$  and  $\sigma = 0.01$ .

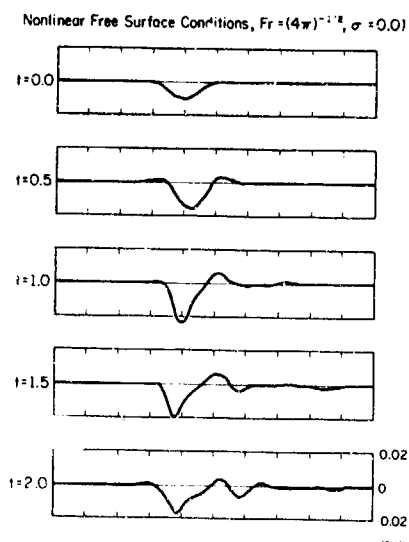


Fig. 5. Time Evolution of Wave Height Computed with Nonlinear Free Surface Conditions.  $Fr = (4\pi)^{-1/2}$  and  $\sigma = 0.01$ .

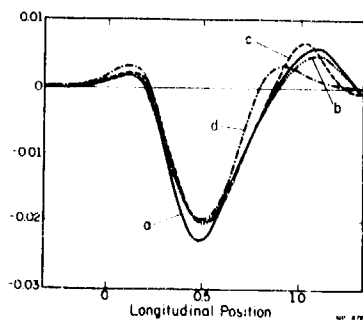


Fig. 6. Comparison of Wave Height.  $\sigma = 0.01$  and  $Fr = (4\pi)^{-1/2}$ .  
a - Nonlinear solution at  $t = 1.0$ .  
b - Linear solution at  $t = 1.0$ .  
c - Linear solution at  $t = 0.96$  by Haussling and Van Eseltine.  
d - Analytic linear steady state solution.

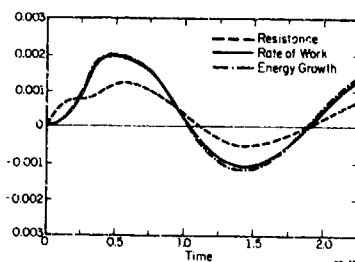


Fig. 7. Variation of Computed Rate of Work, Energy Growth, and Resistance.  $Fr = (4\pi)^{-1/2}$  and  $\sigma = 0.01$ .

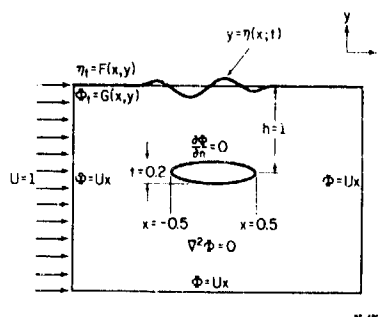


Fig. 8. Schematic of Two-dimensional Problem of a Submerged Elliptic Cylinder.

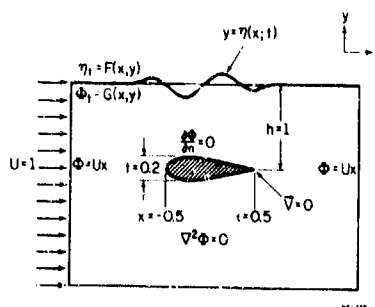


Fig. 9. Schematic of the Hydrofoil Problem.

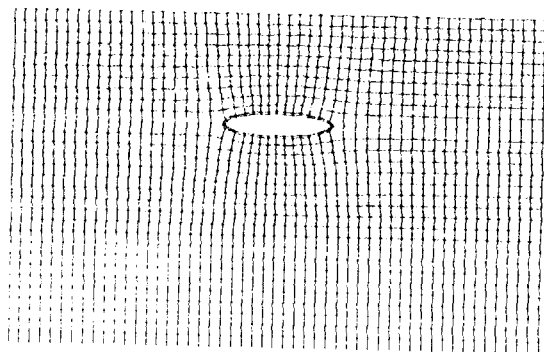


Fig. 10. Initial Mesh System for the Elliptic Cylinder Problem.

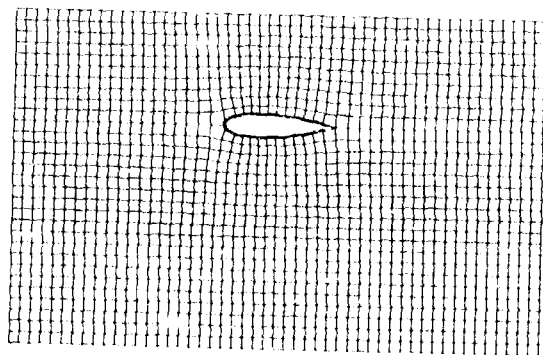


Fig. 11. Initial Mesh System for the Hydrofoil Problem.

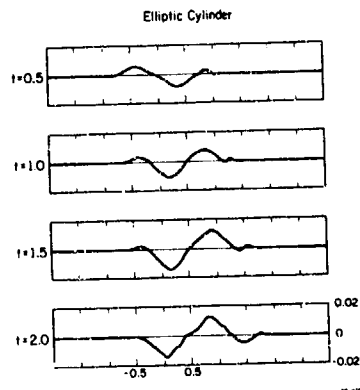


Fig. 12. Development of Wave Heights for the Elliptic Cylinder Problem.

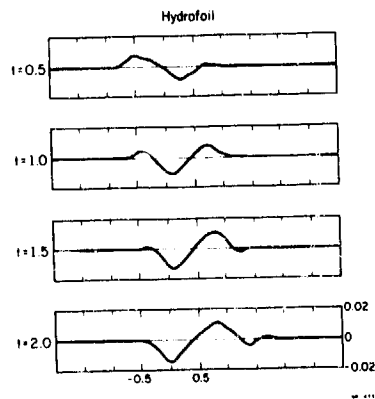


Fig. 13. Development of Wave Heights for the Hydrofoil Problem.

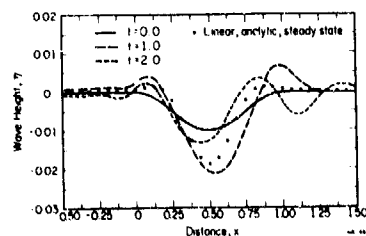


Fig. 14. Wave Profiles at  $t = 0, 1.0$  and  $2.0$ . Comparison with the Linear Steady State Solution.  $Fr = (4\pi)^{-1/2}$  and  $\sigma = 0.01$ .

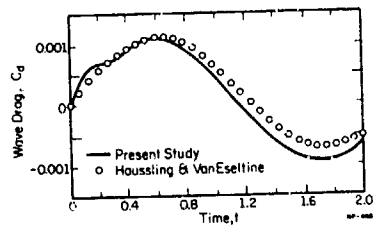


Fig. 15. Comparison of Wave Drag with a Linear Numerical Solution.  $Fr = (4\pi)^{-1/2}$ ,  $\sigma = 0.01$ .

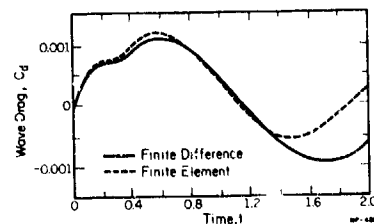


Fig. 16. Comparison of the Finite Element and Finite Difference Calculations of Wave Drag.  $Fr = (4\pi)^{-1/2}$  and  $\sigma = 0.01$ .

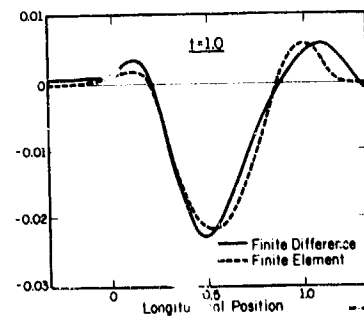


Fig. 17. Comparison of Finite Element and Finite Difference Calculations of Wave Height at  $t = 1.0$ .  $Fr = (4\pi)^{-1/2}$  and  $\sigma = 0.01$ .



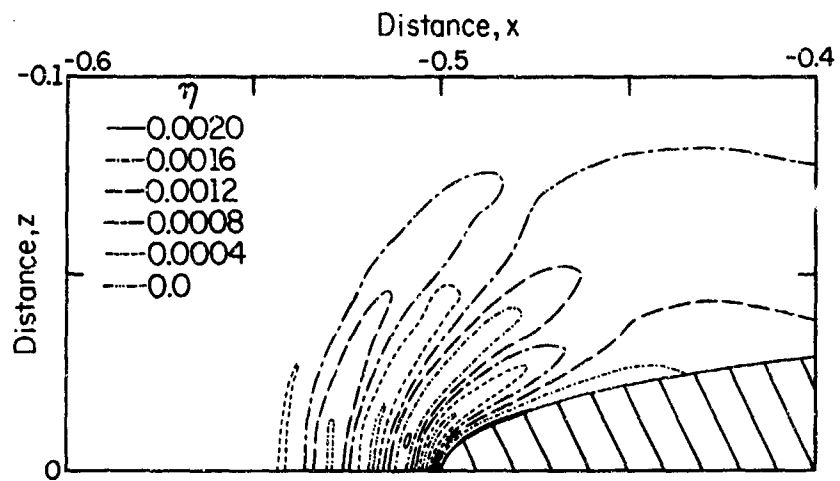


Fig. 18. Contour Plots of the Free Surface Position near the Upstream End of the Strut at  $t = 0.05$ .

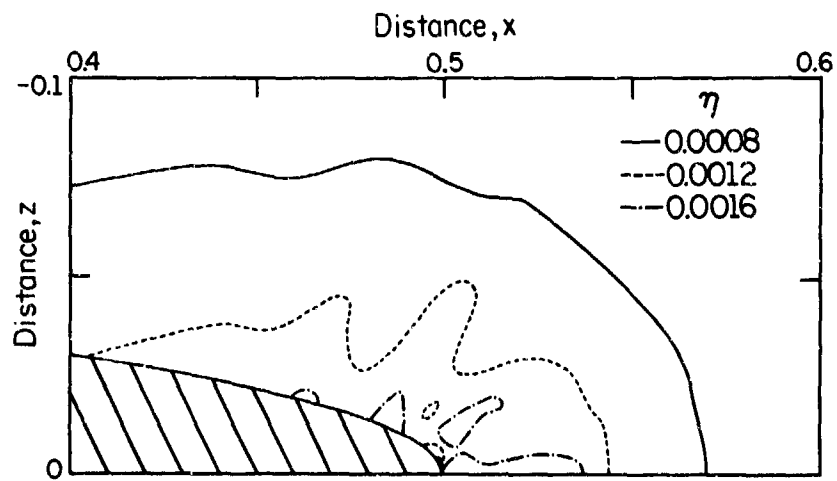


Fig. 19. Contour Plots of the Free Surface Position near the Downstream End of the Strut at  $t = 0.05$ .

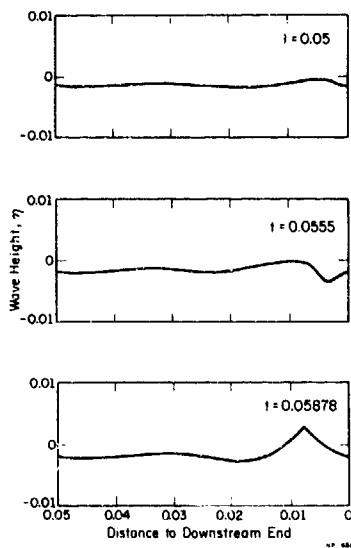


Fig. 20. Sequence of Wave Profiles at the Surface of the Strut vs. the Distance along the Arc of the Strut Prior to and After Wavebreaking.

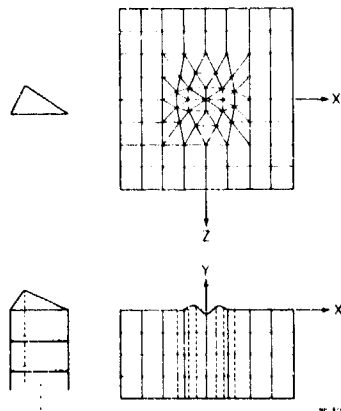


Fig. 21. A Grid System for Implementation of a Hybrid Method. Inner Region for Finite Element Method. Outer Region for Finite Difference Method.

# TRANSIENT FREE-SURFACE HYDRODYNAMICS\*

M. J. Fritts and J. P. Boris  
Naval Research Laboratory  
Washington, D.C. 20375

## Abstract

The control volume approach is used to obtain a finite-difference scheme for a Lagrangian formulation of inviscid incompressible flow using an irregular triangular mesh. The method permits grid reconnections and allows local vertex addition and deletion. Algorithms are presented which conserve divergence, vorticity, mass, momentum and energy even during grid restructuring. Examples are taken from simulations of shear flow and flow over a hydrofoil in which the restructuring algorithms are crucial. Although the structure of the code is highly scalar, techniques are outlined for producing efficient code even for the new vector computers.

## I. Introduction

The hydrodynamics code SPLISH is designed for Lagrangian simulations of transient free-surface phenomena. The present version of the code was developed for inviscid, incompressible flows in two dimensions. The method uses a triangular finite-difference grid in which triangle sides are aligned along free-surfaces, interfaces, boundaries and the perimeters of submerged bodies. The grid internal to these surfaces is left free to reconnect, adjusting to the time-dependent flow.<sup>1,2</sup> In addition, vertices can be added or subtracted as they accumulate or become sparse in convergent and divergent regions of flow. The added flexibility gained through such grid restructuring permits the application of Lagrangian techniques to large classes of problems which were formerly considered solvable only with the aid of diffusive Eulerian rezoning methods.<sup>3,4</sup> For example, the simulation of shear flows about obstacles are possible with only local changes in the grid. This paper will present the formulation and the motivation of several such grid restructuring techniques, the algorithms used in implementing them and examples of their use in SPLISH. Because the lack of global ordering in a reconnecting grid is a drawback to its implementation, a discussion of techniques to produce more efficient codes is included. Examples will be given of calculations performed on NRL's TI ASC pipeline computer.

\* This research was supported by the Office of Naval Research.

## II. The Control-Volume Approach

For a Lagrangian formulation of inviscid, incompressible flow, the basic equations are

$$\rho \frac{d\vec{v}}{dt} = -\vec{\nabla}P - \rho g\hat{y} \quad (1)$$

and

$$\vec{\nabla} \cdot \vec{v} = 0 \quad (2)$$

together with the conservation of mass, momentum and energy. There are, of course, many possible ways to design finite-difference schemes for these equations. However, it is in general not possible to determine which approach will be successful.<sup>5</sup> For the case of triangular grids, and in particular reconnecting grids, there does not exist a literature of proven techniques. Therefore the method chosen for SPLISH was the control-volume approach, in which the finite-difference equations are formulated to satisfy the conservation laws macroscopically, over a computational cell. In this way the conservation of physical quantities is explicitly satisfied by the scheme at the outset, and corrections for non-conservation are eliminated.<sup>6,7,8</sup>

The definition of the control volume will of course depend on the location at which physical variables are applied on the grid. It is natural to specify positions and pressures at vertices, since the Lagrangian surfaces coincide with surfaces on which pressure is defined as a boundary condition. In our formulation velocities and densities are triangle-centered, yielding a staggered mesh. Pressure gradients are therefore piecewise linear within each triangle and discontinuous at triangle sides, as are the triangle velocities and densities. Therefore all the variables in Eq. (1) are triangle-centered and it is easy to advance the triangle velocities either implicitly or explicitly.

The vertex-centered control volumes,  $cv$ , are used to define the new pressures through Eq. (2), expressed as an integral invariant:

$$\oint_{cv} \vec{\nabla} \cdot \vec{v} dV = 0 \quad (3)$$

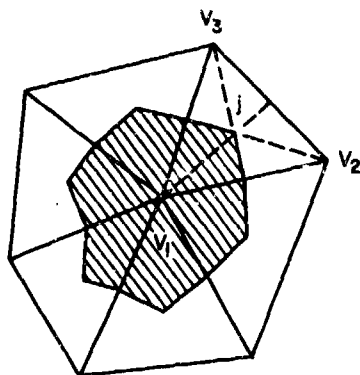


Figure 1. Definition of a control volume about an interior vertex,  $V_1$ . The area of triangle  $j$  is apportioned equally to the control volumes about  $V_1$ ,  $V_2$  and  $V_3$ .

That is, the pressures at the vertices are iterated until the resultant triangle velocities reflect a divergence-free condition for each control volume. An obvious construction for a control volume for this application is shown in Figure 1. The vertex-centered control volume is defined by lines extending from the triangle centroids to the triangle side midpoints. This permits a unique, uniform and complete tessellation of the entire computational region. The control volume for each vertex contains exactly one-third of the area of each of the adjacent triangles. Because pressures are defined as boundary conditions, the control volumes are altered near boundaries as shown in Figure 2. In this way the pressures at vertices near the boundaries enforce a divergence-free condition over the additional area as well.

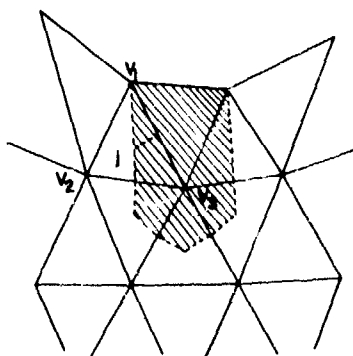


Figure 2. Alteration of a control volume near a boundary. The portion of triangle  $j$  normally assigned to the vertex  $V_1$  is divided between vertices  $V_2$  and  $V_3$ .

There is another constraint implicit in Eq. (1). Taking the curl of both sides, we have

$$\frac{d(\nabla \times \bar{V})}{dt} = -(\nabla \times \frac{\bar{\nabla} P}{\rho}) \quad (4)$$

For homogeneous systems this implies that  $\nabla \times \bar{V}$  is an invariant for every control volume since  $\nabla \times \bar{\nabla} P = 0$ . With a properly defined  $\bar{\nabla} P$ , the finite difference formulation also yields  $\nabla \times \bar{\nabla} P = 0$ , so that the vorticity cannot be altered by the pressure gradients alone. However, this invariant does not ensure the conservation of vorticity over a complete timestep by itself. The velocities are triangle-centered, and advancing the vertex positions means altering the size and shape of the control volumes while leaving the velocities unchanged. In other words, the integrated region is changed but not the integrand. Therefore the updating of vertex positions dictates an accompanying change in triangle velocities to keep the vorticity conserved. This is shown explicitly in Figure 3. The rotation and stretching of the triangle has necessitated a rotation and diminishing of the triangle velocity such that the  $\bar{V} \cdot d\bar{l}$  line integral contributions within the triangle for each of the three vertex control volumes remains constant.

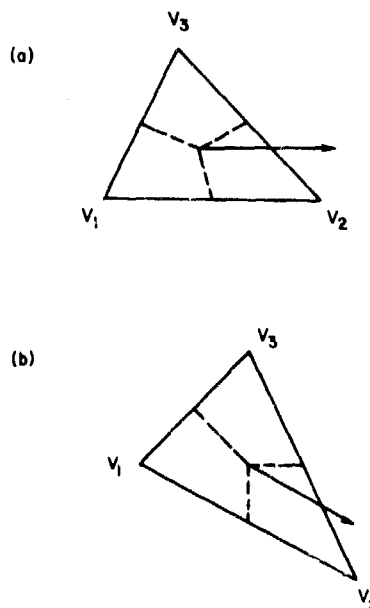


Figure 3. Conservation of vorticity while advancing vertex positions. The triangle velocity is altered such that the  $\bar{V} \cdot d\bar{l}$  line integral contributions within the rotated and stretched triangle remain the same for each vertex.

Thus far we have shown only that a logical extension of the control volume approach is applicable to a general triangular mesh. It can lead to finite-difference formulations which macroscopically conserve appropriate physical quantities, regardless of how irregular the mesh becomes. The real utility of this approach can be seen, however, when we allow the mesh the freedom to reconnect.

### III. Reconnections

Despite the assurance that both the curl and divergence can be conserved, solutions through such Lagrangian algorithms can still yield grossly erroneous results. Figure 4(a) illustrates a sample calculation of shear flow. Triangles below the center of the fluid are moving to the left with velocity  $-U$ , and those above are moving to the right with velocity  $U$ . The vertices lying directly on the shear interface are stationary, while those above and below move with the triangle velocities. The shear layer is in an unstable equilibrium and should persist until round-off errors accumulate enough to perturb the layer. However, even in the absence of round-off in the positions the scheme will quickly fail since the triangles on either side of the boundary will become stretched. Very soon pressure gradients will be calculated which involve vertices far removed from each other as

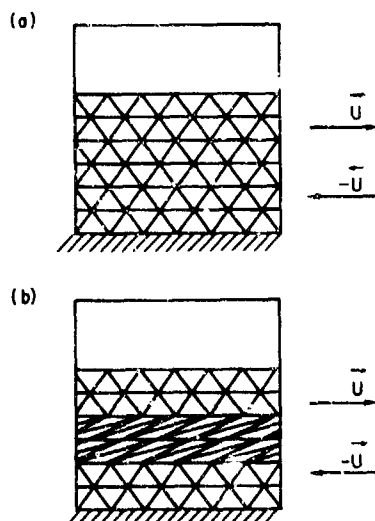


Figure 4. An example of stretched grids in Lagrangian simulations. The initial grid has triangle velocities to the right in the upper half of the fluid and to the left in the lower half of the fluid (a). Periodic boundary conditions are specified on the sides of the region. The grid very quickly distorts in the vicinity of the shear layer (b).

shown in Figure 4(b). Although the area of each triangle remains constant (and each control volume divergence-free) the convergence of the iteration would slow and truncation errors build rapidly as the triangle sides lengthened. The very appearance of the grid reflects the non-physical situation in which pressures far removed from their co-triangular points on the interface directly influence their behavior, whereas those in the immediate vicinity have little effect.

Clearly allowing the mesh to reconnect can solve this dilemma. After reconnection the finite-differences will again only involve neighboring vertices. The most obvious criterion for reconnection is based on this premise. Any interior mesh line is associated with a triangle on either side. The line can therefore be viewed as one of two possible diagonals of the quadrilateral formed by these two triangles. One reconnection prescription is to select the shorter of the two diagonals, provided the resulting triangles are not too unequal in size. This last caveat can be quantified in a number of ways, of course. For example, this algorithm would remove the line from vertex 1 to vertex 3 and subtract a line from vertex 2 to vertex 4 only in Figure 5(a). In Figure 5(b) the new line would lie outside the quadrilateral and in Figure 5(c) the post reconnection triangles would be vastly different in size. Thus reconnection should not be performed.

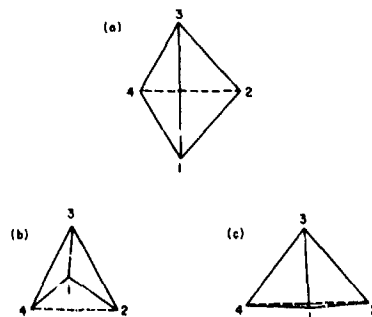


Figure 5. The "nearest neighbor" reconnection algorithm. Lines are reconnected to choose the shortest diagonal of a quadrilateral (a). Lines are not reconnected for "inverted" quadrilaterals even if the exterior diagonal is shorter (b). Nor is the reconnection performed if the resultant triangles are too dissimilar in size (c).

Despite the simplicity and physical motivation of such an algorithm, it is not obvious that it is the preferred one. The expression for a general triangular mesh Poisson equation is<sup>8</sup>

$$\sum_{i \in \text{CV}} \frac{1}{2A_{i+1/2}} [\varphi_i \hat{x}(\vec{r}_c - \vec{r}_{i+1}) + \varphi_{i+1} \hat{x}(\vec{r}_i - \vec{r}_c) + \varphi_c \hat{x}(\vec{r}_{i+1} - \vec{r}_i)] \times \frac{(\vec{r}_{i+1} - \vec{r}_i)}{2} + \hat{z} = A_{cv} (\vec{\nabla} \cdot \vec{\nabla})_{cv} = 0 \quad (5)$$

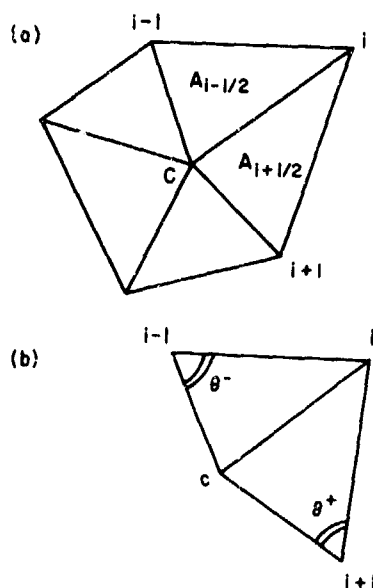


Figure 6. The reconnection algorithm to preserve diagonal dominance of the Poisson Equation. The triangle and vertex labelling used in the Poisson Equation is shown in (a). Figure (b) indicates the angles  $\theta^+$  and  $\theta^-$  used in the reconnection test for the line from vertex c to vertex i.

The vertex c is the central vertex as shown in Figure 6(a). The  $\sum_{i \in \mathcal{N}_c}$  is a sum over all triangles adjacent to c and the labelling for the  $i + \frac{1}{2}$ th triangle is as shown in the figure.  $A_{i+\frac{1}{2}}$  is the area of the  $i + \frac{1}{2}$ th triangle.  $A_{cv}$  is the area of the control volume about vertex c and  $(\vec{v} - \bar{v})_{cv}$  is the finite difference form of Eq. (5). The coefficient  $a_c$  of the  $\psi_c$  term is

$$a_c = - \sum_{i \in \mathcal{N}_c} \frac{|\vec{r}_{i+1} - \vec{r}_i|^2}{4A_{i+\frac{1}{2}}} \quad (6)$$

and is always negative. The coefficient of the  $\psi_i$  term has contributions from just two triangles  $A_{i-\frac{1}{2}}$  and  $A_{i+\frac{1}{2}}$ , and is

$$a_i = - \frac{(\vec{r}_c - \vec{r}_{i+1}) \cdot (\vec{r}_{i+1} - \vec{r}_i)}{4A_{i+\frac{1}{2}}} - \frac{(\vec{r}_{i-1} - \vec{r}_c) \cdot (\vec{r}_i - \vec{r}_{i-1})}{4A_{i-\frac{1}{2}}} \quad (7)$$

This coefficient reduces to

$$a_i = \frac{1}{2} [\cot \theta^+ + \cot \theta^-] \quad (8)$$

where  $\theta^+$  and  $\theta^-$  are shown in Figure 6(b).

Since  $\theta^+$  and  $\theta^-$  are both within the range of  $0^\circ$  to  $180^\circ$  (in positive area triangles), then this

term is negative only when  $\theta^+ + \theta^- > 180^\circ$ , since

$$a_i = \frac{\sin(\theta^+ + \theta^-)}{2 \sin \theta^+ \sin \theta^-} \quad (9)$$

Therefore the matrix represented by Eq. (5) is diagonally dominant if  $\theta^+ + \theta^- \leq 180^\circ$  for each i. This provides another uniquely defined reconnection algorithm, since the sum of both such pairs of angles in the quadrilateral is just  $360^\circ$ . Whenever  $\theta^+ + \theta^- > 180^\circ$ , the line is reconnected to the opposite diagonal. In other words, we have a reconnection algorithm which automatically ensures the diagonal dominance of the Poisson Equation for an irregular triangular mesh. This algorithm also automatically ensures that a diagonal outside the quadrilateral is never chosen.

Whichever reconnection algorithm is chosen, during a reconnection the smallest physically definable cell is the quadrilateral, and not the triangles. It is reasonable then to ensure that quadrilateral properties are unchanged during a reconnection. In other words, the quadrilateral becomes a control volume over which certain variables must be conserved. The reconnection is further complicated by its alteration of the vertex control volumes of each of its vertices, as shown in Figure 7.

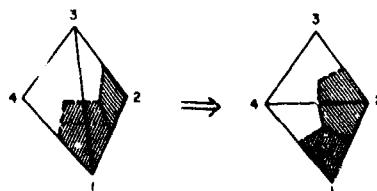


Figure 7. The alteration of control volumes by a reconnection. Portions of the control volumes about vertex 1 and vertex 2 are shown before and after the reconnection.

Nevertheless, it would be desirable that the conservation laws enforced through vertex control volumes remain in force during the reconnection. For example, to keep the vorticity and divergence conserved the portions of

$$\text{the integrals } \int_{cv} \vec{v} \cdot \vec{V} dV \text{ and } \int_{\text{surface}} \vec{v} \times \vec{V} \cdot d\vec{A}$$

within the old and new triangles must be the same before and after the reconnection. Since there are four vertices with two equations for each and only four triangle velocity components to be changed, it would seem that both integrals cannot remain unaltered. In fact, the eight equations are not independent. There exists a unique solution for every interior vertex which satisfies both constraints. It is given by

$$\vec{V}_T = M \vec{V}_T^0$$

where

$$\vec{V}_T = \begin{pmatrix} V_{Tx} \\ V_{Ty} \\ V_{Tx} \\ V_{Ty} \end{pmatrix}, \quad \vec{V}_T^0 = \begin{pmatrix} V_{Rx} \\ V_{Ry} \\ V_{Lx} \\ V_{Ly} \end{pmatrix},$$

$$M = \frac{1}{\vec{R} \cdot \vec{R}} \begin{pmatrix} -\vec{R} \cdot \vec{D} & -2A_F & -\vec{R} \cdot \vec{C} & 2A_F \\ 2A_F & -\vec{R} \cdot \vec{D} & -2A_F & -\vec{R} \cdot \vec{C} \\ \vec{R} \cdot \vec{A} & 2A_B & \vec{R} \cdot \vec{B} & -2A_B \\ -2A_B & \vec{R} \cdot \vec{A} & 2A_B & \vec{R} \cdot \vec{B} \end{pmatrix} \quad (10)$$

where the vector definitions of  $\vec{A}$ ,  $\vec{B}$ ,  $\vec{C}$ ,  $\vec{D}$ , and  $\vec{R}$  are given in Figure 8,  $\vec{V}_R$  and  $\vec{V}_L$  are the triangle velocities before reconnection and  $\vec{V}_B$ ,  $\vec{V}_F$  and  $A_B$ ,  $A_F$  are the triangle velocities and areas after the reconnection.

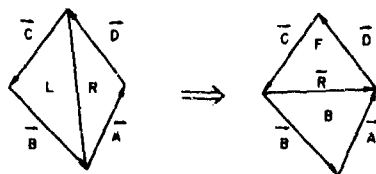


Figure 8. The labelling for triangles and side vectors used in the reversible algorithm to determine new triangle velocities.

This solution includes a valuable bonus. Not only is it unique, but it is reversible. Re-connecting a line yields the original triangle velocities as well as the original vertex control volume configurations. This is a desirable feature since it mirrors yet another implicit property of the basic equations, time reversibility.

As stated above, Eq. (10) also preserves the quadrilateral velocity. That is

$$A_Q \vec{V}_Q = A_R \vec{V}_R + A_L \vec{V}_L = A_F \vec{V}_F + A_B \vec{V}_B \quad (11)$$

where

$$A_Q = A_R + A_L = A_F + A_B \quad (12)$$

The mass of the quadrilateral is just the sum of the triangle masses, or

$$M_Q = A_R \rho_R + A_L \rho_L = A_F \rho_F + A_B \rho_B \quad (13)$$

Therefore strict mass conservation can also be enforced despite the destruction and creation of triangles by constraining the new densities through Eq. (13). By Eqs. (11) and (13)  $V_Q$  and  $M_Q$  are both separately conserved, and therefore so is the quadrilateral momentum and kinetic energy. The pressures are defined at vertices whose positions do not change during reconnection, and the potential energy can be altered only by the different definitions of  $\vec{V}_F/\rho$ . Since we are free to choose both new densities and have only one equation, Eq. (13), to satisfy, we also control the change in potential energy through Eq. (4), which provides the second density constraint. This specifies that the amount of vorticity generated within the quadrilateral is the same before and after the reconnection.

Reconnections then offer a very attractive alternative to global rezoning. The control volume approach leads to algorithms which conserve vorticity and divergence in the control volume about each vertex despite the reconnections. The algorithms also conserve mass, energy and momentum on the basis of triangular and quadrilateral control volumes and further exhibit time reversibility. Finally, the prescription for the occurrence of reconnections can be chosen to preserve ordering by nearest neighbors or to preserve the diagonal dominance of Poisson's equation over the irregular grid.

#### SHEAR FLOW WITH NO PERTURBATIONS

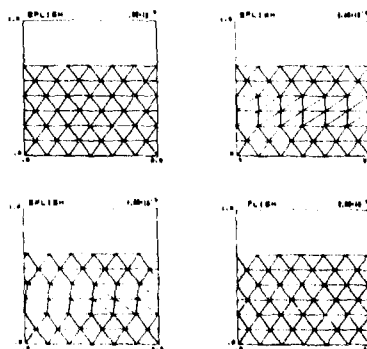


Figure 9. A test of the reconnection algorithm in SPLISH. The grid at various times is presented for a simulation of an unperturbed shear layer. The grid at  $t = 0$  corresponds to that in Figure 4(a). However, here the grid reconnects as it stretches, as shown between  $t = .006$  sec and  $t = .040$  sec. In this simulation  $\delta t = .004$  sec,  $|\vec{U}| = 5$  cm/sec and the length of the system is 2 cm. At  $t = 2.00$  sec each vertex in the upper layer has passed each vertex in the lower layer ten times. Any errors in assignment of triangle velocities would have perturbed the unstable equilibrium of the layer.

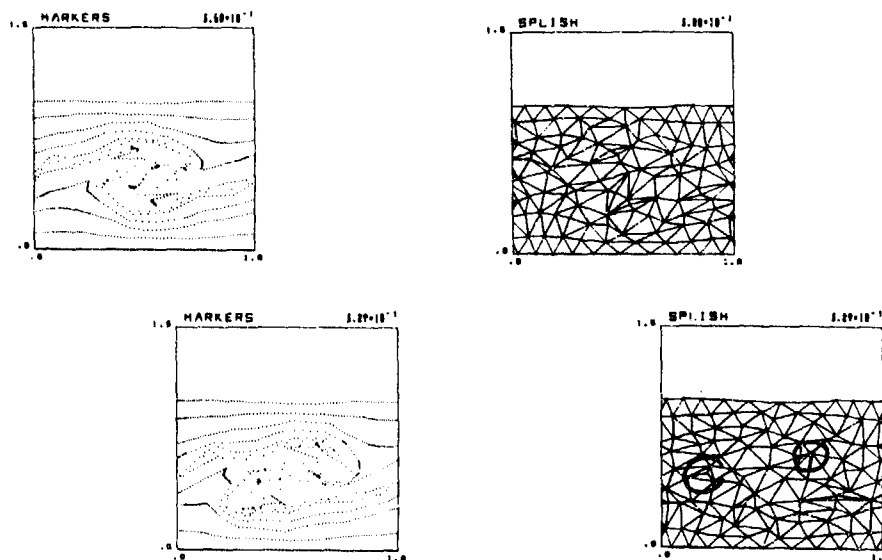


Figure 10. The grid and marker particles at two times in a simulation of a perturbed shear layer. Here  $\delta t = .001$  sec,  $|U| = 5$  cm/sec and the length of the system is 1 cm. At  $t = .300$  sec. the perturbed layer has grown to a mature Kelvin-Helmholtz billow. Only reconnections were used in restructuring the grid. At  $t = .329$  sec the billow is shearing. Two grid anomalies are circled.

These routines have been tested on the problem of shear layer instability.<sup>7</sup> Figure 9 illustrates a simulation in which the initial shear layer was not perturbed. The grid has not changed although each vertex in the upper half of the fluid has traversed the entire grid ten times. Figure 10 shows the grid and a marker particle display for the case of an initial perturbation which has grown to a Kelvin-Helmholtz billow (top row), and after the mature billow begins to shear. The calculation agrees well with the predicted growth rates. Only the reconnection algorithms were used in restructuring the grid, and the grid at  $t = .329$  sec exhibits two irregularities. Two of the vertices have become too close, forming thin elongated triangles, and a third vertex has become enclosed within a triangle. Other grid restructuring is clearly needed. These additional techniques will be discussed in the following section.

#### IV. Vertex Addition and Deletion

The fluid flow near a separatrix is another area in which traditional numerical Lagrangian treatments fail. Figure 11 illustrates a sample grid for a submerged hydrofoil near a free surface. The flow is directed to the right initially with velocity  $U$ . Clearly as the flow develops vertices will tend to accumulate at the forward stagnation point. At the same time the vertices on the hydrofoil will move with the flow along the hydrofoil and accumulate (by pairs) in its wake. After a very short time the gridding will deteriorate

to a denser grid before and after the hydrofoil and a sparse grid along the hydrofoil itself.

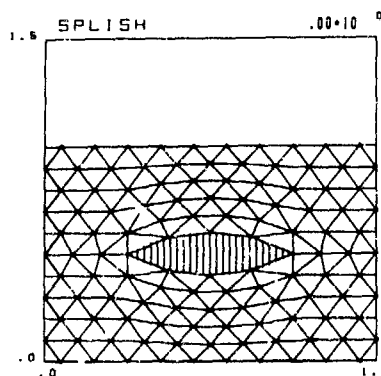


Figure 11. The grid for a hydrofoil near a free surface. The flow is initially directed to the right with velocity  $U$ .

These problems do not derive from an ill-chosen initial grid but are inherent in Lagrangian treatments. By choosing the mid-line of the hydrofoil between an initial row of vertices, a situation develops in which vertices of the same triangle flow toward opposite sides



of the obstacle, leading to a nonsensical calculation of fluid pressure gradients between vertices separated by an obstacle. Fixing the vertices on the hydrofoil surface and allowing reconnections is neither physically desirable nor effective. A tangled grid results from inverted triangles forming over the hydrofoil. The advantage of the present treatment using a control volume formulation is that while these problems are difficult, they are still soluble.

The problem of representing flow near separatrices could be resolved if it were possible to add and subtract vertices from the calculation as needed without altering the physically conserved properties of the flow. Fortunately, such schemes are possible, and may be derived in the same spirit as the reconnection algorithm by using a control volume approach. For example, the simplest way to add a vertex to the fluid is at the centroid of a triangle. Lines are drawn from the new vertex to each of the existing vertices, leaving three new triangles in place of the old one. If all triangle variables are chosen to be identical with the original variables of the old triangle, the behavior of the three triangles clearly does not alter the fluid motion since it is identical to that of the initial triangle. If the vertex pressure is chosen as the average of the three vertex pressures, we have likewise left unaffected the pressure gradients throughout the area occupied by the old triangle. In other words, the three new triangles behave exactly as the former one, and are indistinguishable from it since the vertex remains enclosed within its former boundaries. However, we know that the reconnection algorithm will eventually alter one of the triangle sides if a vertex in the vicinity of the old triangle was really needed. Otherwise the new vertex will continue to behave as if it were not there. But the reconnection is also conservative as shown above, and once a reconnection occurs we have successfully introduced a vertex while maintaining strict conservation of flow properties.

The converse is also true. If a vertex becomes enclosed in a triangle, the behavior of that triangle is not altered if the vertex is removed and the new larger triangle given the velocity

$$A_4 \bar{v}_4 = A_1 \bar{v}_1 + A_2 \bar{v}_2 + A_3 \bar{v}_3 \quad (14)$$

where triangle 4 encompasses the three triangles 1, 2, and 3. Since the mass of the resultant triangle can be defined in a similar manner, the momentum of the larger triangle has not been altered. Therefore for both addition and subtraction of vertices, the larger triangle acts as a control volume in exactly the same sense as the quadrilateral for the reconnections. What has been lost is the information about the behavior of the pressure gradients and velocity gradients within the triangle. This information has been averaged out and replaced by a linear variation across the triangle. All we have suffered is a loss in resolution, exactly what we set out to do in removing the vertex.

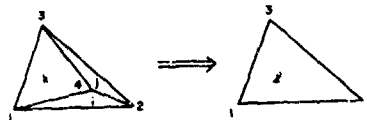


Figure 12. Triangle configurations immediately before and after the removal of a vertex. Vertex 4 is enclosed within triangle 1 either as a result of normal reconnections or by forcing reconnections as it approaches vertex 2.

This claim requires elaboration. The removal of a vertex implies the alteration of four vertex control volumes, one of which is removed, and such a drastic change does not seem consistent with a mere change in resolution. Figure 12 illustrates the triangles before and after vertex removal. Before the vertex is deleted the relevant contribution to the vorticity integrals about each vertex are

$$\begin{aligned} \int \bar{v} \cdot d\bar{l} &= \bar{v}_1 \cdot \frac{(\bar{r}_4 - \bar{r}_2)}{2} + \bar{v}_k \cdot \frac{(\bar{r}_3 - \bar{r}_4)}{2} = \xi_1 \\ \int \bar{v} \cdot d\bar{l} &= \bar{v}_j \cdot \frac{(\bar{r}_4 - \bar{r}_1)}{2} + \bar{v}_1 \cdot \frac{(\bar{r}_1 - \bar{r}_4)}{2} = \xi_2 \\ \int \bar{v} \cdot d\bar{l} &= \bar{v}_k \cdot \frac{(\bar{r}_4 - \bar{r}_1)}{2} + \bar{v}_j \cdot \frac{(\bar{r}_2 - \bar{r}_4)}{2} = \xi_3 \\ \int \bar{v} \cdot d\bar{l} &= \bar{v}_1 \cdot \frac{(\bar{r}_2 - \bar{r}_1)}{2} + \bar{v}_j \cdot \frac{(\bar{r}_3 - \bar{r}_2)}{2} \\ &\quad + \bar{v}_k \cdot \frac{(\bar{r}_1 - \bar{r}_3)}{2} = \xi_4 \end{aligned} \quad (15)$$

After vertex 4 is eliminated, its vorticity must be apportioned to vertices 1 through 3 in some manner;

$$\begin{aligned} \int \bar{v} \cdot d\bar{l} &= \bar{v}_1 \cdot \frac{(\bar{r}_3 - \bar{r}_2)}{2} = \xi_1 + \xi'_1 \\ \int \bar{v} \cdot d\bar{l} &= \bar{v}_j \cdot \frac{(\bar{r}_1 - \bar{r}_3)}{2} = \xi_2 + \xi'_2 \\ \int \bar{v} \cdot d\bar{l} &= \bar{v}_j \cdot \frac{(\bar{r}_2 - \bar{r}_1)}{2} = \xi_3 + \xi'_3 \end{aligned}$$

$$\text{and} \quad \xi'_1 + \xi'_2 + \xi'_3 = \xi_4 \quad (16)$$

Eliminating  $\xi'_1$ ,  $\xi'_2$  and  $\xi'_3$  between Eq. (15) and (16), we have

$$\begin{aligned} \bar{v}_1 \cdot (\bar{r}_4 - \bar{r}_2) + \bar{v}_k \cdot (\bar{r}_3 - \bar{r}_4) &= \bar{v}_1 \cdot (\bar{r}_3 - \bar{r}_2) - 2\xi'_1 \\ \bar{v}_j \cdot (\bar{r}_4 - \bar{r}_1) + \bar{v}_1 \cdot (\bar{r}_1 - \bar{r}_4) &= \bar{v}_j \cdot (\bar{r}_1 - \bar{r}_3) - 2\xi'_2 \\ \bar{v}_k \cdot (\bar{r}_4 - \bar{r}_1) + \bar{v}_j \cdot (\bar{r}_2 - \bar{r}_4) &= \bar{v}_j \cdot (\bar{r}_2 - \bar{r}_1) - 2\xi'_3 \end{aligned} \quad (17)$$

Substituting  $A_4 \bar{v}_4 = A_1 \bar{v}_1 + A_2 \bar{v}_2 + A_3 \bar{v}_3$  into Eq. (17) yields, after some algebra,

$$\epsilon'_1 = A_j \epsilon_h / A_L$$

$$\epsilon'_2 = A_k \epsilon_h / A_L$$

$$\epsilon'_3 = A_i \epsilon_h / A_L$$

where  $\epsilon'_1 + \epsilon'_2 + \epsilon'_3 = \epsilon_h$  since  $A_i + A_j + A_k = A_L$ . Therefore, conserving momentum exactly over the large triangle yields exactly the conservation of vorticity within the affected vertex control volumes. The vorticity carried by the expunged vertex is apportioned by area to the neighboring vertices. If the deleted vertex lies close to one of the remaining vertices, that vertex will carry most of the reassigned vorticity. Therefore the total vorticity is accounted for in a reasonable and natural manner, and momentum is still conserved. Since a similar argument holds for the divergence equations, conservation of flow variables is demonstrated, and a loss in resolution is the only effect.

For the case of an added vertex, the vertex control volume integrals are trivially left unchanged, and the added vertex initially carries no vorticity. Vorticity can accumulate about the added vertex only through reconnections with triangles having dissimilar  $\phi$ . That is, vorticity is generated only by density gradients, as expected.

Therefore, vertices can be added and subtracted within triangles while conserving flow properties exactly. In both cases the usefulness of this result derives from the reconnection algorithm. Used in tandem with addition and deletion within triangles it provides a general algorithm for altering the grid without disturbing the fluid flow. It has already been shown that reconnection used after addition of a vertex at the triangle centroid liberates the vertex in a conservative manner and permits it to behave no longer as the centroid of the triangle. The process can also be reversed. The reconnection algorithm can be used to isolate any vertex within a larger triangle. Once this is accomplished the vertex can be averaged out.



Figure 13. The addition of a vertex at a boundary. The vertices on the boundary are moving along opposite sides of a submerged body (a), and resolution is lost for the leading edge of the body. In (b) a new vertex is added on the boundary. The old triangle is deleted and two new triangles are added.

The utility of this technique is not limited to interior mesh points. Figure 13(a) illustrates a triangle at the leading edge of a submerged body. The flow is forcing the triangle vertices on the boundary in opposite

directions, and resolution of the leading portion of the hydrofoil is being lost. A point may be added along the body as in 13(b). The result may be viewed as the addition of a point within a triangle, but one in which only two of the three smaller triangles survive.

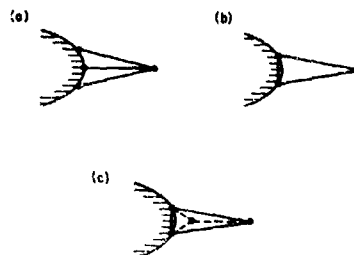


Figure 14. The deletion of a boundary vertex. The flow is converging at the trailing edge of a submerged body (a), resulting in a clustering of vertices and the formation of long thin triangles. In (b) a vertex is removed by drawing a new line to form the enclosing triangle. In (c) a new vertex is added within the elongated triangle to preserve resolution of the flow at the trailing edge. Subsequent reconnections will remove the thin triangles.

Figure 14(a) illustrates the reverse situation at the rear of the hydrofoil. There a new line is drawn to enclose the unwanted vertex in a triangle. In Figure 14(b) the vertex has been removed from the body, leaving the way clear to add a vertex in the fluid, if needed to preserve resolution, as in Figure 14(c).

The use of the control volume approach has therefore made possible the dynamic addition and subtraction of vertices exactly where desired and in a fashion which locally and globally conserves the properties of the fluid flow. The combined use of local resolution alteration and reconnection algorithms permits Lagrangian calculations of extremely complicated flows.

## V. Efficiency

It is obvious that for a code such as SPLISH any global ordering of the grid would soon be invalidated by reconnections and by the addition and deletion of vertices. Since standard fast Poisson solvers rely on such an implicit ordering among vertices, it is appropriate to conclude this paper with some remarks on its efficiency.

The new generation of vector computers provides a good starting point for such a discussion. The increased speed of these computers is attained in large part by their ability to perform quickly a given operation on large numbers of members of an array, which are preferably stored contiguously in memory. Calculations on a vector computer are therefore performed operation by operation for all array

members instead of performing the whole sequence of operations in turn for each member of an array. The ordering of the vertices becomes all important, and a highly disordered code such as SPLISH is almost totally unsuitable for efficient operation. However, despite such obvious problems, the entire SPLISH code has been optimized for the NRL TI ASC vector computer.

Our first example is the reconnection algorithm itself. The heart of the reconnection algorithm is based on the quadrilateral about the line. However, every reconnection that is performed redefines the quadrilaterals for each of the four lines which make up the original quadrilateral. This situation is highly scalar, in that a single reconnection may invalidate the possible reconnection of four neighboring lines. Therefore it is impossible to allow reconnections to proceed in parallel, and the complete calculation for one must be performed before the next is initiated.

However, even in this situation some increase in speed may be gained through efficient coding. Clearly a good deal of the time in the reconnection algorithm is spent in testing each line for a possible reconnection. In general, very few of the lines reconnect for a given timestep. The flow is following local streamlines. Therefore the test can be vectorized provided its output is a list of lines which may want to be reconnected. Each of these (few) lines is then passed through the scalar reconnect routines, in which they are retested and the reconnection performed if it is still desirable. An iteration through this procedure may be desired, but in most cases is not necessary since most reconnections occur remote from each other. In no realistic case tested were more than three iterations required to reach the final grid.

The savings in computer time, of course, depends on the number of lines reconnected. For roughly one percent of the lines reconnecting per timestep (an average case), the vectorized test followed by scalar reconnect is ten times faster. The same is true of all the grid restructuring algorithms. Large saving in time can accrue through vectorizing the tests which must be performed on every line or triangle. The grid alterations must remain scalar, but are relatively few in number.

The second example is the solution of Poisson's Equation. In SPLISH the pressures are adjusted at each vertex iteratively to enforce a divergence-free condition for each vertex control volume. As shown by Eq. (5), coefficients of each term are expressed in terms of the positions of co-triangular vertices. Since there is no global ordering, such a calculation accesses storage almost randomly. That is, the code is highly scalar, and its efficiency on a vector machine is correspondingly poor.

Nevertheless, it is also possible to obtain vectorized code in this situation. The solution is to precompute arrays which duplicate the position data for each neighboring

vertex. These "alias" arrays can be ordered consecutively in core in exactly the ordering necessary for efficient vectorized code. Therefore, although a good deal of extra scalar computation is performed, the increase in speed obtainable for the vectorized code more than compensates for the extra time. The use of "alias" arrays has yielded decreases in computation time of roughly a factor of three. Typical timings for the Poisson solver are now 6.8 milliseconds per iteration for 120 vertices or about 60 microseconds per iteration per vertex.

Although such increases in speed are encouraging, they are not the final solution. Large calculations will require faster solvers. The most promising approach is through the use of direct solvers, rather than iterative ones. Although the matrix representing Eq. (5) does not exhibit the ordering of rectangular meshes, it is nonetheless sparse. Furthermore, if the vertices are preordered by position, the non-zero members will lie along rather diffuse bands. Recently, there has been an increase in interest in fast solvers for such banded matrices and several techniques look particularly encouraging.<sup>9,10</sup> The outlook is very good. Not only is a large class of problems now amenable to Lagrangian calculations, but also at a computational cost per zone competitive with other techniques.

#### References

1. J. P. Boris, M. J. Fritts and K. L. Hain, "Free Surface Hydrodynamics Using a Lagrangian Triangular Mesh," Proceedings of the First International Conference on Ship Hydrodynamics, Oct. 20, 1975.
2. W. P. Crowley, "Flag: A Free Lagrange Method," Proceedings of the Second International Conference on Numerical Methods in Fluid Dynamics, Lecture Notes in Physics, Springer-Verlag, New York, 1971.
3. R.K.-C. Chan, "A Generalized Arbitrary Lagrangian-Eulerian (Gale) Method for Incompressible Flows with Sharp Interfaces," SAI-73-575-LJ, November 1973.
4. C. W. Hirt, "An Arbitrary Lagrangian-Eulerian Computing Technique," Proceedings of the Second International Conference on Numerical Methods in Fluid Dynamics, Lecture Notes in Physics, Springer-Verlag, New York, 1971.
5. P. J. Roache, Computational Fluid Dynamics, Hermosa Publishers, Albuquerque, New Mexico, 1972, p. 25.
6. M. J. Fritts, "A Numerical Study of Free-Surface Waves," SAI-76-528-WA, March 1976.
7. M. J. Fritts, "Lagrangian Simulations of the Kelvin-Helmholtz Instability," SAI-76-632-WA, September, 1976.
8. M. J. Fritts and J. P. Boris, "Solution of Transient Problems in Free-Surface Hydrodynamics," NRL Memorandum Report 3446,

Feb. 1977.

9. D. S. Kershaw, Private Communication.
10. N. K. Winsor, NRL Memorandum Report 3481, June 1977, to be published in Nuclear Science and Engineering.

DISCUSSIONS  
of two papers

FINITE-ELEMENT AND FINITE-DIFFERENCE SOLUTIONS  
OF NONLINEAR FREE-SURFACE WAVE PROBLEMS

S.M. Yen, K.D. Lee and T.J. Akai

TRANSIENT FREE-SURFACE HYDRODYNAMICS

M.J. Fritts and J.P. Boris

Invited Discussion

Aad J. Hermans  
Technische Hogeschool Delft

The authors should be congratulated for their contribution of numerical tools to be used in ship hydrodynamics. Both papers present methods to be used to solve the complete nonlinear free-surface problem in two-dimensional problems, while the paper of Yen et al. presents some results in three dimensions as well. Up to now these problems are considered as too complicated for solving with purely analytical tools. Papers of for instance Ogilvie, Dagan and myself show that the linearized Kelvin-Neuman problem leads to erroneous solutions at low Froude number, at least in certain two-dimensional problems. For three-dimensional problems the same errors are expected locally. Therefore it is suggested that one take into account the non-linearity in the free-surface condition.

With the aid of the very fast new-generation pipeline computer, and perhaps in the future with more sophisticated parallel processors, large computations may be carried out at rather low costs. The disadvantage, however, of the use of highly specialized numerical procedures may be that a gap will grow between numerical specialists and the physicist who likes to obtain a description of a particular physical phenomenon in ship hydrodynamics.

There are some well-known examples where computational results look similar to physical ones, although it is impossible for the mathematical model to have such a solution. However, errors in the numerical procedure make the results look that way. For instance, solutions of models without viscosity may look like solutions of equations with viscosity terms, because of the use of certain difference schemes. Therefore a sufficient amount of testing has to be carried out before the programs can be used generally.

I would like to start my discussion with the last paper where many details are presented concerning a Lagrangian method. The shear-flow problem, treated as an example for the reconnection procedure, brings forth some questions. The nonviscous interaction between two parallel streams of fluid with equal density and opposite

direction is nonstable. Figure 10 shows the development of the nonstable situation. For certain combinations of density and fluid velocity there exists a stable situation. An interesting check of whether the described picture is a physical one or just a numerical failure could be to run the program for a stable situation. I hope that this kind of information can be given in order to furnish more confidence in the method.

The paper of Yen et al. brings up some questions as well. In our paper earlier this morning we presented a numerical technique that may be modified to solve the same class of problems as treated here, but in stationary situation. In shallow-water problems it turns out that the mean surface elevation in front of the disturbance is different from the mean elevation behind the disturbance. This difference in mean level in the steady-state problem is due to a phenomenon described by Brooke Benjamin and drawn to our attention by a paper presented at the IUTAM meeting in Delft by Salvesen and von Kerczek in 1976. It turns out that if one starts at rest and gives the disturbance a constant velocity suddenly, hydraulic jumps move forward and backwards with different heights. These jumps have to be found if one describes the initial-value problem properly in the shallow-water case. Especially in the supercritical case this effect is important. In the deep-water case this effect is of no importance; therefore the results look reasonably good. However, I doubt whether in the shallow-water case the correct physical solution will come out of the numerical treatment. At last I would like to remark that the authors in their paper do not pay much attention to the Kutta condition. It may be of interest to present more details about the vortex that is left behind and its influence on the free-surface elevation.

Discussion

by Kwang June Bai  
of paper by S.M. Yen, K.D. Lee and T.J. Akai

Professor Yen and his associates should be congratulated for their successful attack on an exact nonlinear free-surface flow problem. I have only a few specific comments on their paper. (1) It seems to me that in treating a hydrofoil problem, the boundary condition  $V=0$  at the trailing edge is not convenient for the numerical

solution of potential-flow theory. From my own experience in treating a hydrofoil problem (Bai, 1978), it was convenient to use the 'numerical Kutta condition' following Hess (1972), namely that the tangential velocities on the upper and lower surfaces at the trailing edge have the same magnitude.

(2) When the Kutta condition is used, the domain of the potential flow is no longer a simply-connected region but a doubly-connected region. Therefore, there should be a cut connecting the hydrofoil surface and the outer boundary (i.e., the bottom, the free surface, or the point at infinity).

(3) The mechanism of vortex generation used here for a time-dependent potential-flow problem is not proper. For this initial-value problem, the authors make no provision for the trailing vortices which necessarily lie within a finite domain downstream of the hydrofoil.

(4) In this paper the authors propose a hybrid method that combines the finite-element method and the finite-difference method. However, I do not see any advantage of this hybrid method since it is known that the finite-element method and finite-difference method both reduce to the same final matrix equation if a proper choice of the trial function is made.

Bai, K.J., "A localized finite-element method for two-dimensional steady potential flows with a free surface," (Submitted to J. Ship Research), 1978  
Hess, J.L., "Calculation of potential flow about arbitrary three-dimensional lifting bodies," Douglas Aircraft Company, Long Beach, California, Rep. No. MDC J5679-01, Oct., 1972, 160 pages.

**Author's Reply**  
by S.M. Yen, K.D. Lee and T.J. Akai  
to discussion by Aad J. Hermans

The supercomputers would undoubtedly be useful to us in applying the existing numerical methods (the validity of which has been established) to more complex, large-scale problems such as those encountered in ship hydrodynamics and in developing more accurate computational schemes for solution of these problems. Furthermore, the computation power of such computers will enable us to treat these problems in considerably more detail; therefore, we expect that the numerical solutions obtained from the supercomputers will exhibit more accurately the physical phenomenon to be simulated. The supercomputers do present a problem to the users in that they should understand the machines' architecture (either pipeline or parallel design) in order to obtain the maximum possible computational efficiency in the implementation of a numerical scheme.

Free-surface wave problems introduce computational difficulties in accommodating the free-surface geometry, in satisfying the boundary condition at the free surface, and in treating the radiation condition. Methods devised to deal with these difficulties will introduce errors. The focus of our effort in developing numerical methods to solve these problems is to minimize equally the error from each source.

Equal attention should of course be given to the sources of error that are common to the solution of any fluid-mechanics problem, such as that due to artificial viscosity.

We used the "water table" to study qualitatively the features of high-speed compressible flow in the earlier days; therefore, we can appreciate the comments on the hydraulic jump and other features in the shallow-water free-surface flow. The observation that these flow features may lead to difficulties in solving numerically the initial-value free-surface problem in shallow water serves as a caution to people in their attempt to solve such a problem and suggests a new area of study in the numerical solution of free-surface problems.

The discussion of the treatment of the Kutta condition for the hydrofoil problem is given in the reply to Dr. Bai.

**Author's Reply**  
by S.M. Yen, K.D. Lee and T.J. Akai  
to discussion by Kwang June Bai

Our attempt is to develop numerical methods to solve the nonlinear free-surface wave problems in general. The first step of our effort is to devise computational schemes to deal with the nonlinear free-surface boundary condition, the radiation condition and the free-surface geometry. The second step is to study the feasibility of these schemes by applying them to problems of increasing complexities. In this study, methods used to treat some of the other boundary conditions encountered may have to be simplified in order to facilitate numerical experiments that are necessary to study systematically the accuracy of computations. The third step is to refine our basic computational schemes as suggested by these numerical experiments. The final step is to find the detailed solutions of nonlinear problems of interest by applying the revised methods. It is in this step that we intend to make further refinements of the treatment of boundary conditions, if necessary, that are peculiar to these problems. In our feasibility study, we applied our methods to the nonlinear problems of pressure distribution, submerged bodies and a surface-piercing body. For the hydrofoil problem, we chose a thin, symmetrical hydrofoil and neglected the circulation generated by the free surface. In the future, when we attempt to find the detailed numerical solutions of the lifting-body problems, we will use more accurate implementation of the Kutta condition and consider the potential jump. (The comments made by Dr. Bai on the treatment of the Kutta condition are pertinent, and the method he suggested to implement this condition is of interest and would indeed be useful.)

In our proposed hybrid scheme, our intention is to accommodate more accurately the complex flow geometry (e.g., the free surface in the  $Y$ -direction as shown in Fig. 21) by using the finite-element method in the near field and to facilitate the treatment of the hyperbolic feature of the radiation condition at the free surface by using the finite-difference method in the far field (in the  $X$ - $Z$  plane).

Author's Reply

by M.J. Fritts and J.P. Boris  
to discussion by Aad J. Hermans

We would like to thank Dr. Hermans for his remarks. His suggestion that the program be used to study a stable shear layer is well taken. We have conducted these tests and the detailed results may be found in our reference 7. Specifically we used several combinations of density gradients and shear layer depths at a given wavelength to test whether the unstable growth was indeed restricted to the spectral band which is theoretically predicted. For all of our calculations, the layers were stabilized in agreement with theory. Similarly, whenever the density gradients or layer depths were insufficient to achieve stabilization numerically, the theoretical limits were in agreement.

Although these calculations were performed primarily to test the program and had insufficient resolution for highly accurate results, we feel they carry more than the usual weight associated with routine testing of code. The tests also indicated the presence of symmetrical waves on the stabilized layers which were experimentally observed but not theoretically predicted. Furthermore the long-time solutions indicated that the shear layer between the Kelvin-Helmholtz billows remained stable even during the coalescence of the billows into a turbulent layer. This provided a plausible explanation for the previously unexplained phenomenon of the appearance of density gradients in the micro-layers of late-time turbulent regions formed by shear layers.

# ADVANCES IN THE CALCULATION OF STEEP SURFACE WAVES AND PLUNGING BREAKERS

Michael S. Longuet-Higgins  
Dept. of Applied Mathematics and Theoretical Physics  
University of Cambridge and Institute of Oceanographic Sciences  
Wormley, Surrey, England

## Abstract

This paper describes some new and accurate methods for the calculation of the form of steep gravity waves, and of the time-history of unsteady, breaking waves.

For steady waves, one method has been to use the small-amplitude expansion due to Stokes, but introducing a new expansion parameter which (unlike the first Fourier coefficient) increases monotonically over the permissible range. With the aid of Padé approximants, satisfactory convergence can be obtained with the use of about  $10^2$  terms. These calculations have been facilitated by the recent discovery of a new set of quadratic relations between the coefficients in Stokes's expansion.

The author and M.J.H. Fox have developed a different approach for waves of nearly limiting height, where the wave crest is still rounded. They have shown that the flow near the crest tends to a certain asymptotic form, whose length-scale  $l$  is proportional to the (non-zero) radius of curvature at the crest. This asymptotic form is the same for steady waves of any type, whether in deep or in shallow water. Using this as an "inner solution", and matching it to an "outer solution" representing the rest of the wave (wavelength  $L$ ), they have shown how to describe a steep wave by an expression involving two terms only, for sufficiently small values of  $l/L$ . The expression derived for the phase velocity confirms very accurately the previous calculations by Padé sums, and shows in particular that the phase-speed is not a monotonic function of the wave height: the highest wave is not the fastest.

For unsteady breakers, a new and accurate method was proposed by the author and developed in collaboration with E.D. Cokelet. This semi-Lagrangian method uses the values of the coordinates  $x, y$  and of the velocity-

potential  $\phi$  at the free surface only. At each time-step an integral equation is solved for the normal component of velocity  $\partial\phi/\partial n$ . The method is free of analytical approximations. It was found possible to follow the development of the free surface well beyond the point of overturning.

In more recent work Cokelet has followed the flow to the point where the tip of the breaker touches the forward face of the wave. The momentum in the jet has been found numerically to increase almost linearly with the time after overturning.

A recent calculation of the dynamical stability of steep waves has shown that as well as subharmonic instabilities of the Benjamin-Feir type there also occur local instabilities, on waves whose steepness exceeds about 93 percent of the maximum. These instabilities, and their corresponding growth rates, were calculated by a normal-mode analysis. A quite independent check has now been carried out using the time-stepping method described earlier. This has accurately confirmed the initial rates of growth and displayed the later stages of development of each type of instability. The local instabilities develop rapidly into plunging breakers. The subharmonic instabilities grow more slowly at first, but at a later stage local instabilities develop at the wave crests.

## 1. Introduction

Most theories of surface waves are valid only when the surface slope is sufficiently small, the particle accelerations are small compared to  $g$ , and the particle speeds are much less than the phase speed  $C$ . But observations of waves under the action of wind, or near the caustic of a ship-wave pattern, commonly show the wave form as quite steep and sharp-crested, sometimes breaking by turning over onto the forward face of the wave. Laboratory observations of plunging breakers also



show the particle velocity in the forwards jet may exceed 1.2 times the phase-velocity for low waves of the same length (1).

Here we shall review recent calculations under three heads (a) steep symmetric waves (b) the deformation of the wave which lead to breaking and (c) the flow in whitecaps after breaking. We also describe a new calculation of the normal-mode instabilities of steep gravity waves, which indicates that there are two different types. First, there are subharmonic instabilities of the Benjamin-Feir type. These tend to modulate the wave envelope, so that the difference between high and low waves constantly increases. Secondly there is a local type of instability, concentrated near the wave crest, which leads directly to plunging. The rates of growth of these instabilities have been accurately checked by the independent time-stepping method described under (b).

This paper is about waves without ships. Nevertheless there is reason to suppose that numerical techniques similar to those for pure gravity waves may be extended to problems involving solid bodies, and with analogous results.

## II. Steady symmetric waves

It was Schwartz (2) who discovered that for steep gravity waves, not necessarily the highest, Stokes's series must fail. This is because the parameter used by Stokes, which is effectively the amplitude  $\alpha_1$  of the first Fourier harmonic, does not increase uniformly with the wave height  $2a_1$  at constant wavenumber  $k$ . In fact  $\alpha_1$  reaches a maximum at about  $\alpha k = 0.406$  whereas the highest wave corresponds to  $\alpha k = 0.443$  (see 2, Figure 8). For the same value of  $\alpha_1$ , therefore, there can sometimes be two possible waves of the same length, with differing heights  $2a_1$ .

Schwartz (2) overcame this obstacle by using as expansion parameter not  $\alpha_1$  but  $\alpha k$ , each value of which defines a unique wave. Convergence was accelerated by use of Padé sums.

Soon afterwards (3) it was established that not only each coefficient  $\alpha_n$  but also the phase-speed  $C$  attains a maximum for waves less than the highest, in fact when  $\alpha k = 0.436$  (see Figure 1). The physical reason is connected with the fact that the highest waves are so sharp-crested that their surface profile intersects that of the waves that are slightly lower. So the profile of the higher waves lies below that of the lower waves over most of their wavelength. Hence the potential energy

of the higher waves is actually less, and their speed also.

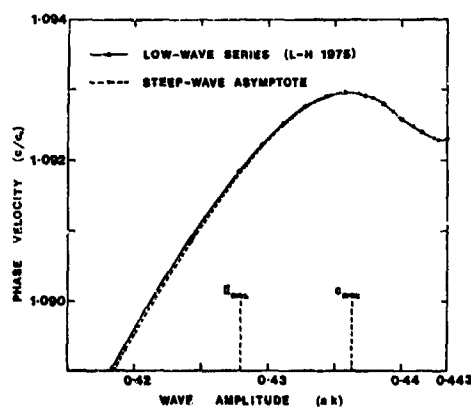


Figure 1. The phase velocity  $C$  of steep gravity waves in deep-water, relative to the speed  $C_0$  of waves of infinitesimal slope. Circles represent calculations by use of small-amplitude series, carried to high order. The broken line represents the asymptotic expressions (3.2).

These results are similar to those found for solitary waves (4). The numerical computations have been extended systematically to waves in water of finite depth  $h$  by Cokelet (5) who has given tables of important wave properties at different values of  $\alpha k$  and  $kh$ .

Numerical calculations have been facilitated by the discovery of a new set of identities between the coefficients in the expansion of the surface elevation  $\eta$  as a function of the velocity potential  $\phi$  at the free surface. Thus in deep water, if  $g = k = 1$  and

$$\eta = \frac{1}{2} H_0 + H_1 \cos \phi/c + H_2 \cos 2\phi/c + \dots$$

and if we write

$$\left. \begin{aligned} a_0 &= 1/c, \\ a_n &= n H_n / c, \quad n = 1, 2, \dots \end{aligned} \right\}$$

then we have

$$\left. \begin{aligned} \lambda a_0 + 1. a_1 a_1 + \frac{1}{2} a_2 a_2 + \frac{1}{3} a_3 a_3 + \dots &= -1 \\ 1. a_1 a_0 + \lambda a_1 + 1. a_1 a_2 + \frac{1}{2} a_2 a_3 + \dots &= 0 \\ \frac{1}{2} a_2 a_0 + 1. a_1 a_1 + \lambda a_2 + 1. a_2 a_3 + \dots &= 0 \\ \frac{1}{3} a_3 a_0 + \frac{1}{2} a_2 a_1 + 1. a_1 a_2 + \lambda a_3 + \dots &= 0 \end{aligned} \right\}$$

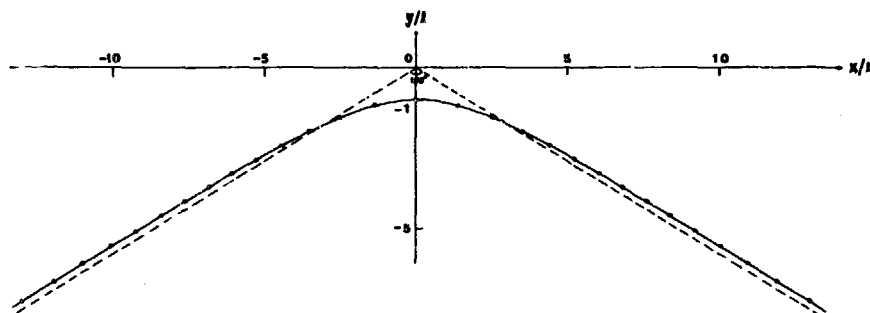


Figure 2 from Longuet-Higgins and Fox (2). Asymptotic form of the profile of a steep, progressive gravity wave.

Here  $\lambda$  is an eigenvalue, equal to  $-H_0 C_0$ . The above relations are quadratic in  $\alpha_0, \alpha_1, \alpha_2, \dots$  and  $\lambda$ . So they are both simpler and more efficient than those previously used (2).

The above relations were discovered accidentally by comparing two columns in the output of a computer program (6). But a formal proof has now been provided (8).

### III. Asymptotic methods

For steep waves, the above methods require summation of series to high order  $N$ , where  $N$  may exceed 80. A different approach (2, 10) reduces the expression of  $C$  and other integral quantities to only two terms.

It was noticed (2) that for very steep waves the forms of the wave profiles at the crest are self-similar, being scaled by the length

$$l = \psi^2 / 2g$$

where  $\psi$  denotes the particle speed at the wave crest, seen by an observer moving with the phase-speed  $C$ . For limiting waves the crest is a stagnation point at which  $\psi$  vanishes. In general  $l$  is proportional to the radius of curvature at the crest. The limiting form of the crest, at distances comparable to  $l$ , has been calculated by Longuet-Higgins and Fox (see Figure 2). Because the profile crosses its asymptotes, the maximum slope slightly exceeds  $30^\circ$ , as suspected by Sasaki and Murakami (11). The actual value is  $30.37^\circ$  (see (2)).

To calculate the complete wave profile (10) we define a small parameter  $\epsilon$  by

$$\epsilon^2 = \psi^2 / 2c_0^2 \quad (c_0^2 = g/k)$$

so that for steep waves  $\epsilon$  is small. The fluid is then divided into three zones of dimensions  $O(\epsilon^2 L)$ ,  $O(\epsilon L)$  and  $O(L)$  respectively (see Figure 3). In the inner zone I the flow is given by the asymptotic solution of reference (2). In the outer zone III the flow is given essentially by Michell's limiting solution for the highest wave, perturbed to order  $\epsilon^3$  so as to accommodate the rounded crest. Matching of the

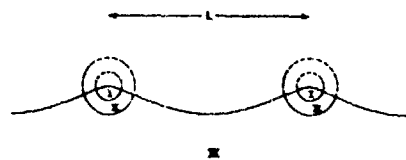


Figure 3. Zones of validity for calculating the almost-highest wave.

inner and outer solutions is accomplished in zone II. We quote the following results (10). To order  $\epsilon^3$ , the wave amplitude  $a$  and phase speed  $C$  are given by

$$\begin{aligned} ak &= 0.443 - 0.5 \epsilon^2 \\ &\quad + 0.503 \epsilon^3 \cos(2.143 \ln \epsilon - 2.54), \\ c^2 k/g &= 1.1931 \\ &\quad - 1.18 \epsilon^3 \cos(2.143 \ln \epsilon + 2.22). \end{aligned}$$

As  $\epsilon \rightarrow 0$ , the cosine gives an oscillation in  $C^2$ , damped by the factor  $\epsilon^3$ . The values are in excellent agreement with those found previously by the summation of high-order series (see Figure 1).

#### IV. Unsteady surface waves

For calculating unsteady motions and breaking waves a fully nonlinear method was proposed by the present author (12) and developed in collaboration with E.D. Cokelet. Though applied first to waves in deep water (12), (14), (15) it has also been extended to finite depth by Fenton and Mills (16).

The motion is assumed to be irrotational and periodic in space (see Figure 4) though not generally periodic in time. All calculations are carried out with the surface values of the space coordinates  $(x, y)$  and of the velocity potential  $\phi$ . For the rates of change of these quantities one has

$$\left. \begin{aligned} Dx/Dt &= \partial\phi/\partial x \\ Dy/Dt &= \partial\phi/\partial y \\ D\phi/Dt &= -p - gy + \frac{1}{2}(V\phi)^2 \end{aligned} \right\}$$

where  $D/Dt$  denotes differentiation following the motion. The last equation follows from the time-dependent Bernoulli equation and the fact that  $D\phi/Dt = \partial\phi/\partial t + (V\phi)^2$ . Hence given the surface values of  $x, y, \phi$  and  $V\phi$  at some instant  $t$  on the surface  $C$  one can calculate  $x, y$  and  $\phi$  at time  $t + dt$  on the displaced surface  $C(t + dt)$ .

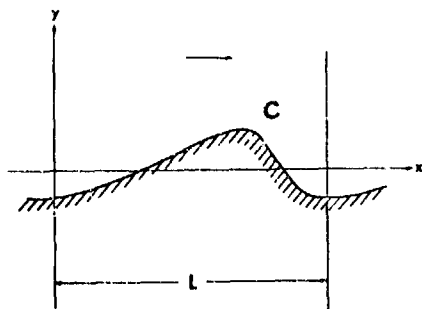


Figure 4. The free surface in the  $(x, y)$  plane.

To proceed to the next time-step we need to know both components of the velocity on  $C(t + dt)$ . We can obtain the tangential component  $\partial\phi/\partial s$  immediately, by differentiating  $\phi(t + dt)$  along the new surface. However we still lack the normal component of velocity  $\partial\phi/\partial n$  on  $C(t + dt)$ .

Now because of the space-periodicity we can transform  $C$  into a closed contour  $C'$  (Figure 5) simply by writing

$$e^{ik(x+y)} = \zeta$$

The domain of the fluid goes into the interior of  $C'$  and the points at infinite depth go into the origin  $O'$ . We then have to solve, in effect, the well-known Dirichlet problem, namely to find  $\partial\phi/\partial n$  on a contour  $C'$ , given  $\phi$  on  $C'$  and

$$\nabla^2\phi = 0$$

everywhere inside  $C'$ .

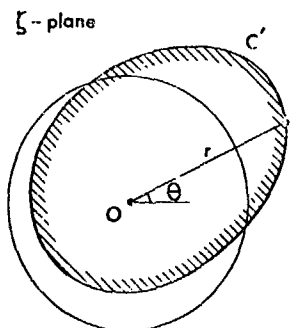


Figure 5. The surface  $C'$  in the transformed plane.

This problem can be solved as follows. Let  $R, \alpha$  denote the polar coordinates of a running point  $P$  on the boundary, relative to a fixed point  $Q$ , also on  $C'$ . Then it follows from Green's theorem that

$$\int_{C'} \left( \frac{\partial\phi}{\partial n} \right)_P \ln R \, ds = -\pi\phi_Q + \int_{C'} \phi_Q \, d\alpha$$

where in the right-hand integral we take the principle value. Since  $\phi$  is known everywhere on  $C'$ , the right-hand is given, and the equation is then a linear equation for  $\partial\phi/\partial n$  with given kernel

ln R. Solution of this equation gives us  $\partial\phi/\partial n$  on  $C(t+dt)$ , and the time-stepping can proceed.

Numerical solution of the integral equation has been carried out by Longuet-Higgins and Cokelet (12) replacing the boundary by a finite number of integration points. Typically for one wavelength. Details of the method, which are vital for its accuracy and success, are given in their paper. The method was tested for accuracy on a free symmetric wave of finite amplitude for which the form and phase-velocity were calculated independently by the method of Section II, and good agreement was obtained.

The method is evidently quite flexible and can be applied with a variety

of initial conditions. We quote three examples.

In (12) the authors assumed an initially regular progressive wave train of finite amplitude and applied to it a surface distribution of pressure such as to raise the energy of the waves smoothly to a level greater than the maximum possible ( $E_{max}$ ) for a steady wave train. The pressure was then released, so that the waves were free. They then became unsymmetric and overturned forwards (see Figure 6).

It will be noticed that the computation points, which are also marked particles, have a welcome tendency to collect near points of maximum curvature, where they are most needed for computational accuracy.

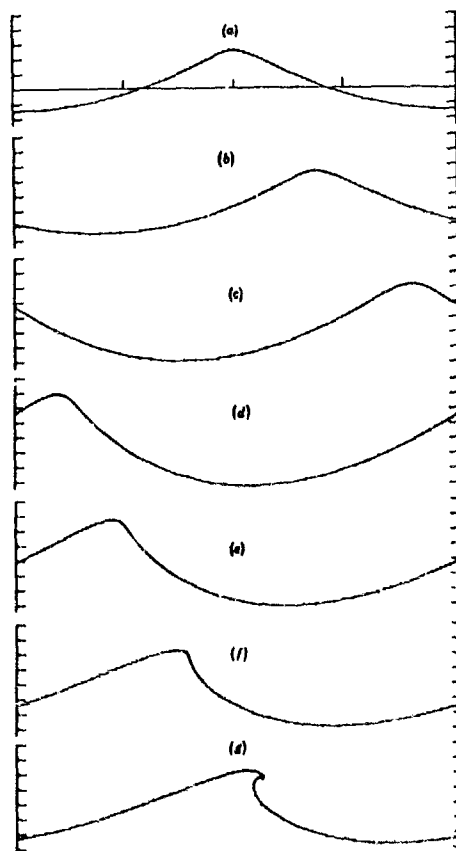


Figure 6 (from Longuet-Higgins and Cokelet (12)). Overturning of a free wave, (d) to (g), when raised to an energy level  $E = 1.88 E_{max}$  by a smoothly applied pressure at the surface, (a) to (c).

In a second example Cokelet (14) has begun with a free wave of exactly sinusoidal form but moderate or large amplitude. Thus it is not a steady wave. Without applying any pressure at the free surface, he follows the development of the wave in time, showing that it, too, curls over forwards (see Figure 7). This occurs though the total energy  $E$  of the wave may be less than  $E_{max}$ . The momentum of the jet, defined as that part of the breaker

which lies between the two vertical tangents to the surface has been followed numerically as a function of the time (see Figure 8). Once started, it appears to increase almost linearly with the time, until the tip of the jet meets the forward face of the wave.

A third example of the application of this method is given in the next section.

$$E/E_{max} = 1.67$$

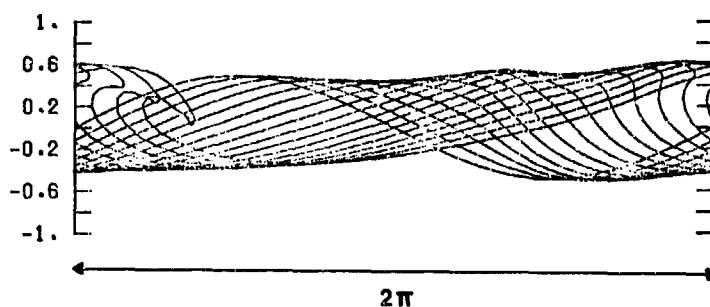


Figure 7. (from Cokelet (14)) Overturning of a free wave, initially a pure sine-wave of finite amplitude.

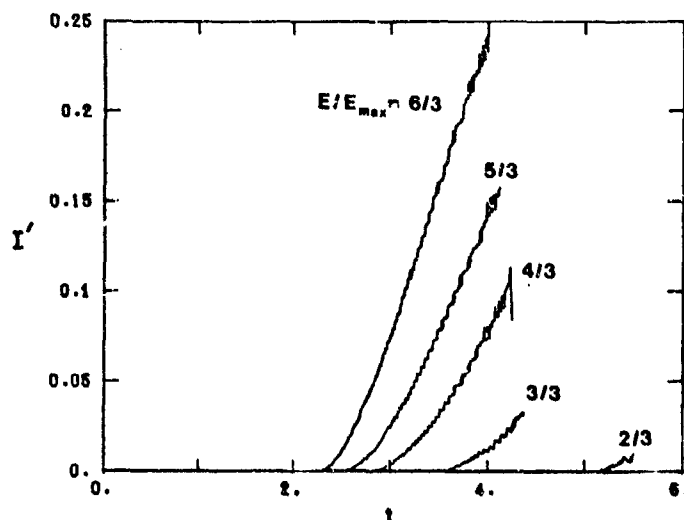


Figure 8. (from Cokelet (14)) Growth of the momentum  $I'$  in the jet as a function of time.

### V. The instabilities of steep gravity waves.

In order to understand the processes leading to wave breaking, the author (6, 7) has recently investigated systematically the stability of regular finite-amplitude gravity waves with respect to arbitrary small perturbations. In a frame of reference moving with the phase-speed of the unperturbed wave, the unperturbed motion is steady. So for the perturbed motion we may write

$$\left. \begin{aligned} x &= X(\phi, \psi) + \xi(\phi, \psi, t) \\ y &= Y(\phi, \psi) + \eta(\phi, \psi, t) \end{aligned} \right\}$$

where  $\phi, \psi$  are the velocity potential and the streamfunction taken as independent variables;  $X, Y$  represent the unperturbed, finite-amplitude wave calculated by Stokes's method or otherwise, and  $\xi, \eta$  are small, time-dependent perturbations. The free surface is given by  $\eta = \bar{F}(\phi, t)$ , where  $\bar{F}$  also is small, and all squares and products of  $\xi, \eta$  and  $\bar{F}$  are neglected.

An arbitrary perturbation may be resolved into normal modes of the form

$$\left. \begin{aligned} \xi(\phi, \psi, t) &= \hat{\xi}(\phi, \psi) e^{-i\sigma t} \\ \eta(\phi, \psi, t) &= \hat{\eta}(\phi, \psi) e^{-i\sigma t} \\ \bar{F}(\phi, t) &= \hat{F}(\phi) e^{-i\sigma t} \end{aligned} \right\}$$

where  $\sigma$  denotes the corresponding eigenfrequency. If  $\sigma$  is real, then the modes are neutrally stable. If on the other hand  $\sigma$  is complex, with a non-zero imaginary part, then the modes will grow or decay in time.

In (6) and (7) the normal modes were computed by resolving  $X, Y, \hat{\xi}, \hat{\eta}$  and  $\hat{F}$  each into a Fourier series in  $\phi$ . The calculations showed that for sufficiently small values of the steepness  $\alpha k$  of the unperturbed wave, all normal-mode perturbations are neutral, and resemble travelling waves with frequency  $n \pm |\alpha|^{1/2}$ , where  $n$  is the wavenumber of the perturbation. Thus  $n = 1$  corresponds to a perturbation that shifts the unperturbed wave through a constant phase. Since the phase-speed of the perturbed wave

is then unaltered, this perturbation is independent of time; its frequency is zero, for all  $\alpha k$ . However, as  $\alpha k$  increases from zero, each of the superharmonics  $n = 2, 3, 4, \dots$  tends generally to decrease in frequency, in this reference frame. The frequency  $\sigma_2$  of the lowest superharmonic tends towards  $\sigma_1 = 0$  at precisely the steepness  $\alpha k = 0.436\dots$  for which the phase-speed  $C$  is a maximum, indicating the onset of a local instability at this critical amplitude.

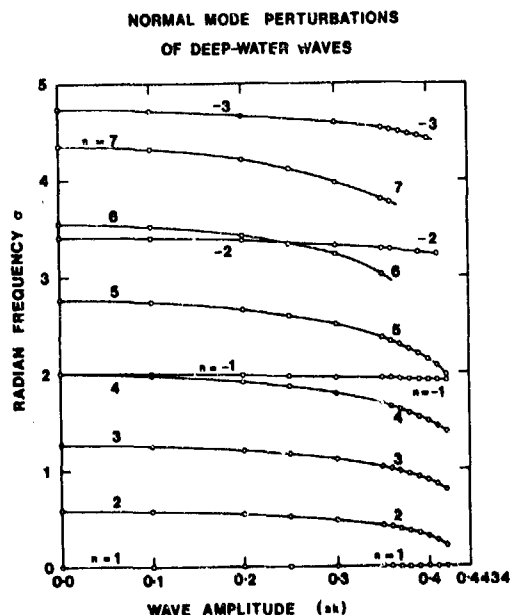


Figure 9. (from Longuet-Higgins (2)) Frequencies of normal-mode perturbations, as a function of the dimensionless amplitude  $\alpha k$  of the unperturbed wave. The ratio  $n$  corresponds to the wavenumber when  $\alpha k$  is small.

Still more interesting are the subharmonic instabilities  $|n| < 1$ , whose frequencies  $Re(\sigma)$  are shown in Figure 10. As  $\alpha R$  increases, the neutral modes  $n = \pm 1/m$  coalesce in pairs to form subharmonic instabilities of the Benjamin-Feir type. Their rates of growth  $Im(\sigma)$  are shown in Figure 10.

Consider for example the subharmonic mode  $\sigma = (4, 1/2)$ , that is to say  $n = (1/2, 1/4)$  whose basic length is twice that of the unperturbed wave. From Figure 10, this first becomes unstable at  $\alpha R = 0.220$ .

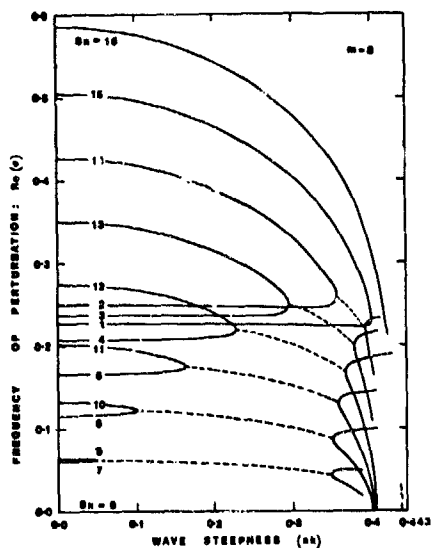


Figure 10 (from Longuet-Higgins, (8)). The frequencies of normal modes of oscillation (subharmonics) having a horizontal periodicity of  $m$  wavelengths, when  $m = 7$ . The real part of the frequency is shown as a function of the steepness  $\alpha R$  of the unperturbed wave.

It has a maximum rate of growth when  $\alpha R \approx 0.32$  and then dies out at about  $\alpha R = 0.366$ . Then at about  $\alpha R = 0.41$  a new instability arises, resulting from a coalescence with the mode  $n = 1$ . It can be shown (7) that this is to be expected at about the value of  $\alpha R$  which makes  $C$  a maximum. The new instability is localised near the crests of the original wave. It has a much greater rate of growth (see Figure 11) and is expected to be the forerunner of a plunging breaker.

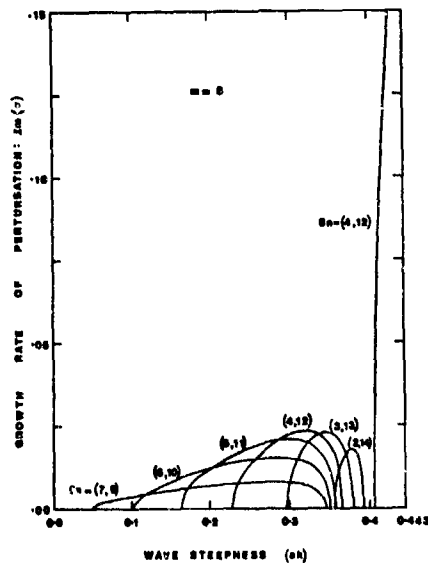


Figure 11 (from Longuet-Higgins, (8)). The rates of growth of normal modes of oscillation (subharmonics) having a horizontal periodicity of  $m$  wavelengths, when  $m = 7$ . The imaginary part of the frequency is shown as a function of the steepness  $\alpha R$  of the unperturbed wave.

To check these conclusions, obtained by a normal-mode analysis, and to extend them in time until the perturbations themselves became nonlinear, the author and E.C. Cokelet (15) have used the time-stepping method described in Section IV to follow the development of the normal mode  $(\frac{1}{2}, \frac{3}{2})$ . The motion satisfies the conditions of the analysis, being periodic in space (not time) but repeating itself every two wavelengths (see Figure 11). The perturbation, being odd, is of opposite sign on adjacent waves.

Figure 12 shows the results for the fastest-growing subharmonic instability, when  $\alpha R = 0.32$ . On the left are shown two wavelengths of the perturbed wave, with time increasing down the page. The wave is progressing to the right, in general. In the right-hand column is shown, at the top the initial perturbation imposed on the wave, with vertical scale exaggerated  $\times 20$ . At subsequent times the perturbation is defined as the difference between the perturbed wave as shown on the left, and

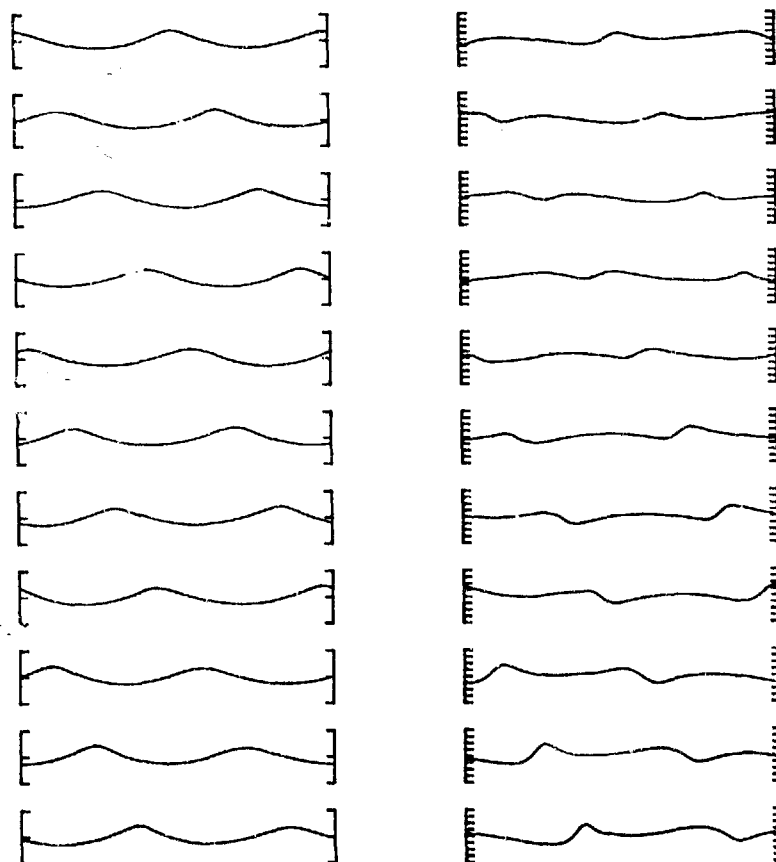


Figure 12. Time-stepped calculation of the growing perturbation  $(\frac{1}{2}, \frac{3}{2})^+$  when  $\alpha R = 0.32$ . On the left is the calculated profile, as it develops through one half-cycle of the perturbation (time increases downwards). On the right is shown the perturbation magnified vertically times 20.



the unperturbed wave advanced to the right with the phase speed. Figure 12 encompasses one half-cycle of the perturbation, during which the perturbation can be seen to have grown and to have reversed in sign, relative to the unperturbed wave. Thus the wave crest which was initially more peaked has become

more flattened, and vice versa.

Figure 13 shows the results of carrying the computation of the unstable mode  $(1/2, 3/2)^+$  for a further half-cycle. By this time the steeper crest has developed a sharp curvature.

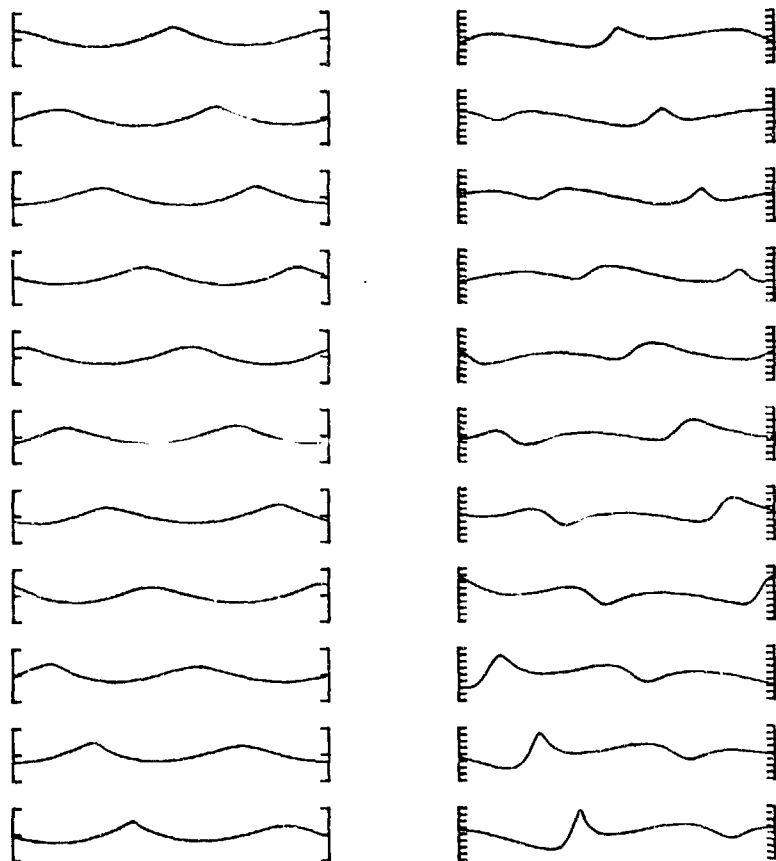


Figure 13. (continuation of Figure 12). Further development of the growing perturbation  $(1/2, 3/2)^+$  when  $\alpha k = 0.32$ .

The rate of growth of the perturbation was calculated as follows. Let  $f_0(x)$  and  $f_t(x)$  denote the perturbations at times  $t = 0$  and  $t/\sigma$  (a half-period) respectively. Then the apparent rate of growth  $\beta'$  was taken as

$$\beta' = t^{-1} \ln (\bar{f}_t / \bar{f}_0)$$

where  $\bar{f}$  denotes the r.m.s. value of  $f$ . In this case the calculated value of  $\bar{f}_t / \bar{f}_0$  was 1.51 giving  $\beta' = .0254$  (see Table 1) compared to the value  $\beta = .0234$  obtained by the normal-mode analysis.

As a check, the correlation coefficient  $C(f_0, f_t, \Delta x)$  between  $f_0(x)$  and  $f_t(x + \Delta x)$  was also calculated, and maximised with respect to  $\Delta x$ . The maximum correlation coefficient  $C(f_0, f_t)$  was in this case 0.039 (see Table 1).

The corresponding decaying perturbation was also tested. The rate of decay was found to be  $\beta' = -0.0175$ . The correlation coefficient  $C(f_0, f_t)$  was only slightly less than for the increasing mode.

Figure 14 shows a close-up of the wave profile of Figure 13 during the final stage of overturning, as seen in a frame of reference moving with the speed  $c_0$ .

of low waves. The interval between successive profiles is only 0.02 of the basic wave period, so that the final overturning takes place very rapidly.

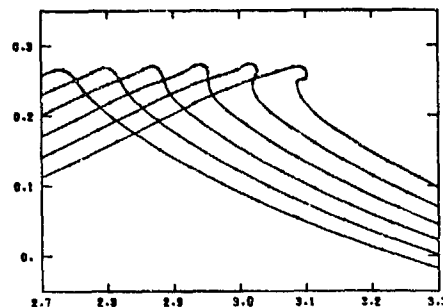


Figure 14. Close-up of the overturning crest corresponding to Figure 13 ( $0.8 = 0.52$ ) in a reference frame moving with speed  $c_0$ . The time between successive profiles is 1/50 of the wave period.

Table 1. Comparison of calculated rates of growth of perturbations.

$uk$	Normal-mode calculation				Time-stepping with integral equation			
	$n$	$Re(\omega)$	$\frac{1}{2}T$	$\beta = Im(\omega)$	$N$	$t$	$C(f_0, f_t)$	$\beta'$
0.10	1/2	.2072	15.17	.0000	90	$\frac{1}{2}T$	.999	.0001
	3/2	.2753	11.41	.0000	90	$\frac{1}{2}T$	.996	-.0001
0.20	1/2	.2098	14.57	.0003	90	$\frac{1}{2}T$	.996	.0001
	3/2	.2406	13.06	.0000	90	$\frac{1}{2}T$	.988	.0
0.25	$(1/2, 3/2)^+$	.2150	14.61	.0132	90	$\frac{1}{2}T$	.990	.0138
	$(1/2, 3/2)^-$	.2150	14.61	-.0132	90	$\frac{1}{2}T$	.985	-.0125
0.32	$(1/2, 3/2)^+$	.1931	16.27	.0234	90	$\frac{1}{2}T$	.939	.0254
	$(1/2, 3/2)^-$	.1931	16.27	-.0234	90	$\frac{1}{2}T$	.880	-.0175
0.38	1/2	.1804	17.41	.0000	90	$\frac{1}{2}T$	.993	-.0009
	3/2	.1309	24.00	.0000	120	$\frac{1}{2}T$	.875	-.0040
0.40	1/2	.1840	17.07	.0000	90	$\frac{1}{2}T$	.855	.0065
0.41	$(1/2, 3/2)^+$	.0000	$\infty$	.064	120	0.5	.96	.065

A crucial test of the normal-mode analysis was carried out on the mode at the basic amplitude  $\alpha R = 0.39$ . According to Figures 9 and 10, the mode at this amplitude should have become neutrally stable, that is, the rate of growth should be zero. At  $\alpha R = 0.39$  there are actually two branches, which for convenience may be designated  $n = 1/2$  (the upper branch) and  $n = 3/2$  (the lower).

Figure 15 shows the development of the mode  $n = 1/2$ . After one half-cycle the perturbation returns closely to its original value, with a change of sign but without appreciable magnification (see Table 1). The magnification of the mode  $n = 3/2$  at this value of  $\alpha R$  is also small.

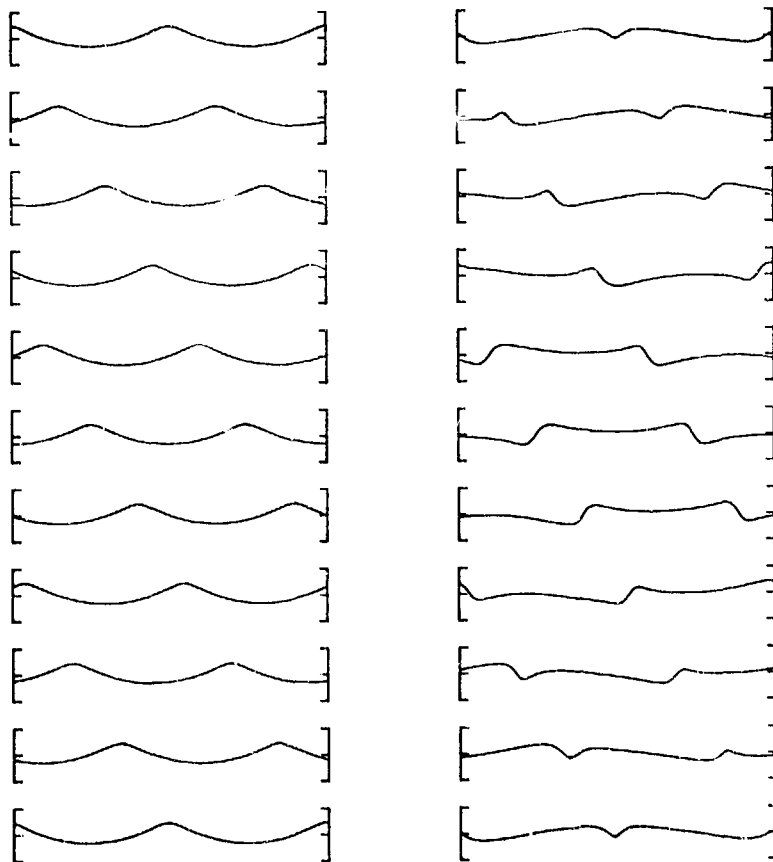


Figure 15. Development of the neutral mode  $n = 1/2$  at  $\alpha R = 0.39$ . On the left is the time-stepped wave profile; on the right is the perturbation enlarged vertically by a factor of 20.

Finally Figure 16 shows the growing mode at  $\alpha k = 0.41$ . The original perturbation is clearly very local, being concentrated at the wave crests. It

grows very rapidly, at about 10 times the rate of the fastest-growing subharmonic instability.

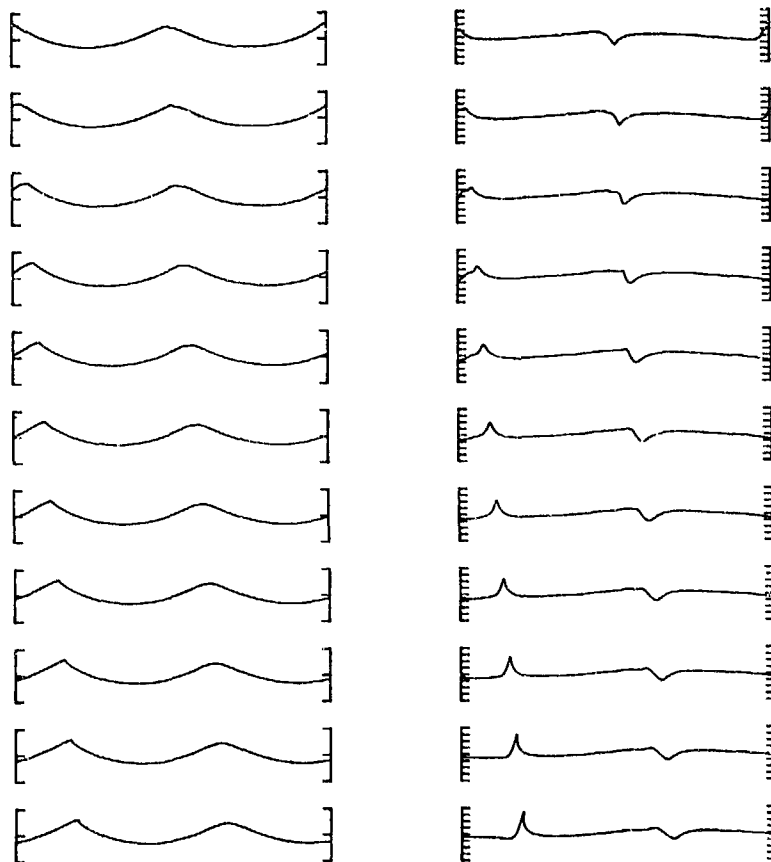


Figure 16. Development of the unstable mode  $n = (1/2, 1/2)^+$  at  $\alpha k = 0.41$ . On the left is the time-stepped wave profile; on the right is the perturbation enlarged vertically by a factor 5.

Figure 17 shows a close-up of the fluid overturning. It is so similar to Figure 14 that we may conclude that in both cases the dynamics of the final overturning are governed by the local flow, and are virtually independent of the rest of the wave.

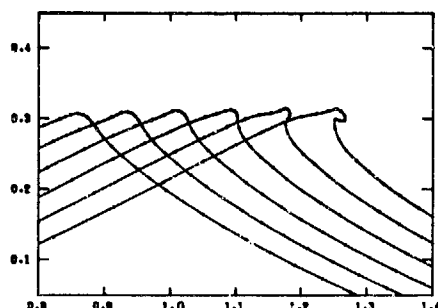


Figure 17 Close-up of the overturning crest corresponding to Figure 16 ( $\Delta R = 0.41$ ) in a frame moving with speed  $C_0$ . The time between successive profiles is  $1/50$  of the wave period.

#### VI. Waves after breaking

The present calculations take no account of surface tension, air currents, shearing in the upper layers of the water, or of finite depth, when this is appropriate. In principle at least, all these effects might possibly be included in the numerical method. However, after the tip of the jet has met the forward face of the wave, an altogether new type of analysis is required, in order to model the entrainment of air and the turbulent diffusion of momentum and vorticity. Whitecaps which are in a quasi-steady state, corresponding to "spilling" breakers, appear to offer the simplest situation for analysis. A model which represents the whitecap as a fluid of lower density riding on the forward face of a steep, steady wave, has been suggested by the authors and J.S. Turner (18). While correctly predicting the conditions necessary for whitecap formation, this simple model will undoubtedly require some modification to take account of the repeated injection of fluid by overturning at the crest, and the continuous loss of buoyancy by air bubbles rising through the surface.

#### References

- (1) Van Dorn, W.G. Laboratory investigation of wave breaking. Part II: Deep water waves. Scripps Institution of Oceanography, AOEL Report 71 (1975).
- (2) Schwartz, L.W. Computer extension and analytic continuation of Stokes's expansion for gravity waves. *J. Fluid Mech.* 62 (1974) 553-578.
- (3) Longuet-Higgins, M.S. Integral properties of periodic gravity waves of finite amplitude. *Proc. R. Soc. Lond. A* 342 (1975) 157-174.
- (4) Longuet-Higgins, M.S. and Fenton, J.D. On the mass, momentum, energy and circulation of a solitary wave. II. *Proc. R. Soc. Lond. A* 340 (1974) 471-493.
- (5) Cokelet, E.D. Steep gravity waves in water of arbitrary uniform depth. *Phil. Trans. Roy. Soc. A* 286 (1977) 183-230.
- (6) Longuet-Higgins, M.S. The instabilities of gravity waves on deep water. I Superharmonics. *Proc. R. Soc. Lond. A* in press, (1978).
- (7) Longuet-Higgins, M.S. The instabilities of gravity waves on deep water. II Subharmonics. *Proc. R. Soc. Lond. A* in press, (1978).
- (8) Longuet-Higgins, M.S. Some new relations between Stokes's coefficients in the theory of gravity waves. *J. Inst. Math. Applic.*, in press, (1978).
- (9) Longuet-Higgins, M.S. and Fox, M.J.H. Theory of the almost-highest wave. The inner solution. *J. Fluid Mech.* 80 (1977) 721-74.
- (10) Longuet-Higgins, M.S. and Fox, M.J.H. Theory of the almost-highest wave. II. Matching and analytic extension. *J. Fluid Mech.*, in press, (1978).
- (11) Sasaki, K. and Murakami, T. Irrotational, progressive surface gravity waves near the limiting height. *J. Oceanogr. Soc. Japan*, 29 (1973) 94-105.

- (12) Longuet-Higgins, M.S. Breaking waves.  
Proc. D.C.A.M.M. Symposium, Lyngby, Copenhagen, March 1973.
- (13) Longuet-Higgins, M.S. and Cokelet, E.D. The deformation of steep surface waves on water. I. A numerical method of computation.  
Proc. R. Soc. Lond. A. 350 (1976) 1-26.
- (14) Cokelet, E.D. Numerical experiments on the deformation of steep water waves.  
Proc. I.M.A. Conf. on Mathematics in Oceanography, University of Bristol, June 1977.
- (15) Longuet-Higgins, M.S. and Cokelet, E.D. The deformation of steep surface waves on deep water. II. Development of normal instabilities.  
In preparation, Sept. 1977.
- (16) Fenton, J.D. and Mills, D.A. Shallowing waves and tsunamis: Numerical solutions of an exact integral equation.  
Proc. IUTAM Symposium on Waves on water of variable depth, Canberra, July 1976.
- (17) Benjamin, T.B. Instability of periodic wavetrains in nonlinear dispersive systems.  
Proc. R. Soc. Lond. A. 299 (1967) 59-67.
- (18) Longuet-Higgins, M.S. and Turner, J.S. An entraining plume model of a spilling breaker.  
J. Fluid Mech. 63 (1974) 1-20.

# NUMERICAL SOLUTIONS OF TRANSIENT NONLINEAR FREE-SURFACE MOTION OUTSIDE OR INSIDE MOVING BODIES

Odd M. Faltinsen  
Division of Ship Hydrodynamics  
Norwegian Institute of Technology  
Trondheim, Norway

## Abstract

A numerical method is derived for study of two-dimensional nonlinear transient problems of a body oscillating in a free surface. At each timestep the velocity potential is represented by a distribution of sources and dipoles over the wetted body surface and the free surface. Properties of fluid particles on the free surface are used to step the solution forward in time. A formula to calculate the exact force on the body is presented. A solution to a linear transient problem is derived. The solution agrees well with the nonlinear transient solution. The sloshing problem is briefly discussed.

## Nomenclature

$(x, y)$  coordinates, (see figure 1)  
 $\phi(x, y, t)$  velocity potential  
 $t$  time variable  
 $\zeta(x, t)$  free surface elevation  
 $g$  acceleration of gravity  
 $\dot{y}_0(t)$  forced vertical velocity of the cylinder  
 $\vec{n}$  unit normal vector to the surface (positive into the fluid)  
 $n_y$  y-component of  $\vec{n}$   
 $S$  wetted body surface (mean wetted surface in linear theory)  
 $S_\infty$  vertical control surfaces at  $x = \pm \infty$   
 $S_F$  free surface  
 $S_B$  horizontal control surface far down in the fluid  
 $b(t)$  is so defined that when  $|x| > b(t)$  the flow can be approximated by a dipole at the centre of the body  
 $V$  volume enclosed by  $S$ ,  $S_F$ ,  $S_\infty$  and  $S_B$   
 $A$  defined by equation (9)  
 $(\xi_j, \eta_j)$  coordinates of endpoints of the segments (see figure 1)  
 $(\bar{x}_j, \bar{y}_j)$  coordinates of midpoints of the segments (see figure 1)  
 $\rho$  mass density of the fluid  
 $A_{33}$  added mass coefficient in heave  
 $B_{33}$  damping coefficient in heave  
 $\omega$  Fourier transform variable  
 $\Omega$  circular frequency of forced oscillation

$\Phi$  Fourier transform of velocity potential  
 $Y_0$  Fourier transform of forced vertical velocity  
 $a$  radius of circular cylinder  
 $\alpha$  small quantity defined by equation (40)  
 $A_3$  amplitude of forced heave motion  
 $F$  Hydrodynamic vertical force on cylinder minus linear restoring force ( $-\rho g 2ay_0(t)$ )

## 1. Introduction

Nonlinear free surface problems are of importance in many ocean engineering contexts. An example is sloshing of fluid in a ship tank. Other examples are the influence of steep surface waves on marine structures and the slow drift oscillations of a moored structure or a low-waterplane area large-volume structure in irregular waves. Linear theory is commonly used in predicting wave-induced motions and loads on a ship. But nonlinear effects cannot be ignored in extreme weather conditions or for extreme shipforms (for example ships with large bowflare).

Nonlinear free surface problems are difficult to solve. The mathematical difficulty of the problem arises essentially from the need to satisfy the condition of constant pressure at a free surface which not only is unknown, but whose form is highly time dependent. Finite element methods and finite difference methods have been applied with good results to some nonlinear free surface problems. But in this paper we apply a Green's function boundary-integral-equation technique which is thought to require less computer storage and computer time than finite difference and finite element methods. This kind of method has gained good reputation in predicting two dimensional added mass and damping coefficients (Frank (1)) and linear wave-induced motions and loads on large offshore structures (Faltinsen and Michelsen (2)). Ogilvie (3) suggested using the boundary-integral-equation technique to solve a nonlinear free surface problem arising in wave resistance

analysis. A similar technique was applied by Longuet-Higgins and Cokelet (4) to study the deformation of steep surface waves. Faltinsen (5) applied and modified Ogilvie's ideas to study sloshing of fluid in a rectangular tank forced to oscillate harmonically in sway mode.

In this paper the boundary-integral-equation technique is applied to a nonlinear two dimensional free surface problem with a body oscillating harmonically with forced vertical velocity in the free surface. The amplitude of oscillation is finite. We neglect viscosity and assume incompressible fluid and irrotational flow. The exact nonlinear free surface conditions are satisfied. The problem is solved as an initial-value problem. When the problem has been solved for one time-instant, the free surface conditions are used to find the free surface position and the velocity potential on the free surface for the next time-instant. At each time instant the velocity potential is represented by a distribution of sources and dipoles over the wetted body surface and the free surface. Unknowns at each timestep are the velocity potential on the wetted body surface and the normal derivative of the velocity potential on the free surface. These are found by solving an integral equation. The numerical calculations are significantly reduced by representing the flow far away from the body by a dipole with singularity in the centre of the body.

A formula to calculate the exact force on the body is presented. In the formula it is only necessary to know the velocity potential on the positions of the free surface and the wetted body surface.

In order to gain some confidence in the nonlinear theoretical predictions, the corresponding linear transient problem is solved. The solution was found by Fourier transform technique. The nonlinear theory agrees well with the linear theory for small amplitudes of oscillation.

The solution to the interior problem, i.e., the sloshing problem is only discussed briefly in this paper, since it will be published separately (Faltinsen (5)).

## 2. Theoretical Formulation

Consider an infinitely long horizontal rigid cylinder of arbitrary cross-section that is forced vertically in a free surface. Let the water be infinite in extent and be of infinite depth. Initially the water is calm. The origin of the coordinate system is in the plane of the undisturbed water surface. The y-axis is positive upwards and goes

through the center of gravity of the cylinder. The y-axis is symmetry line for the cross-section. The x-axis is in the undisturbed water plane.

We assume the fluid to be incompressible and the flow irrotational so that there exists a velocity potential  $\phi$  that satisfies the Laplace equation

$$\frac{\partial^2 \phi}{\partial x^2} + \frac{\partial^2 \phi}{\partial y^2} = 0 \quad (1)$$

in the fluid domain. The pressure is set equal to a constant atmospheric pressure on the free surface. Neglecting surface tension, we can write the dynamic free surface condition as

$$g\zeta + \frac{\partial \phi}{\partial t} + \frac{1}{2} \left[ \left( \frac{\partial \phi}{\partial x} \right)^2 + \left( \frac{\partial \phi}{\partial y} \right)^2 \right] = 0$$

on  $y = \zeta(x, t)$  (2)

Here  $g$  is the acceleration of gravity,  $y = \zeta(x, t)$ , the free surface shape, and  $t$  is the time variable.

The kinematic free surface condition can be written as

$$\frac{\partial \zeta}{\partial t} - \frac{\partial \phi}{\partial y} + \frac{\partial \phi}{\partial x} \frac{\partial \zeta}{\partial x} = 0$$

on  $y = \zeta(x, t)$  (3)

We set the initialvalue condition

$$\phi = 0 \quad \text{on the free surface } \zeta = 0 \quad (4)$$

For a linear system this implies

$$\frac{\partial \phi}{\partial t}(x, 0, 0) = 0 \quad (5)$$

Other initialvalue conditions would have been possible. We write the velocity of the cylinder as  $\dot{y}_0(t)\hat{j}$ , where  $\hat{j}$  is the unit vector along the positive y-axis. The boundary condition on the wetted body surface can be written as

$$\frac{\partial \phi}{\partial n} = \dot{y}_0(t)\hat{j} \cdot \hat{n} \equiv \dot{y}_0(t)n_j \quad (6)$$

where  $\hat{n}$  is unit normal vector to the body and  $\partial/\partial n$  is the derivative along this normal vector. We assume  $\hat{n}$  to be positive into the fluid.

## 3. Solution Procedure

By applying Green's second identity to the velocity potential  $\phi$  and

$$\psi = \log \sqrt{(x-x_1)^2 + (y-y_1)^2}$$

we can write

$$\oint_S \left( \phi \frac{\partial \psi}{\partial n} - \psi \frac{\partial \phi}{\partial n} \right) ds = 0 \quad (7)$$



where

$$S' = S + S_\infty + S_B + S_F + S_1$$

Here  $S$  is the wetted body surface,  $S_\infty$  vertical control surface at  $x = \pm \infty$ ,  $S_B$  horizontal control surface far down in the fluid,  $S_F$  the free surface and  $S_1$  is a cylindrical surface of small radius  $r_1$  and with axis through  $(x_1, y_1)$  which is a point in the fluid domain. The contribution from  $S_B$  and  $S_\infty$  are both zero. Note that for the steady state case the contribution from  $S_\infty$  is not zero.

We can now write

$$\begin{aligned} & -2\pi\phi(x_1, y_1) \\ & = \int_{S_F+S} \left\{ \phi(x, y) \frac{\partial}{\partial n(x, y)} \log \sqrt{(x-x_1)^2 + (y-y_1)^2} \right. \\ & \quad \left. - \log \sqrt{(x-x_1)^2 + (y-y_1)^2} \frac{\partial \phi(x, y)}{\partial n(x, y)} \right\} ds(x, y) \end{aligned} \quad (8)$$

The contribution from the free surface integral can be rewritten. For  $|x| > b(t)$  where  $b(t)$  is a large number dependent on time, we can write

$$\phi(x, y) \sim \frac{Ay}{x^2 + y^2} \quad (9)$$

where  $A$  is at present unknown.

We can write

$$\begin{aligned} & \int_b^\infty \left\{ \phi(x, y) \frac{\partial}{\partial n(x, y)} \log \sqrt{(x-x_1)^2 + (y-y_1)^2} \right. \\ & \quad \left. - \frac{\partial \phi(x, y)}{\partial n(x, y)} \log \sqrt{(x-x_1)^2 + (y-y_1)^2} \right\} dx \Big|_{y=0} \\ & \sim \int_b^\infty \frac{A}{x^2} \log \sqrt{(x-x_1)^2 + y_1^2} dx = I(x_1, y_1) \end{aligned} \quad (10)$$

In a similar way we can write the contribution from integration from  $-\infty$  to  $-b$  in equation (8) as

$$\begin{aligned} J(x_1, y_1) &= \\ &= \int_{-\infty}^{-b} \frac{A}{x^2} \log \sqrt{(x-x_1)^2 + y_1^2} dx \end{aligned} \quad (11)$$

It is possible to show analytically that

$$\begin{aligned} I &= A \left\{ \frac{\ln \sqrt{(b-x_1)^2 + y_1^2}}{b} - \frac{x_1}{x_1^2 + y_1^2} \right. \\ & \quad \left. - \ln \left( \frac{\sqrt{(b-x_1)^2 + y_1^2}}{b} \right) + \frac{y_1}{x_1^2 + y_1^2} \right\} \\ &= \left( \operatorname{sgn}(y_1) \frac{\pi}{2} - \arctg \left( \frac{b-x_1}{y_1} \right) \right) \end{aligned} \quad (12)$$

Further we can write

$$J(x_1, y_1) = I(-x_1, y_1) \quad (13)$$

The problem will be solved by a time step integration procedure. For each timestep equation (8) will be solved with  $\partial\phi/\partial n$  as the unknown along the free surface,  $\phi$  as the unknown along the wetted body boundary and with  $(x_1, y_1)$  as points on the body surface and the free surface.

In the numerical evaluation of equation (8) the free surface  $S_F$  and the wetted body surface  $S$  are divided into a number of segments, and  $\phi$  and  $\partial\phi/\partial n$  are set constant over each segment. An example of the subdivision of one part of the surface is shown in Figure 1 where the  $x-y$  coordinates of the endpoints and midpoints of the segments are denoted by  $(\bar{x}_j, \bar{y}_j)$  and  $(x_j, y_j)$ .

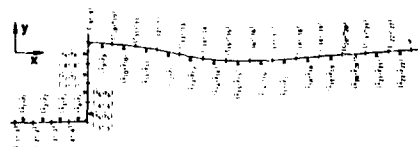


FIGURE 1  
EXAMPLE OF SUBDIVISION OF BODY  
SURFACE AND FREE SURFACE

respectively. In fig. 1 only segments on a small portion of the free surface are shown. In general, it is necessary to have segments over a much larger part of the free surface. But by using (10)-(13) it is unnecessary to cover the complete free surface. Due to the symmetry of the problem, the segments for  $x > 0$  can be reflected about the  $y$ -axis to represent the body and the free surface for  $x < 0$ .

Using the subdivision in figure 1 as an example together with the symmetry properties of the fluid motion we can rewrite the integral equation resulting from equation (8) as a linear algebraic equation with  $\phi(x_j, y_j)$  ( $j=1,8$ ) and  $\frac{\partial \phi}{\partial n}(\bar{x}_j, \bar{y}_j)$  ( $j=9,22$ ) as the unknown, i.e.

$$\begin{aligned} & A_{1,1}\phi(\bar{x}_1, \bar{y}_1) + \dots + A_{1,8}\phi(\bar{x}_8, \bar{y}_8) \\ & + A_{1,9}\frac{\partial \phi}{\partial n}(\bar{x}_9, \bar{y}_9) + \dots + A_{1,22}\frac{\partial \phi}{\partial n}(\bar{x}_{22}, \bar{y}_{22}) \\ & = B_1 \\ & \vdots \\ & A_{22,1}\phi(\bar{x}_1, \bar{y}_1) + \dots + \\ & A_{22,22}\frac{\partial \phi}{\partial n}(\bar{x}_{22}, \bar{y}_{22}) = B_{22} \end{aligned} \quad (14)$$

Here

$$A_{ij} \begin{matrix} i=1,22 \\ j=1,8 \end{matrix} = 2\pi K +$$

$$+ \int_{\Delta_j} \frac{\partial}{\partial n(x,y)} [\log \sqrt{(x-\bar{x}_1)^2 + (y-\bar{y}_1)^2}] ds(x,y)$$

$$+ \int_{\Delta_{-j}} \frac{\partial}{\partial n(x,y)} [\log \sqrt{(x-\bar{x}_1)^2 + (y-\bar{y}_1)^2}] ds(x,y)$$

$$A_{ij} \begin{matrix} i=1,22 \\ j=9,22 \end{matrix} =$$

$$- \int_{\Delta_j} [\log \sqrt{(x-\bar{x}_1)^2 + (y-\bar{y}_1)^2}] ds(x,y)$$

$$- \int_{\Delta_{-j}} [\log \sqrt{(x-\bar{x}_1)^2 + (y-\bar{y}_1)^2}] ds(x,y) + F$$

where  $K=j$  when  $i=j$  and  $K=0$  when  $i \neq j$ . Further  $F$  is zero except when  $j=22$ . Then

$$F = -\bar{x}_{22}^2 \cdot (I(\bar{x}_1, \bar{y}_1) + J(\bar{x}_1, \bar{y}_1)) / A$$

Further

$$B_i = \sum_{j=1}^8 \frac{\partial \phi}{\partial n}(\bar{x}_j, \bar{y}_j) C_{ij} + \sum_{j=9}^{22} \phi(\bar{x}_j, \bar{y}_j) C_{ij} \quad (i=1,22)$$

where

$$C_{ij} \begin{matrix} i=1,22 \\ j=1,8 \end{matrix}$$

$$= \int_{\Delta_j} [\log \sqrt{(x-\bar{x}_1)^2 + (y-\bar{y}_1)^2}] ds(x,y)$$

$$+ \int_{\Delta_{-j}} [\log \sqrt{(x-\bar{x}_1)^2 + (y-\bar{y}_1)^2}] ds(x,y)$$

$$C_{ij} \begin{matrix} i=1,22 \\ j=9,22 \end{matrix}$$

$$= -2\pi K -$$

$$\int_{\Delta_j} \frac{\partial}{\partial n(x,y)} [\log \sqrt{(x-\bar{x}_1)^2 + (y-\bar{y}_1)^2}] ds(x,y)$$

$$- \int_{\Delta_{-j}} \frac{\partial}{\partial n(x,y)} [\log \sqrt{(x-\bar{x}_1)^2 + (y-\bar{y}_1)^2}] ds(x,y)$$

Analytical expressions for the integrals above can be derived (see Faltinsen (5)). The integration is

either over segment no  $j$   $\Delta_j$  or the segment  $\Delta_{-j}$  which is the image of  $\Delta_j$  about the  $y$ -axis. The expression for

$$\frac{\partial \phi(\bar{x}_j, \bar{y}_j)}{\partial n} \quad (j=1,8)$$

follows directly from the body boundary condition.

The expressions for the velocity potential  $\phi$  on the free surface and the free surface position are obtained by the following timestepping procedure. Looking on a fluid particle on the free surface we can write (see equation (2))

$$\frac{D\phi}{Dt} = \frac{\partial \phi}{\partial t} + \frac{\partial \phi}{\partial x} \frac{\partial \phi}{\partial x} + \frac{\partial \phi}{\partial y} \frac{\partial \phi}{\partial y} \quad (15)$$

$$= -g\zeta + \frac{1}{2} \left[ \left( \frac{\partial \phi}{\partial x} \right)^2 + \left( \frac{\partial \phi}{\partial y} \right)^2 \right]$$

Further, from equation (3),

$$\frac{D\zeta}{Dt} = \frac{\partial \phi}{\partial y} \quad (16)$$

and

$$\frac{Dx_F}{Dt} = \frac{\partial \phi}{\partial x} \quad (17)$$

where  $x_F$  is the  $x$ -coordinate of the fluid particle.

Knowing the velocity potential at the free surface and the coordinates of particles on the free surface at some time instants, equations (15), (16) and (17) provide means to find the change with time of these variables.

In the numerical calculation procedure the free surface particles will not always correspond to midpoints on the free surface elements. When the fluid characteristic is known at the midpoints, the fluid characteristic at the fluid particles will be determined by interpolation, and vice versa when the fluid characteristic of the fluid particles are known. The time stepping procedure is performed by the Runge-Kutta method. It is possible that a less time-consuming method could also have been used with satisfactory results.

#### 4. Force Calculation

After the fluid motion has been determined, the Bernoulli equation may be used to obtain the force on the body; however, we will follow another procedure, which will be derived below. Salvesen (6) has used a similar procedure, but one important term is missing in his expression.

The hydroinduced force  $\vec{F}$  on the body

can be written

$$F = -\iint_{S_F} p_1 \vec{n} dS + \iint_{S_F} \rho g y \vec{n} dS \quad (18)$$

where the total pressure  $p$  (excluding atmospheric pressure) is

$$p = p_1 - \rho g y = -\rho \frac{\partial \phi}{\partial t} - \frac{\rho}{2} |\nabla \phi|^2 - \rho g y \quad (19)$$

Applying Gauss' theorem we can write

$$\begin{aligned} -\iint_{S_F} p_1 \vec{n} dS &= -\rho \iint_V \left\{ \nabla \frac{\partial \phi}{\partial t} + \frac{1}{2} \nabla |\nabla \phi|^2 \right\} d\tau \\ &+ \iint_{S_F} p \vec{n} dS + \iint_{S_F} \rho g y \vec{n} dS \\ &= -\rho \iint_{S_\infty} \left\{ \frac{\partial \phi}{\partial t} + \frac{1}{2} |\nabla \phi|^2 \right\} \vec{n} dS \end{aligned} \quad (20)$$

where  $V$  is the volume enclosed by  $S, S_F, S_\infty$  and  $S_B$ . Since  $p = 0$  on  $S_B$  the second integral on the right hand side is equal to zero. We can write:

$$\begin{aligned} \frac{d}{dt} \iint_V \nabla \phi d\tau &= \iint_V \nabla \frac{\partial \phi}{\partial t} d\tau \\ &= -\iint_{S_F} \nabla \phi \frac{\partial \phi}{\partial n} dS \end{aligned} \quad (21)$$

Substituting (21) into (20) gives

$$\begin{aligned} -\iint_{S_F} p_1 \vec{n} dS &= -\rho \frac{d}{dt} \iint_V \nabla \phi d\tau \\ &= -\iint_{S_F} \nabla \phi \frac{\partial \phi}{\partial n} dS \\ &= -\frac{\rho}{2} \iint_V \nabla |\nabla \phi|^2 d\tau + \iint_{S_F} \rho g y \vec{n} dS \\ &= -\rho \iint_{S_\infty} \left\{ \frac{\partial \phi}{\partial t} + \frac{1}{2} |\nabla \phi|^2 \right\} \vec{n} dS \end{aligned} \quad (22)$$

Applying Gauss' theorem we can write

$$\begin{aligned} \frac{d}{dt} \iint_V \nabla \phi d\tau &= -\frac{d}{dt} \iint_{S_F} \phi \vec{n} dS \\ &= -\iint_{S_\infty} \frac{\partial \phi}{\partial t} \vec{n} dS \end{aligned} \quad (23)$$

We can write

$$\begin{aligned} -\iint_{S_F} p_1 \vec{n} dS &= \rho \frac{d}{dt} \iint_{S_F} \phi \vec{n} dS - \rho \iint_{S_F} \nabla \phi \frac{\partial \phi}{\partial n} dS \\ &= \frac{\rho}{2} \iint_V \nabla |\nabla \phi|^2 d\tau + \iint_{S_F} \rho g y \vec{n} dS \end{aligned}$$

$$= \frac{\rho}{2} \iint_{S_\infty} |\nabla \phi|^2 \vec{n} dS$$

Again Gauss' theorem can be used to show that

$$-\iint_{S_F} \nabla \phi \frac{\partial \phi}{\partial n} dS = \frac{1}{2} \iint_V \nabla |\nabla \phi|^2 d\tau$$

We can now write

$$\begin{aligned} -\iint_{S_F} p_1 \vec{n} dS &= \rho \frac{d}{dt} \iint_{S_F} \phi \vec{n} dS + \iint_{S_F} \rho g y \vec{n} dS \\ &+ \rho \iint_{S_\infty} \left\{ \nabla \phi \frac{\partial \phi}{\partial n} - \frac{1}{2} |\nabla \phi|^2 \vec{n} \right\} dS \end{aligned}$$

Hence, the hydrodynamic force is

$$\begin{aligned} \vec{F} &= \rho \frac{d}{dt} \iint_{S_F} \phi \vec{n} dS + \iint_{S_F} \rho g y \vec{n} dS \\ &+ \rho \iint_{S_\infty} \left\{ \nabla \phi \frac{\partial \phi}{\partial n} - \frac{1}{2} |\nabla \phi|^2 \vec{n} \right\} dS \end{aligned} \quad (24)$$

The second term in (24) was not included in the formula derived by Salvesen (6).

In a transient problem we can neglect the contribution from  $S_\infty$ . The hydroinduced force during the transient phase can therefore be written as

$$\vec{F} = \rho \frac{d}{dt} \iint_{S_F} \phi \vec{n} dS + \iint_{S_F} \rho g y \vec{n} dS \quad (25)$$

A special case of this formula is used in wave impact problems, for instance to calculate the wave induced loads on horizontal truss members in the splash zone or to calculate hydrodynamic forces on bowflare sections. In those cases the boundary condition  $\phi = 0$  is used on the undisturbed free surface. Equation (25) can then be written

$$\begin{aligned} \vec{F} &= -\frac{d}{dt} (A_{33}(\omega) \dot{y}_0(t)) \\ &+ \iint_{S_F} \rho g y \vec{n} dS \end{aligned} \quad (26)$$

where  $A_{33}(\omega)$  is the infinite frequency added mass coefficient in heave as a function of submergence. The last term is the hydrostatic pressure force as a function of submergence.

### 5. Linear Theory

In order to gain some confidence in the nonlinear theoretical prediction, a

solution to the corresponding linear transient problem has been derived. Ursell (7) and Maskell and Ursell (8) have studied transient free motion of a two dimensional body in a free surface, while we are interested in the transient forced motion.

The formulation of the linear problem is very similar to the formulation of the nonlinear problem given in Chapter 2. We assume no motion when  $t < 0$ . The velocity potential  $\phi$  satisfies the Laplace equation (1). The linearized free surface condition can be written as

$$\frac{\partial^2 \phi}{\partial t^2} + g \frac{\partial \phi}{\partial y} = 0 \text{ on } y = 0 \text{ outside the body} \quad (27)$$

The body boundary condition is given by (6) but evaluated on the mean body surface position. The initial value conditions are given by (4) and (5). We want to find the force component

$$f_3(t) = -\int_S p n_3 dS = \rho \int_S \frac{\partial \phi}{\partial t} n_3 dS \quad (28)$$

Note that the dynamic effect due to change in hydrostatic force is neglected. This can be written as  $-\rho g B y_0(t)$  where  $B$  is beam at the water line.

We take the Fourier transform with respect to time of the equations. The Fourier transform of the velocity potential and the velocity can be written as

$$\phi(x, y, \omega) = \int_0^\infty e^{i\omega t} \phi(x, y, t) dt \quad (29)$$

$$y_0(\omega) = \int_0^\infty e^{i\omega t} y_0(t) dt \quad (30)$$

where  $i$  is the complex unit.

The integration is only from 0 to  $\infty$  because the variables are zero for  $t < 0$ . The inversion formula is of the form

$$\phi(x, y, t) = \frac{1}{2\pi} \int_{-\infty}^\infty e^{-i\omega t} \phi(x, y, \omega) d\omega \quad (31)$$

By using the initial value conditions (4) and (5) and similar conditions when  $t \rightarrow \infty$  we can write the following equations

$$\frac{\partial^2 \phi}{\partial x^2} + \frac{\partial^2 \phi}{\partial y^2} = 0 \quad (32)$$

$$-\omega^2 \phi + g \frac{\partial \phi}{\partial y} = 0 \text{ on } y = 0 \quad (33)$$

$$\frac{\partial \phi}{\partial n} = y_0(\omega) n_3 \text{ on mean position of the body} \quad (34)$$

To define the  $\phi$ -problem completely an additional condition is necessary. But from equation (31) we note that  $\phi$  can be written as a sum of an infinite number

wave components. This implies

$$\frac{\partial \phi}{\partial r} + \frac{i\omega^2}{g} \phi = 0 \text{ as } r \rightarrow \infty \quad (35)$$

according as  $\omega \geq 0$

The solution to the  $\phi$ -problem may now be obtained. The solution is by no means trivial, but is routine calculation in strip theory calculation of ship motion, (see for instance Ursell (9), Frank (1)).

It is the force that we want to determine here. The Fourier transform of the force, can be written as

$$F_3(\omega) = \int_0^\infty e^{i\omega t} f_3(t) dt \quad (36)$$

$$= -i\omega \rho \int_S \phi(x, y, \omega) n_3 dS - \rho \int_S \phi(x, y, 0) n_3 dS$$

When  $\omega > 0$  we can write

$$F_3(\omega) = -i\omega Y_0(\omega) \{-A_{33}(\omega) - \frac{1}{\omega} B_{33}(\omega)\} - \rho \int_S \phi(x, y, 0) n_3 dS \quad (37)$$

where  $A_{33}(\omega)$  and  $B_{33}(\omega)$  are added mass and damping coefficients in heave, respectively. When  $\omega < 0$  we note that

$$F_3(-\omega) = \overline{F_3(\omega)} \quad (38)$$

where the bar denotes complex conjugate.

When  $F_3(\omega)$  is obtained,  $f_3(t)$  can in principle be obtained by Fourier inversion.

#### Special Case

Consider a circular cross-section with axis in mean free surface. The radius is  $a$ . The forced velocity is written as

$$\dot{y}_0(t) = \cos \Omega t \quad (39)$$

To circumvent mathematical difficulties we write

$$\dot{y}_0(t) = e^{-\alpha t} \cos \Omega t \quad (40)$$

where  $\alpha$  is a small quantity which later will approach zero. We can write (see (30))

$$Y_0(\omega) = \frac{1}{\alpha - i\omega - \Omega^2} + \frac{1}{\alpha - i\omega + \Omega^2} \quad (41)$$

Since  $\dot{y}_0(0) = 1$  and  $\phi(x, 0, 0) = \frac{\partial \phi}{\partial t}(x, 0, 0) = 0$  we can write

$$-\rho \int_S \phi(x, y, 0) n_3 dS = A_{33}(-\omega) \quad (42)$$

This implies that

$$F_3(\omega) = -i\omega \cdot \frac{1}{a-i\omega-i\Omega} + \frac{1}{a-i\omega+i\Omega} \quad (43)$$

$$= (-A_{33}(\omega) - \frac{i}{\omega} B_{33}(\omega)) + A_{33}(\omega)$$

when  $\omega > 0$ .

Using (38) we can write the force on the body as

$$f_3(t) = \frac{1}{2\pi} \int_0^\infty e^{-i\omega t} F_3(\omega) d\omega$$

$$+ \frac{1}{2\pi} \int_0^\infty e^{-i\omega t} F_3(\omega) d\omega \quad (44)$$

The integrals in (44) converge. According to Ursell (9)

$$A_{33}(\omega) - \frac{i}{\omega} B_{33}(\omega)$$

$$= \frac{p\pi}{2} a^2 (1 - \frac{4g}{3\pi\omega^2 a}) \text{ when } \omega \rightarrow \infty \quad (45)$$

This implies  $F_3(\omega) = O(\omega^{-2})$  when  $\omega \rightarrow \infty$  which ensures that the integrals converge. On the other hand they are cumbersome to calculate due to slow convergence and singularities close to the real axis. To circumvent this problem we introduce a path  $C^+$  in the complex plane (see figure 2). The contour of integration is deformed into a contour  $C^+$  which goes from 0 to  $\infty$ ,

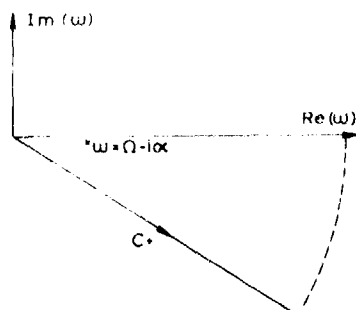


FIGURE 2  
DEFORMATION OF THE CONTOUR  
OF INTEGRATION

which lies entirely in the fourth quadrant, which passes below the pole  $\omega = \Omega - i\alpha$ , and which also satisfies the condition that no other pole lies between the real axis and  $C^+$ . The gap at  $\infty$  between  $C^+$  and the real  $\omega$ -axis is closed at  $\infty$  by a large circular arc. Then by Cauchy's theorem

$$\oint_{C^+} f(\omega) d\omega = -2\pi i (\text{residue at } \Omega - i\alpha)$$

for the contribution from the large circular arc vanishes. We choose the contour of integration along the ray  $\arg(\omega) = -\arctg(\frac{1}{2})$ .

We can now write

$$f_3(t) = 2\text{Re} \left\{ \frac{1}{2\pi} \int_{C^+} e^{-i\omega t} F_3(\omega) d\omega \right\}$$

$$+ \Omega \sin \Omega t A_{33}(\Omega) - \cos \Omega t \quad (46)$$

where  $a$  has been set equal to  $\Omega$  and  $\text{Re}$  means the real part.

The last two terms represent the steady-state solution, i.e., the solution when  $t \rightarrow \infty$ . To calculate the transient term we need to evaluate

$$F_3(\omega) = - \frac{\omega^2}{\omega^2 - \Omega^2} \Lambda_1 + A_{33}(\omega) \quad (47)$$

Here  $\Lambda_1$  is the analytic continuation of  $A_{33} - \frac{i}{\omega} B_{33}$  along the ray  $\arg(\omega) = -\arctg(\frac{1}{2})$ .  $\Lambda_1$  can be calculated in the way presented by Maskell(10). A computer program based on his procedure has been prepared. Numerical results for  $\Lambda_1$  are shown in figure 3.

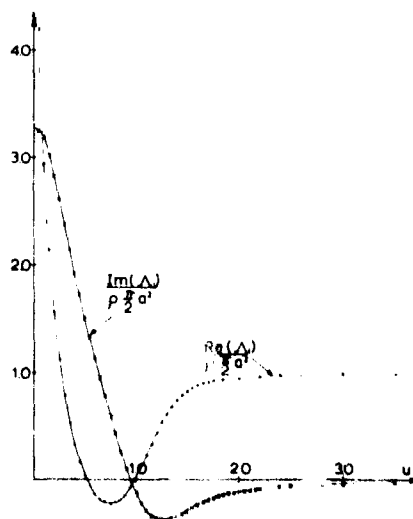


FIGURE 3  
CALCULATION OF FORCE COEFFICIENT  
ALONG THE ARRAY ( $\omega/\Omega = 0.1-0.5$ )

The asymptotic solution when  $\omega \rightarrow 0$  is

$$\frac{A_1(\omega/\frac{a}{g})}{\rho \frac{\pi}{2} a^2} = \frac{8}{\pi^2} \left\{ \frac{-(\ln Ka - \pi i) - \gamma + \frac{3}{2} - 2 \ln 2 + \dots}{1 - \frac{2}{\pi} Ka (\ln Ka - \pi i)} \right\} \quad (48)$$

Here  $Ka = \frac{\omega^2 a}{g}$  and  $\gamma = 0.57725385$ . When  $\omega \rightarrow \infty$ ,

$$\frac{A_1}{\rho \frac{\pi}{2} a^2} \sim 1 - \frac{4}{3\pi Ka} \quad (49)$$

The transient term can be easily calculated when  $A_1$  is obtained. There are no singularities of the integrand close to  $C^+$  and the integrand decays exponentially for large arguments along the integration path.

#### 6. Numerical Results

Results by the nonlinear and the linear transient solution methods are presented in figures 4 to 7. The

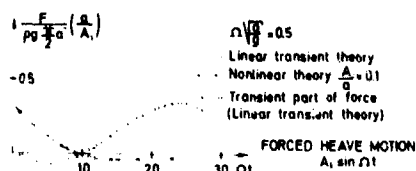


FIGURE 4  
HYDRODYNAMIC FORCE ON CIRCULAR CYLINDER  
(EXCLUDED LINEAR RESTORING FORCE)

forced oscillation frequencies are  $\Omega/\frac{a}{g} = 0.5, 0.8, 1.0$  and  $1.5$ , respectively. The results are for a circular cross-section of radius "a" with axis in

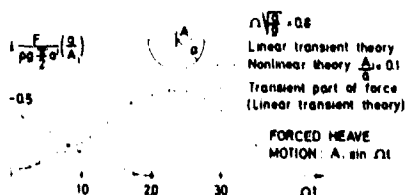


FIGURE 5  
HYDRODYNAMIC FORCE ON CIRCULAR CYLINDER  
(EXCLUDED LINEAR RESTORING FORCE)

the mean free surface. The forced heave motion is  $A_1 \sin \Omega t$  where the nonlinear results are for  $A_1/a = 0.1$ . Fourteen surface elements of equal length were

used on the total wetted cylinder surface. In the case of

$$\Omega/\frac{a}{g} = 0.5, 0.8, 1.0$$

the same length was used initially on the surface elements on the free surface. Number of free surface elements were 60 total. This implies that  $b = 7.73$  when  $\omega = 1$ . In the case of

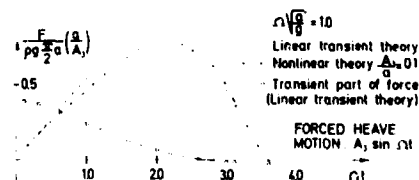


FIGURE 6  
HYDRODYNAMIC FORCE ON CIRCULAR CYLINDER  
(EXCLUDED LINEAR RESTORING FORCE)

$\Omega/\frac{a}{g} = 1.5$ , 40 equal surface elements were used. The results are presented as hydrodynamic vertical force  $F$  on the

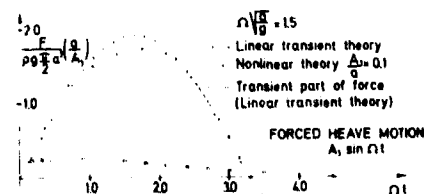


FIGURE 7  
HYDRODYNAMIC FORCE ON CIRCULAR CYLINDER  
(EXCLUDED LINEAR RESTORING FORCES)

cylinder nondimensionalized by  $\rho g \frac{\pi}{2} a A_1$  as a function of  $\Omega t$ . In the hydrodynamic force is excluded the linear restoring force  $-\rho g 2ay_0(t)$ . The nonlinear solution method agrees well with the linear solution method. We note that the transient part of the force is appreciable for small  $\Omega t$ -values except when  $\Omega/\frac{a}{g} = 1.5$ . But the transient-force part dies rapidly out and steady-state oscillation is nearly reached within the first oscillation period.

The numerical results by the nonlinear method will depend on the number and the length of the surface elements. The length of the elements must not exceed a certain fraction of the wave lengths. The number of surface elements will be a function of time,  $\omega$ , to be more precise,  $b$  is a function of time. For instance, the solution procedure becomes invalid when a surface wave has reached  $b$ . In reality the solution pro-

cedure becomes invalid even before that time. This has been studied to some extent by varying  $b$ . The initial length of the free surface elements are kept equal to  $\frac{1}{4}a$ . Results for  $\Omega/\frac{a}{g} = 1.0$  and  $0.5$  are presented in figures 8 and 9. The amplitude ratio  $\frac{A_1}{a}$  is 0.1. Based on these results

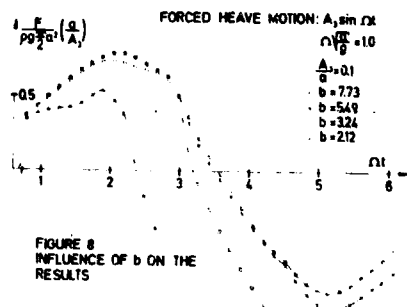


FIGURE 8  
INFLUENCE OF  $b$  ON THE RESULTS

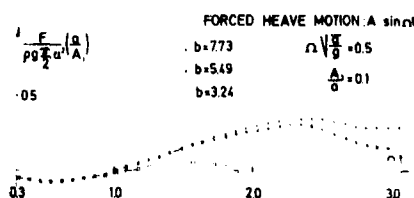


FIGURE 9  
INFLUENCE OF  $b$  ON THE RESULTS

figure 10 has been prepared. It shows  $(\Omega t)_{\text{FAILURE}}$  as a function of

$$\left(\frac{b}{a} - 1\right) \frac{2\Omega^2 a}{g}$$

where  $(\Omega t)_{\text{FAILURE}}$  is defined as the  $\Omega t$

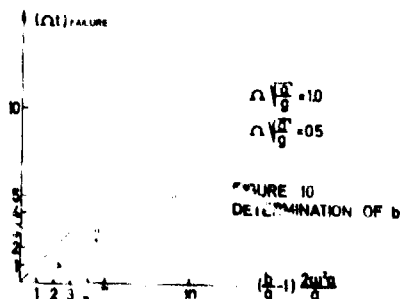


FIGURE 10  
DETERMINATION OF  $b$

when the solution fails for given  $b$ . There will always be some ambiguity involved in determining  $(\Omega t)_{\text{FAILURE}}$ .

One should note that

$$\Omega t = \left(\frac{b}{a} - 1\right) \frac{2\Omega^2 a}{g}$$

defines the time the energy in an Airy wave of circular frequency  $\Omega$  takes to propagate from  $a$  to  $b$ .  $(\Omega t)_{\text{FAILURE}}$  seems to be lower than this value.

The nonlinearity has been studied by varying  $\frac{A_1}{a}$  for given  $\Omega/\frac{a}{g}$ . Results for  $\Omega/\frac{a}{g} = 1.0$  and  $\frac{A_1}{a} = 0.1, 0.2$  and  $0.25$  are presented in figure 11. Results for

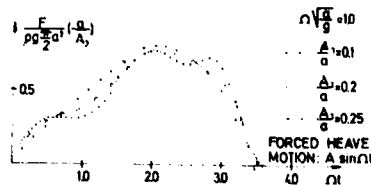


FIGURE 11  
HYDRODYNAMIC FORCE ON CIRCULAR CYLINDER  
(EXCLUDED LINEAR RESTORING FORCES)

$\frac{A_1}{a} = 0.3, 0.4$  and  $0.6$  are presented in figure 12. Number of free surface elements are 40. Their initial lengths are  $0.3a$ . To my knowledge there exist neither analytical methods nor modeltest results to compare with in the transient phase. For steady-state conditions C. M. Lee (11) has presented nonlinear ana-

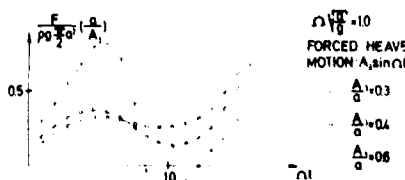


FIGURE 12  
HYDRODYNAMIC FORCE ON CIRCULAR CYLINDER  
(EXCLUDED LINEAR RESTORING FORCES)

lytical results for forced vertical oscillation of a cylinder in a free surface. He assumes small amplitude of oscillation. What small amplitude of oscillation means is a question of experience, but it is questionable if  $\frac{A_1}{a} = 0.4$  and  $0.6$  can be denoted small amplitude of oscillation. C.M.Lee solves the problem by perturbation technique to second order in forced oscillation amplitude. His results include first harmonic and second harmonic forced oscillations in addition to a timeindependent vertical force. C.M.Lee's results do not show a significant influence of nonlinearity. This is logi-

cally inherent in assuming the linear first order harmonic term to be dominating. Our results indicate a more significant influence of nonlinearity. This is especially true when  $A_3/a = 0.6$ . Although the possibility of numerical errors exist, the results for  $A_3/a = 0.6$  can to some extent be rationally explained. The initial phase of small  $\Omega t$ -values correspond to high suddenly exposed forced vertical velocity and resulting high fluid accelerations. As in wave impact problems a good approximation to the vertical hydrodynamic force (excluding the hydrostatic force) would be

$$F = \frac{d}{dt} (A_{33}(\omega) \dot{y}_0(t)) \quad (50)$$

where  $A_{33}(\omega)$  is the infinite frequency added mass in heave as a function of submergence measured relative to initial calm free surface. Equation (50) has been compared with the results by the complete nonlinear transient method. The results are presented in figure 13 and agrees quite well up to  $\Omega t \sim 0.5$  where the result by the complete nonlinear theory starts to decline. This decline

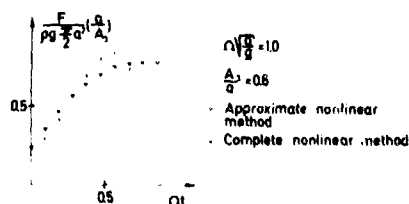


FIGURE 13  
HYDRODYNAMIC FORCE ON CIRCULAR CYLINDER  
(EXCLUDED LINEAR RESTORING FORCES)

cannot be easily explained, but it should be noted that the results for smaller amplitude ratios have a similar behaviour.

#### 7. Interior Problem

The interior problem, i.e. the sloshing problem, has also been studied. No details will be given here since a separate paper has been devoted to this subject (Raitinen (6)). In the sloshing problem we are studying forced harmonic sway-oscillation of a rectangular tank. But the method is thought to be applicable for the case of forced irregular oscillation of a combination of modes and to a wide class of tanks with two-dimensional flow. In general the approach is the same as in the exterior problem presented above. There are differences. These are:

a) The body boundary condition is linearized. In many cases this is no limitation. In resonance condition the

nonlinearity in the free surface condition is much more significant than the nonlinearity in the body boundary condition.

b) The velocity potential is represented as a distribution of sources over the body surface and the free surface. In the exterior problem both sources and dipoles were used. In principle both approaches are right.

c) In the sloshing problem the free surface position and the velocity potential on the free surface are obtained by following "points" on the free surface with constant horizontal coordinate. In the exterior problem we are following fluid particles.

d) In the sloshing problem it is necessary to introduce an artificial damping term of the Rayleigh viscosity type in the nonlinear free surface condition, i.e. we add a term  $\mu \phi$  to the left hand side of the dynamic free surface condition (2). The damping is small, but essential because there is no damping in a potential flow inside a tank. By examining the analytical solution of the linear transient sloshing problem, we will note that transient terms will not die out if damping is not present. In reality (i.e. model tests) a steady-state oscillation is clearly seen. Damping is therefore introduced and represents a substitute for viscous losses primarily in the boundary layer close to the tank wall.

e) In the sloshing problem it is necessary to solve the problem over a substantial number of oscillation periods to achieve steady-state oscillation. In the exterior problem steady-state oscillations will nearly be achieved within the first oscillation period.

An example of the calculations is shown in figure 14 for a rectangular tank that is forced to oscillate harmonically in sway. The tank breadth is

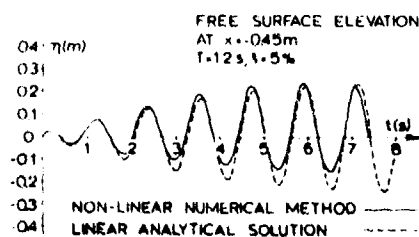


FIGURE 14



1 m and the mean water depth is 0.5 m. The sway amplitude is 0.025 m and the oscillation period is 1.2 s which is close to the natural period 1.18 s for the fluid motion. An artificial damping of 5% of the critical damping is used. The figure shows free surface elevation at the tank wall as a function of time. The nonlinear numerical method is compared with a linear analytical solution which has been derived as a mean to control the numerical results. The agreement is reasonable. The nonlinear solution shows the typical nonlinear behaviour that the distance from mean surface level to the trough is smaller than the distance from the mean surface level to the crest.

The intention with the method is not to study the fine details of the motions i.e. local breaking. We are more interested in the gross-motion of the fluid. This implies that rather few marked points (order of magnitude  $\approx 10$ ) are needed on the free surface to describe the fluid motion. This is advantageous due to the substantial number of oscillation periods necessary to reach steady-state oscillation.

#### Conclusions

Boundary-integral equation technique has been applied to study nonlinear transient problems of bodies oscillating in a free surface and to the sloshing problem. A linear transient theory for the exterior problem has been derived. This solution agrees well with the nonlinear transient method for small amplitude of oscillations. It shows that transient effects die out rapidly. Steady-state conditions are nearly reached within the first oscillation period. The opposite is true in the sloshing problem where an artificial damping term has to be introduced to achieve steady-state oscillations. The nonlinear transient method shows a significant effect of nonlinearity which to some extent can be rationally explained. But before proceeding further with numerical studies it seems wise to perform modeltests for large amplitudes of forced oscillation.

The method presented in this paper is quite general. In principle it applies to any type of forced velocity and cross-sections. But problems are anticipated when the free surface normal and the body surface normal at the intersection between the free surface and the body surface are not close to orthogonal.

#### References

1. Frank, W. "Oscillation of Cylinders in or Between the Free Surface of Deep Fluids", NSRDC, Washington D.C. Report No. 2375, 1967.

Falkenberg, O. and Michelsen, F.C. "Motions of Elastic Structures in Waves at Low Froude Number", International Symposium on the Dynamics of Marine Vehicles and Structures in Waves, University College, London, 1973.

Eqiliv, A.P. "Nonlinear High-Froude Number Ship-Surface Problems", Journal of Engineering Mathematics, 1974, 15-235.

4. Longuet-Higgins, M.H. and Cokelet, E.D. "The formation of steep surface waves on water. A numerical method of computation", Proc. R.Soc. London, 1976, 359-261.
5. Falkenberg, O. "A numerical nonlinear method of sloshing in tanks with two-dimensional flow." To be published in the Journal of Ship Research.
6. Sarpkaya, T. "Second Order Steady-State Effects of Moments on Surface Ship in Oblique Regular Waves", International Symposium on the Dynamics of Marine Vehicles and Structures in Waves, University College, London, April 1974.
7. Ursell, F. "The decay of the free motion of a floating body", J. Fluid Mech., vol. 10, 1962, 9.
8. Maskell, S.J. and Ursell, F. "The transient motion of a floating body", J. Fluid Mech., vol. 14, part 2, pp. 303-313, 1962.
9. Ursell, F. "On the heaving motion of a circular cylinder on the surface of a fluid", Quart. J. Mech. Appl. Math. 2, 218-231, 1949.
10. Maskell, S.J. "Computations on the free motion of a floating body", Ph.D. Dissertation, University of Manchester, 1964.
11. Lee, C.M. "The Second-Order Theory of Heaving Cylinders in a Free Surface", Journal of Ship Research, vol. 12, pp. 313-327, 1968.

## NUMERICAL SIMULATION OF SHIP MOTION BY EULERIAN HYDRODYNAMIC TECHNIQUES\*

G. I. Bourianoff and B. R. Penumallil  
Austin Research Associates, Inc.  
Austin, Texas

\*This work was sponsored by the Office of Maritime Technology of the U.S. Maritime Administration.

### Abstract

A ship motion simulation technique is described which utilizes Eulerian hydrodynamic techniques to solve for the free surface flow field in the vicinity of the ship. The ship constitutes one of the boundaries on the flow field. The ship motion is calculated by summing the hydrodynamic forces and couple on the ship and solving Newton's equation. This technique has been applied to modeling the motion of a moored ship in random beam seas in two dimensions and three degrees of freedom. The computed results agree very well with the model test results.

### I. Introduction

The operation of large ships in shallow coastal waters has created a need for predictive methods to analyze the fluid flow fields and ship motion encountered in this environment. Existing techniques do not in general handle this problem very well. The geometry encountered is complicated enough that analytic methods can solve only very simplified models. Existing numerical techniques generally solve the problem in the frequency domain using linearized boundary conditions and simplified bottom geometries. The Inertial Marker Particle (IMP) method described here is an essentially new approach to the problem of predicting ship motion.

The method involves solving the Euler hydrodynamic equation coupled with the rigid body equation of motion for the ship. The ship constitutes one of the boundaries of the fluid flow region and is treated as a reactive boundary which is free to move in response to forces exerted on it and obeys the appropriate equations of motion.

The boundaries will not in general coincide with the grid lines and it is necessary to interpolate the relevant conditions to the

boundary location. A substantial fraction of the code is devoted to accomplishing this task accurately.

The main features of the existing code are: (1) nonlinear treatment of ship-wave interaction; (2) arbitrary two dimensional geometry; (3) calculating ship motion in irregular or regular waves; and (4) arbitrary mooring forces on the ship.

The code has been validated against model results for a spring moored vessel exposed to irregular beam seas. The computed sway agrees very well with the measured quantities.

The computer code as currently implemented runs approximately four times slower than real time on a CDC 6600 computer system.

Chapter II discusses the Mathematical Formulation of the problem. Chapter III presents the numerical techniques which we have employed. Chapter IV presents the simulation results while Chapter V gives conclusions.

### II. Mathematical Formulation

The equations satisfied by the fluid in the absence of the ship are the incompressible viscous flow equations shown in equations (2.1) and (2.2).

$$\text{div } \vec{V} = 0 \quad (2.1)$$

$$\frac{\partial \vec{V}}{\partial t} + (\vec{V} \cdot \nabla) \vec{V} = - \nabla p + \nabla \cdot (\gamma \nabla \vec{V}) \quad (2.2)$$

where

$\vec{V}$  = fluid velocity vector.

$p$  = pressure normalized to the density.

$\gamma$  = artificial kinematic viscosity.

$\nabla$  = "del" vector differential operator.

This is coupled with the equations of ship motion which are

$$m_s \frac{d\vec{v}_s}{dt} = - \int p \, d\vec{n}_v + m_s \vec{g} \quad (2.3)$$

$$I_n \frac{d\vec{\Omega}}{dt} = - \int \vec{p} \times (p \, d\vec{n}_v) \quad (2.4)$$

where

$m_s$  = mass of the ship

$\vec{v}_s$  = velocity of the center of mass of the ship

$d\vec{n}_v$  = surface area in the direction of  $\vec{v}_s$

$I_n$  = moment of inertia about an axis perpendicular to the plane of  $\vec{\Omega}$

$\vec{g}$  = acceleration due to gravity

$\vec{p}$  = vector from metacenter to the marker particle on surface

$\vec{\Omega}$  = angular velocity about the axis of  $I_n$

The motion of the particles is subject to the fact that the particles are constrained to lie on the surface of a rigid body. If  $(x, y)$  marks the position of a representative inertial marker particle, then

$$x_{\text{new}} = x_{\text{old}} + v_{xs} \delta t - \Omega_z \rho_y \delta t \quad (2.5)$$

$$y_{\text{new}} = y_{\text{old}} + v_{ys} \delta t + \Omega_z \rho_x \delta t \quad (2.6)$$

where

$\rho_x, \rho_y$  are the components of the vector from the metacenter to the IMP under consideration.

$v_{xs}, v_{ys}$  are the components of the translational velocity of the body.

$\Omega_z$  is the rotational velocity of the body.

The kinematical boundary condition at the ship-fluid interface is that the fluid velocity equal the body velocity.

On a stationary curved wall rigid boundary, the requirement is that normal fluid velocity equal zero. Further all rigid boundaries are assumed free slip. The appropriate boundary condition on a free surface is that it cannot support any stress.

### III. Solution Techniques

The solution method to be presented utilizes the salient features of modified SUMMAC [1] method with respect to the computation of flow field and free surface and the ABMAC [2] method with respect to the treatment of curved wall and moving boundaries. The computation is performed over a finite difference mesh encompassing the region of interest. For fluid dynamic calculations it is customary to use a set of staggered meshes one for each of the primitive variables (velocities and pressure). The staggered mesh scheme is the result of considerable experimentation [3] and appears to be the most successful scheme for fluid dynamic calculations. It allows all spatial derivatives to be approximated by centered finite differences. A typical cell from a mesh is shown in Figure 3-1 along with the points of definition of the field variables. Pressure is defined at the center of cell and the velocities are defined at the centers of the cell faces. A typical cell  $(i, j)$  extends from  $x = i\delta x$  to  $(i+1)\delta x$ , and  $y = j\delta y$  to  $(j+1)\delta y$ .

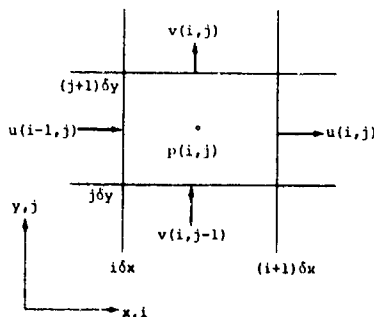


Figure 3-1. Typical Mesh Cell with Points of Definition of Field Variables

Overall calculation for one time step may be divided into three phases all of which are referenced to the Eulerian grid just described.

**PHASE I:** Since we are dealing with arbitrary curved wall and free surface boundaries, the actual boundary seldom exactly coincides with mesh cells. As a result, we need to approximate the true boundary by a boundary of mesh cells. The first step is to find the intersections of the true boundary with the mesh cells. Now the true boundary consists of a number of segments whose union is the total boundary and has zero intersection, each associated with a mesh cell. The second step

of Phase I is to compute the fluid volume of the cell bounded by the boundary segment. If this volume is greater than a set fraction (25% normally) of the cell volume ( $\delta x \cdot \delta y$ ), the cell is flagged a boundary cell.

For the stationary part of the boundary this calculation need be done only once at the beginning of the simulation, but for moving boundary the procedure needs to be repeated every time step. At this stage the boundary is composed of a number of contiguous segments each associated with a boundary mesh cell and characterized by a normal pointing into the fluid, positioned at the midpoint of the segment and whose magnitude equals the area of the segment. The logic of the code is built around flags associated with each cell. A flagging scheme is adopted in which a four digit cell flag is assigned to each and every cell of the computational mesh. The most significant digit indicates whether the cell is empty, full, boundary, or intersection. If the cell is a boundary type, the next significant digit indicates the type of boundary (rigid, stationary, reactive, free surface, outflow, and inflow). The two least significant digits indicate the orientation of the cell in relation to the neighboring cells.

PHASE II: Consists of setting appropriate boundary conditions, advancing the velocities in time and iterating on velocities and pressures until a flow field is obtained which satisfies the incompressibility condition. Viacelli [2] reported a method in which arbitrary free slip rigid wall boundaries (either stationary or moving) are treated as if they were free surfaces with a pressure distribution applied exterior to the fluid in such a way that the free surface position coincides with the wall boundary. The technique involves an iteration method in which velocities and pressures are adjusted simultaneously as opposed to the standard iterative solution of Poisson equation followed by the computation of new velocities as used in the SMAC [4] method. It can be shown, however, that the two techniques are equivalent.

#### Boundary Conditions

Velocities on and exterior to the boundary cells are necessary in differencing the momentum equations as well as to determine the interpolated boundary velocities. The velocities on the boundary are set to make the cell divergence zero. This means for a cell that has only one closed face, we calculate all the other velocities in the usual manner and compute the one on the closed face by setting

$\nabla \cdot \mathbf{v} = 0$ . Cells with more than one closed face have more complicated procedures. The required velocities exterior to the boundary are set equal to the adjacent velocities inside the fluid. The boundary conditions at rigid stationary and reactive boundaries are implicitly implemented through the pressure iteration.

In the free surface boundary cells the pressure is calculated by a linear interpolation from the pressure in the fluid cells immediately below it.

$$P_{i,j} = \alpha p_a + (1-\alpha) P_{i,j-1}$$

where  $p_a$  is the required (or specified) free surface pressure (normally zero) and  $\alpha = \delta y / \delta$ , where  $\delta$  is the distance from the free surface to the center of cell  $(i,j-1)$  and  $\delta y$  is the grid size.

Outflow boundary conditions are the most interesting and difficult to implement. Roache [5] presents a good survey of different types of outflow conditions. The most stable outflow condition is to specify the outflow velocities *a priori*. Unfortunately, the kind of outflow conditions we are interested in are the so-called "continuable" outflow conditions, where the requirement is to permit the fluid to flow out of the mesh with a minimum of upstream influence. Outflow boundary conditions are particularly important in wave propagation problems. A good outflow boundary allows one to use a much smaller mesh than otherwise needed because it eliminates the possibility of reflected waves affecting the calculation. The prescription we implemented involves setting the velocity gradients near the outflow boundary to zero. However, inside the pressure iteration they are free to change with the changes in pressures. This seems to work well, as evidenced by the results presented later.

Inflow boundaries are implemented by specifying velocities as a function of depth. The theoretical velocity distributions of a right running linear gravity wave in water of finite depth are given by McCormick [6].

$$u = \frac{gkh}{\omega} \frac{\cosh(kz + kh)}{\cosh(kh)} \cos(kx - \omega t)$$

$$v = \frac{gkh}{\omega} \frac{\sinh(kz + kh)}{\cosh(kh)} \sin(kx - \omega t)$$

where

$$k = 2\pi/\lambda = \text{wave number}$$

$a$  = wave amplitude  
 $g$  = gravitational constant  
 $\omega$  = wave frequency  
 $z$  = depth coordinate  
 $h$  = depth of water  
 $x$  = coordinate in direction of propagation  
 $t$  = time

In order to specify the velocities at the boundary,  $x$  was set to zero and the velocities were calculated as a function of time and depth. The initial condition from which we start has the free surface and velocity field set to zero. We start generating inflow velocities, thereby creating a wave. It takes several time steps for the wave to reach its steady state amplitude. The waves propagate across the mesh at a phase velocity determined by the  $k$  of the wave and which agrees well with the theoretical phase velocity.

Irregular waves corresponding to a given wave spectrum are assumed to be a superposition of regular waves with different magnitudes and random phase mix.

Pierson-Moskowitz [7] spectrum for fully developed seas is

$$S(\omega) = (A/\omega^5) e^{-(B/\omega^4)} \quad (3.1)$$

$S(\omega)$  = spectral density of wave heights,  $\text{ft}^2 \text{ sec.}$

$A$  =  $172.8 \text{ h}^2 \text{ T}^{-4}$

$B$  =  $691 \text{ T}^{-4}$

$\omega$  = circular frequency,  $\text{rad/sec.}$

$h$  = mean of the 1/3 highest peak to trough values,  $\text{ft.}$

$T$  = average period,  $\text{secs.}$

Irregular waves with any specified spectrum can be modeled by the following equation:

$$x(t) = \sum_{n=0}^N a_n \cos(n\omega_0 t + c_n) \quad (3.2)$$

where

$x$  = free surface height with reference to the still water

$$a_n = \sqrt{2 \omega_0 S(n\omega_0)}$$

$c_n$  = a random number uniformly distributed between 0 and  $2\pi$ .

$N$  = a reasonably large number such that  $(N\omega_0)$  covers the frequency of interest.

A wave corresponding to Eq. (3.2) can be readily generated by the same procedures described for the generation of regular waves.

#### Difference Equations and Pressure Iteration

The specific finite difference equations used to advance the velocities in time are presented in Appendix A. Time derivatives are approximated explicitly, and for space derivatives a factor is built into the equations which controls the amount of donor cell fluxing. A time dependent solution for the problem is obtained by advancing the flow field variables through a succession of time steps. The velocities are advanced using the previous state of the flow to calculate accelerations caused by convection, pressure gradients, viscous stresses, body forces, etc. by an explicit calculation. However, this explicit time advancement does not necessarily yield a velocity field with zero divergence. Therefore, the pressure field is adjusted such that each cell in the computational grid has zero divergence. Since a pressure change in one cell affects velocities in neighboring cells as well, this pressure adjustment is done iteratively until all cells have simultaneously achieved a zero divergence. The following algorithm is employed for pressure iteration. Let  $\delta p$  denote the pressure correction at  $i$ th iteration for a typical cell  $(i,j)$ , i.e.  $\delta p = p(i,j)^{n+1} - p(i,j)^n$  where superscript,  $n$ , denotes iteration number, then for:

Full Cells:

$$\delta p = -\beta D$$

where

$D$  = the cell divergence

$$\beta = \beta_0 / \delta t \left( \frac{1}{\delta x^2} + \frac{1}{\delta y^2} \right)$$

$\beta_0$  = a relaxation factor between 0.5 and 1.0.

Boundary Cells:

$$\delta p = -\frac{1}{\delta} \left( \left[ \vec{v}_{mp} - \vec{v}_{mb} \right] \cdot \vec{n} \right) / \delta$$

$\vec{v}_{mp}$  = the interpolated velocity vector at the midpoint of the segment associated with the boundary cell.

$\vec{v}_{mb}$  = the boundary velocity vector of the midpoint.

$\hat{n}$  = the unit normal at the midpoint, pointing into the fluid

$\cdot$  = symbol for vector dot product

$\delta$  = a mesh parameter.

For rigid stationary boundaries  $\vec{V}_{mb}$  is set identically to zero and for the reactive boundaries  $\vec{V}_{mb} = \vec{V}_b + \hat{n}_b \times \vec{R}$ , where  $\vec{V}_b$  is the translational velocity and  $\hat{n}_b$  is the rotational velocity of the boundary and  $\vec{R}$  is the vector from the center of rotation to the midpoint.

$\vec{V}_{mp}$  is obtained by a bivariate interpolation of the velocity components which are defined on mesh lines to the midpoint of the segment. It is similar to the MAC [3] area weighting procedure used to compute particle velocities.

Intersection cells are the cells that contain both a free surface boundary and some other type of boundary. Several alternate treatments are possible for such cells. After a considerable experimentation, we found that adjusting pressures based on the free surface part of the boundary works best. This may not always exactly satisfy the rigid boundary condition for that part of the rigid boundary associated with the intersection cell. However, from our experience we found that the discrepancies caused by this are minimal.

Since the free surface segment in the intersection cell can lie anywhere in the cell, there is a question as to what surface height need be used to interpolate the pressure. An extrapolated surface height at the center of the column in which the intersection cell lies was utilized because the pressure interpolation is in terms of cell pressures which are defined at the center of cells. Several extrapolation schemes were tried and the most simple linear extrapolation seems to work best. The failure of high order extrapolation is attributable to the fact that these formulas force a dependency over a larger domain and as a result, the height at the intersection cell cannot react freely to the local flow field.

Once a  $\delta p$  has been determined for a cell (i,j) the pressures and velocities are updated as follows:

$$p(i,j) = p(i,j) + \delta p$$

$$u(i,j) = u(i,j) + (\delta t / \delta x) \delta p$$

$$v(i,j) = v(i,j) + (\delta t / \delta y) \delta p$$

$$u(i-1,j) = u(i-1,j) - (\delta t / \delta x) \delta p$$

$$v(i,j-1) = v(i,j-1) - (\delta t / \delta x) \delta p$$

For boundary cells only the velocities on open faces are adjusted and the velocities on closed faces are determined by setting the cell divergence to zero.

One complete iteration consists of adjusting pressures (and thereby velocities) in all the cells by sweeping the mesh in an orderly fashion. It is to be noted that pressure in each cell gets updated once during an iteration, whereas the velocities get updated twice. The iteration is terminated when the ratio of the norm of the pressure changes to the norm of pressures, drops below a small positive number  $\epsilon$ . Usually sufficient accuracy is obtained with an  $\epsilon$  of the order of  $10^{-4}$ . Iteration normally converges in about 4 to 6 iterations, provided the flow variations are not too rapid from time step to next and  $\epsilon$  is not chosen excessively small.

PHASE III: Having obtained a consistent flow field, it is necessary to update the free surface and reactive boundaries in preparation for next time step.

In the early MAC methods a line of particles marked the free surface position. When these particles are moved each time step by computing the velocities of these particles. This is a Lagrangian procedure and tends to be unstable after a large number of time steps. Chan and Street [1] reported, that the round off errors were particularly serious in problems involving waves. To overcome this difficulty an alternative Eulerian approach has been developed for two dimensional problems by Chan and Street [1]. Later the method was applied to 3-D problems by Nichols and Hirt [8]. In this approach the fluid surface is represented by a single valued function and is initially defined by the surface height above the bottom of mesh. The surface height is defined at the center of each column of cells. The change in surface elevation is determined by the local fluid velocity and is governed by the following equation.

$$\frac{\partial h}{\partial t} = v - u \frac{\partial h}{\partial x} - w \frac{\partial h}{\partial z}$$

This equation is solved by a space centered explicit differencing method to obtain the free surface position at new time. This particular difference approximation is unstable because of a negative diffusion truncation error, as a result a stabilizing viscous like term of the form

$$\gamma \left( \frac{\partial^2 h}{\partial x^2} + \frac{\partial^2 h}{\partial z^2} \right)$$

has been added to the surface height equation.  $\gamma$  is a small positive number and is chosen to be greater than  $u^2 \delta t / 2$ . Where  $u$  is the maximum velocity in the flow field. Due to the nature of the difference approximation, a surface height is required in the column immediately outside the fluid region. This is obtained by setting  $\partial h / \partial \eta = 0$ .

#### Reactive Boundaries

These are the boundaries which can move in response to the forces exerted on them in a fashion dictated by the inertial characteristics of these boundaries. Let us assume that the reactive boundary is characterized by a set of  $N$  particles (called Inertial Marker particles [9]) located at the midpoints of the segments associated with the reactive boundary cells.

$\vec{x}_1 = (x_1, y_1)$  denote the position of these particles.

$A_1$  = area of the corresponding segments, note:  $\sum A_1$  = total area of reactive boundary.

Let  $M$  and  $I$  be the mass and inertia tensor of the collection of these particles. Then, if  $\vec{v}_b$  and  $\vec{\omega}_b$  are the instantaneous translational and rotational velocities of the boundary, the dynamics of the boundary is governed by the following equations:

$$M \frac{d\vec{v}_b}{dt} = \vec{F}_1 - M\vec{g}$$

$$I \frac{d\vec{\omega}_b}{dt} = \vec{r}_1 \times \vec{F}_1 - \vec{G} \times \vec{R}_c$$

where

$\vec{F}_1 = \sum_{i=1}^N \vec{F}_i$  is the vector force acting at  $\vec{x}_1$

$p_1$  = the interpolated pressure at  $\vec{x}_1$

$\vec{n}_1$  = the unit normal at  $\vec{x}_1$  pointing away from fluid

$\vec{R}_1$  = the vector from the center of rotation (metacenter) to the point  $\vec{x}_1$

$\vec{g}$  = the acceleration due to gravity

$\vec{G}$  = a vector in the  $y$ -direction whose magnitude is  $M\vec{g}$

$\vec{R}_c$  = the vector from center of rotation to center of mass

$\times$  = symbol for vector cross product

In order to determine  $p_1$  by interpolation, it is sometimes necessary to know the pressures in exterior empty cells for which a pressure is normally not computed. Therefore, before attempting to determine  $p_1$ , pressures are extrapolated to the cell centers of immediately exterior cells by a linear extrapolation procedure.

Now the motion of the boundary is governed by  $d\vec{x}_1/dt = \vec{v}_b + \vec{\omega}_b \times \vec{R}_1$ . It is assumed that the initial condition is that the fluid and the floating body are at rest and hence  $\vec{v}_b$  and  $\vec{\omega}_b$  are zero at time zero. Explicit finite differences are used to solve these equations of motion. After all the inertial marker particles are moved, both the center of rotation and center of mass are moved.

This concludes the computation for one time step. At the conclusion of Phase III, we are ready with a new configuration of the computational region to go into the next time step. A flow chart of program organization is presented in Figure 3-2.

#### Numerical Stability and Accuracy Considerations

1. A criterion, which says, the distance the fluid travels in one time step must be less than one grid length is known as the Courant condition. This restricts the time increment to

$$\Delta t \leq \min \left( \frac{\Delta x}{|u|}, \frac{\Delta y}{|v|}, \frac{\Delta z}{|w|} \right)$$

2. Since free surfaces are present, it is necessary to insure that the distance a surface wave travels during one time step be less than the horizontal cell dimension

$$i.e., c \Delta t \leq \min (\Delta x, \Delta z)$$

$c$  = the wave speed

3. When viscous diffusion terms are present, numerical stability requires

$$\nu \Delta t \leq 0.5 \left( \frac{1}{\Delta x^2} + \frac{1}{\Delta y^2} + \frac{1}{\Delta z^2} \right)^{-1}$$

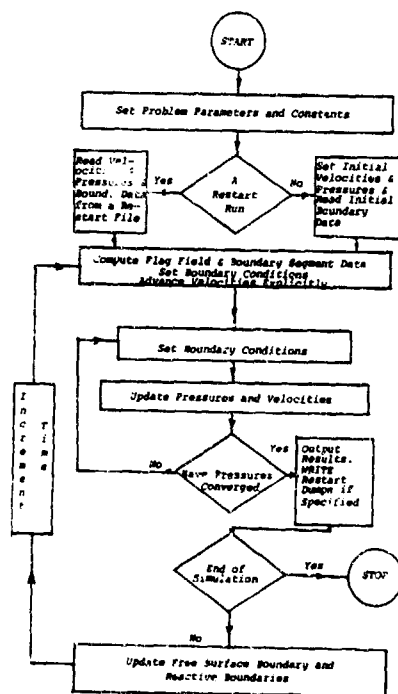


Figure 3-2. Flow Chart

5. Instabilities may arise if there are sharp curvatures in the boundary relative to mesh size. As a general rule at least 3 to 5 cells should be allowed to define a sharp curve in the boundary. By the same token any confined fluid flow regions should be covered by 3 to 5 cells. In otherwords floating bodies must be composed of at least three cells in each direction and fluid flow regions must be at least three cells thick.

6. When once numerical stability is assured, accuracy depends a lot on how well mass (volume) and momentum are conserved. The degree of mass conservation is directly dependent on how stringent the convergence criterion (i.e., how small  $\epsilon$ ) is. Practical experience indicates that below a certain small value, cutting down  $\epsilon$  any further does not improve accuracy. This value is very problem dependent and we do not know any one method to find this value *a priori*, except by trial and error. Momentum conservation is also an important aspect with respect to the accuracy of calculations. In order to achieve this the terms in the transport part of the momentum equations of the form

$$u \frac{\partial u}{\partial x} + v \frac{\partial u}{\partial y}$$

were transformed, using the incompressibility condition to

$$\frac{\partial u^2}{\partial x} + \frac{\partial uv}{\partial y}$$

The difference form of this expression can simply be written such that flux out of one side of cell exactly equals the flux into that same side of the adjacent cell.

#### IV. Results

Several simulations have been carried out for a ship moored between four horizontal springs and subject to beam seas. Results are compared with the model test results conducted at Netherlands Ship Model Basin [10]. A sketch of the model test setup is shown in Figure 4-1.

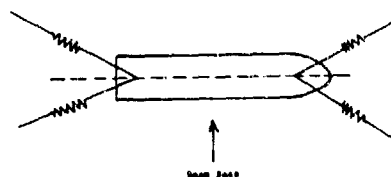


Figure 4-1. Model Test Setup

In order to simulate this situation in two dimensions, it was observed that the length of the ship is large compared to wavelengths of the exciting waves and hence the end effects are assumed negligible. As a result, slab symmetry may be assumed in the third dimension and the simulation may be setup (Figure 4-2) in two dimensions with three degrees of body freedom viz. sway, heave and roll. The mooring system is implicitly incorporated into the body dynamics as follows.

Let  $F_x^h$ ,  $F_y^h$  and  $M^h$  be the forces in  $x$ ,  $y$  directions and moment of rotation about the metacenter of the vessel without the presence of the mooring system. (h superscript denoting hydrodynamic forces.)

With reference to Figure 4-3, let  $(x_p^0, y_p^0)$  be initial (equilibrium) position of point  $p$  where the ropes are attached on the deck.

- $y$  be the height of metacenter below deck
- $k$  be the spring constant for mooring ropes



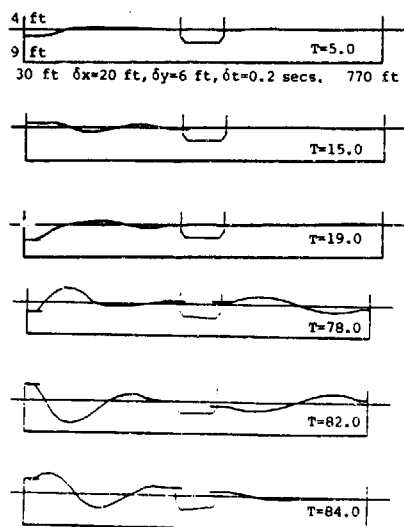


Figure 4-2. Simulation Setup at Various Times. (Wave is shown amplified by a factor of 8)

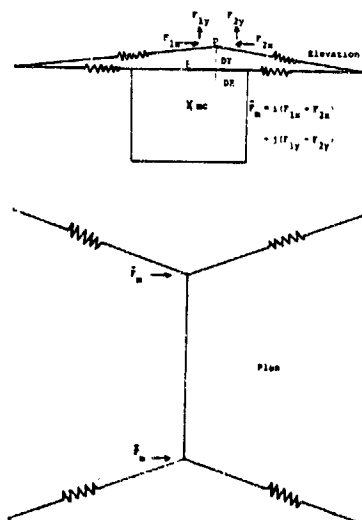


Figure 4-3. Schematic of Mooring Forces

$(x_c^0, y_c^0)$  be the equilibrium position of metacenter

now let  $(x_p^n, y_p^n)$  be the new position of point p due to a translation of  $(\delta x, \delta y)$  of the metacenter and a rotation of  $d\theta$  about the metacenter, then

$$x_p^n = x_p^0 + \delta x - \bar{y} \sin d\theta$$

$$y_p^n = y_p^0 + \delta y - \bar{y}(1 - \cos d\theta)$$

now define DX and DY as

$$DX \equiv x_p^n - x_p^0 = \delta x - \bar{y} \sin d\theta \quad (4.1)$$

$$DY \equiv y_p^n - y_p^0 = \delta y - \bar{y}(1 - \cos d\theta)$$

(DX, DY) = the effective translation of point p with respect to main coordinate system.

By hypothesis,

$$\delta x = (x_c^n - x_c^0)$$

$$\delta y = (y_c^n - y_c^0)$$

where

$$(x_c^n, y_c^n) = \text{the new position of metacenter.}$$

It can be seen that the net force due to mooring system,  $\vec{F}_m = \hat{i} 2k DX + \hat{j} 2k DY$ . Where  $\hat{i}$ ,  $\hat{j}$  are the unit vectors in x, y directions respectively. An assumption has been made here that the magnitudes of DX and DY are such that all four mooring ropes are in the linear operating range all the time.

Since we have two sets of springs (two springs each) total force is

$$\vec{F} = \hat{i} 4k DX + \hat{j} 4k DY = \hat{i} K_{eff} DX + \hat{j} K_{eff} DY$$

re

$K_{eff}$  = the effective spring constant for the total mooring system = 4k

Now the total forces and moment in the combined system of ship and mooring ropes are

$$F_x^n = F_x^h + K_{eff} DX$$

$$F_y^n = F_y^h + K_{eff} DY$$

$$M^n = M^h + K_{eff} DX (\bar{y} \cos d\theta)$$

$$- K_{eff} DY \bar{y} \sin d\theta$$

Thus, if we use  $F_x^n$ ,  $F_y^n$ ,  $M^n$  in computing the new body velocities, instead of  $F_x^h$ ,  $F_y^h$  and  $M^h$ , we are effectively incorporating the mooring system into the problems.

Two different irregular beam seas are used in the simulations whose spectra are shown in Figures 4-4 and 4-5.

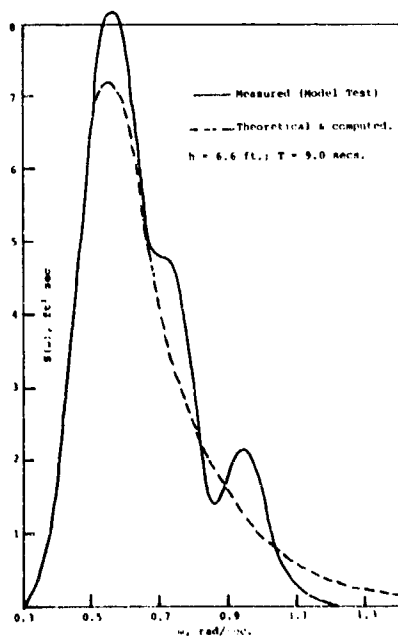


Figure 4-4. Wave Spectrum No. 2

The simulation spectrum and the spectrum generated in the model test are both indicated. The simulation spectrum coincides with the spectrum which the model tests attempted to produce. However, it is to be noted that

noticeable discrepancies exist between the simulation spectrum and the one that was actually generated in the model test. This point is to be borne in mind when comparing the computer simulations to model test data.

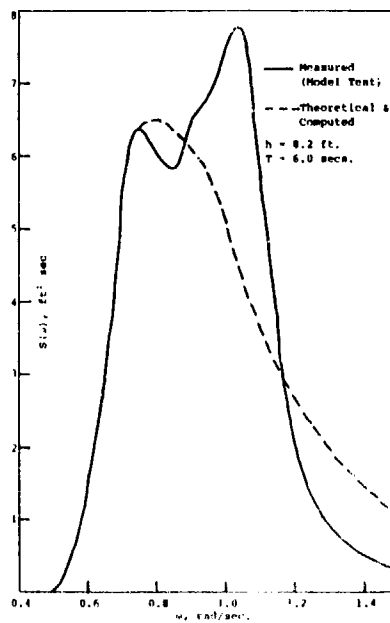


Figure 4-5. Wave Spectrum No. 3

The main particulars of the ship and the mooring system are:

Length to beam ratio	= 5.3
Beam to draft ratio	= 3.65
Block coefficient	= 0.75
Mid-ship section coefficient	= 0.997
Stiffness of each mooring spring	= 5 tons/m

Neither the mass nor one of (length, beam or draft) was reported in the model test report to uniquely determine all the ship's parameters. Hence a typical beam length of 90 ft. was assumed and all other parameters were determined in conformity with this length. A still water depth of 65 ft. was used in all the simulations.

It was pointed out in Chapter III that a minimum amount of viscosity must be present make the numerical calculation stable. This "artificial viscosity" seems to attenuate the wave slightly as the wave propagates down the mesh. Therefore, it is necessary to generate a slightly larger wave at the inflow boundary so

that we get the right magnitude wave near the ship.

The initial condition for the simulation is that the ship and the fluid are at rest. We start the simulation by impressing appropriate velocities at the inflow boundary, thereby creating a wave. The generated waves propagate across the mesh, interact with the ship and smoothly flow out through the outflow boundary (see Figure 4-2). It takes several wave periods for the wave to get setup. Simulation results for the setup period were discarded in the analysis of results presented.

The computer code outputs time records of sway, heave and roll. The second central moment of the sway for two different sea states is shown in Figures 4-6 and 4-7. The test model data for the corresponding cases is also shown in Figures 4-6 and 4-7. No data were presented in the model test report to compare the motions in the other two degrees of freedom viz. heave and roll.

In Reference [10], Verhagen gives a plausibility argument that the standard deviation of the sway amplitude is related to the normalized spectral density function by a linear relationship as shown in Figure 4-8. He conducted three model tests to confirm this hypothesis as shown. We simulated this series of model tests and obtained the results shown in Figure 4-8.

Our results showed some deviation from the linear relationship at large wave amplitudes (approximately 20 ft. waves). We suspect that this is a nonlinear effect which would be born out by the model tests if they were conducted at large amplitude. Our results also show a slightly different linear constant in the low wave amplitude results. This may be attributed to a scaling of the postulated linear relationship to the mass of the ship. The scaled ship displacement was not specified in Reference [10]. We can bracket the above results by assuming different displacements and should be able to reproduce the linear relationship more closely by assuming a slightly larger mass and rerunning the three simulations.

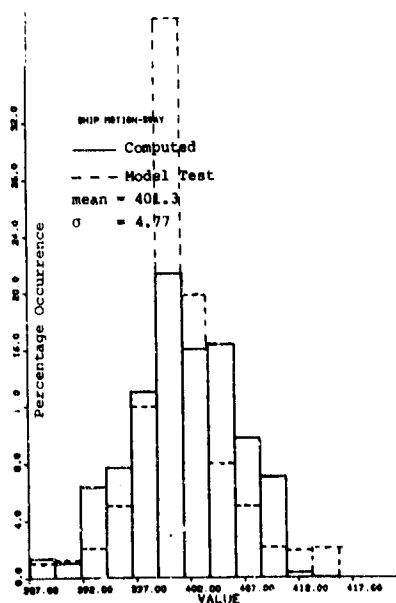
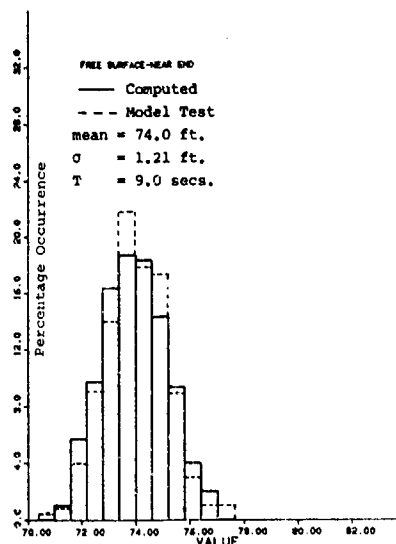


Figure 4-6. Comparison of Wave and Ship Motion Distributions, Spectrum 2

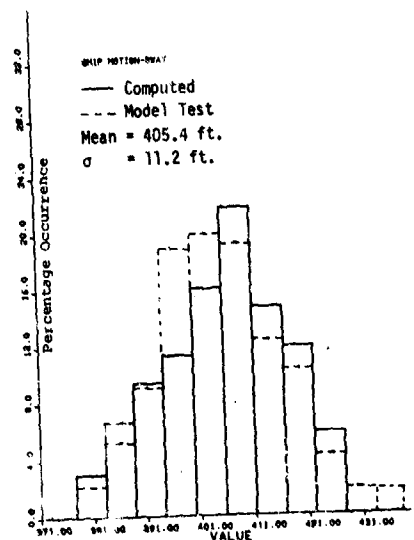
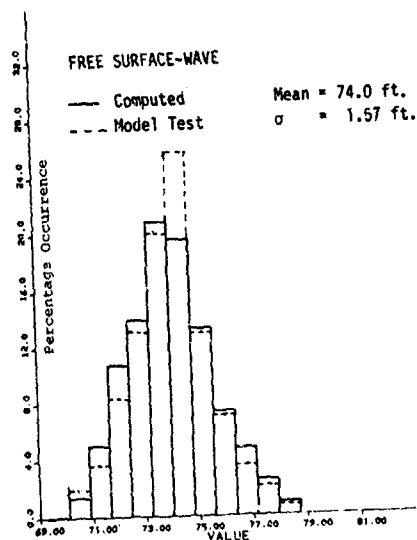


Figure 4-7. Comparison of Wave and Ship Motion Distributions

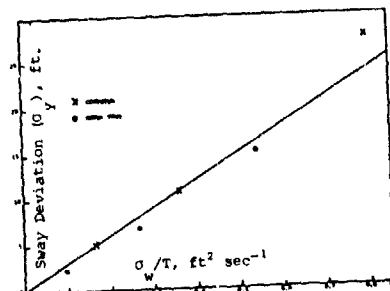


Figure 4-8. Summary Comparison of Model Test and Computer Results

#### V. Conclusions

We have developed an Eulerian hydrodynamic approach to simulating ship motions in random seas. The method treats the ship wave interaction in a completely nonlinear fashion. The code as presently formulated allows arbitrary boundary shapes, arbitrary mooring forces on the ship and arbitrary random wave input spectra. The code results have been validated against model test results and shown good agreement. The method has the capability to be extended to a very general three dimensional predictive technique.

#### Appendix A: Finite Difference Approximations

The finite difference notation used in this paper is:

$p_{i,j}^n$  = pressure at center of cell (i,j) at time level n

$u_{i,j}^n$  = x-direction velocity at middle of right side of cell (i,j) at time level n

$v_{i,j}^n$  = y-direction velocity at middle of top side of cell (i,j) at time level n

The difference approximation representing the continuity equation, Eq. (2.1) for a typical cell (i,j) is

$$\frac{1}{\delta x} \left( u_{i,j}^{n+1} - u_{i-1,j}^{n+1} \right) + \frac{1}{\delta y} \left( v_{i,j}^{n+1} - v_{i,j-1}^{n+1} \right) = 0.$$

The difference equations approximating the Navier-Stokes equations, Eq. (2.2) are,

$$u_{i,j}^{n+1} = u_{i,j}^n + \Delta t \left[ \frac{1}{\Delta x} (P_{i,j}^n - P_{i-1,j}^n) \right.$$

$$\left. + g_x - FUX - FUY + VISX \right]$$

and

$$v_{i,j}^{n+1} = v_{i,j}^n + \Delta t \left[ \frac{1}{\Delta y} (P_{i,j}^n - P_{i,j+1}^n) \right.$$

$$\left. + g_y - FWX - FUY + VISY \right],$$

where the convective and viscous fluxes are defined as

$$FUX = \frac{1}{\Delta x} \left[ (u_{i,j} + u_{i+1,j})^2 + \alpha |u_{i,j} + u_{i+1,j}| \right.$$

$$\times (u_{i,j} - u_{i+1,j}) - (u_{i-1,j} + u_{i,j})^2$$

$$\left. - \alpha |u_{i-1,j} + u_{i,j}| (u_{i-1,j} - u_{i,j}) \right],$$

$$FUY = \frac{1}{\Delta y} \left[ (v_{i,j} + v_{i+1,j}) (u_{i,j} + u_{i,j+1}) \right.$$

$$+ \alpha |v_{i,j} + v_{i+1,j}| (u_{i,j} - u_{i,j+1})$$

$$\left. - (v_{i,j-1} + v_{i+1,j-1}) (u_{i,j-1} + u_{i,j}) \right.$$

$$\left. - \alpha |v_{i,j-1} + v_{i+1,j-1}| (u_{i,j-1} - u_{i,j}) \right],$$

$$FWX = \frac{1}{\Delta x} \left[ (u_{i,j} + u_{i+1,j}) (v_{i,j} + v_{i+1,j}) \right.$$

$$+ \alpha |u_{i,j} + u_{i+1,j}| (v_{i,j} - v_{i+1,j})$$

$$\left. - (u_{i-1,j} + u_{i+1,j}) (v_{i-1,j} + v_{i,j}) \right.$$

$$\left. - \alpha |u_{i-1,j} + u_{i+1,j}| (v_{i-1,j} - v_{i,j}) \right],$$

$$FVY = \frac{1}{\Delta y} \left[ (v_{i,j} + v_{i,j+1})^2 + \alpha |v_{i,j} + v_{i,j+1}| \right.$$

$$\times (v_{i,j} - v_{i,j+1}) - (v_{i,j-1} + v_{i,j})^2$$

$$\left. - \alpha |v_{i,j-1} + v_{i,j}| (v_{i,j-1} - v_{i,j}) \right],$$

$$VISX = \nu \left[ \frac{1}{\Delta x^2} (u_{i+1,j} - 2u_{i,j} + u_{i-1,j}) \right.$$

$$\left. + \frac{1}{\Delta y^2} (u_{i,j+1} - 2u_{i,j} + u_{i,j-1}) \right]$$

and

$$VISY = \nu \left[ \frac{1}{\Delta x^2} (v_{i+1,j} - 2v_{i,j} + v_{i-1,j}) \right.$$

$$\left. + \frac{1}{\Delta y^2} (v_{i,j+1} - 2v_{i,j} + v_{i,j-1}) \right]$$

#### References

1. Robert L. Street, Robert K. C. Chan and Jacob E. Fromm, "Two Methods for the Computation of the Motion of Long Water Waves--A Review and Applications," 8th ONR Symposium on Naval Hydrodynamics, Pasadena, California, 1970, pp. 147-187.
2. James A. Vieceilli, "A Computing Method for Incompressible Flows Bounded by Mooring Walls," Journal of Computational Physics, Vol. 8, No. 1, August 1971.
3. J. E. Welch, et al., "A Computing Technique for Solving Viscous, Incompressible, Transient Fluid Flow Problems Involving Free Surfaces," Los Alamos Scientific Laboratory, Los Alamos, New Mexico, LA-3425, March 1966.
4. Anthony A. Amsden and Francis H. Harlow, "The SMAC Method: A Numerical Technique for Calculating Incompressible Fluid Flows," Los Alamos Scientific Laboratory, LA-4370, 1970.
5. Patrick J. Roache, Computational Fluid Dynamics, Hermosa Publishers, Albuquerque, New Mexico, 1972.
6. Michael E. McCormick, Ocean Engineering Wave Mechanics, John Wiley and Sons, 1973.
7. G. Neumann, and W.J. Pierson, Principles of Physical Oceanography, Prentice-Hall Publishers, Englewood Cliffs, N.J., 1966.

8. B. D. Nichols and C. W. Hirt, "Calculating Three-Dimensional Free Surface Flows in the Vicinity of Submerged and Exposed Structures," *Journal of Computational Physics*, Vol. 12, No. 2, June 1973.
9. G. I. Bourianoff, "Numerical Simulation of Incompressible Viscous Flows with Reactive Boundaries: The IMP Method," Computational Methods in Nonlinear Mechanics, 1974, pp. 121-128.
10. J. H. G. Verhagen, "The Drifting Force on a Floating Body in Irregular Waves," *Eighth Symposium on Naval Hydrodynamics*, ACR-179, August 24-28, 1970.

## COMPUTATION OF NEAR-BOW OR STERN FLOWS, USING SERIES EXPANSION IN THE FROUDE NUMBER

J.-M. Vanden Broeck and E. O. Tuck  
Applied Mathematics Department  
University of Adelaide, Australia

### Abstract

Two-dimensional flow past a semi-infinite body with constant draft  $H$ , is solved by expansion in a formal power series with respect to a parameter  $\epsilon$  related to the draft-based Froude number  $F_H = U/\sqrt{gH}$ . This series is everywhere divergent, but can be summed by standard methods. The sum is not unique, and one particular efficient summation procedure yields a discontinuous but wave-free free surface. Iteration techniques are developed to proceed from this solution as a starting point, to a continuous solution possessing non-linear waves, which can therefore serve as a stern flow. Results are presented for the steepness of the waves generated as a function of  $F_H$ . No continuous wave-free solution appears to exist, and numerical evidence suggests the presence of a re-entrant jet in the corresponding bow-flow problem.

### 1. Introduction

In the present paper, we study further the problem considered first by Dagan and Tulin (1972), of steady flow past a semi-infinite two-dimensional flat-bottomed body of draft  $H$ . In Dagan and Tulin's original problem the body terminates with a vertical face; we generalize this here to include plane faces at an arbitrary angle  $\gamma$  to the horizontal. This geometry can serve as a model for either near-bow or near-stern flow past a barge-like vessel, depending on the sign of the flow magnitude  $U$  at infinity.

Dagan and Tulin found two terms in an expansion in powers of  $U^2/gH$ . We are able to continue this series, in principle indefinitely, but in practice are able to obtain good numerical values for 15 terms in the series. These terms are quite uniquely determined, and are independent of the sign of  $U$ .

However, it is apparent that the magnitude of the terms is increasing at an alarming rate. Indeed, convincing numerical evidence is available to show that the  $(n+1)$ st term is asymptotically a factor of order  $n$  times as large as the  $n$ th term. Hence the rate of growth is factorial, and the series has a zero radius of convergence.

Such everywhere-divergent series can be summed by a number of standard methods. However, there is necessarily a problem of lack of uniqueness about this sum. Indeed, it is fortunate that this should be the case, since the same series represents both bow and stern flows, which are expected to be quite different in character. The major task is then to choose a summation procedure capable of generating whichever of these possible solutions we prefer.

Although work is proceeding (Vanden Broeck and Schwartz, 1978) on development of direct techniques to achieve such a purpose, we use here an indirect technique. First we use a standard summation procedure due to Shanks (1955), which gives good convergence, but appears to generate a physically unacceptable solution, possessing a discontinuous free surface.

Appropriate portions of this solution are then used as a "seed" for a direct numerical attack on the problem, using a form of Newtonian iteration. This procedure is in principle quite independent of the low-Froude number asymptotic series, and can be viewed as a standard numerical solution of the integro-differential equation to which the complete problem can be reduced, at arbitrary Froude number. However, convergence of the iterations is very sensitive to the choice of starting solution, and success has been achieved only by use of the summed series as such a starting solution. The iterations appear to converge extremely well for stern flow, but not for bow flow.

In the case of stern flow, the final solution appears to agree within the accuracy of convergence of the iterations with the summed series, between the body and the discontinuity. Beyond the previous discontinuity, the final solution changes smoothly into a train of waves at infinity. These waves become strongly non-sinusoidal as the Froude number increases. The present non-linear computations provide the first published solution for waves generated by steadily moving semi-infinite bodies; linear theories of wave generation by moving bodies would suggest that the generated wave amplitude tends to zero as the body length tends to infinity.

## 2. Mathematical Formulation

We assume a two-dimensional irrotational flow past a semi-infinite body, consisting of a plane lower surface  $y^* = -H$ ,  $x^* < 0$ , and a face  $y^* = -H + x^* \tan \gamma$  which slopes at an angle  $\gamma$  to the horizontal. Figure 1 shows an idealized flow of this nature, which behaves at infinity as a uniform stream  $U$  in the  $+x^*$  direction, with the free surface ultimately the plane  $y^* = 0$ ,  $x^* \rightarrow +\infty$ . The fine detail of the flow sketched in Figure 1 (e.g. the stagnation point of contact, and the absence of waves) may not be representative of the true flow to be computed; indeed it is part of our task to determine if these features are present. Figure 1 shows a stern flow with  $U > 0$ ; the method is, however, equally applicable to bow flows with  $U < 0$ .

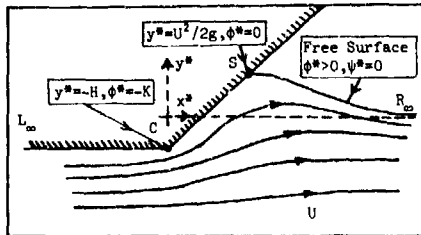


Figure 1. Sketch of dimensional flow

The mathematical problem is thus to determine a dimensional velocity potential  $\phi^*(x^*, y^*)$  satisfying Laplace's equation in the field of flow, with  $\phi^* \rightarrow U x^*$  at infinity, with vanishing normal derivative on both the body and free surface, and with uniform pressure on the free surface, i.e.

$$\frac{1}{2} \left( \frac{\partial \phi^*}{\partial x^*} \right)^2 + \frac{1}{2} \left( \frac{\partial \phi^*}{\partial y^*} \right)^2 + g y^* = \frac{1}{2} U^2. \quad (2.1)$$

Without loss of generality, we can choose the zero level for the potential  $\phi^*$ , such that  $\phi^* = 0$  at the point of contact between the body and the free surface.

We now normalise with respect to a length scale

$$L = K/U, \quad (2.2)$$

where  $-K$  is the value of the velocity potential  $\phi^*$  at the corner point  $x^* = 0$ ,  $y^* = -H$ . Thus we define non-dimensional quantities

$$x = (x^* - (H + \frac{U^2}{2g}) \cot \gamma) / L \quad (2.3)$$

$$y = (y^* + \frac{U^2}{2g}) / L \quad (2.4)$$

$$\phi = \phi^* / K \quad (2.5)$$

$$\text{and} \quad \epsilon = \frac{U^2}{2gL} \quad (2.6)$$

In terms of un-starred variables, the free-surface condition (2.1) becomes

$$\epsilon(\phi_x^2 + \phi_y^2) + y = 0. \quad (2.7)$$

At infinity in non-dimensional co-ordinates, we have a unit free stream  $\phi \rightarrow x$  and a free-surface level  $y = -\epsilon$ . If there is a stagnation point on the free surface, it is necessarily at  $y = 0$ , and  $y < 0$  for all non-stagnant free-surface points. The normalized flow is shown in Figure 2.

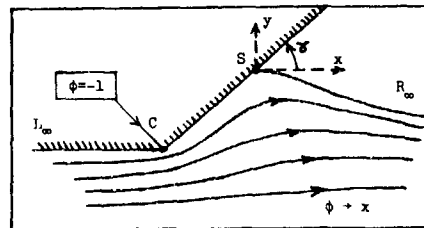


Figure 2. Sketch of non-dimensional flow

We solve this problem in an inverse manner. If  $\psi$  is the stream function, conjugate to  $\phi$ , we write

$$f = \phi + i\psi \quad (2.8)$$

$$\text{and} \quad z = x + iy, \quad (2.9)$$

and solve for  $z$  as an analytic function of  $f$ , in  $\psi \leq 0$ . The free surface and the body are portions of the streamline  $\psi = 0$ , on which (2.7) becomes

$$y(x^2 + y^2) + \epsilon = 0, \phi > 0. \quad (2.10)$$

The boundary condition on the body can be written

$$\begin{cases} y_\phi = 0, \phi < -1 \\ (\sin \gamma)x_\phi - (\cos \gamma)y_\phi = 0, -1 < \phi < 0. \end{cases} \quad (2.11)$$

A solution for a given value of the parameter  $\epsilon$  can be written

$$z(f) = z(f; \epsilon) = x(\phi, \psi; \epsilon) + iy(\phi, \psi; \epsilon). \quad (2.12)$$

Note that the dependent variables also depend implicitly on the angle  $\gamma$  of the body. The inverse problem in the  $f$ -plane is illustrated in Figure 3.

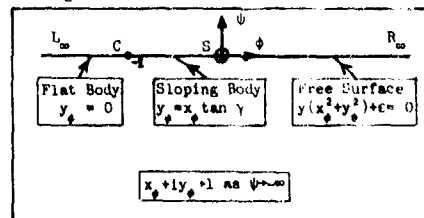


Figure 3. Flow in  $(\phi, \psi)$  plane

In this inverse formulation, it is important to note that the normalization chosen has forced the body's corner point to lie at  $\phi = -1$ ,  $\psi = 0$ . Our solution will then determine the  $y$ -coordinate  $y(-1, 0; \epsilon)$  of this point, and



hence implicitly the normalized draft  $H/L$  of the body. Thus (2.4) implies

$$\frac{H}{L} = -y(-1, 0; \epsilon) - \epsilon \quad (2.13)$$

from which we find the draft-based Froude number

$$F_H = \frac{U}{\sqrt{gH}} \quad (2.14)$$

$$= (-1 - y(-1, 0; \epsilon)/2\epsilon)^{-1/2} \quad (2.15)$$

as a function of the parameter  $\epsilon$ .

The function  $z(f)$  is analytic in  $\psi < 0$  except at the stagnation point  $f = 0$ , where (c.f. Dagan and Tulin, 1972)

$$z'(f) = \begin{cases} f^{-1/2} & , \gamma > \pi/3 \\ f^{-1/3} & , \gamma < \pi/3 \end{cases} \quad (2.16)$$

and at the corner point  $f = -1$ , where

$$z'(f) = (f+1)^{1/2} \quad (2.17)$$

For  $\epsilon = 0$ , the problem has the exact solution

$$z'(f) = \left(\frac{f+1}{f}\right)^{1/2} \quad (2.18)$$

corresponding to flow under a step, the free surface being replaced by the rigid plane  $y=0$ . Note that this is a good local approximation near the stagnation point  $f = 0$  only if  $\gamma > \pi/3$  but gives the wrong asymptotic behaviour if  $\gamma < \pi/3$ .

Consider now the function

$$\chi(f) = \left(\frac{f}{f+1}\right)^{1/2} z'(f) - 1 \quad (2.19)$$

which vanishes at  $\epsilon = 0$  and as  $\psi \rightarrow -\infty$ , and removes the singularity at  $f = -1$ . If  $\gamma > \pi/3$ , it also removes the singularity at  $f = 0$ , but if  $\gamma < \pi/3$ , we have  $\chi \sim f^{1/2-\pi/3}$ . This singularity is weaker than a simple pole, so that in all cases, we can apply Cauchy's theorem to  $\chi(f)$  on a path consisting of the complete streamline  $\psi = 0$  and a semi-circle at  $\psi = -\infty$ . Hence we have for  $\psi < 0$ ,

$$\chi(f) = -\frac{1}{2\pi i} \int_{-\infty}^{\infty} \frac{\chi(\phi)}{\phi-f} d\phi \quad (2.20)$$

since  $\chi \rightarrow 0$  as  $\psi \rightarrow -\infty$ . On letting  $\psi \rightarrow 0^-$ , we obtain

$$\chi(\phi - 10) = -\frac{1}{\pi i} \int_{-\infty}^{\infty} \frac{\chi(\phi)}{\phi-\phi} d\phi \quad (2.21)$$

the integral being of Cauchy principal-value form.

The boundary condition (2.11) on the body  $\phi < 0$  is equivalent to the statement that the imaginary part of the function  $\chi(f)$  vanishes for real negative  $f$ . Hence, on taking the real part of (2.21), we have

$$\Re \chi(\phi) = -\frac{1}{\pi} \int_{-\infty}^{\infty} \frac{\chi(\phi)}{\phi-\phi} d\phi \quad (2.22)$$

i.e. using (2.19) with  $\phi > 0$ ,

$$x_\phi(\phi, 0; \epsilon) = \left(\frac{\phi+1}{\phi}\right)^{1/2} \left[ 1 - \frac{1}{\pi} \int_{-\infty}^{\infty} \left(\frac{\phi}{\phi+1}\right)^{1/2} \frac{y_\phi(\phi, 0; \epsilon)}{\phi-\phi} d\phi \right] \quad (2.23)$$

Upon substitution of the formula (2.23) for  $x_\phi$  into the free-surface boundary condition (2.10) we obtain a non-linear singular integro-differential equation for the unknown quantity  $y(\phi, 0; \epsilon)$ ,  $\phi > 0$ .

Once this equation is solved on  $\phi > 0$ , the solution can be continued to the remainder of the  $f$ -plane using (2.20). In particular, for  $-1 < \phi < 0$  the integral on the right of (2.23) (which is no longer of Cauchy principal-value character when  $\phi < 0$ ), provides a representation for the quantity  $(\cos \gamma)x_\phi(\phi, 0; \epsilon) + (\sin \gamma)y_\phi(\phi, 0; \epsilon)$ . In combination with the boundary condition (2.11), this gives an expression for  $y_\phi$ ,  $-1 < \phi < 0$ , namely

$$y_\phi(\phi, 0; \epsilon) = \sin \gamma \left(\frac{\phi+1}{-\phi}\right)^{1/2} \left[ 1 - \frac{1}{\pi} \int_{-\infty}^{\infty} \left(\frac{\phi}{\phi+1}\right)^{1/2} \frac{y_\phi(\phi, 0; \epsilon)}{\phi-\phi} d\phi \right] \quad (2.24)$$

This can be used to evaluate  $y(-1, 0; \epsilon)$ , and hence the draft-based Froude number  $F_H$ , via (2.15).

### 3. Series in Froude Number

We now assume that the integro-differential equation obtained by combining (2.10), (2.23), possesses a formal power-series solution in the parameter  $\epsilon$ , of the form

$$y(\phi, 0; \epsilon) = \sum_{n=0}^{\infty} y_n(\phi) \epsilon^n \quad (3.1)$$

$$= \sum_{n=0}^{\infty} z_n(\phi - 10) \epsilon^n \quad (3.2)$$

where  $z_n(f) = x_n + iy_n$  is the corresponding coefficient in a power series for the complete solution  $z(f; \epsilon)$ . The leading ( $n=0$ ) term in this expansion is simply the zero-Froude-number solution (2.18), i.e.

$$z_0(f) = \left(\frac{f+1}{f}\right)^{1/2} \quad (3.3)$$

which is real on the free surface  $f = \phi - 10$ ,  $\phi > 0$ . Thus

$$y_0 = 0 \text{ and } x_0(\phi) = \left(\frac{\phi+1}{\phi}\right)^{1/2}$$

Upon substitution of the series (3.2) into the boundary condition (2.10) we find  $y_1 = -(x_0')^{-1}$ , and obtain the recurrence relation

$$\frac{y_n}{y_1} = \sum_{m=1}^{n-1} Q_m y_{n-m}, \quad n = 2, 3, 4, \dots \quad (3.4)$$

where

$$Q_n = \sum_{m=0}^n x_m' x_{n-m}' + y_m' y_{n-m}' \quad (3.5)$$

Since equation (2.23) is a linear relationship between  $y_n$  and  $x_n$ , it can be used to compute each  $x_n$ , once the corresponding  $y_n$  is known, i.e. for  $n = 1, 2, \dots$

$$x'_n(\phi) = -\frac{1}{\pi} \left( \frac{\phi+1}{\phi} \right)^{1/2} \int_0^\infty \left( \frac{\phi}{\phi+1} \right)^{1/2} \frac{y'_n(\phi)}{\phi-\phi} d\phi. \quad (3.6)$$

Some care has to be taken in the numerical evaluation of the derivatives  $y'_n(\phi)$  and the integrals (3.6), since this is the only numerical limitation on the number of coefficients which can be found. In order to work with integrals over a finite interval, we first re-write the relations (3.5) and (3.6) with the new independent variable

$$\beta = \left( \frac{\phi}{\phi+1} \right)^{1/2} \quad (3.7)$$

obtaining

$$Q_n(\beta) = \frac{(1-\beta^{2/\gamma})^{\gamma}}{(\pi/\gamma)2\beta^{2/\gamma-2}} \int_0^1 \left( \frac{\partial x_n}{\partial \beta} \frac{\partial x_{n-1}}{\partial \beta} + \frac{\partial y_n}{\partial \beta} \frac{\partial y_{n-1}}{\partial \beta} \right) d\beta \quad (3.8)$$

and

$$\frac{\partial x_n}{\partial \beta} = -\frac{\beta^{2/\gamma-2}}{(1-\beta^{2/\gamma})^\gamma} \int_0^1 \frac{\delta(1-\delta^{2/\gamma})}{\delta^{2/\gamma} - \beta^{2/\gamma}} \frac{\partial y_n}{\partial \delta} d\delta. \quad (3.9)$$

The interval of discretization is specified as  $E$ ; for example, for  $N$  equal intervals,  $E = 1/N$ . The functions  $y_i(\beta)$ ,  $i \geq 2$ , are evaluated at the points  $\beta_k = (k-1)E$ ,  $k=1, 2, \dots, N$ . The derivatives

$$\frac{\partial y_i}{\partial \beta}, \quad i \geq 2,$$

are computed by cubic splines at the points  $\beta_k$ , and also at the midpoints  $\delta_k = (k-1)E$ ,  $k=2, 3, \dots, N$ , with the end conditions  $y_i(0) = y_i(1) = 0$ ,  $i \geq 2$ . The values  $\partial y_i / \partial \beta$  at the points  $\delta_k$  are used to compute the integrals (3.9), upon application of Monacella's (1967) theorem, which states that the singularity in the numerical evaluation of Cauchy principal-value integrals can be ignored, providing the quadrature is symmetrical with respect to singularity. In the integration routine, a cubic spline fit was used to represent the integrand, and this cubic was integrated exactly.

The program was run in double precision (39 figures) on a CDC 6400 computer, with  $N=100$ , and was found to enable evaluation of terms up to  $y_{10}$  with 5-figure accuracy, and up to  $y_{15}$  with 4-figure accuracy.

#### 4. Divergence and Non-Uniqueness

Evidence has recently been given that the low-Froude-number approximation in problems of the present nature is singular, and leads to formal series in powers of the Froude number with zero radius of convergence (Vanden Broeck, Schwartz and Tuck, 1977). Providing the Froude number is sufficiently small (and it must indeed be extremely small), the series nevertheless retains significance as an asymptotic expansion, with accuracy of the order of magnitude of the first neglected term. However, such very low-Froude-number results are

"uninteresting" in the sense that the departure of the free surface from its limiting plane is required to be quite small, and the inevitable loss of accuracy of the asymptotic expansion takes place before interesting displacements of the free surface (including waves) have a chance to occur.

In the present section we show how the usefulness of the divergent expansion can be improved by a simple approximate series-completion procedure.

We recognise that in practice the following approach is limited by very serious computational difficulties. However we consider it as a useful preliminary motivation for the exact numerical scheme to be used in Sections 6 and 7.

Let us consider the series (corresponding to (3.2)) for  $z'(\phi, 0; \epsilon)$ ,  $\phi > 0$ . In Vanden Broeck, Schwartz and Tuck (1977), a generalisation to the case of complex coefficients of the Domb-Sykes procedure (Domb, C. and Sykes, M.F., 1957) was used to show that, for  $n$  large,

$$\frac{z'_{n+1}(\phi)}{z'_n(\phi)} \sim \frac{1}{n} c_1(\phi) \quad (4.1)$$

for some complex-valued quantity  $c_1(\phi)$ . A reasonable approximation to  $c_1(\phi)$  can be obtained from a finite number of terms, directly from (4.1), or by extrapolation for  $n \rightarrow \infty$ .

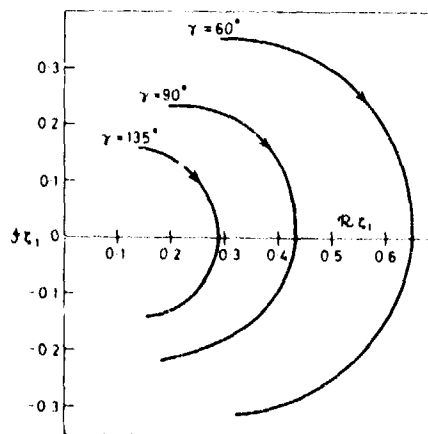


Figure 4. Polar plot of  $c_1(\phi)$ .

In Figure 4 we present polar plots of the function  $c_1(\phi)$  estimated from (4.1) with  $n=11$ , for different values of  $\gamma$ . The points on each curve when moving clockwise correspond to increasing values of  $\phi$ . All these plots appear to be close to a circle through the origin. This result can be shown (see Appendix for details) to

be equivalent to the approximation obtained by replacing the non-linear free surface by a "locally linearised" linear condition. This locally-linearised solution also predicts the form in which this circular plot is parametrized, namely

$$\frac{d}{d\phi} \frac{1}{\zeta_1(\phi)} = \frac{1}{2} (x'_0(\phi))^2, \quad (4.2)$$

a result which appears to be confirmed by the Comb-Sykes plot for  $\phi \gg \phi_c$ , where  $\zeta_1(\phi_c) = D = \text{real}$ . On integrating (4.2) we have

$$\frac{1}{\zeta_1(\phi)} = \frac{1}{D} + \frac{1}{2} \int_{\phi_c}^{\phi} (x'_0(\psi))^2 d\psi \quad (4.3)$$

The approximation (4.1) seems to fail close to the stagnation point  $\phi = 0$ , suggesting a different kind of behaviour in this region. We shall see in Section 5 that this does not constitute a serious limitation to the final numerical scheme.

Solution of (4.1) as a recurrence relation yields

$$z'_n(\phi) = C(\phi)(\zeta_1(\phi))^n (n+a)! \quad (4.4)$$

for some constant  $a$ , and some function  $C(\phi)$  which can be evaluated by fitting the last few coefficients. Recall that all quantities, including  $C$ ,  $\zeta_1$  and  $a$  in (4.4), may depend implicitly on the angle  $\gamma$ . Some preliminary computations seem to suggest that  $a = 0$ . However, this value has to be treated with caution, as an accurate evaluation of the constant " $a$ " based on only 15 terms is difficult. We will therefore develop the following arguments without any assumption on the constant  $a$ .

Following Buchanan (1976) and Dingle (1973), we sum the asymptotic series approximately by assuming that

$$z'_n = C(\phi)(\zeta_1(\phi))^n (n+a)! \quad (4.5)$$

for all  $n \geq N+1$ , where  $N$  is a sufficiently large integer. Therefore we write

$$z'(\phi, \epsilon) = \sum_{n=0}^N \epsilon^n z'_n + C \sum_{n=N+1}^{\infty} \epsilon^n \zeta_1^n (n+a)! \quad (4.6)$$

The infinite series

$$C \sum_{n=N+1}^{\infty} \epsilon^n \zeta_1^n (n+a)! \quad (4.7)$$

can be summed in the Borel sense as

$$-C(\epsilon \zeta_1)^N e^{-\frac{1}{\epsilon \zeta_1}} W_N \left( -\frac{1}{\epsilon \zeta_1} \right) \quad (4.7)$$

where

$$W_N(t) = \int_0^{\infty} \frac{(u-t)^{N+1} e^{-u}}{u} du \quad (4.8)$$

The function  $W_N(t)$  is defined in the complex  $t$ -plane, cut along the negative-real axis. If  $a = 0$ ,  $W_N(t)$  can be expressed in terms of the exponential integral function

(Abramowitz and Stegun, 1964, p.228). The usefulness of the original asymptotic expansion can therefore be increased by replacing the infinite series in (4.6) by its "converging factor", i.e.

$$z'(\phi, \epsilon) \sim \sum_{n=0}^N \epsilon^n z'_n - C(\phi)(\epsilon \zeta_1)^N e^{-\frac{1}{\epsilon \zeta_1}} W_N \left( -\frac{1}{\epsilon \zeta_1} \right) \quad (4.9)$$

Different functions replacing  $W_N(t)$  can be obtained by specifying different cuts in the complex  $t$ -plane. All the resulting solutions differ by a term which is exponentially small in the limit as  $\epsilon \rightarrow 0$  and all have therefore the same asymptotic expansion. The main difficulty about the converging factor is therefore one of non-uniqueness.

In particular we can replace  $W_N(t)$  in (4.9) by either of the following two functions:

$$W_N^+(t) = \begin{cases} W_N(t) & , t > 0, \\ W_N(t) - 2i\pi(-t)^{N+1/2} & , t < 0, \end{cases} \quad (4.10)$$

or

$$W_N^-(t) = \begin{cases} W_N(t) + 2i\pi(-t)^{N+1/2} & , t > 0, \\ W_N(t) & , t < 0. \end{cases} \quad (4.11)$$

One may argue that other arbitrary terms (also exponentially small in the limit as  $\epsilon \rightarrow 0$ ) could have been included in the definition of the converging factor. We believe that this is not the case in the present problem, and that the only non-uniqueness appearing in the present problem is associated with the specification of the branch-cut location. The most convincing argument for this is perhaps the numerical scheme presented in Section 6: the profile predicted by Shanks transformation turns out to be correct for the stern flow close to the body.

Let us consider first the choice (4.8). Since  $W_N(t)$  is defined in the complex  $t$ -plane, cut along the negative-real  $t$ -axis, the corresponding function in (4.9) is defined in the complex  $\zeta_1$ -plane cut along the positive real  $\zeta_1$ -axis. But Figure 4 shows that this branch cut is necessarily crossed at the value  $\phi = \phi_c$ , for any  $\gamma$ . Hence the corresponding solution is discontinuous at  $\phi = \phi_c$ , and therefore not physically acceptable. On the other hand, since the functions  $W_N$  and  $W_N^-$  are defined on a  $t$ -plane cut on the positive real  $t$ -axis, the corresponding functions in (4.9) are defined in the complex  $\zeta_1$ -plane cut along the negative real  $\zeta_1$ -axis, which is not crossed by the curves in Figure 4. Hence both of these solutions are continuous, and can be expected to have a physical meaning. Note that the solution corresponding to  $W_N$  has no waves at infinity and has therefore a bow-flow character, whereas the solution corresponding to  $W_N^-$  possesses a train of waves at infinity, and has a stern-flow character.

More precisely, substituting (4.3) and (4.10) into (4.9), we get for  $\phi > \phi_c$  in the stern-flow case,

$$z(\phi, \epsilon) = \sum_{n=0}^N \epsilon^n z'_n - C(\phi)(\epsilon \zeta_1)^N e^{-\frac{1}{\epsilon \zeta_1}} W_N \left( -\frac{1}{\epsilon \zeta_1} \right) + 2i\pi C(\phi) \frac{1}{(\epsilon \zeta_1)^{1+s}} e^{-\frac{1}{\epsilon \zeta_1}} e^{-\frac{1}{2\epsilon} \int_{\zeta_1}^{\zeta_2} (z_s(v))' dv} \quad (4.12)$$

The last term in (4.12) represents a linear wave on the non-uniform stream defined by the rigid-wall solution. The amplitude of the waves at infinity is given by:

$$\frac{4\pi}{\epsilon} e^{-\frac{1}{\epsilon \zeta_1}} \lim_{\phi \rightarrow \infty} \left| \frac{C(\phi)}{(\zeta_1(\phi))^{1+s}} \right| \quad (4.13)$$

and is exponentially small as  $\epsilon \rightarrow 0$ .

These results are similar to those obtained by Ogilvie (1968), by carrying out a local linearisation about the  $\epsilon = 0$  solution  $z = z_0(f)$ . In Ogilvie's method the waves are completely determined by the rigid-wall solution i.e. the first term of the low Froude number expansion. On the other hand, our method indicates that the amplitude of the waves depends on quantities like  $C(\phi)$ ,  $a$  and  $D$  which can only be evaluated by considering many terms in the low Froude number expansion. We expect our approach to be an improvement on Ogilvie's theory, as the total information about the fully non-linear problem is contained in high-order terms of the expansion. However, our approach seems to present serious numerical difficulties, partly because of the difficulty of evaluating the constant  $a$  from a small number of terms. Other numerical difficulties also arise associated with the above series-completion method, involving errors due to subtraction of large nearly-equal numbers. In the following sections, a more practical numerical method is derived, using a similar philosophy but without the above limitations.

#### 5. Shanks Table Summation

Transformations that accelerate the convergence of slowly-convergent series, can often also be used on divergent asymptotic expansions. For example Baker (1965) proved that Padé sequences are convergent for divergent expansions derived by confluence. In the present paper we make use of the Shanks transformation  $e^{(k)}$  (Shanks 1955). Although this transformation is often more powerful than the Padé sequences for summing divergent expansions, it has not been studied extensively and the reasons for its "magic" power remain obscure.

Useful experience can be gained by considering first the simple divergent expansion

$$\sum_{n=0}^{\infty} x^n n! \quad (5.1)$$

where  $x$  is a complex variable. When applied to the series (5.1), the iterated Shanks transformation  $e^{(k)}$  converges rapidly, so long as  $x$  is not real and positive, to the function

$$-\frac{1}{x} e^{-\frac{1}{x}} E_1 \left( -\frac{1}{x} \right) \quad (5.2)$$

where  $E_1(t)$  is the exponential integral function defined in the complex  $t$ -plane cut along the real negative  $t$ -axis. (Abramowitz and Stegun 1964, p.228). Thus the Shanks table converges in the complex  $x$ -plane cut along the real positive  $x$ -axis.

Other choices for the cut are in principle possible. The reason why the Shanks table selects this particular cut can be established by contradiction. If another cut were selected, the Shanks table applied to the expansion (5.1), with  $x$  real and positive, would have to converge to one of the two complex functions

$$\frac{1}{x} e^{-\frac{1}{x}} \left[ \text{Ei} \left( \frac{1}{x} \right) \pm i\pi \right] \quad (5.3)$$

On the other hand  $e^{(k)}$  is real and cannot therefore converge to a complex number when  $x$  is real. Therefore the only possible choice is to cut the complex  $x$ -plane along the real positive axis. A similar argument has been used before by Shanks (1955) in the case of the function  $\log(1+z)$ .

Our method is now the following. We apply the transformation  $e^{(k)}$  to the complete expansion for  $z'(\phi, 0; \epsilon)$ ,  $\phi > 0$ , obtained in Section 3. The above considerations, combined with the arguments of Section 4, suggest that a Stokes discontinuity has to be expected for  $\phi = \phi_c$ .

This point can be justified intuitively as follows. In Section 4 we have shown that the most-divergent part of the series can be completed with the functions  $W_N(t)$ ,  $W_N^*(t)$  or  $W_N^{**}(t)$ . The solution corresponding to  $W_N(t)$  has a Stokes discontinuity at  $\phi = \phi_c$ , whereas the solution corresponding to  $W_N^*(t)$  possesses a train of linear waves for  $\phi > \phi_c$ . This procedure could in principle be repeated an infinite number of times.

For example, in the second step, we should find a less-divergent expansion by extracting the most-divergent part from the original expansion. We should then complete this new series with appropriate functions  $S(t)$ ,  $S^*(t)$  or  $S^{**}(t)$ . The solution corresponding to  $S(t)$  would have a Stokes discontinuity at  $\phi = \phi_A$  and  $S^*(t)$  would possess, for  $\phi > \phi_A$ , a train of non-linear corrections to the linear waves found in the first step. It seems reasonable to assume that the domain in which we superpose the non-linear corrections coincides with the domain of the linear waves. Therefore  $\phi_A = \phi_c$ .

The Shanks table was found to converge rapidly, and gives results with 4-figure accuracy on almost all the free surface, even for moderately large values of  $\epsilon$ . A good convergence was even found near the stagnation point, where the plots of Figure 4 do not give any information.

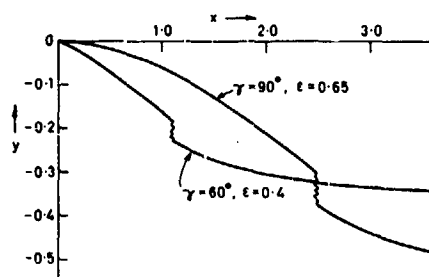


Figure 5. Discontinuous free-surface profiles obtained by Shanks method.

Typical profiles for  $\varepsilon = 0.65$ ,  $\gamma = \pi/2$ , and  $c = 0.40$ ,  $\gamma = \pi/3$ , are shown on Figure 5. These profiles have, as expected, jump discontinuities corresponding to a value of  $\phi$  relatively close to the points  $\phi = \phi_c$  where the circles in Figure 4 cross the real positive  $\zeta_1$ -axis.

By analogy with the properties of the converging factor established in Section 4, we assume that the portion of the free surface given by the Shanks table between the body and the discontinuity is correct for the stern flow, and that the portion of the free surface beyond the discontinuity is correct for the bow flow. In the case of the stern flow, this assumption is confirmed by the numerical scheme of Section 6 and by the fact that the solution given by the Shanks table between the body and the jump satisfies the boundary condition (2.10). The situation with respect to the bow flow is less clear.

#### 6. Stern Flow

In order to solve the fully non-linear problem, a successful numerical scheme was developed in the following way. For a given value of  $\varepsilon$  and  $\gamma$ , we seek a continuous solution of the integro-differential equation defined by (2.10) and (2.23), which matches exactly the solution given by the Shanks table between the body and the discontinuity. We assume, therefore, that

$$y_s(\phi) = y_s^*(\phi), \quad 0 \leq \phi \leq b, \quad (6.1)$$

where  $y_s^*(\phi)$  is given by the Shanks table. The value  $\phi = b$  corresponds to some point between the body and the discontinuity. Since  $y(0) = 0$ , the relation (6.1) implies

$$y(\phi) = y^*(\phi), \quad 0 \leq \phi \leq b, \quad (6.2)$$

where  $y^*(\phi)$  is a known function. Equation (2.23) can now be re-written in the form

$$x_s = F(\phi) - \frac{1}{\pi} \left( \frac{\phi+1}{\phi} \right)^{1/2} \int_0^\phi \left( \frac{\phi}{\phi+1} \right)^{1/2} \frac{y_s}{\phi-\phi'} d\phi', \quad (6.3)$$

where

$$F(\phi) = \left( \frac{\phi+1}{\phi} \right)^{1/2} \left( 1 - \frac{1}{\pi} \int_0^\phi \left( \frac{\phi}{\phi+1} \right)^{1/2} \frac{y_s^*}{\phi-\phi'} d\phi' \right)$$

is a known function of  $\phi$ .

Equations (2.10) and (6.3) define an integro-differential equation for the unknown function  $y_s(\phi)$ ,  $b < \phi < \infty$ , to be solved subject to the matching condition

$$\lim_{\phi \rightarrow b+} y(\phi) = y^*(b). \quad (6.4)$$

After discretisation, the functions  $y_s(\phi)$ ,  $y(\phi)$ ,  $x_s(\phi)$ ,  $b < \phi < \infty$ , are represented respectively by the vectors

$$\underline{y} = (y_1^1, y_1^2, y_1^3, \dots, y_1^N) \quad (6.5)$$

$$\underline{y} = (y^1, y^2, y^3, \dots, y^N) \quad (6.6)$$

and

$$\underline{x}_s = (x_s^1, x_s^2, x_s^3, \dots, x_s^N), \quad (6.7)$$

whose components are the values of the corresponding functions at the mesh points chosen.

The first mesh point is at  $\phi = b$  and the last one is at  $\phi = \phi_\infty$ , where  $\phi_\infty$  is a large number. The error inherent in approximating an infinite integral by a finite interval was found in most cases to be negligible, at a distance less than a wavelength from the last mesh point, for  $\phi_\infty$  sufficiently large. Using the trapezoidal rule and Monacella's theorem to approximate the integrals, we get relations of the form

$$x_s^i = F_i + \sum_{j=1}^N a_{ij} y_j^1, \quad i = 1, 2, \dots, N \quad (6.8)$$

$$y_i^1 = \sum_{j=1}^N c_{ij} y_j^1, \quad i = 1, 2, \dots, N. \quad (6.9)$$

where the  $a_{ij}, c_{ij}, F_i$  are known constants. Substituting in (2.10), we get a system of  $N$  non-linear algebraic equations with  $N$  unknowns  $(y_1^1, \dots, y_N^1)$  that can be written in vector form as

$$\underline{g}(\underline{y}^1) = 0. \quad (6.10)$$

This system is solved iteratively by a Newton method. Thus, if  $\underline{y}_0^1$  is an approximation to the solution, a better approximation is expected to be

$$\underline{y}_1^1 = \underline{y}_0^1 - A^{-1} \underline{g}(\underline{y}_0^1), \quad (6.11)$$

where  $A$  is the matrix  $\partial \underline{g} / \partial \underline{y}_0^1$  with  $(i,j)$ th elements

$$A_{ij} = \partial g_i / \partial (y_j^1)_0.$$

For the first approximation we take  $\underline{y}_0^1 = 0$ . Each iteration requires the computation and inversion of the matrix  $A$ .

The scheme was found to be rapidly convergent, and a solution of the algebraic equations

with an error less than  $10^{-10}$  is obtained in a few iterations. The accuracy of the solution obtained is improved by increasing the number of mesh points. The residual error is a direct measure of the accuracy with which the free-surface condition is satisfied, and in fact can be interpreted as the difference between the computed pressure and the required zero level.

So far, the solution obtained satisfies the free-surface condition for  $b < \phi < \infty$ , and matches the Shanks-table solution near the body. Using (6.3) and (2.10) we can compute  $x_b$  and  $y$ ,  $0 \leq \phi \leq b$ . It is quite remarkable that the function  $y(\phi)$  so computed, turns out to be equal to  $y^*(\phi)$  (see (6.2)) to the same good accuracy as that to which the free-surface condition is satisfied for  $y > b$ . This proves that our solution satisfies the complete integro-differential equation (2.10), (2.23) to this accuracy. It also shows *a posteriori* that our conjecture about the accuracy of the Shanks-table solution near the body was correct. It is worthwhile mentioning that a Newtonian iteration scheme allowing all the points of the free surface to vary, does not converge, even if the starting approximation is correct to three places. This phenomenon is related to the non-uniqueness of the solution.

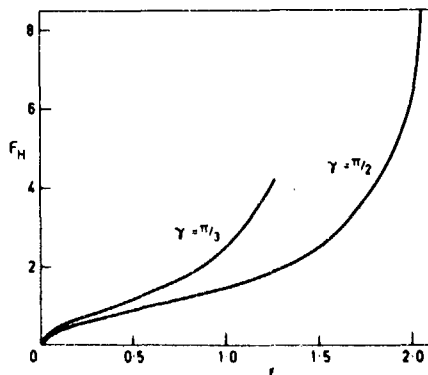


Figure 6. Relationship between  $F_H$  and  $\epsilon$ .

Stern flows for  $\gamma = 60^\circ$ ,  $\gamma = 90^\circ$  were computed by the above numerical scheme for various values of  $\epsilon$ . In each case the corresponding value of the Froude number was computed by use of (2.24) and (2.15). In Figure 6 we present values of the Froude number  $F_H$  versus  $\epsilon$ , for  $\gamma = 60^\circ$  and  $\gamma = 90^\circ$ . For  $\epsilon$  small,  $F_H$  is proportional to  $\sqrt{\epsilon}$ . This result is in agreement with an asymptotic analysis of (2.24) and (2.15) in the limit as  $\epsilon \rightarrow 0$ . For large values of the Froude number, the curves of Figure 6 indicate that all the values of  $F_H$  between 0 and  $\infty$  are mapped onto a finite range of  $\epsilon$ .

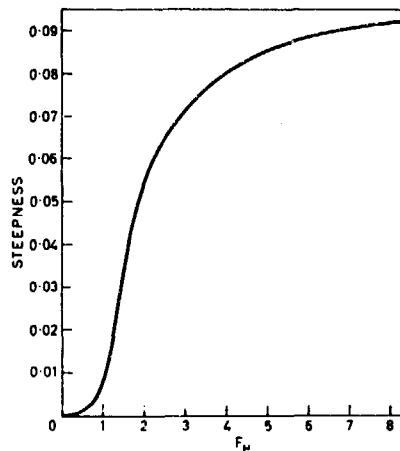


Figure 7. Steepness (wave height/wave length) of the non-linear stern wave as a function of draft-based Froude number at  $\gamma = 90^\circ$ .

As the Froude number increases for a given value of  $\gamma$ , the steepness of the waves (i.e. peak-to-trough wave height divided by the wavelength) increases. Figure 7 shows the steepness of the waves versus the Froude number  $F_H$ , for  $\gamma = 90^\circ$ . When the Froude number is small, the steepness increases rapidly (in fact exponentially) with the Froude number. This behaviour can be expected from the linear approximation of Section 4 (see formula (4.13)). However, when the Froude number is large, non-linear effects become predominant and an extrapolation of the curve of Figure 7 for  $F_H \rightarrow \infty$ , suggests that the steepness tends to a value less than the maximum steepness (0.1412) of Stokes waves (Schwartz, 1974). In other words, when the Froude number increases, both the wave height and the wave length increase but their ratio (i.e. the steepness) remains bounded by a constant less than the maximum steepness. Similar results were found in the case  $\gamma = 60^\circ$ . Note that the mathematical formulation of Section 2 allows in principle negative values of the draft  $H$ , for which waves of higher steepness could be computed.

In Figure 8 we present a typical example of the non-linear computations which can be performed by the present method. The Froude number is 6.3 and the steepness of the waves is of order 0.09. The actual shape of the body ( $\gamma = 90^\circ$ ) is also shown on this figure. Note that the wave height is several times bigger than the draft of the body, and the waves are quite noticeably non-sinusoidal, with sharp peaks and broad troughs. Note also that the horizontal scale has been much compressed compared to the vertical scale. Similar computations have been performed for a large range of  $\gamma$  and  $\epsilon$  values.

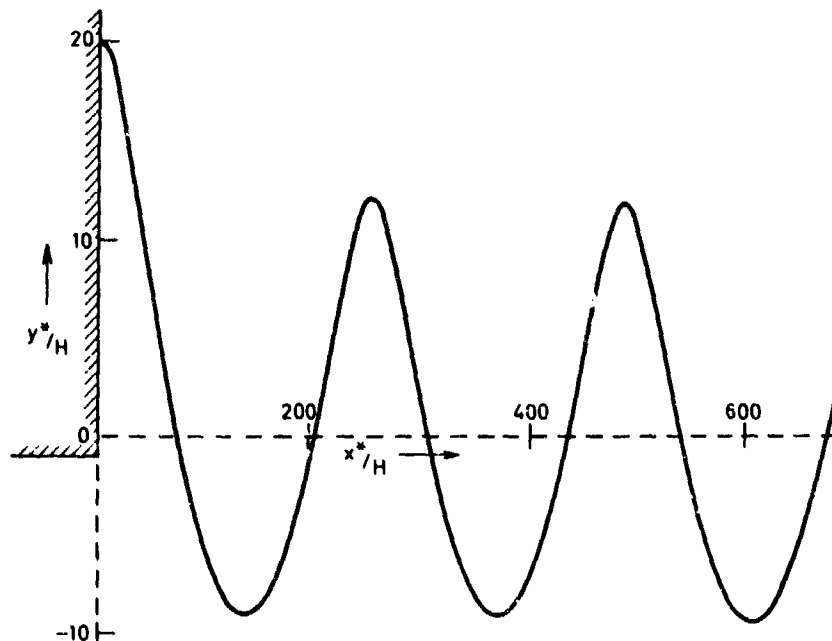


Figure 8. Stern flow for  $\gamma = 90^\circ$ ,  $F_H = 6.3$

#### 7. Bow Flow

In the spirit of Section 5, we may expect the solution given by the Shanks table beyond the discontinuity at  $\phi = \phi_c$  to be correct for the (wave-free) far-field solution for bow flow. It is interesting to note, however, that our numerical results from the Shanks table are slightly less accurate for  $\phi > \phi_c$  than for  $\phi < \phi_c$ . Thus the free-surface pressure computed from this solution is essentially zero (to the accuracy of convergence of the Shanks table) if  $\phi < \phi_c$ , but not quite so for  $\phi > \phi_c$ . This is of potential significance, as discussed below, but since the error is still only very small we ignore it temporarily, and assume that the Shanks table solution is exact for  $\phi > \phi_c$  as a representation of a bow flow.

We now attempt to solve the bow-flow problem in a manner analogous to that for stern flow in Section 6. That is, for a given value of  $\epsilon$  and  $\gamma$ , we seek a continuous solution of the integro-differential equation (2.10) and (2.23), which matches exactly the solution given by the Shanks table for  $\phi > \phi_c$ . We therefore assume

$$y_\phi(\phi) = y_\phi^*(\phi), \quad b < \phi < \infty, \quad (7.1)$$

where  $y_\phi^*(\phi)$  is given by the Shanks table for some constant  $b > \phi_c$ .

Following the procedure outlined in Section 6, an integro-differential equation is derived for the unknown function  $y_\phi(\phi)$ ,  $0 < \phi < b$ . After discretization, we obtain again a set of  $N$  non-linear algebraic equations in  $N$  unknowns, that we try to solve by Newtonian iteration.

This scheme was found to be unstable, and did not converge for a realistically-high choice of the number  $N$  of mesh points. This numerical evidence seems to point strongly to the conclusion that no continuous wave-free solution of the bow-flow problem exists. However, some qualitative information can still be gained from the present numerical procedure.

For example, a careful analysis of the first few Newtonian iterations suggests that the trouble arises in the immediate neighbourhood of the stagnation point. It was found that excellent convergence of the iterations could be achieved by decreasing the number of mesh points in the neighbourhood of the stagnation point, while keeping a large value of  $N$ , with mesh points closely distributed over the remainder of the free surface. A typical free-surface profile ( $\gamma = 90^\circ$ ,  $\epsilon = 0.9$ ) is shown in Figure 9.

This "solution" is clearly very approximate indeed, as the flow between the last point shown and the stagnation point has been completely filtered out. However, it is

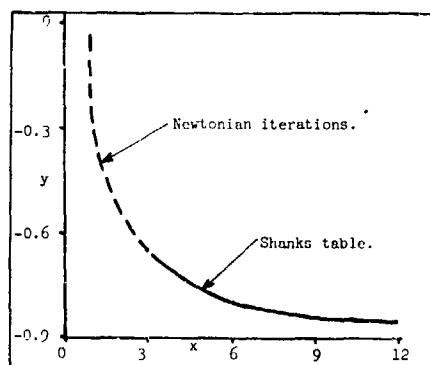


Figure 9. Attempted bow-flow solution

interesting to note that the free surface is becoming almost vertical at the last computed point, and shows no indication of any tendency to approach the stagnation point.

These computations therefore suggest that the true bow-flow solution possesses some kind of jet. We conjecture that the appropriate solution at all Froude numbers is of the form shown in Figure 10, similar to that suggested by Dagan and Tulin (1972) at high Froude number. The fact that the above numerical method, which ignores the presence of this jet, nevertheless converges if we make the mesh sufficiently coarse near the body, is consistent with the whole jet structure being confined to a very small region close to the body.

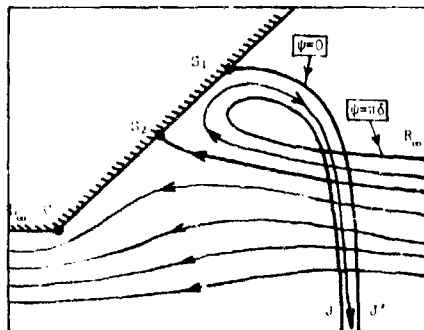


Figure 10. Sketch of conjectured jet-like bow flow

It is clear, however, that the whole analytical and numerical structure of the present paper is in principle invalid for a flow such as that in Figure 10. For example, the  $f$ -plane sketched in Figure 4 is no longer appropriate, and we must insert a cut as shown in Figure 11. Nevertheless, we can recover the original  $f$ -plane geometry by the conformal mapping

$$f = \bar{f} + \delta \log(\bar{f} - \lambda) + i\pi\delta \quad (7.2)$$

which turns the  $f$ -plane of Figure 11 into that of Figure 4, with  $\bar{f}$  instead of  $f$ .

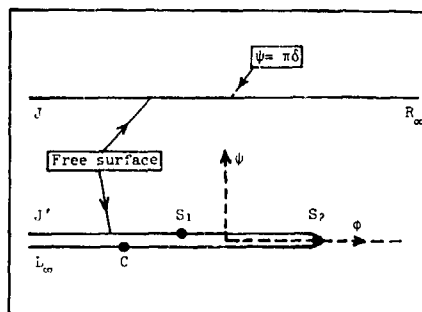


Figure 11. Modified  $f$ -plane with jet

The only effect on the computations is to replace the free-surface condition (2.10) by

$$\epsilon \left( 1 + \frac{\delta}{\bar{f} - \lambda} \right)^2 + y(x_\epsilon^2 + y_\epsilon^2) = 0, \quad (7.3)$$

where  $\delta$  is the non-dimensional jet thickness and  $\lambda$  is its location in the  $\bar{f}$ -plane. Both parameters  $\delta, \lambda$  are unknown and must be determined as part of the bow-flow solution.

Note that if  $\delta = 0$  we recover the continuous assumption used in the remainder of this paper, and  $\bar{f} \equiv f$ . It seems likely that  $\delta$  is exponentially small in the limit as  $\epsilon \rightarrow 0$ . If this is the case, the solution with a jet has exactly the same asymptotic expansion as that without, and the jet structure must be obtained by an appropriate summation technique.

At this point we can see how the slight apparent error in the pressure computation for  $\phi > \phi_c$  could be significant. For if (2.10) is not the appropriate free-surface condition, but rather (7.3), the error obtained by assuming (2.10) will appear to be a non-zero free-surface pressure, proportional to the exponentially-small jet thickness  $\delta$ . Attempts have been made, so far unsuccessful, to exploit this phenomenon to provide an estimate of  $\delta$  and  $\lambda$ .

Direct Newtonian-iteration methods incorporating the jet geometry are presently being investigated. This is a problem of considerable difficulty, since an accurate model of the complete re-entrant jet geometry is needed, and this demands good numerical values for the unknown jet parameters  $\delta$  and  $\lambda$ .

#### Acknowledgement

The authors thank Dr. L.W. Schwartz for assistance given by active discussion of this work, as part of a research project supported by the Australian Research Grants Committee.



## References

1. Abramowitz, M. & Stegun L.A. (eds.) 1964 Handbook of Mathematical Functions, Appl. Math. Ser. No. 55, Nat. Bur. Stand., Washington, D.C.
2. Buchanan, D.J. 1976 Analysis and improvement of divergent series. Quart. J. Mech. Appl. Math. 29, 127-135.
3. Baker, G.A. 1965 The theory and application of the Padé method, in Advances in Theoretical Physics (K. Breuckner, ed.) Vol.1, p.1. Academic Press.
4. Dagan, G. 1975 Waves and wave resistance of thin bodies moving at low speed: The free-surface non-linear effect. J. Fluid Mech. 69, 405-416.
5. Dagan G. & Tulin, M.P. 1972 Two-dimensional free-surface gravity flow past blunt bodies. J. Fluid Mech. 51, 529-543.
6. Dingle, R.B. 1973 Asymptotic Expansions: Their Derivation and Interpretation. Academic Press, London and New York.
7. Domb, C. & Sykes, M.F. 1957 On the susceptibility of a ferromagnetic above the Curie point. Proc. R. Soc. London. A240, 214-228.
8. Monacella, V.J. 1967 On ignoring the singularity in the numerical evaluation of Cauchy principal value integrals. Rep. No. 2356, D.T.N.S.R.D.C., Department of the Navy, Washington, D.C.
9. Newman, J.M. 1976 Linearized wave resistance theory. Int. Sem. Wave Resistance. Proceedings, Soc. Nav. Arch. Japan, Tokyo.
10. Ogilvie, T.F. 1968 Wave resistance: the low-speed limit. Rep. No. 002, Dept. Nav. Arch. & Mar. Eng., University of Michigan, Ann Arbor.
11. Schwartz, L.W. 1974 Computer extension and analytic continuation of Stokes' expansion for gravity waves. J. Fluid Mech. 62, 553-578.
12. Shanks, D. 1955 Non-linear transformations of divergent and slowly-convergent sequences. J. Math. & Phys. 34, 1-42.
13. Vanden Broeck, J.M., Schwartz, L.W. & Tuck, E.O. "Divergent Low-Froude-Number Series Expansion of Non-Linear Free-Surface Flow Problems", Report No. V-01, Applied Mathematics Department, University of Adelaide, January 1977.
14. Vanden Broeck, J.M. & Schwartz, L.W. 1978 A generalized family of series transformations. (In preparation.)

## Appendix

### Asymptotic form of Coefficients for Large $n$

Relation (4.1) can be used to infer the asymptotic form of the coefficients  $z_n$ , by considering contributions to the right-hand side of (3.4) from  $x_{n-1}, y_{n-1}, x_{n-2}, y_{n-2}, \dots$ , noting that  $Q_{n-1}$  depends on all these quantities, but  $Q_{n-2}$  depends only on  $x_{n-2}, y_{n-2}, \dots$ , etc. Thus,

$$\begin{aligned} y_n &= y_1 [Q_1 y_{n-1} + Q_2 y_{n-2} + y_2 Q_{n-1} + O(x_{n-3}, y_{n-3})] \\ &= 2x_0^2 y_1' x_{n-1}' + 2y_1 (y_2 x_0' + y_1 x_1') x_{n-1}' + \dots \\ &\quad + y_1 Q_1 y_{n-1} \quad + y_1 Q_2 y_{n-2} + \dots \\ &\quad + 2y_1^2 y_1' y_{n-1}' + \dots \end{aligned} \quad (A.1)$$

The leading term in (A.1) is normally dominant for large  $n$ , and thus the growth of the coefficients is asymptotically given by

$$y_n \sim 2(x_0')^{-3} x_{n-1}', \quad n \rightarrow \infty. \quad (A.2)$$

Note that the term  $y_1 Q_1 y_{n-1}$  must be of lower order, if the series is everywhere divergent, since this term can produce only a geometrical increase in  $y_n$ , in the absence of the term in  $x_{n-1}'$ . The limiting recurrence relation (A.2) would have arisen from a model linear problem, in which the actual free-surface condition (2.10) was replaced by

$$y - 2\epsilon(x_0')^{-3} x_\phi = R(\phi), \quad (A.3)$$

for any arbitrary function  $R(\phi)$ . Equation (A.3) is a linear mixed boundary condition for the potential function  $y = y(\phi, \psi)$  on  $\psi = 0$ , reminiscent of similar free-surface conditions obtained by previous authors (Ogilvie 1968, Dagan 1975, Newman 1976), by carrying out a "local linearization" about the  $\epsilon = 0$  solution  $z = z_0(f)$ .

If we substitute approximation (4.5) for  $z_1'(\phi)$  into the asymptotic recurrence relation (A.2), we see immediately that this relation holds if and only if  $\zeta_1(\phi)$  is given by (4.2).

## NONLINEAR HYDRODYNAMIC FORCES ON FLOATING BODIES\*

B. D. Nichols and G. W. Hirt  
University of California  
Los Alamos Scientific Laboratory  
Los Alamos, New Mexico 87545

### ABSTRACT

This study investigates the influence of nonlinear effects on two- and three-dimensional cylinders in forced oscillation. For the two-dimensional calculations the publicly available finite-difference code SOLA-SURF is used. This code provides a solution algorithm for the full nonlinear Navier-Stokes equations or, as an input option, the nonlinear potential flow equations. The companion code, SOLA-3D, is used for the three-dimensional calculations. Hydrodynamic forces on two- and three-dimensional triangular cylinders undergoing forced harmonic oscillation in sway are calculated and compared. The hydrodynamic coefficients for the two-dimensional cylinder are numerically determined for several amplitudes of motion. At amplitudes larger than approximately 0.12 beam widths definite nonlinear effects are observed. However, this is not the case for the three-dimensional flow associated with finite length cylinders for amplitudes of motion up to 0.22 beam widths. The numerical data support the use of linear potential theory for predicting the added mass and damping coefficients for two-dimensional cylinders in low amplitude motion (up to 6% of beam width for sway). For finite length cylinders the linear theory appears to hold for much larger amplitudes (at least up to 20% of beam width). The numerical algorithms contained in the SOLA codes are also shown to work well for the calculation of nonlinear flows generated by rigid bodies impacting on a fluid surface. In particular, the impact of a circular cylinder is calculated and found to be in excellent agreement with experimental data.

### I. INTRODUCTION

In this paper we discuss numerically determined hydrodynamic forces on floating cylinders. Particular attention is given to nonlinear effects and to finite length effects. The numerical solution algorithms used for these studies are finite-difference techniques for the nonlinear Navier-Stokes equations. The two-dimensional algorithm is contained in the SOLA-SURF code.<sup>1</sup> This code has been used in extensive numerical studies of the hydrodynamic forces on rectangular and triangular cylinders

in low amplitude forced heave, sway, and roll motions.<sup>2-4</sup> The good agreement obtained in these studies with linear theory and experimental data serves as a validation of the basic calculational procedures. The companion three-dimensional code, SOLA-3D, has been successfully applied to the calculation of wind loading on three-dimensional structures<sup>5</sup> and, in addition, has reproduced selected two-dimensional calculations for heave and sway motions for cross checking against the two-dimensional code.

We have utilized the two- and three-dimensional SOLA codes to investigate nonlinear and three-dimensional effects influencing the hydrodynamic forces on floating cylinders. In this paper we discuss nonlinear effects arising during large amplitude swaying motions of a two-dimensional 60° triangular cylinder. The results of the numerical studies are compared with other data, including nonlinear potential flow numerical computations. An interpretation of the observed nonlinear effects is given. We present a second study that compares two- and three-dimensional calculations of the triangular cylinder in sway. Here the end effects associated with finite length cylinders are noted. Nonlinear finite amplitude effects for the three-dimensional triangular cylinder are also considered. To further validate our numerical methods as useful tools for studying nonlinear flow phenomena, we present the results from a circular cylinder impacting onto a water surface.

### II. NONLINEAR TWO-DIMENSIONAL EFFECTS

#### Low Amplitude Studies

The hydrodynamic coefficients<sup>6</sup> for two-dimensional bodies undergoing low amplitude forced harmonic oscillations in an otherwise quiescent fluid have been determined using the SOLA-SURF code. In this study added mass and damping coefficients are computed and compared with the experimental and analytical work of Vugts.<sup>7</sup> The results of these studies for the rectangular cylinder in forced heave,<sup>8</sup> and the 60° triangular cylinder in forced sway<sup>9</sup> have previously been reported, but are included here

\*This work was performed jointly under the auspices of the United States Energy Research and Development Administration and the Office of Naval Research, ONR Task #NRO62-455.

for completeness. Presented are also data from a 60° triangular cylinder in forced roll motion. The added mass coefficient,  $\mu$ , and the damping coefficient,  $\lambda$ , are given by

$$\mu = \frac{\gamma \cos \beta}{\omega^2 a} \quad (1)$$

and

$$\lambda = \frac{\gamma \sin \beta}{\omega a} \quad (2)$$

where  $a$  is the amplitude of motion,  $\omega$  is the frequency of motion, and  $\gamma$  is the amplitude of the calculated harmonic pressure force on the body. The phase shift  $\beta$  was obtained by comparing plots of the body displacement and pressure force acting on the cylinder as functions of time and measuring the shift in phase. A detailed description of the determination of these coefficients is given in an earlier report.<sup>2</sup> The calculated added mass and damping coefficients for the cylinders in heave, sway, and roll are shown in Figs. 1, 2, and 3, respectively. The coefficients are normalized by  $\rho A$  ( $B^2 \rho A$  for roll) and  $\sqrt{B/2g}$ , where  $\rho$  is the fluid density,  $A$  is the mean submerged area,  $B$  is the cylinder beam, and  $g$  is the acceleration of gravity. Coefficients were calculated for normalized frequencies (i.e.,  $\omega \sqrt{B/2g}$ ) ranging from 0.50 to 1.25 with  $B/T = 2.0$  for the rec-

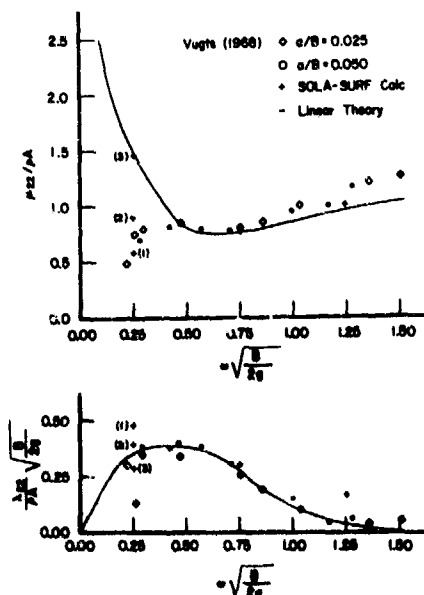


Fig. 1. A comparison of theoretical, numerical, and experimental values of added mass (top) and damping (bottom) coefficients for a rectangular cylinder in forced heave, with  $B/T = 2.0$ .

tangular cylinder and  $B/T = 1.155$  for the triangular cylinder, where  $T$  is the initial draft of the cylinder. The amplitudes of motion, normalized by  $B$ , for the rectangular cylinder were 0.025 and 0.050 and for sway was 0.058. The triangular cylinder in roll motion rotated about an axis located at the horizontal center of the wedge and the initial free surface position. The amplitudes of motion were 0.025 and 0.050 radians.

In general, the numerical data from these calculations are in good agreement with linear theory. The sway (Fig. 2) and roll (Fig. 3) numerical data show some discrepancy with the experimental data, which is believed to result from elastic bending in the support bar used to hold the body in the experimental setup.<sup>7</sup> Although there was secondary flow at the tip of the triangular cylinder in the sway and roll calculations, we found, as Vugts suggested from his observation of these secondary vortices in his experiments, that this did not disturb the net pressure force over the cylinder surface. We believe these numerical experiments reinforce the usefulness of linear, potential flow theory for computing the added mass and damping coefficients for various shaped bodies in low amplitude motions.

#### Large Amplitude Studies

The nonlinear effects associated with large amplitude motions of floating cylinders may be illustrated with a two-dimensional triangular cylinder in finite amplitude forced sway. This study was performed with the two-dimensional SOLA-SURF code. The amplitude of motion in the low amplitude studies discussed above was 0.058 of the cylinder beam width (0.02 m) at the still water level. The cylinder draft was equal to 0.865 beam widths. The finite amplitude studies were performed with amplitudes increased up to a maximum value of 0.430 of the beam width, at a normalized frequency of 1.0. All other parameters remained the same as for the low amplitude studies.

The main effect of this increase in amplitude is to produce a significant decrease in the phase shift of the dynamic pressure force relative to the cylinder displacement phase. Figure 4 shows this phase shift and the amplitude of the dynamic pressure force as functions of the amplitude of motion. The phase shift reaches a maximum of 0.90 radians at 0.04 m amplitude and then decreases nearly linearly for larger displacement amplitudes. This figure also shows, as expected, the linear increase in the force amplitude as a function of the cylinder displacement amplitude. These trends are reflected in the calculation of the hydrodynamic coefficients shown in Fig. 5. Added mass and damping coefficients determined from the linear theory reported by Vugts<sup>7</sup> are included for comparison. The damping coefficient, Eq. 2, follows the trend of the phase shift ( $\beta$ ) shown in Fig. 4. This is expected because for small phase shifts the coefficient is proportional to the phase shift, while the force amplitude ( $\gamma$ ) increases nearly linearly with the displacement amplitude ( $a$ ).

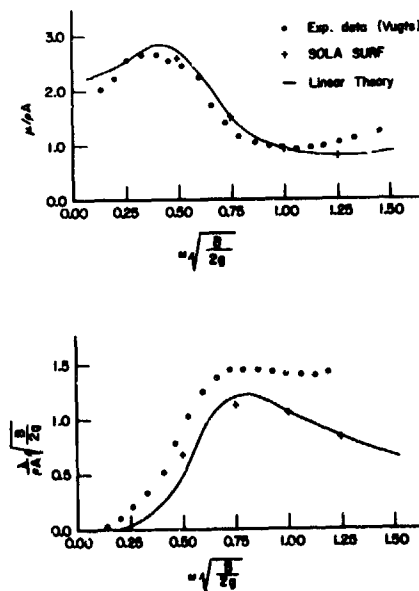


Fig. 2. A comparison of theoretical, numerical, and experimental values of added mass (top) and damping (bottom) coefficients for a 60° triangular cylinder in forced sway, with  $B/T = 1.155$ .

The added mass coefficient, Eq. 1, for the larger amplitudes of motion varies less than 10% from the linear theory values. This follows from its weak dependence on  $B$  for small  $B$ .

These results suggest that the linear theory reported by Vugts does adequately predict the added mass coefficients for the 60° triangular cylinder in sway at this beam to draft ratio and for displacement amplitudes of motion up to nearly 50% of its beam width. For the damping coefficient, however, this is not the case. For displacement amplitudes greater than approximately 25% of the beam width, the damping coefficient is significantly smaller than that predicted by linear theory.

The detailed calculations reveal the reason for the decreasing phase angle  $\beta$  with increasing amplitude. Referring to Fig. 6, we see the velocity field of the fluid after 1.48 periods of motion for the four different amplitudes of motion, 0.02, 0.09, 0.12, and 0.15 m. As the sway amplitude is increased, for a given frequency, the average body velocity increases. This causes the fluid to slosh further up (down) the sides of the body, because surface waves do not move away fast enough. As a consequence the fluid reaction force on the wedge tends to be more in phase with the body, i.e., the phase shift  $\beta$  is reduced. Of course, this trend cannot continue indefinitely, because the

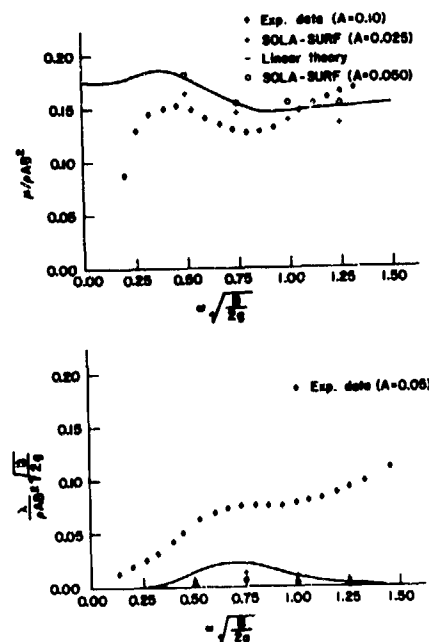


Fig. 3. A comparison of theoretical, numerical, and experimental values of added mass (top) and damping (bottom) coefficients for a 60° triangular cylinder in forced roll, with  $B/T = 1.155$ .

very high amplitudes will cause splashing and turbulence dissipation effects that must contribute to some damping.

#### Potential Versus Nonpotential Flow

The flow field in the two-dimensional calculations of the triangular cylinder in sway shows secondary flow near the cylinder tip (see Fig. 6). As noted above, the presence of this secondary flow vortex has virtually no effect on the net calculated force on the cylinder. In an attempt to understand this, we modified the two-dimensional SOLA-SURF code so that non-linear potential flow can be computed as an input option.

The basis of this modification comes from the observation that the momentum equation difference approximation can be easily cast into the form of the potential flow equations. This is done by eliminating all body, convective, and viscous accelerations, and also zeroing out the previous time step velocity field. The potential function,  $\phi$ , is then formally identified with  $\delta t \cdot P$  in the code, where  $\delta t$  is the time increment and  $P$  is the pressure when the full Navier-Stokes equations are used. The incompressibility condition remains unchanged. The rigid wall boundary conditions also remain unchanged. At the free surface, however, dif-

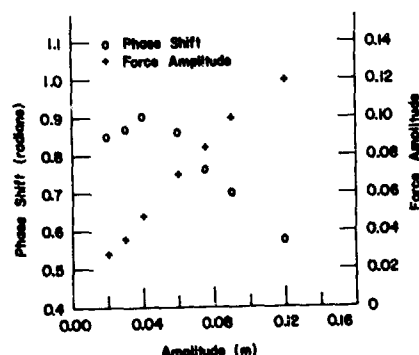


Fig. 4. Phase shift and amplitude of the dynamic pressure force as functions of the 60° triangular cylinder displacement amplitude.

ferent boundary conditions are needed for the variable  $P$  when it is identified with the potential. These conditions are derived under the constraint that the gas pressure at the free surface must equal the pressure outside the liquid. By expressing this condition in terms of the potential, appropriate free surface boundary conditions are determined. We prooftested this potential flow code by calculating the SOLA-SURF test problem,<sup>1</sup> i.e., the formation and propagation of an undular bore. The results compared well with the original SOLA-SURF calculation, which makes use of the full Navier-Stokes equations.

A comparison is shown in Fig. 7 of the velocity fields of a cylinder in sway after 1.48 periods from the SOLA-SURF code with and without the nonlinear potential flow option. The difference between the irrotational and rotational flow fields is obvious. The net calculated forces on the cylinder, however, are nearly identical for the two methods. On the other hand, the pressure profiles along the cylinder boundaries in the two cases do differ. Figure 8 compares the pressure (plotted normal to the boundaries) on the 60° triangular cylinder assuming nonlinear potential flow and using the full Navier-Stokes equations. The amplitude of motion for these calculations is 0.173 beam widths (0.06 m) and the normalized frequency is 1.0. The pressure profile plotted is after 1.48 periods, which corresponds to the velocity fields in Fig. 7. At this time the cylinder velocity is near zero as it approaches the rightmost position of maximum displacement. As expected in the potential flow case, the pressure near the tip on both sides of the cylinder is more negative than elsewhere on the corresponding side, which is necessary to accelerate the flow around the tip. In fact, the pressure is lower over the entire cylinder surface in the potential flow calculation than in the nonpotential flow calculation. Although these pressure profiles differ, the less positive downstream pressures in the potential flow

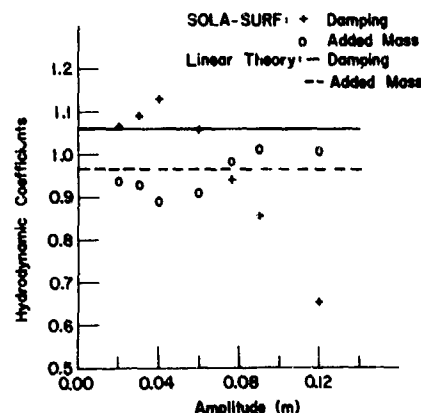


Fig. 5. Normalized added mass and damping coefficients as functions of the 60° triangular cylinder displacement amplitude.

case are compensated for by more negative upstream pressures. As a result, the net forces on the cylinder are nearly the same in the two cases. The eddies generated in the nonpotential case do not carry away kinetic energy because they are alternately generated and destroyed as the body moves to and fro.

### III. NONLINEAR THREE-DIMENSIONAL EFFECTS

Nonlinear and finite length effects influencing the hydrodynamic forces on three-dimensional floating cylinders may be studied using the SOLA-3D code. We utilized this three-dimensional code to investigate the end effects and nonlinear large amplitude effects associated with a finite length 60° triangular cylinder in forced sway.

#### Finite Length

The parameters for these three-dimensional calculations were chosen for comparison with the two-dimensional calculations. Calculations were made with sway amplitudes of motion of 0.058 and 0.116 of the triangular cylinder beam width, i.e., 0.02 m and 0.04 m, at the still water level. The cylinder draft was equal to 0.865 beam widths and the normalized frequency of motion was 1.25. The cylinder length to draft ratio was varied from two to four. The resulting phase shift of the dynamic pressure force relative to the cylinder displacement phase, and the amplitude of the hydrodynamic force per unit length for the three-dimensional calculations were virtually the same as the two-dimensional calculations. This brief study suggests, therefore, that the end effects of the triangular cylinder are not significant for low amplitudes of motion and for cylinder length to draft aspect ratios greater than two. Length to draft ratios less than two were not investigated.

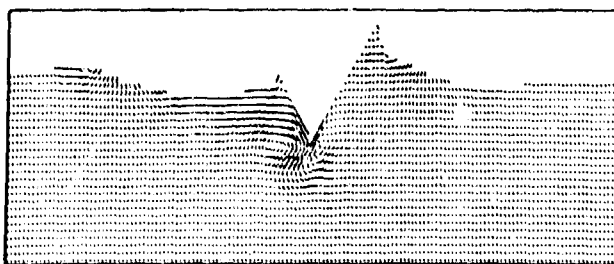
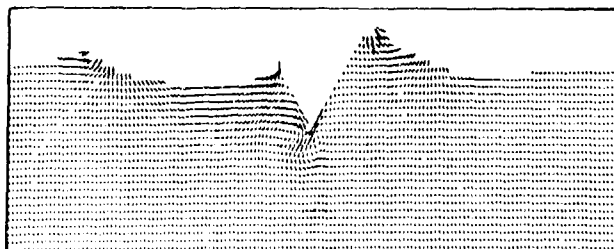
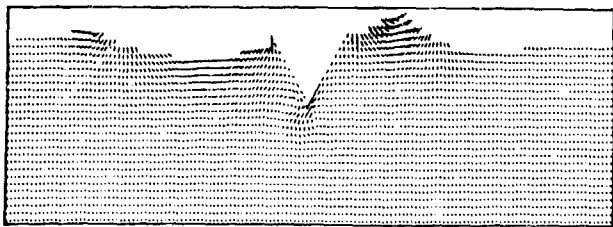
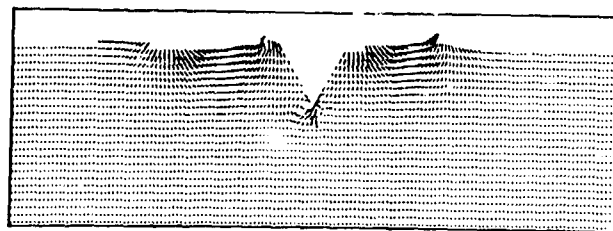


Fig. 6. Velocity vector plots showing the velocity field about a swaying  $60^\circ$  triangular cylinder after 1.48 periods. Reading from top to bottom, the amplitudes of motion are 0.02, 0.09, 0.12, and 0.15 m.

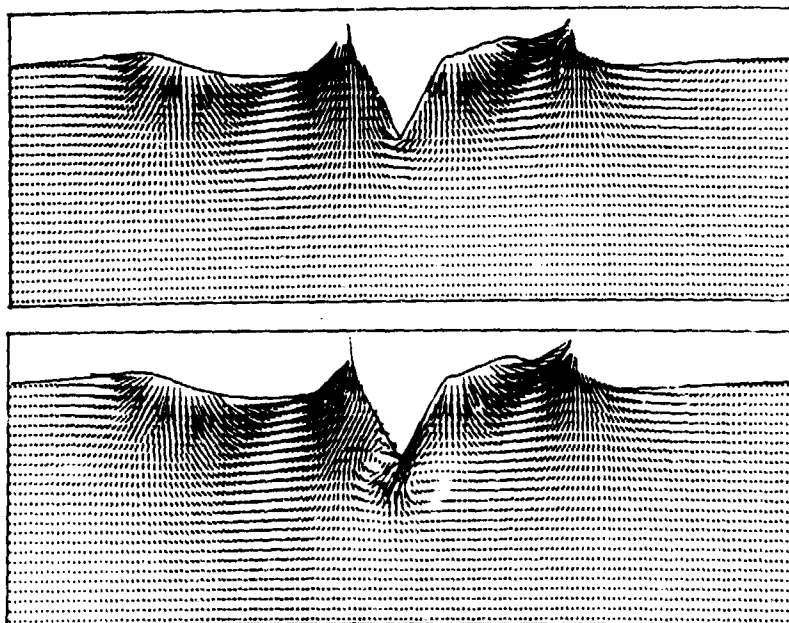


Fig. 7. Velocity fields about a 60° triangular cylinder in sway after 1.48 periods from the SOLA-SURF code with (top) and without (bottom) the nonlinear potential flow option.

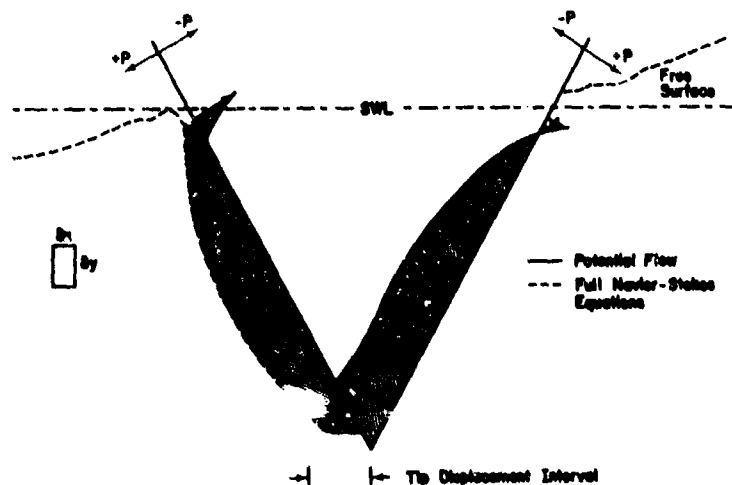


Fig. 8. Pressure profiles on a 60° triangular cylinder in sway determined from the SOLA-SURF code with and without the nonlinear potential flow option.

Typical velocity field plots for these low amplitude calculations are shown in Figs. 9 and 10. The entire velocity field in these planes is not shown, but only the region near the cylinder. Also, the magnification of the velocity vectors varies from plane to plane. Velocity fields in planes normal to the axis of the cylinder are shown in Fig. 9. The left velocity field is of the plane nearest the cylinder end and the right plot is of the velocity field in the plane immediately outside the cylinder end. At the time of these plots the cylinder is moving to the right after 2.11 periods of oscillation. The three-dimensional effect of the flow is clearly shown in the right plot. The larger velocity flow at the left (downstream) edge of the cylinder does not continue past the cylinder end in this plane, but flows around the edge. This is also clearly shown in the right plot of Fig. 10, which is of a horizontal plane near the vertical center of the cylinder. The fluid flows around the downstream side of the cylinder. The velocity field in the vertical plane through the center of the cylinder and parallel to its axis is shown in the left plot in Fig. 10. Secondary vortex flow is seen near the cylinder end in all the planes shown. However, as in the two-dimensional calculations, these vortices appear to have no significant influence on the net hydrodynamic forces on the body.

#### Large Amplitude

The most significant effect of the increase in amplitude in the two-dimensional calculations, as discussed above, was a significant decrease in the phase shift of the dynamic pressure force relative to the cylinder displacement phase. The force amplitude increased linearly with the cylinder displacement amplitude. We made correspondingly large amplitude, three-dimensional calculations to compare with the two-dimensional study.

The three-dimensional calculations were for amplitudes of motion from 0.058 to 0.216 of the beam width, i.e., .020 m to 0.075 m. (At larger amplitudes the free surface slope near the cylinder end violated the code requirement that the slope not be greater than the slope of the cell diagonal.) The draft of the 60° triangular cylinder was 0.865 beam widths and the length to draft aspect ratio was two. As in the two-dimensional case, the force amplitude increased linearly as the cylinder displacement amplitude increased (see Fig. 11). However, as seen in Fig. 12, the decrease in the phase shift of the dynamic pressure force relative to the cylinder displacement phase observed in the two-dimensional case was not observed in these finite-length calculations. The phase shift is less for all amplitudes of motion but does not decrease significantly as the amplitude increases. It is possible, however, that at still larger amplitudes of motion the phase shift would show a decrease.

The added mass and damping coefficients determined from these three-dimensional calculations are compared with the two-dimensional SOLA-SURF data and linear theory in Figs. 13 and 14. In keeping with the two-dimensional data, the added mass coefficients are within a few per cent of the linear theory. The damping coefficient, again, follows the trend of the phase shift.

We earlier noted that in the infinite length case the phase shift decreased as the body velocity increased (i.e., at larger amplitudes of motion at a set frequency) because the fluid sloshed further up (down) the sides of the body and caused the force on the cylinder to be more in phase with the body, i.e., the phase shift was reduced. The probable reason for the phase shift not decreasing significantly in the finite length case is that at large

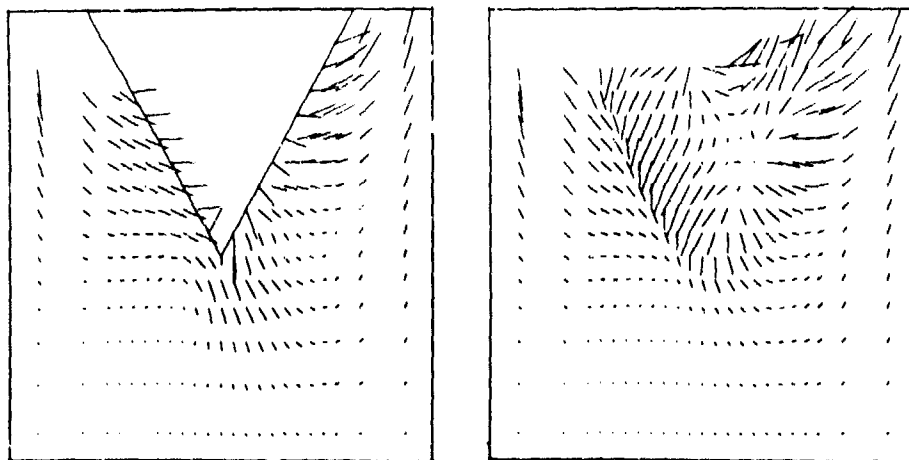


Fig. 9. Local velocities in planes normal to the axis of the three-dimensional triangular cylinder in low amplitude motion after 2.11 periods. The left plot is the plane nearest the cylinder end and the right plot is the plane immediately outside the cylinder end.



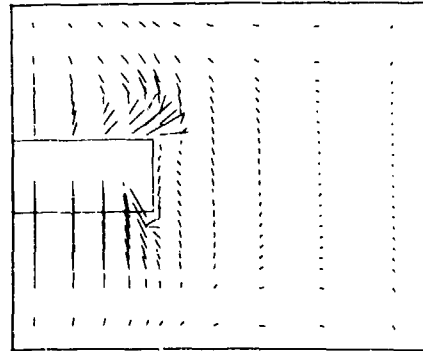
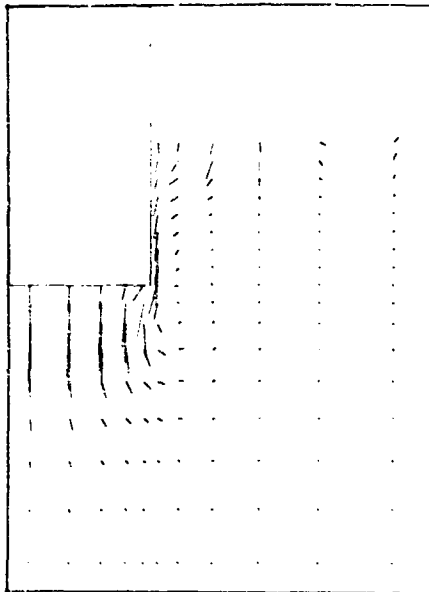


Fig. 10. Velocities in a vertical plane through the center of the cylinder and parallel to its axis (left) and in a horizontal plane near the vertical center of the cylinder (right) after 2.11 periods.

amplitudes of motion fluid flows freely around the cylinder end and does not build up at the sides.

The flow pattern around the cylinder for the large amplitudes reinforces this interpretation. Figures 15 and 16 show the velocity field near the cylinder for an amplitude of 0.173 beam widths (0.06 m) after two periods of oscillation. Again, the magnification of the velocity vectors is different for each of the planes. Velocity fields in planes normal to the axis of the cylinder are shown in Fig. 15. The left velocity vector plot is of the plane nearest the cylinder end. As observed in Fig. 6 for the two-dimensional case, very strong secondary vortex flow is formed near the tip of the cylinder. The right plot in Fig. 15 is of the plane immediately outside the cylinder end. At the time of these plots the cylinder has reached the leftmost point of its displacement after two periods of oscillation. The left plot in Fig. 16 is of the velocity field in the vertical plane through the center of the cylinder and parallel to its axis. This shows the downward motion of the fluid at the end of the cylinder, resulting in the small vortex off the cylinder end. The right plot in Fig. 16 shows the secondary flow on the downstream side of the cylinder in the horizontal plane near the vertical center of the cylinder. These velocity fields in selected planes show the flow around the cylinder end and downward flow near

the end for this time. The resulting free surface configuration is shown in Fig. 17.

#### IV. CIRCULAR CYLINDER IMPACT

The SOLA-SURF code was used to calculate the force of impact on a circular cylinder during constant velocity entry into a pool of water. The cylinder boundary was approximated by straight line segments. The rigid-fluid interface boundary condition applied to each line segment was successfully used for determining the hydrodynamic forces on the rectangular and triangular cylinders in forced motion discussed above. Specifically, at the rigid-fluid interface the cell pressure is derived from the constraint that the normal fluid velocity be equal to that of the cylinder. As a free fluid surface approaches a rigid boundary, a simple linear combination of the rigid and free boundary condition is used. This is needed to eliminate the sudden transition in boundary conditions, which may result in excessively large pressure spikes. For partially submerged bodies moving at relatively small velocities, this ad hoc linear combination of boundary conditions worked very well. For the impact problems, however, a modification was necessary because the fluid did not anticipate the presence of the rigid boundary in sufficient time before impact and the calculation consequently exhibited unacceptable large pressure oscillations. Through a heuristic argument based on the need

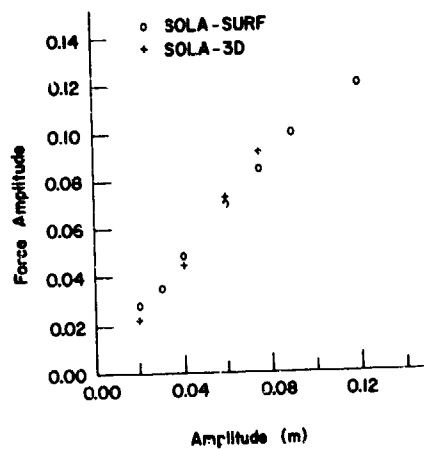


Fig. 11. Amplitude of the dynamic pressure force as a function of cylinder displacement amplitude.

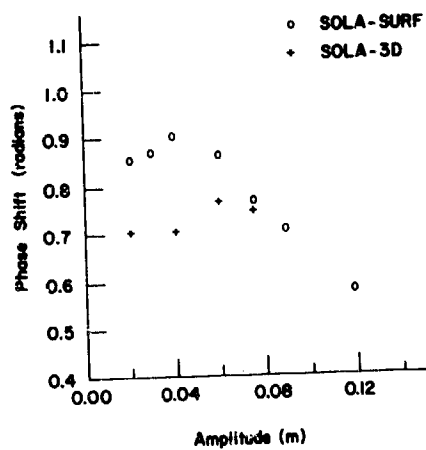


Fig. 12. Phase shift of the dynamic pressure force relative to the cylinder displacement phase as a function of the cylinder displacement amplitude.

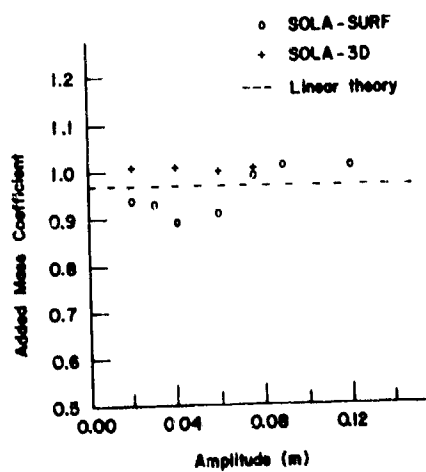


Fig. 13. Normalized added mass coefficient as a function of the cylinder displacement amplitude.

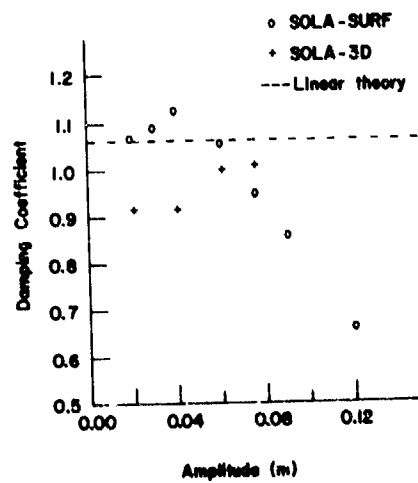


Fig. 14. Normalized damping coefficient as a function of the cylinder displacement amplitude.

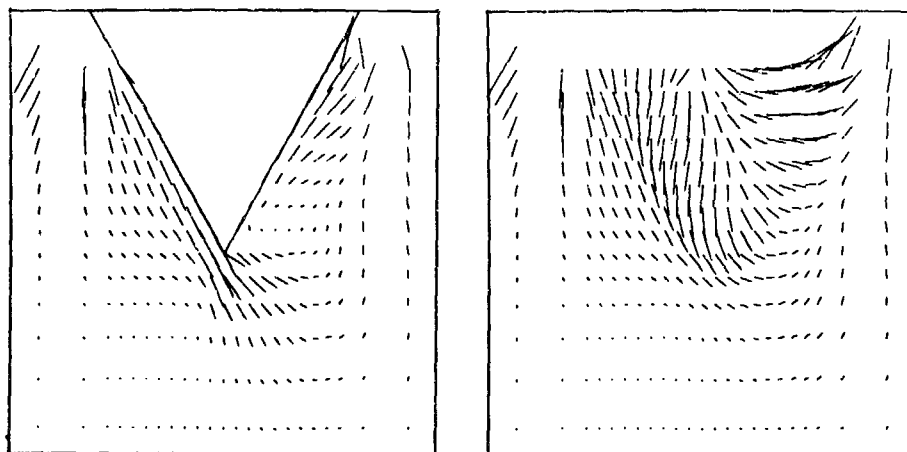


Fig. 15. Local velocities in planes normal to the axis of the triangular cylinder in large amplitude motion after 2.0 periods. The left plot is the plane nearest the cylinder end and the right plot is the plane immediately outside the cylinder end.

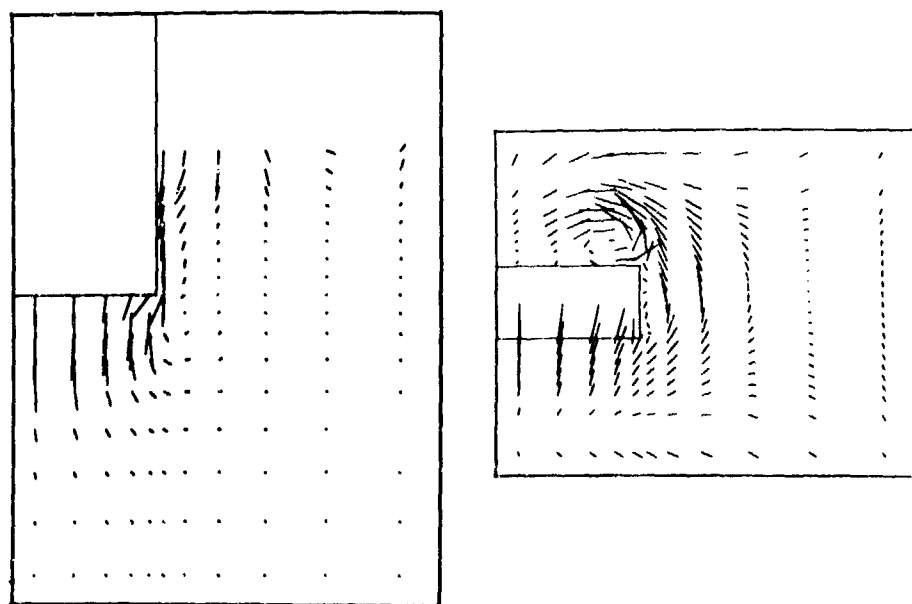


Fig. 16. Local velocities in a vertical plane through the center of the cylinder and parallel to its axis (left) and in a horizontal plane near the vertical center of the cylinder (right) after 2.0 periods.

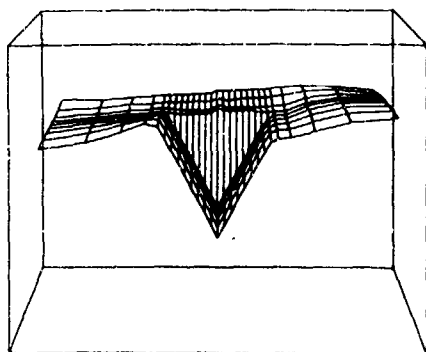


Fig. 17. Local free surface configuration resulting from the triangular cylinder in sway motion after 2.0 periods.

for an applied pressure on the fluid just sufficient to bring the normal component of the fluid and body velocities into agreement at the time of impact, a boundary condition combination was derived that did force a smooth transition between the free and rigid boundary conditions. The new combination uses a quadratic in the relative velocity term instead of the linear term used in the earlier ad hoc expression.

The average pressure on the cylinder, i.e., the vertical force per unit length divided by the cylinder diameter, was determined for a cylinder with a diameter of 8.25 inches and an impact velocity of 7.70 ft/sec. The calculation was run to a time of 18.0 msec. At this time the fluid has reached nearly 90° around the cylinder. Velocity vector plots in Fig. 18 show the velocity field with the free surface and the cylinder boundary at -7.85, 2.48, 10.75 and 18.00 msec. Because the calculation starts some time before the cylinder hits the surface, we shifted the calculated time scale so that the computed and measured peak forces occur at the same time.

A comparison of the numerically calculated average pressure and the experimental data<sup>4</sup> are shown in Fig. 19. (The experimental data are for an impact velocity of 7.65 ft/sec. and the computed data have been scaled from 7.70 ft/sec. to 7.65 ft/sec. for this comparison.) The experiment only had pressure transducers located along a portion of the lower surface of the cylinder. When the cylinder was wetted beyond the highest pressure gauge location the total force was estimated in two ways. In the first, extrapolation was used to estimate the unmeasured surface pressures and resulted in the upper of the two experimental curves appearing in Fig. 19 after  $t=3.0$  msec. The lower curve is the result obtained using only the measured data and ignoring the pressures in the uninstrumented region. The agreement between the computed results and the upper experimental curve is excellent, except for some small, high

frequency pressure oscillations around 6 msec. These oscillations are remnants of the discretization fluctuations that are not completely eliminated by the improved boundary condition combination discussed above.

#### V. CONCLUSIONS

Most ship hydrodynamic problems are solved by linear potential flow methods. Some limits of this approximate theory have been demonstrated by comparisons of calculated results using the SOLA-SURF code for the full, nonlinear Navier-Stokes equations with linear theory and the experimental data of Vughts. An essential assumption made in the linear theory is that the amplitude of motion be small with respect to the dimensions of the cylinder. Indeed, when this is no longer the case, nonlinear effects, as shown by the SOLA-SURF code, can be significant.

Three-dimensional, finite length effects were determined not to be significant for cylinders with either low or relatively high amplitudes of motion. Apparently the flow around the cylinder ends, for the short cylinders studied, minimizes the pile up of fluid at the fore and aft cylinder surfaces, which caused the large amplitude effect in the case of infinitely long cylinders.

The calculations of the cylinder impacting onto the free surface forced a needed improvement of the transition from free to rigid surface boundary conditions. It also served to further validate the SOLA-SURF code as a useful tool for calculating nonlinear fluid flow problems.

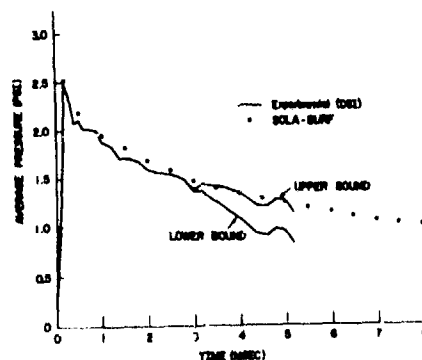


Fig. 19. Comparison of numerically computed and experimental data for the average pressure per unit length on an 8.25 in. diameter cylinder impacting with a constant velocity of 7.65 ft/sec.

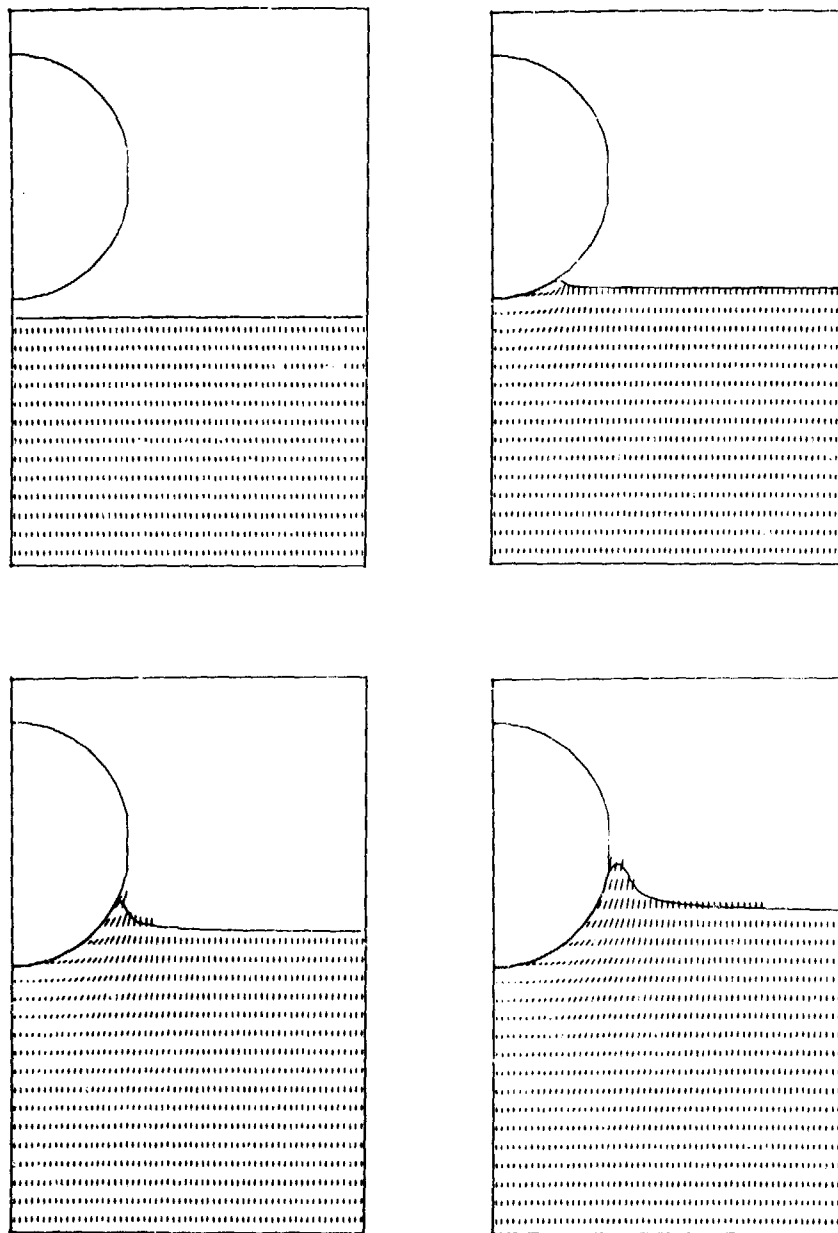


Fig. 18. Velocity vector plots showing the velocity field near the impacting cylinder with the free surface and cylinder boundary at -7.85, 2.48, 10.75, and 18.0 msec.

#### ACKNOWLEDGMENTS

The authors wish to express their appreciation to Leland Stein for writing the SOLA-3D code and for many valuable suggestions in running the three-dimensional problems and to Juanita Salazar for so ably composing the text and figures of this paper.

#### REFERENCES

1. C. W. Hirt, B. D. Nichols, and N. C. Romero, "SOLA - A Numerical Solution Algorithm for Transient Fluid Flows," Los Alamos Scientific Laboratory report LA-5852 (April 1975); LA-5852, Addendum (January 1976).
2. B. D. Nichols and C. W. Hirt, "Methods for Calculating Multi-Dimensional, Transient Free Surface Flows Past Bodies," Proc. of the First Intern. Conf. on Numerical Hydrodynamics, Gaithersburg, MD (1975).
3. B. D. Nichols and C. W. Hirt, "Numerical Calculation of Wave Forces on Structures," Proc. of the Fifteenth Intern. Conf. on Coastal Engineering, Honolulu, HI (1976).
4. B. D. Nichols and C. W. Hirt, unpublished work performed for the Office of Naval Research under contract NR-062-455.
5. C. W. Hirt and J. D. Ramshaw, "Prospects for Numerical Simulation of Bluff Body Aerodynamics," Proc. of the Aerodynamic Drag Mechanisms Symposium presented by General Motors Research Laboratories, Warren, MI (1976).
6. J. V. Mehausen, "The Motion of Floating Bodies," Annual Review of Fluid Mechanics, **3**, 237 (1977).
7. J. H. Vugts, "The Hydrodynamic Coefficients for Swaying, Heaving, and Rolling Cylinders in a Free Surface," International Shipbuilding Progress, **15**, 251 (1968).
8. John J. Carey, Electric Power Research Institute/Developmental Sciences, Inc., private communication (1977).

DISCUSSIONS  
of four papers

NUMERICAL SOLUTIONS OF TRANSIENT NONLINEAR FREE-SURFACE MOTION  
OUTSIDE OR INSIDE MOVING BODIES

Odd M. Faltinsen

NUMERICAL SIMULATION OF SHIP MOTION BY EULERIAN HYDRODYNAMIC TECHNIQUES

G.I. Bourianoff and B.R. Penumallil

COMPUTATION OF NEAR-BOW OR STERN FLOWS,  
USING SERIES EXPANSION IN THE FROUDE NUMBER

J.-M. Vanden Broeck and E.O. Tuck

NONLINEAR HYDRODYNAMIC FORCES ON FLOATING BODIES

B.D. Nichols and C.W. Hirt

Invited Discussion

John V. Wehausen  
University of California, Berkeley

I have very few comments on Faltinsen's paper. Out of curiosity, it might be interesting to know how big a penalty one pays by replacing (9) by  $\phi(x,y) = 0$ . Does  $b(t)$  have to be much larger? It might help some readers if (35) were identified with the "radiation condition". At the bottom of p. 9 the author remarks that C. M. Lee's results do not show a significant influence of nonlinearity. From his point of view he is probably right. However, the differences calculated by Lee, Parissis and by Potash [J. Ship Res. 15 (1971), 295-324] are significant enough to be measurable and show reasonable agreement with experiment when the amplitudes aren't too large, as shown by Tsai & Koterayama [Rep. Res. Inst. App. Mech. Kyushu Univ. 24 (1976), no. 77, 1-39].

I have a few problems with the paper by Bourianoff & Penumallil. The first concerns the use of the Navier-Stokes equations and an "artificial viscosity". Is this aimed at obtaining a more exact model of a fluid or does it have significance only as a device to simplify the numerical analysis? If the former, is the usual viscous-fluid boundary condition satisfied? Another question concerns the equations of motion (2.3) and (2.4). If (2.3) is the equation for the motion of the center of mass, shouldn't the angular motion be referred to a coordinate system fixed in the body with moments taken about the center of mass? Other choices usually lead to more complicated equations. A similar remark applies to some later equations.

Since drift forces are calculated, it would be interesting to see some comparisons with analytically derived expressions by Newman [J. Ship Res. 11, 51-60] and Maruo [J. Ship Res. 4, no. 3, 1-10]. There are also some recent measurements.

The paper by Vanden Broeck and Tuck is very interesting. I think I have understood what has been done, but I have not digested it well enough to comment sensibly.

The numerical analysis in the paper by Nichols & Hirt has been published elsewhere, so

that one can comment only upon the results. Firstly, one can ask the same question here as was asked above about the use of the Navier-Stokes equation by Bourianoff & Penumallil. In particular, is the viscous-fluid boundary condition used? If this condition is not satisfied, I find it strange that vortices can be generated as in Figures 7 and 9. It is, of course, satisfying to have a numerical assessment of the limits of validity of linearized theory. Earlier assessments have been either from experiment or from second-order calculations such as those of Lee, Parissis and Potash cited above. A comparison with the latter would be of interest.

Author's Reply  
by Odd M. Faltinsen  
to discussion by John V. Wehausen

Professor Wehausen asked how large  $b(t)$  has to be in order to approximate  $\phi(x,0)$  by zero when  $|x| > b(t)$ .

I have not examined this systematically, but I found quite erroneous answers by using such an approximation for the  $b(t)$ -values used in my paper.

Author's Reply  
by George I. Bourianoff and B.R. Penumallil  
to discussion by John V. Wehausen

The comment about artificial viscosity can best be answered by first supplying some background information. It is well-known that the explicit forward time differencing of the force equation results in a numerical error that is second order in  $\Delta x$ . This error term can have either positive or negative sign, depending on the direction of local spatial gradients. The "artificial viscosity" is a positive dissipative term that is larger in magnitude than the largest error term. Therefore, the net second-order term (numerical error plus artificial viscosity) will remain positive and the calculation will remain stable.

It is possible to use centered time differencing techniques or predictor-corrector techniques that have smaller or no second-order error. These techniques require more computer time and are more difficult to implement. Therefore, the inclusion of an artificial viscosity

term is simply a device to allow the use of a simple fast numerical technique in the present analysis. The no-slip boundary conditions were used at all fluid-solid interfaces, and hence there is no coupling of the viscous drag force to the floating body.

Dr. Wehausen's second point is well taken since there is a term left out of equation (2.4). The term is included when the equation is rewritten on page 6 and it is included in the calculation.



## CONFERENCE PARTICIPANTS

ADEE, BRUCE H., University of Washington, Seattle, Washington, USA  
 BABA, EIICHI, Mitsubishi Heavy Industries, Nagasaki, Japan  
 BAI, K.J., DTNSRDC, Bethesda, Maryland, USA  
 BANNISTER, KENNETH A., Naval Surface Weapons Center, Silver Spring, Maryland, USA  
 BASTIANON, RICARDO A., Instituto de Tecnología Naval, Buenos Aires, Argentina  
 BORIS, JAY P., U.S. Naval Research Laboratory, Washington, D.C., USA  
 BØRRESEN, ROLF, The Ship Research Institute of Norway, Trondheim, Norway  
 BOURIANOFF, GEORGE, Austin Research Associates, Inc., Austin, Texas, USA  
 BOYNTON, FREDERICK P., Physical Dynamics Inc., Berkeley, California, USA  
 BYERS, DAVID W., Naval Ship Engineering Center, Washington, D.C., USA  
 CAGLE, BEN J., Office of Naval Research, Pasadena, California, USA  
 CAULISAL, SANDER M., U.S. Naval Academy, Annapolis, Maryland, USA  
 CHAN, ROBERT K.-C., JAYCOR, Del Mar, California, USA  
 CHANG, M. S., DTNSRDC, Bethesda, Maryland, USA  
 CHAPMAN, R. B., Science Applications, Inc., La Jolla, California, USA  
 CHASZEYKA, MICHAEL A., Office of Naval Research, Chicago, Illinois, USA  
 CHEN, HSAO-HSIN, American Bureau of Shipping, New York, USA  
 COLEMAN, RODERICK M., DTNSRDC, Bethesda, Maryland, USA  
 COLLATZ, GUENTER, The Hamburg Model Basin, Hamburg, Germany  
 COOPER, RALPH D., Office of Naval Research, Arlington, Virginia, USA  
 CORDONNIER, J.-P. V., Université de Nantes, Nantes, France  
 CUMMINS, WILLIAM E., DTNSRDC, Bethesda, Maryland, USA  
 DAOUD, NABIL, University of Michigan, Ann Arbor, Michigan, USA  
 DAWSON, CHARLES W., DTNSRDC, Bethesda, Maryland, USA  
 DEMANCHE, JEAN FRANCOIS, Bassin d'Essais des Carènes, Paris, France  
 DERN, J. C., Bassin d'Essais des Carènes, Paris, France  
 DOCTORS, LAWRENCE J., DTNSRDC, Bethesda, Maryland, USA  
 EGGERS, KLAUS, Hamburg University, Hamburg, West Germany  
 EUVRARD, DANIEL, ENSTA, Paris, France  
 FALTINSEN, ODD, Norges Tekniske Høgskole, Trondheim, Norway  
 FEIFEL, WINFRIED M., The Boeing Company, Renton, Washington, USA  
 FRITTS, MARTIN J., Naval Research Laboratory, Washington, D.C., USA  
 GADD, G. E., National Maritime Institute, Feltham, Middlesex, England  
 GARRISON, C. J., Naval Postgraduate School, Monterey, California, USA  
 GLEISSNER, GENE H., DTNSRDC, Bethesda, Maryland, USA  
 GOODMAN, THEODORE, Stevens Institute of Technology, Hoboken, New Jersey, USA  
 HAIKOV, ANRI J., BSHC, Varna, Bulgaria  
 HAUSSLING, HENRY J., DTNSRDC, Bethesda, Maryland, USA  
 HERMANS, AAD J., Delft Technical University, Delft, The Netherlands  
 HERSHEY, ALLEN V., Naval Surface Weapons Center, Dahlgren, Virginia, USA  
 HESS, JOHN L., John L. Hess Associates, Long Beach, California, USA  
 HIRT, CYRIL W., Los Alamos Scientific Laboratory, Los Alamos, New Mexico, USA  
 HOLT, MAURICE, University of California, Berkeley, California, USA  
 HONG, YOUNG S., Consulting Naval Architect, Berkeley, California, USA  
 HOSODA, RYUSUKE, University of California, Berkeley, California, USA  
 HSIUNG, CHI-CHAO, Mississippi State University, Mississippi, USA  
 HWANG, ALLEN Y.-L., University of California, Berkeley, California, USA  
 INUI, TAKAO, University of Tokyo, Tokyo, Japan  
 JACOBSEN, BENT K., Danish Ship Research Laboratory, Lyngby, Denmark  
 JIANG, CHEN-WEN, Massachusetts Institute of Technology, Cambridge, Massachusetts, USA

JIANG, CHEN-WEN, Massachusetts Institute of Technology, Cambridge, Massachusetts, USA  
 JONES, GARY, Naval Ship Engineering Center, Washington, D.C., USA  
 KAHN, LAWRENCE A., Operations Research, Inc., Silver Spring, Maryland, USA  
 KENNEL, COLEEN G., Naval Ship Engineering Center, Washington, D.C., USA  
 KINOSHITA, TAKESHI, Yokohama National University, Yokohama, Japan  
 KORVING, CORNELIS, Delft Technical University, Delft, The Netherlands  
 KUSAKA, YUZO, Mitsui Engineering & Shipbuilding Co., Ltd., Tokyo, Japan  
 KUX, JÜRGEN, Universität Hamburg, Hamburg, Germany  
 LANDWEBER, LOUIS, The University of Iowa, Iowa City, Iowa, USA  
 LAROCK, BRUCE E., University of California, Davis, California, USA  
 LARSSON, LARS A., Swedish State Shipbuilding Experimental Tank, Göteborg, Sweden  
 LAU, RICHARD, Office of Naval Research, Pasadena, California, USA  
 LEE, CHONG M., DTNSRDC, Bethesda, Maryland, USA  
 LOKEN, A. E., Det Norske Veritas, Oslo, Norway  
 LONGUET-HIGGINS, M. S., University of Cambridge, England  
 LUNDEGARD, R. J., Office of Naval Research, Washington, D.C., USA  
 MAGNUS, ALFRED, Boeing Company, Seattle, Washington, USA  
 MARIN, SAMUEL, Carnegie Mellon University, Pittsburgh, Pennsylvania, USA  
 MARUO, HAJIME, Yokohama National University, Yokohama, Japan  
 MCCARTHY, JUSTIN H., DTNSRDC, Bethesda, Maryland, USA  
 MILES, MICHAEL D., National Research Council, Ottawa, Ontario, Canada  
 MINER, E. WADE, Naval Research Laboratory, Washington, D.C., USA  
 MOLIN, BERNARD, Institut Français du Pétrole, Rueil-Malmaison, France  
 MONACELLA, VINCENT J., DTNSRDC, Bethesda, Maryland, USA  
 MORGAN, WILLIAM B., DTNSRDC, Bethesda, Maryland, USA  
 MORI, KAZUHIRO, Hiroshima University, Hiroshima, Japan  
 NAGHD, PAUL M., University of California, Berkeley, California, USA  
 NEWMAN, J. NICHOLAS, Massachusetts Institute of Technology, Cambridge, Massachusetts, USA  
 NICHOLS, B. D., Los Alamos Scientific Laboratory, Los Alamos, New Mexico, USA  
 NOWACKI, HORST, Technical University of Berlin, Berlin, West Germany  
 OGILVIE, T. FRANCIS, University of Michigan, Ann Arbor, Michigan, USA  
 OHRING, SAMUEL, DTNSRDC, Bethesda, Maryland, USA  
 PENUMALLI, B. REDDY, Austin Research Associates, Austin, Texas, USA  
 PETTERSEN, BJØRNAR, Technical University of Norway, Trondheim, Norway  
 PINKSTER, JO A., Netherlands Ship Model Basin, Wageningen, The Netherlands  
 POWELL, ALAN, DTNSRDC, Bethesda, Maryland, USA  
 PRITCHETT, JOHN W., Systems, Science & Software, La Jolla, California, USA  
 RATTAYYA, JASTI, Lockheed Missiles & Space Company, Inc., Sunnyvale, California, USA  
 REDDALL, WALTER F., The Aerospace Corporation, El Segundo, California, USA  
 ROGERS, JOEL C.W., Applied Physics Laboratory, Johns Hopkins University, Laurel, Maryland, USA  
 SALVESEN, NILS, DTNSRDC, Bethesda, Maryland, USA  
 SAYER, PHILIP, University of Manchester, Manchester, England  
 SCHMIECHEN, MICHAEL, Berlin Model Basin, Berlin, Germany  
 SCHOT, JOANNA W., DTNSRDC, Bethesda, Maryland, USA  
 SCHUBERT, CHRISTIAN, Technical University of Berlin, Berlin, West Germany  
 SCRAGG, CARL A., DTNSRDC, Bethesda, Maryland, USA  
 SEIDL, LUDWIG H., University of Hawaii, Honolulu, Hawaii, USA  
 SMITH, KEILL, Naval Coastal Systems Laboratory, Panama City, Florida, USA  
 SÖDING, HEINRICH, Technical University of Hannover, Hannover, West Germany  
 SPARENBERG, J. A., University of Groningen, Groningen, Holland  
 STREET, R. L., Stanford University, Stanford, California, USA  
 TELSTE, JOHN G., DTNSRDC, Bethesda, Maryland, USA  
 THOMPSON, JOE F., Mississippi State University, Mississippi, USA  
 THOMPSON, ALEX J., Physical Dynamics Inc., Berkeley, California, USA  
 TSUTSUMI, TAKAYUKI, Ishikawajima Harima Heavy Industries Co., Ltd., Yokohama, Japan

TUCK, E. O., University of Adelaide, Adelaide, Australia  
 TULIN, MARSHALL P., Hydronautics, Inc., Laurel, Maryland, USA  
 URSELL, F., University of Manchester, Manchester, England  
 VANDEN BROECK, J. M., University of Adelaide, Adelaide, Australia  
 VANDER VORST, MICHAEL, JAYCOR, Del Mar, California, USA  
 VAN DYKE, MILTON D., Stanford University, Stanford, California, USA  
 VAN DYKE, PETER, Hydronautics, Inc., Laurel, Maryland, USA  
 VAN OORTMERSEN, GERARD, Netherlands Ship Model Basin, Wageningen, The Netherlands  
 VINJE, TOR, Technical University of Norway, Trondheim, Norway  
 VON KERCZEK, C., DTNSRDC, Bethesda, Maryland, USA  
 WALDEN, DAVID A., U.S. Coast Guard, Washington, D.C., USA  
 WEBSTER, WILLIAM C., University of California, Berkeley, California, USA  
 WEHAUSEN, JOHN V., University of California, Berkeley, California, USA  
 WHITNEY, ARTHUR, Lockheed Missiles & Space Company, Inc., Palo Alto, California, USA  
 WINTER, DONALD F., University of Washington, Seattle, Washington, USA  
 WU, THEODORE Y., California Institute of Technology, Pasadena, California, USA  
 YEN, SHEE-MANG, University of Illinois, Urbana, Illinois, USA  
 YEUNG, RONALD W., Massachusetts Institute of Technology, Cambridge, Massachusetts, USA  
 YIM, BOHYUN, DTNSRDC, Bethesda, Maryland, USA  
 YUEN, HENRY C., TRW Defense & Space Systems, Redondo Beach, California, USA  
 ZARDA, P. RICHARD, DTNSRDC, Bethesda, Maryland, USA  
 ZIEN, T. F., Naval Surface Weapons Center, Silver Spring, Maryland, USA